UNITED NATIONS UNIVERSITY

ORKUSTOFNUN

Geothermal Training in Iceland

2015

Reports of the 6-month UNU Fellows
at the United Nations University
Geothermal Training Programme, 2015

UNITED NATIONS
UNIVERSITY

UNU-GTP
Geothermal Training Programme

Orkustofnun, Grensásvegur 9
IS-108 Reykjavík, Iceland

Geothermal Training in Iceland 2015

Reports of the 6-month UNU Fellows at the United Nations University Geothermal Training Programme in 2015

Edited by
Málfrídur Ómarsdóttir and
Lúdvík S. Georgsson

ISBN 978-9979-68-391-9
ISSN 1670-7400

The photo on the front page shows the Fellows of the 37th annual UNU Geothermal Training Programme in 2015 at the Reykjanes high-temperature field, SW-Iceland, with the Reykjanes geothermal power plant in the background.

Back row from left (standing): Aloysius Otmar (Papua New Guinea), Elizabeth Mwangi-Gachau (Kenya), Kasu Girma (Ethiopia), Kondwani Gondwe (Malawi), Anthony Ngigi (Kenya), Ali Barreh (Djibouti), Lee Monasterial (Philippines), Davar Ebrahimi (Iran), Ali Abdou (Comoros), Antonio Franco (Portugal), Zheng Tingting (China), Patrick Muanza (DR Congo), Fardaneh Ravazdezh (Iran), Jason Gotuato (Philippines), Shammah Kiptanui (Kenya), Jigo Mismanos (Philippines), Peketsa Mangi (Kenya), Fredrick Mutua (Kenya), Nuno Vieira (Portugal), Andrés Lloret (Ecuador), Pedro Ramos (Bolivia).

Front row (kneeling): Hamda Hassan (Djibouti), Nyaso Makwaya (Tanzania), Fridah Kiara (Kenya), Getenesh Hailegiorgis (Ethiopia), Amali Samaranayake (Sri Lanka), Reuben Langat (Kenya), John Mundui (Kenya), Bryan Cacho (Philippines), Ruth Wamalwa (Kenya).

INTRODUCTION

The 37th annual session of UNU-GTP was held from May through October 2015. A total of thirty UNU Fellows from 15 countries in five continents completed the traditional 6-month courses. They came from Bolivia (1), China (1), Comoros Islands (1), D.R. Congo (1), Djibouti (2), Ecuador (1), Ethiopia (2), Iran (2), Kenya (9), Malawi (1), Papua New Guinea (1), Philippines (4), Portugal (2), Sri Lanka (1) and Tanzania (1). UNU Fellows were trained in all eight lines of specialization, in: Geothermal Geology (5 Fellows), Geothermal Utilization (5), Reservoir Engineering and Borehole Geophysics (5), Chemistry of Thermal Fluids (4), Geophysical Exploration (4), Environmental Science (3), Drilling Technology (1) and the new line Project Management and Finances (3). They were all on fellowships from the Icelandic Government and UNU. Seven UNU Fellowships were co-funded by the Kenya Electricity Generating Company (KenGen) and Geothermal Development Company (GDC) in Kenya, the four UNU Fellowships for Philippines were co-founded by the Energy Development Corporation (EDC), the two Portuguese from the Azores were co-funded by the EES-Grants system, and one from Ethiopia was co-funded by ICEIDA. One new country was added in the 6-month training in 2015 with the first UNU Fellow from D.R. Congo. Thus, during 1979-2015, 613 scientists and engineers from 59 countries have completed the annual 6-month courses. Of these, 37% have come from countries in Africa, 36% from Asia, 15% from Latin America and the Caribbean, 11% from Central and Eastern Europe, and 1% from Oceania. Among them have been 127 women (21%). Over 90 professionals have received shorter training in Iceland (2 weeks to 4 months).

Sixteen former UNU Fellows (from Bolivia 1, El Salvador 1, Ethiopia 1, Kenya 7, Malawi 2, Rwanda 1, Tanzania 2 and Yemen 1) undertook MSc studies in 2015 under cooperation agreements with the University of Iceland, and Reykjavík University. The traditional 6-month courses at the UNU-GTP can constitute 25% of the MSc studies. Five (1 from El Salvador, 2 from Kenya, 1 from Rwanda and 1 from Tanzania) defended their MSc theses, while four started their MSc studies in 2015. Forty-five fellows had completed an MSc degree from the University of Iceland at the end of 2015. Two Fellows continued their PhD studies in 2014, and a third started his studies in 2015. All are from Kenya.

Our annual UNU Visiting Lecturer this year was Dr. Meseret Teklemariam from Ethiopia, a geothermal geologist and a former UNU Fellow. She gave a series of lectures on geology and geothermal development in Africa, which were very well attended and received.

The 8th event in the UN Millennium series of Short Courses / Workshops for the Americas was the "*Short Course VII on Surface Exploration for Geothermal Resources in El Salvador*" which was organized and conducted by the UNU-GTP and LaGeo S.A. in Santa Tecla, El Salvador during March 15-21, 2015. The lecturers came from El Salvador (12) and Iceland (4). The number of registered participants was 42 in all, from 13 countries of Latin America and the Caribbean. The 11th annual Millennium event in Africa, *"Short Course X on Exploration for Geothermal Resources",* was held in Kenya, November 9-30, 2015. This was a very well-attended event with 62 participants from 18 African countries (including Yemen) plus 64 lecturers and field instructors (mostly from Kenya, but four from Iceland (ISOR and UNU-GTP), and six from the neighbouring countries (Ethiopia 2, Eritrea, Tanzania, Rwanda and Uganda)). The Short Course was co-hosted by the UNU-GTP, KenGen and GDC. The Millennium short courses were very well received by the participants.

UNU-GTP's intense activities in customer-designed courses continued in 2015. Several short courses were held in Africa financed through the "*Geothermal Exploration Project in E-Africa"*, in cooperation with the Icelandic International Development Agency (ICEIDA), the Icelandic Ministry for Foreign Affairs (IMfFA) and/or the Nordic Development Fund (NDF). Within the project, UNU-GTP has been given the task of geothermal capacity building and assisting in strengthening institutional build-up with regards to geothermal expertise. The first three events of the year were held in Addis Ababa, Ethiopia. First was the *Short Course on Well Design and Geothermal Drilling Technology* held for GSE and EEP in January 12-24. The second was the *Short Course on Preparations of Bankable Geothermal Documents* held during January 26 – February 3, with additional participants from MoWIE, and the final one *Short Course on Geothermal Project Management,* held during February 9-20. The next event

was the *Short Course on Geothermal Project Management* held in Nakuru, Kenya for GDC and KenGen during May 18-28. In the autumn two events were given in Djibouti, *Short Course on Preparation of Bankable Documents for Geothermal Projects* during September 5-10, and the final event of the year in these series, *Short Course on Geothermal Project Management,* held in September 12-21. Both were held for ODDEG, but participants also came from CERD and MoEWNR. Participation was good in all events. Two short courses in the Azores series, funded by the EEA-Grants system, were held in the Azores, *Short course III on Borehole Geophysics in Geothermal Development* during June 15-27 and *Short Course IV on Chemistry of Thermal Fluids* during September 7-19. Both were well received.

The teaching and research supervision of the UNU-GTP in 2015 was carried out as follows: by geothermal specialists from ISOR (Iceland GeoSurvey) 55%, the University of Iceland and Reykjavik University, 15%, and specialists at other institutions, energy utilities and consulting engineering offices, about 30%. In all, more than 100 teachers contributed to the training. Many thanks are due to the teachers and supervisors, and their institutions. The availability of top quality supervisors for the various lines of studies offered is of vital importance to the UNU-GTP operations. Warm thanks are also due to the permanent staff, Thórhildur Ísberg, Ingimar G. Haraldsson, Málfrídur Ómarsdóttir, María S. Gudjónsdóttir (who resigned in the summer) and Markús A.G. Wilde.

The UNU programmes had the honour of hosting Rector David Malone for the first time. The purpose of his visit was to get a direct impression on the activities of the Icelandic programmes and to discuss ideas of a new UNU institute with the Ministry for Foreign Affairs. His impression of our activities was positive.

Finally, we want to remind the readers that the reports presented here are written as a part of an academic exercise, and in most cases under a considerable time pressure. The reports have been written under close guidance of the supervisors. We are grateful for the dedication of the UNU Fellows and the teachers in their work at the UNU Geothermal Training Programme. Furthermore, we would like to point out that all the reports of the UNU-GTP from the start in 1979 are available through our website: *www.unugtp.is,* where they are published in colour.

With warmest regards from Iceland,
Lúdvík S. Georgsson, director

Information about the UNU Geothermal Training Programme

The Geothermal Training Programme of the United Nations University has operated at Orkustofnun (the National Energy Authority) in Iceland since 1979 with 6-month annual courses for professionals who mostly come from the developing countries. Candidates must have a minimum of one-year practical experience in geothermal work in their home countries prior to the training, and, preferably, they should be within 40 years of age. Specialized training is given in geothermal geology, geophysical exploration, reservoir engineering and borehole geophysics, environmental studies, chemistry of thermal fluids, geothermal utilization, drilling technology and project management and finances. Each trainee attends only one specialized course. The training is conducted in English.

The hallmark of the training is to give university graduates engaged in geothermal work very intensive on-the-job training in their chosen fields of specialization. The trainees work side by side with geothermal professionals in Iceland. The training is tailor-made for the individual and the needs of his/her institution/country. The aim is to assist developing countries with significant geothermal potential to build up groups of specialists that cover most aspects of geothermal exploration and development. Priority is given to candidates from institutions where geothermal work is already under way. All candidates are selected by private interviews and receive scholarships (covering tuition, per diem and international travel) financed by the Government of Iceland and the UNU, or others. Upon completion of their training the participants receive a UNU Certificate. Further description can be found at our internet home page: *www.unugtp.is.*

TABLE OF CONTENTS

Page

6. **Abdou, A.S.:** TEM and MT resistivity surveying: data acquisition, processing and 1D inversion with an example from Hágöngur geothermal field, Mid-Iceland.....1

7. **Barreh Adaweh, A.:** Environmental management of Assal-Fiale geothermal project in Djibouti: A comparison with geothermal fields in Iceland.....29

8. **Cacho, B.T.:** A study on different two-phase flow correlations used in geothermal wellbore modelling 69

9. **Ebrahimi, D.:** Structural mapping and subsurface geology compared to thermal gradient and the geothermal system in Mödruvellir, SW-Iceland 89

10. **Franco, A.:** Subsurface geology and hydrothermal alteration of Cachaços-Lombadas sector, Ribeira Grande geothermal field, São Miguel island, Azores 113

11. **Girma, K.:** Assessment of project management maturity at Landsvirkjun – Power Projects department division 161

12. **Gondwe, K.T.:** Geothermal energy utilization model for Nkhotakota geothermal springs in Malawi.....181

13. **Gotuato, J.G.:** The thermodynamics behind initiation flow from geothermal wells.....221

14. **Hailegiorgis, G.:** Processing and joint 1D inversion of MT and TEM data from Alallobeda geothermal field in Tendaho, NE-Ethiopia 241

15. **Hassan Weis, H.:** Borehole geology and hydrothermal alteration of well HE-58, Hellisheidi geothermal field, SW-Iceland.....277

16. **Kiara, F.M.:** Concentrations of selected trace elements and ions in spent geothermal liquid and associated impacts on groundwater, soil and vegetation in the Menengai geothermal field.....303

17. **Kiptanui, S.K.:** Financial assessment of commercial extraction of sulphur and carbon dioxide from geothermal gases in Menengai, Kenya.....329

18. **Langat, R.N.:** Topping unit at Olkaria IV geothermal power plant, Naivasha, Kenya.....357

19. **Lloret C., A.:** Use of geothermal energy for seawater desalination in the Galápagos Islands, Ecuador.....393

20. **Makwaya, N.:** Interpretation of geochemical data from low-temperature geothermal area Fljótin, N-Iceland, compared to selected geothermal samples from Rungwe Tanzania..419

21. **Mangi, P.M.:** Project review of geothermal spas´ construction in Kenya and Iceland.....443

22. **Mismanos, J.W.:** Evaluation of structural permeability in Mahanagdong geothermal field, Philippines using soil gases (220Rn, 222Rn, CO_2 flux) 475

23. **Monasterial, J.L.C.:** Microgravity survey in 2009-2010 around Bacman geothermal field, Philippines - gravity corrections and interpretations 495

Page

24. Muanza, P.K.: Geothermal mapping in Middalur field, Hengill area, SW-Iceland 517

25. Mundui, J.K.K.: Mineral scaling potential of geothermal fluids in well MW01A in Menengai, Kenya.....533

26. Mutua, F.M.: Borehole geology and hydrothermal alteration mineralogy of well MW-19A, Menengai geothermal field, Kenya 549

27. Mwangi-Gachau, E.: Preliminary environmental cost accounting for Olkaria IV geothermal project 585

28. Ngigi, A.M.: Geothermal well design using the new 2015 New Zealand standard and 1991 standard: A case of MW-20a in Menengai, Nakuru county, Kenya 607

29. Otmar, A.T.: Temperature and pressure analysis of wells NJ-13 and NJ-28 in the Nesjavellir geothermal system, SW-Iceland.....641

30. Ramos Sullcani, P.R.: Well data analysis and volumetric assessment of The Sol de Mañana geothermal field, Bolivia 665

31. Ravazdezh, F.: A study on operation and maintenance of flash steam geothermal power plants: Reykjanes power plant 689

32. Samaranayake, S.A.: Seismic monitoring of geothermal fields: A case study of Hellisheidi geothermal field.....727

33. Vieira, N.: Steam and brine gathering system design for Cachaços-Lombadas new production wells in Ribeira Grande geothermal field 755

34. Wamalwa, R.N.: Evaluation of factors controlling the concentration of non-condensible gases and their possible impact on the performance of wells in Olkaria, Kenya.....787

35. Zheng Tingting: Assessment of the Urban Dezhou sandstone geothermal reservoir in North China 809

UNITED NATIONS UNIVERSITY
UNU-GTP
Geothermal Training Programme

Orkustofnun, Grensasvegur 9,
IS-108 Reykjavik, Iceland

Reports 2015
Number 6

TEM AND MT RESISTIVITY SURVEYING: DATA ACQUISITION, PROCESSING AND 1D INVERSION WITH AN EXAMPLE FROM HÁGÖNGUR GEOTHERMAL FIELD, MID-ICELAND

Ali Soumail Abdou
Geological Bureau of Comoros
CEFADER-Mde
COMOROS
abdousoumail@gmail.com

ABSTRACT

Geophysical methods are some of the most effective geothermal exploration methods. Some of them are aimed at parameters that are directly influenced by the geothermal activity, such as resistivity and thermal methods, while others are aimed at geological parameters, and thus referred to as indirect methods. Electrical resistivity methods like magnetotellurics (MT) and transient electromagnetics (TEM) are most successful in identifying geothermal resources. This report discusses these two methods and describes the data acquisition, processing and 1D inversion using a practical example from MT and TEM surveys that were carried out in the Hágöngur area, Mid-Iceland by Iceland GeoSurvey (ÍSOR), in 2011 and 2013. The data were processed and inverted one-dimensionally (1D) using different software like: SSMT2000, MTEditor, TEMX and TEMTD. The results of the 1D joint inversion are presented as resistivity cross-sections and iso-resistivity maps down to different depths. Finally, the geothermal significance of the resistivity model is discussed.

1. INTRODUCTION

Resistivity methods show the variations of resistivity in the subsurface. The use of these methods has accompanied the exploration of geothermal energy, because low-resistivity rocks have always been regarded as a good indicator of the presence of a geothermal reservoir. The experience gained in recent years has shown that the objective is not only to look for conductive bodies corresponding to the clay cap of the reservoir, but also the underlying resistive bodies in basaltic areas that can be associated more directly with the reservoir. Electrical resistivity depends on porosity and the pore structure of the rock, the salinity of the water, temperature, water-rock interaction and alteration, amount of water (saturation), pressure, and steam content in the water.

The most important resistivity methods are magnetotellurics (MT) and transient electromagnetics (TEM). These two methods, MT and TEM, are often used in conjunction since they complement each other. The first one is a passive electromagnetic (EM) exploration method that measures the orthogonal components of the electric and magnetic field at the surface of the Earth. The naturally generated variations in Earth's magnetic field are the source field, providing a wide and continuous spectrum of

EM field waves that induce currents within the earth. The second one is an active EM method that measures the EM response from eddy currents within the earth induced by a current in a loop or grounded wires on the surface.

The Hágöngur high-temperature geothermal area in Mid-Iceland is one of the 25-30 hign-temperature geothermal areas in Iceland. The area is within the central volcanic zone in Iceland, a few kilometres from the western edge of Vatnajökull glacier. Belonging to the central highlands, at an elevation of about 800 m a.s.l., the area is far from habitation and very remote.

In order to establish a fuller knowledge and understanding of the internal geothermal structure of the area, several exploration surveys have been done using different methods such as the resistivity method which is discussed in this report.

An overview of the resistivity of rocks and the theoretical basis of resistivity methods, the magnetotelluric and the transient electromagnetic method is given. This is followed by a description of data acquisition, processing and interpretation of TEM and MT data from Hágöngur area. The static shift problem, skin depth of MT, and the 1D joint inversion of TEM and MT data are also discussed in some details.

2. RESISTIVITY METHODS IN GEOTHERMAL EXPLORATION

It has been proven that resistivity is one of the most useful geophysical parameter in geothermal exploration. Some of the most important factors affecting resistivity in geothermal systems are salinity, temperature, permeability and alteration. A correlation exists between these parameters and the reservoir (Hersir and Árnason, 2009; Flóvenz et al., 2012). The resistivity structure of geothermal systems is imaged better by inverting jointly MT and TEM data.

2.1 Resistivity of rocks

2.1.1 Specific resistivity

Electrical resistivity of a material is usually symbolized by the Greek letter ρ (Ωm). It is an intrinsic property of a given material which shows how strongly the material can oppose the flow of an electric current. By transmitting a current I (A) through a material of length l (m) and measure the potential difference ΔV (V) between the two sides (Figure 1), one can define the resistivity as:

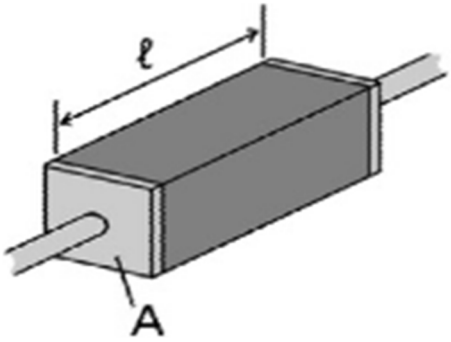

FIGURE 1: A conductive medium of cross-sectional area A and length l.

$$\rho = \frac{\Delta V}{I}\frac{A}{l} \tag{1}$$

where A is the cross-sectional area of the conducting medium (m^2).

For a material which has a cross-sectional area 1 m^2 and is 1 m long, the resistivity is defined as:

$$\rho = \frac{\Delta V}{I} \tag{2}$$

The resistivity ρ can also be defined in terms of the resistance R (Ω) as shown in the following equation:

$$\rho = R\frac{A}{l} \tag{3}$$

The reciprocal of resistivity is conductivity ($1/\rho=\sigma$) measured in Siemens/m.

2.1.2 Temperature

Resistivity of an aqueous solution decreases with increasing temperature, due to the increasing mobility of the ions caused by a decrease in the viscosity of the water (Figure 2). At higher temperatures, above 250°C, a change in density, viscosity and dielectric permittivity of water affects the conductivity of the ions in the solution, hence, an increase in fluid resistivity (Dakhnov, 1962). This is described by the following relationship:

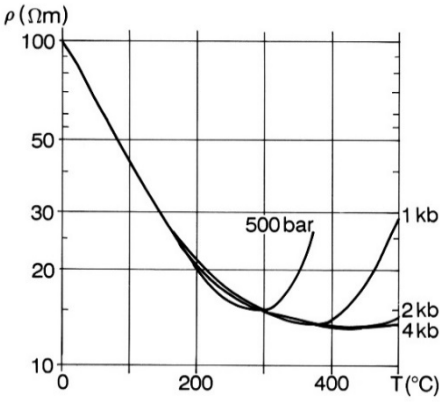

FIGURE 2: Resistivity of a NaCl solution as a function of temperature and pressure (Hersir and Björnsson, 1991; based on Quist and Marshall, 1968)

$$\rho_w = \frac{\rho_{w0}}{1 + \alpha(T - T_0)} \qquad (4)$$

where ρ_w = The resistivity (Ωm) of the fluid at temperature T;
ρ_{w0} = The resistivity (Ωm) of the fluid at temperature T_0;
T_0 = The reference temperature (°C);
α = The temperature coefficient of the resistivity, $\alpha \approx 0.023°C^{-1}$ for $T_0 = 25°C$.

Three main conduction mechanisms are observed (Figure 3): mineral conduction which in most cases is negligible, conduction by dissolved ions in the pore fluid in geothermal which is called pore fluid conduction, and surface conduction which is the conduction caused by the (highly) mobile absorbed ions that form a conductive layer on the surface of the pore walls.

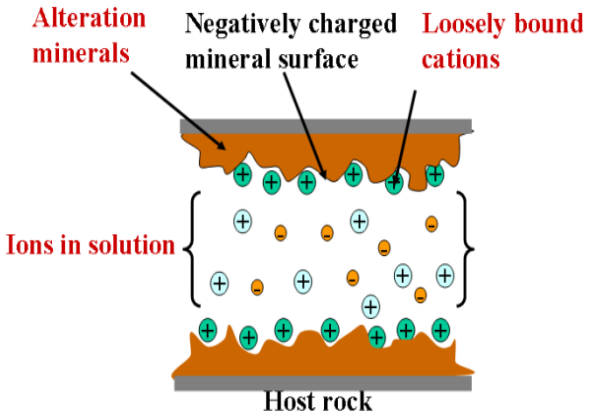

FIGURE 3: Conduction mechanisms (Hersir and Árnason, 2009)

In high-temperature geothermal systems and close to the solidus of the rock, the conductivity of the rock matrix becomes significant. The matrix conductivity follows the Arrhenius formula (see e.g. Flóvenz et al., 2012):

$$\sigma_m(T) = \sigma_0\, e^{-E/kT} \qquad (7)$$

where σ_m = The matrix conductivity (S/m);
σ_0 = The conductivity at infinite temperature (S/m);
E = The activation energy (eV);
k = The Boltzmann constant (eV/°K); and
T = The temperature (°K).

Laboratory measurements of basalts and related material over the temperature range 400-900°C give typical value of 0.80 for E and 300 for σ_m. This shows that the matrix resistivity of basaltic rock is on the order of 1000 Ωm at 400°C and decreases to 10 Ωm at 800°C. At higher temperature, partial melt will still increase the conductivity. Since temperature exceeding 400°C can be expected in the root of the geothermal systems, the matrix conductivity will have an increasing impact on the overall conductivity.

2.1.3 Porosity

Porosity is defined as the ratio of pores to the total volume of the rock. Archie's law (Archie, 1942) has been used for relating the conductivity of a reservoir rock and the conductivity of the fluid contained in the pores. It describes the resistivity dependence on porosity if ionic conduction in the pore fluid dominates other conduction mechanisms in the rocks. For normal rocks, the law is valid only if the resistivity of the pore fluid is 2 Ωm or less and it is a very good approximation if the resistivity is dominated by that of the saturating fluid (Árnason et al., 2000). Archie's law is given by the equation:

$$\rho = \rho_w a \Phi_t^{-n} \tag{5}$$

where ρ = The bulk (measured) resistivity;
ρ_w = The resistivity of the pore fluid (Ωm);
a = An empirical parameter;
Φ_t = The fractional porosity;
n = The cementing factor.

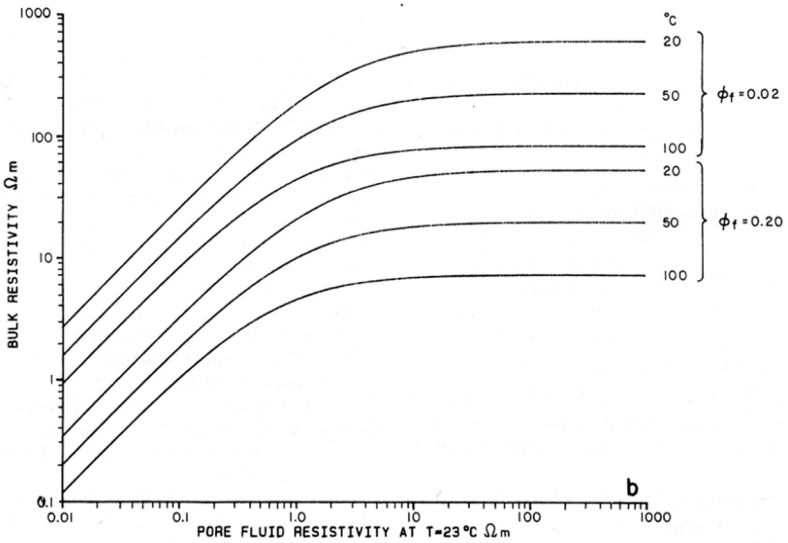

FIGURE 4: Bulk resistivity as a function of pore fluid resistivity for different pressures and porosities (Flóvenz et al., 1985)

The relationship between the bulk resistivity and the pore fluid resistivity for different porosities and temperatures for rocks in the uppermost kilometer of the Icelandic crust outside the volcanic zone is shown in Figure 4. It is based on a model put forward by Flóvenz et al. (1985). The model includes both electrolytic and surface/mineral conduction.

2.1.4 Salinity

The conductivity of the pore fluid depends on the salinity and mobility of ions present in the solution. The conductivity σ of a solution, can be determined by considering the current flow through a cross-sectional area of 1 m^2 at a voltage of 1 V/m. It is described by the equation (Hersir and Björnsson, 1991):

$$\sigma = \mathrm{F} \cdot (c_1 q_1 m_1 + c_2 q_2 m_2 + \cdots), \tag{6}$$

where F = Faraday's number (9.649×10^4 C/mole);
c_i = Concentration of ions;
q_i = Valence of ions;
m_i = Mobility of different ions.

When the amount of dissolved ions in the pore fluid increases, the conductivity also increases. Conduction in a solution is greatly affected by salinity and the mobility of ions present in the solution as shown in Figure 5.

2.1.5 Water rock interaction

Hydrothermal alteration is the interacting of hydrous (liquids), called hydrothermal fluids, reacting with surrounding rock. During the reaction, the composition of the rock is changed, through the replacing of

minerals. The interaction between hot fluids and rocks results in the formation of secondary minerals which is called geothermal alteration (Figure 6). The main factors determining which type of alteration is formed are fluid composition, permeability and temperature (Henley and Ellis, 1983). In high-temperature geothermal systems, there are relationships between alteration, subsurface resistivity, temperature and the conduction mechanism. These relationships for high-temperature geothermal systems in Iceland are shown in Figure 7 and they apply elsewhere where the host rocks are volcanic.

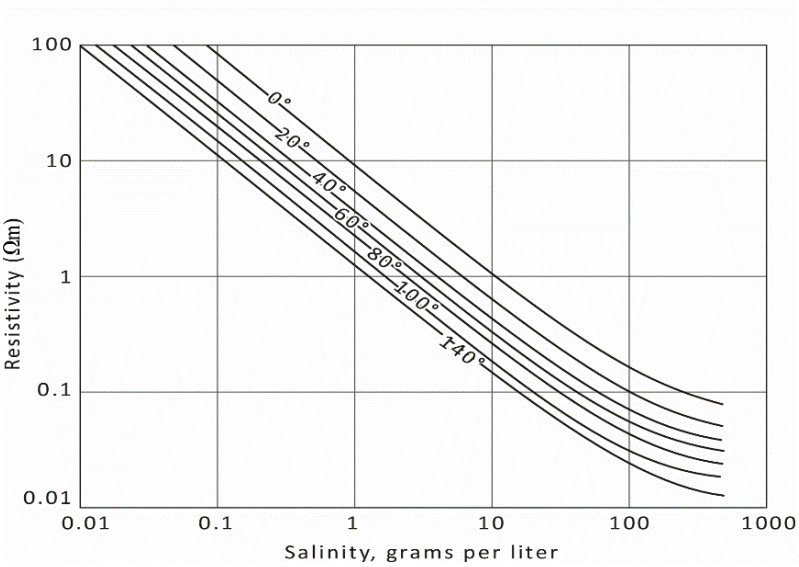

FIGURE 5: The resistivity of solutions of NaCl as a function of concentration and temperature in °C (Flóvenz et al., 2012; based on Keller and Frischknecht, 1966)

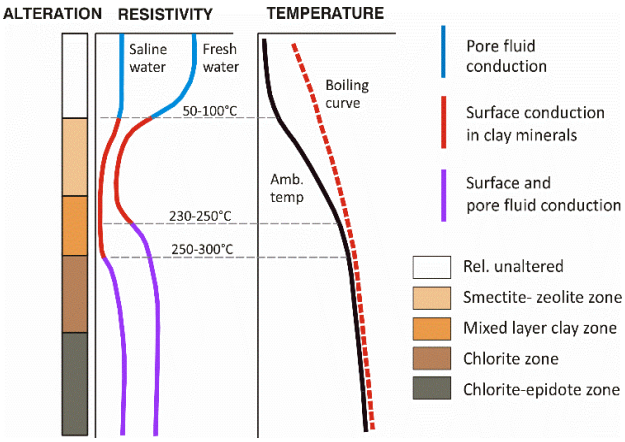

FIGURE 6: The general resistivity structure of the basaltic crust in Iceland summarized, the depth scale is arbitrary (Flóvenz et al., 2012; based on Flóvenz et al., 2005)

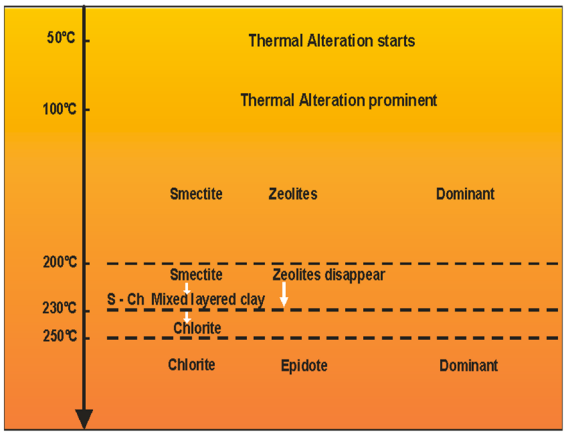

FIGURE 7: Alteration mineralogy and temperature (Hersir and Árnason, 2009)

Resistivity is high in unaltered cold formations near the surface in a typical high-temperature geothermal system. As temperature progressively increases from 50 to 100°C with depth, low-temperature mineral alterations such as smectite and zeolites are formed making the rocks conductive due to their loosely bound cations. Resistivity increases again at moderately high temperatures of about 230-240°C, where the clay minerals are gradually replaced by chlorite as the dominant alteration minerals in the transition zone of mixed-layer clays. At higher temperatures exceeding 250°C, epidote and chlorite dominate, and the system is more resistive due to the bounded ions in the crystal lattice (Árnason et al., 2010).

The subsurface resistivity structure in high-temperature geothermal fields reflects the hydrothermal alteration. The primary minerals in the host rock matrix are transformed into different minerals because of water-rock interaction and chemical transport by the geothermal fluids. Formation of alteration minerals depends on temperature and the type of primary minerals and the chemical composition of the geothermal fluid. If the alteration and temperature are in equilibrium, the subsurface resistivity structure

reflects not only the alteration but can also predict which temperature to expect. This was an important result because if the temperature that produced the alteration mineralogy still prevails, the resistivity structure can be used to predict temperature. But if cooling occurs, the alteration remains and so does the resistivity structure.

2.2 Magnetotelluric method (MT)

The magnetotelluric (MT) method is a passive geophysical prospecting method. Its principle is based on the induction of electromagnetic waves in the subsurface. The MT data acquisition requires the recording of two fields; the electric field and the magnetic field. The recording is done continuously in the time domain. The electric field data are recorded using four non-polarizable electrodes, two perpendicular dipoles. The recording of the magnetic field is done using magnetometers/coils recording two or even three orthogonal components of the magnetic field (Figure 8). The method provides information on the distribution of electrical conductivities in the underground rocks.

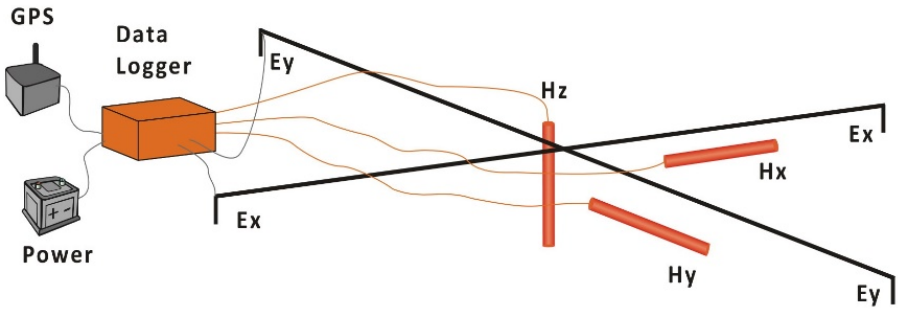

FIGURE 8: Magnetotelluric set up for data acquisition
(Flóvenz et al., 2012)

There are two sources which give rise to the MT signal:

1. At low frequencies, less than one cycle per second, the source of the signal originates from the interaction between the charged particles in the solar wind and the earth´s magnetosphere and particles in the ionosphere.
2. Electromagnetic fields which have frequencies higher than 1 Hz originate from meteorological activities such as lightning discharges.

The magnetotelluric method was developed by Tikhonov (1950) and Cagniard (1953).

2.2.1 Principles

The phenomenon of electromagnetic induction is explained through Maxwell's equations. These equations describe the electric and the magnetic fields as a function of space and time and are given as (Kaufman and Keller, 1983):

Faraday's law:

$$\nabla \times \boldsymbol{E} = -\mu \frac{\partial \boldsymbol{H}}{\partial t} \tag{8}$$

Ampère´s law:

$$\nabla \times \boldsymbol{H} = \boldsymbol{j} + \varepsilon \frac{\partial \boldsymbol{E}}{\partial t} \tag{9}$$

Gauss´s law (magnetic field):

$$\boldsymbol{\nabla} \cdot \boldsymbol{B} = 0 \tag{10}$$

Gauss´s law (electric field):

$$\boldsymbol{\nabla} \cdot \boldsymbol{D} = \eta \tag{11}$$

where $\boldsymbol{E}$ = Electric field (V/m);
$\boldsymbol{B}$ = Magnetic induction (T);
$\boldsymbol{j}$ = Electrical current intensity (A/m^2);
μ = Magnetic permeability (H/m);
ε = Electric permittivity (F/m);
η = Electric charge density of free charges (C/m^3);
$\boldsymbol{D}$ = Electric displacement (C/m^2);
$\boldsymbol{H}$ = Magnetic intensity (A/m).

The fields and fluxes described in Maxwell´s equations above are linked through the constitutive relationships, which for an isotropic medium are:

$$\boldsymbol{B} = \mu\boldsymbol{H};\ \boldsymbol{D} = \varepsilon\boldsymbol{E};\ \ \boldsymbol{j} = \sigma\boldsymbol{E}.$$

A naturally occurring time varying magnetic field induces an electrical field which further induces eddy currents in the ground, measured on the surface in horizontal and orthogonal (E_x, E_y) directions. The electric fields are induced by the corresponding source magnetic fields (H_y and H_x) (Flóvenz et al., 2012); thus, by measuring variations in the magnetic and electrical field on the surface, subsurface resistivity and phase as a function of the frequency of the electromagnetic field are determined using the basic Maxwell's equations given above.

In a homogeneous and isotropic halfspace, using the constitutive relationships above and assuming harmonic time dependence of **E** and **H** $\sim e^{i\omega t}$, Faraday´s and Ampère´s laws may be rewritten as:

$$\boldsymbol{\nabla} \times \boldsymbol{E} = -i\omega\mu\boldsymbol{H} \tag{12}$$

$$\boldsymbol{\nabla} \times \boldsymbol{H} = \sigma\boldsymbol{E} + i\omega\varepsilon\boldsymbol{E} \tag{13}$$

For an incident plane wave in a conductive halfspace, Snell´s law gives:

$$\frac{1}{vo}\sin\theta_i = \frac{1}{v}\sin\theta_t \tag{14}$$

where $v_0 = \frac{1}{\sqrt{\epsilon_0\mu_0}}$ and $v = \sqrt{\frac{2\omega}{\mu_0\sigma}}$ are the velocities of the incident EM wave in the air and in the halfspace, respectively; θ_i is the incidence angle to the surface; θ_t is the refraction angle into the halfspace; and σ the conductivity of the homogeneous earth.

Equation 14 can be rewritten as:

$$\sin\theta_t = \sqrt{\frac{2\omega\epsilon_0}{\sigma}}\sin\theta_i \tag{15}$$

For typical values of the relevant parameters, $\frac{2\omega\epsilon_0}{\sigma} < 10^{-3}$, therefore θ_t is close to zero and the incident waves travel vertically downwards for all angles of incidence θ_i and below the surface, $\frac{\partial}{\partial x} = \frac{\partial}{\partial y} = 0$. By using the above assumptions and applying Maxwell´s equations, this gives:

$$\begin{aligned} \frac{\partial^2 E_x}{\partial z^2} &= k^2 E_x\,,\ \frac{\partial^2 E_y}{\partial z^2} = k^2 E_y \\ \frac{\partial^2 H_x}{\partial z^2} &= k^2 H_x\,,\ \frac{\partial^2 H_y}{\partial z^2} = k^2 H_y \end{aligned} \tag{16}$$

where k is the wave propagation parameter, $k^2 = i\omega\mu(\sigma + i\omega\epsilon)$. Using the extreme values for the conductivity σ and the angular frequency ω: $\sigma \approx 1 - 10^{-4}$ S/m; and $\omega = \frac{2\pi}{T}, T = 10^{-4} - 10^{4}\ s$, this gives $(\omega\epsilon)_{max} \approx 5 \cdot 10^{-5}$ or $\sigma \gg \omega\epsilon$. Then $k^2 \approx i\omega\mu\sigma$.

The general solutions to Equation 16 can be given as :

$$E_{x,y} = \left(A_{xy}e^{kz} + B_{xy}e^{-kz}\right)e^{i\omega t} \tag{17}$$

$$\begin{aligned} H_x &= \frac{1}{i\omega\mu}\frac{\partial E_y}{\partial z} = \frac{k}{i\omega\mu}\left(A_y e^{kz} - B_y e^{-kz}\right)e^{i\omega t} \\ H_y &= -\frac{1}{i\omega\mu}\frac{\partial E_x}{\partial z} = -\frac{k}{i\omega\mu}\left(A_x e^{kz} - B_x e^{-kz}\right)e^{i\omega t} \end{aligned} \tag{18}$$

where $A_{x,y}$ and $B_{x,y}$ are constant to be determined.

By assuming that as z goes to infinity, **H** and **E** go to zero, this gives $A_{x,y} = 0$, and Equations 17 and 18 become:

$$E_x = B_x e^{-kz}e^{i\omega t}\ and\ E_y = B_y e^{-kz}e^{i\omega t} \tag{19}$$

$$\begin{aligned} H_x &= -\frac{k}{i\omega\mu}B_y e^{-kz}e^{i\omega t} = -\frac{k}{i\omega\mu}E_y \\ H_y &= \frac{k}{i\omega\mu}B_x e^{-kz}e^{i\omega t} = \frac{k}{i\omega\mu}E_x \end{aligned} \tag{20}$$

The ratio of the electric and magnetic field, yields the Tikhonov-Cagniard wave impedance as:

$$Z_{xy} = \frac{E_x}{H_y}\ and\ Z_{yx} = \frac{E_y}{H_x} \tag{21}$$

2.2.2 Impedance tensor

The impedance tensor (**Z**) relates the orthogonal components of the horizontal electric and magnetic fields. In matrix notation this is given by:

$$\begin{bmatrix} E_x \\ E_y \end{bmatrix} = \begin{bmatrix} Z_{xx} & Z_{xy} \\ Z_{yx} & Z_{yy} \end{bmatrix}\begin{bmatrix} H_x \\ H_y \end{bmatrix} \tag{22}$$

The linear relationship of the fields can be written as:

$$\begin{aligned} E_x &= Z_{xx}H_x + Z_{xy}H_y \\ E_y &= Z_{yx}H_x + Z_{yy}H_y \end{aligned} \tag{23}$$

where the on-diagonal elements relate fields measured in the same direction whereas the off-diagonal elements relate the orthogonally measured fields.

For a homogeneous half space the diagonal elements Z_{xx} and Z_{yy} are zero and:

$$Z_{xy} = \frac{E_x}{H_y} = \sqrt{\omega\mu\rho}\ e^{i\pi/4}\ and\ Z_{yx} = \frac{E_y}{H_x} = -Z_{xy} \tag{24}$$

The resistivity of a homogeneous half space is given by:

$$\rho_{xy} = \frac{1}{\omega\mu}\left|Z_{xy}\right|^2 = \rho_{xy} = \frac{1}{\omega\mu}\left|Z_{yx}\right|^2 \tag{25}$$

and $$\theta = \frac{\pi}{4} = 45°$$

1D impedance tensor
For layered (1D) earth, the conductivity σ changes only with the depth and the impedance tensor can be written as:

$$\begin{bmatrix} E_x \\ E_y \end{bmatrix} = \begin{bmatrix} 0 & Z_{xy} \\ Z_{yx} & 0 \end{bmatrix} \begin{bmatrix} H_x \\ H_y \end{bmatrix} \tag{26}$$

with $Z_{xx} = Z_{yy} = 0$ and $Z_{xy} = -Z_{yx}$

For an inhomogenous earth, the apparent resistivity and phase are defined as:

$$\rho_{\mathrm{a}} = 0.2\mathrm{T}|z|^2, \theta_a = \arg(z) \neq 45° \tag{27}$$

where z is a linear function of the impedance tensor elements.

The apparent resistivity calculated from the off-diagonal elements of the impedance tensor in the two equations above are the same for a homogeneous and 1D earth. Rotating the impedance tensor for a non-1D earth will change the resistivity values of ρ_{xy} and ρ_{xy}. The rotationally invariant determinant of the impedance tensor, which is a kind of an average value of the apparent resistivity and phase, is commonly used for inversion (Badilla, 2011). The apparent resistivity and phase calculated from the determinant value of the impedence tensor is given by:

$$\rho_{det} = \frac{1}{\omega\mu}|Z_{det}|^2 = \frac{1}{\omega\mu}\left|\sqrt{Z_{xx}Z_{yy} - Z_{xy}Z_{yx}}\right|^2 \; ; \; \theta_{det} = arg(Z_{det}) \tag{28}$$

2D impedance tensor
In a 2D earth environment, resistivity varies with depth and in one horizontal direction. The other horizontal direction has no variations in resistivity and is commonly known as the geoelectrical strike direction. MT impedance tensor data can be mathematically rotated with one axis perpendicular to the geoelectrical strike and the other axis parallel to it, by minimizing the off diagonal elements of the impedance tensor. The same case as in 1D, if $Z_{xx} = Z_{yy} = 0$, but here $Z_{xy} \neq -Z_{yx}$:

$$Z_{2D} = \begin{bmatrix} 0 & Z_{xy} \\ Z_{yx} & 0 \end{bmatrix} \tag{29}$$

Then the field can be split into two independent impedance tensor modes: **E**- and **B**-polarization. Both can be analyzed independently. Transverse Electric (TE) mode or **E**-polarization is when the electric field is parallel to the electromagnetic strike and Transverse Magnetic (TM) mode or **B**-polarization is when the magnetic field is parallel to the electromagnetic strike. The apparent resistivity can be calculated for each of the modes as:

$$\rho_{TE} = \frac{1}{\omega\mu}|Z_{TE}|^2; \; \rho_{TM} = \frac{1}{\omega\mu}|Z_{TM}|^2 \tag{30}$$

If neither of the horizontal axes are aligned along the geoelectrical strike, the diagonal elements of the impedance tensor remain $Z_{xx} = -Z_{yy} = Z$, and the off-diagonal elements Z_{xy} *and* Z_{yx} are independent values:

$$Z_{2D} = \begin{bmatrix} Z & Z_{xy} \\ Z_{yx} & -Z \end{bmatrix} \tag{31}$$

3D impedance tensor
The conductivity σ in a 3D earth case varies in all directions *x, y* and *z*. The general form of the impedence tensor is then:

$$Z_{3D} = \begin{bmatrix} Z_{xx} & Z_{xy} \\ Z_{yx} & Z_{yy} \end{bmatrix} \tag{32}$$

where $Z_{xx} \neq Z_{yy} \neq 0$ and $Z_{yx} \neq Z_{xy}$.

All the elements of the impedence tensor are non-zero for all rotations. A rotational invariant parameter called skew, *S*, is defined as:

$$S = \frac{|Z_{xx} + Z_{yy}|}{|Z_{xy} - Z_{yx}|} \tag{33}$$

This parameter indicates the dimentionality of the impedence tensor. It is close to zero for 1D and 2D earth, but large value of S indicates 3D earth.

Electrical strike shows the direction of the main horizontal geoelectrical/resistivity variation. It is calculated by minimizing the diagonal elements of impedance tensor. Often, the geoelectrical strike direction is the same direction as the geological fractures. To perform two-dimensional analysis of MT data, the impedance tensor should be rotated by an angle α. However, this approach implies a 90° ambiguity in the strike angle, so there is no way to distinguish between α and (α + 90°) using only H_x and H_y. This ambiguity can be solved by using the Tipper based on measuring the vertical component of the magnetic field, H_z.

The vertical component of magnetic field H_z may be expressed as a linear combination of horizontal magnetic field components, H_x and H_y. It is given by:

$$H_z = W_{zx}H_x + W_{zy}H_y \tag{34}$$

where $[W_{zx}\ W_{zy}] = \mathbf{W}$ is the Wiese-Parkinson matrix, also known as the Tipper.

The matrix **W** reflects the symmetry of the excess currents caused by horizontal variation of resistivity. For the 1D model, there are no induced currents in the vertical direction (**W**=0). For the 2D model, the rotation of the coordinate system places x-axis in the strike direction (also known as a T-strike), by minimizing $|W_{zx}|$.

Skin depth

As can be seen from Equations 19 and 20, the electromagnetic fields decay exponentially with depth. The depth at which the electromagnetic field becomes e^{-1} of its surface value is called the skin depth. It is also called the penetration depth. In the case of homogeneous earth, the skin depth is defined by:

$$\delta = \frac{1}{2\pi}\sqrt{10\rho T} \approx 0.5\sqrt{\rho T}\ (km) \tag{35}$$

where δ is the skin depth (km), ρ is the resistivity (**Ω**m) and T is the period (s).

As shown in the Equation 35, this depth is an increasing function of the period; by performing measurements for increasing periods, one thus obtains information on increasing depths of the subsurface.

2.2.3 Static shift problem

The MT method suffers the so called “static shift” problem which manifests itself in a frequency independent unknown multiplicative factor of the apparent resistivity or shift on log-scale. The static shift is a distortion of EM fields due to variations in near surface conductivity resulting in electrical field distortion, current distortion or topographic effects. The main cause is the accumulation of charges at resistivity boundaries causing the electrical field not to be continuous close to this boundary as shown in Figure 9. Consequently, the measured electric fields for the whole frequency range are affected by a

constant shift on a log scale. Thus this effect produces apparent resistivity curves with the correct shape but they are incorrectly located on the vertical logarithmic apparent resistivity axes. The flowing of the current in the ground with a localised resistivity anomaly can be deflected as shown in Figure 10. The causes of static shift can range widely, both where multiple processes and different structures give rise to unknown multipliers, *S* (shifts on log scale), of the apparent resistivity. In most cases those structures are not of great interest, but the interpretation of static shifted MT data will introduce errors in the results. Árnason et al. (2010), point out that shift multiplier 0.1 in MT data will result in conductivity models that have an order of magnitude too high conductivity and 3 times too shallow depths of boundaries.

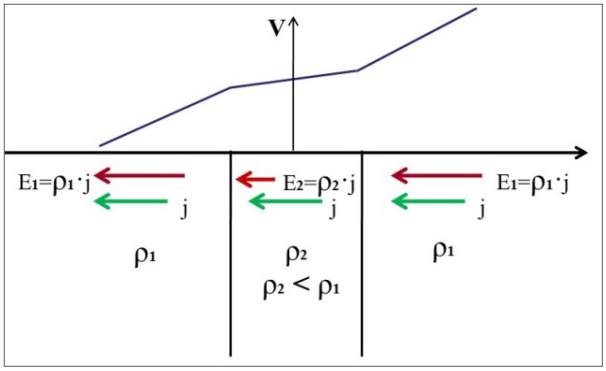

FIGURE 9: Electric field distortion causing shift (Árnason, 2015)

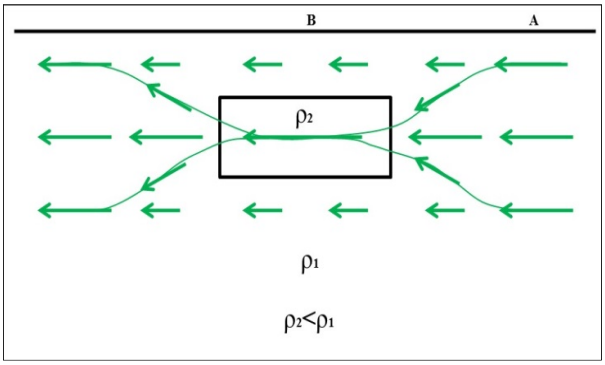

FIGURE 10: Current distortion causing static shift (Árnason, 2015)

To correct the static shift problem in MT data, the transient electromagnetics method (TEM) has been used for jointly inverting both MT and TEM data. This is based on the fact that, for TEM measurements at late time there are no distortions due to near surface inhomogeneities since they do not involve measuring the electrical field. This has been tested and shown to be a useful method to correct the static shifts in MT soundings, at least for 1D resistivity environment (Árnason, 2015).

Field example
MT soundings have been used in high-temperature geothermal fields mostly for deep prospecting. To correct for the static shift problem, ISOR developed a software for joint 1D (layered earth) inversion of MT and TEM data (Árnason, 2006a). For the data collection, TEM and MT soundings are performed in the same place within less than 200 m. The joint inversion is done for the model parameters and one additional parameter called shift multiplier, *S*. This multiplier is an unknown parameter by which the MT apparent resistivity values have to be divided by in order to fit the TEM data with the response of a common model as shown in Figure 11.

Figures 12 and 13 show static shift multipliers of the MT apparent resistivity derived from the determinant of the impedance tensor. The shift multipliers were determined by joint inversion with central-loop TEM soundings at the same spot (within 200 m). Figure 12 shows that half of the MT data in Hágöngur area were shifted down (S<1) due to near surface conductive bodies. The static shift multiplier less than 1 shows that the apparent resistivity curve is shifted downward resulting in decreased depth to the boundaries. S higher than 1 results in higher resistivity and increased depth to the boundaries, causing an upward shift of apparent resistivity over resistive bodies (Árnason, 2015). Figure 13 shows the distribution of shift multipliers in the Hágöngur area.

2.3 Transient electromagnetic method (TEM)

The transient electromagnetics (TEM) method was developed in order to gain information on the electric resistivity of the subsurface. Unlike the magnetotelluric method, the transient electromagnetic method is an active method where a loop of wire is placed on the ground and a current is generated to run in the

loop and then suddenly terminated. The collapsing electromagnetic field induces eddy currents in the conductive underground according to Maxwell's equations. This system of eddy currents produces a secondary magnetic field, whose propagation depends on the conductivity distribution in the subsurface (Figure 14).

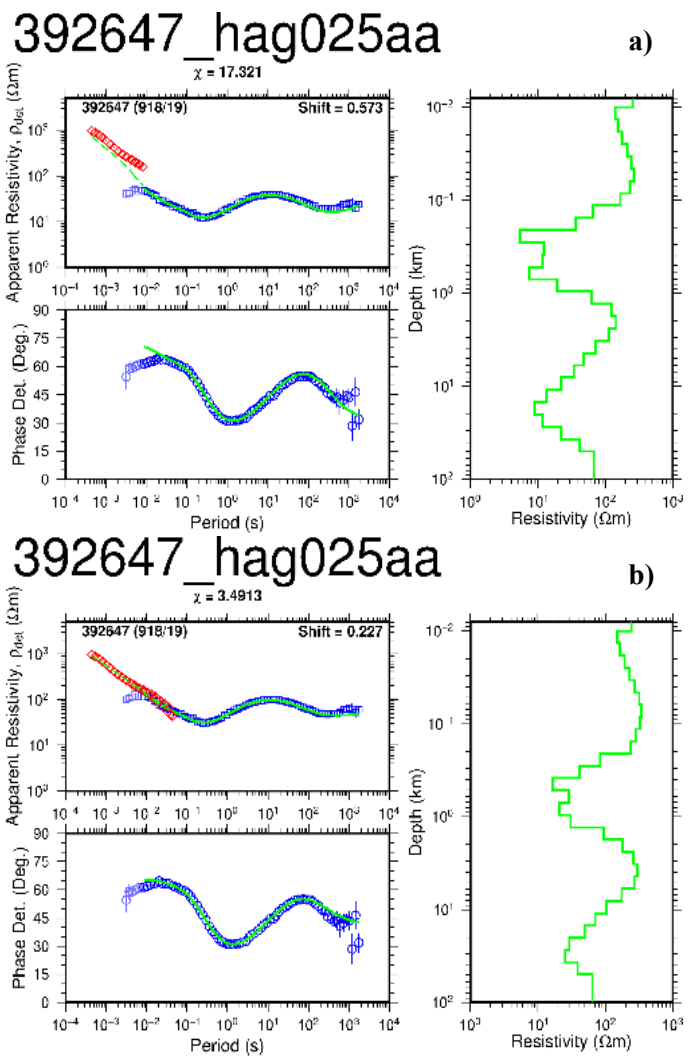

FIGURE 11: A typical result of 1D joint inversion of TEM and MT data from Hágöngur geothermal field. Red diamonds are measured TEM apparent resistivity, blue diamonds and blue circles are determinant of MT apparent resistivity and phase, respectively. Solid lines show the response of the resistivity model to the right. Shift multipliers used are shown in the upper right hand corners of the apparent resistivity panels. In a) the shift multiplier is 0.573 which is obviously an underestimate, not tieing the different curves well together; while in b) it is 0.227, which provides a good fit to the combined TEM and MT data and the model response

The primary magnetic field transient creates eddy currents below the transmitter loop and as the initial near-surface eddy currents decay, they in turn induce eddy currents at greater depths. The rate of change of the secondary field, due to induced eddy currents, is measured using an induction coil. The depth of exploration that will be mapped in a vertical sounding configuration can vary from tens of metres to thousand metres, depending on the transmitter loop size and source current.

As shown in Figure 14 , the transmitter (Tx) transmits bipolar half-duty current, with equal current on and off segments and linear turn-off. The receiver (Rx) records the induced voltage at time gates equally distributed on log-scale during current off. In the central-loop configuration, the induced voltage is measured in a receiver coil at the centre of a circle transmitter loop as shown in Figure 14. The transmitter and the receiver need to be synchronised so that Rx knows when Tx starts to turn off. And also, Rx should know the time (T_{OFF}) it takes to turn off the current. The transient voltage induced decays with time after the current turn-off and is eventually drowned in noise.

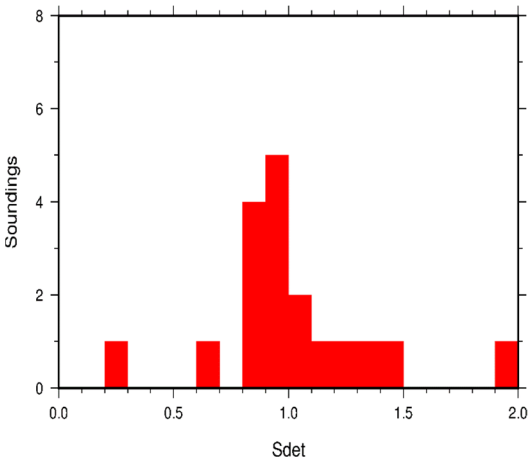

FIGURE 12: Static shift histogram for the Hágöngur high-temperature geothermal field

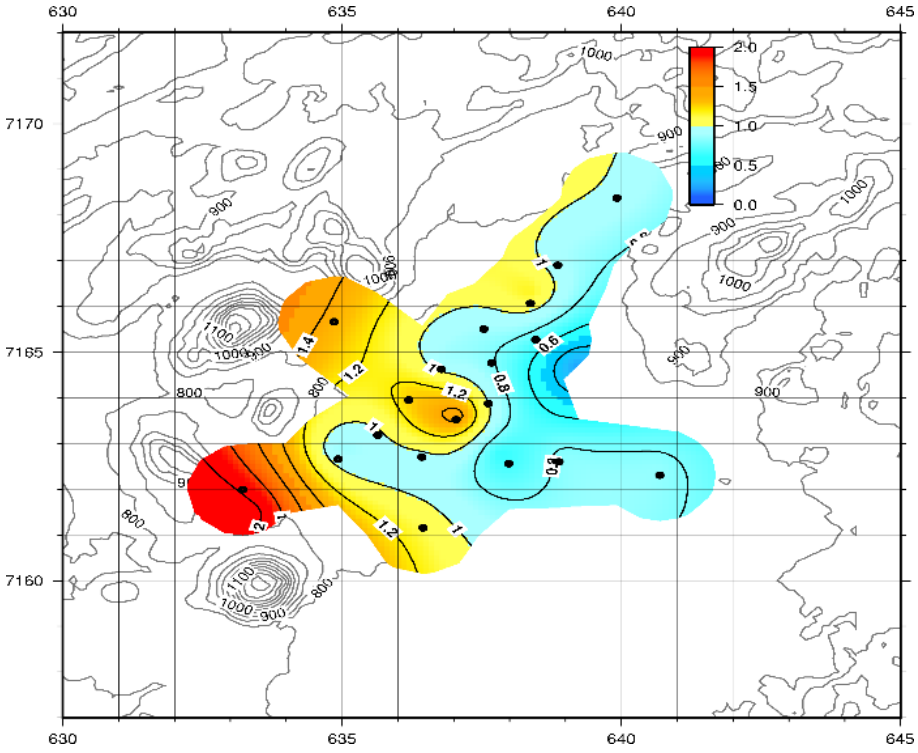

FIGURE 13: Static shift distribution map for Hágöngur, black dots are MT locations

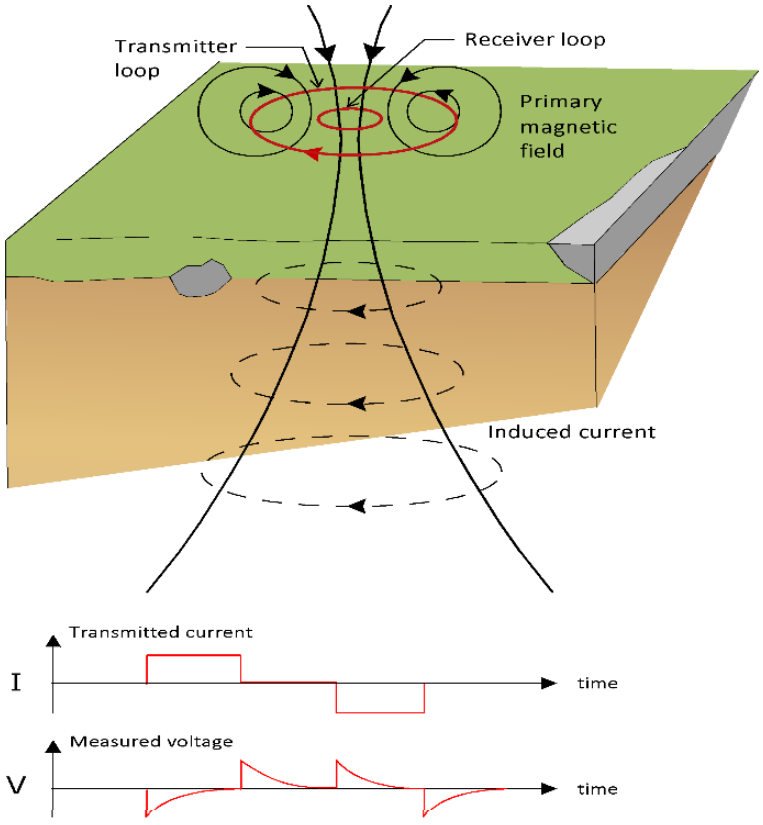

FIGURE 14: Set-up of a TEM sounding and the transient current flow in the ground (modified from Flóvenz et al., 2012)

The induced voltage *V(t,r)* for a central-loop configuration on a homogeneous half space of conductivity σ is given by (Árnason, 1989):

$$V(t,r) = I_0 \frac{C(\mu_0 \sigma r^2)^{3/2}}{10\pi^{1/2} t^{5/2}} \tag{36}$$

where C $= A_r n_r A_s n_s \frac{\mu_0}{2\pi r^3}$;
t = Elapsed time after the transmitter current is turned off (s);
r = Radius of the transmitter loop (m);
A_r = Cross-sectional area of the receiver coil (m^2);
n_r = Number of windings in the receiver coil;
μ_0 = Magnetic permeability in vacuum (H/m);
A_s = Cross-sectional area of the transmitter loop (m^2);
n_s = Number of windings in the transmitter loop;
I_0 = Transmitted current (A);
$V_{t,r}$ = Measured voltage (V).

Equation 36 can be used to define apparent resistivity, $\rho_a(t)$, in terms of induced voltage after the source current is turned off, given by (Árnason, 1989) as:

$$\rho_a = \frac{\mu_0}{4\pi}\left(\frac{2\mu_0 I_0 A_r n_r A_s n_s}{5t^{5/2} V_{t,r}}\right)^{2/3} \tag{37}$$

3. PREVIOUS STUDY AT THE HÁGÖNGUR GEOTHERMAL AREA

3.1 Location and accessibility

Hágöngur high-temperature geothermal area is located in the central highlands within the active volcanic zone, a few kilometres west of the Vatnajökull glacier, in Iceland. This area is very remote. Access to the area is available by using the Sprengisandur highland road, from a mountain track heading towards Vonarskard with an elevation of about 800 m a.s.l.

3.2 Geology

The Hágöngur area has been explored by Landsvirkjun (The National Power Company of Iceland). Geological investigations have been done occasionally in the area between the glaciers Vatnajökull and Hofsjökull. The geology of the Hágöngur is little known except that is being confined to the northern margin of the eastern volcanic zone with abundance of exposed Pleistocene and Holocene volcanics. Jóhannesson and Saemundsson (2003) have presumed that the area is an independent central volcano, but it has also been proposed that the Hágöngur area is in direct relation and a part of an elongated central volcano from Tungnafellsjökull in the northeast, extending southwards to the Hágöngur geothermal area (Fridleifsson et al., 1996). In this area, all exposed volcanic formations have a normal magnetization and as a result they are younger than 700,000 years (Piper, 1979). The area is in many ways quite unique in comparison with other high-temperature geothermal area in Iceland. It is entirely buried in glacio-fluvial sediments, supposedly filling an old lake basin.

3.3 Geophysics

In April 1998, a transient electromagnetic (TEM) survey was carried out in the Hágöngur area in order to get reliable data on the size and thermal conditions of the geothermal system. The TEM survey

revealed a high-resistivity core of about 28 km^2 at 1000 m depth approximately. Including the low-resistivity cap surrounding the high-resistivity core, the size of the high-temperature area is about 50 km^2, comparable to the resistivity depicted at the same level in the Krafla high-temperature area in Northern Iceland (Karlsdóttir, 2000). The resistivity anomaly at sea level is shown in Figure 15 with the low-resistivity cap and high-resistivity core mentioned separately.

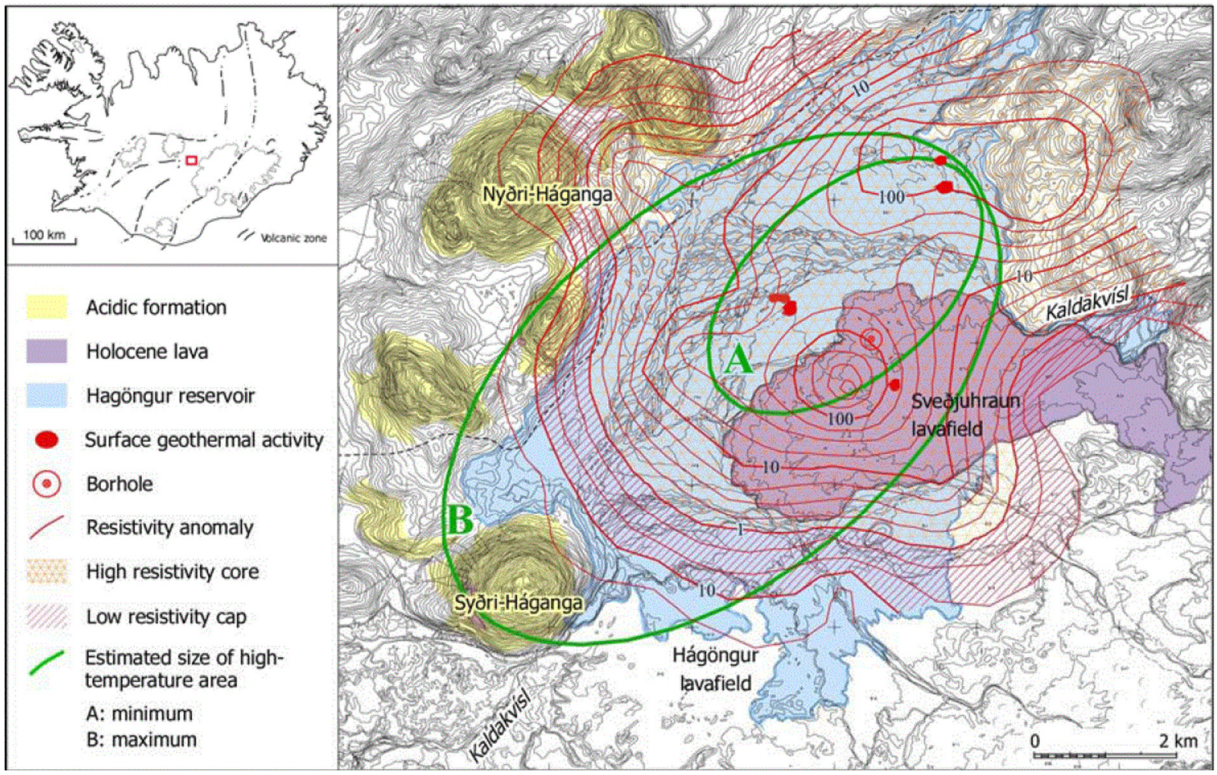

FIGURE 15: Location of the Hágöngur geothermal area and a simplified geological map with the resistivity anomaly (from Karlsdóttir, 2000) in the area at sea level

3.4 Lithology in well HG-01

An exploration well HG-01, the first deep exploration well drilled in the Hágöngur geothermal field, is located above the centre of the high-resistivity core. The well was drilled to a total depth of 2360 m in 2002. The lithology in this well and distribution of alteration minerals from analysis of drill cuttings are simplified in Figure 16.

4. MT AND TEM SURVEY AT HÁGÖNGUR HIGN-TEMPERATURE GEOTHERMAL FIELD

4.1 The location of the MT and TEM measurements

The main aim of this study was to learn about the application of MT and TEM measurements. Data from Hágöngur geothermal field were used for that purpose. The location of MT and TEM soundings in Hágöngur used in this report and the associated resistivity profiles are given in Figure 17. The data were measured by ÍSOR's staff and are used here with the permission of Landsvirkjun (The National Power Company of Iceland). Nineteen MT soundings and eighteen TEM soundings were performed on three profiles. Two of them trend SW-NE direction and the third one SE-NW. The resistivity data and its interpretation are presented in a separate Appendices report (Ali Soumail, 2015).

4.2 Data acquisition and processing

MT data acquisition. For an MT sounding, the equipments needed are data logger, two pairs of electric dipoles and three magnetic sensors. Generally, the data logger has 5 channels, 3 for the orthogonal horizontal and vertical magnetic field (H_x, H_y, H_z), and 2 for the orthogonal horizontal electric field (E_x, E_y). The data logger can control the acquisition process, amplify and filter the data, and convert them to digital format for storage.

The distance between the electrodes of the dipoles is usually in the range of 50-100 m. The measurement of the magnetic fields is made by a magnetic field sensor – coils are oriented in the x, *y and z* direction. The electric field is determined as $E_i = U/D_i$ where U is the voltage and D_i is the distance between a pair of electrodes in the direction of $i = x,y$.

A spirit level and compass are used in the MT set up to align the measurement axes in such a way that the *x, y* directions are horizontal and orthogonal to each other and the *z* direction is vertical. Generally, *x* positive direction is taken as magnetic North, *y* positive direction as magnetic East and *z* positive vertical downwards. After Fourier transforming the recorded time series data are obtained in the frequency range of 300 - 0.001 Hz

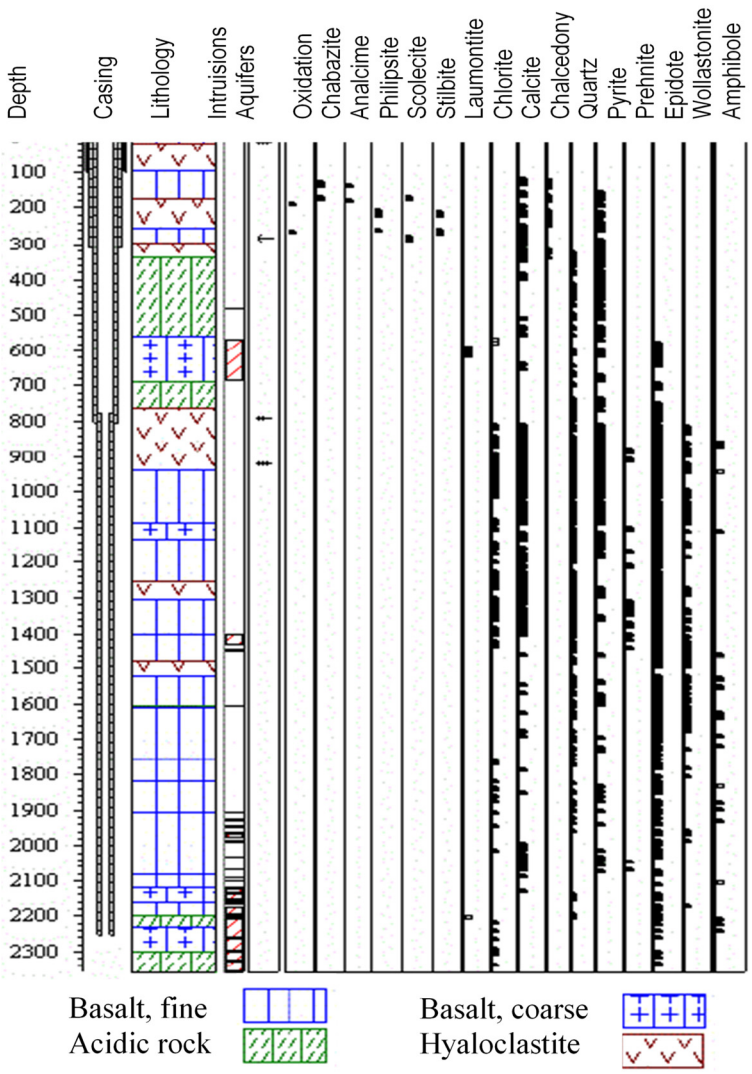

FIGURE 16: Simplified lithology in well HG-01 and distribution of alteration minerals from analysis of drill cuttings (Jónsson et al., 2005)

TEM data acquisition. For a TEM sounding, the instruments needed are generator, receiver, receiver coil(s), a current transmitter and wire for the transmitter loop. The description below applies to the PROTEM-67 system from Geonics, Ltd. At the measurement site, the first thing to do is to turn on the equipments and heat the crystals used for synchronization. Then the receiver and the transmitter are connected by a cable and the crystaltiming synchronized. Usually, the set-up uses a square transmitter loop, 100 m to 300 m each side. A current of about 15-20 A is transmitted into the loop. A prism is used to make the loop as rectangular as possible by determining the right angle directions. The receiver coils are laid down in the centre of the transmitter loop.

After laying out the loops, the power source is started, the current and the turn off time in the transmitter are recorded in the data book. At low frequency (2.5 Hz), the current is measured to get a more stable value, and at high frequency (25 Hz), the turn off time is measured. The current and turn off time values are recorded into the receiver. Repeated measurements are done for different gains and stacking, first at

low frequency and then at high frequency. Low-frequency measurements are performed with a large receiver loop and a smaller standard receiver coil. The high-frequency measurements are made only with the small receiver coil.

4.3 1D inversion of resistivity data at Hágöngur area

4.3.1 TEM data processing and 1D interpretation

The raw TEM data were processed by the programme TemX developed by Árnason (2006b). This program enables visual editing of the raw data to remove outliers and unreliable data points before stacking over repeated measurements and calculating late time apparent resistivity as a function of time. 1D inversion of TEM is achieved by software called TEMTD which is a Linux/UNIX program (Árnason, 2006a). This software assumes that the source loop is a square and that the receiver coil/loop is at the centre of the source loop. The current waveform is also assumed to have equal current-on and current-off time segments. The transient response is calculated both as induced voltage and late time apparent resistivity as function of time. All the TEM soundings in the Hágöngur field have been interpreted by 1D inversion. The inversion was done by the Occam inversion as will be seen later in this report. In 1D inversion it is assumed that the earth consists of horizontal layers with different resistivity and thickness. The 1D interpretation determines the layered model whose response can best fit the measured responses (an example is seen in Figure 18). The remaining TEM soundings and models are given in Appendix I (Ali Soumail, 2015).

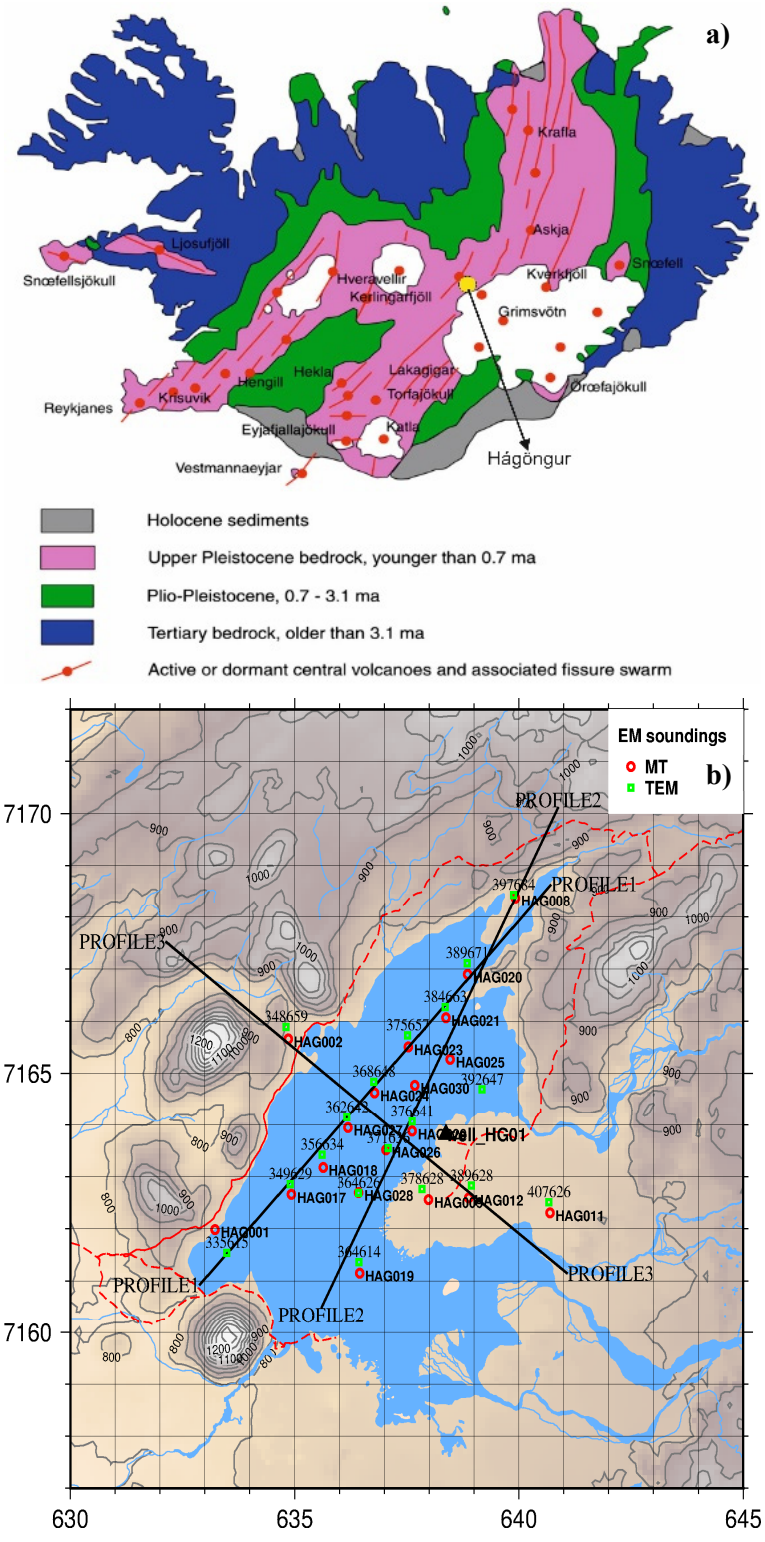

FIGURE 17: Location of the Hágöngur geothermal area (a) and the MT/TEM stations and the resistivity profiles (b). The red cirles are the MT stations, the green squares are the TEM soundings, the black triangle is well HG-01 and red lines are roads

4.3.2 MT data processing and 1D interpreation

The processing of the collected time series data recorded from the MT equipment starts by using the time series viewer option in the SSMT2000 software (Phoenix Geophysics, 2005). It gives a first indication of the data quality that influences decision making on whether to repeat the sounding or not. Then parameter files (tbl) are edited to reflect the setup for the collected data. The resulting time series are Fourier transformed to the frequency domain, and then the different auto- and cross-powers are calculated using the robust processing method (RPM). The data are graphically edited using MTeditor, a Phoenix geophysics software, by masking the outliers to achieve apparent resistivity and phase curves as shown in Figure 19. The resulting MT parameters are all saved as EDI files.

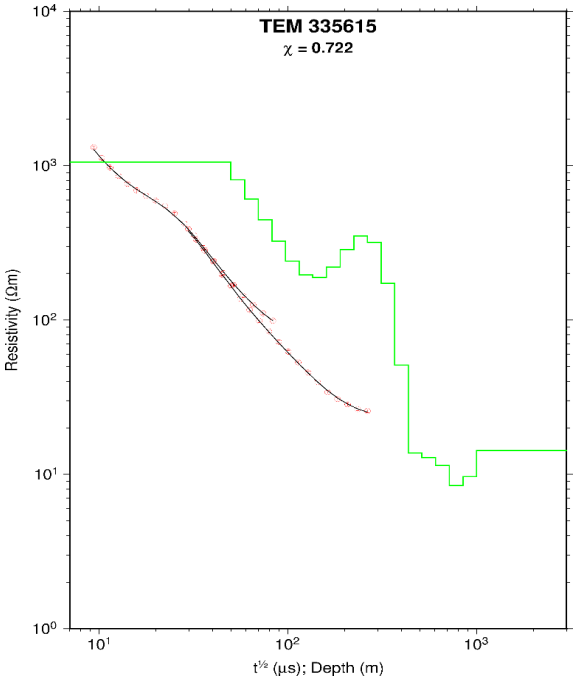

FIGURE 18: 1D inversion results from the TEM sounding 335615; the red dots are the calculated apparent resistivity points from voltage data; the green line shows the layered model generated by TEMTD; the black line is the response from the model

The spectral EDI files from MTeditor are further processed through dos2unix which changes the edi-files from window based environment to a Linux readable format so that the commands spect2edi can calculate various parameters and can give the results in the standard format EDI making these ready to be used for inversion. Some of these programmes were developed at ISOR such as spect2edi. Finally, the inversion will be done through the TEMTD programme. The data were also run through another programme edi2ps to generate PostScript graphs. And finally ps2raster transforms the postscript files to PNG, which is the case of the pictures in this report. The plots in Figure 20 show an example of processed MT data. The remaining processed MT data are given in Appendix II (Ali Soumail, 2015).

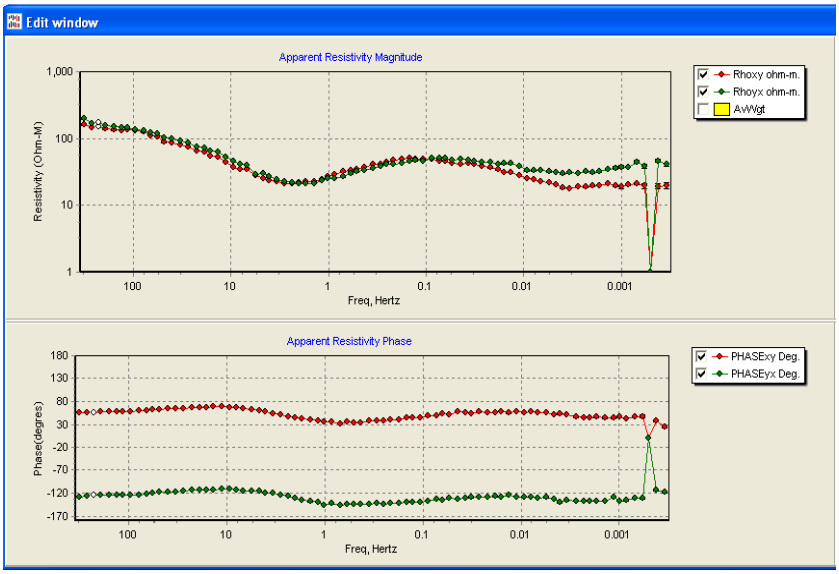

FIGURE 19: MTeditor output showing the apparent resistivity and phase curvesof Hágöngur sounding HAG011

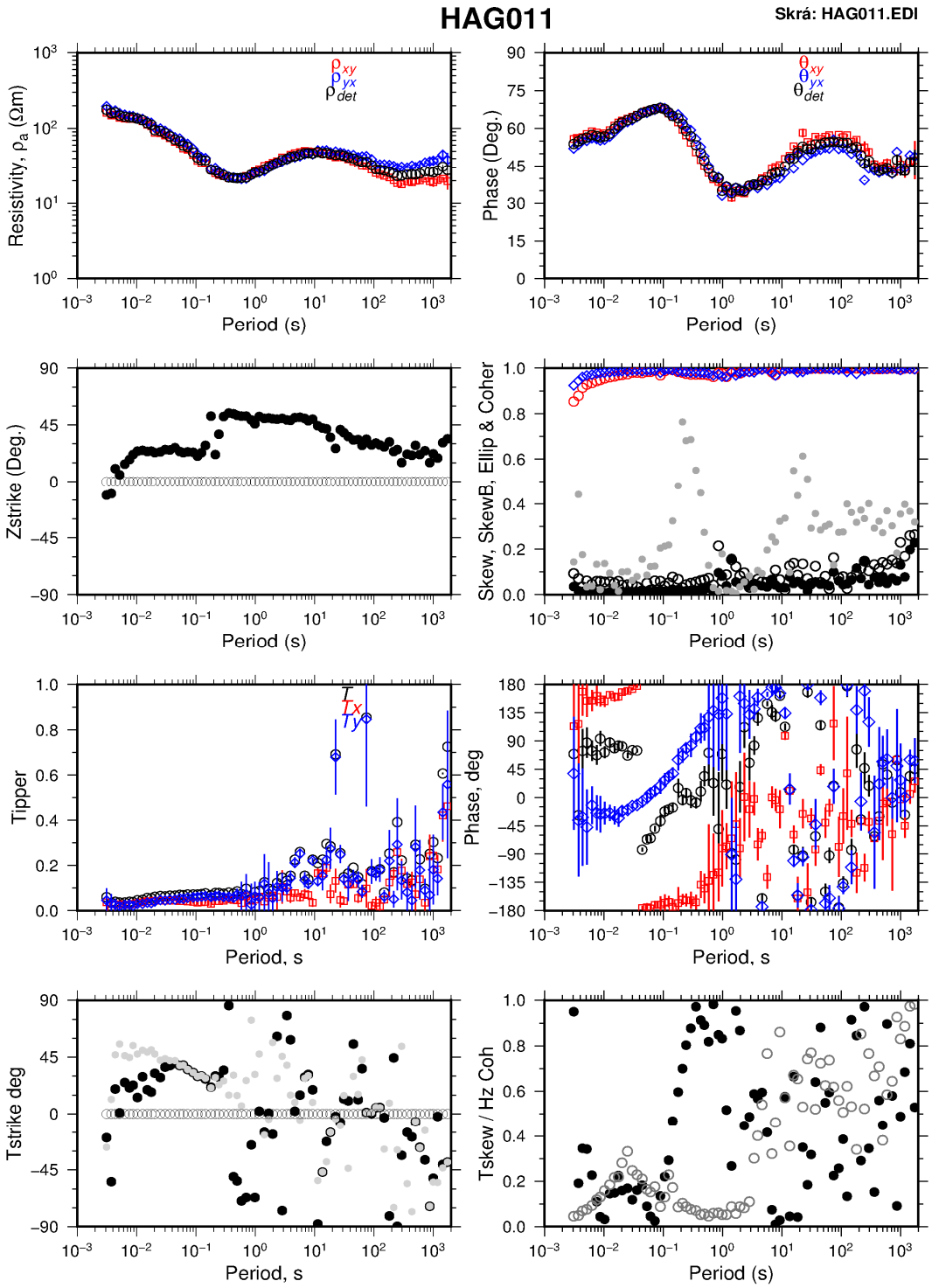

FIGURE 20: Processed MT data for sounding HAG011 from Hágöngur geothermal field; the plots show the apparent resistivity and phase derived from the xy (red) and yx (blue) components of the impedance tensor and the determinant invariant (black), the Z-strike or Swift angle (black dots), and multiple coherency of xy (red) and yx (blue), and skew (black dots) and ellipticity (grey dots). The lowermost four graphs show different representations of the Tipper values

4.3.3 1D joint inversion of MT and TEM

All data were inverted using Occam inversion method with varying first and second order derivatives of the resistivity layers such that the model will be optimized for resistivity smoothness and avoid unnecessary oscillations in their values. The 1D inversion was done with TEMTD. An example is given in Figure 21. The remaining 1D joint inversion soundings are given in Appendix III (Ali Soumail, 2015).

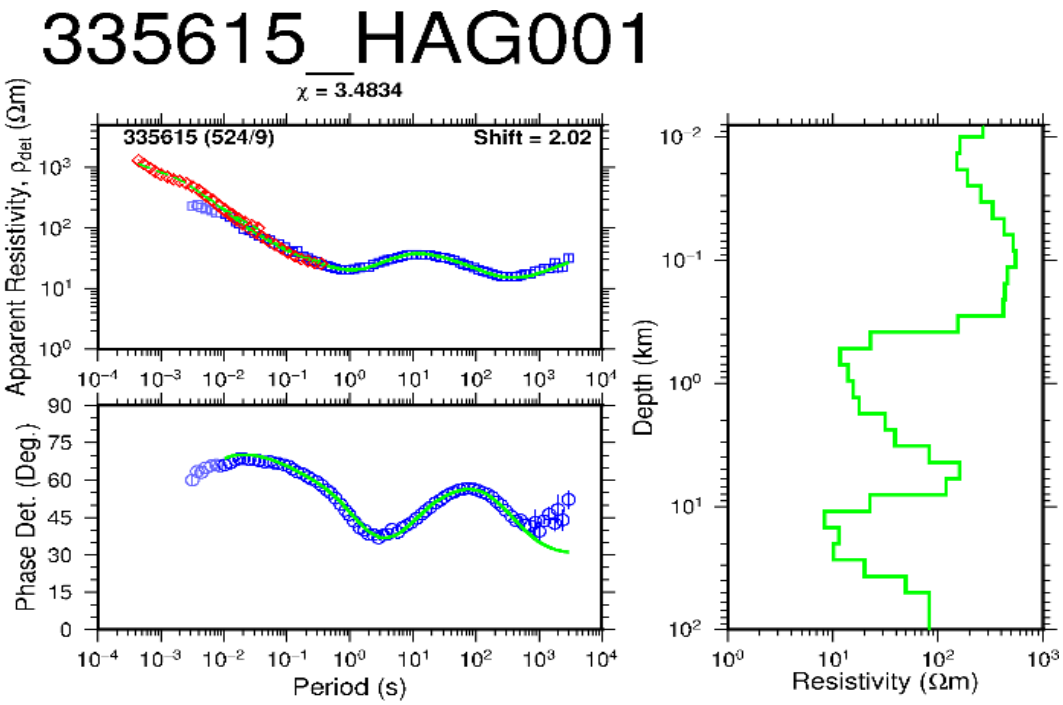

FIGURE 21: Results for joint 1D inversion of TEM and MT data. Red diamonds: TEM apparent resistivities transformed to a pseudo-MT curve; blue squares: measured apparent resistivities; blue circles: apparent phase derived from the determinant of MT impedance tensor; light blue symbols to the left of the green curve: data not used in the inversion; green lines model calcuations; vertical blue lines: error bars. Right panel: results of the 1D resistivity inversion model, in the left panels its synthetic MT apparent resistivity and phase response. Number shown on the top of the figure: HAG001 is the name of the MT station and 335615 is the name of the TEM station. The numbers in parenthesis (524/9) indicates that the two stations were 524 m apart and their elevation difference was 9 m. The Chi square χ is 3.4834, and the shift is 2.02

5. INTERPRETATION AND RESULTS

5.1 Cross-sections

The resistivity cross-sections presented in this report were plotted from results acquired from 1D inversion by a programme developed at ÍSOR called TEMCROSS (Eysteinsson, 1998). This programme calculates the best lines between the selected stations on a profile. Then it plots the resistivity isolines based on the 1D model generated for each sounding.

Three cross-sections were made in the Hágöngur area, as shown on the location map, see Figure 17. Two cross-sections (profile1 and profile2) are trending SW-NE and one (profile3) in SE-NW direction. All are presented in two versions, down to 2000 m b.s.l. and down to 10,000 m b.s.l.

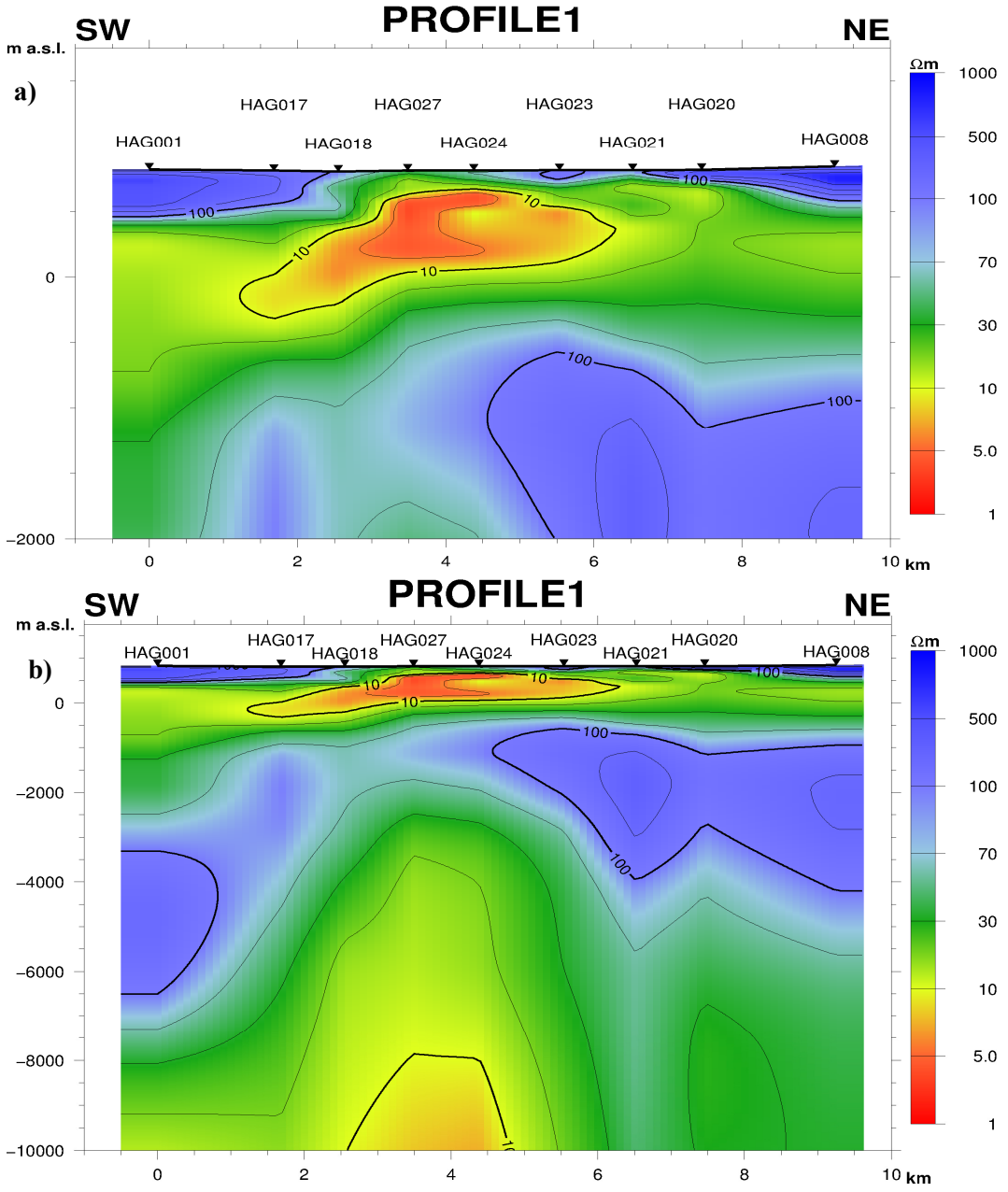

FIGURE 22: Resistivity cross-section profile1; a) Down to 2000 m b.s.l.; b) Down to 10,000 m b.s.l.; the location of the profile is shown on Figure 17

Cross-section profile1 (Figure 22) has 9 soundings and is about 9 km long. It shows a thin resistive layer near the surface which can be interpreted as unaltered basaltic lavas underlain by low-resistivity layer with resistivities less than 10 Ωm in the central part of the profile. This conductive layer, which lies roughly between 500 m a.s.l. and 500 m b.s.l., can be correlated with clay cap rocks such as smectite, zeolites or mixed-layer clays, indicating alteration temperatures somewhere between 100 and 220°C. Below this, a high-resistive layer is observed which may correspond to alteration zone with epidote,

chlorite. This indicates the presence of alteration temperatures above 250°C. This layer reaches down to 4-5000 m b.s.l. Further down lower resitivities are seen again.

Cross-section profile2 (Figure 23) has 6 soundings and is about 5 km long. This profile shows similar resistivity structures as the first one. But in addition to this, there is an indicationof a fault trending NW-SE below -1000 m b.s.l.

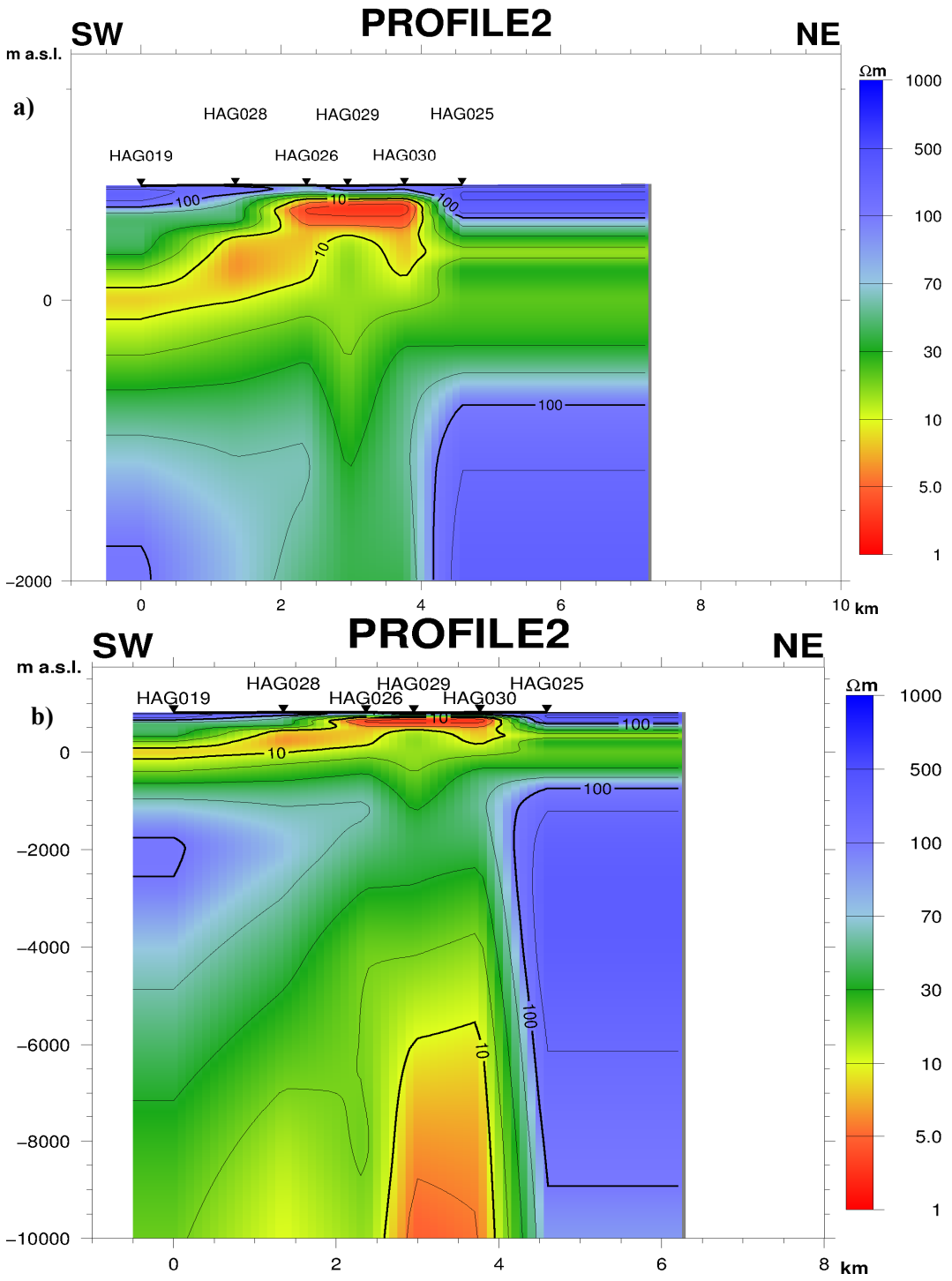

FIGURE 23: Resistivity cross-section profile2; a) Down to 2000 m b.s.l.; b) Down to 10,000 m b.s.l.

Cross-section profile3 (Figure 24) has 6 soundings and is about 7 km long. It shows the same resistivity structures. An upflow zone appears to be seen in this profile which trends from the deep conductive layer seen in soundings HAG26 and HAG24 which may correspond to the heat source.

A correlation between these profiles and well HG-01 drilled in this area has been found, and confirmed the assumptions on the different resistivity structures and the alteration minerals.

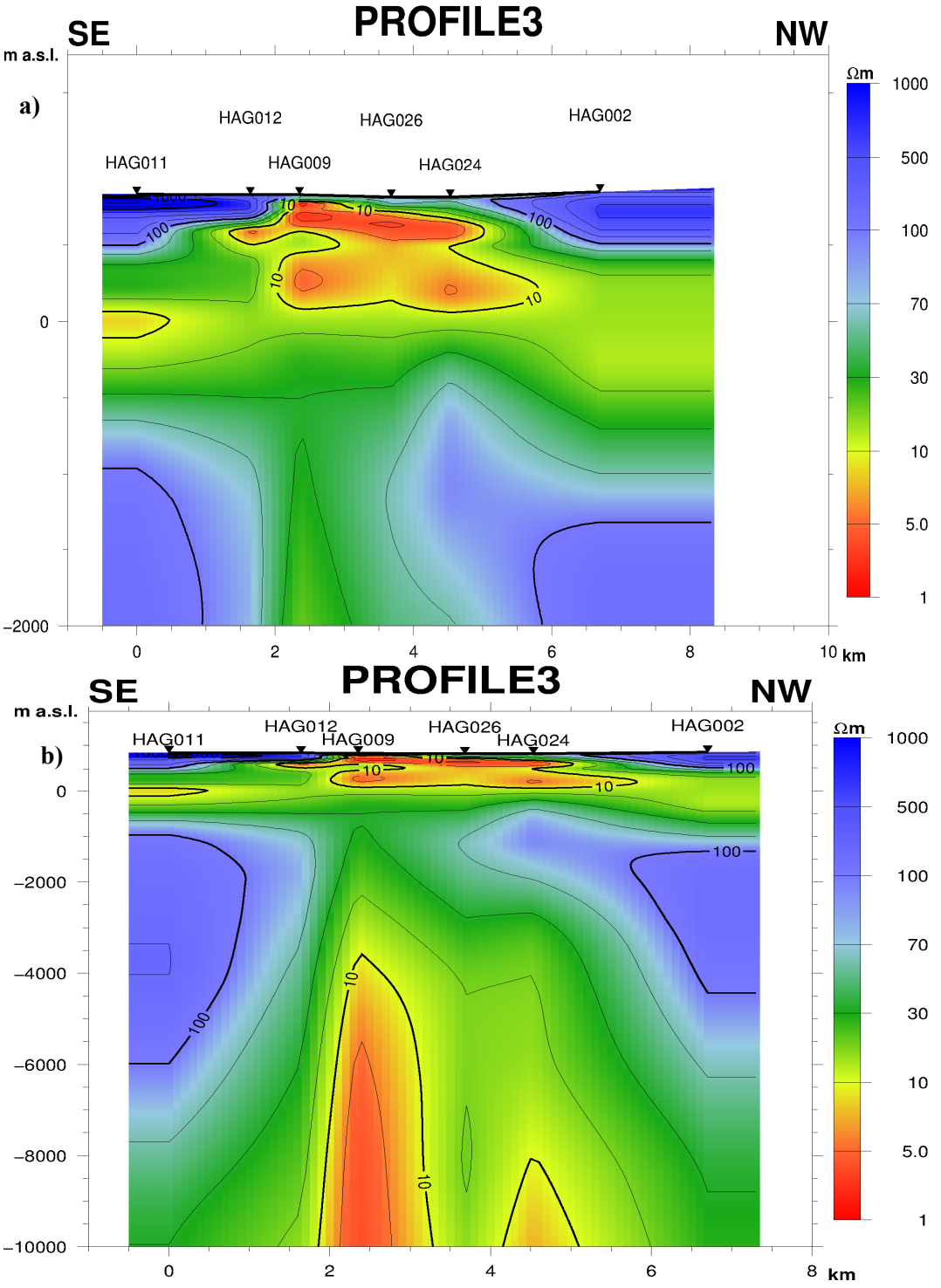

FIGURE 24: Resistivity cross-section profile3; a) Down to 2000 m b.s.l.; b) Down to 10,000 m b.s.l.

5.2 Iso-resistivity maps

Iso-resistivity maps using the TEMMAP program (Eysteinsson, 1998) were made to display the resistivity at different depths in Hágöngur geothermal field. Several iso-resistivity maps were made, in this report four of them are displayed. However, it should be kept strictly in mind that the maps are based on relatively few soundings with non-uniform distribution.

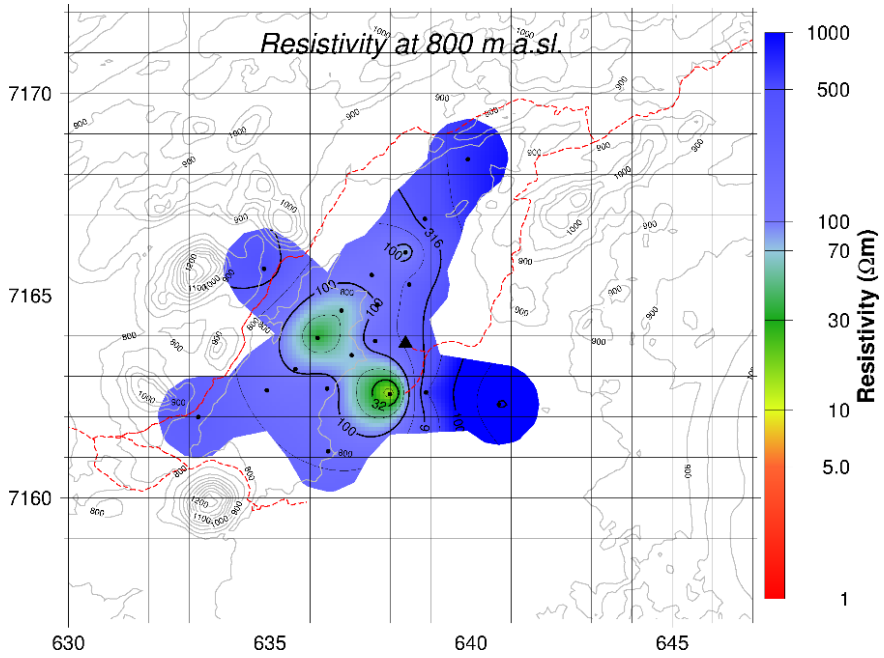

FIGURE 25: Iso-resistivity map at at 800 m a.s.l.; black dots denote MT soundings, the black triangle is well HG-01 and red lines are roads

Resistivity map at 800 m a.s.l. (Figure 25): The map shows a fairly uniform resistivity of about 100 Ωm or slightly more, representing relatively unaltered rocks, except in the central part of the map, where the resistivity is about 30 Ωm.

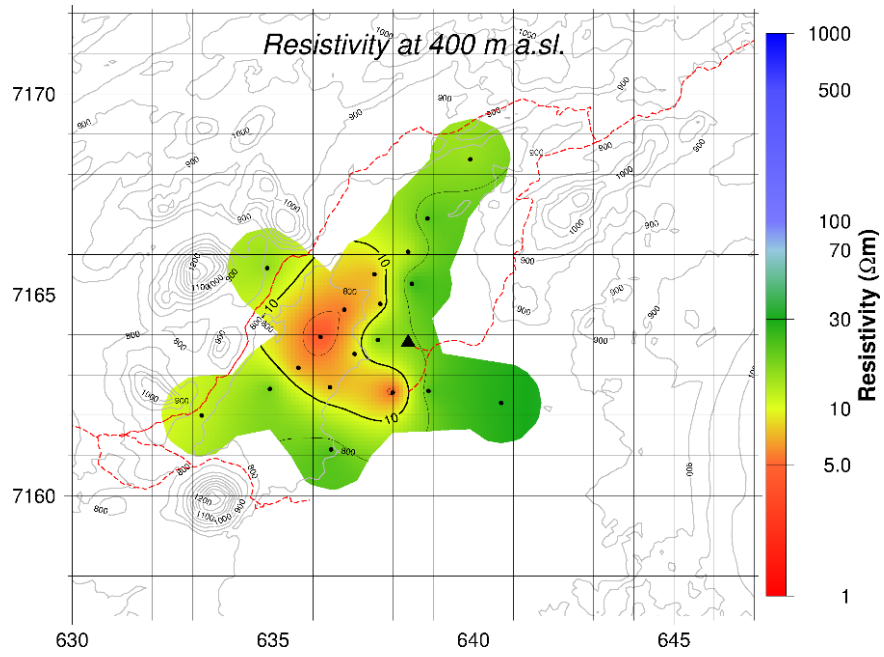

FIGURE 26: Iso-resistivity map at at 400 m a.s.l.; for figure legend, see Figure 25

Resistivity map at 400 m a.s.l. (Figure 26): A uniform conductive layer appears at this depth. It is more conductive in the centre part of the lake, with resistivities less than 10 Ωm. Else, it ranges between 10 and 30 Ωm. The conductive layer correlates with the clay cap rocks around the geothermal system.

Resistivity map at 1000 m b.s.l. (Figure 27): The map shows a fairly uniform layer with resistivities around 30 Ωm at the centre to the southeast of the lake; outside this main area the resistivity is greater than 100 Ωm. The resistivities are probably controlled by high-temperature alteration minerals, dominated by epidote and chlorite, which could be the geothermal reservoir.

Resistivity at 7500 m b.s.l. (Figure 28): At these deep levels the rocks are more conductive, specially in the centre of the lake, with resistivities less than 10 Ωm, but outside, they range between 10 and 30 Ωm. The conductive body might be associated with the heat source.

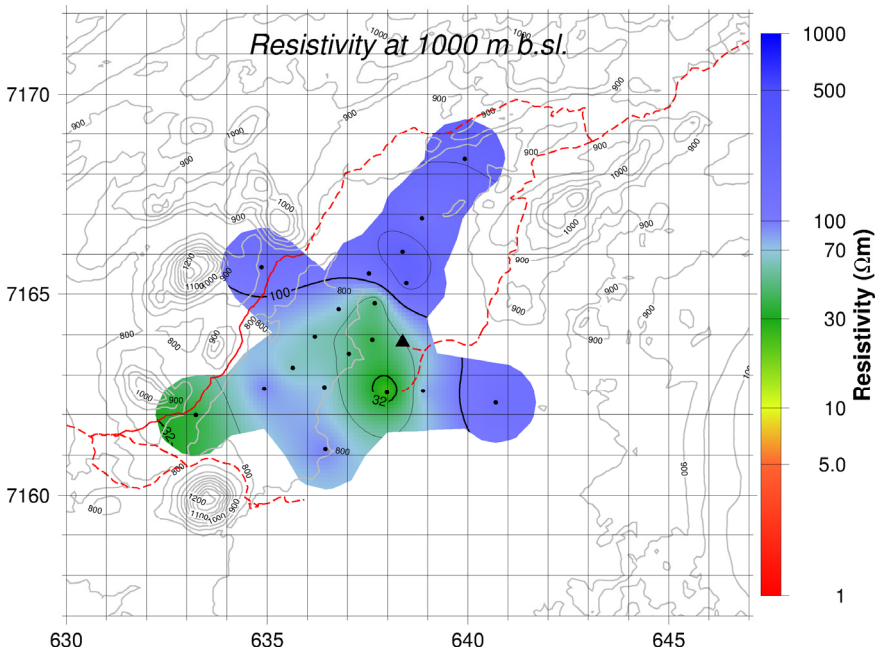

FIGURE 27: Iso-resistivity map at 1000 m b.s.l.;
for figure legend, see Figure 25

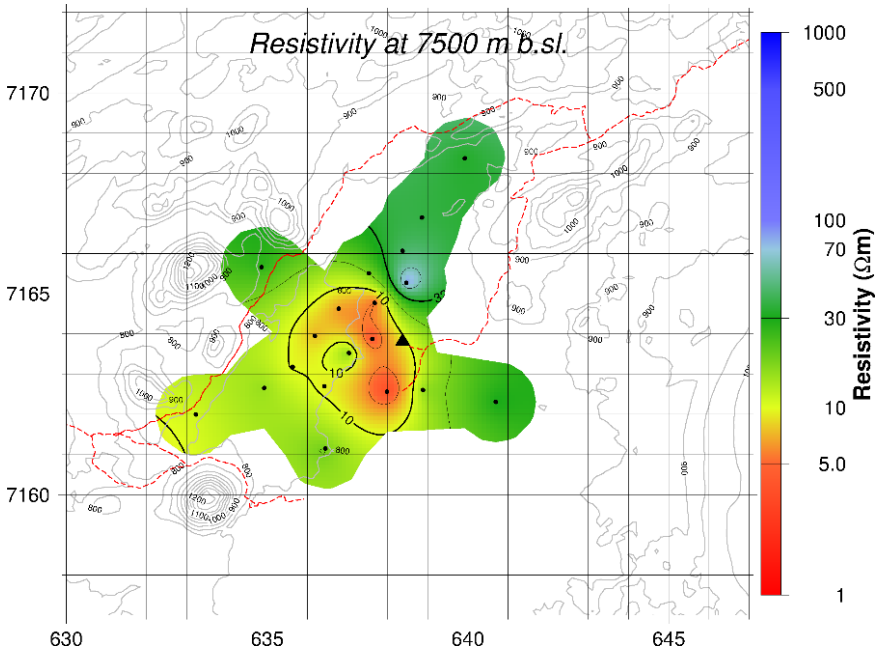

FIGURE 28: Iso-resistivity map at 7500 m b.s.l.; for figure legend,
see Figure 25

5. CONCLUSIONS

According to the results of the resistivity survey in Hágöngur, as presented through 3 cross-sections and several iso-resistivity maps at different depths, and comparison with data from geothermal well HG-01, the area has a geothermal potential. The classical subsurface resistivity structures for geothermal systems in volcanic regions appears in the three profiles with high-low-high-low resistivity pattern. The following resistivity layers are displayed:

- High resistivity near surface caused by unaltered rocks;
- This is followed by low resistivity at around 400 m a.s.l. due to low-tempera-ture alteration minerals, reching down to about 1000 m b.s.l.,
- At 1000 m b.s.l. a resistive core is found similar to what can be expected from high-temperature altera-tion minerals in a high-temperature geothermal system.
- Finally, at 6-8 km depth there appears to be a deep conductor, which may be the heat source of Hágöngur geothermal system.

The centre of the geothermal reservoir seems to be localised between MT sounding HAG17 and HAG23 at levels below 900 m a.s.l. and there is an indication of a fault trending NW-SE below 1000 m b.s.l. An upflow zone can be seen in profile3 in the vicinity of resistivity stations HAG24 and HAG26.

These results of the resistivity structure of Hágöngur geothermal area show that the MT method is a powerful tool in mapping subsurface conductivity variations. It can investigate the electrical resistivity at great depth, even down to some tens of km, reveal geological faults and delineate the geothermal system. The joint inversion of MT/TEM is helpful in correcting static shift.

ACKNOWLEDGEMENTS

I would like to express my gratitude to the United Nations University Geothermal Training Programme (UNU-GTP) of Iceland for granting me the opportunity to be a fellow in this excellent programme and Landsvirkjun (National Power Company of Iceland) for providing the data. Many thanks go to director Mr. Lúdvík S.Georgsson, deputy director Mr. Ingimar G. Haraldsson, Ms. Thórhildur Ísberg, Ms. Málfrídur Ómarsdóttir and Mr. Markús A.G. Wilde, for their terrific support and facilitation of the training programme.

Special thanks to my supervisors, Mr. Gylfi Páll Hersir and Mr. Knútur Árnason for always being there for me and working with me full time during this research work. Furthermore, I wish to give my thanks to Mr. Arnar Már Vilhjálmsson for his assistance with my project. More thanks to my colleagues at UNU-GTP in Geophysical Exploration section for their fruitful discussions and sharing of knowledge. To the entire UNU Fellows of 2015, many thanks.

To my family, your support during these six months away was paramount. Most importantly, thanks to the Almighty Allah who taught mankind by the pen what they didn't know.

REFERENCES

Abdou, A.S., 2015: *Appendices to the report "TEM and MT resistivity surveying: Data acquisition, processing and 1D inversion with an example from Hágöngur geothermal field, Mid-Iceland*". UNU-GTP, Iceland, report 6 appendices, 30 pp.

Archie, G.E., 1942: The electrical resistivity log as an aid in determining some reservoir characteristics. *Tran. AIME, 146*, 54-62.

Árnason, K., 1989: *Central loop transient electromagnetic sounding over a horizontally layered earth*. Orkustofnun, Reykjavík, Iceland, report OS-89032/JHD-06, 129 pp.

Árnason, K., Karlsdóttir, R., Eysteinsson, H., Flóvenz, Ó. G., and Gudlaugsson, S.T., 2000: The resistivity structure of high-temperature geothermal systems in Iceland. *Proceedings of the World Geothermal Congress 2000, Kyushu-Tohoku, Japan,* 923-928.

Árnason, K., 2006a: *TEMTD (Program for 1D inversion of central-loop TEM and MT data)*. ÍSOR-Iceland GeoSurvey, Reykjavík, Iceland, short manual, 16 pp.

Árnason, K., 2006b: *TemX short manual*. ÍSOR-Iceland GeoSurvey, Reykjavík, internal report, 17 pp.

Árnason K., Eysteinsson, H., and Hersir, G.P., 2010: Joint 1D inversion of TEM and MT data and 3D inversion of MT data in the Hengill area, SW Iceland. *Geothermics*, 39, 13-34.

Árnason, K., 2015: The static shift problem in MT Soundings. *Proceedings of the World Geothermal Congress 2015, Melbourne, Australia*, 12 pp.

Badilla, E.D., 2011: Resistivity imaging of the Santa Maria sector and the northern zone of Las Pailas geothermal area, Costa Rica, using joint 1D inversion of TDEM and MT data. Report 8 in: *Geothermal training in Iceland 2011*. UNU-GTP, Iceland, 85-118.

Cagniard, L., 1953: Basic theory of the magneto-telluric method of geophysical prospecting. *Geophysics, 18*, 605-635.

Dakhnov, V.N., 1962: Geophysical well logging. The application of geophysical methods; electrical well logging. *Q. Colorado Sch. Mines*, *57-2*, 445 pp.

Eysteinsson, H., 1998: *TEMMAP and TEMCROSS plotting programs*. ÍSOR – Iceland GeoSurvey, Reykjavík, unpublished programs and manuals.

Flóvenz, Ó.G., Georgsson, L.S., and Árnason, K., 1985: Resistivity structure of the upper crust in Iceland, *J. Geophys. Res*., *90*, 10,136-10,150.

Flóvenz, Ó.G., Spangerberg, E., Kulenkampff, J., Árnason, K., Karlsdóttir, R., Huenges, E., 2005: The role of electrical interface conduction in geothermal exploration. *Proceeding of the World Geothermal Congress 2005, Antalya, Turkey,* 9 pp.

Flóvenz, Ó.G., Hersir, G.P., Saemundsson, K., Ármannsson, H., and Fridriksson Th., 2012: Geothermal energy exploration techniques. In: Sayigh, A. (ed.), *Comprehensive renewable energy, vol 7*. Elsevier Oxford, United Kingdom, 51-95.

Fridleifsson, G.Ó., Ólafsson, M., and Bjarnason, J.Ö., 1996: *Geothermal activity in Köldukvíslarbotnar*. Orkustofnun, Reykjavík, Iceland, report OS-96014/JHD-04 (in Icelandic), 32 pp.

Henley, R.W. and Ellis, A.J., 1983: Geothermal systems, ancient and modem: A geochemical review. *Earth Sci. Reviews*, *19*, 1-50.

Hersir, G.P., and Björnsson, A., 1991: *Geophysical exploration for geothermal resources. Principles and applications*. UNU-GTP, Iceland, report 15, 94 pp.

Hersir, G.P., and Árnason, K., 2009: Resistivity of rocks. *Paper presented at "Short Course on Surface Exploration for Geothermal Resources", organized by UNU-GTP and LaGeo, Santa Tecla, El Salvador*, 8 pp.

Jóhannesson, H., and Saemundsson, K., 2003: *Active central volcanoes in Iceland*. ÍSOR, Reykjavík, Iceland, unpublished map (in Icelandic).

Jónsson, S.S., Gudmundsson, Á., and Pálsson, B., 2005: The Hágöngur high-temperature area, Central-Iceland. Surface exploration and drilling of the first borehole, lithology, alteration and geological setting. *Proceeding for the World Geothermal Congress 2005, Antalya, Turkey*, 6 pp.

Kaufman A.A., and Keller, G.V., 1983: *Frequency and transient sounding. Methods in geochemistry and geophysics, vol. 16.* Elsevier Scientific Publishing Co., Amsterdam, Netherlands, 685 pp.

Karlsdóttir, R., 2000: *The high-temperature area in Köldukvíslarbotnar. TEM-survey in 1998*. Orkustofnun, Reykjavík, Iceland, report OS-2000/060 (in Icelandic), 60 pp.

Keller, G.V., and Frischknecht, F.C., 1966: *Electrical methods in geophysical prospecting*. Pergamon Press Ltd., Oxford, United Kingdom, 527 pp.

Phoenix Geophysics, 2005: *Data processing. User guide´s*. Phoenix Geophysics, Ltd., Toronto.

Piper, J.D.A., 1979: Outline of volcanic history of the region west of Vatnajökull, Central Iceland. *J. Volcanol. & Geothermal Res., 5,* 87-98.

Quist, A.S., and Marshall, W.L., 1968: Electrical conductances of aqueous sodium chloride solutions from 0 to 800°C and at pressures to 4000 bars. *J. Phys. Chem., 72*, 684-703.

Tikhonov, A.N., 1950: Determination of the electrical characteristics of the deeper strata of the earth's crust. *Dokl. Akad. Nauk, 73*, 295-297 (in Russian).

UNITED NATIONS UNIVERSITY
UNU-GTP
Geothermal Training Programme

Orkustofnun, Grensasvegur 9,
IS-108 Reykjavik, Iceland

Reports 2015
Number 7

ENVIRONMENTAL MANAGEMENT OF ASSAL-FIALE GEOTHERMAL PROJECT IN DJIBOUTI: A COMPARISON WITH GEOTHERMAL FIELDS IN ICELAND

Ali Barreh Adaweh
Ministry of Energy in charge of Natural Resources
Cite Ministerielle, Djibouti
REPUBLIC OF DJIBOUTI
alibarreh@gmail.com

ABSTRACT

The geological characteristics of the Assal rift are favourable for the development of geothermal energy in Djibouti. The Government plans to exploit the geothermal resources in the Assal region to enable public access to a reliable, renewable and affordable source of energy. The Assal-Fiale geothermal project is located on a site that has scientific, ecological and tourist importance. Using the geothermal resource is believed to be a positive way to generate electricity in the area but improper management of the resource can cause possible negative impacts on the environment. Environmental impacts assessment will help to understand and minimize negative impacts of the project and with good management can support the environmental, economic and social goals of sustainability. This report presents the possible environmental impacts of the project and their management which aims to minimize them in accordance with national and international regulations and the geothermal utilization experience gained in Iceland.

1. INTRODUCTION

1.1 Purpose of this study

The geothermal potential in Djibouti is estimated around 1000 MWe, distributed among thirteen sites and mainly located in the Lake Assal region. The government's plans, with its first geothermal project, are to exploit the geothermal resources in the Lake Assal region to enable public access to a reliable, renewable and affordable source of energy. The aim of the project is to quantify the technical and financial feasibility of using geothermal resources of the Assal Rift for mass production of electricity. The project includes an exploration drilling program of four production wells in the area of Fiale, north of Lava Lake.

The Assal-Fiale geothermal project is located on a site that has scientific, ecological and tourist importance. Using the geothermal resource is believed to be a positive way to generate electricity in the area but the utilisation of the resource can cause possible negative impacts on the environment.

Therefore, the evaluation and the management of environmental impacts will help to minimize the possible negative impacts of the project and can support the environmental, economic and social goals of sustainability. The study will provide information on the process of assessing the environmental impacts and implementing appropriate mitigation actions and their management.

1.2 Objective

The goal of this study is to:

i. improve knowledge regarding the EIA process and implementing appropriate mitigation actions;
ii. improve the monitoring at the different stages of the projects development;
iii. create an Environmental Management Program which identifies the possible key environmental and social impacts associated with the development of the geothermal field in Assal-Fiale in Djibouti and minimises negative impacts with good management. Some comparison will be to Hellisheidi, Svartsengi and Reykjanes geothermal fields in Iceland.

1.3 Scope/methodology

The research work consists of a literature review, observing the similarities with comparable projects in Iceland and other countries in order to find the most common and important impacts. Leading experts in the geothermal field in Iceland, including chemists, geologists and experts on environmental impact assessments were consulted to understand better the possible effects of a geothermal development in the area and how to prepare the project to minimize negative impacts.

The environmental aspects of the Assal project are essentially covered in the following sources: (Fichtner, 2012), (REI, 2008) and (AFDB, 2013). Other main sources used are (Van Nguyen et al., 2015) and (Hunt, 2000).

In the table below is a list of the persons that were interviewed or got written questions and whose answers are in Appendix I.

TABLE 1: Persons interviewed or contacted

Person interviewed	Organisation	Type of function	Date	Contact information
Thoroddur F. Thoroddsson	National Planning Agency	Specialist, Environmental Assessment	August-October	doddifr@gmail.com
Jónas Ketilsson	Orkustofnun	Expert geotherm. utilization	October	jonas.ketilsson@os.is
Ómar Sigurdsson	HS Orka	Reservoir engineer	September – October	os@hsorka.is
Hólmfrídur Sigurdardóttir	Reykjavik Energy	Head of Environmental Affairs	September	holmfridur.sigurdardottir@or.is
Halldór Ármannsson	ISOR	Geochemist	October	halldor.armannsson@isor.is

2. LITERATURE REVIEW

2.1 Geothermal system

Geothermal energy is described as a clean, sustainable and renewable resource that provide energy using heat derived from the earth. An important exploitable source of geothermal energy are the reservoirs that form underground when groundwater trapped along fault lines, fractures in the rocks and porous rock is heated by magma that has been pushed up from the earth‘s core (Van Nguyen et al., 2015).
The use of geothermal resources is divided into two main groups:

- Direct use: geothermal reservoirs of low to intermediate temperature (20-150°C) are exploited, either with heat pumps or directly for heat production (houses in cold climates). Electricity is also generated using intermediate-temperature (70-149°C) geothermal resources (and binary electric generation).
- Power generation: High temperature geothermal reservoirs (150-300°C) are exploited for indirect use by producing electricity.

There are three main categories of geothermal power plants, depending on the chemistry, fluid temperature and pressure involved (Van Nguyen et al., 2015):

- Condensing power plants, with dry steam and single- or double-flash systems;
- Back-pressure turbines, which release into the atmosphere; and
- Binary plants, which use lower temperature water or separated brine.

2.2 Geothermal energy development

Whatever technology is applied (which is mainly depending on the properties of the geothermal fluid), the main phases of the development are (Rybach, 2003):

1) Exploration:
This is the first step in the development of a geothermal area and the goal is to gather as much information on the geological, geophysical and geochemical characteristics of the field to help reduce the risk in the next phase (the drilling). The impacts of this phase is generally temporary and of relatively small magnitude, because of the little interaction with the environment or the short duration of these activities. Impacts resulting from exploration activities can be associated with the development of access roads, if needed, including: localized ground clearing, vehicular traffic and noise producing activities.

2) Production test or drilling and well testing:
Most impacts resulting from these activities can be associated with the development of access roads, exploratory and flow testing wells (Ármannsson and Kristmannsdóttir, 1992). These include: localized ground clearing, vehicular traffic, seismic testing, positioning of equipment, drilling and emission of non-condensable gases and drilling muds. Most of these impacts can be mitigated or reduced by the use of good industry practices and by restoring the disturbed areas once the drilling and testing have been completed.

3) Construction:
Impacts during construction phase are more extensive but similar to the ones present during the exploration and drilling/testing. Most of the land disturbing activities occur during the construction phase because the need of removing and contouring land and the use of heavy equipment. The workforce needed during this phase is also high, compare to other phases. Depending on the location of the site it could cause negative impacts. Activities during the construction that may cause impacts include site preparation (e.g., clearing and grading); facility construction (e.g. geothermal power plant, pipelines, transmission lines, drill pads); and vehicular and pedestrian traffic. The construction of the

typical 50 MW geothermal power plant would disturb about 6 to 10 hectares of land. Transmission line construction would disturb about 0.5 hectares of land per mile of line.

4) Operation and maintenance:

Normal activities during this phase, in a typical power plant could be, operation and maintenance of production and injection wells and pipeline systems, operation and maintenance of the power plant, waste management, and maintenance and replacement of facility components. Possible impacts due to these activities are related to noise, water demand, waste management, land use conflicts, visual effects of facilities and steam plumes, potential spills and increased traffic at the project site.

5) Decommissioning and site reclamation:

Geothermal power plants have to be dismantled and removed from their sitting sites after their normal useful life, this procedure is known as the decommissioning, after this the site has to be restored to its original state (or approximately its original state in accordance to what has been stated in the environmental national and local law) in a process known as reclamation. Typical activities during the decommissioning/reclamation phase include closure of all facilities and wells; removal of above ground components and gravel from well pads, access roads (if not maintained for other uses), and other ancillary facility sites; re-contouring the surface; and re-vegetation. Also, remediation of contaminated sites is an activity done in this phase if any accidental spillage of toxic substances occurred during the other phases and has not yet been cleaned or dealt with. The impacts caused by these activities would be similar to those listed for the construction phase because the use of heavy machinery is also needed; however, most of these impacts would have a lower magnitude and because of the relatively short period of time in which this phase is completed. The procedure of restoration of the environment during the decommissioning and reclamation phase would have to ensure that the impacts of the geothermal development would not go beyond the life span of the power plant and that those impacts remaining after the removal of all structures are minimized, mitigated and compensated if necessary (Hunt, 2001).

2.3 Potential environmental impacts of energy development

The potential impacts of geothermal energy development depend on many factors, such as how special the environment is, how sensitive it is, the use of the land, people affected, and the size of land used for access roads and drilling, the construction activities implemented, the number of well pads and the technology in the power plant. The environmental impacts may be positive or negative, temporary or long term, irreversible or not and include e.g.:

- *Landscape and land use:* due to the land disturbance related to the construction of power plants and transmission lines. Pressure drop and decreased production of wells in the area, can call for new wells to be drilled every year. This could lead to expanded production area or increased pressure to drill in more sensitive areas than was originally planned.
- *Ecological resources:* when construction activities destroy or disturb wildlife by disturbing feeding, breeding and migration patterns, reduce habitat quality and species diversity, both flora and fauna.
- *Gaseous emissions:* resulting from the discharge of non-condensable gases. The most common gases are carbon dioxide (CO), hydrogen sulphide (H_2S) and other low-concentration gases such as methane, hydrogen, sulphur dioxide and ammonia (Van Nguyen et al., 2015).
- *Water pollution:* dissolved minerals in the geothermal water, both high quantity of common minerals like in sea water and low concentration of heavy metals that can be poisoning e.g., boron, mercury and arsenic. The chemicals in the geothermal fluid generated during exploration, testing and production phases may poison surface or groundwater. They can harm people, drinking water and also flora and fauna on dry land or in lakes and rivers (MIT-led interdisciplinary panel, 2006; Van Nguyen et al., 2015).
- *Noise pollution:* primary sources of noise are associated with exploration activities such as the well drilling and testing when noise levels are in the range of 80-115 decibels at the site boundary

(Van Nguyen et al., 2015). Severe noise can also be during maintenance in the power plant during operation time.
- *Solid waste: e.g. c*uttings from the drilling, used oil and building materials.
- *Land subsidence, seismicity:* during the production phase the pressure drop in the geothermal system has in some areas lead to land subsidence, increased seismic activity is e.g. known in connection with reinjection, especially if the injection water is pumped down in large amounts and under high pressure.

2.4 Environmental Impact Assessment (EIA)

Focus on environmental protection has increased more and more in the last 40-50 years and was the goal of the United Nations Summits in Rio (1991), Kyoto (1997) and Johannesburg (2001). In 1971 the first act of EIA came in to force in USA. In the following years the EIA process was introduced in the legislation of many countries, e.g. in Iceland 1994 which is in accordance with EU-directives. Many countries have adopted their own Environmental Impact Assessment (EIA) procedures and it is now as a tool that is most widely used in the preparation stage of projects and a part of environmental management.

The World Bank and several other financing institutions have also adapted the EIA process to their standard procedure which must be fulfilled if the plan is to get a project financed by them. All of this is supporting nations to take better care of the environment in the spirit of the UN summits.

The EIA process identifies the impacts of a proposed project during construction and operational phases. An EIA considers short-, medium-, and long-term impacts, local and global impacts, as well as direct, indirect, secondary, cumulative, permanent and temporary, positive and negative effects of the project (Heath, 2002). It is known that exploration and later utilisation of geothermal areas, can have negative impacts on the environment. Possible impacts must therefore be identified, quantified and if necessary avoided or mitigated in order to comply with environmental regulations.

3. OVERVIEW OF GEOTHERMAL EXPLORATION IN DJIBOUTI

3.1 History of geothermal exploration

The Republic of Djibouti has an exceptionally geological context favourable for the development of geothermal energy. Djibouti is located in the Afar depression at the junction of three important tectonic structures: The Eastern Africa Rift zone, the Red Sea Rift and the Gulf of Aden (Figure 1). The rift zone is still expanding by about one millimetre per year. This geodynamic context of rifting is characterized by intense volcanic activity and geothermal manifestations marked by fumaroles and hot springs found in different parts of the country. The exploration of the geothermal activities has a 40 year long history in Djibouti and can be divided into six major steps:

- 1970 to 1975: The first exploration drilling was in 1975 by BRGM including two exploration wells in the Assal area (Assal 1 and 2). The two wells have shown good temperatures but only one of them has produced geothermal fluid (Assal 1) but too salty.
- 1980 to 1985: The Djibouti government conducted a detailed general inventory of geothermal resources and several areas of interest were identified, including Assal, Hanlé, Lake Abbé, Obock, North Goubbet, Dorra, and Arta.
- 1987 to 1988: The second deep geothermal exploration was conducted by AQUATER. Two wells were drilled in Hanle (Hanle 1 and 2) and three wells in the Assal Rift (Assal 3, 4, 5). One exploration well was also drilled by ISERST in the Assal Rift (Assal 6). The Hanlé wells were

negative (no geothermal gradient). The wells Assal 3 and 6 have proven to be productive but the wells Assal 4 and 5 dry but with too high temperatures (359°C).

- 1989 to 1990: A geothermal scaling/ corrosion study was carried out on well Assal 3, with the objective to assess the effect of scaling and corrosion and to study possible ways to reduce the negative impact of the salinity (Virkir-Orkint, 1990).
- In 1995: Further TEM measurements were carried out in a part of the Assal region in order to understanding better the sub-surface structures (Árnason and Flóvenz, 1995).
- 2007 to 2008: A prefeasibility study was carried out in the Assal rift by Iceland GeoSurvey and Reykjavik Energy Invest (REI). The geological (Khodayar, 2008) and geophysical (Árnason et al., 2008) results of the prefeasibility phase identified Fiale caldera in the Assal rift as a favourable production sector. (Figure 2).

FIGURE 1: The East African Rift and location of Djibouti. Volcanoes (red triangles) with known inferred Holocene eruptions (Smithsonian Institution, 2013)

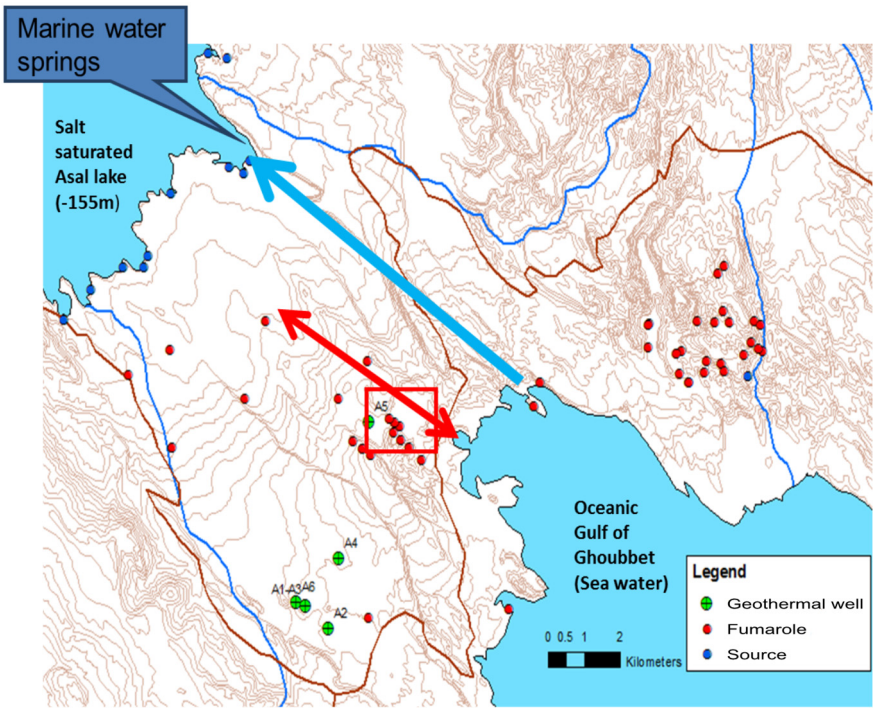

FIGURE 2: Location of the drilled sites (in green, numbered) and main fumaroles (red dots) of the Assal rift on the topographic map. The first wells (A1 to A3) and later A4 et A6 were drilled on the SE side of the rift, at a fair distance from the active volcanic axis of the rift (double red arrow) as well as from the seismo-tectonically active axis along which an important ground sea water flow cross through from Ghoubbet to Lake Assal -155m b.s.l. (blue arrow). The site of the present feasibility project is the red square (source: J. Varet ARGeo-C5)

The results from these six wells have shown the existence of a shallow geothermal reservoir and a deep reservoir. The shallow reservoir at depth ranging from 240 m to 600 m is showing high permeability and temperatures between 140 and 190°C, but has not been tested. The deep reservoir is situated below 2000 m depth with temperatures ranging from 250 to 360°C. The geophysical data correlated with the well logs is suggesting a continuity of the shallow reservoir in the whole rift area, which is not the case for the deep reservoir (Orkustofnun, 1988). Comparison of the chemical and temperature data shows that the shallow reservoir was thermally protected and with a salinity around 50g/l. The depth to the magma chamber is between 2 and 5 km depth. The geothermal gradient observed, has a thermal anomaly characteristic of large global geothermal fields, it is 25°C/100 m. The values of the heat flow obtained are 3.9 Mcal/cm²/s. The seawater flowing through fractures in the rift of the centre tends to lower the surface gradient.

The geophysical survey done by ISOR for Reykjavik Energy Invest (2008) enabled the elaboration of a new conceptual model taking into consideration available data including the results from the previous deep drilling. This allowed sitting the 4 exploration wells that are now planned in the central part of the rift axis within Fiale caldera and its immediate surroundings. After REI withdrew its interest in the project, the program was taken as a base of reference for the World Bank to propose the feasibility study presently being engaged. Following these references, 4 wells have been planned to be drilled down to 2800 m with large production diameters (9 inches) and deviated in the reservoir (below 2000 m) in order to maximize the chances to intersect open productive fissures supposedly vertical in this axial part of the rift.

3.2 Assal-Fiale geothermal project

3.2.1 Objective and location

The Assal-Fiale geothermal project is located in the Fiale area, with a focal point in Lava Lake, a circular depression filled with young lava flows, where maximum spreading takes place in the Rift and with intensive micro earthquake activity. This area is the focus of the planned exploration-drilling project due to a set of observations that point towards a possible good resource. Firstly, coexistence of large and active faults, intersection of fault systems, a high resistivity anomaly underneath a low resistivity layer, lava production centre and seismic and fumaroles activity. Secondly the brine is expected to have salinity close to that of seawater and lower than in wells 1 and 2 in the old wellfield and therefore better suitable for utilization. Finally, the Lava Lake resistivity anomaly appears to be on the order of 4 km^2 at 1000 m depth and enlarges when going deeper. It should therefore prequalify as a resource that can support a minimum of 50 MW station, using a conservative 10 MW/km^2 generating capacity as a reference.

Based on the conceptual model from pre-feasibility study four well locations were determined and drilling targets were specified.

The objective of the planned exploration-drilling project is to quantify the technical and financial feasibility of using the geothermal resources of Assal rift for mass production of electricity. The project comprises an exploration drilling program of 4 production wells in Fiale region north of the Lava Lake.

The primary objective is to reach and test the intermediate/shallow reservoir (at 240 to 600 m). The temperatures there are ranging from 140°C to 190°C which is high enough to generate electricity for commercial purposes using a binary cycle power plant.

3.2.2 Project phases

The Assal-Fiale geothermal project is part of a geothermal energy development program aimed at improving the quality of life for the public in Djibouti by increasing access to electricity through an

expansion of the national energy production capacity. Structured as a public-private partnership (PPP), the programme will be executed in 3 phases:

(i) Phase I comprises the exploration of the Lake Assal geothermal vapour field and confirmation of the characteristics of the field's geothermal resources;
(ii) Phase II involves the development of the geothermal field and construction of a geothermal power station with an installed capacity of 20 MW;
(iii) and Phase III will involve expanding the capacity of the geothermal power station to 50 MW.

Phase I, financed with concessional resources, is currently ongoing and is aimed to minimise exploration risks in order to pave the way for private sector participation under Phases II and III.

3.2.3 Main components and activities in Phase I

Phase I of the project will comprise the following components: (A) Drilling activities; (B) Technical assistance; (C) Project implementation; and (D) Environmental and social management. This phase will be executed until May 2016. The geothermal power station, which will be developed in Phases II and III, and financed by a private investor, is planned to be implemented once the geothermal resource has been confirmed by the feasibility study in Phase I.

TABLE 2: Description of activities in Phase I

No.	Component name	Component description
A	Drilling activities	Execution of a drilling programme for 4 exploration/production wells, including civil engineering works, drilling services, procurement of equipment and testing.
B	Technical assistance	Recruitment of an expert to develop the exploration programme, including drilling, testing and the feasibility study for the geothermal power station
C	Project implementation	Operation of the Project Implementation Unit (PIU), including costs related to the recruitment of the International Manager of the PIU.
D	Environmental and social management	Execution of the Environmental and Social Management Plan

Main construction phases:

- Construction of an access road from the Djibouti-Tadjourah RN9 highway to the drilling sites;
- Opening of one or more quarries to obtain backfill material;
- Construction of 4 drilling platforms, each having a surface area of 6,000 to 10,000 m^2. To each platform will be added two watertight tanks, one for mud (1,000 m^3), and the other for collecting geothermal fluids produced during production tests (2,000m^3). In event of a positive drilling result, the equipment needed to conduct various tests, such as a separator and a silencer, as well as fluid processing equipment, will also be installed on these platforms.
- Preparation of the land at least for storage of equipment and/or temporary premises for the drilling team;
- Drilling works (4 boreholes created through rotary directional drilling with an initial diameter of 23 inches, a final diameter of 9 inches, and a target depth 2000 to 2,500 metres).
- Laying of discharge pipes for geothermal fluids, and a water intake pipe for preparation of drilling mud;
- Establishment of a camp for workers and security officers.

3.2.4 Development phase

The intermediate goal is to commission a 50 MW plant in Djibouti. Once the capacity of the source has been confirmed with drilling, the project will proceed by continuing drilling production and re-injection

wells in the area as well as having conceptual design done of the resource and the power plant (Figure 3). The development consists of access roads, service roads, production wells, water supply system, steam transmission pipes, steam separator stations, power house, cooling towers/units, steam exhaust stacks, a groundwater supply system, water tanks, hot-water transmission pipe, quarrying, storage site, discharge system, injection areas and connection to the power grid (Hjartarson et al. 2010).

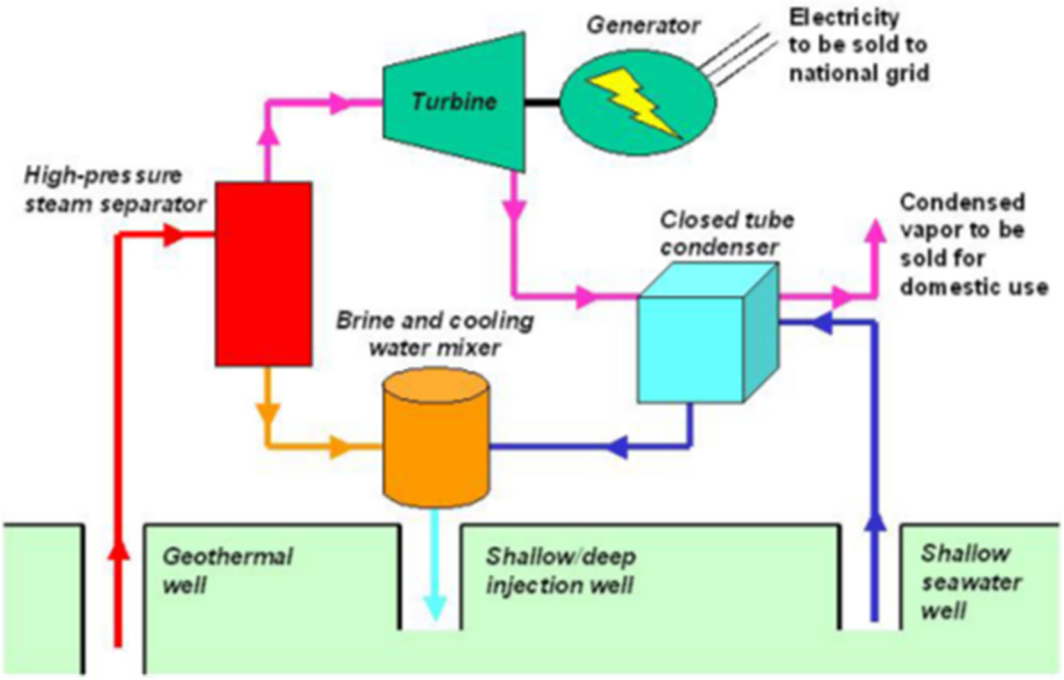

FIGURE 3: A conceptual design of a power plant proposed by Reykjavík Energy Invest, 2009 (Hjartarson et al., 2010)

4. ENVIRONMENTAL CHARACTERISTICS OF THE ASSAL GEOTHERMAL AREA

4.1 Physical environment

Geology

The Assal geothermal system is located on the isthmus between Lake Assal and Ghoubbet el Kharab gulf (Figure 4) at a distance of about 120 km from Djibouti City. Altitudes range from -151 m at Lake Assal to +300 m at the highest point of the Rift valley floor. The area is bounded by the high plateaus of Dalha to the north (above 1000 m elevation) and by 400-700 m high plateaus to the south. The most remarkable signs of recent and current volcanic activity in the Assal Rift are the presence of hot springs, fumaroles, various craters and the Ardoukoba volcano that started erupting in November 1978.

Seismicity

Because of the peculiar tectonic situation, the Assal Rift is impacted by tectonic faults, that are still active and the area is a very seismically active region. Earthquakes are quite frequent although their intensity is low. The region was hit by an earthquake in March 1992 that rippled through the Gulf of Tadjourah, with its epicentre located at sea, 2 km off the coast of Arta, and seismic tremors that exceeded 4 on the Richter scale. These earthquakes did not cause much damage. The average period of occurrence of an earthquake with a magnitude exceeding 5 in a given region is estimated 16 years (± 5

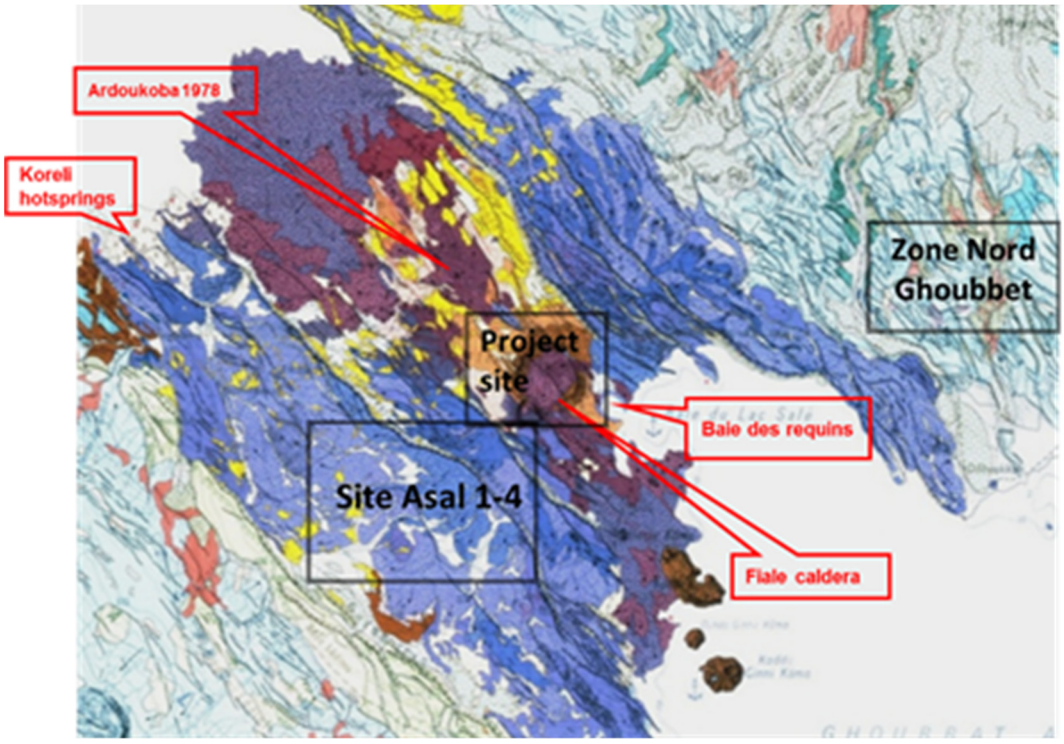

FIGURE 4: Geological map of the Assal Rift (Stieltjes, 1978); hyaloclastites are in orange, recent basalts in deep blue and violet. Early rift basalts (300.000 – 100.000 y.) are in pale blue; the stratoid series (3 to 1 My) is in very pale blue colour; lacustrine deposits (diatomite) in yellow

years). A magnitude of 6 on the Richter scale is estimated to be the maximum for the Gulf of Tadjourah (Didier, 2001).

Climate and water resources

The region is arid desert, with an average rainfall of 130 mm per year, but can be highly variable in certain years. The climate, which is far from uniform all over the national territory, varies over time and with each region. Generally, the climate in the coastal regions is characterized by a cold season (from October to April) and a hot and dry season (from May to September).

Humidity ranges between 40% and 90%, while average air temperature is 25°C in winter and 35°C in summer. The quantity of fresh water resources in the project area is very limited because of low rainfall. The groundwater in the Lake Assal region is of poor quality, with a salinity of >2.000 mg/l (CERD, 2009). Hydrogeological studies of the region show a general groundwater flow towards Lake Assal, which is the lowest point of the area, and is a salty lake saturated with sodium chloride and calcium sulphates.

4.2 Protected areas and ecosystems

Djibouti has currently 7 protected areas comprising 4 on land (Day and Mabla forests, Lake Abbé and Lake Assal) and 3 at sea (the Islands of Musha and Maskali, Sept-Frères-Khor Angar-Godoria and Harramous). They are all classified as protected areas under Djibouti law, but do not directly match the categories of the IUCN.

Lake Assal

Lake Assal, is situated 155 m below sea level in a volcanic area. It is the third deepest depression in the world and is considered to be one of the geological wonders of the country. Lake Assal is surrounded by an expanse/area of solid salt of variable thickness that exceeds 60 metres at certain points with a surface area of 60 km^2. This briny body of water, which is saturated with mineral salts (up to 340 g/l), has a surface area of 50 km^2 and a maximum depth of 25 m. Its reserves are deemed to be inexhaustible,

since 6 million tonnes of salt flow in each year (filtering in from Ghoubbet sea and from brackish hot springs). From time immemorial, this lake has always been a focus of interest to the nomadic peoples of the region whose main livelihood is small-scale mining of salt that is exported by caravan to Ethiopia.

Lake Assal has been declared a protected area under Articles 1 and 7 of Law No. 45/AN/04/5L. Nevertheless, the exact boundaries of the protected areas and their managerial measures/conservation strategy have not yet been defined. There is no accurate map of protected areas in the country. The statute determining the protection boundaries of Lake Assal has not been adopted, but provision is made for protecting the lake itself and its salt banks (solid salt expanse). The distance between the drilling site and the banks of Lake Assal is approximately 8 km. The proposed drilling site is located (maximum 1 km) close to the area where water from Ghoubbet sea filters into Lake Assal.

Ghoubbet-Kharab
Ghoubbet is a sensitive ecological area separated from the Gulf of Tadjourah by a narrow strait that is 40 m wide and 40 m deep. Ghoubbet sea is more than 200 metres deep. Sea water salinity ranges from 39.3 g/l at a depth of 125 m in November to 37.7 g/l at the surface in June. Surface temperatures fluctuate between 28°C and 30.5°C. Ghoubbet is a potential marine protected area according to Ministry of Housing, Urbain planning and Environment (MHUE). The distance between the drilling site and Ghoubbet-Kharab is an approximately 2 km airline and 5 km by road.

4.3 Biological environment

Flora
In general, the vegetation of Assal-Ghoubet region is grass and shrub steppe with *Dracaenae ombet*, *Acacias tortilis* and *mellifera* as well as *Acacia asak* in the more humid areas. Acacia leaves are the main food for goats. The land around the proposed drilling site and around "Lava Lake" is uneven terrain, covered mainly by basaltic lava with very little vegetation in general.

Fauna
The presence of wildlife in the Lake Assal is limited to the confluence of springs flowing into the lake where the water is less saline. The presence of small fish (*Cyprinodon* sp.) has been confirmed.

The Ghoubbet marine basin is a spawning area for most pelagic fish and coral reef fish of Djibouti (National Monograph, 2000). Ghoubbet is the habitat of several species mentioned in Decree No. 2004-0065/PR/MHUE on the protection of biodiversity, especially dugongs, dolphins, turtles, sharks and whale sharks *(Rhincodon typus)* which deserve special protection.

4.4 Socio-economic environment

The Fiale caldera, located near the scheduled drilling area, is used as pastureland by the local community and transhumant herds. At the same time, the site is also traversed by the access road leading to the Ardoukoba volcano and Lava Lake which are sites of touristic interest (African Development Bank, 2013).

Human and socio-economic environment
The project is located in Tadjourah region, 79 km from Tadjoura town and 127 km from the capital. It is 7 km away from the border of the Arta region and 25 km away from Karta village (Arta region), where the nearest school is found. The closest community is currently located at Daba le Gahar (76 households) on the former camp site of the Yugoslavian company that built the RN9 highway, situated approximately 5 km from the proposed drilling site. The total population of the villages of Daba le Gahar, Laïta and Ardoukoba (called Carrefour) is 298 "sedentary" households who still mine salt using caravans. In addition to the settled population, 248 "semi-nomadic" households (practicing

transhumance) live in the area. The population of the study area is 546 households, the closest of which live in Daba le Gahar, 5 km from the proposed drilling site. Traditionally, the Assal zone is not recognized as a permanent settlement site because of its harsh climatic conditions, lack of drinking water and scanty vegetation.

In the past, it used to be a periodic transit area between two seasons (cold season and hot season) used by transhumant herders as they moved from North to South or from South to North. There are no basic services, no basic infrastructure, no health posts or schools. However, it was also the area that experienced the first intensive salt extraction activities. The region had the greatest number of caravans travelling from the salt banks of Lake Assal to Ethiopia.

The important archaeological sites within the region are concentrated along the Ghoubbet coast, South-East of the study area.

In the project area, there are several tourist attractions of varied potential:

- Lake Assal and the salt caravans;
- "Lava Lake";
- Ardoukoba volcano with its peculiar geology;
- Ghoubbet-el-Kharab, the shark pool, Devil Island;
- The camps of “Dankalêlo / Ghoubbet” and “Afar Rift”.

Drinking water
The leading priority for the local population is drinking water. There is no drinking water source, since groundwater is saline. The villages are supplied with water only once a week by a tank truck from the regional administration.

Education
There is no school in Assal sub-prefecture. Children from the villages attend the nearest school in Karta (15 km). Out of the 170 in the communities, 59 children attend school. Since there is no school bus, the children trek to and from school.

Health
There are no statistics on the health situation of Assal region. Public health is not developed. There is no dispensary/health centre in Assal sub-prefecture. In theory, an ambulance service exists in Tadjourah town, but because of the long distance, it is expensive and in fact unavailable.

Electricity
The villages have electricity only when there is gasoil for an existing generator (at least for some households). The project for building interconnection lines from the future geothermal power station will not improve the situation in the villages unless a low-tension line for rural electrification is constructed.

5. ENVIRONMENTAL REGULATION APPLICABLE TO THE ASSAL-FIALE PROJECT

Djibouti's environmental policy is based on laws, agreements and international treaties that contribute to socioeconomic development of the country. Since the 2000s, many national and international laws were adopted.

5.1 National legislation

The Assal geothermal project will have to comply with the following regulations regarding the environment:

- Act No. 106/AN/00/4L on the environmental CODE 2009;
- Act No. 45/AN/04/5L on terrestrial and marine protected areas;
- Act No. 66/AN/94/3L on the mining code;
- Decree No. 2004-0092/PR/MHUE establishing the National Commission on Sustainable Development (CNDD);
- Decree No. 2001-0011/PR/MHUE on environmental impact studies;
- Decree No. 2011-029/PR/MHUE revising the assessment procedure of environmental impact.

Environmental Code Act:
Law No. 51/AN/09/6th L on the Environmental Code is to set the ground rules and basic principles of national policy in the field of protection and management of the environment in order to ensure sustainable development, in accordance with multilateral environmental agreements.

In this project, the Articles 19-26 concerning the protection and preservation of water resources as well as Articles 27-31 concerning the protection and conservation of the soil and subsoil require special consideration.

In Articles 75-88, the Environmental Code specifies the status and treatment of waste.

In Articles 39-41, the Act to the Environmental Code also strengthens the protection and preservation of plant and wildlife.

According to the Environmental Code, the creation of protected areas Land and Marine enacted thereunder Law No. 45/AN/04/5th L remains in force.

Protected Areas Act:
Act No. 45/AN/04/5th L Establishment of Protected Land and Marine Areas. Under the special provisions of the Convention on Biological Diversity, the Ramsar Convention on Wetlands and the Framework Law on the Environment, Terrestrial Protected Areas, and the sites below have been listed:

- Forest Day;
- Forest Mabla;
- Lake Abbé;
- Lake Assal.

The draft report the Ghoubbet-Kharab as a marine protected area has been communicated by the MHUE, but to date there is no documentation of these forecasts.

Mining Code:
The Mining Code No. 66/AN/94/3L, establishes the exclusive ownership of the state over all land resources and the earth and marine subsoil whose management and operation are ensured by public authorities (Article 2 of Law No. 66/AN/94/3L).

The Code grants licenses for prospection ("research"), exploration, mining development, and refining and smelting.

Articles 11-13 of the Code specifically apply to mineral and geothermal waters and brine. These grant the Government the right to authorize prospection, exploration and development/utilisation of these resources according to rules and formalities to be specified by specific Government order. Accordingly,

the Government may decree the provisions of the Law that it deems appropriate to be applicable. The volume of mineral water, geothermal fluid, or brine to be produced and its calorific value will be subject to government authorization. The mode of extraction of secondary products (contained minerals) and of the production and use, as well as the reinjection of waste geothermal fluid may also to be determine.

This Code is supplemented by Decree No. 97-0064/PR/MIEM "permit and the taxation of research-related activities, exploration and mining".

Environmental Impact Studies (2001/2009/2011):
A national law and two decrees address the issue of environmental impact studies:

a) The Law No. 51/AN/09/6th L Environmental Code Chapter VII: "Integration Mechanisms for Environmental" provides details with respect to environmental studies and evaluation. The environmental impact study should include at least:

- An analysis of the initial state of the site and its environment;
- A project description;
- A study of changes that the project is likely to generate, and measures considered to remove, reduce or offset the negative impacts of the activity on the environment and health;
- A cost of these measures before, during and after the project;
- An achievement of an environmental management plan;
- A public hearing.

b) Decree No. 2001-0011/PR/MHUE is concerning definition of the environmental impact assessment procedure and the environmental management of major projects. This decree targets mainly:

- The integration of environmental concerns in all phases of a project, from design to post-closing through its operations;
- Inventorying all change vectors in the project area;
- Identification of any negative impacts and/or positive and suggest consistent and sustainable mitigation.

The decree emphasizes the obligation of the environmental impact study and due process for all projects, whether public or private, consisting of works, facilities, agricultural, mining, crafts, commercial or transport, whose implementation is likely to harm the environment.

c) Decree No. 2011-029/PR/MHUE revises the environmental impact assessment procedure and specifies as follows:

- in Article 4, the Ministry of Environment is responsible for the categorization of EIA. The decree divides the EIA in 2 categories (summary and detailed);
- in Articles 5 and 6 the necessity and procedure of environmental permit by the Ministry in charge of environment. The environmental permit is issued for a period of five years from the start of the project and is renewable after an environmental audit.

The procedure for developing and approving the impact study is defined in Title IV, Articles 12-29 of the Decree, including information on public participation and organization of a public hearing meeting. Surveillance and environmental monitoring are covered in Articles 30-34, stating the specifications, institutional responsibility and the Environmental and Social Management Plan (ESMP) accommodations. A possible modification of original project requires a new environmental impact assessment according to Article 37.

In accordance with Articles 35-38, the sponsor must at the end of the project, conduct an environmental audit, the implementation arrangements will be decided by the Ministry of Environment in

environmental technical guidelines. The audit report must be submitted to the Ministry of Environment for review and issuance of environmental discharge.

The audit and its environmental management plan are sanctioned by an environmental discharge by the Ministry for the Environment. The Environmental Management Plan resulting from the audit is a set of specifications for the developer.

National Action Program on Biological Diversity:
The Government also adopted Decree No. 2004-0065/PR/MHUE of 22 April 2004 on the protection of biodiversity. The decree made under the Convention of Biological Diversity, lists the animal species, endemic or endangered, and as such benefiting from special protection.

The decree stipulates that the hunting, capture, trade, export, and import of these species and their products are prohibited. The decree also states that the felling, removal, bleeding, and plucking of endemic or endangered plant species is strictly prohibited.

The enforcement of this decree is provided by Directorate of Physical Planning and Environment with the support of the departments concerned.

In accordance with Articles 1 and 7 of Law No. 45/AN/04/5L, Lake Assal is a protected area. The exact boundaries of protected areas in Djibouti and management measures are not yet established and there is no exact map of protected areas and will be detailed in regulations. The regulation determining the Lake Assal protection limit has not yet been enacted.

5.2 International legislation

International Conventions and Treaties which Djibouti has signed and ratified will also need to be respected during the execution of the project:

- The United Nations Convention on Biological Diversity (1992);
- The United Nations Framework Convention on Climate Change (1992);
- The Kyoto Protocol to the United Nations Framework Convention on Climate-change;
- The RAMSAR Convention on Wetlands and bird species that live there (1971);
- The Basel Convention on the Control of Transboundary Movements of dangerous waste;
- The Convention on Migratory waterbirds;
- The United Nations Convention on the Law of the Sea;
- The International Convention on trade in animal and plant species with extinction (1973).

World Bank Operational Policies applied in the Environmental Assessment:

a. 4.01 "Environmental Assessment";
b. 4.04 “Natural Habitats”;
c. 4.11 “Cultural Property”;
d. 4.12 “Involuntary Resettlement”;
e. 4.10 “Indigenous People”;
f. Environmental, health and safety guidelines of the World Bank group for geothermal power generation (DRAFT Environmental and Social Management Framework for the ARGeo project);
g. The “Equator Principles”.

5.3 Standards

The Assal geothermal project must comply with the following regulations regarding the effluent discharge, gases emissions, and noise:

- Environmental, Health and Safety Guidelines Mining, IFC/World Bank, 2007;
- Human exposure limit of WHO, IFC/WB;
- The World Bank and the African Development Bank safeguard policies.

5.4 Environmental screening

According to the decree no. 2001-0011/PR/MHUEAT on Environmental Impact Assessment, thermal power stations (category 7 of the Annex) are subject to environmental impact study. However, drilling of geothermal wells is not listed in the Annex.

The World Bank undertakes environmental screening of each proposed project to determine the appropriate extent and type of Environmental Assessment. The Bank classifies the proposed project into one of four categories, depending on the type, location, sensitivity, and scale of the project and the nature and magnitude of its potential environmental impacts (The World Bank Operational Manual OP 4.01, 1999).

a. Category A: If the proposed project is likely to have significant adverse environmental impacts that are sensitive, diverse, or unprecedented. These impacts may affect an area broader than the sites or facilities subject to physical works. The proposed project requires full Environmental Assessment.
b. Category B: If the proposed project's potential adverse environmental impacts are less adverse than those of Category A projects. These impacts are site-specific; few if any of them are irreversible; and in most cases mitigation measures are readily designed. The proposed project requires a more targeted Environmental Assessment or just an EMP.
c. Category C: If the proposed project is likely to have minimal or no adverse environmental impacts. The proposed project is beyond screening, no further Environmental Assessment actions are required.
d. Category FI: If the proposed project involves investment of Bank funds through a financial intermediary, in subprojects that may result in adverse environmental impacts.

It should be stressed here that according to the Icelandic Environmental Impact Assessment Act no. 106/2000, which is in accordance with the European Union Directive 85/337/EEC and 97/11/EC the following applies:

- Drilling of production/research wells in high-temperature geothermal regions are projects which *may be subject to* environmental impact assessment and are assessed on a case by-case basis.
- Geothermal power plants with a heat output of 50 MW or more and other power installations with an electricity output of 10 MW or more *shall always be subject to* Environmental Impact Assessment.

When considering the type and scale of the drilling and testing of the four geothermal wells in the Assal area, the rating of the sensitivity of the proposed site and taking the experience of the impacts of similar projects in Iceland into account, REI's opinion is that the drilling and testing of the feasibility study should be classified, according to the World Bank as Category B project.

5.5 Responsible authority

The Ministry of Housing, Urban Development, Environment and Land Use Planning (MHUEAT) is in charge of environmental issues. According to article 5 in the decree no. 2001-0011/PR/MHUEAT the Minister for the Environment grants a development permit.

The implementation of the national policy for the protection of the environment and for a sustainable development of the country is under the responsibility of the Prime Minister. A decision on

Environmental Assessment and grant of a development permit for drilling and testing of geothermal wells has to be based on a common decision between numerous administrations like:

- The Ministry of Housing, Urban Development, Environment and Land Use Planning (MHUEAT);
- The Ministry of Interior;
- The Ministry of Energy and Natural Resources;
- The Ministry of Water, Agriculture, Livestock and Sea;
- The Ministry of Youth, Sports and Tourism;
- The municipalities Tadjourah and Dikhil. The proposed drilling and testing site for the drilling operation of the feasibility study is in the Tadjourah municipality. The Dikhil municipality border is only few km away as the border between these two districts runs alongside Lake Assal's southern shore and ends at the Ghoubbet El Kharab basin. Both communities will be actively involved in the project as the camp sites and other logistic activities may be in the Dikhil municipality.

5.6 Comparison of EIA process in Iceland and Djibouti

The first law on Environmental Impact Assessment in Iceland is from 1994. Major changes were done in the new law no. 106/2000 when the scoping process was introduced but the latest change is in law 60/2013 when the main change is that projects are in three groups instead of two.

In article 12 of law 60/2013 it says that in Annex 1 there are projects in three groups/categories A, B, and C. Projects in category A are always subject to an EIA but projects in category B and C may be subject to an EIA and that is assessed in every case with respect to the type /nature, scale, and location of the project. Following is the list of geothermal projects and projects related to geothermal utilization (Table 3).

TABLE 3: Categories of projects subject to an EIA in Iceland
(Law on EIA nr. 106/2000, changes by law 138/2014)

Paragraph	Projects	Category
2.06	i. Drilling of exploration and production wells in high temperature areas.	B
	ii. Drilling in low temperature areas where mineral water sources, hot pools or hot springs are on the surface or in the nearby vicinity.	B
3.02	Geothermal power plants with a heat output > 50 MWh or more and other power plants with electric output > 10 MWe or more.	A
3.07	Industrial installation for production of electricity, steam and hot water and thermal processing from geothermal areas, 2.500 kW gross power or more.	B
3.08	Overhead transmission lines 66 kV or more. Submarine cables for transport of electricity 132 kV or more, 20 km or longer.	A
3.09	Pipes for carrying gas, steam or hot water in connection with industrial projects.	B

The Figure 5 shows that developers in Iceland, have to apply first for a research license from the Ministry of Industries and Innovation. Then, the developer notifies to the National Planning Agency (NPA) of the proposed exploration drilling project and the NPA decides whether the project needs to be subjected to an EIA. If the project is subjected to an EIA and, it is accepted, or if it was not subjected to EIA, the developer needs to apply for a development permit to the National Energy Authority in order to start exploration drilling. After the exploration drillings and a feasibility study the developers have to submit a scoping document for the EIA for a proposed power plant that needs to be revised and accepted by the

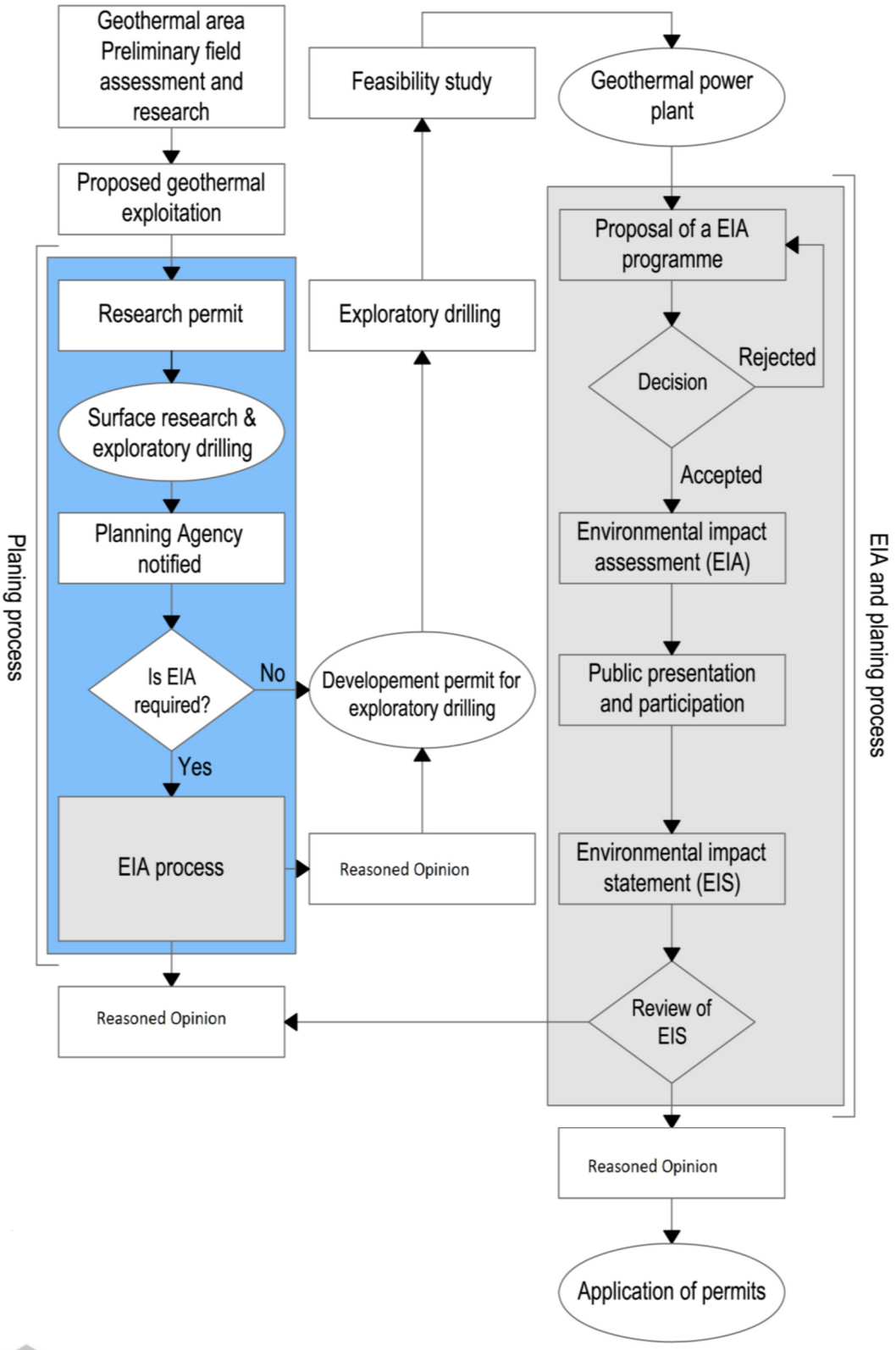

FIGURE 5: Flowchart of regulatory framework of EIA in Iceland (Rodas, 2015)

NPA. When the ruling is positive the developer carries out the EIA and goes through the normal stages of presentation and public participation before the preliminary EIA statement/document (EIS) is sent to the NPA for revision. The NPA makes the preliminary EIS public, seeks comments from other statutory agencies and delivers, with the publics comments included, to the developer. The developer inserts all comments and his responses to them into the preliminary EIS and sends the final EIS to the NPA. The NPA gives a reasoned opinion on the project's EIS which is the basis for development permits published by the local municipality. The project must also be in accordance with spatial plans, regional and municipal development plans, but if not then the planning process must be considered as part of the preparation stage. The last step is to apply for all necessary permits like operation and utilization permits to the National Energy Authority, the environmental permit to the Municipal Health Committees and construction and building permits to the local municipalities.

In Djibouti, the Ministry of Environment holds the responsibility to revise and approve the Environmental Impact Assessments.

The first difference that can be noticed when reviewing the law in both countries is that in Djibouti the resources of the subsurface belong to the State no matter if the resource is located on a private land or if it is located under the territorial sea. On the other hand, in Iceland the ownership of the underground resource is linked to the owner of the land in which it is located, if the resource is in a public land then it is property of the State. Nevertheless, the development and use of the resource is subject to licensing. The EIA process in both countries presents the same principle, unless the state or one of its organisms are the developers. In conclusion, the main difference between the EIA processes in the countries that could affect the development of geothermal energy, is the absence of specific norm to different resources in Djibouti.

6. POSSIBLE ENVIRONMENTAL IMPACTS OF THE ASSAL-FIALE PROJECT

The potential impacts, positive and negative, can be classified into 3 categories:

- physical,
- biological, and
- social and economic impacts.

6.1 Positive impacts

The Assal-Fiale project will have significant positive impacts including stabilization of electricity generation in Djibouti, promotion of economic growth in the country and contribution to the Government revenue. The project will also be improving socio-economic conditions of the local population by the creation of employment, access to social amenities (education, health, water, transport, and roads), development of tourism, and the improvement in gender equality. The project will offer opportunity for training and acquisition of skills.

6.2 Negative impacts

6.2.1 Potential impacts on physical environment

Geology and land

During exploration: Exploration can be divided into two phases. First is the surface geophysical studies which will not have any significant impact on geology and land. The second part of exploration includes

drilling experimental wells to obtain a geothermal gradient map which can have some impact such as soil disposal.

During drilling: Road construction and preparation of drill sites can cause unstable earth conditions and change or damage geological formations. During well testing, care should be taken not to discharge the wastewater directly to steep areas, but sumps should be made to contain this waste water, as failure to do this can cause serious gullying.

During operation: Subsidence and induced seismicity are the main possible effects on the land around the power plant and the surrounding areas. A monitoring program for subsidence in this area is recommended.

Effects on air
During all phases: Gas emission into the air would take place during all phases of the proposed project.

During the construction and decommissioning phases: Dust would result from surface disturbances and vehicle travel on unpaved roads.

During well drilling and testing and during power plant operations: Non-Condensable Gases (NCGs), including hydrogen sulphide (H_2S) and carbon dioxide (CO_2), will be released from the geothermal fluid.

During all phases: Oxides of Nitrogen, Carbon monoxide, and oxides of Sulphur emitted from internal combustion engines will be released during all phases of the project.

A summary of the effects on air during such a project:

- Small quantities of critical air pollutants will be released from mobile construction equipment and other vehicles, but this impact will be below the level of significance;
- Large quantities of critical air pollutants, in particular oxides of nitrogen (NOx), will be released from drilling rig engines during well drilling operations, but this impact will not be significant if wells are drilled one by one, and only one active drill rig is operated at any one time;
- Hydrogen Sulphide will be released during well flow testing from well pads and during power plant operation, and it is necessary to control the concentration of H_2S in the atmosphere and keep it below levels specified in international standards;
- The project will release "greenhouse gases" which will contribute to global warming. These gases consist mainly of carbon dioxide (CO_2) and some methane (CH_4). But a prediction of the amount of carbon dioxide released to the atmosphere per kilowatt of electricity shows it to be approximately 20 times smaller than the amount of "greenhouse gases" released from a fossil-fuel power plant for an equivalent amount of electricity.

During drilling test and operation, a monitoring programme, including the monitoring of pollutant gases such as H_2S in the atmosphere, should be carried out, and if the concentrations of these gases become higher than limits set by standards, measures must be taken to reduce their amounts in the atmosphere.

Effects on water
The wells, which will be drilled in this area for high-temperature geothermal fluid will be deep and may require up to 50 l/s of water for periods of several months, depending on the number of wells to be drilled. The amount of water used as drilling fluid is enormous and should be recycled or discharged with utmost care into well-designed sumps, or possibly re-injected as this can affect the quality of the groundwater in the area.

The concentration of dissolved solids and gases in geothermal water and steam are greater than in shallow ground water. Therefore, it is necessary to monitor the effect of geothermal fluid on surface water and shallow groundwater after the installation of a power plant.

Noise effects
In the Assal-Fiale geothermal field, there will not be serious noise impacts during geothermal project activities such as drilling, well testing, and operation. Only during well testing will there be some temporary noise, which will affect wildlife in the vicinity of the drill rig. Workers on-site will need to wear appropriate hearing protection as a necessary safety precaution. The greatest noise effects during power plant operation are from the cooling tower, transformer, and turbine-generator building. When power plant operation starts, noise mufflers must be used to keep the noise level below the 65 dB limit set by the U.S. Geological Survey (Kestin et al., 1980). With a reduced level of noise, workers, tourists, and wildlife will not be seriously affected.

6.2.2 Potential impacts on biological environment

The Assal-Fiale geothermal project can have potential impacts on the ecosystems. In case of negligent treatment, muddy waters from drilling and geothermal fluids generated during the trial phase could potentially flow over the land's surface or through shallow faults into Lake Assal. Given the probability that the heavy metal content (or other dangerous substances) of these fluids exceed that of the receiving waters of Lake Assal, it is imperative to ensure that such fluids and other waste or dangerous substances do not reach the lake.

The drilling project could have a high negative impact on protected areas, the sensitive ecosystems and the coastal areas, especially if drilling sludge and geothermal fluids are dumped into the waters of Lake Assal or Ghoubbet el Kharab. Although the latter has not yet been declared a protected area, it is the habitat of several vulnerable species that are on the red list of the International Union for the Conservation of Nature (IUCN), such as the whale shark and the dugong.

6.2.3 Potential impacts on socio-economic environment

Potential loss of part of the transhumance corridor
Part of the transhumance corridor runs over the drilling project area. The length of the corridor in the potentially affected drilling area is approximately 2-3 km, starting from the seismograph station up to the great fault behind the former Assal 5 drilling site. The passage of animals requires a corridor that has a minimum breadth of 2 m (when limited to a short distance); on flat land, animals need a larger corridor that is 1 to 2 km wide. The herds pass along the current access road and its surrounding area where the land so permits. Herders from the northern part of Tadjourah region and from the south of Dikhil region use the transhumance corridor regularly, at least twice (and often 3 to 4 times) a year, depending on the abundance of rainfall, which has remained irregular in recent years. Route No. 7 transits directly through the project area. During consultations with the affected population, the sub-prefect of the region stated that several thousands of animals transit regularly through the project area and pass through the drilling project site.

Closure of the transhumance corridor would imply that the population will no longer have access to this important transhumance resource. Under the customary law of the Afars, right of passage is defined by the Sultan of Tadjourah. If the transhumance corridor along the current route is effectively closed, an alternative route will need to be constructed.

Visual impacts
The drilling facilities and pipes will leave an enormous visual impact on the area.

Impacts Related to STDs/HIV-AIDS
Workers' camps are often a potential source of negative impacts on local women: sexual harassment, prostitution and sexually-transmitted diseases (AIDS, etc.). Women are often vulnerable to single workers living without their families in the camps and have to be protected against all forms of abuse. Given the drilling project's limited number of workers, short duration of construction activities, and recruitment of local labour, this impact is evaluated as low. An awareness-raising drive on sexually-transmitted diseases will be conducted by a local NGO to be jointly selected with the Ministry of Women's Advancement.

6.3 Risks of accidents

According to the report of the Environmental and Social Management Plan of the African Development Bank, the main environmental risks/accidents of the project are:

Well blowouts
Well blowouts may occur during drilling of wells, leading to the emission of drilling and geothermal fluids. Rising drilling fluids may have high temperatures with risks of burning for workers. The risk of an induced phreatic or volcanic eruption is low, but the impact on staff is potentially harmful and provision should be made for mitigation measures.

Accidental fluid emissions
Pipes may break during well drilling or testing, causing emissions of geothermal fluids and hydrogen sulphide from the geothermal reservoir. The potential impact of a broken pipe on staff and the environment is deemed to be high, and provision should be made for mitigation measures.

Seismic and volcanic events
Considering that the project is located in a zone of intense seismic and volcanic activities, there is a certain risk of seismic (earthquakes) and volcanic incidents. The consequences of such an incident are potentially catastrophic for the staff and local population.

7. COMPARISON OF SVARTSENGI, REYKJANES, AND HELLISHEIDI TO ASSAL-FIALE GEOTHERMAL FIELDS

7.1 Facts about geothermal energy in Iceland

Geothermal development in Iceland begins around the mid-20th century when low temperature geothermal fields were utilized for space heating in public areas such as schools, state hospitals and swimming pools. Presently, 90% of all houses are heated with geothermal energy. In the last decade of the 20th century, high temperature geothermal fields were developed and now geothermal energy accounts for 24% of the country's installed capacity with a total electrical power production of 665 MW (Björnsson and Steingrímsson, 1991. This success was achieved through the following strategies:

1. Power potential for each geothermal field analysed through detailed surface exploration and drilling. Design and construction of power plant;
2. Testing of the field by small power plant until full potential of the geothermal field was developed;
3. To keep the production constant, 1-2 wells drilled per year e.g. Hellisheidi.

Despite this strategy, the building of the geothermal power plants at Reykjanes and Hellisheidi were done in large initial steps. Reykjanes produced 100 MWe from the start and Hellisheidi 120 MWe which expanded to 303 MWe in 2011. This lead to dropping pressure which is still dropping and new wells are needed, probably earlier than was planned in the beginning. In the case of Hellisheidi, the utilization

has increased and steam is piped from longer distance than planned in the beginning to keep up the electric production.

Orkustofnun (the national energy authority in Iceland) is the authority that issues licenses for research and utilization of the geothermal resources. Decisions, in this regard, made by Orkustofnun can be appealed to the ruling committee for the resources act.

According to Jónas Ketilssson (personal communication, October 2015) from Orkustofnun, the utilization licenses sometimes stipulate limitations for the acceptable pressure drawdown if deemed necessary by Orkustofnun due to the rate of exploitation. This applies in particular to geothermal power plants. An example is the Theistareykir geothermal field in north Iceland where the pressure drawdown is not allowed to be more than stipulated. It is also stated that the annual decrease in steam production cannot be more than 3% per year on average over the past five years.

If these requirements are not met the situation is analysed. Firstly, the models are re-calibrated and if issues for long-term utilization are below thresholds the license holder may have to increase reinjection, enlarge the production area and possibly even change utilization strategy.

In Hellisheidi the pressure drawdown is not more than predicted and allowed in the license. But at Reykjanes there is no limit in the utilization license that was published by the Ministry for industry in year 2004. However, in a new license issued by Orkustofnun in 2011, there are limitations, but that license is not in effect until the power plant is enlarged.

Two of the geothermal areas, Svartsengi and Reykjanes are on the southwest tip of the Reykjanes peninsula. The third geothermal system is Hellisheidi which is located on the northeast part of the peninsula.

7.2 Svartsengi geothermal field

The first electrical power plant in Svartsengi was built in 1976-1978. It was the world's first geothermal power plant utilizing high-temperature geothermal systems to produce electricity and hot water for district heating. Since 1976, the power plant has been upgraded in six stages. The current capacity of the plant is 150 MWth for district heating and electrical power capacity is 74.4 MW. At the moment the Svartsengi power plant is utilizing high and low pressure steam as well as binary units for the waste heat from the condensing units. Some 30 geothermal wells have been drilled by Iceland GeoSurvey (ISOR).

In an interview with Mr Ómar Sigurdsson (personal communication, September-October 2015), a reservoir engineer at HS – Orka, he said that in 2014 the average year production was 488 kg/s and the injection 293 kg/s. As the Svartsengi is a liquid dominated reservoir the reinjection plays a large role there in holding the drawdown rate at an acceptable stabilization. The future plan is to increase reinjection slightly (10-15%). Some effluent is used by the Blue Lagoon and is disposed to shallow formations, the rest will be discharged to the sea. He was also asked about surface subsidence in the centre of the area and if it has had any problems for the utilization and he said that the total subsidence at Svartsengi is on the order of 45-50 cm. It has so far not caused problems as constructions in the area have been in steps so it has compensated for much of this subsidence (Appendix I).

It shall be noted that the Blue Lagoon is a world famous tourist destination with probably over 700.000 visitors per year with significant economic and social impacts in the area and for the tourism in Iceland.

7.3 Reykjanes geothermal field

The Reykjanes geothermal system is located at the tip of the Reykjanes Peninsula, while the Svartsengi geothermal system is found about 10 km to the east-northeast of it. Geothermal fluids in Reykjanes have the same salinity as seawater but in Svartsengi the salinity is about 2/3 of seawater as mentioned above.

The Reykjanes reservoir fluid, has reacted with the basaltic host rock at temperatures between 270-340°C. The concentrations of metals and trace elements in the reservoir fluid collected at 1350–1500 m depth are; Cu ~15 mg/kg, Zn 5-25 mg/kg, Fe 10-140 mg/kg, Mn ~2.5 mg/kg, Pb 100-300 µg/kg, Ag 30-100 µg/kg and Au 1-6 µg/kg (Hardardóttir et al., 2010). Its chemical properties have long been studied for the purpose of producing salt and valuable minerals.

According to Mr Ómar Sigurdsson a reservoir engineer at HS-Orka, the geothermal reservoir fluid of Reykjanes geothermal reservoir is a steam dominant two-phase zone in the top part while the reservoir is liquid dominated at greater depth. Most of the production wells have some connection to the steam zone as it is not cased off in them. Of the current 16 producing wells there are 3 shallow wells that only produce from the steam zone.

Presently, the pressure drawdown in the central part of the production field is about 40 bar and becomes less with distance from the centre. The drawdown was very rapid during the first 2-3 years but has almost stabilized now at a rate of about 1 bar/year.

As reinjection is used as a tool to work against the pressure drop in the geothermal system, Mr Sigurdsson pointed out that in 2014 the average year production was 518 kg/s and the reinjection 82 kg/s. This is an infield injection and can therefore not be increased as it can cool wells and quench steam. Reinjection wells are under construction at the outskirts of the field and plans are to triple the injection using these outer wells.

It is a known fact that the Reykjanes area is a tourist attraction and geological features are of special interest, such as geothermal manifestations, lava flows, craters and open fissures which are the results of plate tectonics and the fact that the Mid Atlantic ridge “coms on shore” there. There have been changes in the geothermal manifestations on the surface and Mr. Sigurdsson was asked how much surface area is impacted by increasing heat from the start of the power plant and what could be the main reasons. He replied that the changes in thermal surface manifestation have been very dynamic over the decades. Therefore, the selection of a reference point matters and the difference is only true over the compared period. Over longer or different time period the results may be quite different. If the reference is the start of the power plant the change in surface area that has been impacted by thermal activity has about doubled. The size of influenced area is today around 0.3 km^2.

What is of special interest at Reykjanes is the salinity of the brine as is the case in the Lake Assal region in Djibouti and therefore important to learn from the experience at Reykjanes.

The salinity of the brine can create big problems of scaling in the wells and that has been studied at Reykjanes and what happens there is that as the fluid ascends from a well it starts to boil due to pressure decrease resulting in precipitations of mainly sphalerite (Zn,Fe)S) up the well from about -1200 m depth. At surface downstream of an orifice plate a sudden decrease in pressure from ~37 bar down to 22 bar, results in rapid boiling (flashing) resulting in abundant precipitation of sulphides. In order to better understand the build-up of scales and the resulting decrease in fluid-flow in the surface pipeline, a detailed geochemical and mineralogy study has been done on the scales by Hardardóttir (2011), and her co-workers (Hardardóttir et al., 2010). The scales are primarily composed of sphalerite, less of chalcopyrite ($CuFeS_2$) with minor of galena (PbS) and traces of other sulphides (mainly Cu-sulphides like bornite (Cu_5FeS_4) and digenite (Cu_9S_5) (Hardardóttir, 2011).

The wells RN-12 and RN-11 are currently the most productive wells of the Reykjanes power plant in terms of electricity and in amount of scaling (Sigurdsson, 2015).

The existence of TENORM in the Reykjanes scales with a higher value in the activity of Po-210 has now been confirmed for the first time in Iceland. NORM and TENORM is included in the Icelandic Act on Radiation Protection and any potential radiation protection issues associated with TENORM in geothermal applications will be addressed as needed by the Icelandic Radiation Safety Authority (Sigurdsson, 2015).

Because of the expected high salinity at Assal-Fiale it was decided to contact Dr Halldór Ármannsson who has worked in Djibouti and studied the chemistry of the older wells and done experiments to find out solutions regarding scaling and reinjection of the geothermal water.

According to Dr Halldór Ármannsson (Appendix I): It can be expected that quite a high salt concentration will be in the geothermal fluid in Assal-Fiale and that there may be problems in getting rid of the fluid on the surface, immediately during the testing of wells. Therefore, it is correct to assume that it may be necessary to drill injection wells for the fluid, especially if the testing of the wells lasts for months as would be desirable. Further studies / experiments on deposits from the geothermal fluid are needed to ensure a suitable permanent way of disposal. Disposal of the geothermal fluid in the sea may cause deposit problems and negative effects on the ecosystem in the vicinity of the outlet, because of chemicals in the liquid.

- The sulphide scaling can be dealt with by inhibition, but iron silicates and amorphous silica deposits by pressure (temperature) control.
- As the plan in Djibouti is to drill four exploration wells in the Assal-Fiale area Halldór recommended that two wells would be drilled in the beginning and after testing 6-12 months (flowing) the other two wells would be drilled in the light of the results from the first ones.
- Regarding the problems associated with gas from geothermal fluids, as the high content of H_2S coming from the Hellisheidi Power plant, Halldór believes that based on available data that problems because of H_2S is very unlikely and as the area is considerably windy the risk of accumulation should be low.

The attention came also to the radioactivity measured in deposits from wellheads in Reykjanes Power plant and that it is worth to have such measurements as a part of the monitoring program at the Assal-Fiale geothermal area.

7.4 Hellisheidi geothermal field

The Hengill Area is an active volcanic systems consisting of Mt. Hengill and fracture zone to the NW and to the SW (Sæmundsson, 1967, Franzson et al., 2005). Two power plants have been built in the area; one in Nesjavellir in the northern part of the area and one in Hellisheidi in the southern part. At least two other geothermal fields in the area are believed to be feasible for electrical power production; the Bitra and the Hverahlíd Fields (Gunnarsson, 2011). The total production capacity of the Hellisheidi Power plant is 303 MWe (Gunnarsson, 2011). The power plant also consists of a heating unit with 400 MWh capacity.

The history of energy utilisation on Hellisheidi is short and considerable uncertainty is expected in forecasting what will be the respond of the geothermal system to extraction in future. Measurements in 2014 show that the drawdown in the system is following the forecasts as in previous years and within limits under development license. Studies show that the current processing area will not cover the full production of Hellisheidi power plant permanently. The energy production area that was estimated for the plant is smaller than the preliminary research expected. Therefore, it was considered to be better to enlarge the extraction area and provide additional steam for the production of electricity and hot water

by utilizing wells who had already been drilled at Hverahlíd rather than drilling new wells in the existing extraction area (Sigurdardóttir and Thorgeirsson, 2014).

According to Hólmfrídur Sigurdardóttir (personal communication, september2015, Appendix I), head of environmental affairs at Reykjavík Energy, the need for new wells will be 1-2 wells per year to keep the production at 300 MWe and they will probably be both at the Hellisheidi power plant production area and nearby areas.

The reinjection has posed a major problem in the operation of the Hellisheidi Power Plant. The temperature at the originally planned reinjection zone proved to be very high (>300°C) when injection wells were drilled there. In order to be able to use that zone for production a new reinjection zone was planned. The new zone has been promising despite problems in operating the new injection wells. The wells are drilled into a fault that is active and injection tests have resulted in swarms of small earthquakes. The injectivity of the wells in the new reinjection zone is highly dependent on temperature of the reinjected water. This dependence can be explained by thermo-mechanical effects on fractures in the fracture governed reservoir. Thinning the geothermal brine with condensate water and cooling it with heat exchangers makes it possible to inject it all into the reservoir and solve the environmental problem of brine disposal. The long term effects of this solution on the geothermal reservoir are not known and have to be studied further by monitoring the system's response and by simulations (Gunnarsson, 2011). According to Hólmfrídur Sigurdardóttir (personal communication, septembre 2015, Appendix I) 17 injection wells had been drilled at the end of 2013 and she explains the history of reinjection experiments.

According to Gunnar Gunnarsson (2011), the rate of silica precipitation from the separated water was slowed down substantially under laboratory conditions by lowering the pH of separated water from pH 9.3 to below 6.3. Dilution of the separated water with 15% condensate water additionally decreased the precipitation rate making it a favourable inhibition method to prevent silica scaling from spent geothermal brine at Hellisheidi power plant. Prevention of silica scaling is in the case of Hellisheidi a key element for successful injection of brine.

Future experiments to prevent scaling from the geothermal brine involve injecting sulfuric acid, produced in other experimental facilities at the Hellisheidi power plant, into the separated water and pumping the water to reinjection wells.

Hólmfrídur Sigurdardóttir was asked how many wells have been drilled and how many are used as production wells and reinjection wells and she answered that at the end of 2013, a total of 57 steam wells had been drilled south and east of the mountain Hengill. This includes 47 at the current Hellisheidi power plant production area, 3 in the Bitra area, 6 at Hverahlíd area and 1 by Gráuhnúkar area. In November 2014, a total of 33 wells were connected to the plant. Many wells are drilled in the same drilling site/well pad to reduce the environmental impact of the plant. The wells are not all connected to the plant as some are drilled to explore the edge of the area and others have not produced as much as hoped. Some of these wells are used for monitoring as it is important that some wells will be used to monitor temperature and pressure conditions in the area. Two steam wells that did not serve as production wells were connected with the reinjection system in 2014. A new steam extraction hole was drilled in the summer of 2015.

As it is known that the amount of H_2S and CO_2 from the Hellisheidi power plant is critical, Hólmfrídur Sigurdardóttir (Appendix I) was asked what the current amount of CO_2 is coming from the power plant and how much of it is reinjected. She said that in 2014, 2400 tonnes of CO_2 were pumped back down into the bedrock and since the CarbFix project started until the end of August 2015, 3600 tonnes of CO_2 have been pumped down to the bedrock. According to Reykjavík Energy homepage the amount of CO_2 from the power plant in 2014 was 55.440 tonnes.

She was also asked about the H_2S and reinjection of that and she answered that in the year 2014, 1500 tonnes of H_2S was pumped back down to the bedrock (since the CarbFix project started until the end of August 2015 about 2750 tonnes of H_2S have been pumped down to the bedrock). According to the Reykjavík Energy homepage the amount of H_2S released to the atmosphere from Hellisheidi and Nesjavellir power plants was 17.760 tonnes in 2014.

7.5 Subsidence and gravity changes at Reykjanes

The subsidence at Reykjanes has been studied since 1986 with a maximum of 6 mm/year (Eysteinsson, 2000).

- The subsidence bowl around the Svartsengi field is connected to the Eldvörp geothermal field. That, along with the fact that those two geothermal systems are pressure related (Björnsson and Steingrímsson, 1991), suggest that the two fields have a common origin. This is further confirmed by a resistivity survey in the area (Eysteinsson, 2000). The total integrated subsidence volume around Svartsengi is 10% of the total volume of fluid subtracted from the reservoir. Although the fluid production for the power plant at Svartsengi has been explained as the cause of the subsidence, another possible source could be a reduced pressure in a solidifying magma chamber within the crust beneath Svartsengi (Eysteinsson, 2000).
- The gravity changes on the outer part of the Reykjanes peninsula are small and mainly limited to the Svartsengi and Eldvörp geothermal areas. The maximum reduction in gravity is located at the same place as maximum subsidence where it is around 5 μgal/year. The integrated gravity reduction is equivalent to 2.4 Mt/year mass loss in the area. This is about 30% of the total mass drawn out of the geothermal field. No gravity change is observed at the Reykjanes geothermal field.
- The subsidence at Svartsengi is greater than has been observed in other utilized geothermal fields in Iceland. At Nesjavellir (SW Iceland) small subsidence has been observed over a limited area around the power plant at the rate of 5 mm/year, but recent observations show that the land is rising, probably due to natural tectonic processes in the area. No gravity changes have been observed in the area that could be related to the exploitation of the geothermal field. In Krafla geothermal field (north Iceland) there have been large elevation and gravity changes over the last 25 years due to the volcanic eruption period from 1975 to 1985. In this area land has lifted over 3 meters and in limited area there has been subsidence of over 1 meter. Since 1989, when land lifting reached the peak, and to 1995, land has subsided up to 250 mm. During this period a subsidence bowl is observed around the bore field in Krafla which corresponds to 30 mm/year subsidence, a part of that is probably related to utilization of that field. Observed gravity changes in Krafla field are only related to tectonics during the eruption period.

7.6 Comparison of the geothermal fields

- All the fields are within volcanic areas;
- All fields are considered to be high-temperature areas with a geothermal fluid >200°C at 1000 m;
- Assal-Fiale and Reykjanes are in coastal areas with reservoir fluids with high salinity which especially creates scaling problems and can have complications with disposal of the geothermal water, especially reinjection. Disposal of the water on the surface can create lagoons which can harm the environment but can also be utilized as the Blue lagoon in Svartsengi.
- Permeability, reinjection and earthquakes, scaling and corrosion are all common factors that makes utilization of the geothermal resources complicated.
- In Hellisheidi the amount of H_2S is higher than in the other areas and creates specific mitigations.
- The proposed development site in Djibouti is in a protected area and the three power plants in Iceland are all in areas of natural interest mainly because of volcanic craters, lava flows and

geothermal activity on the surface like fumaroles, mud pots and colourful transformations and precipitations.

- Vegetation in the Assal-Fiale is scarce because of hot climate, lack of water and unfertile soil. But the Bay of Ghoubbet has a sensitive ecosystem. The three areas in Iceland have lava fields with sensitive moss and some contain ecosystems that depend on the geothermal heat, warm soil, especially at Reykjanes.
- All the areas are tourist attractions although the number of tourists in Assal-Fiale is still very low. The area in Svartsengi was not a tourist, or recreation area, before the power plant was built and the geothermal water created the Blue lagoon in the lava field. Hellisheidi area was a ski resort and highly used for outdoor recreation, now it is still a recreation area and the powerhouse is a popular tourist attraction. Reykjanes was a tourist area before the power plant was built and still is and the powerhouse is a popular tourist attraction.

7.7 Environmental parameters to be considered in management programme Assal-Fiale geothermal development

- Managing of the scaling and reinjection;
- Survey of the effects of different reinjection schemes on the properties of the reservoir;
- Monitoring of the system response, simulations and radiation.

8. ENVIRONMENTAL MANAGEMENT AT ASSAL-FIALE GEOTHERMAL PROJECT

8.1 General

Environmental Management is a set of policy, regulatory, advocacy and market based mechanisms which transforms human behaviour to achieve society's goals for the environment. As with all management functions, effective management tools, standards and systems are required. The Environmental Management System (EMS) based on the ISO 14001 involves all aspects of the operation of the geothermal development in order to manage and to minimize the environment impact.

EMS of ISO 14001 requirements include the following stages (Figure 6) (Moeljanto, 2004):

1. **Planning**
   - Environmental aspects
   - Legal and other requirements
   - Objective and targets
   - Environmental management programmes
2. **Implementation and operation**
   - Structure and responsibility
   - Training, awareness and competence
   - Communication
   - Environmental management system documentation
3. **Checking and corrective action**
   - Monitoring and measurement
   - Non-conformance and corrective and preventive action
   - Records
   - Environmental management system audit
4. **Management review**

FIGURE 6: EMS of ISO 14001 (Moeljanto, 2004)

8.2 Environmental Impact Assessments

A full EIA should be carried out prior to the drilling and plant construction should include Environmental Management Plans and costs in the project's design and budget. The ecosystems should be mapped and ranked in order of protection value or sensitivity before project starts and the results used to decide mitigations before commencing any activities of the project.

8.3 Best practice, mitigation measures and monitoring

Best practice is the way a project is carried out according to all laws and regulations, the practice that may be learned from previous projects etc. If despite that a project will have negative impacts of some sort, then mitigation measures must be found to reduce the impact and if that is not enough the impacts may be compensated e.g. a land is bought from the landowner. All these actions are designed to prevent, decrease or reduce negative environmental impact.

8.3.1 Protective measures for local ecosystems

In order to protect the area's ecosystems, it is recommended that the sensitive ecosystem of the Bay of Ghoubbet should not be affected and that water for drilling purposes should rather be pumped from a well near the drilling site. It is also recommended to reinject fluids into their reservoir of origin or dispose of/inject treated fluids into shallow wells.

8.3.1.1 Measures for the development of drilling infrastructure

To minimise the impact of access road and field development, the following best practice measures should be envisaged:

- Design the road alignment in such a way as to limit impact on the landscape and geology to a strict minimum;
- Carry out minimum excavation works to protect the geology, soils, topography, landscape and vegetation;
- Take appropriate erosion-control measures and avoid vegetation areas;
- Follow the alignment of the existing road where possible. For the areas where the current road crosses over Lava Lake, there are plans to change the alignment and avoid the lava area;
- Alignments of the current road that have been replaced should be closed.

Before and during operation of a quarry, the following mitigation measures should be taken:

- Establish a General Safety and Health Plan (GSHP) for the operation of the quarry;
- Optimize the planning of proposed extractions to minimize impacts on geology, topography, vegetation, etc.;
- Choose adequate extraction equipment and techniques to minimize impacts on noise levels and air quality and reduce the risk of accidents;
- Accurately plan extraction works to avoid all types of accidents caused by rockslides, landslides, etc. especially after the use of explosives;
- Regulate access of quarry trucks to national highways (road signs, speed limits, etc.).
- Reduce noise by using appropriate equipment;
- Provide noise protection gear;
- Reduce dust generation;
- Provide protective respiratory masks for workers;
- Ensure proper transportation and storage of explosives;
- Secure the quarry site against all types of accidents or subsequent damage, and rehabilitate the site upon completion of the works.

Specific measures for drilling operations:

- **Management of drilling fluids**

Best practice measures for drilling fluid management include the following:

- Use of storage tanks or special basins lined with a water-tight membrane for collection and storage of fluids, mud and spoils;
- Re-utilisation of drilling fluids as much as possible;
- Use of water-tight casing to line the walls right down to the appropriate depth of the geological formation to avoid leakage of drilling fluids at levels far above the geothermal reservoir;
- Preference for biodegradable products when manufacturing drilling mud;
- Where a decision has been taken to dispose of the liquid resulting from separation, the quality of effluents must be up to standards; this could involve treating fluids prior to disposal;
- The quality of liquids to be disposed must be controlled regularly;
- Where foam would be used, special measures must be taken to protect against wind;
- The drilling mud treatment facilities and water intake and/or drilling fluid disposal pipes must be dismantled upon completion of works.
- The treated effluents must be disposed/injected into shallow wells.

- **Management of geothermal fluids**

The option to dispose of geothermal fluids into the Gulf of Ghoubbet or Lake Assal, even when treated, is not feasible. It is recommended that the technical study should investigate whether the Assal 5 well can be used for reinjection of treated fluids.

The treatment method to be adopted depends very much on the chemical composition of the geothermal fluids, and should be determined by the drilling contractor once the geothermal drilling fluids have been analysed through laboratory tests:

- If all the geothermal fluids are not re-injected into their reservoir of origin, the quality of effluents must be up to standard. This may imply bringing the temperature and concentrations of effluent down to the prescribed limits. The quality of water that is disposed of must be controlled regularly;
- If it is decided that the fluids will be re-injected into their reservoir of origin, the groundwater contamination potential must be reduced to a minimum by lining the injection wells with water-tight case right down to the level where the geological formation containing the geothermal reservoir is located;
- Where applicable, the temporary treatment facilities and pipes for disposal of geothermal fluids produced during the tests must be dismantled after completion of works.

Protective measures against risk of water and soil contamination

- Regular maintenance of machines;
- Proper transportation and storage of fuels;
- Collection and proper disposal of used and potentially polluting fluids (oils, break fluids, etc.).

8.3.1.2 Solid waste management

The drilling contractor should present a Waste Management Plan that includes dangerous waste, prior to commencement of drilling works.

In case of dangerous waste, adequate management must include its proper onsite storage and confinement prior to its final treatment and disposal in an appropriate waste management facility. Waste treatment essentially includes dewatering of sludge. Assuming that the waste contains heavy metals mainly composed of sulphides and hydroxides, any waste stabilized in this manner may be disposed of

in a household waste treatment facility, so long as it is protected from rain water. Given the low rainfall in Djibouti, the risk of heavy metal build-up is generally deemed to be low.

The decision on the final destination of dangerous waste disposal must be taken by the Djiboutian authorities. The main options are landfilling or export. Considering that there is no controlled landfilling in Djibouti to date, the export of small quantities of potentially dangerous waste is probably the preferred option. Mitigation measures on household waste management comprise at least:

- A program to minimize waste, including waste sorting, reuse and recycling;
- On site waste collection;
- Transportation of the waste to a household garbage dump.

With regard to wastewater, the measures to be envisaged are:

- The installation of mobile toilets on the project site;
- Regular evacuation to a wastewater treatment plant.

8.3.1.3 General safety and health plan (GSHP)

After preparing the technical study and selecting the drilling methods, the drilling consultant should prepare a general safety and health plan (GSHP) prior to commencement of works. The role of the GSHP is to highlight the general risks on the project site. It comprises a detailed analysis of the risks, and defines safety and health measures, covering aspects related to drilling machinery, external companies, work equipment, individual protection gear, noise, explosives, vehicles, surface traffic, asbestos, ionizing radiation, electricity, protection against corrosion, protection against explosions, evacuation and rescue means, safety drills, drilling programme, installation and dismantling, casings and general safety of the site.

The specific health and safety problems of geothermal products could result from exposure to:

- Gas coming from the geothermal reservoir;
- Heat; and
- Noise.

The problems could also be caused by exceptional accidents (breakage of pipes, well blowouts, volcanic eruptions, earthquakes, etc.).

Exposure to gas
As regards the risk of exposure to dangerously high concentrations of hydrogen sulphide, it is necessary to envisage the following measures:

- Install a non-stop surveillance and early-warning system. Where the H2S concentration exceeds the WHO guideline value of 10 ppm, the drilling works or testing should be halted;
- Prepare an emergency intervention plan in case of accidental hydrogen sulphide emission, covering all the necessary aspects from evacuation to resumption of normal operations;
- Install hydrogen sulphide detectors or distribute personal detectors, and also install autonomous respiratory equipment in areas with high risk of exposure;
- Install adequate ventilation mechanisms to prevent a build-up of hydrogen sulphide;
- Distribute brochures or any other information medium to workers on the chemical composition of liquid and gaseous phases, explaining their potential risks to health and safety.

Exposure to heat
Accidental exposure to heat may occur during drilling in case of well blowouts and malfunction of heat confinement and conveyance mechanisms. Recommendations on controlling exposure to heat include the following:

- Reduce work time in high temperature environments and provide access to drinking water points;
- Establish protective surfaces in areas where workers work near hot equipment, especially pipes;
- Use appropriate individual protection gear, especially insulated gloves and shoes;
- Follow appropriate safety procedures during drilling works.

Exposure to noise
Noise is usually generated by well drilling works and vapour expulsion. The noise level can temporarily exceed 100 dB(A) during certain drilling and vapour expulsion operations. Workers operating in the drilling area should use individual protective gear such as ear defenders if the noise level exceeds 85 dB (A).

Well blowouts
The drilling consultant should cover these risks in his Emergency Intervention Plan (EIP). The plan should specify the following:

- Define measures for controlling a blowout using a blowout preventer stack and stocking of material for quelling the blowout (water, barite);
- Define personal safety measures;
- Define other emergency measures;
- The staff working on the drilling site should be trained on the measures to be adopted.

Volcanic eruptions and earthquakes
The following mitigation measures should be taken:

- Establish an evacuation plan;
- Develop emergency measures;
- Train staff on the risks and the measures to be adopted.

The GSHP, including the EIP, should be included in the Bidding Documents for the drilling contractor.

Socio-economic measures
Compensate for or avoid the transhumance and tourist routes
Two alternatives were discussed in the impact assessment: constructing a new route (recommended by the local population); and leaving the current road open to herders during the project.

It is recommended that the technical drilling study should select drilling sites in such a way as to maintain a safe distance without closing the route used by transhumant livestock. Where possible, the transhumance route should be slightly modified, but it must still pass through Fiale in order to guarantee access to pastureland and the traditional right to the transhumance route. The specific ESMP of the drilling contractor should specify mitigation measures, where necessary.

Although the impact assessment recommends that the current route should be left open, the matter has not yet been concluded and requires closer consultation with the PMU, the local population and the Directorate for the Environment.

Similarly, the project should not block the route that leads to Lava Lake and Ardoukoba Volcano. The passage should remain open, but a safe distance must be maintained during construction of the drilling platforms. If this is not possible, an alternative route should be constructed. It would be appropriate to install display and information panels.

Prior to implementation of the project, it is mandatory to display a detailed plan of the project sites and consult the local population and local administrative authorities. It should be explained that landowners newly settled on the proposed drilling sites will not be compensated.

Institution of a procedure for "chance finds" of cultural monuments
The proposed sites (access roads, drilling area, quarry etc.) should be inspected by an archaeologist prior to commencement of construction works. In case of a chance find during the project, all works should be suspended and an archaeologist called in. However, a procedure for "chance finds" historical sites or cultural monuments has been suggested for use during the eventual modification of the current alignment of the access road, the selection of a quarry, etc.

Temporary abandonment
In case of temporary abandonment of the site, the following measures should be taken:

- Installation of a blowout preventer to reduce the risk of blowout;
- Regular surveillance of temporarily abandoned wells;
- Construction of a fence around the drilling site to prevent access by unauthorized persons or animals.

Temporary abandonment is possible only when:

- The casings are properly installed;
- Cementation between the casing and the soil ensures the insulation of the permeable levels;
- The duration of temporary abandonment should be agreed upon with the competent authorities.

Permanent abandonment
Where a well turns out to be unproductive or where the risk of blowout is too high, the geothermal well should be abandoned permanently. Once such a decision is taken, the products needed to insulate the permeable levels should be used to cover/fill the entire initially drilled section of the well. After complete closure of the well, a closure file should be prepared by the drilling consultant giving an exhaustive and precise description of the status of the well and all details of the closure procedure. After completion of the works, the drilling site should be rehabilitated.

8.4 Monitoring programmes

Monitoring of the environmental effects of the geothermal utilization can be carried out through programmes which consist of systematic observation, measurements and evaluation of the various parameters using appropriate methods and technology. A monitoring programme must cover all aspects of the physical, biological and socioeconomic environment for the exploration, construction, utilization/operation and decommissioning project phases.

8.4.1 Preliminary action

Before the exploration activities is commenced, baseline data must be gathered to validate and assess the environmental impacts. The objective of this is to be able to compare detailed information on the geothermal areas prior to, during and after geothermal utilization.

8.4.2 During the production test / drilling and well testing

During the production test, the following operations are to be implemented:

a. Planning phase (prior to the works)
- The Djiboutian Office of Geothermal Energy Development (ODDEG) should ensure that the technical solution proposed by the drilling consultant is in conformity with environmental and social standards;
- A detailed Environmental and Social Management Plan (ESMP), a General Health and Safety Plan (GHSP), an Emergency Intervention Plan (EIP) and a Solid Waste Management Plan (SWMP) should be prepared and validated;
- Commencement of the institution of support projects for the local population.

b. Preparatory works phase
- Monitoring of the application of health and safety standards and measures;
- Consultation with the local population to verify whether the problem of the transhumance corridor and the tourist route has been solved;
- Consultation with village communities of Assal area (Daba le Gahar, Laïta, Carrefour) and local authorities, traditional institutions and women/men's associations to find out whether mitigation measures have been implemented.

c. Drilling works phase
- Control of the application of the best technology, control of the application of the environmental precautions (works, storage of chemical substances, treatment of drilling mud and geothermal fluids, storage of materials, etc.);
- Control of the implementation of safety measures at work: noise, heat, geoth. gas emissions, etc.;
- Regular analysis of the chemical composition of emitted gases;
- Quality control when disposing of fluids resulting from treatment of drilling mud;
- Analysis of generated waste (drilling spoils) to determine means of disposal;
- Visual control of the drilling site and storage and/or treatment facilities;
- Control of protective measures for wells, in case of temporary or permanent abandonment of the drilling site.

d. Testing phase
- Control of the implementation of safety measures at work; noise, heat, geothermal gas emissions;
- Quality analysis of geothermal fluids prior to commencement of testing;
- Regular visual control of the processing facilities, pipes, etc.;
- Regular quality control for treated fluids prior to disposal (where applicable);
- Regular analysis of the chemical composition of emitted gases;
- Analysis of the waste generated (precipitates, residue from geothermal fluid treatment) to determine means of disposal;
- Consultation of the population concerned to verify whether the mitigation and support measures have effectively been implemented and whether the implementation process was transparent.

e. Completion phase
- Control of site rehabilitation (quarry, drilling, etc.);
- Project appraisal;
- Planning of subsequent stages.

8.4.3 During the operation

During the operation phase, the following monitoring programs must be carried out at Assal-Fiale geothermal project:

1. Monitoring of the wells, during testing and later production, heat, pressure, amount of water, modelling of the geothermal reservoir;
2. Monitoring the social impacts, jobs, tourism (increase/decrease), transhumance route etc.
3. Monitoring of noise emissions at sensitive receptor sites;
4. Hydrogen Sulphide gas monitoring;
5. Meteorological weather monitoring;
6. Precipitation chemistry monitoring;
7. Chemical elements of environmental significance in wastewater, soil and vegetation;
8. Monitoring of vegetation patterns;
9. Monitoring of water quality (surface and groundwater);
10. Monitoring of subsidence.

8.5 Other environmental tools

Environmental baseline studies
Prior to any final decision to proceed with full development, a number of studies would be required to

verify that resources at risk are properly characterized and that impacts can indeed be reduced to acceptable levels:

- Hydrologic studies of ground water, including their categories, flow patterns qualitative and quantitative indicators, water use, water discharge/disposal, water system or its separate parts and other characteristic features, including an assessment of potential effects of development on the hot springs;
- Detailed surveys of flora and fauna within a kilometre of the plant site and at transmission line tower sites, including specific flora composition and habitat conditions;
- Detailed survey of the plant site and the transmission line route for physical artefacts and historical sites or cultural monuments value;
- Detailed evaluation of potential induced development in the region or elsewhere in Djibouti;
- Evaluation of emissions of carbon dioxide or other greenhouse gases, as levels of CO_2 from geothermal development may be an appreciable fraction of that generated by an equivalent fossil fuel plant.

These studies and others would inform the full feasibility study and ESIA and inform the final decision of the Government whether to proceed.

Environmental audits for operations
Internal and external audits covering all environmental aspects management must be realized at least twice a year.

Communication
Consultations with stakeholders is important in the development of the geothermal project.

9. DISCUSSION AND RECOMMENDATION

- ✓ The experience of the geothermal development in Iceland shows that the exploration and utilization of geothermal reservoirs are complicated and there are several uncertain and critical points in predicting production capacity of a geothermal resource and the response of the reservoir. The reality is often that things are more complicated than expected. For that it is important to conduct a progressive development of geothermal resources exploitation to earn good knowledge and control of the unforeseen with minimum negative environmental impacts and social and financial risks and for a sustainable energy production;
- ✓ The success of an environmental monitoring program depends on the baseline data gathering to establish the background information that is valuable for comparing changes in the environmental conditions during a geothermal development, as well as for identifying natural variations, not related to the activities of a proposed project;
- ✓ It is essential to implement an environmental management system for optimal environmental protection.

10. CONCLUSIONS

The proposed project has great economic significance to the country because of the increasing demand for electrical power. The environmental effects of developing the geothermal energy in Djibouti need to be investigated in full and a careful choice of electrical power and geothermal field has to be made. It is now generally acknowledged that geothermal fields have to be carefully monitored for several years prior to development in order to ensure the most viable field in environmental terms, as well as sustainable energy production and the least negative impacts on the environment in general. The Assal-

Fiale geothermal resources can be exploited in a sustainable way if all the preventive and protective measures for the environment are taken.

The regulatory institutions play an important role in the EIA process and decisions on exploration and utilization of a geothermal resource as well as in monitoring and follow up of a geothermal project and they must provide general guidelines for the developers to carry out monitoring surveys. Official monitoring reports are important tools in enabling relevant authorities to assess the management of a geothermal system under development. A very important factor in monitoring is that results and reports can be made available to the public and obtainable from the consent authority.

It is necessary that a monitoring program can be discussed and agreed upon so developers and regulatory institutions are able to state the monitoring parameters and frequency of data collection according to the interests of the parties. The responsibility for protecting the environment during a geothermal development rests with the developer that is working according to his consent and permits, this responsibility cannot be shifted to the regulatory authorities or the government.

The information contained in this report can be used as a general reference/guide by regulatory institutions in Djibouti to enhance the surveillance and follow up conferred upon geothermal projects.

ACKNOWLEDGEMENTS

I wish to extend my gratitude to the Government of Iceland and the United Nations University Geothermal Training Program, for the opportunity to participate in this training program. My sincere gratitude to the Director, Mr Lúdvík S. Georgsson and the Deputy Director Mr Ingimar G. Haraldsson, for their undivided dedication to this training. I am grateful to Ms Málfrídur Ómarsdóttir, Ms Thórhildur Ísberg, and Mr Markús A.G. Wilde, for their generous help, care and advice during the whole training period. Special thanks to my ministry in Djibouti for giving me the opportunity to participate in this program. To my dedicated supervisors, Mr Thóroddur F. Thóroddsson and Dr Brynhildur Davídsdóttir, this research could not have been completed without your guidance and input. Much appreciation goes to Ms Hólmfrídur Sigurdardóttir of Reykjavík Energy, Mr Ómar Sigurdsson at HS Orka, Ólafur Árnason at Efla Consulting, Dr Halldór Ármannson at ISOR and Mr Jónas Ketilsson at Orkustofnun for their generous information. Finally, my deepest thanks for my family, my lovely wife, Fatouma Barreh, my daughters, Taslim and Deksan, and my mother Aicha Waiss, for their unwavering support and encouragement, this report is dedicated to you.

REFERENCES

African Development Bank (AFDB), 2013: *Djibouti – Geothermal exploration project - Summary environmental and social management plan (ESMP)*. Africa Development Bank, 29 pp.

Ármannsson, H., and Kristmannsdóttir, H., 1992: Geothermal environmental impact. *Geothermics, 21-5/6,* 869-880.

Árnason, K., and Flóvenz, Ó.G., 1995: Geothermal exploration by TEM-Soundings in the Central Asal Rift in Djibouti, East Africa. *Proceedings of the World Geothermal Congress 1995, Florence, Italy,* 933-938.

Árnason, K., Eysteinsson, H., and Vilhjálmsson, A.M., 2008: *The Asal geothermal field, Djibouti. Geophysical surface exploration, 2007-2008.* ÍSOR - Iceland GeoSurvey, report ISOR-2008/019, prepared for REI (closed report), 74 pp.

Björnsson, G., and Steingrímsson, B., 1991: *Temperature and pressure in the Svartsengi geothermal reservoir*. Orkustofun, Reykjavík, report OS-91016/JHD-04 (in Icelandic with English summary), 69 pp.

Fichtner, 2012: *Environmental and social impact assessment (ESIA) framework, geothermal resources evaluation project, Djibouti*. World Bank, report (in French), 174 pp.

Gunnarsson, G., 2011: Mastering reinjection in the Hellisheidi field, SW-Iceland - A Story of successes and failures. *Proceedings of the Thirty-Sixth Workshop on Geothermal Reservoir Engineering, Stanford University*, Stanford, CA, United States, 8 pp.

Hardardóttir, V., 2011: *Metal-rich scales in the Reykjanes geothermal system, SW Iceland: Sulfide minerals in a seawater-dominated hydrothermal environment*. University of Ottawa, PhD dissertation, 311 pp.

Hardardóttir, V., Hannington, M., Hedenquist, J., Kjarsgaard, I., and Hoal, K., 2010: Cu-rich scales in the Reykjanes geothermal system, Iceland. *Economic Geology, 105*, 1143-1155.

Hjartarson, G., Gísladottir, V., Gíslason, G., and Ólafsson, K., 2010: Geothermal development in the Assal area, Djibouti. *Proceedings of the World Geothermal Congress 2010, Bali, Indonesia*, 8 pp.

Eysteinsson, H., 2000: Elevation and gravity changes at geothermal fields on the Reykjanes peninsula, SW Iceland. *Proceedings of the World Geothermal Congress 2000, Kyushu-Tohoku, Japan,* 6 pp.

Hunt, T.M., 2001: *Five lectures on environmental effects of geothermal utilization.* UNU-GTP, Iceland, report 1-2000, 109 pp.

Khodayar, M., 2008: *Results of the 2007 surface geothermal exploration in the Assal Rift and transform zones, Djibouti: Tectonics and geothermal manifestations (revised version, May 2008)*. Iceland GeoSurvey, report ÍSOR-2008/008 prepared for REI (closed report), 81 pp.

MIT-led interdisciplinary panel, 2006: *The future of geothermal energy: Impact of enhanced geothermal systems (EGS) on the United States in the 21st century*. Massachusetts Institute of Technology, MA, United States, 372 pp.

Moeljanto, 2004: Evaluation of the enviromental impact at the Kamojang geothermal field in Indonesia applying the EMS of ISO 14001. Report 11 in: *Geothermal training in Iceland 2004*. UNU-GTP, Iceland, 209-238.

Orkustofnun, 1988: *Geothermal Resistivity Survey in the Asal Rift in Djibouti*. Volume 1: Main text prepared for the UND-OPS and ISERST. Report OS-88031/JHD-05, September 1988

Reykjavik Energy Invest, 2008: *Drilling and testing of geothermal exploration wells in the Assal area, Djibouti - Environmental management plan*. Reykjavik Energy Invest (REI), report REI-2008/Assal 1, 58 pp.

Rodas, Mario A., 2010: *Preliminary environmental impact assessment for the geothermal field Chachimbiro in Ecuador. A case comparison with Bjarnarflag geothermal field in Iceland*. University of Iceland, MSc thesis, 147 pp.

Rybach, L., 2003: Sustainable use of geothermal resources: renewability aspects. *Presented at "International Geothermal Conference IGC2003", Reykjavík, Iceland*, 15 pp.

Sigurdardóttir, H., and Thorgeirsson, Th.A. (eds.), 2014: Reykjavik Energy environment report 2014 (in Icelandic). Reykjavik Energy, Reykjavik, Iceland, 90 pp.

Sigurdsson, Th., 2015: TENORM in geothermal application in Iceland. *Presented at the "NSFS XVII conference", Roskilde, Denmark*, 9 pp.

Van Nguyen, M., Arason, S., Gissurarson, M., and Pálsson, P.G., 2015: *Uses of geothermal energy in food and agriculture - Opportunities for developing countries*. United Nations Food and Agriculture Organization, Rome, Italy, 2015. 62 pp.

Virkir-Orkint, 1990: *Djibouti. Geothermal scaling and corrosion study.* Virkir-Orkint, Reykjavík, report, 109 pp.

APPENDIX I: Interviews and discussions with experts from Reykjanes, Svartsengi, Hellisheidi power plants, ISOR and Orkustofnun

Interview 1: **Ómar Sigurdsson from HS Orka**

Reykjanes

1. How much the has the surface area which is impacted by heat increased from the start of the power plant? What is the main reason?

Ans: Changes in thermal surface manifestation have been very dynamic over the decades. Therefore, selection of reference point matters and the difference is only true over the compared period. Over longer or different time period the results may be quite different. If the reference is the start of the power plant the change in surface area that has been impacted by thermal activity has about doubled. The size of influenced area is today around 0.3 km^2.

2. What is the current situation with the pressure in the geothermal reservoir and how has it changed from the start of the power plant?

Ans: Currently the pressure drawdown in the central part of the production field is about 40 bar and becomes less with distance from the centre. The drawdown was very rapid during the first 2-3 years but has kind of stabilized now at a rate of about 1 bar/year.

3. What is the total amount of geothermal water from the power plant and how much of it is reinjected? What are the main results (lessons learned) of the reinjection?

Ans: In 2014 the average year production was 518 kg/s and the reinjection 82 kg/s. This is an infield injection and can therefore not be increased as it can cool wells and quench steam. Under construction is reinjection to wells at the outskirt of the field. Plans are to triple the injection with the main portion to these outer wells.

4. What is the number of wells, deep wells and shallow in to a steam pillow?

Ans: At Reykjanes we do not have steam cap or pillow as you call it. In the top part of the geothermal reservoir is a steam dominant two-phase zone while the reservoir is liquid dominated at greater depth. Most of the production wells have some connection to this steam zone as it is not cased off in them. Of the current 16 producers there are 3 shallow wells that only produce from the steam zone.

Svartsengi

5. What is the total amount of geothermal water from the power plant and how much of it is reinjected? What are the main results of the reinjection?

Ans: In 2014 the average year production was 488 kg/s and the injection 293 kg/s. Svartsengi is a liquid dominated reservoir and the reinjection plays a large role there in holding the drawdown rate at acceptable stabilization.

6. What will be the future solutions to dump the geothermal water?

Ans: Reinjection will be increased slightly (10-15%), effluent used by the Blue Lagoon and what goes to the lagoon from steering control of the power plant is disposed to shallow formations, the rest will be discharged to the sea.

7. How much is the surface subsidence in the centre of the area and has it had any problems for the utilization of the area?

Ans: The total subsidence at Svartsengi is on the order of 45-50 cm. It has so far not caused problems as construction in the area has been in steps so it has compensated for much of this subsidence.

Interview 2: **Hólmfrídur Sigurdardóttir, head of environmental affairs, Reykjavik Energy**

The answer to the first three questions are to be found in OR Environment report 2014 which is in English at the homepage: https://www.or.is/en/energy-environment

1. What is the current amount of CO_2 coming from the power plant and how much of it is reinjected?

Ans: See appendix 12 and 13 and the chapter Emissions of other geothermal gases (carbon dioxide, hydrogen and methane)

In 2014 2400 tonnes of CO_2 was pumped back down into the bedrock (since the CarbFix project started until the end of August 2015 3600 tonnes of CO_2 have been pumped down to the bedrock).

2. What is the current amount of H_2S coming from the power plant and how much of it is reinjected? See app 12 and 13 and the chapter Emissions of hydrogen sulphide.

Ans: The year 2014, 1500 tonnes of H_2S was pumped back down to the bedrock (since the CarbFix project started until the end of August 2015 about 2750 tonnes of H_2S have been pumped down to the bedrock).

3. How much is the pressure drop from the starting of the power plant?

Ans: See appendix 2b and discussion in the chapter managing high-temperature geothermal resources

4. How many wells have been drilled and how many are used as production wells and reinjection wells?

Ans: At the end of 2013, a total of 57 steam wells had been drilled south and east of the mountain Hengill; including 47 at the current Hellisheidi power plant production area, 3 in the Bitra area, 6 at Hverahlíd area and 1 by Gráuhnúkar area. In November 2014, a total of 33 wells were connected to the plant. Many wells are drilled in the same drilling site/well pad to reduce the environmental impact of the plant. The holes are not all connected to the plant as some are drilled to explore the edge of the area and others have not produced as much as hoped. Some of these wells are used for monitoring as it is important that some wells will be used to monitor temperature and pressure conditions in the area. 2 steam wells that did not serve as production wells were connected with the reinjection system in 2014. A new steam extraction hole was drilled in the summer of 2015.

At the end of 2013, 17 injection wells had been drilled to bring the separated water back into the geothermal reservoir. The wells have been drilled in four places. The first 3 wells were drilled in the Svínahraun lava field by the highway which is now abolished. The first two wells were vertical wells, but were not enough permeable/leaking to take the separated water. This area, and the wells have been used for the CarbFix project where the carbon dioxide is injected in order to bind it as mineral underground.
Next it was drilled in an area closer to the hillside under Gráuhnúkar. In this area have been drilled 6 wells that are accepting a lot of water.
By the hill Húsmúli north of the Hellisheidi power plant was drilled one exploratory well in order to explore the large faults that are in the Húsmúli area and are believed to be the western edge of the great rift valley which the geothermal activity is connected to. This well gave favourable hopes that there could be an area suitable for reinjection of the water from the separators. One another well was drilled in the same area, but its performance was not as good. In this area was then drilled 6 wells. Wells utilized as injection wells are 16 of which 2 are steam wells that did not serve as such and were connected to the injection system in 2014.

Over twenty groundwater holes have been drilled to explore the groundwater in the Hengill area plus other shallow wells, including wells for water for drilling and to lead the separated water from blowing wells below the surface.

5. What is the need for new wells pr. year/5 years to keep the production at 300 MWe? Will they be in the same area as the existing wells or is a need to expand the area?

Ans: 1-2 wells per year, cf. the chapter on geothermal power plants in the OR environmental report for 2012 : https://www.or.is/um-or/utgefid-efni#umhverfi.

As stated above, a new steam well was drilled on Hellisheidi summer of 2015. In 2016, 4 steam wells that were drilled few years ago at Hverahlíd area will be connected to the Hellisheidi power plant. Continued drilling steam wells will probably be both at the Hellisheidi power plant production area and other areas.

Minutes of the discussion with: **Jónas Ketilssson, Orkustofnun**

Orkustofnun is the authority that issues licenses for research and utilization of the geothermal resources. Decisions, in this regards, made by Orkustofnun can be appealed to the ruling committee for the resources act.

The utilization licenses sometimes specify limitations for the acceptable pressure drawdown if thought necessary by Orkustofnun due to the rate of exploitation. This applies in particular to geothermal power plants. An example is the Theistareykir geothermal field in north Iceland where the pressure drawdown is not allowed to be more than stipulated. It is also stated that the annual decrease in steam production cannot be more than 3% /year on average over the past five years.

If these requirements are not met the situation is analysed. Firstly, the models are re-calibrated and if issues for long-term utilization are below thresholds the license holder may have to increase reinjection, enlarge the production area and possibly even change utilization strategy.

Research on reinjection is recommended from the start of a power plant because it is a complicated process and needs normally some time consuming tests and even drilling of several wells.

In Hellisheidi the pressure drawdown is not more than predicted and allowed in the license. But at Reykjanes there is no limit in the utilization license that was published by the Ministry for industry in year 2004. However, in a new license issued by Orkustofnun in year 2011 there are limitations but that license is not in effect until the power plant is enlarged.

Link to the license of Reykjanesvirkjun:
http://www.os.is/media/leyfi-2011/Virkjunarleyfi-HS-Orka-fylgibref-15092011.pdf
Link to the license for Theistareykir:
http://www.os.is/media/utgefin%20leyfi/jardhiti-theistareykjum-ny%CC%81tingarl.pdf
http://www.os.is/media/utgefin%20leyfi/fylgibref-jardhiti-theistar.pdf
Link to the license for Hellisheidi:
http://www.os.is/media/leyfi-2011/virkjunarleyfi_OR_03.06.2011.pdf

Minutes of the discussion with: **Dr. Halldór Ármannsson, Iceland GeoSurvey**

Dr. Halldór Ármannsson took part in a comprehensive scaling/corrosion study in Assal, Djibouti (Virkir-Orkint 1990).

At the beginning of the conversation, the knowledge gained in previous research drilling and studies of precipitation associated with it was discussed. It was stated that of course is not possible to ascertain the composition of the brine from the wells in the new area until after drilling. Resistivity measurements and general geological studies on the surface can however give an indication of this, and are considered to suggest that a lower concentration of salt will be in the geothermal liquids in the Assal-Fiale are than in the areas where previous wells were drilled.

It can be expected that quite a high salt concentration will be in the geothermal fluid in Assal-Fiale and that there may be problems in getting rid of the fluid at the surface, immediately during the testing of wells. Therefore, it is correct to assume that it may be necessary to drill injection wells for the fluid, especially if the testing of the wells lasts for months as is desirable. Further studies / experiments on deposits from the geothermal fluid are needed to ensure a suitable permanent way of disposal. Disposal of the geothermal fluid in the sea may cause deposit problems and negative effects on the ecosystem in the vicinity of the outlet, because of chemicals in the liquid.

It emerged that that considerable deposits can be expected from the geothermal fluid and it is important what the wellhead pressure will be as well as the enthalpy. If there is high enthalpy (mainly steam) then the pressure matters little. Earlier studies in Assal (Geochemical patterns of scale deposition in saline high temperature geothermal systems: H. Ármannson and V. Hardardóttir Iceland GeoSurvey, Grensásvegur 9, IS-108, Reykjavík, Iceland) show that the pattern of deposition is such at pressure >16 bar that the major scales are sulphides, but at lower pressure iron silicate scales predominate down to amorphous silica saturation. The sulphide scaling can be dealt with by inhibition, but iron silicates and amorphous silica deposits by pressure (temperature) control.

As the plan in Djibouti is to drill four exploration wells in the Assal-Fiale area Halldór recommended that two wells would be drilled in the beginning and after testing 6-12 months (flowing) the other two wells would be drilled in the light of the results from the first ones.

Regarding the problems associated with gas from geothermal fluids, such as the high content of H_2S coming from the Hellisheidi Power plant, Halldór believes that based on available data that problems because of H_2S is very unlikely and as the area is considerably windy, the risk of accumulation should be low.

The attention was also drawn to the radioactivity measured in deposits from wellheads in Reykjanes power plant and that it is worth to have such measurements as a part of the monitoring program at the Assal-Fiale geothermal area.

UNITED NATIONS UNIVERSITY
UNU-GTP
Geothermal Training Programme

Orkustofnun, Grensasvegur 9,
IS-108 Reykjavik, Iceland

Reports 2015
Number 8

A STUDY ON DIFFERENT TWO-PHASE FLOW CORRELATIONS USED IN GEOTHERMAL WELLBORE MODELLING

Bryan T. Cacho
Energy Development Corporation - EDC
38/F One Corporate Centre Building
Julia Vargas corner Meralco Avenue
Ortigas Center, Pasig City, 1605
PHILIPPINES
cacho.bt@energy.com.ph

ABSTRACT

There are various flow correlations available to estimate the pressure drop associated with two-phase flow in a geothermal well. A number of previous studies on the different flow correlations have been conducted to assess their applicability in geothermal wellbore modelling. In this study, the performance of five flow correlations was evaluated and compared using discharge data from 39 geothermal wells that cover a wide range of wellhead conditions. The wellhead parameters were utilized to simulate the flowing pressure and temperature profiles using the wellbore simulator Simgwel. Different analyses were performed to identify which of these correlations would perform best depending on the condition of the fluid in the wellbore up to the wellhead.

1. INTRODUCTION

Geothermal wellbore modelling is one of the methods that reservoir engineers use for resource management decisions because it can provide vital information about the geothermal reservoir. It is the process of characterizing the behaviour of a geothermal well by reproducing the measured pressure and temperature profile and determining the relative contribution, fluid properties and fluid composition of each feed zone for a given discharge condition (Aunzo et al., 1991). Wellbore simulation can be used for optimizing the utilization of geothermal wells and improving reservoir models (Freeston and Gunn, 1993). Wellbore models are also being utilized to estimate improvements in well performance after carrying-out well interventions such as mechanical workover, relining of casing and acid injection (Fajardo and Malate, 2005). Based on its aforementioned applications, wellbore simulation is an important tool for resource optimization and management.

It is necessary to have a good understanding of the main aspects concerning the two-phase fluid flow in geothermal wells when performing wellbore simulations. Having in-depth knowledge about fluid flow can help predicting the pressure drop in the well more accurately and give better predictions if changes were to occur on mass flow or pressure in the well (Thórisdóttir, 2013). Various flow correlations have been developed to estimate the pressure drop in two-phase flow. These flow correlations greatly affect the simulated pressure drop in a geothermal well (Hsu and Graham, 1976). Accurately predicting the pressure drop in a geothermal well requires detailed information on:

1) Estimated feed zone contribution at a given wellhead condition;
2) Flash point location (used to determine the setting depth for calcite inhibition system in lieu of an actual survey);
3) Fluid velocity profile (required to predict required bottom hole assembly weight, throttling or threshold wellhead pressure to minimize erosion and sometimes to determine required throttling to run-in downhole tools); and
4) Fluid enthalpy changes.

All four aspects affect the simulated discharge parameters. Therefore, it is worthwhile to investigate the performance and applicability of these flow correlations. In this study, five two-phase flow correlations were used to predict the discharge pressure and temperature profiles of 39 geothermal wells using a wellbore simulator. The simulated pressure and temperature profiles were compared to the actual discharge data to evaluate and compare the performance of each flow correlation. The flow correlations used in this study are Orkiszewski, Armand, Duns and Ros, Hagedorn and Brown and Duns and Ros modified by Ros. The main objective of this study is to evaluate and compare the performance of these two-phase flow correlations and determine their applicability with given wellhead conditions.

2. THEORY ON TWO-PHASE FLOW IN GEOTHERMAL WELLS

In a high-temperature liquid-dominated reservoir, geothermal fluid generally undergoes flashing as it travels up through the wellbore. This flashing, which occurs due to pressure loss experienced by the fluid while travelling up through the wellbore, leads to two-phase flow. The pressure drop associated with two-phase fluid transport in a well is the sum of the pressure losses due to the frictional, gravitational and acceleration forces. In single-phase flow, the pressure drop can be easily determined because the fluid properties are well defined (Probst et al., 1992). However, in two-phase flow, accurately predicting the pressure drop is difficult because two-phase flows are complex and, under some conditions, the vapour moves with a higher velocity than the liquid. In addition, the velocity of the liquid phase along the casing wall of the wellbore can vary considerably over a short distance and resulting in variable friction loss. And under other conditions, the liquid is almost completely entrained in the gas and has very little friction loss due to contact with the casing wall. Therefore, the difference in velocity and the geometry of the two phases are very significant in predicting pressure drop in two-phase flow (Aunzo et al., 1991).

2.1 Single-phase flow

As mentioned above, pressure drop in single-phase flow through pipes can be easily estimated. In fluid mechanics literature by White (1979) the flow of single-phase fluid in pipes was investigated intensively. The flow calculations are performed with linear equations assuming that the fluid properties remain relatively constant (Björnsson, 1987). The components of the total pressure drop (pressure loss due to friction, gravity and acceleration) are given by:

$$\left[\frac{dP}{dz}\right]_{fri} = \frac{fG^2}{4r_w\rho} \quad (1)$$

$$\left[\frac{dP}{dz}\right]_{pot} = \rho g sin\theta \quad (2)$$

$$\left[\frac{dP}{dz}\right]_{acc} = \frac{d(Gu)}{dL} \quad (3)$$

where $\left[\frac{dP}{dz}\right]_{fri}$ = Pressure drop component due to friction [Pa/m];

$\left[\frac{dP}{dz}\right]_{pot}$ = Pressure drop component due to gravity [Pa/m];

$\left[\frac{dP}{dz}\right]_{acc}$ = Pressure drop component due to acceleration [Pa/m];
f = Friction factor;
G = Mass flux [kg s^{-1} m^{-2}];
r_w = Well radius [m];
ρ = Density of fluid [kg/m^3];
g = Gravitational constant [m/s^2];
θ = Deviation angle from horizontal [degree]; and
u = Average fluid velocity [m/s].

Thus, the total pressure drop equation can be written as:

$$\frac{dp}{dz} = \left[\frac{dP}{dz}\right]_{fri} + \left[\frac{dP}{dz}\right]_{pot} + \left[\frac{dP}{dz}\right]_{acc} \quad (4)$$

The friction factor f is given by White (1979):

If $Re < 2400$:

$$f = \frac{64}{Re} \quad (5)$$

If $Re \geq 2400$:

$$\frac{1}{f} = -2.0log_{10}\left[\frac{\in}{3.7(2r_w)} + \frac{2.51}{Ref^{0.5}}\right] \quad (6)$$

where Re = Reynold's number; and
$\in$ = Pipe roughness [m].

2.1.1 The continuity equation

The continuity equation describes the transport of conserved quantity (conservation of mass):

$$\frac{d}{dz}(\dot{m}) = 0 \quad (7)$$

If the diameter of the pipe is assumed to be constant, Equation 7 could be written in terms of cross sectional area of the pipe and fluid density as:

$$\frac{d}{dz}(\rho u) = 0 \quad (8)$$

2.1.2 The energy equation

From the first law of thermodynamics, the energy conservation equation contains a kinetic, potential and enthalpy part. The first term represents the change in kinetic energy due to the change in velocity, the second term is the change in potential energy as a result of change in elevation and the third term is the change in enthalpy:

$$\dot{m}u\frac{du}{dz} + \dot{m}g + \dot{m}\frac{dh}{dz} + \dot{Q} = 0 \quad (9)$$

where $\dot{Q}$ = Heat loss from the pipe per unit length [W/m]; and
h = Enthalpy of the fluid [kJ/kg].

2.1.3 The momentum equation

The momentum equation is divided into four terms: inertia, pressure changes, hydrostatic pressure and

head losses. The first term represents the change in inertia caused by velocity change, the second term is the pressure change of the fluid, the third term is the change in hydrostatic pressure and the last term is the head loss due to friction. The term $|u|u$ is used in order to consider the flow in both directions since the head loss is always in the direction of the flow:

$$\rho u \frac{du}{dz} + \frac{dp}{dz} + \rho g + \frac{\rho f}{2d}|u|u = 0 \tag{10}$$

where d = Diameter of the pipe [m].

2.1.4 Matrix form of the equations

The equations in the last three subsections need to be solved simultaneously. In order to do so, the equations were assembled in matrix form by Pálsson (2011). The matrix can also be solved using numerical integration from the bottom of the well to the top.

$$\begin{bmatrix} \rho & u\frac{\partial \rho}{dp} & u\frac{\partial \rho}{\partial h} \\ \dot{m}u & 0 & \dot{m} \\ \rho u & 1 & 0 \end{bmatrix} \frac{d}{dz}\begin{bmatrix} u \\ p \\ h \end{bmatrix} + \begin{bmatrix} 0 \\ \dot{m}g + \dot{Q} \\ \rho g + \frac{\rho f}{2d}|u|u \end{bmatrix} = \begin{bmatrix} 0 \\ 0 \\ 0 \end{bmatrix} \tag{11}$$

2.2 Two-phase flow

All the basic laws of fluid mechanics also apply to two-phase flow. However, equations describing two-phase flow are more complicated than those describing single-phase flow because the liquid and vapour phases have different thermodynamic properties (Thórisdóttir, 2013). The three main equations which are continuity, momentum, and energy will have to take both phases into account. To characterize two-phase flow, two important auxiliary parameters, steam mass fraction and void fraction, are introduced (Pálsson, 2011). The steam mass fraction is defined as the ratio of the mass of steam to the total mass of the mixture. The steam mass fraction x, also called as dryness, is given as:

$$x = \frac{\dot{m}_g}{\dot{m}} = \frac{\dot{m}_g}{\dot{m}_g + \dot{m}_l} \tag{12}$$

where $\dot{m}_g$ = Mass of steam or vapour [kg/s];
$\dot{m}_l$ = Mass of liquid [kg/s]; and
$\dot{m}$ = Total mass of the mixture [kg/s].

The steam mass fraction can also be expressed in terms of enthalpy:

$$x = \frac{h - h_l}{h_g - h_l} \tag{13}$$

where h_g = Enthalpy of the steam or vapour [kJ/kg]; and
h_l = Enthalpy of the liquid [kJ/kg].

Void fraction α is defined as the fraction between the area of steam and the total area of a given cross-section of a pipe (Pálsson, 2011). It is also called steam saturation and expressed as:

$$\alpha = \frac{A_g}{A} = \frac{A_g}{A_g + A_l} \tag{14}$$

where A = Cross-sectional area of the well [m^2];
A_g = Cross-sectional area occupied by vapour [m^2]; and
A_l = Cross-sectional area occupied by liquid [m^2].

In two-phase separated flow, there are two velocities present, liquid velocity u_l and vapour velocity u_v. Pálsson (2011) simplified the expression of flow velocities into a single variable, u. Where u is defined as the velocity that would be experienced if the liquid was flowing alone in the pipe, but with the same mass flow as the total flow:

$$u = \frac{\dot{m}}{\rho_l A} \tag{15}$$

Pálsson (2011) also incorporated u and x to the actual velocities where liquid velocity becomes:

$$u_l = \frac{\dot{m}_l}{\rho_l A_l} = \frac{(1-x)\dot{m}}{\rho_l(1-\alpha)A} = \frac{1-x}{1-\alpha}u \tag{16}$$

and the vapour velocity:

$$u_v = \frac{\dot{m}_g}{\rho_g A_g} = \frac{x\dot{m}}{\rho_g \alpha A} = \frac{x\rho_l}{\alpha\rho_g}u \tag{17}$$

where ρ_l = Density of the liquid [kg/m^3]; and
ρ_g = Density of the vapour [kg/m^3].

2.2.1 The continuity equation

The continuity equation for two-phase flow consists of liquid and vapour phases. Assuming that the pipe diameter is constant, the equation can be written as:

$$\frac{d}{dz}(\dot{m}_l + \dot{m}_v) = \frac{d}{dz}\left(\rho_l u_l A_l + \rho_g u_g A_g\right) = 0 \tag{18}$$

Equation 18 was also simplified by Pálsson (2011) using the void fraction definition:

$$\frac{d}{dz}\left(\rho_l u_l(1-\alpha) + \rho_g u_g \alpha\right) = 0 \tag{19}$$

$$\frac{d}{dz}(\rho_l(1-x)u + \rho_l x u) = 0 \tag{19}$$

$$\frac{d}{dz}(\rho_l u) = 0 \tag{20}$$

2.2.2 The energy equation

The energy equation for two-phase flow can be written as:

$$\frac{d}{dz}\left(\dot{m}_l\left(\frac{u_l^2}{2} + gz + h_l\right) + \dot{m}_v\left(\frac{u_g^2}{2} + gz + h_g\right)\right) + \dot{Q} = 0 \tag{21}$$

Introducing γ in the equation and following the derivation of Pálsson (2011) would give:

$$\gamma = \frac{(1-x)^3}{(1-\alpha)^2} + \frac{\rho_l^2 x^3}{\rho_g^2 \alpha^2} \tag{22}$$

$$\gamma u\frac{du}{dz} + \frac{u^2\partial\gamma dp}{2\partial p dz} + \left(1 + \frac{u^2}{2}\frac{\partial\gamma}{\partial h}\right)\frac{dh}{dz} + g + \frac{\dot{Q}}{\dot{m}} = 0 \tag{23}$$

2.2.3 The momentum equation

The momentum equation in two-phase flow has to consider the inertial part and the gravitational part where the density has to be an averaged value with respect to the void fraction (Pálsson, 2011):

$$\rho_{\propto} = (1-\alpha)\rho_l + \alpha\rho_g \tag{24}$$

Hence, the momentum equation can be written as:

$$\frac{d}{dz}\left(\dot{m}_l u_l + \dot{m}_g u_g\right) + A\frac{dp}{dz} + \left((1-\alpha)\rho_l + \alpha\rho_g\right) gA + \Phi^2 \frac{\rho_l f A}{2d} u^2 \tag{25}$$

where Φ^2 = Correction factor for the frictional pressure loss in two-phase flow.

The momentum equation is simplified by introducing η:

$$\eta = \frac{(1-x)^2}{1-\alpha} + \frac{\rho_l}{\rho_g}\frac{x^2}{\alpha} \tag{26}$$

Finally, the momentum equation can be written as:

$$\eta\rho_l u\frac{du}{dz} + \left(1 + \rho_l u^2\frac{\partial\eta}{\partial p} + \eta u^2\frac{\partial\rho_l}{\partial p}\right)\frac{dp}{dz} + \rho_l u^2\frac{\partial\eta}{\partial h}\frac{dh}{dz} + \left((1-\alpha)\rho_l + \alpha\rho_g\right) g + \frac{\Phi^2\rho_l f}{2d}u^2 = 0 \tag{27}$$

2.2.4 Matrix form of the equations

The three governing equations were assembled in a similar manner as in single-phase flow by Pálsson (2011) in matrix form which can also be solved by using numerical integration from the bottom to the top of the well.

$$\begin{bmatrix} \rho_l & u\frac{\partial\rho_l}{dp} & 0 \\ \gamma u & \frac{u^2}{2}\frac{\partial\gamma}{\partial p} & \left(1 + \frac{u^2}{2}\frac{\partial\gamma}{\partial h}\right) \\ \eta\rho_l u & \left(1 + \rho_l u^2\frac{\partial\eta}{\partial p} + \eta u^2\frac{\partial\rho_l}{dp}\right) & \rho_l u^2\frac{\partial\eta}{\partial h} \end{bmatrix} \frac{d}{dz}\begin{bmatrix} u \\ p \\ h \end{bmatrix} + \begin{bmatrix} 0 \\ g + \frac{\dot{Q}}{\dot{m}} \\ \left((1-\alpha)\rho_l + \alpha\rho_g\right) g + \frac{\Phi^2\rho_l f}{2d}u^2 \end{bmatrix} = \begin{bmatrix} 0 \\ 0 \\ 0 \end{bmatrix} \tag{28}$$

2.2.5 Liquid holdup

Liquid holdup (H_l) is defined as the fraction of a unit volume of pipe which is occupied by liquid at same instant (Carrascal, 1996). It is expressed as:

$$H_l = \frac{volume\ of\ liquid\ in\ a\ pipe\ segment}{volume\ of\ pipe\ segment} \tag{29}$$

3. TWO-PHASE FLOW CORRELATIONS

Many empirical correlations and models have been developed to estimate the pressure drop associated with two-phase flow in geothermal wells (Probst et al., 1992). These correlations use different methods in calculating the three components of the total pressure gradient (see Equation 4). Some of these correlations will be described later.

Two-phase flow models were divided into two categories: homogenous and separate flow models. The assumption in homogenous flow model is that the liquid and vapour phases travel at the same velocity and the slippage between the phases are ignored. In separated flow models, it is considered that the vapour phase flows faster than the liquid phase and that the phases flow concurrently (Gudmundsdóttir, 2012). The difference between liquid and vapour velocities is called "slip velocity" (Probst et al., 1992). According to Björnsson (1987), it is customary to use the method of separated flow models where the flow of liquid and vapour are treated separately using the well-established theory of single-phase flow. Then, the equations for the two phases are extended for two-phase flows using empirical correlations. These empirical correlations are also called two-phase flow correlations.

3.1 Orkiszewski correlation

The Orkiszewski correlation (Orkiszewski, 1967) is based on the study of several published correlations used to determine the pressure drop in oil and gas systems. Orkiszewski selected different two-phase flow correlations and evaluated them by comparing correlation predictions to actual data. A total of 148 wells were used in the investigation. The results show that no single correlation was accurate enough to predict the pressure gradient in a well for a wide set of different flow conditions.

Two-phase flow correlations were classified by Orkiszewski (1967) according to their similarity in theoretical concepts and separated into three categories:

1. The liquid holdup is neglected in the determination of the mixture density which is just corrected by pressure and temperature. The liquid holdup and the pressure losses are correlated in an empirical friction factor. Flow regimes are neglected.
2. The liquid holdup is considered in the calculation of the mixture density. It is correlated separately or in combination with friction losses. The friction losses are calculated using the properties of the mixture. Flow regimes are neglected.
3. The liquid holdup is used to calculate the mixture density. The liquid holdup is determined using the concept of slip velocity (difference between gas and liquid velocities). The friction losses are determined using the continuous phase. Flow regimes are considered.

There are four flow regimes that were considered in the Orkiszewski correlation. These flow regimes are: bubble, slug, transition (slug-annular) and mist. Orkiszewski (1967) used different methods for predicting pressure drop and chose which among them is the most appropriate to use for each flow regime. For bubble flow, Griffith-Wallis (1961) correlation was used without any modifications done in the correlation. For slug flow, the same correlation was used but it was modified because it is not reliable in the higher flow rate range of slug. The modification of the Griffith-Wallis correlation (for the slug flow) included a parameter for the liquid distribution, the liquid film and the liquid entrained in the gas bubble. This parameter accounts for the liquid holdup at the higher flow velocities. Orkiszewski used the data from the Hagedorn and Brown (1965) model to evaluate the liquid distribution coefficient or holdup (Bellarby, 2009). For mist flow, the Duns and Ros correlation (1963) was used. Flow correlations that were used in Orkiszewski method for different flow regimes are listed in Table 1.

TABLE 1: Correlations used in Orkiszewski method

Method / correlation	Flow regime
Griffith	Bubble
Griffith and Wallis	Slug (density term)
Orkiszewski	Slug (friction gradient term)
Duns and Ros	Transition
Duns and Ros	Mist or annular

3.1.1 Flow regimes considered in Orkiszewski correlation

In the case of two-phase flow, the distribution of liquid and gas phases may vary depending on the velocity, the inclination of the well and the amount of each fluid. Flow regimes can be considered as the distribution of each phase with respect to each other in a well. Determining the flow regimes in a vertical well is much easier than in a horizontal well because in the horizontal flow pattern, the phases tend to separate due to gravity. For a two-phase fluid flowing up through an incline pipe, the flow pattern is slug or mist for most of the cases (Carrascal, 1996). As mentioned above, there are four flow regimes that were considered by Orkiszewski (1967), their names and descriptions are as follows:

- *Bubble* - In this flow regime, the liquid phase is the continuous phase and occupies most of the pipe volume. The gas is distributed in the pipe in form of bubbles that have different sizes and moving in different velocities. The effect of gas on the pressure gradient is small because of its density value. Therefore, the liquid phase is decisive in the pressure gradient calculation.
- *Slug* - The liquid phase in this regime remains as the continuous phase, but the bubbles have increased in number and form a single bubble that may have a size close to the pipe diameter. The bubbles are surrounded by a liquid film. The liquid around the film may move upward (in direction of bulk flow) or it may move downward. The gas bubbles have higher velocity than the liquid. Both liquid and gas contributes in the total pressure gradient.
- *Transition* - In this regime, the gas phase becomes the continuous phase and some liquid is entrained as small droplets into gaseous phase. The gas phase is more dominant than the liquid phase. Thus, the gas has a greater influence on the total pressure gradient than the liquid.
- *Mist* - The gas phase is the continuous phase and the liquid is entrained in the gas where gas is the predominant factor. The gaseous phase controls the pressure gradient and liquid causes secondary effects.

An illustration of how the fluid looks in different flow regimes (bubble, slug, transition and mist), taken from Orkiszewski (1967), is presented in Figure 1.

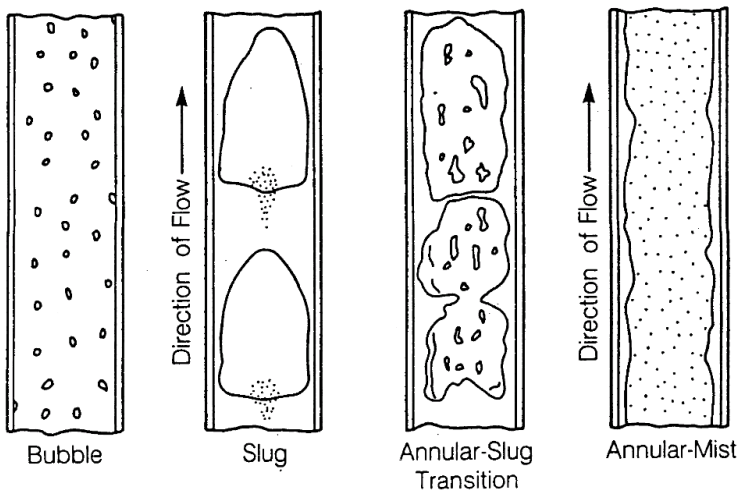

FIGURE 1: Illustration of the four flow regimes in the Orkiszewski correlation (Orkiszewski, 1967)

3.2 Duns and Ros correlation

The Duns and Ros (1963) correlation is the result of intensive laboratory experiments. About 4,000 two-phase flow tests were conducted in a 185 ft. high vertical-flow loop. Pipe diameters used are ranging from 1.3 to 5.6 inches. Most of the tests were near atmospheric conditions using air (for the gas phase) and liquid hydrocarbons or water (for the liquid phase). The authors expressed the energy equation as a pressure balance equation. They defined three terms in the pressure balance equation: the static gradient term, the wall friction gradient term and the acceleration gradient term. In the static gradient term, the effects of liquid holdup were considered and were kept separated from the effects of friction (Carrascal, 1996). Duns and Ros (1963) developed a flow regime map which is used as the basis of parameters of superficial gas and liquid velocities. The flow regime map is divided into three regions and the liquid holdup is calculated differently in each region (Bellarby, 2009). The three regions are determined by the

continuity, or lack of continuity, of the liquid and gas phases. These regions were defined by Duns and Ros (1963) as follows:

- *Region I* - The liquid phase is continuous and bubble flow, plug flow and part of the froth flow regime exists.
- *Region II* - In this region, the phases of liquid and gas alternate. The region covers slug flow and the remainder of the froth flow regime.
- *Region III* - The gas is in a continuous phase and the mist flow regime exists.

The diagrams and regions are illustrated in Figure 2. There is also a transition zone between regions II and III (see Figure 2). The Duns and Ros correlation is widely used for pressure drop prediction in mist flow regime (Bellarby, 2009). The correlation was developed for oil and gas mixtures, however, the authors claim that the method should also be accurate for water and gas mixtures (Probst et al., 1992).

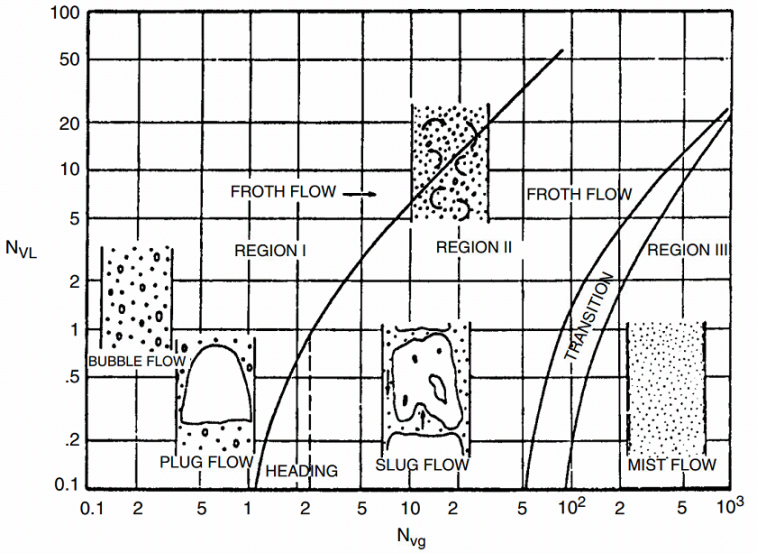

FIGURE 2: Region of occurrence of different flow regimes as described by Duns and Ros (1963); figure adapted from Lyons (2010)

3.3 Duns and Ros modified by Ros correlation

Duns and Ros modified by Ros correlation was developed from tests on a vertical pipe using air-water and air-liquid hydrocarbon mixtures. The only difference between this correlation and the Duns and Ros correlation is the treatment of pressure drop due to acceleration and friction. Duns and Ros modified by Ros correlation uses a two-phase multiplier based on Martinelli and Nelson and modified by Chisholm, while Duns and Ros correlation uses their own two-phase multiplier to correct the single-phase pressure drop due to friction (McGuinness, 2014).

3.4 Hagedorn and Brown correlation

Hagedorn and Brown (1965) developed an empirical correlation using a small-diameter, 1500-ft. vertical experimental well. In the experimental analysis, tubing diameters ranging from 1 to 2 in. were considered along with five different fluid types, namely water and four types of oil with viscosities ranging between 10 and 110 cP (at 80°F). This correlation does not consider different flow regimes. The liquid holdup is used as a correlating parameter in the calculation of the total pressure drop for an incremental length of pipe. Nevertheless, this correlation is effectively a prediction for slug flow, although further study was done to verify whether the flow was in the bubble flow regime (Lyons, 2010).

Having been one of the frequently used correlations, Hagedorn and Brown method has been derived several times subsequently, ensuring that the predicted holdup would not go below the no-slip hold-up in the calculations as this tends to produce better results (Bellarby, 2009).

Furthermore, this correlation was generated using data measured for a wide range of gas-liquid ratios and differing fluid properties. Hence, this correlation is commonly used in oil wells including those with

pumps. In spite of their increasing gas to liquid ratios, gas-lifted wells still frequently produce slug flow and the Hagedorn and Brown correlation therefore, remains applicable (Ravindran and Horne, 1993).

3.5 Armand correlation

The Armand (1946) correlation is one of the first correlations for predicting the void fraction while considering the non-homogenous nature of two-phase flow (Aunzo et al., 1991). Also, Armand's empirical correlation was used to calculate the velocities of gas and liquid phases that are needed in the evaluation of momentum flux and energy equations (Bhat et al., 2005). According to the study of Spedding and Chen (1982), Armand correlation only applies to the bubble and slug flow regimes.

3.6 Previous studies

Many researchers have conducted studies on the different correlations used in various two-phase flow, or pressure drop models. Gould (1974) is one of the first researchers who assessed the applicability of different pressure drop models to the geothermal industry. Gould evaluated the performance of three correlations namely, Hagedorn and Brown (1965), Aziz (1972) and Orkiszewski (1967) correlations, simulating data primarily taken from the wells of Wairakei and Broadlands fields in New Zealand. However, Gould only considered the effect of dissolved solids and ignored the effects of non-condensable gasses. Consequently, Gould provisionally concluded that one modification of Hagedorn and Brown correlation was the most consistent in performance.

Another pair of investigators is Ambastha and Gudmundsson (1986) who noted that the general applicability of flow correlations cannot be demonstrated if a number of pressure drop models are compared on a single or only few data sets. The authors decided to check on which geothermal conditions Orkiszewski (1967) correlation performs satisfactorily by collecting well test data from 10 geothermal wells demonstrating a wide range of characteristics (although pure water was assumed in all cases). Eventually, the authors were able to conclude that the Orkiszewski (1967) correlation is generally applicable; however, it obtains better results when the steam mass flux (steam flow per unit area) is greater than 100 kg s^{-1} m^{-2}.

A comparison of Orkiszewski (1967) correlation with another correlation was the study of Tanaka and Nishi (1988). There the authors matched the Orkiszewski (1967) correlation with another correlation for sixteen tests of eight wells, thirteen of which were incorporated with carbon dioxide content. All production data have wellhead dryness fractions of 10% or less. With this, Tanaka and Nishi observed that the Orkiszewski correlation did not perform satisfactorily. On the other hand, Freeston and Hadgu (1988) compared five wellbore simulators, three of which were based on the Orkiszewski (1967) correlation and one being the simulator developed by Barelli et al. (1982) which was the only one capable of handling non-condensable gases. Freeston and Hadgu (1988) tested the simulators on production data from eleven wells with broad and different characteristics and concluded that none of the five simulators were applicable to all conditions.

4. PERFORMANCE EVALUATION OF FLOW CORRELATIONS

4.1 Geothermal well data

Prior to the evaluation of flow correlations, discharge data from 39 two-phase production wells were collected. The geothermal wells are located in five geothermal fields in the Philippines: BacMan, Leyte, Mindanao, Northern Negros and Southern Negros. Additionally, one well located in Reykjanes, Iceland, was used. The data that were utilized in this study cover a wide range of wellhead conditions. The

wellhead pressure ranges from 5 to 60 bar-a, the enthalpy from 900 to 2500 kJ/kg and the total mass flowrate from 7 to 70 kg/s. Most of the wells are standard diameter wellbores (9 5/8" production casing diameter). The discharge data, wellhead diameter and depth of the wells are shown in Table 2.

TABLE 2: Discharge test data used for the flow correlation comparisons

Well	Mass flow (kg/s)	Wellhead dryness (%)	Depth (m)	Wellhead diameter (in)	Well	Mass flow (kg/s)	Wellhead dryness (%)	Depth (m)	Wellhead diameter (in)
1	Moderate	Low	1927	13 3/8"	20	Low	Medium	1210	13 3/8"
1.1	Moderate	Low	1927	13 3/8"	21	High	Low	1731	9 5/8"
2	Moderate	Medium	1179	9 5/8"	22	Moderate	Medium	623	9 5/8"
3	Moderate	Low	1334	13 3/8"	23	Low	Low	609	9 5/8"
4*	Low	Low	1460	9 5/8"	24	Low	Medium	599	9 5/8"
5	Low	Medium	652	9 5/8"	25	Low	Medium	654	9 5/8"
6	High	Low	862	13 3/8"	26	Low	Low	637	9 5/8"
7	High	Low	1561	9 5/8"	27	Low	Medium	1454	9 5/8"
8	Low	Low	667	9 5/8"	28	Low	Low	1283	9 5/8"
9	Low	Medium	902	9 5/8"	29	Low	Low	1285	9 5/8"
10	Moderate	Low	1947	13 3/8"	30	Moderate	Low	963	9 5/8"
11	Low	Low	1955	9 5/8"	31	High	Low	1176	9 5/8"
12	Low	Medium	1220	13 3/8"	32	Moderate	Low	1760	9 5/8"
13	High	Low	601	9 5/8"	33	Moderate	Low	1407	9 5/8"
14	Moderate	Low	1014	9 5/8"	34	High	Low	1056	9 5/8"
15	Low	Medium	733	9 5/8"	35	Low	Medium	1610	9 5/8"
16*	Low	Low	680	9 5/8"	36	Moderate	Low	1224	9 5/8"
17	Moderate	Low	862	9 5/8"	37	Moderate	Low	1260	9 5/8"
18	Moderate	Low	1001	9 5/8"	38	Moderate	Low	1747	9 5/8"
19	High	Low	1747	9 5/8"	39	Moderate	Low	1430	9 5/8"

** perforated wells*

The total mass flowrates were classified as low (< 20 kg/s), moderate (20 - 40 kg/s) and high (> 40 kg/s). Wellhead dryness was classified as low (< 1500 kJ/kg), medium (1500 - 2500 kJ/kg) and high (> 2500 kJ/kg). The depth indicated in Table 2 is not the total depth of the well. The depth considered in this study is the depth where the top of the slotted liner (TOL) is located. And for perforated wells, the depth was set just above the perforated section. Also, note that one of the wells has two sets of discharge data. Both data were used, named Well 1 and Well 1.1.

The parameters used for evaluating the performance of the flow correlations are summarized below:

- Wellhead parameters (wellhead pressure, total mass flow and enthalpy);
- Casing geometry of the well;
- Pressure and temperature logs during discharge.

The total mass flowrate and enthalpy of the wells at the wellhead were calculated using the James lip pressure method while pressure and temperature logs were taken using Kuster pressure and temperature gauge. For some of the wells, flowing pressure and temperature were measured using a memory type PTS (Pressure-Temperature-Spinner) measuring tool.

4.2 Wellbore simulation

The flowing pressure and temperature profiles in the cased portion of the wells were simulated using the earliest version of wellbore simulator Simgwel (ver. 9.21) developed by Marsan Consulting, Ltd. and Energy Development Corporation (Marquez et al., 2015). The core of Simgwel is based on the research tool GWELL and completely written in Fortran95. The wellbore simulator solves coupled steady-state mass, momentum and energy conservation equations for liquid, vapour and two-phase fluids containing carbon dioxide up a geothermal well (McGuinness, 2013). The capabilities of Simgwel as enumerated by Marquez et al. (2015) are:

1) Models liquid, steam and two-phase fluid flow where CO_2 content is considered;
2) Considering of the effect of heat transfer between the reservoir and the well;
3) Giving options for using different parameters in well geometry (i.e. roughness, inner diameter of casing or liner and deviation of the well);
4) Performing feed zone to wellhead and wellhead to feed zone simulations for single- or multi-feed production and injection wellbore models;
5) Producing simulated liquid and vapour velocities, flash point, flow pattern or flow regime, mass fraction of CO_2, enthalpy, static and dynamic steam fraction, flowing pressure and temperature across a well's depth;
6) Providing well's output for different wellhead pressures using estimated deliverability parameters (i.e. steam coefficient, linear drawdown factor, quadratic drawdown coefficient and viscosity-independent productivity index) given other feed parameters (i.e. reservoir pressure, mass flow and enthalpy);
7) Giving data points and graphical plots of simulated flowing pressures and temperatures, fluid velocities and bore output curves; and
8) Considering setting of the bottom hole pressure range of the simulated output curve.

The wellhead parameters in Table 2 were utilized to simulate the flowing pressure and temperature profiles using the five two-phase flow correlations: Orkiszewski (1967), Armand (1946), Duns and Ros (1963), Hagedorn and Brown (1965) and Duns and Ros modification by Ros (1961). Top-down simulations were performed wherein the calculations start from the wellhead down to TOL (or just above the shallowest feed, for perforated wells). Simulations only covered the cased-off section of the wells to limit the number of simulation variables that need to be controlled and to remove modeller bias that may result from modeller inputs of feed contribution and enthalpy. Modeller bias in the feed zone inputs is a concern because most of the studied wells do not have spinner data making it difficult to estimate the mass flow distribution across the feed zones. The effects of heat loss or gain from the formation to wellbore were also ignored. It is also assumed that the casing of the wells is clear from obstruction and scaling. The casing roughness assumed for all of the wells is 46 μm. Probst et al. (1992) stated that wellbore roughness is significant to the calculation of pressure drop because as the enthalpy of the fluid increases, the frictional component of the pressure drop also increases. A minimal mass fraction of CO_2 content (~0.001) was assumed in all simulations. This is a reasonable value, since it is a little less than the equilibrium value for water in contact with air at atmospheric condition (McGuinness, 2014).

4.3 Comparison of simulated and measured flowing profiles

To measure the accuracy of the flow correlations, the error between the measured and simulated flowing pressure and temperature profiles are calculated at every 15 m depth interval. The error is defined as:

$$e_i = measured\ value - predicted\ value \tag{30}$$

The calculated errors are used to apply the method of root-mean-square error (RMSE). The root-mean-square error is mostly used to measure the differences between values predicted by a model and the values actually measured or observed (Koehler and Koehler, 2006):

$$RMSE = \sqrt{\frac{1}{n}\sum_{i=1}^{n} e_i^2} \tag{31}$$

Then, the average of the pressure and temperature RMS-error is assumed to be the total error and used as the basis for evaluating the performance of each flow correlation:

$$Total\ error = \frac{RMSE_{press.} + RMSE_{temp.}}{2} \tag{32}$$

The correlation with the lowest total error would be the best match for that specific well. It is also possible that two or more correlations could give the best match on the pressure and temperature profile of the well. An example of that case is illustrated in Figure 3.

Figure 3 shows the plots of the measured and simulated temperature and pressure values of well 39 using five correlations. In this case, the Orkiszewski, and the Duns and Ros (modified by Ros) correlations performed equally well.

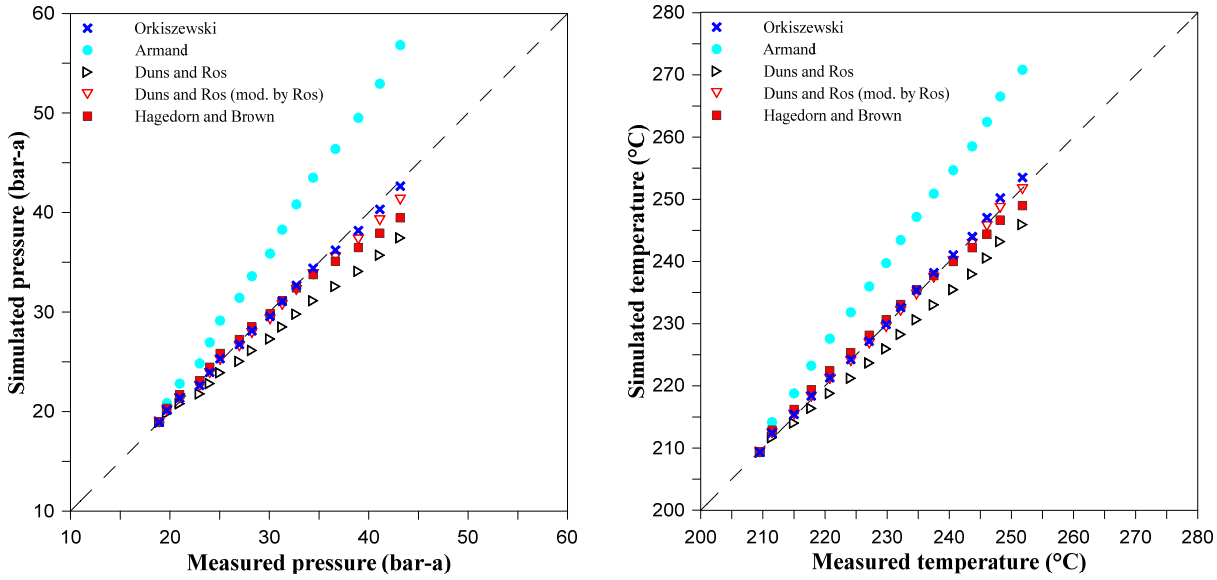

FIGURE 3: Measured vs. simulated pressure and temperature from wellhead to the top of slotted liner of well 39

4.4 Performance of flow correlations based on the number of wells matched

The performance of flow correlations was first evaluated based on the number of wells matched. The number of wells matched by each correlation and the mean error (based on wells matched) are summarized in Table 3. The results show that the Orkiszewki correlation matched 10 wells in which wellhead pressure is ranging from 10 to 50 bar-a and a total mass flow rate ranging from 7 to 70 kg/s (same as the data sets range of mass flow rate). It is also noted that the Orkiszewski correlation has the lowest mean error based on the results. The Armand correlation, on the other hand, matched 7 wells having a wellhead pressure ranging from 10 to 40 bar-a and mass flow rate ranging from 10 to 40 kg/s. However, the Armand correlation's performance is very poor based on both its number of wells matched and mean error.

TABLE 3: Number of wells best matched by the flow correlations based on average pressure and temperature RMS-error

Flow correlation	Number of best-matches	Mean error of best-matches (bar-a °C)
Orkiszewski	10	4.3
Armand	7	8.1
Duns and Ros	14	6.4
Duns and Ros (mod. by Ros)	12	4.7
Hagedorn and Brown	13	8.4

The Duns and Ros correlation performed the best among the tested correlations based on the total number of wells matched. Wells matched using this correlation have a wellhead pressure ranging from

5 to 30 bar-a and a mass flow rate ranging from 10 to 70 kg/s. As for the Duns and Ros (modified by Ros) correlation, it performed well in simulating flowing pressure and temperature profiles of wells having wellhead pressure within the range of 10 - 40 bar-a and mass flow rate within the range of 10 - 70 kg/s. Lastly, the Hagedorn and Brown correlation also performed well based on the number of wells matched, though its mean error is considerably higher. The wells matched by this correlation have wellhead pressure ranging from 8 to 60 bar-a and a mass flow rate ranging from 10 to 60 kg/s.

4.5 Performance of flow correlations based on error distribution

The histogram of the average RMS-errors of each flow correlations were constructed to further evaluate and compare their performances based on the distribution of the errors produced by each correlation. In the paper of Probst et al. (1992), it was suggested that an error of 3 - 4 bar-a in predicting pressure drop might be acceptable. In this analysis, an error of 3 bar-a for pressure and 5°C for temperature was considered and getting their average would give an error value of approximately 4 bar-a °C. This error value was then used as the maximum acceptable error in evaluating the performance of the flow correlations.

In Figure 4, the distribution of the errors of each flow correlation is illustrated. Based on their histograms, Duns and Ros correlations apparently have the most satisfactory results of all correlations. However, it was observed that the Orkiszewski correlation did also perform well in simulating the given discharge data sets based on its error distribution. And it can be noticed that there is only a very little difference between the results of Orkiszewski and Duns and Ros correlations (based on their frequency of errors that is less than 4). Duns and Ros (modified by Ros) correlation comes to be third best according to its error distribution. Though, using this correlation, the possibility of getting an error (higher than the acceptable error) could be expected.

Furthermore, even though the Hagedorn and Brown correlation seems to perform well based on the number of wells matched, its error distribution suggests that there is a greater possibility that big errors would be obtained if used in simulating wells with wide range of wellhead conditions. And finally, the Armand correlation, gives unsatisfactory results based on its error distribution. It also gives poor results even without considering the error. Thus, it could be an indication that Armand correlation is not applicable to the wellhead conditions used in this study.

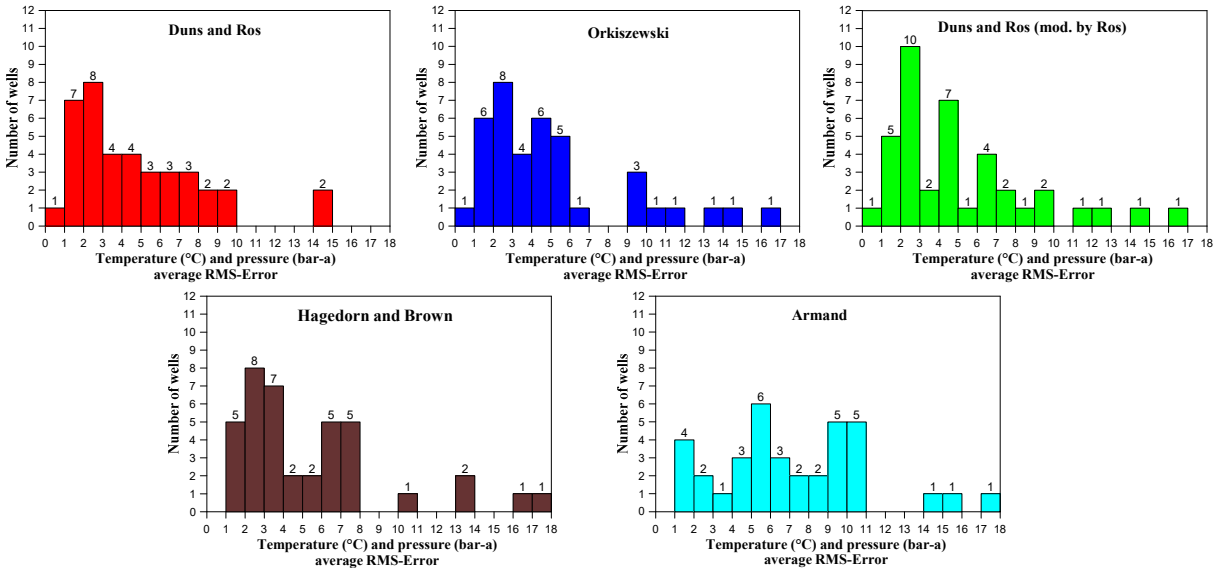

FIGURE 4: Distribution of the temperature (°C) and pressure (bar-a) average root-mean-square errors of the five flow correlations; dashed lines mark the acceptable error

The cumulative frequency distributions of the error of five flow correlations were also plotted in Figure 5. The plot shows that Duns and Ros correlation is slightly better than Orkiszewski, Hagedorn and Brown and Duns and Ros (modified by Ros) correlation, but this could be the result of statistical errors. The Armand correlation is obviously not applicable in a wide range of wellhead condition. Also, based on the plot the probability of getting an acceptable error (≈ 4 bar-a °C) using the five flow correlations are: 48% for Orkiszewski, 18% for Armand, 45% for Duns and Ros (modified by Ros) and 50% for both Duns and Ros and Hagedorn and Brown.

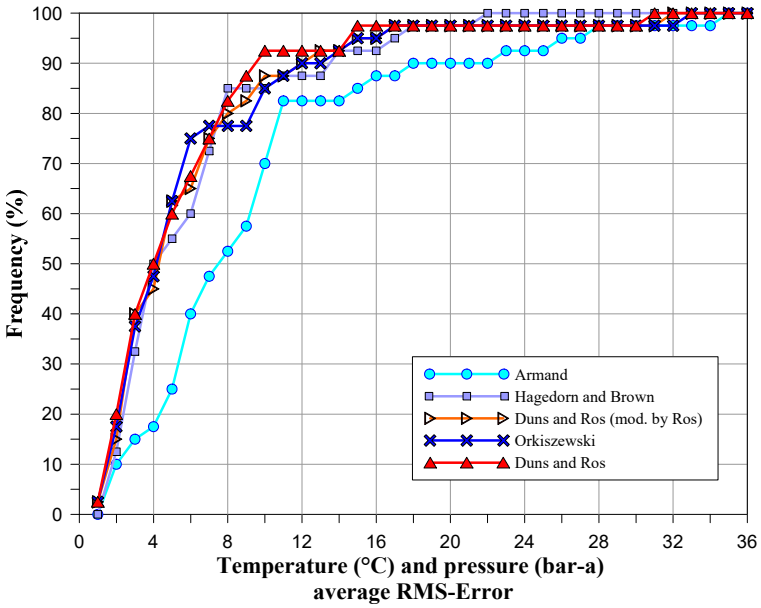

FIGURE 5: Cumulative frequency distribution of temperature and pressure average RMS-error

4.6 Performance of flow correlations based on wellhead conditions

Based on the previous analyses, it appears that Orkiszewski, Duns and Ros, Duns and Ros (modified by Ros) and Hagedorn and Brown correlations could have a general applicability in geothermal wellbore simulation. However, it would be better to identify under what conditions these flow correlations would perform the best by considering other parameters. In order to identify their applicability based on specific wellhead condition, several trials were performed such as plotting wellhead pressure versus total mass flow rate, steam fraction versus total mass flow rate and mass flow rate versus enthalpy. Then, it was observed that by plotting wellhead pressure versus wellhead steam mass flux, the wells matched by different flow correlations seem to form a cluster (see Figure 6). Steam mass flux considers different parameters at the wellhead such as dryness, enthalpy, mass flow and diameter. It can be expressed as:

$$Steam\ mass\ flux = \frac{\dot{m}_g}{\pi r^2} \tag{33}$$

where r = Radius of the well at the wellhead [m].

As illustrated in Figure 6, the wells matched by the Duns and Ros correlation mostly have wellhead pressure less than 30 bar-a and steam mass flux greater than 100 kg s^{-1} m^{-2}. This means that the Duns and Ros correlation performs best under such condition. On the other hand, the Orkiszewski and the Duns and Ros (modified by Ros) correlations could be expected to produce good results if the wellhead pressure is less than 20 bar-a and the steam mass flux is higher than 100 kg s^{-1} m^{-2}. Then, the wells matched by the Armand correlation apparently lie within the wellhead pressure range of 10 - 40 bar-a and less than 200 kg s^{-1} m^{-2} steam mass flux which clearly shows that Armand correlation could produce good results under such condition. Also,

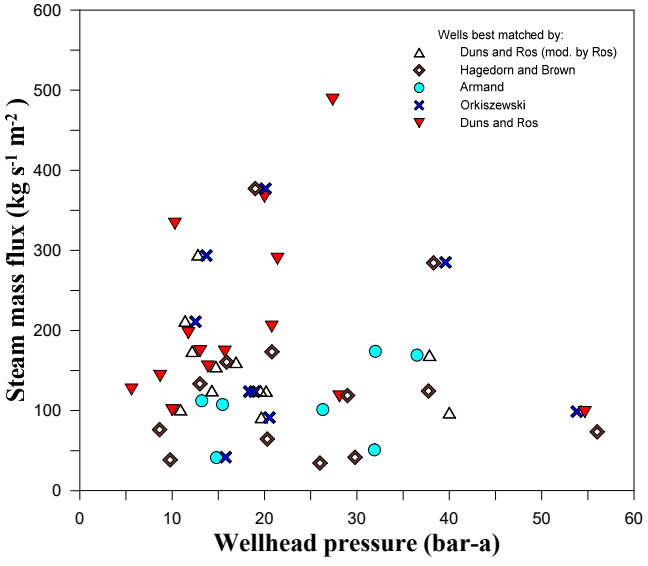

FIGURE 6: Wellhead pressure vs. steam mass flux

Hagedorn and Brown performs well under conditions almost similar to Armand correlation, with the addition that Hagedorn and Brown could match wells having wellhead pressure less than 10 bar-a. Seen in Table 4 are the conditions at the wellhead where each of the flow correlations performed well.

TABLE 4: Conditions where the different flow correlations performed well

Flow correlation	Wellhead pressure	Steam mass flux
Duns and Ros	< 30 bar-a	> 100 kg s^{-1} m^{-2}
Armand	10 - 40 bar-a	< 200 kg s^{-1} m^{-2}
Orkiszewski	< 20 bar-a	> 100 kg s^{-1} m^{-2}
Duns and Ros (mod. by Ros)	< 20 bar-a	> 100 kg s^{-1} m^{-2}
Hagedorn and Brown	< 40 bar-a	< 200 kg s^{-1} m^{-2}

4.7 Performance of flow correlations based on wellhead enthalpy

The flow correlations were also evaluated based on the enthalpy of the well. In this analysis, the classification of wells based on wellhead dryness mentioned in Section 4.1 was used. Out of 40 wells, 29 have enthalpy less than 1500 kJ/kg while the rest have enthalpy ranging from 1500 to 2500 kJ/kg. This is to identify which correlation will give a good result in reproducing the flowing pressure and temperature of a well having an enthalpy less than 1500 kJ/kg or in the range 1500 - 2500 kJ/kg. In Figure 7, the mean errors obtained by the flow correlations on two classifications of wellhead enthalpy or dryness are illustrated. Duns and Ros correlation noticeably gives the most accurate result in wells having an enthalpy ranging from 1500 to 2500 kJ/kg. For wells with less than 1500 kJ/kg enthalpy, the result suggests that all correlations except Armand could give good results.

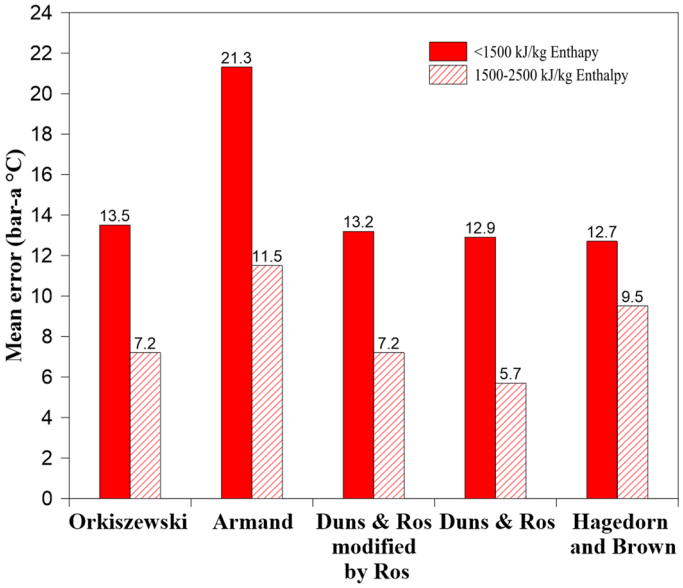

FIGURE 7: Performance of flow correlations on wells having an enthalpy of < 1500 kJ/kg and 1500 - 2500 kJ/kg

4.8 Performance of flow correlations based on fluid flow regime

An analysis was performed to identify the reason why other correlations did not perform well with the given sets of discharge data. Since all of the correlations which performed well, except Hagedorn and Brown (1965), are dependent on the pressure drop calculated assuming a certain flow regime, this could be one of the reasons why other correlations have unsatisfactory results. Hence, it was decided to use flow regime map to predict the flow pattern of the fluid flowing through the wells.

The flow regime map is one of the commonly used maps in predicting flow patterns for inclined flow. It was developed by Aziz et al., (1972), but here it is based on the paper of Ehizoyanyan et al. (2015). Initially, the superficial velocities of the two phases obtained from the simulation using each correlation were plotted to verify if there was a difference with the predicted flow regimes for each correlation. Then it was observed that the flow correlations were producing almost the same fluid flow regimes

throughout the cased-off section of the wells. An example of this is shown in Figure 8 where well 21 is experiencing slug flow at the top of liner and annular/mist flow at the wellhead while well 34 has an annular/mist flow from top of liner up to the wellhead. It was also observed that the flow correlations produce almost the same superficial velocities of liquid and gas at the top of liner of the wells. And Orkiszewski, Duns and Ros and Duns and Ros (modified by Ros) correlations calculate the same value of superficial velocities of the two phases throughout the cased-off section of the wells.

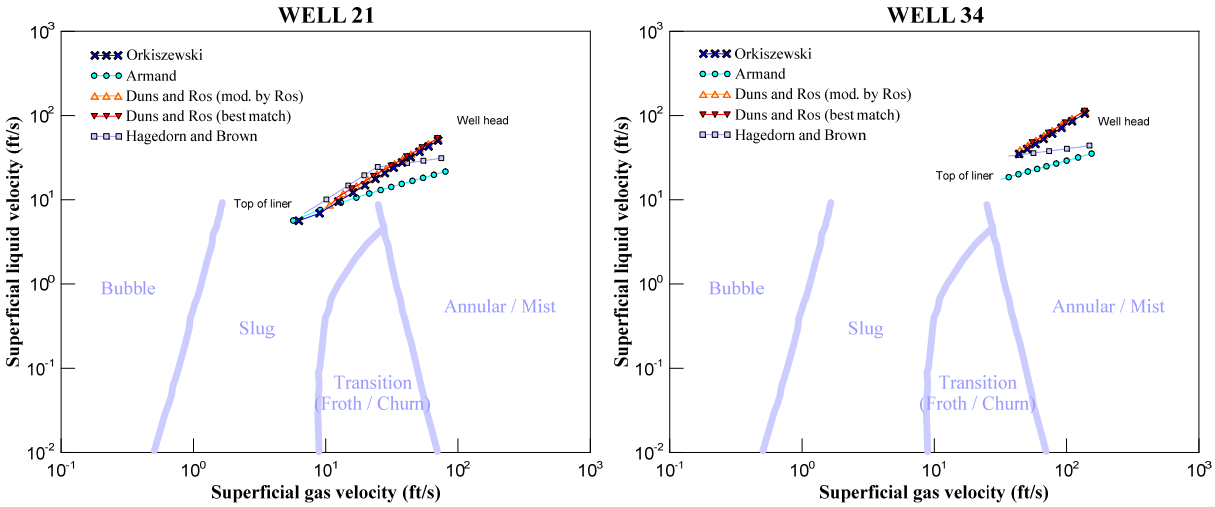

FIGURE 8: Predicted flow regimes of the fluid throughout the cased-off section of well 21 and well 34 based on Aziz et al., (1972) flow pattern map

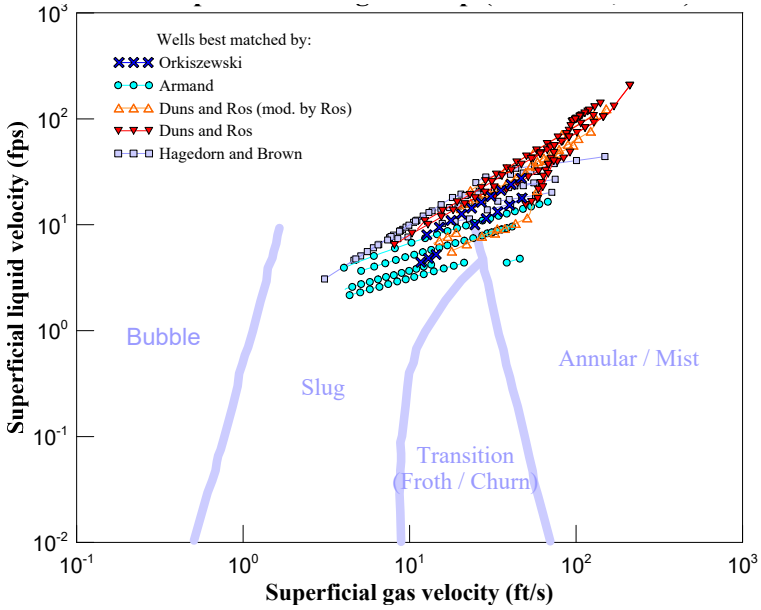

FIGURE 9: Predicted flow regimes of the fluid throughout the cased-off section of the wells based on Aziz et al., (1972) flow pattern map

To check the fluid flow regime of all of the wells, the same process was repeated, though in this case the superficial velocities of the two phases based on the well's best matched correlation were used (see Figure 9). And it was observed that most portions of the wells were experiencing annular/mist flow. According to Bellarby (2009), the Duns and Ros correlation gives an accurate result in predicting the pressure drop of two-phase fluid flow specifically in mist flow. This could be the reason why the Duns and Ros correlation performs best of the correlations. Likewise, Orkiszewski and Duns and Ros (modified by Ros) correlations also performed well because both used the method of Duns and Ros correlation in mist flow. It is also noted that the Armand correlation seems to have a good performance on wells which have lower superficial liquid velocity (slug flow). And the Hagedorn and Brown correlation, although it does not consider the flow regime in pressure drop calculations, still gives good matches for wells experiencing slug and annular/mist flow. Lastly, the Armand correlation seems to perform well in slug flow which also agrees with the study of Spedding and Chen (1982) that the Armand correlation is only applicable to bubble and slug flow regimes.

5. CONCLUSIONS AND RECOMMENDATIONS

In this study, different analyses were performed to evaluate and compare the performance of different flow correlations as implemented in EDC's in-house simulator Simgwel. Based on these analyses, it can be concluded that each flow correlation has a different applicability depending on the condition of the fluid in the wellbore up to the wellhead. The accuracy of flow correlations in simulating flowing pressure and temperature profiles of a geothermal well may greatly depend on the condition of the fluid and its flow regime. The Duns and Ros correlation gives an accurate result if the fluid flow regime is mist. And based on the 40 sets of discharge data that were simulated, it would give good matches between the calculated and measured profiles if the steam mass flux is higher than 100 kg s^{-1} m^{-2} and wellhead pressure is less than 30 bar-a.

The Orkiszewski correlation gives good results if used in mist flow and would also perform well in simulating geothermal wells having wellhead pressure of less than 20 bar-a and steam mass flux greater than 100 kg s^{-1} m^{-2}. Duns and Ros (based on Ros) correlation also performs well in mist flow but there is still a possibility that it will give unsatisfactory results. It can also produce accurate results if the wellhead pressure is less than 20 bar-a and the steam mass flux higher than 100 kg s^{-1} m^{-2}. The Hagedorn and Brown correlation on the other hand, can give a good match on wells with wellhead pressure less than 40 bar-a and steam mass flux less than 200 kg s^{-1} m^{-2}. However, it should be used with caution because of the possibility that it may give a significantly large error. Furthermore, the performance of Armand correlation is unsatisfactory based on the error obtained between the measured and predicted flowing profiles. Although, it may give good results if the steam mass flux at the wellhead is less than 200 kg s^{-1} m^{-2}, further evaluation is necessary to confirm this result.

In conclusion, it should be noted that these evaluations still need to be validated through an intensive study having a substantial amount of data and considering other important parameters such as chemical composition of the fluid (non-condensable gas content and total dissolved solids) and casing blockage or scale. In the case of modelling a geothermal well, it is recommended to first predict the fluid flow regime. This would help the reservoir engineer to decide what flow correlation to use.

ACKNOWLEDGEMENTS

Sincere gratitude is hereby extended to the following who have never ceased to support and helped me in all aspects throughout my venture and until this paper is structured:

To Mr. Lúdvík S. Georgsson, director of UNU-GTP and Mr. Ingimar Gudni Haraldsson, deputy director of UNU-GTP, for the opportunity to participate in the six-month training programme. To the UNU-GTP staff, Markús, Frída and Thórhildur, thank you for all of your precious time and efforts that guided us through life in Iceland. To Rósa Jónsdóttir, thank you for sending me the copy of all the books and references that I needed.

To my supervisors Mr. Lárus Thorvaldsson and Dr. Jean-Claude Berthet whose expertise and guidance highly contributed to the success and completion of this study. To Valdís Gudmundsdóttir and my colleagues in EDC, Yam Alcaraz, Julius Rivera and Daryl On, thank you for sending me all the data that I needed. To Ms. Kristine Eia Antonio, thank you for all the encouragements, comments, patience and effort in checking this study. To Mr. Jaime Austria, thank you for checking and sharing your ideas for the project. To Ms. Selna Marquez, for also sharing your ideas in this study, thank you very much.

To the management of the Energy Development Corporation, President Richard Tantoco and GREG SVP Manny Ogena, thank you for supporting me in this training. To Mr. Francis Sta. Ana, Mr. Dave Yglopaz, Mr. Jericho Omagbon and Mr. Anthony Ciriaco, thank you for nominating me for this training.

To my brothers here in Iceland, Jigo Mismanos, Jason Gotuato and Lee Monasterial, thank you for all the good times and experiences we have shared together that made my stay more enjoyable and unforgettable here in Iceland.

To my parents Reynaldo and Nora and my siblings Reygie, Roxanne, Niño and Beverlyn who are my motivations to give my best to finish this work. To all my friends and Church mates, for the unwavering moral support and words of encouragements that helped me pull through, thank you very much. To my beloved Ms. Jemimah Keren Rivera, thank you for all the encouragements and taking time to help me finish this project.

Above all, utmost appreciation offers to my GOD Almighty for the divine favour and for giving me strength throughout this journey. With You, all things are possible.

REFERENCES

Ambastha, A.K., and Gudmundsson, J.S., 1986: Pressure profiles in two-phase geothermal wells: Comparison of field data and model calculations. *Proceedings of the 11th Workshop on Geothermal Reservoir Engineering*, *Stanford University, Stanford, CA, United States,* 183-188.

Armand, A.A., 1946: *The resistance during the movement of a two-phase system in horizontal pipes.* Izv. Vses. Teploteck. Inst., Vol. 1, 16-23.

Aunzo, Z., Björnsson, G., and Bödvarsson, G., 1991: *Wellbore models GWELL, GWNACL, and HOLA user's guide.* Lawrence Berkeley Laboratory, Berkeley, CA, United States, report LBL-31428 / UC-251, 102 pp.

Aziz, K., Govier, G.W., and Fogarasi, M., 1972: Pressure drop in wells producing oil and gas. *J. Canadian Petroleum Technology, 11,* 31-38.

Barelli, A., Corsi, R., Del Pizzo, G., and Scali, C., 1982: A two-phase flow model for geothermal wells in the presence of non-condensable gas, *Geothermics, 11,* 175-191.

Bellarby, J., 2009: *Well completion design*. Elsevier, 711 pp.

Bhat, A., Swenson, D., and Gosavi, S., 2005: Coupling the HOLA wellbore simulator with TOUGH2. *Proceedings of the 30th Workshop on Geothermal Reservoir Engineering, Stanford University, Stanford, CA, US,* 3-6.

Björnsson, G., 1987: *A multi-feedzone geothermal wellbore simulator.* University of California / Lawrence Berkeley Laboratory, MSc thesis, report LBL-23546, 102 pp.

Carrascal, J.F., 1996: *Multiphase flow application to esp pump design program*. Texas Tech University, Thesis in Petroleum Engineering, 134 pp.

Duns Jr., H., and Ros, N.C.J., 1963: Vertical flow of gas and liquid mixtures in wells. *Proceedings of the 6th World Petroleum Congress, Frankfurt am Main, Germany,* 22-106.

Ehizoyanyan, O., Appah, D., and Sylvester, O., 2015. Estimation of pressure drop, liquid holdup and flow pattern in a two phase vertical flow. *International J. Engineering and Technology, 4,* 241-253.

Fajardo, V.R., and Malate, R.C.M., 2005: Estimating the improvement of Tanawon production wells for acid treatment, Tanawon sector, BacMan geothermal production field, Philippines. *Proceedings of the World Geothermal Congress 2005, Antalya, Turkey,* 5-7.

Freeston, D., and Hadgu, T., 1988: Comparison of results from some wellbore simulators using a databank. *Proceedings of the 10th New Zealand Geothermal Workshop, Auckland University, Auckland, NZ,* 4-7.

Freeston, D., and Gunn, C., 1993: Wellbore simulation – case studies. *Proceedings of the 18th Workshop on Geothermal Reservoir Engineering, Stanford University, Stanford, CA, US,* 3-6.

Gould, T., 1974: Vertical two-phase steam-water flow in geothermal wells. *J. Petroleum Technology, 26,* 833-842.

Griffith, P., and Wallis, G.B., 1961: Two-phase slug flow. *J. Heat Transfer, 83*, 307-318.

Gudmundsdóttir, H., 2012: *A coupled wellbore-reservoir simulator utilizing measured wellhead conditions.* University of Iceland, MS thesis, 119 pp.

Hagedorn, A.R., and Brown, K.E., 1965: Experimental study of pressure gradients occurring during continuous two-phase flow in small diameter vertical conduits. *J. Petroleum Technology, 4*, 475-484.

Hsu, Y.Y., and Graham, R.W., 1976: *Transport processes in boiling and two-phase systems*. Hemisphere Publishing Corp., NY, US, 559 pp.

Koehler, A., and Koehler, H.R., 2006: Another look at measures of forecast accuracy. *International J. Forecasting, 22,* 679–688.

Lyons, W., 2010: *Working guide to petroleum and natural gas production engineering*. Elsevier, Oxford, United Kingdom, 316 pp.

Marquez, S., Sazon, T.A., Omagbon, J., and Sazon, T.A., 2015: SIMGWEL: EDC's new geothermal wellbore modeling software. *Proceedings of the World Geothermal Congress 2015, Melbourne, Australia*, 4 pp.

McGuinness, M.J., 2013: *Geothermal wellbore simulation.* Short Course on Geothermal Well Bore Simulation, held for Energy Development Company, Manila, Philippines.

McGuinness, M.J., 2014: *Simgwel User Manual Version 9.10*. Wellington: Marsan Consulting Ltd.

Orkiszewski, J., 1967: Predicting two-phase pressure drops in vertical pipes. *J. Petroleum Technology, 19,* 829-838.

Pálsson, H., 2011: *Simulation of two-phase flow in a geothermal well.* University of Iceland, lecture notes, 8 pp.

Probst, A., Gunn, C., and Andersen, G., 1992: A preliminary comparison of pressure drop models used in simulating geothermal production wells. *Proceedings of the 14th New Zealand Geothermal Workshop, Auckland, NZ,* 139-144.

Ravindran, N., and Horne, R., 1993: *Multivariate optimization of production systems - the time dimension.* Stanford University, Petroleum Research Institute, Stanford, CA, US, report DOE/BC/14600-42, 114 pp.

Ros, N.C.J.: 1961: Simultaneous flow of gas-liquid as encountered in well-tubing. *J. Pet. Tech., 10*, 37-49.

Spedding, P.L., and Chen, J.J.J., 1982: *Holdup in inclined two-phase flow.* University of Auckland and University of Hong Kong, 7 pp.

Tanaka, S., and Nishi, K., 1988: Computer code of two-phase flow in geothermal wells producing water and/or water-carbon dioxide mixtures. *Proceedings of the 13th Workshop on Geothermal Reservoir Engineering*, *Stanford University, Stanford, CA, US,* 159-164.

Thórisdóttir, Th.H., 2013: *Estimation of slip ratios for pressure drop calculations in geothermal wells*. University of Iceland, MSc thesis, 50 pp.

White, F.M., 1979: *Fluid mechanics.* McGraw-Hill, NY, US, 847 pp.

UNITED NATIONS UNIVERSITY
UNU-GTP
Geothermal Training Programme

Orkustofnun, Grensasvegur 9,
IS-108 Reykjavik, Iceland

Reports 2015
Number 09

STRUCTURAL MAPPING AND SUBSURFACE GEOLOGY COMPARED TO THERMAL GRADIENT AND THE GEOTHERMAL SYSTEM IN MÖDRUVELLIR, SW ICELAND

Davar Ebrahimi
Niroo Research Institute
Poonak bakhtari Blvd., Shahrak-e-Ghods
P.O.Box 146655-517, Tehran
IRAN
davar.ebrahimi@gmail.com

ABSTRACT

The Mödruvellir geothermal field is a low-temperature geothermal resource located in southwest Iceland. Exploration in this region started in 1978 by drilling shallow gradient wells and using them for temperature measurements. At present there are two production wells and 22 gradient wells in the area. This study is based on an investigation of the surface geology, analyses of gradient well data and subsurface geology. Stratigraphical units in this area belong to the sequences of Late Tertiary to early Quaternary and approximately 480 m of basalt with intercalations of hyaloclastites are exposed in this area. Several faults and fractures were plotted on geological map. These faults have two main trends, NE-SW and ENE-WSW, some were observed and measured in the field while others were deduced from examination of aerial photographs. The geothermal gradient method was applied to locate a geothermal anomaly and a thermal map showing temperatures at 50 m depth in the gradient wells revealed two anomalies that are related to a local structural pattern in this area. Five different temperature zones were revealed on the local geothermal gradient map, the highest temperature zone on the map was within the highest gradient zone. Subsurface geology in this area was based on an analysis of drill cutting samples of two vertical wells, and the main rock types that comprise the subsurface geology of the studied wells were basaltic lavas and minor hyaloclastites. Correlation between subsurface lithological unites showed that displacement of these units are related to the normal dip of topography in this area. Based on this study the first conceptual model for the Mödruvellir low-temperature geothermal system is proposed.

1. INTRODUCTION

Geothermal energy constitutes one of the most important natural resources in Iceland and has been extensively harnessed, particularly for house heating, but also for greenhouses, farming, power generation and various industries (Gudmundsson and Pálmason, 1987; Arnórsson, 1991). Bödvarsson (1961) classified geothermal areas in Iceland as either high- or low-temperature areas. The high temperature areas are located within the active volcanic zones of Iceland but geothermal activity of low

FIGURE 1: Location of study area

temperature, which is defined by reservoir temperatures ranging from just above ambient to about 150°C, is widely distributed in Quaternary and Tertiary formations (Arnórsson, 1995a). In the Hvalfjördur area in SW Iceland, several low-temperature fields have been located, one of which is in Mödruvellir to the northeast of Mt. Esja (Figure 1). There are two production wells and 22 gradient wells in this area. This study combines detailed field data on the faults and dykes, an interpretation of a geothermal gradient map and borehole geology of wells MV-19 and MV-24 in the Mödruvellir low-temperature field. This paper is submitted as a requirement for the partial fulfilment and attainment of a six-month postgraduate course on geothermal geology at the United Nation University Geothermal Training Programme (UNU-GTP) in the period between May and October 2015.

1.1 Previous work

The first comprehensive study of the geology of the area was done by Fridleifsson (1973). This research included the petrology and structural geology of Mt. Esja in SW Iceland (Figure 1), and a regional geological map of the area on the scale 1: 25,000 was republished by Orkustofnun after mapping by Fridleifsson (1973). There are no surface manifestations of geothermal activity in the region. However, drilling resulted in the discovery of an 80°C hot geothermal reservoir in Hvalfjördur. The anomaly is N-S elongated suggesting that the hot aquifer is related to a fractured zone in this area. The anomaly was defined on the basis of 60 m deep boreholes. Kristinsson, (2009) studied the stratigraphy, tectonics and alteration of the Hvalfjördur central volcano, and divided this central volcano into three major units. The oldest one is the western part of the volcano made of tholeiite lavas and some rhyolite, and this part is crosscut with dykes and mainly cone sheets. A middle unit is more complex with thick basalt lavas, hyaloclastites and rhyolite lavas. The youngest unit is the caldera filling with 150 to 200 m thick sediments, hyaloclastites and some lava. Other studies have also been completed about the surrounding study area. Kristjánsson et al., (1980) worked on the stratigraphy and paleomagnetism of Esja, Eyrarfjall and Akrafjall mountains, SW Iceland. Weisenberger and Selbekk (2007) studied multi-stage zeolite facies mineralization in the Hvalfjördur area. Tibaldi et al., (2008) investigated strike-slip fault tectonics and the emplacement of sheet laccolith systems in Thverfell area. The last effort in the exploration of the geothermal resource in this area was the drilling of two deep wells, MV-19 in 2011 and MV-24 in 2014.

1.2 Location of study area and accessibility

The Mödruvellir area is located about 40 km NE of Iceland's capital Reykjavik, sitting behind the Esja Mountain. The area is accessed by road from Reykjavik as shown in Figure 1.

2. GEOLOGICAL SETTING

2.1 Iceland

Iceland is located in the North Atlantic Ocean at 63°23´N to 66°30´N. It is believed to have been built from the interaction of a mantle plume with the north Atlantic divergent plate boundary (Schilling, 1973; Gudmundsson, 2000; Jacoby and Gudmundsson, 2007). The mid Atlantic ridge defines the constructive plate boundary between the American and Eurasian plates and from magnetic anomalies to the north and south of Iceland, the spreading rate has been estimated as 2 cm/year. This region is known as the Icelandic basalt plateau, which rises more than 3000 m above the surrounding ocean floor and covers about 350,000 km^2 of which 103,000 km^2 is above sea level (Thórdarson and Höskuldsson, 2002). The stratigraphical succession of Iceland spans three geological periods, that of late Tertiary (Miocene and Pliocene), the Quaternary or Pleistocene and the Holocene (Figure 2).

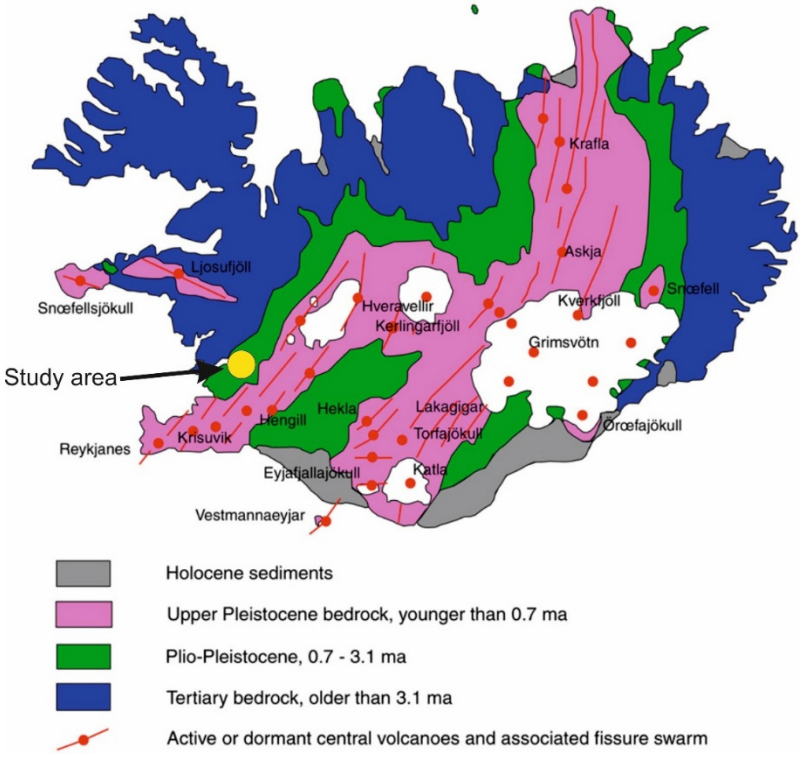

FIGURE 2: Bedrocks of Iceland and distribution of central volcanic systems (Thórdarson and Höskuldsson, 2002)

Geothermal areas in Iceland are divided into two main groups, high-temperature and low-temperature areas. The high temperature areas are found only within the area of active volcanism within the rift zones and are usually ascribed to intrusive activity at high levels within the upper crust (Flóvenz and Saemundsson, 1993). Geothermal activity of low-temperature type, which is defined by reservoir temperature ranging from just above ambient to about 150 °C, is widely distributed in Quaternary and Tertiary formations west of the belts of active volcanism and rifting in Iceland. They are located on the American plate east of these belts, (Arnórsson, 1995b).

2.2 Geology of study area

The study area Mödruvellir is in the Hvalfjördur region. Hvalfjördur belongs to a sequence of late Tertiary to early Quaternary flood basalts with a minor interlayer of hyaloclastites and rhyolites (Figure 3). Rock formations from the Hvalfjördur central volcano can be seen on both sides of the fjord. They are from the Gauss magnetic polarity epoch (3.1-2.4 Ma), and represent the time from Mammoth paleomagnetic event to the Gauss/Matuyama boundary, about 600-700,000 years. The local dip of the lava pile in the area is 5-10°C at the coast.

The Hvalfjördur central volcano can be divided into three major units (Kristinsson, 2009). The oldest one is the western part of the volcano made of tholeiite lavas and some rhyolite. In this part the alteration is high, with chlorite/epidote facies on the coast. This western part is crosscut with dykes, mainly cone sheets with NE-SW strike and a 25-40° dip.

The middle unit is more complex, with thick basalt lavas, hyaloclastites and rhyolite lavas. Rocks in this unit dip over 20° in some parts to the south but mainly dip to the southeast. Alteration is less prominent, quartz/laumontite, at the coast. There are basaltic intrusions (dolerite) and three diamictite and/or hyaloclastite units within the middle part. The middle part represents the caldera of the central volcano. The calderas are two, the western rim of the larger one is defined at the Hrafnabjörg intrusion

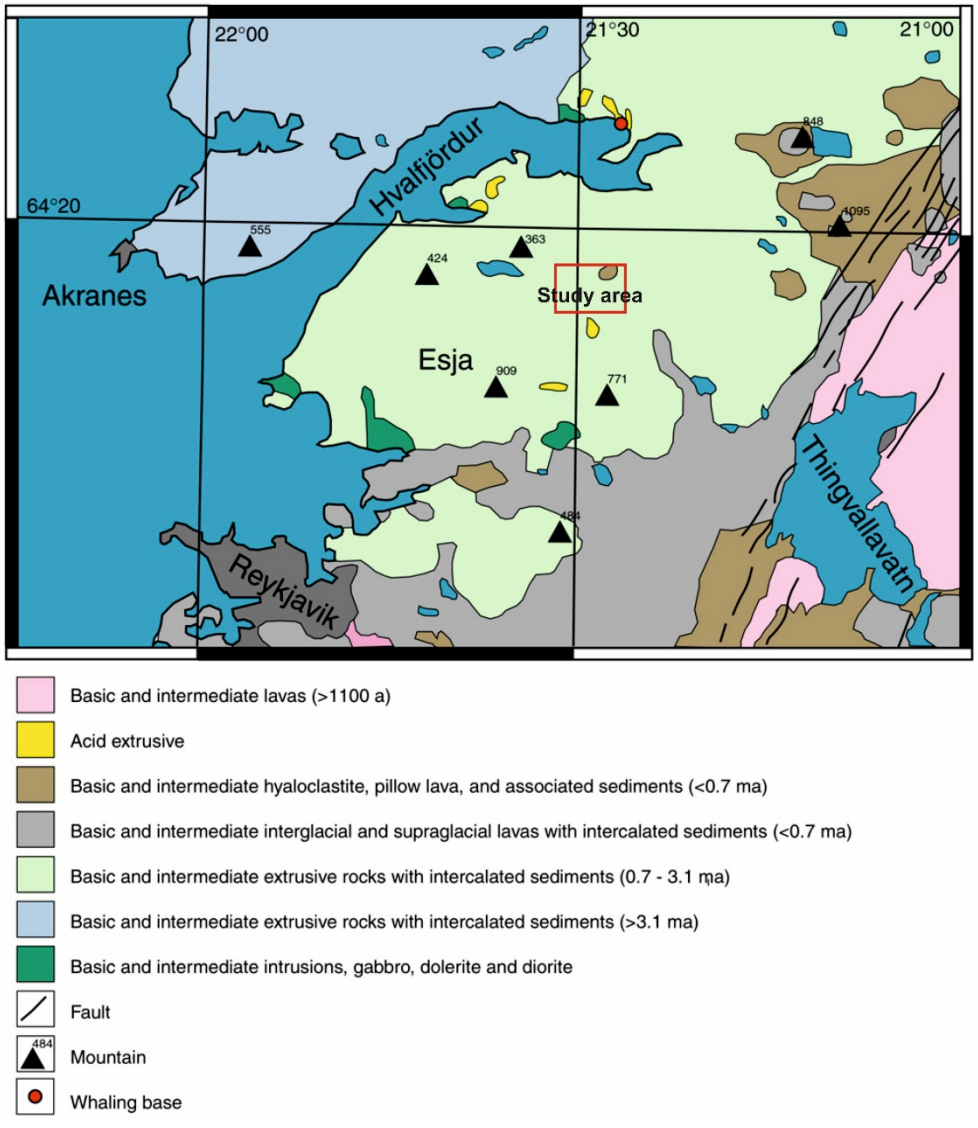

FIGURE 3: Geology map of Hvalfjördur area (Weisenberger, 2005)

and the eastern rim near Bláskeggsá. The smaller caldera is within the other, the western rim is the same but the brittle structures and tilting of the strata up of Stapi mark the eastern rim. The youngest unit is the caldera filling with 150-200 m thick sediments, hyaloclastites and some lavas (Kristinsson, 2009).

The basalt is affected by low-temperature zeolite facies alteration, caused by the burial of the lava succession and a higher heat flow influenced by the Hvalfjördur central volcano. The high alteration represents the garnet-epidote field. The coast from Hálshólar at the Hvammsvík peninsula is altered with chlorite and laumontite. The northern coast from Saurbær to Hrafnabjörg has the same alteration except from a local epidote-granat zone near Ferstikla (Kristinsson, 2009).

The low-temperature zeolite facies in the basaltic lavas in Thyrill and Midfell at the western and eastern sides of the volcano represents the mesolite-scolecite zeolite zone (Walker, 1960). That indicates that nearly 1 km has been eroded off the lava pile.

The Esja mountain (Figure 1) is located between the western rift zone and Tertiary basalts NW of the rift. This transitional zone incorporates a succession of basaltic lava flows and hyaloclastites (Fridleifsson, 1973), known as the Plio-Pleistocene formation on the geological map of Iceland by Jóhannesson and Saemundsson (1998). These lava units, totalling a thickness of 1300 m and comprising the core of the Esja, were erupted 2.8, 2.0 and 1.7 Ma ago (Thórdarsson and Höskuldsson, 2002) from the Thverfell, Midsandur and Stardalur magmatic complexes (Villemin et al, 1994). When the volcanic activity ceased, the Esja was dissected by glacial erosion, which exposed the inner structure of three magmatic complexes (mainly doleritic intrusions).

The latest and most detailed map of the Esja (Fridleifsson, 1973) depicts a doleritic body surrounded by lavas and hyaloclastites. These lavas and hyaloclastites succession is associated with the Thverfell and Stardalur complexes and is locally intruded by inclined sheets, some of which were already mapped by Fridleifsson (1973). The structure features of the area were first described by Fridleifsson (1973) and later in more detail by Villemin et al, (1994). Both reported NE to NNE striking normal faults and dykes and Villemin et al, (1994) reported the occurrence of transcurrent faults in the area but noted their minor importance relative to normal faults.

The succession of volcanic rocks becomes generally older to the northwest, away from the NNE- striking Thingvellir central graben (Saemundsson, 1992) (Figure 3). The lake Thingvallavatn lies in the recent graben system, with historic subaerial basaltic products surrounded by table mountains comprising hyaloclastites and pillow-lavas that were formed under subglacial conditions (Saemundsson, 1992). The bedrock of Esja Mountain and of the southern and north eastern Hvalfjördur area rocks are of Plio-Pleistocene age (0.7-3.1 Ma). The Plio-Pleistocene sequence is formed of alternating successions of lava flows, hyaloclastite and glacial deposits (Saemundsson and Einarsson, 1980; Saemundsson, 1992).

Fridleifsson (1973) descripted the stratigraphy and chronology succession in Esja. He divided the rocks into 26 units, some of these units are located in the research area.

2.3 Eruption history

Volcanism was active in the Esja region for just over one million years and during this time span, at least ten glaciations occurred in the region (Fridleifsson, 1973). The stratigraphy succession is therefore, characterised by a sequence of lava flows intersected with thick subglacial hyaloclastite units. Two central volcanos were active in the Esja region; the Kjalarnes volcano for about 0.6 million years which was succeeded after a short interval by the Stardalur volcano, which remained active for about 0.3 million years. Flood basalt volcanism was concomitant with the central volcanism and most of the olivine tholeiites are considered to have been erupted in fissures and shield volcanoes unrelated to the central volcanoes (Fridleifsson, 1973).

3. GEOLOGICAL AND GEOTHERMAL MAPPING

Mapping of geothermal manifestations, structures and hydrothermal alteration is an essential part of any geothermal survey. Geological mapping helps to define many important parameters which control the flow of hydrothermal fluids, such as rock types, alteration, strike and dip of rock formations and the location of faults, fractures and dykes (Saemundsson and Einarsson, 1980). Surface activity in low-temperature geothermal areas in Iceland is distinctly different from that of the high temperature areas. Sometimes low-temperature activity in an area is represented by a single, isolated thermal spring, although clusters of springs forming a field or an area are also a common feature, Arnórsson (1995b). During this research the published geology map of the study area (scale 1:25,000, Hjartarson and Kristinsson, 2007) and aerial photographs were used to study the geology.

The research area has no surface manifestations and geothermal exploration was carried out by measuring temperatures in shallow drill holes (gradient wells), which have been drilled in this area. Geothermal mapping, including mapping of the main structures like faults, fractures and dykes, was carried out in the Mödruvellir area.

3.1 Stratigraphical units

The study area is about 4 km long and 3 km wide and includes the superficial deposits on the flats and lava flows, and hyaloclastite formations in two flanks (Figure 4). Stratigraphical units in this area belong to the sequences of Late Tertiary to early Quaternary and exposed in this area are approximately 480 m of basalt with intercalations of hyaloclastites. The volcanic succession dips towards the southeast.

Stratigraphic units in this area are divided into four major units, these units are described below (Fridleifsson, 1973):

Unit mf8: Olivine tholeiite lavas: Fine grained olivine tholeiite lavas spread over the region. The unit thickness in this area is about 100 m and most of the lavas here are of olivine tholeiite.

Unit mf9: Tholeiite lavas: The olivine tholeiites of unit mf8 are capped by a few tholeiite lavas, which, because of their higher resistance to erosion, form escarpments. In this region the thickness of unit mf9 is about 60 - 100 m.

Unit mf10: Basaltic hyaloclastite, 50 to 100 m thick. During the glaciation that followed the extrusion of lava unites mf8 and mf9, the volcanism was most active in this region and gave rise to a rugged hyaloclastite mountain. In this area the unit consist of tuffaceous hyaloclastite and breccia.

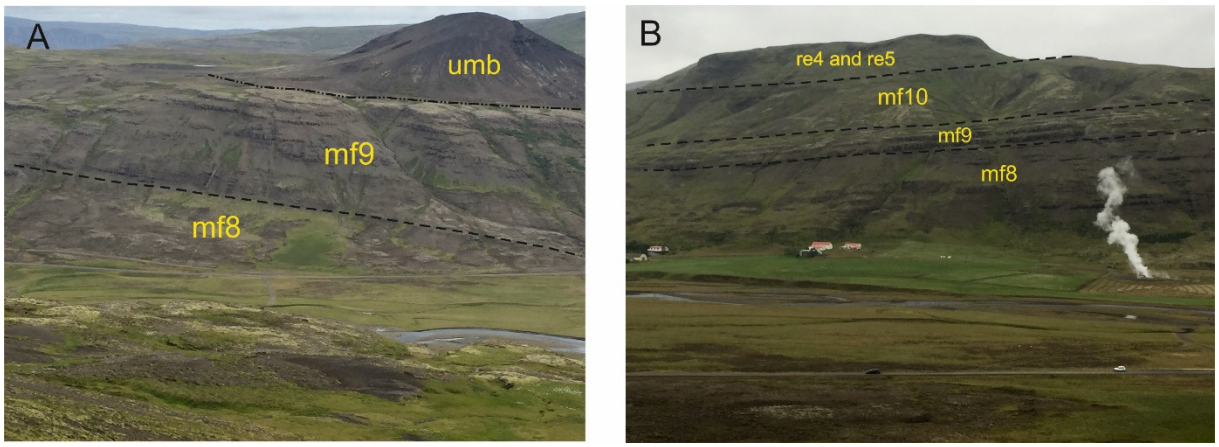

FIGURE 4: Sequences of lava flow and hyaloclastite unite in Mödruvellir geothermal area. A: North eastern flank, B: South western flank

Unit ref4: Tholeite lava: this unit has a small outcrop in the upper part of the south western flank of the study area. The thickness of this unit is about 50 m.

Other minor units are shown on the geology map. The central part of the study area is covered by superficial sediments (unit lj). This unit consists of sedimentary rocks like clay, silt, sand and gravel that were transported by streams and deposited on the flats. Sandfell Mountain in the north eastern part of the study area is made of hyaloclastite (unit umb) and was deposited on top of the eroded surface, forming an unconformity. This unit is formed of younger hyaloclastite and was formed by feeder dykes that cut the oldest units and reached Sandfell Mountain (Figure 5A and 5C).

There are several scoria layers at the boundaries between lava flows, containing numerous vesicles and many type of zeolites (Figure 5B). Soil horizons and sedimentary layers are often deposited in scoria parts.

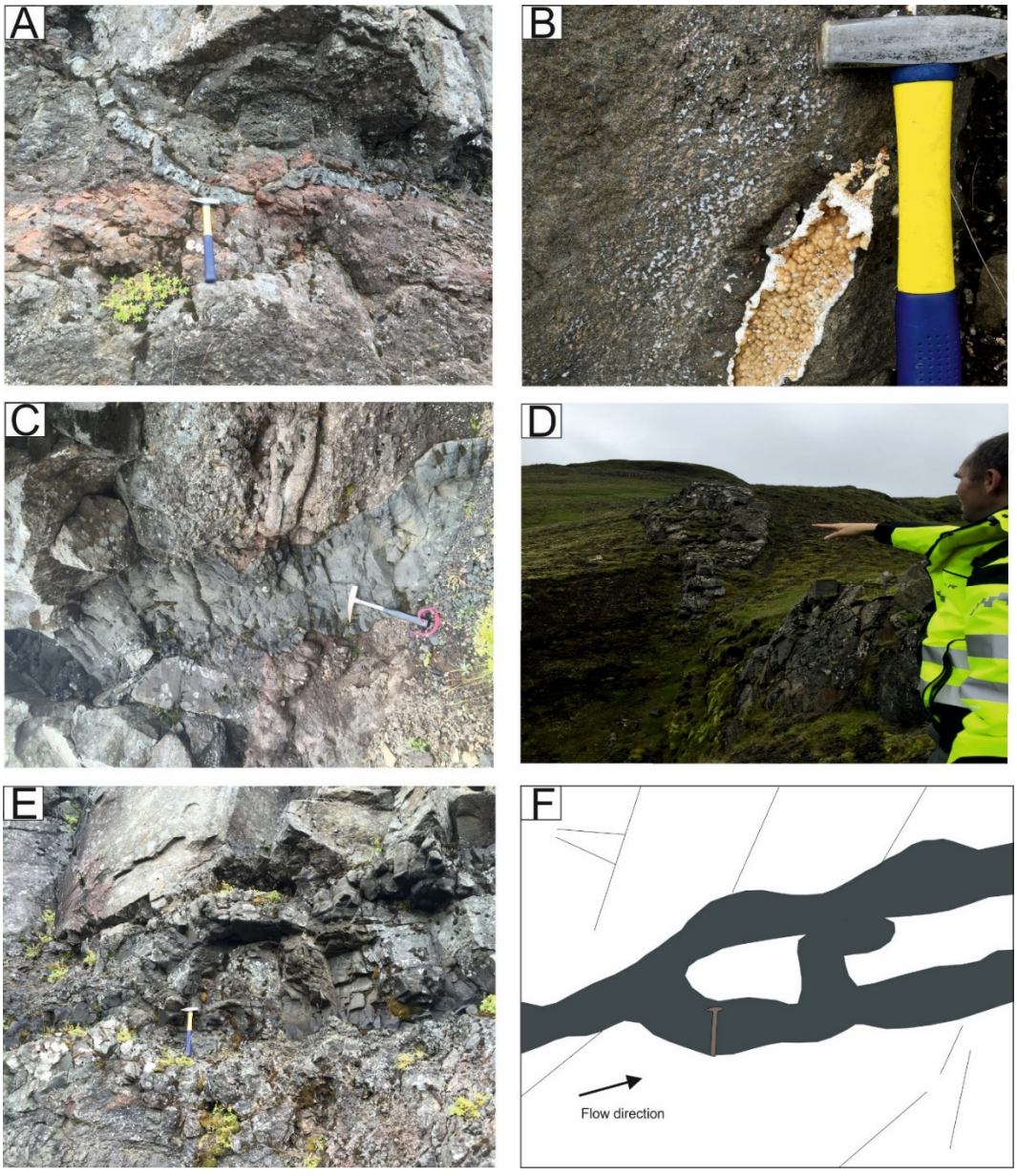

FIGURE 5: Field observations, A: scoria between lava flows, B: Zeolites in vesicle part of lava flow, C: Vesicular dyke, D: Big dyke in the south eastern part of the area, E and F: Photograph and interpretation illustrating the strike of the veins and direction of a thin sheet

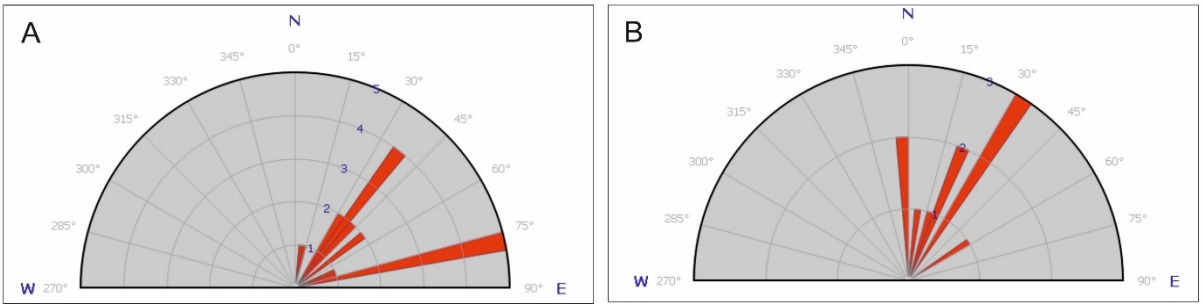

FIGURE 6: The main strike of faults (A) and strike of dykes (B) in the study area

Most of the dykes that were measured in the field have a NE-SW trend (Figure 6) and some of them were plotted on the geological map (Figure 7).

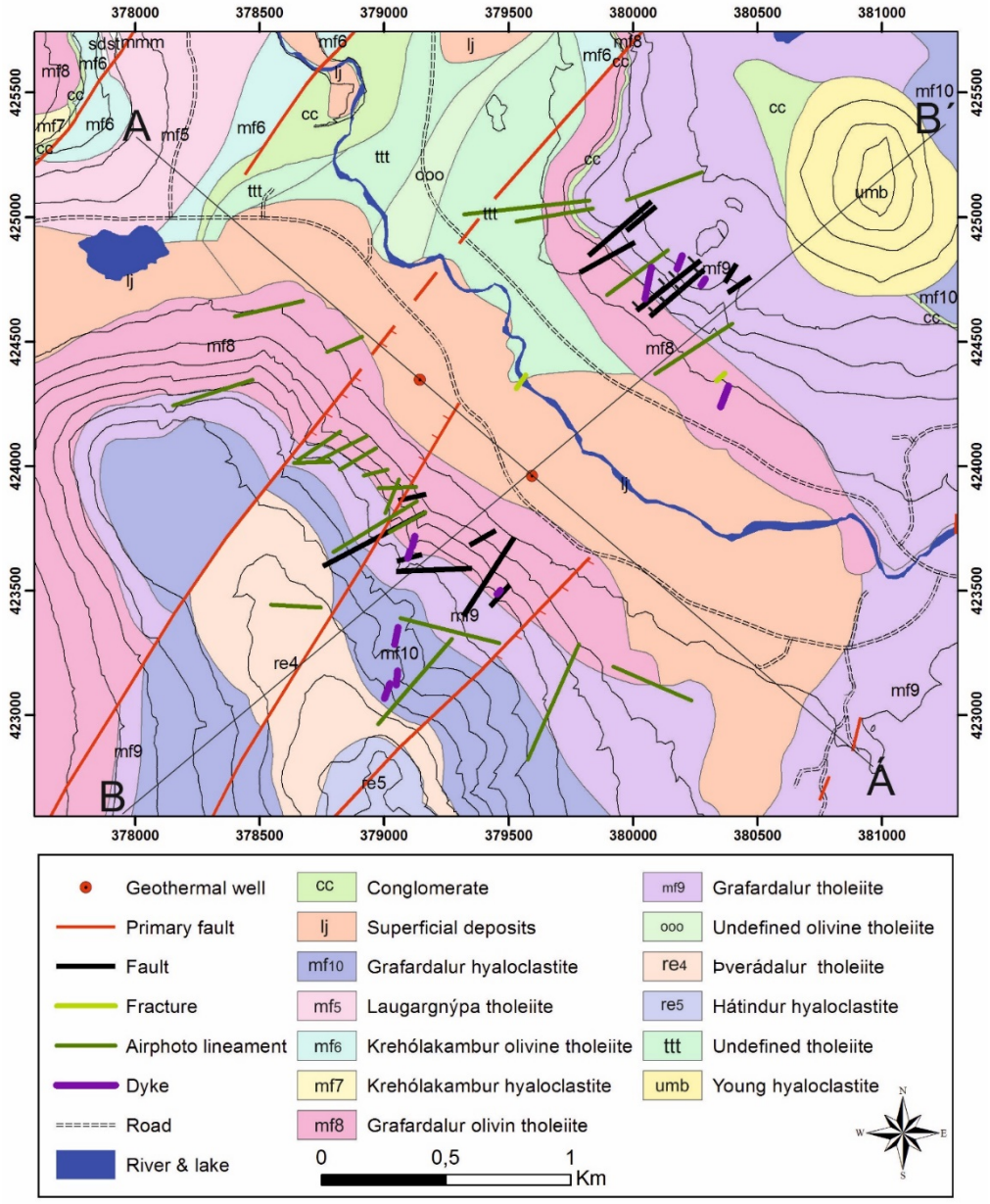

FIGURE 7: Geology map of the study area (modified from Fridleifsson, 1973; Hjartarson and Kristinsson, 2007). Cross sections A-A´ and B-B´ are shown in Figure 15 and Figure 16, respectively

3.2 Structural mapping

Mapping of faults and fractures is important in geothermal prospecting, as such structures may control the flow of hydrothermal fluids. Analysis of structural mapping included plotting faults and lineaments on a geological map and trend distribution on rose diagrams.

Mödruvellir area is characterized by several faults and fractures, most of them having a NE-SW trend. Three NW-SE faults occur parallel to each other and are already marked on the 1:25,000 scale geology map. Some of the faults that have been mapped in the study area were observed in the field, and others were deduced from examination of aerial photographs. Geological features are typically large and applications therefore require small scale imagery to cover the extent of the element of interest. Aerial photos can be used in some areas. During the field study, 18 faults and fractures were mapped with GPS in the field. In addition, 22 lineaments were derived from aerial photos and plotted on a geology map. Most of these faults and fractures have a general NE-SW trend and some have ENE-WSW trends (Figure 6) that appear to crosscut the NE-SW faults, (Figure 7).

Based on analysis of aerial photos, there are some lineaments that have WNW-ESE trends, and were not seen during the field study. These lineaments are located in the southern part of the study area.

4. GRADIENT WELLS

Drilling of gradient wells is a method used in exploration of both high and low-temperature geothermal areas. In Iceland many low-temperature geothermal systems have been discovered with this method where there were no surface manifestations. The temperature gradient in Iceland is mainly dependent on four factors: (1) the regional heat flow through the crust, (2) hydrothermal activity, (3) the permeability of the rock and (4) residual heat in extinct volcanic centres (Flóvenz and Saemundsson, 1993). In high temperature areas in Iceland, the gradient method is not used as an early step in subsurface exploration, except where resistivity surveys alone indicate a resource. More often, deep exploratory boreholes are drilled to follow up surface exploration if the results of the various methods correlate tolerably well, (Saemundsson, 2007). In the low-temperature areas, the method is used to outline the areal extent of an anomaly. It is important to avoid disturbances from the internal flow inside the well. In fracture controlled low-temperature fields, shallow wells give the best results (Saemundsson, 2007). Beside these, a heat flow map of Iceland has newly been released (Figure 8) and around 1000 wells have been used to construct the map (Hjartarson et al, 2015).

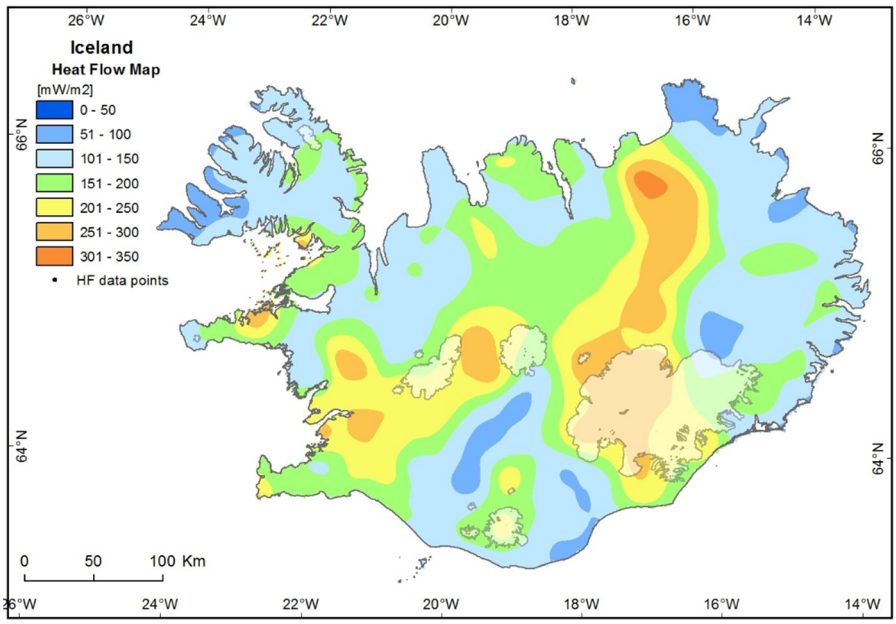

FIGURE 8: Heat flow map of Iceland (Hjartarson, et al., 2015)

As the basalt becomes buried the pores close due to lithostatic pressure and in formations of secondary minerals below 500 to 1000 m depth in uneroded lava pile, the

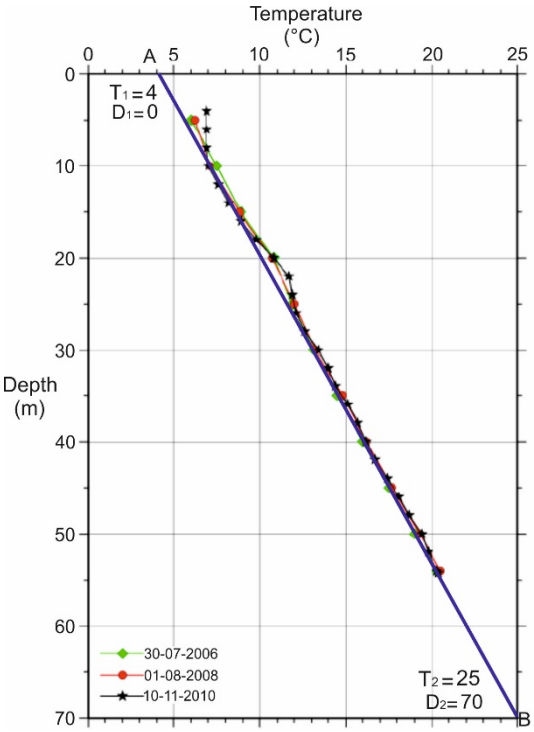

FIGURE 9: Temperature versus depth in well MV-14

heat is mainly transported by conduction. In the lowlands and valleys of Iceland outside the volcanic rift zone, 1000 to 1500 m of the original lava pile has been eroded, leaving thermal conduction as the most important heat transport mechanism (Flóvenz and Saemundsson, 1993).

There are no surface manifestations in the Mödruvellir area, so the gradient method was applied to locate geothermal anomalies, and the drilling of shallow gradient wells revealed geothermal activity. Today there are 22 gradient wells in the area, and Table 1 shows the characteristics of the wells. In this study, two geothermal anomalies were defined on the basis of temperature at 50 m depth and the thermal gradient in wells.

The regional geothermal gradient must also be known as a baseline for recognizing thermal anomalies (Saemundsson, 2007). It is well established that temperature increases with depth, indicating that heat is generated at depth and transferred through rock and sediment layers to the surface (Forrest et al., 2007). Thermal gradients were calculated for all gradient wells based on the gradient equation. Figure 9 presents an example for this calculation, and shows temperature versus depth for well MV-14. A-B is a straight line which cuts the maximum points of temperature versus depth points. The gradient well logs are presented in Appendix I.

TABLE 1: Characteristics of the gradient wells in Mödruvellir area

Well	Coordinate system		Temperature at 50 m depth	Gradient °C/ km	Depth (m)
	x	y			
MV-6	379666	423651	14	205	75
MV-7	379848	423502	14	183	73
MV-8	379541	423856	18	265	58
MV-9	379266	424200	18	272	59
MV-10	379400	424036	17	245	59
MV-11	379187	424364	19	300	60
MV-12	378908	424435	15	190	59
MV-13	379208	424325	19	297	60
MV-14	379147	424388	19	300	54
MV-15	379051	424372	19	282	71
MV-16	379274	424393	19	275	70
MV-18	379251	424502	19	290	70
MV-20	379492	423944	17	257	69
MV-21	379388	423832	17	256	71
MV-22	379646	423781	16	230	70
MV-23	379639	423958	16	265	90
EJ-5	379792	424149	13	160	51
KM-3	379571	424698	16	210	51
KM-4	379624	424674	16	236	45
KM-5	379343	424884	12	160	64

Gradient equation:

$$G = \frac{\Delta T}{\Delta Z} = \frac{T2 - T1}{D2 - D1}$$

In Figure 9: T1= 4°C; T2= 25°C and D1= 0 m; D2= 70 m

Gradient equation yields:

$$G = \frac{25-4}{70-0} = 0.3°C/m$$
$$= 300°C/km$$

The thermal gradient was calculated for 22 gradient wells by using this equation. Figure 10 shows the temperature gradient map in this area. There are five different temperature zones on the map, the highest temperature gradient is >270°C/km and the lowest is <180°C/km. This map can be considered a portrayal of the subsurface temperature distribution.

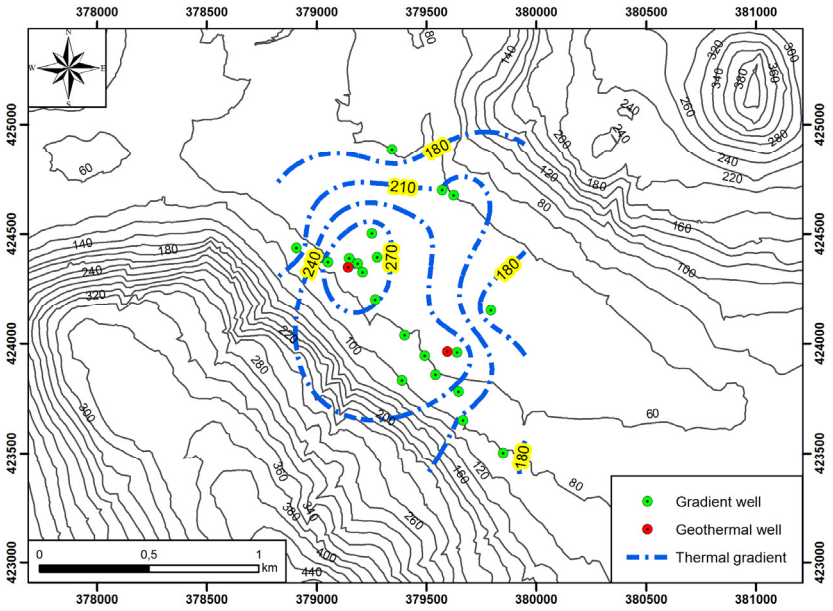

FIGURE 10: Thermal gradient map of the Mödruvellir geothermal area

In Figure 11, a map shows the temperature at 50 m in the gradient wells. There are two temperature anomalies in this area, the main anomaly is clearly related to fractures trending NE-SW and another has a WNW-ESE trend, suggesting that the hot water flow is related to both the fractured zones.

Figure 12 illustrates a comparison between the thermal and gradient maps. It shows that the highest temperature zone on the thermal map is within the highest gradient zone. Based on Figure 12 the main temperature anomaly is located between two major faults in this area.

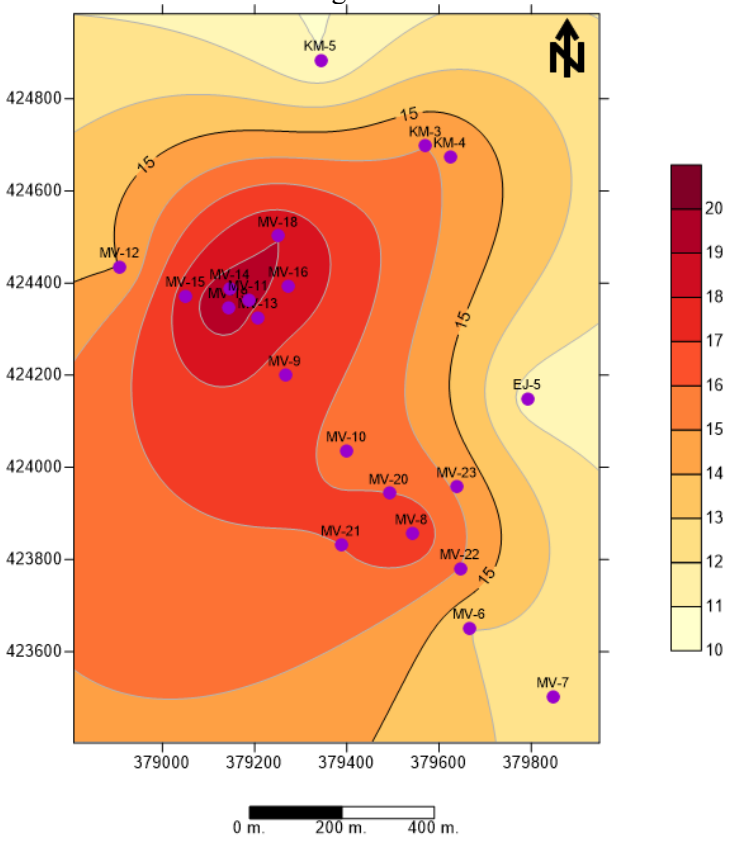

FIGURE 11: Temperature map at 50 m depth in the gradient wells

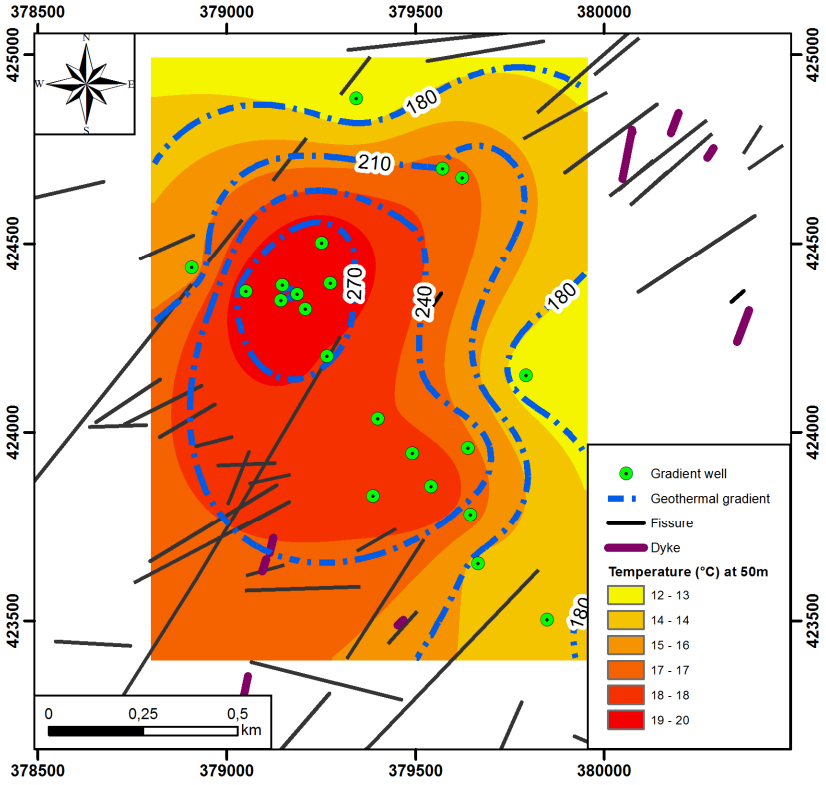

FIGURE 12: Comparison between thermal map and gradient map in Mödruvellir area

5. SUBSURFACE GEOLOGY

After the surface mapping of a geothermal system, further exploration and evaluation of the geothermal system is mainly based on information gained from wells. This development has led geologists to measure various parameters directly from boreholes and get in-depth information about the geothermal system.

Subsurface geology in this area is based on an analysis of drill cutting samples from two vertical wells, MV-19 (820 m) and MV-24 (1704 m). The sample cuttings were analysed using a binocular microscope. Rock cuttings had been collected at 2 m intervals and a total of 1200 samples of drill cuttings for both wells were analysed in this study. The analysis consisted of identifying lithological units, secondary minerals, vein fillings, oxidation and subsurface structures like fractures and veins (Figure 13 and Figure 14). Studies of drill cuttings have provided important information on the subsurface stratigraphy and rock units. Based on these studies five distinct volcanic units were defined in the study wells.

5.1 Subsurface stratigraphy

The main rock types that comprise the subsurface geology of the studied wells are basaltic lava and minor hyaloclastites.

The crystalline basalt formations have been differentiated based on their composition being tholeiite, olivine tholeiite and olivine basalt.

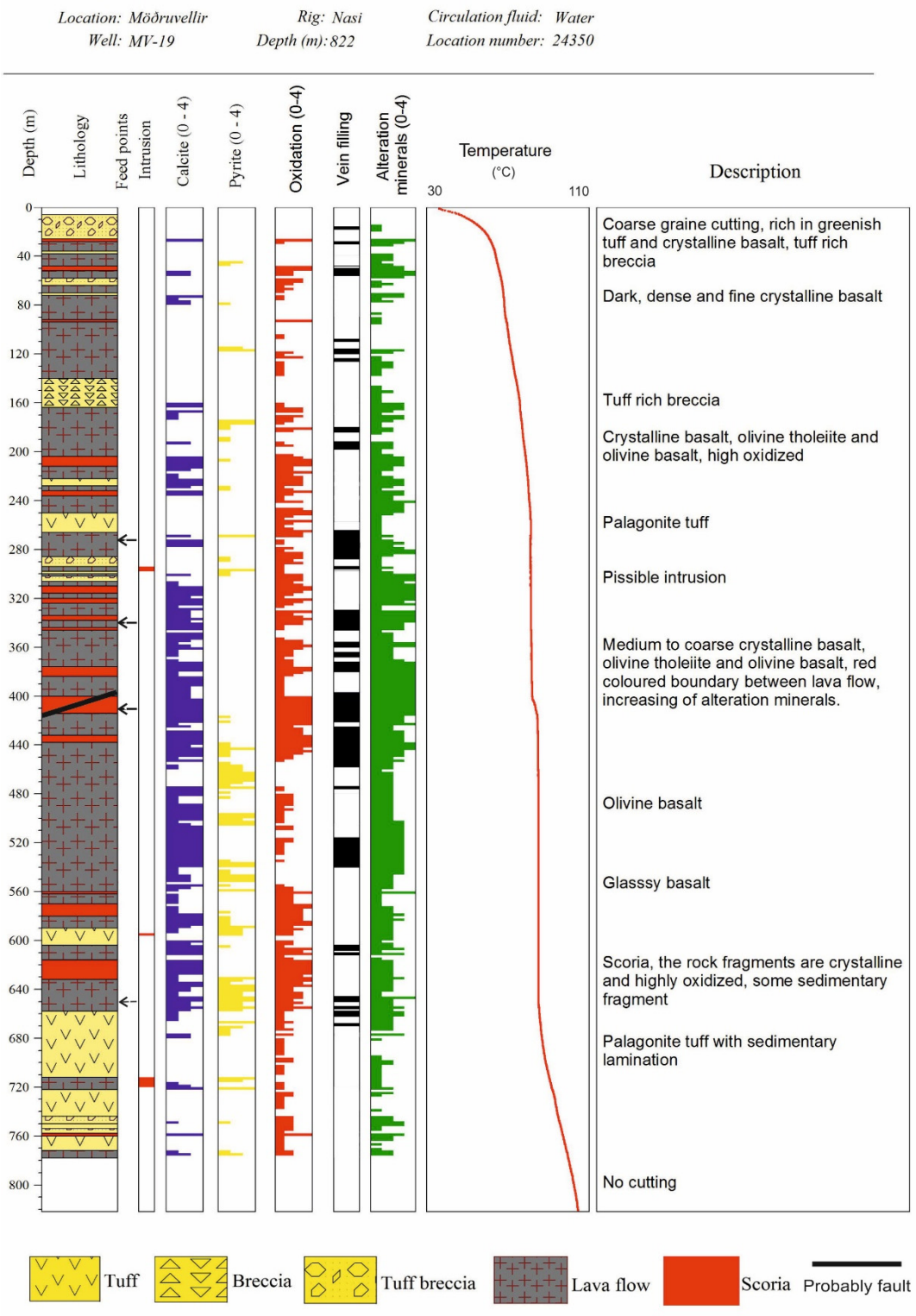

FIGURE 13: Lithology, selected alteration minerals and temperature log of MV-19

Lithological units in well MV-19 are comparable with the mf4, mf5, mf6, mf7, and mf8 units. In well MV-24 the lithological units are similar to unites mf1 (tholeiite), mf4 (hyaloclastite), mf5, mf6, mf7, mf8. These units are tholeiite lavas, basaltic hyaloclastites, olivine tholeiite lavas and olivine basalt lavas. Lithological logs from well MV-19 and MV-24 are presented in Figure 13 and Figure 14, respectively. Based on these studies, the different lithological units are described below.

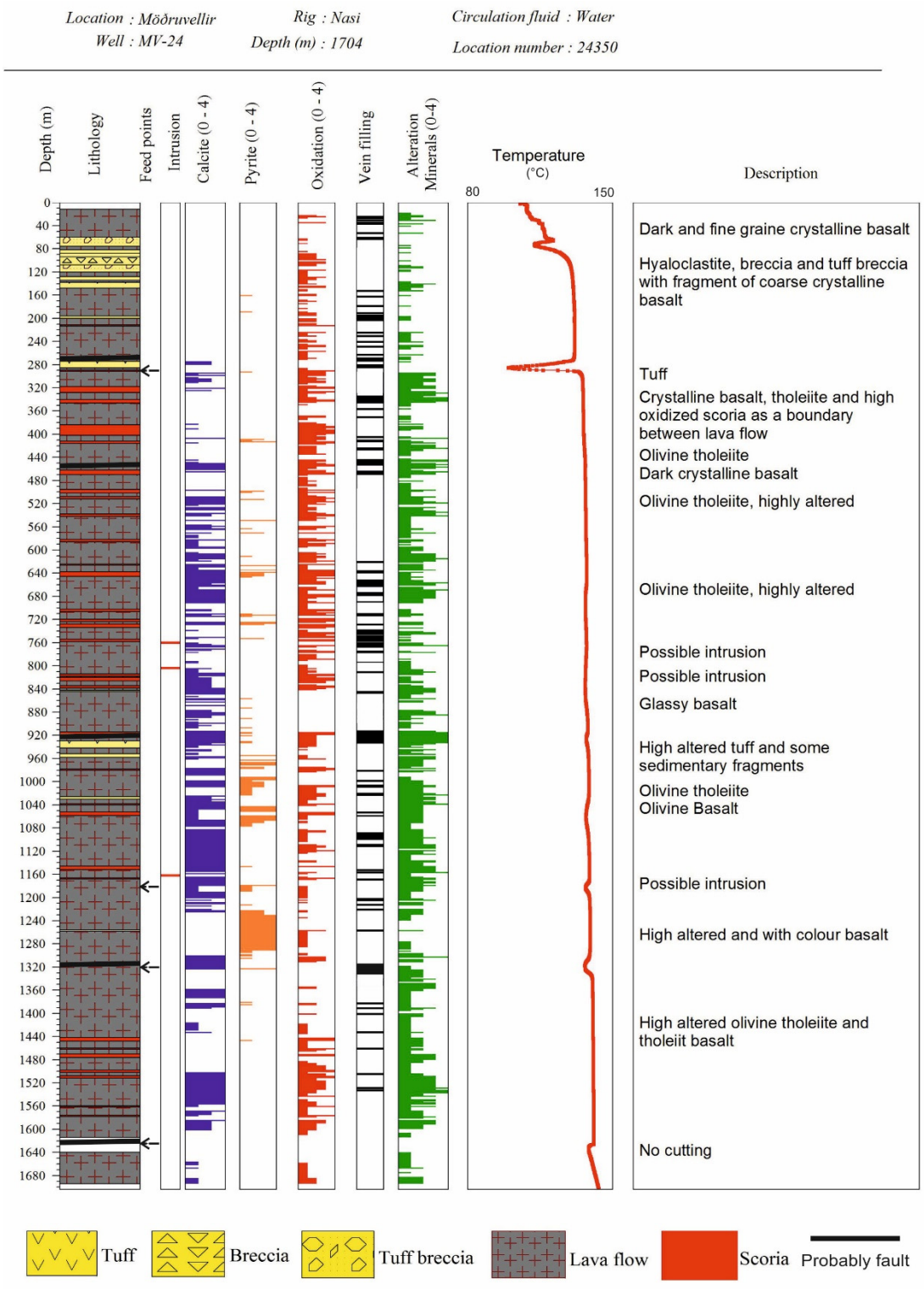

FIGURE 14: Lithology, selected alteration minerals and temperature log of MV-24

Tuff:
Mostly reworked tuff, greenish and red colour, fine to medium grained, mixed with fragments of crystalline basalt and secondary minerals are scarce. Tuff was found from 222 to 228 m, 250 to 266 m, 590 to 604 m, 660 to 744 m, 760 to 772 m depth in well MV-19, and 82 to 88 m, 128 to 134 m, 142 to 148 m, 196 to 200 m, 274 to 286 m, 930 to 942 m, 952 to 958 m, 1026 to 1030 m, in well MW-24. Tuffs occur as brown colour palagonite tuff in the lower part of well MV-19, which were formed in a lacustrine

environment but this sedimentary interval is not present in well MV-24. The tuff in the lower intervals of well MV-24 is highly altered to clays.

Tuff breccia and breccia:
Various type of tuff mixed with pieces of fine to medium grained crystalline basalt in certain intervals. These hyaloclastite units were noted between 6 to 26 m, 36 to 38 m, 58 to 64 m, 70 to 72 m, 286 to 294 m, 302 to 306 m, 744 to 750 m, 754 to 758 m, 140 to 164 m in well MV-19, and 60 to 76 m, 94 to 120 m in well MV-24. In these intervals the amount of secondary minerals is relatively small but zeolites can be seen.

Lava flow:
The majority of the units in both wells consist of lava flows. There is a range in composition from tholeiite to olivine basalt; fine to medium grained and oxidized basalt, moderately altered in well MV-19 and strongly altered in lower part of well MV-24. There are boundaries between these lava flows. Alteration minerals in vesicular part are zeolites and calcite. Pyrite is also formed in many intervals of the crystalline basalt. The lava flows are sometimes partly glassy.

Scoria:
Highly oxidized, red in colour, very porous and the amount of alteration minerals increases in the scoria parts. Scoria sits at boundaries between lava flows. There are 16 scoria boundaries in well MV-19 and 32 scoria boundaries between lava flows in well MV-24.

5.2 Feed points and permeability

Feed point locations have been estimated by using the temperature log and they are shown in Figure 13 and Figure 14. The main source of permeability in the wells is related to lithological boundaries and fractures.

5.3 Intrusions

Table 2 shows a list of possible intrusive rocks in well MV-19 and MV-24. These intrusive rocks are characterized by fresh appearance, coarse graining and dark basalt, and an increase in alteration in the surrounding formations.

TABLE 2: intrusive rocks determined from drill cutting from well MV-19 and MV-24

Well	Depth interval (m)	Type
MV-19	292-298	Possible intrusion
MV-19	596-598	Possible intrusion
MV-19	712-722	Possible intrusion
MV-24	758-762	Possible intrusion
MV-24	802-806	Possible intrusion
MV-24	1160-1166	Possible intrusion

5.4 Alteration minerals

Alteration minerals in these wells are zeolites, calcite, and to a lesser extent quartz. Zeolites form the majority of alteration minerals in this study. Zeolites are formed during alteration and precipitation in vugs and vesicles. Zeolites are often classified by shape into three main categories, fibrous, tabular and granular and some of them are variable in shape. Most of the zeolites in both wells have fibrous and tabular shapes. Zeolites in this study include mesolite, thomsonite, stilbite and scolecite. Epidote is found

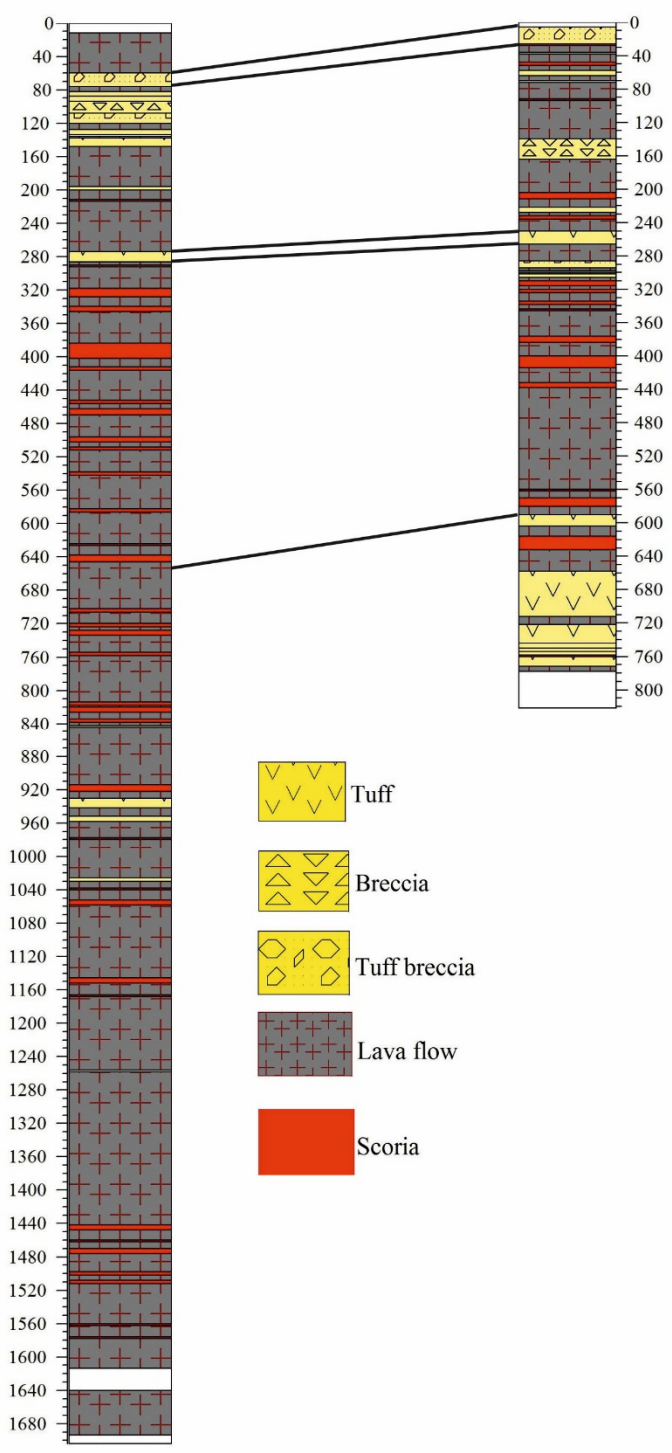

FIGURE 15: Stratigraphic correlation between wells MV-19 and MV-24 in Mödruvellir area

in the lower part of well MV-24, from 1400 m depth to the bottom. This epidote is deformed without any crystal shape and is not related to the low-temperature geothermal system but probably to some older geothermal system. In order to identify the alteration minerals and types of clay minerals, thirteen samples were prepared for XRD analysis. Each sample was prepared and analysed in three conditions: untreated, glycolated and heated. The peaks recorded from the analysis were interpreted, and the XRD analysis showed the presence of different type of zeolites and smectite that indicate a temperature in the range 50 - 200°C. Some examples of the XRD analysis are shown in Appendix II.

5.5 Subsurface correlation

Correlation between wells MV-19 and MV-24 is difficult because there are no clear marker horizons or key beds in these wells. For the subsurface correlation some tuff layered units that have sedimentary layers and lamination were used. In addition, the type of lava flow composition between these layers helped. Correlation between subsurface lithological units is shown in Figure 15. It seems that the displacement of units is related to the normal dip of topography in the area (Figure 4 and Figure 16).

6. CONCEPTUAL MODEL

In order to interpret the subsurface geology and examine the geothermal system in Mödruvellir, two cross sections A-A´ and B-B´ on the geological map (Figure 7) were used. A conceptual model for the low-temperature geothermal system is based on an analysis of the geological information and is shown in Figures 16 and 17. Geology cross sections across these wells show the correlation of the lithological units at the surface and subsurface. Based on the interpretation of the data collected from the studied wells and thermal gradient map, two upflow zones were found in the area. The NE-SW, ENE-WSW faults and fractures act as upflow zones and the main upflow zone is close to well MV-19. This anomaly is restricted between two major faults in the area, which have opposite dips and form a mini graben. It seems that the intersection of these faults has an important role in the formation of the temperature anomaly. Another temperature anomaly is close to well MV-24. Geothermal gradient in

Figure (16) shows a lower temperature for this anomaly and based on Figure (12) this anomaly occurs above fractures and fault that have ENE-WSW trend.

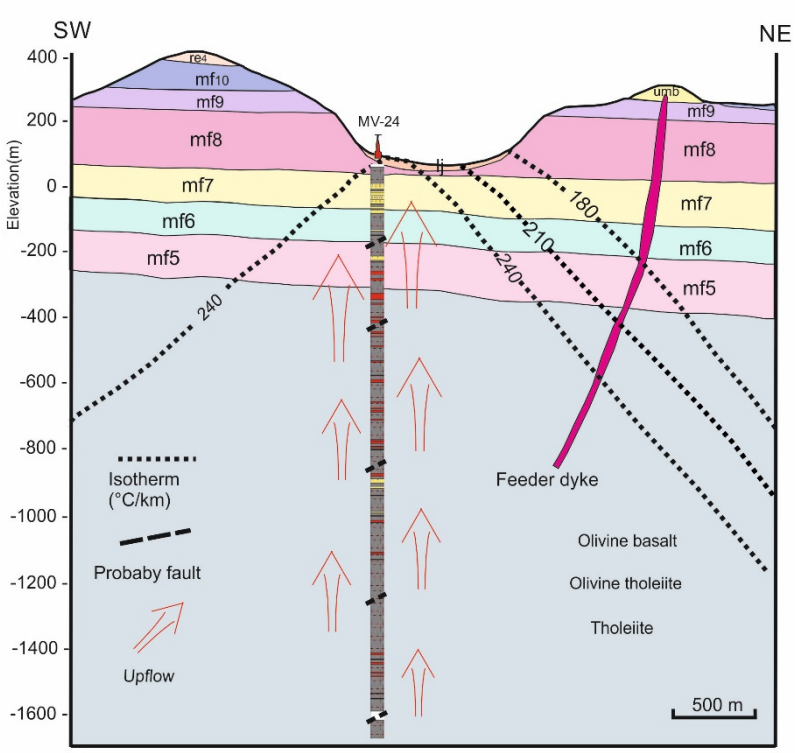

FIGURE 16: Geological cross section and conceptual model along A-A´ shown in Figure 6

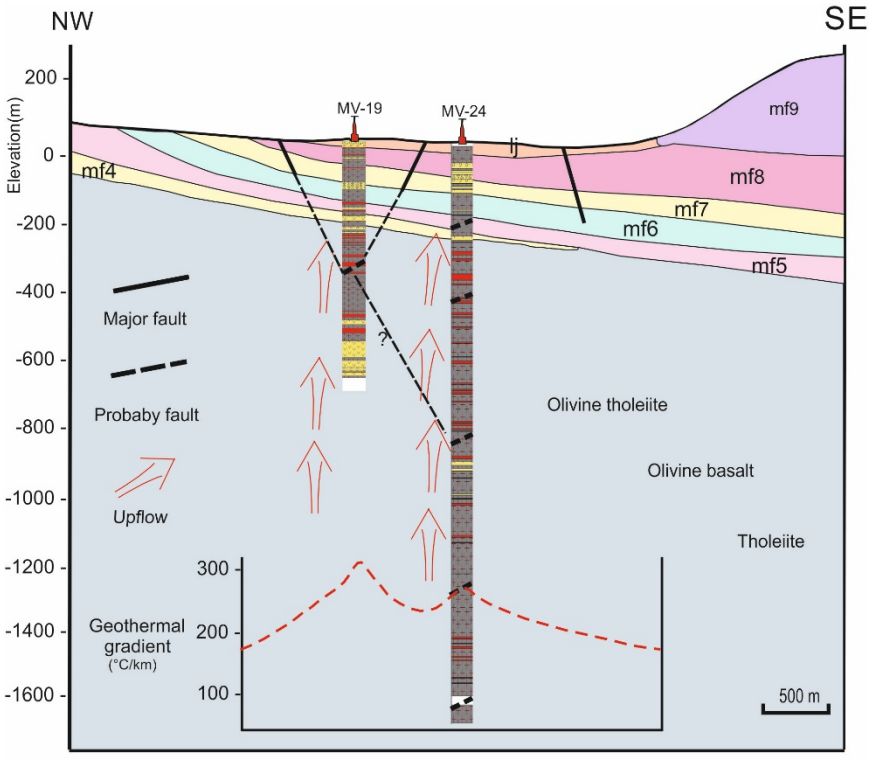

FIGURE 17: Geological cross section and conceptual model along B-B´ shown in Figure 6

7. CONCLUSION

The main conclusions drawn from this work are as follows:

- Geology structures that control the flow of the fluids upwards, have three main directions, NE-SW, WSW-ENE and WNW-ESE.
- The mini graben in the area that was formed between two major faults with different dips, has an important role in increasing the permeability in the north western part of the study area.
- Based on the analysis of the temperature map, there are two temperature anomalies in this area that are related to fracture zones.
- The highest temperature zone in the temperature map is within the zone with the highest geothermal gradient.
- The lithostratigraphy of wells MV-19 and MV-24 is similar and is composed of different lithological units: Crystalline basalt, tuff, tuff breccia, and scoria.
- Secondary minerals in these wells are zeolites, calcite and to some extent quartz.
- Oxidation in this area is very high and there are 16 scoria boundaries between lava flows in well MV-19 and 32 scoria boundary in well MV-24.
- Based on a conceptual model in this area, the best place for future drilling is in the north western part of the study area, close to well MV-19.

ACKNOWLEDGMENTS

I would like to express my heartfelt gratitude to the Government of Iceland and the United Nations University, Geothermal Training Programme (UNU-GTP) for awarding me the fellowship to take part in the UNU-GTP 2015 programme. I thank Mr. Lúdvík S. Georgsson, the Director of the United Nations University Geothermal Training Programme, for my acceptance to this training programme. Mr. Ingimar Gudni Haraldsson (Deputy Director), Mr. Markús A.G. Wilde (Service Manager), Ms. María Gudjónsdóttir (Project Manager), Ms. Málfrídur Ómarsdóttir (Environmental Scientist) and Thórhildur Ísberg (School Manager) for their assistance and support during my stay in Iceland. Thanks to my supervisors, Mr Björn S. Hardarson and Mr Sigurdur G. Kristinsson for sharing their experience during this project. I am grateful to Mr. Sigurdur Sveinn Jónsson for the X-ray diffraction (XRD) analysis. I would like to thank the UNU-GTP 2015 fellows for their friendship. Finally, I am deeply grateful to my wife, Sarvin Ghazanfari and my family for giving me all the support to finish my training in six months.

REFERENCES

Arnórsson, S., 1991: Geochemistry and geothermal resources in Iceland. In: D´Amore, F. (co-ordinator), *Applications of geochemistry in geothermal reservoir development.* UNITAR/UNDP publication, Rome, 145-196.

Arnórsson, S., 1995a: Geothermal systems in Iceland: Structure and conceptual models – I. High-temperature areas. *Geothermics, 24,* 561-602.

Arnórsson, S., 1995b: Geothermal systems in Iceland: Structure and conceptual models – II. Low-temperature areas. *Geothermics, 24*, 603-629.

Bödvarsson, G., 1961: Physical characteristics of natural heat resources in Iceland. *Jökull, 11,* 29-38.

Forrest, J., Marcucci, E. and Scott, P., 2007: Geothermal gradients and subsurface temperature in the northern Gulf of Mexico. *GCAGS Transactions, 55*, 233-248.

Flóvenz, Ó.G. and Saemundsson, K., 1993: Heat flow and geothermal processes in Iceland. *Tectonophysics, 225*, 123-138.

Fridleifsson, I.B., 1973: *Petrology and structure of the Esja Quaternary volcanic region SW Iceland*. Oxford University, PhD dissertation, 208 pp.

Gudmundsson, A., 2000: Dynamics of volcanic systems in Iceland: Example of tectonism and volcanism at juxtaposed hot spot and mid-ocean ridge systems. *Annual Review of Earth and Planetary Sci., 28*, 107-140.

Gudmundsson, J.S. and Pálmason, G., 1987: The geothermal industry in Iceland. *Geothermics, 16*, 567-573.

Hjartarson, Á. 2015: Heat flow in Iceland. *Proceedings of the World Geothermal Congress 2015, Melbourne, Australia*, 4 pp.

Hjartarson, Á. and Kristinsson, S.G., 2007: *Kjalarnes – Botnsdalur. Bedrock map 1:25,000 and descriptions of strata*. ÍSOR – Iceland GeoSurvey, ÍSOR-2007/064 (in Icelandic).

Jacoby, W. and Gudmundsson, M.T., 2007: Hotspot Iceland: An introduction. *J. Geodynamics, 43*, 1-5.

Jóhannesson, H. and Saemundsson, K., 1998: *Geological map of Iceland 1:500,000. Tectonics* (2nd ed.). Icelandic Institute of Natural History, Reykjavík, Iceland.

Kristjánsson, L., Fridleifsson, I.B. and Watkins, N.D., 1980: Stratigraphy and paleomagnetism of Esja, Eyrarfjall and Akrafjall Mountains, SW-Iceland. *J. Geophys., 47*, 31-42.

Kristinsson, S.G., 2009: *The Hvalfjördur central volcano, stratigraphy, tectonics and alteration*. University of Iceland. MSc thesis (in Icelandic), 93 pp.

Saemundsson, K., 1992: Geology of the Thingvallavatn area. *Oikos, 64,* 40-68.

Saemundsson, K., 2007: Geology and gradient wells. *Presented at "Short Course II on Surface Exploration for Geothermal Resources", organized by UNU-GTP and KenGen, Lake Naivasha, Kenya,* 11 pp.

Saemundsson, K. and Einarsson, S., 1980: *Geological map of Iceland, sheet 3, SW-Iceland* (2nd ed.). Museum of Natural History and the Iceland Geodetic Survey, Reykjavík, Iceland.

Schilling, J.G., 1973: Iceland mantle plume: geochemical study of Reykjanes Ridge. *Nature, 242*, 565-571.

Tibaldi, A., Vezzoli, L., Pasquare, F.A. and Rust, D., 2008: Strike-slip fault tectonics and the emplacement of sheetelaccolith systems: The Thverfell case study (SW Iceland). *J. Structural Geology, 30*, 274-290.

Thórdarson, T. and Höskuldsson, A., 2002: *Iceland (Classic Geology in Europe 3).* Terra Publishing, Reykjavík, 200 pp.

Weisenberger, T. and Selbekk, R.S., 2007: Multi-stage zeolite facies mineralization in the Hvalfjördur area, Iceland. *Int. J. Earth Sci (Geol Rundsch), 98,* 985-999.

Weisenberger, T., 2005: Zeolite facies mineralisation in the Hvalfjördur area, Iceland. Freiburg: Albert Ludwigs Universitat Freiburg, Diploma thesis, 142 pp.

Walker, G.P.L., 1960: Zeolite zones and dyke distribution in relation to the structure of the basalts of eastern Iceland. *J. Geol., 68,* 515-528.

Villemin, T., Bergerat, F., Angelier, J. and Lacasse, C., 1994: Brittle deformation and fracture patterns on oceanic rift shoulders: The Esja peninsula, SW Iceland. *Journal of Structural Geology, 16*, 1641-1654.

APPENDIX I: Gradient well logs in Mödruvellir geothermal field

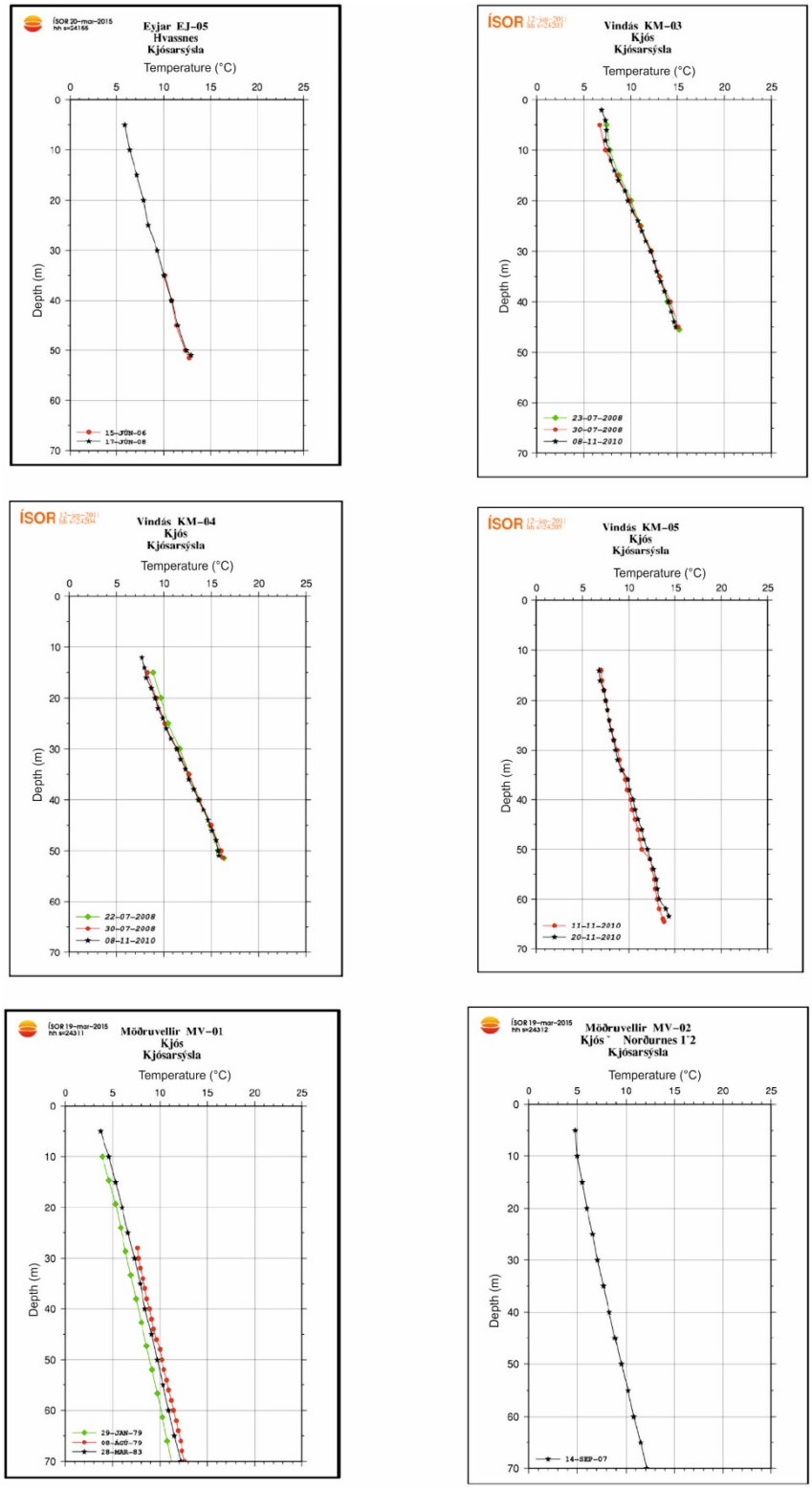

FIGURE 1: Temperature versus depth in wells EJ05, KM3, KM4, KM5, MV01 and MV02

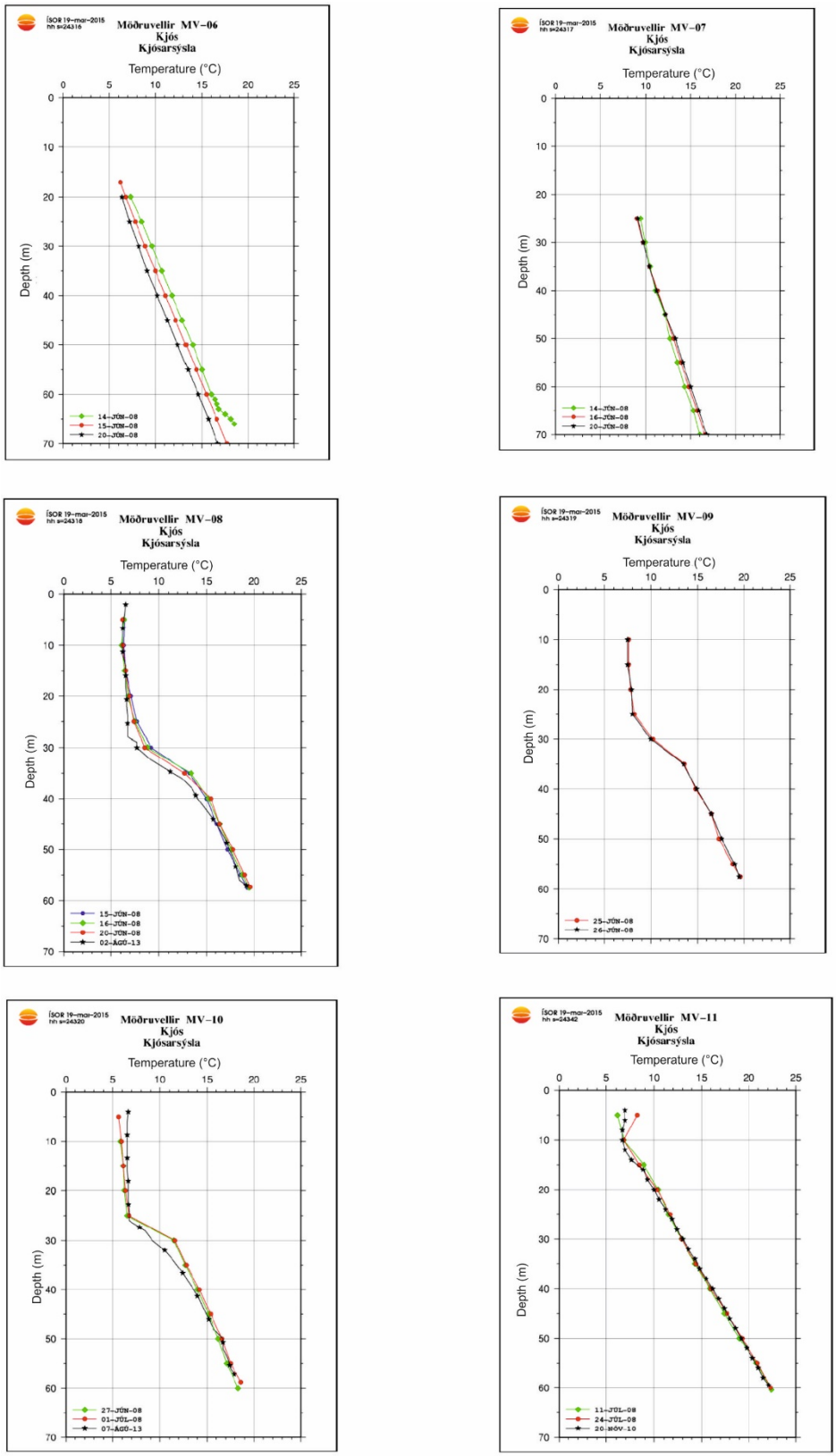

FIGURE 2: Temperature versus depth in wells MV06, MV07, MV08, MV09 and MV10

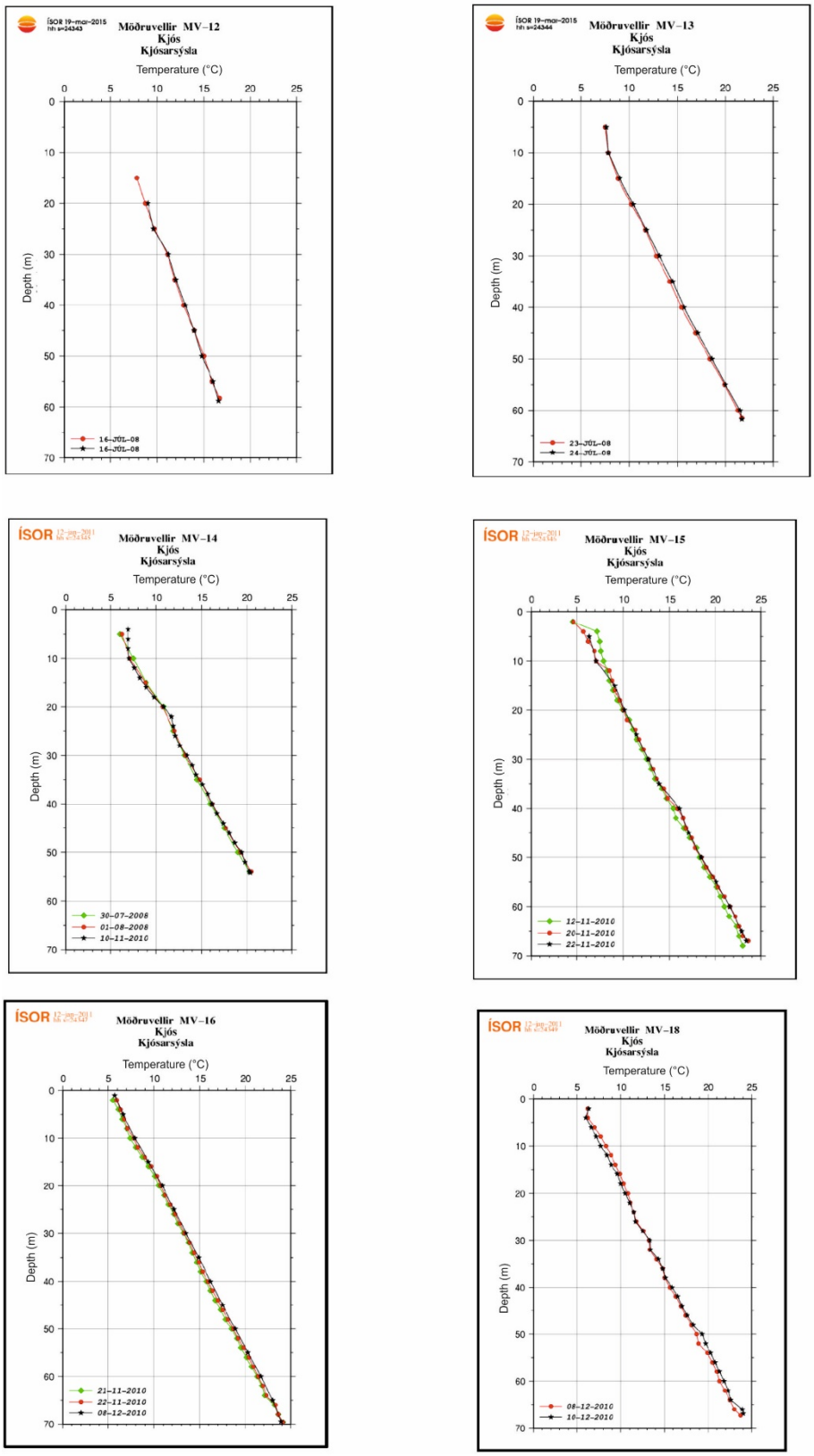

FIGURE 3: Temperature versus depth in wells MV12, MV13, MV14, MV15 and MV16

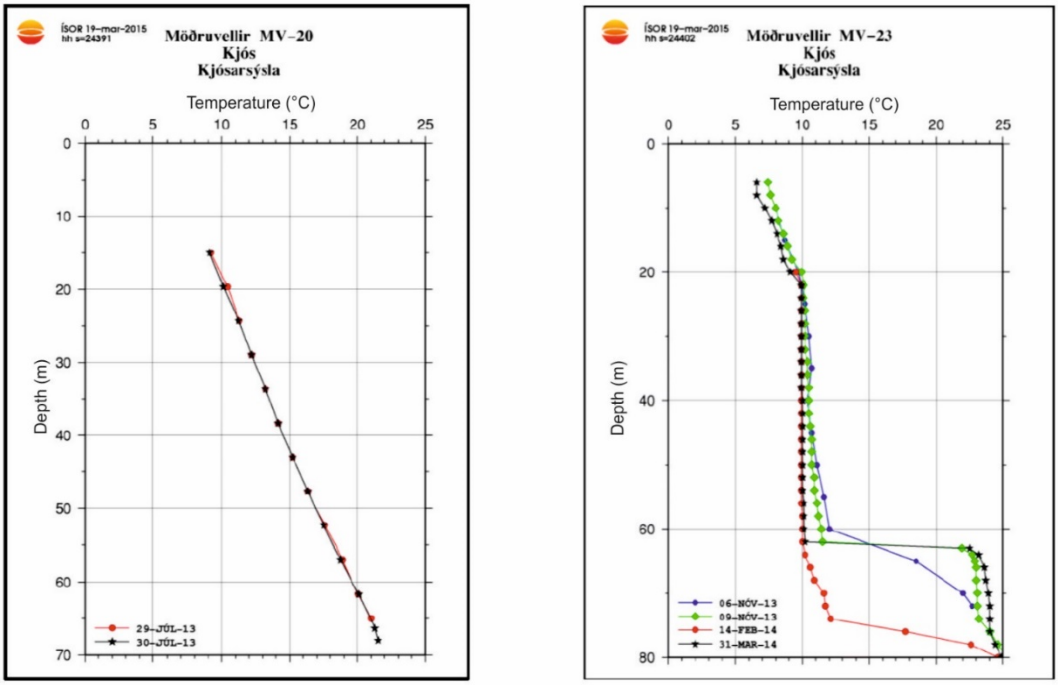

FIGURE 4: Temperature versus depth in wells MV20 and MV23

APPENDIX II: The XRD measurements for clay minerals and zeolites in wells MV-19 and MV-24

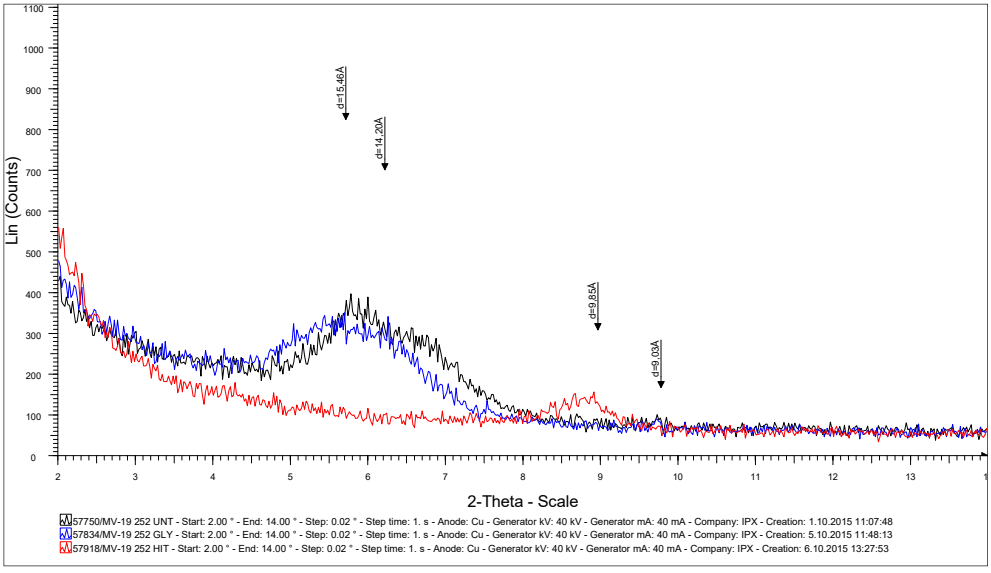

FIGURE 1: Well MV-19, XRD analysis from 252 m

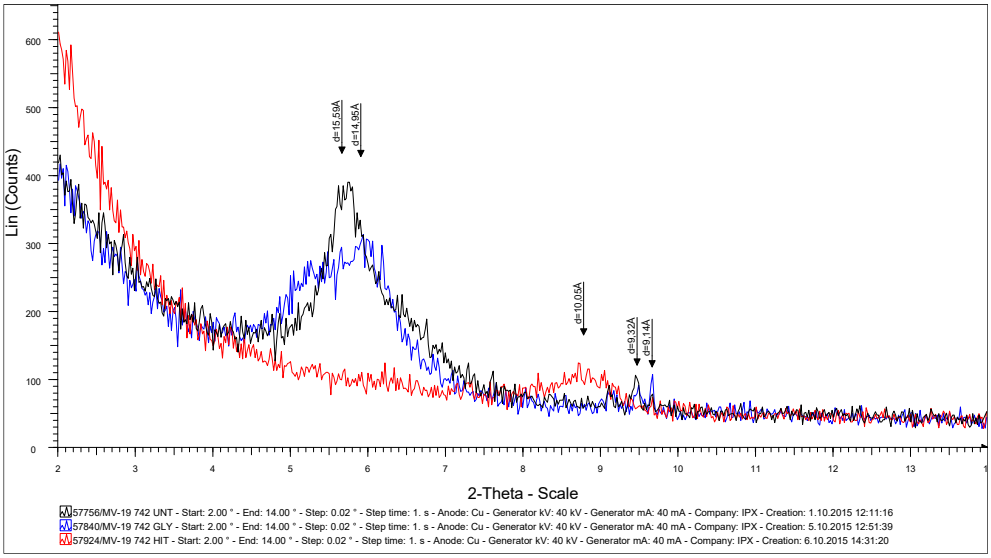

FIGURE 2: Well MV-19, XRD analysis from 742 m

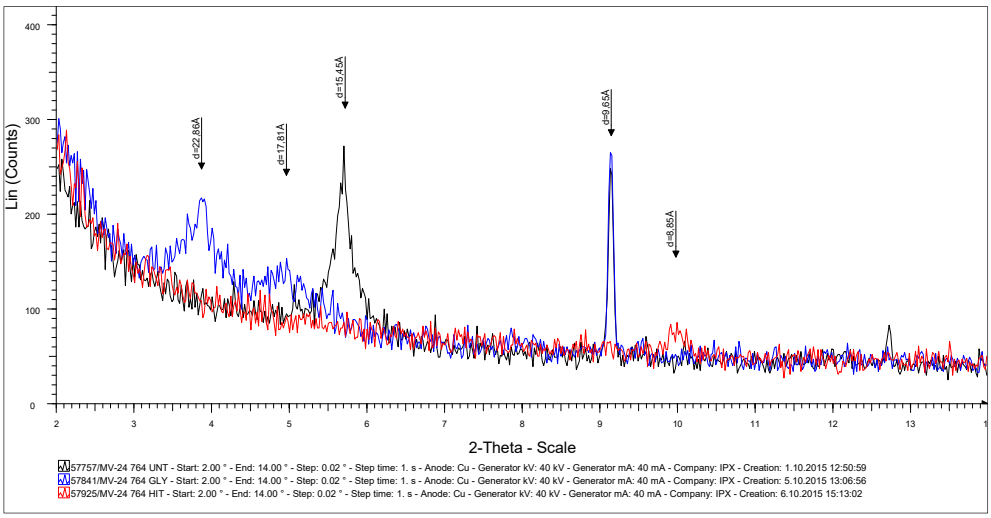

FIGURE 3: Well MV-24, XRD analysis from 764 m

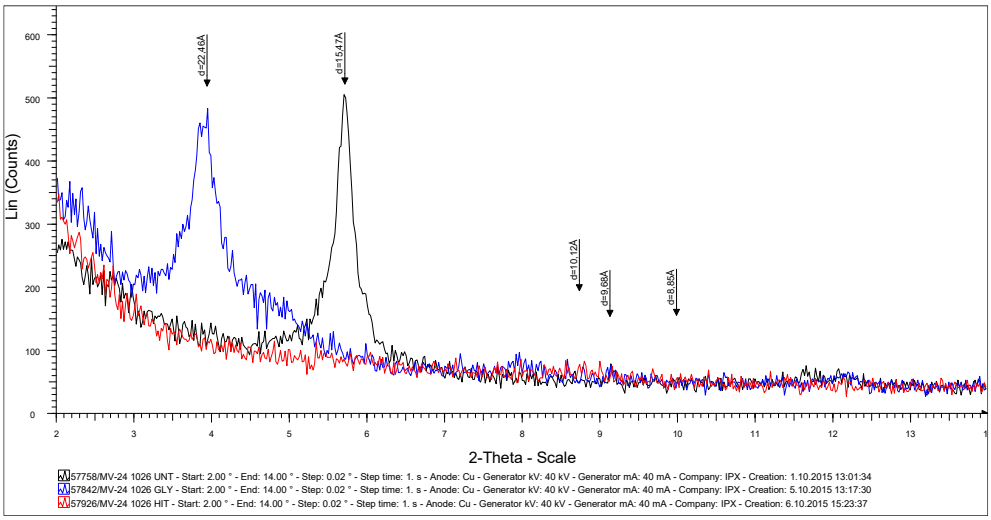

FIGURE 4: Well MV-24, XRD analysis from 1026 m

UNITED NATIONS UNIVERSITY
UNU-GTP
Geothermal Training Programme

Orkustofnun, Grensasvegur 9,
IS-108 Reykjavik, Iceland

Reports 2015
Number 10

SUBSURFACE GEOLOGY AND HYDROTHERMAL ALTERATION OF CACHAÇOS-LOMBADAS SECTOR, RIBEIRA GRANDE GEOTHERMAL FIELD, SÃO MIGUEL ISLAND, AZORES

António Franco
EDA RENOVÁVEIS
Rua Francisco Pereira Ataíde, 1
9504-535 Ponta Delgada, Acores
PORTUGAL
antonio.l.franco@eda.pt

ABSTRACT

The present report focuses on the high temperature geothermal area of Cachaços-Lombadas in the 245°C two-phase liquid dominated Ribeira Grande geothermal system in São Miguel Island. Subsurface geology and hydrothermal alteration are studied, using data from four of the eight existing wells. Emphasis is laid on the determination of the lithostratigraphy and identification of possible correlations between the geological units and the permeability encountered in the wells, including the analysis of tectonic structures inferred in the area. The present work reveals that pyroclastic rocks dominate the upper part of the subsurface geology, locally interrupted by trachyte lava flows and, at deeper levels, basalt lavas are the predominant lithological unit. Furthermore, the results show that north-northwestern trending structures probably play a very important role in the distribution of permeability in the Cachaços-Lombadas area.

Temperature distribution in the area was also investigated and the results are consistent with the main conclusions from previous studies, showing a clear boundary of the geothermal system in the southern part of the area and suggesting that the location of the upflow zone of the geothermal system is likely to be in the east to northeastern parts of the Cachaços-Lombadas area.

The alteration mineralogy allowed determining the alteration zoning pattern in the Cachaços-Lombadas area, identifying two zones of hydrothermal alteration, smectite zone and chlorite zone, beneath a shallow zone of relatively unaltered rocks. The hydrothermal alteration investigations were complemented with the study of fluid inclusions, allowing determination of the thermal history of the geothermal system. The results reveal that the geothermal system was hotter at some point in the past. However, since cooling has occurred, the system has been in equilibrium, with evidence of some fluctuations of the fluid levels within the geothermal reservoir.

1. INTRODUCTION

1.1 Geographical location of the Azores

The Azores Archipelago is a group of nine islands located in the middle of the Atlantic Ocean (Figure 1), 1600 km away from Portugal and 3800 km from the east coast of the USA. The population is approximately 240,000 inhabitants and of those about two thirds live on the largest island, São Miguel. The islands are spread along 600 km and, because of that, each island must be energy self-sufficient. Thus, the very small energy market, associated with the remote and isolated location of the region make the energy projects less attractive to private investors and, therefore, geothermal development must be publically driven (Rangel et al., 2011).

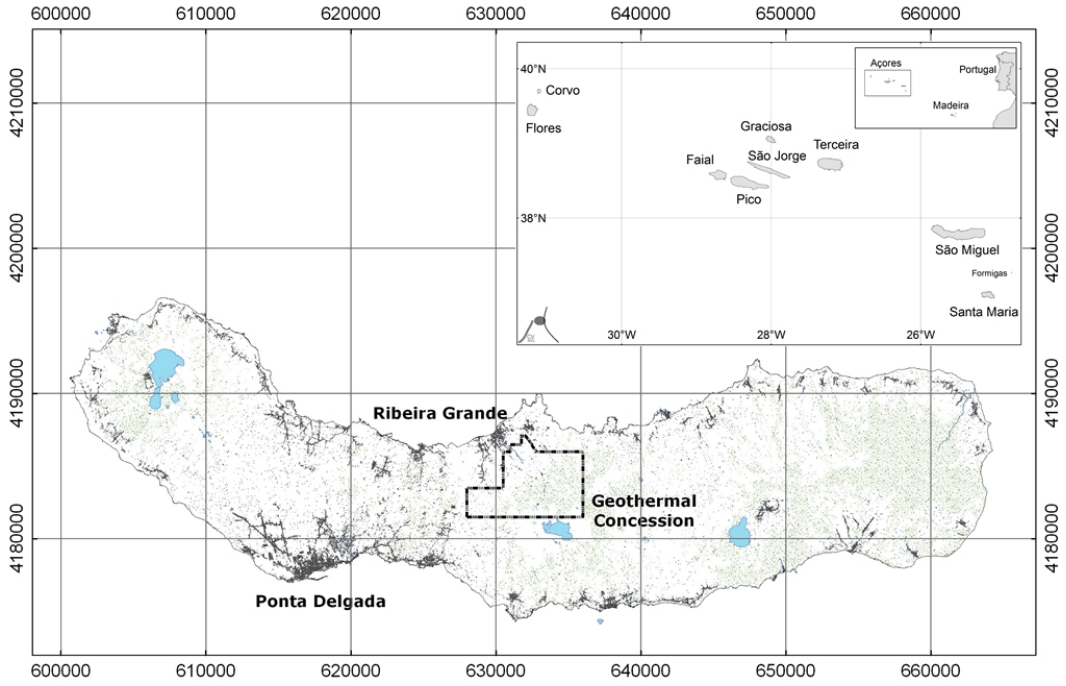

FIGURE 1: Geographical location of São Miguel Island, showing the location of Ribeira Grande geothermal concession (map provided by EDA RENOVÁVEIS)

1.2 History of geothermal projects in the Azores

Geothermal exploration in São Miguel Island started in 1976, with the execution of geophysical surveys (geoelectric and magnetotelluric), which identified a resistivity anomaly in the northern flank of Fogo volcano (Figure 2) which is possibly related to the presence of a geothermal system. This exploration was spurred by the findings in 1973 when a well was drilled to 981 m depth close to the city of Ribeira Grande (Figure 2) and encountered steam productive zones and temperatures exceeding 200°C (Muecke et al., 1974). This well was part of the ‘‘Deep Drill’’ project, developed by scientists at Dalhousie University and Lamont-Doherty Geological Observatory, and was planned to enhance the understanding of the structure, petrology and geochemistry of oceanic islands (Muecke et al., 1974).

In 1973, six thermogradient wells were drilled to 200 m depth and confirmed the existence of an extensive temperature anomaly in the northern flank of the Fogo volcano. These were followed by drilling of five exploratory wells (RG1, RG2, PV1, PV2 and SB1) from 1978 to 1981 which confirmed the existence of a high temperature geothermal reservoir (Hennerberger and Nunes, 1990), finding temperatures up to 230-235°C at -150 to -200 m mean sea level (m.s.l.).

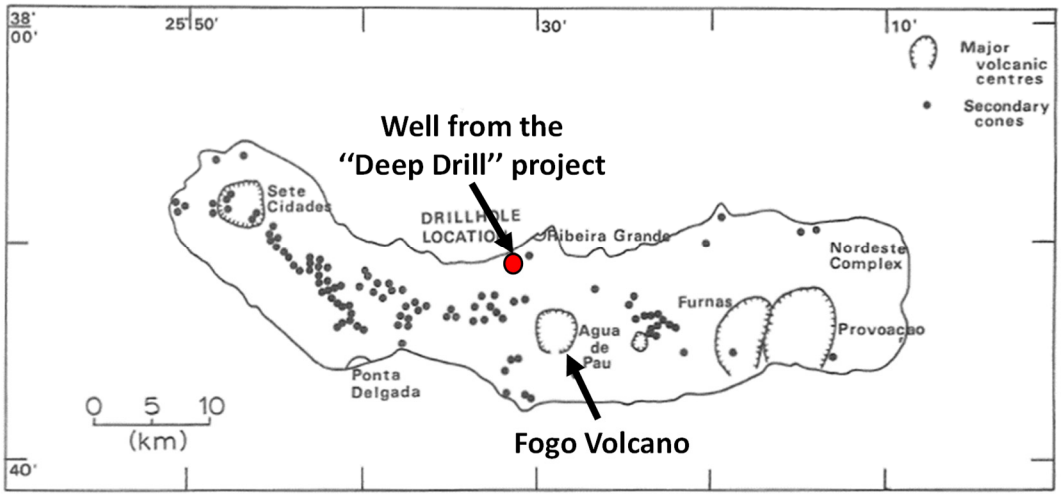

FIGURE 2: Location of the well drilled in the scope of the "Deep Drill" project (adapted from McGraw, 1976)

PV1 led to the installation of a small 3 MW geothermal pilot power plant, flash type, with a backpressure turbine which operated from 1980 to 2005 (Ponte, 2012). This project represented the first milestone of geothermal power production in the Azores and it was a very important breakthrough for the geothermal project because the pilot plant acted as a school for the technical staff who learned how to operate the industrial equipment and allowed to enhance the knowledge of the geothermal resource.

From 1989 to 1994, four wells (CL1, CL2, CL3, and CL4) were drilled in the southern part of the geothermal field, at higher elevations on the Fogo volcano and production of these wells was more than sufficient to supply Phase A of the Ribeira Grande plant (5 MW organic binary cycle) (Granados et al, 2000). The power plant went online in 1994, starting the industrial geothermal power production in the Azores. The wells were relatively prolific and the power plant was later expanded to 13 MW in 1999. During the past twenty-five years, three make-up wells were drilled for additional fluid supply to the power plant in order to maintain the load factor at high levels. This was the case for wells CL5 (2000), CL6 (2005) and CL7 (2010). More recently, well CL4-A was drilled in 2012 to serve, in combination with CL4, the reinjection of the effluent (brine and steam condensate) from the power plant, returning it back into the geothermal reservoir.

Meanwhile, in 2005, the pilot power plant at Pico Vermelho was dismantled and a new 10 MW power plant was installed in the same area (Cabecas et al., 2010) after the drilling of 6 additional wells was completed (PV3, PV4, PV5, PV6 and PV7 and PV8). This power plant was online by the end of 2006. Since then, it has achieved consistent production results with high availability (> 99%) and high load factor (> 99%) (Rangel et al., 2011). Within the first year in operation, numerical modelling studies had shown the possibility of thermal breakthrough within the reservoir due to reinjection in wells PV5 and PV6 (Ponte et al., 2010). Therefore, three new injection wells (PV9, PV10 and PV11) were drilled in 2009 and reinjection of brine and steam condensate from Pico Vermelho power plant is now being employed in these wells.

Since 1990, the geothermal development was driven by SOGEO (Sociedade Geotérmica dos Acores, S. A.), following the work of previous regional government institutions (Rangel et al., 2011). Meanwhile, in 2014, SOGEO merged with the EEG (Electricidade e Gás, S.A.), the company that exploits hydro and wind resources, and changed its denomination to EDA RENOVÁVEIS. In 2014, the geothermal contribution to total generation reached an average of 44% in São Miguel Island, representing about 23% of the overall power produced in the Azores (EDA, 2014). Therefore, the geothermal project of the Azores provides a significant contribution to the energy self-sufficiency of this remote and isolated region, offering clean, secure and cost-competitive energy, diminishing the needs for the use of fossil fuels.

2. OBJECTIVES

This work aimed at investigating the subsurface geology and hydrothermal alteration in the Ribeira Grande geothermal field, focusing on the Cachaços-Lombadas sector, located in the southern part of the field, and possibly providing some valuable information regarding what to expect in future wells to be drilled within this area. The main objectives of the study are described below:

- Establishing a correlation between the geological formations intersected by the geothermal wells and, if possible, try to identify the transition from subaerial to submarine deposits (phreatic breccias);
- Determining if there is any consistent relation between the geology and the permeability of the reservoir;
- Making a first determination of the alteration zone and determine the thermal evolution of the geothermal system, namely, weather if it is in equilibrium, heating or cooling.

3. GEOLOGICAL BACKGROUND

3.1 Tectonic setting of the Azores and the Fogo volcano

The Azores Islands are located on the triple-junction of the Azores where the Eurasian, African and American tectonic plates meet. As Figure 3 shows, the nine islands of the Archipelago are divided into three groups with Flores and Corvo located on the North American plate whilst the eastern (São Miguel and Santa Maria islands) and the central group (Faial, Pico, São Jorge and Terceira islands) are located along the Terceira Rift which corresponds to the western segment of the Azores-Gibraltar fault zone. The islands from the eastern and central groups follow a WNW-ESE trend and emerge above the sea in the Azores Plateau which is defined by the bathymetric line of 2000 m (Rangel et al., 2011) and marks the transition to the nearby abyssal planes with depths of over 3500 m.

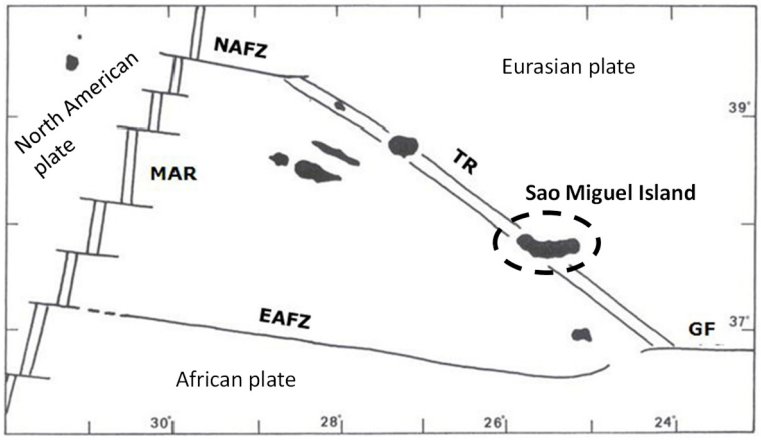

FIGURE 3: Main tectonic structures in the Azores region: MAR – Mid Atlantic Ridge; NAFZ – Northern Azores Fault Zone; EAFZ – Eastern Azores Fault Zone; TR – Terceira Rift; GF – Glória Fault (adapted from Gaspar, 1996)

According to Carmo (2013), the fault pattern in the Azores is characterized by two main fault systems with oblique slip, each of which is composed of two sets dipping in opposite directions: WNW-ESE to NW-SE normal dextral faults and conjugated NNW-SSE to N-S normal lateral structures. With this arrangement, the fault pattern exhibits a horizontal maximum compressive stress trending NW-SE (σ1), a horizontal minimum compressive axis trending NE-SW (σ3) and a vertical intermediate compressive stress axis (σ2). The resultant deformation is accommodated by several active faults where significant volcanic and seismic activity occurs.

São Miguel Island is located near the southeast end of the Terceira Rift and its most important tectonic structures follow the general pattern of the Azores Plateau with main directions NW-SE and WNW-ESE

(Silva et al., 2011). Therefore, the island is characterized by significant seismicity associated with these NW-SE and WNW-ESE structures (Queiroz, 1997; Ferreira, 2000).

The most important tectonic structure of the Fogo volcano is the graben of Ribeira Grande (Figure 4). The identification of tectonic structures at the surface is somewhat difficult in the Fogo volcano, due to the fact that most of the faults are covered by thick layers of pyroclastic units or are obscured by dense vegetation. Therefore, most of the structures are inferred by lineaments formed by the volcanic structures and from the linear river streams/creeks.

According to Carmo (2013), the orientation of the main structures of Ribeira Grande graben is in agreement with the main direction of the regional tectonic stresses, associated with the Terceira Rift. The graben itself extends over most of the northern flank of the volcano and its limits are defined by two lineaments of volcanic peaks. The western limit is given by the fault zone of Ribeira Grande, a lineament with about 7 km in extension formed by Pico da Varanda, Pico da Madeira, Pico dos Carneiros, Pico Queimado and the scoria cone of Rochão. The eastern limit corresponds to the fault zone of Falca which is defined by a 9 km lineament formed by the volcanic peaks of Cintrão, Pico da Vinha, Lameiro, Coroa da Mata, Pico Redondo and Monte Escuro.

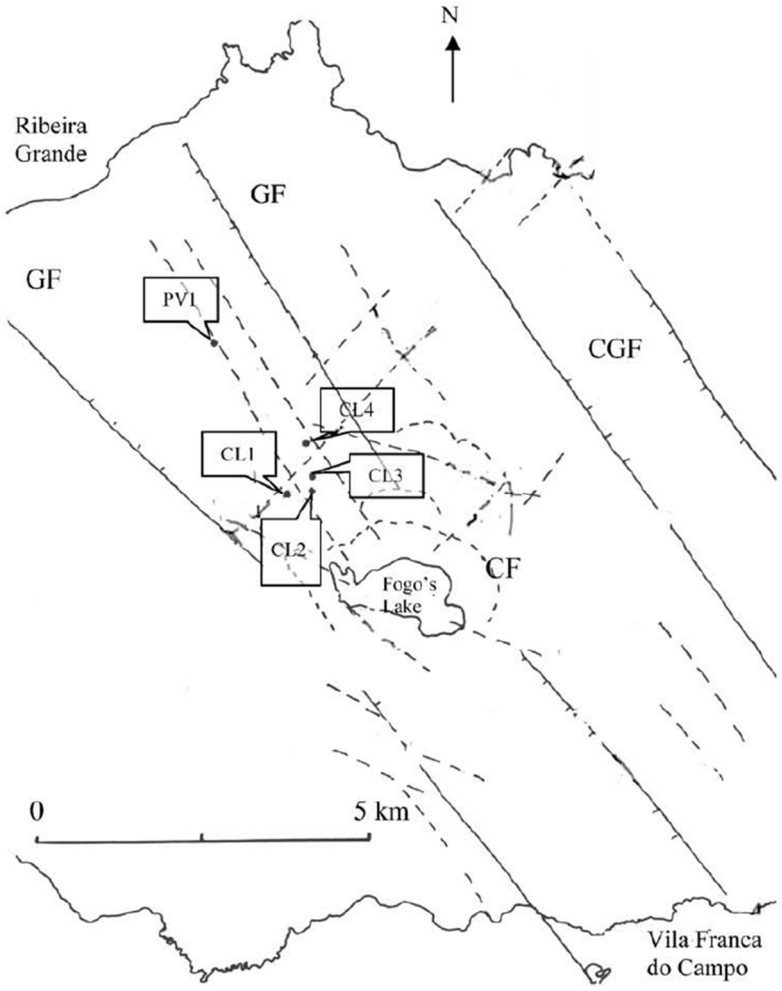

FIGURE 4: The graben of Ribeira Grande, showing the location of the geothermal wells (PV1, CL1, CL2, CL3 and CL4). GF denotes the Graben faults; CF denotes caldera faults; and CGF denotes Congro's fault system. Solid lines denote known faults, dashed lines inferred faults (modified from Carvalho et al., 2006)

As shown in Figure 4, the main structures observed in the graben of Ribeira Grande are NW-SE and NNW-SSE trending. The vertical displacement of the normal faults that limit the graben is uncertain because this tectonic valley has been filled with successive volcanic material from recent eruptions, such as the FOGO A unit, which can reach up to 20 m in thickness (Carmo, 2013). Furthermore, according to Muecke et al., (1974), based on the geological data collected from core samples in a well drilled in 1973 in the scope of the "Deep Drill" Project the graben of Ribeira Grande has suffered subsidence of about 650 m in the last 690,000 years. This was suggested by the appearance of submarine deposits at only about 700-800 m depth with the uppermost part of the well lithology consisting only of subaerial facies.

Moreover, the fact that there are no surface expressions of the normal fault zones that correspond to the boundaries of the graben suggests that volcanic activity and the rate of the material filling the graben exceeds the tectonic activity associated with the graben faults (Carmo, 2013).

3.2 Geology of Fogo volcano

Along with Sete Cidades and Furnas, Fogo is one of the three late Quaternary stratovolcanoes of São Miguel Island. Located in the central part of the island (Figure 5), Fogo is a central volcano with a summit about 900 meters above sea level, truncated by a 3 km wide caldera where the lake "Lagoa do Fogo" lies. Furthermore, the volcano morphology is characterized by an older outer caldera about 7x4 km across, which is preserved in the western, northern and eastern part of the volcano (Moore, 1991).

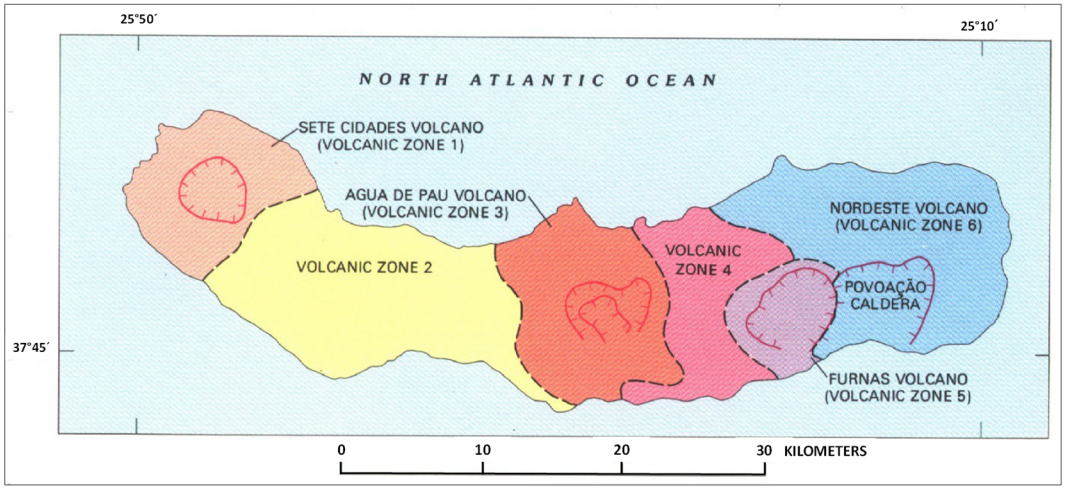

FIGURE 5: Location of Fogo volcano, identified as Agua de Pau volcano (Moore, 1991)

Inside the calderas there is only evidence of explosive activity, whereas several trachyte and mafic lava flows were erupted from vents located on the flanks of the volcano prior to and following the caldera formation (Moore, 1991). According to Booth et al. (1978), during the last 5,000 years at least five eruptions of trachyte pumice have occurred from vents located within the inner caldera.

The rock types show geochemical bimodality with the trachyte compositions dominating and the intermediate compositions representing a minor volumetric part of the eruptions. The lava flows and the pyroclastic deposits of the Fogo volcano are classified as alkali basalt-trachyte (Irvine and Barager, 1971).

As shown in Figure 6, the Fogo volcano stratigraphy can be divided into the following main units:

- *The Pleistocene units* correspond to the oldest subaerial rocks and according to Moore (1990), these include a trachyte dome (181,000 years old) on the southern flank, a trachyte flow (121,000 years old) near the summit and a trachyte welded tuff (103,000 years old) deposits on the northeast coast. The main edifice of the volcano was built around 40,000 to 100,000 years ago and it consists of trachyte lava flows, domes and pyroclastic deposits (Moore, 1990);
- *Older caldera – outflow deposit:* This corresponds to the collapse episodes of the summit caldera. Although this might have occurred several times, only two deposits show clear evidence of such episodes. These mostly correspond to several cubic meters of welded and non-welded pumice which can be found in outcrops on the north eastern and south eastern flanks of the volcano as well as exposures of welded tuff deposits on the northern and south eastern flanks of the volcano which can be seen filling the canyons near the margins of the early trachyte flows and overlying trachyte flows;
- *Post-outer caldera units:* There is no evidence for the occurrence of any eruptions within the outer caldera limits for about 15,000 to 30,000 years. Nevertheless, a few eruptions of tristanite and possibly mafic lavas occurred from vents located on the flanks of the volcano.
- *Younger caldera – outflow deposit:* The inner caldera was formed about 15.200 years ago as a result of a large Plinian eruption which produced large volumes of non-welded pumice and

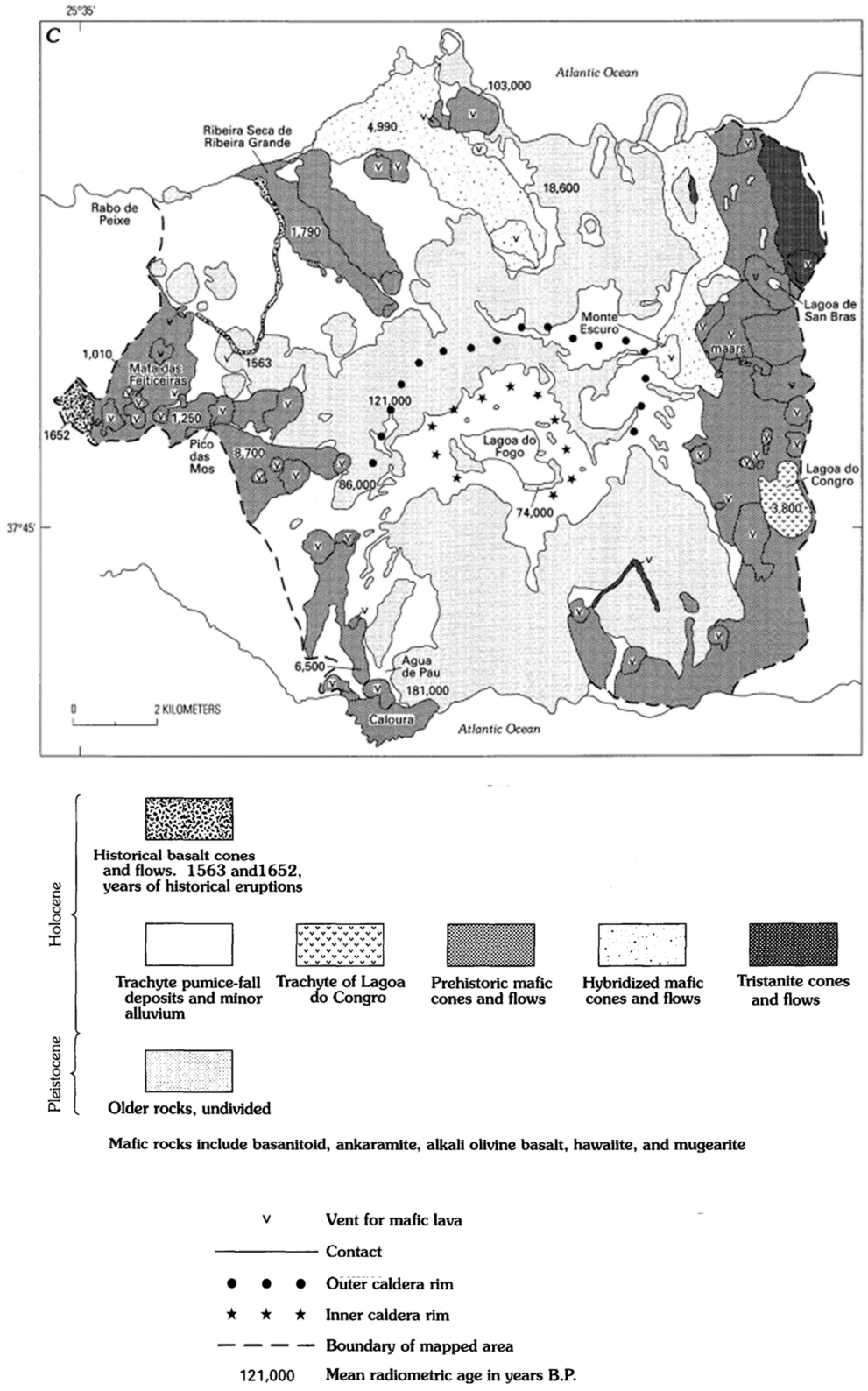

FIGURE 6: Geological map of Fogo volcano (Moore, 1991)

- locally welded pyroclastic flows. Exposures of these deposits can be found on the southern flank of the volcano with the best outcrops being located in the sea cliffs between Trinta Reis and Pisoes.
- *Post-inner caldera units*: According to Moore (1990), until about 10,000 years ago no important eruptions occurred within the inner caldera. Nevertheless, six trachyte domes and associated

flows were formed just outside the outer caldera rim on the western and north western flanks of the volcano.

- *Holocene units* are resulting mostly from the activity in the inner caldera about 5,000 years ago. These include the large Plinian fall deposit Fogo A which was probably formed in at least five separate eruptions (Moore, 1990) as well as other minor pyroclastic and mudflows (Walker and Crossdale, 1970). The Fogo A deposit is one of the most valuable chronostratigraphic marker beds because no other major trachytic eruption is known on central and eastern São Miguel at this time.

3.3 Historical eruptions and seismic activity

Due to its geodynamic setting, the Azores are frequently associated with seismic and volcanic activity. Since settlement in the 15th century, 30 earthquakes of tectonic origin were felt in the Azores, killing approximately 5000 people and causing significant damage (Carvalho et al., 2001). Some of these earthquakes are estimated to have reached magnitudes of up to 7 on the Richter scale. During this period, about 30 volcanic eruptions took place in the Azores, causing about 240 deaths. The last volcanic eruption was in 1998 and it was located in the sea, west of Terceira Island. The last major earthquake was felt in Faial in 1998, reaching a magnitude of 6 on the Richter scale (Carvalho et al., 2001).

The source of the volcanic activity in the Azores has been considered to be related to the presence of a mantle plume (Madureira et al., 2005, 2014) and the region is considered as a typical example of hot spot-ridge interaction but this has been under intense debate (Métrich et al., 2014). Since the settlement three volcanic eruptions have occurred in São Miguel Island, two in Furnas Volcano in 1439-43 and 1630 (Booth et al., 1978; Cole et al., 1995) and one in Fogo in 1563 (Figure 7) (Wallenstein et al., 2007).

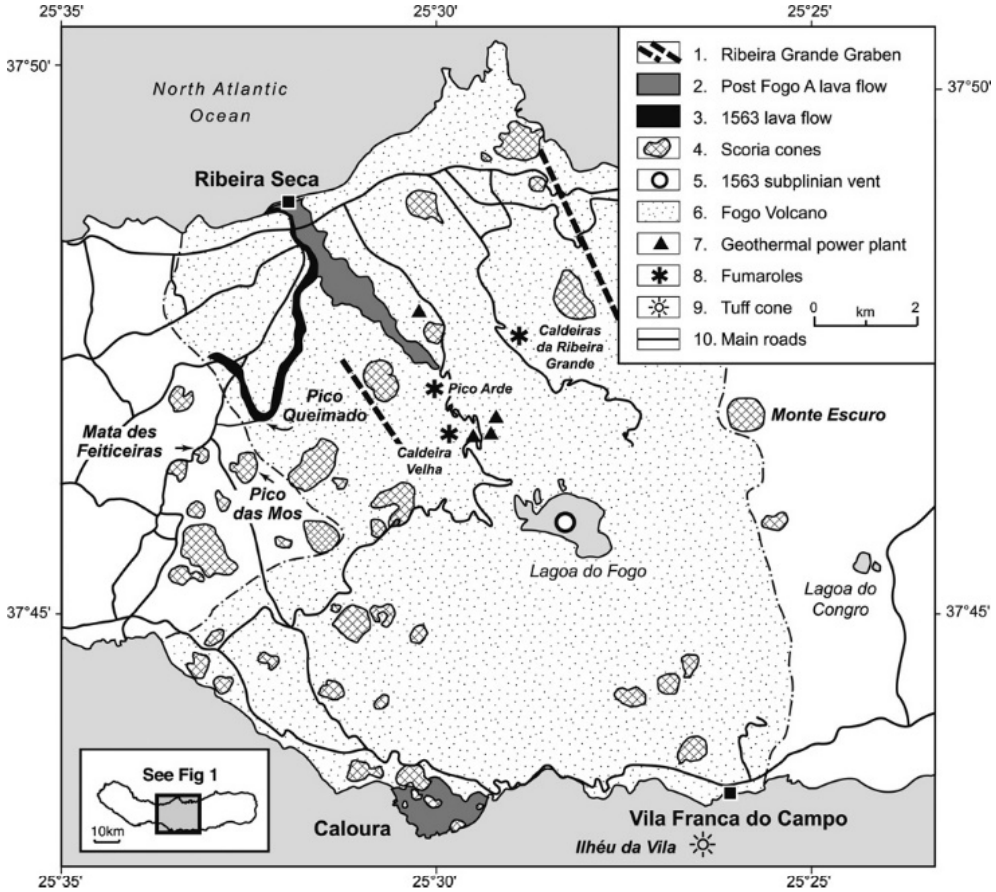

FIGURE 7: Volcanic structures and geothermal surface manifestations in the Fogo volcano, showing also the location of the 1563 eruptions (Wallenstein et al., 2007)

The 1563 eruption started as a Plinian eruption inside the inner caldera and, just a few days later, a Strombolian eruption started in a vent located in the north western flanks of the volcano (Pico Queimado) with the latter extruding a mafic lava flow that reached the villages of Ribeira Seca and Ribeira Grande located in the north coast of São Miguel Island (Figure 7).

At present time, the Fogo volcano is considered to be dormant. Several geothermal surface manifestations in the area include active fumarole fields, hot springs and soil diffuse degassing areas. As shown in Figure 7, these manifestations are mainly located in the northern flank of the Fogo volcano and are associated with NW-SE faults (Ferreira, 2000) with the main features being present at Pico Vermelho (near Pico Arde), Caldeira Velha and Caldeiras da Ribeira Grande.

Since the early 80´s, the seismic network of the Azores, operated by CIVISA (Centro de Informação e Vigilância Sismovulcânica dos Açores), has been monitoring the seismic activity of the Azores, registering hundreds of earthquakes and micro earthquakes. These data allowed delineating the major seismic areas of the Region. As shown in Figure 8, the seismic swarms are located along the Terceira Rift and on the Middle Atlantic Ridge and in their associated areas. This is the case of D. João de Castro submarine volcano, located between the Terceira and São Miguel islands or the seismic swarm located southeast from São Miguel Island. Additionally, it is important to note that seismicity in the region has been characterized by the occurrence of frequent low to moderate magnitude events, up to 2-3 on the Richter scale, but, as mentioned above, some strong earthquakes of magnitude 7 also occur.

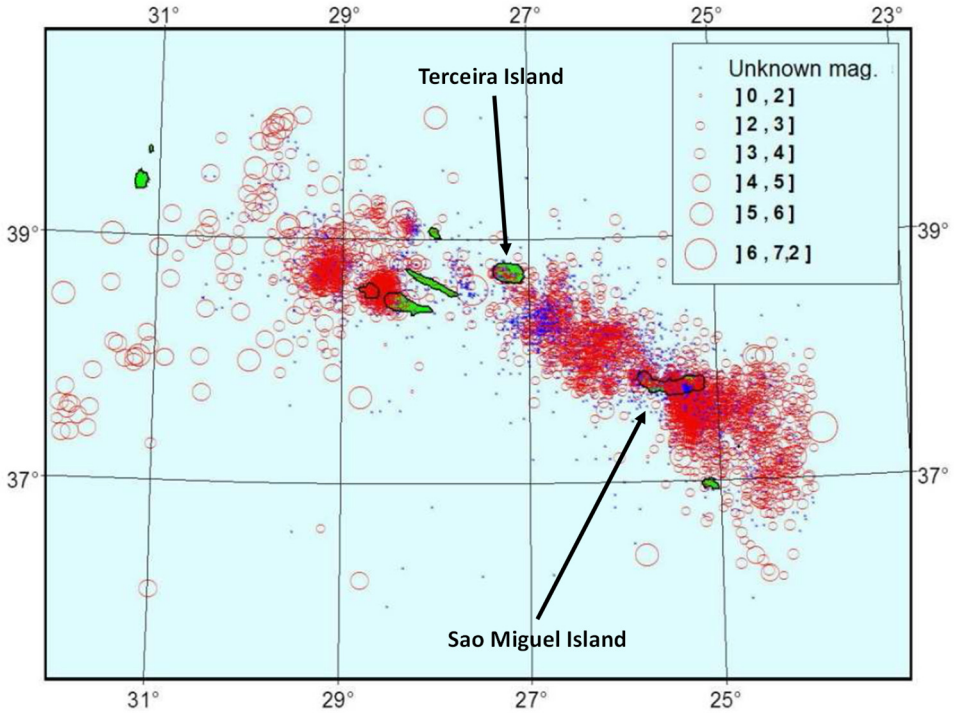

FIGURE 8: The Azores epicentral map for 1915 to 2011
(adapted from Rodrigues and Oliveira, 2013)

3.4 Ribeira Grande geothermal field

The main hydrothermal system of the Fogo volcano is located on the northern flank, associated with the northwest-southeast fault system corresponding to the graben of Ribeira Grande (Figure 4). The Ribeira Grande geothermal system is a high temperature system with temperatures up to 245°C, hosted by volcanic rocks, mainly pyroclastic units and lava flows. The system is elongated in a north-western direction and its boundaries probably follow the same strike (GeothermEx, 2008; Ponte et al., 2009).

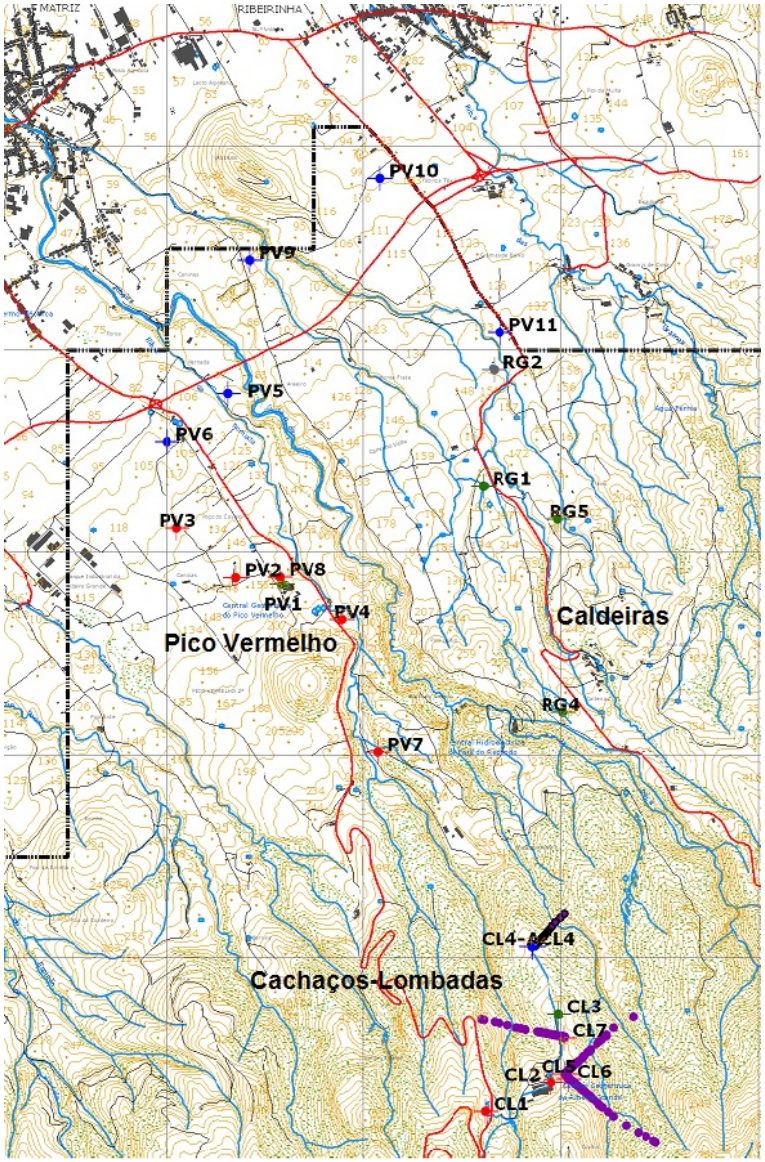

FIGURE 9: Location of the wells in the Ribeira Grande geothermal field (Rangel, 2014; provided by EDA RENOVÁVEIS)

The heat source is most likely related to a magmatic body or young intrusive rocks associated with the activity of the Fogo volcano (GeothermEx, 2008; Ponte et al., 2009; Pham et al., 2010; Ponte et al., 2010). In this respect, many studies have suggested that a trachytic magma chamber underlies the Fogo volcano (Booth et al., 1978; Duffield and Muffler, 1984; Gandido et al., 1984) and seismic studies undertaken by Dawson et al., (1985) indicated that the magma chamber is likely to be located at 10 to 12 km depth.

The subsurface geology and the geothermal reservoir conditions have been investigated by surface exploratory work and by drilling of shallow and deep geothermal wells. Based on the available data, the upflow to the geothermal system is located in the south eastern part of the geothermal field, probably east to northeast of wells CL3 and CL7 (Figure 9). The fluid subsequently moves upwards and northwestward, following the fault system of the Ribeira Grande graben and the outflow of the geothermal system which is likely towards the sea, in the northern part of the field (Figure 10) (GeothermEx, 2008; Ponte et al., 2009; Pham et al., 2010; Ponte et al., 2010).

The reservoir is two-phase and liquid dominated, the fluid composition being sodium-chloride type with total dissolved solids of 6 to 7 g/l and pH of 8-9. The chloride content is typically about 1500-1600 mg/l, the silica content ranges from 400 to 600 mg/l and the alkalinity is about 500 mg/l (Rangel et al., 2011). The permeability is mainly associated with fracture zones located within the basalt lava flows, likely to be associated with the northwest trending fault system of the Ribeira Grande graben. Furthermore, the fluid composition in the geothermal system is fairly homogeneous, indicating that good and well distributed permeability can be found in most of the field (GeothermEx, 2008). Additionally, oxygen and deuterium isotope analyses have shown that recharge of the geothermal system is of meteoric origin (Ponte et al., 2010; Rangel et al., 2011).

The cap rock of the geothermal system is composed of a sequence of pyroclastic units which are altered to clay, forming a relatively impermeable cap at the top of the reservoir. Because of the topography, the cap rock is found deeper in the wells located in the southern part of the field, namely at 500-650 m depth in the Cachaços-Lombadas sector (identified as Ribeira Grande area in Figure 10), whereas it is found at 300-400 m in the wells located further north in the Pico Vermelho sector.

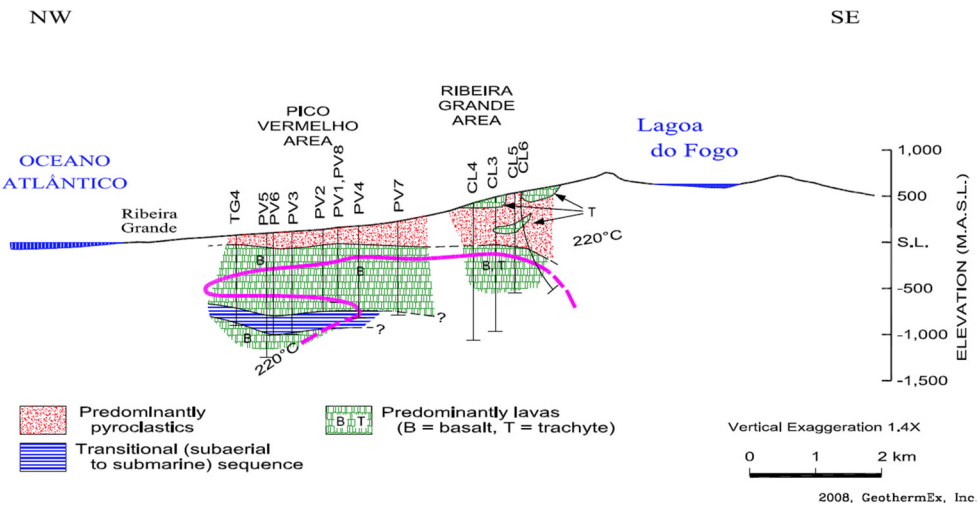

FIGURE 10: Generalized cross-section of the Ribeira Grande geothermal system (GeothermEx, 2008)

4. LITHOLOGY LOGS

All rocks intersected by the Cachaços-Lombadas wells are volcanic and correspond to the eruptive products of the Fogo volcano. The rock types include pyroclastic rocks, such as fine-grained tuffs and coarser tuffs with variable amounts of lithic fragments, pumice and crystals and different types of lavas, varying in composition from trachyte, basalt and intermediate. Based on binocular analyses of drill cuttings, the detailed descriptions of the lithological units and the stratigraphy of wells CL4-A, CL5, CL6 and CL7 is presented, respectively, in Appendices I and II. In summary, the different formations can be divided into three main units:

- *Pyroclastic rock units*. These incorporate all the glassy components (mostly ash and pumice) including tuffs, lithic tuffs with variable amounts of lava fragments, pumice and scoria, crystal rich tuffs and pumice deposits and they correspond to the predominant lithology in the uppermost part of the wells.
- *Crystalline trachyte lavas*. A shallow and relatively thick (up to 100-150 m thick) sequence of trachyte lavas is found near surface in five of the eight wells and it has very high secondary permeability. Below 200 m, at least three sequences of trachyte lavas can be identified and these are frequently found interspersed with the pyroclastic rock units. In general, the trachytes are massive, fine-grained with sugary appearance, commonly porphyritic with sparse sanidine phenocrysts.
- *Crystalline basalt lavas*. The darker lavas are more commonly found below sea level and form the predominant lithology in the reservoir interval. In general, the basalt flows are massive, fine-grained, with textures that vary from aphanitic to porphyritic with olivine and sparse pyroxene phenocrysts.

4.1 Correlation between the wells

4.1.1 Lithostratigraphic correlation

In the present study, drill cuttings from wells CL4-A, CL5, CL6, and CL7 were analysed jointly with previously acquired data on the lithology of the other wells in Cachaços-Lombadas area. In summary, the lithostratigraphy of the area can be described as follows:

- At shallow levels from the surface to about 250-300 m m.s.l., five wells intersect a thick sequence of trachyte lava. This is the case in CL1, CL2, CL3, CL4 and CL4-A. The sequence of trachyte lavas is absent in the wells CL5, CL6 and CL7, possibly because they thin out or are eroded away at these locations (Figure 11). It is important to note that this shallow sequence of trachyte lava is very permeable and caused severe losses of circulation fluid during drilling.
- A thick sequence of pyroclastic rocks is the predominant lithological unit from the surface to about -100 m m.s.l. At CL5, CL6, and CL7 it reaches about 600 m thickness, but is thinner in CL4-A where it is 300-400 m thick. This sequence of pyroclastic rocks underlies the sequence of trachyte lavas described above when the lavas are present. When the shallow trachyte lavas are not present, the pyroclastic rocks outcrop at the surface.
- The sequence of pyroclastic rocks, chiefly of trachytic character, is locally interrupted by lava flows of variable thickness which constitute a minor fraction of the total rock volume. These lava flows are mostly of trachyte composition, even though basalt and possibly intermediate types are present, too. Here, four sequences of lava give a good correlation between the wells in the area, namely two sequences of trachyte lava and two sequences of basalt lavas which are described below:
- The second sequence of trachyte lavas is found in about 240-160 m m.s.l., giving a good correlation between the wells CL6, CL5, and CL4-A. However, it is important to note that this intermediate-depth trachyte is thinner in CL7 than in CL5 and CL6 and the fact that this sequence of trachyte lava seems to thin out towards northwest could help explaining its absence in CL4-A. Additionally, the different depths of penetration into wells CL5 and CL6 indicates that this lavas dip north-westwards, which is consistent with the structure of the Fogo volcano;
- A third trachyte lava sequence is found at about 50-90 m m.s.l. It is thinner than the one described above but is present in all wells with the exception of CL5 where it possibly thins out;
- The first sequence of basalt lavas is found at about 100-200 m m.s.l. in wells CL4-A and CL7 but it only has a significant expression in well CL4-A where it is 90 m thick, whereas in CL7 this lava flow is very thin (4 m).
- A second sequence of basalt lavas is found at -30 to -60 m m.s.l. and there is a good correlation between wells CL5 and CL4-A. The second sequence of basalt lavas is not found in CL7 and keeping in mind that CL7 was drilled directionally towards NW, whereas CL5 and CL4-A were both drilled directionally towards NE, this could be related to the fact that these basalt lavas thin out towards NW.
- The pyroclastic rock units show a progressive increase of hydrothermal alteration with depth, particularly to clay minerals. This is consistent with the reduced permeability that is observed in the middle and at the bottom of the pyroclastic rock sequence. Here, secondary clays form the caprock of the geothermal system, limiting vertical flow and isolating the geothermal reservoir from the shallower groundwater.
- Below sea level and underlying the pyroclastic rock sequence, the subsurface geology is dominated by basalt lavas down up to about -600 m m.s.l. This is more prominent in CL4-A. Elsewhere, the extent of this of the lava dominated interval is rather uncertain, particularly in the area of wells CL6, CL5, and CL7 where this interval was drilled without returns. Low penetration rates while drilling in CL5 are consistent with the possibility that lavas are the predominant lithology in this interval. However, for wells CL6 and CL7 the rates of penetration did not show a major variation and cannot be used as a guide for estimation of the lithology types.
- No intrusive or subvolcanic rocks were identified in this study (except as clasts within pyroclastic deposits with the most commonly found being syenite). However, such rocks may occur at greater depths;
- The geological record from wells CL4-A, CL5, CL6, and CL7 did not allow the identification of the transition from subaerial to submarine deposits as no pillow lavas or phreatic breccias were observed in any of these wells. This observation is consistent with the high subsidence rate that the Ribeira Grande graben has suffered, as described in section 3.1 above, and to the fact that Cachaços-Lombadas wells are often drilled without returns below 600 m m.s.l.

4.1.2 Correlation between permeability and lithology

Based on the drilling data, geological data and the temperature logs taken during heat recovery after completion of the wells, it was possible to identify the location of the permeable zones in CL4-A, CL5, CL6, and CL7. These are indicated in Figure 11 and in Appendix II. A summary of the distribution of permeability with depth is presented below.

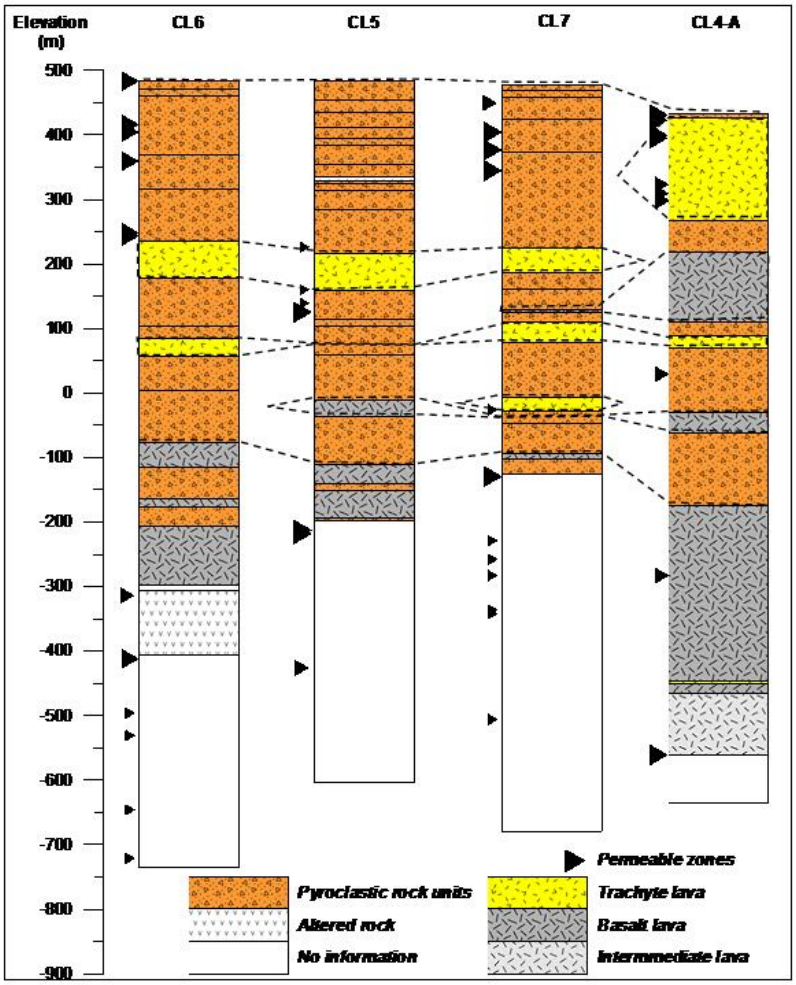

FIGURE 11: Schematic SE-NW lithology cross-section of Cachaços-Lombadas sector

The majority of the Cachaços-Lombadas wells, including CL4-A, intersect a shallow sequence of trachyte lava which is highly fractured and, therefore caused severe losses of circulation fluid during drilling. Wells CL5, CL6, and CL7 did not intersected this shallow sequence of trachyte lava but still significant permeable zones were found in these wells from about 500 to 350 m m.s.l., often related to zones of high porosity within the pyroclastic rock units or in the boundaries between units. Here, it is important to note that no significant permeable zones were reported in well CL5 at shallow depths because this well was drilled to 150 m using air-rated drilling, thus not allowing the identification of permeability with precision.

From 200 to -100 m m.s.l. permeability is very limited. Nevertheless, a few permeable zones were identified in CL5 and CL6 and these are mostly related to fracture zones within the trachyte lava flows or are located at their top and bottom boundaries.

Below -100 m m.s.l. the basaltic sequence predominates and marks the entry into reservoir conditions. Here, a zone of very high permeability is observed from -150 to -400 m, where frequently the fluid returns are lost during drilling of the wells. In most of the Cachaços-Lombadas wells, this is the zone were the most prolific feed zones are located. From there and down to about -700 m, the permeability is minor when compared to the zone above. The only exception to this was well CL4-A where a major permeable zone was found deeper at -561 m m.s.l.

4.1.3 Correlation between permeability and alteration minerals

Porosity and permeability are the primary factors that control movement and storage of fluids in the rock formations leading to the deposition of minerals, either in veinlets, veins or amygdales. In the Ribeira Grande geothermal field, some secondary minerals such as calcite, pyrite and silica phases (opal,

chalcedony and quartz) are commonly found in or adjacent to aquifers, occurring as products of the alteration of the host rocks during water-rock interaction or as precipitates, filling open-spaces such as fractures, fissures or vesicles. Therefore, the occurrence and abundance of these minerals can serve as indicators of the presence of permeability.

A summary of the main findings from the comparison between the locations of the permeable zones against the abundance of the alteration minerals in the Cachaços-Lombadas wells is presented below:

- In CL4-A, pyrite abundance has good correlation to the permeability found in the well as the depths of the pyrite peaks found at 620 and 900-910 m have a good match to losses of circulation fluid during drilling (Appendix II). On the other hand, the distribution of calcite and silica minerals did not allow any correlation with the permeable zones found in the well. Calcite and silica appear at around 200-250 m depth and their abundance peaks at 300-320 m. A second peak is observed at about 420 m and then they become fairly common to the bottom of the well. However, during drilling, no significant permeable zones were seen here. Furthermore, where permeability was identified it is difficult to relate it to any specific abundant zone of calcite or silica, mostly because below 420 m and down to the depth of the last sample recovery these minerals are found in relatively high abundance;
- In CL5, the major permeable zone encountered at 710-715 m is just preceded by a peak in the silica and pyrite veining (Appendix II). Other peaks in the abundance of silica and pyrite are seen at 460-500 m and 540-620 m but no permeability was observed here, suggesting that the majority of the open-spaces within the rock formation were sealed by the precipitation of the secondary minerals.
- In CL6, the permeable zones are accompanied by peaks in the abundance of secondary minerals. As shown in Appendix II, the permeable zone at 260 m depth matches a peak of pyrite and the feed zones at 800 and 900 m are accompanied by vein peaks of the calcite, pyrite and quartz.
- In CL7, pyrite was found and it was fairly abundant at about 120-160 m depth, quite shallow in comparison to the other Cachaços-Lombadas wells (Appendix II). This pyrite peak corresponds to a zone of high permeability found in the well. Other pyrite peaks were found at 200-240 m, 300-340 m and 460-500 m and these were accompanied by calcite and silica peaks. However, no permeable zones were identified in these intervals, suggesting that permeability was present there at some point in the past but it is now sealed.

4.1.4 Relation between permeability and tectonic structures

The geological structure of the Ribeira Grande geothermal field is influenced by tectonic and volcanic stresses which combine to form a local pattern of faulting and fracturing. Regional tectonic stresses are associated with the triple junction of the Azores, more specifically with the Terceira Rift, whereas the local stresses are related to the Fogo volcano and its caldera faulting. The identification of tectonic structures applying common surface mapping techniques is rather difficult for the Fogo volcano because they are obscured by dense vegetation and are covered by thick pyroclastic rock units. Therefore, most of the structures mapped in the previous studies were inferred by topographic trends and lineaments from the volcanic structures. As described above in Section 3.1 and as shown in Figure 4, these lineaments indicate that over the entire Ribeira Grande geothermal field there is a predominant north-westward structural trend, associated with the graben of Ribeira Grande.

The lithological data from the wells, described in Section 4.1.1, does not allow for direct identification of any faults that might be present in the Cachaços-Lombadas area. The lava flows can be used locally as marker horizons, particularly the sequences of trachyte lavas that are intersected by the wells from 500 to about -100 m depth, but where they are present, the correlation between these marker horizons often indicates that the lava flows tend to dip towards north or northwest which is coincident with the structure of the Fogo volcano. Additionally, where there are significant vertical displacements between the depths of penetration of marker horizons in the different wells, the data is not decisive enough to be

able to conclude with confidence about whether there is a tectonic structure present or if it was the case of the lava having been eroded or thinned out.

Keeping this in mind, other features were tested to verify if there was any positive relation between the permeability and the tectonic structures inferred in the area of Cachaços-Lombadas, such as plotting the location of the major permeable zones encountered in each well against the tectonic lineaments inferred in the area.

As referred to above, the entry into reservoir conditions is marked by the transition into the basalt lava sequence. Here, most of the permeability seems to occur between -150 and -400 m m.s.l. It is noticeable that the location of the permeable zones identified in CL4-A, CL5, and CL6 coincides roughly with the alignment of an inferred fault, oriented NNW-SSE, as shown in Figure 12. The same is observed with CL7 which was drilled towards WNW, crossing a NNW trending fault at about -300 m m.s.l. The location of the major permeable zone at CL7 is at -130 m m.s.l., and therefore higher than the expected

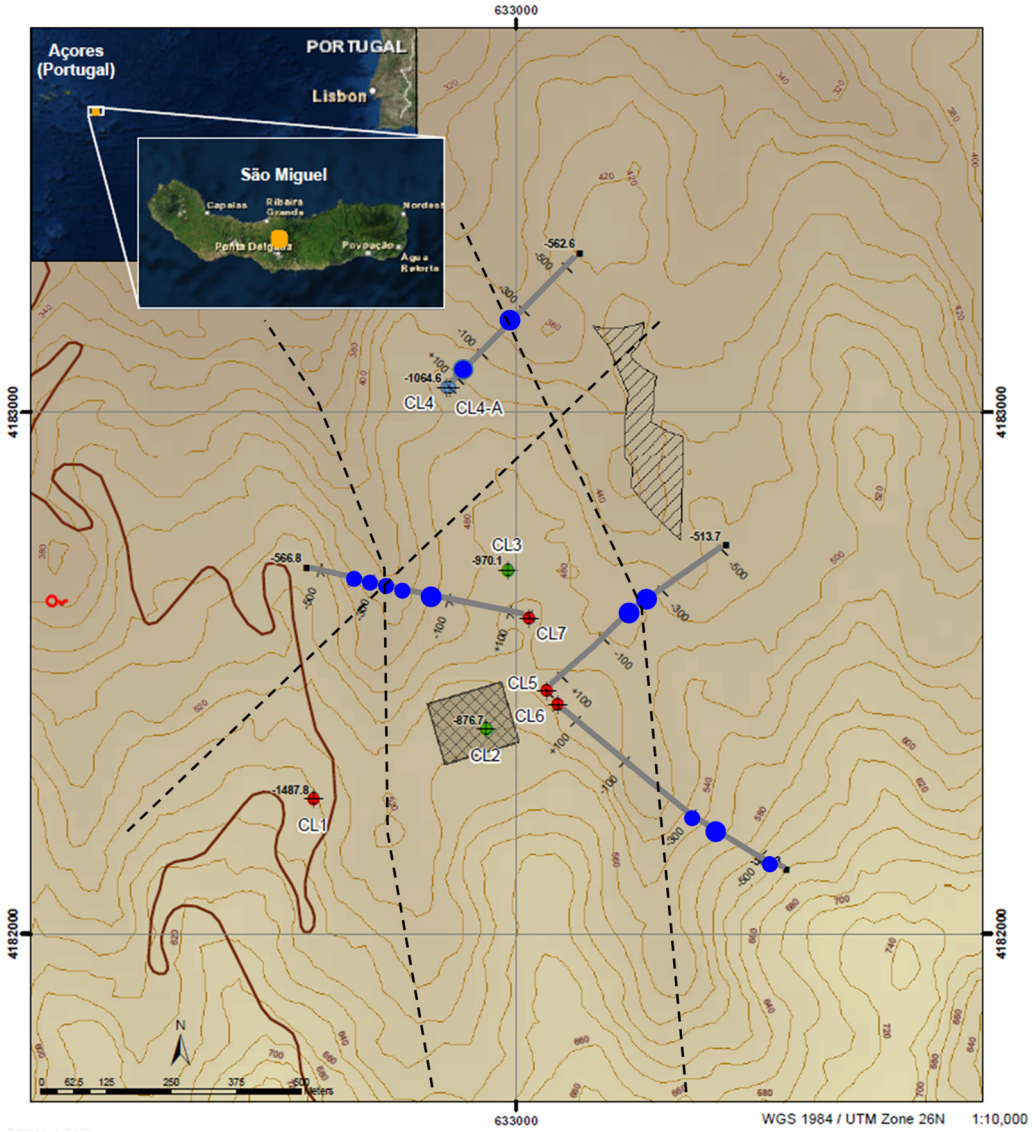

FIGURE 12: Map of Cachaços-Lombadas sector, Ribeira Grande Geothermal Field (adapted from GeothermEx, 2014). The map shows the location and well-path of the geothermal wells, including the location and size of the permeable zones (marked in blue circles) and the Ribeira Grande power plant, marked as a grey square. The dashed lines correspond to the inferred faults by Carvalho et al., 2006

intersection with the fault zone. However, it is noticeable that several minor feed zones were identified in CL7 at about -280 to -340 m m.s.l. and these are possibly related to the fault zone.

Either way, if the inferred faults indeed extend from the surface to deeper levels (this is uncertain), at least down to -400 m m.s.l., the deviated wells must have intersected the fracture zone related to these faults at some point. In this respect, it is worth noticing that the most prolific wells in the area are, by this order, CL7 with a wellbore trending to WNW and CL5 with a wellbore trending to NE. Additionally, well testing at CL4-A also revealed that this well could be an adequate producer. Therefore, this suggests that deviated wells that have intersected the NNW structural trend tend to be more productive.

5. FORMATION TEMPERATURE

The formation temperatures, based on stabilized profiles taken prior to injection or flowing, were gathered and plotted as a function of the elevation for all the Cachaços-Lombadas wells. In general, the temperature profiles show a similar pattern. As shown in Figure 13, the temperature gradient is relatively high to about -100 m m.s.l. and from there on the profiles are relatively isothermal, reaching maximum temperatures of about 230-240°C. A slight temperature reversal is observed in most of the wells (CL1, CL2, CL3, CL4, CL4-A). This strongly indicates that the main upflow zone of the geothermal system is not located in the central parts of the project development, in the area of Cachaços-Lombadas. Additionally, as shown in the Appendix III, most of the wells have a two-phase or steam zone on the top of the reservoir, with the only exception being CL6, located further to the south which only exhibits the liquid phase.

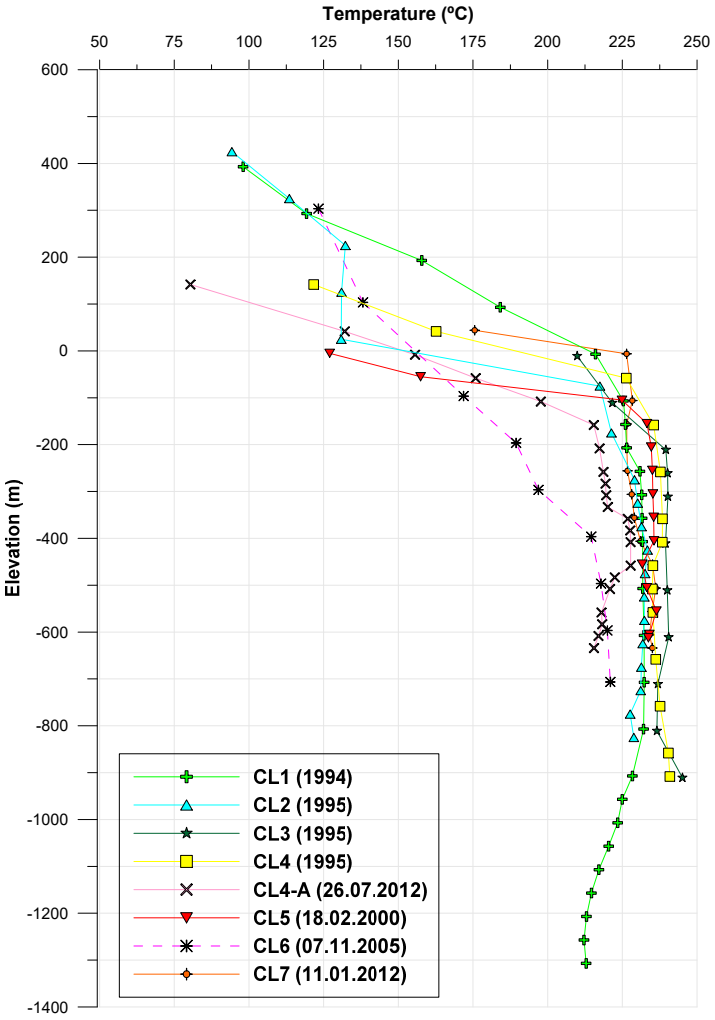

FIGURE 13: Formation temperature profiles of the Cachaços-Lombadas wells

The distribution of the formation temperature at four different elevations (0 m, -300 m, -600 m and -900 m m.s.l.) was inferred from temperature profiles. Figure 14 shows the temperatures contour maps drawn at 0, -300, -600 and -900 m m.s.l. The main findings from the analysis of the temperature distribution are in line with the conclusions from Ponte et al. (2010) and they can be summarized as follows:

- The temperature distribution at 0 m, still above the reservoir, shows that higher temperatures are found in the central and southwestern part of the Cachaços-Lombadas project development, with temperatures higher than 210°C being found in the wells CL7, CL2, and CL1;

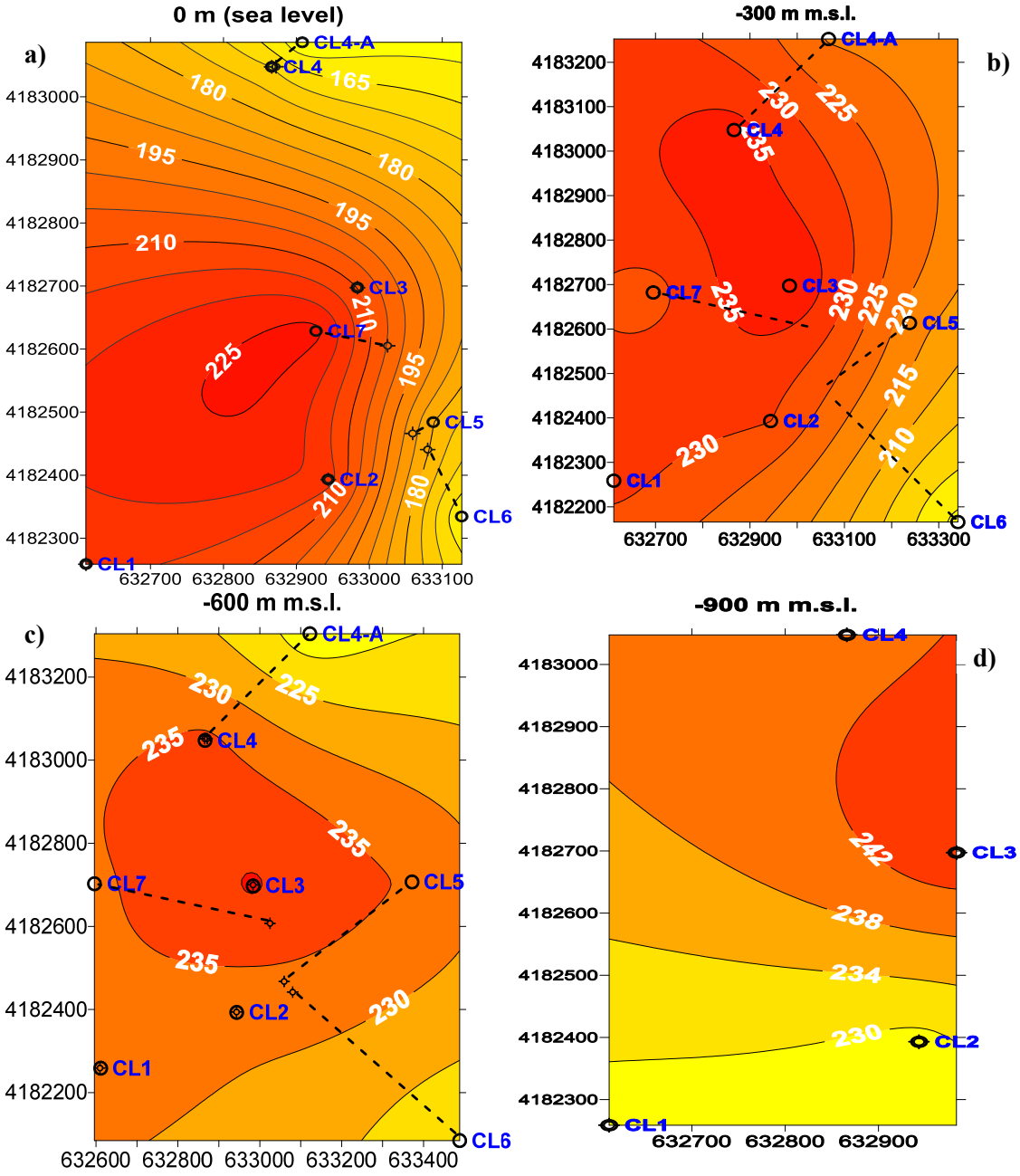

FIGURE 14: Temperature distribution in the area of Cachaços-Lombadas at 0 m (a), -300 m m.s.l. (b), -600 m m.s.l. (c) and -900 m m.s.l. (d). The dashed lines show the well-path of the deviated wells

- At -300 and -600 m m.s.l. the temperature maps are near isothermal with the temperatures ranging from 230-235°C in most of the area and with the highest temperatures being measured at CL3 (240°C). This depth interval corresponds to the core of the geothermal reservoir.
- With increasing depth, the temperatures continue to increase towards north and northeast whereas in the southern part of the area the temperatures tend to decrease. In fact, reservoir temperatures decrease towards CL6 which is somewhat cooler than the other wells, with maximum reservoir temperature that does not exceed 222°C.
- The data are insufficient to precisely locate the upflow zone because the majority of the wells were drilled only to about -600 to -700 m m.s.l. Nevertheless, as it deepens, the temperature distribution suggests that the main upflow zone may occur at some undetermined location to the east or northeast of wells CL3 and CL7.

6. HYDROTHERMAL ALTERATION

Reaction of geothermal fluids with the host rocks in the Cachaços-Lombadas sector has resulted in a progressive hydrothermal alteration sequence with increasing depth. However, it is important to note that the type and intensity of the alteration in the area also varies depending on the rock type present, showing locally strong or weakly altered zones. Commonly, the pyroclastics are less dense and tend to be more easily altered, whereas the dense lava flows tend to be fresher looking, although strong veining zones can occur within the lavas.

The alteration minerals assemblages found in Cachaços-Lombadas are typical for the wells in the Ribeira Grande field and are similar to what is found in other geothermal fields around the world in similar environments. Secondary minerals that were identified by binocular analysis included clay minerals, iron oxides (mostly hematite), silica minerals (such as opal, chalcedony and quartz), calcite, pyrite and zeolites.

Detailed petrographic analysis was limited to samples from well CL6. In this respect, the present study uses the findings from the investigation performed by the Foundation of the Science Faculty at the University of Lisbon which was contracted in 2005 by EDA RENOVÁVEIS, at that time denominated as SOGEO, to analyse thin sections from twenty drill cutting samples. The results from 2005 confirmed the occurrence of the minerals described above and allowed to identify others that are typical from high enthalpy hydrothermal systems such as secondary albite, epidote, prehnite and different zeolite types, including low and high temperature ones.

Additionally, X-ray diffractometric (XRD) analysis performed on selected samples from all the wells allowed the identification of the type of secondary clay minerals present. A total of twenty-seven samples were analysed using Bruker AXS D8 Focus Diffractometer at ISOR (Icelandic GeoSurvey) with the objective of determining the alteration zones within the Cachaços-Lombadas area. The present study also incorporates results from XRD investigations executed in 2005 by the Foundation of the Science Faculty at the University of Lisbon and in these are included seven samples from CL6 and three samples from CL5. The complete results from the XRD analysis are shown in the Appendix IV.

The abundance and the first appearance of the alteration minerals as function of depth is shown in the geological logs in Appendix II. Based on the occurrence, distribution and relative abundance of the secondary minerals it was possible to delineate the alteration zone diagrams from wells CL4-A, CL5, CL6, and CL7, described below in sections 6.1 to 6.4. The diagrams reflect the range of hydrothermal minerals that were found in each well and in general these vary from low temperature zeolites to high temperature minerals like chlorite, prehnite, epidote, and albite.

6.1 CL4-A

In CL4-A, based on the results from the binocular analysis to the drill cuttings and the XRD analysis to 9 samples, three alteration zones were inferred. As shown in Figure 15, these are unaltered to weakly altered zone, smectite zone and chlorite zone, which are summarized below:

0-185 m: *Unaltered to weakly altered zone*. This zone corresponds mainly to the thick sequence of trachyte lavas intersected in the well from 24 to 182 m. These lavas are relatively fresh and unaltered, exhibiting only weak clay alteration and locally oxide staining in the sanidine phenocrysts.

185-512 m: *Smectite zone*. The top of the zone is marked by the peaks in the clay and iron oxides alteration, identified at the bottom of the trachyte lava. In this zone, smectite is the dominant clay type, locally found associated with traces of illite. Calcite first appears at 196 m, becoming common thereafter. In this respect, two peaks in the abundance of calcite were identified, a first one at 320-340 m and a second one at 480-500 m. Secondary silica first appears at 230 m with opal and chalcedony

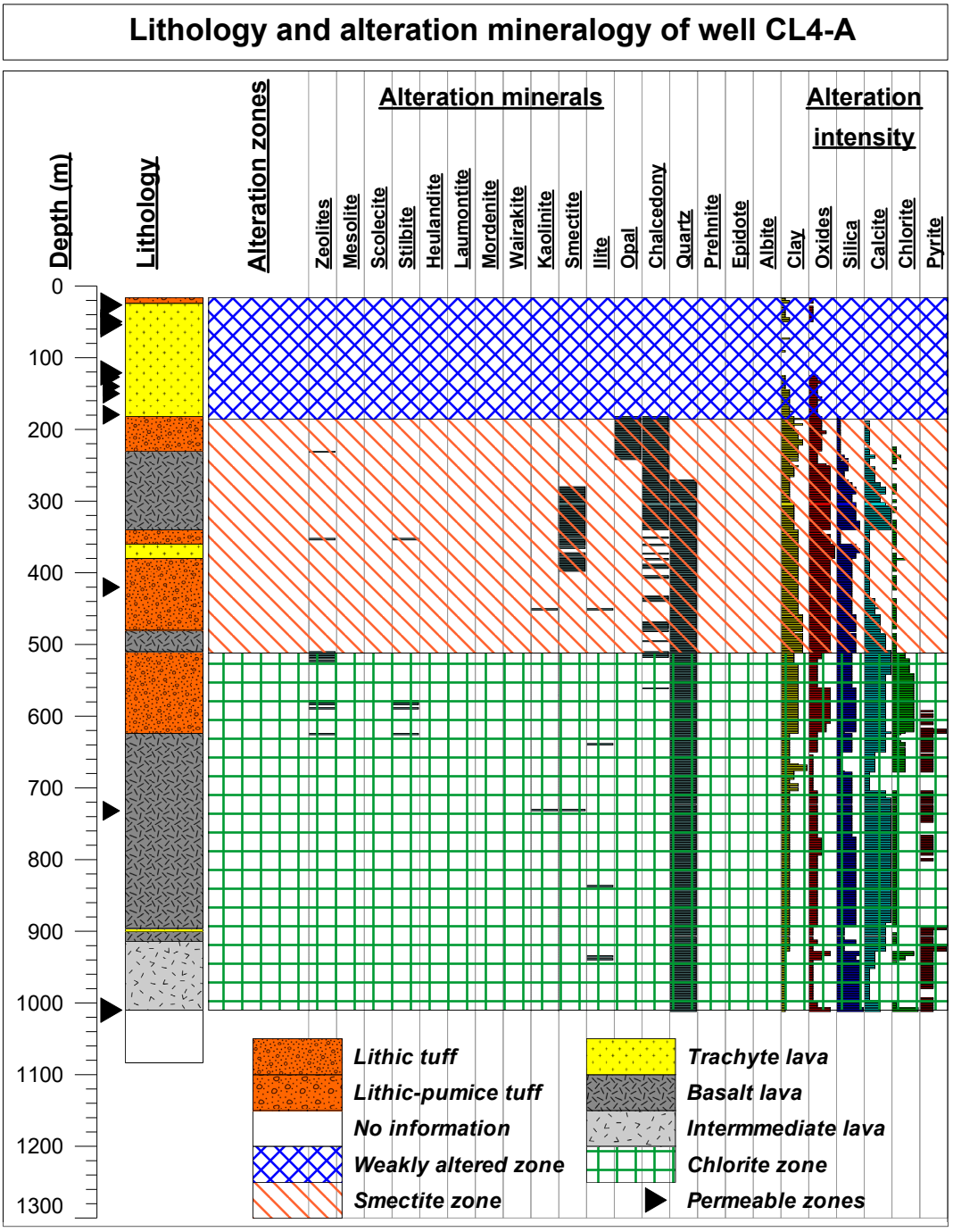

FIGURE 15: Alteration zones interpreted in CL4-A

amygdales in vesicular basalt lava. First appearance of microcrystalline quartz is at 270 m in veins and veinlets, where it is associated with calcite and possibly very fine chlorite. From there, quartz becomes common and persists down to the bottom of the zone. Chalcedony and possibly zeolite amygdales are also found intermittently at the bottom of the zone, but the positive identification of the latter could only be possible by a detailed petrographic analysis.

512-1010 m: *Chlorite zone*. The upper part of this zone is marked by a peak of open-space fillings found at 510-520 m with the mineral assemblage mainly composed of different associations of chlorite, quartz and calcite. Pyrite appears at 564 m and this is relatively deep compared to the other existing wells. From there, pyrite persists to the depth of the last sample recovery but it is seen intermittently and in minor quantities. In this zone, the ash matrix of the pyroclastics is often altered to clay with the chlorite and minor traces of illite forming the main clay types. The ash matrix is locally indurated by

silicification, likely as result of deposition of chalcedony or microcrystalline quartz. With depth, veins, veinlets and amygdales of the assemblage calcite + quartz + chlorite continue to be generally abundant, mainly occurring within the lavas intersected in this interval. It is important to note that chlorite abundance decreases with depth but it peaks again just before a major permeable zone was found at 1010 m.

6.2 CL5

In CL5 (Figure 16), based on the data from the binocular analysis complemented by XRD difractometry analysis to 8 samples and petrographic analysis to three samples (620, 670 and 703 m), three alteration

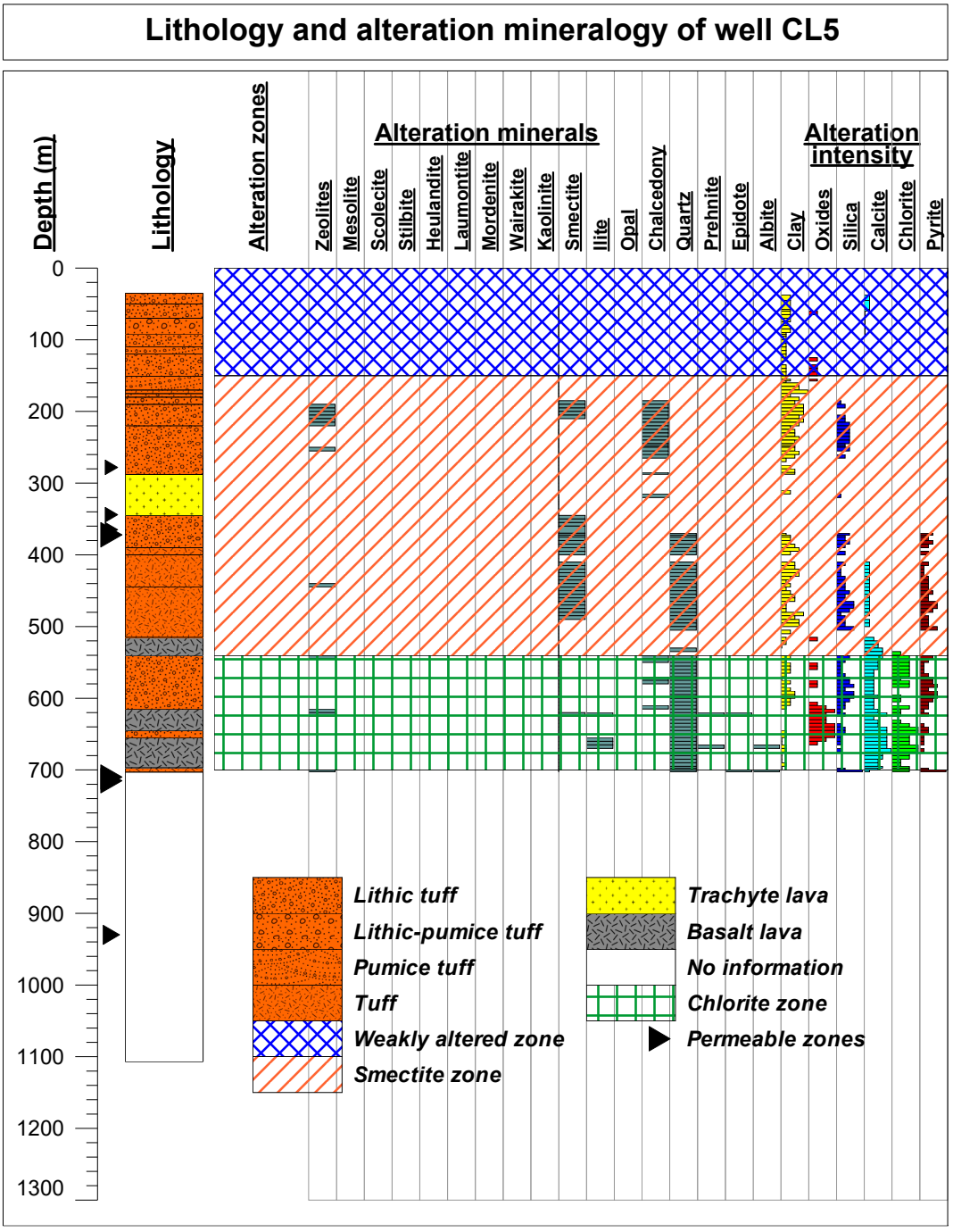

FIGURE 16: Alteration zones interpreted in CL5

zones were interpreted. These are weakly altered zone, smectite zone and chlorite zone, and they are summarized below:

0-345 m: *Weakly altered to unaltered zone*. The alteration within the first 150 m consists mainly of the conversion of the glassy components (ash and pumice) of the pyroclastic rocks to clay minerals. Iron oxides are locally abundant. Small amounts of calcite and opal appear at 50 m and are present to the bottom of the zone in small quantities.

150-540 m: *Smectite zone*. A trend induration of the matrix of the pyroclastic units begins at 150-200 m and it becomes more intense at about 250 m, as a result of the deposition of silica (probably opal). Silica persists with depth but it stops in the trachyte lava intersected at 288-345 m which is relatively fresh and unaltered. Underlying the trachyte lava, the pyroclastic rocks are variable altered. This zone is characterized by the abundance of smectite clay and silica minerals which are more crystalline when compared to the upper zone, suggesting that chalcedony and microcrystalline quartz are now the dominant silica mineral phases, replacing opal which dominated above. At this respect, the first appearance of quartz is logged at 370 m. Veining appears to be absent, with the only exception being a scoria unit at 445-555 m, exhibiting silica veins.

540-700 m: *Chlorite zone*. Alteration peaks at 540 m with the chlorite and calcite becoming the most abundant secondary minerals, occurring as replacements of most of the rock components but also in veins and other open-space fillings. Quartz and pyrite complete the secondary mineral assemblage. Hematite is also locally important, particularly in the basalt lava found at 615-645 m, being found in many places where it has been clearly recrystallized and sometimes mobilized as a vein mineral. Hematite and pyrite often coexist, with pyrite replacing hematite in some places. In this zone, veining appears to increase in intensity with depth, reflecting increasingly intense hydrothermal activity. The vein minerals include quartz, calcite, chlorite, pyrite and hematite, found in various different assemblages. The detailed petrographic analyses from 2005 revealed that prehnite is found locally at 620 m, being associated with calcite. The same is with epidote which first appears at 620 m. The bottom of the zone is marked by the appearance of secondary albite which is often found with epidote + calcite + quartz + chlorite.

6.3 CL6

In CL6, three alteration zones were interpreted as shown in Figure 17. These are a weakly altered zone, a smectite zone and a chlorite zone. They are summarized below:

0-196 m: *Weakly altered to unaltered zone*. At shallower depths and down to 196 m the alteration consists predominantly of the conversion of ash and pumice into clay minerals. Iron oxides are locally present in minor amounts but most of these are likely a product of superficial weathering prior to burial. Opal is locally present.

196-590 m: *Smectite zone*. Below 196 m smectite is the predominant clay mineral, locally associated with illite aggregates. The zeolites found in the top of this zone are low temperature types such as mesolite, scolecite, stilbite and heulandite/laumontite, commonly appearing in amygdales. Other open space fillings found at the top of this zone are mostly chalcedony and microcrystalline quartz, but calcite and very fine chlorite are also present with the latter being identified in the petrography analysis. Overall the alteration is low-grade but it peaks near 270 m. There is a zone of stronger mineralization within the trachyte lava intersected at this depth with clusters of pyrite, calcite and microcrystalline quartz. The same formation was intersected by the nearest well CL5 but this mineralized zone was not found in CL5, suggesting that the mineralization may be associated with a specific fracture zone passing through the lava in the area of CL6. Below 350 m the microcrystalline quartz becomes more abundant comparatively with chalcedony and the more abundant zeolites are heulandite and laumontite. Below 500 m veining becomes common, with mineral assemblages of quartz, calcite, fine chlorite along with silicification of the rock, namely the interstitial spaces of the rock fragments.

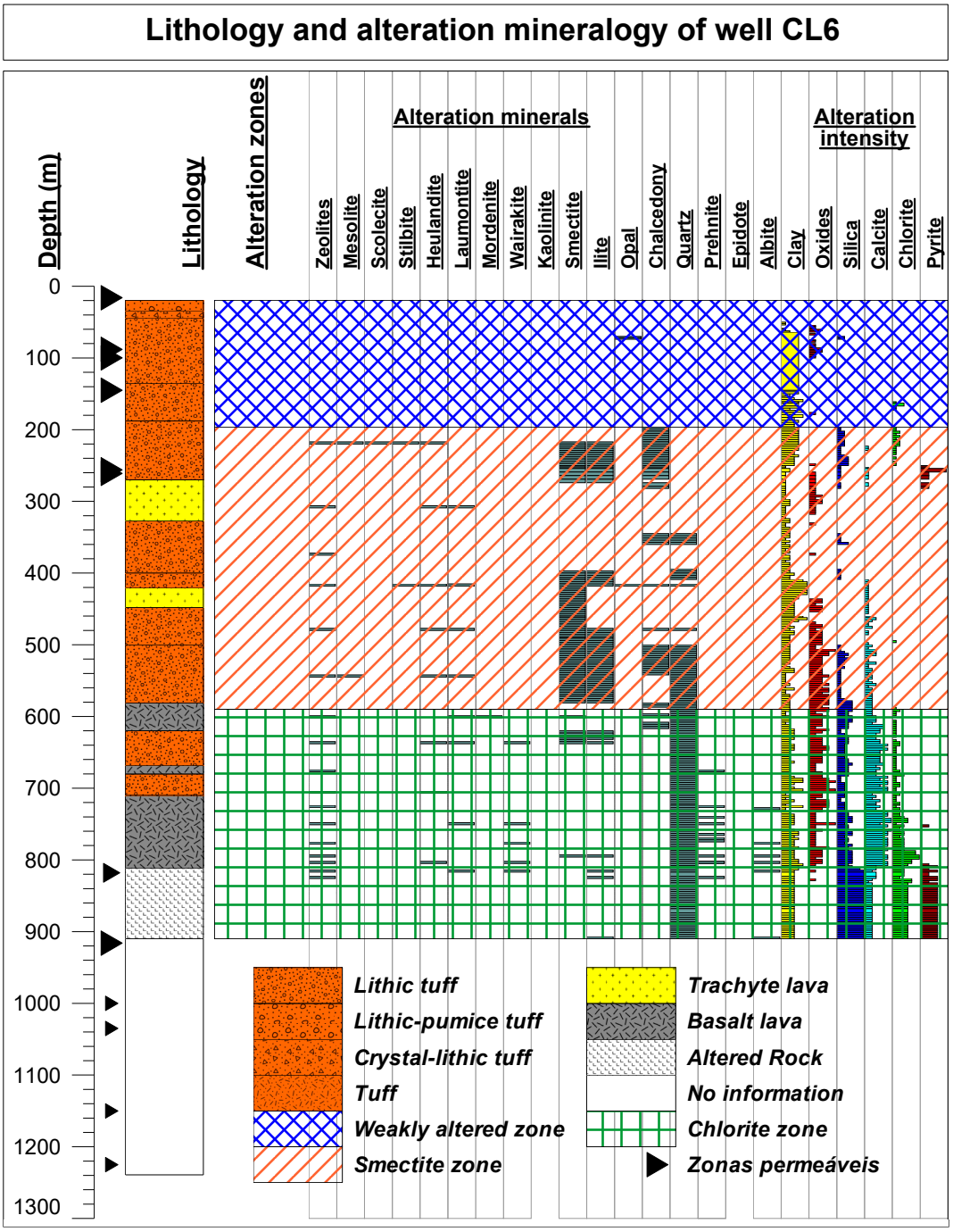

FIGURE 17: Alteration zones interpreted in CL6

590-775 m: *Chlorite zone*. Chlorite is rare above 590 m but it becomes abundant thereafter, marking the top of this zone. The alteration assemblage of quartz + calcite + chlorite is common throughout this zone, appearing as open-space fillings, suggesting that the basalt lava and pyroclastics found at these depths are characterized by a large net of veins and veinlets filled with secondary minerals. Here, it is important to note that the abundance of calcite and chlorite increases with depth, whereas the abundance of the other secondary minerals appear to vary within more a less constant ranges. At the top of the zone the predominant zeolite type is laumontite, but heulandite and mordenite are also found in minor amounts. Wairakite appears at 635 m, suggesting alteration temperatures of up to 200°C. Detailed petrography from 2005 identified also the presence of high temperature minerals. Epidote was identified at 674 m, becoming common thereafter, associated with quartz, calcite, chlorite and prehnite. Secondary albite was identified at 775 m, locally associated with epidote. The mineral assemblages found at the

bottom of the zone consist mainly of epidote + albite + chlorite + prehnite + calcite + quartz, indicating alteration temperatures in the range of 230-250°C.

6.4 CL7

In general, the alteration found in CL7 (Figure 18) is similar to the other wells in Cachaços-Lombadas area but the occurrence of a strong alteration zone at about 125-200 m is unusual. This zone is characterized by the abundance of white to light grey clay (mostly smectite and kaolinite) and disseminated pyrite (present in clusters and as well-developed cubic crystals with size up to 2 mm). This type of mineralization is typical of acidic environments, so this zone could be the product of a now

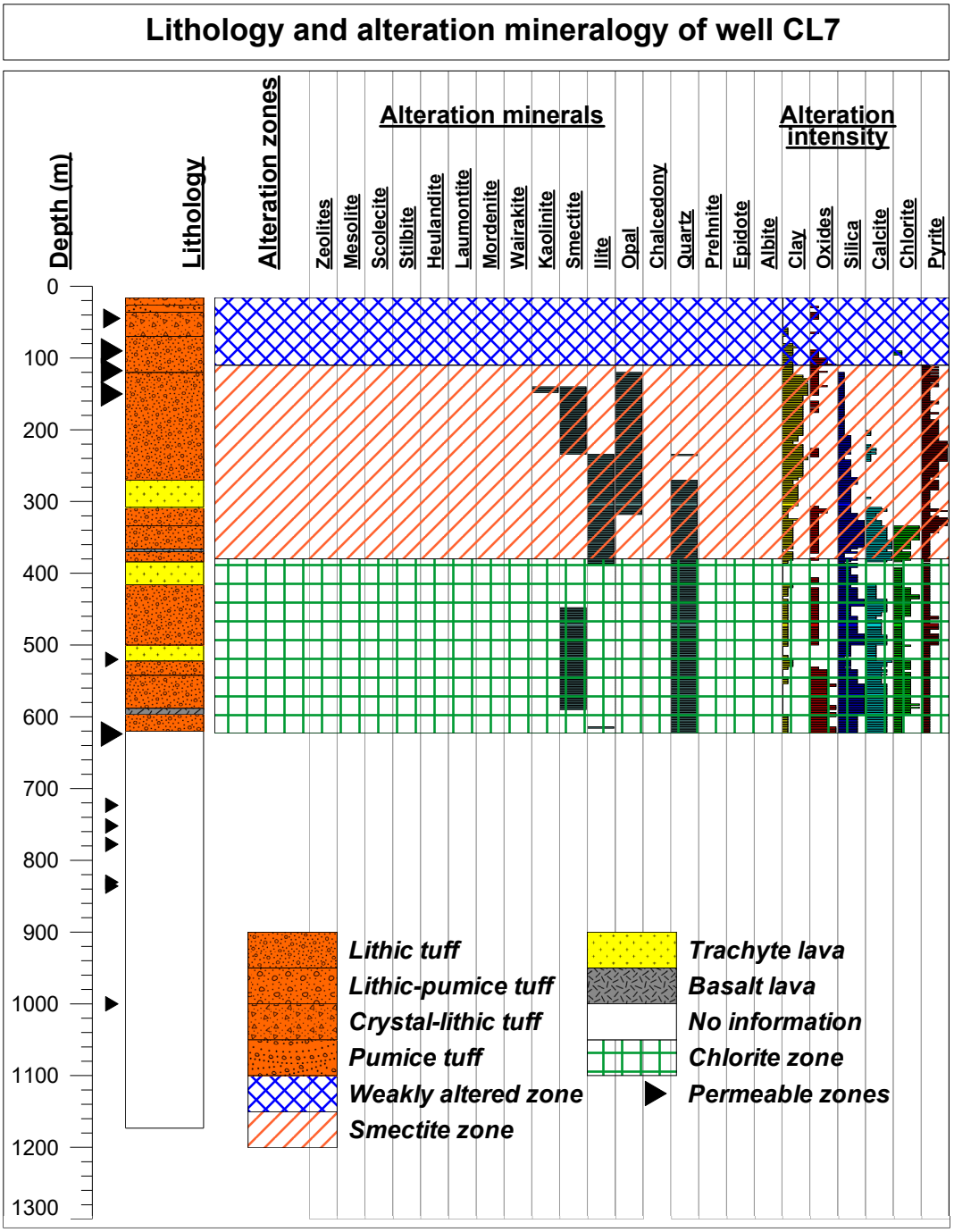

FIGURE 18: Alteration zones interpreted in CL7

extinct steam heated aquifer. No similar style of alteration was found in similar intervals in the wells CL4-A, CL5, or CL6.

0-110 m: *Unaltered to weakly altered zone*. The alteration consists mainly of the conversion of the glassy components (ash and pumice) of the pyroclastic rocks to clay minerals. Iron oxides are locally abundant but these may be a product of superficial weathering prior to burial.

110-380 m: *Smectite zone*. From 110 m the ash matrix of the pyroclastic rocks becomes indurated as a result of deposition of silica (likely as opal). Pyrite appears at 110 m and it is continuously encountered throughout the remainder of the well. The appearances of pyrite and quartz (found at 234 m) are relatively shallow compared to the neighbouring wells. In the bottom part of the trachyte lava occurring at 270-300 m, the formation is strongly altered to clay (mainly illite) and is overall mineralized with clusters of pyrite, calcite and probably microcrystalline quartz. From 360-384 m some well-developed hexagonal quartz crystals up to 1 cm in size were found. This is rather unusual as crystals of this size were not found in any of the other Cachaços-Lombadas wells.

380-622 m: *Chlorite zone*. The top of this zone is clearly marked by a peak in the chlorite alteration with the mineral assemblage being composed by clays (chlorite is dominant while illite appears in small trace amounts), silica, chlorite, pyrite, calcite and iron oxides. In the top part of this zone, a second sequence of trachyte lavas are found at 384-416 m and alteration appears to be more intense near the top, mostly corresponding to veining. Below 422 m, the pyroclastic units are moderately altered and contain abundant pyrite, including some well-formed cubic crystals. With depth, the formations continue to show increasing hydrothermal alteration and it becomes difficult to distinguish the original rock type. Overall, the rock formations are moderately altered to clay. Chlorite is the dominant clay type but smectite is consistently present as well, whereas illite was found only in minor traces below 614 m. Below 520 m there is a notable peak in open-space fillings abundance with different mineral assemblages of chlorite + silica + hematite + calcite + pyrite.

7. ALTERATION ZONING

The present study reveals two zones of hydrothermal alteration beneath a shallow zone of relatively unaltered rocks. A summary of these zones is presented below:

- *Weakly to unaltered zone.* Extending from the surface to about 150-200 m depth, the formations in this zone are relatively fresh and unaltered, with little or no signature of alteration or development of any secondary minerals. Pyroclastic rocks are the predominant lithological unit and the alteration consists of the conversion of ash and pumice into weak clay and locally minor oxide staining of the feldspars in the lithic fragments;
- *Smectite zone (<200-220°C)*. The hydrothermal alteration generally starts at 150-200 m and this marks the beginning of the smectite zone which extends down to 510-590 m. In this zone, smectite is the predominant clay type, mostly resultant from the alteration of the ash matrix of the pyroclastic rock units. It is important to note that the lava flows found in this zone are denser than the pyroclastics so the clay alteration is generally less intense in these, even though veining is often seen in the lavas. The smectite zone is also characterized by the increasing silicification of the rock formations with depth which is accompanied by the progressive deposition of the silica mineral phases, namely opal, followed by chalcedony and quartz. Overall, the alteration in this zone is generally low grade and the mineral assemblage at the bottom of this zone indicates alteration temperatures that do not exceed 200-220°C.
- *Chlorite zone* (>230°C). The transition to the chlorite zone is marked by the peak in the chlorite abundance, commonly found in mineral assemblages along with calcite and quartz which are found in open-space fillings. This indicates that the formations in this depth range (predominantly basalt lavas) are characterized by dense net of veins and veinlets filled with secondary minerals. It is important to note that, at the top of this zone, chlorite and smectite

were seen to coexist in some places (see Appendix V), indicating that the upper part of the chlorite zone might correspond to a transition zone. Furthermore, with increasing depth, smectite disappears and chlorite becomes the dominant clay mineral. The Chlorite zone is also marked by the appearance of high temperature minerals such as prehnite, epidote and albite which were identified in CL5 and CL6 below 650 m. This corresponds to the reservoir interval where the mineral assemblage is frequently completed with chlorite and indicates alteration temperatures above 240-250°C.

The alteration zones from the four wells were plotted together with the lithology and temperature isograds from key index minerals in order to understand the general distribution of the alteration temperatures in the Cachaços-Lombadas area. As shown in Figure 19, the alteration zones have a consistent distribution with depth and show a relatively good correlation from well to well. The zoning pattern indicates that smectite and chlorite zones are shallower in CL7 when compared to the other wells. This becomes more evident for the chlorite zone which was found at 100 m m.s.l in CL7, whereas in CL4-A, CL5 and CL6 it was found at -80 to -100 m m.s.l. Therefore, the zoning pattern indicates that higher alteration temperatures were found shallower at the location of CL7, suggesting that CL7 is probably closer to the heat source than the other wells. It is important to note that this evidence is consistent with the formation temperature distribution within the area as discussed in section 5.

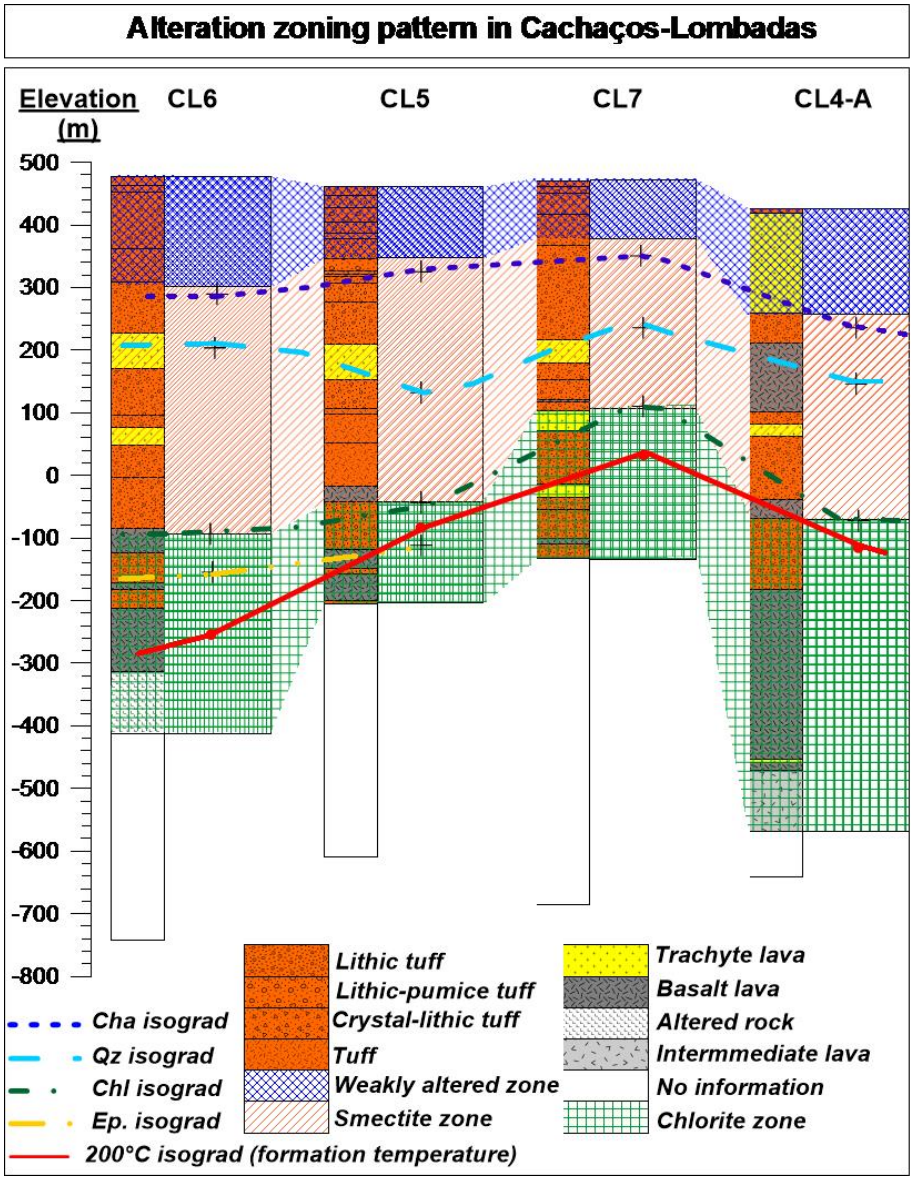

FIGURE 19: Alteration zoning diagram of Cachaços-Lombadas area

Additionally, by comparing the alteration temperature isograds from key index minerals against the isograd of 200°C (formation temperature) it is possible to observed that the chlorite isograd, which indicates past temperatures of at least 230°C, is found above the 200°C isograd in all the wells. This evidence indicates that higher temperatures were present shallower at some point in the past.

8. STUDY OF FLUID INCLUSIONS

The study of fluid inclusions can be used for geothermometry and it is most commonly applied to study the evolution of geothermal systems as a complement to the information provided by the alteration mineralogy. Additionally, fluid inclusions are an important tool to determine the chemical compositions of the geothermal fluid in the past.

8.1 Heating studies

In the attempt to determine the thermal history of the geothermal system in the area of Cachaços-Lombadas a total of nine samples from CL4-A, CL5, and CL7 were used in heating studies for determination of the homogenization temperatures (Ht). This investigation complemented by the identification of the first appearance and abundance of key index secondary minerals (as described in sections 6 and 7 above) provided valuable data on the historical deep temperatures and contributed to the determination of the alteration temperature curves. During the present study, it was noticeable that quartz samples from the Cachaços-Lombadas wells contain different types and numerous generations of fluid and gas inclusions and special care must be taken in the assignment of a given inclusion or group of inclusion to a particular paragenetic stage.

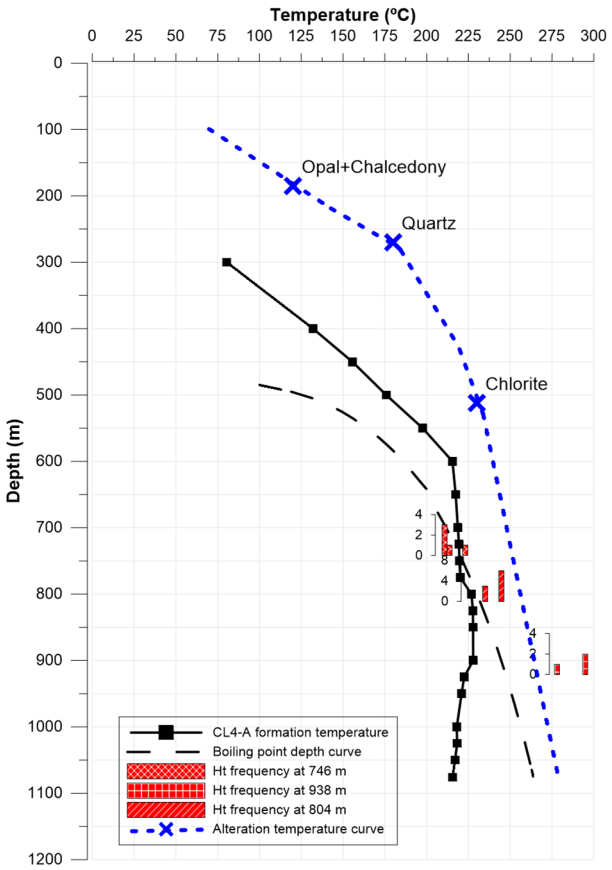

FIGURE 20: Homogenization temperature range from fluid inclusions of CL4-A along with the formation and alteration temperature curves

8.1.1 Samples from CL4-A

CL4-A is the well that has the deepest geological record available in the area of Cachaços-Lombadas because total losses of circulation were only encountered at 1010 m what is significantly deeper in comparison to the other Cachaços-Lombadas wells. This allowed for sampling of an important sequence of the reservoir interval. During the binocular analysis of the rock samples, quartz crystals from veins found in samples from 746, 804, and 938 m were selected for the study of fluid inclusions. This selection was based on the crystal abundance at those intervals (samples 804 and 938 m) as well as the proximity or direct occurrence at inferred permeable zones of the well (sample from 746 m).

As shown in Figure 20, the results show increasing Ht with depth with temperatures ranging between 211-223°C at 746 m to 278-295°C at 938 m. Noticeably, homogenization temperatures at 746 m have a good fit with the formation temperature but with increasing depth there is a growing shift between the formation and the homogenization temperatures, suggesting that

the geothermal system at the location of CL4-A was at some point in the past significantly hotter that it is today reaching temperatures close to 300°C.

8.1.2 Samples from CL5

The entry into reservoir conditions is well marked at CL5 by the abundance of veining in the interval from about 540 to 660 m depth. Thus, quartz crystals from samples at 550, 610 and 650 m were selected for the study of fluid inclusions (Figures 21 and 22).

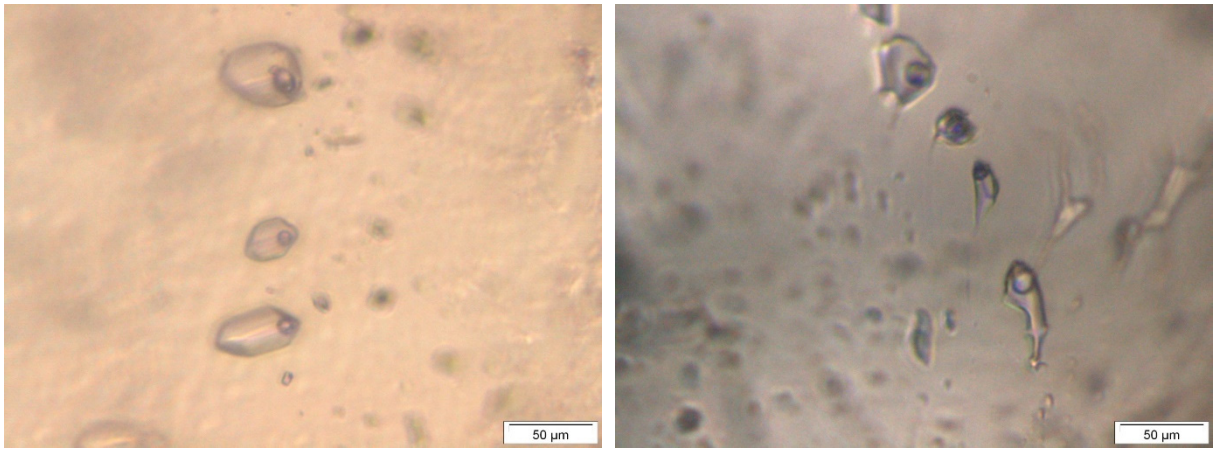

FIGURES 21 and 22: Fluid inclusions of quartz crystals from CL5. To the left inclusions from the 550 m sample are shown and to the right inclusions from the 610 m sample are shown

As shown in Figure 23, the homogenization temperatures in the CL5 range from 200 to 270°C with the lowest temperature being measured at 610 m. Nevertheless, considering the frequency of the Th measurements, the most common temperatures are ranging from 225 to 260°C. Additionally, there is an evident tendency for the homogenization temperatures to increase with depth and this is a similar pattern to what was seen in CL4-A but here the Th gradient is smaller than in CL4-A.

Moreover, the homogenization temperatures are slightly higher than the formation temperatures, suggesting that at the location of CL5 temperatures within the geothermal system could have been slightly hotter at some point in the past than they are today, possibly ranging from 235-270°C. Moreover, based on the Th results, reservoir temperatures (above 225°C) were present in the past at 550 m what is slightly shallower than at present times. This observation suggests that the fluid level within the reservoir was at some point in the past at slightly shallower depths than today. This is consistent with the secondary mineralogy found at around 540 m depth where the rock formation starts to show abundant veining which becomes common and

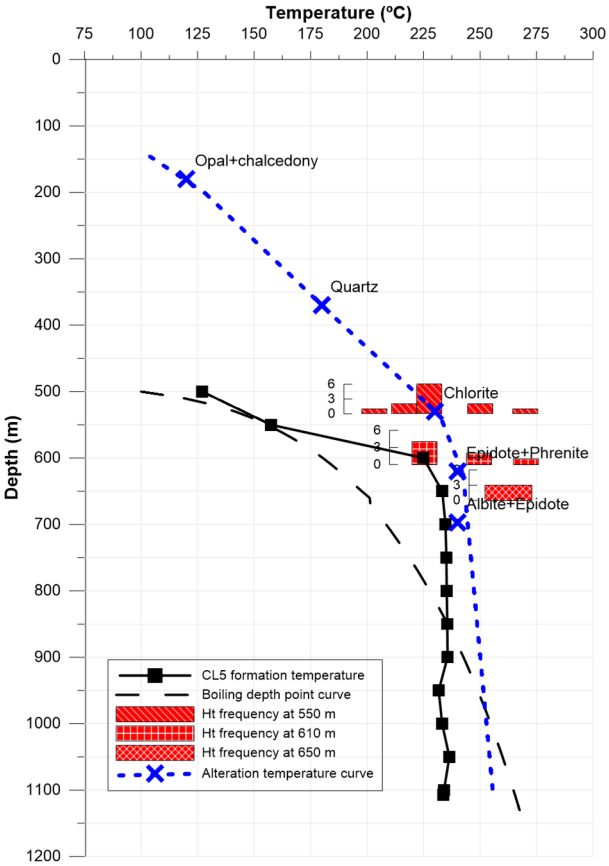

FIGURE 23: Homogenization temperature range from fluid inclusions of CL5 along with the formation and alteration temperature curves

appears to increase in intensity with depth, reflecting an increase in the hydrothermal activity. Here, the vein mineral assemblages include calcite, quartz, chlorite, pyrite and hematite which can be found in different combinations. Thus, the common association of calcite and quartz, as well as the identification of deposition of different calcite generations with distinct grain size and optical properties (Foundation of the Science Faculty at the University of Lisbon, 2005), suggests that fluid levels within the geothermal system had been fluctuating in the past.

8.1.3 Samples from CL7

From well CL7 the selection of samples was limited to the initial 620 m because almost the entire reservoir interval was drilled without returns. CL7 shows strong silica alteration starting from 150-200 m depth onwards with initial deposition of opal. With depth, first chalcedony and then microcrystalline quartz replace opal as the silica phase. In the interval from 200 to 500 m two samples of well-developed hexagonal quartz were found at 234 and 464 m and these were selected for the study of fluid inclusions. It is noteworthy that the size of the quartz sample found at 464 m (1.3 cm) is not very common in the Ribeira Grande field but similar size quartz crystals were occasionally found in other wells (for example at 254 m in well RG4, drilled in the Caldeiras sector of the Ribeira Grande Geothermal Field).

The fluid inclusions found in the quartz sample at 234 m showed homogenization temperatures ranging from 243 to 272ºC what is significantly higher than the estimated formation temperatures at this depth. The absence of logging points above 500 m depth in the temperature profiles obtained from the well makes it difficult to be certain of the precise formation temperature at 234 m depth but it is unlikely to exceed 175ºC which is the formation temperature measured at 500 m depth. It is noticeable that at about 150-250 m depth the rock formation exhibits intense argillic alteration with abundant white clay. X-ray diffraction results indicate that smectite is the dominant clay type at this depth where it was found coexisting with kaolinite at the top of the interval and with illite below 200 m. This type of clay alteration is a characteristic of acidic environments, suggesting that this could be the result of a now extinct steam heated aquifer.

The size of the 464 m quartz crystal allowed it to be cut in four transversal sections which are each about 1 mm thick for detailed fluid inclusion studies. From these samples, one from the top and another from the bottom were selected and heated to determine the homogenization temperatures of the fluids trapped in them.

The quartz sections were analysed under the microscope and it was possible to observe that they contained different generations of fluid inclusions which can be summarized as three types: i) some well-formed growth zones outlined by groups of primary fluid inclusions (Figure 24) predominantly correspondent to gas inclusions; ii) a few groups of secondary inclusions found aligned along micro fractures and were mostly liquid (water) but gas inclusions were also found; iii) isolated primary fluid inclusions with no specific relation to any growth zone of the crystal or any specific microfractures; these are predominantly liquid inclusions.

The primary inclusions were formed during the growth of the quartz crystal. During crystallization the quartz was fractured and when these micro fractures healed they trapped small quantities of the surrounding liquid or gaseous fluids in the host crystal, forming secondary inclusions. Both primary and secondary fluid inclusions were heated to determine the homogenization temperatures in an attempt to understand the thermal evolution of the geothermal system during the crystal grow. The main findings are described below.

- At the bottom of the crystal, the primary inclusions (primary to the growth of the crystal), show Ht of 240 to 290°C;
- Primary inclusions at the top of the crystal show Th of 227 to 251°C, meaning that a cooling episode of the geothermal system has occurred during the period of time at which the crystal was growing;

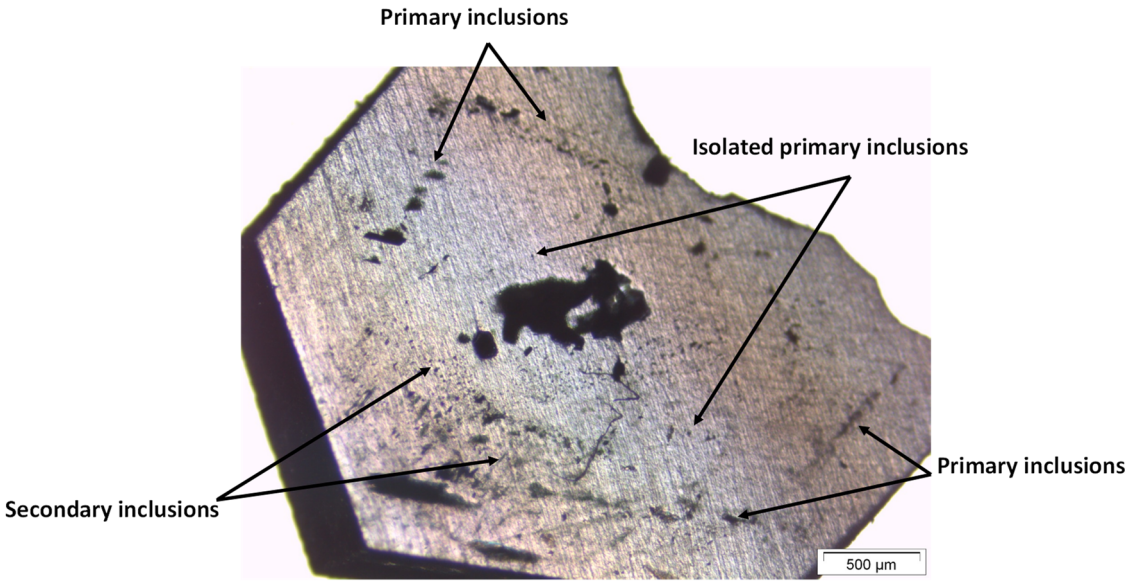

FIGURE 24: Top section of the 464 m quartz sample from well CL7

- Secondary inclusions found at the bottom (Figures 25 and 26) and at the top of the crystal show consistent Th in the range of 233-241°C. These are similar to the Th range shown by the primary inclusions found on the top of the crystal, indicating that the geothermal system was in equilibrium since the end of the crystal growth;
- When comparing the secondary fluid inclusions Th (233-241°C) with the formation temperatures seen today we observe that the range of temperatures given by the fluid inclusions is very similar to the present time reservoir temperatures found in the Ribeira Grande field, meaning that the geothermal system is in equilibrium since the end of the crystal growth;
- As shown in Figure 27, Th results seem to indicate that higher reservoir temperatures were present at shallower depths in the past what points at possible fluctuations in the fluid level within the reservoir;
- A significant number of gas inclusions were found in all the samples from CL7 (see Figure 28). This indicates that boiling was occurring when the gas was trapped during the quartz crystallization.

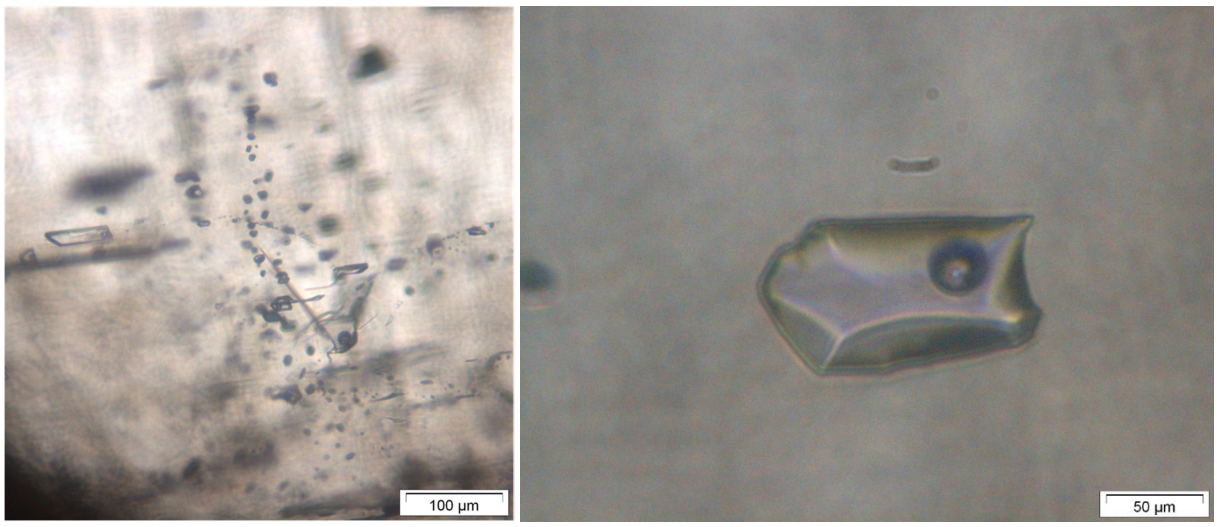

FIGURES 25 and 26: Secondary liquid inclusions with vapour bubble found at 464 m (bottom section of the quartz crystal)

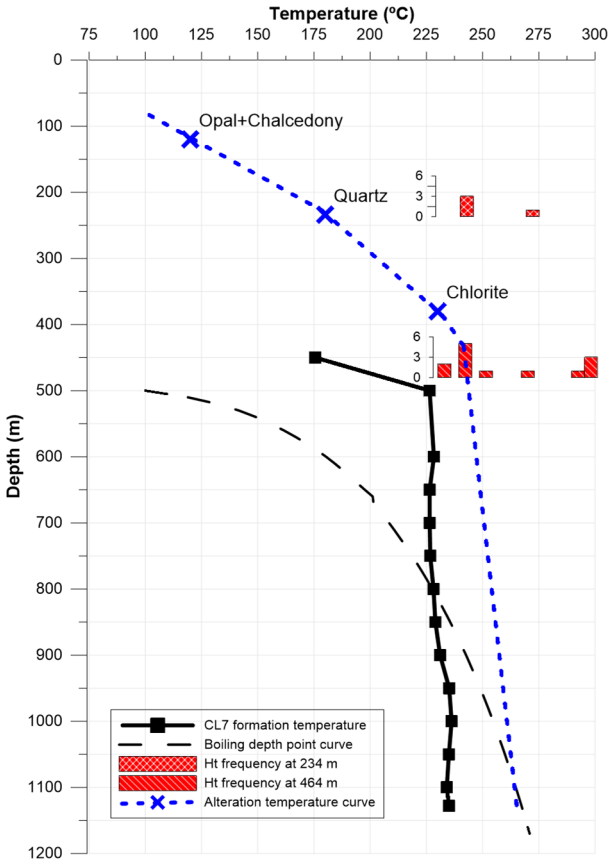

FIGURE 27: Homogenization temperature range from fluid inclusions of CL7 along with the formation and alteration temperature curves

8.2 Freezing studies

Two samples from CL7, namely the top and bottom sections of the 464 m quartz described in section 8.1.3, were frozen to determine the melting point temperatures (Tm) and investigating the composition of the liquids trapped in them (Figure 29). The melting temperatures were consistently -0.3ºC. According to Bodnar and Vityk, 1994, these melting temperatures correspond to 0.53wt% of sodium chloride salinity equivalent. These results indicate that the fluid within the geothermal system has consistently been composed of fresh water. This is in line with the present time chemical data from the geothermal fluid given by isotopic analysis which indicates that the recharge into the geothermal system is meteoric water (GeothermEx, 2008; Ponte et al., 2009; Pham et al., 2010; Ponte et al., 2010; Rangel, 2014).

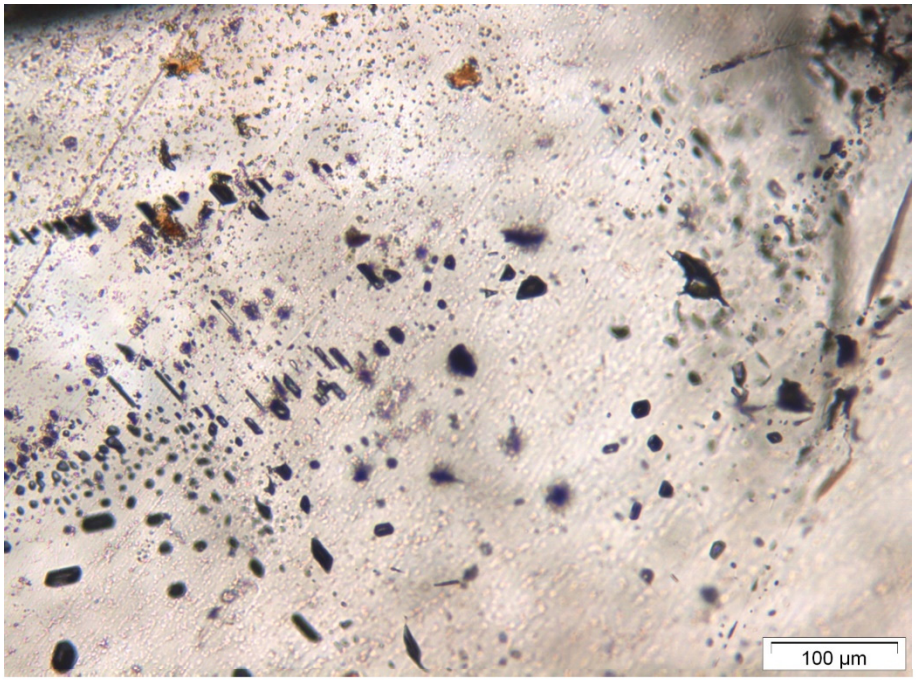

FIGURE 28: Groups of predominantly gas inclusions found in the 464 m sample (to section of the quartz crystal). The photo was taken at room temperature (22°C)

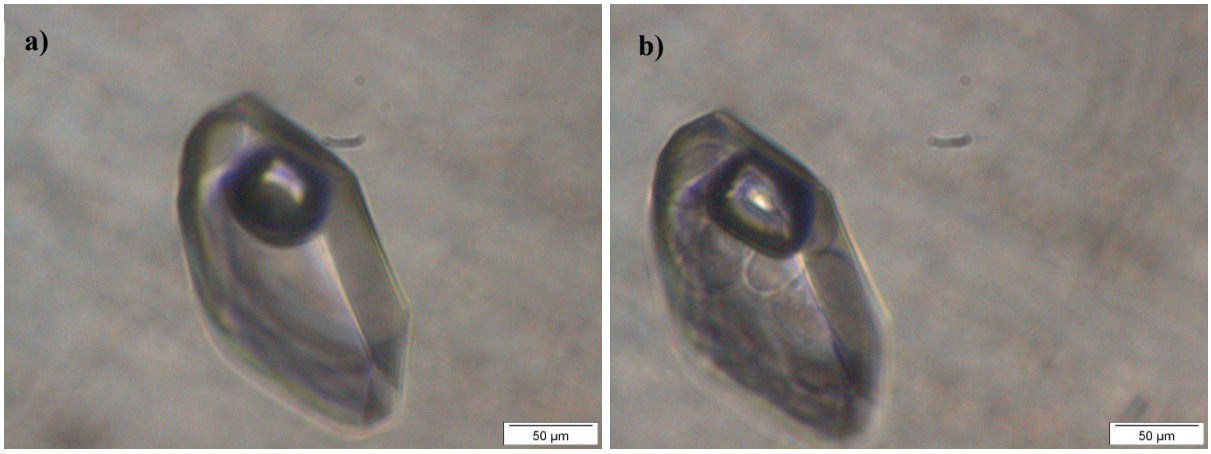

FIGURE 29: Fluid inclusion studied in the 464 m quartz of CL7. To the left the freezing stage is at -10.0°C and to the right the freezing stage is at -0.3°C where the ice melting becomes evident

9. COMPARISON BETWEEN THE ALTERATION TEMPERATURE AND FORMATION TEMPERATURES

The present study analyses temperature data from the Cachaços-Lombadas wells in two ways. The formation temperature corresponds to the stabilized profiles taken in the wells after warm-up and the alteration temperature was assessed according to the occurrence and distribution of the secondary minerals. In this respect, a correlation between the formation and the alteration temperature curves is shown in Figure 30 which allows inferring the thermal evolution of the geothermal system.

The alteration temperatures from all wells are shifted to the right of the formation temperatures indicating that at some point in the past the geothermal system was slightly hotter, reaching temperatures up to 260°C. In the uppermost part of the reservoir down to 600 m depth, this shift is more pronounced in CL6 where the temperature difference is about 40-45°C while in the other wells the shift is only about 10 to 20°C. Additionally, the alteration temperature curves suggest that the geothermal system was shallower than today (about 50-100 m

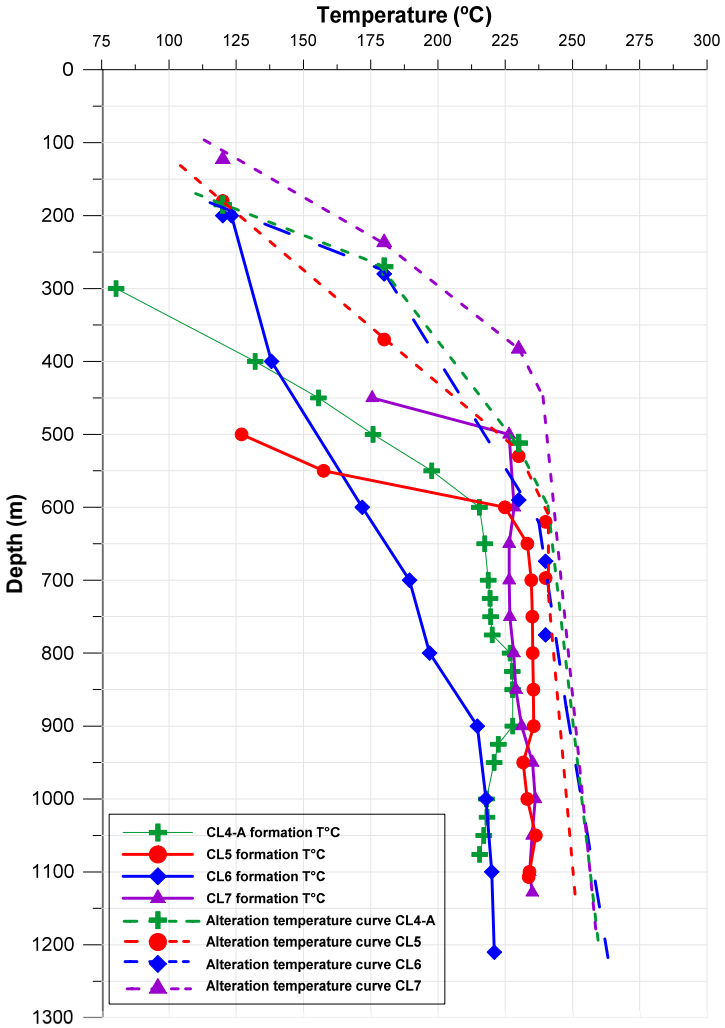

FIGURE 30: Formation and alteration temperature curves of wells CL4-A, CL5, CL6, and CL7

shallower at this location), suggesting that fluid levels within the geothermal system have been fluctuating with time.

The comparison of the alteration and formation temperatures indicates that cooling has occurred at some point in the past. During the binocular analyses, no significant evidence of retrograde alteration was found filling the open-spaces within the rock formations of the Cachaços-Lombadas wells. However, this does not exclude its presence. In this respect, it is important to note that the detailed petrography, performed in 2005 by the Foundation of the Science Faculty at the University of Lisbon, allowed to identify both retrograde and prograde alteration in thin sections from cutting samples of well CL6 (Figures 31 and 32) and these observations are consistent with the hypothesis that cooling has occurred at some point in the past.

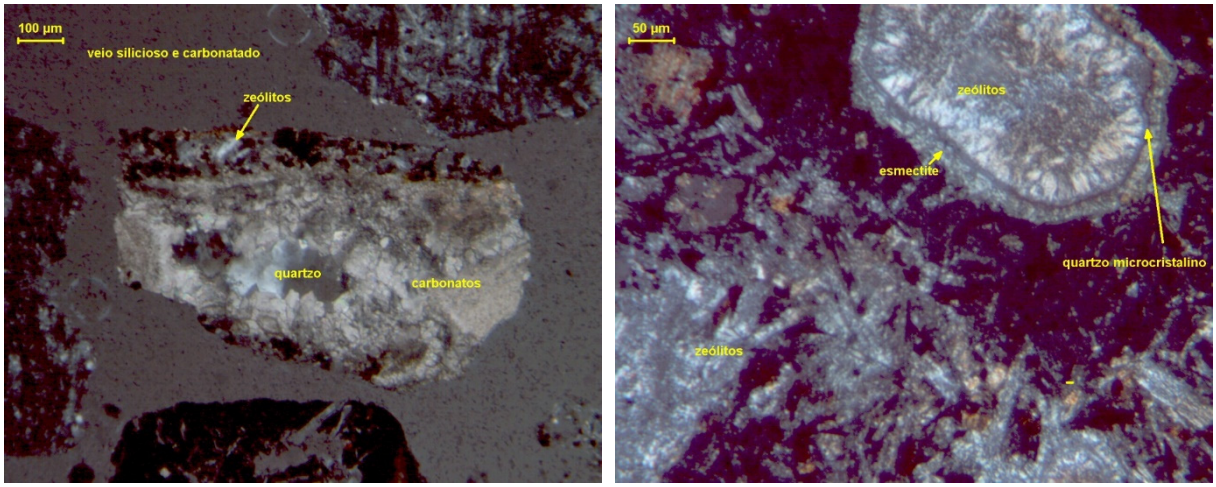

FIGURES 31 and 32: Samples from well CL6. In Figure 31 to the left, a vein is identified at 635 m composed of 1) zeolites, 2) calcite and 3) quartz, showing a prograde alteration. In Figure 32 to the right, a vesicle is identified at 542 m filled with 1) quartz, 2) smectite and 3) zeolites, showing retrograde alteration in a vesicle at CL6 (photos from Foundation of the Science Faculty at the University of Lisbon, 2005)

The investigation of the mineral sequences should be performed using detailed petrographic analysis and this was only executed thoroughly in well CL6 (CL5 only three samples were analysed). Therefore, the available data is not sufficiently conclusive regarding the existence of any retrograde or prograde alteration tendency and how these are distributed over the Cachaços-Lombadas area. Nevertheless, the rank of the alteration minerals, particularly the ones identified under the petrographic microscope in wells CL5 and CL6 such as prehnite, epidote and albite, suggest that the geothermal system was at slightly higher temperatures than the ones observed at present times.

The hypothesis that fluctuations of the reservoir fluid level have occurred in the past is more convincing (this is quite evident in CL5 and CL7) and is supported by the results from the fluid inclusion studies and by the observation of high abundance of calcite and quartz veins at about 0 to -150 m m.s.l. in most of the Cachaços-Lombadas wells.

10. CONCLUSIONS

All rocks intersected by the Cachaços-Lombadas wells are volcanic and correspond to the eruptive products of the Fogo volcano. The lithostratigraphy of the area can be summarized as follows:

- At shallow levels from the surface to about 250-300 m m.s.l. five wells intersect a thick sequence of trachyte lavas which are very permeable. This is the case of CL1, CL2, CL3, CL4 and CL4-

A. These trachyte lavas are absent in the wells CL5, CL6 and CL7, possibly because they thinned out or it were eroded in these locations;
- A thick sequence of pyroclastic rocks is the predominant lithology from the surface to about -100 m m.s.l. In CL5, CL6 and CL7 the sequence reaches about 600 m thickness but is thinner at CL4-A where it is 300-400 m thick. The sequence of pyroclastic rocks is locally interrupted by lava flows (mostly trachytes) of variable thickness. Here, four lava units have relatively good correlation between wells, working as marker horizons;
- The pyroclastic rock units show a progressive increase in the intensity of the hydrothermal alteration with depth, particularly to clay minerals which form the caprock of the geothermal system;
- Below sea level the subsurface geology is dominated by basalt lavas down up to about -600 m m.s.l. This is most prominent in CL4-A. Elsewhere, the extent of this lava dominated interval is rather uncertain, particularly in the area of wells CL6, CL5, and CL7 because this interval was drilled without returns;
- No intrusive or subvolcanic rocks were identified in the study but they may occur at greater depth;
- No pillow lavas were found in the depth interval logged down to -600 m m.s.l. This confirms the high rate of subsidence that the graben of Ribeira Grande has suffered.

The lithological data from the wells does not allow for direct identification of any faults. However, the location of the major permeable zones encountered in the Cachaços-Lombadas wells roughly coincide the NW and NNW trending inferred faults in the area, suggesting that the NNW trend structures may be associated with high permeability.

Boiling occurs in most of the wells, creating a two-phase or steam zone at the top of the reservoir. The only exception is well CL6, located further to the south, which only exhibits the liquid phase. Furthermore, the temperature distributions at 4 different elevations indicate:

- The temperature gradient is relatively high to about -100 m m.s.l. (in the range of 250-300°C/km);
- From -100 m m.s.l., the reservoir is near isothermal with temperatures ranging from 230-235°C in most parts of the area. This depth interval corresponds to the core of the geothermal reservoir where the most prolific feed zones are located;
- A slight temperature reversal is observed in the bottom part of most of the Cachaços-Lombadas wells, indicating that the main upflow zone of the geothermal system is not located in the central parts of the project development area of Cachaços-Lombadas;
- With increasing depth, the temperatures continue to increase towards NNE whereas in the southern part of the area the temperatures tend to decrease. This strongly indicates a boundary of the geothermal field in the south. Furthermore, the data are insufficient to locate precisely where the upflow zone is but the temperature distribution suggests that it may occur at some undetermined location to the east or northeast of CL3 and CL7.

The alteration mineral assemblage shows a trend where low temperature minerals like zeolites and opal form in the upper part of the wells and are gradually replaced by moderate temperature minerals like chalcedony and quartz which in turn give way to higher temperature minerals such as chlorite, prehnite, epidote and albite.

The occurrence and distribution of alteration minerals allowed the identification of two zones of hydrothermal alteration beneath a shallow zone of relatively unaltered rocks. A smectite zone (< 200-220°C) was identified from 150-200 to 500-590 m and a chlorite zone (> 230°C) below 500-590 m. Additionally, the alteration zoning pattern within the area indicated that higher alteration temperatures are found shallower in CL7 when compared to wells CL4-A, CL5, and CL6, suggesting that CL7 is closer to the upflow zone of the geothermal system.

Alteration temperatures, based in the first appearance of key index secondary minerals and in the homogenization temperatures of fluid inclusions, indicate that the geothermal system was hotter than today at some point in the past, with maximum temperatures up to 270-300°C, but it has been in equilibrium since then with some fluctuations of the fluid level in the reservoir.

Freezing studies carried out with fluid inclusions in quartz samples from CL7 confirmed that fresh water was the fluid of the geothermal system when the inclusions were trapped during the crystallization of the secondary quartz crystals and this is consistent with the composition of the reservoir fluid at the present time.

ACKNOWLEDGEMENTS

I wish to address my gratitude to the United Nations University – Geothermal Training Programme, in particular to Mr. Lúdvík S. Georgsson, director of the Geothermal Training Programme of the United Nations University (UNU-GTP) and to all the technical staff, namely Mr. Ingimar G. Haraldsson, Ms. Málfrídur Ómarsdóttir, Ms. Thórhildur Ísberg and Mr. Markús A.G. Wilde for their kind assistance and arrangements. These are extended to all the 2015 UNU fellows for their friendship and caring support during the training in Iceland. Special thanks to my fellow geologists Davar Ebrahimi, Frederick Mutua, Hamda Wais and Patrick Muanza for the continuous share of knowledge and ideas.

Sincere thanks to Dr. Björn S. Hardarson from ISOR for his advice and guidance during the development of this project. These are extended to Mr. Sigurdur Jónsson for the assistance in the X-ray diffraction analysis and to Dr Gunnlaugur Einarsson and Jóhann Kristjánsson from Orkustofnun for the support with the Petrel software. I am also thankful to Dr. Kristján Saemundsson for the valuable comments throughout the development of the project. A kind appreciation is also addressed to Professor Eniko Bali of the University of Reykjavik for the support during the fluid inclusion studies.

Finally, but not the last, a special word of appreciation is addressed to EDA Renováveis, S.A., for the support given during the training in Iceland and for allowing the use of the Ribeira Grande geothermal field data for the purpose of the present work.

REFERENCES

Booth, B., Croasdale, R., and Walker, G.P.L., 1978: A quantitative study of five thousand years of volcanism on São Miguel, Azores. *Royal Society of London Philosophical Transactions, 288*, 271-319.

Cabeças, R., Carvalho, J., Nunes, J., 2010: Portugal country geothermal update 2010. *Proceedings of the World Geothermal Congress 2010, Bali, Indonesia*, 10 pp.

Carmo, R., 2013: *Neotectonic studies in São Miguel Island, a contribution for the study of seismic risk in the Azores.* PhD dissertation in Geology, specialty in Volcanology (in Portuguese). Department of Geoscience, University of the Azores, 307 pp.

Carvalho, M., Forjaz, V., Almeida, C., 2006: Chemical composition of deep hydrothermal fluids in the Ribeira Grande geothermal field (São Miguel, Azores). *J. Volcanology and Geothermal Research, 156*, 116–134.

Carvalho, A., Sousa, M., Oliveira, C., Campos-Costa, A., Nunes, J., and Forjaz, V., 2001: Seismic hazard for the central group of the Azores Islands. *Boll.Geofisica Teorica ed Applicata, 42-1/2*, 89-105.

Cole, P., Queiroz, G., Wallenstein, N., Gaspar, J., Duncan, A., and Guest, J., 1995: An historic subplinian/phreatomagmatic eruption: the 1630 AD eruption of Furnas volcano, São Miguel, Azores. *J. Volcanology and Geothermal Research, 69*, 117-135.

Dawson, P., Silva, A., Lyerl, H., and Evans, J., 1985: Seismic study of the Agua de Pau geothermal prospect, São Miguel, Azores. *Geothermal Resources Council Transactions, 9*, 401-406.

Duffield, W.A., and Muffler, L.J.P., 1984: *Geothermal resources of São Miguel Island, Azores, Portugal*. U.S. Geological Survey, open-file report 84–287, 21 pp.

EDA – Electricidade dos Açores, 2014: *Demand and offer of electricity (in Portuguese).* Electricidade dos Açores (EDA), Planning, Control of manageament and regulation (PLCOR), Ponta Delgada, São Miguel, Azores, Portugal, 32 pp.

Ferreira, T., 2000: *Characterization of the volcanic activity in São Miguel Island (Azores), recent basaltic volcanism and degassing areas. Risk assessment.* PhD dissertation (in Portuguese), Geoscience Department, University of Azores, 248.

Foundation of the Science Faculty at the University of Lisbon, 2005: *Petrographic and diffractometric characterization of selected samples from wells CL5 and CL6, Ribeira Grande geothermal field (in Portuguese)*. University of Lisbon, report for Sociedade Geotérmica dos Acores, S.A. (SOGEO), 22.

Gaspar, J.L., 1996: *Graciosa Island (Azores), volcanological history and assessment of hazards.* University of the Azores, Azores, PhD dissertation (in Portuguese), 256 pp.

GeothermEx, 2008: *Update of the conceptual and numerical model of the Ribeira Grande geothermal reservoir, São Miguel, Açores*. GeothermEx Inc., report for Sociedade Geotérmica dos Açores, S.A. (SOGEO), 190 pp.

GeothermEx, 2014: *Selection of new drilling sites in the Cachaços-Lombadas sector, Ribeira Grande geothermal field, São Miguel, Açores*. GeothermEx Inc., report for EDA Renováveis, 46 pp.

Granados, E., Hennerberger, R., Klein, C., Sanyal, S., Ponte, C., Forjaz, V., 2000: Development of injection capacity for the expansion of the Ribeira Grande geothermal project, São Miguel, Açores, Portugal. *Proceedings of the World Geothermal Congress 2010, Kyushu-Tohoku, Japan*, 3065-3070.

Hennerberger, R., and Nunes, J., 1990: A new discovery well in the upper Água de Pau geothermal system, São Miguel Island, Azores: results of drilling and testing. *Geothermal Resources Council Transactions, 14*, 1449-1452.

Irvine, T.N., and Barager, W.R.A., 1971: A guide to the chemical classification of the common volcanic rocks. *Canadian Journal of Earth Sciences, 8*, 523-548.

Madureira, P., Moreira, M., Mata, J., and Alle`gre, C., 2005: Primitive neon isotopes in Terceira Island (Azores archipelago). *Earth and Planetary Science Letters, 233*, 429–440.

Madureira, P., Moreira, M., Mata, J., Nunes, J., Gautheron, C., Lourenco, N., Carvalho, R. and Abreu, M., 2014: Helium isotope systematics in the vicinity of the Azores triple junction: constraints on the Azores geodynamics. *Chemical Geology, 372*, 62–71.

McGraw, P., 1976: *A petrological/geochemical study of rocks from the São Miguel drillhole, São Miguel, Azores.* MSc dissertation, University of Dalhousie, 194 pp.

Métrich, N., Zanon, V., Créon, L., Hildenbrand, A., Moreira, M., and Marques F., 2014: Is the 'Azores hotspot' a wetspot? Insights from the geochemistry of fluid and melt inclusions in olivine of pico basalts. *Journal of Petrology, 55*, 377–393.

Moore, R., 1990: Volcanic geology and eruption frequency, São Miguel, Azores. *Bulletin of Volcanology, 52*, 602–614.

Moore, R., 1991: Geology of three late Quaternary stratovolcanoes on São Miguel, Azores. *US Geological Survey Bullettin 1990*, 46 pp.

Muecke, G., Ade-Hall, J., Aumento, F., MacDonald, A., Reynolds, P., Hyndman, R., Quintina, J., Opdyke, N., and Lowrie, W., 1974: Deep drilling in an active geothermal area in the Azores. *Nature, 252*, 281-285.

Pham, M., Klein, C., Ponte, C., Cabeças, R., Martins, R., and Rangel, G., 2010: Production/injection optimization using numerical modeling at Ribeira Grande, São Miguel, Azores, Portugal. *Proceedings of the World Geothermal Congress 2010, Bali, Indonesia*, 6 pp.

Ponte, C, 2012: Case study – Use of geothermal resources for power production in the Azores (in Portuguese). *Ingenium magazine, September/October edition*, 67-67.

Ponte, C., Cabecas, R., Rangel, G., Martins, R., Klein, C., Pham, M., 2010: Conceptual modelling and tracer testing at Ribeira Grande, São Miguel, Azores, Portugal. *Proceedings of the World Geothermal Congress, Bali, Indonesia*, 11 pp.

Ponte, C., Cabeças, R., Martins, R., Rangel, G., Pham, M., and Klein, C., 2009: Numerical modeling for resource management at Ribeira Grande, São Miguel, Azores, Portugal. *Geothermal Resources Council Transactions, 33*, 847-853.

Queiroz, G., 1997: *Sete Cidades volcano (São Miguel Island, Azores) – eruptive history and hazard assessment.* PhD dissertation (in Portuguese), University of the Azores, 226 pp.

Rangel, G., Franco, A., Cabeças, R., Ponte, C., 2011: Use of geothermal resources in the Azores Islands: A contribution to the energy self-sufficiency of a remote and isolated region. *Geothermal Resources Council Transactions, 35*, 1209-1214.

Rangel, M.G., 2014: Temperature model and tracer test analysis for the Ribeira Grande geothermal system, São Miguel Island, Azores. Report 29 in: *Geothermal training in Iceland 2014*. UNU-GTP, Iceland, 615-642.

Rodrigues, M, and Oliveira, C., 2013: Seismic zones for Azores based on statistical criteria. *Natural Hazards Earth System Sciences, 13*, 2337–2351.

Silva, R., 2011: *Evaluation of spatial and temporal seismicity patterns in the central region of São Miguel (Azores): implications for whole-island seismic hazard assessment*. University of the Azores, PhD dissertation, 236 pp.

Walker, G., and Croasdale, R., 1970: Two Plinian-type eruptions in the Azores. *J. Geological Society of London, 27*, 17-55.

Wallenstein, N., Duncan, A., Chester, D., and Marques, R., 2007: Fogo volcano (São Miguel, Azores): a hazardous edifice. *Géomorphologie: Relief, Processes, Environment, 3*, 259-270.

APPENDIX I: Detailed description of the lithological units of wells CL4-A, CL5, CL6, AND CL7

CL4-A

Well CL4-A was drilled to 1076.4 m during June 3 and July 26, 2012. The 13-3/8´´ production casing was set at 613.5 m and the 9-5/8´´ slotted liner was installed at 1,067.4 m, hanging at 588.4 m depth inside the production casing (note: all depths correspond to total measured depths from the ground floor level). The lithological units intersected by the well can be summarized as follows:

0-24 m: *Pyroclastic deposits*. Three pyroclastic units can be distinguished, with a tuff rich scoria at the top, followed by lithic tuff and a pumice bed at the bottom.

24-182 m: *Trachyte lava*. White to light grey, hard, porphyritic with sanidine phenocrysts. Locally it is slightly vesicular. Common oxide stains in the felsic groundmass which peak at 174 m. From 124 m loose sanidine crystals are abundant. This could be the same sequence of lava found in CL1 and CL2, located in the southern part of Cachaços-Lombadas sector, or some separate but similar sequence of lava.

182-230 m: *Lithic tuff*. The formation is brownish grey and poorly consolidated. Matrix of ash, tan to brownish grey, partially altered to clay. Lithics of mostly fresh lava, exhibiting oxidation. The first appearance of calcite is at 196 m. Opal and chalcedony are common as open space fillings, mainly as amygdales in the lithics of vesicular lava which are found in minor quantities.

230-340 m: *Basalt lava*. Dark brownish grey, moderately consolidated. The lava is pervasively altered to clay, vesicular, with light grey-green to white fillings likely microcrystalline quartz or chalcedony. The groundmass is mottled by clay alteration (mainly smectite). At 238 m sulphur crystals were found, suggesting that at same point in the past this corresponded to an open permeable zone, likely a fracture through which steam was circulating onwards from 270 m the first veins of quartz and calcite appear. The lava in the uppermost part of this interval seems to be decomposed, possibly by weathering prior to burial.

340-360 m: *Lithic tuff*. Brown to brownish grey, poorly consolidated. Matrix of ash is altered to brownish clay (mainly smectite). Lithics of different lavas: dark grey basalt lava, fine-grained, locally with replacements and veins of calcite + quartz; light grey to grey lava, porphyritic with feldspar phenocrysts, moderately hard to soft, pervasively altered to clay and with oxide spots. Minor reddish-orange lava, strongly oxidized and silicified and greenish grey lava with abundant amygdales filled with smectite + opal, with the groundmass mottled by clay alteration.

360-380 m: *Trachyte lava*. The lava flow sequence is light grey to brownish grey, moderately hard, porphyritic with sparse hyaline feldspar phenocrysts (sanidine). At the top it is vesicular with white opal fillings/coatings, locally with calcite + quartz replacements.

380-480 m: *Lithic tuff*. The deposit is grey to brownish grey, poorly consolidated to moderately consolidated. Matrix of ash altered to clay, was mostly washed away during drilling, appears as coatings on the lava lithics. Lithics of dark grey to brownish grey lava, porphyritic with sanidine phenocrysts, locally with chlorite + quartz replacements and with calcite + quartz + hematite veins. Common lithics of light grey lava and reddish brown lava, strongly oxidized, as well as light grey vesicular lava with white to white green fillings. Minor syenite fragments and loose quartz, the latter probably from open-space fillings (veins). Weak to moderately altered, mostly clay (likely smectite), calcite (veins, veinlets and replacements), silica (quartz veins and replacements, and opal fillings). Chlorite appearance is at 450 m, becoming more common with increasing depth.

480-510: *Basalt lava*. The lava flow sequence is grey to dark grey, compact, hard, with calcite + quartz veinlets and veins, locally associated with chlorite. Common loose quartz + calcite, likely from open space fillings (veins). Additionally, locally the lava exhibits patchy hematite. Weak to moderately altered, mainly calcite, quartz, chlorite and hematite.

10-624 m: *Lithic tuff*. The pyroclastic deposits are brownish grey to grey, poorly consolidated. Matrix of ash has been mostly washed away but is locally indurated by silicification, related to the deposition of microcrystalline quartz or chalcedony. Lithics of mostly grey to brownish grey lava, with abundant calcite + chlorite replacements, strongly oxidized. Minor lithics of light grey lava with opal fillings, the groundmass mottled by clay alteration. Locally with very fine pyrite at 564 m. Common loose quartz + chlorite, probably from open-space fillings (veins) which are very abundant at the top (510-516 m). At 582 m found amygdales filled with calcite + quartz + chlorite. Calcite is abundant in the whole interval. Moderately altered.

624-896 m: *Basalt lava*. Dark grey, hard, aphanitic to locally porphyritic with pyroxene phenocrysts, locally with quartz + calcite replacements, veins and veinlets (all locally associated with chlorite and pyrite). Occasionally, the pyroxene phenocrysts exhibit oxide staining. The groundmass is relatively fresh, fine grained but locally is chloritized at 688-702 m. Minor presence of white altered rock, silicified, with very fine disseminated pyrite, appears at 682 m and at 700-724 m. Oxidation peaks up at 702 m and the same occurs with the white open space fillings (quartz and quartz + calcite. Red jasper is found locally at 724 m and the chlorite replacements peak at 724 m.

896-900 m: *Trachyte lava*. The lava is white to light grey, moderately hard, fine grained, with calcite + chlorite replacements, locally with very fine cubic pyrite.

900-914 m: *Basalt lava*. Dark grey, moderately hard, fine grained, with calcite + quartz replacements, locally with patchy hematite. Minor loose calcite + quartz from open-space fillings with most of the crystals being hyaline.

914-1010 m: *Intermmediate lava*. The lava is grey to light grey, moderately hard. Fine grained, aphanitic. Calcite is less abundant than above. Common loose white and hyaline crystals mostly quartz and quartz + calcite, from open-space fillings (veins). Locally with fine disseminated pyrite and with hematite stains.

1010-1083 m: *No information*. Drilled without returns.

CL5

Well CL5 was drilled to 1,132.0 m during October 31, 1999 to January 31, 2000. The 13-3/8´´ production casing was set at 613.5 m and the 9-5/8´´ slotted liner was installed at 1,067.4 m, hanging at 588.4 m depth inside the production casing. The lithological units intersected by the well can be summarized as follows:

0-288 m: *Pyroclastic rock units*. Relatively unconsolidated pyroclastics rock units (mostly lithic tuffs and pumice deposits) dominate from surface to about 288 m. Light grey to tan pumice beds are found at 110-120 m and interlayered with lithic tuff from 151-170 m.

288-345 m: *Trachyte lava*. Light grey, moderately hard to hard. Consists at least of two flow units separated at 315-320 where there is a brown clay matrix and minor weathering of some of the lava. Overall, the lava is massive, fine grained with sugary appearance. Sparse phenocrysts of sanidine and rarely amphibole can be seen. Unaltered to weakly altered, only locally some hematite on weathered surfaces (310-320 m).

345-515 m: *Pyroclastic rock units*. This interval may contain several units but the most prominent are the lithic tuff units found at 345-390 and 400-445 m which are interlayered with two main tuff units, a consolidated tuff from 390-400 m which seems to be indurated by silicification, and at the bottom from 445 to 515 m the ash matrix is overall altered to clay and silicified with common very fine disseminated pyrite. A scoria unit is found at 445-555 m.

515-540 m: *Basalt lava*. The lava flow sequence is grey to brownish grey, hard, fine grained. Weakly to moderately altered, with partial replacements of calcite, chalcedony and possibly zeolite veins. First appearance of chlorite is at 525 m and it becomes common down to the bottom of the well.

540-615 m: *Lithic tuff.* The lithics of lava make up from 20 to 70%. Veins of chalcedony, quartz, chlorite, pyrite and occasionally hematite are common.

615-645 m: *Basalt lava*. Dark grey to grey, hard, massive, fine grained. The lava is pervasively altered, with abundant calcite replacements and locally with patchy chlorite. Hematite is locally intense. Veins are common, in various assemblages, such as calcite + quartz, quartz + pyrite, quartz + pyrite + chlorite, calcite + chlorite.

645-655 m: *Lava breccia*. The formation is red to grey, corresponding to a breccia zone between two lava flows. Alteration is strong to moderate, mostly calcite + chlorite, some silicification and hematite.

655-697 m: *Basalt lava*. The lava flow sequence is dark grey to grey, hard, massive and fine-grained. Mostly is pervasively altered, with abundant calcite and chlorite replacing the groundmass minerals.

Veining is locally abundant, mainly quartz + chlorite + pyrite + calcite and rarely quartz + pyrite + hematite.

697-703 m: *Tuff*. White to tan, moderately consolidated. Pervasively silicified. The tuff is replaced by chalcedony and chlorite. Very fine disseminated pyrite is abundant. Veining is rare.

703-1076 m: *No information*. Drilled without returns.

CL6

Well CL6 was drilled to 1,239.2 m between January 26th and April 27th, 2005. The 13-3/8´´ production casing was set at 719.8 m and the 9-5/8´´ slotted liner was installed at 1,227 m, hanging at 693 m depth inside the production casing. The lithological units intersected by the well can be summarized as follows:

0-135 m: *Lithic tuff, lithic-pumice tuff and pumice beds*. Poorly consolidated to unconsolidated pyroclastic deposits are predominant with the intersection of several tuff and lithic tuff units from the surface to a depth of 270 m. Two pumice beds are found at 21-25 m and 91-93 m and from 34 to 44 m there is a crystal rich tuff with abundant loose crystals of sanidine.

135-188 m: *Lithic tuff*. The formation is grey to yellow-brown, poorly to moderately consolidated. Matrix of ash partially altered to tan, white and yellow clay (mostly likely smectite), contains also very fine silte to sand size crystals and lithics. Lithics of compact grey lava, porphyritic with sanidine phenocrysts, locally vesicular with white clay fillings. Minor loose crystals of sanidine and grey to yellow-orange pumice, the latter making up to 5-10%. Rare volcanic glass. Scoria bed is present at 136-140 m.

188-270 m: *Lithic tuff*. The formation is grey-green, moderately consolidated. Matrix of tan to light greenish grey ash, containing very fine silt size crystals, altered to clay (possibly smectite and minor chlorite), locally indurated by silification. Lithics of grey, light grey and grey-green compact lava, often oxidized. Some lava lithics are vesicular, with tan to yellow fillings (likely smectite and zeolites). Rare syenite fragments.

270-327 m: *Trachyte lava*. Light grey to white, moderately hard to hard, fine grained, massive, porphyritic with sanidine phenocrysts, locally exhibiting oxide stains. Locally the lava is soft where it is decomposed to clay. At 285 m abundant pyrite clusters were found associated with microcrystalline quartz. Additionally, yellow sulphur was found at 285 to 291 m, suggesting the possibility that some fault/fracture is or was present in that zone through which steam is or was flowing. The logging team at drilling site did not identify the sulphur crystals, but reported that samples had a strong sulphur smell. Note also that this is possibly the same trachyte unit encountered from 288-345 m in CL5. The different depths of intersection in the two wells suggest that this lava dips northward or north westward which is consistent with the structure of the Fogo volcano. Also important to note is that near the top of this trachyte lava there is a zone of stronger mineralization with clusters of pyrite, calcite and quartz. This zone does not occur in CL5, suggesting that the mineralization may be associated with a specific fracture zone passing through the lava. This is consistent with the sulphur crystals reported above.

327-400 m –*Lithic tuff and pumice-lithic tuff*. The formation is light grey to tan, moderately consolidated. Matrix of white to tan ash, partially altered to clay, comes up mainly as clusters and as coatings on the lithics but locally is also indurated by silicification. Lithics of light grey to dark grey lava, porphyritic with sanidine phenocrysts. Grey pumice is not found much in the whole interval but is dominant at 333 m, suggesting that a pumice bed could had been deposited here.

420-448 m - *Trachyte lava*. The lava is light grey to light brownish grey, moderately hard, with abundant oxide stains, fine grained, porphyritic with sanidine phenocrysts.

448-500 m – *Lithic tuff and crystal-lithic tuff*. The formation is light grey to brown and purple, poorly to well consolidated. Matrix of ash altered to white to grey clay, mostly washed away during drilling but appears as coatings on the lithics. Lithics of lava include trachyte and basalt types, some scoria and minor altered rock.

500-581 m – *Lithic tuff*. The formation is dark grey to brownish and purple grey. Matrix of ash altered to brown clay (mainly smectite). Lithics of mostly grey to dark grey lava, fine-grained, porphyritic with sparse sanidine phenocrysts, locally with calcite replacements. Minor lithics of trachyte lava and volcanic glass. Common loose feldspar and loose silica fragments (likely microcrystalline quartz or chalcedony), the later from open space fillings (veins and veinlets). The lava lithics exhibit common oxide staining. At 541 m vesicular lithics of lava with chalcedony amygdales were found. It is noticeably that the amount of the silica veins increases with depth.

581-620 m - *Basalt lava*. The lava sequence is dark grey, moderately hard, fine grained, with common calcite + quartz replacements, veins and veinlets (locally associated with chlorite). The interval has abundant white to hyaline loose crystals, from open space fillings (veins and veinlets), mainly corresponding to quartz and quartz + calcite. Moderately altered, mainly open space fillings and replacements of silica, calcite. The groundmass is locally chloritized onward from 587 m.

620-668 m – *Lithic tuff*. The formation is dark grey to brownish grey. Matrix of brown to red-brown altered ash, altered to clay and moderately indurated by silicification from the deposition of microcrystalline quartz. Lithics of mostly basalt lava, dark grey, aphanitic, vesicular with calcite + quartz and quartz fillings, locally plus chlorite with hematite on the rims. Clear calcite and quartz crystals are relatively common and loose microcrystalline quartz + calcite crystals are relatively abundant.

668-680 m - *Basalt lava.* The lava is dark grey, aphanitic, fine-grained, with quartz + calcite + chlorite replacements. Abundant white to white green open space fillings from amygdales, veins and veinlets. Common silica eggs likely quartz. Moderately altered, mainly clay, silica, chlorite and iron oxides.

680-710 m - *Lithic tuff*. The formation is variable coloured, dark grey, dark brown and light brown-green, moderately consolidated. Matrix of dark brown to light brown clay, locally indurated by silicification. Lithics of grey to blue-green, grey and dark grey lavas with common calcite + quartz replacements (locally plus chlorite). Moderately altered, mainly clay, calcite, silica, chlorite and iron oxides.

710-811 m - *Basalt lava*. The lava is dark grey, hard to moderately hard, porphyritic with olivine and sparse pyroxene phenocrysts. This appears to be a relatively continuous sequence with only minor breaks, caused by brecciation between lava flows. Hyaline and white loose crystals are relatively abundant from open-space fillings (veins and veinlets) with the most common assemblages found being quartz, quartz + calcite and quartz + calcite + chlorite, locally with hematite (abundant at 716 m). From 750 m the lava sequence is weakly chloritized but the chloritization peaks and is intense below 787 m. Rare occurrence of red jaspe, likely from veins. According to the detailed petrographic analysis, prehnite is also occasionally present, often associated with calcite. Additionally, at 775 m growing aureoles of secondary albite were found around the plagioclase phenocrysts.

811-910 m - *Altered rock*. The formation is white to greenish grey, moderately hard, pervasively altered to silica and chlorite. The alteration obscures the original lithology of the formation but relict textures suggest that at least part of this sequence may be pyroclastic. In this interval, calcite is common but its intensity is significantly weaker than above. The cuttings become very fine below 826 m, making it even more difficulty to identify the rock type. The rock is overall silicified and with very fine disseminated pyrite. XRD and detailed petrographic analysis revealed that there is abundant zeolite within the rock fragments (probably laumontite or wairakite) as well as secondary albite. The appearance of epidote is at 823 m.

910-1239 m – No information. Drilled without returns.

CL7

Well CL7 was drilled to 1,166 m between February 27 and April 8, 2010. The 13-3/8´´ production casing was set at 599 m and the 9-5/8´´ slotted liner was installed at 1,147 m, hanging at 567 m depth inside the production casing. The lithological units intersected by the well can be summarized as follows:

0-120 m: *Pyroclastic rock units*. The deposits include lithic tuff, crystal-pumice tuff and pumice beds. Variable amounts of loose crystals of sanidine are found in this interval but they are abundant at 40-46 m. Two pumice beds are found in this interval at 26-36 m and 104-108 m.

120-270 m: *Lithic tuff*. Light grey to light greenish grey, poorly to moderately consolidated. Matrix of ash altered to white and light grey clay (mostly smectite, coexisting with kaolinite at the top and from 200 m with illite), locally silicified likely due to the deposition of opal and/or chalcedony. Lithics of mostly light grey trachyte lava. Clay alteration peaks at 126 m and silicification is stronger below 240 m. Pyrite appears at 110 m and quartz appears at 234 m.

270-308 m: *Trachyte lava*. White to light greenish grey, moderately soft, mostly altered to clay and locally indurated by silicification. Common fine disseminated pyrite.

308-384 m: *Pyroclastic rock units*. Two lithic tuff units are present at 308-366 m and 370-384 m, interrupted by a thin basalt lava flow at 366-370 m. The tuff is pervasively altered to white and white-green clay (mainly illite, coexisting with chlorite at the bottom of the interval) and is weakly to strongly silicified, locally with patchy chlorite. The lithics of lava are mostly of basaltic composition, with calcite + quartz replacements.

384-416 m: *Trachyte lava*. Light grey, fine-grained, compact, with quartz replacements. The alteration is more intense in the top of the interval in the less dense part of the lava flow. This sequence differs from the trachyte lavas commonly found in geothermal field, as the sanidine phenocrysts that are often present in these type of lavas are not evidently present in this section, possibly eroded due to alteration.

416-500 m: *Lithic tuff*. The formation is light grey to grey, moderately consolidated. Matrix of ash is pervasively altered to white and light greenish grey clay, indurated by silification and locally chloritized. Lithics are mostly trachyte lava. Common loose quartz, quartz + calcite crystals whose abundance peaks at 464 and at 476 m; additionally, loose pyrite is abundant in the whole interval.

500-522 m: *Trachyte lava*. The lava is light grey to white, moderately hard, fine-grained, with sugary appearance, locally with feldspar phenocrysts being replaced by clay, hematite and quartz.

522-588 m: *Pyroclastic rock units*. At least two lithic tuff deposits are found in this interval. The ash matrix is overall silicified and chloritized. The lithics of lava are predominantly of basalt with common quartz + calcite veinlets and replacements.

588-596 m *Basalt lava*. Dark grey, hard, aphanitic, with calcite + quartz replacements and patchy hematite. Locally chloritized.

596-620 m: *Lithic tuff*. Moderately consolidated, this unit is more homogeneous than the pyroclastic units found above from 522-588 m.

620-1173 m: No information, drilled without returns.

APPENDIX II: Lithology logs of wells CL4-A, CL5, CL6, and CL7

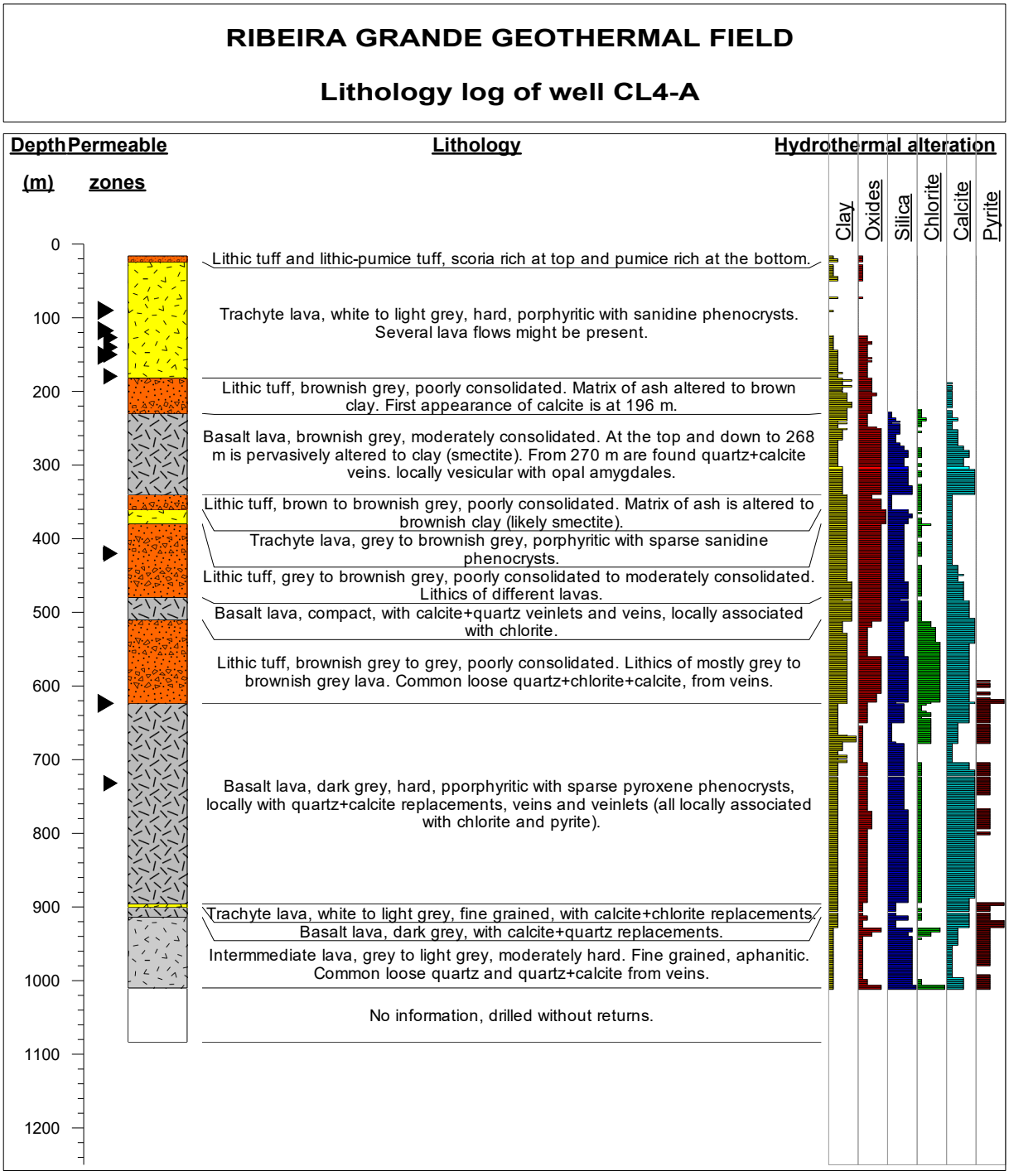

Company Name: EDA RENOVÁVEIS, S.A.
Drilling Contractor: Iceland Drilling; Drilling rig: Jotunn
Drilling dates: June 3 - July 26, 2012; Total drilling time = 56 days
Well Coordinates (UTM WGS 84 - Zone 26N):
East = 632.872 m; North = 4.183.047 m; Elevation = 441 m Drilled depth = 1173 m

RIBEIRA GRANDE GEOTHERMAL FIELD

Lithology log and alteration zones of well CL5

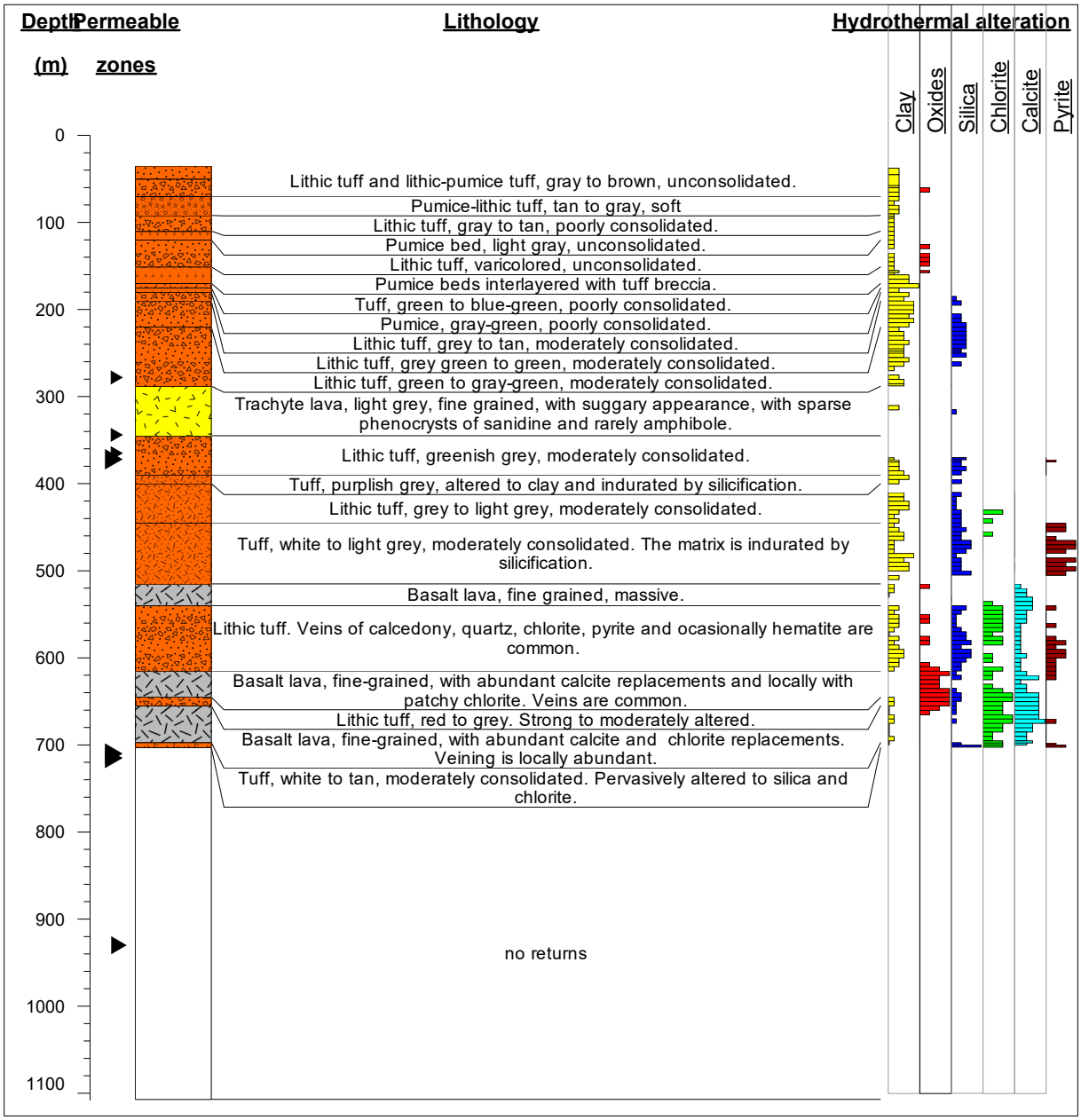

Company Name: EDA RENOVÁVEIS, S.A.
Drilling Contractor: Iceland Drilling; Drilling rig: Jotunn
Drilling dates: Oct, 31st, 1999 to Jan, 17th, 2000; Total drilling time = 62,0 days
Well Coordinates (UTM WGS 84 - Zone 26N):
East = 633.028,2 m; North = 4.182.428,20 m; Elevation = 495,0 m Drilled depth = 1.139,0 m

RIBEIRA GRANDE GEOTHERMAL FIELD

Lithology log of well CL6

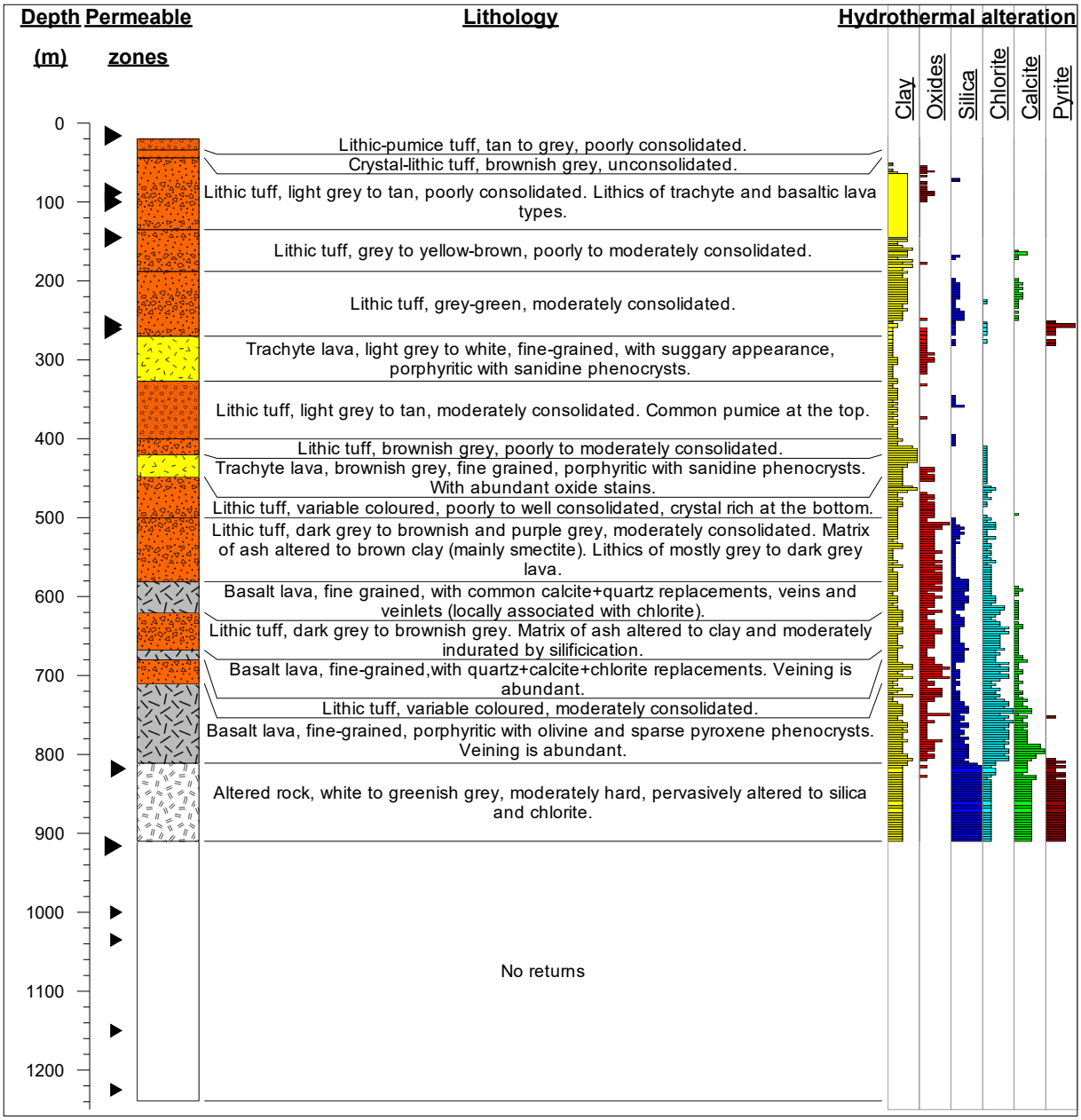

Company Name: EDA RENOVÁVEIS, S.A.
Drilling Contractor: Iceland Drilling; Drilling rig: Ingerssol Rand RD20 (1st stage. from 0 to 135 m); Jotunn
Drilling dates: January, 26th to April, 27th, 2005; Total time for operations = 54 days
Well Coordinates (UTM WGS 84 - Zone 26N):
East = 633.048,9 m; North = 4.182.402,50 m; Elevation = 503.5 m Drilled depth = 1239.2 m

RIBEIRA GRANDE GEOTHERMAL FIELD

Lithology log of well CL7

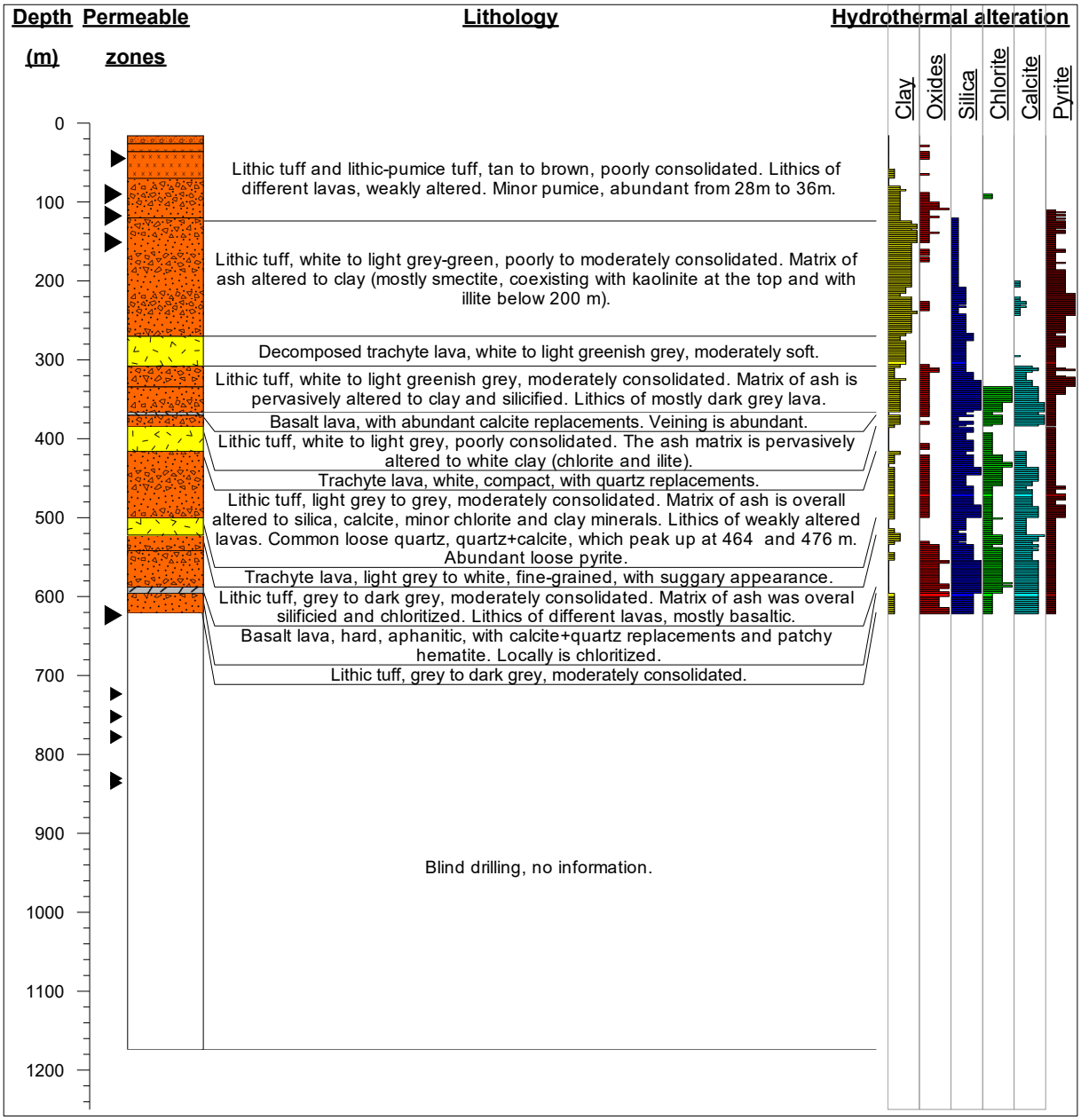

Company Name: EDA RENOVÁVEIS, S.A.
Drilling Contractor: Iceland Drilling; Drilling rig: Jotunn
Drilling dates: February 27 - April 8, 2010; Total time for operations = 40 days
Well Coordinates (UTM WGS 84 - Zone 26N):
East = 633.024 m; North = 4.182.605 m; Elevation = 487 m Drilled depth = 1173 m

APPENDIX III: Formation temperature profiles of wells CL1, CL2, CL3, CL4, CL4-A, CL5, CL6, CL7, and CL8

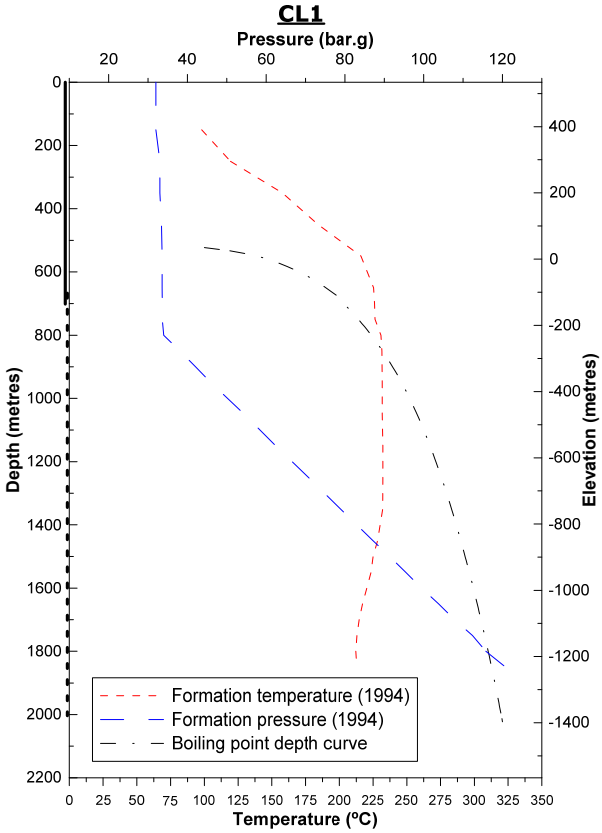

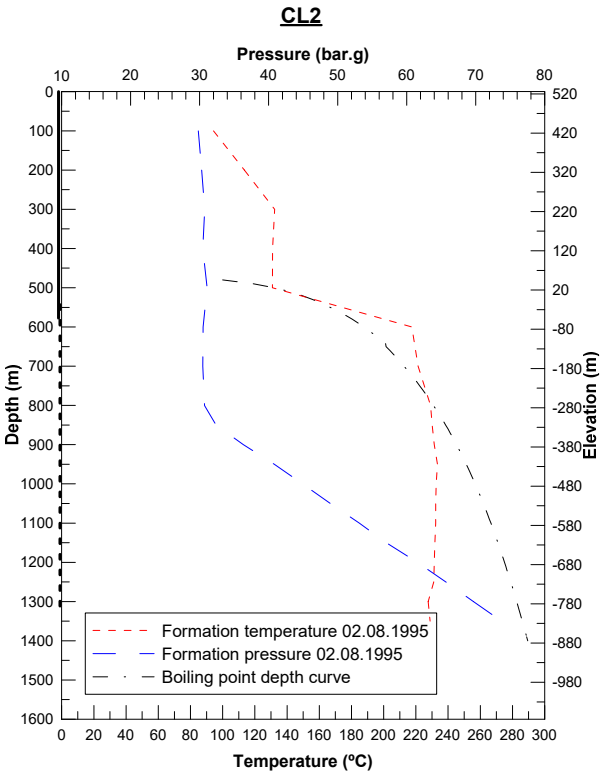

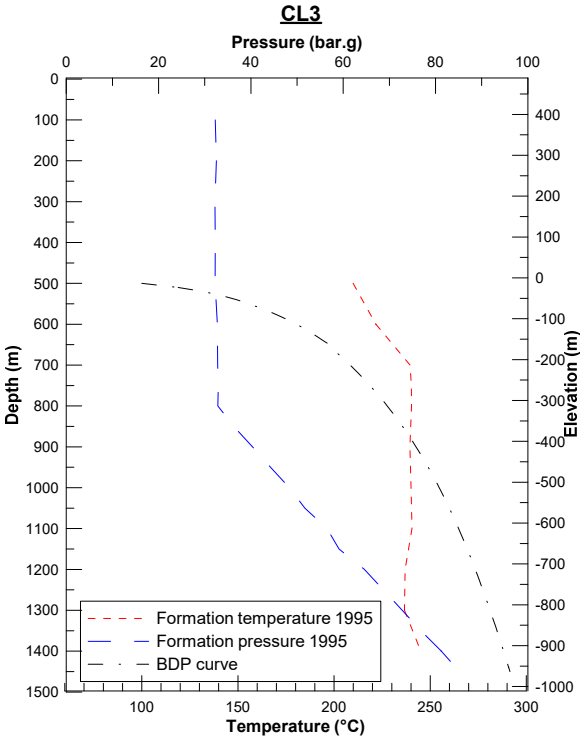

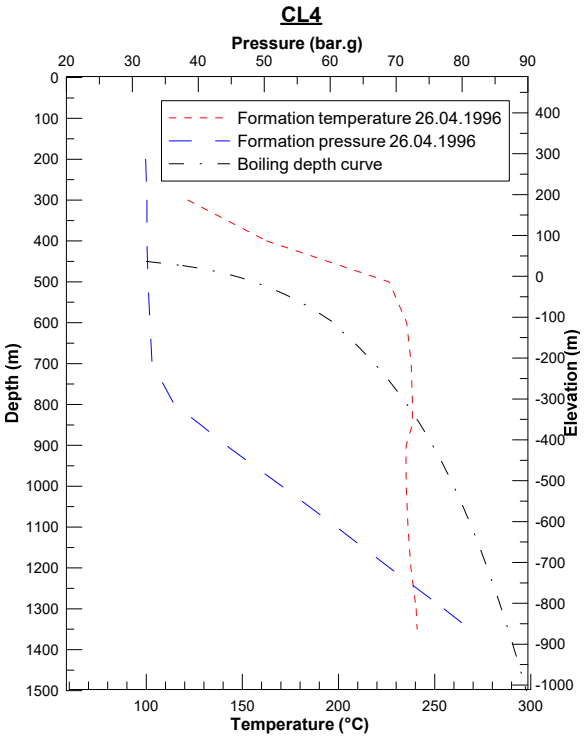

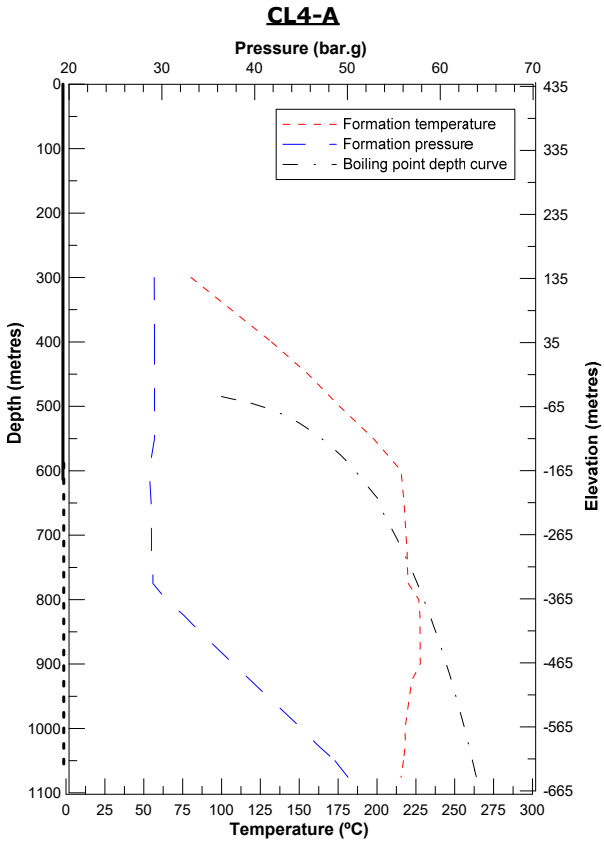
CL4-A
Pressure (bar.g)
Formation temperature
Formation pressure
Boiling point depth curve
Depth (metres)
Elevation (metres)
Temperature (ºC)

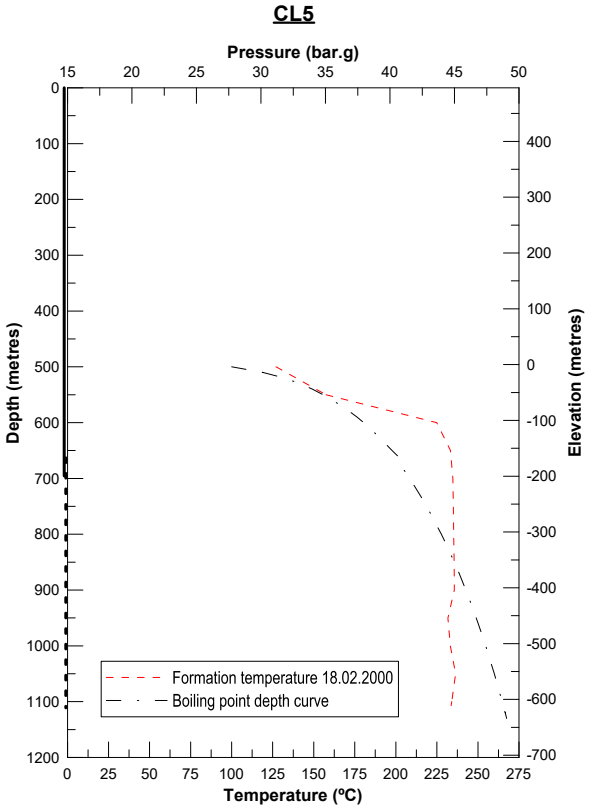
CL5
Pressure (bar.g)
Formation temperature 18.02.2000
Boiling point depth curve
Depth (metres)
Elevation (metres)
Temperature (ºC)

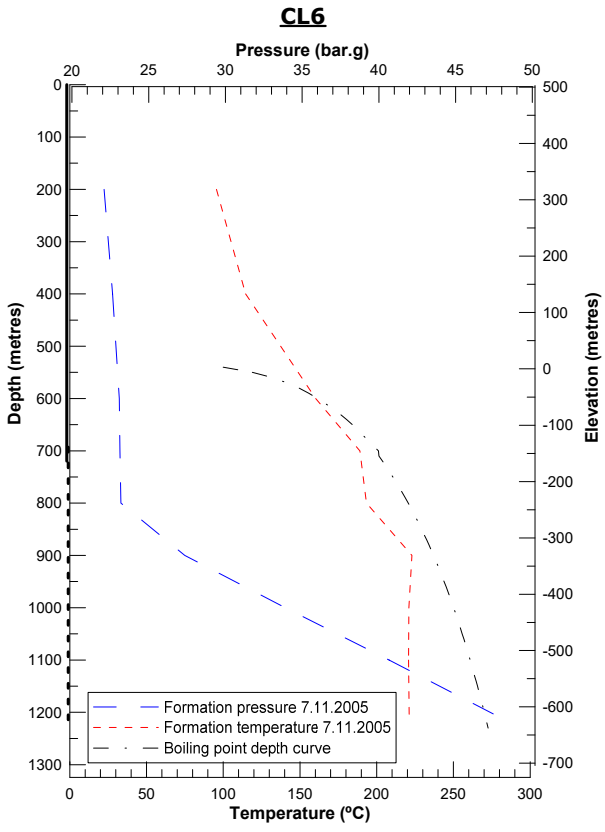
CL6
Pressure (bar.g)
Formation pressure 7.11.2005
Formation temperature 7.11.2005
Boiling point depth curve
Depth (metres)
Elevation (metres)
Temperature (ºC)

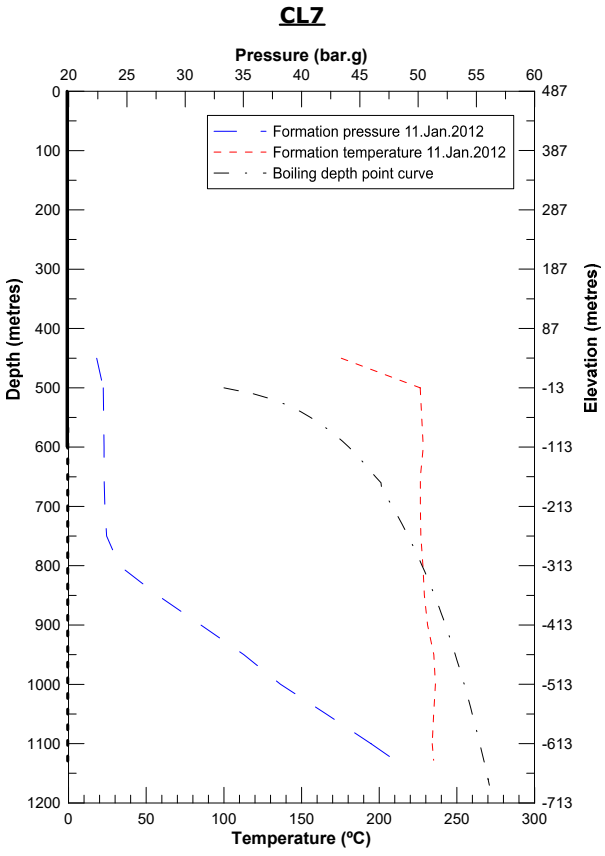
CL7
Pressure (bar.g)
Formation pressure 11.Jan.2012
Formation temperature 11.Jan.2012
Boiling depth point curve
Depth (metres)
Elevation (metres)
Temperature (ºC)

APPENDIX III: X-ray diffractometry results from wells CL4-A, CL5, CL6, and CL7

X-ray diffractometry analyzis conducted at ISOR laboratory (2015)

Well	Depth (m)	Untreated (Å)	Glycolated (Å)	Heated (Å)	Minerals identified
CL4-A	236	n.d.	n.d.	n.d.	no clays
CL4-A	280	13.02	14.22	10.08	Smectite
CL4-A	348-350	13.02	14.22	10.13	Smectite
CL4-A	450-452	10.94/7.21	10.94/7.21	10.29/n.d.	Kaolinite. Ilite is probably present but there is a odd shift in the heated peak.
CL4-A	550-552	14.83/10.03	14.83/10.03	7.24/10.03	Chlorite and minor traces of ilite
CL4-A	638	14.62/10.14	14.62/10.14	7.24/10.14	Chlorite. Ilite might be present, but the fact that the heated peak is higher than the untreated is kinda odd.
CL4-A	730-732	12.86/7.20	14.05/7.02	9.96/n.d.	Smectite. Minor traces of kaolinite
CL4-A	934	14.71/10.58	14.71/10.58	7.2/10.58	Chlorite + Ilite
CL4-A	836	14.69/10.30	14.69/10.30	7.22/10.30	Chlorite and minor traces of ilite
CL4-A	1008	14.37	14.37	7.14	Unstable chlorite
CL5	170-175	n.d.	n.d.	n.d.	no clay
CL5	220-250	6.62	6.62	6.62	no clay. Traces of some type of feldspar.
CL5	345-390	12.37/6.58	13.51/6.58	10.11/6.58	Smectite. Traces of some type of feldspar
CL5	490-495	6.59	6.59	6.59	No clay. Traces of some type of feldspar
CL5	525	n.d.	n.d.	n.d.	no clay
CL5	590-605	14.34/14.34	14.3/14.34	13.99/7.20	Unstable chlorite
CL5	655	14.34/14.34/10.23/6.43	14.34/14.34/10.23/6.43	14.34/7.18/10.23/6.43	Unstable chlorite. Minor traces of ilite and some type of feldspar
CL5	705	17.48/11.46	17.48/11.46	n.d.	Residual peaks at 17 and 11A, but no positive identification
CL7	140-148	17.48/7.32	17.48/7.32	10.26/n.d	Smectite + kaolinite
CL7	198	13.75/6049	15.65/6.49	10.01/6.49	Smectite. Traces of some type of feldspar
CL7	234	10.38	10.38	10.38	Possibly ilite, but there is a rather weird heated peak, which is higher than the glyco and untreated peaks (these are very low, almost absent)
CL7	280-286	10.53	10.53	10.53	Ilite
CL7	380	14.52/10.79	14.52/10.79	7.31/10.79	Chlorite + Ilite, almost equally abundant.
CL7	448-452	14.34/12.80	14.34/13.15	7.24/10.07	Chlorite coexisting with smectite (not MLC), almost equally abundant.
CL7	540	14.54/14.54	14.54/14.54	7.18/10.07	Chlorite + smectite, equally abundant.
CL7	560	14.45/12.78	14.45/13.38	7.18/10.03	Chlorite+Smectite, with chlorite more abundant.
CL7	614	14.32/10.03	14.32/10.03	7.18/10.03	Chlorite and minor ilite
					n.d. = no difraction

X-ray diffractometry analyzis conducted at Faculdade de Ciencias da Universidade de Lisboa (2005)

Well	Depth (m)	Untreated (Å)	Glycolated (Å)	Heated (Å)	Minerals identified
CL6	217	n.a.	n.a.	n.a.	Sanidine, Clorite and ilite
CL6	397	n.a.	n.a.	n.a.	Sanidine, quartz and ilite
CL6	415	n.a.	n.a.	n.a.	Sanidine and ilite
CL6	563	n.a.	n.a.	n.a.	Sanidine, quartz and ilite
CL6	704	n.a.	n.a.	n.a.	Quartz, sanidine, hematite and ilite
CL6	727	n.a.	n.a.	n.a.	quartz, hematite, albite and chlorite (nimite)
CL6	793	n.a.	n.a.	n.a.	Quartz, hematite, chlorite (nimite) and ilite (?)
CL6	814	n.a.	n.a.	n.a.	quartz, albite, Chlorite and ilite
CL6	910	n.a.	n.a.	n.a.	Quartz, ortoclase, albite and traces of ilite
CL5	703	n.a.	n.a.	n.a.	Albite, quartz and chlorite
					n.a. = not available

UNITED NATIONS UNIVERSITY
UNU-GTP
Geothermal Training Programme

Orkustofnun, Grensasvegur 9,
IS-108 Reykjavik, Iceland

Reports 2015
Number 11

ASSESSMENT OF PROJECT MANAGEMENT MATURITY AT LANDSVIRKJUN – POWER PROJECTS DEPARTMENT DIVISION

Kasu Girma
Ethiopian Electric Power – EEP
Aluto Geothermal Project Office
P.O. Box 1233
Addis Ababa
ETHIOPIA
girmakasu@gmail.com

ABSTRACT

This report is focused on assessment of project management maturity at Landsvirkjun-Power Projects Department Division. Interviews, a five level project management maturity model and the ten Project Management Body of Knowledge (PMBoK) areas were used as the main assessment tools. The results indicate that, the project management maturity level at the Power Projects Department is at level 3. A future plan is proposed to do a similar assessment in a power company in the home country of the author.

1. INTRODUCTION

1.1 General overview

Project management practice can be applied in project based organisations as well as in business organisations. According to the Project Management Body of Knowledge (PMBoK) (PMI, 2013), project management is the application of knowledge, skills, tools, and techniques to project activities to meet the project requirements. This application of knowledge requires the effective management of the project management processes. Such management process is very important in project based organizations, for instance, in the energy sector. This applies especially in geothermal energy research and development as geothermal project activities can be take a long time to meet project deliverables. Integrated and well organized management processes like organizational project management are therefore very important for such projects and others. Organizational Project Management (OPM) is a strategy execution framework utilizing project, program, and portfolio management as well as organizational enabling practices to consistently and predictably deliver organizational strategy producing better performance, better results, and a sustainable competitive advantage (PMI, 2013).

An organization measures its capabilities, then plans and implements improvements towards the systematic achievement of best practices (PMI, 2013). One way of measuring capability or maturity of organization project management practices is deploying of an assessment tool by using interviews and different maturity models. Different project management maturity models are developed to measure project management maturity of organizations. The PM solutions project management maturity model is one of the maturity model tools that was adopted and used to measure project management maturity

level of the Projects Department Division of Landsvirkjun, the national power company of Iceland. The purpose of the assessment is to measure the maturity of project management practices at the Power Projects Department and give recommendations for future improvement.

1.2 Scope

The scope of the project was:

- To assess the project management maturity level at Landsvirkjun, Power Projects Department Division;
- To establish the department's progress in maturity level and give recommendations for future improvement

1.3 Methodology

The maturity assessment was done through following steps:

1. Document review;
2. Assessing project management practices at selected department offices by using a sample questions survey and conducting face to face interviews;
3. Evaluate the gathered information and determine the maturity level of each knowledge area through using the five levels of PM maturity model.

1.4 Why do assessments?

As stated by Alice Zavala (2005) doing the maturity assessment at organization can give the following stated benefits to organization. The Power Projects Department also can benefit from the assessment through other advantages as the assessment:

- Provides a clear picture of current state and define future state;
- Identifies the gaps and provides a roadmap for organization change;
- Motivates the organization to reach a better state;
- Motivates individuals to grow and develop current skills and educate the organization on best practices.

During the assessment, interviews were only conducted with a few selected people at the department.

1.5 Description of the company

Landsvirkjun is exploring a number of potential power projects all over the country (approximately 20). These projects are at varying stages within the preparation and authorization process which involve a detailed feasibility and environmental study. There is also a long-term planning and authorization process during which institutions, stakeholders and the public are given the opportunity to provide feedback during the various stages of each project. Good quality information is essential for preparing the initial power project layout to ensure minimum environmental impact (Landsvirkjun, 2014).

The Research and Development division is responsible for developing new power projects from prefeasibility design phase and up to tendering and construction phase when Construction Division takes over. Within the Research and Development Division, Power Projects Department ”owns“ the projects and provides most of the project managers, Research Department provides project managers for exploration and resource research, Environmental Department provides project managers for

environmental and planning activities and Internal Department provides project control. The organizational chart of the company is shown in Figure 1.

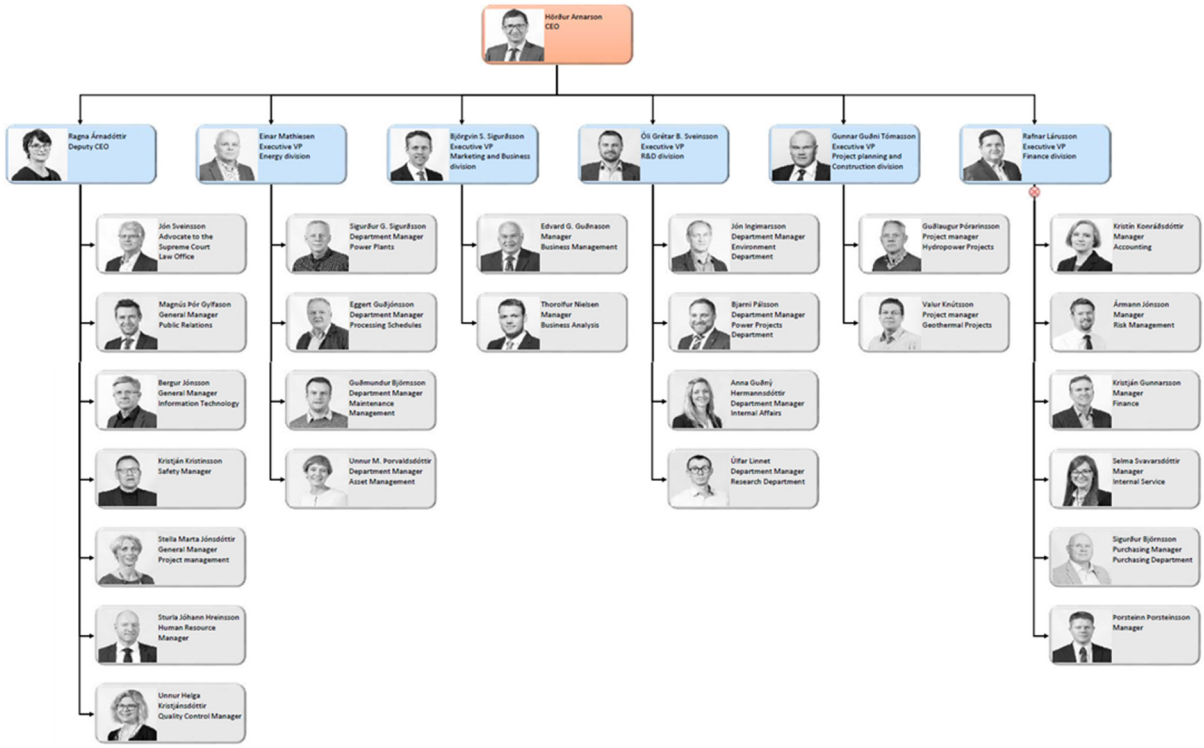

FIGURE 1: Landsvirkjun organisational chart

2. LITERATURE REVIEW

Project management maturity refers to the progressive development of project management practice in project, program and portfolio management in a project based organization. Before dealing with the maturity assessment it is important to understand the project management terminology definitions and concepts as described below.

2.1 Project and project management

A project is a temporary activity which has definite starting and end. According to PMBoK, project management is the application of knowledge, skills, tools, and techniques to project activities to meet the project requirements. Project management is accomplished through the appropriate application and integration of 47 logically grouped project management processes, which are categorized into five process groups (initiating, planning, executing, monitoring and controlling, and closing) (PMI, 2013).

2.2 Program and portfolio management

According to PMBoK (PMI, 2103), program is defined as a group of related projects, subprograms, and program activities managed in a coordinated way to obtain benefits not available from managing them individually while program management is the application of knowledge, skills, tools, and techniques to a program in order to meet the program requirements. A project may or may not be part of a program but a program will always have projects.

A portfolio refers to projects, programs, sub-portfolios, and operations managed as a group to achieve strategic objectives while portfolio management refers to the centralized management of one or more portfolios to achieve strategic objectives. The projects or programs of the portfolio may not necessarily be interdependent or directly related (PMI, 2013).

2.3 Project Management Maturity Model (PMMM)

Project management maturity refers to the progressive development of an enterprise-wide project management approach, methodology, strategy and decision making process. Project Management Maturity Model (PMMM) is a formal tool developed by PM Solutions and used to measure an organisation's project management maturity. Once the initial level of maturity and areas for improvement are identified, the PMMM provides a roadmap, outlining the necessary steps to take toward project management maturity advancement and performance improvement (Crawford, 2006).

2.4 Project Management Body of Knowledge (PMBoK)

Project management body of knowledge describes that the overall knowledge with in the profession of project management and includes tools and techniques used to manage project management process and practices. There are ten knowledge areas according to the PMBoK guide (PMI, 2013) as described below.

1. Project integration management
Project integration management includes the processes and activities to identify, define, combine, unify, and coordinate the various processes and project management activities within the project management process groups.

2. Project scope management
Project scope management includes the processes required to ensure that the project includes all the work required and to complete the project successfully. Managing the project scope is primarily concerned with defining and controlling what is and is not included in the project.

3. Project time management
Project time management includes the processes required to manage the timely completion of the project. Plan schedule, define and sequence activity, resource and duration estimation, develop and control schedule are the processes required in project time management.

4. Project cost management
Project cost management includes the processes involved in planning, budgeting, financing, funding, managing, and controlling costs so that the project can be completed within the approved budget.

5. Project quality management
Project quality management includes the process and activities of the performing organization that determine quality polices, objectives, and responsibilities so that the project will satisfy the needs for which it was undertaken. It works to ensure that the project requirements, including product requirements, are met and validated.

6. Project human resource management
Project human resource management includes the processes that organize, manage, and lead the project team. The project team is comprised of the people with assigned roles and responsibilities for completing the project.

7. Project communications management
Project communications management includes the processes required to ensure timely and appropriate planning, collection, creation and distribution, storage, retrieval, management, control, monitoring and the ultimate disposition of project information.

8. Project risk management
Project risk management includes the processes of conducting risk management planning, identification, response planning, and controlling risk on a project. The objectives of project management are to increase the likelihood and impact of positive events, and decrease the likelihood and impact of negative events in the project.

9. Project procurement management
Project procurement management includes the processes necessary to purchase or acquire products, services, or results needed from outside to the project team. The organization can be buyer or seller of the products, services, or results of a project. It includes the contract management and change control processes required to develop and administer contracts or purchase orders issued by authorized project team members.

10. Project stakeholder management
Project stakeholder management includes the processes required to identify the people, groups, or organizations that could impact or be impacted by the project, to analyse stakeholder expectations and their impact on the project, and to develop appropriate management strategies for effectively engaging stakeholders in project decisions and execution.

3. METHODOLOGY

The main methods used in this assessment were interview and five levels of maturity model from PM Solutions project management maturity model.

3.1 Interview

Face to face interviews with 5 project managers were conducted in this assessment to gather data about the project management practices at Landsvirkjun-Power Projects Department. They were conducted with 5 project managers at the Power Projects Department in their offices. The department manager and four project managers were selected for interviews, as listed below:

1. Dr. Bjarni Pálsson, manager, Power Projects Department, R&D Division.
2. Ms. Anna Gudný Hermannsdóttir, manager internal matters, Power Projects Department, R&D Division.
3. Dr. Egill Júlíusson, project manager geothermal projects, Research Department, R&D Division.
4. Mr. Kristján Einarsson, project manager geothermal projects, Power Projects Department, R&D Division.
5. Mr. Albert Gudmundsson, project manager hydro power projects, Power Projects Department, R&D Division.

These managers were selected for interview based on their knowledge and experience they had regarding project management practices. General criteria for the selection of people to interview was:

- To limit the scope of the assessment and minimize the complexity because it is impossible to assess the whole company within a short time;
- To get information easily from those who have more knowledge and experience about project management practices at the department.

The sample interview questions used in this report are prepared based on ten knowledge areas of PMBoK and by reviewing the maturity assessment documents done by Holmes and Walsh (2005) and Temesgen (2013) for guidance as described in Table 1 Appendix I.

3.2 Model

The model used in this assessment was adopted from project management maturity (Pennypacker and Grant, 2003) but it is redrawn based on the recent PMBoK by using the ten knowledge areas (PMI, 2013) and five level maturity of PM solutions project management maturity model as shown in Figure 2 below. The key characteristics of the five level maturity model were used as criteria to evaluate each component of knowledge areas based on the qualitative data result obtained from conducted interviews.

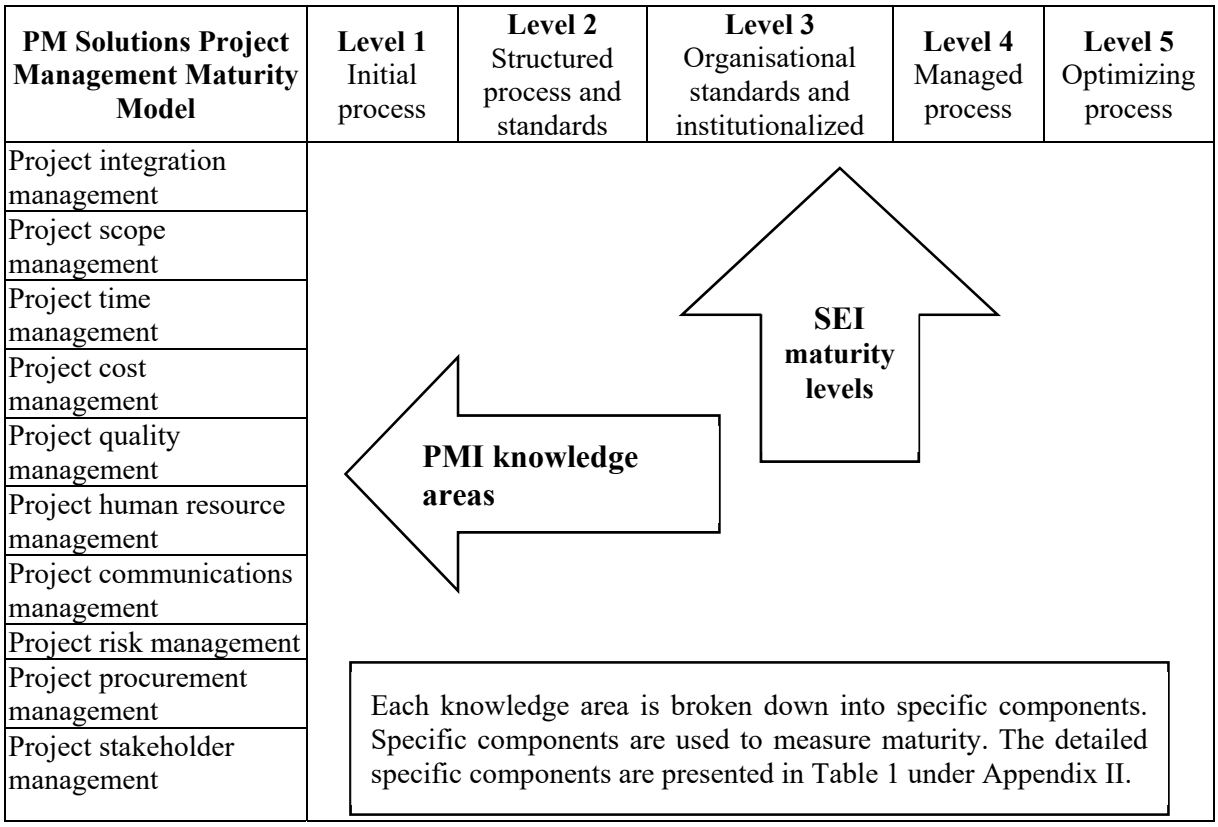

FIGURE 2: PM Solutions project management maturity model

The five maturity levels of PM solutions project management maturity model (Pennypacker & Grant, 2003) similar to those in the SEI capability maturity model are described here below.

Level 1: Initial process
"There is recognition on project management processes but there are not established practices and standards, and individual project managers are not held to specific accountability by any process standards. Documentation is loose and ad hoc and metrics are informally collected on an ad hoc basis. Management understands the definition of a project, that there are accepted processes and is aware of the need for project management" (Pennypacker, 2001).

Level 2: Structure process and standards
"Many project management processes exist in the organisation, but they are not considered organisational standards. Documentation exists on these basic processes and management supports the implementation of project management, but there is neither consistent understanding, involvement, nor

organisational mandate to comply for all projects. Functional management is involved in the project management of larger, more visible projects and these are typically executed in a systematic fashion. There are basic metrics to track project cost, schedule, and technical performance, although data may be collected/correlated manually. Information available for managing the project is often a mix between summary level data and detailed level data" (Pennypacker, 2001).

Level 3: Organisational standards and institutionalized process
"All project management processes are in place and established as organisational standards. Nearly all projects use this process with minimal exception – management has institutionalized the processes and standards with formal documentation existing on all process and standards. Project management processes are typically automated and management is regularly involved in input and decision making. Each project is evaluated and managed in light of other projects" (Pennypacker, 2001).

Level 4: Managed process
"Project is managed by considering the past performed and future expectation. Management uses efficiency and effectiveness metrics to make decisions and understands the impacts on other projects and to evaluate all projects, changes and issues from cost estimates, baseline estimates, and earned value. Project information, project management processes and standards are integrated with other corporate systems and processes. Processes and standards are documented. Management clearly understands its role in project management process and execute it well, managing at right level. Management styles and project management requirements for different sizes/complexities of projects are clearly differentiated" (Pennypacker, 2001).

Level 5: Optimizing process
"Processes are in place and actively used to improve project management activities. Lessons learned are regularly examined and used to improve project management processes, standards, and documentation. Management and organisation are not only focused on effectively managing projects but also on continuous improvement. The metrics collected during execution are used to understand performance of projects and for making organisational management decision for the future" (Pennypacker, 2001).

4. RESULTS

The direct results of the assessment gathered by using interviews are presented in Appendix I but the summary of the results is described below for each knowledge areas.

4.1 Project management knowledge areas

Project integration management
The direct result from interviews for the project integration management is given in Table 1 as shown in Appendix I and similar procedure for the rest of the knowledge areas. Project management processes were applied to power projects, especially to large projects. All projects were executed in a professional manner but sometimes the goals were not achieved within the planned time and cost, because in many cases unforeseen events lead to additional costs and time. For instance, permit issues, and geology are the main events. The project charter includes information regarding 'what, when, where, how and to whom' is available for project activities. Overall change control was performed by steering committee meetings to identify, evaluate, recommend and update plan of the changes. Generally, there was a coordinated system to plan, execute, monitor and control the project's activities.

Project scope management
The project scope is determined based on the project portfolio, company strategy and functional targets of project by steering committee (management) in meeting minutes. Management plan scope, collect

requirements, define scope, create work breakdown structure (WBS) and control scope processes were effectively used in the entire project activities. Scope change control was handled by steering committee to determine the causes of changes and evaluate before updating the plan.

Project time management
Project management software, MS Project and standard MS Excel, were the common systems used at organizational level for scheduling, estimating and work packages. Milestone plan and Gantt chart were the main tools used in time management process. The full Gantt chart was saved in house software share point (GoPro) – filing documentation system. The colour indictors (green, yellow and red lights) were used to manage time in '*villi*' **(**project overview system or VERKEFNAYFIRLIT)**.** The project time management document was available to project members by standard Excel template and also via department's web. The baseline schedules were not always maintained for each project because of different problems that could occur during the progress (sometimes in case of design).

Project cost management
The central database - MS Dynamics Ax (company software), Cognos, Earned Value and homemade Project Overview System 'Villi' were built for tracking cost changes. The standard Excel template was used for small projects and standard document was available for project team members. Both scope changes and cost estimations can be approved by management but sometimes scope changes were not approved in a formal way. The project cost was assigned based on project size, tasks and time.

Project quality management
Power Projects Department uses the organizational quality standards defined by the company. Regular ISO 9001, ISO 14000, ISO 18000, internal and external audits, stage gate process and external permit related process such as EIA, development permits were standards recognized by the company for quality assurance process and used to identify and measure product quality. The quality metrics (internal and external review process), process analysis (stage gate process), and project documents (Villi) were tools used to manage project quality.

Project human resource management
The project department has defined roles and responsibilities for project plan, execution and control in a simple organisational chart. Organization charts, networking, expert judgment, and meetings were tools used for planning HR management. Sometimes the project management attended training courses provided by project management office or project department and also informally through internal and external online. Furthermore, encouragement was given to project management members to apply for International Project Management Association (IPMA) certificates. The skill level of PM was defined based on experience and education as well as the department started to define PM to IPMA, at least level D, C or B and use IPMA guideline as reference.

Project communications management
The standard Excel sheet and Share Point (GoPro) were used to plan communications management for all projects. The most common communication management tools were meetings and sometimes external web and internal project 'Villi', email, and mobile phone were used. The final reports, lessons learned and previous experience were documented in the filing system Share Point (GoPro) and utilized informally for other projects.

Project risk management
Risk identification was done for each project at stage gate process, before any field exploration and during the whole project. Monte Carlo analysis for cost, decision trees are used typically for deciding drilling targets, scenario analysis, SWOT analysis, contingency plan and @Risk techniques were used in risk management. There was a defined and implemented process used to measure derivable risk lights (red, yellow and green) by standard Excel sheet and available to project team members.

Project procurement management
The procurement management process was available as written formal working procedure and formats for procurement plan execution. Not only procurement department but also project team and project managers had responsibilities on planning and requisitioning items as per organizational evaluation criteria. The schedules and cost targets were available during the purchasing process depending on the project size.

Project stakeholder management
The stakeholder management process was required to identify the people, groups and organisations that could impact or be impacted by projects. The stakeholder analysis, expert judgment and meetings tools were used to identify stakeholders. Project manager had responsibility to plan, manage, control and for decision making in stakeholder management. Most of the time the availability of relevant information for identified stakeholders was based on the communication plan.

4.2 Lessons learned

Lessons learned, final reports, previous experience and other related files were saved in house software share point (GoPro – filing documentation system), and available for all project team and utilized for other projects depending on the type of projects and their relevancy. Project managers were nominated and assigned to projects based on the necessary experience, knowledge and education level. Generally, there was good project management processes application to all projects and a plan for continuous improvement.

5. DISCUSSION

Five people were selected for interviews. Most of their responses on interview were in good alignment, even if there some different ideas were experienced. The interviews took one month, more than the planned time. The main reason was that the selected people were busy and hence it was difficult to schedule the face to face interviews.

A sum up of the final results is shown Table 1 below. A detailed evaluation of each knowledge area, by using the key characteristics of the five levels maturity as criteria, is shown in Table 1 under Appendix II. From the result, it is concluded that most of knowledge areas are at maturity level 3 while a few of them are below level 3. This indicates that all organizational standards and processes were not applied to all knowledge areas.

TABLE 1: Maturity results of each knowledge area

No.	Knowledge areas	PM solutions PM maturity levels					Actual
		1	2	3	4	5	
		Initial process	Structur. process	Org. standards	Manag. process	Optimiz. process	
1	Project integration management			3			3
2	Project scope management			3			3
3	Project time management			3			3
4	Project cost management			3.67			3.67
5	Project quality management			3			3
6	Project human resource management		2.50				2.5
7	Project communications management			3.33			3.3
8	Project risk management		2.83				2.8
9	Project procurement management			3.50			3.5
10	Project stakeholder management		2.50				2.5
	Power projects dept. maturity level						**3**

As we can see from the result project management integration had maturity level of 3. Most of power projects were executed in professional manner by applying the organizational standards and processes, but sometimes the goals were not achieved within the planned time and cost, because in many cases unforeseen events lead to additional cost and time. There were the integrated systems and process of knowledge areas in execution and controlling of project activities.

The scope, time, cost and quality management also were at maturity level 3. This means that standardized, documented, repeatable processes were available and applied to most of projects. The schedule integration process of scope, time, cost and quality were developed and implemented with program schedules at organizational standard's level. The organization had a standardized and documented quality system (ISO 9001, 14000, 18000) used at organizational level for most of power projects.

Project human resource and stakeholder management had maturity level greater than 2. It indicates that basic processes of HRM were well defined and applied to all projects. In the case of stakeholder management, also basic processes were defined and applied to most projects. Management supports and encourages staff to apply the stakeholder management process more in project management practice.

Project communications and risk management were at maturity level 3. It indicates that all organisational standards and repeatable processes were applied to most projects. The standard Excel sheet and share point (GoPro) were used to plan communications management for all projects. The standard project risk management plan was available to identify, analyse and mitigate risks before all filed exploration and during whole project progress for each project but not all processes were applied to all projects. There was a defined process which was applied to most of projects to measure derivable risk lights (red, yellow and green) by standard Excel sheet and Share Point (GoPro).

Project procurement had maturity level greater than 3. This indicates that all standards and repeatable processes were applied to all projects. There was a standard working procedure for executing procurement processes. Generally, the demonstration of each knowledge area's maturity level results of project maturity at Power Projects Department is shown using spider diagram as shown in Figure 3 below.

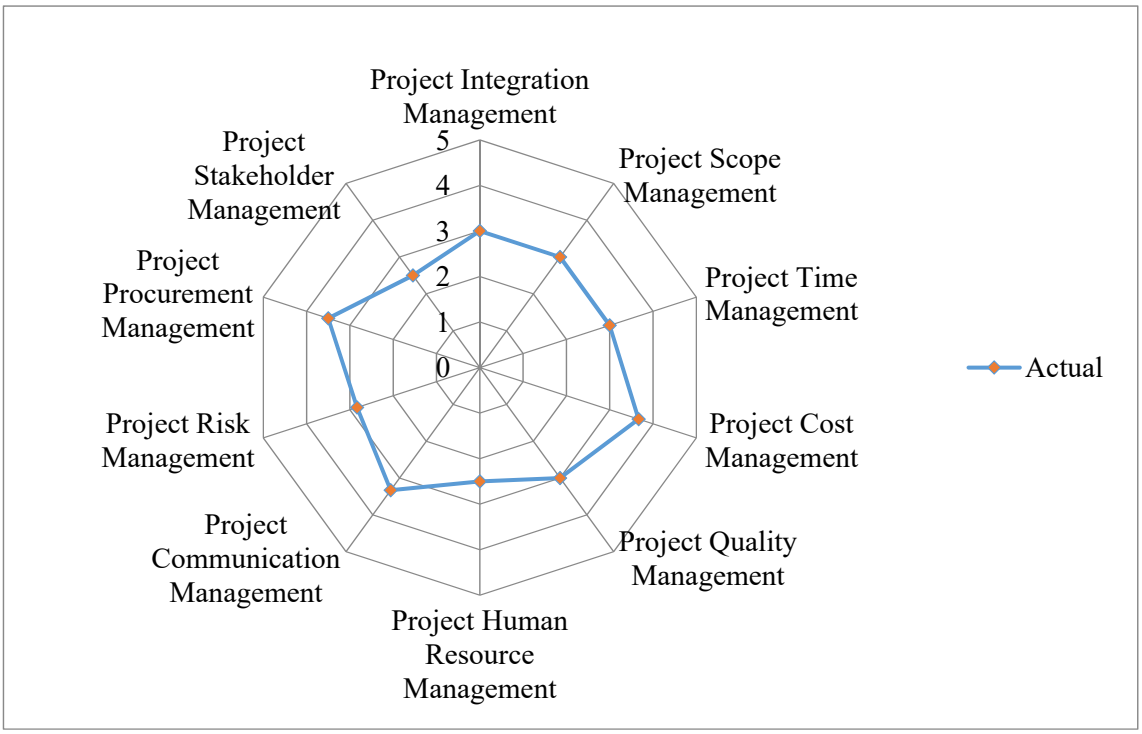

FIGURE 3: Actual result of maturity level of each knowledge areas

6. CONCLUSIONS AND RECOMMENDATIONS

Results from the assessment indicated that the Power Projects Department has used a lot of organisational standard resources in the implementation of most of power projects, especially large projects. But sometimes the baseline schedule (in case of some projects) was not kept within the planned resources, because in many cases unforeseen events occurred and lead to additional resources being required.

It is concluded that the overall project management maturity at Power Projects Department is at maturity level 3. This indicates that most organizational standards and processes were achieved by most of project management knowledge areas and applied to all projects. However, in some cases, knowledge areas were not completely standardized and thus processes not applied properly and ineffectively. The assessment tool also identifies areas to be focused on for improvement.

It is recommended that formal training be provided based on project management knowledge areas including organisational standards, and processes of project management, for the project team and others. This can increase the ability to implement all the standards and processes to all projects easily and will increase department as well as organisation performance, project deliverables and organisation changes, including individuals.

The act of measuring the project management maturity can help this organization to improve its effectiveness in project delivery. Doing more assessments at the Power Projects Department as well as to the whole company will thus help to understand the current status, measure performance, identify problem areas and plan future continuous improvements.

It is proposed to do a similar future assessment in a power company in the home country of the author. The plan is described in Appendix III.

ACKNOWLEDGEMENTS

I would like to express my gratitude to the Director of UNU-GTP, Mr. Lúdvík S. Georgsson, and his staff, Deputy Director, Mr. Ingimar Gudni Haraldsson, Ms. Málfrídur Ómarsdóttir, Ms. Thórhildur Ísberg, Ms. María S. Gudjónsdóttir and Mr. Markús A.G. Wilde. I would also like to thank other UNU-GTP staff and teachers for their support, guidance, time and help from the beginning to the end of the training that made it successful for me. I would also like to thank Ethiopian Electric Power Company for their support and encouragement to me to participate in the training, especially the Manager of Aluto Geothermal Project, Mr. Mulugeta Asaye.

I am greatly indebted to my supervisor Prof. Helgi Thór Ingason, Reykjavik University, for his great support and guidance through the course and report writing as well as Ass. Prof. Haukur Ingi Jónasson**,** Reykjavik University.

Special thanks to the Power Projects Department Manager Dr. Bjarni Pálsson and all the R&D members at Landsvirkjun - National Power Company, for their great contribution, time and willingness that made the report successful.

I would like to thank and appreciate my colleges Mr. Peketsa Mwaro Mangi, and Mr. Shammah Kipkogei Kiptanui, for their great guidance and support, and all other UNU-GTP fellows for the memorable time I enjoyed with them.

Finally, I would like to thank my lovely family for the support, moral, encouragement, and help during my stay in Iceland.

REFERENCES

Crawford, J.K., 2006: Project management maturity model (2nd ed.). Auerbach Publications, Taylor & Francis Group, Boca Raton, FL, US, 235 pp.

Holmes, S.J, and Walsh, R.T., 2005: *Conducting effective project management maturity assessment interviews.* Integrated Management Systems, Inc., Ann Arbor, MI, US, 32 pp.

Landsvirkjun, 2014: Potential power projects – Annual report 2014. Landsvirkjun, website: *http://annualreport2014.landsvirkjun.com/research-and-development/power-projects.*

Pennypacker, J.S., and Grant, K.P., 2003: Project management maturity: An industry benchmark. *Project Management Journal, 34*, 4-11.

PMI, 2013: *A guide to the project management body of knowledge PMBOK® guide* (5th ed.). Project Management Institute Inc. (PMI), Newton Square, PA, US, 589 pp.

Temesgen, T.W., 2013: *Assessment of project management capability (a case study at Mesfin Industrial Engineering PLC, Mekelle – Ethiopia)*. KTH Royal Institute of Technology, Stockholm, Sweden, MSc thesis, 36 pp.

Zavala, A, 2005: *Organizational project management maturity assessments*. Project Management Institute Inc. (PMI), San Francisco, California, United States, 45 pp.

APPENDIX I: Project Management Maturity assessment at Landsvirkjun – Power Projects Department Division - summary of results and sample of interview questions

TABLE 1: Project integration management results

No.	Project integration management	Mark 'x' in circle if you agree
1	Are all the projects executed in professional manner within planned time and cost?	○ Yes - **X**, but in many cases unforeseen events lead to additional cost and time. E.g. permit issue, geology, etc. ○ No ○ Not sure /Not applicable
2	Do you use the project charter?	○ Yes – **X**, in the project overview system; VERKEFNAFIRLIT/ "Villi" ○ No ○ Not sure /Not applicable
3	Does the overall change controls manage actual changes when they occur?	○ Yes – **X**, in the project overview system decision taken in the steering committee meetings. ○ No ○ Not sure /Not applicable
4	Who has responsibility in project planning, execution, and control? And approved by whom?	○ General Manager **– X**, approved by general manager ○ Deputy Manager ○ Project Manager -**X**, prepared by project managers
5	Does all project process management apply to all projects?	○ Yes – **X**, mostly apply to large power projects. ○ No ○ Not sure /Not applicable

TABLE 2: Scope management results

No.	Scope management	Mark 'x' in circle if you agree
1	Do you use all the scope management processes and apply to projects?	○ Collect requirements – **X**, this can be accepted at steering committee meetings stated in ○ Define scope – **X**, meeting minutes and presented in an updated project dates in Villi. ○ Create WBS - **X** ○ Verify scope - **X** ○ Control scope – **X**
2	Do you provide standard scope management documents for customers?	○ Yes – **X**, it is special template but most use only steering committee meeting minutes ○ No ○ Not sure
3	How is scope of project determined?	○ Direction from management? – **X**, it depends; most projects are aimed to support the project portfolio and company strategy but have a lot of external restrictions. ○ Developed from functional targets? – **X** ○ Direction from customers**?** ○ Other, if so describe _____
4	How is scope changed and controlled?	○ Direction from management? – **X**, by decision in steering committee ○ Direction from customers? ○ Change notice form project office? ○ Other, if so describe _____

TABLE 3: Time management results

No.	Time management	Mark 'x' in circle if you agree
1	What type of documents do you use for time management?	○ Milestone plans – **X**, ○ Project plans - Gantt chart - **X** ○ System plans ○ Master schedule plan - **X** ○ Other, if so describe
2	What type of tools/ techniques do you use for time management process?	○ Project management software -MS Project – **X** ○ MS Excel – **X**, in some cases (small projects) ○ List of tasks - **X** ○ Other, if so describe – **X**, In house software (share point – GoPro)
3	Is the baseline schedule maintained for each projects?	○ Yes- **X,** most of the time but it depends on the type of projects. ○ No ○ Not sure

4	Is the planned schedule available for all project teams via web or email?	○ Yes – **X,** an overview should be in 'Villi' but the full Gantt chart and MS project is saved in GoPro - filing system and restricted access to only those concerned, i.e. project team ○ No ○ Not sure

TABLE 4: Cost management results

No.	Cost management	Mark 'x' in circle if you agree
1	What systems / tools do you currently use to manage your project cost? Is standard method practiced for resource planning, cost estimation and budgeting? Yes /No – **Yes**	○ Project management software - MS Project ○ MS Excel – **X,** for small projects ○ Earned Value Management / Forecasting ○ Other, if so describe - **X,** MS Dynamics Ax, Cognos, Villi
2	How are project costs assigned?	○ By project - **X** ○ By tasks and time - **X** ○ By department ○ WBS ○ Other, if so describe _____
3	What method do you use for tracking costs? Is there a built system for cost tracking? Yes/No - **Yes**	○ Central database - **X,** MS Dynamics Ax, Cognos, Villi ○ Project manager maintains a spreadsheet ○ Project engineers' spreadsheet ○ Other, if so describe _____
4	Are scope changes and cost estimates approved by management?	○ Yes - **X,** by management but sometimes scope changes are not approved in a formal way ○ No ○ Not sure/Not applicable

TABLE 5: Quality management results

No.	Quality management	Mark 'x' in circle if you agree
1	Is there software based systems / tools that you currently use to manage your project quality? Is the company ISO certified? Yes/No- **Yes**	○ Quality management and control tools – **X,** IS O 9001, 14000, 18000 ○ Seven Basic Quality Tools ○ Quality metrics and audits - **X,** Review process (external review and stage gate process) ○ Process analysis - **X** ○ Project documents – **X,** Project overview system - Villi ○ Not applicable

2	Are quality goals methods and systems established for each project?	○ Yes ○ No - **X,** they have to meet internal and external criteria ○ Not sure
3	Are quality assurances processes established and recognized by your organization?	○ Yes - **X,** Regular ISO 9001, 14000 and 18000, internal and external audits, stage gate process, and external permit related process such as; EIA, development permits, etc. ○ No ○ Not sure
4	Are there performance/quality standards used to identify and measure project's product quality?	○ Yes – **X**, ISO 9001, 14000, 18000 ○ No ○ Not sure

TABLE 6: Human resource management results

No.	HR management	Mark 'x' in circle if you agree
1	Are your project management practices and process consistent across divisions and functional groups?	○ Yes - **X** ○ No ○ Not sure
2	What systems / tools do you currently use to plan HR management in your projects?	○ Organization charts and position descriptions - **X** ○ Networking - **X** ○ Organizational theory ○ Expert judgment - **X** ○ Meetings - **X** ○ Other, if so describe
3	Are PM training courses identified and training provided?	○ Yes - **X,** internal online, external and encourage Project managers to take IPMA certificates and sometimes PMO also provides the training ○ No ○ Not sure
4	Do you have defined roles and responsibilities for all project members?	○ Yes - **X,** in most cases some projects team and others are described in a simple organization chart ○ No ○ Not sure/Not applicable
5	Do you have a defined skill level for project manager?	○ Yes - **X,** usually based on experience and education level, but currently at least IPMA level D, C, B ○ No ○ Not sure/Not applicable

TABLE 7: Communications management results

No.	Communications management	Mark 'x' in circle if you agree
1	What kind of techniques and tools do you use to plan communications?	○ Communication requirements analysis ○ Communication technology – **X,** external web and internal project Villi ○ Communication models and methods - **X,** on standard Excel template (who will take to who, when, how often) for all projects ○ Meetings – **X,** primary tool ○ Other, if so describe _____
3	Does project manager share lessons learned with project members?	○ Yes - **X,** informal – experience shared at department meetings ○ No ○ Not sure /Not applicable
4	Are final reports, lessons learned and previous experiences well organized, documented and utilized for other projects?	○ Yes – **X**, but not very well organized ○ No ○ Not sure

TABLE 8: Risk management results

No.	Risk management	Mark 'x' in circle if you agree
1	When is project risk analysed?	○ Before all field exploration -**X** ○ After every project phase - **X,** stage gate process ○ After accomplishing every key event ○ After reaching every milestone ○ After every progress evaluations ○ Other, if so describe - **X,** during the whole projects
2	Are the areas of risk identified and mitigated for each project?	○ Yes – **X,** standard Excel sheet ○ No ○ Not sure/Not applicable
3	Is there a defined process to measure deliverables?	○ Yes - **X,** standard Excel sheet ○ No ○ Not sure /Not applicable
4	What methods or tools do you use to manage and control risk?	○ Monte Carlo analysis - Modelling and simulation - **X,** for cost ○ Decision tree analysis - **X,** typical for deciding drilling targets ○ Scenario analysis ○ Gantt charts ○ SWOT analysis - **X** ○ Other, if so describe - **X,** @Risk, contingency plans

5	Are there standard documents provided of risk management for project members and customers?	○ Yes – **X,** in Excel sheet form ○ No ○ Not sure /Not applicable
6	Is the risk analysis done for each project?	○ Yes - **X,** has to be in place to go through a stage gate, ○ No

TABLE 9: Procurement management results

No.	**Procurement management**	
1	Is there a written formal working procedure and format for procurement works?	○ Yes - **X,** documented in the quality system ○ No ○ Not sure /Not applicable
2	Is the procurement management process applied to all projects?	○ Yes - **X,** to most of projects ○ No ○ Not sure /Not applicable
3	Does the procurement department take lead on planning, requisitioning items?	○ Yes - **X,** always included with the project team and procurement department assists PM with planning and requesting ○ No ○ Not sure /Not applicable

TABLE 10: Stakeholder management results

No.	**Stakeholder management**	**Mark 'x' in circle if you agree**
1	Is the stakeholder management process required to identify the people, groups or organisations that could impact or be impacted by the project?	○ Yes - **X** ○ No ○ Not sure /Not applicable
2	What tools do you use to identify stakeholders in your project?	○ Stakeholder analysis - **X,** they fill in a standard form in meetings with various experts ○ Expert judgment - **X** ○ Meetings - **X** ○ Other, if so describe
3	Is the relevant information available for all identified stakeholders?	○ Yes - **X,** most of the time and they have plan to do better according to the communication plan ○ No ○ Not sure /Not applicable

4	Who has a responsibility to plan, manage, control, and make decisions in stakeholder management process?	○ General Manager ○ Deputy Manager ○ Project Manager- **X,** PM develops and executes the stakeholder plan but steering committee/ sponsor has to approve the plan ○ Primary customers ○ Other, if so describe _____

APPENDIX II: Detailed evaluation of knowledge areas

Based on the result obtained from interview the maturity level of 47 detailed components of knowledge areas were evaluated (Table 1 below) using some key characteristics of five level maturity model as criteria to find the overall maturity level of project management at Power Projects department. The key characteristics were taken from project management maturity model (Crawford, J.K., 2006).

Level 1: Initial process
- Ad hoc process and management awareness

Level 2: structured process and standards
- Basic processes, not standard on all projects, used on large, highly visible projects
- Management supports and encourages use

Level 3: organizational standards and institutionalized management
- All processes, standards for all projects, repeatable
- Summary and detailed information

Level 4: Managed process
- Process integrated with corporate process
- Management uses data to make decisions specific

Level 5: Optimizing process
- Process to measure project effectiveness and efficiency
- Process in place to improve project performance
- Management focuses on continuous improvement

TABLE 1: Assessment result of each knowledge area maturity level

No.	PMI knowledge areas	PM solutions maturity levels					
		1	2	3	4	5	Mean
		Initial process	Struct. process	Org. standards	Managed process	Optim. process	
	Project Integration Management						**3**
1	Develop project charter			3			
2	Develop project management plan				4		
3	Direct and manage project work			3			
4	Monitor and control project work			3			
5	Perform integrated change control		2				
6	Close project or phase			3			
	Project Scope Management						**3**
7	Plan scope management				4		
8	Collect requirements			3			
9	Define scope			3			
10	Create WBS			3			
11	Validate scope		2				
12	Control scope			3			
	Project Time Management						**3**
13	Plan schedule management				4		
15	Activity definition			3			
15	Activity sequencing			3			
16	Estimate activity resource			3			
17	Estimate activity duration			3			
18	Schedule development			3			
19	Schedule control		2				
	Project Cost Management						**3.67**
20	Cost estimating				4		
21	Cost budgeting				4		
23	Determine budget			3			
	Project Quality Management						**3**
24	Plan quality management			3			
25	Perform quality assurance			3			
26	Quality control			3			
	Project Human Resource Management						**2.5**
27	Plan HRM			3			
28	Aquire project team			3			
29	Develop project team		2				
30	Manage project team		2				
	Project Communications Management						**3.33**
31	Plan communications management				4		
32	Manage communications			3			
33	Control communications			3			
	Project Risk Management						**2.83**
34	Plan risk management			3			
35	Identfy risks			3			
36	Perform qualitative risk anaysis			3			
37	Perform quantitative risk anaysis			3			
38	Plan risk responses		2				
39	Control risks			3			
	Project Procurement Management						**3.50**
40	Plan procurement management				4		
41	Conduct procurements			3			
42	Control procurements			3			
43	Close procurments				4		
	Project Stakeholder Management						**2.5**
44	Identify stakeholderes			3			
45	Plan stakeholder management			3			
46	Manage stakeholder engagement		2				
47	Control stakeholder engagement		2				

APPENDIX III: Future plan – Assessment at Ethiopian Electric Power (EEP)

The plan is to carry out a similar assessment at Ethiopian Electric Power company using the project maturity tools studied in Iceland. The objective of the assessment is to establish the level of project maturity in the company and recommend areas of improvement.

Why do assessments at the company?
As stated by Alice Zavala (2005) doing the maturity assessment at organization can give the following stated benefit to organization. The Power Company can benefit from the assessment through other advantages as the assessment:

- Provides a clear picture of current state and define future state;
- Identifies the gaps and provides a roadmap for organization change;
- Motivates the organization to reach a better state;
- Motivates individuals to grow and develop current skills and educate the organization on best practices.

The assessment will be carried out through the following procedure:

a. Prepare for interviews
   - Document and review interview guidelines,
   - Prepare questions,
   - Determine interview team,
   - Prepare supporting templates and documentation guidelines.

b. Conduct interviews
   - Individual interviews or small-groups, it depends.

c. Assessment findings
   - Analysing results, comparing scores, information sorting,
   - Prepare and complete assessment deliverables,
   - Create report and presentation of findings and recommendations,
   - Report to management.

The assessment will be carried out according to the planned schedule as shown in Table 1 below.

TABLE 1: Time schedule of project management maturity assessment

No.	Stage description	Months											
		1	2	3	4	5	6	7	8	9	10	11	12
1	Preparing proposal												
2	Approval of proposal												
3	Preparing interview Schedule/Questionnaire survey												
4	Booking appointments												
5	Conduct interviews												
6	Evaluating and analysing the result												
7	Report writing												
8	Checking by supervisor												
9	Finalize the report												
10	Approval of report by supervisor												
11	Presentation to management of company												

UNITED NATIONS UNIVERSITY
UNU-GTP
Geothermal Training Programme

Orkustofnun, Grensasvegur 9,
IS-108 Reykjavik, Iceland

Reports 2015
Number 12

GEOTHERMAL ENERGY UTILIZATION MODEL FOR NKHOTAKOTA GEOTHERMAL SPRINGS IN MALAWI

Kondwani Thapasila Gondwe
Mzuzu University
Private Bag 201, Mzuzu 2
MALAWI
gondwe.k@mzuni.ac.mw

ABSTRACT

Malawi is endowed with huge potential of low-enthalpy geothermal as manifested by several hot springs in different geothermal fields across the country. None of these fields have been developed into useful economic activities. The main purpose of this study was to come up with potential direct utilization technologies for economic development of Malawi's geothermal fields. Three geothermal fields of Kasitu, Linga and Benga in Nkhotakota district were considered. Four technologies which included swimming pools and spas, greenhouse tomato production, indoor fish drying and raceway aquaculture of tilapia were analysed. Using the heat loss method for greenhouses, swimming pools and spas and aquaculture raceways, and the mass and energy balance method for the fish dryer, energy and hot water requirements were calculated. In addition, economic feasibility was done on each of the technology by calculating internal rate of return (IRR), payback period and net present value (NPV) discounted at 10% discount rate for a 10-year period.

Results indicate a total energy requirement of 5.2 MWth with 4.2 MWth being for aquaculture demanding total hot water requirement of 35 l/s for Linga field and 26 l/s for Kasitu field. Excluding aquaculture, the total energy requirement is 1 MWth with corresponding hot water requirement of 8 l/s for Linga and Benga fields and 6 l/s for Kasitu field. Economic evaluation indicates positive IRR ranging from 17% for aquaculture to 29% for spas and positive NPV for all the technologies with highest being with aquaculture at US$ 2.1 million and the lowest being US$ 0.04 million for greenhouse tomato production.

Based on the findings, Malawi can effectively develop greenhouse tomato production, swimming pools and spas, indoor fish drying and intensive aquaculture of tilapia in its geothermal fields dependent on the source temperatures. This would greatly boost the tourism industry and achieve sustained availability of high quality tomato and fish (both fresh and dried) throughout the year, thereby contributing to food security and improved livelihood in the areas of development. However, to achieve and maintain flow rates required for aquaculture, there is need for shallow drilling up to 300 m into deeper aquifers below. The use of greenhouses to produce vegetables and intensive fish farming will bring awareness among policymakers and the general public on the potential of the technologies to improve quality and quantity of yields throughout the year.

1. INTRODUCTION

Malawi is endowed with low-enthalpy geothermal resources as manifested by the numerous hot springs along the rift on the western side of Lake Malawi and through Kirk Range and the Shire Valley and through Zomba, Phalombe and Mulanje districts. However, these resources have not been put into economic use except the Nkhotakota's Mawira springs which were used for hot water supply during the colonial era (Harrison and Chapusa, 1975). Currently most hot springs are only used for local bathing while some springs in Nkhatabay are used for curing cassava for flour production. This project looks at some of the economic uses by which the low-enthalpy geothermal water could benefit Malawi in its economic challenges. The target areas are in Agriculture through greenhouse vegetable production, Fisheries through aquaculture and fish drying and Tourism through nature baths (spa) and swimming pools based on the hot springs in Nkhotakota district.

National development goals and related policy targets
Malawi development is guided by the Malawi Growth Development Strategy II (MGDS II) in line with the Vision 2020. MGDS II recognizes food security as being important to economic growth and creating wealth. Strategic objectives of MGDS II for agriculture and food security are:

- To increase agricultural productivity and diversity;
- To ensure sustained availability and accessibility of food to all Malawians at all times at affordable prices;
- To move up the value chain in key crops and increase agro-processing for both domestic and export markets;
- To increase agricultural production and productivity through intensification of irrigation.

In line with the MGDS II, the Agricultural Sector Wide Approach has come up with the five key focus areas of:

- Food security and risk management;
- Commercial agriculture, agro processing business and market development;
- Sustainable land and water management;
- Technology development and dissemination;
- Institutional development and capacity development (Ministry of Agriculture and Food Security, 2011).

Some of the energy policy strategies are: *"to ease pressure on destructive natural resources exploitation, particularly the depletion of forests for wood fuel, the improvement in availability and quality of energy services to the poor by creating jobs both farm and nonfarm, thus reducing overall unemployment and opening up more diverse livelihood.*" In addition, the energy policy recommends that for the energy sector to be effective, it is important to invest in the other beneficial sectors of the economy (Ministry of Energy and Mining, 2003).

The tourism policy promotes the need for community involvement in projects to ensure direct benefit for the hosting communities.

Sector status for agriculture, fisheries and tourism
Malawi agriculture is basically rain based and the effect of drought and flooding due to climate change has greatly affected food security. More than 2.8 million people will suffer due to hunger. About 47% of under-five children suffer from stunting with 13% being underweight due to malnutrition (World Food Programme, 2015).

Fish farming is in its early stages with most of the fish ponds being for small scale production. Currently most of the fish available in Malawi is the catch fish. There is very high demand for fish, making Malawi a net importer of fish. Fish production contributes 4% of GDP and captured fish is the one that contributes greatly to the national food security. There is a very high potential for aquaculture both for commercial and small scale production to meet the ever increasing fish demand (FAO, 2008; Chimatiro and Chirwa, 2005).

Geothermal energy development efforts
Geothermal application at hot springs in Malawi has been there for quite a long time. Notable use has been in Mawira in Nkhotakota, which was used to supply hot water through pipes that run 2 km to the district administrative centre where it supplied St Anne's hospital. The water was taken from collection tanks at the spring site all the way to the distribution tanks near the hospital.

With support from the British Geological Survey, most of the hot springs were recorded in the geological survey bulletin. In early 2000, the Geological Survey Department, through Dr. Dulanya, visited the documented springs (Dulanya et al., 2010). In 2010, Geothermal Development Company under the auspices of the Geothermal Projects Malawi conducted a reconnaissance of the documented springs. In the same year Gondwe and Allen carried out a cataloguing exercise where additional undocumented springs were added to the list.

A number of persons have been trained in geothermal energy resource exploration and specialized courses with the United Nations University Geothermal Training Programme (UNU-GTP) since 2010 and the government with support from World Bank has since identified a consultant to carry out detailed feasibility study for possible geothermal development.

The project
This project seeks to promote investment in the energy beneficial sectors of Agriculture through greenhouse vegetable production, in Fisheries through aquaculture production and fish drying and in Tourism and Health Sectors through promotion of hot spring sites, swimming pools and spas. Training in swimming will contribute to physical education and investment in education, youth, sports and culture. Greenhouses and aquaculture farms will be able to recruit local personnel thereby contributing to the reduction of the overall unemployment. Fish dryers will provide both employment and fight the ever increasing deforestation caused by burning wood for fish smoking. The spas and swimming pools are intended to contribute to human health and employment while enhancing tourism development.

The use of greenhouses to produce vegetables and intensive fish farming will bring awareness among policymakers and the general public on the potential of the technologies to improve quality and quantity of yields throughout the year. This will help to have sustained growth of vegetables and fish throughout the year and at faster growth rates. Fish drying will reduce fish loss due to spoilage and bring awareness to the general public on good quality of dried fish. Improved quality will be attained throughout the year irrespective of the weather. Sustained production of vegetables and reduced loss of fish during drying will contribute to the national food security.

2. GEOTHERMAL POTENTIAL IN MALAWI

2.1 Current status

Geothermal manifestations
Malawi is located in the western arm of the great East African Rift valley. It is to the southern end of the rift at 8-18° South and 32-36° East. Geothermal manifestations are mostly through hot springs and altered grounds though the existence of geothermal grass as an additional manifestation in some of the sites has been recorded (Omenda, 2010).

The hot springs are guided by the faulting within the rift. The greatest faulting occurs in the Vipya mountainous area from northern part of Nkhotakota, to the northern part of Nkhatabay, bounded by the pre-rift dislocation zone. The greatest number of hot springs is within the mountainous faulting zone of Kajilirwe/Kavuzi area to the south west of Mzuzu. They lie along the rift from Chinunkha in Chitipa at northern end all the way to Muloza in Mulanje at the southern end.

The highest recorded temperature is 84°C at Chiweta followed by 78°C at Chiwi hot springs. Chemical geothermometry indicate reservoir temperatures of as high as 270°C on average for Kanunkha hot springs (Msika, et al., 2014) also referred to as Karwe hot springs in Nkatabay. Chemical geothermometry of some hot springs is shown in Table 1.

No advanced exploratory work that would lead to actual locating of production wells for power production has been done. The resource lies untapped despite the fact that there is massive shortage of electricity in the country, marked with massive power cuts. The outage is greatest in the world at 77 days per annum (Foster and Shkaratan, 2010).

TABLE 1 Geothermometry temperatures of some hot springs in Malawi
(Dulanya et al., 2010; Msiska et al., 2014)

Hot spring	District	Surface temp. (°C)	Temp (°C) SiO_2	Temp (°C) Na-K	Temp (°C) Na-K-Ca
Chiweta	Rumphi	84	-	-	-
Chiwi	Nkhotakota	78	-	-	-
Mtondolo	Nkhatabay	74	-	126	144
Mawira	Nkhotakota	65	130.5	100.2	99.5
Liwonde	Machinga		-	182.1	142.9
Chikwidzi	Nkhotakota	55	124.2	88.9	93.3
Chombo	Nkhotakota	64	-	-	-
Ling'ona	Nkhotakota	61	-	-	-
Mwankenja	Karonga	53.4	117.3	106.8	104.0
Chinunkha	Chitipa	29	-	213.6	164.6

Underground aquifers
Documentation on aquifers in Malawi is limited to a depth of less than 100 m as applied to boreholes for potable water use. The aquifers are grouped into the basement and alluvial aquifers. The basement aquifers are low yielding and low mineralised (Mapoma and Xie, 2014) with yield of 1-2 l/s for the weathered and 2-4 l/s for the un-weathered fractured basement. Alluvial aquifers lie along the rift valley and have yield greater than 10 l/s. Most of the alluvial aquifers are semi-confined to unconfined but with high mineral contents (Chimphamba et al., 2009).

Need for detailed exploration
Malawi needs to do detailed geothermal exploration to have a quantified estimate of the energy potential in all the geothermal fields. Currently Malawi is hit with serious energy shortage with electricity just at 10% and biomass dominating in cooking and hot water supply. To come up with a reliable energy sector, diversity in energy source would be paramount. Geothermal energy would provide an environmentally sustainable source to meet the electrical base load and the provision of hot water supply.

There is a need for detailed investigations to include geophysical surveys to delineate the precise orientations of the fault conduits that bring hot water to the surface, combined with continuous discharge and various hydrochemical parameters and isotopic analysis to estimate the depth of these reservoirs (Gondwe et al., 2015). Currently, Malawi has engaged an Italian company to carry out the detailed resource assessment under the World Bank's funded project, Energy Sector Support Programme – ESSP. Not downplaying the donor support, the government should be able to plan and manage its energy sector if it is to grow to a middle income state.

2.2 Geothermal hot springs in Nkhotakota District

Nkhotakota is one of the districts in the central region of Malawi. It is located within 12°S and 34°E. It borders Nkhatabay to the north, Mzimba to the north - west, Salima to the south, Kasungu to the west

and Ntchisi to the south - west. It is within the rift plain to the southern arm of the western arm of the Great East African Rift Valley.

The geology of Khotakota is bound with extensive faulting within the Ntchisi Mountains and major faulting along the lakeshore. The outstanding faults are the Liwaladzi, Mphalanyongo and the Sani faults along the lakeshore. The structural map of Nkhotakota - Benga area has been provided in Appendix I. With the new district boundary shifted from Dwangwa to Dwambazi, the additional area can be found in the bulletin for South Viphya (Peters, 1965).

There are three known geothermal fields and a total of five sets of hot springs in the district. Brief descriptions of the fields and their related hot springs have been outlined below. Their locations are shown on the map in Figure 1.

2.2.1 Kasitu geothermal field

There are two springs, one on the beach at the foot of a small Kalari hill at the shoreline of Lake Malawi and one is 10 m into the lake at Kasitu. The temperature recorded is 78°C (Peters, 1965) though lower values that can be obtained in some parts of the year. The difference could be based on the different mixing rates with cold water depending on the period of the year. They occur on the north-northwest trending faults and are at the intersection point of the Kaungozi fault and the lines of Khuyu and Mkoma II faults. So far, this is the second hottest spring in Malawi and the hottest in Nkhotakota, located 78 km north of Nkhotakota boma.

The hot springs are within the fishing village of Kasitu and a small tourist beach lodge is being constructed at the top of the Kalari hill. The beach is 3 km from the town centre and the main lakeshore road, M5. Chiwi hot springs are also referred to as Kalari hot springs or Kasitu hot springs.

2.2.2 Linga geothermal field

There are three sets of hot spring in the field within a radius of 5 km from the district headquarters. The hot springs are of nearly same average temperature.

Chombo hot springs
Chombo hot springs are about 1.5 km south of Chombo primary school and about 4 km north - west of Nkhotakota boma. The most referenced spring is a pool at the base of the bank of the Chombo marsh. The measured temperatures are 64°C close to the edge of the pool at the bank and 36°C in the pool 5 m away, this is a clear indication that there is a lot of cold water mixing within the same spot.

Recent revelations indicate that there are several springs over a range of 200-300 m with the main pool being close to mid-way. A flexible deposition of close to 60 cm overlay a mass volume of hot water below it for a length exceeding 50 m, though with an undetermined water depth. The springs are at the lower end of the Mphalanyongo fault close to its junction with the Sani fault towards the mouth of Kaombe River (Harrison and Chapusa, 1975).

Mawira hot springs
Mawira hot springs are located 2 km south of Nkhotakota boma, and within 100 m to the west of M5 road. There are about 7 hot springs with the average temperature of 65°C. A cold spring is just 14 m from the hottest spring indicating a bounding structure between them. The hot Mawira stream flows into the cold Mchandilu stream just 8 m away. The springs are to the east of the Sani fault.

Ling'ona hot spring
Ling'ona hot spring is about 1.5 km southwest of Mawira hot spring. It flows at the bank of Ling'ona River. The measured temperatures are 61°C at the source and 38°C in the bathing pool. The springs lie along the Sani fault.

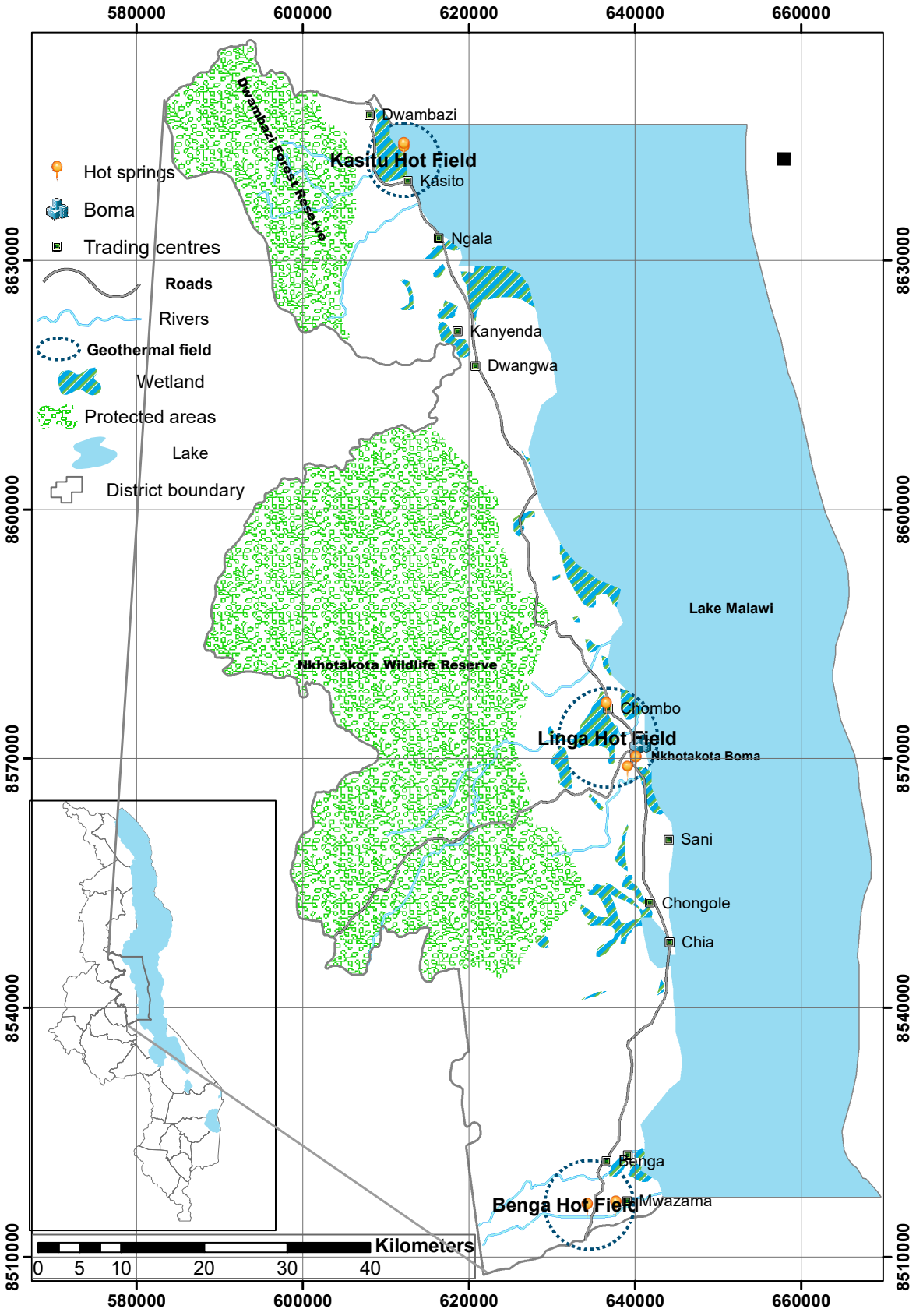

FIGURE 1: Map of Nkhotakota District showing the three geothermal (hot) fields (modified from Nkhotakota District Council, 2010)

2.2.3 Benga geothermal field

There are two hot springs at Chikwidzi, 1.5 km apart. This is about 10 km south of Benga and 56 km South of Nkhotakota Boma. The hotter spring with a temperature of 55°C lies about 100 m to the west of M5 road at Chiwidzi Bridge. Water bubbles from several places. The second spring is 1.5 km east of the road and has a measured temperature of 42°C. Benga is one of the vegetable growing areas of Nkhotakota. Benga is the southernmost geothermal field in the district.

2.3 Potential utilization

Depending on the nature of the geothermal resource, different applications can be used. Electricity generation using flash systems requires temperatures greater than 150°C while binary plants can start at as low as 80°C depending on the cycle used. Industrial application can vary from low to high temperature depending on the final required temperature.

Much as Malawi has high temperatures even for power production, this report considers direct utilization especially in agriculture and agro-industry. The potential uses of geothermal energy in agriculture and agro-industry are shown in Figure 2. Small binary production will be considered where there is need for electricity to power auxiliary equipment. Potential uses other than those shown in Figure 2 can be obtained from the standard Lindal diagram provided in Appendix II.

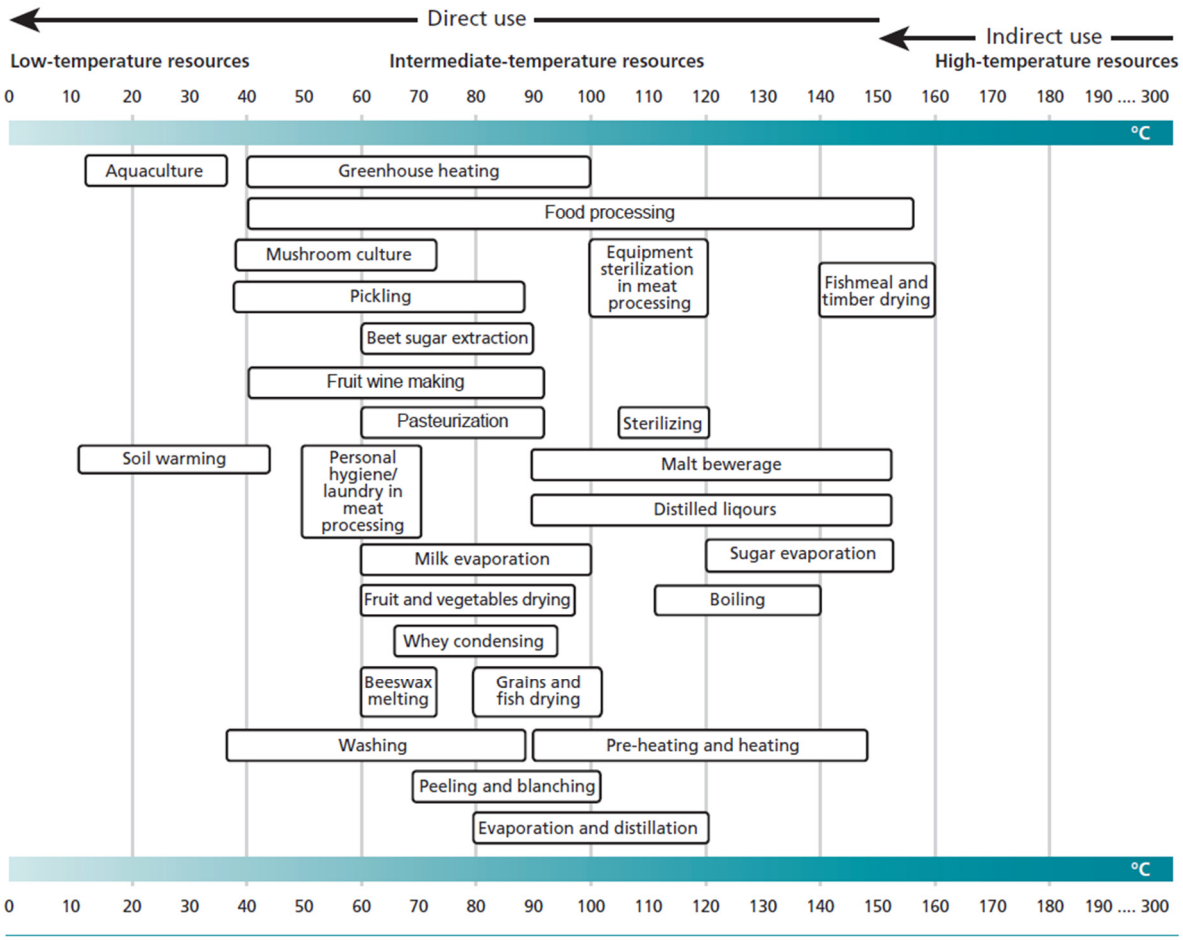

FIGURE 2: Lindal diagram of potential uses of geothermal energy in agriculture and agro-industries (Van Nguyen et al., 2015)

3. DIRECT UTILIZATION MODEL OF NKHOTAKOTA HOT SPRINGS

3.1 Selected direct uses

Considering that the fields in Nkhotakota are of temperatures 78°C, 65°C and 55°C on surface, respectively, and expected reservoir temperatures for Linga and Benga fields are 130.5 °C and 124.2°C (no records for Chiwi), the following applications have been selected.

Tourism and health: Activities being considered are swimming pools for Linga and Kasitu fields, and spas for all fields.

Agricultural activities: Activities to be considered are greenhouses for vegetable production, aquaculture farms and fish drying. Greenhouses are targeted for all the three fields while aquaculture and fish drying are being targeted for Kasitu and Linga fields.

In addition to the technologies covered in this report, other applications to be considered for future work are *district space cooling* and *binary power production*.

3.2 Swimming pools

Swimming pools in Malawi are basically in hotels and some very few well to do homes. This is associated with the well-to-do group. This project however wants to break that mentality by bringing awareness that the pools can be used for different purposes. In this section we will have two swimming pools of same surface area but with different depth to allow for the beginners to get trained in swimming. The pools will be heated and maintained at 28°C during the cold period May to August when the average temperature is 15.1°C (LaCroix et al., 1991).

3.2.1 Swimming pool dimensions

The size of a swimming pool is determined based on its intended purpose. Swimming pools could basically be used for recreational purposes, swimming competition and swimming lessons or just bathing for those who don't know how to swim. According to Karras (1996), there are three approved lengths that meet the international standards for swimming competitions. The lengths are 50 m for the Olympic Standards, 25 m for up to 400 m swimming and 33.3 m as an intermediate. Lane requirement for each swimmer is 2 m width.

Depth should be 1 m on the shallow side and 1.8 m on the deep side for a professional pool (Karras, 1996; Svavarsson,1990) and 0.8 m on the shallow side and 1.2 m (maximum) on the deep side for the non-swimmers (Jalili-Nasrabadi, 2004). Jalili-Nasrabadi further states that if the swimming pool is to be used only for swimming (excluding diving), a depth of 1.5 m or less at the deeper end for a professional pool would be more appropriate.

This project therefore considers two swimming pool sizes, one for professional swimming of up to 400 m and the other for swimming lessons and bathing for non-swimmers. Both pools will be 25 m long and 13 m wide. The depth for the professional pool will be 1 m on the shallow side and 1.8 m on the deep side while the pool for the swimming lessons will be 0.5 m and 1 m, respectively. This gives a surface area of 325 m^2 and volumes of 455 m^3 and 243.75 m^3, respectively.

Given the space requirement of 4.5 m^2 per swimmer in the deeper pools (Maharjan, 1995; Karras, 1996) and 2 m^2 per person for the shallower pools (Maharjan, 1995), the total capacity for the pools would be 72 persons for the professional pool and 162 persons for the regular pool. Considering a two thirds capacity at maximum patronage, the appropriate numbers would be 48 persons for the professional pool and 108 persons for the regular pool.

3.2.2 Swimming pool and pipe layout

There will be 28 inlet sprouts points for either pool. The main inlet and outlet lines are at the deeper end of the pool. The sprouts will be evenly distributed at the pool base while the outlet will be trough overflow around the pool. To achieve full circulation of the pool water in 6 hours, the flow rate of 21.1 l/s (Volume (m^3) × 1000 (kg/m^3) ÷ (6 hr × 3600 s/hr) is required for the professional pool and 16.93 l/s for the regular pond with a water change of 4 hrs. The outlet is through two overflow collection lines connected to a single line leading to a balance tank. The basic layout of the pools is given in Figure 3.

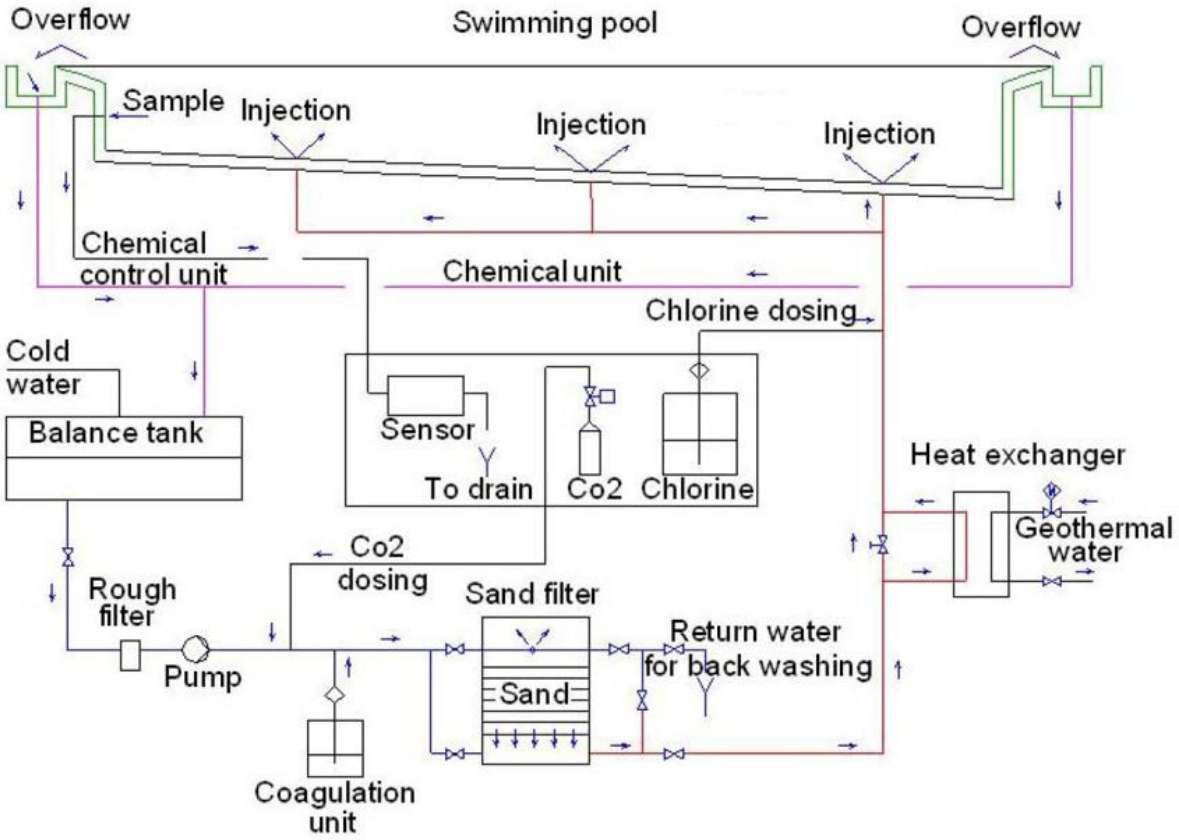

FIGURE 3: Proposed swimming pool layout (Jalili-Nasrabadi, 2004)

3.2.3 Pipe and equipment selection

There are two ways to go about the pipe selection. The pipe sizes are basically selected based on their maximum allowable pressure drop. This can be done by going to pipe sizing sheets provided by the manufacturers. Table 2 shows pipe selection chart for swimming pools and spas based on swimming pool installation manual. In this report however the pipe selection sheet as provided by pipe manufacturers were applied. It must be clearly stated that values in Table 2 fall out of range in the manufacturers flow sheet where the velocity is limited to 5 ft/s (1.52 m/s). Table 3 (a and b) has been developed based on the pipe manufacturers. Conversions used in Tables 2 and 3 are: 1 ft = 0.3048 m, 1 ft/s = 0.3048 m/s, 2.3 ft/ 100 ft = 22.46 kPa/100 m. Total pressure drop calculated is 41 kPa, which a pump has to overcome in addition to the elevation head at the site.

TABLE 2: Pipe selection based on maximum velocities
(modified from Sta-Rite Industries: Basic Training Manual, 2003)

Flow rate at water velocity of 2.1 m/s (l/s)	Flow rate at water velocity of 2.4 m/s (l/s)	Flow rate at water velocity of 3.1 m/s (l/s)	Pipe diameter (“)	Pipe diameter (mm)
0.8	0.9	1.1	¾	19
1.1	1.4	1.8	1	25
2.1	2.3	3.0	1 ¼	31
2.8	3.3	3.9	1 ½	38
4.7	5.4	6.9	2	50
6.9	7.4	7.9	2 ½	63
10.1	11.7	14.8	3	75
17.4	19.6	24.9	4	100
34.1	45.7	53.6	6	150

TABLE 3a: Pressure drop in regular swimming pool circulation system

Flow rate (l/s)	Line component	Quantity	Inside diameter (mm)	Length (m)	Equivalent length (m)	Total equi-valent length (m)	Pressure drop (kPa/100m)	Line press. drop (kPa)
0.75	Pipe	1	65	4		4		
	Pipe	7	65	0.3		2.1		
	Elbow	1	65		2.1	2.1		
	Adapter	7	65		1.68	11.76		
						19.96	2.47	0.49
1.5	Pipe	1	80	4		4		
						4	1.12	0.04
2.26	Pipe	1	80	4		4	2.7	0.11
3.01	Pipe	1	80	4		4	4.04	0.16
3.76	Pipe	1	80	4		4		
	Adapter	1			1.98	1.98		
						5.98	5.84	0.35
4.51	Pipe	1	100	4		4	2.47	0.10
5.27	Pipe	1	100	4		4		
	Elbow	1			3.66	3.66		
	Adapter	1			2.74	2.74		
						10.4	3.14	0.33
21.06	Pipe	1	150	15		15		
	Elbow	2			5.4	10.8		
	Tee	1			9.97	9.97		
						35.77	6.74	2.41
	Loss in pipes							**3.99**
21.06	Heat exchanger	1						25
21.06	Sand filter	3						12
	TOTAL							**40.99**

Pump and filter selection:
Based on past reports, filters of Astral (865) were selected. Data for other type of filters were not available so the same filter has been adopted for this purpose. However, locally available filters in Malawi will be assessed and calculations revised appropriately. Astral 865 filter´s specifications are presented in Table 4.

With the pool volume of 455 m^3 and a recycle time of 6 hrs, the flow is 75.8 m^3/h or 21.06 l/s. The regular pool is 243.75 m^3 and recycle time is 4 hrs and the resulting flow is 61 m^3/h or 17 l/s. This would require 3 filters for the professional pool while 2 filters will be enough for the regular pool. Pumps less than 1 kW will be required for each of the pools. Detailed specifications will be obtained from swimming pool installers in Malawi.

TABLE 3b: Pressure drop in professional swimming pool circulation system

Flow rate (l/s)	Line component	Quantity	Inside diameter (mm)	Length (m)	Equivalent length (m)	Total equi-valent length (m)	Pressure drop (kPa/100m)	Line press. drop (kPa)
0.6	Pipe	1	65	4		4		
	Pipe	7	65	0.3		2.1		
	Elbow	1	65		2.1	2.1		
	Adapter	7	65		1.68	11.76		
						19.96	1.8	0.36
1.21	Pipe	1	65	4		4		
	Elbow	1			2.1	2.1		
						6.1	6.51	0.40
1.81	Pipe	1	80	4		4	1.57	0.06
2.42	Pipe	1	80	4		4	2.02	0.08
3.02	Pipe	1	80	4		4		
	Adapter	1			1.98	1.98		
						5.98	4.04	0.24
3.63	Pipe	1	80	4		4	5.84	0.23
4.23	Pipe	1	80	4		4		
	Adapter	1			1.98	1.98		
						5.98	7.64	0.46
16.93	Pipe	1	150	15		15		
	Elbow	2			5.4	10.8		
	Tee	1			9.97	9.97		
						35.77	4.27	1.53
	Loss in pipes							**3.36**
16.93	Heat exchanger	1						25
16.93	Sand filter	2						12
	TOTAL							**40.36**

TABLE 4: Specification of Astral 865 sand filter

Capacity	30 m^3/h
Filtering speed	20 m^3/m^2h
Filter surface area	1.54 m^2
Volume	2 m^3

3.2.4 Heating energy requirement

Energy required for a pool is energy required to compensate for energy losses from the pool through convection, evaporation, conduction, radiation and the effect of rain and the energy required to heat fresh water for the pool. Based on formulae provided in lecture notes (Ragnarsson, 2015), the energy losses are computed as follows:

Convection heat loss
Convection heat loss is basically dependent on the atmospheric air temperature (ambient) and the wind speed just above the water surface. Convection heat loss has been calculated using Equation 1:

$$Q_c = h_c(T_w - T_a) \quad (1)$$

where Q_c = Convective heat loss [W/m^2];
h_c = $k + 1.88\ v_2$ [W/m^2 °C];
k = $3.89 + 0.17\ (T_w - T_a)$;
T_w = Pool water temperature [°C];
T_a = Ambient air temperature [°C];
v_2 = Wind velocity 2 m above the ground [m/s].

Values of $(T_w - T_a)$ and v_2 can be obtained in Appendix III.

Evaporative heat loss

Evaporative heat loss is the energy lost due to evaporation of the pool water. In addition to the dependence on ambient air temperature and wind velocity, evaporative heat loss is also greatly affected by the difference in partial pressures of steam just above the water surface and that in air above the pool. Computing evaporative heat loss is done using Equation 2:

$$Q_e = (1.56k + 2.93v_2) \times (\mathrm{e}_w - \mathrm{e}_a) \quad (2)$$

where Q_e = Evaporative heat loss [W/m^2];
e_w = Partial (saturation) pressure of steam in the air at the water surface [mbar];
e_a = Partial pressure of steam in the air above the water surface [mbar];
(saturation pressure at air temperature × relative humidity).

Values of $(\mathrm{e}_w - \mathrm{e}_a)$ can be obtained from Appendix III.

Radiative heat loss

Radiative heat is mainly dependent on the solar radiation and effect of cloud cover. The standard formula for computing radiative heat loss is given in Equation 3 (Ragnarsson, 2015) and can also be found using Equation 4 (Karras, 1996):

$$Q_r = 4.186((13.18 \times 10^{-9} \times (0.46 - 0.06\,\mathrm{e}_\mathrm{a}^{0.5}){T_a}^4 - G_o(1-a)) \times (1 - 0.012N^2) + 13.18 \times 10^{-9}({T_w}^4 - {T_a}^4)) \quad (3)$$

$$Q_r = 0.51 \times 10^{-8} \times [(492 + 1.8T_w)^4 - (492 + 1.8T_a)^4] \quad (4)$$

where Q_r = Radiative heat loss [W/m^2];
G_o = Solar radiation in clear weather [cal / s m^2];
a = Natural reflection of water;
N = Cloudiness factor (0 – 8);
e_a = Partial pressure of steam in the air above the water surface [mbar];
(saturation pressure at air temperature × relative humidity).

Conductive heat loss

Conductive heat loss is dependent on the thermal conductivity of the construction material and their thickness. The conductive heat loss is calculated by Equation 5. In this report, concrete of thickness 18 cm and rock wool of thickness 6 cm have been used as pool construction and insulation materials respectively:

$$Q_{cd} = \frac{\Delta T_{soil}}{\frac{l_1}{k_1} + \frac{l_2}{k_2}} \quad (5)$$

where ΔT_{soil} = $T_w - T_{soil}$ [°C] (values can be obtained in Appendix III);
T_{soil} = Outside soil temperature [°C];
l_1 = Thickness of construction material (1) – concrete in this case [m];
l_2 = Thickness of construction material (2) – rock wool in this case [m];
k_1 = Thermal conductance of concrete = 1.82 [W/m°C];
k_2 = Thermal conductance of rock wool = 0.042 [W/m°C].

Highest computed values are for the month of August. These values are shown in Table 5.

TABLE 5: Maximum energy losses from the swimming pools

Pool type	Q_c[Wm^{-2}]	Q_e[Wm^{-2}]	Q_r[Wm^{-2}]	Q_{cd}[Wm^{-2}]	Q_f[W]	Q_{total}[kW]
Regular	169	626	74	7	46,339	396
Professional	169	626	68	7	20,595	371

The calculated heat losses are multiplied with corresponding effective area. Summing the products together with loss due to heating the refill water Q_f, gives the total effective energy loss from the pool. The areas considered in this report are L × W for Q_c, Q_e and Q_r while the area for conductive heat loss is the total interior wall surface area. This is given by; $(L \times W) + (2 \times \text{L}\times\text{D}) + (2 \times W \times D)$ where D is the average pool depth, L is the length and W is the width.

Considering a water renewal of 30 l/person and that the operational time is 8 hrs per day, the additional cold water flows would be 0.4 kg/s for the professional pool and 0.9 kg/s for the other pool. The energy required for heating fresh water, originally at ambient temperature is 20.60 kW for the professional pool and 46.34 kW for the regular pool. This has been computed using Equation 6:

$$Q_f = m_f C_p (T_w - T_f) \tag{6}$$

where Q_f = Energy needed to heat refilling water [kW];
T_f = Refill water temperature [°C];
m_f = Mass flow rate of fresh cold water [kg/s];
C_p = Specific heat capacity of water [kJ/°C].

The total energy required from the geothermal water will thus be 370.66 kW for the professional pool and 396.07 kW for the regular pool. To estimate the required flow rate of geothermal water, different surface temperatures of 55°C, 65°C and 78°C have been considered, as well as respective temperatures of 78°C and 95°C at 400 m depth for Linga and Kasitu. These have been computed using Equation 7 and are shown in Table 6:

$$m_h = \frac{Q_{total}}{C_p (T_h - T_w)} \tag{7}$$

where Q_{total} = Total energy requirement [kW];
T_h = Geothermal water temperature [°C];
m_h = Mass flow rate of geothermal water [kg/s].

TABLE 6: Maximum hot water requirement for the swimming pools at different source temperatures

Pool type	Power (kW)	Hot water requirement (l/s)			
		55°C	**65**°C	**78**°C	**95**°C
Professional	370.66	3.28	2.39	1.77	1.32
Regular	396.07	3.50	2.56	1.89	1.41
Combined	766.73	6.78	4.95	3.66	2.73

3.2.5 Nature baths

Unlike the use of swimming pools which are used by the elite group, geothermal nature baths are used by the poor locals in the locality. This is basically due to the fact that nearly all sites are not cared for and the areas and the waters are untidy and unhygienic. The waste cases occur with Chiweta hot springs where businessmen treat killed pigs for the removal of the fur from the skin at the hot water source.

This project however aims at improving the sites to a state acceptable to all groups of people including the elite. There will be two sets of spas to be developed which will include commercial spas of the level of the Blue Lagoon in Iceland and non-commercial improvement of the existing pools. The non-commercial ones will be available for the local community for free while the commercial ones will be open to all with locals paying a lower fee. A distinction between the current nature bath at Chombo in Malawi and an improved commercial nature bath of Mývatn in Iceland is shown in Figure 4. Developing the nature bath in Figure 4a into a similar bath to Figure 4b would allow all levels of people to patronize the facility and promote tourism.

(a) Chombo Nature Bath – Nkhotakota, Malawi

(b) Myvatn Nature Bath – Iceland

FIGURE 4: Undeveloped (a) vs. developed (b) nature baths

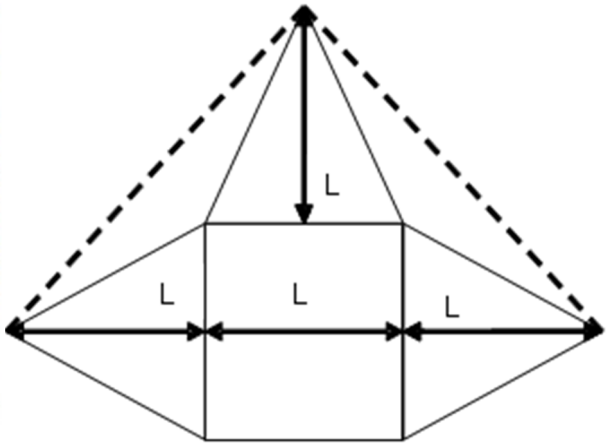

FIGURE 5: Proposed plan for the spa

Pool design and dimensions

The spa will be designed with three triangular segments attached to a central square section as shown in Figure 5. The square section will be at the entry point with the temperature setting of 38°C while the triangular sections will be at 40°C, 42°C and 45°C. For the purpose of this project, the depth of the square section will be 0.75 m while the depth of the triangular sections will be 1 m. The base and height of the triangular shape shall be equal the side of the square section. Computation of evaporation losses, energy losses and the mixing ratios has been based on side length of 3 m as shown in Figure 5.

Based on the operation of the Blue Lagoon (Iceland), the hot brine will be delivered at a central receiving point where it will be distributed to the four sections through smaller pipes. The mixing will be regulated by an automatic control valve based on temperature.

Energy losses and water requirement

Energy losses have been computed based on Equations 1, 2, 3 and 5 in Section 3.2.3. Control of temperature is based on the temperature activated switches allowing just enough amount of water to mix with the pool water to maintain the required temperature. Using Equation 7, the minimum and maximum hot water requirements were calculated and are shown in Table 7.

TABLE 7: Maximum hot water requirement for the spa at different source temperatures

Power (kW)	**Hot water requirement (l/s)**			
	55°C	**65**°C	**78**°C	**95**°C
62.45	0.995	0.597	0.393	0.271

3.3 Greenhouses

Greenhouses are structures covered with transparent or translucent materials that are used to provide desirable climatic conditions for plant growth. Depending on the construction materials and operation control capabilities, greenhouses vary greatly in their cost.

Greenhouses are used to provide the optimum temperature and humidity (Canakci et al., 2013) and light intensity for the crops while protecting them from extreme winds, rain contact, snow and excessively high or low temperatures. In temperate regions the main aim is to protect the crops from extremely low temperature, effect of snow, extreme winds and increase light capture or provide artificial lighting in very short days. In the tropics however the primary reason for using the greenhouse is to exclude pests, protection from excessive solar radiation, protection from heavy rains and wind (Hickman, 2010) and for humidity control.

Greenhouse operation is characterised by an intensive production and year round operation. It involves high investment cost and high energy consumption (Djevik and Dimitrijevic, 2009). Good locations are crucial in planning and production of greenhouse crops (Canakci and Akinci, 2006).

Greenhouse production aims at producing higher quality yield outside the cultivation season, which is possible by maintaining the optimum temperatures at every stage of the crop (Shethi and Sharma, 2008). Greenhouse effectiveness is defined as its capability to increase light input, reduce heat losses during cold weather and maximise heat removal during hot weather (Fabrizio, 2012).

In tropical areas of Africa, very few areas have the optimum growing conditions required for a high value crop. Polyethylene covered, non-ventilated greenhouses are mostly used for a month or two for start-up of vegetable plants. To achieve high quality crop throughout the year, ventilated greenhouses are required (Mrema et al., 2011). Greenhouses in hot and humid environments should be able to protect plants from extreme temperatures, rain, wind and insects, in such a way that the optimal growing conditions are attained. The inside temperature and relative humidity are controlled through natural and mechanical ventilation, evaporative cooling and shading (Shamshiri and Wan Ishmail, 2014).

Some of the advantages of using greenhouses in tropics are:

- Higher yield and better quality
- Better use of fertilizers and pesticides
- Less susceptibility to diseases due to less wetting and exclusion of heavy rainfall
- All year production ensures reliable market availability (Von Zabeltitz, 1997).

3.3.1 Site selection

Site selection is of great importance for the sustainability and profitability of greenhouse vegetable production. Based on Mrema et al. (2011), the factors to be considered in locating a greenhouse include: A nearly level topography with good quality and quantity of water for irrigation, well drained, clear areas with wind break, proximity to road and power networks and labour availability. The area should be flat in the width and 0 to 0.5% slopes in the main axes. Urban areas with high air pollution should be avoided (Castilla and Baeza, 2013).

The sites chosen are all within reach to the main road. Linga and Kasitu are also close to trading centres while Benga trading centre is about 10 km from the greenhouse sites. In addition to these local markets the major market would be in Lilongwe and Kasungu and some share going to Nkhatabay and Mzuzu. Flat areas are located within the geothermal field and the actual site would depend on negotiations with the community leaders, district officials and agricultural extension workers.

In all the three sites, irrigation water could be taken from nearby rivers or from the lake where necessary. Labour availability should not be a problem at Kasitu and Linga while operations at Benga may require additional labour force from other areas.

Despite the fact that all the areas have access to grid electricity, electricity in Malawi is very much unreliable with frequent and extended blackouts and load shedding being the norm of the day.

3.3.2 Climatic data for the selected area

It has been a challenge getting climatic data for Nkhotakota district from the responsible administrators for the district and data used is the best available based on internet sourced data. Considering that the information provided in the District development profile was not consistent within the document, the district official was requested to provide an official stand, however, he opted not to cooperate. For this reason, data used in this report is based on NASA data obtained through RET Screen programme, LaCroix et al., (1991) publication on Orchids of Malawi, Feeble online weather data and some from Metrological department in Malawi in some of their 10-day weather reports. Reasonable mean for each set was established and applied in this report.

Nkhotakota can be described as a sub-tropical climate with mean monthly temperatures ranging from 20°C in cold months (May to August) to as high as 37°C in hot months (September to January). It is however important to note that on a daily basis there is a wide variation between day and night temperatures. On average, temperatures between 8:00 am and 7:00 pm are generally above 17°C in hot months, but those from 7:00 pm to about 7:30 am are basically below 13°C. Mean monthly minimum temperatures range from 15°C in cold season to 22°C in the hot period. Up to 30 days per year experience extreme cases with a daily mean temperature of as low as 7-9°C.

The variation in temperature results in an inverse corresponding relative humidity. In the night the humidity would range from about 64% to as high as 93 % (around midnight) while during the day it can go as low as 30% or even lower between 1:00 pm and 2:00 pm.

3.3.3 Structural design and dimensions

Greenhouses can be made of different materials for both frame and covering. Material used in greenhouse construction range from locally available materials like bamboo stems to most expensive steel frames. Use of cheap poly plastic and wooden poles or bamboo sticks is being promoted to assist small holder farmers in the tropics (Pack and Mehta, 2012).

There are basically two types of greenhouses based on their structural shape. Most polyethylene sheet roofed greenhouses are of Quonset (or D-frame) type where the arched shape allows the transfer of the load to the ground. These can be with or without walls as indicated depending on design. Most glass greenhouses are of the A – frame type. These have trusses that form the roof and the gables and all the load is transferred to the ground through the side walls. A-framed greenhouses could be stand alone or gutter connected multiples (Mrema et al., 2011).

It is recommended that for tropical climates, tall greenhouses should be used. The minimum height from floor to gutter should be at least 3 m with an addition of at least 1.2 m to the ridge. Taller structures provide bigger air volumes which contribute to improved climate uniformity through the slowed response to external weather conditions (Kumar et al, 2009). However, for effective light capture, the greenhouse in the tropics should have an east-west orientation for single span and north-south orientation for multi-span with gutter connection (De Gannes et al., 2014). In this project the construction of the frame will be of aluminium bars and the covering of fibreglass.

The sizes of the greenhouses would be 36 m in length, 7 m in width and the wall height 3 m. A roof slope (pitch) angle between 25 and 30° will be used. A ventilation area of 15-30% of the floor area will be provided based on desired requirements (Kumar et al., 2009; Kittas et al., 2013). To achieve efficient ventilation, openings must be placed at the roof, gable and sidewalls (Kittas et al., 2013). In this project, openings will be on the windward sidewalls for cold air inlet and on the leeward roof for the warm air outlet. A rough sketch of the proposed design is shown in Figure 6.

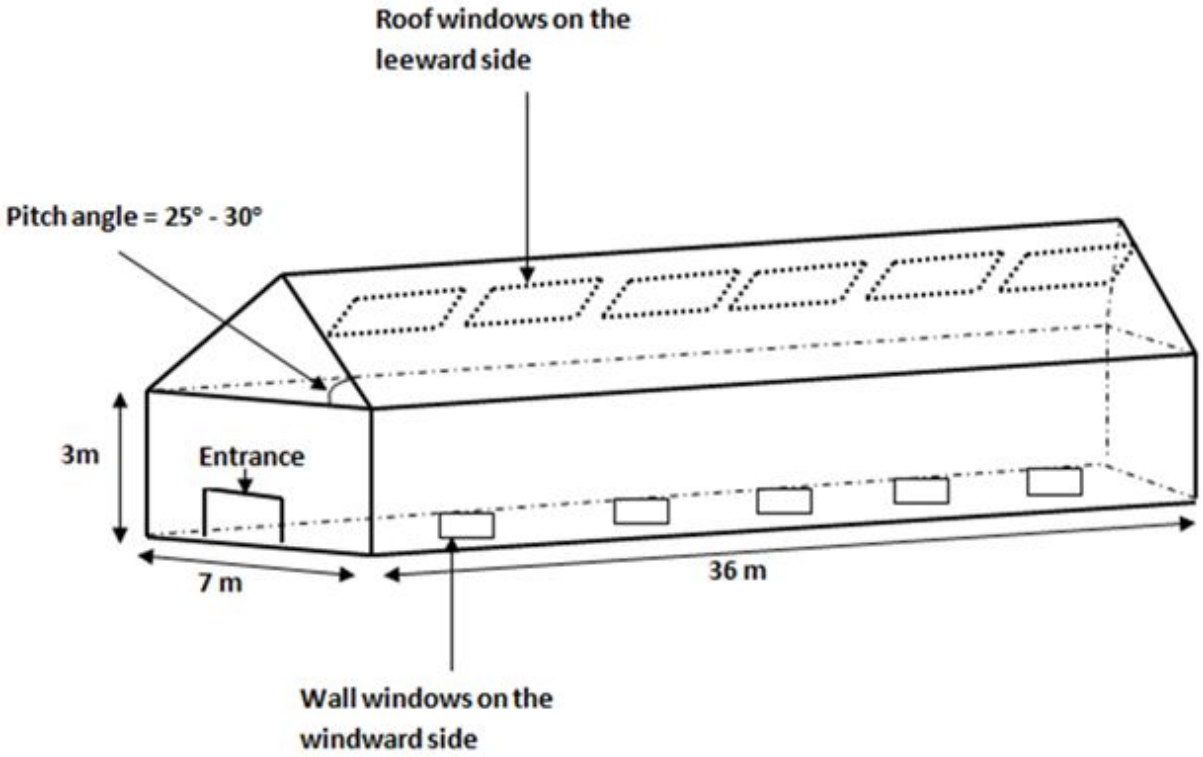

FIGURE 6: Sketch of the proposed greenhouse

Climate control could be either active or passive. Active control is where humidification and dehumidification is done with the help of mechanical devices while in passive control this is achieved through natural convection. Passive climate control is less costly but achieves irregular production and good quality can only be obtained in limited periods while with active control, despite being costly, production is regular and good quality is assured all year round (Montero et al., 2013). It is therefore imperative that both passive and active climate control will be used in this project. The combination will be used in such a way that when passive control can be effective, it is the one to be used and active control will be employed only in extreme cases. This will require lower investment cost while achieving the required production and quality levels.

3.3.4 Heating and cooling requirement

It is difficult to accurately determine the behaviour of greenhouse with static designing methods. But for simplicity, static design can be used with conditions set with no solar gains (Emeish, 1999). This is basically calculated for the worst case which generally occurs at early morning hours in winter (NGMA, 2015). In this project however the assumption affects greatly the cooling design load which is greatest when the solar radiation is greatest. Heating load has been assumed to be during the night or days of very low solar radiation.

To determine the heating requirement, heat losses are required to be known. With the static design method, the heat loss in a greenhouse is composed of two major components; transmission losses through the walls and roof and the infiltration and ventilation losses due to the infiltration of the cold outside air (Kasapoglu and Parlaktuna, 2005). In principle the energy required is the net energy loss obtained by subtracting all energy gains from the total energy losses as given in Equation 10 (Joudi and Hasan, 2013)

$$Energy\ Required\ = \Sigma Heat\ Loss - \Sigma Heat\ Gains \quad (10)$$

Transmission loss through the walls and the roof
Transmission losses through the walls and the roof are given by equation 11:

$$Q_t = UA(T_i + T_o) \quad (11)$$

Where Q_t = Transmission heat loss through walls and roof [W];
U = Heat transfer coefficient [W/m^2°C];
A = Total surface area of the walls and roof [m^2];
T_i = Inside design temperature [°C];
T_o = Outside design temperature [°C].

The heat transfer coefficient (*U*) for the covering materials is dependent on the type of material and on the wind speed of a particular area. This means that the values will be different even if the material is the same but if the wind speeds are different. The *U* values of different covering materials as adopted from Rafferty, 1998 (cited by Kasapoglu and Parlaktuna, 2005) are given in Table 8.

From Table 8 trend lines with the order of three were obtained and used to compute different values of the *U* values at different wind speeds. The higher the order the more precise it becomes but in this project an order of three was thought appropriate. The obtained trend lines are given in Table 9 as polynomials of the order three.

TABLE 8: U values of common covering materials as a function of wind speed as adopted from Rafferty, 1998 (cited by Kasapoglu and Parlaktuna, 2005)

V(m/s) / Material	0.00	2.24	4.47	8.94	11.18	13.41
Glass	4.34	5.40	5.91	6.47	6.59	6.70
Fibreglass	3.95	4.91	5.39	5.87	6.01	6.12
Single Poly	4.60	5.68	6.19	6.76	6.87	6.98
Double Poly	3.04	3.58	3.83	4.07	4.13	4.18

TABLE 9 : Polynomials for commputing *U*-values with wind speed (v)

Covering material	Polynomials for computing *U*-value
Glass	$U = 0.0015v^3 - 0.0475v^2 + 0.5393v + 4.3582$
Fibreglass	$U = 0.0015v^3 - 0.0446v^2 + 0.4958v + 3.9647$
Single Poly	$U = 0.0015v^3 - 0.0483v^2 + 0.5480v + 4.6191$
Double Poly	$U = 0.0009v^3 - 0.0261v^2 + 0.2788v + 3.0494$

Infiltration heat loss
Infiltration heat loss basically depends on the rate at which the inside air is replaced by the cooler air from outside. This is a function of the temperature difference between the inside and the outside air and also the wind speed at the site. The infiltration energy loss is calculated using Equation 12.

$$Q_i = V \times ACH \times \rho_a \times C_p(T_i - T_o)/3600 \quad (12)$$

where Q_i = Infiltration heat loss [W];
V = Greenhouse volume [m^3];
ACH = Air changes per hour;
ρ_a = Air density [kg/m^3];
C_p = Specific heat capacity of air [J/kg°C];
T_i = Inside design temperature [°C];
T_o = Outside design temperature [°C].

Cooling is required if the heat gains are larger than the heat losses. It is basically calculated by Equation 10 and can be considered as the negative heating load. The negative sign to the heating load indicates that the heat has to be removed from the system.

From the Excel calculation on the average temperatures, the system shows that it will require heating between May and September and cooling between October and April. However, the critical heating is required at night throughout the year to avoid condensation when the night temperature falls below dew point.

Heating pipe requirement
The bare pipe length is determined by the empirical Equation 13.

$$L = \frac{3.6Q_t}{11.345A\left[4.422 \times \left(\frac{1}{D}\right)^{0.2} \times (1/(1.8T_{ave}+32)^{0.181} \times (\Delta T)^{1.266} + 15.7 \times 10^{-10}[(1.8T_1+32)^4 - (1.8T_2+32)^4]\right]} \quad (13)$$

where L = Pipe length [m];
Q_t = Total heat loss [W];
D = Outside pipe diameter [mm];
T_{ave} = $255.6 + (AWT + T_{air})/2$ [°C];
AWT = $T_{wi} - \Delta T/2$ [°C];
T_{wi} = Heating water inlet temperature [°C];
T_{air} = Greenhouse inside design air temperature [°C];
ΔT = Heating water temperature drop [°C];
T_1 = $255.6 + AWT$ [°C];
$AUST$ = Average unheated surface temperature [°C];
T_3 = $(AUST + T_{air})/2$ [°C];
T_2 = $255.6 + T_3$ [°C];
A = Outside surface area of the pipe per unit length [m^2/m].

The number of pipes required is then obtained by dividing the pipe length by the greenhouse length given by Equation 14:

$$n = L_{pipe}/L_{greenhouse} \quad (14)$$

The pipes will be put at 0.5 m and 2 m above the ground. The value for the number of pipes (n) is thus rounded to the nearest even integer in Excel computation. This gives a total number of pipes, 12, with a total length of 397 m. The pipes will be at 1 m and 2.5 m from the walls giving a door passage space of 2 m between the inner pipes. Inputs and calculated outputs for the heat requirement and hot water piping are show in Table 10.

TABLE 10: Input and calculated data for greenhouse heating requirement

Input parameters		**Output parameters**	
Outdoor air temperature	15.1°C	Total energy loss (design)	9954 W
Wind speed	3.86 m/s	Max geothermal water flow rate	0.242 l/s
Greenhouse floor area	252 m^2	Total pipe length	397 m
Total glass area	488 m^2	Number of pipe required	12
Volume	785 m^3	Total energy consumption	188 GJ/year
Inside design temperature	18 °C	Specific energy consumption	0.75 (GJ/m^2) / year
Air changes	3 ACH	Geothermal water consumption	4,575 m^3/year
Tubing outside diameter	32 mm		
Water supply temperature	55°C		
Water temperature drop	10 °C		
Brine density	985 kg/m^3		
Annual load factor	0.6		

3.3.5 Greenhouse cooling

Greenhouses in the tropics require cooling especially between 10 AM and 3 PM during the hot months when the temperatures are above the crop requirement. In Nkhotakota, cooling will be required from end of August to mid-February. There are several ways of greenhouse cooling, however for the purpose of this report only those to be employed are explained.

Natural ventilation
Natural ventilation works on the principle of temperature difference and density. Hot air is lighter and tends to rise. In a greenhouse, openings are on the windward wall side for cold air inlet and on the leeward roof side for the hot air exit. When the air is heated it rises creating space for the cold air. It is mainly used due to its low energy requirement. Its dependency on the natural external conditions makes it non-efficient at times and other techniques have to be used in combination (Montero et al., 2013).

Shading
Shading is used to reduce the incoming solar radiation by providing shading materials either inside or outside the greenhouse walls. These materials could be either shade cloth, shading nets or some other liquid foams. Much shading is good for low-light requiring crops, but it greatly lowers productivity in high-light requiring crops like tomatoes if used over long periods.

Evaporative cooling
Evaporative cooling based on the principle of conversion of sensible heat into latent heat through evaporation of water. It is the least expensive way in greenhouse cooling. According to Kumar et al., 2009, evaporative cooling is the most effective method in greenhouse microclimate regulation. It can be achieved either by passing water through an evaporator pad or through mist or fog spray. Mist spray achieves uniform distribution of both humidity and temperature throughout the greenhouse.

To achieve effective microclimate control, this project will use a combination of natural ventilation, mist evaporative cooling and fan and pad evaporative cooling.

3.3.6 Irrigation water requirement

The irrigation water requirement (IWR) is found by summing the crop water requirement (CWR) and the soil leaching requirement (SLR). To determine the irrigation water requirement, it is thus important to know the evapotranspiration upon which the CWR is greatly dependent.

To determine the evapotranspiration rate, the Penman-Monteith equation is derived and applied. The equation is a combination of the original latent heat flux and the aerodynamic resistance as described in the guidelines for computing crop water requirement (Allen et al., 1998). Reference evapotranspiration is calculated using Penman-Monteith equation as given in Equation 15 and monthly crop water requirement is found using Equation 16 (von Zabeltitz, 2011).

$$ET_o = 0.408 \times \Delta \times (R_n - G) + (\gamma \times \frac{900}{T_{mean} + 273}) \times v \times (u_s - u_a) \div (\Delta + \gamma \times (1 + 0.34v)) \quad (15)$$

where ET_o = Reference evapotranspiration [mm/day];
Δ = The slope of vapour pressure curve [kPa/°C];
R_n = Net radiation at crop surface [MJ/m^{2}day];
G = Soil heat flux density [MJ/m^{2}day];
γ = Psychometric constant [kPa/°C];
T_{mean} = Mean daily air temperature at 2 m [°C];
v = Wind speed at 2 m height [m/s];
u_s = Saturation vapour pressure [kPa];
u_a = Actual vapour pressure [kPa].

and

$$CWR_m = CWR_d \times d_m \quad (16)$$

where CWR_m = Monthly crop water requirement [mm/month];
d_m = Number of days in a month;
CWR_d = $AET_c \times (1 + l_i) \times A_{crop}/A_{greenhouse}$ [mm/day];
AET_c = Actual evapotranspiration for a particular crop coefficient [mm/day];
l_i = Irrigation loss factor [%];
A_{crop} = Area covered by the crop [m^2];
$A_{greenhouse}$ = Area of the greenhouse [m^2].

A detailed computation of the irrigation water requirement for each of the three sites need to be calculated using the standard method. For the purpose of this project however, a requirement of 50 millilitres per plant per day for new plants and 2.7 litres per plant per day (Snyder, 1914) has been assumed. With an average plant population of 615, a total maximum irrigation requirement of 1,660 litres per day is needed. Based on Snyder 1914, plant population is calculated by dividing the greenhouse area by 0.37 m^2 per plant (for maximum) and by 0.46 m^2 per plant (for minimum) population.

3.4 Fish dryer

Fish is highly perishable since it contains as high as 80% of water by mass. This calls for drying to remove the water to a level that inhibits microbial growth (Hubackova et al., 2014). In Malawi, fish drying is mostly done through open sun drying for smaller fish like Utaka, Usipa, Matemba and small size Mcheni, while the bigger fish like Chambo (Tilapia), Kampango, Mlamba and Batala are smoke dried. Frequently the smaller fish is also sun dried where they are roasted first and then sun dried or they could be boiled and then sundried. A lot of fish is lost due to spoilage and animals. The quality of fish is usually denatured due to uncontrolled drying. Smoking of fish has also resulted in deforestation along the fishing areas making it even more difficult for such drying, especially during the rainy season.

According to Kapute, 2008, close to 40% of landed fish is lost due to poor processing. It is unfortunate to note that even the national fishing company Maldeco is using traditional ways of drying fish. Due to lack of information in respect to fish quality and safety, most Malawians consume fish with an unacceptable quality. Studies indicate that such fish is sold in most of the supermarkets in the country (Makawa et al., 2014).

Air dryer design
The principle of air drying is to pass air of low humidity over the mass to be dried. As it passes it absorbs the water from the material, thereby drying it. The rate of drying is mainly influenced by the temperature and the humidity difference between the drying air and the material being dried. The velocity of the drying air has also great effect on drying rate.

Drying can be done as a single stage or through two stages. In a two-stage drying system, fish is dried at a faster drying rate at the beginning up to a moisture ratio referred to as critical moisture content. From this point, the fish is transferred to a slower drying for a longer period. This helps to avoid the surface from becoming impermeable to the inner moisture and ensures thorough drying.

Principle of fish drying
In the tropics fish drying is done through simple sun-drying of split fish on racks. Much as it is simple and cheap, huge losses result from spoilage and insects and dust contamination, especially where fish is dried on or near to the ground. Rains and dew, especially at early hours in the morning, leads to spoilage from moulds (Ruddle, 1990). It is usually difficult to obtain a uniform product with sun drying since it is weather dependent (Sankat and Mujaffar, 2004; Al Rawahi et al., 2013).

Optimal drying conditions for tropical fish seem not clearly defined but higher temperatures of 40-50°C with corresponding relative humidity of 50-60% have been used (Mujaffar and Sankat, 2005). However, it is recommended that temperatures between 60 and 63°C be used to prevent microbial growth without denaturing the product (Rahman, 2015). This increases the storage life due to the lower moisture content achievable with high temperature controlled drying (Al Rawahi et al., 2013).

Much as drying rate is of great importance in fish drying, very little information is available on the kinematics of water removal from the fish (Mujaffar and Sankat, 2005). Drying rate is very high at the initial drying stage and then decreases exponentially as the water content decreases (Toujani et al., 2012). It is also dependent on the moisture content, volume and temperature of the drying air (Seveda, 2012).

Mass balance

Mass of water evaporated by primary drying is found by subtracting mass of semi-dried product from the intitial mass before drying while that evaporated by the secondary drying is found by subtracting the mass of the dried product from the mass of the semi-dried product. It must be noted that the solid mass does not change (Sengar et al., 2009). The percentage moisture content is then computed using Equations 17 and 18 below:

$$MC_{wb} = ((W_1 - W_2)/W_1) \times 100 \quad (17)$$

$$MC_{db} = ((W_1 - W_2)/W_2) \times 100 \quad (18)$$

where MC_{wb} = Moisture content wet basis [%] ;
MC_{db} = Moisture content dry basis [%];
W_1 = Product weight before drying [kg];
W_2 = Product weight after drying [kg].

Energy requirement

In principle, the drying product needs energy to raise its temperature from its initial temperature to the temperature of the drying air. To evaporate the moisture to the required level, a further energy of vaporisation at the drying temperature is required. The basic way the energy requirement for drying can be calculated is given by Equation 19 (Seveda, 2012). It is a common practice though to use a combined specific heat capacity of wet fish as opposed to have separate specific heat capacities of water and solid matter and this is then presented as Equation 20 (Sengar et al., 2009; Earle and Earle, 2004).

$$Q = (1 - MC_{wb})W_1 \times C_{pd} \times (T_a - T_f) + (MC_{wb} \times W_1) \times C_{pw} \times (T_a - T_f) + (w \times L_v) \quad (19)$$

$$Q = W_1 \times C_{pf} \times (T_a - T_f) + (w \times L_v) \quad (20)$$

where Q = Energy requirement for drying [W];
C_{pd} = Specific heat capacity of solid fish material [kJ/kg°C];
C_{pw} = Specific heat capacity of water [kJ/kg°C];
C_{pf} = Specific heat capacity of whole fish [°C];
T_a = Drying air temperature [°C];
T_f = Initial fish temperature [°C];
w = Amount of water to be evaporated [kg];
L_v = Latent heat of evaporation of water [kJ/kg].

In this project, since there are two stages of drying, the corresponding equations for the energy requirement are Equation 21 for primary drying and Equation 22 for secondary drying. The total energy required to dry fish from the initial moisture content to the final required moisture content is the sum of the primary and secondary energy requirements.

$$Q_p = W_1 \times C_{pf} \times \left(T_{a_p} - T_{f_p}\right) + (w_p \times L_v) \quad (21)$$

$$Q_s = B \times C_{pf} \times \left(T_{a_s} - T_{f_s}\right) + (w_s \times L_v) \quad (22)$$

where Q_p = Energy requirement for primary drying [kJ];
Q_s = Energy requirement for secondary drying [kJ];
B = Mass of semidried fish [kg];
w_p = Moisture to be removed during primary drying [kg];
w_s = Moisture to be removed during secondary drying [kg];
T_{a_p} = Heating air temperature in the primary dryer [°C];
T_{a_s} = Heating air temperature in the secondary dryer [°C];
T_{f_p} = Initial fish temperature in the primary dryer [°C];
T_{f_s} = Initial fish temperature in the secondary dryer [°C].

To have a good heat transfer between the air and the fish being dried, it is advised to have turbulent air flow within the drying chamber (Maharjan, 1995). Temperatures between 45 and 150°C and air flow of 0.7-8.14 $kgs^{-1}m^{-2}$ are recommended.

Dimensions of the dryer
In the tray dryer the hot air passes over the fish along the length. The drying area is thus the tray area of the fish ($L \times W$) while the area in respect to air flow is the cross-sectional area of the dryer ($W \times H$). These may be the same if the air flow is vertical or in the horizontal flow, if the dryer is a cuboid. In this project, the air flow is horizontal in the primary section and vertical in the secondary section. The primary dryer section is given in Figure 7.

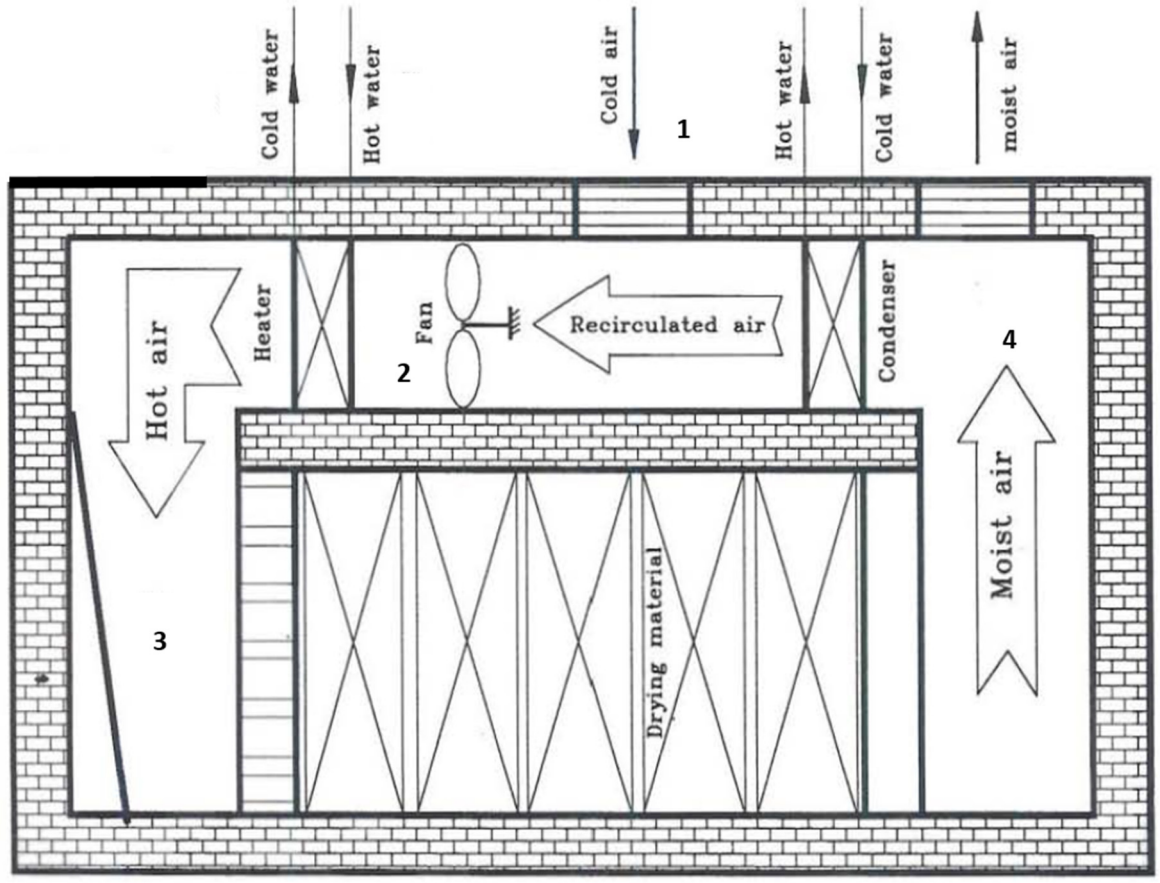

FIGURE 7: Tray dryer, primary section, (modif. from Maharjan, 1995)

The dryer has been designed to dry 10,000 kg of fish with a moisture content of 80% down to 55% in the primary dryer and down to 15% in the secondary one. The dryer is designed for drying Chambo but smaller fish species can also be dried with shorter drying times. Different winter and summer ambient conditions, drying air conditions and exit conditions have been examined. Maximum energy requirement occurs in winter and the results are shown in Table 11.

Air flow required is found by dividing water to be evaporated by the change in moisture ration between point 4 and point 3 in the primary dryer and point 3 and point 2 for the secondary dryer. With w_p = 6000 kg/ h and w_s = 1882.4 kg/h, the air requirement is:

$$Air\ flow\ rate = 6000 \text{ kg/h} \div (6.2/1000) \text{ kg/kg} = 24{,}193 \text{ kg/h for the primary dryer}$$

and

$$Air\ flow\ rate = 1882.4 \text{ kg/h} \div (3.5/1000) \text{ kg/kg} = 5{,}378 \text{ kg/h for the secondary dryer}$$

TABLE 11: Air condition at different points of the dryer

Position number	**Air temperature [℃]**	**Relative humidity [%]**	**Moisture ratio (x) [kg/kg]**	**Enthalpy (i) [kJ/kg]**
Primary				
1	19	75	10.2	45
2	25	90	18.3	72
3	45	30	18.3	93.5
4	30	90	24.5	93.5
Secondary				
1	19	50	7	36.5
2	48	9.5	7	66
3	40	24	10.5	66

The energy requirement is found by multiplying the air flow rate by the change in enthalpy $(i_4 - i_2)$ for primary and $(i_3 - i_2)$ for the secondary dryer. This gives:

$$Air\ flow\ rate = 24{,}193 \text{ kg/h} \times 21.5 \text{ kJ/kg} = 520 \text{ MJ/h} = 144 \text{ kW for the primary dryer}$$

and

$$Air\ flow\ rate = 5{,}378 \text{ kg/h} \times 29.5 \text{ kJ/kg} = 159 \text{ MJ/h} = 44.07 \text{ kW for the secondary dryer}$$

3.5 Intensive aquaculture facility

3.5.1 Current status

Fish farming has great interest among smallholder farmers. Facilitated by development agencies, small scale fish farming has been promoted in many parts of Malawi. Over 4000 fish farmers with a total number of fish ponds amounting to 7000 exist in the country at present (Tall, 2009). Most of these are open earthen ponds. Most of these practice extensive system with low inputs and very low yield (Nyanja et al., 2005). The most cultured species are *Oreochromis Shiramus* and *Tilapia Rendalli.* One commercial farm, Chambo Fisheries (Pacific), farms Nile Tilapia using biofloc system. It was difficult to ascertain production levels for the purpose of this report.

Most of these farmers are not satisfied with the slow growth, stunted growth and early maturity of the cultured fish (Chimatiro and Chirwa, 2005). Much as most researchers believe that Chambo is difficult to be cultured to full market size due to its early maturity, others have argued that it is the poor environment and feeding that leads to early maturity. The government's target is to raise the current low

production of 750 kg/ha/yr. to about 1500 kg/ ha /yr. but this is very far from reaching the ever increasing demand. To meet the fish demand and achieve an export level, Malawi needs to promote the intensive commercial aquaculture.

3.5.2 Design of an aquaculture farm

Much as the major target is promoting pond farms with smallholder farmers due to its simplicity and cheapness, the farmer has no or little control over the several external factors that affect the fish growth and production. For ideal intensive culture conditions, it is appropriate to use either tank or raceway culture where the farmer can have full control over the inputs (Nyanja et al., 2005). Tanks and raceway farms provides an opportunity for highly intensive fish farming due to the ability to control external factors and inputs (Pillay and Kutty, 2005; White and Rigby, 2003).

Water quality and temperature are critical for good aquaculture production. Good water with high oxygen levels is required for the fish. Waste from the pond should be removed to avoid concentration of ammonia. The growth and reproduction of fish is greatly affected by the water temperature. Spawning and fish growth tend to decrease below or above optimum temperature for each fish species. Optimal temperatures for Tilapia are 27-30°C for growth and 22-32°C for spawning (Ísaksson, 2015). For the Chambo in Malawi, research shows that temperatures between 27 and 29°C are recommended for reduced hatching period and increased hatchability and fry survival (Valeta et al., 2013). It is observed that in unheated earthen ponds and natural waters, the spawning season lasts from August to March with peak between November and December when the ambient temperatures are above 22°C (Banda et al., 2005). It is also observed that fry production and growth greatly lowered in the cold season which normally ranges from May to early part of September (Brummett and Noble, 1995).

Based on the above recommendations the proposed fish farm will have a hatchery with ponds at a temperature of 29°C to reduce hatching period and the rearing ponds with a temperature of 28°C. It may also be considered to have all ponds at either temperature.

To ensure continuous removal of waste from the water, raceway farm will be adopted. Raceways are basically designed in a way that there is continuous water throughflow and the typical ratios of length to width to depth are 30:3:1 (Stinkney, 2005). However, the first test farm will be of sizes 25 m by 4 m by 1.2 m for the rearing raceway ponds and 25 m by 2 m by 0.75 m for the hatching ponds.

3.5.3 Water and energy requirement

Fresh water requirement
The water requirement in a raceway is determined by the rearing density to maintain a good level of oxygen for fish survival. The total pond water requirement is given by Equation 23:

$$Q_r = \frac{\left(V_f + V_{rf} + L_e + L_s + L_c - V_{ra}\right)}{86400T} \quad (23)$$

where Q_r = Annual water requirement [l/s];
V_f = $A \times h$ = Pond volume to be filled [m^3];
V_{rf} = $N_o \times V_f$ = Pond volume to be refilled [m^3];
L_e = $A \times E$ = Evaporation losses [m^3];
L_s = $A \times T \times S$ = Seepage losses [m^3];
L_c = $A_c \times E \times 1.2$ = Canal transmission losses [m^3];
V_{ra} = $A_{eff} \times R_a$ = Inflow due to rainfall [m^3];
A = Average pond water surface area [m^2];
h = Average pond water depth [m];
N_o = Number of refilling per year;
E = Mean annual evaporation [m];

T = Operational time [days];
S = Seepage coefficient [m/day];
A_c = Water surface area of a canal [m^2];
A_{eff} = Total pond area exposed to rain [m^2];
R_a = Mean annual rainfall [m].

In this project, L_s, L_c *and* V_{ra} have been assumed to be zero and L_e is equated to W_p in Equations 24 and 25.

Energy requirement
Like in swimming pools, aquaculture ponds lose heat through evaporation, convection, radiation and conduction. Geothermally heated aquaculture farms are restricted in size based on the maximum available heat from the geothermal source. To determine the total heat requirement, we need to sum all the associated heat losses.

Evaporative heat loss (Rafferty, 2003; Lund, 1996)
This is the greatest heat loss associated with ponds. It is basically considered as the amount of energy required to evaporate the amount of water mass. With heat of evaporation of 2,440 kJ required to evaporate 1 kg of water, the total heat loss through evaporation can be found by multiplying the amount of water evaporated by the unit heat of evaporation. The amount of water evaporated is obtained through the equation describing the rate of evaporation as given in Equations 24 and 25 for outdoor ponds and Equation 26 for indoor ponds:

$$W_p = \left(11.0 + (4.30 \times v)\right) \times (p_w - p_a) \times A \quad (24)$$

$$W_p = \frac{2930v}{1.8T_s + 492} \times (p_w - p_a) \times A \quad (25)$$

$$W_p = 14.46 \times (p_w - p_a) \times A \quad (26)$$

where W_p = Rate of evaporation [kg/h];
A = Pond surface area [m^2];
v = Air velocity [m/s];
p_w = Saturation vapour pressure of pond water [bar – absolute];
p_a = Saturation pressure of air at dew point [bar – absolute];
or saturation pressure at air temperature × relative humidity;
T_s = Water surface temperature [°C].

Evaporative heat loss is therefore given by Equation 27:

$$q_{ev} = W_p[\tfrac{kg}{h}] \times h_{ev}\left[\tfrac{kJ}{kg}\right] \quad (27)$$

where W_p = Rate of evaporation [kg/h];
q_{ev} = Evaporative heat loss [kJ h^{-1}];
h_{ev} = Specific heat of evaporation for water at temperature,T_s [kJ/kg].

Convective heat loss
Convective heat loss is the heat loss associated with the passing of cold air over the surface of pond water. This is basically influenced by the temperature difference between the cold air and the warm water surface and the velocity of the cold air. Convective heat loss is computed by Equation 28:

$$q_{cv} = 9.045v \times A \times (T_w - T_a) \quad (28)$$

where q_{cv} = Convective heat loss [kJ/h];
v = wind velocity [m/s];
A = Pond area [m^2];
T_w = Pond water temperature [°C]
T_a = Ambient air temperature [°C].

Conductive heat loss
Conductive heat loss is basically the heat lost due to conduction through all the wall area. Since it is usually very small compared to other heat losses, it is usually omitted in most design cases. However conductive heat loss is calculated by Equation 29:

$$q_{cd} = \{[(L + W) \times 12.45] + (L \times W \times 0.4084)\} \times [(T_w - T_a) - 8.33] \quad (29)$$

where q_{cd} = Conductive heat loss [kJ/h];
L = Length of the pond [m];
W = Pond width [m].

Radiative heat loss
Radiative heat loss is due to the heat transfer from the water to the air due to their temperature difference and is given by Equation 30:

$$q_{rd} = 1.836 \times 10^{-8} \times [(492 + 1.8T_w)^4 - (492 + 1.8T_a)^4] \times A \quad (30)$$

where q_{rd} = Radiative heat loss [kJ/h].

To maintain the hatchery ponds at 29°C and the rearing ponds at 28°C, the thermal power requirement and hot water requirement are summarized in Table 12. The greatest energy requirement is in August amounting to 4,154 kW.

TABLE 12: Maximum hot water requirement for the fish farm at different source temperatures

Power (kW)	**Hot water requirement (l/s)**			
	55°C	**65°C**	**78°C**	**95°C**
4,154	36.83	26.87	14.89	14.84

4. ECONOMIC ANALYSIS OF THE SELCTED DIRECT USES

Economic feasibility of any project can be measured using different financial management tools. In this report the Payback Period, Net Present Value (NPV) and the Internal Rate of Return (IRR) are considered.

Simple Payback Period
Payback Period is the duration the project´s cash inflows are expected to repay the investment cost. It is recommended that the Payback period is kept as low as possible for the project to be profitable. This is determined by dividing the investment cost by the annual cash inflow.

Net Present Value (NPV)
This is an analysis tool in which all cash inflows and outflows are discounted to their present value. If the Net Present Value is positive, the project should be accepted. This is basically dependent on the discounting rate. Lower discounting rates, as low as 4%, are commonly used for government projects to be considered viable. A discounting rate of 10% has also been greatly applied (Freeston and Browne, 1994). NPV is computed using Equation 31 (Schmidt, 2014-2015):

$$\text{NPV} = \sum_{n=1}^{n} (\text{FV}_\text{n}) \times (1/(1+r)^n) \quad (31)$$

where NPV = Net Present Value [monetary units];
FV = Future value [monetary units];
n = Number of years;
r = Discount rate [%].

Internal Rate of Return (IRR)
Internal rate of return is the value of the discount rate (r) at which the net discounted cash flows exactly equals the investment cost. It is thus the value of the discount rate that makes Equation 31 equal to zero. A higher IRR is recommended for viability of the project; it should be greater than the desired discount rate.

Based on (ACCA, 2015), IRR is computed by using Equation 32. A discount rate r_a is chosen and NPV is calculated using Equation 31. A second rate r_b is chosen such that NPV is either negative if the first one is positive or positive if the first one is negative. With the two values of r and the two NPV's, IRR is computed as follows:

$$\text{IRR} = r_a + \frac{\text{NPV}_\text{a}(r_b - r_a)}{\text{NPV}_a - \text{NPV}_\text{b}} \quad (32)$$

where IRR = Internal Rate of Return [%];
r_a = Lower discounting rate [%];
r_b = Upper discounting rate [%];
NPV_a = NPV at r_a [monetary units].

However, with the use of MS Excel, IRR is easily found by using Goal Seek function to determine the discount rate by setting the value of the NPV equal to Zero.

4.1 Feasibility of swimming pools and spas

4.1.1 Swimming pools

In swimming pools, the major costs are the investment cost, cost related to chemicals, labour, advertising, maintenance and other supplies. Apart from the initial investment cost, chemicals for water purification and PH control and energy for pumps in the recirculation system are the main contributors to the variable cost. The cost and revenues have been listed in Table 13 and the NPVs for a 10-year period and a discounting rate of 10% have been plotted in Figure 8 as an example for the other technologies. Construction cost estimates are based on Clean Pool and Spa (2015) while road works are costed based on Ministry of Transport and Public Infrastructure (2010). Fees were based on prevailing hotel charges in Malawi.

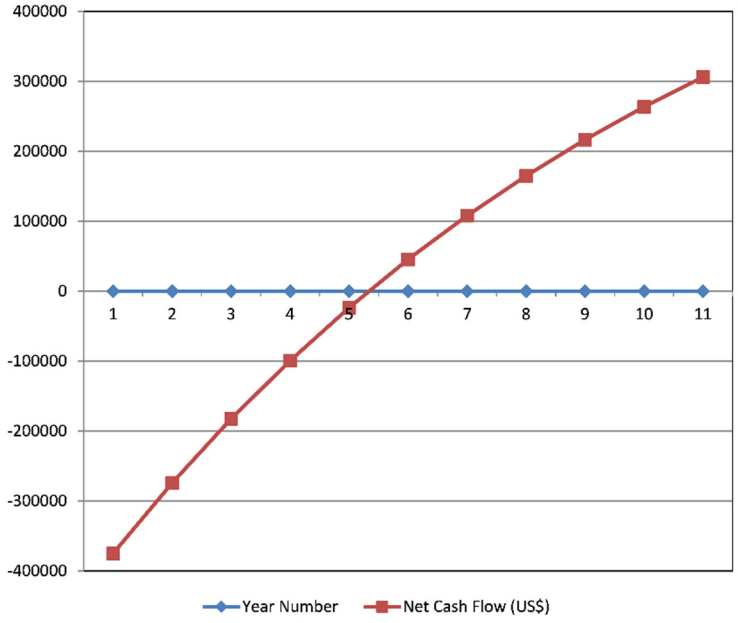

FIGURE 8: Discounted cash flows for computing NPV for swimming pools

With net annual revenue of US$ 110,880 against an initial investment cost of US$ 375,000, we get the values as follows:

IRR = 27%
NPV = US$ 306,292
Discounted Payback period (breakeven point) = 4.21 yrs.
Simple Payback period = 3.4 yrs.

TABLE 13: Estimated cash inflows and outflows for swimming pools

Description	Item	Quantity	Unit Price (US$)	Cash flow (US$)
Investment cost	Pool construction	1	25,000	(25,000)
	Building and access road	1	350,000	(350,000)
Total investment cost				**(375,000)**
Variable cost	Collective cost	12 months	2,500/month	(30,000)
Revenue	Fee collection	12 months	11,740/month	140,880
Net cash flow				**110,880**

4.1.2 Feasibility of a spa

Unlike in swimming pools, in geothermal nature baths, there are no circulation, filtering and PH control systems. The major cost is the investment cost, labour, advertising, maintenance, and other supplies. These are far much lower as compared to those of swimming pools. The cash flows are shown in Table 14.

TABLE 14: Estimated cash inflows and outflows for hot spas

Description	Item	Quantity	Unit Price (US$)	Cash flow (US$)
Investment cost	Pool construction	1	10,000	(10,000)
	Building and access road	1	250,000	(250,000)
Total investment cost				**(265,000)**
Variable cost	Collective cost	12 months	1,000/month	(12,000)
Revenue	Fee collection	12 months	11,740/month	128, 070
Net cash flow		**1 yr.**		**116, 070**

With net annual revenue of US$ 116,070 against an initial investment cost of US$ 265,000, we get the values as follows:

IRR = 43%
NPV = US$ 453,200
Discounted Payback period (breakeven point) = 2.5 yrs.
Simple Payback period = 2.2 yrs

4.2 Feasibility of greenhouse tomato production

In geothermal greenhouse tomato production, major costs are those related with the structure, irrigation and heating network, packaging, storage and labour. For tomato production to be profitable, it is recommended that the product be sold before planting, thus the market should be established before planning to grow the crop. The cash flows are shown in Table 15. Current open field tomato production in Malawi yields on average 950 kg/ha with one cycle per year (Mango et al., 2015). It is anticipated that with proper management the greenhouse tomato yield will reach an average 10 kg per plant giving a total of 6.1 tonnes per cycle. This is an equivalent of 48.4 tonnes per hectare per year.

Greenhouse and tomato production cost and selling prices were based on Pena (2005) and Smith et al. (2015) and some prevailing market prices in Malawi.

TABLE 15: Estimated cash inflows and outflows for greenhouse tomato production

Description	Item	Quantity	Unit price (US$)	Cash flow (US$)
Investment cost	Greenhouse structure	1	65/m^2	(32,760)
	Buildings	1	15,000	(15,000)
	Irrigation	1	25,000	(25,000)
	Packaging and Storage	1	20,000	(20,000)
Total investment cost				**(92,760)**
Variable cost	Collective cost	1	30/m^2	(15,120)
Revenue	Sales	25 tonnes	1.5/kg	36,900
Net cash flow				**21,780**

With net annual revenue of US$ 21,780 against an initial investment cost of US$92,760, we get the values as follows:

IRR = 20%
NPV = US$ 41,069
Discounted Payback period (Breakeven point) = 5.5 yrs.
Simple Payback period = 4.3yrs

4.3 Feasibility of intensive aquaculture facility

The main cost associated with intensive raceway aquaculture is investment cost, pumping cost if water is not supplied by gravity, cost of seed (fingerlings) if there is no on farm hatchery and fish feed if it is not produced on farm. Other costs include labour for harvesting, processing and transport. In this project it is proposed that feed and hatching will be on the farm, purchase will be done in the first year only. The cash flows are shown in Table 16. Expected yield and cost are based on personal information collected from Chambo fisheries in Malawi.

TABLE 16: Estimated cash inflows and outflows for fish farming

Description	Item	Quantity	Unit Price (US$)	Cash flow US$)
Investment cost	Raceway construction	1	6,000,000	(6,000,000)
	Building and access road	1	650,000	(650,000)
Total investment cost				**(6,650,000)**
Variable cost	Collective cost	1 yr.	250,000	(250,000)
Revenue	Fish sales	420 tones	4	1,680,000
Net cash flow				**1,430,000**

With net annual revenue of US$ 1,430,000 against an initial investment cost of US$6,650,000 we get the values as follows:

IRR = 17%
NPV = US$ 2,136,731
Discounted Payback period (breakeven point) = 6.3 yrs.
Simple Payback period = 4.7 yrs.

4.4 Feasibility of indoor fish drying

The major challenge in computing profitability of the fish drying process is that the final product for sale is about 22% in mass as compared to the fresh fish bought. This leads to the processed fish having very high market price per kg – much higher than the fresh fish. The major costs are the investment cost,

the equipment and labour and the actual buying of the raw material (fresh fish) while the income is through sales. The cash flows are shown in Table 17.

TABLE 17: Estimated cash inflows and outflows for indoor fish drying

Description	Item	Quantity	Unit Price (US$)	Cash flow (US$)
Investment cost	Structure and equipment	1	2,600,000	(2,600,000)
	Other cost	1	200,000	(200,000)
Total investment cost				**(2,800,000)**
Variable Cost	Fresh fish purchase	500 tones	1.5 / kg	(750,000)
Revenue	Dried fish sales	106 tones	13 / kg	1,376,471
Net cash flow				**626,471**

With net annual revenue of US$ 626,471 against an initial investment cost of US$2,800,000, we get the values as follows:

IRR = 18%
NPV = US$ 1,049,391
Discounted Payback period (breakeven point) = 6.1 yrs.
Simple Payback period = 4.5yrs

5. CONCLUSIONS AND RECOMMENDATIONS

From the energy and hot water requirement calculations, it has been shown that it is possible for Malawi to develop the existing geothermal fields in Nkhotakota for economic activities like commercial swimming pools, spas, greenhouse tomato production and fish drying. Intensive aquaculture would however require at least some minimal drilling of within 400 m to have enough hot water supply. The economic analysis of all the technologies yielded high Internal Rate of Return and positive Net Present Value though the greenhouse requires a minimum of double the design area to achieve a positive NPV.

I would like to recommend that a detailed social economic status and market analysis be done to come up with a more realistic estimates of the sales of both products and services from the geothermal field development. I would also like to recommend that shallow slim wells of the size of borehole for portable water be drilled and their yield be tested to ascertain sustainable availability of the hot water supply. However, with the existing flows, swimming pools, spas and greenhouses can be developed.

There is need to have similar evaluations done for all geothermal fields in Malawi and determine potential direct utilization technologies which could be implemented while waiting for advanced exploration and deep drilling activities.

ACKNOWLEDGEMENTS

I also would like to express my greatest thanks to my supervisor, Árni Ragnarsson for his untiring effort in his guidance throughout the project work. In addition, I would like to thank Dr. Robert Ridley, Vice Chancellor of Mzuzu University for accepting my attendance to the specialized geothermal training. Great thanks also go to Mr. Lúdvík S. Georgsson and the entire staff of UNU-GTP for accepting me to participate in the programme.

Special thanks go to all the lecturers and the fellows, especially Malawian MSc students and the Geothermal Utilization (2015) class for their great support in areas where I required support to understand system performance and behaviour.

My great lovely thanks should go to my wife, Fausta, and the children together with my mum, Tamalirapo Nyachavula, for their continued encouragement and prayers while I was away participating in the six-month long programme away from home.

Lastly, I would like to express my greatest thanks to God for allowing me to undergo the specialized geothermal utilization training without any serious health challenges.

REFERENCES

ACCA, 2015: *The internal rate of return*. Association of Chartered Certified Accountants. Website: *www.accaglobal.com/in/en/student/exam-support-resources/foundation-level-studyresources/ffm/ffm-technical-articles/the-internal-rate-of-return.html.*

Al Rawahi, Z.N.A., Munusami, A., and Kaithari, D.K., 2013: Performance analysis of solar drying systems for marine products of Oman. *International J. of Students Research in Technology and Management, 1-6*, 610-613.

Allen, G., Pereira, L.S., Raes, D., Smith, M., 1998: *Crop evapotranspiration. Guidelines for computing crop water requirements*. United Nations Food and Agriculture Organization, FAO irrigation and drainage paper 56, 300 pp.

Banda, M.C., Kanyerere, G.Z., and Rusuwa, B.B., 2005: The status of Chambo in Malawi: Fisheries and biology. In: Banda, M., Jamu, D., Nyanja, F., Makuliwa, M., and Maluwa, A. (eds.), *The Chambo restoration strategic plan. Proceedings of the National Workshop held on 13 – 16 May 2003 at Boadzulu Lakeshore Resort, Mangochi.* The WorldFish Center, Penang, Malaysia, 1-7.

Brummet, R.E., and Noble, R., 1995: *Aquaculture for African small holders*. ICLARM – The WorldFish Centre, Penang, Malaysia, 65 pp.

Canakci, M., and Akinci, I., 2006: Energy use pattern analyses of greenhouse vegetable production. *Energy, 31*, 1243-1256.

Canakci, M., Emekli, N.Y., Bilgin, S., and Caglayan, N., 2013: Heating requirement and its cost in greenhouse structures: A case study for Mediterranean region of Turkey. *Renewable and Sustainable Energy Review, 24*, 483-490.

Castilla, N., and Baeza, E., 2013: Greenhouse site selection. In: Duffy, R., (English language ed.), *Good agricultural practices for greenhouse vegetable crops. Principles for Mediterranean climate areas.* United Nations Food and Agriculture Organization, FAO plant and production protection paper 217, 21-33.

Chimatiro, S.K., and Chirwa, B.B., 2005: *National aquaculture sector overview, Malawi*. United Nations Food and Agriculture Organization, National aquaculture overview fact sheets. Website: *www.fao.org/fishery/countrysector/naso_malawi.*

Chimphamba, J., Ngongondo, C., and Mleta, P., 2009: Groundwater chemistry of basement aquifer: A case study of Malawi. In: Titus, R., Beekman, H., Adams, S., and Stranchan, L., (eds.), *The basement aquifers of Southern Africa.* Water Research Commission, Gezina, South Africa, report no. TT 428-09, 39-44.

Clean Pool and Spa, 2015: Cost of swimming pool installation. Clean Poola and Spa, webpage: *www.clean-pool-and-spa.com/cost-of-swimming-pool.html.*

DeGannes, A., Heru, K.R., Mohammed, A., Paul, C., Rowe, J., Sealy, L., and Seepersad, G., 2014: *Tropical greenhouse growers' manual for the Caribbean*. The Caribbean Agricultural Research and Development Institute (CARDI), University of West Indies, St. Augustine, Trinidad and Tobago, 157 pp.

Djevik, M., and Dimitrijevic, A., 2009: Energy consumption for different greenhouse constructions. *Energy, 34*, 1325-1331.

Dulanya, Z., Morales-Simfors, N., and Sivertun, A., 2010: A comparison between silica and cation geothermometry of Malawi hot springs. *Proceedings of the World Geothermal Congress 2010, Bali, Indonesia*, 6 pp.

Earle, R.L., and Earle, M.D., 2004: *Unit operations in food processing*. The New Zealand Institute of Food Science and Technology Inc., web edition. Website: http://www.nzifst.org.nz/unitoperations/

Emeish, M.S., 1999: Geothermal heating system for Jordanian greenhouses. Report 2 in: *Geothermal training in Iceland 1999*. UNU-GTP, Iceland, 41-70.

Fabrizio, E., 2012: Energy reduction measures in agricultural greenhouses heating: Envelope, system and solar energy collection. *Energy and Buildings, 53*, 57-63.

FAO, 2008: *Nutrition country profile: Republic of Malawi*. United Nations Food and Agriculture Organization (FAO), 57 pp. Website: *ftp.fao.org/ag/agn/nutrition/ncp/mwi.pdf.*

Foster, V., and Shkaratan, M., 2010: Malawi's infrastructure: A continental perspective. The International Bank for Reconstruction and Development / The World Bank, Washington DC, United States, AICD country report, 35 pp.

Freeston, D.H., and Browne, P.R.L., 1994: *Teaching the teachers: Geothermal technology*. Geothermal Institute, University of Auckland, Auckland, New Zealand, 146 pp.

Geothermal Education Office, 2005: *Geothermal energy uses*. Geothermal Education Office, poster, webpage: *www.geothermal.marin.org*

Gondwe, K., Allen, A., Georgsson, L.S., Chakhala. H., and Tsokonombwe, G., 2015: Geothermal Development in Malawi – a Country Update. *Proceedings of the World Geothermal Congress 2015, Melbourne, Australia*, 9 pp.

Harrison, D.R., and Chapusa, F.W.P., 1975: The geology of the Nkhotakota – Benga area. *Bull. Geol. Surv. Malawi, 32*, 33 pp.

Hickman, G.W., 2010: Tropical greenhouses: *Design, construction and supply lists*. Cuesta Roble Consulting, CA, United States, 2 pp.

Hubackova, A., Kucerova, I., Chrun, R., Chaloupkova, P., and Banout, J., 2014: Development of solar drying model for Cambodian fish species. *The Scientific World Journal, 2014*, 10 pp.

Ísaksson, Á., 2015: *Aquaculture: Global status, technology and development. Teaching manual*. UNU-GTP, unpublished lecture notes, Iceland, 35 pp.

Joudi, K.A., and Hasan, M.M., 2013: Cooling and heating a greenhouse in Baghdad by a solar assisted desiccant system. *J. Engineering, 19*, 933-951.

Kapute, F., 2008: *Fish quality and processing in Malawi: Responding to challenges through institutional capacity building*. United Nations University Fisheries Training Programme (UNU-FTP), Iceland, final project, 28 pp.

Karras, E., 1996: Prospectives for exploiting the geothermal resources of Ikaria, Greece. Report 6 in: *Geothermal training in Iceland 1996*. UNU-GTP, Iceland, 103-133.

Kasapoglu, H., and Parlaktuna, M., 2005: A technical feasibility study on the use of Çavundur geothermal field for greenhouse heating. *Proceedings of the World Geothermal Congress 2005, Antalya, Turkey*, 9 pp.

Kiruja, J., 2011: Use of geothermal energy in dairy processing. Report 16 in: *Geothermal training in Iceland 2011.* UNU-GTP, Iceland, 303-326.

Kittas, C., Katsoulas, N., Bartzanas, T., and Bakker, S., 2013: Greenhouse climate control and energy use. In: Baudoin, W., Nono-Womdim, R., Lutaladio, N., Hodder, A., Castilla, N., Leonardi, C., De Pascale, S., Qaryouti, M. and Duffy, R., (English language ed.), *Good agricultural practices for greenhouse vegetable crops. Principles for Mediterranean climate areas.* United Nations Food and Agriculture Organization, Rome, FAO plant and production protection paper 217, 63-95.

Kumar, K.S., Tiwari, K.N., and Madan K.J., 2009: Design and technology for greenhouse cooling in tropical and subtropical regions: A review. *Energy and Buildings, 41*, 1269-1275.

LaCroix, I., LaCroix, A.E.S., and LaCroix, T.M., 1991: *Orchids of Malawi: The epiphylitic and terrestrial orchids from South and East Central Africa.* A.A. Balkema, Rotterdam, Netherlands, 358 pp.

Lund, J.W., 1996: *Lectures on direct utilization of geothermal energy*. UNU-GTP, Iceland, report 1, 123 pp.

Maharjan, R., 1995: Design of dryer and a swimming pool using geothermal water. Report 7 in: *Geothermal training in Iceland 1995*. UNU-GTP, Iceland, 155-184.

Makawa, Z., Kapute, F., and Valeta, J., 2014: Effect of delayed processing on nutrient composition, pH and organoleptic quality of pond raised Tilapia (Oreochromis Shiranus) stored at ambient temperature. *African J. of Food, Agriculture, Nutrition and Development, 14-3*, 8872-8884.

Mapoma, H.W.T., and Xie, X., 2014: Basement and alluvial aquifers of Malawi: An overview of groundwater quality and policies. *African J. Environmental Science and Technology, 8-3*, 190-202.

Ministry of Agriculture and Food Security, 2011: *Malawi agricultural sector wide approach: a prioritised and harmonised agricultural development agenda: 2011-2015*. Malawi Government, 181 pp.

Ministry of Energy and Mining, 2003: *National energy policy 2003-2008*. Malawi Government, 170 pp.

Ministry of Transport and Public Infrastructure, 2010: Investment programme for road sector in Malawi 2010 – 2020. Malawi Government, 73 pp.

Montero, J.I., Teitel, M., Baeza, E., Lopez, J.C., and Kachira, M., 2013: Greenhouse design and covering materials. In: Baudoin, W., Nono-Womdim, R., Lutaladio, N., Hodder, A., Castilla, N., Leonardi, C.,

De Pascale, S., Qaryouti, M. and Duffy, R., (English language ed.), *Good agricultural practices for greenhouse vegetable crops. Principles for Mediterranean climate areas.* United Nations Food and Agriculture Organization, Rome, FAO plant and production protection paper 217, 35-62.

Mrema, G.C., Gumbe, L.O., Chepete, H.J., and Agullo, J.O., 2011: *Rural structures in the tropics. Design and development.* United Nations Food and Agriculture Organization, The Technical Centre for Agricultural and Rural Cooperation (CTA), Rome, 486 pp.

Msika, B.J.W., Saka, J.D.K., and Dulanya, Z., 2014: Spatial distribution, chemistry and subsurface temperatures of geothermal springs in Nkatabay, Malawi. *African J. Environmental Science and Technology, 8-8*, 464-475.

Mujaffar, S., and Sankat, C.K., 2005: The air drying behaviour of shark fillets. *Canadian Biosystems Engineering, 47*, 3.11-3.21.

Jalili-Nasrabadi, S., 2004: Geothermal district heating and swimming pool in the Sabalan Area, Iran. Report 7 in: *Geothermal training in Iceland 2004*. UNU-GTP, Iceland, 99-130.

NGMA, 2015: *Heat loss*. National Greenhouse Manufacturers Association (NGMA), Harrisburg, PA, United States, 5 pp.

Nkhotakota District Council, 2010: Nkhotakota District social economic profile. Malawi Government, Nkhotakota District Council, 158 pp.

Nyanja, F., Jamu, D., Kaunda, E.K.W., and Ford, A., 2005: Culture – based production systems: Options for the Chambo in Lake Malawi and Lake Malombe. In: Banda, M., Jamu, D., Nyanja, F., Makuliwa, M., and Maluwa, A., (eds.), *The Chambo restoration strategic plan – Proceedings of the national workshop held on 13 – 16 May 2003 at Boadzulu Lakeshore Resort, Mangochi.* The WorldFish Center, Penang, Malaysia, 113 pp.

Omenda, P.A., 2010: The geology and geothermal activity of the East African Rift. *Presented at "Short Course V on Exploration for Geothermal Resources", organized by UNU-GTP, GDC and KenGen, at Lake Bogoria and Lake Naivasha, Kenya,* 18 pp.

Pack, M., and Mehta, K., 2012: Design of affordable greenhouses for East Africa. *2012 IEEE Global Humanitarian Technology Conference, Seattle, WA, United States*, 104-110.

Pena, J.G., 2005: Greenhouse vegetable production economic considerations, marketing and financing. Aggie Horticulture, webpage: *aggie-horticulture.tamu.edu/greenhouse/hydroponics/economics.html.*

Peters, E.R., 1975: The geology of South Viphya Area. *Bull. Geol. Surv. Malawi, 36*, 38 pp.

Pillay, T.V.R., and Kutty, M.N., 2005: *Aquaculture: Principles and practice* (2nd ed.). Blackwell Publishing, Oxford, UK, 640 pp.

Rafferty, K.D., 2003: Aquaculture technology. In: Dickson, M.H., and Fanelli, M. (eds.), *Geothermal energy, utilization and technology.* UNESCO, Bangalore, India, 121-128.

Ragnarsson Á., 2015: *Geothermal bathing and swimming. Teaching notes*. UNU-GTP, unpublished lecture notes, 56 pp.

Rahman, S.M., 2015: Drying of fish and seafood. In: Mujumdar, A.S., (ed.), *Handbook of industrial drying* (4th ed.). CRC Press, Taylor & Francis Group, Boca Raton, FL, United States, 1334 pp.

Ruddle, K., 1990: Fish processing technologies for entrepreneurial development in Bangladesh. In: *Transfer for entrepreneurial development in Bangladesh*. U.N. Economic and Social Commission for Asia and the Pacific (ESCAP), Bangkok, 67-85.

Sankat, C.K., and Mujaffar, S., 2004: Sun and solar cabinet drying of salted shark fillets. *Drying 2004 – Proceedings of 14th International Drying Symposium (IDS 2004), Vol. C*, 1584-1591.

Schmidt, M., 2015: *Discounted cash flow DCF, net present value NPV, time value of money explained: Definitions, meaning, and calculated examples*. Solution Matrix Limited, Business Encyclopedia. Website: *www.business-case-analysis.com/discounted-cash-flow.html.*

Sengar, S.H., Khandetod, Y.P., and Mohod, A.G., 2009: Low cost solar dryer for fish. *African J. of Environmental Science and Technology, 3-9*, 265-271.

Seveda, M.S., 2012: Design and development of walk-in hemicylindrical solar tunnel dryer for industrial use. *International Scholarly Research Network, 2012*, 9 pp.

Shamshiri, R., and Wan Ishmail, W.I., 2014: Investigation of climate control techniques for tropical low land greenhouses in Malaysia. *Journal of Applied Sciences, 14-1*, 60-65.

Shethi, V.P., and Sharma, S.K., 2008: Survey and evaluation of heating technologies for world-wide agricultural greenhouse applications. *Solar Energy, 82*, 832-859.

Smith, J., Hewitt, T., Hochmuth R. and Hochmuth, G., 2015: A profitability and cash flow analysis of a typical greenhouse production in North Florida using tomato as an example. Webpage: *smallfarms.ifas.ufl.edu/crops/hydroponics/pdf/cashflowanalysis.pdf.*

Snyder, R.G., 2001: *Greenhouse tomato handbook*. Mississippi State University, Starkville, MS, US, 28 pp.

Sta-Rite Industries, 2003: *Basic training manual* (3rd ed.). Sta-Rite Industries, 66 pp, webpage: *www.pentairpool.com/pdfs/staritecommTM.pdf*

Stickney, R.R., 2005: *Aquaculture: An introductory text.* CABI Publishing, Oxfordshire, UK, 278 pp.

Svavarsson, G., 1990: *Designing swimming pools*. University of Iceland, Reykjavik, BSc thesis, 52 pp.

Tall, A., 2009: Fisheries in landlocked Malawi – potential for development. *INFOFISH International, 6*, 61-65.

Toujani, M., Hassini, L., Azzouz, S., and Belghith, A., 2012: Experimental study and mathematical modelling of Silverside fish convective drying. *J. of Food Processing and Preservation, 37*, 930-938.

Valeta, J.S., Likongwe, J.S., Kassam, D., and Maluwa A.O., 2013: Temperature-dependent egg development rates, hatchability and fry survival rate of Lake Malawi Tilapia (Chambo), Oreochromis karongae (Pisces: Cichlidae). *International J. of Fisheries and Aquaculture*. 4, 55-59.

Van Nguyen, M., Arason, S., Gissurarson, M., and Pálsson, P.G., 2015: *Uses of geothermal energy in food and agriculture – Opportunities for developing countries.* United Nations Food and Agriculture Organization, Rome, 52 pp.

Von Zabeltitz, C., 1997: Why greenhouses in the tropics? *Der Tropenlandwirt, Beitrage zur tropischen Landwirtschraft und Veterinarmedizin, 98*, 237-244.

Von Zabeltitz, C., 2011: *Integrated greenhouse systems for mild climates: Climate conditions, design, construction, maintenance, climate control*. Springer – Verlag, Berlin Heidelberg, 361 pp.

White P. and Rigby, M., 2003: *Shallow raceway design Solemates Programme.* Academia website: *www.academia.edu/10232191/Shallow_raceway_design_for_aquaculture,* 26 pp.

World Food Programme, 2015: *The cost of hunger in Malawi – Implications on national development and vision 2020.* World Food Programme, 63 pp. Website: http://www.documents.wfp.org/stellent/ groups/public/ documents/newsroom/wfp274603.pdf.

APPENDIX I: Structural map of Nkhotakota – Benga Area (Harrison and Chapusa, 1975)

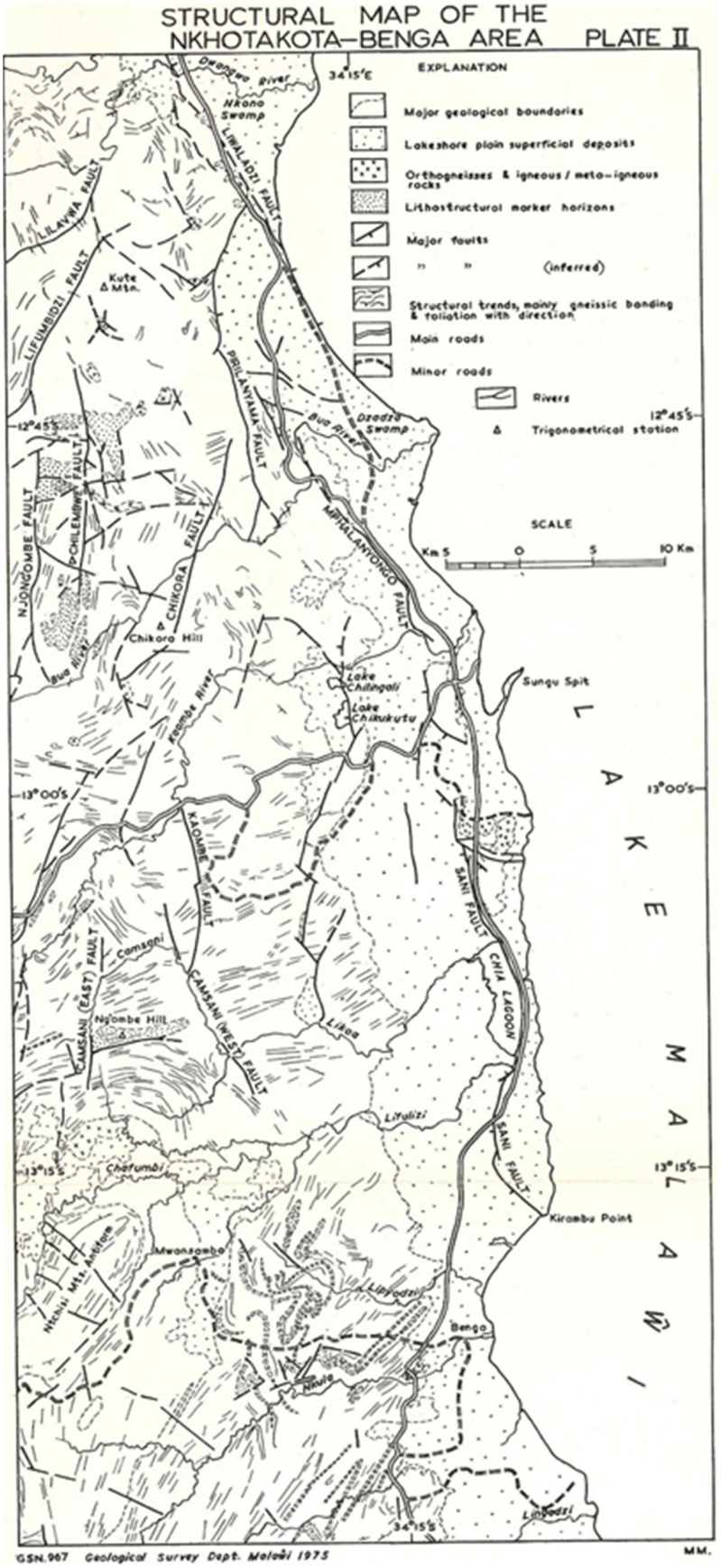

APPENDIX II: Lindal diagram and pictorial modified Lindal diagram
(Kiruja, 2011; Geothermal Education Office, 2005)

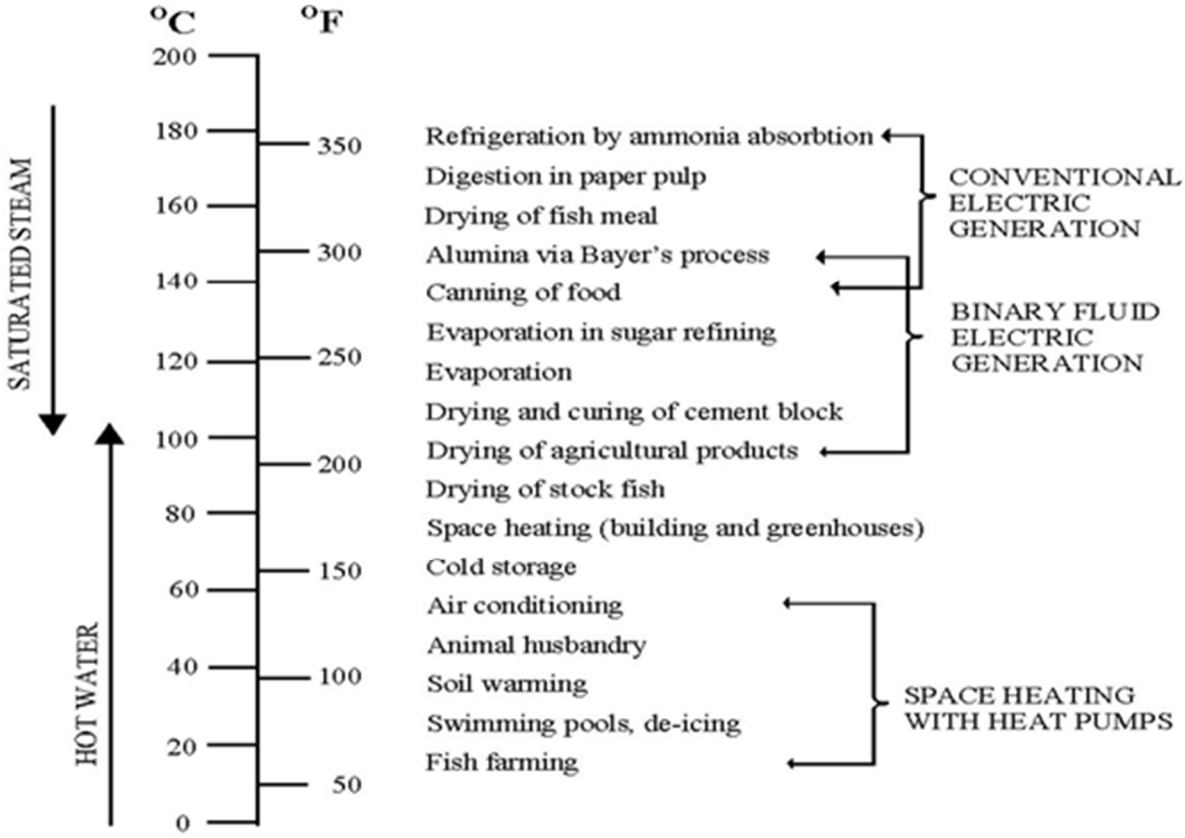

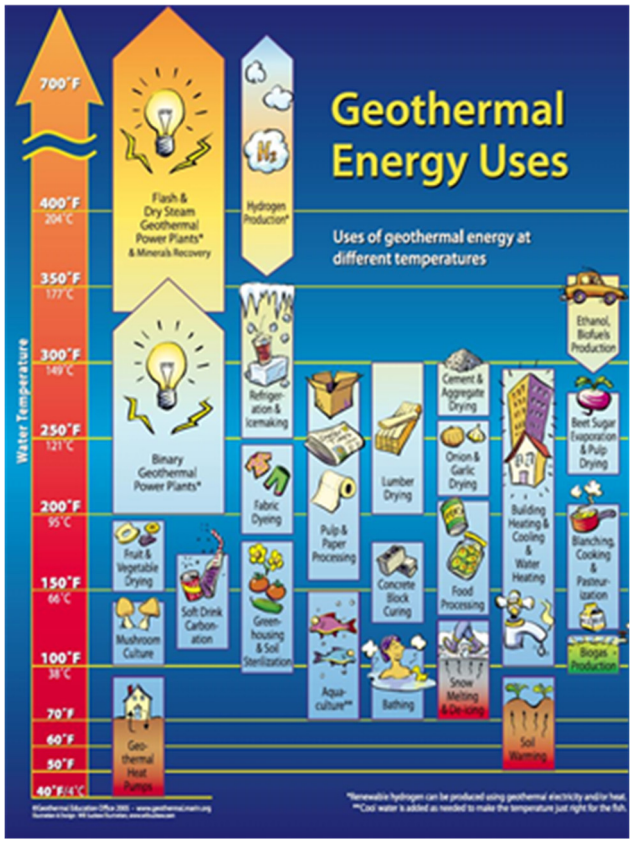

APPENDIX III: Swimming pool, spa and aquaculture ponds water to air temperature differences and their corresponding partial pressures

Month	Mean monthly min. temperat. (°C)	Wind velocity (m/s)	RH (%)	Vapour saturation pressure (mbar)	Partial pressure of air (mbar)	pw - pa (28°C)	pw - pa (29°C)	pw - pa (38°C)	pw - pa (40°C)	pw - pa (42°C)	pw - pa (45°C)	pw - pa (47°C)
Jan	21.1	2.81	80	35.03	28.13	9.70	11.96	38.19	45.71	53.96	67.81	78.13
Feb	21.1	2.63	79	35.03	27.74	10.09	12.35	38.58	46.10	54.35	68.20	78.52
Mar	20.7	2.72	77	24.43	18.88	Q	a.21	47.44	54.96	63.21	77.06	87.38
Apr	20.1	2.98	68	23.54	15.98	21.85	24.11	50.34	57.86	66.11	79.96	90.28
May	17.7	3.33	58	20.26	11.73	26.10	28.36	54.59	62.11	70.36	84.21	94.53
Jun	15.6	3.68	56	17.73	9.96	27.87	30.13	56.36	63.88	72.13	85.98	96.30
Jul	15.1	3.86	54	17.17	9.19	28.64	30.90	57.13	64.65	72.90	86.75	97.07
Aug	15.7	4.12	48	17.84	8.58	29.25	31.51	57.74	65.26	73.51	87.36	97.68
Sep	17.7	4.21	44	20.26	8.93	28.90	31.16	57.39	64.91	73.16	87.01	97.33
Oct	20.5	4.30	47	24.13	11.24	26.59	28.85	55.08	62.60	70.85	84.70	95.02
Nov	22.1	3.77	57	26.61	15.03	22.80	25.06	51.29	58.81	67.06	80.91	91.23
Dec	21.6	3.07	73	25.81	18.82	19.01	21.27	47.50	55.02	63.27	77.12	87.44

Month	Mean monthly min. temperat. (°C)	ΔT(28)	ΔT(29)	ΔT(38)	ΔT(40)	ΔT(42)	ΔT(45)	ΔT(47)
Jan	21.1	6.9	7.9	16.9	18.9	20.9	23.9	25.9
Feb	21.1	6.9	7.9	16.9	18.9	20.9	23.9	25.9
Mar	20.7	7.3	8.3	17.3	19.3	21.3	24.3	26.3
Apr	20.1	7.9	8.9	17.9	19.9	21.9	24.9	26.9
May	17.7	10.3	11.3	20.3	22.3	24.3	27.3	29.3
Jun	15.6	12.4	13.4	22.4	24.4	26.4	29.4	31.4
Jul	15.1	12.9	13.9	22.9	24.9	26.9	29.9	31.9
Aug	15.7	12.3	13.3	22.3	24.3	26.3	29.3	31.3
Sep	17.7	10.3	11.3	20.3	22.3	24.3	27.3	29.3
Oct	20.5	7.5	8.5	17.5	19.5	21.5	24.5	26.5
Nov	22.1	5.9	6.9	15.9	17.9	19.9	22.9	24.9
Dec	21.6	6.4	7.4	16.4	18.4	20.4	23.4	25.4

Partial pressure at water surface (RH =100%)	
T(°C)	Ps (mbar)
28	37.83
29	40.09
38	66.32
40	73.84
42	82.09
45	95.94
47	106.26

UNITED NATIONS UNIVERSITY
UNU-GTP
Geothermal Training Programme

Orkustofnun, Grensasvegur 9,
IS-108 Reykjavik, Iceland

Reports 2015
Number 13

THE THERMODYNAMICS BEHIND INITIATION OF FLOW FROM GEOTHERMAL WELLS

Jason G. Gotuato
Energy Development Corporation - EDC
38/F One Corporate Centre Building
Julia Vargas corner Meralco Avenue
Ortigas Center, Pasig City, 1605
PHILIPPINES
gotuato.jg@energy.com.ph / jasongotuato@yahoo.com

ABSTRACT

Air-lift pumping and air compression are two techniques used to initiate flow from medium- and high-temperature geothermal wells. This paper aims to explain further the thermodynamic concepts of these methods. Spreadsheet models were developed to gain understanding of the technical requirements for a successful well discharge, and in planning the aforementioned methods of stimulation.

1. INTRODUCTION

Geothermal wells are the conduit for geothermal fluids to flow from the reservoir to the surface. They can be characterized into: low temperature (< 150°C), medium temperature (150-200°C) and high temperature (> 200°C) wells. Figure 1 illustrates a typical schematic diagram of a casing program for a high-temperature geothermal well. The low-temperature wells are used for district heating or direct use and high-temperature wells for power generation. These wells can be further subdivided based on the formation pressure into two: artesian and non-artesian wells. Artesian wells are wells which have a water level above the surface and will flow when the wellhead valve is opened. Non-artesian wells have a water level below the surface and must be pumped or stimulated in order to self-flow. Some non-artesian wells will build up gas or steam pressure on top when shut-in and will flow when opened, due to boiling deep in the well (Steingrímsson, 2015). Figures 2 and 3 show typical pressure per depth plots of artesian and non-artesian wells for both low- and high-temperature wells, respectively.

Some high-temperature geothermal wells are capable of self-discharge or are simply self-flowing wells. These wells are usually from vapour-dominated systems and those within the naturally-two-phase regions of 1iquid-dominated reservoirs. Many wells, however, are non-artesian. Discharge of these wells can often be initiated by certain methods (Buning et al., 1998).

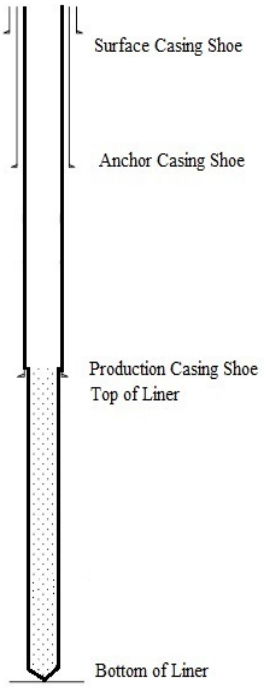

FIGURE 1: Schematic diagram of a geothermal well

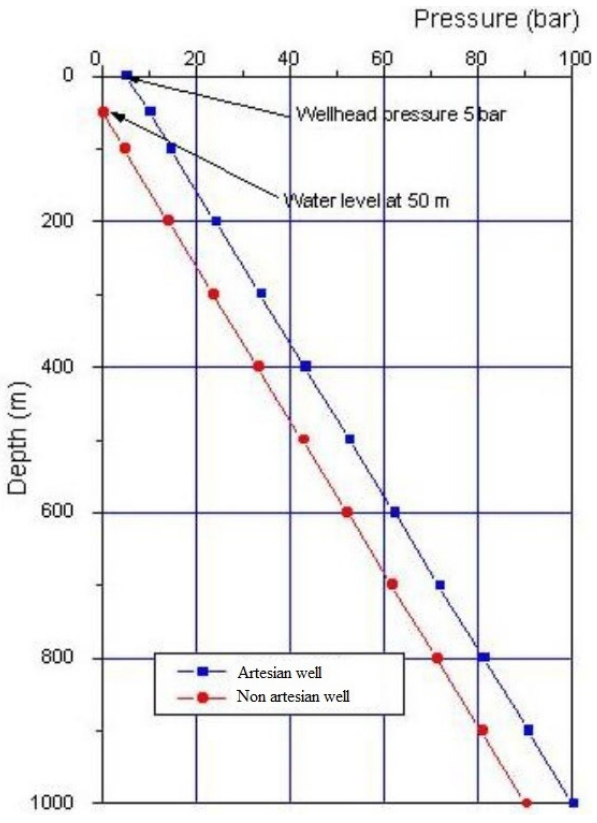

FIGURE 2: Artesian and non-artesian wells for low-temperature systems (Steingrímsson, 2015)

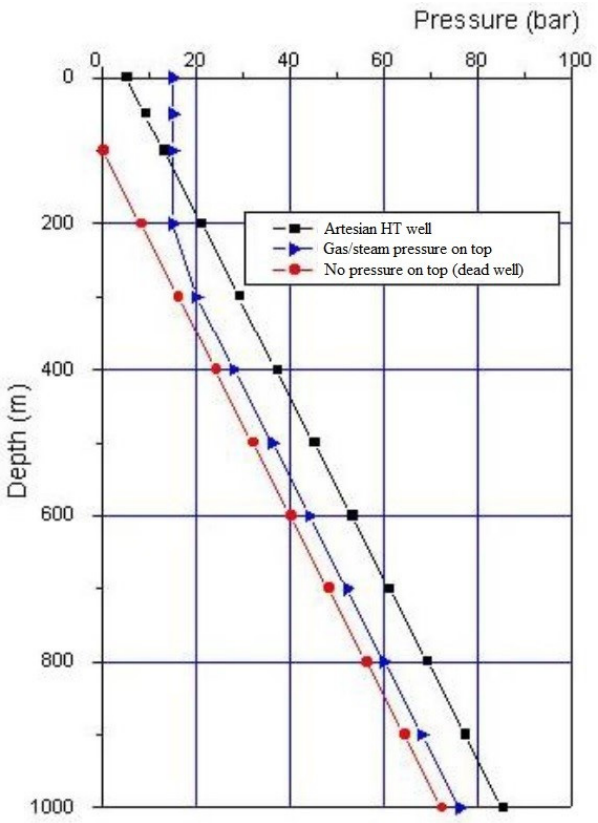

FIGURE 3: Artesian and non-artesian wells for high-temperature systems (Steingrímsson, 2015)

Air-lift pumping and air compression are two methods commonly employed to initiate discharge from geothermal wells. Both methods involve air injection into the well using an air compressor. With the air-lift pumping method, air is injected through a coiled tubing or a drill pipe run into the well to a depth below the water level. The low-density air will lift the water out the well to initiate self-flow, once it is hot enough so boiling of the water supplies sufficient steam to overtake the "air-lifting". With the air compression stimulation, air is injected through a valve (kill line) on the wellhead, depressing the water level. The cold water is pushed down into the hot part of the well to reach the formation temperature at that depth, eventually allowing the well to self-flow once the pressure is rather rapidly released and boiling in the water lifts the fluid to the surface.

2. OBJECTIVE

The objective of the study is to explain the thermodynamics behind the two methods: air-lift pumping and air compression. What are the technical requirements for a successful discharge by air-lifting and compressing of the well?

For the air-lift pumping the questions are, what submergence (distance below the water table) the coiled tubing or drill pipe is required, and what air-compressor rating (pressure and air flow) is necessary for a successful discharge? For air compression, the questions are; what air-compressor rating is required for a certain job and how long does it take to compress a well from zero (initial) to final pressure? What is the minimum water level suppression required to discharge the well successfully by compression alone? What other key factors need to be considered for a well to attain successful discharge and to maintain self-flow?

3. METHODOLOGY

The two methods, air-lift pumping and air compression, will be explained operationally and technically, using concepts learned from thermodynamics and fluid dynamics. Literature research will be the first step in describing these concepts. The discussion will focus on what is really happening inside the wellbore.

Spreadsheet models were developed as part of this report to aid in the analysis and guide the design of these two procedures. MS Excel will be used to develop these models together with X-Steam, an add-in function in Excel for steam properties (http://xsteam.sourceforge.net/). The first spreadsheet model for air-lift pumping aims to simulate success of the air-lift operation, if the flow will reach the surface after inputting certain parameters, such as air volume injected trough the coiled tubing below the water level in the well. The second spreadsheet model for the air compression aims to simulate how much air volume, or what capacity of compressor is needed to compress a well, given the initial and desired pressure and compressor time. The third spreadsheet model, also for air compression aims to simulate success of air compression, if the pressure profile attained immediately after the air discharge is sufficient for the well to self-flow, given the reservoir formation temperature and pressure. The fourth spreadsheet model was developed to simulate the flowing pressure and temperature profile from the bottom to the top of the well. This is a two-phase simulator that aims to answer whether the well will sustain self-flow or not. The HOLA wellbore simulator program (Björnsson et al., 1993) was also used to calculate the temperature and pressure profiles of flowing wells. The spreadsheet model results are compared to the HOLA results and to actual measurements made in flowing wells (dynamic logs).

Actual field data gathered from initiating jobs for wells to flow and flowing wells in the Philippines are used for this project to confirm the model predictions. Data, such as initial wellhead pressure, downhole temperature and pressure logs, duration of stimulation method, target wellhead pressure, compressor rating etc., will be used. The data are analysed and serve as an actual example after learning the physics behind the stimulation process.

4. AIR-LIFT PUMPING

In air-lift pumping or gas-lifting, coiled tubing, drill pipes, or hoses are run into the hole from the wellhead to depths below the water level in the well. Compressed air or nitrogen gas is then injected through the pipes, causing the water column in the annulus to bubble as the air flows back to the surface. The fluid density at the water/air column will then decrease, causing the aerated fluid level to rise. This method is commonly applied to freshwater wells, often referred to as air-lift pumping. In the oil industry, this type of method is also used for producing oil wells that have stopped producing because of severe pressure drawdown in the reservoir (Sarmiento, 2011). The schematic diagram for the typical air-lift pumping in freshwater wells is shown in Figure 4. The arrangement in geothermal wells is similar except the production casing serves as the eductor pipe and the wellhead diverter is more robust.

The common terms are the following:

- *Discharge level* is the level where the discharge line is.
- *Static water level* is the depth where the water level is at static condition.
- *Pumping water level* is the depth where the water level is during air-lift pumping.
- *Eductor pipe* is a temporary pipe installed in large diameter groundwater wells but is not practical to install in high-temperature geothermal wells.
- *Air line* is the coiled tubing, drill pipe, or hose installed from the wellhead to set depth below the water level.
- *Starting submergence* is the length of the air line submerged below the static water level.

- *Pumping submergence* is the length of the air line submerged below the pumping water level.
- *Total starting lift* is the distance from the discharge level to the static water level.
- *Total pumping lift* is the distance from the discharge level to the pumping water level.

To start and maintain air-lift pumping, air pressure and volume flow rate are essential. To overcome the initial pressure the air pressure must reach the starting submergence pressure at the lower end of the air line. The air volume flow rate injected becomes the most essential factor in the success of an air-lift pumping after the pressure has initiated flow (Australian Drilling Industry Training Committee, Ltd., 1997). Figure 5 shows how the addition of different volumes of air affects the water flow pattern in the borehole.

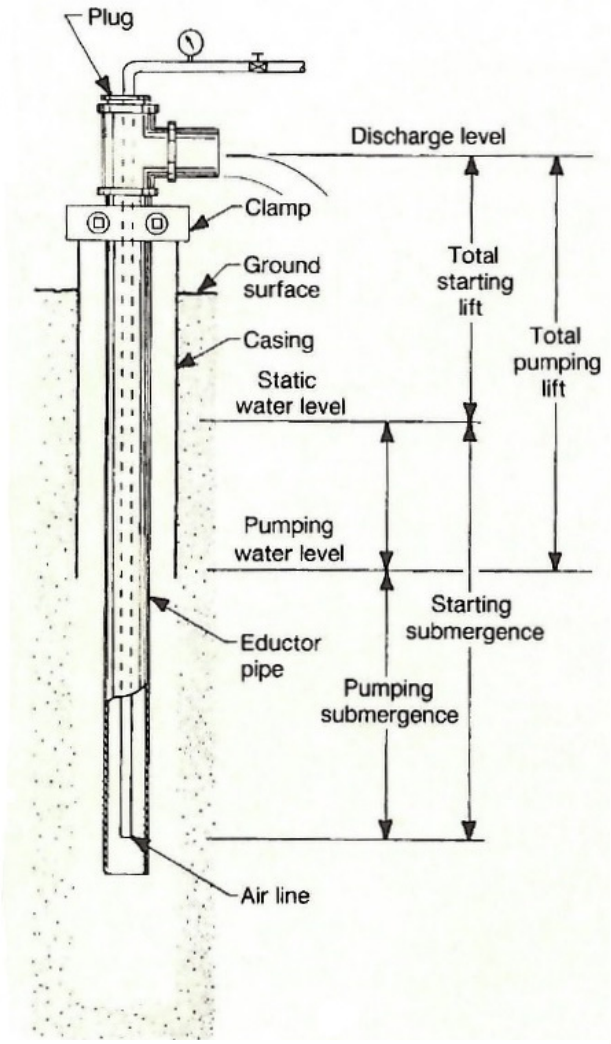

FIGURE 4: Schematic diagram of a typical air-lift pumping set-up with the common terms used (Ingersoll-Rand, 1971, in Driscoll, 1986)

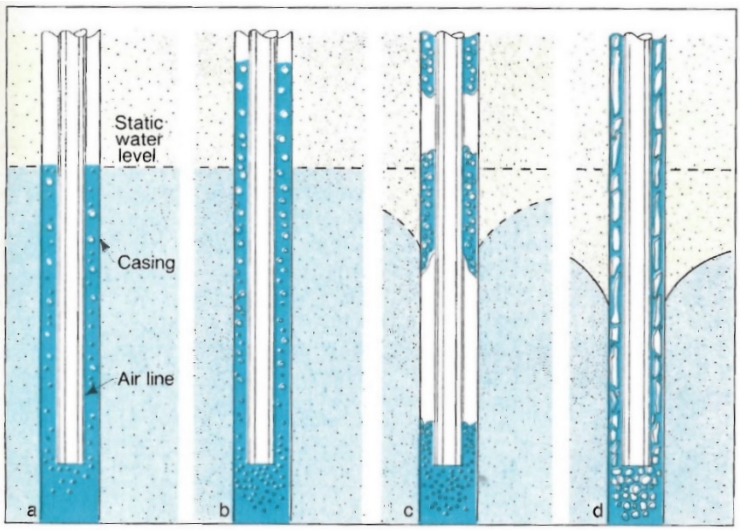

FIGURE 5: This diagram shows how the two-phase (air and water) flow behaves during air-lift pumping; (a) Introduction of air into the well shows no change at the water level because the first air injected is just enough to overcome the initial head exerted by the water column; (b) As the volume of injected air increases, the water becomes partly aerated as it rises up the well; (c) Aerated water surges or is lifted out of the casing irregularly as the air injected further increases; (d) If injected air is sufficient, aerated water will flow steadily out of the well, but note that excessive air volume might actually decrease the flow rate of water (Driscoll, 1986)

5. AIR COMPRESSION

Stimulation by air compression involves mobilizing and connecting a high-pressure air compressor to the wellhead. The air injected will cause the cold water column to be pressed down and into the hotter portion of the well. The well is then shut for hours or days to give ample time for the suppressed cold water to heat up. If the fluid heats up to a sufficient temperature, it should overcome pressure and heat losses as it rises up the wellbore and initiate boiling. Once the valve of the well is opened for discharge, the flow should reach the surface if the attempt for discharge is successful (Sarmiento, 2011).

Prior to the start of compression, the field engineer shall gather the relevant well information for the stimulation work, such as casing burst pressure, branch limit pressure, wellhead conditions, target wellhead pressure, temperature and pressure profile of the well, casing depth, etc. The engineer and operators shall mobilize the air compressor to the site with all the accessories: pressure rated hose, swivel joints and pipe, wing valve adaptor, fuel, stud bolts, seal ring and other necessary tools. The set-up of the air compressor, and the arrangement of the swivel joints and pipe from the valve of the well to be compressed to the discharge line of the air compressor, shall be planned accordingly and have whip-stop cables on connections for safety. After the installation of the pressure rated hose, swivel joints, and pipes, the connections should be checked for leakages and if they are securely in place. The installed pressure gauges at the wellhead must also be inspected to ensure that they are in good working condition and calibrated.

The wellhead pressure build-up should be monitored during the compression. The engine and the discharge line going to the well should be checked for any abnormal conditions. Leaks should also be checked and repaired immediately if any are observed. The pressure in the discharge line should be released before the repairs. The switch on the air compressor should be changed from load to unload after achieving the desired wellhead pressure of the well. The pressure build-up on the wellhead can take hours or days, depending on the capacity of the compressor and the wellhead pressure considered necessary to stimulate the well to flow. When the wellhead pressure is reached, the well is kept shut-in for a number of hours or days (sometimes a week) for heating up until the well is ready for discharging.

Figure 6 shows a hypothetical well pressure and temperature profiles prior to and after air compression. The wellhead pressure prior to air compression is 1 bar-a and the water level is at 500 m with a temperature of about 80°C, at that depth. During the air compression, the wellhead pressure rises up to 70 bar-a and the water level becomes depressed to 1500 m, to the production casing shoe, where the temperature is about 300°C. At around 1400-1600 m, the temperature profile overlaps with the boiling point depth curve, which indicates a tendency of boiling around that depth.

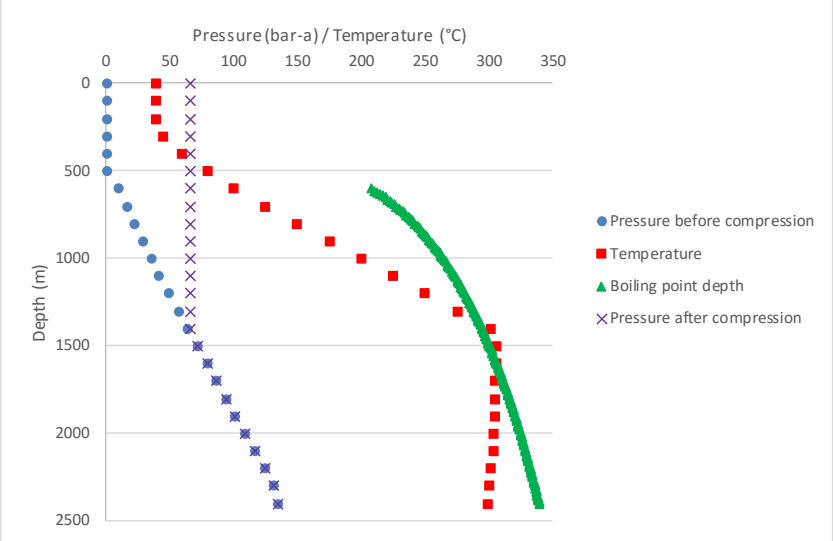

FIGURE 6: Temperature and pressure downhole profiles of a non-artesian well prior to air compression

The water column that is depressed encounters high formation temperature which increases its energy content (enthalpy). The rapid release of pressure is made by opening the valve at the wellhead and

allowing the air to escape. Pressure reduction then occurs which causes the fluid to flow up the wellbore. Some of the water flashes to steam due to the energy released during pressure reduction (Colina et al., 2008). The boiling process for the model calculations is adiabatic (iso-enthalpic) as the heat loss is minor from the well to the formations.

The maximum depth to which the water level can be compressed is down to the first loss zone, but typically only down to the depth of the production casing shoe, because the next section is the open hole with a slotted liner, and air injected there will just diffuse out into the formation. Usually, the well is compressed to the maximum allowable pressure, taking in consideration the pressure rating of the discharge lines and of the wellhead.

6. MODELS

Spreadsheet models are developed as part of this report for air-lift pumping, air compression, and two-phase simulation. The design, formulas, input and output parameters are discussed in the following sections. Practical guidelines or “rules of thumb” from handbooks/guidelines were used to select parameters to be used for a successful air-lift pumping. To verify the two-phase simulator model results a wellbore simulator program called HOLA, and dynamic well logging measurements were used.

6.1 Air-lift

6.1.1 Rule of thumb

Guidelines for designing air-lift pumping operations have been established based on field experience as described by Driscoll’s "*Groundwater and wells* (1986 - 2nd ed.)" book and the manual from the Australian Drilling Industry Training Committee Ltd. (1997) entitled "*Drilling: the manual of methods, applications, and management*". The design procedure will be explained by the following example.

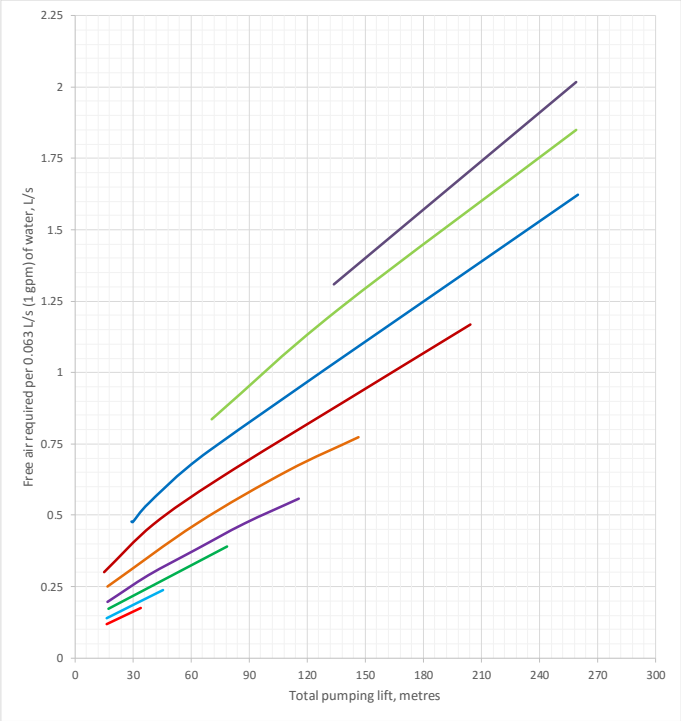

FIGURE 7: Air volume (cfm) required to pump 0.063 L/s (1 gpm) of water for various submergence percent and total pumping lift combinations (modified from Ingersoll-Rand, 1971, in Driscoll, 1986)

To overcome initial head created by the submergence of the air line into boreholes 90-120 m deep, the compressor used for air supply should have a minimum pressure of 8.6 bars. The air volume flow rate is the most important factor in successful air-lift pumping once the pressure initiates flow. The rule of thumb is that for each 0.063 L/s (1 gpm) of water, the proper compressor capacity for air-lift pumping is to provide about 0.35 L/s (3/4 cfm) of air.

The total pumping lift, the pumping submergence, and the cross-sectional area of the casing are the factors to be considered for the air volume requirement to operate air-lift pumping efficiently in freshwater wells. Figure 7 shows the

graphical relation of some of these factors. For maintaining steady flow, the air-volume requirements will usually be greater than those given in the figure. The actual volume of air required may be two to three times the volume shown in the figure for deep boreholes with low static water levels. Table 1, on the other hand shows the suggested sizes of eductor pipes (not applicable as the casing is used) and air line for air-lift pumping, but some changes in sizes may be necessary for practical reasons.

TABLE 1: Recommended pipe sizes for air-lift pumping (modified from Driscoll, 1986)

Pumping rate*		**Size of well casing if eductor pipe is used**		**Size of eductor pipe (or casing if no eductor pipe is used)**		**Minimum size of air line**	
gpm	**L/s**	**in**	**mm**	**in**	**mm**	**in**	**mm**
30-60	1.8-3.79	4	102, or larger	2	51	½	13
60-80	3.79-5.05	5	127, or larger	3	76	1	25
80-100	5.05-6.31	6	152, or larger	3 ½	89	1	25
100-150	6.31-9.46	6	152, or larger	4	102	1 ¼	32
150-250	9.46-15.8	8	203, or larger	5	127	1 ½	38
250-400	15.8-25.2	8	203, or larger	6	152	2	51
400-700	25.2-44.2	10	254, or larger	8	203	3	64
700-1000	44.2-63.1	12	305, or larger	10	254	3	64
1000-1500	63.1-94.6	16	406, or larger	12	305	4	102

*Actual pumping rate is dependent on percent submergence

The length of the air line below the pumping water level, divided by the total length of air line suspended in the well, and multiplied by 100 is equal to the pumping submergence percentage. When the pumping submergence is about 50 percent, the air-lift pumping is quite efficient for wells with about 60-150 m of total pumping lift and 40 percent for 150-270 m. Figure 8 shows the guideline for optimum submergence for a given pumping lift.

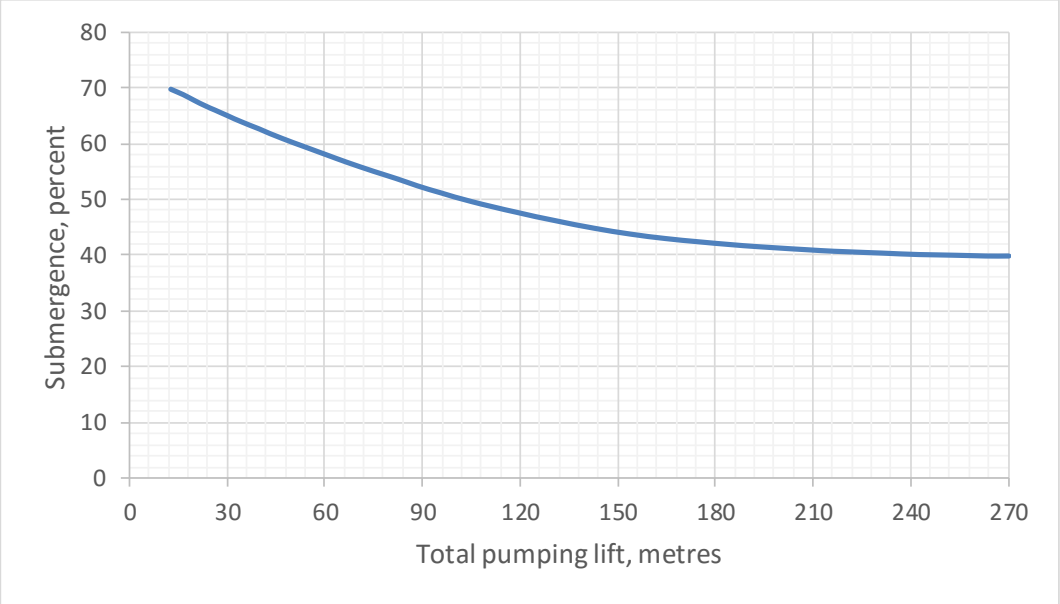

FIGURE 8: This graph serves as a guideline of pumping submergence for optimum air-lift efficiency (modified from Ingersoll-Rand, 1971 in Driscoll, 1986)

Not taking time to analyse and consider the operational characteristics of an air-lift may lead to inefficient pumping, lost time, and in some cases, failure to pump any water. The example below from

Driscoll's book "Groundwater and wells", shows the factors that should be considered for designing a successful air-lift pumping operation.

Figure 9 shows, as an example, a 254-mm (10-in) diameter cased well with a total depth of 123 m and screened from 110 to 123 m. Static water level is at 30 m. It is decided to air-lift pump at a rate of 38 L/s (600 gpm), 20 percent above the design rate of 31.5 L/s (500 gpm). Pumping water level would be at 61 m. The following are the steps for selecting the proper size of equipment for air-lift and for estimating the potential efficiency of the system:

- Step 1 is to determine the diameter of the eductor pipe, if required, and the air line. Use Table 1 for this step. It shows that a 203-mm (8-in) eductor and a 76-mm (3-in) air line should be used for the 254-mm (10-in) casing. A smaller diameter eductor can be chosen, but the air-pressure requirements would rise because of the additional friction effects.
- Step 2 is to determine the length of the eductor pipe and the air line. The bottom of the eductor pipe is set at 122 m, reasonable distance above the bottom of the screen, with the air line set at 120 m.
- Step 3 is to determine the submergence.

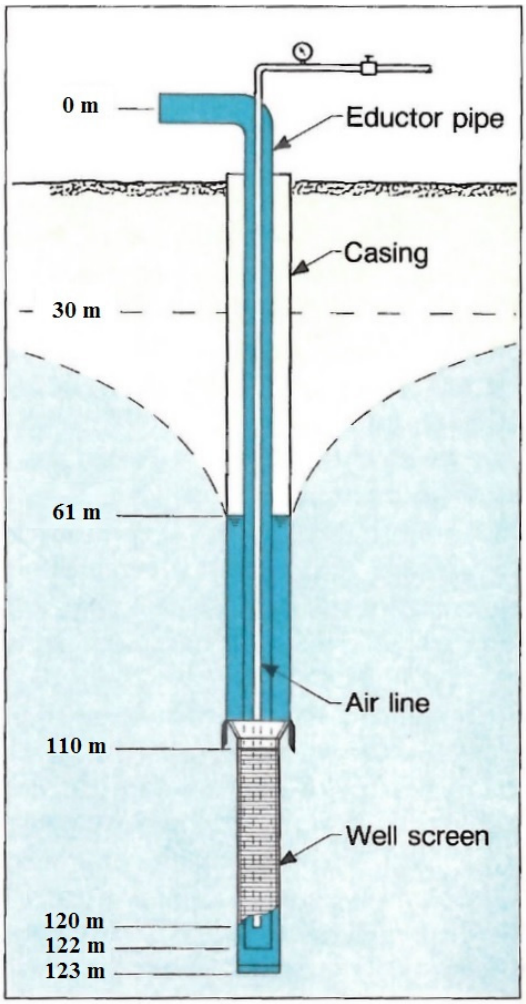

FIGURE 9: Sample well for air-lift designing (modified from Driscoll, 1986)

The pumping submergence is given by this formula:

$$\%\ pumping\ submergence = \frac{length\ of\ air\ line\ below\ pumping\ water\ level}{total\ length\ of\ air\ line} \cdot 100 \qquad (1)$$

$$= \frac{120 - 61}{120}$$

$$\approx 50\%$$

Figure 8 shows that at this pumping submergence, the air-lift will be reasonably efficient considering that the volume of water pumped is acceptable.

- Step 4 is to determine the air-volume requirements. Figure 7 shows that for a total pumping lift of 61 m and pumping submergence of about 50%, 0.47 L/s (1 cfm) of air is required to pump 0.063 L/s (1 gpm) of water. Thus, 283 L/s (600 cfm) of air are required to pump 38 L/s (600 gpm) of water.
- Step 5 is to determine whether the compressor has sufficient pressure to initiate flow in the air line.

$$Minimum\ pressure\ requirement\ (bar) = \frac{density\ of\ water\ \cdot 9.8 \cdot (length\ of\ air\ line - static\ water\ level)}{100000} \qquad (2)$$

$$= 1000 \cdot 9.8\ (120.4 - 30.48)/100000$$

$$= 8.8\ \text{bar}$$

The minimum pressure requirement to start the air-lift for the starting submergence chosen is at 8.8 bar, and a safety factor of 25% is usually added to this pressure figure. The pressure requirement decreases almost by half once the flow has been established as the head acting on the air line decreases.

To have some assurance that the air-lift development procedures will work as desired, the steps mentioned above must be done properly. The steps, including the design and operational parameters, however, are not mathematically precise. Thus, the air-lift design may have to be changed depending on the well condition or available equipment. The engineer must be prepared to make appropriate adjustments. Generally, the air-lift pumping will be most efficient if the static water level is high, the casing diameter is relatively small, and the capacity of the compressor is adequate.

6.1.2 Spreadsheet model

A spreadsheet model was made as a part of this report to simulate the success of an air-lifting operation. The input parameters are: the volume rate of air to be injected, air line setting depth, pressure and temperature at the air line setting depth, and the expected water flow from the wellbore. After inputting the said parameters, the model will calculate the pressure versus depth up to the surface based on the density profile. It will show whether the input parameters are sufficient to make the fluid flow to the surface or not. A successful discharge will yield a minimum of 2 bar-a, at the wellhead.

The pressure at depth h is calculated by using the formula:

$$P = P_o - \rho g h \tag{3}$$

where P = Pressure (bar-a);
P_o = Pressure at deeper depth (bar-a);
ρ = Density of two-phase flow (kg/m^3);
g = Acceleration of gravity (9.8m/s^2);
h = Depth (m).

The air volume per depth is calculated using the ideal gas law:

$$PV = nRT \tag{4}$$

By isolating the air volume (V), the equation will be:

$$V = \frac{nRT}{P} \tag{5}$$

where V = Air volume per second (L/s);
n = Number of moles per second (n/s);
R = Universal gas constant (0.08314 L bar/K mol);
T = Temperature (K);
P = Pressure (bar-a).

The number of moles per second is calculated from the input parameters of the air volume injected. After inputting the air volume at standard cubic feet per minute (scfm) for the compressor, it will be converted to litres per second (L/s) and then finally to number of moles per second. One mole of an ideal gas will occupy 22.4 L at standard temperature (0°C) and pressure (1 atm) so the volume in L/s will be divided by 22.4 L to get the number of moles. The output rating of air compressors is reported in standard cubic feet per minute (scfm) but the criteria for "standard" temperature varies, either 0°C (STP) or in the United States 68°F but the pressure is always 1 atm. The former criterion is used in this report.

The density of the two-phase flow is calculated using the formula:

$$\rho = \frac{M}{V} \tag{6}$$

where ρ = Density of two-phase flow (kg/L);
M = Total mass flow of air and water (kg/s);
V = Total volume of air and water (L/s).

The total mass flow is equal to the sum of the air injected in kg/s and the mass flow rate of water. The density of water is retrieved from steam tables (X-Steam) based on the temperature given. The total volume is found by adding the air volume injected and the assumed water flow.

The submergence depth is calculated using the formula:

$$S = h - \frac{P}{\rho g} \tag{7}$$

where S = Submergence depth, length of air line submerged in water (m);
h = Air line setting depth (m);
P = Pressure at the air line setting depth (bar-a);
ρ = Density of water (kg/m^3);
g = Acceleration of gravity (9.8 m/s^2).

The pumping submergence percentage is calculated by dividing the submergence depth by the air line setting depth, then multiplying it by 100.

In addition to the plot of pressure versus depth in the wellbore, the pressure inside the air line is also plotted. The initial pressure required at the wellhead to be supplied by the compressor is calculated by adding the pressure drop to the pressure at the submergence depth. The pressure drop in the compressed air line is calculated by using the empirical formula (modified from The Engineering Toolbox, 2015):

$$dp = \frac{7.42q^{1.85}L \cdot 10^4}{d^5 p} \tag{8}$$

where dp = Pressure drop (bar);
q = Air volume flow at atmospheric conditions (m^3/min);
L = Length of pipe (m);
d = Inside diameter of pipe (mm);
p = Initial absolute pressure (kg/cm^2)

The air volume flow from the given parameter is converted to m^3/min. The length of the pipe is equal to the depth where the air line is set. The inside diameter of the pipe is as per the design. The initial absolute pressure is equal to the absolute pressure at the submergence depth, converted to kg/cm^2.

6.2 Air compression

6.2.1 Spreadsheet model (for planning)

A spreadsheet model was made as a part of this report to calculate how much total air volume is required, and what capacity of compressor is required in order to stimulate a high-temperature well to flow. The input parameters are: the production casing diameter size, static water level in the well, production casing shoe depth, the initial wellhead pressure, the target or final wellhead pressure during the air compression, the initial and final temperature in the airspace, and the compression or pumping time. After inputting the parameters, the model will calculate the initial and final casing air volume, the initial and final number of moles, the amount of moles that need to be injected into the wellbore, and finally, the corresponding air flow to be injected in litres per second (L/s) and in standard cubic feet per minute (scfm). The user can play around with the model by changing the necessary parameters. For example, if the user only has a low flow capacity compressor, he or she can change the length of pumping time in order to reach the target wellhead pressure.

The initial casing volume with air is calculated using the formula:

$$V_i = \pi r^2 h_i \tag{9}$$

where V_i = Initial casing volume with air (m^3);
r = Casing radius (m);
h_i = Water level (m).

The final casing volume with air is calculated using the formula:

$$V_f = \pi r^2 h_f \tag{10}$$

where V_f = Final casing volume with air (m^3);
h_f = Casing shoe depth or maximum water level suppression for target pressure (m).

The initial number of moles is calculated using the ideal gas law. By isolating the moles on the other side of the equation, the formula becomes:

$$n = \frac{P_i V_i}{R T_i} \tag{11}$$

where n = Number of moles;
P_i = Initial wellhead pressure (bar-a);
V_i = Initial casing volume with air (m^3);
R = Universal gas constant (0.08314 L bar/K mol);
T_i = Initial temperature (K).

The final number of moles is calculated using the formula:

$$n = \frac{P_f V_f}{R T_f} \tag{12}$$

where P_f = Final wellhead pressure (bar-a);
V_f = Final casing volume with air (m^3);
T_f = Final temperature (K).

The difference between the final and initial number of moles is equal to the total air that needs to be injected by the compressor. One mole of an ideal gas will occupy 22.4 L at standard temperature and pressure (STP) so the number of moles can be converted to litres per second (L/s) by multiplying it by 22.4. The volume in L/s is also converted to standard cubic feet per minute (scfm) for ease in finding compressor capacity suitable for actual operation.

This model can also be used in reverse. The volume flow capacity and the time it takes to compress a well from initial to final state can be interchanged so the volume capacity will be the input parameter and the time will be the output. The same concept and formulas will be used. After inputting the air volume capacity of a sample compressor in standard cubic feet per minute (scfm), it is converted to L/s and then eventually to number of moles per second by dividing it by a factor of 22.4. Finally, the time is calculated by getting the difference between the final and initial number of moles, and dividing this number by the number of moles per second. The time is calculated in seconds, then converted to hours. This can help in planning out an air compression job. The user can now have an estimate of how long the compression job will take just by knowing the condition of the well, the target wellhead pressure, and the compressor capacity.

6.2.2 Spreadsheet model (for predicting success)

A spreadsheet model was made for this report to simulate if the well will successfully discharge by attaining a certain pressure at the wellhead after releasing the air. The input parameters are the depth, static temperature and pressure profiles and target wellhead pressure. After inputting the parameters for a static well, the model will predict (or calculate) after the air release. The calculation of flowing pressure and temperature profile, steam quality, and density per depth is based on shifting the deep water up into the shallow portions of the well. The shift corresponds to the pressure of compression, by how much the water moves up. The model will then, based on the reassigned enthalpies vs. depth, calculate new values of pressure, temperature, steam quality, and density up to the surface. The pressure vs. depth is calculated by using Equation 3. The spreadsheet results will tell us if the well will successfully discharge by building up a certain wellhead pressure during the initial discharge just modelled. A criterion for successful discharge should be a minimum of 2 bar-a, at the wellhead.

6.3 Two-phase simulator

After stimulating the well to flow either by air-lift pumping or air compression successfully, the well will continue to discharge and self-flow. A spreadsheet model was created to determine if the well has sufficient pressure and enthalpy to flow successfully. The simulator program HOLA was also used to compare the results with the model, as well as actual temperature and pressure logs from flowing wells (dynamic).

6.3.1 Spreadsheet model

A spreadsheet model was made as a part of this report to simulate temperature and pressure profiles to assess whether the well will flow or not, depending on the inflow parameters of the well (in this case assumed to be for the bottom conditions). The model then calculates flowing profiles from bottom to top. The input parameters should be for the main inflow but in this exercise: the bottom depth, the pressure at the bottom, the average enthalpy of the well discharge, and assumed pressure loss due to two-phase friction. After inputting the parameters, the spreadsheet model will give the pressure vs. depth up to the surface, the temperature vs. depth, the quality of steam, and density vs. depth based on the pressure and enthalpy. The pressure vs. depth is calculated by using Equation 3. A pressure drop with units of bar per kilometre factoring in friction losses is also incorporated in the model, and this value will be subtracted from the calculated pressure vs. depth. The results are displayed on a graph with the simulated pressure vs. depth inside the wellbore superimposed with the measured downhole data. It will also show if the well has a positive wellhead pressure and flow to the surface. The minimum pressure criterion to obtain sustainable flow at the surface ranges from 2 to 4 bar-a.

6.3.2 HOLA

HOLA is a software program, a wellbore simulator, which simulates a well temperature and pressure profile from the top to the bottom of the well. The input parameters are wellhead conditions (wellhead pressure, flow and enthalpy), casing geometry, and location of feedzones. After inputting the parameters, the program will give the downhole profile down to the bottom.

The user is first asked to enter the input parameters and they are:

- *Textlines.*
- *Wellhead parameters* - wellhead pressure (bar-a), wellhead enthalpy (kJ/kg), and wellhead flow (kg/s).
- *Heat loss parameters* (usually entered with default/assumed values) - rock thermal conductivity (2 W/m/°C), rock density (2800 kg/m^3), rock heat capacity (1000 J/kg/°C), and time passed (0.8640 10^5 s).

- *Wellbore geometry* - depth of well (m), number of well sections, length of each sections (m), well inner radius (m), well roughness (default/assumed value of 0.05 mm), and distance between nodal points (m).
- *Feedzone properties* (flow and enthalpy).

The user then has the option to select phase velocity method: Armand, Orkiszewski, Chisholm, or Björnsson (9-5/8" wells) but the default method is Orkiszewski (1967). Finally, the user can choose to calculate the wellbore conditions (temperature and pressure), write the results to a file, and then plot the results.

7. EXAMPLES

7.1 Air-lift pumping

As an example, a hypothetical well was made and its properties were entered into the air-lift spreadsheet model. The conditions are like for a cold well as the initial conditions for air-lift pumping. Only after first successfully unloading the cold water will the effects of flash-steam kick in as the well heats up. The effects of flashing are not a part of this model, only the air-lift pumping part to initiate the flow. The following are the input parameters:

- *Air volume flow:* 500 scfm.
- *Air line setting depth*: 400m.
- *Pressure at the air line setting depth*: 20 bar-a.
- *Temperature at the air line setting depth*: 20°C.
- *Expected water flow out the wellbore*: 25 L/s.
- *Air pipe inside diameter*: 50 mm.

Figure 10 shows the snapshot of the spreadsheet model while Figure 11 shows the results.

Air flow	scfm	L/s	n/s	kg/s	m3/min
	500	235.97	10.53	0.29	14.16

Depth	Press	Temp	Air volume	Water flow	Total volume	Total mass flow	Density (water)	Density (2 phase fluid)	Air volume flow	Pipe length	Air pipe (inside diameter)
(m)	(bar-a)	(°C)	(L/s)	(L/s)	(L/s)	(kg/s)	(kg/L)	(kg/m3)	m3/min	m	mm
0	2.11	20	121.59	25	146.59	25.25	1.00	172.24	14.16	400	50
20	2.50	20	102.71	25	127.71	25.25	1.00	197.70			
40	2.94	20	87.30	25	112.30	25.25	1.00	224.84			
60	3.44	20	74.67	25	99.67	25.25	1.00	253.32	Initial abs	dP	dP
80	3.99	20	64.29	25	89.29	25.25	1.00	282.77	pressure (kg/cm2)	(kg/cm2)	(bar)
100	4.60	20	55.72	25	80.72	25.25	1.00	312.78	20.41	0.64	0.63
120	5.28	20	48.62	25	73.62	25.25	1.00	342.97			
140	6.01	20	42.70	25	67.70	25.25	1.00	372.96	Press air line	Depth (m)	
160	6.80	20	37.74	25	62.74	25.25	1.00	402.44	20.63	0	
180	7.64	20	33.56	25	58.56	25.25	1.00	431.13	20	400	
200	8.55	20	30.03	25	55.03	25.25	1.00	458.83			
220	9.50	20	27.02	25	52.02	25.25	1.00	485.39			
240	10.50	20	24.44	25	49.44	25.25	1.00	510.71			
260	11.55	20	22.22	25	47.22	25.25	1.00	534.72			
280	12.64	20	20.30	25	45.30	25.25	1.00	557.41			
300	13.78	20	18.62	25	43.62	25.25	1.00	578.79			
320	14.95	20	17.16	25	42.16	25.25	1.00	598.88			
340	16.16	20	15.87	25	40.87	25.25	1.00	617.73			
360	17.41	20	14.74	25	39.74	25.25	1.00	635.40	Submergence	Water	Submergence
380	18.69	20	13.73	25	38.73	25.25	1.00	651.94	depth (m)	level (m)	%
400	20	20	12.83	25	37.83	25.25	1.00	667.43	195.75	204.25	48.94

FIGURE 10: Snapshot of the air-lift pumping spreadsheet model

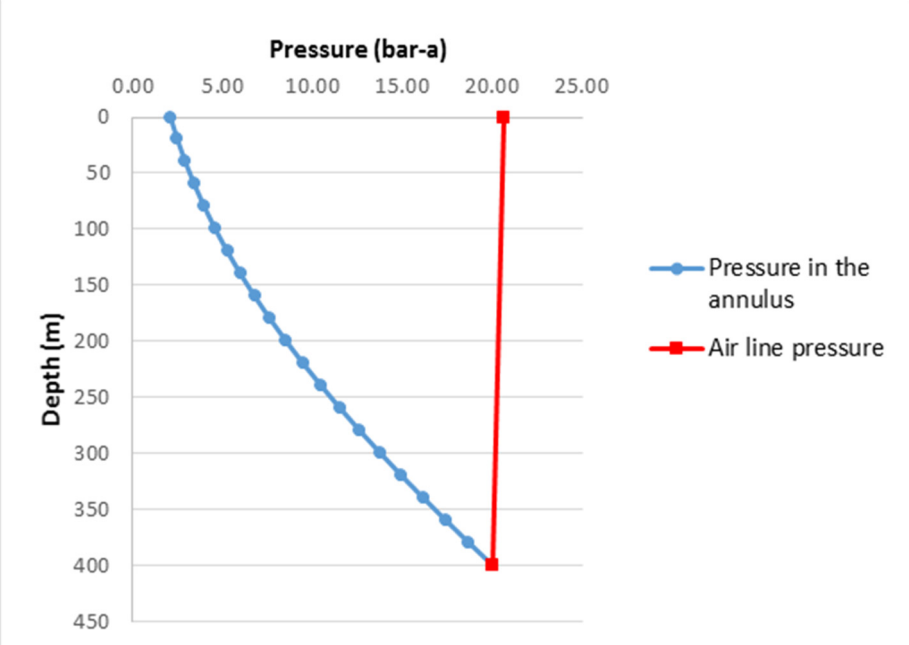

FIGURE 11: The spreadsheet model graph tells us that with the given air-lift pumping design parameters, the well will flow at the surface at 2.1 bar-a wellhead pressure, and the pressure at the air line will drop from 20.64 bar-a at the surface to 20 bar-a at the end of the air line at 400 m depth

7.2 Air compression (for planning)

Energy Development Corporation (EDC) uses an air package for air compression operations. An air package is a combination of an air compressor and an air booster. This equipment is important in reviving some of the production wells for augmenting the supply of steam. See Table 2 below for the compressor specifications.

TABLE 2: Air package specification

Equipment	Compressor	Booster
Discharge pressure	24.13 bar (350 psi)	149.96 bar (2175 psi)
Capacity	1350 scfm	1800 scfm @ two stage
Fuel consumption	200 litres/4 hours	250 litres/4 hours

As an example, actual field data from a well in the Philippines is used in the air compression spreadsheet model. Here are the input parameters for well 1:

- *Casing size:* 9-5/8”
- *Initial water level:* 1000m
- *Final water level:* 1700m
- *Initial pressure:* 1 bar-a
- *Final pressure:* 58 bar-a
- *Pumping time:* 2 h
- *Initial temperature:* 158°C
- *Final temperature:* 240°C

Model output – Air capacity: 707 scfm

This tells us that the primary air compressor alone will not be able to carry out the job, even though the volume capacity is sufficient. The maximum pressure requirements of 58 bar-a cannot be met without

adding a booster. A combination of the compressor and booster is more than sufficient, and that is the set-up that is usually used in the Philippines.

In order to achieve a wellhead pressure of 58 bar-a in two hours, an air flow of 707 scfm is required. If we take the reverse and enter an air capacity of 350 scfm as input, the time will be 4.1 hours. This means that to reach the target pressure while using a small capacity compressor, it will take about twice as long to finish the job and build up the target wellhead pressure. Figure 12 shows the snapshot of the air compression spreadsheet model.

	Diameter (in)	Fraction	Radius (m)
Casing size (in)	9	5/8	0.122
Water level (m)	1000		
Target depth (m)	1700		
Initial casing vol (m^3)	46.97	Initial P (bar-a)	1
Final casing vol (m^3)	79.84	Final P (bar-a)	58
Initial casing vol (liters)	46965.74	Initial temp (°C)	158
Final casing vol (liters)	79841.76	Final temp (°C)	240
Initial moles (n)	1310.22	Pumping time (hr)	2
Final moles (n)	108543.48	(seconds)	7200
Δ (n/s)	14.89		
L/s	333.82		
SCFM	**707.34**		
Reverse:			
SCFM	350	Time (seconds)	14812.45
L/s	162.26	Hours	**4.11**
n/s	7.24		

FIGURE 12: Snapshot of the air compression spreadsheet model (for planning)

7.3 Air compression (for predicting success)

Well 1 described above was also used as an example for this model. The input parameters are the following: Bottom depth of 2100m, static temperature and pressure profiles, and target wellhead pressure of 58 bar-a, which is the pressure at the production casing shoe.

The pressure at the bottom, which is 80 bar-a, will be subtracted from the pressure to be injected, which is 58 bar-a. The difference is equal to 22 bar, which is at a depth of 1400 m, based on the flowing pressure per depth. The user will then use the second table to enter the second set of parameters which are the depth of 1400 m, the static pressure at this depth which is 33.3 bar-a and shift the enthalpy from the bottom of the well to this depth which is 991 kJ/kg. The other enthalpy figures are likewise shifted upwards as to simulate the effects of the air being released and the heated water moving up the well. Projecting these parameters to the surface tells us that this well will not discharge because the value at the surface is less than 2 bar-a. Figure 13 shows the snapshot of this spreadsheet model while Figure 14 shows the downhole profiles before compressing and after releasing the compressed air. This agrees with the field results, the well could not self-flow.

As a second example for testing this model, well 2 was used. The initial wellhead pressure is at 1 bar-a, and the water level is at 600 m. The target wellhead pressure is 66 bar-a, because this is the pressure at the production casing shoe, which is located around 1500 m. The input parameters are the following: bottom depth of 2400m, static temperature and pressure profile, and target wellhead pressure by air compression of 66 bar-a.

The pressure of the bottom, which is 135 bar-a, will be subtracted from the pressure to be injected, which is 66 bar-a. The difference is equal to 69 bar, which is at depth 1300 m based on the flowing pressure per depth. The user will then use the second table to enter the second set of parameters which are the depth of 1300 m, the static pressure at this depth which is 60 bar-a and the shifted enthalpy from the bottom of the well to this depth which is 1341 kJ/kg. All other enthalpy vs. depth figures are likewise shifted upwards. Projecting these parameters to the surface tells us that this well will discharge, since the pressure at the wellhead (surface) will be 33 bar-a. Figure 15 shows the downhole profiles before compressing and after releasing the compressed air.

Static Press (bar-a)	Depth (m)	Flowing Press (bar-a)	Static Temp (°C)	Enthalpy (kJ/kg)	Quality X	Dens (kg/m³)
1	0	#VALUE!	36.02	150.91	#VALUE!	#VALUE!
1	100	#VALUE!	36.02	150.91	#VALUE!	#VALUE!
1	200	#VALUE!	36.02	150.91	#VALUE!	#VALUE!
1	300	#VALUE!	36.02	150.91	#VALUE!	#VALUE!
1	400	-8.97	57.47	240.58	#VALUE!	#VALUE!
1	500	0.55	82.27	344.47	0	970.36
1	600	0.68	105.03	440.34	0.029	14.10
1	700	0.79	116.90	490.64	0.044	10.56
1	800	0.94	116.97	490.91	0.036	15.30
1	900	1.43	118.15	495.93	0.016	50.44
8	1000	1.52	161.12	680.44	0.095	9.12
13.06	1100	10.25	177.58	752.53	0	889.61
20.13	1200	14.54	200.48	854.55	0.01	437.26
26.52	1300	19.61	214.52	918.39	0.01	516.52
33.27	1400	23.36	227.11	976.69	0.02	382.65
40.34	1500	31.40	235.25	1014.94	0	820.08
46.67	1600	39.44	236.82	1022.40	0	818.67
54.42	1700	47.44	239.64	1035.82	0	815.43
57.53	1800	55.52	234.13	1009.66	0	824.18
63.70	1900	63.74	224.88	966.29	0	837.67
73.88	2000	71.92	228.03	980.99	0	834.24
80.08	2100	80.08	230.33	991.75	0	831.93

Depth (m)	Press (bar-a)	Temp (°C)	Enthalpy (kJ/kg)	Quality X	Dens (kg/m³)
0	0.74	91.47	490.64	0.05	9.38
100	0.87	95.70	490.91	0.04	12.87
200	1.52	111.73	495.93	0.01	66.36
300	1.62	113.62	680.44	0.09	9.99
400	10.34	177.60	752.53	0.00	889.62
500	12.13	188.44	854.55	0.03	181.72
600	13.27	192.57	918.39	0.05	116.68
700	14.13	195.49	976.69	0.07	87.97
800	14.91	198.00	1014.94	0.09	78.58
900	15.73	200.55	1022.40	0.09	83.79
1000	16.57	203.08	1035.82	0.09	86.40
1100	17.71	206.33	1009.66	0.07	116.00
1200	20.10	212.64	966.29	0.03	243.58
1300	25.16	224.29	980.99	0.01	515.37
1400	33.27	230.29	991.75	0.00	827.23

FIGURE 13: Snapshot of the air compression spreadsheet model (for predicting success)

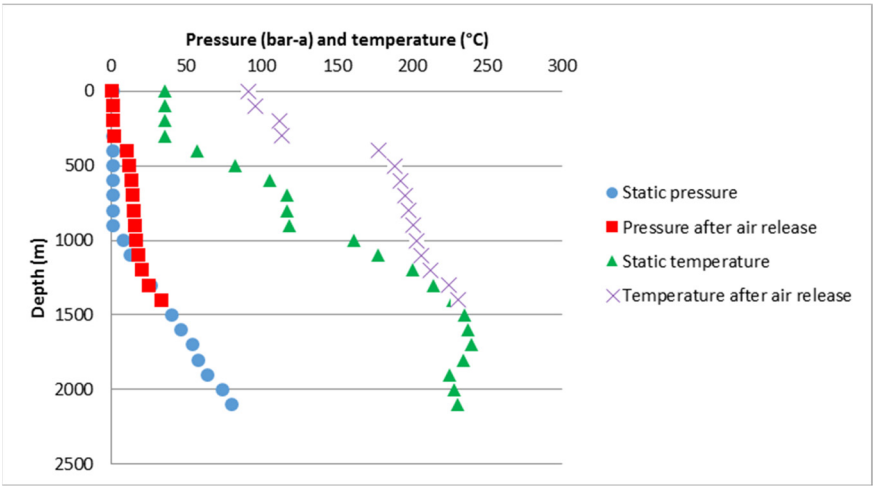

FIGURE 14: Downhole profiles of well 1 before air compression and after releasing compressed air

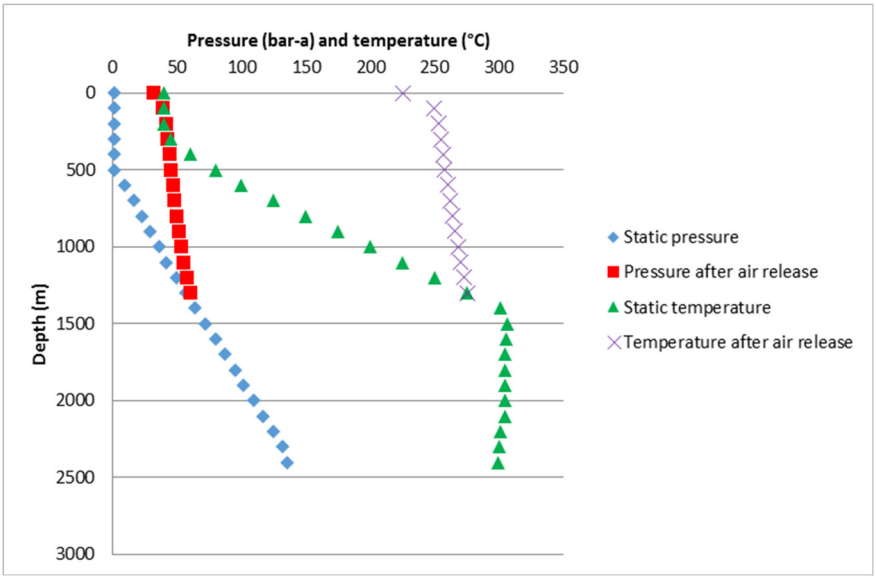

FIGURE 15: Downhole profiles of well 2 before air compression and after releasing compressed air

7.4 Flowing wells

Down-hole measurements from flowing wells (dynamic logs) are used as actual examples to validate predictions by the spreadsheet model and the HOLA program.

Input parameters are used from a number of wells in the two-phase spreadsheet model. The assumed two-phase pressure drop (assumed) in the well was varied from values 4 to 7 (bar/km). After a number of runs and testing a number of wells, a value within the range 4-7 produced good predictions.

The input parameters for well 3 in the spreadsheet model are the following:

- *Bottom depth*: 2700 m
- *Pressure at bottom depth*: 69.9 bar-a
- *Pressure drop*: 5.35 bar/km
- *Enthalpy*: 1228 kJ/kg

Figure 16 shows the snapshot of the two-phase simulator model.

The input parameters for well 3 in the HOLA program are the following:

- *Wellhead pressure*: 12.2 bar-a
- *Wellhead enthalpy*: 1228 kJ/kg
- *Wellhead flow*: 29 kg/s
- *Rock thermal conductivity*: 2 W/m/°C
- *Rock density*: 2800 kg/m^3
- *Rock heat capacity*: 1000 J/kg/°C
- *Time passed*: 0.8640 E^5 s
- *Depth of well*: 2500 m (vertical depth)
- *Number of well sections*: 2 (production casing and slotted liner)
- *Length of section 1 (production casing):* 1600 m (vertical depth)
- *Well inner radius*: 0.120 m
- *Well roughness*: 0.05 mm
- *Distance between nodal points*: 2 m
- *Length of section 2 (slotted liner)*: 900 m (vertical depth)
- *Well inner radius*: 0.089 m
- *Well roughness*: 0.05 mm
- *Distance between nodal points*: 2 m
- *Number of feed-zones*: 1

Depth (m)	Press (bar-a)	dP bar/km	Temp (°C)	Enthalpy (kJ/kg)	Quality X	Dens (kg/m^3)
0	12.22	5.35	**188.80**	1228	0.21	28.29
67.5	12.78	5.35	**190.84**	1228	0.21	30.01
135	13.35	5.35	**192.85**	1228	0.21	31.80
202.5	13.94	5.35	**194.84**	1228	0.20	33.69
270	14.54	5.35	**196.81**	1228	0.20	35.66
337.5	15.15	5.35	**198.76**	1228	0.20	37.73
405	15.77	5.35	**200.69**	1228	0.19	39.90
472.5	16.41	5.35	**202.60**	1228	0.19	42.18
540	17.07	5.35	**204.51**	1228	0.18	44.58
607.5	17.74	5.35	**206.41**	1228	0.18	47.12
675	18.43	5.35	**208.29**	1228	0.18	49.79
742.5	19.14	5.35	**210.18**	1228	0.17	52.62
810	19.87	5.35	**212.06**	1228	0.17	55.62
877.5	20.62	5.35	**213.94**	1228	0.17	58.80
945	21.39	5.35	**215.82**	1228	0.16	62.17
1012.5	22.19	5.35	**217.70**	1228	0.16	65.77
1080	23.01	5.35	**219.59**	1228	0.15	69.62
1147.5	23.86	5.35	**221.49**	1228	0.15	73.73
1215	24.74	5.35	**223.40**	1228	0.15	78.14
1282.5	25.65	5.35	**225.33**	1228	0.14	82.89
1350	26.60	5.35	**227.27**	1228	0.14	88.02
1417.5	27.58	5.35	**229.23**	1228	0.13	93.58
1485	28.60	5.35	**231.22**	1228	0.13	99.63
1552.5	29.66	5.35	**233.23**	1228	0.12	106.23
1620	30.77	5.35	**235.28**	1228	0.12	113.48
1687.5	31.94	5.35	**237.36**	1228	0.11	121.48
1755	33.16	5.35	**239.48**	1228	0.11	130.37
1822.5	34.45	5.35	**241.66**	1228	0.10	140.31
1890	35.82	5.35	**243.89**	1228	0.10	151.52
1957.5	37.27	5.35	**246.20**	1228	0.09	164.28
2025	38.81	5.35	**248.58**	1228	0.09	178.97
2092.5	40.47	5.35	**251.06**	1228	0.08	196.13
2160	42.27	5.35	**253.65**	1228	0.07	216.49
2227.5	44.23	5.35	**256.38**	1228	0.07	241.17
2295	46.39	5.35	**259.30**	1228	0.06	271.95
2362.5	48.81	5.35	**262.45**	1228	0.05	311.78
2430	51.60	5.35	**265.92**	1228	0.04	366.21
2497.5	54.92	5.35	**269.88**	1228	0.03	447.39
2565	59.19	5.35	**274.70**	1228	0.01	590.31
2632.5	64.54	5.35	**278.35**	1228	0	753.51
2700	**69.9**	**5.35**	**278.40**	**1228**	0	754.28

FIGURE 16: Snapshot of the two-phase simulator spreadsheet model

It is important to note that the feedzone is assumed to be one and the depths entered should be the vertical depths and not the measured depths of a deviated well. If there are discrepancies or errors with the values, it could be attributed to these factors. Figure 17 shows the measured data and the simulated data from the spreadsheet model and HOLA program. The model results agree well on the wellhead pressure (WHP) but show a slightly lower pressure deep in the hole as compared to HOLA and the measured values. The figure includes a sample well profile from another well (blue X) that will not self-flow by inputting a low value for enthalpy (temperature profile of the well) in the model.

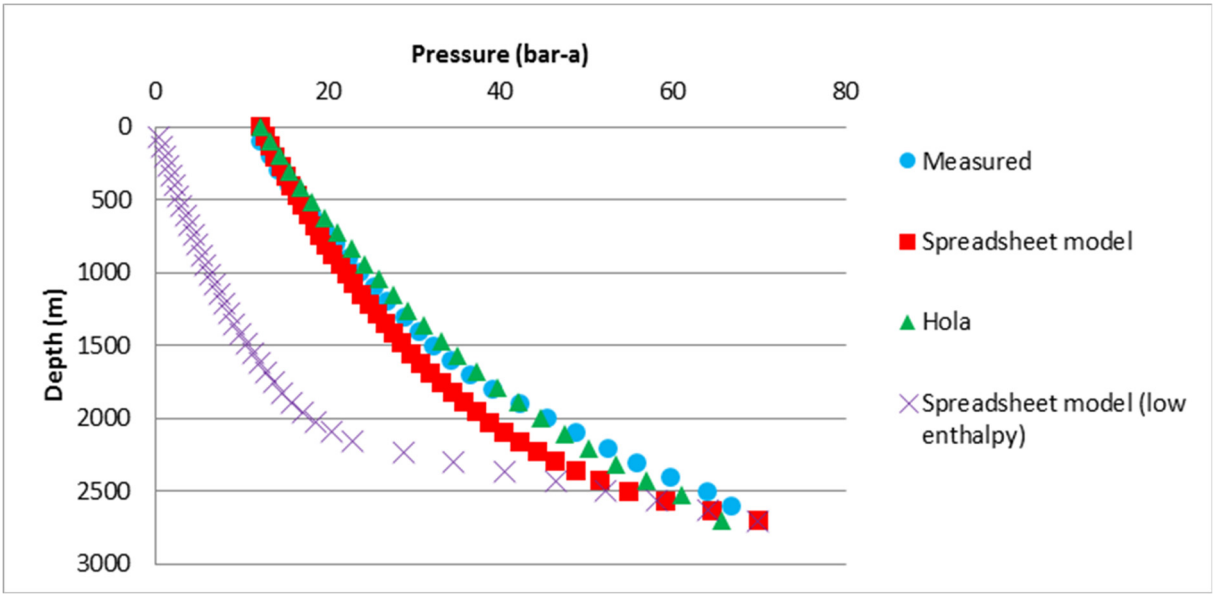

FIGURE 17: Results of the simulated data using the spreadsheet model and HOLA vs. the measured data of well 3

8. CONCLUSIONS

To conclude, let us go back to the main objective which was to answer the question: "What are the technical requirements for a successful discharge by air-lifting and compressing the well?"

For the air-lift pumping, what submergence of the coiled tubing or drill pipe and air-compressor rating (pressure and air flow) are required?

- Based on air-lift graphs, 50% of pumping submergence is required for efficient air-lift with wells about 60-150 m of total pumping lift. This percentage decreases as the pumping lift increases, such as 40% for 150-270 m. The minimum wellhead (or compressor) pressure requirement to initiate flow in the air line is calculated by getting the difference of the air line setting depth and static water level, then multiplying by the water density and g (9.8). For the air volume requirement, the total pumping lift, pumping submergence and the size of air pipe or line and casing are the factors needed to be considered. Practical guidelines from air lift pumping of water wells were applied.
- Based on the spreadsheet model, the success of an air-lift set up can be assessed based on the air volume and expected water flow (air/water ratio) and the submergence depth.

For air compression, what volume capacity of compressor is required for a certain job and how long does it take to compress a well from initial to final pressure? What air pressure is needed to discharge the well by compression alone?

- Based on the spreadsheet model results, the capacity of the compressor in terms of air volume flow rate can be computed by knowing the well conditions and downhole profile of the initial and desired state of air compression, well geometry, and duration of compression. The user can play around with the model, making the capacity the known variable and duration of pumping the unknown. This is good for planning the compression job, estimating capacity and time, even before going into the field.

- For a compression job, one should maximize the water level depression, whether at the first loss zone or at the production casing shoe, considering also the pressure rating of the wellhead and the pipes used at the surface. Because the water level is typically compressed down to the production casing shoe depth, the optimum wellhead pressure one can achieve by compressed air depends on the reservoir pressure at this depth. With this factored in, the next important factor is the temperature (enthalpy) of inflow. With sufficient temperature, the well should flow. Based on the spreadsheet model for predicting success of compression, the combination of downhole pressure and temperature and the casing shoe depth dictates whether a well will flow at the surface or not after rapidly releasing the compressed air.

What other key factors are considered necessary for a well to attain successful discharge and maintain self-flow?

- Based on the developed two-phase simulator (simulating from bottom to top), attaining successful discharge and maintaining self-flow depends on the bottom pressure, well inflow enthalpy, and pressure loss due to friction up the hole. This model was compared to the HOLA wellbore simulator (simulating from top to bottom) and the results were also comparable with downhole logging data.

ACKNOWLEDGEMENTS

First I would like to thank the UNU-GTP director, Lúdvík S. Georgsson and staff, Ingimar G. Haraldsson, Markús A.G. Wilde, Málfrídur Ómarsdóttir, Thórhildur Ísberg, and María Gudjónsdóttir, thank you very much for the opportunity and for supporting each and every fellow. To my best advisers, Sverrir Thórhallsson and Benedikt Steingrímsson, I highly appreciate your eagerness to teach and guide me with this project. “Takk fyrir”!

To our (EDC) President, Mr. Richard B. Tantoco, our (GREG) Senior Vice-President, Mr. Manuel S. Ogena, our (GREG) Assistant Vice-President, Mr. Francis Xavier M. Sta. Ana, our Department Manager, Mr. David M. Yglopaz, and Section Supervisor, Mr. Edson B. Emoricha, thank you for the opportunity and for nominating me for this geothermal programme. To my colleagues back home, thank you for suggesting project ideas, and for providing me with much needed data, special thanks to Ms. Kristine Antonio, Ms. Selnalyn Marquez, Ms. Emma Rose Baula, Mr. Renan Jhon Guerra, Mr. Ramil Derecho, Mr. Joselito "Yam" Alcaraz II, Mr. Gualbert Gerona, and Mr. Bryan Cacho.

To the UNU Fellows, thank you for the time well spent together, hope our paths will cross someday.

To my family, thank you for always being there for me, especially my dad who even went to Iceland to visit me. To all our Filipino friends who are living in Iceland, thank you for making our stay warmer, happier, and much more exciting. Lastly, to my mom, who I know has always been my greatest fan, I dedicate this accomplishment to her.

Finally, I would like to thank God. With him, anything is possible.

REFERENCES

Australian Drilling Industry Training Committee, Ltd., 1997: *Drilling: The manual of methods, applications, and management.* Lewis Publishers, 624 pp.

Björnsson, G., Arason, P., Bödvarsson, G.S., 1993: *The wellbore simulator HOLA. Version 3.1. User's guide*. Orkustofnun, Reykjavík, Iceland, 36 pp.

Buning, B.C., Gonzaga, L.D., Aqui, A.R., Salera, J.R.M., and Sarmiento Z.F., 1998: Discharge initiation by gas-lifting: PNOC-EDC experience in Philippine geothermal wells. *Proceedings of the 23rd Workshop on Geothermal Reservoir Engineering, Stanford University, Stanford, CA, US,* 379-383 pp.

Colina, R.N., Omagbon, J.B., Austria, J.J.C., Sta. Ana, F.X.M., Malate, R.C.M., 2008: *Review of guidelines in predicting discharge stimulation success using selected air compressed wells from 1993 to 2008*. Energy Development Company (EDC), research paper, 10 pp.

Driscoll, F.G., 1986: *Groundwater and wells* (2nd ed.). Johnson Screens, St. Paul, MN, US, 1089 pp.

Orkiszewski, J., 1967: Predicting two-phase pressure drops in vertical pipes. *J. Petroleum Technology, 19,* 829-838.

Sarmiento, Z.F., 2011: Application of well testing in assessing geothermal resources. *Presented at "Short Course on Geothermal Drilling, Resource Development and Power Plants", organized by UNU-GTP and LaGeo, Santa Tecla, El Salvador*, 13 pp.

Steingrímsson, B., 2015: *Discharge measurement and injection* tests. UNU-GTP, Iceland, unpublished lecture notes, 64 pp.

The Engineering Toolbox, 2015: *Compressed air – Pressure drop in pipe lines – Online pressure drop calculator.* The Engineering Toolbox, website: *http://www.engineeringtoolbox.com/pressure-drop-compressed-air-pipes-d_852.html*

UNITED NATIONS UNIVERSITY
UNU-GTP
Geothermal Training Programme

Orkustofnun, Grensasvegur 9,
IS-108 Reykjavik, Iceland

Reports 2015
Number 14

PROCESSING AND JOINT 1D INVERSION OF MT AND TEM DATA FROM ALALLOBEDA GEOTHERMAL FIELD IN TENDAHO, NE-ETHIOPIA

Getenesh Hailegiorgis
Geological Survey of Ethiopia
P.O. Box 2302
Addis Ababa
ETHIOPIA
getenesh19@gmail.com, getegio@yahoo.com

ABSTRACT

Geophysical methods play a big role in geothermal resource exploration, for instance in revealing the electrical conductivity of the subsurface. Magnetotelluric (MT) and time domain electromagnetic resistivity methods are currently the most widely used resistivity methods. Resistivity is an important parameter because it is directly related to the physical properties of the reservoir.

Tendaho is one of the high-temperature geothermal fields in the Main Ethiopian Rift, NE-Ethiopia, and a promising area for geothermal development with respect to both its size and location. Alallobeda is one of the three prospects found in Tendaho geothermal field. Understanding the resistivity structure of the Alallobeda prospect could give a good understanding of the subsurface and enhance the possibility of developing the geothermal resource.

A total of 132 MT and Transient Electromagnetic (TEM) sounding pairs were acquired in 2014 and 2015 by the Geological Survey of Ethiopia (GSE) and the Italian consulting company Electro Consult (ELC) financed by the Icelandic International Development Agency (ICEIDA) and the Nordic Development Fund (NDF). Technical supervision for review and monitoring was done by Iceland GeoSurvey (ÍSOR). In this report, 54MT soundings were processed and almost the same number of TEM soundings. The soundings were1D inverted. TEM was used for static shift correction of the MT data from the same site. Some of the MT stations were inverted using MT data only based on a static shift correction given by the Italian consultant. The results are presented in the form of 1D models for individual stations, iso-resistivity maps and cross-sections. Three main resistivity layers were observed. The first is a thin layer of very low resistivity (< 10 Ωm) at shallow depth down to about 300 m b.s.l. which is correlated to sedimentary formation or a smectite- zeolite zone. Below the low resistivity a high-resistivity core appears with values between 100 and 1000 Ωm down to a depth of 1000 to 5000 m b.s.l. which can be correlated to the less permeable Afar Stratoid basalt series and high-alteration minerals like chlorite and epidote. Beneath the high-resistivity layer down to a depth of 5000 m b.s.l. a deep conductor is revealed that could be associated with the heat source.

1. INTRODUCTION

Geophysical methods, especially resistivity methods, and in particular magnetotellurics (MT) and Transient Electromagnetics (TEM) play an important role in geothermal exploration. The main reason is that resistivity is highly sensitive to temperature, salinity, porosity and geothermal alteration and it is directly related to the physical properties of the reservoir. Resistivity surveys identify variations in the electrical resistivity of the subsurface that are caused by different rock types and ground water. The main task of geophysical methods in geothermal exploration is to detect geothermal prospect, delineate geothermal resources and to further the understanding of their characteristics, as well as locating the exploitable reservoir and to help placing boreholes through which hot fluids can be extracted from depth. Geophysical exploration methods are different from other methods like geology and geochemistry in exploring geothermal resources because they use equipment that measure directly some physical parameters on the surface that reflect physical properties at depth in the earth´s crust (Flóvenz et al., 2012).

Geothermal exploration began in the Main Ethiopian Rift (MER) in 1969, carried out by the Ethiopian Government and the United Nation Development Programme (UNDP) (Bekele, 2012). In 1980, the Italian company Aquater began a detailed geological, geophysical and geochemical survey including a regional isotopic study in 1994 as well as monitoring of the deep Tendaho wells, drilled in the 1990s. The isotopic information highlighted that the recharge of the geothermal reservoir in the Tendaho Graben originates from the Western Escarpment (elevations above 2000 m) and excludes local recharge.

The geothermal prospects in Ethiopia lie in the MER system. Presently the total number of identified prospects is 23. Tendaho is one of the most promising geothermal areas in the MER system. A detailed geoscientific exploration survey was conducted in Alallobeda geothermal field, one of Tendaho´s three subfields in 2014-2015 by GSE and an Italian consulting company ELC, financed by ICEIDA and NDF. A part of the project was a resistivity survey, consisting of MT and TEM measurements. A total of 132 MT and 132 TEM soundings were done in 2014-2015, in addition to 27 MT soundings which had been done in 2013. The aim of the MT and TEM survey was to reveal the subsurface resistivity structure, to investigate whether a heat resource exists, to develop a conceptual geothermal model of the area and to propose sites of exploratory/production drilling targets.

In this project, geophysical methods applied in geothermal exploration, particularly electromagnetic methods, are discussed. In addition, TEM and MT soundings from the Alallobeda field in Tendaho are processed and 1D inverted.

2. THE TENDAHO GEOTHERMAL FIELD

2.1 Location of the study area

Tendaho geothermal field (see Figure 1) is located 600 km northeast of the capital city, Addis Ababa, in the central Afar depression. The area is bound between latitude 11°30´-12°N and longitude 41°00´-41°30´E. Alallobeda geothermal prospect is one of the three geothermal areas in Tendaho graben, the other two are Dubti and Ayrobera. Alallobeda geothermal prospect is located in the western part of the Tendaho Graben 15 km southwest of Dubti plantation, south-southeast of Logiya. It is characterized by flat plain land and a stratified mountainous range. The elevation of the area varies from 300 to 800 m.

The region´s population is mostly living of the breeding of camels, goats, sheep and donkeys. Due to the fertile alluvial soil and water supply of the Awash River, the most important economic activity during the past 4-5 decades has been the cultivation of cotton at Dubti, Det Bahri, Tangaye koma and Asayita plantation. Currently, the main agricultural product of the area is sugar and in some places of

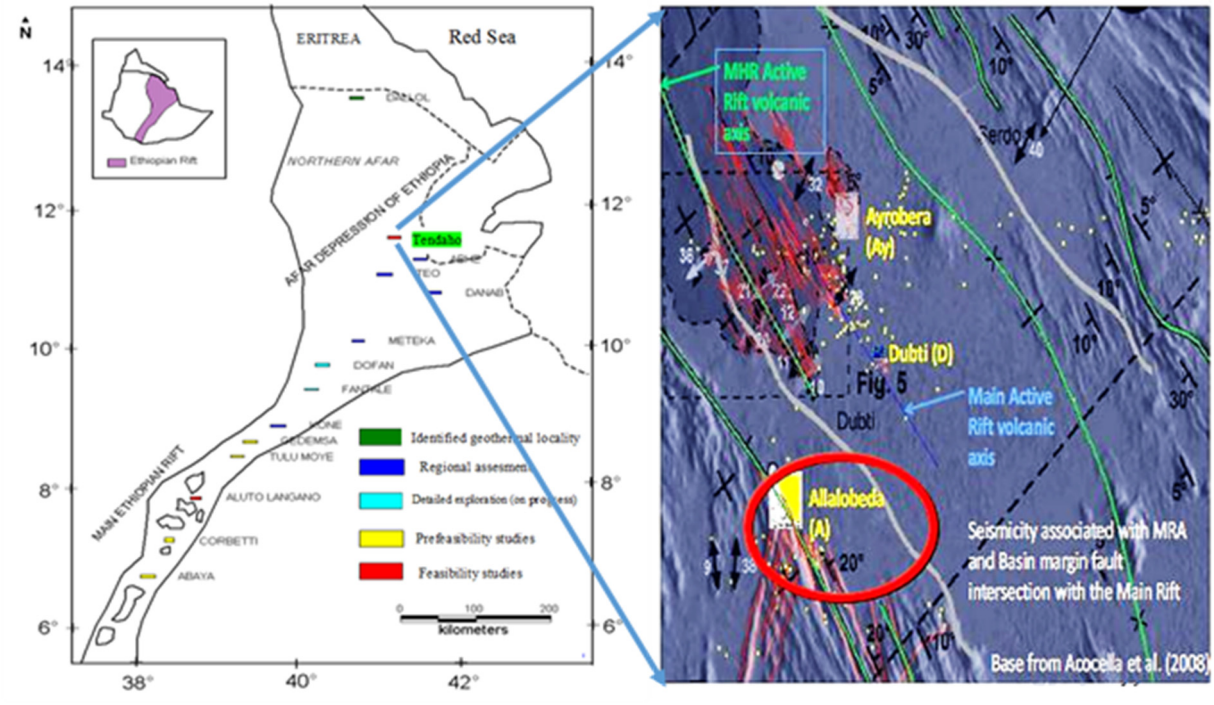

FIGURE 1: Location map of Tendaho

maize along the Awash River and utilizing water of the Awash Dam which is directed through canals at Dubti, Det Bahri, Tangaye Koma and Asayita.

An asphalt road from Addis Ababa branches at Semera to continue to Djibouti and Assab. Currently, the only sea-route out of Ethiopia is through Djibouti. Because of these circumstances, a temporary storage facility area has been built in Semera to minimize the cost for portal service. The traffic on the highway and the services needed in association with this have benefitted to the growth of the town Logiya. Semera, which started out as a road maintenance camp, has also served as the campsite for the geothermal exploration project since the 1990s. Semera became the capital city of the Afar region in 2004 and is growing fast.

The energy consumed by the rural population is mainly obtained from biomass fuel: wood from acacia trees, crop residue and camel and goat droppings. However, all four towns have electric supply, used primarily for household lighting and in the commercial sector. Dubti and Logiya are now connected to the EEPCo diesel generator in Semera. Dubti farm generates its own electricity for use at its ginnery and workshop and for air conditioning and lighting. Diesel fuel is used to generate power for irrigation and drainage pumping.

In the Afar region, the climate is of arid type and it is one of the hottest places in the country.

2.2 Geologic and tectonic setting of the Tendaho prospect area

The Afar depression is a part of the MER and is a triple junction (Figure 2) where three rifts separate three tectonic plates, the Nubian (Africa) plate, the Arabian plate and the Somalian plate. Two rifts are oceanic (Red Sea and Gulf of Aden rift) and one is continental (East African Rift). Tendaho is one of the high-temperature geothermal fields in the MER and a promising area for geothermal development with respect to its size and location. Several geothermal explorations have been carried out there since 1969.

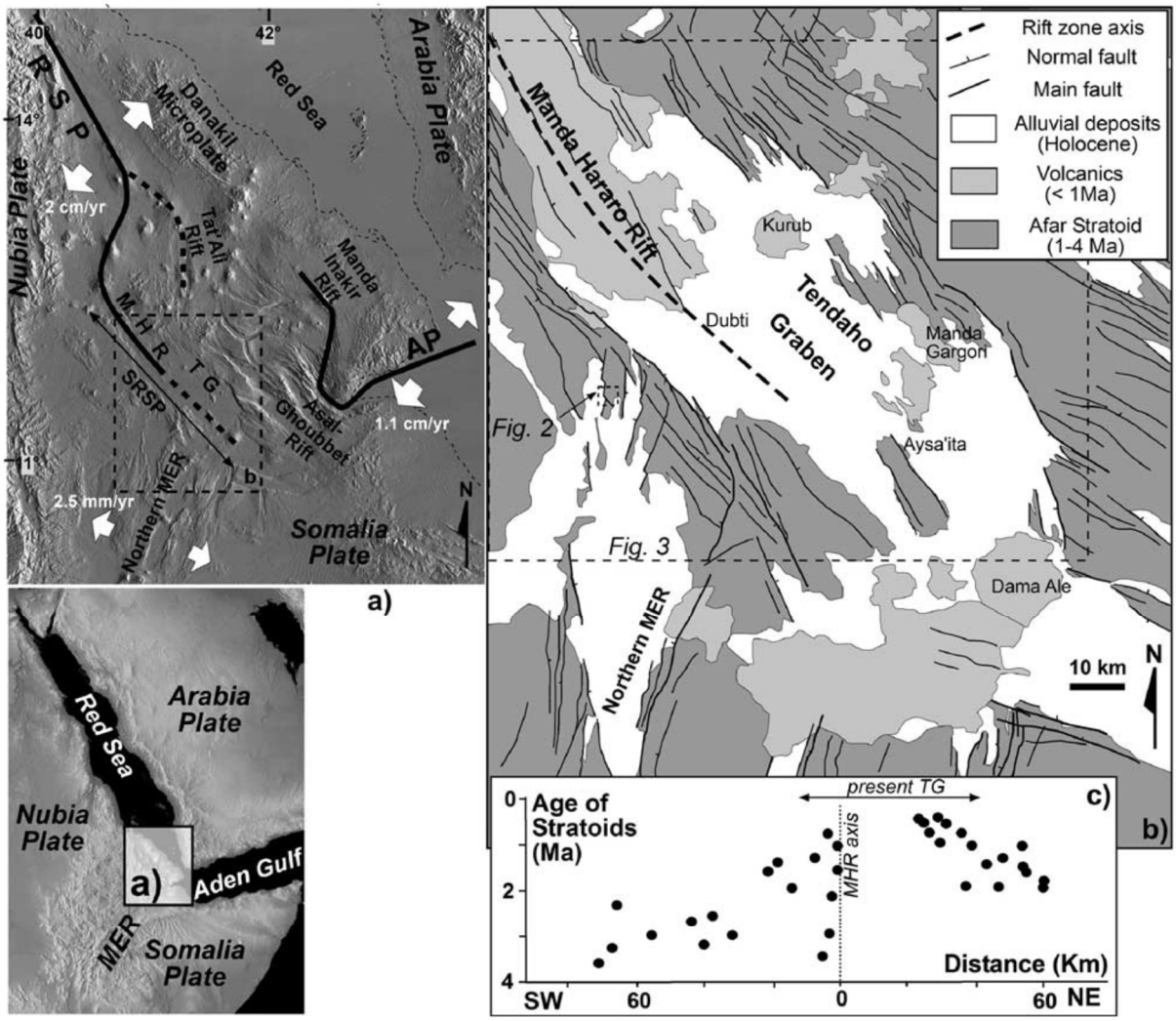

FIGURE 2. Regional setting of Afar region (bottom right): (a) General structure of the Afar triple junction. RSP, Red Sea propagator; SRSP, southern Red Sea propagator; AP, Aden Propagator; EAR, Erta Ale Range; MHR, Manda Hararo Rift; TG, Tendaho Graben; (b) Geology of Tendaho Graben area; (c) Projection of the age (in Ma) of the Afar Stratoid deposits along a NE-SW section perpendicular to the present MHR axis (age data from Barberi et al. (1975), Lahitte et al. (2001, 2003a, 2003b), and Kidane et al. (2003)); the figure is taken from Acocella et al., 2008

The northern Tendaho rift is tectonically characterized by open fissures and active faults which define a pattern of NW-SE elongated blocks with typical wave length of some hundreds of metres. In accordance with this tectonic trend, a general transtensive tectonic regime affects the area as pointed out by Aquater (1996) who carried out a micro-seismic survey. Satellite imagery and field observations show that the main lineament is NW-SE, indicating the prevalence of the Red Sea trend. At the western margin, NW-SE and NE-SW trending lineaments crisscross each other forming grid faults. Within the graben E-W and N-S trending structures are observed, though they are not prominent (Mamo and Bekele, 2014).

As shown in Figure 2, the Afar region is an area of active extensional tectonism and volcanism where the Red Sea, East African Rift system and Gulf of Aden Rift meet. Rifting in Afar began during lower Miocene on a continental arc where significant basaltic activity was probably in progress. The Afar depression is believed to have formed during the Pleistocene period with the formation of an axial ridge. Intense tensional tectonics affect the entire depression, thus, forming a complex mosaic of horsts and

grabens that are still active and contain localized sedimentary basins. From west to east, these are the Tendaho Graben, Dobi Graben, Gaggade Graben and Assal Graben (Megersa et al., 2006).

The northeast-trending Tendaho Graben, where the Alallobeda manifestations are located, has a width of about 50 km and joins the Ethiopian Rift close to Dama Ale the volcano west of Lake Abhe. The border of the graben consists of products of the Afar Stratoid Series (ASS) and the graben itself is filled with lacustrine and alluvial deposits and post-Stratoid basalt flows. The filling is overlain by recent volcanoes, including the historically active Kurub volcano (young products: 4,000-10,000 years) and Dama Ale (younger products: 2,500 years). In Tendaho Graben, under the recent sediments and the trachybasalt; the plagioclase pyric and perlite basalt rocks could be important aquifers due to their micro-fractures and close jointing and constitute reservoir formations for the geothermal system of Alallobeda.

There are different opinions on where the triple junction is located. Wolfenden (2003) states: "Magmatic segments of the main Ethiopian Rift terminate at the Tendaho Gda´ad discontinuity, which separates axial volcanic ranges, faults and fissures trending NW-SE, parallel with the incipient and diffuse Africa-Arabia plate boundary in central and northwest Afar, from north-northeast-trending magmatic segment in the MER. Termination of the MER at the Tendaho Graben Goba´da discontinuity marks the current Afro-Arabian triple junction. The current triple junction is therefore a broad sub-circular area of about 300 km in diameter centred on the Afar Depression, in which the three rift arms overlap, rather than a point".

In the vicinity of geothermal areas, the most identifiable point of intersection is near Alallobeda, where NNE-SSW-trending faults of the MER terminate and deflect into the major NW-SE-trending that bounds the graben on its southwest edge (Stimac et al., 2014).

2.3 Previous geophysical work

In 1969, a joint programme was performed by the Ethiopian government and the UNDP which included the study of the regional geology, geochemistry and hydrology of hot springs of the East African Rift System in Ethiopia (UNDP, 1973). In Tendaho, the first reconnaissance survey was done by UNDP and EIGS in 1973 (Megersa and Getaneh, 2006). Regional and semi-detailed geophysical studies were carried out in the Afar Depression and Tendaho geothermal field to find and investigate the deep structures and to delineate possible geothermal reservoirs. The geophysical methods included MT (e.g. Berktold, 1975), vertical electrical soundings (VES), a magnetic and gravity survey (e.g. Aquater, 1980) and others. Below, some of the surveys that have been done in Afar Depression are described.

An MT survey was carried out in the Afar region in 1971 to investigate the electrical resistivity distribution at depth (Berktold, 1975). The survey included 316 stations arranged on three profiles with a total length of 900 km. Profile I passes through the west of the plateau into the Afar Depression in an E-W direction (Dessie-Bati-Serdo) and crosses the study area. The results of the cross-structural model from profile I in the Afar Depression and under the western plateau have shown that the electrical resistivity layers vary from 200-500 Ωm in the uppermost kilometre, to 5-10 Ωm at about 15 km depth. The temperature at a depth of 15 km in the Afar Depression ranges from 800 to 1200°C corresponding to a mean gradient of about 60°C/km (Berktold, 1975).

In 1972 seismic measurements were made on five profiles, each 120-300 km in length. Along the profiles 350 stations were installed. Four of the profiles were located in the Afar lowland and one in the Ethiopian highlands. The interpretation shows a crustal thinning and upwelling of hot upper-mantle material underneath Afar (Berckhemer and Baier, 1975).

A gravity survey was carried out by Aquater (1980) with a total of 2086 stations. In the southeast centre of Tendaho (Dubti) plantation, a gravity low with a minimum value of -57 mgal was located. This may be caused by the thicker sediment accumulation in the graben which was also detected.

A ground magnetic survey by Aquater (also carried out in 1980) resulted in a map of the total magnetic field that shows a general magnetic low anomaly extending from NW to SE along the Tendaho Graben axis with minor anomaly perturbation, probably due to near surface inhomogeneities.

A micro-seismic survey was carried out by Aquater (1995) in the Tendaho Graben. It shows that the hypocentres of earthquakes are aligned along a line trending NW-SE, and are mostly located at 5 and 10 km depth.

A geophysical survey, which was carried out in 2013 (Kebede et al., 2013), reveals, based on impedance strike and tipper strike at different depth levels, that most of the stations show a general NW-SE strike direction which is coincident with the major trend of the Tendaho rift axis N25°W.

MT surveys were carried out in Tendaho by Lemma et al. (2012). The results show three major resistivity structures of variable thicknesses. Low resistivity associated with sediments and lateral flow of geothermal fluid or zeolite clay alteration zone (Aquater, 1996) is found near the surface. Below the conductive layers, higher resistivity of 8 Ωm is found, which can be correlated to Afar Stratoid basalt or epidote alteration zone, confirmed from alteration zones of wells TD1, TD2 and TD3 (Aquater, 1996). Then, a conductive layer is found at great depth, which can be correlated to magmatic melt associated with the heat source of the geothermal system.

2.4 Previous geochemical work

Water samples were collected from the Northern Afar Region for chemical and isotopic analyses (Gonfiantini et al., 1973). Later, gas samples were collected in fumaroles which can be found almost in the whole Ethiopian Rift valley. Craig (1977) conducted a regional chemical and isotopic study covering most of the Ethiopian Rift valley. Environmental isotopes of ^{18}O, D, tritium, ^{4}He, ^{14}C and ^{13}C were analysed and interpreted. The results of the exploration activities confirmed the existence of circulating high-temperature geothermal fluid at great depth that could be used for electrical power generation.

A radon soil gas survey was conducted in the Dubti geothermal prospect in 2010 with the help of the BGR (German Geological Survey) experts and led to the conclusion that the anomalous area is to the southeast of the drilled wells.

In 2012, another radon soil gas survey was conducted by Teclu and Mekonen (2013) in Ayrobera geothermal prospect and it identified anomalous structures trending NNE-SSW and in NNW-SSW. These structures also cross each other. The distribution of the thoron anomaly shows broken consecutive NNE-SSW, NNW-SSE and N-S directions.

The radon soil gas geochemical survey by Teclu and Mekonen (2013) also reveals the distribution of buried faults, joints or fractures. The investigation confirms that the anomalous values are concentrated along structures with NNE-SSW and N-S directions in the Alallobeda area.

Tendaho was the second area to be drilled after the Lakes district. In Tendaho geothermal field, six wells were drilled from 1993 to 1998 by the Italian government and Geological Survey of Ethiopia. Three deep wells namely TD1, TD2 and TD3 were drilled to a depth of 2196, 1811, and 1989 m, respectively. Three shallow wells, TD4, TD5 and TD6 were drilled to a depth of 466, 516 and 505 m, respectively. TD2, TD4, TD5 and TD6 are productive while TD1 and TD3 are non-productive. The elevation (m a.s.l.) of wells TD1, TD2, TD3, TD4, TD5 and TD6 is 365.9, 365.7, 366.8, 365.2, 366.3 and 366, respectively. The temperatures in the wells range from 200 to 270°C.

A preliminary production test and techno-economic study indicate that the shallow productive wells could supply enough steam to operate a pilot power plant of about 5 MWe and the potential of the deep reservoir is estimated to be about 20 MWe (Teklemariam and Kebede, 2010).

3. GEOPHYSICAL METHODS IN GEOTHERMAL EXPLORATION

3.1 Introduction

Geophysical methods are some of the most important methods in exploring geothermal areas. They use equipment that measure from the surface physical parameters which are directly related to physical properties or processes at depth in the earth´s crust. Combined with other geothermal exploration methods, their results can be used to find the size of geothermal fields and the likely successful drill sites.

The primary aim of geophysical exploration of geothermal areas is to:

- Find geothermal prospects;
- Outline drilling fields;
- Find the depth of reservoir;
- Locate aquifers and site wells;
- Estimate properties of the system.

Geophysical exploration is a fairly young scientific discipline which with regards to geothermal was developed in the mid twentieth century. With large advance in electronics, computer technology and model calculations during the past decades, it has developed more rapidly. Different parameters are measured in geophysical exploration, depending on the geophysical methods used.

Geophysical exploration methods can be classified into indirect and direct methods.

3.2 Indirect methods (structural methods)

The structural methods include gravity, magnetic and seismic measurements. Structural methods give information on anomalies caused by the associated geological formations or structures (e.g. fault and dykes).

Magnetics measurements: The spatial variations in the strength of the earth´s magnetic field are measured either on the ground or in an aeromagnetic survey. Surface bound magnetic surveys can trace narrow linear features like dykes and faults where the basement is covered with soil. In aeromagnetic surveys correlation has been found between magnetic anomalies and zones of intense hydrothermal alteration.

Magnetic methods are routinely employed for geothermal studies to outline structural lineaments which could be associated with faults and fractures as potential conduits for geothermal fluid circulations. Magnetic maps are used for structural purposes, locating intrusions, dykes, faults, buried lava and hydrothermally altered areas (Flóvenz et al., 2012).

Gravity surveys: Gravity anomalies are caused by spatial lateral density variations in the subsurface. Density variations are a result of compositional variations, porosity, differential weathering, hydrothermal alterations, fracturing of rocks and different structures. In geothermal areas possible sources of local gravity anomalies are dominantly hydrothermal alteration, intrusions and structural features, such as faults, calderas and basement structures (Nure, 2001).

Seismic surveys: Seismic methods can be divided into passive and active seismic methods depending on whether the source of seismic energy is natural or man-made.

Passive seismic methods detect seismic activity in the earth and can give information about velocity, attenuation, S-wave shadows, depth to the brittle/ductile boundary which indicates partial melt and magma chambers. Seismic activity that is studied in geothermal exploration is:

Ground noise (micro-seismicity) generated by the geothermal system through boiling.
Micro-earthquakes and earthquakes on active fault planes, hydraulic fracturing and tensile cracking of cooling intrusions.

An earthquake is a movement of crustal material along a new or pre-existing fault or fissure caused by a regional stress field. The non-elastic rupture is usually some tens or hundreds of metres for a small earthquake and can be regarded as a point source from a distance. The source location is called hypocentre and its projection to the surface of the earth is called epicentre.

A measure of the energy release (E) is the Richter M factor or magnitude which is on a logarithmic scale.

$$\log E = A + B \cdot M; B \approx 1.4 \quad (1)$$

An earthquake of magnitude 5 is about 10 times stronger (ten times more energy release) than an earthquake of magnitude 4. Earthquakes and micro-earthquakes give information on the stress field and the tectonic nature of the area where they occur. Stress is the internal force (per unit area) associated with strain which is the relative change in shape or size of an object due to an external applied force. Observation of seismic waves gives information on the properties of the transmission path from source to receiver (seismometer).

The location of a hypocentre is estimated from the arrival times of P-waves and S-waves at several stations. Thereby, it is assumed that the source is a point source and that the seismic wave travels through a transversely uniform earth (horizontal layers). In principle, an epicentre can be found from four P-arrival times. For increased accuracy, both S- and P-arrival times from three or more stations are used.

Some geothermal areas are characterized by an increased number of earthquakes, other show similar seismic activity as the region around the geothermal areas or even define a seismic gap (no seismic activity). Seismic studies have been used to investigate the regional tectonics where a geothermal area is located. As the tectonics and geological settings control the nature of most geothermal areas, the passive seismic method can deliver valuable information about the nature of geothermal systems (Hersir and Björnsson, 1991).

In general, passive seismic methods in geothermal exploration are used to map the location of the heat source, to map high cracking density zone, to determine the fluid zones, reservoir size and fault structure.

Active seismic methods detect sound velocity distribution and anomalies in the earth and its attenuation. The sound velocity distribution gives structural information about temperature and fluid-filled fracture zones (Hersir and Björnsson, 1991).

3.3 Direct methods

The direct methods include thermal and resistivity methods, including SP. Their success is based on them giving information on anomalies that are related to the geothermal activity. These are key methods in the exploration of geothermal systems, especially the resistivity methods.

Thermal methods: These are the most direct methods in geothermal exploration. The measurements can be carried out in the soil or in a borehole at a few metres depth. Temperature measurements in the boreholes delineate aquifers and can be used to estimate the temperature gradient which is a basic knowledge on a high-enthalpy geothermal system. Temperature measurements in the soil can also be useful in finding linear anomalies near hot springs and fumaroles, relating upflow to hidden linear structures.

Resistivity methods can be divided into DC methods and electromagnetic methods:

DC (direct current) resistivity methods are based on sending DC current into the earth and monitoring the potential signal it creates. There are several DC methods which have been used for decades in geothermal exploration. Some of these are Schlumberger and Wenner soundings, Head on profiling, Dipole soundings and profiling (Hersir and Björnsson, 1991).

Electromagnetic methods (EM): Using natural sources; magnetotellurics or MT is a passive method based on the natural electric field in the earth, created through natural variations in the earth's magnetic field. On the other hand, TEM is an active method based on creating a magnetic field in the earth and monitoring its response related to its decay as the source is turned off. Both methods are widely used in geothermal exploration, and the state of the art in modern geothermal research is the combination of these two methods.

S*elf-potential (SP)*: This is a passive method that measures the naturally occurring potential difference in the earth. It does not require electrical currents to be injected into the ground.

Geophysical well loggings and borehole methods: These are valuable tools for direct exploration and detection of physical parameters. Geophysical logging offers an opportunity to determine the composition, variability and physical properties of the rocks around the well enabling a proper understanding of the subsurface at a lower cost (Ofwona, 2010).

4. RESISTIVITY OF ROCKS

Resistivity of a material is defined as the electrical resistance in Ohms (Ω) between the opposite faces of a unit cube of the material (Kearey and Brooks, 1994). For a conducting cylinder of resistance R, length L and cross-sectional area A, the resistivity is given by:

$$\rho = \frac{RA}{L} \tag{2}$$

where ρ = Resistivity of the material (Ωm);
R = Resistance (Ω);
L = Length (m); and
A = Cross-sectional area (m^2).

The specific resistivity ρ depends on the material and is defined through Ohm´s law:

$$\boldsymbol{E} = \rho \boldsymbol{j} \tag{3}$$

where $\boldsymbol{E}$ = Electric field (V/m);
$\boldsymbol{j}$ = Current density (A/m^2).

The reciprocal of resistivity is conductivity ($1/\rho = \sigma$) and is given in Siemens per m.

The main electrical conduction mechanisms are mineral conduction, pore fluid conduction and surface conduction. Mineral conduction within the rock matrix itself is negligible in most cases, the rock matrix normally acts as an insulator except for very high temperatures > 800°C. The main electrical conduction mechanisms in geothermal fields are pore fluid conduction, which is conduction by dissolved ions in the pore fluid, and even more importantly, surface conduction by absorbed ions on the pore's surface.

Electrical resistivity of rocks depends on the parameters discussed briefly in the next subsections.

4.1 Porosity, permeability and the pore structure of the rock

Porosity and permeability are related to the properties of the rocks which are among others the number, size and connection of rock openings. Porosity is defined as the ratio between the pore volume and the total volume of a material.

$$\phi_t = \frac{V_V}{V_T} \tag{4}$$

where ϕ_t = Porosity;
V_V = Volume of void space (m^3);
V_T = Total or bulk volume of the material (m^3).

There are three main types of porosity (Hersir and Björnsson, 1991):

Intergranular: The pores are the spaces between grains or particles in a compact material like sediments and volcanic ash.
Joints-fissures: This is a net of fine fractures caused by tension and cooling of the rock common in igneous rocks and lava.
Vugular: As material is dissolved, big and irregular pores are formed and the material washed away. These can also be pores formed by gas as in volcanic rocks and limestone.

Pore space must be interconnected and filled with water so that the rock can conduct electricity. In all types of porosity there are large voids, called storage pores, and finer connected pores. Most of the resistance to electric current flow (and fluid flow) is in the connecting pores.

It has been observed in many cases that resistivity of water-bearing rocks varies approximately with the inverse square of the porosity. This empirical law, called Archie´s law (Archie, 1942), describes how resistivity depends on porosity if ionic conduction in the fluid dominates other conduction mechanisms in the rock.

$$\rho = \rho_w a \phi_t^{-n} \tag{5}$$

where ρ = Bulk (measured) resistivity (Ωm);
ρ_w = Resistivity of the pore fluid (Ωm);
ϕ_t = Porosity in proportion of total volume;
a = Empirical parameter, varies from < 1 for intergranular porosity to > 1 for joint porosity, usually around 1; and
n = Cementing factor, an empirical parameter, varies from 1.2 for unconsolidated sediments to 3.5 for crystalline rocks, usually around 2.

Archie´s law is valid if the resistivity of the pore fluid is in the order of 2 Ωm or less, but becomes less reliable if the resistivity is much higher (Flóvenz et al., 1985). However, Archie´s law seems to be a fair approximation when the conductivity is dominated by the saturating fluid (Árnason et al., 2000).

Permeability: This is the ability of the rock (material) to transmit water or fluid. It is the amount of fluid of a specified viscosity, under the influence of a given pressure, that passes through a sample having a certain cross-sectional area and thickness. It is mainly dependant on the size and shape of the pores in the materials.

4.2 Salinity of the water

Salinity is a measure of the total amount of salts in water or soil. Salts are highly soluble in surface and ground water and are transported with the water. Ground water may contain a variety of salts in the solution. Therefore, equivalent salinity is defined as the salinity of a NaCl-solution with the same resistivity as the particular solution. Mobility of the ions does not vary widely and equivalent salinity is

therefore close to true salinity. The bulk resistivity of a rock is mainly controlled by the resistivity of the pore fluid which is dependent on the salinity of the fluid. Figure 3 shows how conductivity changes with salinity.

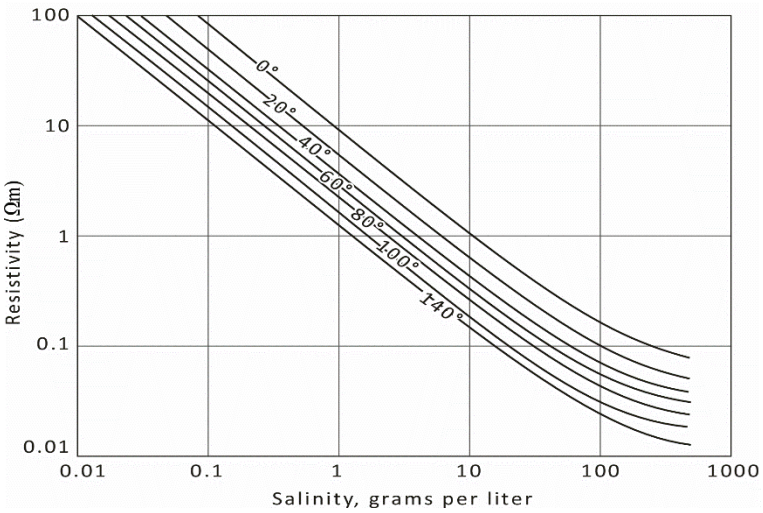

FIGURE 3: Electrical resistivity of NaCl solutions as a function of concentration and temperature (Flóvenz et al., 2012; based on Keller and Frischknecht, 1966)

In aqueous salt-solutions the ions of the solid separate and start to move freely in the solution. If the amount of dissolved solids in the pore fluid increases, the conductivity also increases as shown in Figure 3. Therefore, the conductivity of a solution is a function of salinity and the mobility of the ions present in the solution. The mobility of the ions depends on temperature (viscosity) and on concentration. The conductivity of a solution can be expressed by the following equation (Hersir and Björnsson, 1991):

$$\sigma = F(c_1 q_1 m_1 + c_2 q_2 m_2 + \cdots) \quad (6)$$

where σ = Conductivity (S/m);
F = Faraday´s number (9.65 x10^4 C/mole);
c_i = Concentration of ions;
q_i = Valance of ions**;** and
m_i = Mobility of different ions.

4.3 Temperature

At moderate temperatures, between 0 and 200°C, resistivity of aqueous solutions decreases with increasing temperature as shown on Figure 4. This is because of increasing mobility of ions at increasing temperature caused by a decrease in the viscosity of the water. Dakhnov (1962) has described this relationship:

$$\rho_w = \frac{\rho_{wo}}{1 + \alpha(T - T_o)} \quad (7)$$

where ρ_{wo} = Resistivity of the fluid at temperature T_0 (Ωm);
α = Temperature coefficient of resistivity $(°C^{-1})$ (≈ 0,023 $°C^{-1}$ for T_o = 25 °C).

At high temperatures, a decrease in the dielectric permittivity of the water results in a decrease in number of dissociated ions in the solution. Above 250°C the resistivity of the fluid starts to increase (Quist and Marshall, 1968).

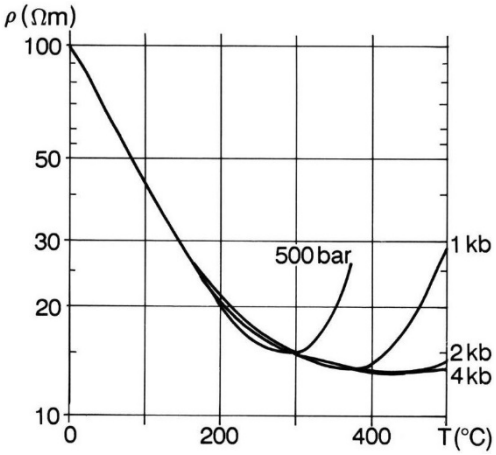

FIGURE 4: Electrical resistivity of NaCl solution as a function of temperature at different pressures (Hersir and Björnsson, 1991; based on Quist and Marshall, 1968)

4.4 Water rock interaction and alteration mineralogy

Water-rock interaction is the interaction of water with rocks which not only extracts the heat but also causes changes in the chemistry of both the water and the rock. Alteration minerals are formed through hydrothermal alteration processes when hydrothermal water reacts with the rock.

The alteration processes and the resulting type of alteration minerals are dependent on the type of primary minerals and the chemical composition of the geothermal fluid and temperature (see right part of Figure 5). The intensity of the alteration is further dependent on the contact time and texture of the host rocks. Alteration intensity is normally low for temperatures below 50°C. At temperatures below 220°C, low-temperature zeolites and the clay minerals smectite are formed. Smectite has hydrated and loosely bound cations between the silica plates, making the mineral conductive and provides it with a high cation exchange capacity (Árnason et al., 2000).

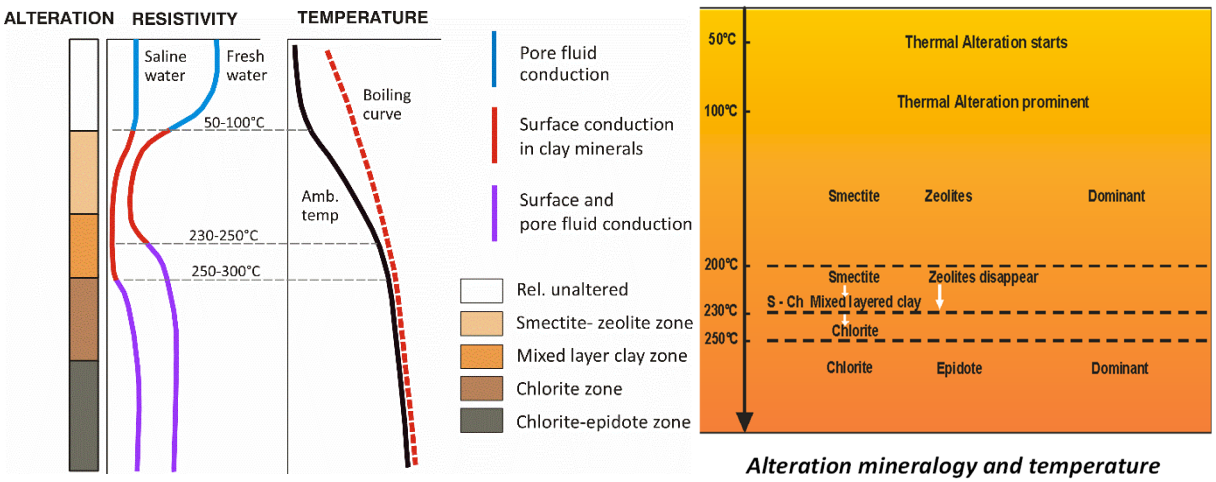

FIGURE 5: The general resistivity structure of a high-temperature geothermal system in basaltic environment showing resistivity variations as a function of alteration and temperature (Flóvenz et al., 2012)

In the temperature range from 220 to about 240-250°C, the low-temperature zeolites disappear and smectite is transformed into chlorite in a transition zone, the so-called mixed-layered clay zone, where smectite and chlorite coexist in a mixture. At about 250°C smectite disappears and chlorite is the dominant mineral, marking the beginning of the chlorite zone. Hence, with increased resistivity, since chlorite minerals have cations that are fixed in a crystal lattice, the mineral is much more resistive. At still higher temperature about 250-270°C, epidote becomes abundant in the so-called chlorite-epidote zone (Árnason et al., 2000).

As shown in the left part of Figure 5, in high-temperature areas in basaltic environment the resistivity in the upper-most part of the subsurface is relatively high and the main conduction mechanism is pore fluid conduction, no alteration is found. Resistivity decreases as the temperature increases and smectite and zeolite become the dominant alteration minerals (temperature > 100°C). The conduction mechanism is surface conduction in clay minerals. Below the smectite alteration, chlorite and mixed-layered clay dominate and the resistivity increases again. This is because chlorite has bound cations that are fixed in the crystal lattice making them resistive. Here, surface and pore fluid conduction are dominant. At greater depth where epidote becomes dominant, the resistivity is high due to the crystal lattice formation, the conduction mechanism is surface and pore fluid conduction.

Resistivity is directly proportional to the alteration minerals and not necessarily related to temperature, since the geothermal system might be fossil.

5. MT AND TEM RESISTIVITY METHODS IN GEOTHERMAL EXPLORATION

5.1 Basic theory of electromagnetic methods

Electromagnetic (EM) methods are commonly used in surface exploration of geothermal areas to determine the spatial distribution of the electrical conductivity in the subsurface. The MT method has found to be the most effective EM method in delineating conductivity at great depth. The TEM method is used to investigate the resistivity structure at shallow depths and also for static shift correction of MT data.

The behaviour of electromagnetic fields at a given frequency can de described by Maxwell´s equations in a conductive media:

$$\boldsymbol{\nabla} \times \boldsymbol{E} = -\frac{\partial \boldsymbol{B}}{\partial t} \tag{8}$$

$$\boldsymbol{\nabla} \times \boldsymbol{H} = \boldsymbol{j} + \frac{\partial \boldsymbol{D}}{\partial t} \tag{9}$$

$$\boldsymbol{\nabla} \cdot \boldsymbol{B} = 0 \tag{10}$$

$$\boldsymbol{\nabla} \cdot \boldsymbol{D} = \eta \tag{11}$$

where **E** = Electric field (Vm^{-1});
B = Magnetic induction (T);
D = Electric displacement (Cm^{-2});
$\boldsymbol{j}$ = Electric current density (Am^{-2});
η = Electric charge density owing to free charges (Cm^{-3});
$(\nabla \times)$ = Curl and $(\nabla \cdot)$ = div.

A harmonic dependency of the oscillating electromagnetic fields **E** and **H** is assumed as: $\sim e^{i\omega t}$. For a linear and isotropic media, the vector fields in Maxwell's equations (Equations 8-11) can be related through the constitutive relationships, $\boldsymbol{j} = \sigma \boldsymbol{E}$, $\boldsymbol{B} = \mu \boldsymbol{H}$ and $\boldsymbol{D} = \varepsilon \boldsymbol{E}$.

According to Snell's law, we have:

$$\frac{1}{v_o} \sin \theta_i = \frac{1}{v} \sin \theta_t$$

V_o and V are the velocities in the air and in the half-space, respectively and can be described as:

$$V_o = \frac{1}{\sqrt{\varepsilon \mu}} \text{ and } v = \sqrt{\frac{2\omega}{\mu \sigma}}$$

Hence:

$$\sin \theta_t = \sin \theta_i \sqrt{\frac{2\varepsilon\omega}{\sigma}} \text{ and } \frac{2\varepsilon\omega}{\sigma} < 10^{-3}$$

θ_t is therefore close to zero; incident plane waves travel vertically downwards for all angles of incidence θ_i.

5.1.1 MT methods

MT is a passive EM method that measures the fluctuations in the natural electric field **E** and magnetic field **B** in orthogonal directions at the surface of the earth to determine the electrical conductivity distribution of the earth at depth ranging from a few hundred metres to tens of kilometres. The

fundamental MT theory was first introduced by Tikhonov (1950, reprinted 1986) and, in more details, by Cagniard (1953).

The depth of penetration of the EM wave into the earth is inversely proportional to rock conductivity. In a uniform earth, **E** and **H** decay exponentially with depth; the more conductive the earth, the less is the penetration.

At the depth $\delta(T)$, the so called skin depth, EM wave are attenuated to e^{-1} of their amplitudes at the surface of the earth. Hence, in MT studies, one electromagnetic skin depth is generally equated with the penetration depth of electromagnetic wave into the earth. In MT studies of the earth, μ is usually the free space value ($\mu_o = 4\pi \times 10^{-7} Hm^{-1}$) and the skin depth can be written as:

$$\delta(T) \approx 500\sqrt{T\rho_a}\ (\text{m}) \qquad (12)$$

where, $\delta(T)$ = Electromagnetic skin depth in m for a given period T (s); and
ρ_a = Apparent resistivity, or the average resistivity of an equivalent uniform half space.

From the above equation we can conclude that for a given period, the depth achieved by the EM wave will be dictated by the average conductivity of the overlying earth that is penetrated (Simpson and Bahr, 2005).

AMT and MT techniques are essentially the same, differing only in the frequency range and the different sources. MT Phoenix equipment acquires data in the frequency range from 400-0.0000129 Hz. AMT acquires data in the frequency range of about 100-10.000 Hz (roughly the range of human hearing, hence the audio designation). Therefore, MT is used for deeper and AMT for shallow investigation.

Magneto hydrodynamic processes within the Earth´s outer core generate the greater part of the Earth´s magnetic field. It is the superimposed, more transient, lower amplitude fluctuation of external origin that MT sounding seeks to exploit. The power spectrum of these plummets is in the range 0.5-5 Hz frequency, minimizing at frequency of ~1 Hz. So for MT the frequency between 0.5-5 Hz is called the dead band frequency, the MT soundings lack data quality in this range. For AMT the dead band frequency around $\sim 1 - 10$ kHz .

Source of MT sounding: Figure 6 shows one of the sources of MT soundings. In the MT methods time variations in the earth´s magnetic field are used to probe the surface resistivity structure. The earth´s EM field contains a wide frequency spectrum, high frequencies >1 Hz (periods shorter than 1 second) are due to thunderstorms near the equator which are distributed in the form of guided waves between

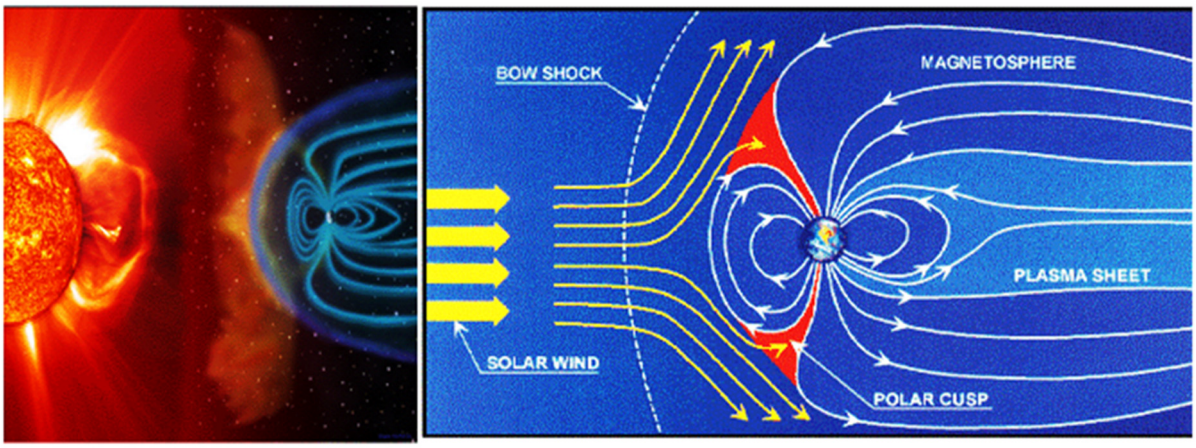

FIGURE 6: Interaction of solar wind with the magnetosphere, source of low frequency natural EM (Adapted from Sky and Telescope (2015) and CNES Scientific Missions (2015))

the earth and ionosphere. The lower frequencies <1 Hz (periods longer than 1 second) are generated by ionospheric and magnetospheric currents caused by plasma interfering with the earth's magnetic field.

The largest geomagnetic field variations on the order of a few hundred nT occur during magnetic storms, which happens due to a sporadic increase in the rate at which plasma is ejected from the sun. Magnetic storms last for several days, they become visible at high latitudes in form of Aurora Borealis and Aurora Australis, or northern and southern lights, respectively (Simpson and Bahr, 2005). Aurora is a natural light displayed in the sky and it is associated with solar wind, a flow of charged particles continuously flowing away from the sun. The earth´s magnetic field traps these particles, many of which travel toward the poles where they are accelerated towards the earth (Lemma, 2010).

The MT method depends on the penetration of electromagnetic energy into the earth. The measurements are absolute and the apparent resistivity calculations from MT measurements are accurate for the true resistivity values. Their interpretation gives true resistivity values and true depths, not just anomalies. Depth interpretation based on MT data is therefore much more definitive than interpretation of gravity or magnetic data (Vozoff, 1972).

Impedance: If the electromagnetic wave propagates through a homogeneous and isotropic medium, the electric and magnetic field vectors are orthogonal. The ratio of the orthogonal components of the electric and magnetic field are derived from Maxwell's equations. The characteristic impedance is denoted by **Z**. The impedance tensor elements describe the relationship between the electric and magnetic fields in matrix form.

$$\begin{pmatrix} E_x \\ E_y \end{pmatrix} = \begin{pmatrix} Z_{xx} & Z_{xy} \\ Z_{yx} & Z_{yy} \end{pmatrix} \begin{pmatrix} H_x \\ H_y \end{pmatrix} \tag{13}$$

$$E_x(\omega) = Z_{xx}(\omega)H_x(\omega) + Z_{xy}(\omega)H_y(\omega) \tag{14}$$

$$E_y(\omega) = Z_{yx}(\omega)H_x(\omega) + Z_{yy}(\omega)H_y \tag{15}$$

$$Z_{xy} = \frac{E_x}{H_y} = \frac{i\omega\mu_o}{k} \tag{16}$$

$$Z_{yx} = \frac{E_y}{H_x} = \frac{-i\omega\mu_o}{k} \tag{17}$$

where Z_{xy}, Z_{yx} = Characteristic impedance elements;
ω = Angular frequency ($2\pi f$) where f is frequency (Hz);
k = $\sqrt{i\omega\mu(i\omega\varepsilon + \sigma)}$, stands for the propagation constant.

Assuming $\sigma \gg \omega\varepsilon$, the wave propagation constant k can be simplified to the quasi-stationary approximation $k = \sqrt{i\omega\mu\sigma}$. Substituting this into Equations 16 and 17 gives:

$$Z_{xy} = \frac{E_x}{H_y} = \frac{i\omega\mu}{\sqrt{i\omega\mu\sigma}} = \sqrt{i}\sqrt{\omega\mu\rho} = \sqrt{\omega\mu\rho}\, e^{i\pi/4} \tag{18}$$

$$Z_{yx} = \frac{E_y}{H_x} = \frac{-i\omega\mu}{k} = -Z_{xy} \tag{19}$$

This shows that there is phase difference of $\pi/4$ or 45° between E_x and H_y as shown in Figure 7. If the earth is homogenous and isotropic, the true resistivity is related to the characteristic impedance using Equation 18 through the relation:

$$\rho = \frac{1}{\omega\mu}\left|Z_{xy}\right|^2 = \frac{1}{\omega\mu}\left|Z_{yx}\right|^2 \tag{20}$$

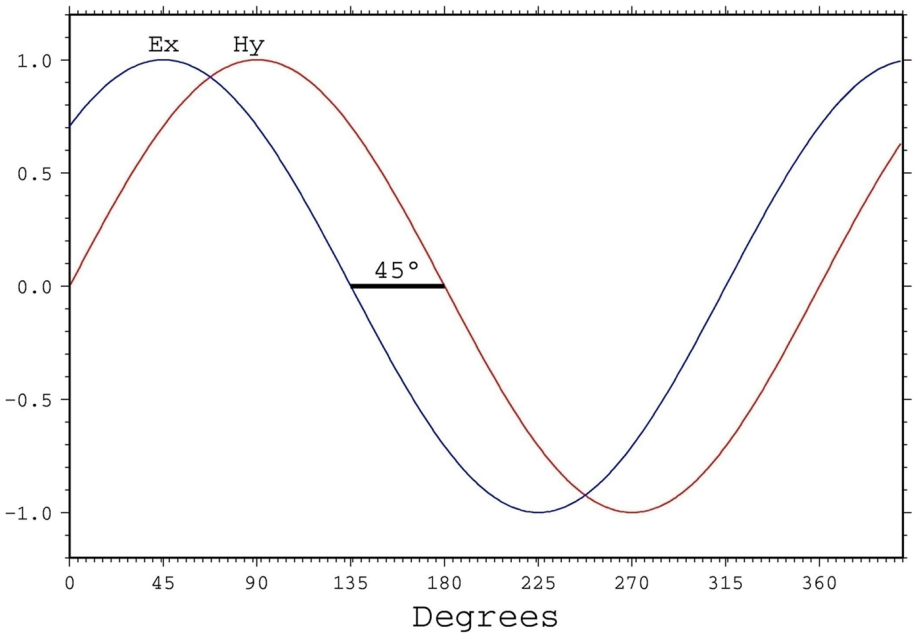

FIGURE 7: The phase difference between the **E** and **H** field
for homogenous half space

In general:

$$\rho = \frac{1}{\omega\mu}|Z|^2 \tag{21}$$

Equation 21 can be re-written using magnetic field intensity $\boldsymbol{B} = \mu\boldsymbol{H}$ in the unit Tesla (T) and electric field $\boldsymbol{E}$ in the practical unit mV/km. For a homogeneous earth, ρ and Z are independent of T:

$$\rho = \frac{T}{2\pi\mu} = \left|\frac{E_x 10^{-6}\mu}{B_y 10^{-9}}\right|^2 = \frac{T\mu}{2\pi}\left|\frac{E_x}{B_y}\right|^2 10^6 = 0.2T\left|\frac{E_x}{B_y}\right|^2 \tag{22}$$

or

$$\phi = arg(Z) = {}^{\pi}/_{4} = 45° \tag{23}$$

For a non-homogeneous earth, ρ and Z depend on T and the apparent resistivity (ρ_a) and phase (ϕ_a) are defined as:

$$\rho_a(T) = 0.2T|Z_o|^2 = 0.2T\left|\frac{E_x}{B_y}\right|^2 \quad and\ the\ phase \quad \phi_a(T) = arg(Z_o) \neq 45° \tag{24}$$

where Z_o = Impedance at the surface.

Impedance tensor: This tensor describes the relationship between the orthogonal electric and magnetic field at a given frequency:

$$\begin{bmatrix} E_x \\ E_y \end{bmatrix} = \begin{bmatrix} Z_{xx} & Z_{xy} \\ Z_{yx} & Z_{yy} \end{bmatrix} \begin{bmatrix} H_x \\ H_y \end{bmatrix} \tag{25}$$

Depending on the spatial distribution of the electrical conductivity the impedance tensor components reduce to a particular expression. The spatial distribution, also called geo-electric dimensionality, can be classified as 1D, 2D or 3D.

Definition of apparent resistivity – non-homogenous media
1D impedance tensor: For a 1D layered earth the resistivity distribution varies only with depth. The diagonal element of the impedance tensor Z_{xx} and Z_{yy} are zero and the off-diagonal elements of the impedance tensor Z_{xy} and Z_{yx} are equal in magnitude but opposite in sign. Therefore, from Equation 25 the impedance tensor for 1D can be written as:

$$Z_{1D} = \begin{vmatrix} 0 & Z_{xy} \\ Z_{yx} & 0 \end{vmatrix} \tag{26}$$

The corresponding apparent resistivity and phase for 1D earth can be defined as:

$$\rho_a = \frac{1}{\mu\omega}|Z|^2 \text{ and } \phi_a = \tan^{-1}\left(\frac{ImZ}{ReZ}\right) \tag{27}$$

The impedance phase gives additional information about the resistivity structure. It can be determined as the tangent inverse of the ratio of imaginary to real component of the tensor.

2D impedance tensor: For a 2D earth, the resistivity is constant in one horizontal direction but varies in the other horizontal direction and with depth. The direction along which the resistivity is constant is known as the geo-electrical strike or electromagnetic strike direction. The diagonal elements of the impedance tensor are equal to zero, but the off-diagonal elements are different in magnitude $\left(Z_{xy} \neq -Z_{yx}\right)$.

If the x-direction is parallel to the strike and the y-direction is perpendicular to it, the diagonal elements of the impedance tensor become zero $\left(Z_{xx} = Z_{yy} = 0\right)$ and the impedance tensor can be written as:

$$Z_{2D} = \begin{vmatrix} 0 & Z_{xy} \\ Z_{yx} & 0 \end{vmatrix} \tag{28}$$

where $Z_{xy} = Z_{TE} = \frac{E_x}{H_y}$; and $Z_{yx} = Z_{TM} = \frac{E_y}{H_x}$

For the 2D electrical resistivity structure, the magnetic field splits into two independent modes:

1. Transverse magnetic (TM) mode: the magnetic field is parallel to the electric strike direction;
2. Transverse electric (TE) mode: the electric field is parallel to the electric strike direction.

In TM mode or B-polarization the magnetic field is polarized parallel to the electromagnetic strike, in TE mode or E-polarization the electric field is polarized parallel to the electromagnetic strike. In TM mode or B-polarization the electric field is polarized perpendicular to the electromagnetic strike, and in TE mode or E-polarization the magnetic field is polarized perpendicular to the electromagnetic strike as shown in Figure 8.

3D impedance tensor: The resistivity varies in all three directions ($\rho = \rho(x, y, z)$). In this case the impedance tensor takes the general form ($Z_{xx} \neq Z_{yy} \neq 0$ and $Z_{xy} \neq Z_{yx}$). The impedance tensor in Equation 25 can be written as:

$$Z_{3D} = \begin{vmatrix} Z_{xx} & Z_{xy} \\ Z_{yx} & Z_{yy} \end{vmatrix} \tag{29}$$

There exists no rotational direction where both diagonal elements of the impedance tensor or any component of the tipper vector will vanish. If the tensor elements are non-zero there is a resistivity boundary.

Skew: This is the ratio of the amplitude of the diagonal impedance elements to the off-diagonal impedance elements. Skew is another measure of 3D dimensionality. It does not change with rotation of the coordinates.

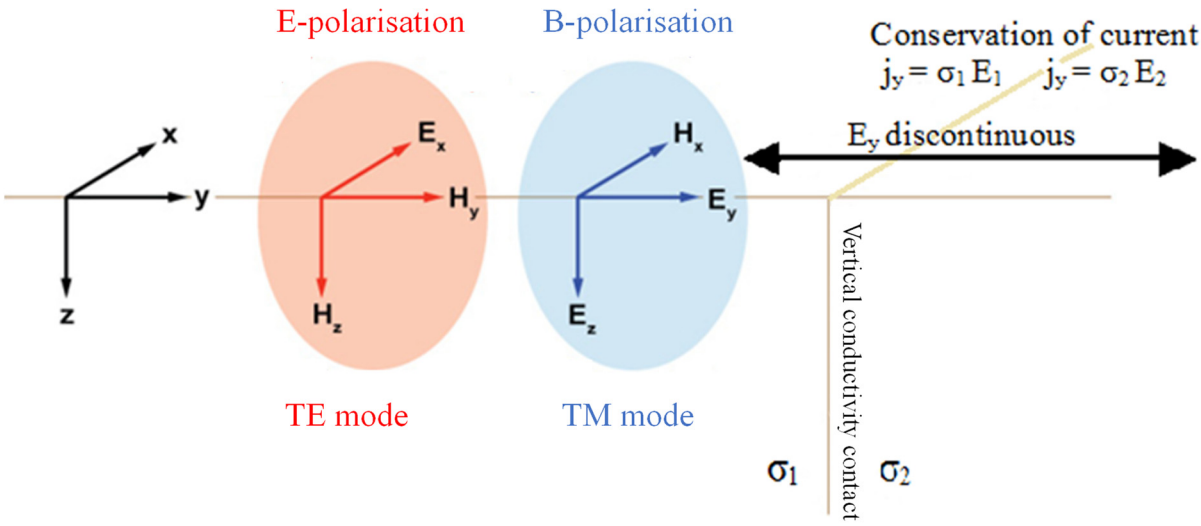

FIGURE 8: 2D model and the concept of polarizations in magnetotelluric (Teklesenbet, 2012)

$$Skew = \left| \frac{Z_{xx} + Z_{yy}}{Z_{xy} - Z_{yx}} \right| \tag{30}$$

In 1D and 2D cases, the skew should be close to zero. Large deviations from zero are an indicator of three-dimensionality. Typical values below 0.2 were taken to indicate that the response could be interpreted in a 1D or 2D manner (Simpson and Bahr, 2005; Berdichevsky and Dmitriev, 2002).

5.1.2 TEM methods

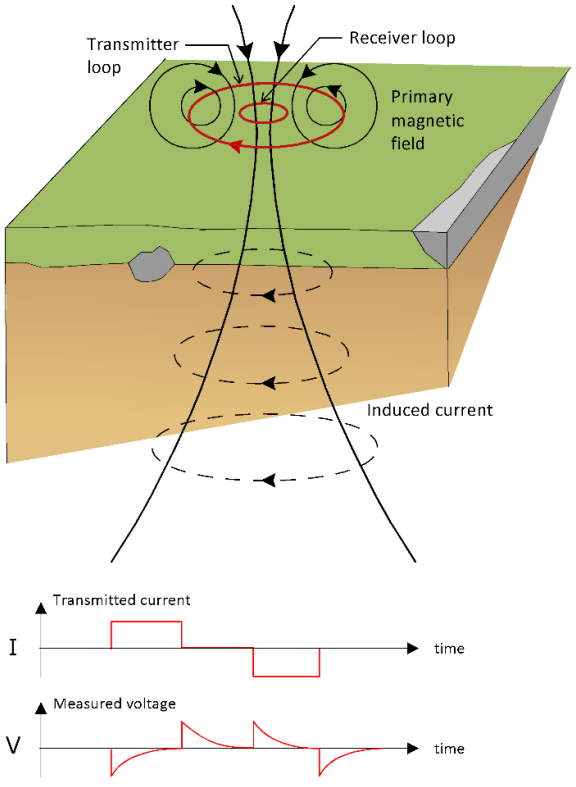

FIGURE 9: The central loop TEM sounding configuration (Flóvenz et al., 2012; based on Hersir and Björnsson, 1991)

TEM is an active EM geophysical exploration method used in exploration of geothermal resources. TEM surveys are also very common in mineral exploration, ground water surveys and in environmental mapping. It is used throughout the world in both onshore and offshore applications. Generally, TEM methods are able to determine subsurface electrical properties, but they are also sensitive to subsurface magnetic properties in applications like unexploded ordnance (explosive weapons like bombs, shells, land mines, etc.) detection and characterization.

In the volcanic zones where the surface is mostly covered by lava, current injection into the ground is a major problem when using Schlumberger soundings. In the TEM method no current is injected into the ground, but into a source loop on the surface. The EM method is classified as frequency domain or time domain, depending on the measuring techniques employed. Time domain electromagnetic methods (TEM) are further classified as grounded or loop source methods depending on how the source field is introduced into the ground (Kebede, 2001).

The setup of the central-loop TEM method is shown in Figure 9. A loop of wire is placed on the ground

and a constant magnetic field of known strength is built up by transmitting a constant current into the loop. The current is then turned off abruptly. The decaying magnetic field induces an electrical current in the ground. This current induces a secondary magnetic field which decays with time (Figure 9). The decay rate of the secondary magnetic field is monitored by measuring the voltage induced in a receiver coil (or small loop) at the centre of the transmitter loop. The current distribution and the decay rate of the secondary magnetic field depends on the resistivity structure of the earth. The decay rate, recorded as a function of time after the current in the transmitter loop is turned off, can therefore be interpreted in terms of the subsurface resistivity structure.

The depth of penetration in central loop TEM-soundings is dependent on how long the induction in the receiver coil can be traced in time before it is drowned in noise. At late times, the induced voltage in the receiving coil on homogeneous half space of conductivity σ is approximately given by (Árnason, 1989).

$$V(t,r) = I_o \frac{C(\mu\sigma r^2)^{3/2}}{10\pi^{1/2}t^{5/2}} \tag{31}$$

where C $= A_r n_r A_s n_s \frac{\mu_o}{2\pi r^3}$;
A_r = Cross-sectional area of the receiver coil (m^2);
n_r = Number of turns in receiver loop;
A_s = Area of transmitting loop (m^2);
n_s = Number of turns in transmitter loop;
t_r = Time elapsed after the current in the transmitter is turned off (s);
μ = Magnetic permeability (H/m);
V(t,r) = Transient voltage (V);
r = Radius of the transmitter loop (m);
I_o = Current in the transmitter loop (A).

Substitution of $\sigma = {}^1/_\rho$ gives the late time apparent resistivity as a function of time after the current is turned off at the transmitter:

$$\rho_a = \frac{\mu}{4\pi}\left[\frac{2\mu I_o A_r n_r A_s n_s}{5t^{5/2}V(t,r)}\right]^{2/3} \tag{32}$$

where ρ_a = Late time apparent resistivity (Ωm).

The apparent resistivity curve is inverted in terms of a horizontally layered Earth´s model with homogenous and isotropic layers (1D model). The model helps to interpret the data because both the resistivity and thickness of the layers can vary in the inversion. The most common 1D interpretation is Occam (minimum structure) inversion of each sounding. In Occam inversion, the smooth variations are approximated by numerous thin layers of fixed thicknesses and the data is inverted for the values of the resistivity (Flóvenz et al., 2012).

Central loop TEM-sounding method has several advantages over conventional DC-sounding methods:

1. The transmitter couples inductively to the earth and no current has to be injected into the ground. This is of great importance in areas where the surface is highly resistive (Árnason, 1989).
2. The fact that the monitored signal is a decaying magnetic field rather than an electric field at the surface makes the results much less dependent on local resistivity conditions at the receiver site (Sternberg et al., 1988). Distortion due to local resistivity inhomogeneities at the receiver site can be a severe problem in DC-soundings as well as in MT soundings (Árnason, 1984).
3. It is less sensitive to lateral resistivity variations than the DC methods. The reason is that in the TEM method, the current induced in the ground can be visualized as a diffuse current ring which at early times, after the current in the transmitter loop is turned off, simulates the current in the transmitter loop (Hoversten and Morrison, 1982). With time this current ring diffuses downwards and outwards resulting in an increased depth of penetration with time. The monitored signal at

the surface is primarily dependent on the resistivity structure inside the diffuse current ring. The central loop TEM-soundings are thus much more downwards focused than DC-soundings, where increased depth of penetration is obtained by increasing the distance between the current injection electrodes and the receiver dipole, making the monitored electric field dependent on a much large volume of rocks.

4. TEM field survey needs less man power and is faster. It gives a more detailed model of the geothermal system. However, TEM soundings are more sensitive to man-made noise than DC methods (like Schlumberger).

6. DATA PROCESSING AND INVERSION OF TEM AND MT

6.1 Inversion

Inversion is used to estimate the model parameters using the measured data. To solve the inversion problem one has to know how to calculate the forward problem. At first a starting model is chosen and the forward algorithm calculates the response. If the calculated response does not fit with the measured data, an inversion algorithm improves the model in order to improve the fit with the measured data.

Forward modelling is a process of predicting data based on some physical or mathematical model with a given set of model parameters. Forward modelling is an important part of the inversion method, and it has to be accurate, fast and reliable. The inversion process uses forward modelling to compute the sensitivity matrix and the response for calculating the misfit. Inversion is used to estimate the quality of the predicted model parameters and to determine which model parameters are the most important in constraining the estimated model parameters. The most commonly used inversion method for geoelectric soundings is the least-square inversion method. After each iteration step we get a sensitivity matrix which gets us nearer the exact model, characterized by the chi-square (χ).

6.2 TEM data processing and inversion

The TEM data in Alallobeda were acquired using two instruments from different manufacturing companies, Zonge GDP-32 and Phoenix V8 TEM systems. For most of the TEM measurement a 200 m × 200 m square source loop was used and in some difficult terrain a 100 m × 100 m square. With Zonge TEM the measurements were made at the frequencies 32, 16, 8 and 4 Hz, and with Phoenix equipment at 25, 5 and 1 Hz.

To read and process the TEM data, a software called TemX was used (Árnason, 2006a). The TemX programme reads TEM raw data files acquired by the PROTEM digital receiver of Zonge. The programme calculates average and standard deviations of repeated transient voltage measurements and calculates late time apparent resistivity as a function of time. The program has a graphical interface, offering the possibility of editing or omitting outliers of noisy raw data. In this project the raw data from Zonge were processed by using the software temxUSF.

The TEMTD programme for the inversion process assumes that the source loop is a square loop and that the receiver coil/loop is at the centre of the source loop (Árnason, 2006b). The current wave form is assumed to be a half-duty bipolar semi-square wave with exponential current turn-on and linear current turn-off. The program is written in ANSI-C and runs under UNIX/LINUX operating systems. It uses the gnuplot graphics program for graphical display during the inversion process.

The inversion algorithm used in the programme is the Levenberg-Marquardt non-linear least square inversion as described by Árnason (1989). The misfit function is the root-mean-square difference between measured and calculated values (chi-square), weighted by the standard deviation of the

measured values. The user can choose whether the program fits the measured voltage values or the late time apparent resistivity values.

The programme offers the possibility to keep models smooth, both with respect to resistivity variation between layers (actually logarithm of conductivities) and layers thicknesses (actually logarithm of ratio of depth to top and bottom of layers). The program can be used to perform minimum structure (Occam) inversion. The input file for TEMTD is the *.inv file produced by the TemX program.

All the TEM sounding were 1D inverted using TEMTD and Occam inversion. An example is given in Figure 10. The TEM and magnetotellurics data from the Alallobeda geothermal prospect and the results of the processing are published in a separate appendices report (Hailegiorgis, G., 2015). All the TEM soundings curves and the associated 1D models are presented in Appendix I. An initial model is given and the best fitting model based on a layered model followed by running TEMTD. The output from the layered model is used as an initial model in the Occam inversion. To get a smooth model and good fit, several parameters can be changed.

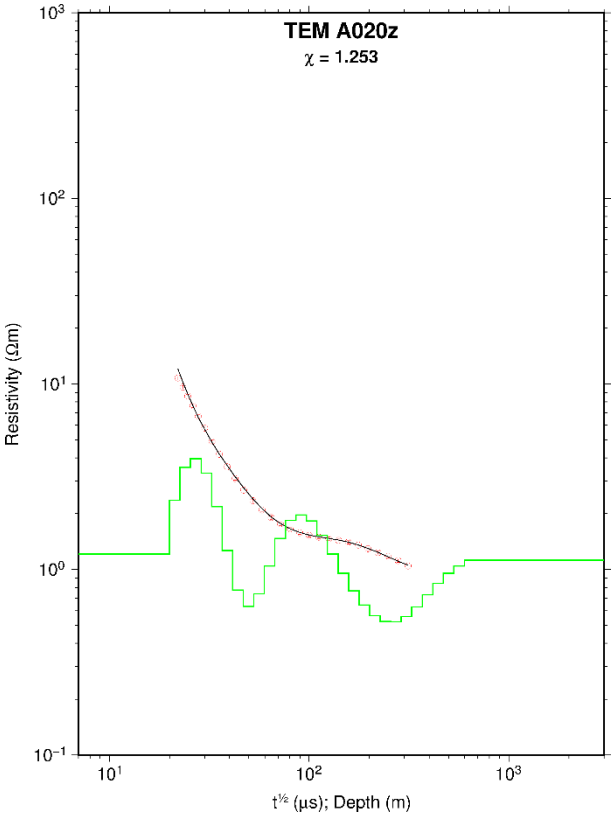

FIGURE 10: A typical TEM sounding from Alallobeda prospect and its 1D Occam inversion; red circles: measured late-time apparent resistivity; black line: apparent resistivity calculated from the model shown in green. The number on the top of the figure (A020z) corresponds to the name of the station

6.3 MT data processing and inversion

MT data were collected using a 5-channel MTU unit data acquisition system from Phoenix Geophysics Company Canada. In this project work 54 soundings were processed from the time series data and used for interpretation.

The time series data were downloaded from the compact flash card of MTU-5A units and viewed using the Synchro Time Series View program. This program allows imaging and printing of graphical representations of the raw time-series data, it computes power spectra densities derived from the time-series data and coherence between pairs of orthogonal channels. The SSMT2000 program, which is provided by Phoenix Geophysics in Canada (Phoenix Geophysics, 2005), takes as input raw time series files, calibration files and site parameter files. In an intermediate step, it produces Fourier coefficients which are then reprocessed with data from reference sites, using robust routines. The output are MT plot files (MTH and MTL) containing multiple cross powers for each of the frequencies. The program MTeditor takes the output from the SSMT2000 program and displays resistivity and phase curves as well as the individual cross powers that are used to calculate each point on the curve. Cross powers that were affected by noise can be automatically or manually excluded from the calculation. When the final cross power and auto-powers as well as all relevant MT parameters have been calculated, the files are converted and stored to industry-standard EDI (Electronic Data Interchange) files suitable for use with Geophysical interpretation software like TEMTD where a joint inversion with TEM data from the same site is carried out. In this project work, EDI files were processed and inverted with the program TEMTD (similar as inversion with the TEM data, as mentioned in Section 6.1). In the project, the rotationally invariant apparent resistivity and phase calculated from the determinant of the impedance were jointly

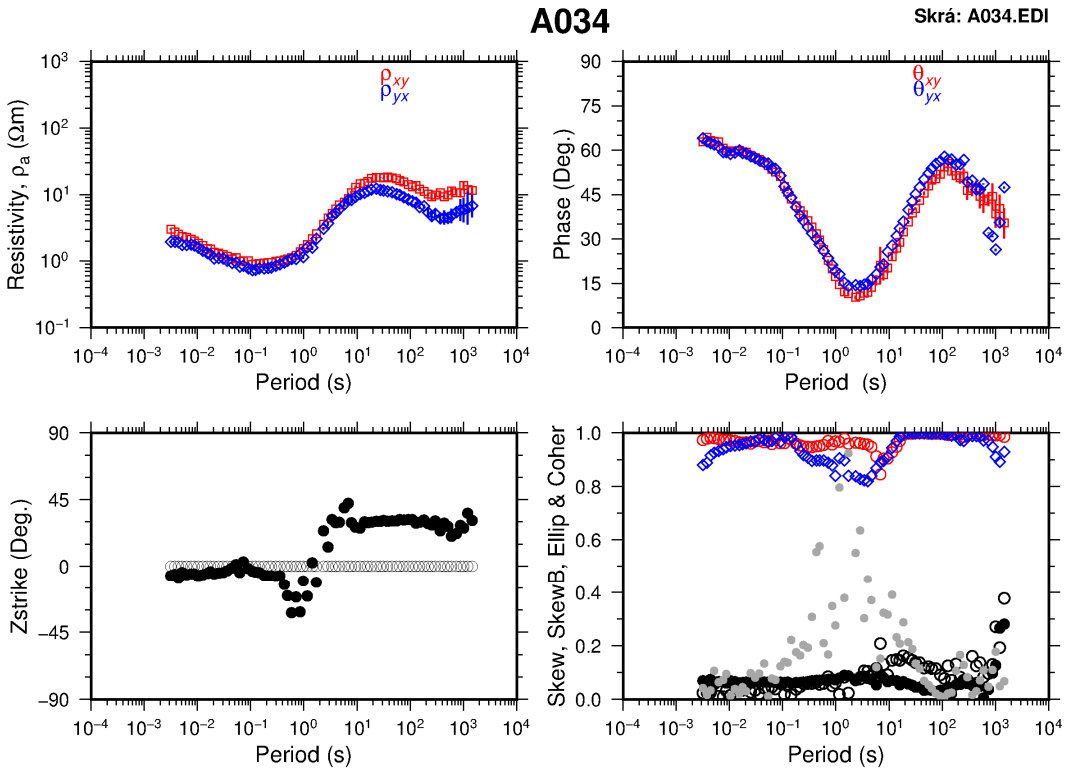

FIGURE 11: An example of processed MT data from the Alallobeda prospect area. The plots show the apparent resistivity and phase derived from the xy (red) and yx (blue) components of the impedance tensor, the Z-strike or Swift angle (black dots), multiple coherency of xy (red) and yx (blue), skew (black dots) and ellipticity (gray dots)

inverted with the TEM data using Occam inversion. The TEMTD programme determines the best static shift parameters for MT data.

The EDI files were converted from DOS to Unix format. The script spect2edi is used to transform the data into EDI form and then the edi2ps script is used to produce PostScript plots of all relevant available parameters of the EDI file. Ghost view (gv) is used to view the apparent resistivity, phase, Zstrike, Tstrike etc. An example of the processed MT data is given in Figure 11. The processed data of all the MT soundings are shown in Appendix II (Hailegiorgis, G., 2015).

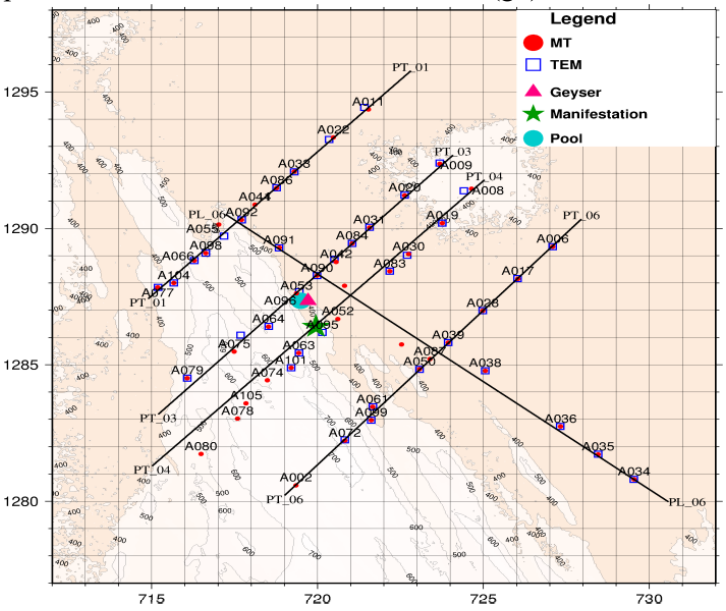

FIGURE 12: Location map of TEM and MT soundings

At some of MT stations, the TEM data from the same site which was acquired using the Phoenix instrument could not be used. Those were inverted by fixing the static shift value by running the script for MT only. For these stations the static shift was given by the ELC-Consult.

Figure 12 shows the location of TEM and MT soundings, the black lines show the profiles that were used for cross-sections.

6.4 Static shift correction

Static shift occurs because of near surface resistivity inhomogeneities and topographic effects. It is due to electric field distortion because of the dependency of electric field on the resistivity of the material where the voltage difference is measured. Static shift due to the topographic effect results in current distortion. The induced current density which is mostly flowing laterally is spread out in local topographic highs but concentrated in topographic lows. So the apparent resistivity value on topographic highs is low and vise versa. Furthermore, MT suffers from static shift problems. Unlike the electric field, the magnetic field is relatively unaffected by local or near surface inhomogeneities. Therefore, static shift due to near- or sub-surface inhomogeneities and topographic effects can lead to severe problems in the interpretation of MT data. The apparent resistivity curve is shifted upward due to low-resistivity slab and shifted downward due to high resistivity when it is plotted on log scale. This shifting gives a wrong resistivity model. Figure 13 shows the histogram of the static shift parameters and reveals how the apparent resistivity curve of the MT data is shifted upwards or downwards. The multiplier for all 54 MT soundings is given, with all except one found to be in the range of 0.2-1.6.

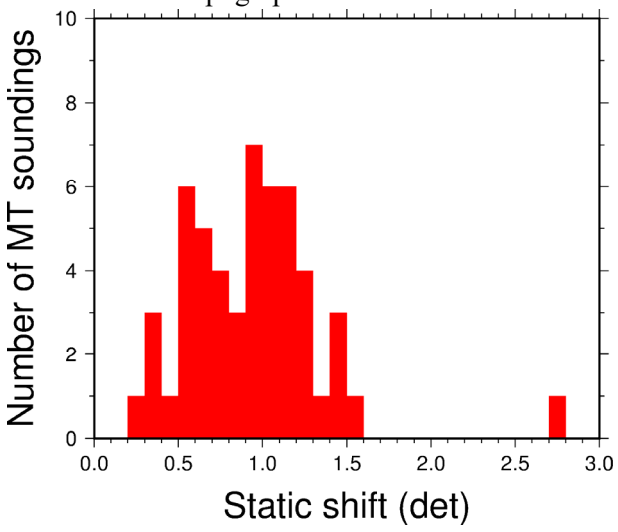

FIGURE 13: A histogram of static shift parameters for Alallobeda prospect

Static shift is frequency independent and is not visible in the phase. Static shift causes a frequency independent offset in apparent resistivity curves so that they are plotted parallel to their true level but scaled by a factor. These static shift factors cannot be determined directly from MT data recorded at one single site. A parallel shift between two polarizations of apparent resistivity curves is a reliable indicator that static shift is present in the data. However, lack of shift between two apparent resistivity curves does not necessarily guarantee an absence of static shift, since both curves might be shifted by the same value. The correct level of the apparent resistivity curves may lie above, below or between the measured levels. If MT data are interpreted applying 1D modelling without correcting for static shift, the depth to the conductive body will be shifted by the square root of the factor by which the apparent resistivities are shifted ($\sqrt{s}$) and the modelled resistivity will be shifted by s. 2D and 3D models may contain extraneous structure if static shift is ignored. Figure 14 shows the spatial distribution of static shift multipliers in the Alallobeda prospect. In most of the area, the MT apparent resistivity is shifted downwards, but upwards at its border.

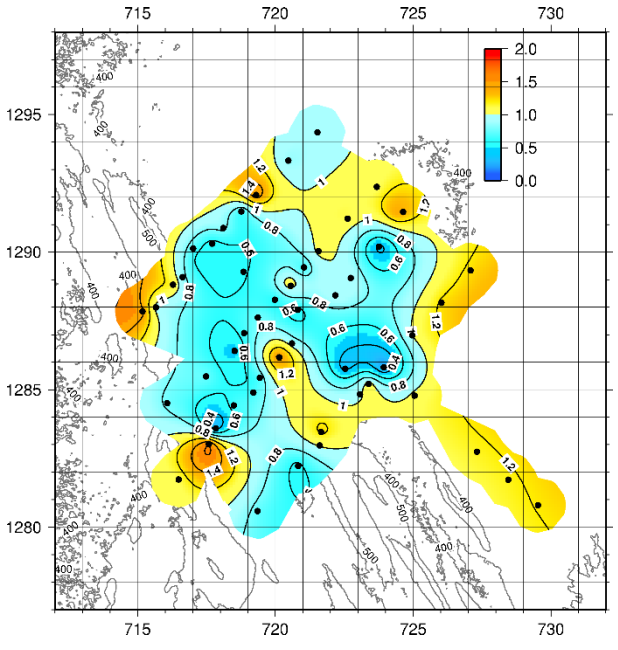

FIGURE 14: Spatial distribution of static shift parameters in the Alallobeda prospect

Static shift can be corrected by short period corrections relying on active near-surface measurements like TEM. TEM does not have the static shift problems that affect MT soundings. Because TEM does not use electrodes and because it does not require electrical contact with the earth for data acquisitions and magnetic field

is not much affected by static shift problems except at very high frequencies (Groom and Bailey, 1989) while the electric field can be severely affected. The static shift problem occurs because the electromagnetic field is distorted by shallow resistivity anomalies near the MT station or close to the electrodes or by the topographic effect. TEM can be used in conjunction with MT data from the same site to correct static shift in MT data. Apparent resistivity curves derived from MT data can be scaled so that they tie-in with TEM curves or can be jointly inverted with TEM data (Sternberg et al., 1988). These techniques are only effective for correcting static shift arising from near-surface inheterogeneities. If the impedance phases are split at high frequencies which are expected to have similar penetration depth for TEM data, then there is no justification for supposing that the apparent resistivity curves for the two polarizations should lie at the same level.

6.5 Joint 1D Occam inversion of TEM and MT soundings

The inversion programme TEMTD (Árnason, 2006b) was used to perform joint 1D Occam inversion of TEM and MT data using the apparent resistivity and phase derived from the rotationally invariant determinant of the impedance tensor. The programme determines the best static shift parameter for the MT data.

Figure 15 shows an example of a joint 1D Occam inversion of TEM and MT data. A complete set of all the 1D joint inversion results is shown in Appendix III (Hailegiorgis, G., 2015). On the right side is shown the response of the resistivity model with depth. The red curve shows the measured value of the TEM sounding, the dark blue line shows measured values of the MT sounding, while in light blue deleted point are marked. Also shown are the values of chi and static shift.

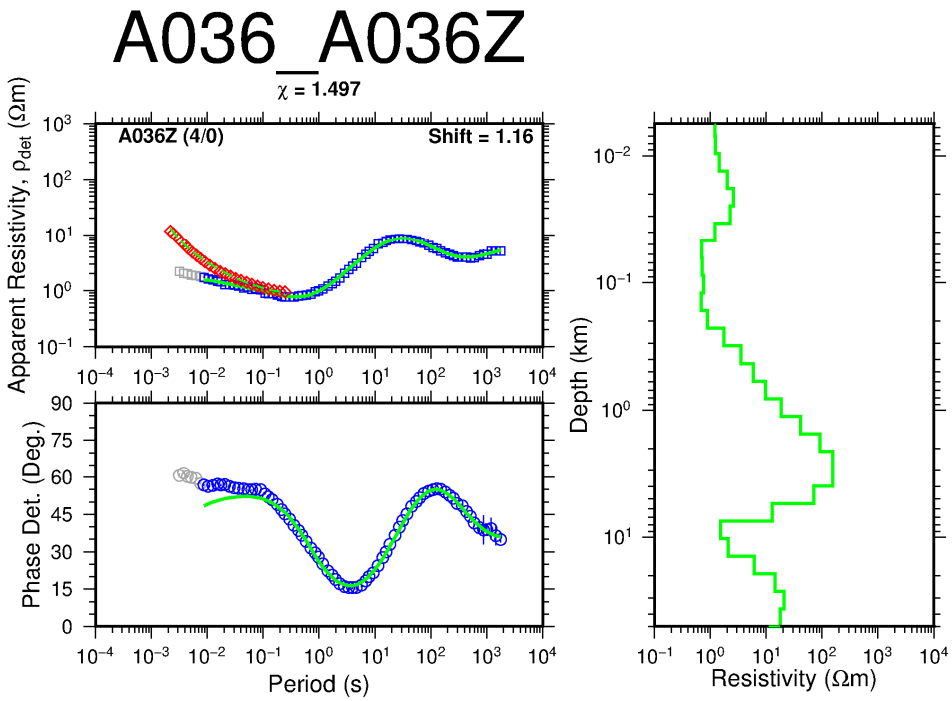

FIGURE 15: Joint 1D inversion of MT and TEM soundings with TEM apparent resistivities transformed to a pseudo-MT curve; blue circles: apparent phase derived from the determinant of MT impedance tensor; light blue symbols to the left of the green curve: data not used in the inversion; vertical blue lines: error bars. Green lines show the response of the model calculation. On the right are shown results of the 1D resistivity inversion model, while on the left its synthetic MT apparent resistivity and phase response. Number on the top of the Figure: A036 is name of the MT station and A036Z is the name of the TEM station. The numbers in parenthesis (4/0) indicates that the two stations were 4 m apart and their elevation difference was 0 m. Static shift correction was 1.16

7. RESULTS AND DISCUSSION OF MT AND TEM SURVEY

7.1 Resistivity cross-sections

The programme TEMCROSS, which was developed at ÍSOR (Eysteinsson, 1998), was used to create the resistivity cross-sections based on the joint 1D Occam inversion models of the TEM and MT data shown in Appendix III (Hailegiorgis, G., 2015). The cross-sections are plotted to a depth of 10,000 m and some also only down to 2,000 m. Their locations are given in Figure 12. Four cross-sections run perpendicular to the tectonic structure (PT_01, 03, 04, and 06) and one parallel to it (PL_06). Additional cross-sections are given in Appendix IV (Hailegiorgis, G., 2015). Generally, it can be said that the resistivity structure seen in the cross-sections is quite similar, with three main resistivity layers. At the top is a fairly thin (few hundred metres) low-resistivity layer (< 10 Ωm) which can be correlated to shallow sedimentary formations. Below that, there is usually a thick high-resistivity formation (> 100 Ωm), which correlates with the highly resistive Afar Stratoid series basalt. At the bottom the resistivity is again low, usually < 10 Ωm, which may indicate a deeper lying conductor that could be related to the heat source. In more detail, the following can be said:

Resistivity cross-section PL_06 is shown in Figure 16 down to a depth of 10,000 m but in Figure 17 only down to 2,000 m. It runs NW-SE parallel with the main geological structure and crosses the main

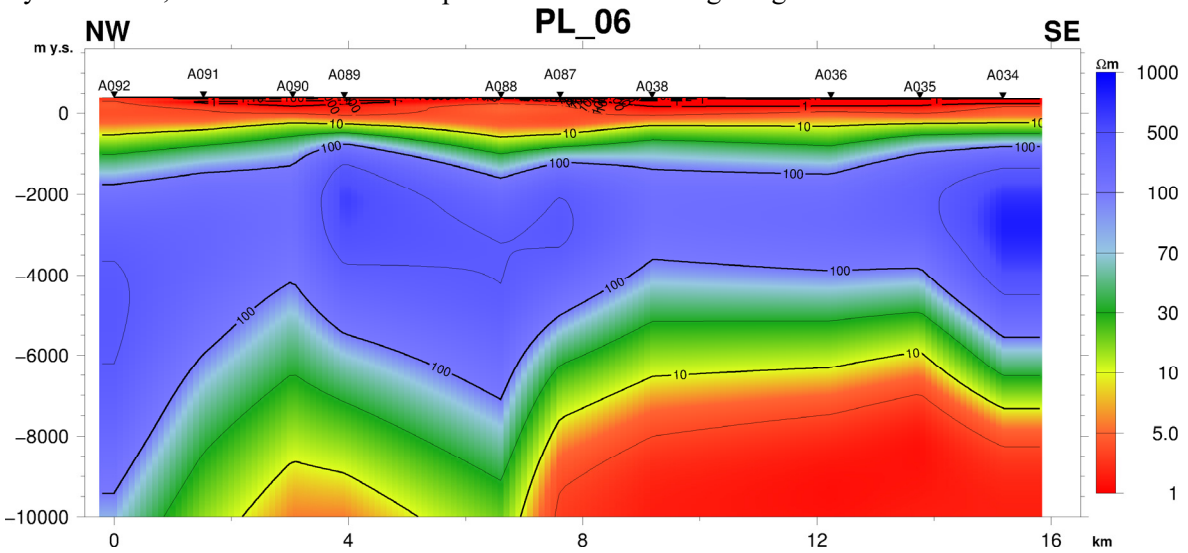

FIGURE 16: Resistivity cross-section PL_06 down to 10,000 m b.s.l.; for location see Figure 12

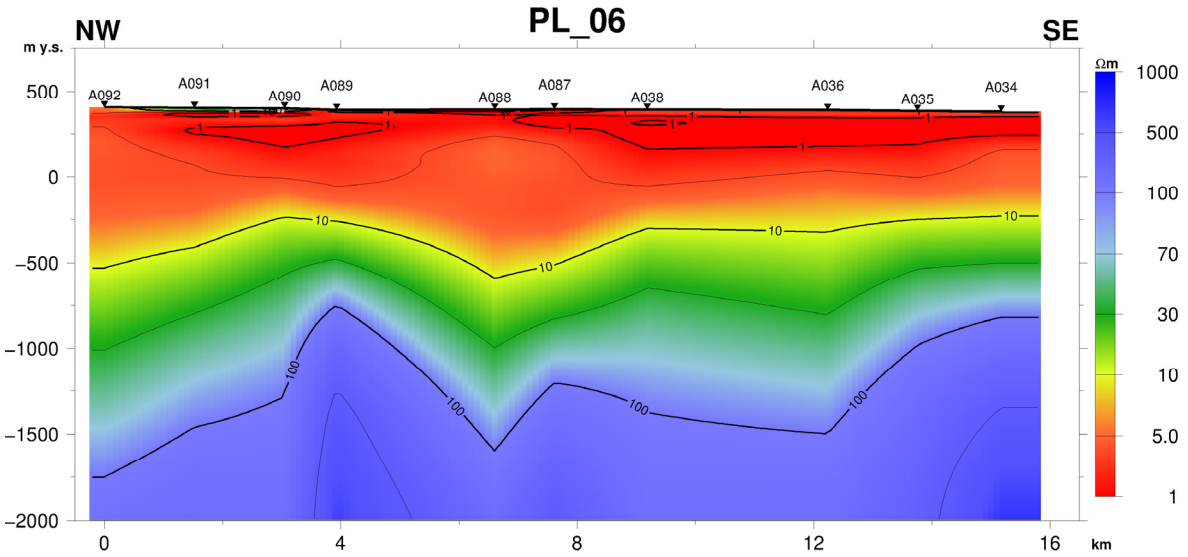

FIGURE 17: Resistivity cross-section PL_06 down to 2,000 m b.s.l.

area of surface manifestations. Down to a depth of 300 m b.s.l., the cross-section is characterized by a thin layer of very low resistivity (< 10 Ωm) correlated to the shallow sedimentary formation. Below that the resistivity increases considerably, with this layer showing resistivity values > 100 Ωm, reaching down to a depth of 4000-6000 m b.s.l., corresponding with the highly resistive Afar Stratoid series basalt, but high-temperature alteration minerals chlorite and epidote may also contribute here. At greater depth the resistivity decreases to a value of < 10 Ωm which may indicate the deeper lying conductor.

Resistivity cross-section PT_01 is shown in Figure 18, down to a depth of 10,000 m. It runs from SW-NE, perpendicular to the main geological structures. The cross-section is characterized by the low-resistivity anomaly, < 10 Ωm, down to a depth of approx. 300 m b.s.l., associated with the shallow sedimentary formation. Around station A086 an upflow zone is seen. Below the low resistivity the high-resistivity layer is found with resistivity values around 100 Ωm down to depths varying between 1000 and 5000 m from the surface. This high resistivity is believed to be mainly related to the highly resistive Afar Stratoid basalt series. At greater depth the resistivity decreases to a value of < 10 Ωm, indicating the deeper lying conductor that may be related to the heat source. This low-resistivity body is seen both in the southwest and northeast part of the cross-section, while between stations A066 and A033 the resistivity is high, around 100 Ωm.

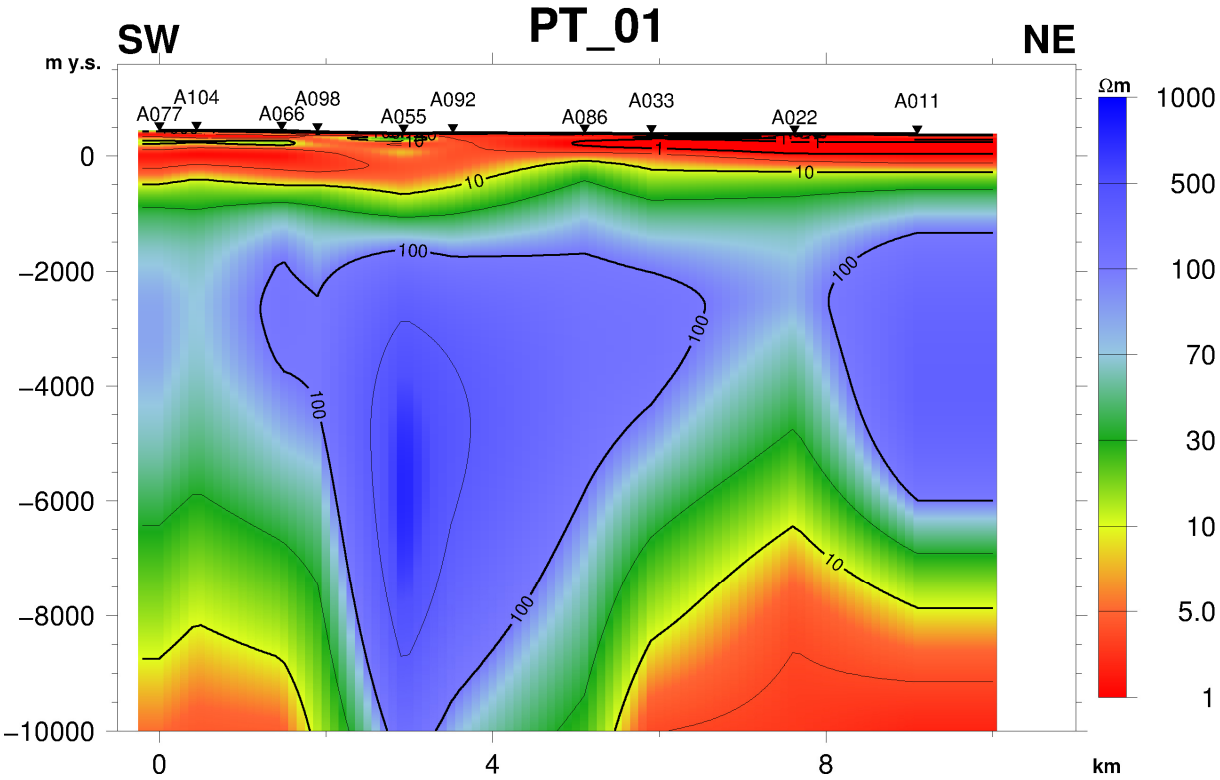

FIGURE 18: Resistivity cross-section PT_01, down to 10,000 m b.s.l.; for location see Figure 12

Resistivity cross-section PT_03 is shown in Figure 19 and runs NE-SW perpendicular to the geological structure. The uppermost part of the cross-section is characterized by a thin layer of very low resistivity, < 10 Ωm, down to a depth of 200 m b.s.l. Below stations A053 and A079 the resistivity is slightly higher, with a value of 10 Ωm, indicating unaltered lava. This low-resistivity layer is associated with the sedimentary formation and possibly also influenced by low-temperature alteration minerals like smectite and zeolites. Below the low-resistivity top layer there is a high-resistivity body with resistivity values about 100 Ωm reaching from approx. 700 m down to the depth 5000 m b.s.l., correlating to the Afar Stratoid basalt series possibly with some influence from high-temperature alteration minerals like chlorite and epidote. This high-resistivity layer is mainly seen in the southwest part of the profile, while in the northeast part a low-resistivity anomaly is dominant. Like in the other cross-sections, at greater

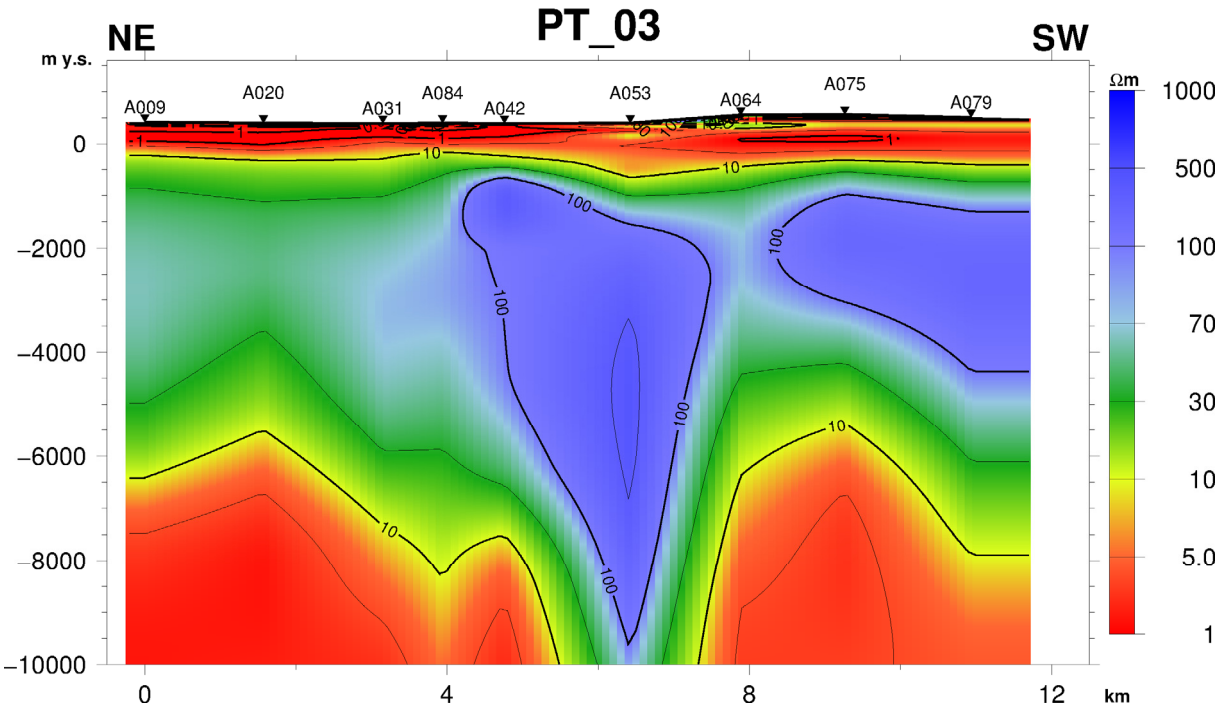

FIGURE 19: Resistivity cross-section PT_03, down to 10,000 m b.s.l.

depth the resistivity decreases to a value of < 10 Ωm. This low-resistivity layer is seen both in the northeast and southwest part of the profile, while between stations A084 and A053 the deep resistivity is high with a value of 100 Ωm seen to the bottom of the cross-section.

Resistivity cross-section PT_04 is shown in Figure 20 down to 10,000 m b.s.l. and in Figure 21 down to 2000 m b.s.l. It runs NE-SW, perpendicular to the geological structures. The uppermost part of the cross-section is characterized by a thin layer of very low resistivity (< 10 Ωm) down to a depth of 400 m b.s.l., associated with the sedimentary formations. Below, the high-resistivity layer with resistivity values between 100 and 1000 Ωm is seen, reaching down to depths of 1000-5000 m b.s.l. The resistivity

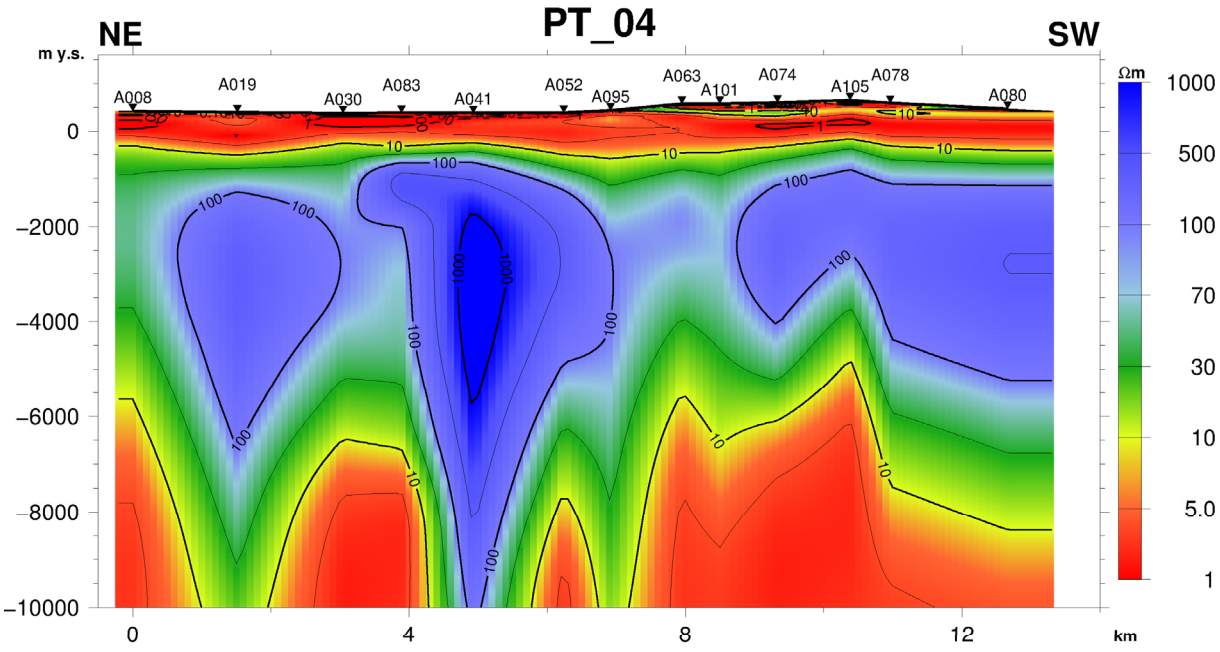

FIGURE 20: Resistivity cross-section PT_04, down to 10,000 m b.s.l.

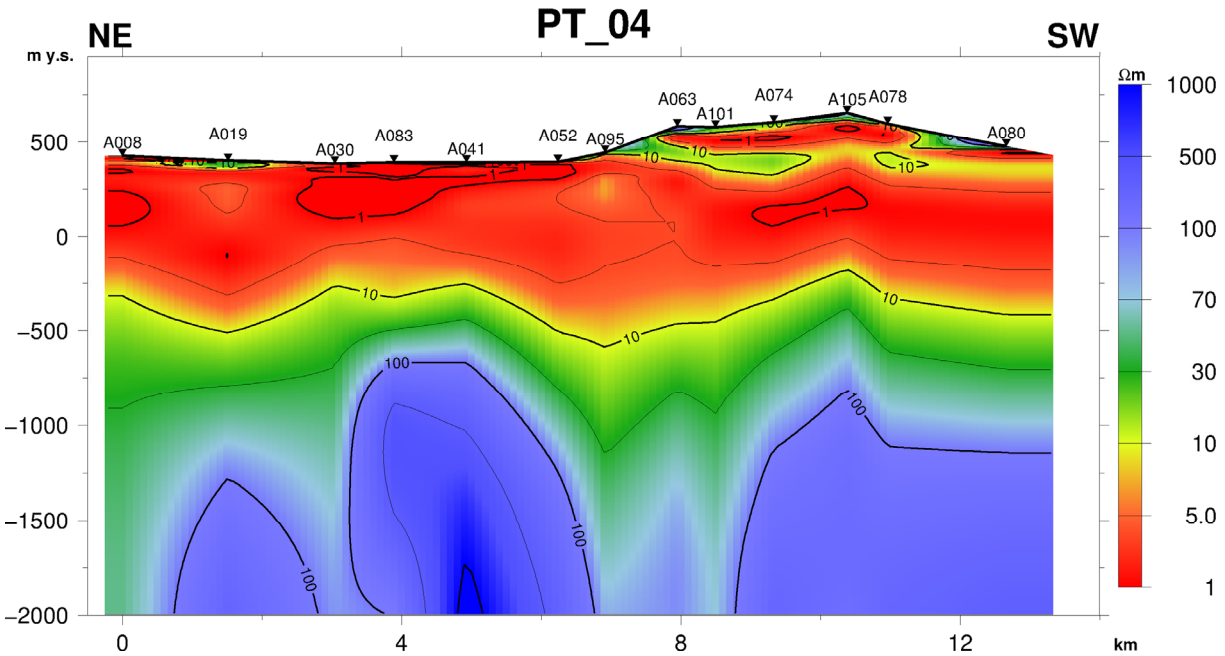

FIGURE 21: Resistivity cross-section PT_04, down to 2,000 m b.s.l.

structure around stations A041, A083 and A105 may indicate an upflow zone in that area. As before, the high resistivity is believed to correlate to the Afar Stratoid basalt series, possibly also influenced by high-temperature alteration minerals like chlorite and epidote. At greater depth the resistivity decreases again, reaching quite low values, < 10 Ωm which may indicate the deeper lying conductor, related to the heat source. This low-resistivity zone is found below all stations except station A041 which shows very high resistivity down to great depth.

Resistivity cross-section PT_06 is shown in Figure 22. It runs NE-SW, perpendicular to the main geological structures. The shallow part of the cross-section is characterized by the thin low-resistivity layer, with a resistivity of 1 Ωm, reaching down to a depth of 200 m b.s.l., associated with the shallow sedimentary formations and low-alteration minerals like smectite and zeolite. Below the low-resistivity

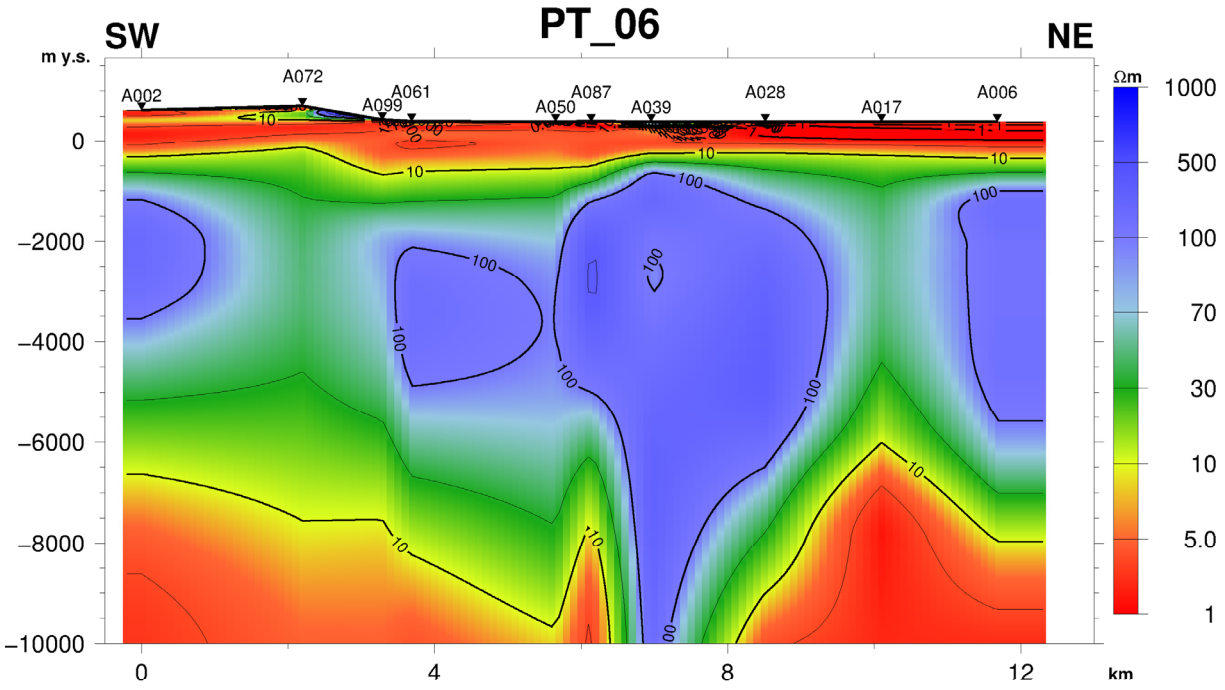

FIGURE 22: Resistivity cross-section PT_06, down to 10,000 m b.s.l.

top, there is high-resistivity layer, the resistivity increases to a value of around 100 Ωm, reaching down to a depth of at least 4,000 m b.s.l., reflecting the Afar Stratoid basalt series. At greater depth the resistivity decreases again, to values of < 10 Ωm, as in other cross-sections, probably indicating a deeper lying conductor possibly related to heat source. This low-resistivity zone is seen both in the southwest and northeast parts of the cross-section. Below station A039 the high resistivity reaches greater depths, separating the deep low-resistivity conductors.

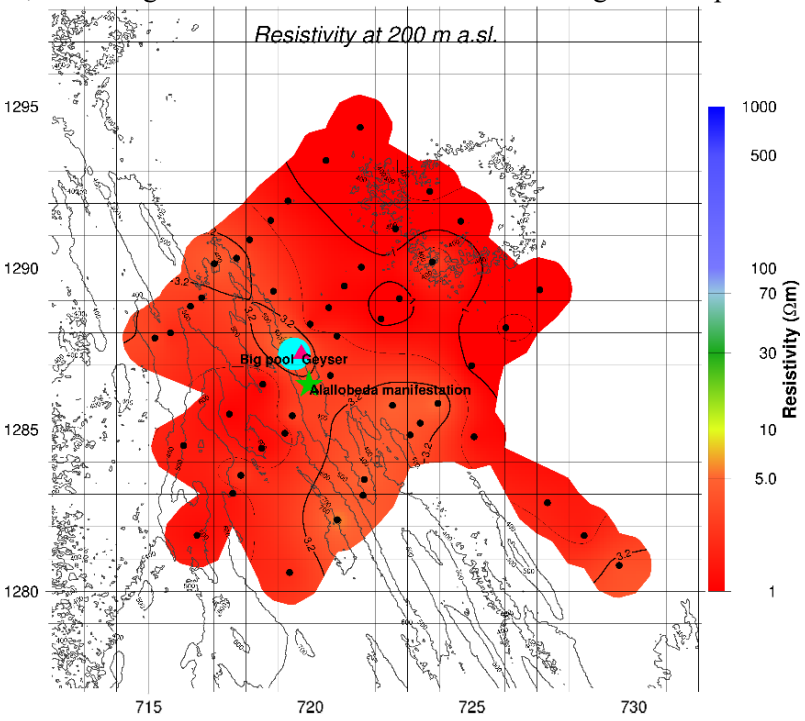

FIGURE 23: Iso-resistivity map of Alallobeda prospect at 200 m a.s.l.; the black dots indicate locations of MT soundings, light blue filled circle the big geothermal pool, with the pink triangle denoting the Geysers; and the green star indicates surface manifestations

7.2 Iso-depth resistivity maps

The programme TEMRESD developed at ÍSOR (Eysteinsson, 1998) was used to plot the iso-resistivity maps based on the joint 1D Occam inversion models of the TEM and MT data presented in Appendix III (Hailegiorgis, G., 2015). The programme runs in Linux environment. The elevation of the Alallobeda geothermal field varies from 200 to 800 m a.s.l. The iso-resistivity maps are presented from 200 m a.s.l. to 8000 m b.s.l. Here 4 maps are shown with additional maps given in Appendix IV (Hailegiorgis, G., 2015).

Resistivity map at 200 m a.s.l. is shown in Figure 23. The resistivity is very low (< 10 Ωm) for the whole area and reflects the sedimentary formation found at shallow levels in the area and low-temperature alteration minerals like smectite and zeolites.

Resistivity map at 300 m b.s.l. is presented in Figure 24. The higher resistivities associated with the Afar Stratoid basalt series are influencing the map, with resistivities around 30 Ωm seen at this depth level. A structure of relatively low

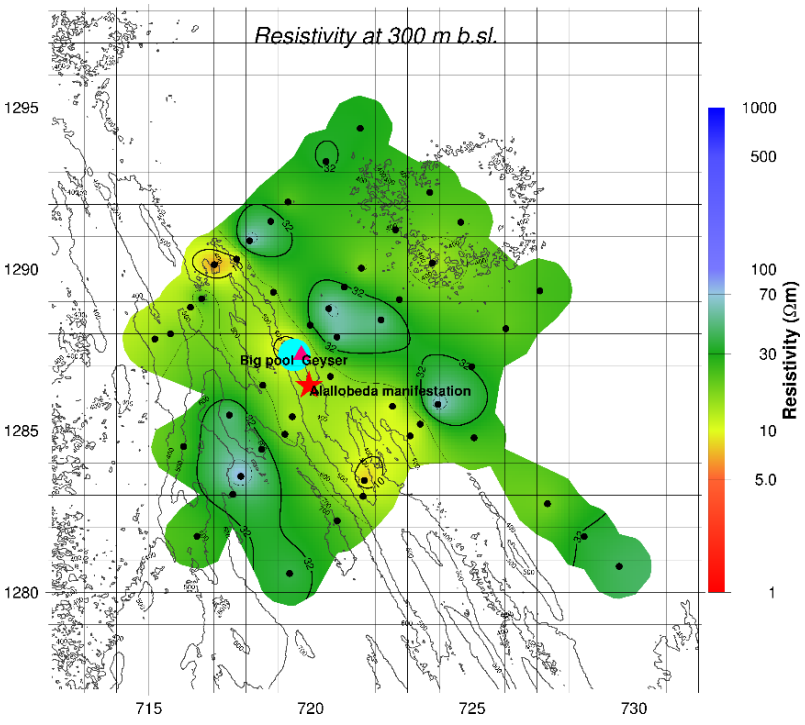

FIGURE 24: Iso-resistivity map in Alallobeda prospect at 300 m b.s.l.; for figure legend see Figure 23

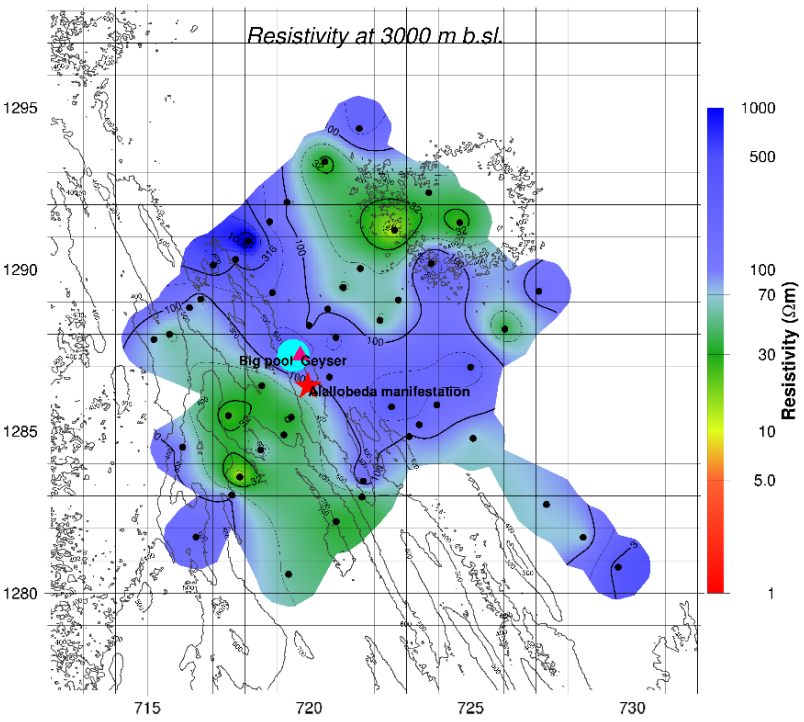

FIGURE 25: Iso-resistivity map in Alallobeda prospect at 3000 m b.s.l.; for figure legend see Figure 23

resistivity is seen along the geological NW-SE structure. This might be correlated with lateral flow of geothermal fluids, fractures or low-temperature alteration minerals like smectite and zeolite.

Resistivity map at 3000 m b.s.l. is shown in Figure 25. The resistive layer correlated with the Afar Stratoid basalt series is seen in the whole area with the resistivity showing values above 100 Ωm. However, along the geological structures trending NW-SE the resistivity is still fairly low at this depth, indicating lateral flow of geothermal fluids along the main fractures, and low-temperature alteration minerals like smectite and zeolites.

Resistivity map at 8000 m b.s.l. is shown in Figure 26. Here the deep lying low-resistivity zone is clearly manifested, with an average resistivity of approximately 3.2 Ωm. This explanation for this deep lying conductor is not certain, but it may be related to the heat source or deep saline sediments. Interestingly, a resistivity anomaly can be seen along the main geological structure trending NW-SE, including the big pool, with slightly resistivities (10 Ωm), supporting geothermal activity along this structure.

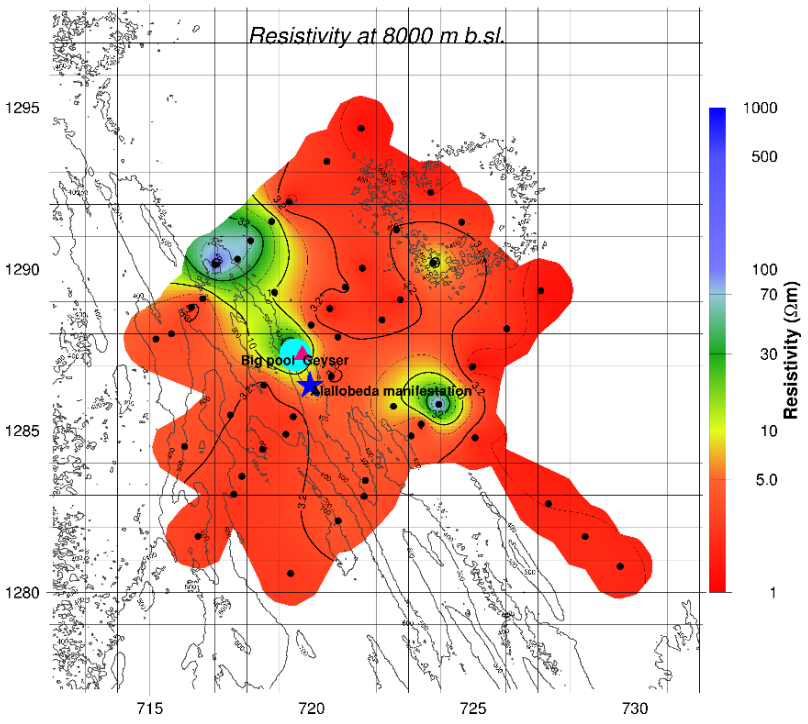

FIGURE 26: Iso-resistivity map in Alallobeda prospect at 8000 m b.s.l.; for figure legend see Figure 23

8. STRIKE ANALYSIS

Strike directions give information on the dimensionality of rock formation and the direction of the main resistivity contrast. Here it is not important if the resistivity distribution is 2D or 3D. This can be shown through the Zstrike which is based on H_x and H_y (see 5.1.2) and through induction arrows which are calculated from H_z. Two maps are presented here with additional maps given in Appendix V (Hailegiorgis, G., 2015). Figure 27 shows the Zstrike calculated from H_x and H_y at 0.01-0.1 s corresponding to a shallow depth of some hundreds of m. The strike is parallel to the main resistivity contrast and coincides with the geological strike direction in the Alallobeda geothermal field.

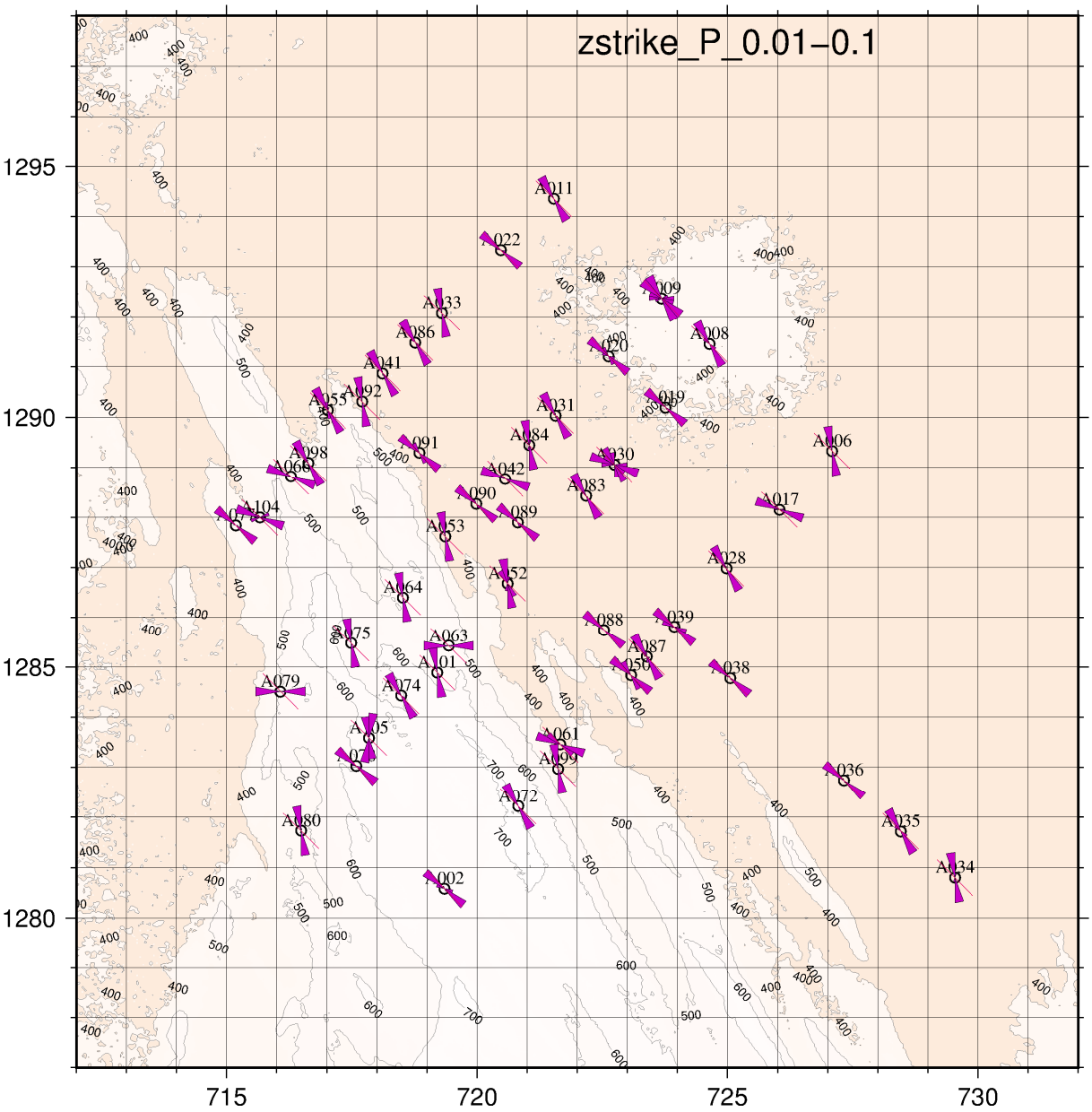

FIGURE 27: Rose diagram of the electrical strike direction based on the Zstrike calculated from H_x and H_y at 0.01-0.1 s corresponding to a shallow depth of some hundreds of metres. The strike is parallel to the main resistivity contrast and coincides with the geological strike direction

Figure 28 shows the anomaly directions for induction arrows. The The real induction arrows (blue colour) point away from a zone of low resistivity. The induction arrows are consistent with the resistivity contrast.

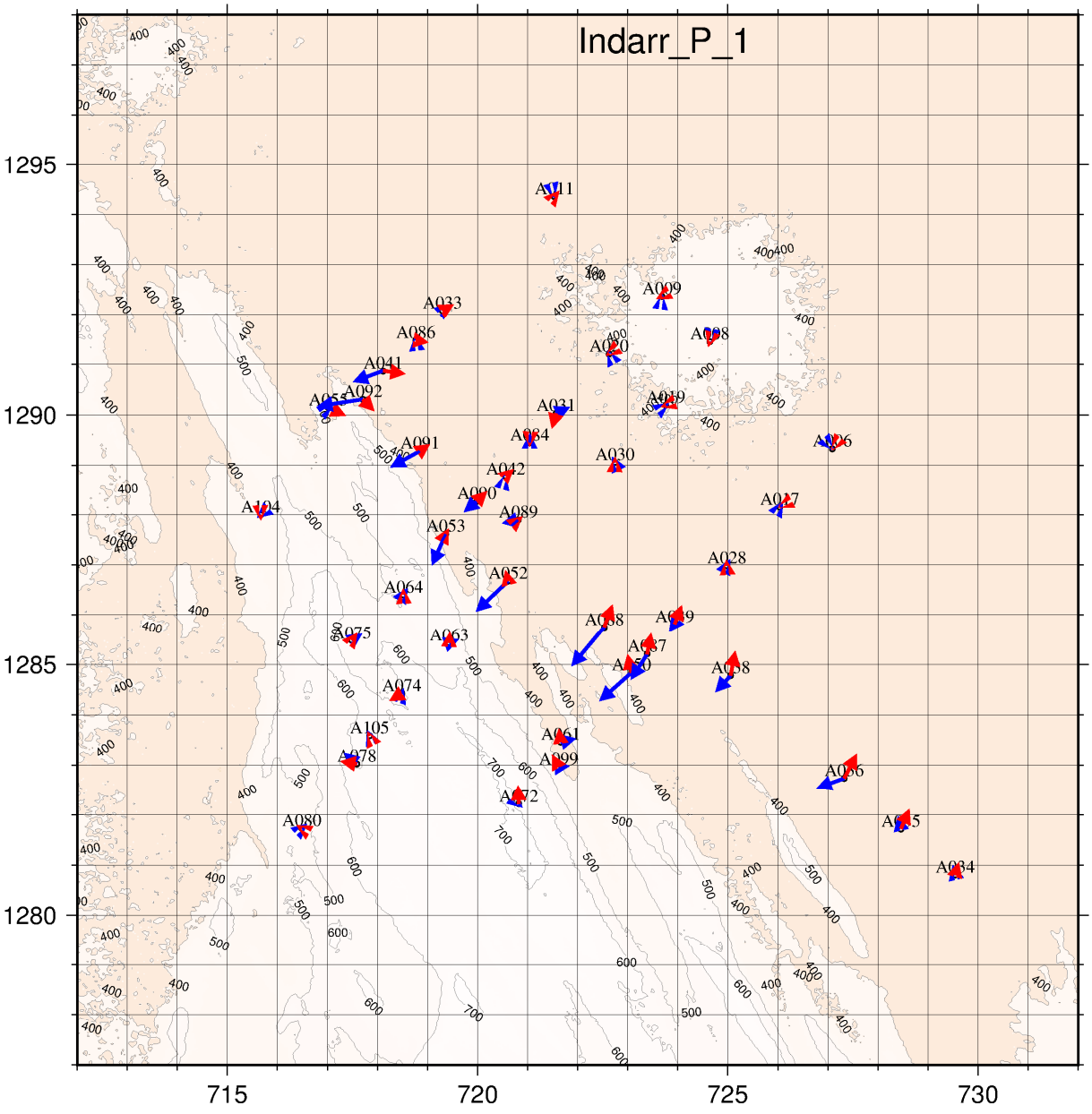

FIGURE 28: Induction arrows for the period 1 s, corresponding to a depth of a few km; blue arrows denote the real part and red arrows the imaginary part

9. CONCLUSIONS

Based on the result of the joint 1D inversion of 54 MT and TEM soundings, the resistivity structure reveals three main resistivity layers seen in the cross-sections presented:

- At shallow depths down to about 500 m b.s.l., a thin layer of low resistivity values exists (< 10 Ωm), which can be correlated to the shallow sedimentary formations in the area, with some influence noted from lateral flow of geothermal fluid in fractures.
- Below the sediments, the resistivity increases considerably and reaches values of about 100 Ωm at a depth of 1000 m b.s.l. This layer is associated with the low-permeability Afar Stratoid basalt series. As can be seen from the cross-sections, this layer stretches to deep levels often of the order of 5-6000 m b.s.l.
- Below the high-resistivity layer, another low-resistivity layer is seen (< 5 Ωm). This deep conductor is either related to the heat source or highly saline sediments at deep levels.
- Effect of geothermal upflow is seen in the iso-resistivity maps associated with known geothermal structures.
- Results of the strike analysis are in an agreement with the resistivity model.

ACKNOWLEDGEMENTS

It has been a great pleasure to participate in this training. I would like to express my special gratitude towards the UNU-GTP director Mr. Lúdvík S. Georgsson, and his deputy Mr. Ingimar G. Haraldsson for the opportunity to participate in the 6-month geothermal training programme in Iceland. I am highly indebted to the UNU-GTP staff members Ms. Málfrídur Ómarsdóttir, Ms. Thórhildur Ísberg and Mr. Markús A.G. Wilde for their guidance and help. I wish to give my thanks to all lecturers and staff members of ÍSOR for their comprehensive presentations and willingness to share their knowledge and experience.

I would like to express my sincere gratitude to my advisors Gylfi Páll Hersir and Knútur Árnason for continued support for my project, for their patient, motivation and immense knowledge. You have set an example of excellence as advisor, instructor and role model.

I would like to express my special gratitude and thanks to ICEDA people for giving me the opportunity to use the data for my project. I am highly indebted to ELC-Consult Company people for providing all the necessary information and data regarding my project and also for their support in completing my project.

I would like to offer my special thanks to Ato Hunda Meleka chief geologist of Geological Survey of Ethiopia, Ato Solomon Kebede Geothermal Resource Exploration and Evaluation Assessment directorate, granting me permission to attend this training and for their continued support, help and encouragement. I express my deep sense of gratitude to Mr. Yiheyis Kebede and all my colleagues in the geothermal department back home giving all necessary information for my project and people who have willingly helped me out with their abilities.

I would like to express my deepest appreciation to my devoted family and friends for their love, prayers, encouragement and motivation.

I would like to thank all 2015 UNU fellows for making my stay in Iceland more pleasurable. Special thanks to my geophysicist UNU Fellows Amali, Ali and Lee and also Fredrick for sharing their experiences and knowledge. Special thanks to Nyaso and Hamda for the good time we spent together.

I would like to thank the Almighty God who helped me all the way. May he bless all of you.

REFERENCES

Acocella, V., Abebe, B., Korme, T., and Barberi, F., 2008: Structure of Tendaho Graben and Manda Hararo rift: implications for evolution of the southern Red Sea propagator in central Afar. *Tectonics, 27,* 17 pp.

Aquater, 1980: *Geothermal resource exploration project Tendaho area, feasibility study - Phase II.* EIGS and Ministry of Foreign Affairs of Italy, San Lorenzo in Campo, report.

Aquater, 1995: *Micro seismic study, final report.* EIGS and Ministry of Foreign Affairs of Italy, San Lorenzo in Campo, report.

Aquater 1996: *Tendaho geothermal project, final report.* MME, EIGS - Government of Italy, Ministry of Foreign Affairs, San Lorenzo in Campo, report.

Archie, R.G., 1942: The electrical resistivity log as an aid in determining some reservoir characteristics. *Trans. AIME, 146,* 54-67.

Árnason, K., 1984: The effect of finite electrode separation on Schlumberger soundings. *54th Annual International SEG Meeting, Atlanta, Expanded Abstracts,* 129-132.

Árnason, K., 1989: *Central loop transient electromagnetic sounding over a horizontally layered earth*. Orkustofnun, Reykjavík, report OS-89032/JHD-06, 129 pp.

Árnason, K., Karlsdóttir, R., Eysteinsson, H., Flóvenz, Ó.G., and Gudlaugsson, S.Th., 2000: The resistivity structure of high-temperature geothermal systems in Iceland. *Proceedings of the World Geothermal Congress 2000*, *Kyushu-Tohoku, Japan,* 923-928.

Árnason, K., 2006a: *TemX, short manual.* ISOR, Reykjavík, internal report, 17 pp.

Árnason, K., 2006b: *TEMTD (Program for 1D inversion of central-loop TEM and MT data)*. ISOR, Reykjavík, short manual 16 pp.

Barberi F., Ferrara G., Santacroce R., and Varet J., 1975: Structural evolution of the Afar triple junction. In: Pilger, A., and Roesler, A. (eds.), *Afar Depression of Ethiopia". Bad Bergzarben, F.R. Germany,* 38-54.

Bekele, B., 2012: *Review and reinterpretation of geophysical data of Tendaho geothermal field*. GSE, Addis Ababa, unpublished report, 96 pp.

Berckhemer, H., and Baier, B, 1975: Deep seismic sounding in the Afar region and on the highland of Ethiopia. *Proceedings of the International Symposium on the Afar Region and Related Rift Problems. Schweizerbart, I, Stuttgart,* 89-107.

Berdichevsky, M.N., and Dmitriev, V.I., 2002: *Magnetotellurics in the context of the theory of ill-posed problems*. Society of Exploration Geophysicists, USA, 215 pp.

Berktold, A., 1975: Magnetotelluric measurements in the Afar area. Afar Depression of Ethiopia. *Proceedings of the International Symposium on the Afar Region and Related Rift Problems, Schweizerbart, I, Stuttgart*, 262-275.

Cagniard, L., 1953: Basic theory of the magneto-telluric method of geophysical prospecting. *Geophysics, 18,* 605-645.

CNES Scientific Missions, 2015: Interaction with solar wind. CNES, webpage: *missions-scientifiques.cnes.fr/OVH/*

Craig, H., 1977: *Isotopic geochemistry and hydrology of geothermal waters in Ethiopian Rift Valley*. Scripps Institution of Oceanography, Isotopic Laboratory, report 77-14, 147 pp.

Dakhnov, V.N., 1962: Geophysical well logging. *Q. Colorado Sch. Mines, 57-2*, 445 pp.

Eysteinsson, H., 1998: *TEMRESD, TEMMAP and TEMCROSS plotting programs*. ÍSOR – Iceland GeoSurvey, unpublished programs and manual.

Flóvenz, Ó.G., Georgsson, L.S., and Árnason, K., 1985: Resistivity structure of the upper crust in Iceland, *J. Geophys. Res., 90-B12,* 10,136-10,150.

Flóvenz, Ó.G., Hersir, G.P., Saemundsson, K., Ármannsson, H., and Fridriksson, Th., 2012: Geothermal energy exploration techniques. In: Sayigh, A. (ed.), *Comprehensive Renewable Energy, 7.* Elsevier, Oxford, UK, 51-95.

Gonfiantini R., Borsi, S., and Ferrara, G., 1973: Isotopic composition of waters from the Danakil Depression, Ethiopia. *Earth and Planetary Science Letter, 18,* 13-21.

Groom, R.W., and Bailey, R.C., 1989: Decomposition of the magnetotelluric impedance tensor in the presence of local three-dimensional galvanic distortion. *J. Geophys. Res., 94*, 1913-1925.

Hailegiorgis, G., 2015: *Appendices to the report "Processing and joint 1D inversion of MT and TEM data from Alallobeda geothermal field in Tendaho, NE-Ethiopia".* UNU-GTP, Iceland, report 14 appendices, 106 pp.

Hersir, G.P., and Björnsson, A., 1991: *Geophysical exploration for geothermal resources. Principles and applications*. UNU-GTP, Iceland, report 15, 94 pp.

Hoversten, G.M. and Morrison, H.F., 1982: Transient fields of a current loop source above a layered earth. *Geophysics, 47,* 1068-1077.

Kearey, P., and Brooks, M., 1994: *An introduction to geophysical exploration* (2nd ed.). Blackwell Scientific Publ., London, 236 pp.

Kebede, Y., 2001: Application of the resistivity method in the Krísuvík geothermal area, Reykjanes Peninsula, SW-Iceland. Report 6 in: *Geothermal Training in Iceland 2001*. UNU-GTP, Iceland, 115-142.

Kebede, Y., Mengiste, A., Woldesemayet, B., Abera, F., Hailegiorgis, A.G., Dandir, K., and Mengesha, K., 2013: Magnetotelluric survey in Tendaho geothermal prospect North-East Ethiopia. Afar National Regional Government and GSE, Addis Ababa, unpubl. report.

Keller, G.V., and Frischknecht, F.C., 1966: *Electrical methods in geophysical prospecting*. Pergamon Press, NY, 527 pp.

Kidane, T., Courtillot, V., Manighetti, I., Audin, L., Lathittle, P., Quidelleur, X., Gillot, P.Y., Gallet, Y., Carlut, J., and Haile, T., 2003: New paleomagnetic and geochronologic results from Ethiopia Afar: Block rotations linked to rift overlap and propagation and determination of a ~ 2 Ma reference pole to stable Africa. *J. Geophys. Res*., 108 (B2), 10.1029/2001 JB000645.

Lahittle, P., Coulie, E., Mercier, N., Kidane, T., and Gillot, P.Y., 2001: K-Ar chronology and TL southern volcanism propagator for Red Sea Afar, since 300 ka, C.R. *Acad. Sci. Paris, Earth planet. Sci., 332*, (in French), 13-20.

Lahitte, P., Gillot, P.Y., and Courtillot, V., 2003a: Silicic central volcanoes as precursors to rift propagation: The Afar case. *Earth planet. Sci. Lett., 207*, 103-116.

Lahitte, P., Gillot, P.Y., Kidane, T., Courtilllot, V., and Abebe, B., 2003b: New age constraints on the timing of volcanism in central Afar, in the presence of propagating rifts, *J. Geophys. Res.,* 108 (B2), 2123.

Lemma Didana, Y., 2010: *Multidimensional inversion of MT data from Krýsuvík high-temperature geothermal field, SW-Iceland, and study of how 1D and 2D inversion can reproduce a given 2D/3D resistivity structure using synthetic MT data.* University of Iceland, Reykjavík, MSc thesis, UNU-GTP, report 4, 94 pp.

Lemma Didana., Y., Abera, F., Dendere, K., and Kebede, Y., 2012: *Magnetotelluric survey at Tendaho geothermal field in North East Ethiopia*. GSE, Addis Ababa, unpubl. report, 39 pp.

Mamo, T., and Bekele, B., 2014: Surface geological mapping at Tendaho geothermal field, Ethiopia. *Proceedings of the ARGeo-C5 Congress, Nairobi, Kenya,* 12 pp.

Megersa, G., and Getaneh, E., 2006: *Geological, surface hydrothermal alteration and geothermal mapping of Dubti-Semera area, Tendaho geothermal field.* GSE, Addis Ababa, unpubl. report, 66 pp.

Nure, K., 2001: *Gravity data interpretation of Gedemsa-Tullu Moye geothermal prospect area in the main Ethiopia rift (MER)*. GSE, Addis Ababa, unpubl. report, 48 pp.

Ofwona, C., 2010: Introduction to geophysical well logging and flow testing. *Presented at Short Course V on Exploration for Geothermal Resources, organized by UNU-GTP, GDC and KenGen, Naivasha, Kenya*, 6 pp.

Phoenix Geophysics, 2005: Data processing. User guide´s. Phoenix Geophysics, Ltd., Toronto.

Quist, A.S., and Marshall, W.L., 1968: Electrical conductances of aqueous sodium chloride solutions from 0 to 800°C and at pressures to 4000 bars. *J. Phys. Chem., 72,* 684-703.

Sky and Telescope, 2015: What is the solar wind? Sky and Telescope, webpage: *www.skyandtelescope.com/astronomy-resources/solar-wind/*

Simpson, F., and Bahr, K., 2005: *Practical magnetotellurics*. Cambridge University Press, Cambridge, UK, 254 pp.

Sternberg, B.K., Washburn, J.C., and Pellerin, L., 1988: Correction for the static shift in magnetotellurics using transient electromagnetic soundings. *Geophysics, 53-11,* 1459-1468.

Stimac, J., Armadillo, E., Rizzello, D., Mandeno, E., 2014*: Geothermal resource assessment of the Tendaho area.* Completed for UNEP and the Geological Survey of Ethiopia, report, 83 pp.

Teclu, A., and Mekonen, M., 2013: *Preliminary radon soil geochemical survey at Alallobeda geothermal prospect (Tendaho geothermal field).* GSE, GREAD, Addis Ababa, unpubl. report, 55 pp.

Teklemariam, M., and Kebede, S., 2010: Strategy for geothermal resource exploration and development in Ethiopia. *Presented at World Geothermal Congress*, *Bali, Indonesia*, 9 pp.

Teklesenbet Beyene, A., 2012: *Multidimensional inversion of MT data from Alid geothermal area, Eritrea; comparison with geological structures and identification of a geothermal reservoir*. University of Iceland, MSc thesis, UNU-GTP, report 1, 92 pp.

Tikhonov, A. N., 1950: The determination of electrical properties of the deep layers of the Earth´s crust (in Russian). *Dokl. Acad. Nauk. SSR 73*, 295-297.

Tikhonov, A. N., 1986: On determining electrical characteristics of the deep layers of the Earth´s. In Vozoff, K. (ed.), *Magnetotelluric methods*. Soc. of Expl. Geophys., 2-3.

UNDP, 1973: *Geology, geochemistry and hydrology of hot springs of the East African Rift System within Ethiopia*. UNDP, December report DD/SF/ON/11, NY.

Vozoff, K., 1972: The magnetotelluric method in the exploration of sedimentary basins. *Geophysics, 37,* 98-141.

Wolfenden, E., 2013: *Evolution of the southern Red Sea Rift: Birth of a magmatic margin.* Royal Holloway, University of London, PhD Thesis.

UNITED NATIONS UNIVERSITY
UNU-GTP
Geothermal Training Programme

Orkustofnun, Grensasvegur 9,
IS-108 Reykjavik, Iceland

Reports 2015
Number 15

BOREHOLE GEOLOGY AND HYDROTHERMAL ALTERATION OF WELL HE-58, HELLISHEIDI GEOTHERMAL FIELD, SW-ICELAND

Hamda Hassan Wais
Ministry of Energy in charge of Natural Resources
Cite Ministerielle, P.O. Box 10010, Djibouti
REPUBLIC OF DJIBOUTI
Ebyane_hassan@hotmail.fr

ABSTRACT

Well HE-58 is located in the Hellisheidi high temperature field within the Hengill geothermal area in SW-Iceland. This directional well was drilled to a total depth of 2531 m. An analysis of the uppermost 1200 m is presented in this report. Binocular microscope, petrographic microscope, XRD-analysis, a fluid inclusion analysis and geophysical logs were used to gather data which are published and interpreted in the paper.

Following binocular and petrographic analyses, it can be concluded that the lithology of well HE-58 mostly comprises hyaloclastite units. The rock types within these hyaloclastite units are: pillow basalts, basaltic breccia, and basaltic tuff. There are also basaltic intrusions at depths of 1050-1060 m and 1142-1148 m.

Four feeder zones were identified using temperature, neutron and caliper logs. These zones show an association with circulation losses and lithological boundaries in the upper levels but occur in relation to a basaltic intrusion at depth.

Four alteration zones were identified in this well: a zone of no alteration at 0-100 m depth; a zeolite-smectite zone (<200°C) from 200 to 450 m; a chlorite zone (230-250°C) from 450 to 760 m and a chlorite-epidote zone (250-280°C) from 760 to 1200 m.

Fluid inclusion studies show a wide range of homogenization temperature which range from 220-386.7°C. The homogenization temperature appears to be in equilibrium with the alteration mineralogy. However, it was not possible to compare the alteration with the formation temperature, because the well was still heating up at the time of the study.

1. INTRODUCTION

1.1 Purpose of the study

The purpose of this study report is to explore the subsurface geology of a geothermal field using data obtained by drilling. Drill cuttings, rig data and geophysical logs were used to study the lithology,

hydrothermal alteration, and the location of aquifers. Well HE-58 in the Hellisheidi geothermal field was chosen to serve these objectives, but this well is the latest make up well for the Hellisheidi power plant.

The main objective of this study is to evaluate the geothermal conditions in the system based on the lithology, hydrothermal mineralization, deposition of alteration minerals in veins and vesicles, and finally the location of aquifers to evaluate permeability and the success of the well. This geological study is mainly based on data available during drilling.

1.2 Geology of Iceland

Iceland is geologically a young country. It lies astride one of Earth's major diverging fault lines, the Mid-Atlantic ridge. This is the boundary between the North American and Eurasian tectonic plates. The two plates are moving apart at a rate of about 2 cm per year (Saemundsson, 1979). Iceland is an anomalous part of the ridge where deep mantle material wells up and creates a hot spot of unusually excessive volcanic productivity. This makes Iceland one of the few places on Earth where one can see an active spreading ridge above sea level. As a result of its location, Iceland is one of the most tectonically active places on Earth, resulting in a large number of volcanoes and hot springs. The volcanic succession of Iceland can be divided into four zones based on the age of the rocks (Figure 1): the upper Tertiary flood basalt formation which is older than 3,1 M.y., the Upper Pliocene and Lower Pleistocene (grey basalt) formation, which are between 0.7 and 3.1 M.y., the Upper Pleistocene (hyaloclastite) formation which is younger, and Postglacial lavas which formed during the last 13.000 years (Saemundsson,1979).

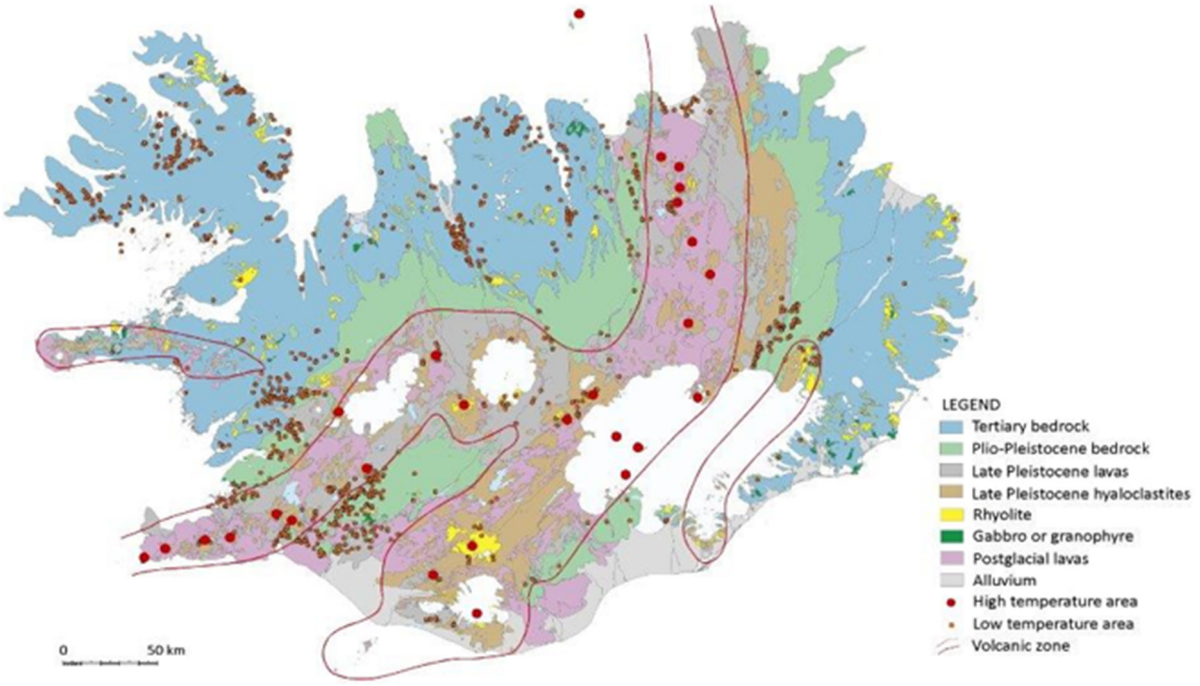

FIGURE 1: Geological map of Iceland (Jóhannesson and Saemundsson, 1999)

The Iceland Geothermal systems (Figure 1) are divided into two groups, high temperature fields (volcanic geothermal systems) and low-temperature fields (non-volcanic systems). The high temperature fields are located in the active zone of volcanism and rifting and temperatures exceed 200°C at 1000 m depth. The low-temperature fields are widely distributed in Quaternary and Tertiary formations and have lower temperatures (150°C at 1000 m depth) (Fridleifsson, 1979).

1.3 Hengill high-temperature geothermal area

The high temperature geothermal area associated with the Hengill central volcano is located in the volcanic rift zone in SW Iceland, approximately 40 km east of Reykjavik. It is located on a triple junction between the southern part of the Western Volcanic Zone, the eastern part of the Reykjanes Peninsula and the South Iceland Seismic Zone and is composed of a complex of fissure swarms and volcanoes (Figure 1).

Three fields have been developed within the greater Hengill area: 1) Nesjavellir where a 120 MW power plant is currently in operation, 2) Hellisheidi where a 303 MW power plant is currently in operation, and 3) Hveragerdi, where the geothermal resource is utilized directly by the local community (Björnsson et al., 2003; Franzson et al., 2005).

Hellisheidi is one of the geothermal areas within the Hengill system, located in the southern part. The Hellisheidi power plant, situated in the south western part of the Hengill area, was commissioned in 2006. The production capacity of the plant is 303 MWe using a water-steam mixture from 34 wells in the area (Gunnarsson, 2011).

1.3.1 Geology and tectonics of the Hengill area

Hengill central volcano (Figure 2) is mainly built up of sub-glacial hyaloclastite formations. Interglacial subaerial lavas erupting within the volcano flowed down the flanks of the volcano and accumulated in

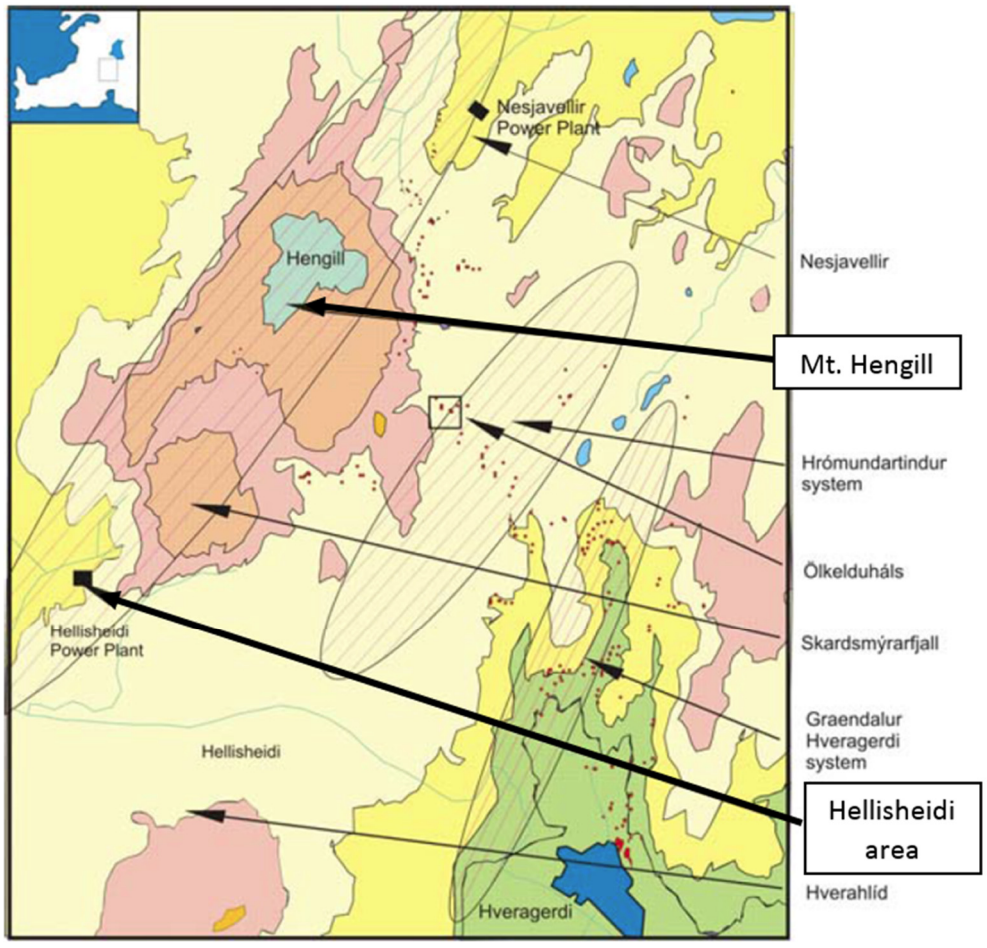

FIGURE 2: Location map of the Hengill volcanic complex
(from Pendon, 2006)

the surrounding lowlands. The age of the volcano has been assessed at around 400,000 years (Franzson et al., 2005).

The Hengill volcanic area is commonly divided into three volcanic systems; the youngest and most active one is Mt. Hengill system itself, located in the west of the area within the axial rift zone. The second youngest is the Hrómundartindur system, further to the east, which is much smaller in distribution.

The third one, the Hveragerdi system, furthest to the east (Figure 2), is now extinct and was considerably eroded in Pleistocene time. The oldest rocks, about 0.8 my old from the Matuyama epoch, are located in the lowlands southeast of the town of Hveragerdi, and the youngest are the Holocene lava flows from the fissure swarm cutting the Hengill volcano in the west. The Hrómundartindur system also includes an early Holocene lava flow from the Tjarnarhnúkur volcanic cone, extending into western Ölkelduháls (Saemundsson, 1967). An age of about 0.4 million years is proposed for the Hengill central volcano which puts a lower age limit on the geothermal system (Franzson et al., 2005). Tectonically, Hengill is the easternmost of a series of four closely spaced basaltic fissure systems that cut diagonally across the Reykjanes Peninsula. It is traversed by a graben about 10 km broad which runs NE-SW parallel to the hyaloclastite ridges. This graben is part of a greater structure which accompanies the Reykjanes-Langjökull volcanic zone. The western part of the Hengill area is split up by numerous sub parallel normal faults. These constitute a 5 km broad inner graben of intense faulting and fissure volcanism. During Postglacial time, six fissure eruptions occurred within this graben, four south of and two north of the mountain (Franzson et al., 2010). Faults and major fractures strike mostly NE-SW and are most conspicuous in the east and west, marking the boundaries of the fault and fissure zones of the volcano. Postglacial volcanism includes three fissure eruptions of ages 9000, 5000 and 2000 years. The two younger NE-SW volcanic fissures are believed to provide an inflow of colder water towards the reservoir of the main geothermal system (Franzson et al., 2005).

1.4 Geophysical studies in the Hengill area

Extensive resistivity surveys have been conducted in the Hengill region, including the Hellisheidi geothermal field, such as Schlumberger and TEM resistivity measurements (Björnsson et al., 1986; Árnason and Magnússon, 2001). Aeromagnetic and gravity surveys have, furthermore, been done in the Hengill geothermal area, including Hellisheidi (Björnsson et al., 1986). The DC resistivity surveys delineated a 110 km^2 low-resistivity area at 200 m b.s.l., and the magnetic survey showed a negative and transverse magnetic anomaly coherent with the most thermally active grounds. Recent transient electro-magnetic soundings (TEM) have led to a revision of the resistivity map (Figure 3).

A correlation exists between resistivity anomalies and alteration of the rocks. Low resistivity is connected with the smectite-zeolite zone (forming at temperature between 50 and 200°C). Below the low resistivity, there is a core of high resistivity as Figure 3 shows. This high-resistivity core is related to the chlorite-epidote zone located under a chlorite zone, indicating alteration temperature of more than 240°C (Árnason et al., 2000).

1.5. Hellisheidi high temperature field

The Hellisheidi geothermal field is located in the southern part of the Hengill area, approximately 20 km southwest of the Nesjavellir high-temperature field (Figure 2). The present well field in Hellisheidi covers around 12 km^2. The first exploration well was drilled in 1985 at Kolvidarhóll (KhG-1) at the western boundary of the field. A total of 58 production or exploration wells and 17 reinjection wells have been drilled in the Hellisheidi area. Production plans for the Hellisheidi power plant aimed at a capacity of 300 MWe electrical generation and 400 MWt thermal energy production. Two steam turbines (45 MWe each; 90 MWe total) have been online since December 2006 and a 33 MWe back-

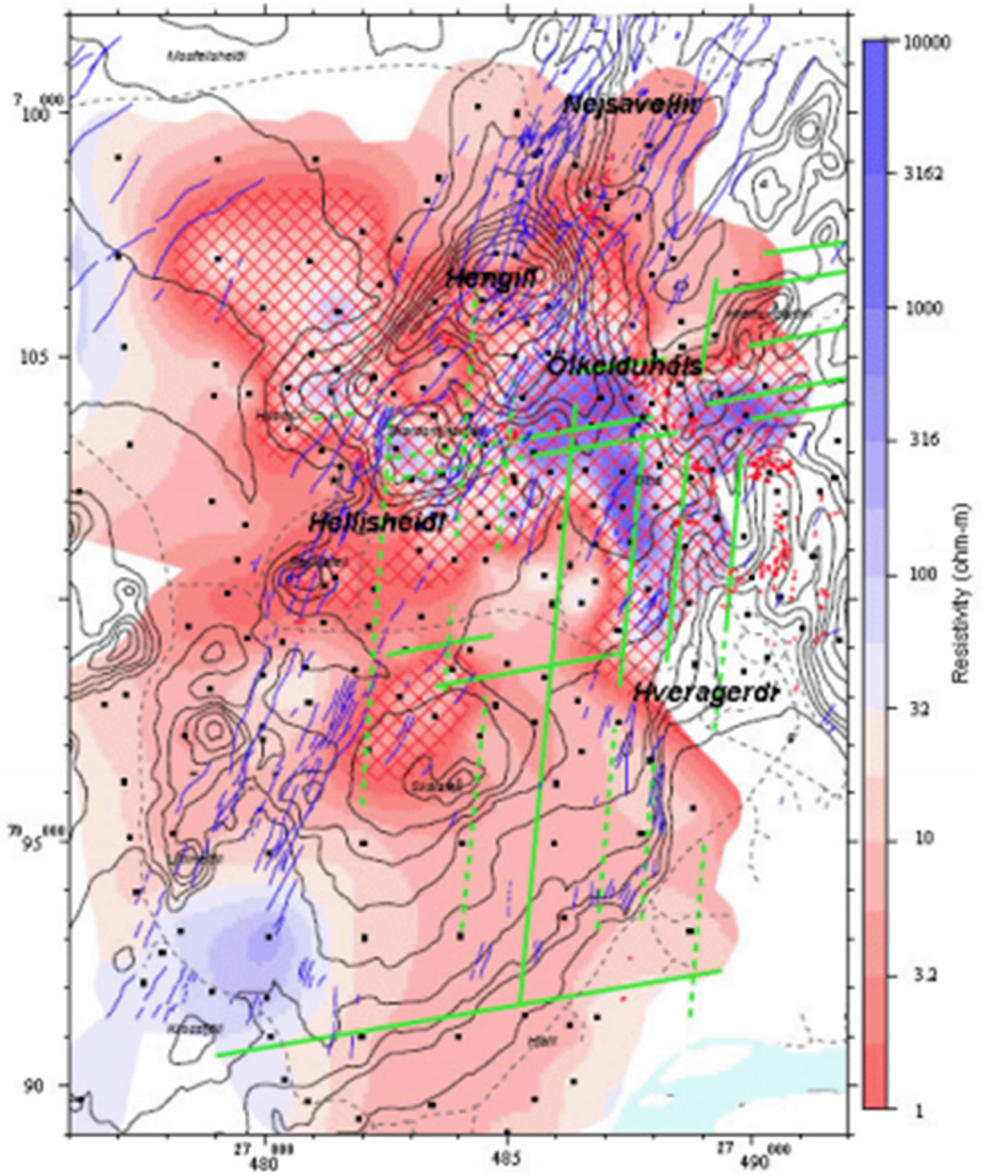

FIGURE 3: Resistivity at 600 m b.s.l. High resistivity cores are shown with red, crossed lines. Surface geothermal springs as red dots. Surface fissures and faults as blue lines. Green lines are fissures and faults defined by earthquake locations and yellow lines are post glacial (< 12 ka) fissures (Árnason, 2007; Árnason and Magnússon, 2001)

pressure turbine since 2007. The plant's purpose is to meet increasing demand for electricity and hot water for space heating in the industrial and domestic sectors of the greater Reykjavík area (Elmi, 2008).

2. BOREHOLE GEOLOGY OF WELL HE-58

2.1 Drilling of well HE-58

Well HE-58 is located east of the Hellisheidi power plant (Figure 4). It shares the same drill pad as HE-41, HE-42 and HE-45. The well was directionally drilled towards WNW, just north of the HE-45 well path. The intention was to reach an upflow zone connected to the NE-SW striking faults of the Hengill graben (Gunnarsdóttir et al., 2015). The well's coordinates (ISN93) are as follows:

X=383860,83 Y=394396,07 Z= 352 m a.s.

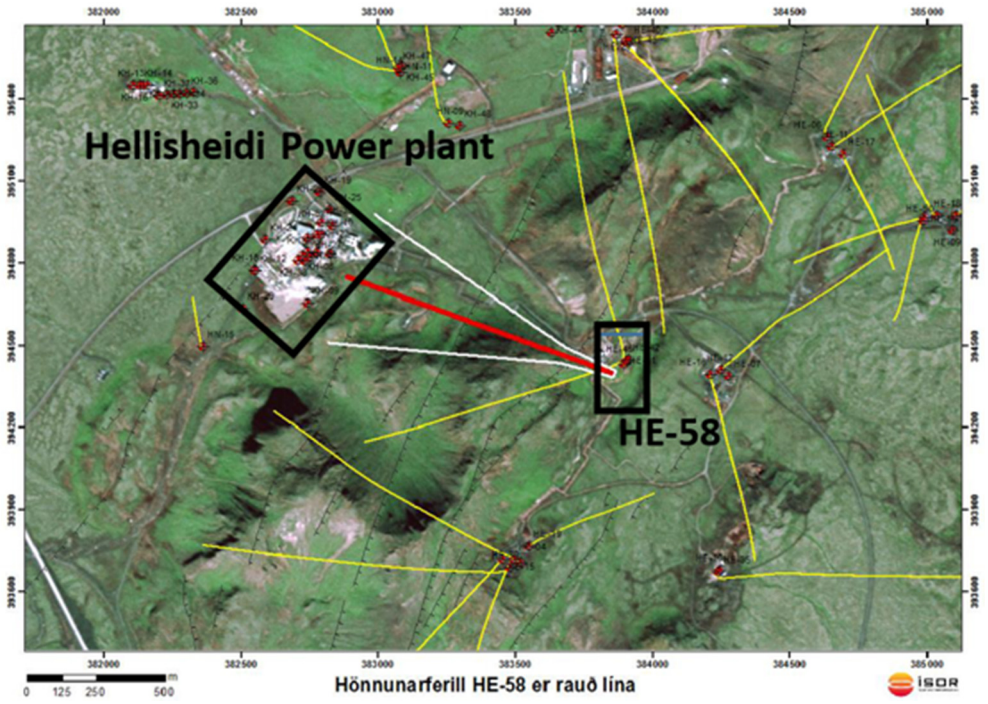

FIGURE 4: Location of HE-58 and red line shows the proposed well path of HE-58

There were four sections of drilling (Figure 5), pre-drilling with the drill rig Nasi (Ræktunarsamband Flóa og Skeida), and 1st to 3rd sections with the drill rig Thor (Iceland Drilling Ltd.). All drill depths in this report refer to Thor's rig floor which is at 9.0 m above ground.

Pre-drilling with 23" drill bit to 98,2 m started on the 9th of July 2015 and ended the next day. 22½" surface casing was run in to 89 m. Thor's work on the 1st section began the 25th of July 2015 with the last preparations of the rig. The run in of a 21" drill bit began shortly after midnight and drilling commenced just before noon on the 26th of July. Drilling continued for two days until 289 m were reached. No circulation losses occurred during drilling. Temperature and caliper logs were finished on the 29th after a period of water circulation and pulling out of the drill string. Following the logging an 18⅝" anchor casing was run in to 267.6 m and then cemented on the 30th of July. When the cement had set the top of the casing was cut on the 1st of August, marking the end of the 1st section.

The second section of the well was drilled from 289 m with a 17½" drill bit with a motor and MWD equipment. Directional drilling commenced at 304 m intending to reach 30° inclination and 290° direction in the second section. Because of the close proximity of other wells on the drill pad, care needed to be taken with the directional drilling. No circulation losses occurred during the drilling of this section. On the 5th of August drilling was stopped at 769 m. Temperature and caliper logs were then performed but on the way up the caliper logging tool got stuck and was eventually lost. Casing with a 13⅜" production casing was finished on the 8th of August followed by cementing.

The third section of the well started on August 11th when a drill bit was run in for grinding of the cement and the caliper logging tool that was lost in the hole. The next day a drillstring with motor, MWD and a 12¼" drill bit was run in. Drilling was smooth until at 1550 m where the torque was beginning to get higher. It was decided to change the drill bit and the next day drilling with a new bit started again. At 2115 m the inclination of the well was getting too low and it was decided to pull out and change the assembly of the drill string as well as the drill bit. Drilling then continued until 2500 m but the well was extended by 31 m because of a feed zone close to the bottom. Drilling stopped on the 29th of August and was followed by geophysical logging, running in of a 9⅝" slotted liner and injectivity tests. The last workday of well HE-58 was the 4th of September.

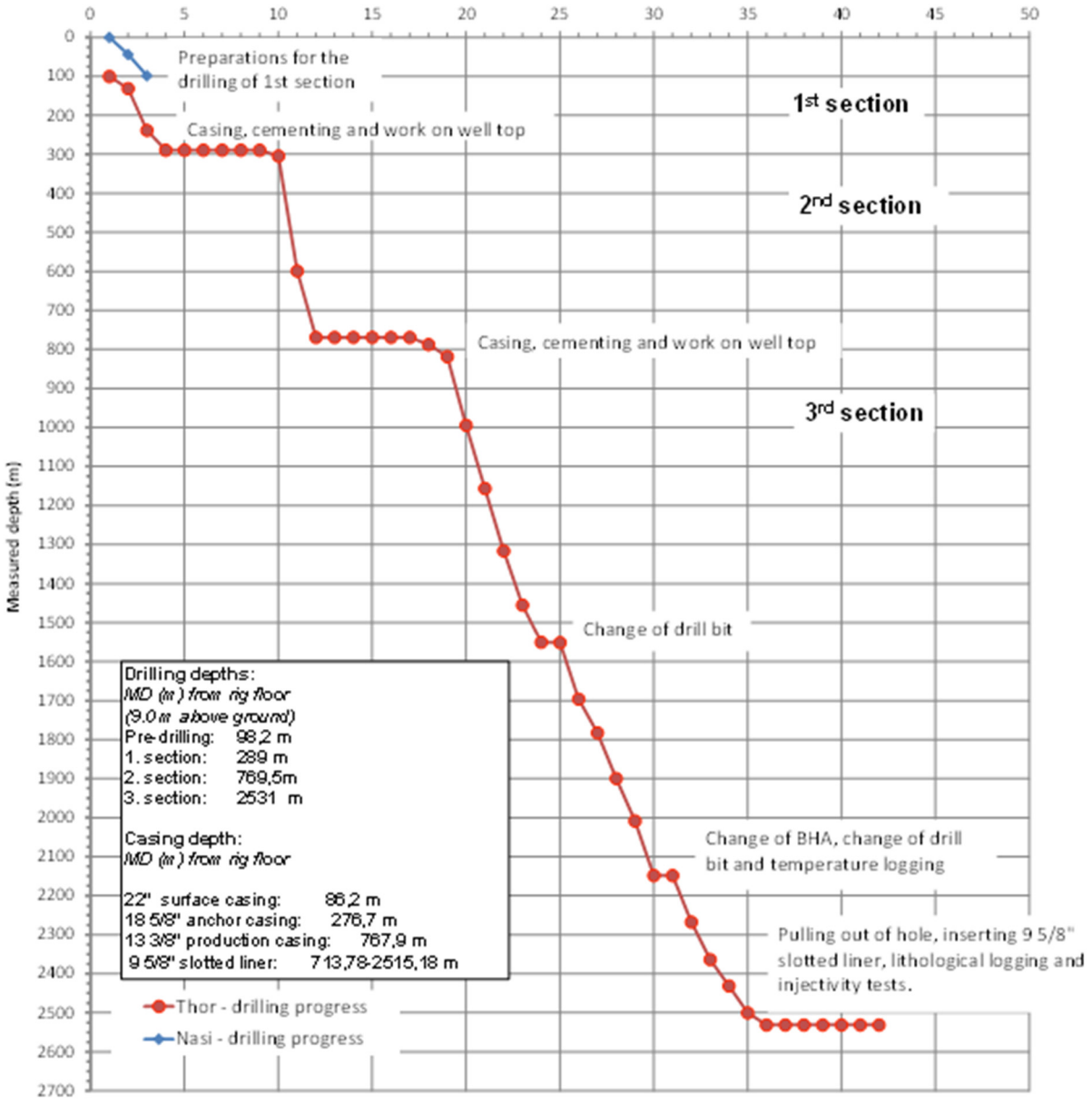

FIGURE 5: Drilling progress of well HE-58 and logging carried out during the drilling

2.2 Methodology and analytical techniques

The samples for this research project were acquired during the drilling of HE-58. Samples were collected at 2 m intervals and a preliminary analysis using binocular microscope was executed at the drill site. The main objective was to identify the lithology, alteration of primary minerals, temperature dependent alteration minerals, fractures and foreign materials present in the cuttings (e.g. metal shreds from casing, drill pipes or drill bit).

This allows for the design of the preliminary stratigraphy, the estimated alteration temperature and fracturing, which are all useful geotechnical aspects for the drilling and necessary for siting the depths of casings. Subsequently the samples were taken to the ISOR labs in Reykjavik and analysed in greater detail.

Four principle methods were used in the study of the drill cuttings. These were binocular analysis and petrographic analysis to determine the rock type, texture, alteration mineralogy, alteration sequences and possible feed-zones. XRD techniques were used to identify the clay chemistry and fluid inclusions to study the alteration history further.

2.2.1 Binocular microscope analysis

Binocular analysis of drill cuttings was done at the time of drilling with the use of a binocular microscope (Olympus SZX12). The samples were washed with tap water to eliminate impurities and dust in order to improve the visibility. The noted properties of the cuttings were, for example, the colour of the rock, grain size, texture, vein fillings if present, alteration mineralogy and degree of alteration. From these observations, the rock types and their properties were identified. Diluted HCl was used to identify the presence of calcite. Samples of interest were selected for XRD analysis and calcite and quartz grains were observed for fluid inclusion geothermometry analysis.

2.2.2 Petrographic microscope analysis

The petrographic microscope is a useful tool for the analysis and study of drill cuttings in a thin section. The thin sections were analysed using a Leitz Wetzler petrographic microscope at the ISOR laboratories. The objective was to confirm the rock types previously determined by the binocular microscope as well as the alteration minerals and other minerals that were possibly overlooked before. In addition, the petrographic analysis was aimed at determining the paragenetic sequence of the alteration minerals as observed in veins and vesicle filling.

2.2.3 X-Ray diffractometer analysis

The X-ray diffractometer (XRD) is mainly used in geothermal research to identify different types of clays, and some alteration minerals like zeolites and amphiboles, in a given hydrothermal system. Clays are used to determine the boundaries between alteration zones and give an indication of the alteration temperature of the well. To perform the XRD analysis a Bruker AXS, D8 Focus Diffractometer was used. Samples were selected among the various stratigraphic units and then prepared for analysis, which involved dissolving the clays from the drill cuttings. Samples were then run in the XRD machine, subsequently glycolated samples were run and finally clay samples that had been heated to 550°C. All the peaks for the different runs were recorded and subsequently analysed using specialized computer software. Results of the XRD analyses are summarized in Table 1 in Appendix 1 along with some raw data results.

2.2.4 Fluid inclusion analysis

Among the different methods of analyses performed in borehole geology studies of a well, is the analysis of fluid inclusions where fluid trapped in vacuoles inside mineral grains during growth or recrystallization are analysed. In particular minerals of calcite and quartz are used for these studies. The trapped fluids give an approximate temperature from the time of the fluid being trapped in the mineral grain. The crystal is heated until the fluid inclusion reaches the homogenization temperature (Th). In this study the crystals were under the petrographic microscope on a Linkam THSMG 94 stage at the University of Iceland. The results are compared to the alteration mineralogy giving important information on the thermal history of the geothermal system. In the case of well HE-58 temperature logs available in this study did not give accurate information about the formation temperature as not enough time had passed for the heating up of the well.

2.3 Stratigraphy

In this study, the upper 1200 m of well HE-58 were analysed showing that the lithology consists mostly of hyaloclastite formations; some crystalline basaltic lava flows and a few intrusions were also

encountered. The hyaloclastite formations contain different types of rocks such as basaltic tuff, basaltic breccia and pillow basalts (glassy basalt). Approximately 550 samples were analysed using binoculars and 15 thin sections were analysed using a petrographic microscope. The lithology, geophysical loggings, some alteration minerals and temperature logs are found in Figures 6.

0 – 100 m: Cuttings were not available during this study.

100 – 152 m: *Basalt breccia.* Light grey to reddish, fine-grained basaltic breccia with occasional olivine, pyroxene and plagioclase crystals. Tuff lenses were seen, mostly brown palagonite. Fresh glass patches were frequently seen within the palagonite.

152 - 158 m: No cuttings due to mistakes in sampling.

158 – 258 m: *Basalt breccia*. Basaltic breccia, serrated and aphanitic texture. The fine- to medium-grained olivine tholeiite is mixed with slightly oxidized tuff. Crystalline fragments are slightly plagioclase and olivine phyric. Zeolites, such as mesolite and thomosonite are found at 198 m and 204 m respectively and scolecite and stilbite at 214 m and 220 m.

258 – 270 m: *Glassy basalt*. Mixture of grey, fine-grained basalt fragments and black glass materials. Vesicular basalt with olivine and plagioclase. The formation is not oxidized. Amorphous silica and zeolites occur.

270 – 288 m: No cuttings due to mistakes in sampling.

288 – 328 m: *Glassy basalt*. Pillow basalt. Plagioclase porphyritic and rather vesicular rock. Clay is noted in some of the vesicles in the glass.

328 – 354 m: *Glassy basalt*. Same formation as above but increasing amount of glass. Amorphous silica and clay occurs.

354 – 372 m: No cuttings due to mistakes in sampling.

372 – 398 m: *Glassy basalt*. Dark grey, fine- to medium-grained rock with increasing amount of glass, perhaps pillow breccia in some samples. Same alteration as before. Clay and amorphous silica occurs but zeolites are absent.

398 – 418 m: *Basalt breccia*. The same formation but now classified as basaltic breccia. Calcite and pyrite occur in small quantities.

418 – 660 m: *Basalt tuff*. Partly greenish tuff. Quartz is seen in the fractures at the depth of 430 m and crystalline quartz (rocks crystal) is found at 446 m. This unit is somewhat fractured below 450 m depth.

660 – 684 m: *Basalt breccia.* Dark-grey to greenish, highly altered basalt breccia, mixed with light-brown to greenish basalt tuff. The rock contains plagioclase and olivine tholeiite crystals. Wairakite occurs at a depth of 670 m.

684 – 716 m: *Glassy basalt*. Fine-grained olivine tholeiite basalt fragments and altered glass. Epidote occurs at 714 m along with prehnite.

716 – 726 m: No cuttings.

726 – 770 m: *Glassy basalt*. This sequence is moderately to highly altered. Calcite and pyrite are very common in this sequence, and quartz was identified at all depths. Veins and vesicles are filled with various unidentified minerals as they were too small.

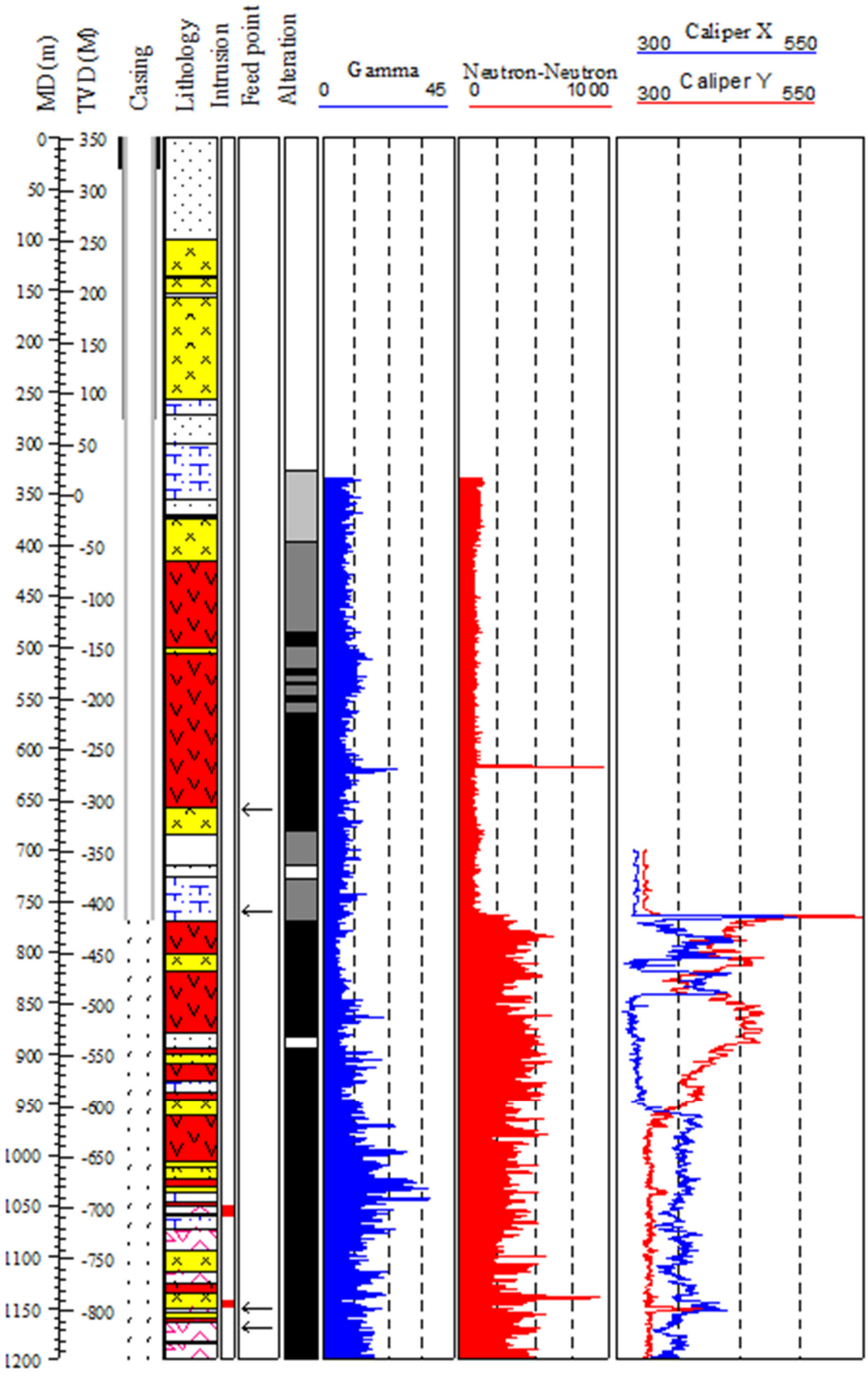

FIGURE 6: Simplified lithology and geophysical logs of well HE-58

770 – 802 m: *Basalt tuff*. Light grey to greenish highly altered tuffs, with some dark basalt fragments. The rock is basaltic tuff with white precipitates of calcite and no oxidation. Chlorite, quartz, and chalcopyrite occur.

802 – 818 m: *Basalt breccia*. Light grey pillow breccia, a mixture of tuff and more crystallized olivine tholeiite. Epidote, quartz and chlorite occur at this depth.

818 – 880 m: *Basalt tuff*. Tuff and tuff rich breccia, cuttings are extremely fine. Coarse- and medium-grained clay, quartz, calcite and chalcopyrite are always present but epidote only occasionally. The formation is homogeneous.

880 – 894 m: No cuttings.

894 – 900 m: *Basalt tuff*. Light grey to greenish tuffs, with dark basalt fragments, highly altered. Same formation as above. Quartz and chalcopyrite fairly common.

900 – 910 m: *Basalt breccia*. Tuff rich breccia, with light grey basaltic fragments, brown tuff and calcite precipitates. Highly altered, intermediate oxidation with sub-ophitic to intergranular textures.

910 – 928 m: *Basalt tuff.* Same tuff formation with high alteration, mixed tuffs and breccia. Cuttings are very fine.

928 – 938 m: *Glassy basalt*. Pillow lava/pillow breccia. Not porous but highly altered. The rock is glassy basalt, but pillow breccia in places. Epidote, quartz and prehnite occur regularly.

938 – 946 m: *Basalt tuff*. Highly altered whitish tuff. The abundance of calcite increases as well as the overall alteration of the rock.

946 – 962 m: *Basalt breccia.* Tuff rich breccia. The tuff is highly altered, whitish and poorly bound together. A 950 m there is a sudden increase in calcite and pyrite, indicating permeability.

962 – 992 m: *Basalt breccia*. Tuff rich breccia, grey to greenish highly altered basalt breccia mixed with light-brown or greenish basalt tuff. Considerable increase in calcite but the amount decreases again below 980 m.

992 – 1006 m: *Basalt tuff*. The rock is basaltic tuff, white and highly altered. The main alteration minerals are quartz and calcite along with epidote.

1006 – 1012 m: *Glassy basalt*. Hypo crystalline or very finely crystallised basalt, porous and highly altered.

1012 – 1022 m: *Basalt breccia*. Tuff rich breccia, highly altered. Same alteration mineralogy as before although alteration minerals are very few.

1022 – 1030 m: *Basalt tuff*. Whitish brown tuff mixed with darker altered, fine-grained crystallized basalt.

1030 – 1046 m: *Glassy basalt.* Altered pillow basalt. Epidote becomes more apparent and more crystalline. Some sedimentary grains are seen.

1046 – 1050 m: *Basalt tuff.* White highly altered and dense tuff.

1050 – 1058 m: *Fine- to medium-grained basalt*. Finely crystallized basalt, possibly an intrusion, quite dense and less altered than the hyaloclastite formation above and below. Clay, calcite and pyrite are seen in vesicles.

1058 – 1072 m: *Glassy basalt*. Porous and very altered pillow basalt, fine grained and mixed with highly altered tuff and hypocrystalline basalt.

1072 – 1092 m: *Fine-grained basalt*. Fine-grained partially altered basalt. Probably a lava flow. Alteration is reduced but the alteration minerals are found in larger crystals, indicating that vesicles in this formation are larger than in the hyaloclastite formation above.

1092 – 1114 m: *Basalt breccia*. Tuff-rich breccia. White and very altered. Increasing amount of alteration minerals, particularly calcite.

1114 – 1126 m: *Fine-grained basalt*. Dense fine-grained basalt, highly altered. Most likely a lava flow. Epidote, quartz, chlorite, and calcite are the most prominent alteration minerals.

1126 – 1136 m: *Basalt tuff*. Highly altered, white and somewhat vesicular tuff.

1136 – 1150 m: *Basalt breccia*. The same formation, but with higher amount of hypocrystalline grains.

1150 – 1154 m: *Fine- to medium-grained basalt*. Dark, fine- to medium-grained and compact basalt, possibly an intrusion.

1160 – 1162 m: *Basalt tuff*. White, very altered tuff lens with high amount of alteration minerals. Wollastonite occurs at 1150 m, suggesting an alteration temperature of 260°C. The amount of calcite is reduced.

1162 – 1200 m*: Fine- to medium-grained basalt*. Basalt lava flow with high alteration. Potentially plagioclase phyric. Nicely crystallized alteration minerals such as epidote, quartz, calcite and prehnite are seen.

2.3.1 Intrusions

An intrusion is a magma body that solidifies below the surface. They generally have relatively coarse textures compared to the host rock as the magma cools slowly to give time for crystal growth (Franzson et al., 2010). However, thin dykes may crystalize quicker resulting in fine- to medium-grained rocks. Intrusive rocks are characterized by their massive character and low alteration compared to the country rock. Indeed, two possible intrusions were identified in the uppermost 1200 m of well HE-58 (Figure 6) and these are described below:

- Intrusive unit I (1050-1058 m): This intrusion is fine to medium grained, dark grey, quite dense and much less altered than the country rock;
- Intrusive unit II (1150-1158 m): Fine- to medium-grained basaltic intrusion. The rock is light grey in colour, and characterized by plagioclase phenocrysts.

2.4 Hydrothermal alteration

Hydrothermal alteration is when a change in the textural, mineralogical, and chemical composition of the host rocks occurs, caused by the action of hydrothermal fluids, steam and/or gas (Henley and Ellis, 1983). The primary minerals are replaced by secondary minerals as a result of change in the physio-chemical conditions affecting the rock. These physio-chemical changes are mainly variations in temperature, pressure, or chemical conditions. The hydrothermal minerals are geothermometers that can

be used to help determine the casing depth and also to determine the alteration temperature in wells, and thereby help assessing if the geothermal system in a particular area is heating, cooling or in equilibrium. Hydrothermal minerals can also be used in estimating the pH of fluid and other chemical parameters, as well as predicting the fluid tendencies of scaling and corrosion, measuring permeability, possible cold-water influx and as a guide to the hydrology (Reyes, 1990). When the rock heats up, especially in active volcanic areas, the rock will release ions into solution. This hydrothermal solution, after undergoing further heating, will rise up as a mineral rich fluid. The mineral rich fluid will tend to crystallize out of the solution onto open cavities and/or open structures depending on temperature, rock type, pressure, permeability, fluid composition and duration of activity. For example, epidote starts to appear at about 230°C, as shown in Table 1 along with temperatures of other well-known alteration minerals (Kristmannsdóttir, 1979; Franzson, 1998).

TABLE 1: Some temperature dependent index minerals in high temperature areas in Iceland (Kristmannsdóttir, 1979; Franzson, 1998)

Minerals	**Min. temperature** (°C)	**Max. temperature** (°C)
Zeolites	40	120
*Laumontite	120	180
*Wairakite	200	
Smectite		<200
**MLC	200	230
Chlorite	230	>300
Calcite	50-100	280-300
Quartz	180	>300
Prehnite	240	>300
Epidote	230-250	>300
Wollastonite	260	>300
Actinolite	280	>300

*Belong to the zeolite group; **Mixed-layer clay

2.4.1 Alteration of primary minerals

Most rocks in geothermal areas contain some primary minerals which are unstable in geothermal environments. These have a tendency to be replaced by new minerals that are stable, or at least metastable, under the new conditions. The replacement hydrothermal minerals record the interactions between the wall rocks and the hydrothermal fluids, while minerals filling open space reflect the processes that affected the circulating fluids (Browne, 1978).

Primary minerals are minerals that form during the solidification and crystallization of the rock. These minerals include both the essential minerals used to assign a classification name to a rock and they form in a sequential group as dictated by the physio-chemical conditions under which the magma solidifies. These minerals become unstable at temperatures prevailing in a geothermal system and, therefore, alter to secondary minerals when subjected to hydrothermal conditions (Browne, 1978). Figure 7 shows the mineral alteration zones in Iceland and the alteration of primary minerals with temperature.

Iceland is mostly composed of igneous or volcanic rocks of which about 80-85% are basaltic rocks in composition (Saemundsson, 1979). The main primary minerals in their order of susceptibility to alterations (Table 2), are:

1. Glass (amorphous, fresh);
2. Olivine;
3. Plagioclase;
4. Pyroxene;
5. Opaques.

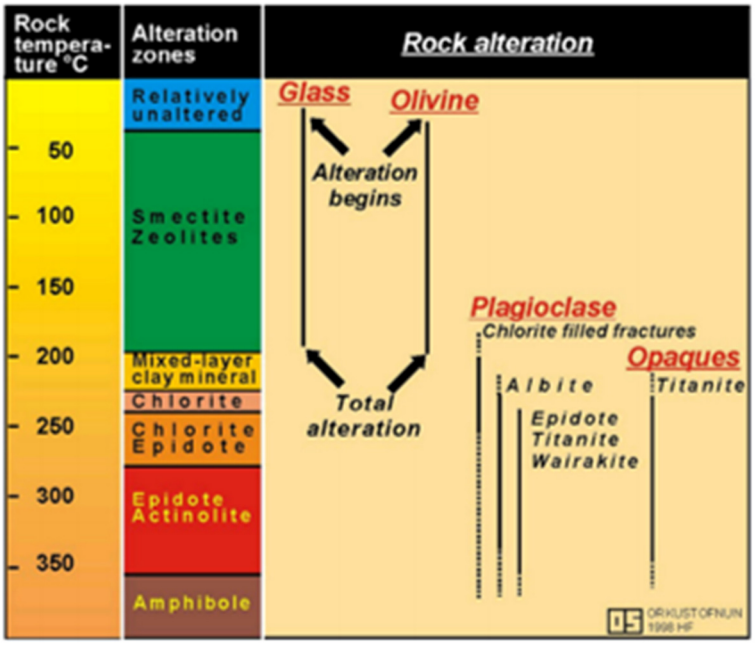

FIGURE 7: Hydrothermal alteration in Iceland with increasing temperature (alteration of primary minerals, alteration products and alteration zone) (from Franzson, 1998)

Volcanic glass: is amorphous and therefore not really a crystal but it forms as magma cools fast. It shows a highly vitreous lustre and good conchoidal fractures. It is the first constituent to be altered and replaced by alteration minerals. The replacement products of volcanic glass are clays, zeolites (e.g. mordenite, laumontite), quartz and calcite (Browne, 1978). In well HE-58 it was replaced by clay minerals.
Olivine: is a term for a serial composition made based on the proportion of magnesium to iron. It is one of the primary minerals that forms basaltic rocks (e.g. olivine tholeiite) and is very susceptible to alteration. It is distinguished in thin section by its high birefringence, distinctive irregular fracture pattern, lack of cleavage, and alteration products, usually clay, forming along rims and fractures. It is completely replaced by clay and minerals such as calcite at depth.

Plagioclase: is common in the microcrystalline ground-mass and as a phenocryst in basalt. In crystalline rocks it is readily identified by its low relief and conspicuous polysynthetic twinning. This is seen throughout the well where crystallization has taken place, and is obvious where the rock is plagioclase porphyritic. It is observed to be progressively altered as temperature increases and is finally replaced by albite and occasionally by calcite, wairakite, chlorite and epidote. In well HE-58 it was replaced by clay, calcite, quartz and chlorite (Table 2).

Pyroxene: like olivine it has compositional series. Augite is the most common form of pyroxene in Iceland. It is black or dark green in colour, and forms prismatic crystals with vitreous lustre and perfect cleavage. It is translucent or transparent, streak is grey or green, and fracture uneven. Pyroxene was seen altered to chlorite and actinolite in the well.

Opaque minerals in basalt in Iceland are mostly magnetite, one of the most common iron oxides. No alteration of the opaque minerals was noted in the uppermost 1200 m of the well.

TABLE 2: Primary mineral alteration in well HE-58 (the arrow shows decreasing susceptibility to alteration

Altered/Unaltered	**Alteration results**
Glass ↓	clay, zeolite, calcite, quartz
Olivine	clay, calcite,
Plagioclase	clay, calcite, quartz, chlorite
Pyroxene	clay, chlorite, actinolite

2.4.2 Distribution of alteration minerals

Hydrothermal minerals are formed as a result of the alteration of primary minerals. Hydrothermal alteration depends on many factors or parameter such as temperature, permeability, fluid chemistry, rock type, pressure and rock structure (Kristmannsdóttir, 1978; Reyes, 1990; Browne, 1978; Malapitan, 1995).

In well HE-58, different hydrothermal minerals were observed, but the most common minerals in the upper 1200 m were calcite, pyrite, zeolites, chalcedony, chalcopyrite, epidote, quartz, clay, prehnite, chlorite and wollastonite. A geothermal system is always associated with H_2S and CO_2, which contribute to the forming of calcite and pyrite. A description of the alteration minerals along with their occurrence in the well is described below and their distribution is shown in Figure 8:

Calcite. It is one of the most abundant and widely distributed secondary minerals in the well, appearing from 398 m and seen all the way to the bottom of the 1200 m section of the well. It is frequently seen in the pores of hyaloclastite units and lava flows, but less in the more compact intrusions. Calcite either occurs as a replacement of primary minerals or as a direct depositional mineral. Hydrochloric acid was used to identify it in the cuttings.

Pyrite. Some pyrite is seen in most samples below ca. 400 m in the well but never abundant. It occurs as precipitation in veins, vesicule and chalcopyrite.

Chalcedony. Chalcedony is one of the varieties of silica polymorphs that have temperature equilibrium of less than 180°C (Fournier, 1985). It occurs at around 400 m in well HE-58. In thin sections, it can be seen as a thin-layered lining in vesicles.

All of the minerals below are associated with certain temperatures in geothermal systems in Iceland and can be used to identify the thermal evolution of the system:

Zeolites: are hydrous secondary minerals (sodium calcium aluminium silicates). Zeolites are generally white or colourless, but sometimes yellow by minor impurities. Zeolites both occur as precipitations in vesicles as well as replacing glass and sometimes plagioclase. In nature, zeolites are temperature dependent which can help in determining the temperature at a given depth in geothermal systems. In well HE-58 zeolites appear at 198 m and can be found down to 302 m. The different types of zeolites in well HE-58 are described below:

> *Mesolite*: It was found with binocular microscope at depths of 198 m, 226 m, 242 m, 256 m, 260 m and 264 m. It is characterised by fibrous radiating clusters. Mesolite is finer and fainter in colour when compared to scolecite in a petrographic microscope. It forms at approximately 70°C;
> *Thomsonite*: This member of the zeolite family was observed in the binocular microscope at 204 m, 212 m, 218 m, 228 m, 232 m, 240 m, 262 m, and 268 m. It has radiating, elongated and slightly flattened crystal habit. Thomsonite crystallises at around 40°C;
> *Scolecite*: It was found with binocular microscope at 210 m, 214 m, 222-226 m, 230 m, 234 m, 246-248 m, 258-260 m, and with the last appearance at 302 m. Scolecite precipitates between 70 and 120°C;
> *Stilbite*: Under the microscope, stilbite is characteristically radial and with fan-like aggregates, and shows good cleavage. Stilbite was found at these depth intervals 216-236 m, and 248-270 m and is indicative of the temperature range 90-120°C.

Quartz: It is a white, transparent mineral. Quartz was first seen at a depth of about 430 m and continued to the bottom of the well. It was also noted in thin sections at 380 m and 600 m (Figure 8). Quartz forms at temperature above 180°C.

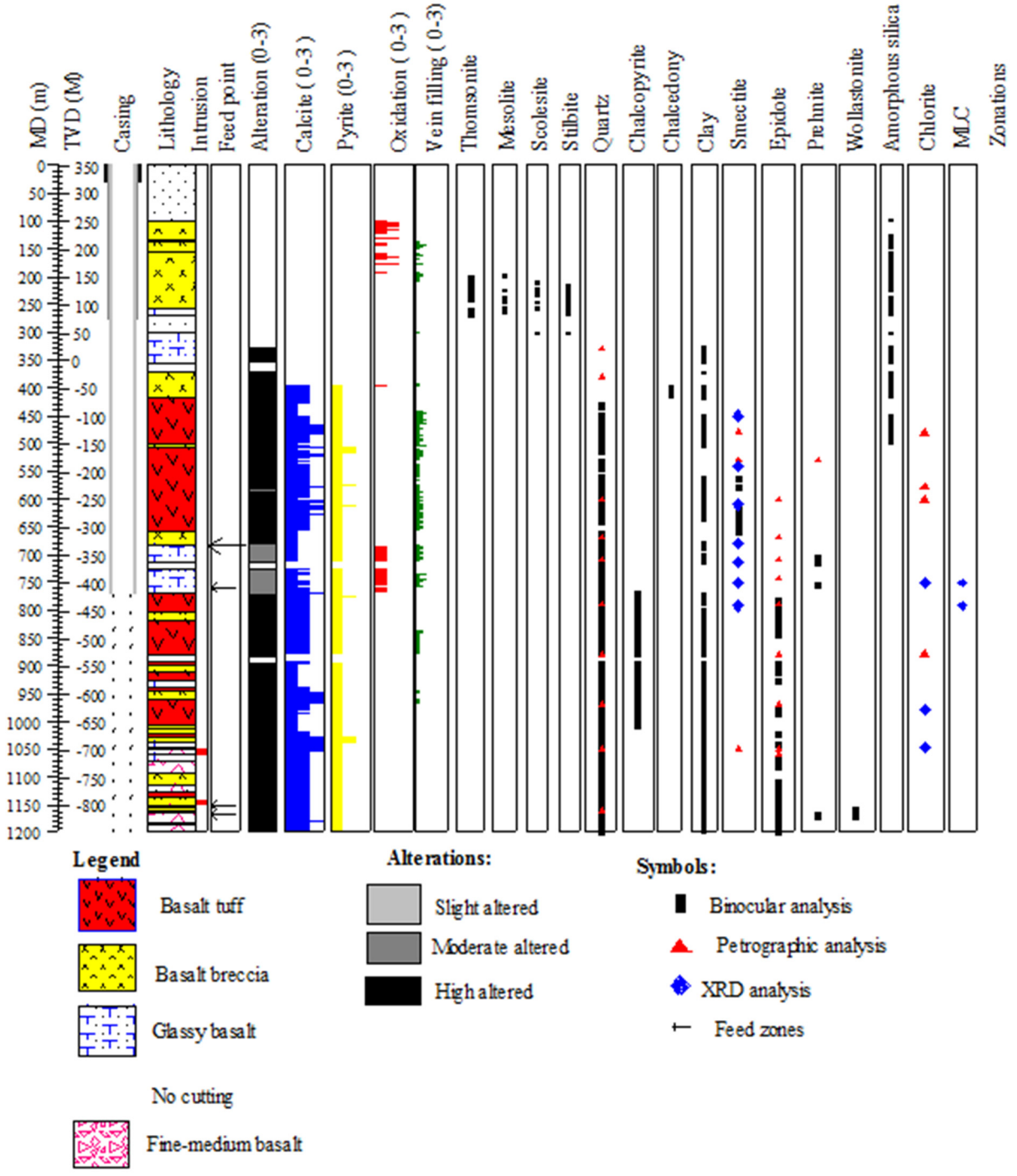

FIGURE 8: Distribution of hydrothermal alteration minerals, location of aquifers and alteration intensity

Epidote: Epidote is a common mineral in hydrothermal processes. It is a high-temperature mineral that has a lower temperature stability formation between 230 and 260°C in volcanic rocks (Browne, 1978), but in Iceland it forms at temperatures exceeding >240° (Franzson, 1998). In this well, it appeared more or less continuously from around 760 m showing euhedral to subhedral minute prismatic and radiating needle-like crystals. It was also noted occasionally in thin sections from 600 m (Figure 8).

Prehnite: Prehnite begins to crystallise at temperatures above 240°C. Commonly, it is found in veins or vesicles. The first appearance of prehnite was observed at 706 m. However, it was also identified in a

thin section at 530 m. Normally, prehnite occurs along with epidote and other high temperature minerals and as a part of simple to complex mineral assemblages.

Wollastonite: a hairy-like high-temperature mineral, first appearance was at the interval depth of 1160-1170 m. In the thin sections, wollastonite seemed to crystallise after epidote. The upper boundary of wollastonite indicates a temperature of around 260°C.

Clay minerals: The clay minerals are the most voluminous alteration minerals. Their formation involves the chemical reactions and physical movement of hydrothermal fluids and, in many cases, there is a zonal arrangement of the clay minerals around the source of alteration, depending on the parent rock and the nature of the hydrothermal solutions (Gebrehiwot, 2010). The composition, structure and morphology of clay minerals depend on a number of environmental parameters – temperature, fluid composition/amount, pH, etc. (Njue, 2010). Clay minerals are alteration products of basaltic glass, olivine, plagioclase, and partly pyroxene, as well as vesicle fillings. Smectite, mixed-layer clays and chlorite comprise the different types of clays in the well:

Smectite is a low-temperature clay formed by the alteration of glass and ferromagnesian primary minerals such as olivine, commonly replacing them completely (Lugaizi, 2011). Smectite has a brownish colour and is found in patches or as thin coatings in altered rocks. In well HE-58 it was first found at 450 m depth (XRD). Under the petrographic microscope, smectite is fine grained with a dark-brownish colour.

Mixed-layer clays: Mixed-layer clay (MLC) minerals are intermediate products of pure end-members of clays (Sradon, 1999) most commonly forming interlayers of smectite and chlorite in Icelandic rocks. MLC was identified in two XRD samples at 752 m and 792 m (Figure 8).

Chlorite: The presence of chlorite indicates temperatures above 230°C (Franzson, 1998). Under the petrographic microscope, the mineral appears light-green and non-pleochroic in plane polarized light; under crossed polars it is greyish. Chlorite was identified in thin sections from 480 m and with XRD analysis from 752 m (Figure 8).

2.4.3 Alteration zones

Many hydrothermal minerals in Iceland are highly temperature dependent and definite mineralogical changes are seen to take place with increasing temperature (Kristmannsdóttir and Tómasson, 1978; Malapitan, 1995). In the Icelandic geothermal setting, low-temperature zeolites and amorphous silica form below 120°C, chalcedony below 180°C, quartz above 180°C, wairakite above 200°C, epidote above 230-250°C and garnet and amphibole above 280°C (Kristmannsdóttir, 1979; Saemundsson and Gunnlaugsson, 2002; Franzson, 1998). Clay minerals such as smectite crystallize below 200°C, mixed-layer clays at 200-230°C, and chlorite above 230°C (Kristmannsdóttir, 1977). Based on binocular, petrographic and XRD analysis, four alteration zones were distinguished in HE-58 (Figure 9). The zones were revealed by considering the distribution of secondary minerals as well as the abundance of certain minerals. Alteration zones in well HE-58 are:

Unaltered zone (0-200 m): This zone is composed of fresh rocks with almost no signature of alteration or precipitation of secondary minerals other than cold groundwater minerals. The zone is signified by low-temperature minerals from 0 to 50°C.

Zeolite-smectite (200-450 m): Low-temperature alteration zone which is characterized by the presence of zeolites and low-temperature clays (smectite). The upper boundary of this zone is represented by the first appearance of zeolites at 200 m. The zeolites present as secondary minerals in this zone are commonly thomsonite/mesolite, stilbite and scolecite. Smectite indicates temperature less than 200°C and is first found in XRD analysis at around 450 m.

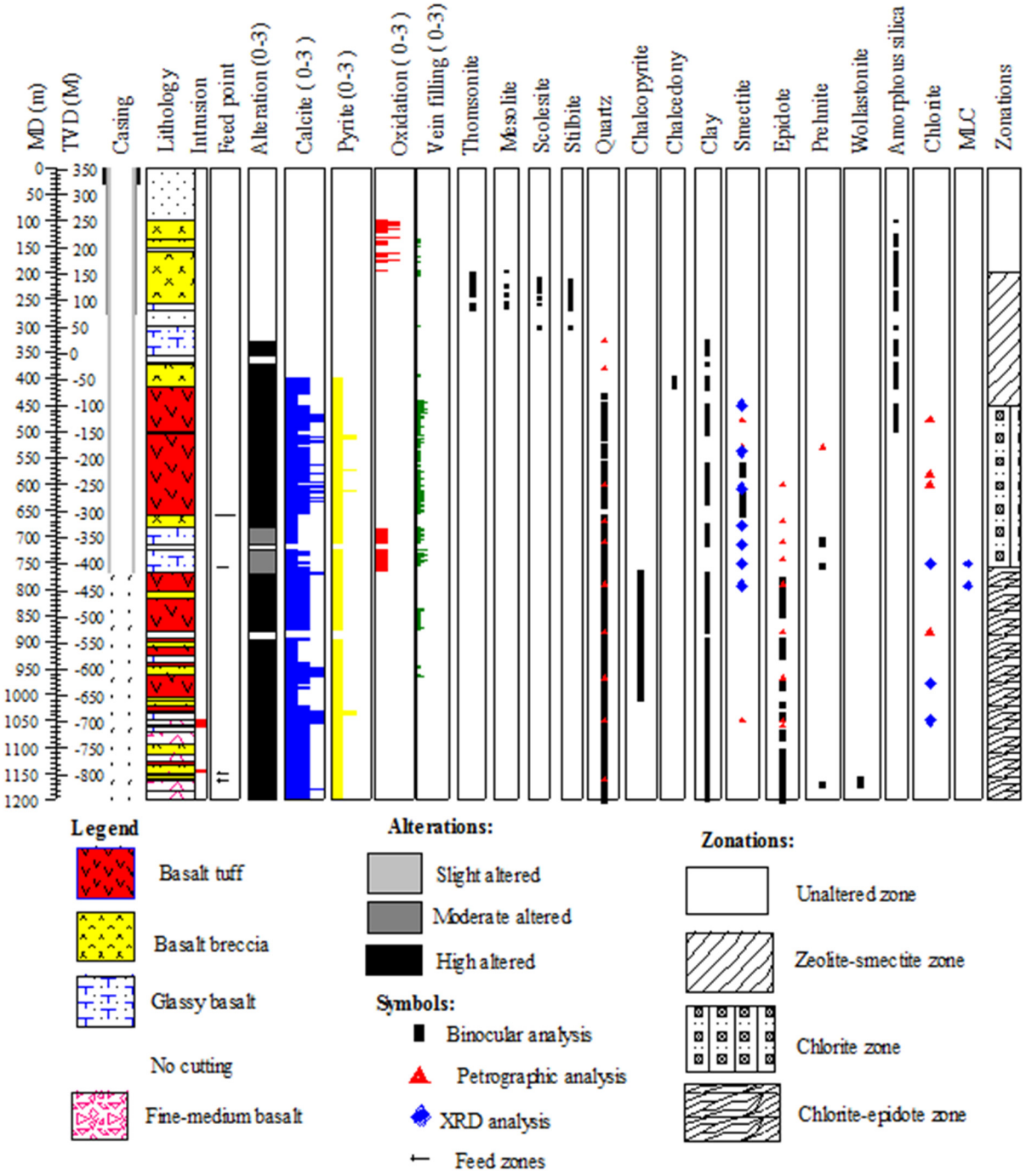

FIGURE 9: Alteration minerals and alteration zones of well HE-58

Chlorite zone (450-760 m): Chlorite is a high-temperature clay mineral which signifies temperature above 230°C and its first appearance marks the top boundary of this zone (Browne, 1978; Franzson, 1987). Chlorite is first identified in thin section at around 480 m but XRD analysis shows chlorite at around 752 m.

Chlorite-epidote zone (760-1200 m): This alteration zone is composed of high temperature secondary minerals such quartz, epidote and chlorite. Mixed-layer clay is also identified in XRD analysis at the same depth as chlorite appears in XRD. Wollastonite appears at around 1160 m (260°C). The characteristic temperature range of this zone in Iceland is about 250-280°C. The upper boundary of this zone was determined from the depth where epidote became common.

3. AQUIFERS

Aquifers are typically water-saturated regions in the subsurface which produce quantities of water to a well. The movement of subsurface water is controlled by the type of rock formations, the characteristics of its permeability and porosity, the temperature and pressure of the subsurface environment, natural recharge, and the hydraulic gradient. The presence of structural formations such as faults, fractures, and joints, lithological contacts, clasts and fragmented matrixes, and paleosols are positive indications of geothermal feed zones (Reyes, 2000). Pillow basalts have higher effective permeability than any other rock type encountered by drilling in Icelandic geothermal areas (Fridleifsson, 1978).

Loss of circulation may vary from minor or weak lossesto total circulation losses that are characterized by highly permeable formations. In the geothermal settings of Iceland, the highest permeable zones intercepted are associated with dykes and faults (Arnórsson, 1995; Pendon, 2006).

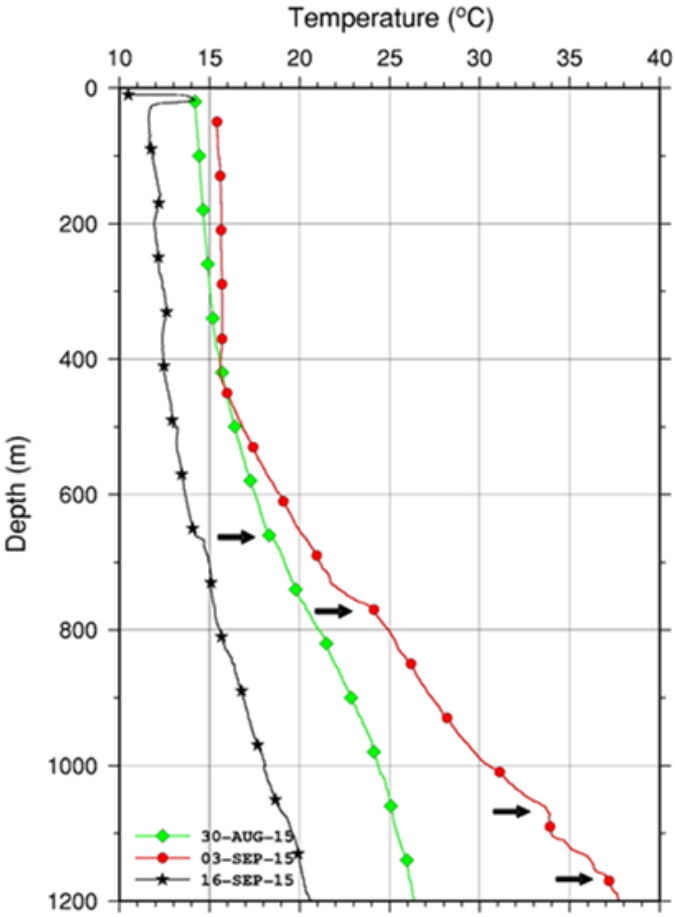

FIGURE 10: Temperature logs from HE-58 while injecting 25 l/s (green), injecting 15 l/s during injectivity test (red) and following stimulation (black) showing the location of permeable zones

In well HE-58, the permeable zones were identified by temperature and geophysical logs (caliper, neutron and gamma logs), increasing alteration minerals (e.g. calcite and pyrite), and circulation losses. Four possible permeable zones were identified at 660 m, 750 m, 1050 m, and 1150 m and they are described below:

Aquifer 1: This feed zone, at around 660 m, was identified by a temperature increase in logs from the 30th of August and 16th of September (Figure 10), located in a tuff and breccia formation.

Aquifer 2: This feed zone is at around 760 m, identified by an increase in temperature and a high peak in the caliper log (Figures 10 and 6). At 770 m (uncorrected depth) there is a lithological contact between glassy basalt and a tuff formation, both rich in calcite and pyrite.

Aquifer 3: This aquifer is at 1050 m indicated by a small increase in temperature, slight peak in the caliper log and a high peak in the gamma ray log as well (Figures 10 and 6). At 1050-1058 m there is a possible intrusion present and there is an increase in both calcite and epidote around that depth.

Aquifer 4: This permeable zone is located at approximately 1150 m in highly altered basaltic breccia, but also rather close to a possible intrusion at 1150-1154 m. The aquifer was seen by an increase in the temperature log from the 3rd of September (Figure 10) and high peak in the caliper log and neutron log (Figure 6). At this depth there is an increase in calcite and epidote and at 1160 m (uncorrected depth) there is significant alteration and abundant wollastonite.

4. FLUID INCLUSIONS

Fluid inclusions are tiny defects in crystals, known as microscopic vacuoles, which are found in minerals such as quartz and calcite, and are trapped inside the crystals during crystallisation (primary inclusion) or recrystallization (secondary inclusion). Secondary inclusions are confined, or trapped, along restored cracks in the crystals and they provide crucial information about the history and condition of the geothermal system, in particular, records of compositional and temperature conditions at the time the inclusions were formed (Roedder, 1984).

A total of 16 fluid inclusions were analysed from well HE-58. The analysis was executed at the University of Iceland using a petrographic microscope and a Linkam THSMG 94 stage. In this study, only quartz and calcite were collected for the analysis. The study was conducted in order to assess whether the geothermal system is heating, cooling or in equilibrium. Samples were collected at the depth of 820-840 m.

Ten inclusions were measured in quartz samples while six came from calcite. The inclusions in the quartz crystals exhibit a range of homogenization temperatures varying from 220 to 264.4°C. One inclusion homogenised at 386.7°C and this may be explained by boiling in the system. On the other hand, calcite inclusions have homogenization temperatures ranging from 262.5 to 271.7°C (Figure 11 and Table 3).

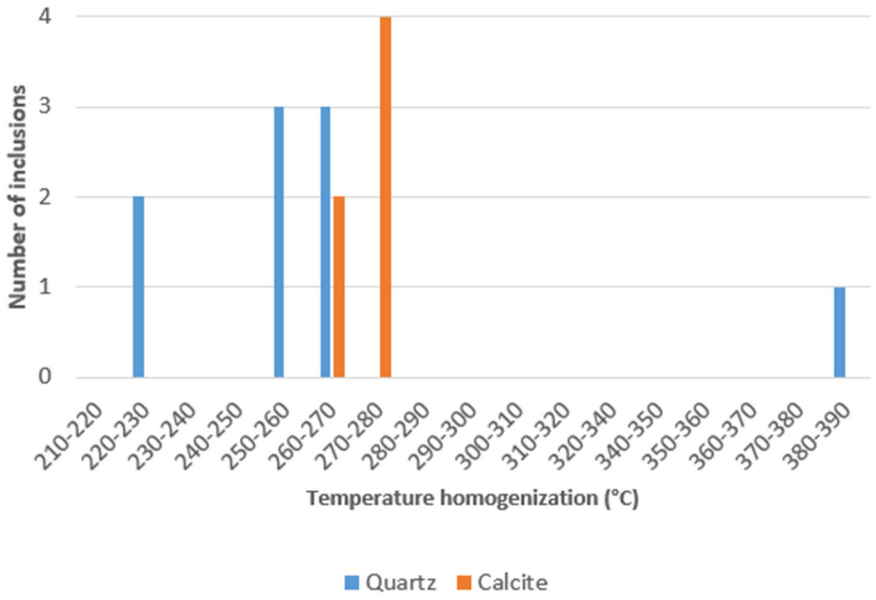

FIGURE 11: Distribution of fluid inclusion homogenization temperatures at 820-840 m in well HE-58

TABLE 3: Fluid inclusion homogenization temperatures in well HE-58

Depth (m)	No. of fluid inclusions	Homogenization temp. (Th) (°C)	Type of crystals
820 - 840	2	220.0	Quartz
	3	250.6	Quartz
	3	264.3	Quartz
	1	386.7	Quartz
	2	262.5	Calcite
	4	271.0	Calcite

5. DISCUSSION

Generally, the stratigraphy of the uppermost 1200 m of well HE-58 consists of hyaloclastite units (basaltic tuff, basaltic breccia, and glassy basalt), with occasional basaltic lava flows (fine- to medium-grained basalt) and basaltic intrusions. The observed basaltic intrusions are identified by their massive and compact character as well as less alteration in comparison to the surrounding lithology.

In borehole geology, the main objective is to discover the characteristics of a geothermal system, that is to say whether the system in question is cooling or heating by studying the different parameters of this discipline.

Geological studies of hydrothermal alteration show that the degree and intensity of alteration of rocks and distribution of mineral alteration increase with depth in well HE-58. Below 750 m depth, the degree of alteration increases rapidly as temperature increases.

Thus, the alteration temperature can be evaluated depending on the appearance of temperature dependent hydrothermal alteration minerals. Minerals are subjected to chemical reactions with respect to the change in the physio-chemical conditions that leads to the formation of diverse assemblage of secondary minerals. Based on these assessments, three alteration zones were identified below an unaltered zone.

These zones are a smectite-zeolite zone, a chlorite zone and a chlorite-epidote zone. The sequence of mineral deposition within the upper part of the well generally shows the hydrothermal system to have evolved from low to high temperature conditions, ranging from zeolites and smectite at the upper part to chlorite, epidote and wollastonite as the well deepens.

The sequence of mineral deposition within the upper part of the well generally also shows the hydrothermal system to have evolved from low to high temperature conditions, e.g. wollastonite following epidote precipitation.

The distribution of fluid inclusion homogenization temperature of quartz and calcite samples generally shows temperatures around 250-270°C. The fluid inclusions appear to be in equilibrium with the alteration mineralogy (Figure 12). The available temperature logs do not show the true formation temperature, since the well was still heating up at the time of the study. Therefore, it is difficult to assess whether the system at this location is heating up, cooling down or in equilibrium.

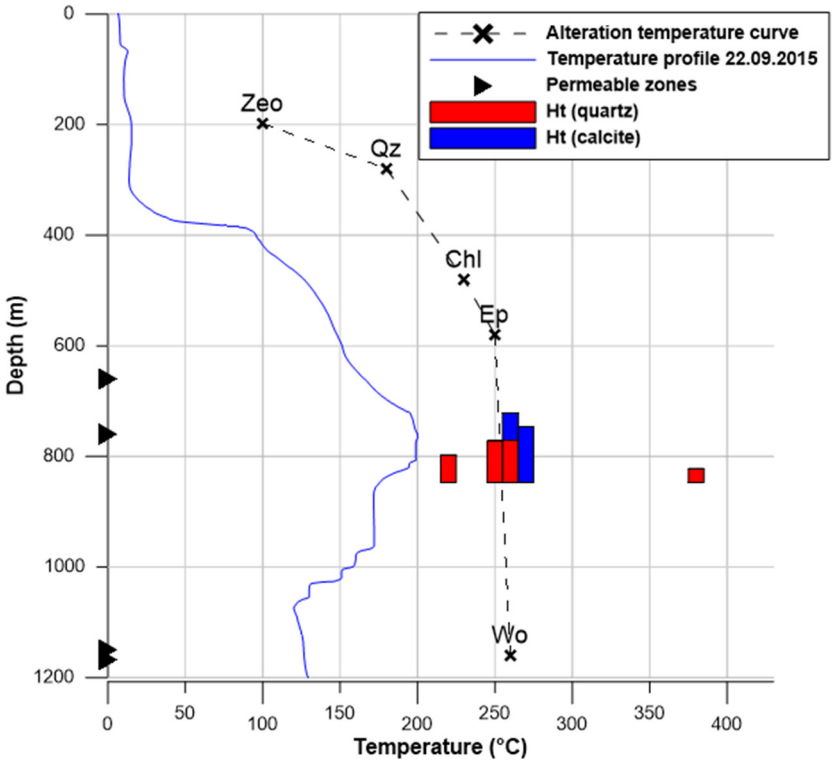

FIGURE 12: Temperature log (blue line) and alteration (black dashed line) with homogenization temperatures of fluid inclusions

6. CONCLUSIONS

The following conclusions can be deduced from the geological study of well HE- 58:

- The stratigraphy of the first 1200 m of well HE-58 consist of hyaloclastite formation (basaltic breccia, basaltic tuff and glassy basaltic), some crystalline basaltic lava flow (fine- to medium-grained basalt), and a couple of possible basaltic intrusions.
- Alteration mineral distribution shows a general tendency to gradual increasing alteration with depth where low-temperature minerals such as zeolites, are gradually replaced by moderate temperature minerals such as quartz, which are quickly followed by high temperature mineral assemblages such as chlorite, prehnite, epidote and wollastonite.
- According to the distribution of alteration minerals, four alteration zone were identified and arranged according to the first appearance of key index minerals. Unaltered zone (<50°C), a zeolite-smectite zone (<200°C), a chlorite zone (230-250°C) and a chlorite-epidote zone (250-280°C).
- Based on the geophysical logs and the intensity of alteration, four permeable zones were distinguished, located at 660 m, 760 m, 1050 m and 1150 m.
- Fluid inclusion temperature at 820-840 m is generally between 250 and 270°C. When compared to the prevailing alteration temperature at that depth, we can deduce that the fluid inclusions appear to be in equilibrium with the alteration mineralogy. Comparison with the formation temperature was not possible as the well was still heating up at the time of this study.

ACKNOWLEDGEMENTS

I wish to express my sincere gratitude to the Government of Iceland and the United Nations University (UNU), for granting me a fellowship to undertake specialized training at the UNU-Geothermal Training Programme.

Indeed, the success and final outcome of this project required a lot of guidance and assistance from many people and I am extremely fortunate to have gotten this for the completion of my project. That I have done this is only due to such guidance and assistance and I will not forget to thank them. Special thanks to the UNU-GTP Director, Dr. Lúdvík S. Georgsson for awarding me the opportunity to study in Iceland; many thanks to Mr. Ingimar Gudni Haraldsson, Ms. Málfrídur Ómarsdóttir, Mr. Markús A.G. Wilde, Ms. Thórhildur Ísberg and Ms. María Gudjónsdóttir for their support and help in the programme.

My heartfelt and sincere thanks also go to my supervisor, Dr. Björn S. Hardarson and my second supervisor Ms. Helga Margrét Helgadóttir, for their excellent supervision, their cordial helpfulness, valuable advice and encouragement during the entire project period. I would like to thank all the lecturers and the staff members at Orkustofnun and ISOR for the knowledge, assistance and valuable comments given to us during the lecture sessions. I also thank the dear UNU Fellows of 2015 for their unbelievable friendship and cooperation during our training time, especially my brothers and gentlemen geologists.

My very sincere gratitude goes to my wonderful amazing family, sisters, brothers and friends, especially my lovely mom, my beloved auntie and the first man in my life my dad for their encouragement and motivation.

Above all, I praise God, the almighty for providing me with this opportunity and granting me the capability to proceed successfully.

REFERENCES

Árnason, K., Karlsdóttir, R., Eysteinsson, H., Flóvenz, Ó.G., and Gudlaugsson, S.Th., 2000: The resistivity structure of high-temperature geothermal systems in Iceland. *Proceedings of the World Geothermal Congress 2000, Kyushu-Tohoku, Japan,* 923-928.

Árnason, K., and Magnússon, I.Th., 2001: *Geothermal activity in the Hengill area. Results from resistivity mapping.* Orkustofnun, Reykjavik, report, OS-2001/091 (in Icelandic with English abstract), 250 pp.

Arnórsson, S., 1995: Geothermal systems in Iceland; structures and conceptual models; I, high temperature areas. *Geothermics, 24*, 561-602.

Björnsson, A., Hersir, G.P., and Björnsson, G., 1986: The Hengill high-temperature area SW-Iceland: Regional geophysical survey. *Geothermal Resources Council, Trans., 10,* 205-210.

Björnsson, G., Hjartarson, A., Bödvarsson, G.S., and Steingrímsson, B., 2003: Development of a 3-D geothermal reservoir model for the Greater Hengil volcano in SW-Iceland. *Proceedings of TOUGH Symposium 2003, Lawrence Berkeley Laboratory, Berkeley, California, USA*, 11 pp.

Browne, P.R.L., 1978: Hydrothermal alteration in active geothermal fields. *Annual Reviews of Earth and Planetary Science, 6,* 229-250.

Elmi H., D., 2008: *Geothermal resource assessment through well testing and production response.* University of Iceland, MSc thesis, UNU-GTP, report 1, 73 pp.

Franzson, H., 1987: The Eldvörp high-temperature area, SW Iceland. Geothermal geology of the first exploration well. Proceedings of the 9th New Zealand Geothermal Workshop, Auckland, NZ, 179-185.

Franzson, H., 1998: Reservoir geology of the Nesjavellir high-temperature field in SW-Iceland. *Proceedings of the 19th Annual PNOC-EDC Geothermal Conference, Manila*, 13-20.

Franzson, H., Árnason, K., Saemundsson, K., Steingrímsson B., and Gunnlaugsson E., 2010: The Hengill geothermal system, conceptual model and thermal evolution. *Proceedings of the World Geothermal Congress 2010, Bali, Indonesia*, 9 pp.

Franzson, H., Kristjánsson, B.R., Gunnarsson, G., Björnsson, G., Hjartarson, A., Steingrímsson, B., Gunnlaugsson, E., and Gíslason G., 2005: The Hengill Hellisheidi geothermal field. Development of a conceptual geothermal model. *Proceedings World Geothermal Congress 2005, Antalya, Turkey,* CD, 7 pp.

Fridleifsson, I.B, 1978: Applied volcanology in geothermal exploration in Iceland. *Pageoph, 117*, 242-252.

Fridleifsson, I.B., 1979: Geothermal activity in Iceland. *Jökull, 29,* 47-56.

Gebrehiwot Mesfin, K., 2010: *Subsurface geology, hydrothermal alteration and geothermal model of northern Skardsmýrarfjall, Hellisheidi geothermal field*. University of Iceland, MSc thesis, UNU-GTP, report 5, 65 pp

Gunnarsson, G., 2011: A story of success and failures, mastering reinjection in the Hellisheidi field,SW-Iceland. *Proceedings of the 36th Workshop on Geothermal Reservoir Engineering, Stanford University, Stanford, Ca*, 8 pp.

Gunnarsdóttir, S.H., Tryggvason, H. and Hardarson, B.S., 2015: *Pre-drilling, 1st and 2nd sections: Drilling for surface casing to 98 m, safety casing to 289 m and production casing to 769 m depth.* ÍSOR - Iceland GeoSurvey, report ÍSOR-2015/044 (in Icelandic).

Henley, R.W. and Ellis, A.J. 1983: Geothermal systems ancient and modern: a geochemical review. *Earth Science and Reviews, 19,* 1-50.

Kristmannsdóttir, H., and Tómasson, J., 1978: Zeolite zones in geothermal areas in Iceland. In: Sand, L.B., and Mumpton (eds.), *Natural zeolites, occurrence, properties, use*. Pergamon Press Ltd., 277- 284.

Kristmannsdóttir, H., 1977: Types of clay minerals in altered basaltic rocks, Reykjanes, Iceland (in Icelandic). *Jökull, 26,* 3-39.

Kristmannsdóttir, H., 1979: Alteration of basaltic rocks by hydrothermal activity at 100-300°C. In: Mortland, M.M., and Farmer, V.C. (editors). *International Clay Conference 1978.* Elsevier Scientific Publishing Co., Amsterdam, 359-367.

Malapitan, R.T., 1995: Borehole geology and hydrothermal alteration of well KR-9, Krýsuvík, SWIceland. Report 8 in: *Geothermal Training in Iceland 1995*. UNU-GTP, Iceland, 185-206.

Njue, M.L.M., 2010: Borehole geology and hydrothermal mineralisation of well HE-27, Hellisheidi geothermal field, SW-Iceland. Report 24 in: *Geothermal training in Iceland 2010.* UNU-GTP, Iceland, 463-492.

Lugaizi. I., 2011: Borehole geology and hydrothermal mineralisation of well HE-32, Hellisheidi geothermal field, SW-Iceland. Report 20 in: *Geothermal training in Iceland 2011.* UNU-GTP, Iceland, 417-465.

Pendon, R.R., 2006: Borehole geology and hydrothermal mineralisation of well HE-22, Ölkelduháls field, Hengill area, SW-Iceland. Report 17 in: *Geothermal training in Iceland 2006.* UNU-GTP, Iceland, 357-390.

Reyes, A.G., 1990: Petrology of Philippine geothermal systems and the application of alteration mineralogy to their assessment. *J. Volc. Geoth. Res., 43*, 279-309.

Reyes, A.G., 2000: *Petrology and mineral alteration in hydrothermal systems: from diagenesis to volcanic catastrophes*. UNU-GTP, Iceland, report 18-1998, 77 pp.

Roedder, E., 1984: *Fluid inclusions*. Mineralogical Society of America, Washington, DC, Reviews in Mineralogy, 12, 646 pp

Saemundsson, K., and Gunnlaugsson, E., 2002: *Icelandic rocks and minerals*. Edda and Media Publishing, Reykjavík, Iceland, 233 pp.

Saemundsson, K., 1979: Outline of the geology of Iceland. *Jökull, 29*, 7-28.

Saemundsson, K., 1967: *Vulkanismus und Tektonik des Hengill-Gebietes in Sudwest-Island*. Acta Nat. Isl., II-7 (in German), 195 pp.

Sradon, J., 1999: Nature of mixed-layer clays and mechanisms of their formation and alteration. *Annu. Rev. Earth Planet. Sci., 27*, 19-53.

APPENDIX I: XRD clay mineral analysis results from well HE-58

TABLE 1: List of samples with XRD clay mineral analysis results upper at 1200 m from well HE-58

Samples no	Depth (m)	D (001) untreated sample	d (001) glycolated sample	d (001) heated sample	d (002)	Mineral
1	302	0	0	0	0	No clay
2	450	12.96	13.74	10.00	9.15	Smectite
3	540	12.87	13.46	10.00	9.20	Smectite
4	610	15.91	17.29	10.00	0	Smectite
5	680	13.42	13.44	10.00	0	Smectite
6	714	12.99/12.87	14.77	12.99	0	Smectite
7	752	14.65	16.69	10.47	7.31	Smectite
8	792	15.16	16.93	10.07	7.37	MLC
9	810	13.61	15.16	10.23	0	MLC
10	844	15.16	17.11	10.17	0	Smectite ??
11	930	0	0	0	0	No clay
12	980	15.16	15.64	10.17	7.34	Chlorite
13	1048	14.75	0	0	1.34	Chlorite
14	1150	0	0	0	8.75	??

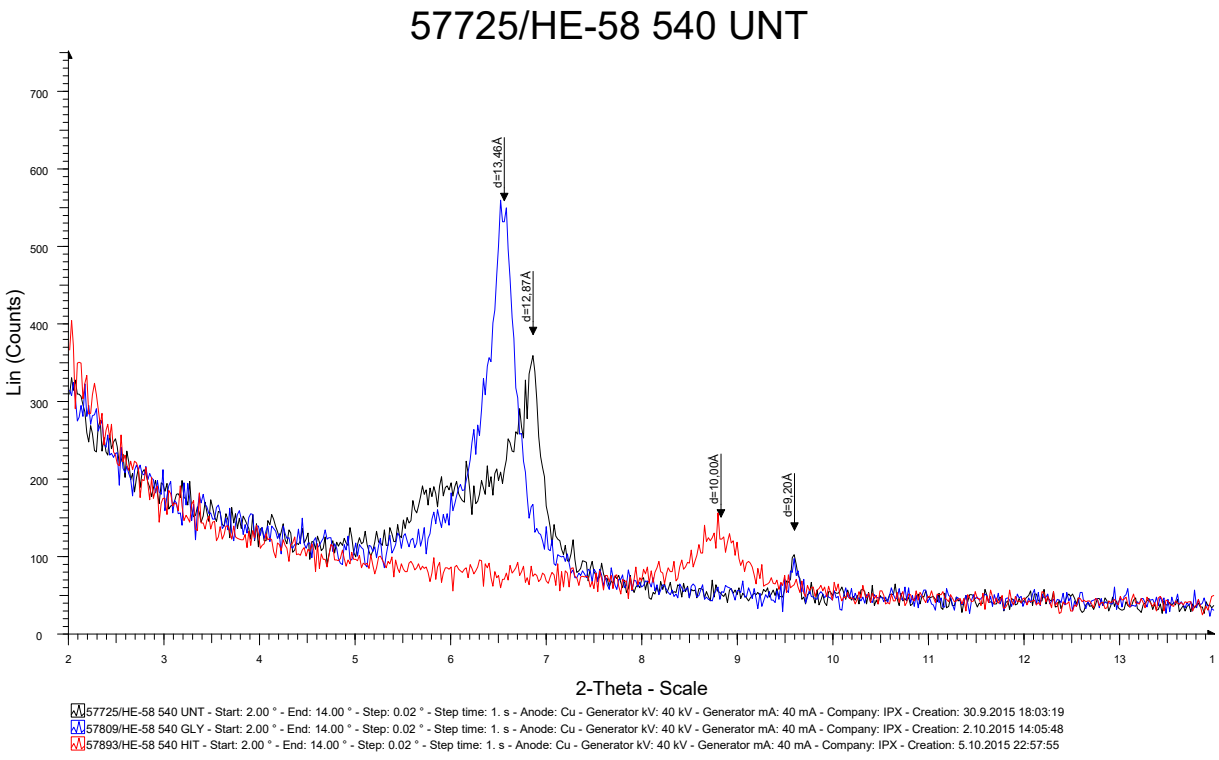

FIGURE 1: HE-58, XRD analysis of a sample 1 from 540 m

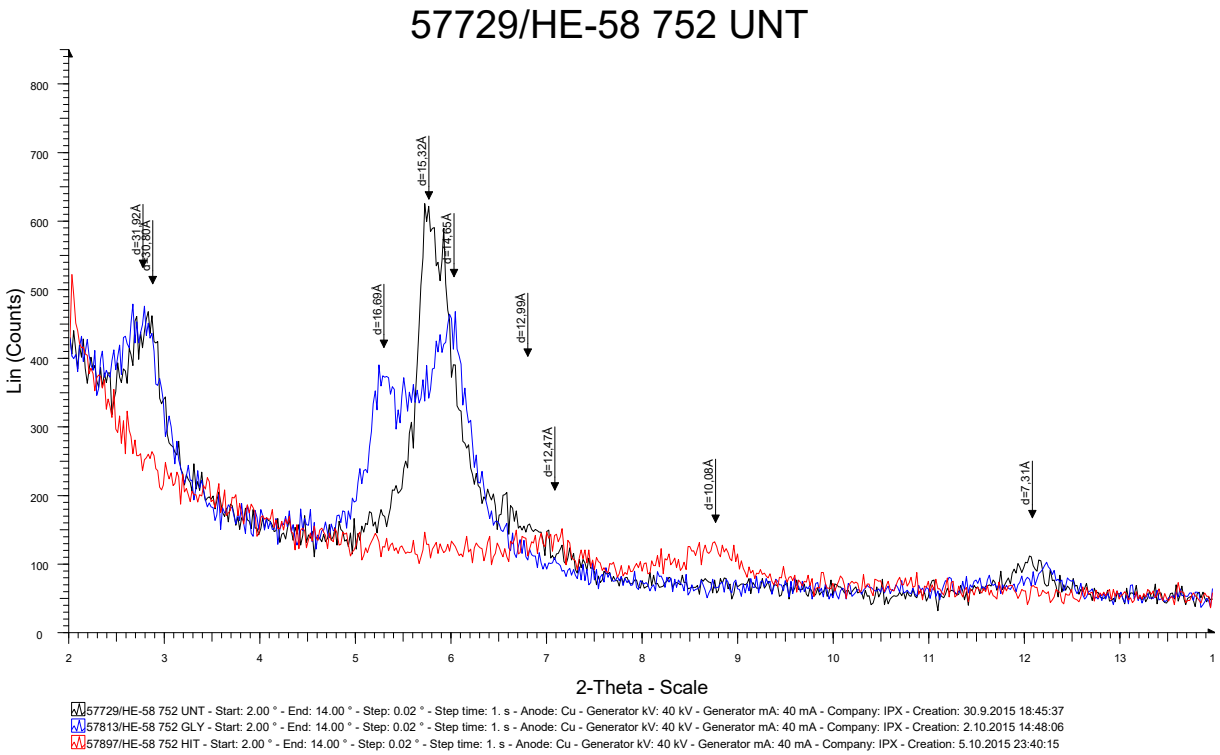

FIGURE 2: HE-58, XRD analysis from 752 m

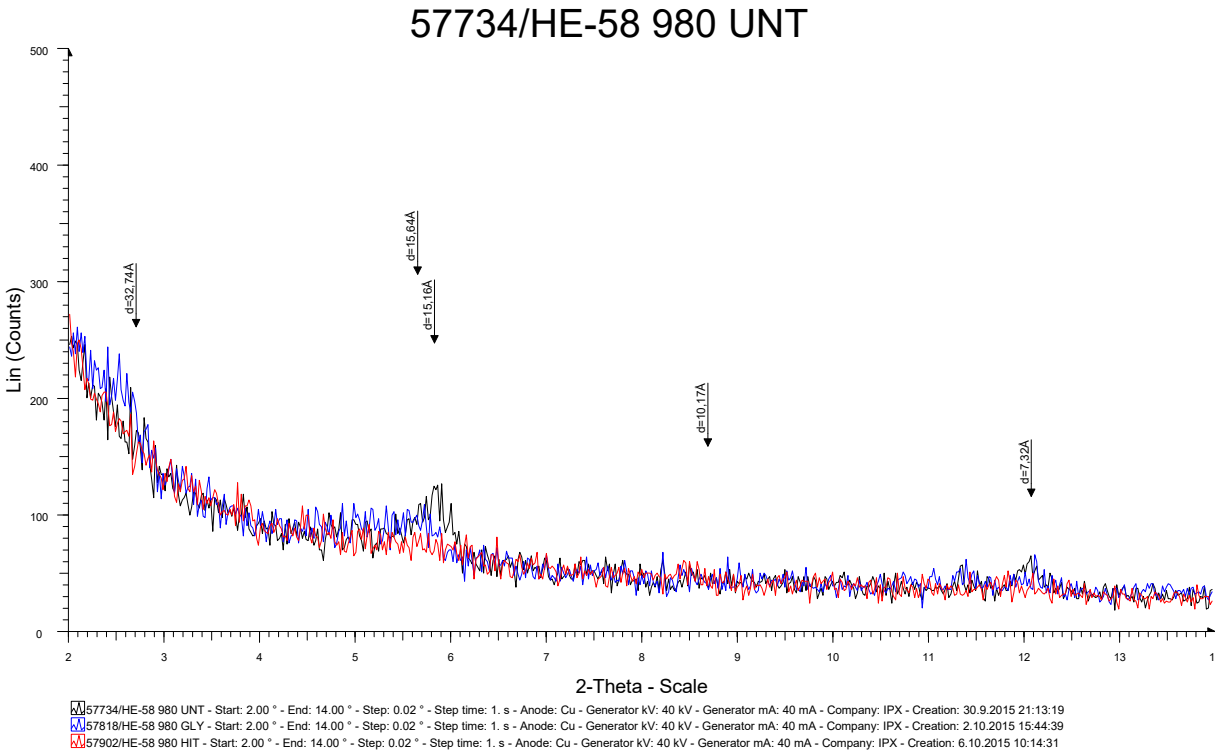

FIGURE 3: HE-58, XRD analysis from 980 m

UNITED NATIONS UNIVERSITY
UNU-GTP
Geothermal Training Programme

Orkustofnun, Grensasvegur 9,
IS-108 Reykjavik, Iceland

Reports 2015
Number 16

CONCENTRATIONS OF SELECTED TRACE ELEMENTS AND IONS IN SPENT GEOTHERMAL LIQUID AND ASSOCIATED IMPACTS ON GROUNDWATER, SOIL AND VEGETATION IN THE MENENGAI GEOTHERMAL FIELD

Fridah Nkatha Kiara
Geothermal Development Company
P.O Box 17700-20100, Nakuru
KENYA
fnkatha@gdc.co.ke

ABSTRACT

To assess the effect of spent geothermal liquids from discharging wells at the Menengai geothermal field on the environment, the concentrations of Na, Cl, K and F ions and the trace elements B, As, Hg, Cd, Cr and Pb in spent geothermal liquid from six geothermal wells and groundwater from four boreholes were analysed. Soils and vegetation in the vicinity of two of the six geothermal wells were also assessed for the concentrations of the trace elements B, As, Hg, Cd, Cr and Pb. Furthermore, the concentrations in spent liquids and groundwater were compared to the local standards for effluent released into the environment and the World Health Organization (WHO) drinking water standards. The soil and vegetation were compared to a reference site 2.5 km away from the discharging wells and further compared to the Food and Agricultural Organization (FAO) standards. The results showed concentrations of the ions Na, Cl and F and the trace elements As, Hg, Cr and Pb in the spent geothermal liquid from some the wells above the requirements of the local effluent standards. In groundwater, the fluoride concentration was double the WHO drinking water standard of 1.5 mg/l, which is typical for groundwater in the Kenyan Rift Valley. All the trace element concentrations were below the WHO drinking water standards except for Pb in two boreholes. In soil and vegetation, all the trace element concentrations were within the reference site levels and the FAO standards. To estimate the effect of the spent geothermal liquid on the groundwater, soils and vegetation, separate linear models were run. The model results indicated no contamination of groundwater, surrounding soils and vegetation by spent geothermal liquid. However, there was limited data for this study and therefore more data is needed to evaluate future impacts. More adequate measures on proper management of the spent geothermal liquid need to be emphasised before reinjection. Measures, such as routine maintenance of High Density Polyethylene (HDPE) liners to avoid seepage of the spent geothermal liquid into the environment, should be considered. Moreover, continuous monitoring of ions and trace elements with more ecosystem components such as other dominant vegetation should also be implemented.

1. INTRODUCTION

1.1 Background

The exploitation of geothermal energy is typically referred to as clean when compared to alternative energy sources such as fossil fuels due to the fact that the potential negative impacts can be mitigated to a larger extent (Kristmannsdóttir and Ármannsson, 2003). The energy is obtained from the earth by drilling into underground geothermal reservoirs. Deep geothermal wells are drilled to a depth of about 1000 m to 3000 m. Hot fluids from the deep geothermal reservoirs are used for electricity generation and other direct uses. During development and utilization of geothermal energy, especially in high temperature liquid dominated systems, dry steam is separated from the fluid for utilization and the remaining product*, spent geothermal liquid* is discharged to the surface. Depending on the geothermal reservoir, the volume of the discharged spent geothermal liquid may vary between wells and fields. In most cases large volumes are reported, for example the Hellisheidi 303 MWe geothermal power plant in Iceland produced 23 million tonnes of spent geothermal liquid in 2014 (Sigurdardóttir and Thorgeirsson, 2014).

The spent geothermal fluids contain several elements and compounds at elevated levels that can pose threats and adverse effects on the environment if not properly contained or discharged, particularly because the fluids are produced during various stages of geothermal development and utilization. The spent geothermal fluids occur in two forms, i.e. either as steam or liquid. Steam plumes are discharged into the atmosphere, especially during well testing, and primarily consist of 95–98% water vapour and uncondensed gases with traces of heavy metals and other elements (Axtmann, 1975). The liquid on the other hand is discharged during drilling, well testing and as separated water from the power plants. During these geothermal development processes, the steam plumes are allowed to disperse into the air while the spent geothermal liquid is directed to ponds which are lined with impervious material for temporary containment awaiting further disposal in either surface water ways or through deep reinjection. In the ponds, the geothermal liquid is contained to cool and reduce its effect on surface water ways during disposal. The containment methods may however be inefficient especially during well testing, which normally lasts a month or longer, resulting in the production of large volumes of spent liquids that may exceed the size of the ponds' carrying capacity and thereby spilling into the nearby environment occurs. The spillages can then get in direct contact with the soil, vegetation and surface water with chances of percolating into sub-surface water and ultimately contaminating the groundwater.

The composition of the spent geothermal fluids primarily consists of dissolved ions and trace elements such as sodium (Na), potassium (K), calcium (Ca), magnesium (Mg), iron (Fe), chloride (Cl), molybdenum (Mo), silica (Si), aluminium (Al), arsenic (As), cadmium (Cd), chromium (Cr), mercury (Hg), lead (Pb), selenium (Se) and boron (B) (Ármannsson and Fridriksson, 2009). The concentrations may vary between reservoirs depending on the rock composition, chemical and physical conditions of the weathering solution, the contribution from magmatic gases and adsorption of metal ions on oxide particles (Aiuppa et al., 2000). These ions and elements are well known to have detrimental short or long term effects on organisms if they deposit and bio-accumulate in vegetation, soils and water resources above tolerable levels. Some of these ions and trace elements such as F, and Cr at low concentrations are essential for the normal growth and development of living organisms. However, others like As and Hg in both low and high concentrations have the potential to contaminate the surface and groundwater adversely affecting aquatic ecosystems (Webster and Nordstrom, 2003).

During the early decades of utilization of geothermal energy, the impacts of spent geothermal liquids on the environment had not been widely studied as there were no strict environmental laws and regulations in place. The liquids were discharged onto the surface or into the nearby surface water ways owing to the low awareness on the associated environmental impacts and because these were the least cost methods available for disposal. During the 1960s for example, an 82 km long canal was constructed for disposal of spent geothermal liquid from the Ahuachapán geothermal field in El Salvador to the Pacific Ocean (Goff and Goff, 1997). A decade later, the effects of spent geothermal liquids on the environment

became evident as environmental awareness levels advanced with the onset of Environmental Impact Assessment (EIA) studies and the subsequent monitoring and management plans to avoid adverse environmental effects. Today, proper disposal methods of spent geothermal liquids guided by policies that specify their proper handling in order to minimize environmental pollution have been developed and continue to improve based on new research findings. Presently, studies on the impacts of spent geothermal liquids on the environment in most geothermal fields around the world have become important. However, there is very limited information documented on the effects of spent geothermal liquids on soils and vegetation. In line with every geothermal projects' environmental management plan, conservation of biodiversity is important. It is therefore necessary to understand the impacts of spent geothermal liquid on the ecosystem for enhanced mitigation measures to minimise or avoid environmental degradation.

In Kenya, the generation of electricity from geothermal resources began in the early 1980s at the Olkaria geothermal field. Prospecting for the resource and drilling of wells commenced in the 1950s. The Olkaria field is located within the Hell's Gate National Park (HGNP) which is managed by the Kenya Wildlife Service (KWS). The geothermal project co-exists harmoniously with the wild life in accordance to a Memorandum of Understanding (MoU) between the KWS and the Kenya Electricity Generating Company Ltd (KenGen) which stipulates proper management of all environmental concerns. Presently, there are about two hundred geothermal wells and four geothermal power plants, i.e. Olkaria I, II, III, IV with an installed electric capacity of 630 MWe in the Olkaria geothermal area. At Olkaria, one of the main environmental challenges is the large volume of spent geothermal liquids produced at various stages of geothermal development and utilization and the consequent environmental effects. However, stringent measures on proper handling and disposal of these liquids have been enforced following an environmental management plan. Proper containment and re-injection of these liquids is practised at Olkaria and various geothermal fields all over the world today, not only for environmental reasons but because the process is also known to maintain the reservoir pressure. A study by Were (2007) on the speciation of trace elements concentration in spent geothermal liquid and the potential effects on the environment at the Olkaria geothermal field revealed elevated As, Hg, Mo and F concentrations beyond the Kenyan maximum permissible limits for recreational water and effluent discharged to the terrestrial environment. The other elements in the study, i.e. Al, As, Cd, Hg, Cu, Pb and Zn were below permissible limits.

The Menengai geothermal field is the second largest field to be developed in Kenya after the Olkaria geothermal field. Similar to Olkaria and other geothermal fields in the world, large volumes of spent geothermal liquid are produced. Nonetheless, studies on the potential environmental impacts are not fully explored. An Environmental Impact Assessment (EIA) for drilling of geothermal wells at the Menengai geothermal field was carried out in 2008 before drilling commenced. The study provided baseline data on the surface water chemistry of two seasonal streams, i.e. Kanduturi and Wanyororo streams which flow within the caldera, before geothermal activities started. The baseline data on the water quality was therefore important for correlation with future monitoring efforts of the same streams and other environmental components to assess potential contamination with the onset of exploitation activities in the geothermal field for planning of mitigation measures. The physical and chemical parameters that were analysed in the streams include, but are not limited to, pH, Na, SiO_2, Pb, Cu, Cd, B, Cl, F and Li, which were all within the National Drinking water standards except for Pb and F (Wetang'ula et al., 2008). However, in the EIA study, baseline data on the physical and chemical composition for the soil and vegetation at the Menengai geothermal field was not provided.

In this study, the concentrations of selected ions and trace elements in spent geothermal liquid, groundwater, soils and vegetation in the vicinity of geothermal wells at the Menengai geothermal field were assessed and presented. Furthermore, the impact of these element concentrations on soils, vegetation, and groundwater was evaluated to determine patterns that could infer possible contamination. The findings of this study are important to provide baseline information which will strengthen the environmental monitoring programmes and aid in improvement of current mitigation measures.

This study is specifically sought to:

1. Assess the concentrations of Na, Cl, K and F ions and the trace elements B, As, Hg, Cd, Cr and Pb in spent geothermal water from six appraisal wells and to compare the results with the local standards for discharge into the environment (Republic of Kenya, 2006).
2. Assess the concentrations of Na, Cl, K and F ions and the trace elements B, As, Hg, Cd, Cr and Pb in groundwater from four boreholes and to compare the results with the World Health Organization (2008), standards for drinking water.
3. Assess the concentrations of the trace elements B, As, Hg, Cd, Cr and Pb in soils and vegetation in the vicinity of two appraisal wells and compare with the FAO soil and vegetation standards.
4. To assess the potential environmental impacts of spent geothermal liquid on soils, vegetation and groundwater.

2. PREVIOUS STUDIES

Studies on the environmental impacts that arise during development of geothermal resources have been done intensively in various geothermal fields all over the world today. Some studies have been done on the impacts of spent geothermal liquids on the environment in various countries utilizing geothermal energy. For instance in Tuscany, central Italy, Bargagli et al. (1997) studied the environmental effects of trace elements emissions from geothermal power plants in mosses, organs of small mammals, fodder-plants and vegetables for human consumption grown within a 1-2 km radius from the geothermal power plant. A notable increase was detected in the deposition of Hg, B, As, and Sb in the biological samples collected a few hundred meters away from the geothermal power plants. The amounts decreased with increasing distance from the geothermal plant. Due to the trend of the high trace element concentrations in these components decreasing with increasing distance, the implication was that part of these trace elements emanated from the geothermal power plants emission. Concentrations of Hg, B, As and Pb were below permissible levels for vegetables and fodder crops consumption in the vicinity of the power plant and were suitable for human consumption (Bargagli, et al., 1997).

In the Philippines at the Northern Negros geothermal project, a similar study on the effect of spent geothermal fluid during well testing on the surrounding vegetation was done (Tuyor et al., 2005). The results showed significant impacts of elevated concentrations of Na, Cl, and B on the vegetation in the vicinity of the wells. According to the study, the vegetation was subject to long term and higher negative effects during well testing especially when wells blew over a month for adequate measurements and evaluation of the reservoir capacity to generate electricity. The results indicated that salinity and other associated ions of geothermal fluids could be a possible cause of leaf drying which later leads to abnormal defoliation of the exposed vegetation in the vicinity of a well during well testing and that the environmental impacts were widespread during vertical discharge compared to horizontal discharge (Tuyor et al., 2005).

In Iceland, spent geothermal liquids from the Hellisheidi and Nesjavellir geothermal power plants are reinjected back into the reinjection wells and part of the liquid is released to the surface. At Nesjavellir geothermal plant about half of the spent liquid is reinjected and half of it is released on the surface and finds its way into Lake Thingvallavatn. Hellisheidi, on the other side, obtained a permit that allows the release of the spent liquid onto the surface in case of emergencies but most of the liquid is re-injected. Continuous monitoring of the spent geothermal liquid has been on-going at the two power plants in order to assess any potential effects to the nearby surface water resources. The spent geothermal liquids at both power plants showed elevated levels of As, Al and K concentrations which were beyond the Icelandic limits tolerable for groundwater (Sigurdardóttir and Thorgeirsson, 2014). The As concentration of spent liquid from Nesjavellir power plant were pointed out as a major threat of contamination to the nearby and conserved Lake Thingvallavatn, thus posing a high risk of damaging effects to the aquatic life and surrounding terrestrial plants (Wetang'ula, 2004).

In Kenya, a few studies have also been done on the impacts of spent geothermal liquids on the environment, particularly in the Olkaria geothermal field (Simiyu and Tole, 2000; Wetang'ula, 2004 and Were, 1998; 2007). Simiyu and Tole, (2000) studied the concentration of selected trace elements, i.e. Pb, Zn, Cu, Cd, B, As, and Hg in spent geothermal liquid around the Olkaria wells and the potential effects on the food chain through soils and plants in contact with the liquid. The findings of their study revealed higher levels of Pb, Cd, Cu, and B in spent liquid compared to the nearby Lake Naivasha located approximately 12 km SW of Olkaria, which was also used as the reference site. In addition, the soils and vegetation in contact with the spent geothermal liquids also showed concentrations of the elements by factors of between 13 and 6000 compared to concentrations in the overlying spent liquid. In another study, Wetang'ula, (2004) assessed the trace elements concentration in spent geothermal liquids at Olkaria. The findings showed elevated concentrations of As, Mo, Al, and B in spent geothermal liquid compared to the Canadian environmental quality guidelines for plants and livestock. The indication was that these levels posed an eco-toxicological hazard to the environment. All these studies done in Olkaria recommended stringent measures on proper disposal of spent liquids, i.e. containment of spent liquid in lined ponds and continuous reinjection of spent liquid in order to trace elements accumulation in the soils and their uptake by plants and animals, therefore contaminating the food chain.

2.1 Review of selected trace elements and toxicity on the ecosystem

Boron is released into the environment through natural weathering of rocks and from volcanic and other geothermal activities. Boron is found both in geothermal steam and liquid. The addition of B to the environment can also be anthropogenic which include the use of borate containing fertilizers and herbicides and as waste released from borate mining process (Koç, 2007). In trace amounts, it is an essential nutrient for normal growth and development in some plants. However, in high concentration B can be toxic to plants, aquatic and micro-organisms. Plants in general, are far more sensitive than animals to boron toxicity. High levels of boron accumulate in plants and might lead to chlorosis and necrosis eventually burning and scorching the leaves (WHO, 2008). Naturally B is present in surface and underground water primarily as a result of leaching from rocks and soils containing borates and borosilicate, however if excess B is ingested through drinking water for a long period, the immune system can be highly affected (WHO, 2008). An example is given by Guo et al., (2008) where high concentrations of B of up to 3.82 mg/l were measured downstream in the Zangbo River in China, which was due to the discharging of spent geothermal liquid from the geothermal power plant at Yangbajing, which had extremely high B concentration levels of up to 119 mg/l. The geothermal power plant at Yangbajing area in China affected the water quality of the Zangbo river thus causing health problems of the people living in the downstream of Yangbajing area.

Arsenic is also found naturally in the minerals in the earth's crust and in soil, rock, water, and air. There are various sources of arsenic including natural sources such as volcanic activities, geothermal processes, and those caused by human activities which are the main contributors of As concentrations in the environment today. Arsenic was declared a human carcinogen contributing to a high incidence of skin and other cancers in populations exposed to high levels of arsenic leading to As concentration standards in water being lowered from 0.05 mg/l to 0.01 mg/l (Nordstrom, 2002). The element is mostly present in active and fossil geothermal systems and can cause contamination of surface and underground waters and can accumulate in plants and soils. For instance, As released into a river will interact with plants, biota, suspended material, and bed sediments thus potentially contaminating the food chain. Webster and Nordstrom (2003) indicated that the higher As concentrations in suspended sediments of the Waikato river were a function of their proximity to geothermal activity, i.e. where the river passes through the area of geothermal activity and that 7-8% of the As entering the river was adsorbed by the sediments.

High levels of mercury (Hg) in the environment have been recorded in areas where there is discharge and emissions from coal, hydro and geothermal power plants, mining and industrial activities. For

instance, Axtmann, (1975) reported elevated Hg concentrations in the Waikato River compared to the spent geothermal liquid from the Wairakei plant in New Zealand which was adversely affecting the aquatic life and quality of the water. Mercury present in the air is deposited into water because of its ability to travel long distances in the air and the bacteria in the surface waters and sediments then converts elemental Hg into organic Hg compounds such as methylmercury. Methylmercury accumulates in fish at levels that may harm the fish and other aquatic life hence leading to mercury accumulation through the food chain.

Cadmium is generally present in the environment at low levels. It is naturally released to the environment through volcanic activities, weathering and erosion. However, human activities have greatly contributed to its increase into the environment through mining, smelting, industrial activities and, utilization of fossil fuels among others. The element has been classified as a human carcinogen by WHO. Moreover, Cd is primarily present in naturally occurring geothermal waters like the hot springs and also in spent geothermal liquid according to the findings by Simiyu and Tole (2000). The study reported Cd concentrations in the naturally occurring hot spring at Olkaria and the spent geothermal liquids from the wells to be in the range of 0.002-0.009 mg/l. The WHO drinking water recommended limit for Cd is 0.003 mg/litre. The Cd concentration in soil and vegetation in contact with the spent geothermal liquid were also reported to be in the range of 18.1–80 mg/l and 0.8–1.0 mg/l, respectively which is below the FAO soil and vegetation standards. High Cd levels in the environment can cause adverse health effects since Cd in soil and water can be taken up by certain crops and aquatic organisms and accumulate in the food-chain, hence affecting human beings especially the kidneys and the skeletal and respiratory system (WHO, 2008).

In the case of chromium, two valence states exist in soil, water and air through natural and anthropogenic sources which are chromium (III) and chromium (VI). Chromium (III) is an important nutrient needed by humans and shortages may cause heart conditions, metabolisms trouble, and even diabetes, but an increased uptake can cause health effects such as skin rashes while chromium (VI) is hazardous to humans and animals and may cause cancer and even death (Zayed and Terry, 2003). Chromium (III) and (VI) occurs mainly in the steel, leather, and textile industries. Most of the chromium present in the air settles in soil or water. Since chromium attaches strongly to soil particles, chromium that settles in soils will not leak into groundwater and chromium settling in water will absorb on sediment and become immobile. Therefore, crop uptake of chromium is generally very low hence there is very little effects on plants. Exposure to chromium can occur through ingestion, inhalation or through skin contact with chromium or chromium compounds. The Cr concentration in spent geothermal liquid from Menengai geothermal wells ranged from 0.01 to 0.1 mg/l and the recommended level of chromium for drinking water is usually as low as 0.05 mg/l.

Lead naturally occurs in the earth's crust usually as lead sulphide (PbS). However, due to human activities, it can also be found in many forms, mainly lead (II) sulphate ($PbSO_4$) and lead carbonates ($PbCO_3$). Lead may leach into the environment from various anthropogenic sources such as mining, steel industries, crop enhancers and improper disposal of batteries among others. When Pb is released into the environment, it makes its way into the air, soils and water sources and has a tendency to accumulate in soils and plants which restricts soil yields and enters the food chain thus affecting the human health. Lead in soil does not biodegrade or decay and absorption by plants is not rapid, therefore contamination of plants by uptake from the soil is rare, although when plants are exposed to lead dust, absorption of the metal dust through their leaves usually occurs, thus accumulating in plants (WHO, 2008). Lead is rarely found in tap water unless as a result of plumbing systems containing lead in the pipes and fittings or the service connections to homes. The amount of lead dissolved from the plumbing system usually depends on the physical and chemical composition of the water including pH, i.e. acidity or alkalinity of the water, temperature and water hardness (WHO, 2008). In geothermal water Pb may occur in high concentrations relative to the WHO drinking water standards depending on the rock mineral composition and water-rock interaction. For examples, Were, (2007) reported two wells in Olkaria with Pb concentrations of 0.247 to 0.373 mg/l, which is an order of a magnitude higher than the WHO recommended limit of 0.01 mg/l.

3. METHODOLOGY

3.1 Study area

The study area is located within the Menengai geothermal field (Figure 1). The Menengai geothermal field is a trachytic central caldera volcano situated in the Kenya Rift within the Eastern sector of the African Rift system and is among 14 geothermal prospects in Kenya. The geothermal field is located on the outskirts of Nakuru Town, about 180 km northwest of Nairobi, few kilometres south of the equator and covers an area of approximately 2,183 km^2 (Mutia and Simboyi, 2015). The geothermal field encompasses the Menengai volcano, the Ol-Rongai volcanoes, Ol-Banita plains and parts of the Solai graben to the northeast bounded by the coordinates 36°01′E and 36° 07′ E and 0° 09′ S and 0° 15′ S. The surface of Menengai geothermal field is covered by volcanic rocks and soils. The visible rocks at the surface of the caldera are mainly the Menengai massif building lava (pre-caldera formations), the pyroclastic (explosive) that accompanied the collapse of the caldera (syn-caldera) and glassy lavas that erupted after the caldera collapse (Njue, 2011). The volcanic soils are usually the dominant soil in young volcanic landscapes areas surrounding Menengai caldera.

The dominant vegetation within the caldera floor includes patches of bushed grassland, mixed bushland and open grasslands. The plant species include *Tarchonanthus camphoratus* (popularly known as leleshwa), *Acacia drepanolobium* and the grass species *Chloris gayana, Digitaria abyssinica* and *Fimbristylis exilis* (geothermal grass) among others (Wetang'ula et al., 2008). *T. camphoratus* is an evergreen shrub that grows to a height of about 9 m. It is favoured by deep soils and it is commonly found on stony soils in grassland, dry forest margins or secondary deciduous bushland. This shrub has been used since time immemorial for various purposes including as fodder for cattle, firewood, construction of the traditional huts, for making of essential oils and it has also been used for various medicinal purposes. Environmentally, it is very important as it controls soil erosion, helps in land reclamation and improves the fertility of the soil.

The local hydrogeology at Menengai is characterised by N-S trending fault/fracture systems which provide underground channels resulting in water disappearing underground in some places (Lagat, 2010). The surface drainage can be observed from the eastern and western rift scarps. On the rift floor, the drainage can mainly be found from Menengai caldera northwards with the exception of drainage from the southern inclines of the caldera into Lake Nakuru. The Menengai geothermal field has no permanent surface waters except for two seasonal streams, i.e. Kanduturi and Wanyororo streams which flow within the caldera. The permanent rivers are Molo and Rongai in the northwest part of the Menengai area, whereas other surface water bodies around include Lakes Nakuru and Lake Solai and the Olbanita swamp.

The rainfall regime in the project area is bimodal with long rains occurring from March to July and short rains from September to November (Wetang'ula et al., 2008). Automatic weather stations installed at the highest and lowest points of the caldera capture data on an hourly basis within the project area. During the period of July 2014 to June 2015 the annual average rainfall recorded ranged from 1000 mm to 316 mm at the highest and lowest points respectively. The rainfall events were concentrated at the centre/peak of the Menengai caldera. The temperature varied with topography with minimum and maximum temperatures of 15.7°C and 21.7°C respectively whereas the average wind speed recorded ranged from 4.53 m/s to 7.53 m/s at the lowest and highest points respectively.

Human settlement within the Menengai field is minimal since it is public land owned by the Kenya Forestry Service (KFS). Settlement is concentrated outside the caldera floor on the southern and western sectors that includes Nakuru municipality and Bahati divisions. The local people occupying the northern and north eastern parts of the prospect area practice small-scale mixed farming that include livestock keeping which mostly graze inside the caldera.

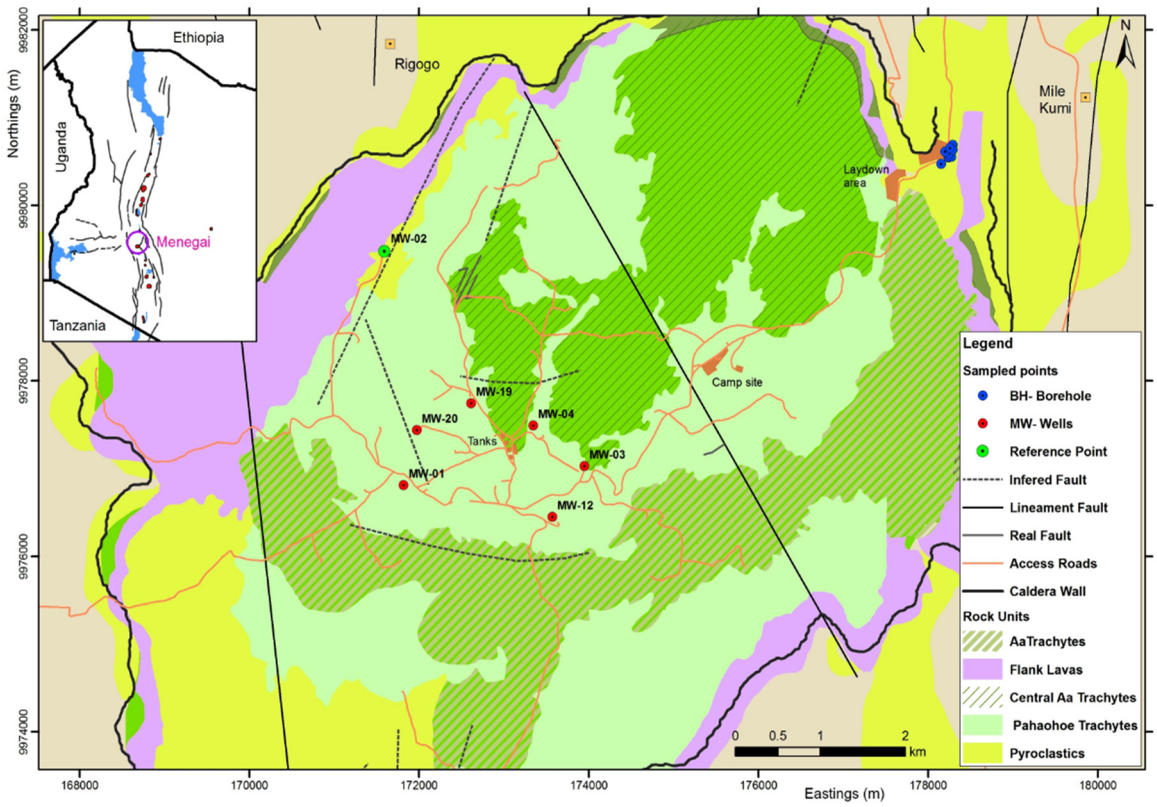

FIGURE 1: Map showing the location of Menengai geothermal field and the sampled points

3.2 Geothermal development at Menengai

Development of geothermal resources in Menengai began in 2004. KenGen undertook surface geoscientific studies to prove the existence of geothermal resources. The results indicated a geothermal potential in excess of 1600 MWe (Republic of Kenya, 2011). To develop the field in bid to meet the country's energy demand, an Environmental Impact Assessment (EIA) study for drilling of geothermal wells was conducted in 2008 by KenGen. The EIA drilling license was then obtained following a laid down Environmental and Social Management Plan (ESMP). However, with the establishment of the Geothermal Development Company (GDC), a state owned parastatal to oversee and develop most geothermal fields in Kenya, the EIA license was transferred from KenGen to GDC.

GDC was established in 2009 to accelerate and deploy geothermal energy in Kenya. This is in line with the country´s policy termed ´Kenya Vision 2030´, which aims at transforming Kenya into a middle income economy by the year 2030 with the provision of affordable and renewable energy as the major driver (Republic of Kenya, 2011). The mandate of GDC includes surface exploration, drilling, resource assessment and promotion of direct utilization of geothermal energy in Kenya. The Menengai geothermal field is the first geothermal field to be fully developed by GDC and the second largest field under development after the Olkaria field in Kenya. To date, geothermal development at this field, since the project was commissioned in 2010, has led to the successful drilling of about 25 deep exploration and production wells with over 2 km depth. GDC is developing the field step-by-step and intends to put up a 105 MWe geothermal power plant. Three Independent Power Producers (IPPs) namely Quantum energy, Sossian Energy and Orpower 22, have been licenced to operate each a 35 MWe modular power plant to achieve the 105 MWe.

As part of the drilling programme in the caldera, ten boreholes within the caldera (Fig 1) were drilled to supply water for drilling, infrastructural works and domestic uses for staff working within the project.

The boreholes were sunk to depths ranging between 100 and 250 m and produce 360 m^3/hr on average (GDC, 2013). The extraction is within the aquifer potential and the recharge is, in general, sufficient. GDC is also linked to the Nakuru Water and Sewerage Company (NAWASCO) to supplement the water resources through piped water services for the project area.

As part of the Environmental Social Monitoring Plan (ESMP) that was adopted in the EIA for drilling of geothermal wells, among the main environmental issues of concern was the containment of spent liquids from discharging wells. According to the plan, the spent liquids were to be contained in HDPE lined ponds with frequent chemical and discharge monitoring. Additionally, to manage the discharge, deep reinjection methods (Wetang'ula et al., 2008) and reuse of the liquids for drilling or other direct uses were proposed for mitigation to avoid contact with the environment.

The spent geothermal liquids from discharging wells in the field are temporarily contained in ponds lined with High Density Polyethylene (HDPE) liners and later on cooled and reused for drilling. Based on the fluid composition, the dissolved solids may potentially contaminate the surrounding surface water, groundwater, soils and vegetation during well testing caused by the steam sprays and overflown liquids. Reinjection of the spent geothermal liquid has not been done although future plans to carry out reinjection after commissioning of the power plants are in place. Routine monitoring of major ions and trace element concentrations in geothermal liquids from the discharging wells is carried out on quarterly basis as well as monitoring of the same elements in the surface and groundwater resources, surrounding soils and vegetation within the vicinity of the wells. However, it is worth noting that the impact of the spent geothermal liquids on the surrounding soils, vegetation and groundwater resources is not addressed in detail in any study.

3.3 Sampling and treatment

Sample collection for this study was done in such a way that all the risks of contamination were minimized and the relevant preservation requirements were met. Proper sample collection was very important in order to acquire data which will reveal the impact of geothermal utilization in Menengai.

3.3.1 Sampling of geothermal spent liquid and groundwater

Six geothermal well sites out of the twenty five drilled wells were selected for sampling of spent geothermal liquid. Four out of the ten groundwater boreholes that have been sunk in Menengai geothermal field by GDC were sampled for this study because they are located in a similar geological area. The ten boreholes have numbers from one to ten. The sampling abbreviations were as follows;

i. Geothermal wells sampled: MW1, MW3, MW4, MW12, MW19, and MW20; and
ii. Groundwater boreholes: BH1, BH2, BH3, and BH4.

Sampling of the geothermal wells was done during the specific time each well was discharging. MW01 discharged at intervals between May 2011 and April 2015 and sampling was done at each interval. Similarly for the other wells, MW3 discharged between September 2012 and June 2013 and was sampled during the same period, MW4 between October 2011 and April 2012, MW12 between February 2013 and May 2014, MW19 discharged from April 2014 to July 2014 whereas MW20 discharged between March 2014 and July 2015 and sampling was done during the same periods with samples collected from the ponds where the spent geothermal liquids were contained.

Samples were collected from all these wells (Figure 1) for the analysis of physical and chemical parameters. The samples for the analysis of the physical parameters, i.e. pH, conductivity and temperature were analysed in the field. The other samples for the chemical parameters were collected in two batches from each sampling point, i.e. one batch for the determination of trace elements which

were labelled as Filtered acidified (Fa) and the other batch for the determination of anions and B which were labelled as Filtered untreated (Fu).

These samples were collected in new and pre-washed 500 ml polyethylene sampling bottles. The bottles were rinsed with the sample before samples were collected. During sampling of the spent liquid, the samples were collected from the ponds and the sampling bottles were immersed in the spent water to a depth of approximately 15 cm, wearing plastic hand gloves to prevent contamination. The groundwater was sampled directly from the taps at the borehole site. The bottles were capped immediately after sampling in order to exclude air and wrapped in plastic bags and then transported to the GDC laboratory for immediate treatment.

3.3.2 Treatment and analysis

The samples labelled Fa were for the determination of trace elements, i.e. As, Hg, Pb, Cd, and Cr. In the laboratory, these samples were filtered through a 0.45 µm millipore membrane to remove suspended matter and prevent sample interaction with these materials and immediately acidified using 1.0 ml of Ultrex Supra pure Nitric acid (HNO_3) to prevent the trace elements from adsorbing to the walls of the polyethylene sampling bottles.

The samples labelled Fu were also filtered through a 0.45 µm millipore membrane for the determination of Na, Cl, K, and B. The Fu samples were analysed at the GDC laboratory. The Fa samples were stored in airtight containers sealed with new plastic bags to avoid any kind of contamination and transported to the internationally accredited Kenya Bureau of Standards (KEBS).

The physical parameters, i.e. pH, temperature and conductivity were analysed on-site using a portable pH/conductivity meter. Boron concentration was determined by the Curcumin method using the Perkin Elmer spectrophotometer. The concentrations of Na, K, and Cl were determined using the Mohr titration technique while F was analysed using the Selective Ion Electrode (ISE) sensitive to F. All these analyses were done following the work instructions stipulated in the International Organization for Standardization (ISO) 9001, Quality Management Systems (QMS) procedures (GDC, 2010). Finally, the trace elements As, Cr, Pb, Hg, and Cd were determined with an Atomic Absorption Spectrophotometer (AAS) at KEBS.

3.3.3 Soil and vegetation sampling

To determine if any potential contamination of the environment exists around the discharging wells, sampling of soil and vegetation was done in the immediate vicinity of the discharged wells MW1 and MW3. The sampling sites were chosen along the prevailing wind and steam plume direction adjacent to the wells. This was because there had been no brine spillages on soils and vegetation at the well sites and so it was assumed that the steam's chemical composition would be similar to spent geothermal liquid in the ponds. The most abundant bushed grassland vegetation species, *T. camphoratus,* was chosen for sampling. One site (MW2) was established as a reference point since the well has never discharged and it is located about 2.6 km and 2.5 km from MW1 and MW3, respectively (Figure 1).

Replicate samples of the upper 5.0 cm soil were collected at each sampling site for analysis at each sampling period, similarly two samples of the *T. camphoratus* upper leaves were collected at the same sampling point as the soil samples. Soil was collected using a plastic scoop into polyethylene bags and sealed. The leaves of *T. camphoratus* samples were also randomly collected from *T. camphoratus* shrubs growing at the same position as the soil samples and stored in polyethylene bags. Sampling of soil and vegetation was done while wearing plastic gloves to prevent any kind of contamination. The soil and vegetation samples were immediately transported to the KEBS laboratory for treatment and analysis.

3.3.4 Treatment and analysis

The soil and vegetation samples were transported to KEBS laboratory where treatment and analysis were carried out. At the laboratory, soil samples were sun dried for 96 hours in direct sunlight in a secure area to prevent further contamination and later on sprayed with 0.1 m NaOH and then dried in the oven for two days at a temperature of 45°C. The soil samples were sieved to < 2 mm particles after oven drying and digested with aqua regia to extract the trace elements. The extract obtained was analysed for trace elements using the Atomic Absorption Spectrophotometer.

The leaves of the *T. camphoratus* samples collected were washed with 100 ml of deionized water and sprayed with 0.1 m NaOH and then oven dried for two days at a temperature of 45°C. The vegetation samples were then digested with aqua regia and analysed for the trace elements using AAS.

3.4 Data analysis

All statistical analysis was done using the program R version 3.2.2. All the data was plotted for exploration and presented as boxplots in Appendix I. Furthermore, the data was grouped into five matrices, i.e. spent liquid concentration, groundwater concentration, soil concentration, and vegetation concentration, and the predictor variable (location) and the observations were plotted. Analysis of Variance (Anova) was separately performed for each element in each of the matrices to test for differences in concentrations of the elements across the different sampled locations. The model diagnostics were also performed to ensure normality. In cases where the normality assumptions were not met, mainly because of zero inflation (concentrations with zero values), the data was log transformed with the equation Log_e (x+v), where x is the variable and v the minimum value of the variable. Descriptive statistical analysis was performed to assess the concentration of selected ions and trace elements in spent geothermal liquid, groundwater, soil, and vegetation and the data is presented as mean ± SE.

To assess the effects of spent geothermal liquid on the groundwater, soils, and vegetation, separate linear models were performed. In the models, groundwater, soil, and vegetation were the response variables while the spent geothermal liquid and well discharge locations were the predictors. Because the concentrations of the selected ions and trace elements in the spent geothermal liquid groundwater, soil, and vegetation did not differ significantly with location, they were treated as replicates for further statistical analysis.

4. RESULTS

4.1 Spent geothermal liquids

4.1.1 Physical parameters and selected ions

The temperature of the spent geothermal liquid at all the sampled points ranged from 22 to 31°C while pH values ranged from 8.8-9.6 (Appendix I). The mean temperature and pH values are presented in Table 1. The range of pH of spent geothermal liquid across all sampled wells was above the local limits for effluent discharge into the environment (Republic of Kenya, 2006; Table 1).

The Na, Cl, K and F concentrations in spent geothermal liquid ranged between 1638 and 3468 mg/l, 516 and 806 mg/l, 151 and 240 mg/l and 91 and 161 mg/l, respectively.

The F, Na, and Cl concentrations were above the limits of the local water quality regulations for effluent standards whereas the limits for the concentrations of K are not defined in the standard (Table 1).

There was a significant variation with well discharge locations between MW1 and MW4 for the concentration of Cl and K (Appendix II). The concentration of K was significantly different between all the sampled wells with highest concentrations at MW4. Meanwhile, Cl concentrations were significantly lower at MW4 compared to the rest of the wells. The concentrations of the Na and F ions in spent geothermal liquids did not show a statistically significant difference across the sampled well discharge locations (Appendix II). The major cation and anion present in high concentrations in spent geothermal liquid were Na and Cl respectively.

TABLE 1: Temperature (°C), pH and concentrations (mg/l; mean ±S.E) of Cl, F, Na and K in spent geothermal liquid from Menengai Wells (MW) compared to permissible levels, *n=36.*
Bold letters show concentrations which exceeded the local limits
for effluent discharge into the environment

Wells	Temp	pH	Cl	F	Na	K
MW1	27.3 ± 0.79	9.1 ± 0.04	**718.50 ± 16.87**	**151.58 ± 1.77**	**2483.16 ± 172.63**	223.72 ± 5.75
MW3	25.2 ± 0.94	9.0 ± 0.14	**703.09 ± 35.10**	**129.01 ± 10.85**	**2594.39 ± 233.40**	189.25 ± 10.30
MW4	27.5 ± 0.87	8.8 ± 0.17	**605.40 ± 28.25**	**133.72 ± 4.23**	**2235.08 ± 107.40**	172.02 ± 5.04
MW12	25.3 ± 0.97	9.6 ± 0.11	**668.16 ± 15.92**	**119.38 ± 4.21**	**2469.07 ± 107.96**	177.65 ± 3.51
MW19	27.2 ± 0.85	9.5 ± 0.09	**682.83 ± 11.15**	**131.23 ± 5.00**	**2545.73 ± 69.23**	179.51 ± 4.79
MW20	24.7 ± 0.82	9.3 ± 0.14	**676.46 ± 15.66**	**135.17 ± 5.95**	**2517.98 ± 184.25**	182.67 ± 8.33
Local standards for effluent discharge into the environment (2006)	NLS*	6.5 - 8.5	250	1,5	200	NLS*

*NLS - No limit specified

4.1.2 Trace elements

The concentration of trace elements in the spent geothermal liquid ranged between 0.020 and 2.070 mg/l of B, 0.001 and 2.000 mg/l of Hg, 0.001 and 7.680 mg/l of As, 0.002 and 0.850 mg/l of Pb, 0.003 and 0.300 mg/l of Cr, and 0.001 to 0.010 mg/l of Cd across all the sampled wells (Appendix I). The mean concentrations are presented in Table 2.

The mean concentrations of B and Cd in spent geothermal liquid were below the recommended local water quality regulations for effluent standards at all the six sampled well discharge locations whereas the concentration of Pb was beyond the permissible limit (Table 2). Elevated Hg concentration in spent

TABLE 2: Mean concentrations (± S.E) of the trace elements concentrations (mg/l) in spent geothermal liquid from Menengai wells (MW) compared to permissible levels, *n=36.*
Bold letters show concentrations which exceeded the local standards
for effluent discharge into the environment

Wells	B	Hg	As	Pb	Cr	Cd
MW1	0.157 ± 0.050	0.001 ± 0.001	0.001 ± 0.001	**0.013 ± 0.001**	0.009 ± 0.001	0.002 ± 0.001
MW3	0.200 ± 0.130	**0.240 ± 0.210**	**0.112 ± 0.050**	**0.087 ± 0.030**	**0.093 ± 0.030**	0.002 ± 0.001
MW4	0.400 ± 0.340	0.002 ± 0.001	**0.310 ± 0.160**	**0.049 ± 0.020**	0.018 ± 0.020	0.001 ± 0.001
MW12	0.668 ± 0.330	**0.082 ± 0.070**	**3.044 ± 1.610**	**0.570 ± 0.030**	0.051 ± 0.030	0.002 ± 0.001
MW19	0.091 ± 0.030	**0.281 ± 0.250**	**0.172 ± 0.150**	**0.069 ± 0.010**	0.020 ± 0.020	0.001 ± 0.001
MW20	0.274 ± 0.120	**0.400 ± 0.360**	0.020 ± 0.020	**0.227 ± 0.140**	**0.070 ± 0.050**	0.002 ± 0.001
Local standards for effluent discharge into the environment (2006)	1,000	0,010	0,020	0,010	0,050	0,010

geothermal liquid occurred at MW3, MW12, MW19, and MW20 while for As, concentrations were elevated at MW3, MW4, MW12, and MW19. High Cr concentration occurred in the spent geothermal liquid at MW3 and MW20 (Table 2).

Nonetheless, the concentrations of As, Cd, Cr, B, Pb, and Hg in spent geothermal liquid across all the wells did not statistically vary with location except for the concentrations of As at MW12 and Cr at MW3 which were significantly higher compared to the other wells (Appendix II).

4.2 Groundwater

4.2.1 Physical parameters and selected ions

The physical parameters did not vary widely in the four groundwater boreholes. The temperature ranged from 25.6°C to 28.8°C and the pH between 7.1 and 7.8. In comparison with the WHO drinking water standards, the pH was within the recommended level of between 6.5 and 8.5 (Table 3).

The Na, Cl, K and F concentrations ranged from 59.5 to 73.6 mg/l, 14.0 to 19.0 mg/l, 1.0 to 1.4 mg/l and 2.6 to 4.2 mg/l, respectively (Appendix I). The mean concentrations are presented in Table 3. All the measured ions were below the WHO required limits for drinking water except F where the concentrations exceeded the 1.5 mg/l limit (Table 3).

TABLE 3: Temperature (°C), pH and mean concentrations (mg/l; ± S.E) of Na, Cl, K and F in groundwater from Menengai boreholes compared to permissible levels, *n=16.*
Bold letters show concentrations which exceeded the WHO drinking water standards

Boreholes	**Temp**	**pH**	**Na**	**Cl**	**K**	**F**
BH1	27.25 ± 0.50	7.48 ± 0.05	71.93 ± 0.71	17.50 ± 0.80	1.22 ± 0.02	**3.50 ± 0.20**
BH2	26.13 ± 0.20	7.54 ± 0.10	70.63 ± 1.00	17.50 ± 0.50	1.25 ± 0.02	**3.25 ± 0.16**
BH3	26.80 ± 0.08	7.29 ± 0.03	60.00 ± 0.33	14.75 ± 0.37	1.23 ± 0.03	**3.15 ± 0.18**
BH4	26.88 ± 0.22	7.23 ± 0.04	65.29 ± 0.75	14.50 ± 0.22	1.95 ± 0.01	**3.37 ± 0.12**
WHO (2008) Drinking water stds.		6.5 - 8.5	200	250	NLS	1,5

*NLS - No limit specified

Concentrations of Na and Cl appear to be location dependent (Appendix II). The concentration of Na was significantly lower at BH3 whereas Cl concentration was significantly lower at MW4 compared to the rest of the wells. The concentrations of Cl, K, and F in groundwater did not show significant differences across the different boreholes sampled, i.e. BH1, BH2, BH3, and BH4 (Appendix II). The major cation and anion present in high concentrations in groundwater was Na and Cl respectively.

4.2.2 Trace elements

The concentrations of the trace elements in groundwater ranged from 0.001 to 0.060 mg/l B, 0.001 to 0,002 mg/l Hg, 0.001 to 0.021 mg/l As, 0.001 to 0.003 mg/l Cr, 0.001 to 0.003 mg/l Cd and 0.009 to 0.030 mg/l Pb across all the sampled boreholes (Appendix I).

The concentrations of the trace elements, i.e. Hg, Cr, B, As, and Cd in the groundwater were below the recommended WHO drinking water levels expect for Pb at BH1 and BH4 (Table 4).

TABLE 4: Mean concentrations (± S.E) of the trace elements concentration (mg/l) in groundwater from Menengai boreholes compared to permissible levels, *n=16*

Boreholes	B	Hg	As	Pb	Cr	Cd
BH1	0.010 ± 0.001	0.001 ± 0.001	0.010 ± 0.001	**0.020 ± 0.001**	0.001 ± 0.001	0.001 ± 0.001
BH2	0.001 ± 0.001	0.001 ± 0.001	0.001 ± 0.001	0.010 ± 0.001	0.001 ± 0.001	0.001 ± 0.001
BH3	0.001 ± 0.001	0.001 ± 0.001	0.010 ± 0.001	0.001 ± 0.001	0.001 ± 0.001	0.001 ± 0.001
BH4	0.030 ± 0.001	0.001 ± 0.001	0.001 ± 0.001	**0.020 ± 0.001**	0.001 ± 0.001	0.001 ± 0.001
WHO (2008) Drinking water stds.	0,500	0,006	0,010	0,010	0,050	0,003

4.3 Soils and vegetation

4.3.1 Trace elements

The concentrations of trace elements in soils ranged between 0.001 and 3.110 mg/l of B, 0.001 to 0.190 mg/kg of Hg, 0.001 to 3.760 mg/kg of As, 2.370 to 36.20 mg/kg of Pb, 0.015 to 2.620 mg/kg of Cr, and 0.021 to 2.200 mg/kg of Cd at the MW1, MW3, and Reference site (MW2) (Appendix I). In vegetation, the concentration ranged from 0.057 to 3.120 mg/kg of B, 0.001 to 0.190 mg/kg of Hg, 0.001 to 2.380 mg/kg of As, 0.014 to 4.800 mg/kg of Pb, 0.021 to 2.200 mg/kg of Cr, and 0.001 to 0.050 mg/kg of Cd (Appendix I). The mean concentrations are presented in Table 5.

TABLE 5: Mean concentrations (± S.E) of the trace elements concentration (mg/l) in soil and vegetation (mg/kg) from Menengai wells (MW) compared to permissible levels, *n=18*

Sample	Site	B	Hg	As	Pb	Cr	Cd
Soil	MW1	0.548 ± 0.470	0.056 ± 0.032	1.026 ± 0.590	15.955 ± 3.660	0.500 ± 0.390	0.247 ± 0.220
	MW3	0.131 ± 0.120	0.001 ± 0.001	0.070 ± 0.060	21.364 ± 6.210	0.416 ± 0.140	0.001 ± 0.010
	Ref*	0.144 ± 0.071	0.004 ± 0.001	0.080 ± 0.040	14.198 ± 3.530	0.330 ± 0.130	0.042 ± 0.030
FAO soil standards		5,00	15,00	50,00	300,00	400,00	3,00
T.camphoratus	MW1	1.239 ± 0.452	0.001 ± 0.001	0.960 ± 0.410	1.030 ± 0.700	0.287 ± 0.260	0.008 ± 0.001
	MW3	0.233 ± 0.150	0.057 ± 0.050	0.137 ± 0.120	0.210 ± 0.100	0.424 ± 0.330	0.001 ± 0.001
	Ref*	0.097 ± 0.040	0.001 ± 0.001	0.072 ± 0.060	0.226 ± 0.090	0.281 ± 0.170	0.040 ± 0.021
FAO vegetation standards		2,00	15,00	50,00	300,00	400,00	3,00

*Ref - Reference site

The concentrations of B, As, Hg, Pb, Cr, and Cd in soil and vegetation were below the recommended FAO standards in both soil and vegetation across the three sites. The trace elements concentrations in soil across the three sites did not show a wide variation, even though statistically higher concentrations of Hg and As were measured in the soils at MW1 compared to MW3 and the reference site MW2 (Appendix II). The average trace element concentrations in soil at MW3 were in the same range or lower compared to the reference site except for Pb which was high at MW3. The concentration of the trace elements in vegetation showed a wide variation in the concentration of B and As being significantly higher in vegetation at MW1 (Appendix II).

4.4 Potential effect of spent geothermal liquid on groundwater, soils and vegetation

The effect of the trace elements B, As, Hg, Cd, Cr, and Pb in spent geothermal liquid on soil was not significant. Nonetheless, the model estimates that the concentration of Cr in spent geothermal liquid around the wells shows a positive association with Cr in surrounding soils, although the relationship is not significant (Appendix III).

The concentrations of B, As, Hg, Cd, Cr, and Pb in spent geothermal liquid showed no significant effects on the surrounding vegetation, however model estimates showed that B concentration in the spent geothermal liquid was correlated with the B concentration in vegetation although the association was not significant (Appendix III).

The effect of B, As, Hg, Cr, and Pb concentrations in spent geothermal liquid on the groundwater within Menengai was not significant, although elevated Cd concentrations were observed. The model estimates also showed the concentration of Cd and Cr in spent geothermal liquid and groundwater was positively associated.

5. DISCUSSION

5.1 Spent geothermal liquid

Spent geothermal fluids are well known to contain some trace elements and ions which in high concentration have the potential to contaminate the environment. The spent geothermal liquids from the sampled wells at the Menengai geothermal field were alkaline in nature with elevated pH levels beyond the recommended local water quality regulations for effluent standards of 6.5–8.5 due to the high concentrations of total dissolved carbonates in the spent geothermal waters. These findings are similar to the spent geothermal liquid at Olkaria from discharging geothermal wells (Were, 2007).

The average concentrations of the ions analysed, i.e. Na, F, K, and Cl in the spent geothermal liquid were found to be in concentrations over 30 times higher compared to the groundwater. This is quite common for spent geothermal liquids especially in high temperature geothermal areas where chemical constituents like Na and Cl ions occur in abundance, with Cl concentrations ranging from 1000 to 10,000 mg/kg (Barbier, 2002). The geothermal liquid that ascends up contains variable solute concentrations which depend on various factors such as the fluid source or mixing, rock type or temperature of the fluids (Arnórsson et al., 2007). As a result of these processes, elevated concentrations of dissolved solids in spent geothermal liquids might cause vegetation damage such as drying of the leaves and abnormal defoliation (Tuyor et al., 2005) if not properly disposed. This is in line with a study on the fluid chemistry, feed zones and boiling in the first exploration well at Menengai (MW1) in Kipng'ok, (2011) classified the aquifer water for MW1 as Na-HCO_3 type with relatively high Cl values of greater than 500 ppm. In comparison to the thermal groundwaters of Vulcano Island in Sicily, similar results of elevated Na, Cl, K, and F were reported (Aiuppa et al., 2000). The variations observed in the K and Cl concentration between MW1 and MW4 could not be established due to limited data.
From an environmental perspective, it is important to monitor the trace element concentrations in the spent geothermal liquid in Menengai geothermal field, considering it is a forest reserve. Elevated levels of trace element concentrations such as Pb, As, Hg, and Cr in the spent geothermal liquid were measured in some of the wells. These trace elements are considered toxic to the environment due to their ability to bio accumulate in terrestrial and aquatic living organisms through the food chain thus causing adverse environmental and health effects. For this reason, proper disposal of spent geothermal liquid needs to be highly emphasised. However, comparing this finding to other geothermal waters, i.e. spent geothermal liquid or naturally occurring geothermal water such as hot springs, the trace elements concentrations in the spent geothermal liquids from Menengai are in the same range or lower in concentration. For example, the trace element concentration in hot springs at Olkaria reported in Simiyu

and Tole (2000) occurred in similar range as the spent geothermal liquids of Menengai except for As and Cr which were high in the hot springs. In comparison to other fields such as the Yangbajing geothermal field in China, the concentration of As and B in spent geothermal liquids in Menengai were very low compared to the spent geothermal liquid collected from the production wells of the Yangbajing geothermal power plants in Guo et al. (2008).

The concentrations of As at MW12 and Cr at MW 3 showed a wide variation in concentrations compared to the other wells which is not expected considering they have a similar reservoir composition and the trace elements' occurrence in geothermal waters including spent geothermal liquid is generally depending on factors such as rocks chemical composition, physical conditions of the weathering solution (temperature, acidity and redox conditions) and the contribution of magmatic gases (Aiuppa et al., 2000). This can be attributed to the different sampling seasons or the variation in As concentration could also be explained partly by the adsorption to silica polymers in the ponds.

5.2 Groundwater

The water quality for the groundwater in Menengai geothermal field from four boreholes was determined. F concentrations were more than double the permissible limit of 1.5 mg/l in all the boreholes measured which is typical in the Kenyan rift due to the underlying geological formation. Similar findings were reported in the pre-drilling EIA for Menengai where two seasonal streams that flow within the caldera showed elevated concentrations of Pb and F levels (Wetang'ula et al., 2008). Human consumption of water with high levels of F concentration can lead to mottling of teeth and in severe cases it might cause crippling skeletal fluorosis (WHO, 2008).

The trace elements concentrations in the groundwater were also below the recommended drinking water limit (WHO, 2008) except for Pb at BH1 and BH4. The elevated Pb concentration in the groundwater may be attributed to the rock composition of Menengai area and not from geothermal activities considering Pb was still high in the pre-drilling report. In the Menengai field, being a volcanic area, Pb is naturally present in the underground rock and soil. Another source of Pb could be from the metallic piping material where the boreholes water is channelled since Pb can easily react with water depending on the physical and chemical composition of the water. Risks from elements such as Pb are intensified by their high ability to increase in concentration as they move up the food chain and children are more susceptible to the most damaging effects of Pb toxicity as they absorb 4-5 times higher Pb concentration than adults after exposure (WHO, 2008).

The variation in the concentration of Na and Cl in the groundwater at BH1 and BH4 could be due to sampling and analytical errors. The model estimates showed that the trace elements concentrations (B, Hg, Pb, Cr, As, and Cd) in the spent geothermal liquid does not have an effect on the groundwater. Although detailed studies on the potential effects of the spent geothermal liquid on the groundwater within Menengai need to be carried out due to insufficient data for this study.

5.3 Soil and vegetation

The trace elements concentrations, i.e. B, As, Hg, Cd, Cr, and Pb in the soil and vegetation in the vicinity of MW1 and MW3 were not different compared to the reference site MW2. All three sites had very low trace elements concentrations that originate from the crust with no potential effects coming from the spent geothermal liquid. The trace elements did not show any accumulation in the soil and vegetation and seems unlikely to pose any risk for the livestock that graze within the project area. Therefore, geothermal activities in Menengai have not had any impact on the concentration of the soils and vegetation at these sites. However, detailed studies are highly recommended for the other well sites within the project area. Although these findings are not similar to the study by Simiyu and Tole, (2000) on the trace elements concentrations in waters, soil and plants in the Olkaria geothermal field. In the

study, higher concentration of B, As, and Hg in soils in contact with the spent geothermal liquid were reported at Olkaria compared to the soil concentration in Menengai. Vegetation samples in contact with the spent geothermal liquid at Olkaria also showed higher B concentrations compared to the vegetation in Menengai.

6. CONCLUSIONS AND RECOMMENDATIONS

The spent geothermal liquid at the Menengai geothermal field showed elevated levels of ions and trace elements, i.e. Cl, Na, Hg, As, Pb, and Cr in spent geothermal liquid in all wells relative to local water quality regulations for effluent discharge into the environment.

The concentrations in the groundwater were within the WHO drinking water levels except for F which is typical in the Kenyan rift. The elevated levels of Pb are caused by the natural geothermal processes and the rocks and soils composition of Menengai area or the piping material for channelling the groundwater. Since this groundwater is mainly used for drilling and civil activities there is no cause for alarm, but before this water is used for human consumption it should undergo proper treatment.

The trace element concentration in soils and vegetation in the vicinity of the three wells, i.e. MW1, MW2, and MW3 were within the recommended FAO levels for soil and vegetation and there is no evidence of trace elements accumulation. There were no differences in trace element concentration at MW1 and MW3 in comparison with the reference site, however more investigation is required since statistically higher concentrations of Hg and As in soil and B and As in vegetation were observed at MW1.

The geothermal activities in Menengai field and specifically the discharge of spent geothermal liquid has not had any effect so far on the surrounding soil, vegetation and groundwater, however further studies are necessary since data for this study was quite limited.

The Menengai geothermal field being a forest reserve, it is important from an environmental perspective to properly contain these spent geothermal liquids to avoid direct contact with the environment. Therefore, this study recommends:

I. Reinjection of spent geothermal fluids to be adopted since the output for these spent liquids is projected to increase with further development.
II. Routine maintenance of the HDPE liners should also be carried out to avoid seepage into the ground and ponds should not be filled beyond their maximum capacity.
III. Frequency in the monitoring of the trace elements concentrations in the spent geothermal liquid, groundwater, soil, and vegetation in the vicinity of all the wells in Menengai should be increased from quarterly to monthly to establish a good database for modelling effects.
IV. Detailed study on the different types of the dominant vegetation species in Menengai which need to be sampled and analysed for the saline ions and trace elements since only one species type was assessed and as part of baseline, other dominant species should be included in the routine monitoring.
V. Assessment of the trace elements mobility, speciation and distribution in the spent geothermal liquid from the different wells.

ACKNOWLEDGEMENTS

I wish to thank the United Nations University Geothermal Training Programme and the government of Iceland for this wonderful training opportunity. My sincere gratitude goes to the Director, Mr. Lúdvík S. Georgsson, and Deputy Director, Mr. Ingimar Guðni Haraldsson for their support during this training. Many thanks to the UNU staff, Ms. Málfríður Ómarsdóttir, Mr. Markús A. G. Wilde, Thórhildur Ísberg for their guidance and support during my stay in Iceland and to the librarian Ms. Rósa S. Jónsdóttir.

I appreciate Geothermal Development Company for giving me this opportunity to participate in this programme with special thanks to Mr. Gabriel Wetang'ula, the Manager Environment at GDC.

To my dedicated supervisors, Ms. Thecla Mutia and Mr Dadi Thorbjörnsson, without their assistance, ideas and valuable advice throughout the entire project period, this study would not have been possible.

Finally, I would like to thank my daughter Ariana Siantei for her patience throughout this period.

REFERENCES

Aiuppa, A., Dongarra, G., Capasso, G., and Allard, P., 2000: Trace elements in the thermal groundwaters of Vulcano Island (Sicily). *J.Volcanol. Geotherm. Res, 98-1*, 189-207.

Arnórsson, S., Stefánsson, A., and Bjarnason, J.Ö., 2007: Fluid-fluid interaction in geothermal systems. *Reviews in Mineralogy and Geochemistry*, *65,* 229-312.

Axtmann, R.C., 1975: Environmental impact of a geothermal power plant. *J. Scientific Research, 187*, 795-803.

Ármannsson, H., and Fridriksson, Th., 2009: Application of geochemical methods in geothermal exploration. *Presented at "Short Course on Surface Exploration for Geothermal Resources", organized by UNU-GTP and LaGeo, Ahuachapán and Santa Tecla, El Salvador*, 12 pp.

Barbier, E., 2002: Geothermal energy technology and current status: an overview. *Renewable and Sustainable Energy Reviews, 6-1/2,* 3-65.

Bargagli, R., Cateni, D., Nelli, L., Olmastroni, S., and Zagarese, B., 1997: Environmental impact of trace element emissions from geothermal power plants. *Archives of Environmental Contamination and Toxicology, 33-2*, 172-181.

GDC, 2010: *Quality manual*. GDC, Kenya, unpublished internal report, 196 pp.

GDC, 2013: *Water resources management plan*. Geothermal Development Company (GDC), Nakuru, Kenya, internal report, 29 pp.

Goff, S., and Goff, F., 1997: Environmental impacts during development: Some examples from Central America. *Proceedings of NEDO International Geothermal Symposium, Japan,* 242-250.

Guo, Q., Wang, Y., and Liu, W., 2008: B, As, and F contamination of river water due to wastewater discharge of the Yangbajing geothermal power plant, Tibet, China. *Environmental Geology, 56-1*, 197-205.

Kipng'ok, J.K., 2011: Fluid chemistry, feed zones and boiling in the first geothermal exploration well at Menengai, Kenya. Report 15 in: *Geothermal training in Iceland 2011.* UNU-GTP, Iceland, 281-302.

Koç , C., 2007: Effects on environment and agriculture of geothermal wastewater and boron pollution in Great Menderes Basin. *Environmental Monitoring and Assessment*, *125*, 377-388.

Kristmannsdóttir, H., and Ármannsson, H., 2003: Environmental aspects of geothermal energy utilization. *Geothermics, 32*, 451-461.

Lagat, J., 2010: Direct utilization of geothermal resources in Kenya. *Proceedings of the World Geothermal Congress 2010, Bali, Indonesia*, 7 pp.

Mutia, T.M., and Simboyi, H., 2015: Environmental audit score-card for Menengai geothermal project, Kenya. *Proceedings of the World Geothermal Congress 2015, Melbourne, Australia*, 9 pp.

Njue, L.M., 2011: The Menengai caldera structure and its relevance to geothermal potential. *Geothermal Resources Council Transactions, 35*, 1201-1208.

Nordstrom, D.K., 2002: Worldwide occurrences of arsenic in groundwater. *Science, 296*, 2143–2145.

Republic of Kenya, 2006: *Environmental Management and Co-ordination (Water Quality) Regulations*, *Legal Notice No. 121*, Republic of Kenya, Government Printers, Kenya, 30 pp

Republic of Kenya, 2011: *Updated Least Cost Power Development Plan. Study Period: 2011 – 2031*. Energy Regulatory Commission, Geothermal Development Company, Kenya Electricity Generating Company, Kenya Power, Rural Electrification Authority, and KETRACO on behalf of the Republic of Kenya, 203 pp.

Sigurdardóttir, H., and Thorgeirsson, A.T. (ed), 2014: *Environmental report*. Reykjavik Energy, Reykjavík, Iceland, 83 pp.

Simiyu, G., and Tole, M., 2000: Concentrations of trace elements in waters, soils and plants of Olkaria geothermal field, Kenya. *Proceedings of World Geothermal Congress 2000, Kyushu-Tohoku, Japan*, 681-688.

Tuyor, J.B., de Jesus, A.C., Medrano, R.S., Garcia, J.R.D., Salinio, S.M., and Santos, L.S., 2005: Impact of geothermal well testing on exposed vegetation in the Northern Negros geothermal project, Philippines. *Geothermics, 34*, 252-265.

Webster, J.G., and Nordstrom, D.K., 2003: Geothermal arsenic. In: Welch, A.H., Stollenwerk, K.G., (eds.), *Arsenic in groundwater: Geochemistry and occurrence*. Kluwer Academic Publishers, Boston, Massachusetts, 101-126.

Were, J.O., 1998: Aspects of waste management and pollution control in Olkaria geothermal field, Kenya. Report 16 in: *Geothermal training in Iceland 1998.* UNU-GTP, Iceland, 423-460.

Were, J.O., 2007: *The speciation of trace elements in spent geothermal fluids and implications for environmental health around Olkaria, Kenya.* University of Iceland, MSc thesis, UNU-GTP, Iceland, report 1, 73 pp.

Wetang'ula, G.N., 2004: *Assessment of geothermal waste water disposal effects, case studies: Nesjavellir (Iceland) and Olkaria (Kenya) fields.* University of Iceland, MSc thesis, UNU-GTP, Iceland, report 2, 76 pp.

Wetang'ula G.N., Were, J.O., Kubo, B., Omenda, P., Onacha, S., 2008: *Menengai geothermal drilling project, Nakuru. Environmental impact assessment study report*. Kenya Electricity Generating Company Ltd., Kenya, 138 pp.

WHO, 2008: *Guidelines for drinking water quality* (3rd ed.). World Health Organization (WHO), Geneva, Switzerland.

Zayed, A.M., and Terry, N., 2003: Chromium in the environment: Factors affecting biological remediation. *Plant and Soil, 249-1*, 139-156.

APPENDIX I: Selected ions and trace elements concentration (mg/l) in spent geothermal liquid, groundwater, soil, and vegetation

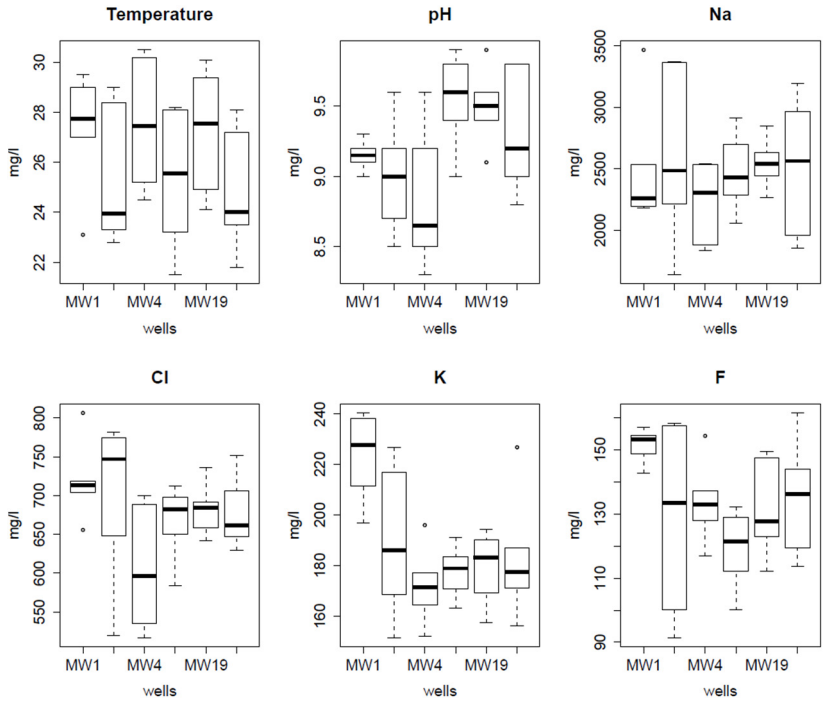

FIGURE 1: Physical parameters and ion concentrations (mg/l) in spent geothermal liquid at Menengai wells. The x-axis represents the sampled wells in the following order, MW1, MW3, MW4, MW12, MW19, and MW20

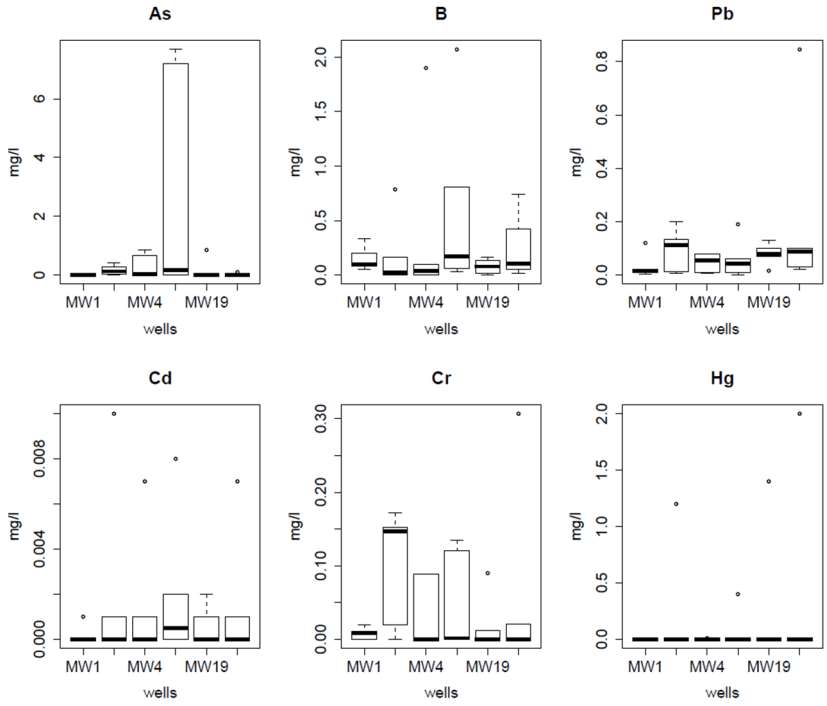

FIGURE 2: Trace elements concentrations (mg/l) in spent geothermal liquid at Menengai wells. The x-axis represents the sampled wells in the following order, MW1, MW3, MW4, MW12, MW19, and MW20

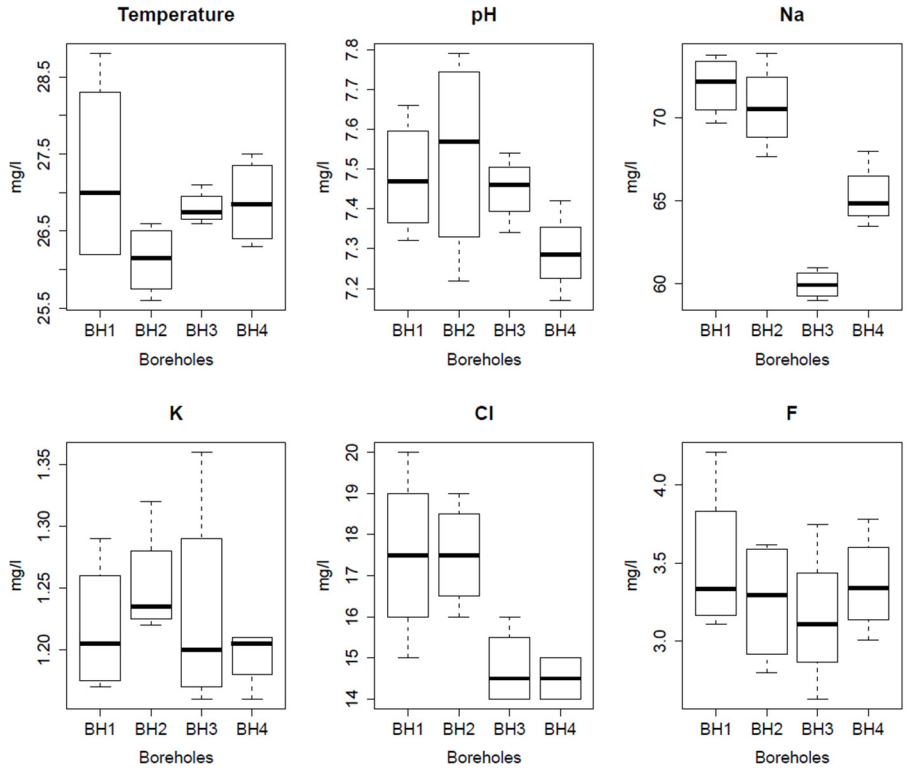

FIGURE 3: Physical parameters and ion concentrations (mg/l) in groundwater from Menengai boreholes - BH1, BH2, BH3, and BH4

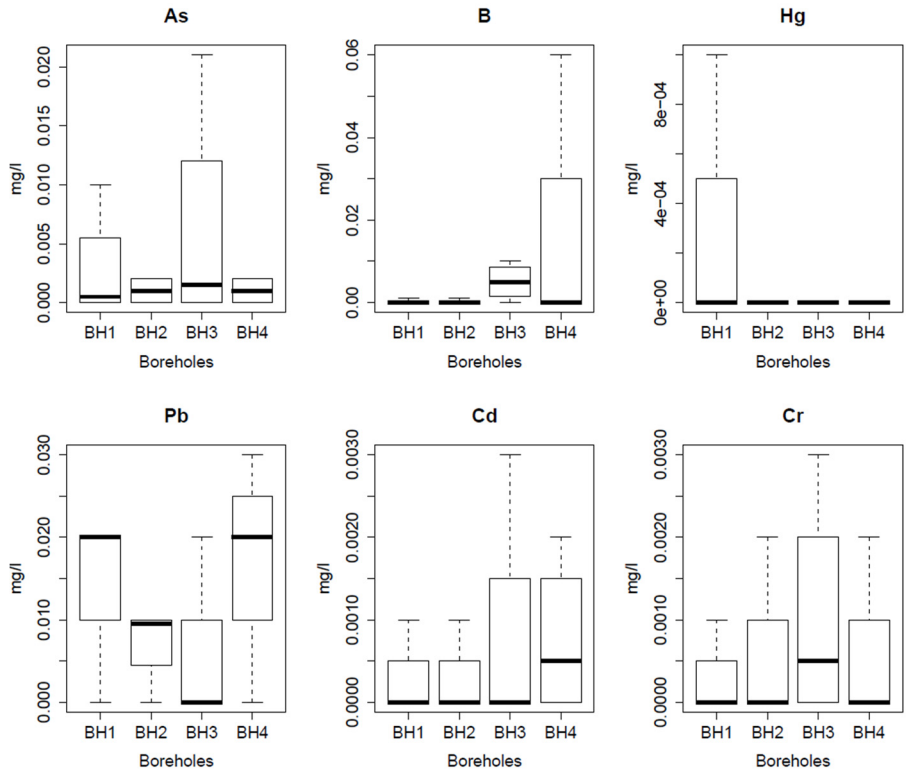

FIGURE 4: Trace elements concentrations (mg/l) in groundwater from Menengai boreholes - BH1, BH2, BH3, and BH4

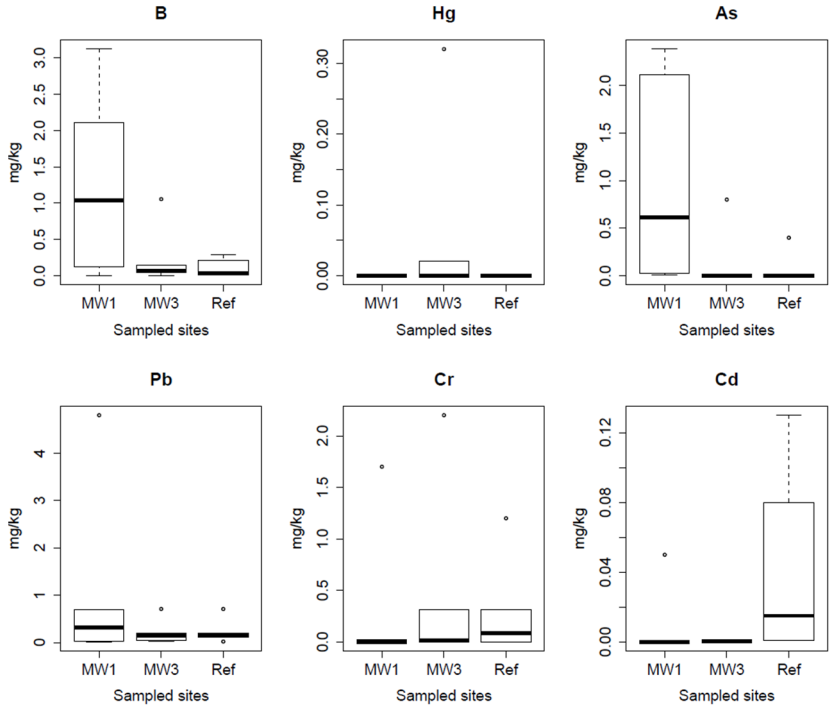

FIGURE 5: Trace elements concentrations (mg/kg) in vegetation samples in the vicinity of Menengai wells - MW1, MW3, and Reference site (MW2)

APPENDIX II: Analysis of Variance (Anova) results for spent geothermal liquid and groundwater across the different sampled locations

TABLE 1: Analysis of Variance (Anova) results for the concentrations of Na, Cl, K, and F in spent geothermal liquid across the different sampled locations from Menengai wells

Response	Predictor	Estimate	Std Error	t-value	P-value
Na concentration in spent geothermal liquid	Intercept-Location MW1	2483,16	184,70	13,444	**0,000**
	Location MW12	-14,09	261,21	-0,054	0,957
	Location MW19	62,57	261,21	0,240	0,812
	Location MW20	34,81	261,21	0,1333	0,895
	Location MW3	111,23	261,21	0,426	0,673
	Location MW4	-248,07	261,21	-0,950	0,350
Residual standard error: 452.4, DF: 30					
Cl concentration in spent geothermal liquid	Intercept-Location MW1	718,15	26,18	27,441	**0,000**
	Location MW12	-50,35	37,03	-1,360	0,184
	Location MW19	-35,67	37,03	-0,963	0,343
	Location MW20	-42,04	37,03	-1,135	0,265
	Location MW3	-15,41	37,03	-0,416	0,680
	Location MW4	-113,1	37,03	-3,054	**0,005**
Residual standard error: 64.13, DF: 30					
K concentration in spent geothermal liquid	Intercept-Location MW1	223,71	7,93	28,22	**0,000**
	Location MW12	-46,06	11,21	-4,109	**0,000**
	Location MW19	-44,21	11,21	-3,943	**0,000**
	Location MW20	-41,05	11,21	-3,661	**0,001**
	Location MW3	-34,47	11,21	-3,074	**0,001**
	Location MW4	-51,70	11,21	-4,611	**0,000**
Residual standard error: 19.42, DF: 30					
F concentration in spent geothermal liquid	Intercept-Location MW1	151,58	7,12	21,304	**0,000**
	Location MW12	-32,2	10,06	-3,200	0,050
	Location MW19	-20,34	10,06	-2,022	0,050
	Location MW20	-16,41	10,06	-1,631	0,113
	Location MW3	-22,57	10,06	-2,243	0,060
	Location MW4	-17,86	10,06	-1,775	0,086
Residual standard error: 17.43, DF: 30					

*Estimates indicate the effects of the predictors compared to the intercept and followed by a test statistic

TABLE 2: Analysis of Variance (Anova) results for the concentrations of B, Hg, As, Cd, Cr, and Pb in spent geothermal liquid across the different sampled locations from Menengai wells

Response	**Predictor**	**Estimate**	**Std Error**	**t-value**	**P-value**
log B concentration in spent geothermal liquid	Intercept-Location MW1	0,171	0,960	0,178	0,860
	Location MW12	0,400	1,357	0,300	0,766
	Location MW19	-0,068	1,357	-0,050	0,961
	Location MW20	0,094	1,357	0,069	0,945
	Location MW3	0,021	1,357	0,015	0,988
	Location MW4	2,570	1,357	1,894	0,068
Residual standard error: 2.35, DF: 30					
log Hg concentration in spent geothermal liquid	Intercept-Location MW1	0,001	0,221	0,005	0,996
	Location MW12	0,068	0,313	0,217	0,830
	Location MW19	0,235	0,313	0,752	0,458
	Location MW20	0,333	0,313	1,065	0,296
	Location MW3	0,535	0,313	1,708	0,098
	Location MW4	0,001	0,313	0,004	0,997
Residual standard error: 0.542, DF: 30					
log As concentration in spent geothermal liquid	Intercept-Location MW1	0,020	0,064	0,032	0,975
	Location MW12	2,530	0,905	2,795	**0,001**
	Location MW19	0,134	0,905	0,149	0,883
	Location MW20	0,010	0,905	0,010	0,991
	Location MW3	0,155	0,905	0,171	0,865
	Location MW4	0,255	0,905	0,281	0,781
Residual standard error: 1.568, DF: 30					
log Cd concentration in spent geothermal liquid	Intercept-Location MW1	0,001	0,001	0,613	0,544
	Location MW12	0,001	0,001	1,084	0,287
	Location MW19	0,000	0,001	0,217	0,830
	Location MW20	0,001	0,001	0,759	0,454
	Location MW3	0,001	0,001	1,084	0,287
	Location MW4	0,001	0,001	0,759	0,540
Residual standard error: 0.003, DF: 30					
log Cr concentration in spent geothermal liquid	Intercept-Location MW1	0,013	0,028	0,454	0,653
	Location MW12	0,035	0,040	0,879	0,386
	Location MW19	0,009	0,040	0,229	0,820
	Location MW20	0,047	0,040	1,17	0,251
	Location MW3	0,098	0,040	2,458	0,020
	Location MW4	0,021	0,040	0,546	0,589
Residual standard error: 0.069, DF: 30					
log Pb concentration in spent geothermal liquid	Intercept-Location MW1	0,004	0,057	0,632	0,532
	Location MW12	0,027	0,081	0,330	0,742
	Location MW19	0,049	0,081	0,602	0,552
	Location MW20	0,164	0,081	2,030	0,051
	Location MW3	0,065	0,081	0,799	0,430
	Location MW4	0,017	0,081	0,208	0,837
Residual standard error: 0.140, DF: 30					

* Estimates indicate the effects of the predictors compared to the intercept and followed by a test statistic

TABLE 3: Analysis of Variance (Anova) results for the concentrations of the ions Na, Cl, K , F, and trace elements, B, As, Hg, Cd, Cr, and Pb in groundwater boreholes across the different sampled locations

Response	**Predictor**	**Estimate**	**Std Error**	**t-value**	**P-value**
Na concentration in ground water	Intercept Location-BH1	71,930	0,948	75,915	**0,000**
	Location BH2	-1,298	1,340	-0,968	0,352
	Location BH3	-11,975	1,340	-8,937	**0,000**
	Location BH4	-6,643	1,340	-4,957	**0,000**
Residual standard error: 1.895, DF: 12					
K concentration in ground water	Intercept Location-BH1	1,218	0,029	41,431	**0,000**
	Location BH2	0,035	0,042	0,842	0,416
	Location BH3	0,013	0,042	0,301	0,769
	Location BH4	-0,023	0,042	-0,541	0,598
Residual standard error: 0.059, DF: 12					
Cl concentration in ground water	Intercept Location-BH1	1,750	6,731	25,997	**0,000**
	Location BH2	1,538	9,520	0,000	1,000
	Location BH3	-2,750	9,520	-2,889	**0,014**
	Location BH4	-3,000	9,520	-3,151	**0,009**
Residual standard error: 1.346, DF: 12					
F concentration in ground water	Intercept Location-BH1	3,498	0,212	16,461	**0,000**
	Location BH2	-0,245	0,301	-0,815	0,431
	Location BH3	-0,348	0,301	-1,156	0,270
	Location BH4	-0,13	0,301	-0,433	0,673
Residual standard error: 0.425, DF: 12					
log B concentration in ground water	Intercept Location-BH1	7,500	7,582	0,099	0,923
	Location BH2	7,512	1,072	0,000	1,000
	Location BH3	4,750	1,072	0,443	0,666
	Location BH4	1,450	1,072	1,376	0,194
Residual standard error: 0.015, DF: 12					
log Hg concentration in ground water	Intercept Location-BH1	0,000	0,000	6,000	**0,000**
	Location BH2	0,000	0,000	-1,414	0,183
	Location BH3	0,000	0,000	-1,414	0,183
	Location BH4	0,000	0,000	-1,414	0,183
Residual standard error: 0.0002, DF: 12					
log As concentration in ground water	Intercept Location-BH1	0,008	0,003	2,737	**0,018**
	Location BH2	-0,002	0,004	-0,437	0,670
	Location BH3	0,003	0,004	0,812	0,433
	Location BH4	-0,002	0,004	-0,437	0,670
Residual standard error: 0.005, DF: 12					
log Cd concentration in ground water	Intercept Location-BH1	7,500	4,787	1,567	0,143
	Location BH2	-3,130	6,770	0,000	1,000
	Location BH3	5,000	6,770	0,739	0,474
	Location BH4	5,000	6,770	0,739	0,474
Residual standard error: 0.009, DF: 12					
log Cr concentration in ground water	Intercept Location-BH1	0,000	0,001	1,455	0,171
	Location BH2	0,000	0,001	0,343	0,738
	Location BH3	0,000	0,001	1,029	0,324
	Location BH4	0,000	0,001	0,343	0,738
Residual standard error: 0.001, DF: 12					
log Pb concentration in ground water	Intercept Location-BH1	0,025	0,005	5,117	**0,000**
	Location BH2	-0,007	0,007	-1,122	0,284
	Location BH3	-0,010	0,007	-1,447	0,173
	Location BH4	0,003	0,007	0,362	0,723
Residual standard error: 0.010, DF: 12					

*Estimates indicate the effects of the predictors compared to the intercept and followed by a test statistic

TABLE 4: Analysis of Variance (Anova) for the concentrations of B, As, Hg, Cd, Cr, and Pb in soil and vegetation in the vicinity of Menengai wells

Response	**Predictor**	**Estimate**	**Std Error**	**t-value**	**P-value**
log B concentration in soil	Intercept-Location MW1	0,5478	0,305	1,794	0,0929
	Location MW3	-0,417	0,4317	-0,967	0,3491
	Location MW2 (Reference site)	-0,4702	0,4317	-1,089	0,293
Residual standard error: 0.73, DF: 15					
log Hg concentration in soil	Intercept-Location MW1	0,056	0,019	2,861	**0,012**
	Location MW3	-0,055	0,028	-1,987	0,066
	Location MW2 (Reference site)	-0,052	0,028	-1,867	0,082
Residual standard error: 0.037, DF: 15					
log As concentration in soil	Intercept-Location MW1	1,0258	0,3719	2,758	**0,0146**
	Location MW3	-0,9557	0,526	-1,817	0,0089
	Location MW2 (Reference site)	-0,997	0,526	-1,896	0,078
Residual standard error: 0.911, DF: 15					
log Cd concentration in soil	Intercept-Location MW1	0,2467	0,1439	1,714	0,107
	Location MW3	-0,246	0,2035	-1,209	0,245
	Location MW2 (Reference site)	-0,2048	0,2035	-1,006	0,33
Residual standard error: 0.37, DF: 15					
log Cr concentration in soil	Intercept-Location MW1	0,5	0,275	1,822	0,0885
	Location MW3	-0,083	0,388	-0,216	0,8322
	Location MW2 (Reference site)	-0,1705	0,388	-0,439	0,667
Residual standard error: 0.637, DF: 15					
log Pb concentration in soil	Intercept-Location MW1	15,995	5,077	3,143	**0,007**
	Location MW3	5,409	7,179	0,753	0,4628
	Location MW2 (Reference site)	-1,757	7,179	-0,245	0,8099
Residual standard error: 12.937, DF: 15					
log B concentration in vegetation	Intercept-Location MW1	1,234	0,2994	4,139	0,000
	Location MW3	-1,006	0,4235	-2,376	0,030
	Location MW2 (Reference site)	-1,0143	0,4235	-2,698	0,017
Residual standard error: 0.07, DF: 15					
log Hg concentration in vegetation	Intercept-Location MW1	0,008	0,003	0,016	0,987
	Location MW3	0,05	0,004	1,313	0,209
	Location MW2 (Reference site)	0	0,004	0,004	0,997
Residual standard error: 0.66, DF: 15					
log As concentration in vegetation	Intercept-Location MW1	0,96	0,2716	3,534	**0,003**
	Location MW3	-0,055	0,3842	-2,142	0,05
	Location MW2 (Reference site)	-0,8894	0,3842	-2,316	0,035
Residual standard error: 0.73, DF: 15					
log Cd concentration in vegetation	Intercept-Location MW1	0,008	0,013	0,623	0,54
	Location MW3	-0,007	0,018	-0,414	0,685
	Location MW2 (Reference site)	0,032	0,018	1,69	0,112
Residual standard error: 0.037, DF: 15					
log Cr concentration in vegetation	Intercept-Location MW1	0,286	0,285	1,004	0,331
	Location MW3	0,1368	0,404	0,339	0,74
	Location MW2 (Reference site)	-0,006	0,404	-0,016	0,988
Residual standard error: 0.698, DF: 15					
log Pb concentration in vegetation	Intercept-Location MW1	1,0297	0,448	2,299	**0,036**
	Location MW3	-0,82	0,6335	-1,294	0,215
	Location MW2 (Reference site)	-0,8033	0,6335	-1,268	0,2241
Residual standard error: 1.937, DF: 15					

* Estimates indicate the effects of the predictors compared to the intercept and followed by a test statistic

APPENDIX II: Linear models for the trace element concentrations of B, As, Hg, Cd, Cr, and Pb in groundwater, soil, and vegetation

TABLE 1: Linear models for the trace element concentrations of B, As, Hg, Cd, Cr, and Pb in groundwater, soil, and vegetation

Response	Predictor	Estimate	Std Error	t-value	P-value
log B concentration in soil	Intercept	0,376	0,307	1,224	0,249
	B in spent geothermal liquid	-0,079	0,315	-0,251	0,807
Residual standard error: 0.937, DF: 10					
log Hg concentration in soil	Intercept	0,0313	0,020	1,584	0,144
	Hg in spent geothermal liquid	-0,026	0,057	-0,456	0,658
Residual standard error: 0.065, DF: 10					
log As concentration in soil	Intercept	0,677	0,402	1,685	0,123
	As in spent geothermal liquid	-2,475	3,837	-0,645	0,533
Residual standard error: 1.207, DF: 10					
log Cd concentration in soil	Intercept	0,150	0,141	1,063	0,313
	Cd in spent geothermal liquid	-21,020	47,222	-0,445	0,666
Residual standard error: 0.443, DF: 10					
log Cr concentration in soil	Intercept	0,438	0,276	1,586	0,144
	Cr in spent geothermal liquid	0,471	3,693	0,127	0,901
Residual standard error: 0.786, DF: 10					
log Pb concentration in soil	Intercept	22,890	4,070	5,624	**0,000**
	Pb in spent geothermal liquid	-41,850	21,520	-1,945	0,080
Residual standard error: 11.92, DF: 10					
log B concentration in Vegetation	Intercept	0,517	0,311	1,663	0,127
	B in spent geothermal liquid	0,476	0,319	1,493	0,166
Residual standard error: 0.950, DF: 10					
log Hg concentration in Vegetation	Intercept	0,030	0,030	1,015	0,334
	Hg in spent geothermal liquid	-0,008	0,084	-0,095	0,926
Residual standard error: 0.096, DF: 10					
log As concentration in Vegetation	Intercept	0,697	0,293	2,381	**0,039**
	As in spent geothermal liquid	-2,85	2,800	-1,020	0,332
Residual standard error: 0.880, DF: 10					
log Cd concentration in Vegetation	Intercept	0,005	0,005	1,124	0,287
	Cd in spent geothermal liquid	-0,728	1,587	-0,459	0,656
Residual standard error: 0.015, DF: 10					
log Cr concentration in Vegetation	Intercept	0,424	0,277	1,533	0,156
	Cr in spent geothermal liquid	-1,612	3,699	-0,436	0,672
Residual standard error: 0.787, DF: 10					
log Pb concentration in Vegetation	Intercept	0,067	0,479	1,405	0,190
	Pb in spent geothermal liquid	-0,531	2,533	-0,210	0,838
Residual standard error: 1.403, DF: 10					
log B concentration in ground water	Intercept	0,006	0,004	10367	0,193
	B in spent geothermal liquid	-0,003	0,008	-0,395	0,699
Residual standard error: 0.015, DF: 14					
log Hg concentration in ground water	Intercept	0,000	0,000	1,001	0,334
	Hg in spent geothermal liquid	0,000	0,000	-0,252	0,805
Residual standard error: 0.0003, DF: 14					
log As concentration in ground water	Intercept	0,003	0,002	2,101	0,054
	As in spent geothermal liquid	-0,005	0,005	-0,859	0,405
log Residual standard error: 0.005, DF: 14					
log Cd concentration in ground water	Intercept	0,000	0,000	1,511	0,153
	Cd in spent geothermal liquid	0,267	0,039	6,89	**0,000**
Residual standard error: 0.0004, DF: 14					
log Cr concentration in ground water	Intercept	0,000	0,000	0,998	0,335
	Cr in spent geothermal liquid	0,006	0,003	1,632	0,125
Residual standard error: 0.0009, DF: 14					
log Pb concentration in ground water	Intercept	0,013	0,004	3,538	**0,003**
	Pb in spent geothermal liquid	-0,036	0,044	-0,803	0,436
Residual standard error: 0.010, DF: 14					

* Estimates indicate the effects of the predictors compared to the intercept and followed by a test statistic

UNITED NATIONS UNIVERSITY
UNU-GTP
Geothermal Training Programme

Orkustofnun, Grensasvegur 9,
IS-108 Reykjavik, Iceland

Reports 2015
Number 17

FINANCIAL ASSESSMENT OF COMMERCIAL EXTRACTION OF SULPHUR AND CARBON DIOXIDE FROM GEOTHERMAL GASES IN MENENGAI, KENYA

Shammah Kipkogei Kiptanui
Geothermal Development Company - GDC
P.O Box 17700- 20100
Nakuru
KENYA
skiptanui@gdc.co.ke, skkiptanui@gmail.com

ABSTRACT

This study presents a financial viability assessment of commercial extraction of elemental sulphur and carbon dioxide (CO_2) from non-condensable gases (NCG) in Menengai geothermal field, Kenya. A brief overview of the geothermal gases in geothermal production and technology options for sulphur removal and carbon dioxide purification and liquefaction suitable for the field are presented. An Excel based profitability assessment model was applied to determine the profitability using gas chemistry data from 11 production wells and budget information received from technology suppliers. It is found that the capital cost of setting up the plant with annual production capacity of 5,655 tons of elemental sulphur and 17,382 tons of industrial liquid CO_2, equivalent 5%, is approximately US$9,779,415. The project´s Net Present Value (NPV) and NPV of Net Cash Flow are $2,033,178 and $2,028,446, respectively, while the equity Internal Rate of Return (IRR) is 31%. These numbers indicate that extraction is viable from the financial point of view and would provide a second option for the power company to generate an additional stream of revenue, and also eliminate the environmental effects of hydrogen sulphide (H_2S) and CO_2. It is found that production of sulphur as a single product is financially unattractive. Market analysis carried out indicates that Kenya is a net importer of sulphur and the Menengai production could provide an alternative local supply source. According to a risk assessment analysis the biggest risk that the production faces is the significantly high sensitivity of IRR to changes in prices both of sulphur and CO_2.

1. INTRODUCTION

Geothermal power production in high-temperature geothermal fields releases non-condensable gases (NCG) as by-products. The concentrations of these non-condensable gases in the geothermal steam can range from less than 0.2% to over 25% depending on the reservoir characteristics. The composition of NCG is mainly carbon dioxide (CO_2), hydrogen sulphide (H_2S), ammonia (NH_3), methane (CH_4), hydrogen (H_2), nitrogen (N_2) and argon (Ar); CO_2 and H_2S being the largest components (Rodríguez et al, 2014).

Carbon dioxide significantly contributes to the global greenhouse effect. Globally, CO_2 emission from geothermal power plants in high temperature fields are about 120 g/KWh^{-1} by weight on average (Ármannsson et al, 2005). Hydrogen sulphide (H_2S) on the other hand is known for its toxic effect and for being a possible cause of acid rain (Padilla, 2007). The environmental effect of these two gases, albeit being significantly lower in comparison to traditional fossil fuels, have led to increased interest in developing alternative methods not only for eliminating them but also creating valuable products that can be of economic value. There exist various abatement methods and processes for eliminating and treating these gases with the re-injection method being currently the most popular abatement scheme in several geothermal producing countries (Rodríguez et al, 2014, Padilla, 2007).

The conversion of NCG into valuable products that can generate a market value is an alternative approach that has gotten more important over the last decade. The key attraction of this method is that it allows primary production of geothermal power to continue without contributing significantly to greenhouse warming as well as providing an additional revenue stream for the company. The hydrosulphide can be removed and converted into mercantile elemental sulphur while the resulting CO_2 is purified and liquefied for sale either as liquid or as dry ice.

Examples of geothermal fields that are currently converting these gases into marketable products include a 500 kg/h liquid CO_2 production plant in South Iceland (Ragnarsson, 2015, and personal comm.), a 120,000 tons/year liquid CO_2 plant in Kizildere, Turkey (Mertoglu et al., 2015; Şimşek et al., 2005) and George Olah renewable methanol plant in Iceland utilizing CO_2 from the Svartsengi geothermal power plant (technology.com, 2015). In addition, two wells in Armenia produce CO_2 for supplying it to a mineral water bottling company and a factory producing dry ice (Lund and Boyd, 2015).

Tests carried out by Geothermal Development Company (GDC) in Menengai to ascertain the gas chemistry of the steam found out that the proportion of NCG in the steam is 5.9% by weight on average. The CO_2 and H_2S components in the NCG are 98% and 1.59% by weight on average, respectively. A potential problem in this field therefore, is the downstream elimination of these gases without disregarding their economic importance. There are several options under consideration including using H_2S as a raw material for elemental sulphur production and further purifying and liquefying CO_2 to produce industrial or food grade liquid CO_2. This strategic option would minimize the environmental effect associated with these gases but also provide an avenue to optimize the utilization of the resources.

Elemental sulphur and liquid CO_2 extracted from a geothermal field can be used for a number of industrial applications as discussed in Section 2.5. However, before the option is considered, a technical, financial and economic assessment is required in order to determine the capital and operational cost of extraction, technological availability as well as the sustainability and profitability of the production.

The objective of this study is to determine financial viability of retrofitting a sulphur recovery and CO_2 purification plant into the 105 MW (3×35MW) Menengai geothermal plants. The aim of the financial assessment is to identify the project capital and investment requirements, the production and operation costs and specifically to assess whether the project will generate acceptable financial returns. This study will also carry out a market analysis to identify the market for the products as well as carry out a risk assessment to identify the effects of various parameters on the profitability of the project.

In Section 2, this report includes a brief discussion of geothermal gases and the chemical characteristics and composition of geothermal gases at the Menengai wells. It gives an overview of the technology options available on the market for sulphur recovery and CO_2 purification and liquefaction in Section 3; the methodology of financial assessment including the market analysis are discussed Section 4, together with the results of the modelling and of the risk analysis. Conclusion are provided at the end.

1.1 Reviewed literature

A few studies have been conducted so far on available technologies and cost estimates for CO_2 extraction in the geothermal industry. However, the cost data which is available are not complete enough for investment decision making. A study by Bogarín Chaves (1996) found out that it is technically feasible and financially viable to produce commercial liquid CO_2 to maximize the geothermal resource in the value chain. The study is however, not backed by financial assessment of the cost of production.

Rodríguez et al. (2014) reviewed the methods available for H_2S abatement in geothermal power plants including the development of a screening tool for technology selection based on field chemistry and type of the geothermal power plant. The study generally describes costs of the different abatement methods but makes no financial assessment of the commercialization of the CO_2 and sulphur production process.

Padilla (2007) carried out a preliminary study on the emission abatement and utilization of geothermal gases for commercial uses in El Salvador. Different methods of abating H_2S and subsequent process of cleaning CO_2 from the Berlin geothermal power plant are discussed. Cost estimation of sulphur and CO_2 production using costs data indexed from 2000 prices from the Svartsengi power plant is also done. Although the study is comprehensive, it lacks more recent information based on the current cost and development in the geothermal industry. This paper will therefore, expand and bring up to date this information on the current costs as well as the financial soundness of commercializing the production processes.

2. GASES IN GEOTHERMAL PRODUCTION

2.1 General background of Kenya's geothermal market

Globally, Kenya is ranked among the leading countries with geothermal potential of between 7,000 and 10,000 MW (Onyango, 2012). The high-temperature geothermal fields are located in the Rift Valley. As in September 2015 the country's total installed electricity generation capacity was 2,177 MW with geothermal power generation contributing 630 MW (27% of installed capacity), mainly from the Olkaria geothermal field. Geothermal Development Company (GDC) is currently developing 105 MW in Menengai geothermal field, 200 MW in Baringo - Silali and 150 MW in Suswa.

2.2 The Menengai geothermal field

Menengai is a high-temperature field located within the Kenyan Central Rift Valley, north of Lake Nakuru and south of Lake Bogoria. The field is the third field to be developed outside of the Olkaria prospects. Nakuru is Kenya´s fourth largest city and a major agricultural and manufacturing town. Menengai is located within a region of intra-continental crustal triple rift junction with the complex dominated by a central volcano approximately 12 km in diameter. The field measures approximately 850 km^2 with an estimated potential of over 700 MW (Onyango, 2012; Omenda and Simiyu, 2015).

The Menengai field is located in the Menengai caldera formed in the Quaternary and built of trachyte lavas and associated intermediate pyroclastic. Resurgent post-caldera activity (< 0.1 Ma ago) occurred on the caldera floor with an eruption of thick piles of trachyte lavas from various centres. Seismology indicates seismic wave attenuation at < 6 km depth underneath Menengai Caldera suggesting the existence of shallow magma bodies which are believed to be associated with the heat sources for the geothermal system.

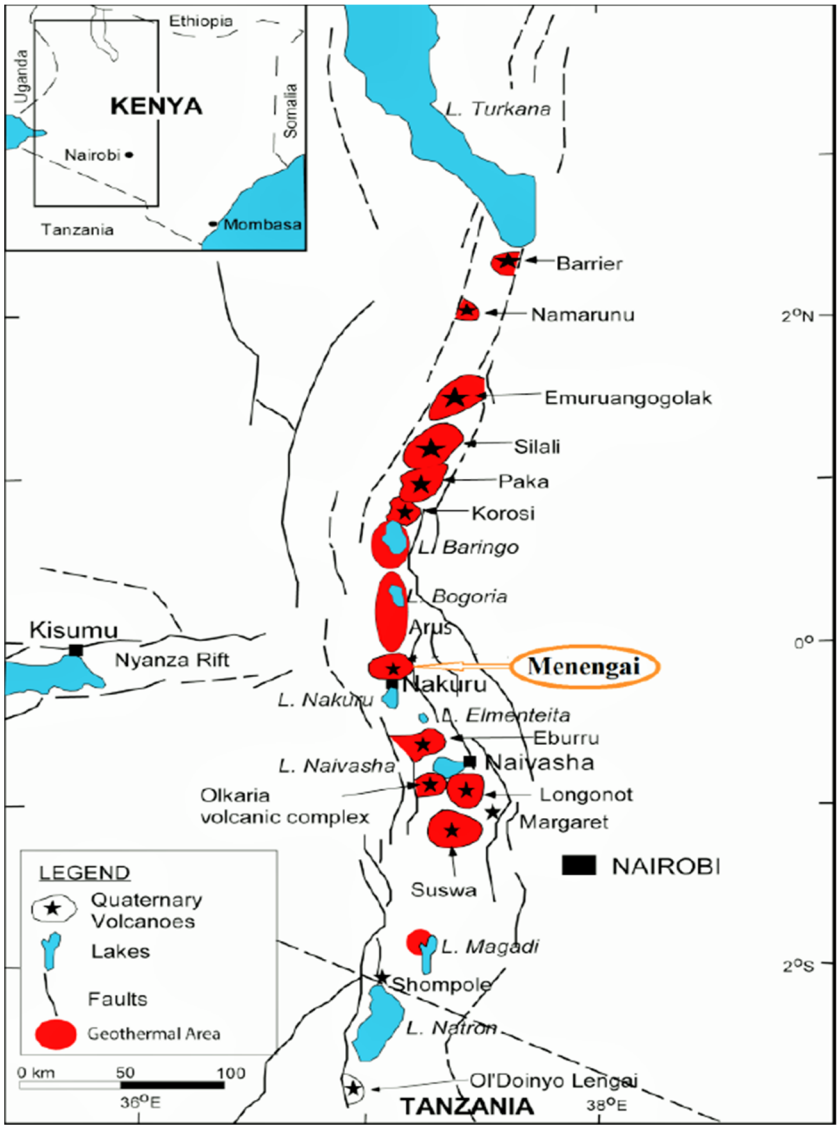

FIGURE 1: Geological map of Kenya showing the location of Menengai

The gas geothermometry based on H_2S and CO_2 indicates that the reservoir temperatures are greater than 250°C. The volcano has been active since about 0.8 Ma ago (Omenda and Simiyu, 2015). The location of Menengai geothermal fields is shown in Figure 1.

2.3 Composition of non-condensable gases (NCG) from Menengai field

By July 2015, 130 MW of steam equivalent had been measured on the well heads in the Menengai field and three companies Sosion Energy, Quantum East Africa and Orpower 22 contracted to operate a 35 MW modular power plant each for a period of 20 years from 2017. These geothermal plants are expected to release non-condensable gases as by-products and measuring them and monitoring is important because these gases can affect the performance of a power plant as well as have environmental effects.

Discharge test results carried out by GDC show that the average share of the NCG in steam from the Menengai field is about 5.9% by weight out of which 98% is CO_2 while 1.59% is hydrogen sulphide (see Table 1). This data was used to determine the quantities of hydrogen sulphide and CO_2, and also as a basis for obtaining budget information from the technology suppliers which is used to estimate the cost (see Section 4).

TABLE 1: Composition of NCG from Menengai field

NCG component	Gas content (%wt)
CO_2	97.9
H_2S	1.59
H_2	0.37
CH_4	0.16
Total	100

2.4 Direct application of non-condensable geothermal gases

In Kenya, commercial direct use applications of geothermal energy are only carried out by the Oserian Development Company where 50 hectares of greenhouses are being heated using geothermal energy from an exploration well. Other small scale applications can be found at the Eburru area where the local community uses 95°C hot steam from a borehole to dry pyrethrum and the condensate as domestic water. Lake Bogoria hotel located near the L. Bogoria geothermal prospect uses water from a nearby warm spring to heat its spa pool (Omenda and Simiyu, 2015).

Besides thermal energy, non-condensable gases and other geothermal by-products geothermal fluids contain can be captured and used for a number of industrial applications in order to achieve a holistic approach. CO_2 and H_2S in particular are the prime gases that can be harnessed for commercial use in the Menengai field.

2.5 Use of elemental sulphur

Elemental sulphur from the Menengai field can be used in the following potential market areas:

- *Chemical production* – Sulphur is the primary source for the production of sulphuric acid. Elemental sulphur can be sold to industries involved in making sulphuric acid. The size of the market of sulphuric acid is discussed in Section 5.
- *Fertilizer manufacturing* – Sulphur is used in the fertilizer manufacturing as one of the essential plant nutrients, along with nitrogen, phosphorous and potassium.
- *Industrial uses* – Potential industrial uses of elemental sulphur includes non-ferrous metals, textile, rubber making such as tyres and boots, pharmaceuticals, agricultural pesticides, personal care products, cosmetics, synthetic rubber vulcanization, water treatment, detergents, paper and carpet making.

2.6 Use of liquid CO_2

CO_2 from the field can be used for a number of applications including the following:

- *Food and beverage industry:* CO_2 can be supplied to food and beverage industry as a key food additive and acidity regulator. CO_2 is also used in carbonate soft drinks, beers, wine and soda/mineral water and to prevent fungal and bacterial growth (modified atmosphere packaging). CO_2 provides fizz to the beverages.
- *Agricultural and biological applications:* Potential customers under his category include large horticultural farms in Nakuru. Plants require CO_2 for photosynthesis and the yields of plants grown in green houses can increase by 20% when air inside the green house is enriched with CO_2. The target level for enrichment is typically a CO_2 concentration of 1000 ppm.
- *Refrigeration (freezing and chilling):* Liquid and solid CO_2 are important refrigerants, especially in the food industry where they are used during the transportation and storage of frozen foods to protect the taste and texture of food products by maintaining proper temperature control.
- *Methanol:* CO_2 can be used as a feed stock and converted into renewable methanol (RM) for usage as fuel, in the production of biodiesel, making of plywood, paints and other products.
- *Medical applications:* In health care, CO_2 is used for insufflation and is often mixed with oxygen or air as a respiratory stimulant to promote deep breathing.
- *Firefighting:* Liquid CO_2 under pressure is used to extinguish small flames from flammable liquids and electrical fires.

3. TECHNOLOGY OPTIONS FOR SUPHUR AND CO_2 RECOVERY

3.1 Overview

This section discusses briefly the main methods that currently exist for the removal of sulphur and purification of CO_2. Independent of the technology type chosen, the process of extracting elemental sulphur and CO_2 from geothermal gases for commercial purposes always involves two main stages. The first stage is the removal of H_2S from the streams of NCG and converting it into elemental sulphur, the second stage involves the purification and liquefaction of the remaining CO_2 (Padilla, 2007). The two-staged production process is briefly discussed here below.

3.2 Stage 1: Removal of hydrogen sulfide (H_2S)

There exist various methods and processes in the geothermal industry for removing H_2S from the stream of NCG exiting the condenser. These processes include liquid redox methods (Stretford, Unisulf, Sulferox and LO-CAT), AMIS, NCG gas injections, the Peabody-Xertic process, the Fe-C1 hybrid method, the Selectox process, biological or THIOPAQ, the Burner-scrubber process, re-injection, the H_2O_2 process, the BIOX process, the copper sulphate process, the steam reboiler process, the alkali scrubbing process, catalytic oxidation, steam stripping, the burner-scrubber process and the Claus process (Bogarín Chaves, 1996; Rodríguez, et al., 2014, Padilla, 2007; Sanopoulos and Karabelas, 1997). The selection of the appropriate process depends on several factors including the condenser type, the gas chemistry, the expected quality of sulphur and regulatory policies regarding gas emissions.

Using the decision tool developed by Rodríguez et al. (2014) for selection of appropriate methods for hydrogen sulphide (H_2S) removal in different geothermal conditions, Table 2 outlines commercial processes that can be applied in the Menengai field. Other processes have not been considered due to their inapplicability (condenser type, gas chemistry, the expected quality of sulphur, economics and regulations for gas emissions) in the Menengai conditions.

The removal of H_2S from NCG from the power plants should involve the application of one of the methods listed above. Price information received from one of the vendors indicated that the capital costs for the full equipment package (including cost for equipment, engineering, initial chemical supply, training and start up support services) for the LOCAT system for the recovery of 15.3 metric tons of sulphur per day is approximately $16M excluding installation costs of approximately $4M. The operating expenses per day on a power plant for chemical purchase are about $2.5M annually. The electricity required totals 4,200 kW for both the equipment electricity load (1100 KW) and the inlet compressors (3100 kW). This process was therefore, eliminated as an option due to its high capital costs, high operating costs associated with the chemicals purchase and high electricity consumption. For the purposes of this study, Thiopaq desulphurization unit has been selected based on economics and budget information received from vendors.

The THIOPAQ process was originally developed by Paques B.V. for the treatment of biogas. The process was further improved by Paques in co-operation with Shell Global Solutions (2008) for the application in the oil and gas industry. The first application of the process was in 1993 in Netherlands and over 100 systems have been installed since. The THIOPAQ process involves the use of naturally occurring bacteria/microorganisms to oxidize the H_2S to elemental sulphur that can be used in the fertilizer production. The process of removing H_2S from the NCG through the THIOPAQ process consists of three stages as shown in the Figure 2 below.

The first stage is the absorption stage/section where hydrogen sulphide is absorbed in a packed tower. The washing liquid from the aerobic reactor is sprayed downwards from the top of the tower. The washing fluid exits the tower at the bottom and is directed to the aerobic reactor. The second stage is the aerobic reactor stage where the microorganisms contained in the aerobic reactor oxidizes absorbed

TABLE 2: H_2S removal processes suitable for the Menengai field

Process type	Brief process description	Pros, cons and costs
1. BIOX process	The BIOX is a downstream process where the off-gases are compressed and mixed with the condensate before entering the cooling tower. An oxidizing biocide is used for biological growth control in the cooling tower which, in combination with oxygen, converts dissolved H_2S to soluble sulphates.	• Eliminates at least 95% of the H_2S in the NCG and at least 98% of the H_2S in the portion of condensate used as cooling tower makeup water • It is suitable for both large and small power plants • The process can be used in both surface and direct contact condenser • Low capital and operational cost
2. THIOPAQ process	The Process involves the use of microorganisms for oxidizing the H_2S to elemental sulphur. The gas containing H_2S is absorbed in an alkaline solution under pressure in a first absorption step. The dissolved sulphide is then oxidized into elemental sulphur in a reactor. The elemental sulphur slurry in the reactor can be separated in a centrifuge to different purities.	• Final H_2S removal of up to 99,99% efficiency with a reactor oxidation to amorphous sulphur between 95 and 98% • Used mostly in the gas industry • Minimal chemical consumption relative to other processes • Low capital costs • The biological sulphur cake can be used for agricultural use
3. Fe-CI hybrid	This method utilizes a highly acidic iron solution through which the off-gas from the condenser is bubbled. The solid sulphur precipitates with nearly 100% turndown of H_2S at solution temperature between 70 and 75°C. The separation of elemental sulphur is done using a rotary drum vacuum filter. Sulphur is obtained as a by-product.	• It has only been laboratory tested and is still under development • The process has potential to generate profit • The iron solution is highly acidic and would require an appropriate selection of materials. • Low capital cost and operational cost
4. Amine/Claus process	Amine/Claus process is a two stage process involving oxidation of stream of gas with air at high temperature to produce sulphur, water and SO_2 followed by a catalytic reaction of H_2S and SO_2 to produce sulphur and water. The liquid sulphur obtained in the process is collected.	• Sulphur recovery of 97% can be achieved • High heat required • No experience in geothermal power plants
5. Wet gas sulphuric acid process (WSA)	WSA is a catalysis process based on diatomaceous earth silica carrier impregnated with vanadium-pentoxide and sodium/potassium pyrosulphates to obtain commercial quality sulphuric acid.	• High quality sulphuric acid (97%) obtained • 95-99% H_2S removal efficiency achieved • Sulphuric acid can be sold commercially • Proper material selection must be done (corrosion) • Low capital costs
6. XERGY process	The XERGY process is still a new technology applicable for HS sulphur recovery in a sour gas stream. There are two different versions of the process, the sub sulphur dew point and the above sulphur dew point. Sulphuric acid is recovered through condensation.	• Sulphur obtained can be sold commercially • There are no stream emissions • The process can be adopted to different H_2S abatements requirements
Sources: Rodríguez et al., 2014; Bogarín Chaves, 1996; Padilla, 2007; Sanopoulos and Karabelas, 1997		

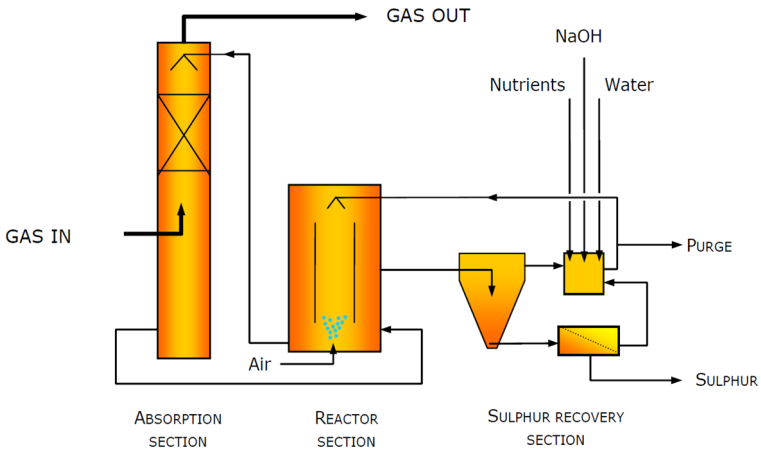

FIGURE 2: THEOPAQ desulphurization process

sulphide into elemental sulphur. The reactor effluent is recycled in the absorber column. The conversion process requires nutrients for good operation. Salt is also required for biomass growth and maintenance.

At the last stage of sulphur recovery, a settling unit is used to separate the produced sulphur from the liquid. The elemental sulphur slurry in the reactor can be separated in a centrifuge to obtain dry-solid concentration of about 60%. The THIOPAQ system will reduce the level of H_2S in the NCG to less than 22 ppm on average.

3.3 Stage 2: Purification of CO_2

After the removal of hydrogen sulphide (H_2S) is completed in stage 1, the remaining CO_2 is purified in order to make it suitable for commercial and industrial use. There is no single standard process designed for the process of recovering and purifying CO_2 after elimination of hydrogen sulphide. Currently, there are five main downstream technologies of removing CO_2 from various gas streams that are available on the market. The five technologies are: chemical solvents, physical solvents, membrane separation, cryogenic separation and adsorption/desorption. The final pressure, temperature and concentration of the CO_2 in the non-condensable gases stream as well as the purity of the final product will determine which technology is most suitable for the extraction process. Most of these technologies are mainly applied in the separation and capturing of CO_2 from coal and gas fired power plants. The purification method most commonly used is the treatment with potassium permanganate, potassium dichromate or active carbon. A typical CO_2 purification process includes the following operational steps (Quintero, 1987; Bogarín Chaves, 1996; Padilla, 2007):

Step i: Compression: After the elimination of H_2S, the next step is compression. The compression stage is a two or more step process which allows the liquefaction of some condensable gases mixed with the CO_2..

Step ii: Phases separation: At this stage, differentiation is carried out based on the gases densities, liquid and gas content.

Step iii: Scrubbing: After differentiation, water or potassium permanganate is normally used to remove some soluble compounds from the gas.

Step iv: Filtration: The next process is the removal of a variety of inorganic impurities by the use of adsorbents such as carbon activated or absorbent compounds.

Step v: Dehumidification: Dehumidification is done using desiccant material in order to reduce the moisture content in the gas.

Step vi: Condensation and liquefaction: During this stage, a refrigerant is used to cool and condense the gas into a liquid form by decreasing the temperature (to approximately -30°C) in combination with high pressure.

Step vii: Storage: The purpose of the storage tank, insulated and with a cooling system, is to contain the liquid CO_2 at high pressures of 15 bar-g and a temperature of approximately -30°C. The cooling could be provided by the CO_2 produced in the process or supplied by an independent cooling device.

The purity of the CO_2 recovered by the process following these steps makes it suitable for usage in the food and beverage industry, agricultural applications and other industrial ones including methanol production and medical applications. The product can be sold liquefied, or solidified as dry ice.

3.4 Current separation of elemental sulphur and CO_2 from geothermal plants

Sulphur is obtained from different sources including coal, gas power plants, crude petroleum, tar sands, oil shale, coal and geothermal brines, metal sulphides such as pyrites, sulphate materials or traditionally mined in native and volcanic deposits (Padilla, 2007). Currently, there are no known documented sources on the production of mercantile sulphur from geothermal power plants.

3.4.1 The Haedarendi CO_2 plant

The power plant at Haedarendi in Grímsnes, South Iceland, has been commercially producing liquid CO_2 food grade (99.99% purity) from two geothermal boreholes since 1988 (Ragnarsson, 2015). The Haedarendi geothermal field is a medium-temperature geothermal field with a temperature of 160°C and a gas content of 1.4% by weight. The plant produces liquid CO_2 for commercial use by utilizing the high concentration of CO_2 gas discharged from the wells which is almost pure CO_2 (Bogarín Chaves, 1996).

The concentration of hydrogen sulphide in the CO_2 gas is approximately 380 ppm, reducing the complex purification process of eliminating it (Bjarnason, 2005). The plant uses approximately 6 l/s of fluid and produces approximately 4,500 tons annually (525 kg/h) of liquid CO_2 (Orkustofnun, 2015; AGA, personal communication).

The production from this facility is sufficient to supply 75% of the total Icelandic CO_2 market requirements of 6,000 tonnes annually. The supply gap is met by imports. The plant was set up at investment costs of $4.7 million. The liquid CO_2 from the power plant is mainly used in green houses, carbonating beverages and in the food industry. The plant is shown in Figure 3.

The production process involves four cleaning stages: cleaning, compression, dehumidification and storage. The cleaning of the gas is performed by a water dispenser where the condensation of some gas takes place at low temperatures. The removal of the remaining portion of H_2S is done using an active carbon filter.

The next stage is a two-stage compression process where cooling and condensate trapping is done at every stage before the final compression is done applying 15 bar-g. At the dehumidification stage, the drying process is carried out in a packed column with silica gel, using a second column for regeneration cycle.

The purified final product (liquid CO_2) is kept in a storage tank with a cooling system to keep the temperature close to -26.5°C. The plant has 225,000 litre capacity storage tanks installed at the site from where liquid is picked up for delivery to customers all over Iceland. The plant itself consumes 17 m^3 of cooling water per hour (AGA, personal communication).

FIGURE 3: Haedarendi carbon dioxide plant in S-Iceland

3.4.2 The CO_2 production from Kizildere field, Turkey

Geothermal resources with high enthalpy in Turkey contain high concentrations of non-condensable gases, especially CO_2. The CO_2 concentration from these fields is probably the highest in the world, ranging from 1 to 2.5% by weight of the geothermal fluid. The Kizilder geothermal field, located at the eastern end of the E-W trending Buyuk Menderes Graben in Western Anatolia, Turkey, is a high-temperature field with a total current production of 95 MWe and 50 MWt. The Kizildere-Denizli power plant was the first geothermal power plant to be built in Turkey in 1984 with an initially installed capacity of 15 MW (Serpen et al., 2015).

In addition to electricity generation, part of the non-condensable gases discharged from Kizildere power plant condenser is piped and passed to a commercial dry ice production plant integrated to the power plant which produces dry ice and liquid CO_2. The CO_2 is filtered through a chemical adsorption process in order to remove minor amounts of sulphur compounds, hydrocarbons and other potential contaminants. Since 1986, the CO_2 plant operated with an initial dry ice and liquid CO_2 production of 40,000 tons per year of clean gas. The production capacity of the plant was increased in 2000 to 120,000 tons per year (Şimşek et al., 2005). Currently, the plant supplies more than 90% of the food grade CO_2 demand required by the Turkey carbonated soft drink market (Simsek et al., 2015). Through this process, the facility is able to generate with zero emission and is at the same time benefiting from the income from commercial sale of CO_2 and through carbon emission trade. Green houses also consume 4,000 tons of CO_2 per year from geothermal resources (Aksoy et al., 2015).

3.4.3 George Olah CO_2 to renewable methanol (RM) plant, Iceland

The George Olah methanol plant located in Grindavík, Reykjanes Peninsula, SW-Iceland, is the world's first commercial CO_2 to methanol plant (see Figure 4). It is the first plant in the world to demonstrate a commercially viable way of generating a synthetic liquid fuel (i.e. liquid electricity for cars) directly from CO_2. The pilot plant started operating in 2007 with a capacity of 50,000 litres per year while an industrial plant began operating in 2011 (Carbon Recycling International, 2015).

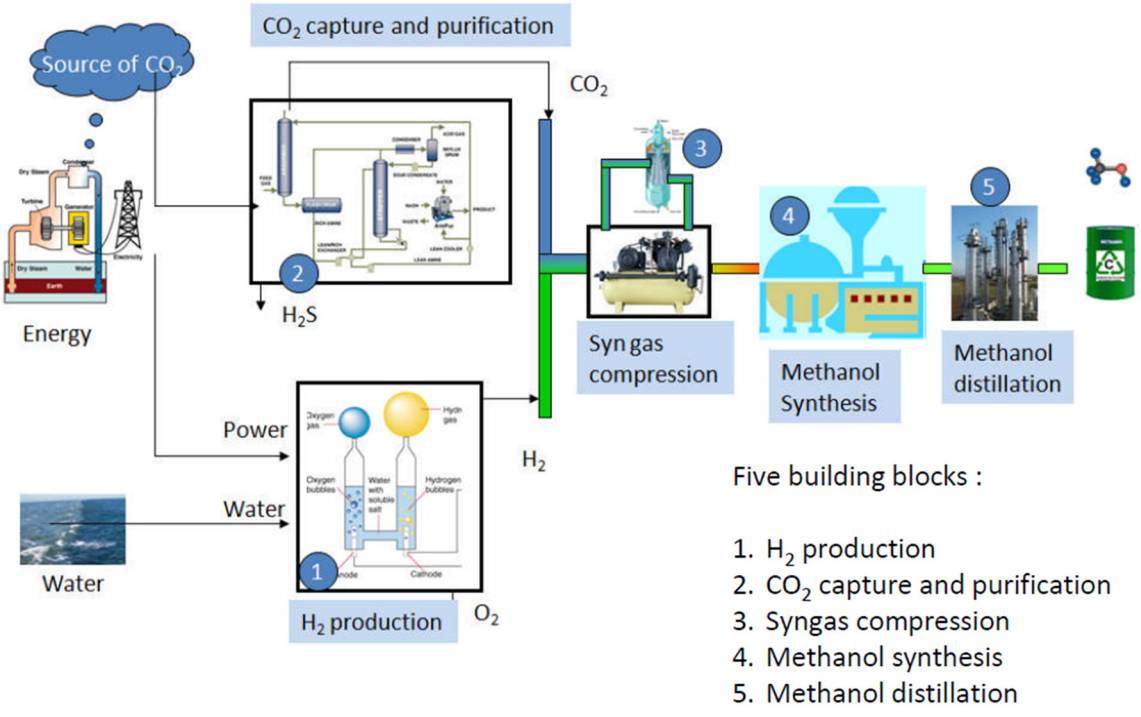

FIGURE 4: Simplified scheme showing the carbon dioxide to fuel process

The industrial plant developed at an investment cost of $8 million uses CO_2 in steam from the Svartsengi geothermal power plant and hydrogen as feed stock and converts this into renewable methanol (RM) for use as a fuel and for making plywood, paints and other products. The water provides the required hydrogen to convert CO_2 to methanol. The only by-product from this process is oxygen (Chemicals-Technology.com, 2015).

The renewable methanol which is sold under the brand Vulcanol is used in bio diesel production, blended with normal gasoline and used as transport fuel for cars both in Iceland and internationally. The renewable facility has a production capacity of fifty million litres of renewable methanol per year which is sufficient to meet approximately 2.5% of the Iceland's gasoline demand. The approximately 5 MW of electricity which the plant requires for its production and electrolysis processes is obtained from the same CO_2 feed stock supplier, the Svartsengi geothermal power plant (Tran, 2010). The facility reclaims approximately 5,500 tons/year of CO_2.

The separation and subsequent conversion process of CO_2 into the final products is based on emission to liquid (ETL) technology, developed by and proprietary of Carbon Recycling International (CRI). The process simply involves splitting of water into hydrogen and oxygen using electricity (electrolysis) and combining CO_2 (feed stock) extracted from the geothermal steam in a ratio of 1:3 to produce renewable methanol (Tran, 2010; Chemicals-technology.com, 2015). A simplified CO_2 to fuel schematic process is shown in Figure 4 above.

3.4.4 Gas separation at the Hellisheidi power plant, Iceland (SulFix and CarbFix Processes)

Reykjavik Energy, in a bid to tackle the gas emission effects at its Hellisheidi Power Plant, has developed a gas abatement method for lowering the H_2S and CO_2 emissions. This method aims at dissolving the geothermal gases in effluent water from the power plant based on their solubility and re-inject them back into the geothermal reservoir. Carbfix involves the isolation of the CO_2 and re-injecting it back into the basaltic formation while SulFix involves reinjection of CO_2 into the geothermal system. A pilot scale gas separation station was operated at the field to determine the commercially feasibility of separating the gases into streams of H_2S and CO_2 rich gas and a stream of less soluble geothermal gases i.e. H_2, N_2, CH_4 and Ar prior to the reinjection of the gases into the reservoir. The company is currently implementing an industrial scale gas injection system based on the success of the pilot project (Júlíusson, 2015; Gunnarsson et al., 2015).

During the pilot phase, three technologies where being tested for their viability; a membrane system for H_2S removal, a system comprising of adsorption and desorption towers for separating soluble gases CO_2 and H_2S from the rest of the geothermal gases and a distillation column to separate CO_2 from H_2S. The pilot scale gas separation is carried out in two steps. The first step involves the separation of soluble gases, CO_2 and H_2S, from the rest of the insoluble geothermal gases (H_2, N_2, CH_4, and Ar) using an absorption/desorption or membrane system. In the second step a distillation column is used to separate CO_2 from H_2S based on the difference in their physical properties (Júlíusson, 2015; Gunnarsson et al., 2015).

There is an interest in developing alternatives of utilizing the resource in the most sustainable and energy efficient way and creating valuable products from all available sources. The stream of purified CO_2 which is separated in the process is a valuable product and can be used in greenhouses to increase the production of crops in Iceland, particularly for tomatoes, algae production, bio fuel production and aquaculture (Júlíusson, 2015). A study to assess the feasibility of the production of renewable methanol and sulphuric acid from hydrogen sulphide and CO_2 emissions from the Hellisheidi geothermal power plant was carried out in 2014 and found that the Icelandic market for sulphur and sulphuric acid was too small, and exporting it was not feasible economically (Júlíusson, 2015; Gunnarsson et al., 2015).

The projects described above demonstrate examples of areas where commercial CO_2 emitted from geothermal plants is captured and converted into marketable products.

4. FINANCIAL ASSESSMENT

4.1 Methodology and model framework

The main criteria for estimating the financial feasibility (profitability) of the investment are the Net Present Value (NPV) and the Internal Rate of Return (IRR) of cash flows. A modified Microsoft Excel-based profitability assessment model developed by Jensson (2006) was applied. The model which consists of different spreadsheets for investment, operations, cash flows and profitability is a simulation model based on an initial investment and subsequent operations of the plant over a determined period of time. The model is set up including a twenty-five year planning period in line with the assumed lifetime of the plant. Using this model, other parameters like the capital requirement, working capital, cash flow, financial ratios and charts can be deduced.

The profitability model is based on the premise that sulphur removal and CO_2 purification plant is a downstream process and will involve retrofitting into the 105 MW Menengai power plants. The model is based on given assumptions (see Section 4.4) which are deterministic but allows random variables to be added. The model´s key input which is costs for the desulphurization unit are based on budget information from the THIOPAQ process supplier. The cost estimates for the CO_2 purification and liquefaction unit are based on budget information presented by a technology supplier in 2012 for the production of 1,000 kg/h liquid in Iceland. The purification costs have been indexed to 2014 prices using the Chemical Engineering Plant Index (CEPCI).

Other model input including the cost for civil works and site preparation, land purchase, labour, utility costs, licences and permitting have been estimated for the Kenyan case. The estimated values used in the modelling might not be the most optimal, but will nevertheless provide a preliminary estimate with a probable accuracy of within ± 20% and be sufficient for decision making.

The key outputs from the model are the discounted NPV and IRR of cash flow and profitability yard sticks for the project. Risk assessment using sensitivity analysis was also carried out to evaluate and compare the effects of various parameters on the profitability (IRR) of the plant. For simplicity, we assume that the prices for elemental sulphur and liquid CO_2 are the same over the modelling time span.

4.2 Data

Gases chemistry data from eleven production wells from the Menengai field and normalized at 7 bar-a (165°C) using WATCH 2.4 program were collected and used to obtain budget quotation from commercial vendors and/or manufacturers for the desulphurization unit. This approach was adopted to ensure that the estimates reflect the present market cost and that they are as realistic as possible.

The THEOPAQ process was selected for this study based on budget information received, plant economics and the suitability of the process in the field. Data on prices of nutrients, sulphur and liquid CO_2 was obtained from secondary sources including market reports, United Nations Commodity Trade Statistics Database and the U.S Geological Survey. Additional data for the purification and liquefaction of CO_2 were obtained via personal communication with AGA, Orka Náttúrunnar (ON) and Carbon Recycling International staff, Iceland.

4.3 Rational for financial assessment

The primary objective of the financial assessment is to determine the net financial impact of the elemental sulphur and CO_2 production plant on GDC. The assessment has been performed from GDC's perspective as the project developer and owner, and hence considers the cash flows that have a direct impact upon GDC or are directly attributed to the development or operation of the plant. The results

from the model should provide an indication on whether it is economically viable or not to invest in the project.

4.4 Technological, cost and financial assumptions

The input data for the model includes information on the expected annual production of elemental sulphur and liquid CO_2 in tons, associated annual expenses, estimated capital costs, operational costs, the Marginal Attractive Rate of Return (MARR) for the project and equity, dividend payments and other technical and financial assumptions.

4.4.1 Technological and production assumptions

- Project start date - January 1, 2017 with one-year construction period.
- Full commercial operation start date - January 1, 2018.
- The desired final compression pressure of the purified liquid CO_2 is 15 bar-g and a temperature of -30°C.
- The planning horizon is 25 years (PPA period).
- Four people are needed to operate the plant (2 engineers per shift).

4.4.2 Cost estimation assumptions

- Total equipment costs are the combined costs for plant and equipment, piping and piping installation, instrumentation, controls, electrical system and installation, cooling tanks, storage tanks for the sodium hydroxide, insurance and freight from the vendor's country to Menengai, engineering, supervision and commissioning. Storage tanks with the capacity to hold NAOH, Paques nutrients and liquid CO_2 for 14 days were considered.
- Cost for buildings and services including the costs for site and yard improvements (fencing, grading, roads, sidewalks, landscaping), as well as auxiliary facilities and service (water, electricity connection, fire protection). These costs have been estimated for Kenya.
- Others investment costs include costs for contracting, licensing and permits and general contingency. Costs for licenses and permits are real values from Kenya (National Environmental Management Authority fees (licenses Environmental and Social Impact Assessment for the plant and site excavation) of 0.1% of the total project costs), royalties of 0.5% of gross sales value and construction levy of 0.5% of the total contract value of the project.
- Fixed costs includes the annual maintenance and repair cost estimated to be 5% of total capital costs, annual plant overhead and administrative expenses estimated to be 6% and 15%, respectively, of the sum of annual operating labour and maintenance and repair costs (Peters and Timmerhaus, 1991; Towler, and Sinnott, 2012). Annual operating labour costs are estimated for Kenya.
- Price of caustic NAOH (20%) estimated to be $ 300 /ton CFR (Cost and Freight) in Kenya. NAOH requirements are 792 litres/hour.
- The Paques nutrient solution's (Nutrimix 34/32) standard price is € 1.699 /litre or $ 1.911 /litre (Shell Global Solutions, 2008). The nutrients requirement is assumed to be 381 litres/day. Indexed to 2014 prices.
- Demineralized water (1.0 $/m^3$) estimated 2 m^3/ton of CO_2.
- Cost for land acquisition is not included in cost estimates as it is already owned by the company.
- Kenya´s corporate tax of 30%.
- Electricity to be supplied from the nearby power plant at US Cents 7 for kWh.
- Cooling water costs are not considered, have to be obtained from the condenser.
- Cost for transportation of liquid CO_2 to the customer premises and storage facilities, costs at the clients' yard, are not included in the estimates.

A summary of cost components for the desulphurization and the CO_2 is given in Tables 3 and 4 below:

TABLE 3: Desulphurization unit

Cost item	Component	Cost ($
Capital investment		
Buildings	Buildings & civil works, auxiliaries and installation	259,701
	Land purchase	-
	Buildings Total	**259,701**
Equipment	Plant and equipment, piping and piping installation, instrumentation and controls, electrical system and installation, engineering, supervision and commissioning, insurance and freight, storage tank for NAOH & cage ladder on scrubber tank	6,197,684
	Equipment total	**6,197,684**
Other investment	Contracting and other fees	230,334
	Licensing, permits, other fees	63,868
	General contingency	645,739
	Other investment total	**939,941**
Total capital investment		**7,397,326**
Production costs		
Fixed costs	Maintenance and repairs ($/yr.)	322,869
	Operating labour and supervision ($/yr.)	45,714
	Plant overhead ($/yr.)	221,150
	Administrative expenses ($/yr.)	55,288
	Fixed costs total	**645,021**
Variable costs	Caustic (NAOH) 20% and Paques nutrient solution (Nutrimix 34/32) ($/yr.)	3,461,387
	Electricity ($/yr.)	807,672
	Water ($/yr.)	-
	Variable costs total	**4,269,059**

TABLE 4: CO_2 purification and liquefaction unit

Cost item	Component	Menengai cost ($)
Capital investment		
Buildings	Buildings & civil works, auxiliaries and installation	129,850
	land purchase	
	Buildings total	**129,850**
Equipment	Plant and equipment, piping and piping installation, instrumentation and controls, electrical system and installation, engineering, supervision and commissioning, CO_2 storage tank	1,887,471
	Total equipment costs	**1,887,472**
Other investment	Contracting and other fees	23,033
	Licensing and permits	
	General contingency	201,732
	Total other investment	**224,767**
	Total capital	**2,242,089**
Production cost		
Fixed costs	Maintenance and repairs ($/yr.)	100,866
	Operating labour and supervision ($/yr.)	45,714
	Plant overhead ($/yr.)	87,948
	Administrative expenses	21,987
	Total fixed costs	**256,516**
Variable costs	Electricity	180,708
	Demineralized water ($/M3)	36,593
	Total variable	**217,300**
	Total production	**473,816**

4.4.3 Project financing

- The project financing is 30% equity and 70% debt
- Loan repayment period is 8 years
- Interest rate on the loan is 6%

5. MARKET ANALYSIS FOR ELEMENTAL SULPHUR AND CO_2

5.1 Elemental sulphur demand, supply and price

In 2014, the global sulphur production was about 72.4 million tonnes, with production from oil and gas contributing 97%. China, the United States and Canada are the biggest producers with their production accounting for approximately 15%, 13% and 11% respectively of the global supply. Africa produces paltry less than 1% share of the global production (U.S. Geological Survey, 2015a). The world sulphur production from all sources is expected to grow at an average annual rate of between 4-6% from 2014 to 2019 with elemental sulphur growing by 6% (IHS, 2014) with the highest growth expected in the Middle East and Canada. Kenya´s known sources of sulphur are small and uneconomical and therefore, the country relies mostly on imported sulphur. In 2013, Kenya produced 23,000 metric tons of sulphuric acid.

The global demand for sulphur in 2014 was dominated by fertilizer production (56%) while base metals and industries consume 32%. Phosphate fertilizer production consumed about 85% of the 56% consumed in fertilizer production, followed by ammonium sulphate production (IHS, 2014). Global consumption increased by 38% from 2000 to 2014 and is expected to grow by 11% per year until 2019 depending on the stability of the world economy and growth in demand for sulphuric acid (IHS, 2014). A surge in demand from major end-use industries is also projected to positively influence growth in global sulphur demand. China is the largest consumer of sulphur. Africa is expected to continue to import high levels of sulphur for phosphate production (U.S. Geological Survey, 2015a).

In 2013, Kenya imported 5,335 metric tons of sulphur in all forms from Russia, Saudi Arabia, United Arab Emirates, India, Jordan and other countries with a trade value of $1.393 million and exported 28 tons valued at $12,964 (United Nations Commodity Trade Statistics Database, 2015).

Kel Chemicals, a sulphuric acid producing plant in Nairobi, produces 14,600 metric tons of sulphuric acid mainly from imported sulphur (Yager, 2015).

Kenya has a total fertilizer demand of 500,000 tonnes annually but only produces 300,000 tonnes. All sulphur required for the manufacturing process is imported. To bridge the demand-gap a new factory with a production capacity of 100,000 tonnes of fertilizer is being set up in Nakuru (15 km away from Menengai field) and is expected to start operation in November 2016. A second factory owned by Toyota Tshusho Corporation is also being built in Eldoret (150 km away from Nakuru). The two companies could provide a locally available demand for the Menengai by-product.

The average contract price for exported elemental sulphur in the U.S in 2014 was $ 157 (FOB) per ton and $ 169 (FOB) per ton between January and June 2015 (U.S. Geological Survey, 2015b). According to Gordon (2015) the price of sulphur between January and March 2015 has been ranging from $ 155 to $ 175 per ton as shown in Figure 5. In September 2015, the Free On Board prices for elemental sulphur in China and the Middle East ranged between $ 120-130 and $ 123-135 /ton respectively (Meehan, 2015).

The average price of imported sulphur in Kenya for the fertilizer production is $150 (personal communication with a fertilizer manufacturing company).

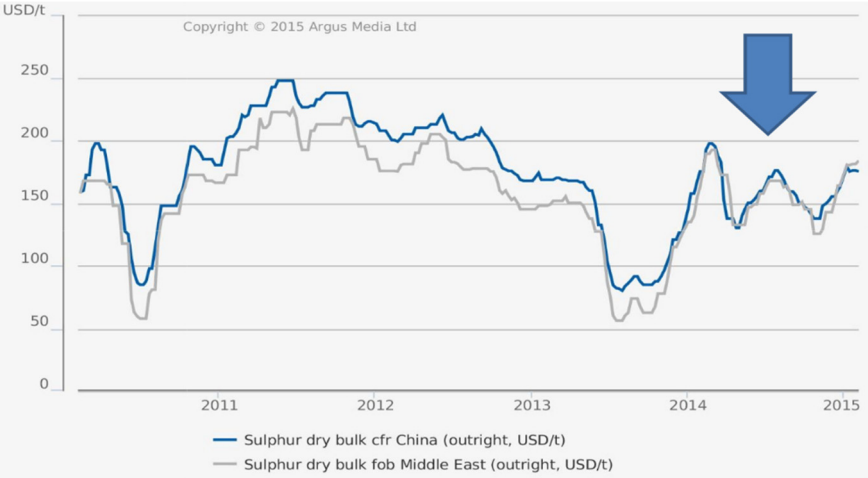

FIGURE 5: Trend of sulphur prices (Gordon, 2015)

5.2 Carbon dioxide demand, supply and price

The market for commercial liquid CO_2 is driven today by demand of the food and beverage industry. The beverage industry has been a consistent consumer of high purity CO_2 for decades with a consumption of more than 300 million tons worldwide. The food and beverage industries consumed almost half of this amount while metal production markets consumed about 15%. China is the leading user with a consumption of almost 34% of the global CO_2 produced in 2014. It is then followed by North America with a demand of 23%, Asia/Oceanic with 16% and the Middle East is accounting for 8% (IHS, 2015).

During the years 2014 to 2019, the total global liquid CO_2 market is expected to grow annually by 2.6% with the average growth rates forecasted to be the highest in Africa with a rate of 9.6%, followed by Latin America and the Middle East at a rate of 5.3% and China at a rate of 4.5% (IHS, 2015; Klemes et al., 2007).

The market for CO_2 in Kenya is an oligopolistic supply, mainly coming from Carbacid (CO_2), Ltd., BOC Kenya, Ltd. (BOC), Chemigas, Noble Gases, Welgas, Crown Gases and Synergy Gas. The industry is divided into a tonnage supply scheme composed of large volumes producers supplying directly via gas pipelines from the on-site production facility, merchant or bulk liquid market where suppliers fill the cryogenic tanks at the customers' sites and cylinder gas deliveries involving small scale supply using gas cylinders.

Carbacid, Ltd. is the biggest CO_2 trading company and controls the majority share of pure CO_2 and other gases market in the East African region. The biggest and major market is the food industry, drink bottlers and breweries in Kenya, Uganda, Tanzania, Rwanda, Burundi, Ethiopia, Uganda, Zambia, Southern Sudan and Somali. The company obtains its natural CO_2 by mining from its underground reservoir wells, 70 km from Nairobi. In 2013, Carbacid´s annual production from its plant in Nairobi was 35,000 tons while the annual production of CO_2 from natural sources was 18,900 tons. Due to increasing regional and local demand for the product, the company increased its capacity in 2014 by 10,000 tons at its mining site at Kereita Forest (Yager, 2015).

BOC Kenya, Ltd. (BOC) sells its CO_2 in the East Africa Region in bulk food grade liquid form, bulk industrial grade liquid CO_2, compressed CO_2, dry ice pellets or as industrial gas in cylinders. In 2013, Kenya exported 12,371 tons of food grade and industrial CO_2 valued at $5,323,477 (equivalent to $430/ton) and imported 9,821 tons valued at $17,781 (United Nations Commodity Trade Statistics

Database, 2015). Information on the actual size of the CO_2 market in Kenya is very scanty due to the nature of the market but this study estimates that the production is approximately 50,000 tons per year.

Currently, the major consumers of CO_2 are the food and beverage industries (beer, wine, fizzy drinks and bottled juices). Some of the biggest consumers include regional bottlers particularly in the East Africa Region including Uganda, Nile, Braliwa and East Africa breweries, Coca Cola, Keroche Industries and flavoured juice manufacturers who use it as a preservative or products enhancer. Demand for the product is further expected to rise parallel with the growth in the soft drinks industry in the East African Region. The carbonated drink production increased by 19.1% in the year 2013.

The price of liquid industrial CO_2 in Iceland is approximately 26-28 ISK/kg (202 to 218 $/ton, exchange rate September, 2015) (AGA Iceland, personal communication in September 2015). For some industries the price is 50 ISK/kg. For this analysis, a price of 393 $/ton was used.

6. MAIN RESULTS OF PROFITABILITY MODEL

This section presents results from the profitability assessment model. From the model results, this study is able to deduce the financial conditions and operating performance of the investment and forecast the future performance of production. The results are based on an annual production of 5,287 tons of elemental sulphur and 17,382 tons of liquid CO_2. This amount of CO_2 is equivalent to 5% of the CO_2 released from the 105 MW power plant as roughly estimated in this study. The prices for elemental sulphur and liquid CO_2 are assumed to be $ 150 and $ 393 per ton, respectively, as indicated in Section 5).

6.1 Project capital requirements

The capital investment required for the project is $ 9,639,415 to be allocated as follows: $ 389,552 for buildings, $ 8,085,156 for equipment and $ 1,164,707 for other investment cost. The project would also require an additional investment in working capital during the first year of the project. From the model, the project´s estimated working capital requirement is $ 140,000. A fixed cost and variable cost of approximately $ 901,537 annually and 198 $/ton will be required throughout the operation period. See Appendix I for detailed information on the financial model of the project.

6.2 Profitability of the project

Net Cash Flows and Pre-Tax Cash Flows: In 2017, the total net cash flow is negative since this is the period where the initial investment is made and construction of the production plant is taking place. This is also the year where funding is required for the purchase of equipment, buildings, civil works as well as installation of the plant. A working capital of $ 140,000 is also required to cover other expenditures.

In 2018, the first full year of operation, pre-tax and net cash flows are forecasted to be approximately $ 2,236,123 and $ 952,877.

As seen in Figure 6, the net cash flows increase until 2027 from where it stabilizes at $ 1,569,961 after the clearing of the loans. This project could generate net cash flow of $ 32,389,601 in its entire 25 year lifetime. If the company decides to produce sulphur only, the pre-tax and net cash flows will be negative.

Net Present Value (NPV): The Net Present Value is a valuable indicator recognizing the time value of money. It is a common tool for evaluating an investment and represents the sum of the discounted cash flows from a given time period. Projects whose NPV is positive are attractive because they are profitable.

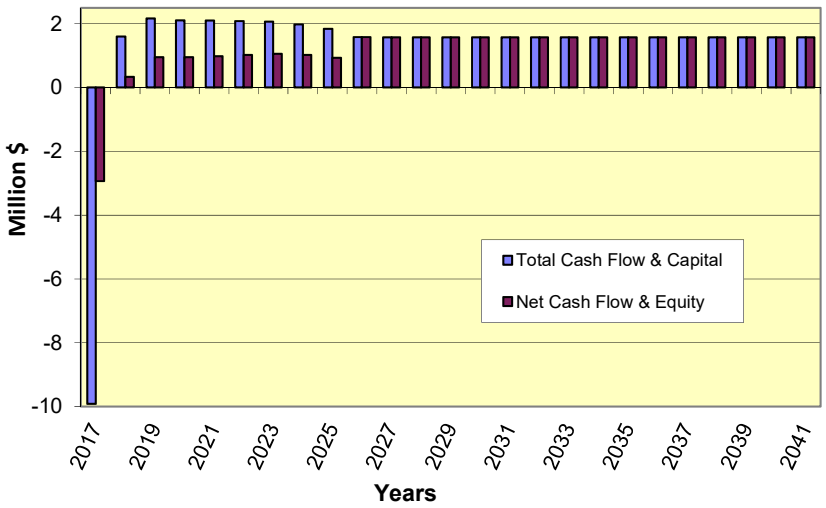

FIGURE 6: The total cash flow and net cash flow

The Net Present Value was calculated for this project to determine profitability of the project and to compare the future cash flows resulting from the investment with other investment alternatives (marginal attractive rate of return or MARR).

In this project, the NPV for total capital with discount rate (MARR) of 15% is $ 2,033,178 while NPV for equity with discount rate (MARR) of 20% is $ 2,028,446. The continued operation of the plant results in NPV of total cash flows and NPV of net cash flows being positive. As the trend of accumulated NPV shows in Figure 7, the NPV for total capital turns positive after ten years while NPV for equity turns positive after five years. In this case, a discount rate of 15% for the total project and 20% for equity was used.

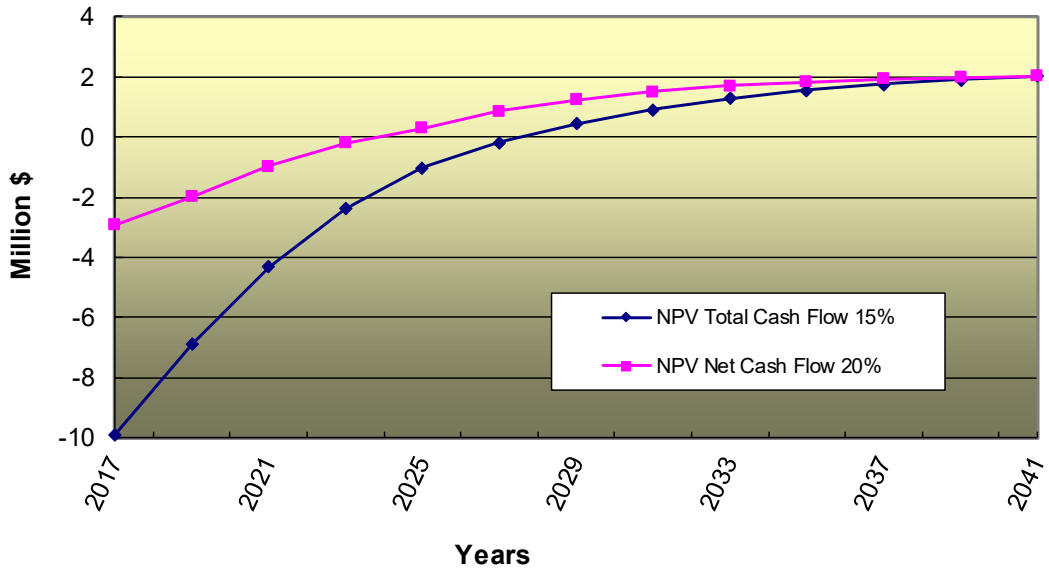

FIGURE 7: Net Present Value of total and net cash flow for the project

Internal Rate of Return (IRR): The Internal Rate of Return is defined as the discount rate at which the after tax NPV is equal to zero. It is a measure of determining the level of annual return (profitability) over the lifespan of an investment. The higher the IRR of a project, the more attractive and viable it is to invest in. This study calculated internal rate of return of the cash flow stream of the project to determine if the IRR meets the marginal attractive rate of the return (MARR) criterion which requires that the lowest acceptable limit for IRR should be greater than MARR or WACC or the hurdle rate.

In this study, the IRR of total cash flow and IRR of net cash flow are 19% and 31%, respectively (Figure 8). These values are higher compared to the total project MARR and equity MARR of 15% and 20%, respectively.

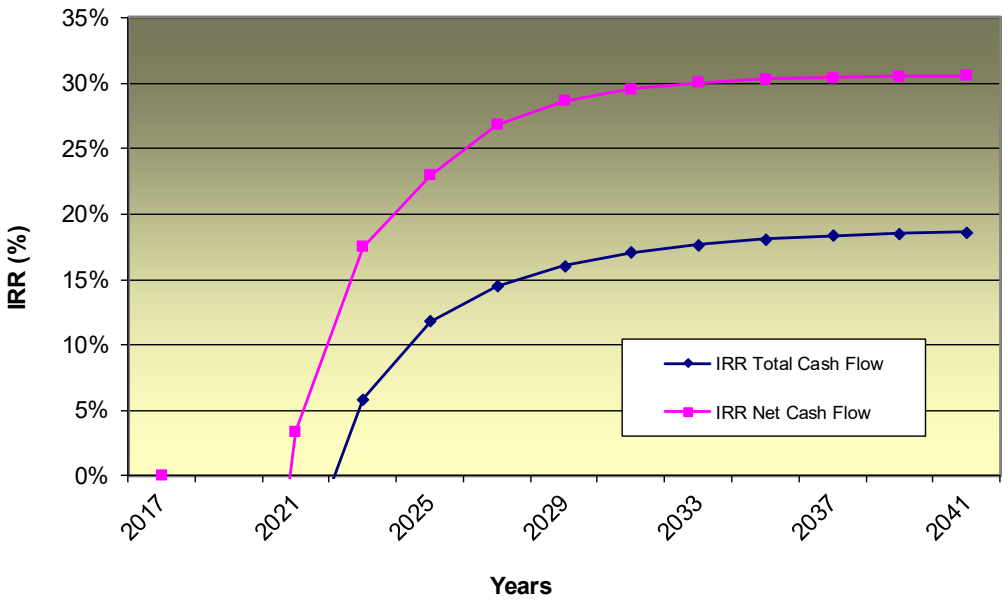

FIGURE 8: Internal Rate of Return (IRR) for the project

6.3 Financial indicators/ratios

The debt service coverage (DSCR) of the project was computed for this project to determine the after tax cash flow of the project on a year-to-year basis relative to the amount of money for loan repayment (principal and interest). The debt service coverage rises from 1.8 in 2018 to reach a stable high of 2.0 in 2023.

Similarly, the loan life cover ratio (LLCR) was also computed to show the number of times the after tax cash flow throughout the life time of the project can be able to repay the outstanding debts. The loan life cover ratio is 2.5 on average and hence higher than the minimum acceptable threshold of 1.5 (Figure 9).

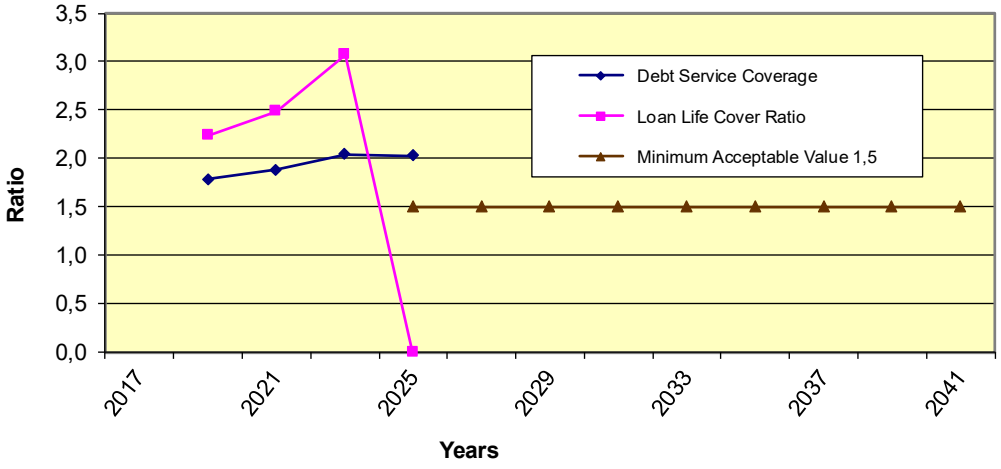

FIGURE 9: Debt service coverage ratio and loan life cover ratio

6.4 Risk assessment analysis

Impact analysis: As part of the financial assessment, risk assessment using sensitivity analysis was carried out to determine the sensitiveness of equity IRR relative to a given change in input parameters. The sensitiveness and size of impact of prices and sales quantities of both elemental sulphur and liquid

CO_2, and buildings and equipment costs on the project IRR was carried out. One variable at a time was changed by a specified percentage, both above and below the most-likely value, while the other variables were held constant at the base case value. The output was then calculated for the new value; in this case the output being IRR of equity. The results of the one-way sensitivity analysis for all variables are as shown in Figure 10 below.

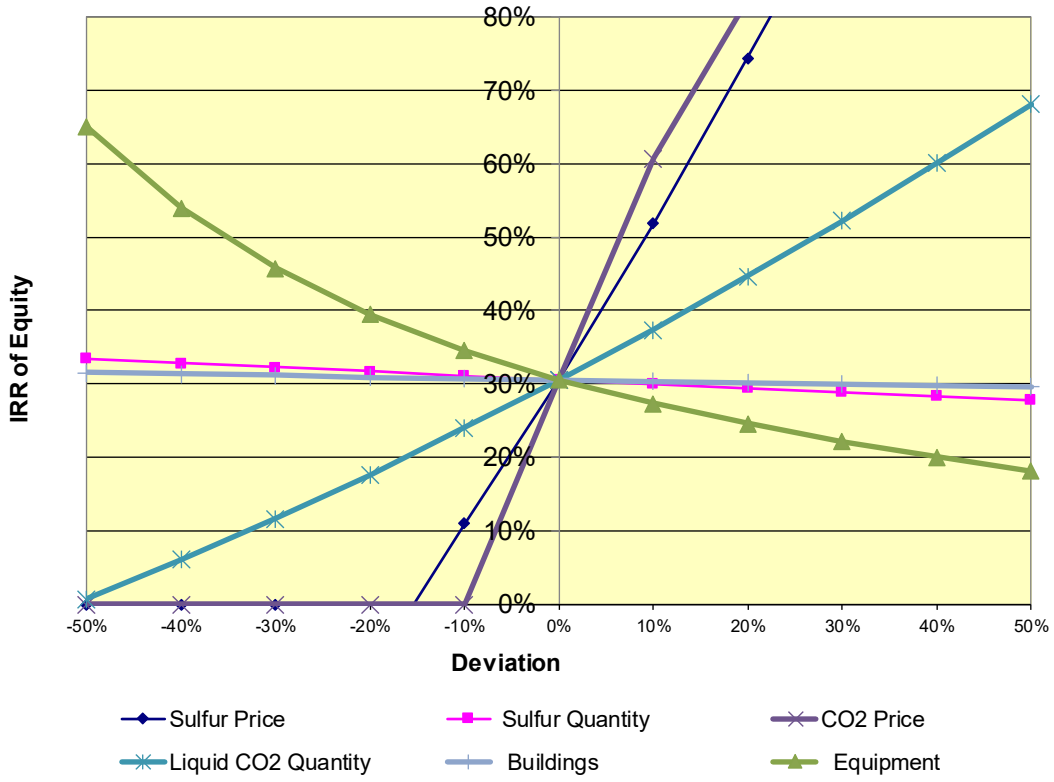

FIGURE 10: Impact analysis of the project

The line of CO_2 price is the steepest compared to others factors implying that the equity IRR is very sensitive to the selling price and quantities of CO_2. When the CO_2 price increases by 10% equity IRR increases by 61%.

On the contrary, GDC will lose profits if the sales price of CO_2 goes down by 5% which would result in a decrease of equity IRR of 14%. Equity IRR is also very sensitive to the sales price of sulphur. However, its impact is not as big as that of the price of CO_2. In addition, equity IRR is also sensitive to the cost of equipment. A 50% decrease in the cost of equipment will increase the equity IRR by 66%, while a 50% increase will increase equity IRR by 21%.

7. DISCUSSION

It is noted that the biggest component of the total capital investment (79%) is used for the desulphurization unit while the rest will be needed for the CO_2 purification and liquefaction unit.

The NPV of total cash flows and NPV for equity are both positive. The positive NPV demonstrates that the proposed project is acceptable or profitable. The production of elemental sulphur alone will not generate sufficient revenues for the project to break even. At a price of 150 $/ton, the production of elemental sulphur will not be able to pay its variable cost of 198 $/ton. A decrease in the demand below the capacity used in this study will make the project non-profitable.

The IRR of total cash liabilities and IRR of net cash flows of 19% and 34% are greater than the marginal attractive rate of return of equity (MARR) of 15% and 20%, respectively. The debt service coverage ratio and loan life cover ratio (LLCR) are also higher than the acceptable minimum acceptable threshold of 1.5. Consequently, on the basis of the results of the IRR and financial ratios the project is profitable enough to operate over the planned period.

Sensitivity analysis shows that the IRR of the project is significantly affected by changes in prices and quantity of liquid CO_2 and elemental sulphur. A drop in the price of sulphur and CO_2 by10% and16%, respectively, will make the IRR negative. A drop in the sales volume from the base value of 17,382 tons will make the investment uneconomical. This means that GDC's priority in the project will be to have long term contracts and assured markets for the 17,382 tons of CO_2 produced. Other parameters including the operational and maintenance, buildings and equipment costs have less impact on the profitability of the plant.

Revenue that may accrue to the project as a result of trading in the certified emission reductions (CERs) have not been taken into consideration in this study due to the recent collapse of the CERs markets and Kenya´s current ineligibility to trade its CERs in the European Union – Emission Trading Scheme.

8. CONCLUSIONS

This study demonstrates that the extraction of elemental sulphur and liquid CO_2 for commercial purposes is financially viable, i.e. results in positive NPV and IRR. Production of elemental sulphur alone is uneconomical but a combination of the two products can generate sufficient cash flows for meeting the project´s operational costs as surplus/profit. The surplus cash flows can significantly improve the economics of the project.

Through this project, Menengai field can provide alternative local elemental sulphur supply and reduce the country´s reliance on imports. Market analysis carried out in this study indicate that the two new fertilizer manufacturing factories being erected in Nakuru and Eldoret could provide a ready market for the 5,655 tons of elemental sulphur which are expected to be produced from the field.

To mitigate risks, further assessment on the accuracy and reliability of the demand for liquid CO_2 is proposed. This study also recommends identification of opportunities for further utilization of the remaining 95% CO_2 not considered. These large quantities could provide a source of potential revenues in the future.

Logistic and distribution chain requirements (costs and risks) for the two products are recommended before positioning the products in the market.

Protection of the environment is an increasingly important consideration in the current production of energy from geothermal sources. An avenue for minimizing the environmental impact of the harmful geothermal gases hydrogen sulphide and CO_2 is therefore, to convert them into marketable products. The emissions avoided during the extraction process as demonstrated in this study proves that the extraction process is an option that can be successfully applied in other geothermal fields in the world with high NCG concentrations. The net effect is the elimination of the effects of the two gases on the environment as well as improving the economics of geothermal power plants.

ACKNOWLEDGEMENTS

I wish to express my gratitude to the United Nations University Geothermal Training (UNU-GTP) Programme and my employer Geothermal Development Company for giving me the opportunity to be among the three pioneer UNU Fellows in the UNU-GTP 2015 new line of study, Project Management and Finances.

I am also grateful to my supervisor, Prof. Páll Jensson for his professional guidance and valuable advice throughout this research. I would also like to thank the entire UNU-GTP staff for their assistance and support. Further, I thank Bjarni Már Júlíusson of ON Power, Ómar Sigurbjörnsson of Carbon Recycling International (CRI) and Mr. Gudmundur K. Rafnsson and Thorlákur Kjartansson for giving me time for an interview despite your busy schedules. A special thanks to all teachers who impacted knowledge on me during the introductory and specialized lecturers and all the fellows for their company and friendship.

Finally, I would like to thank the Almighty God for his love and protection throughout this study.

REFERENCES

Aksoy, N., Gok, O.S., Mutlu, H., and Kilinc, G., 2015: CO_2 emission from geothermal power plants in Turkey. *Proceedings of the World Geothermal Congress 2015, Melbourne, Australia*, 7 pp.

Ármannsson, H., Fridriksson, Th., and Kristjánsson, B.R., 2005: CO_2 emissions from geothermal power plants and natural geothermal activity in Iceland. *Geothermics*, *34*-3, 286–296.

Bjarnason, J.Ö., 2005: Haedarendi well HE-07: Fluid chemistry and carbonate scaling, ISOR – Iceland GeoSurvey, Reykjavík, report ISOR-05236.

Bogarin Chaves, R., 1996: Geothermal gases as a source of commercial extraction of CO_2, in Miravalles, Costa Rica and Haedarendi, Iceland. Report 3 in: *Geothermal training in Iceland 1996.* UNU-GTP, Iceland, 23-44.

Carbon Recycling International, 2015: *Methanol*. Carbon Recycling International, website: *www.carbonrecycling.is/index.php?option=com_content&view=article&id=64&Itemid=32&lang=en*

Chemicals-technology.com, 2015: *George Olah CO_2 to renewable methanol plant, Reykjanes, Iceland.* Website: *www.chemicals-technology.com/projects/george-olah-renewable-methanol-plant-iceland/*

Gordon, F., 2015: *Sulphur and sulphuric acid: Hopes and fears for 2015*. Argus, London, presentation, 20 pp.

Gunnarsson, I., Júlíusson, B.M., Aradóttir, E.S., Sigfússon, B., and Árnason, M.Th., 2015: Pilot scale geothermal gas separation, Hellisheidi power plant, Iceland. *Proceedings of the World Geothermal Congress 2015, Melbourne, Australia,* 8 pp.

IHS, 2014: *Chemical economics handbook: Sulfur*. IHS, website: *www.ihs.com/products/ sulphur-chemical-economics-handbook.html*

IHS, 2015: *Chemical economics handbook: CO_2*. HIS, website: *www.ihs.com/ products/carbon-dioxide-chemical-economics-handbook.html*

Jensson, P., 2006: Profitability assessment models. *Workshop on fisheries and aquaculture in Southern Africa: development and management.* Windhoek, Namibia, ICEIDA and UNU-FTP, 18 pp.

Júlíusson, B.M., 2015: *H_2S abatement in geothermal power plants: Gas separation in NCG exhaust system/from waste to value*. UNU-GTP, Iceland, unpublished lecture notes

Klemes, J., Bulatov, I., and Cockerill, T., 2007: Techno-economic modelling and cost functions of CO_2 capture processes. *Computers and Chemical Engineering, 31*, 445-455.

Lund, J.W., and Boyd, T.L., 2015: Direct utilization of geothermal energy 2015 worldwide review. *Proceedings of the World Geothermal Congress 2015, Melbourne, Australia,* 31 pp.

Meehan, J., 2015: *Sulphur prices in China fall again on poor demand*. ICIS, website: */www.icis.com/resources/news/2015/09/11/9923083/sulphur-prices-in-china-fall-again-on-poor-demand/*

Mertoglu, O., Simsek, S., and Basarir, N., 2015: Geothermal country update report of Turkey (2010-2015). *Proceedings of the World Geothermal Congress 2015, Melbourne, Australia,* 9 pp.

Omenda P., and Simiyu, S., 2015: Country update for Kenya 2010-2014. *Proceedings of the World Geothermal Congress 2015, Melbourne, Australia,* 11 pp.

Onyango, S.O., 2012: Preliminary design of the Menengai Phase I steam gathering system. Report 26 in: *Geothermal training in Iceland 2012*. UNU-GTP, Iceland, 601-641.

Orkustofnun, 2015: *Direct utilization: Industrial uses*. Orkustofnun – National Energy Authority, Reykjavik. Orkustofnun, website: *www.nea.is/geothermal/directutilization/industrial -uses/*

Padilla, E.K., 2007: Preliminary study on emission abatement and use of gas from geothermal power plants in El Salvador. Report 18 in: *Geothermal training in Iceland 2007*. UNU-GTP, Iceland, 417–446.

Peters, M.S., and Timmerhaus, K.D., 1991: *Plant design and economics for chemical engineers* (4^{th} ed). McGraw-Hill, New York, NY, United States, 910 pp.

Quintero, M., 1987: A potential remotion process and utilization of the non-condensable gases CO_2 and H_2S from the geothermal wells in Cerro Prieto. *Geothermal Resource Council, Trans.*, *11*, 143–148.

Ragnarsson, Á., 2015: Geothermal development in Iceland 2010-2014. *Proceedings of the World Geothermal Congress 2015, Melbourne, Australia*, 15 pp.

Rodríguez, E., Harvey, W.S., and Ásbjörnsson, E.J., 2014: Review of H_2S abatement methods in geothermal plants. *Proceedings of the 38^{th} Workshop on Geothermal Reservoir Engineering, Stanford University, Stanford, CA, US,* 9 pp.

Sanopoulos, D., and Karabelas, A.J., 1997: H_2S abatement in geothermal plants: Evaluation of process alternatives. *Energy Sources, 19-1*, 63–77.

Serpen, U., Aksoy, N., and Ongur, T., 2010: 2010 Present status of geothermal energy in Turkey. *Proceedings of the 35^{th} Workshop on Geothermal Reservoir Engineering, Stanford University, Stanford, CA, US,* 7 pp.

Shell Global Solutions, 2008: *Confidential technical proposal - PPGJ project: CPP Gundih AGTU*. Shell Global Solutions, 25 pp, website: *xa.yimg.com/kq/groups/19104170/424004216/ name/Tekim.pdf*

Şimşek, Ş., Yıldırım, N., and Gülgör, A., 2005: Developmental and environmental effects of the Kızıldere geothermal power project, Turkey. *Geothermics*, *34*-2, 234–251.

Towler, G., and Sinnott, R.K., 2012: *Chemical engineering design: Principles, practice and economics of plant and process design* (2nd ed.). Butterworth-Heinemann, Oxford, United Kingdom, 1320 pp.

Tran, K.C., 2010: *Making renewable fuel by carbon recycling*. Carbon Recycling International, Reykjavik, Iceland, 17 pp. Website: http://newenergy.is/gogn/Radstefnur/3mai2010/carbon_recycling_international__cri____overview.pdf

United Nations Commodity Trade Statistics Database, 2015: *UN comtrade database*. Website: *http://comtrade.un.org/*

U.S. Geological Survey, 2015a: *Mineral commodity summaries 2015.* U.S Geological Survey, Reston, VA, United States, 196 pp. USGS, website: *minerals.usgs.gov/minerals/pubs/mcs/2015/mcs2015.pdf*

U.S. Geological Survey, 2015b: *Mineral industry surveys: Sulphur in June 2015*. U.S. Geological Survey, Reston, VA, United States, 5 pp. USGS, website: *minerals.usgs.gov/minerals/pubs/commodity/ sulphur/mis-201506-sulfu.pdf*

Yager, T., 2015: *2013 minerals yearbook: Kenya. The mineral industry of Kenya* [advance release]. U.S. Geol. Survey, 7 pp. Website: *minerals.usgs.gov/minerals/pubs/country/ 2013/myb3-2013-ke.pdf*

APPENDIX I: Financial model of the project

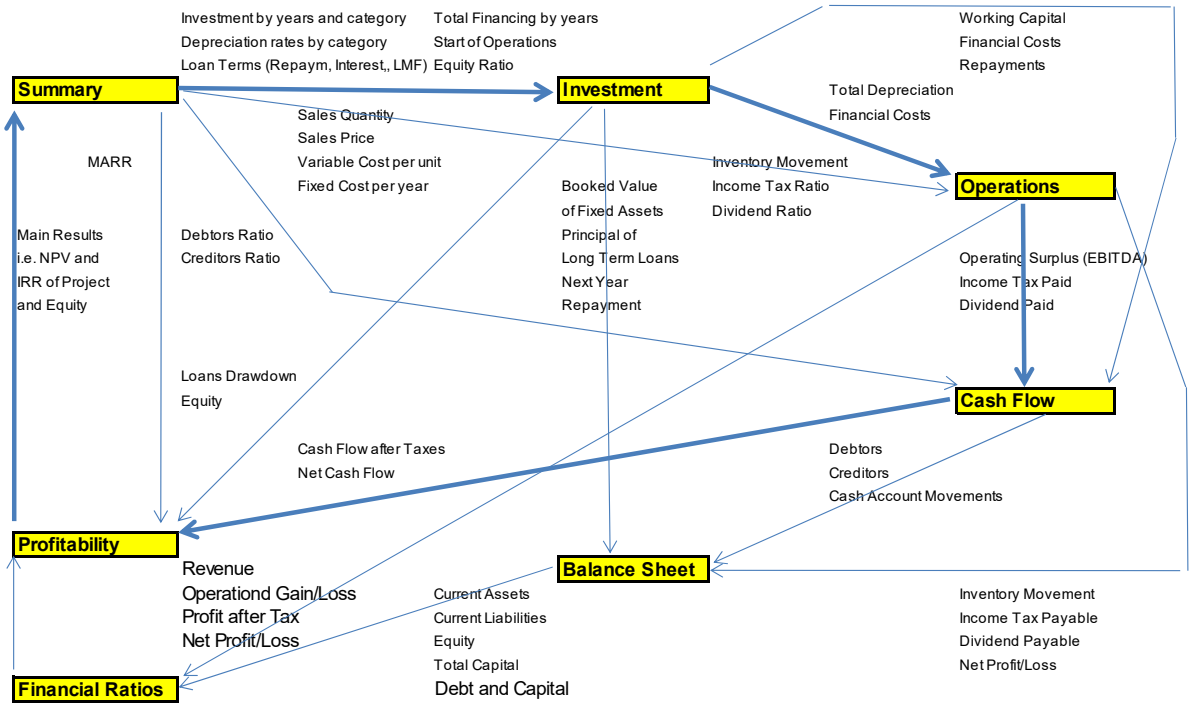

FIGURE 1: Profitability model summary

Investment

Investm and Financing		2.017 1	2019 3	2021 5	2023 7	2025 9	2027 11	2029 13	2031 15	2033 17	2035 19	2037 21	2039 23	2041 25	Total
Investment:															
Buildings		389.552	0	0	0	0	0	0	0	0	0	0	0	0	**389.552**
Equipment		8.085.156	0	0	0	0	0	0	0	0	0	0	0	0	**8.085.156**
Other		1.164.707	0	0	0	0	0	0	0	0	0	0	0	0	**1.164.707**
		9.639.415	**0**	**0**	**0**	**0**	**0**	**0**	**0**	**0**	**0**	**0**	**0**	**0**	9.639.415
Booked Value of Fixed Assets															
Buildings		389.552	358.388	327.224	296.059	264.895	233.731	202.567	171.403	140.239	109.075	77.910	46.746	15.582	
Equipment		8.085.156	5.659.609	3.234.062	808.516	0	0	0	0	0	0	0	0	0	
Other		1.164.707	698.824	232.941	0	0	0	0	0	0	0	0	0	0	
Total Booked Value		**9.639.415**	**6.716.821**	**3.794.227**	**1.104.575**	**264.895**	**233.731**	**202.567**	**171.403**	**140.239**	**109.075**	**77.910**	**46.746**	**15.582**	39.686.146
Depreciation:															
Depreciation Buildings	4%	-	15.582	15.582	15.582	15.582	15.582	15.582	15.582	15.582	15.582	15.582	15.582	15.582	**342.806**
Depreciation Equipm.	15%	-	1.212.773	1.212.773	1.212.773										**5.659.609**
Depreciation Other	20%	-	232.941	232.941											**698.824**
Total Depreciation		**-**	**1.461.297**	**1.461.297**	**1.228.355**	**15.582**	**15.582**	**15.582**	**15.582**	**15.582**	**15.582**	**15.582**	**15.582**	**15.582**	6.701.239
Financing:															
Equity	0	2.933.824	-	-	- -	0 -	0								**2.933.824**
Loans	1	6.845.590	-	-	- -	0 -	0								**6.845.590**
Total		**9.779.415**	**-**	**-**	**- -**	**0 -**	**0**								9.779.415
Loans:															
Drawdown		6.845.590	0	0	0	0	0	0	0	0	0	0	0	0	
Repayment	8		**855.699**	**855.699**	**855.699**	**855.699**									**6.845.590**
Principal	-	6.845.590	5.134.193	3.422.795	1.711.398	-	0	0	0	0	0	0	0	0	
Interest	0	-	359.393	256.710	154.026	51.342	0	0	0	0	0	0	0	0	**1.848.309**
Loan Managem. Fees	2%	136.912	0	0	0	0	0	0	0	0	0	0	0	0	**136.912**

TABLE 1: Investment

Operations

Operations Statement		2.017	2.019	2.021	2.023	2.025	2.027	2.029	2.031	2.033	2.035	2.037	2.039	2.041	Total
Operations Statement															
Sales Sulfur		-	5.287	5.287	5.287	5.287	5.287	5.287	5.287	5.287	5.287	5.287	5.287	5.287	**126.886**
Sales Liquid CO2		-	17.382	17.382	17.382	17.382	17.382	17.382	17.382	17.382	17.382	17.382	17.382	17.382	
Sulfur Price		-	150	150	150	150	150	150	150	150	150	150	150	150	
Liquid CO2 Price		-	393	393	393	393	393	393	393	393	393	393	393	393	
Revenue Sulfur		-	**793.035**	**793.035**	**793.035**	**793.035**	**793.035**	**793.035**	**793.035**	**793.035**	**793.035**	**793.035**	**793.035**	**793.035**	
Revenue Liquid CO2		-	**6.830.985**	**6.830.985**	**6.830.985**	**6.830.985**	**6.830.985**	**6.830.985**	**6.830.985**	**6.830.985**	**6.830.985**	**6.830.985**	**6.830.985**	**6.830.985**	**163.943.649**
Revenue		-	**7.624.020**	**7.624.020**	**7.624.020**	**7.624.020**	**7.624.020**	**7.624.020**	**7.624.020**	**7.624.020**	**7.624.020**	**7.624.020**	**7.624.020**	**7.624.020**	**182.976.479**
Variable Cost	198		4.486.360	4.486.360	4.486.360	4.486.360	4.486.360	4.486.360	4.486.360	4.486.360	4.486.360	4.486.360	4.486.360	4.486.360	**107.672.637**
Fixed Cost	901.537		901.537	901.537	901.537	901.537	901.537	901.537	901.537	901.537	901.537	901.537	901.537	901.537	**21.636.886**
Diverse Taxes															
Operating Surplus (EBITDA)		-	**2.236.123**	**2.236.123**	**2.236.123**	**2.236.123**	**2.236.123**	**2.236.123**	**2.236.123**	**2.236.123**	**2.236.123**	**2.236.123**	**2.236.123**	**2.236.123**	**53.666.956**
Inventory Movement		-	-												
Depreciation		-	1.461.297	1.461.297	1.228.355	15.582	15.582	15.582	15.582	15.582	15.582	15.582	15.582	15.582	**9.623.833**
Operating Gain/Loss (EBIT)		-	**774.826**	**774.826**	**1.007.768**	**2.220.541**	**2.220.541**	**2.220.541**	**2.220.541**	**2.220.541**	**2.220.541**	**2.220.541**	**2.220.541**	**2.220.541**	**44.043.124**
Financial Costs		136.912	359.393	256.710	154.026	51.342	0	0	0	0	0	0	0	0	**1.985.221**
Profit before Tax		**-** **136.912**	**415.433**	**518.117**	**853.742**	**2.169.199**	**2.220.541**	**2.220.541**	**2.220.541**	**2.220.541**	**2.220.541**	**2.220.541**	**2.220.541**	**2.220.541**	**42.057.903**
Loss Transfer	0	- 136.912	-	-	-	-	-	-	-	-	-	-	-	-	
Taxable Profit		-	415.433	518.117	853.742	2.169.199	2.220.541	2.220.541	2.220.541	2.220.541	2.220.541	2.220.541	2.220.541	2.220.541	
Income Tax	30%	-	124.630	155.435	256.123	650.760	666.162	666.162	666.162	666.162	666.162	666.162	666.162	666.162	**12.617.371**
Profit after Tax		**-** **136.912**	**290.803**	**362.682**	**597.619**	**1.518.439**	**1.554.379**	**1.554.379**	**1.554.379**	**1.554.379**	**1.554.379**	**1.554.379**	**1.554.379**	**1.554.379**	**29.440.532**
Dividend	0%	-	-	-	-	-	-	-	-	-	-	-	-	-	-
Net Profit/Loss		**-** **136.912**	**290.803**	**362.682**	**597.619**	**1.518.439**	**1.554.379**	**1.554.379**	**1.554.379**	**1.554.379**	**1.554.379**	**1.554.379**	**1.554.379**	**1.554.379**	**29.440.532**

TABLE 2: Operations

Cash Flow

		2.017	2.019	2.021	2.023	2.025	2.027	2.029	2.031	2.033	2.035	2.037	2.039	2.041	Total
Cash Flow															
Operating Surplus (EBITDA)		-	2.236.123	2.236.123	2.236.123	2.236.123	2.236.123	2.236.123	2.236.123	2.236.123	2.236.123	2.236.123	2.236.123	2.236.123	53.666.956
Debtors	0	-	635.335	635.335	635.335	635.335	635.335	635.335	635.335	635.335	635.335	635.335	635.335	635.335	
Debtor Changes		-	-	-	-	-	-	-	-	-	-	-	-	-	635.335
Greditors	0	-	-	-	-	-	-	-	-	-	-	-	-	-	
Creditor Changes			-	-	-	-	-	-	-	-	-	-	-	-	-
Financing - Expenditure (Wcap)		140.000	-	-	-	0	0	0	-	-	-	-	-	-	140.000
Cash Flow before Tax		140.000	2.236.123	2.236.123	2.236.123	2.236.123	2.236.123	2.236.123	2.236.123	2.236.123	2.236.123	2.236.123	2.236.123	2.236.123	53.171.621
Paid Taxes		-	68.154	140.032	170.838	392.803	666.162	666.162	666.162	666.162	666.162	666.162	666.162	666.162	11.951.208
Cash Flow after Tax		140.000	2.167.969	2.096.091	2.065.286	1.843.321	1.569.961	1.569.961	1.569.961	1.569.961	1.569.961	1.569.961	1.569.961	1.569.961	41.220.413
Interest & Loan Man Fee		136.912	359.393	256.710	154.026	51.342	0	0	0	0	0	0	0	0	1.985.221
Repayment		-	855.699	855.699	855.699	855.699	-	-	-	-	-	-	-	-	6.845.590
Net Cash Flow		3.088	952.877	983.682	1.055.561	936.280	1.569.961	1.569.961	1.569.961	1.569.961	1.569.961	1.569.961	1.569.961	1.569.961	32.389.601
Paid Dividend			-	-	-	-	-	-	-	-	-	-	-	-	-
Cash Movement		3.088	952.877	983.682	1.055.561	936.280	1.569.961	1.569.961	1.569.961	1.569.961	1.569.961	1.569.961	1.569.961	1.569.961	32.389.601
Cash Flow ratios:															
Debt Service Coverage			1,8	1,9	2,0	2,0									
Loan Life Cover ratio:															
NPV of Cash Flow	6%		11.497.531	8.509.085	5.258.264	1.738.982	4.468.119	6.884.841	9.035.715	10.949.985	12.653.679	14.169.961	15.519.446	16.720.482	
Principal			5.134.193	3.422.795	1.711.398										
Loan Life Cover Ratio			2,2	2,5	3,1	-									
Minimum Acceptable Value	**1,5**					1,5	1,5	1,5	1,5	1,5	1,5	1,5	1,5	1,5	

TABLE 3: Cash flow

Balance

Balance Sheet		2017	2019	2021	2023	2025	2027	2029	2031	2033	2035	2037	2039	2041	
Assets															
Cash Account	0	3.088	1.290.319	3.221.745	5.296.927	7.254.825	10.410.150	13.550.071	16.689.993	19.829.915	22.969.836	26.109.758	29.249.680	32.389.601	
Debtors		-	635.335	635.335	635.335	635.335	635.335	635.335	635.335	635.335	635.335	635.335	635.335	635.335	15.248.040
Stock	0	-	-	-	-	-	-	-	-	-	-	-	-	-	-
Current Assets		3.088	1.925.654	3.857.080	5.932.262	7.890.160	11.045.485	14.185.406	17.325.328	20.465.250	23.605.171	26.745.093	29.885.015	33.024.936	375.288.682
Fixed Assets		9.639.415	6.716.821	3.794.227	1.104.575	264.895	233.731	202.567	171.403	140.239	109.075	77.910	46.746	15.582	39.686.146
Total Assets		9.642.503	8.642.475	7.651.307	7.036.837	8.155.056	11.279.216	14.387.973	17.496.731	20.605.488	23.714.246	26.823.003	29.931.761	33.040.519	414.974.828
Debts															-
Dividend Payable		-	-	-	-	-	-	-	-	-	-	-	-	-	-
Taxes Payable		-	124.630	155.435	256.123	650.760	666.162	666.162	666.162	666.162	666.162	666.162	666.162	666.162	12.617.371
Creditors		-	-	-	-	-	-	-	-	-	-	-	-	-	-
Next Year Repayment		855.699	855.699	855.699	855.699	-	-	-	-	-	-	-	-	-	6.845.590
Current Liabilities		855.699	980.329	1.011.134	1.111.821	650.760	666.162	666.162	666.162	666.162	666.162	666.162	666.162	666.162	19.462.961
Long Term Loans		5.989.892	4.278.494	2.567.096	855.699	-	0	0	0	0	0	0	0	0	
Total Debt		6.845.590	5.258.823	3.578.230	1.967.520	650.760	666.162	666.162	666.162	666.162	666.162	666.162	666.162	666.162	
Equity	0	2.933.824	2.933.824	2.933.824	2.933.824	2.933.824	2.933.824	2.933.824	2.933.824	2.933.824	2.933.824	2.933.824	2.933.824	2.933.824	
Profit & Loss Balanc	0 -	136.912	449.828	1.139.252	2.135.493	4.570.471	7.679.229	10.787.986	13.896.744	17.005.502	20.114.259	23.223.017	26.331.774	29.440.532	
Total Capital		2.796.913	3.383.653	4.073.077	5.069.317	7.504.296	10.613.053	13.721.811	16.830.568	19.939.326	23.048.084	26.156.841	29.265.599	32.374.356	
Debts and Capital		9.642.503	8.642.475	7.651.307	7.036.837	8.155.056	11.279.216	14.387.973	17.496.731	20.605.488	23.714.246	26.823.003	29.931.761	33.040.519	

TABLE 4: Balance sheet

TABLE 5: Profitability

Profitability

Profitability Measurements	2.017	2.019	2.021	2.023	2.025	2.027	2.029	2.031	2.033	2.035	2.037	2.039	2.041	Total
NPV and IRR of Total Cash Flow														
Cash Flow after Taxes	- 140.000	2.167.969	2.096.091	2.065.286	1.843.321	1.569.961	1.569.961	1.569.961	1.569.961	1.569.961	1.569.961	1.569.961	1.569.961	40.940.413
Total Capital	- 9.779.415	-	-	-	-	-	-	-	-	-	-	-	-	9.779.415
Total Cash Flow & Capital	- 9.919.415	2.167.969	2.096.091	2.065.286	1.843.321	1.569.961	1.569.961	1.569.961	1.569.961	1.569.961	1.569.961	1.569.961	1.569.961	31.160.998
NPV Total Cash Flow 15%	- 9.919.415	- 6.888.129	- 4.301.341	- 2.373.991	- 1.027.051	- 188.321	442.568	919.611	1.280.324	1.553.075	1.759.314	1.915.260	2.033.178	
IRR Total Cash Flow		-44%	-8%	6%	12%	14%	16%	17%	18%	18%	18%	19%	19%	
NPV and IRR of Net Cash Flow														
Net Cash Flow	3.088	952.877	983.682	1.055.561	936.280	1.569.961	1.569.961	1.569.961	1.569.961	1.569.961	1.569.961	1.569.961	1.569.961	32.389.601
Equity	- 2.933.824	-	-	-	0	0	-	-	-	-	-	-	-	2.933.824
Net Cash Flow & Equity	- 2.930.736	952.877	983.682	1.055.561	936.280	1.569.961	1.569.961	1.569.961	1.569.961	1.569.961	1.569.961	1.569.961	1.569.961	29.455.777
NPV Net Cash Flow 20%	- 2.930.736	- 1.990.388	- 967.541	- 204.273	298.590	859.402	1.246.781	1.515.795	1.702.610	1.832.342	1.922.434	1.984.998	2.028.446	15.035.359
IRR Net Cash Flow	0%	-37%	3%	18%	23%	27%	29%	30%	30%	30%	30%	31%	31%	
Financial Ratios														
Profit+Interest/Debt+Capital (ROI)		8%	10%	14%	31%	23%	17%	14%	12%	10%	9%	8%	7%	
Profit/Sharehl. Capital (ROE)		9%	10%	13%	25%	17%	13%	10%	8%	7%	6%	6%	5%	
Asset Turnover Ratio		83%	94%	106%	105%	78%	59%	48%	40%	34%	30%	27%	24%	
Equity Ratio		39%	53%	72%	92%	94%	95%	96%	97%	97%	98%	98%	98%	
Net Current Ratio		2,0	3,8	5,3	12,1	16,6	21,3	26,0	30,7	35,4	40,1	44,9	49,6	
Liquid Current Ratio		2,0	3,8	5,3	12,1	16,6	21,3	26,0	30,7	35,4	40,1	44,9	49,6	
Internal Value of Shares		1,2	1,4	1,7	2,6	3,6	4,7	5,7	6,8	7,9	8,9	10,0	11,0	
Price/Earnings Ratio		11,6	11,2	8,5	4,9	6,8	8,8	10,8	12,8	14,8	16,8	18,8	20,8	

UNITED NATIONS UNIVERSITY
UNU-GTP
Geothermal Training Programme

Orkustofnun, Grensasvegur 9,
IS-108 Reykjavik, Iceland

Reports 2015
Number 18

TOPPING UNIT AT OLKARIA IV GEOTHERMAL POWER PLANT, NAIVASHA, KENYA

Reuben Kipngeno Langat
Kenya Electricity Generating Company Ltd. - KenGen
P.O. Box 785-20117, Naivasha
KENYA
rklangat@kengen.co.ke, ruben.langat@gmail.com;

ABSTRACT

A study on the optimization of the current set up of Olkaria IV geothermal power plant by utilizing high-pressure fluid is presented. The study is applied on the Olkaria IV geothermal wells to determine the additional electrical energy output that could be generated. A total steam mass-flow of 280 kg/s is passed through a back-pressure turbine acting as a topping unit, operating between 11.8 bar absolute inlet pressure and 6 bar absolute exhaust pressure. Thermodynamic cycle model simulation done using Engineering Equation Solver (EES) shows that 10-26 MW of electricity can be produced in the topping unit assuming turbine isentropic efficiency of 85%. The additional gross power generated will also provide environmental benefits. The application of the proposed model can help to utilize the untapped geothermal energy without additional drilling costs, thereby increasing the profitability of the operating plants.

1. INTRODUCTION

1.1 General background

Renewable energy is a priority in today's global energy outlook due to drastically increasing prices of fossil fuels and associated greenhouse gas emissions. Geothermal energy is considered to be an attractive renewable energy option. It originates from the thermal energy present in the Earth's crust. Geothermal energy has been used since ancient times in many countries in the world, mainly used for bathing, cooking and washing. Current applications of geothermal energy include electricity production, district heating, green house farming, fish farming, drying, snow melting, and others (Geirdal, 2013). Commercial electricity power generation from geothermal power plant started in 1914 when a 250 kW unit at Larderello, Italy provided electricity to the nearby cities of Volterra and Pomarance (DiPippo, 2007). Since then, many geothermal power plants have been installed. There are many aspects that make electricity production from geothermal energy to be feasible technically, economically and environmentally such as high availability, high capacity factor, ability to be used as a base load, low operational and maintenance cost, and low CO_2 emissions.

Geothermal power plants can be divided into two main groups based on the enthalpy of the geothermal fluid: those that utilise steam cycles which are used at higher fluid enthalpies and binary cycles for lower enthalpies In steam cycles, the geothermal fluid from liquid-dominated reservoirs boils partly due to

flashing in the wells, the steam is then separated from the brine and finally expanded in a turbine to produce work. Usually the brine is released into the environment (e.g. re-injected to the reservoir or released onto the surface), or it can be flashed again at a lower pressure. The first type of cycles in which the fluid boils and the brine is separated at a high pressure and then rejected directly to the environment is called single flash cycle (SF), and the second type in which the brine is flashed again at a lower pressure is called double flash cycle (DF). A binary cycle uses a secondary working fluid in a closed power generation cycle. A heat exchanger is used to transfer heat from the geothermal fluid to the working fluid, and the cooled brine is then released into the environment or reinjected back into the ground. The organic Rankine Cycle (ORC) and Kalina cycle, used to exploit low to medium enthalpy geothermal resources are both binary cycles.

Geothermal resources have been classified as low, intermediate or high-enthalpy resources according to their reservoir temperatures. The temperature ranges used for these classifications are arbitrary and they are not generally agreed upon (Lee, 1996). Temperature is used as the classification parameter because it is the easiest to measure and understand. In addition, temperature or enthalpy alone can be ambiguous defining a geothermal resource because two independent thermodynamic properties are required to define the thermodynamic state of the fluid. Geothermal energy exists in the form of heat, which is a low grade form of energy and work is a high grade form of energy, and from the Second Law of Thermodynamics, all work can be converted into heat but not vice versa. Therefore, geothermal resources should be classified based on exergy, a measure of the amount of maximum work that can be produced from a given heat source. (DiPippo, 2007). Exergy analysis can be done for all components of the power plant to identify the exergy efficiencies or sometimes called Second Law efficiencies or utilization efficiencies.

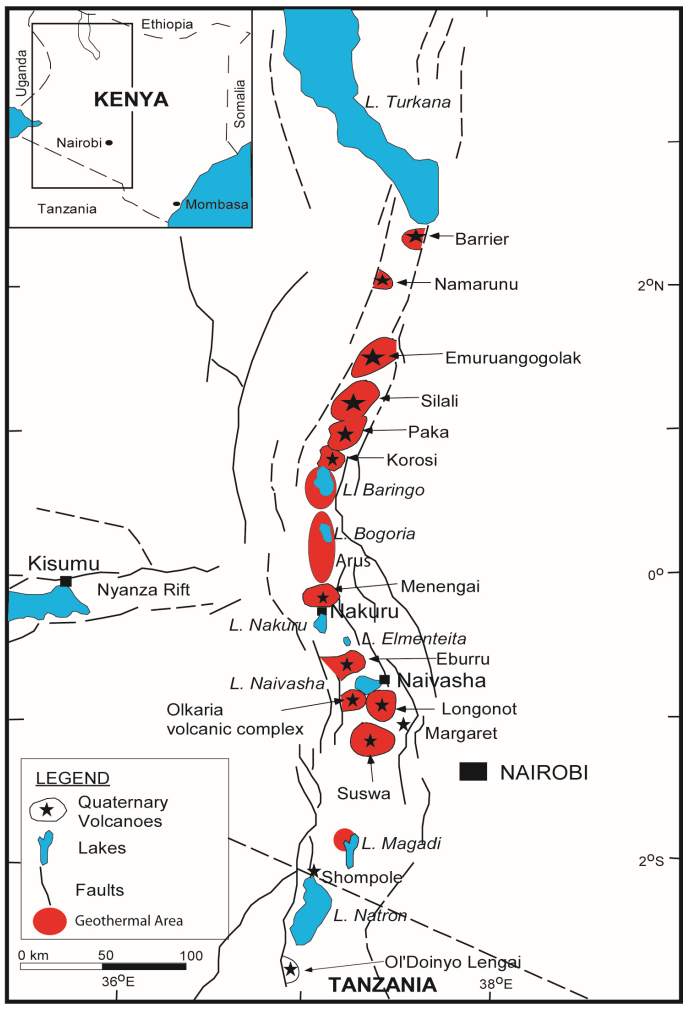

FIGURE 1: Map of Kenya showing the location of Olkaria geothermal area (Lagat, 2004)

1.2 Area of study

The Olkaria geothermal system is one of the several geothermal systems along Kenya's rift valley as shown in Figure 1. The geothermal system is related to plate tectonics involving faulting and rifting of the continental plate and the resulting volcanic activity during the formation of the African rift valley. Fluid flow and hydrothermal features in the field are mainly controlled by faults (Lagat, 2004). The heat sources to the systems are magmatic intrusions located at depths of 5-8 km. The geothermal reservoir is a high-temperature liquid-dominated type with reservoir temperature ranging from 200-340°C and an average of 230-260°C. The chemistry of the fluids shows chloride waters with alkaline pH and low total dissolved solids (TDS) and bicarbonate content. Chloride concentrations range from 100 to 1100 ppm and the non-condensable gases (NCG) are about 0.25% of the steam (Karingithi, 2002).

The Olkaria IV Domes geothermal field is located in the Olkaria geothermal field which is one of the seven geothermal fields

that make up the Olkaria geothermal system. It lies within an approximately circular 17 km^2 area as shown in Figure 2 and now has one power plant (Olkaria IV) with an installed capacity of 140 MWe which is owned and operated by Kenya Electricity Generating Company Ltd, (KenGen). Other power plants in the greater Olkaria field are Olkaria I with an installed capacity of 45 MWe, Olkaria II with an installed capacity of 10 MWe, Olkaria IAU units 4 & 5 with an installed capacity of 140 MWe and Olkaria III, owned by Ormat, and has an installed capacity of 148 MWe.

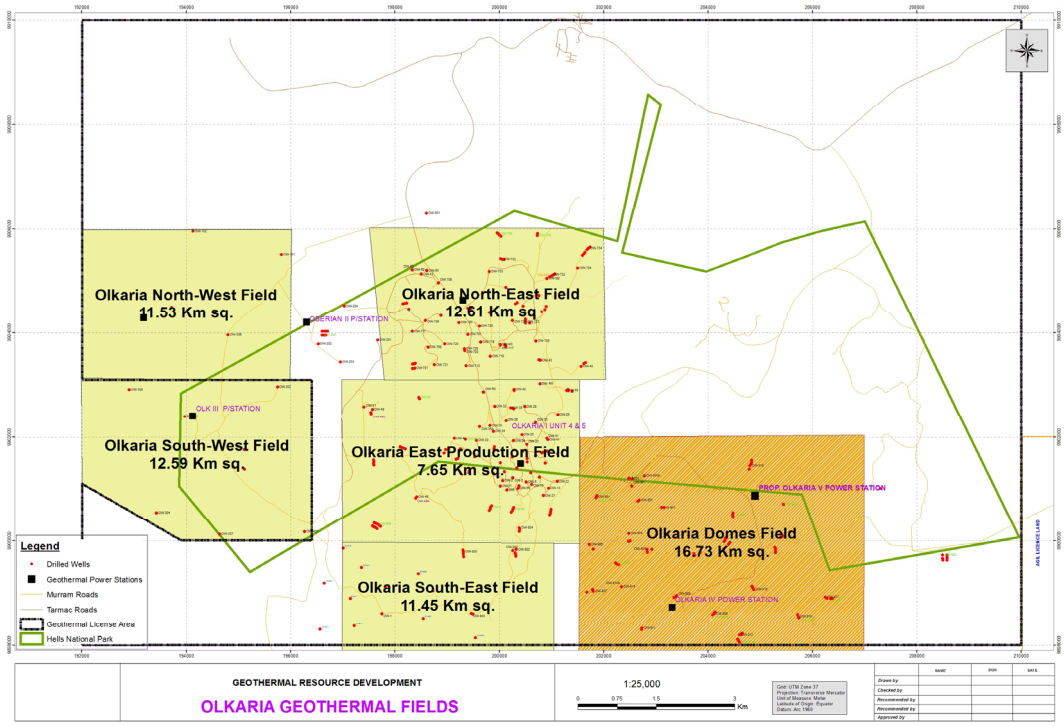

FIGURE 2: The Olkaria geothermal fields

The idea behind the model proposed in this study is the addition of a non – condensing turbine, commonly known as a back pressure turbine unit. This can be installed into the existing system instead of reducing pressure by the process of throttling using a pressure reducing valve, i.e. Pressure Reducing Valve (PRV), in order to further utilize the geothermal energy of the resource that has been harnessed in the high-pressure system of separation stations, and connected to the Olkaria IV power plant through a network of separation stations, namely SD1, SD2 and SD3. The motivation behind this project is to increase the overall efficiency when utilizing the high-pressure steam from the field. Data obtained over the years have shown significant stability of the well pressures in this field.

1.3 Literature review of topping units

The design inlet pressure for condensing steam turbines is often below 8 bar-a pressure, however some of the geothermal well fields produce steam at much higher pressure than required for the condensing steam turbine, which could be considered as unused energy. In this situation, the steam pressure must be reduced to the required inlet pressure of the turbine. Usually, the inlet pressure of the condensing steam turbines is fixed and it cannot be increased, and therefore the need of using a back-pressure turbine to extract this unused energy and to reduce the pressure has become attractive.

The technology of using a back-pressure turbine to extract energy from the excess steam pressure in condensing turbine geothermal power plants, which is sometimes called topping unit, was used in the Leyte Geothermal Optimization Project in the Philippines in 1997, and was done by ORMAT as a EPC turnkey contract. The project consisted of four individual power plants, three of which used a topping unit and the fourth one which used another technology called a bottoming unit. The total net power

gained by using this technology was 49 MW which represented almost 10% of the total installed capacity of the four power plants of 502.5 MW. The net power gained was 35.65 MW from topping units and 13.35 MW from the bottoming unit. The three power plants that used topping units are: Tongonan Power Plant, Mahanagdong A and Mahanagdong B (Kaplan and Schochet, 2000).

Tongonan topping plant

The total installed capacity of the main Tongonan Power Plant is 112.5 MW. The inlet pressure of the plant is 6.83 bar-a with flow of 1008 tons/hr and the steam pressure from well field is 11.14 bar-a. The ORMAT topping units were added to generate maximum power while reducing the pressure from 11.14 to 6.83 bar-a. The topping unit consisted of two 3.25 MW back-pressure turbines with high efficiency and reliability and were easily installed. Each turbine was directly coupled to each side of a generator. The Tongonan Topping Plant has three topping units generating 16.95 MW net power (Kaplan and Schochet, 2000).

Mahanagdong A topping plant

The total installed capacity of the main Mahanagdong A Power Plant is 120 MW. The inlet pressure of the plant is 6.83 bar-a with flow rate of 817 tons/hr while the resource pressure is 10.8 bar-a. The ORMAT topping units were added to generate maximum power while reducing the pressure from 10.8 to 6.8 bar-a. The Mahanagdong A Topping Plant consists of two topping units generating 12.45 MW net output (Kaplan and Schochet, 2000).

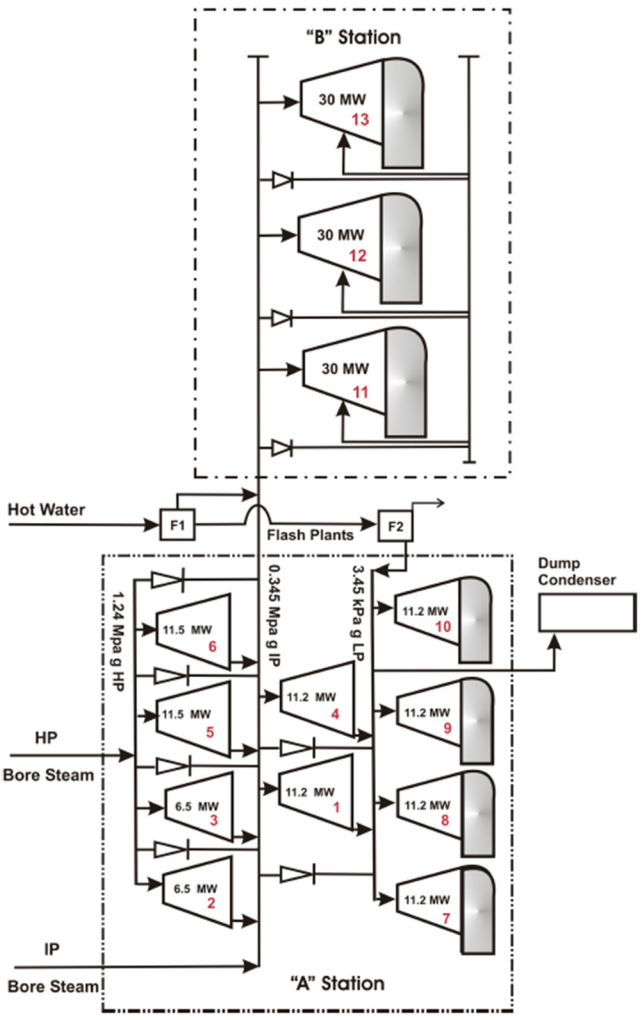

FIGURE 3: Schematic diagram of Wairakei power plant (Thain and Carey, 2008)

Mahanagdong B topping plant

The total installed capacity of the main Mahanagdong B Power Plant is 60 MW. The inlet pressure of the plant is 6.83 bar-a and the resource pressure is 10.8 bar-a. The ORMAT topping unit was added to generate maximum power while reducing the pressure from 10.8 to 6.8 bar-a. The Mahanagdong B Topping Plant consists of one topping unit generating 6.25 MW net (Kaplan and Schochet, 2000).

The total net power gained from the three topping plants is 35.65 MW (Kaplan and Schochet, 2000).

This technology has also been used in Wairakei Power Project, New Zealand in 1956 when it was redesigned by replacing the machines of a heavy water distillation plant with new turbines. Wairakei Geothermal Power plant had a total capacity of 47 MW. The redesign resulted in an implementation of a new plant called B station beside the old plant which is called A station and addition of new turbines in A station itself.

Wairakei A station

This plant consists of three pressure levels: high pressure, intermediate pressure and low pressure as shown in Figure 3. The high pressure is 13.5 bar-a which enters two 11.5 MW turbines and two 6.5 MW turbines, and exits at 4.45 bar-a intermediate pressure and is

then collected in the intermediate pressure manifold. The steam from the intermediate pressure manifold goes through two branches to the intermediate pressure turbines and to the B station. Two 11.2 MW intermediate pressure turbines receive steam at 4.45 bar-a and exit pressure of 1.0345 bar-a. The steam at 1.0345 bar-a enters four 11.2 MW low pressure turbines which are condensing turbines with exit pressure below vacuum (Thain and Carey, 2008).

Wairakei B station
The Wairakei B station consists of three 30 MW condensing turbines. The turbines work at an intermediate pressure of 4.45 bar-a inlet pressure and exit pressure under vacuum. The turbines also accept the pass- in steam from low pressure at 1.1 bar-a (Thain and Carey, 2008).

The total installed capacity of Wairakei geothermal power plant increased from 47 MW to 193.2 MW which is 103.2 MW from A station and 90 MW from B station as in Table 1 (Thain and Carey, 2008).

TABLE 1: Wairakei units rating (Thain and Carey, 2008)

Type	Units	MWe
High pressure (HP)	G2, G3	6.5
High Pressure (HP)	G5, G6	11.5
Intermediate pressure (IP)	G1, G4	11.2
Low pressure (LP)	G7, G8, G9, G10	11.2
Mixed pressure (MP)	G11, G12, G13	30

2. CURRENT STATUS IN OLKARIA IV

2.1 Current operations

Olkaria IV 140 MWe geothermal power plant is one of the two largest power plants in Kenya, the other one being Olkaria 1 ~~a~~dditional Units, with installed capacity of 140 MWe.

Electricity generation in Olkaria IV started in September 2014 when two 70 MWe turbines were commissioned and complete commercial operation was achieved in December 2014. There are plans to increase the capacity by adding extra units in the future. The turbines installed are produced by Toshiba, low-pressure turbines with steam requirement of 504 tons/hr and 5.2 bar-a inlet conditions and an exit pressure of 75 mbar absolute.

The steam is collected from wells in the Olkaria Domes field through a network of four separation stations, SD, named as SD1, SD2, SD3 and SD4 (Figure 4) (Brookes, 2011).

The separator stations comprise a series of vertical modular separators (Figure 5), design to separate two-phase steam at 11.8 bar-a pressure. The separated steam is then piped to a common header that leads to the final steam scrubber vessel before being admitted to the main turbine of the main plant.

During the design phase it was recognised that the separation pressure needed to be higher because of the risk of scaling. At that time the steam system was designed for a pressure of 13.5 bar for the separators and the steam piping. The decision was then made to install pressure let down stations (PLDS) at Olkaria IV to increase the steam field pressures much as possible, given the pressure limitation of the separators and steam piping. The PLDS are now operational, and the design separation pressure increased to around 12.2, 11.8, 11.8 and 12.3 bara for SD1, SD2, SD3 and SD4 respectively. The pressure upstream of the Olkaria IV PLDS is between 10.0 and 10.5 bar (KenGen, 2011).

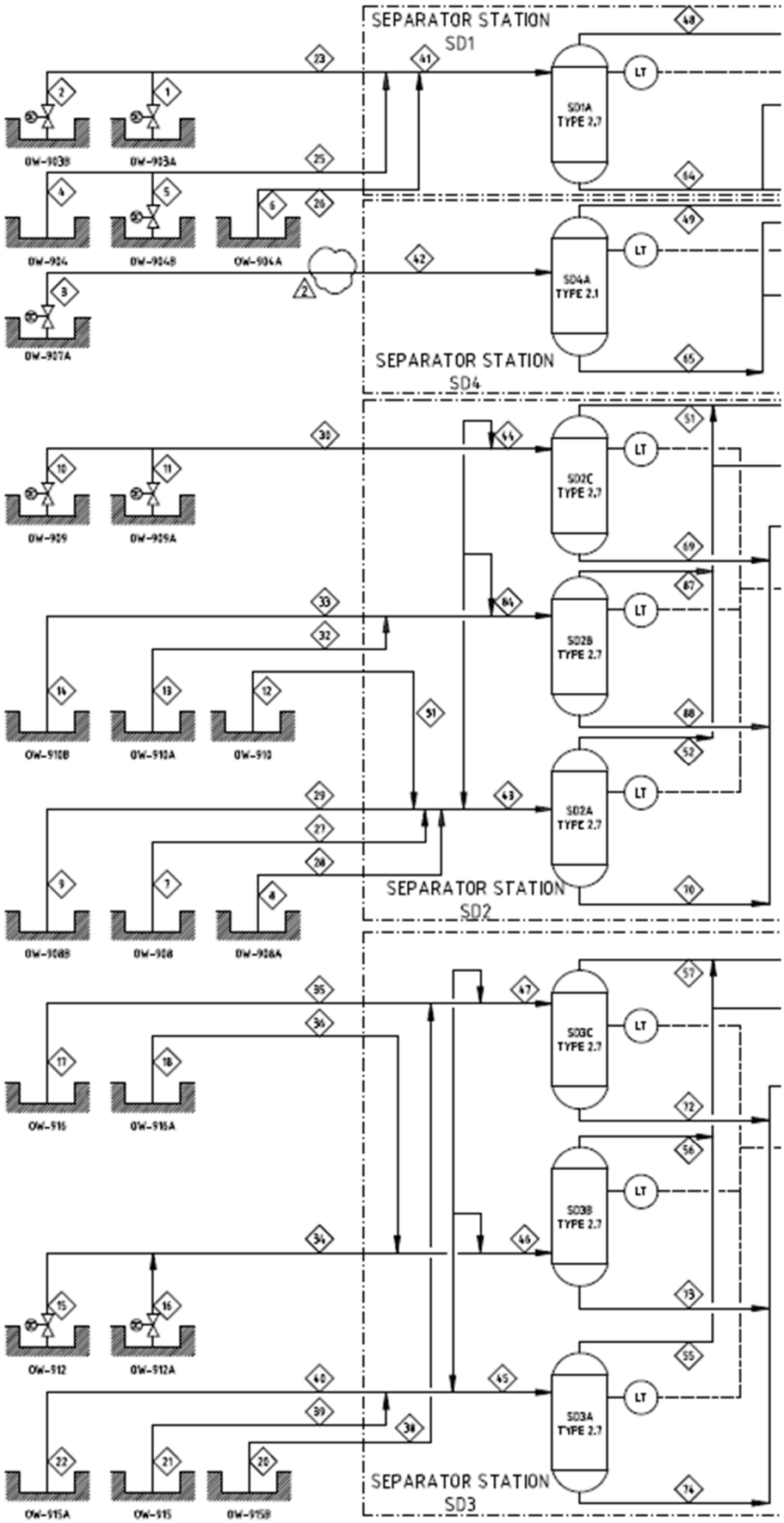

FIGURE 4: Modular separation stations

2.2 Modular separation stations

The steam is collected from the wells in the steam field and is separated in a common central separator station that serves multiple production well pads. The advantage in this modular separation is that the variation between design data and actual production flows in one well's output may be balanced by variations in the outputs of other wells. Figure 5 shows a schematic diagram of a modular separation station.

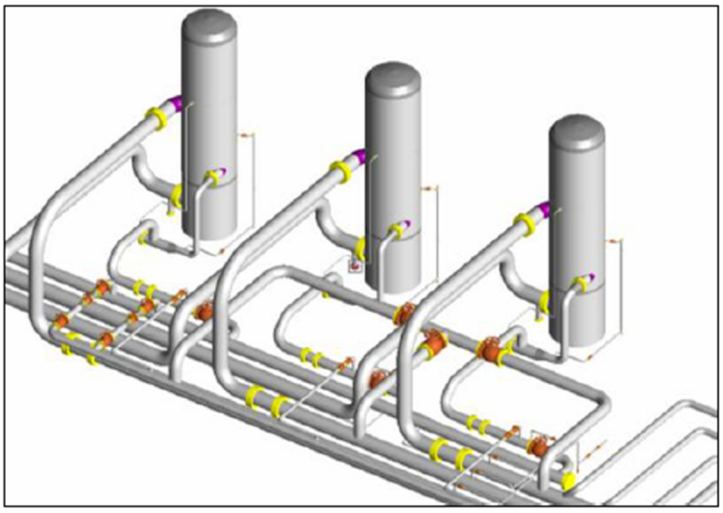

FIGURE 5: Typical modular separation station

Figure 6 shows the well locations, pipe routes, the separator stations and the site of the existing power plant. The two-phase fluid is gathered and conveyed to the common primary modular separators in Figure 5, located near the power plant.

For the gathering of the two-phase geothermal fluid, proper evaluation was made to find the optimum diameter of pipe by optimizing pipe routes in order to minimize the loss of electricity production due to corresponding pressure drop due to frictional losses. The power station site, as seen on the geographic map of Olkaria IV power plant, is at a lower elevation than the separator stations SD2 and SD3, so the

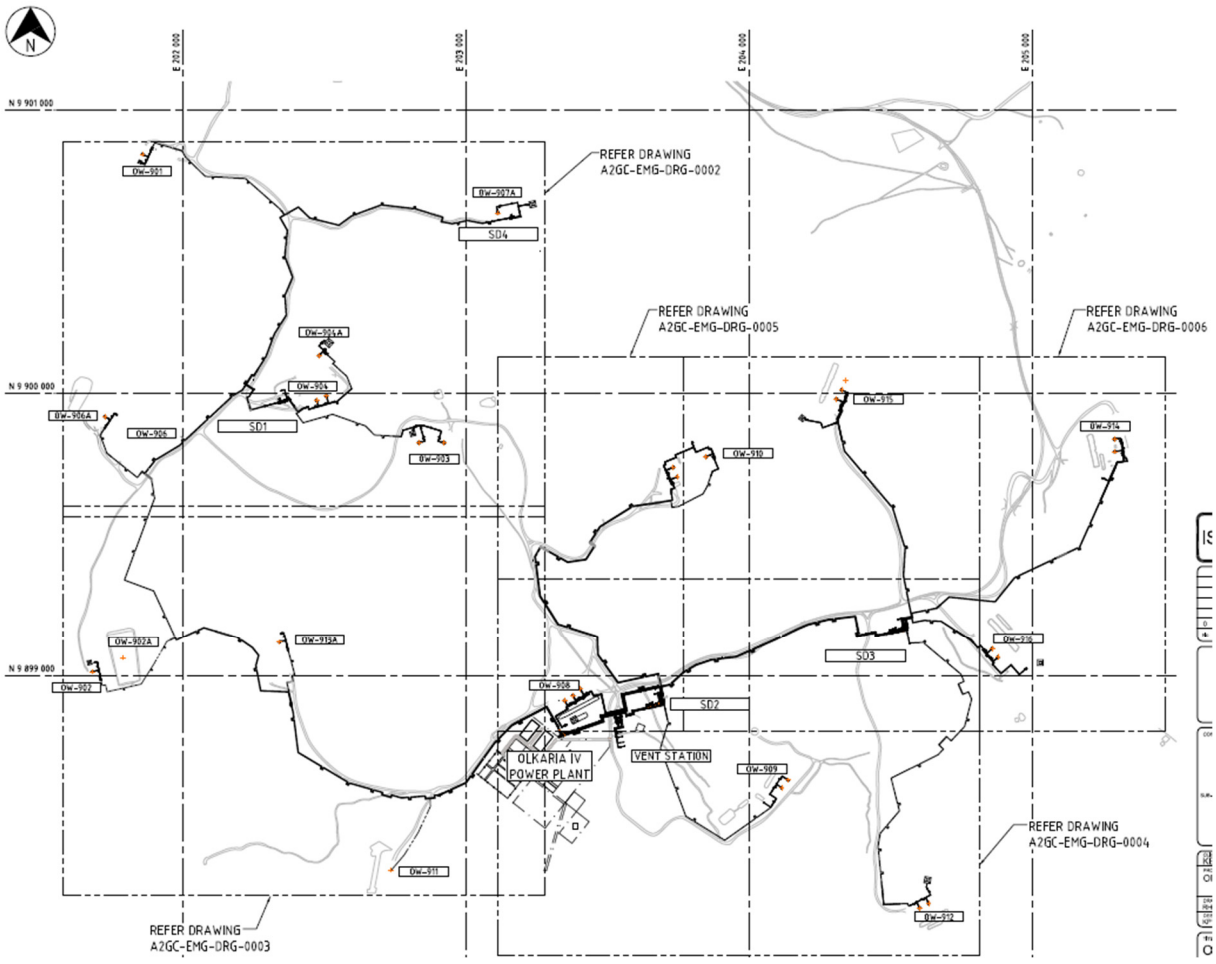

FIGURE 6: Wells locations and pipe routes

fluid gains static head. The static head gain would compensate for the acceleration head loss, however that effect is neglected, so for the two-phase flow calculation of the pipe loss, only the frictional pipe loss is taken into account and not the compensation due to elevation differences. The steam field pressure drops are not considered in this report. Figure 7 shows the existing Olkaria IV power plant as well as the location of SD3 separator station. PLDS and the vent station are located in the vicinity of the power plant. This will be the area where the project for developing the topping unit is planned.

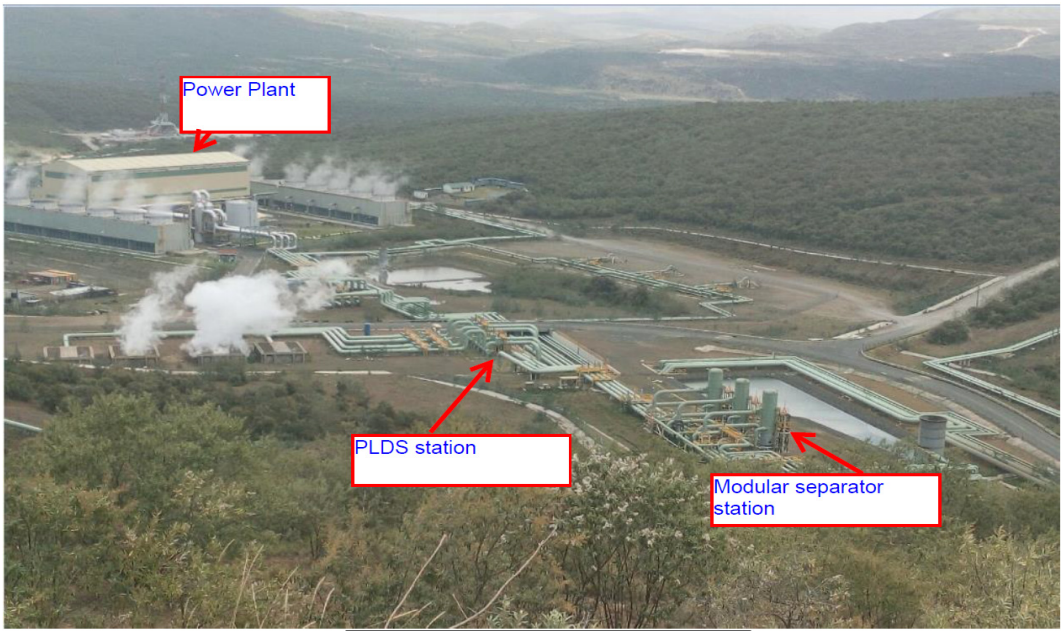

FIGURE 7: Existing Olkaria IV power plant

From the data available on the wells considered, it is clear that the geothermal fluid can be separated at different pressures than the design pressure of the current separator stations, and to meet the power plant inlet steam pressure of 5.2 bar gauge pressure. It is therefore of interest to investigate the feasibility of installing a high pressure topping with back pressure turbine that will exhaust to a new low-pressure separation station to be used in the main power plant downstream. The backpressure turbine is expected to be permanently installed and to be in operation for the life span of the power plant.

3. PROPOSED MODELS

3.1 Introduction

This study aims to analyse the amount of electrical power output that could be obtained from using a back pressure turbine which could be installed after the separator stations to lower the high separation pressure to a pressure closer to the main turbine inlet pressure. It will also compare the benefits of using this back pressure turbine instead of using throttling valve or a Pressure Let Down Stations, PLDS. The schematic arrangement of options available in connecting high-enthalpy wells is presented in Section 3.3.

3.2 Basic design data

The developmental plan for every power plant starts by analysing the available basic resource data. When considering geothermal resources, it is customary to evaluate the condition of the fluid and output characteristics of each well before designing the power plant. This is performed with the available resources at hand or with assumptions based on related studies. The well test data are reviewed in order

to form a list of well production characteristics. Table 2 shows the discharge test results of wells in consideration for the topping plant (KenGen, 2012)

TABLE 2: Well data output

Separator station	Well no.	WHP bara	Two-ph t/h	Enthalpy kJ/kg	Min H kJ/kg	Max H kJ/kg	Steam t/h	Brine t/h
SD1A	W-1	13.0	65	1700	1650	1740	29.4	35.6
SD1A	W-2	13.3	65	1450	1375	1550	21.2	43.8
SD1A	W-3	16.1	90	1425	1375	1475	28.3	61.7
SD1A	W-4	13.0	120	1275	1240	1330	28.6	91.4
SD1A	W-5	12.6	57	1625	1550	1700	23.7	33.3
SD4A	W-6	12.6	95	1750	1650	1800	45.4	49.6
SD2A	W-7	14.9	30	2200	2130	2250	21.2	8.8
SD2A	W-8	17.5	115	1420	1380	1470	36.1	78.9
SD2A	W-9	14.7	87	2050	2000	2100	54.9	32.1
SD2C	W-10	12.9	130	2000	1900	2100	78.8	51.2
SD2C	W-11	12.4	100	1820	1700	1870	51.5	48.5
SD2A	W-12	18.3	60	1950	1900	2000	34.8	25.2
SD2B	W-13	18.1	110	2250	2150	2350	80.5	29.5
SD2B	W-14	18.6	210	2000	1700	1900	127.3	82.7
SD3B	W-15	12.6	40	1950	1900	2000	23.2	16.8
SD3B	W-16	12.6	64	2520	2480	2575	55.5	8.5
SD3C	W-17	14.0	130	2475	2425	2550	109.8	20.2
SD3B	W-18	13.4	65	2150	2050	2250	44.3	20.7
SD3A	W-19	16.3	75	2070	1900	2150	48.1	26.9
SD3A	W-20	15.3	110	2450	2375	2525	91.5	18.5
SD3C	W-21	15.4	105	2200	2150	2250	74.1	30.9
	Total		**1923**				**1108**	**815**

There are four modular separation stations, with two main ones being SD2 and SD3. The other two separator stations SD1 and SD4 are meant to tie in steam to the main steam headers to make sure adequate steam is available for the main steam turbines. Table 3 shows the separation pressures and the steam mass flow from all the separators.

The mass flow from the separator stations in Table 3 has been used to determine the total two-phase flow rate that would be required to pass through the high-pressure separator station in order to meet the main plant steam inlet requirement. It is therefore of interest to investigate the feasibility of installing high-pressure separation stations that use a back pressure turbine that will exhaust to lower pressure to be used in the main power plant downstream.

TABLE 3: Separator stations separation pressures and basis flows

Separator	Inlet P (bara)	Sep DP (bara)	Outlet P (bara)	Outlet T (degC)	2P flow (t/h)	Enthalpy (kJ/kg)
SD1A	12.22	0.08	12.14	188	397	1457
SD2A	11.82	0.10	11.72	187	292	1797
SD2B	11.82	0.10	11.72	187	320	2086
SD2C	11.82	0.10	11.72	187	230	1922
SD3A	11.93	0.09	11.84	187	185	2296
SD3B	11.93	0.09	11.84	187	169	2243
SD3C	11.93	0.09	11.84	187	235	2352
SD4A	12.26	0.02	12.24	189	95	1750

In this report, six options are discussed and compared:

1. The single flash, with current operation set up;
2. The single flash with back pressure topping unit;
3. The double flash system with back pressure topping unit;
4. The double flash system and back pressure topping unit with a mist eliminator;
5. The optimized case of scenario 3 mentioned above with main turbine inlet pressure fixed;
6. The optimized case of scenario 3 with both high and low separator pressures optimized.

3.3 Options selection

The options selected are all based on the current status where all the wells are separated in common modular separator stations. The steam obtained is that of the main steam turbine with a steam inlet requirement of 280 kg/s.

3.3.1 Current operations

The current operations setup is such that steam is collected from a steam gathering system and transported to a modular separation stations at four different locations named SD1, SD2, SD3 and SD4, with separation pressures of 11.8 bar-a for both SD2 and SD3 and 12.2 bar-a and 12.3 bar-a for SD1 and SD4 respectively. SD2 and SD3 are located close to the power plant while SD1 and SD4 are located about 1 km away from the power plant and are mainly meant to provide steam to tie into the main steam headers coming from SD2 and SD3.

The steam is separated at a high pressure of 11.8 bar-a and then conveyed to the main steam headers in the pressure let down stations (PLDS) installed with pressure reducing valves (PRVs) to reduce the pressure to the design inlet turbine pressure of 5.2 bar gauge.

There are two steam turbines installed at Olkaria IV, each with a steam inlet pressure of 5.2 bar gauge and a steam consumption of 140 kg/s. The maximum power output is 70 MWe at a nominal continuous rating (NCR) for one turbine. In this report, both steam turbines are considered as one and so the total steam requirement would be 280 kg/s for a power generation of 140 MW. Figure 8 shows a process flow diagram of the setup.

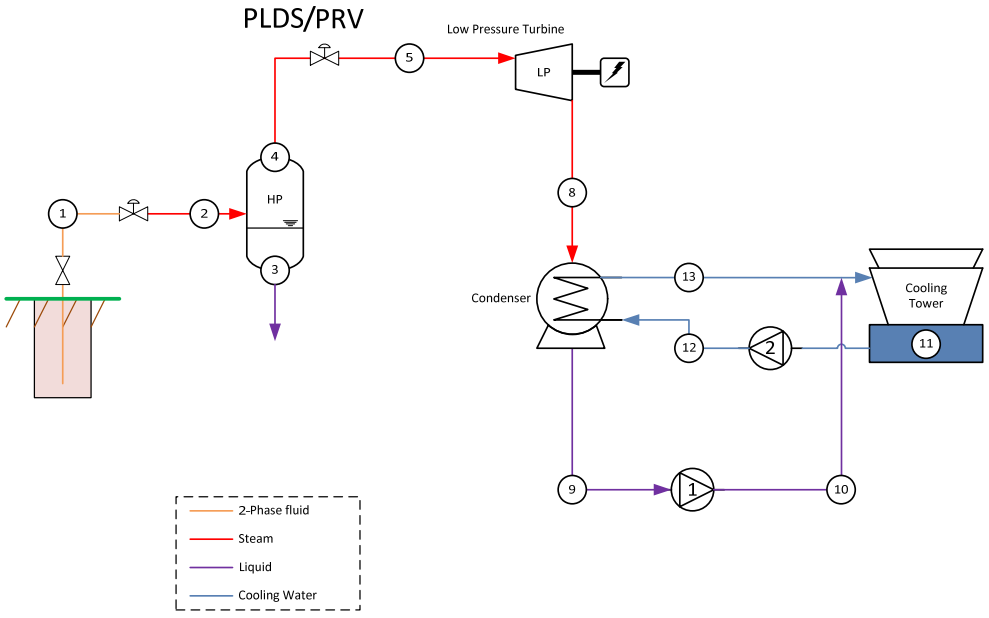

FIGURE 8: Schematic flow diagram of current operations

3.3.2 Single flash with a back pressure topping unit, case 1

The first proposed model is to modify the current operation setup to include a back pressure turbine installed immediately after the separator stations as shown in Figure 9. The back pressure turbine will act as a pressure reducing valve in the process of isentropic expansion of total steam, while at the same time generating electrical power.

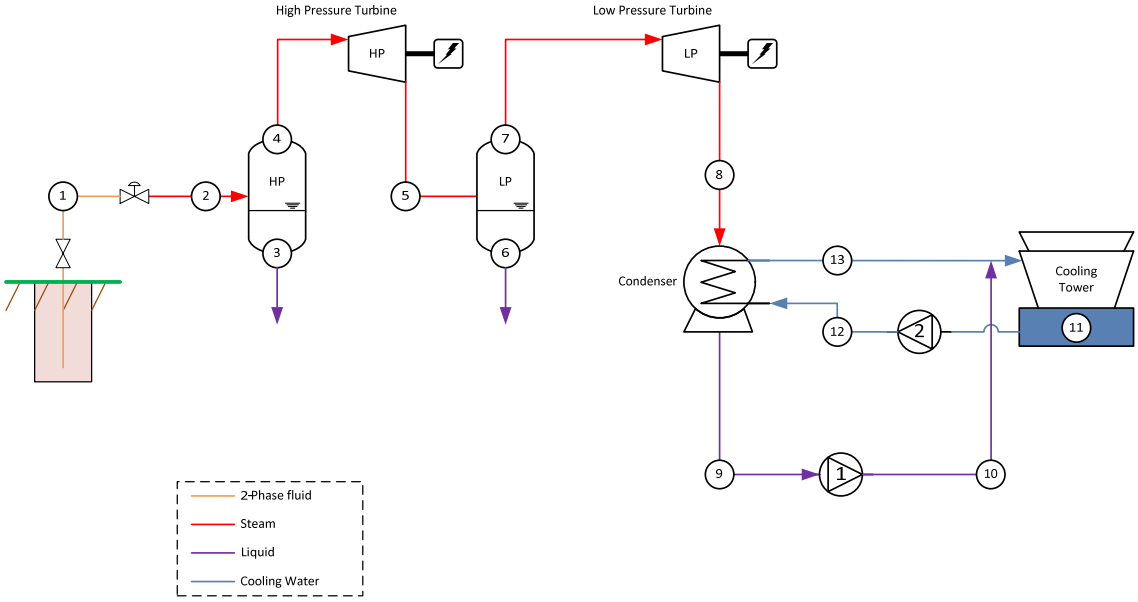

FIGURE 9: Schematic flow diagram, case 1

A mist eliminator is installed to remove any droplet that would have condensed during the expansion in the back pressure turbine.

3.3.3 Double flash system with a back pressure turbine, case 2

In this model, the back pressure turbine is installed after the separation station similar to case 1. The brine from the high-pressure separation station is combined with the exhaust steam from the back pressure turbine to be flashed again at a new low-pressure separation station. The steam obtained from the low-pressure separator is then conveyed to the existing low-pressure steam turbine (Figure 10).

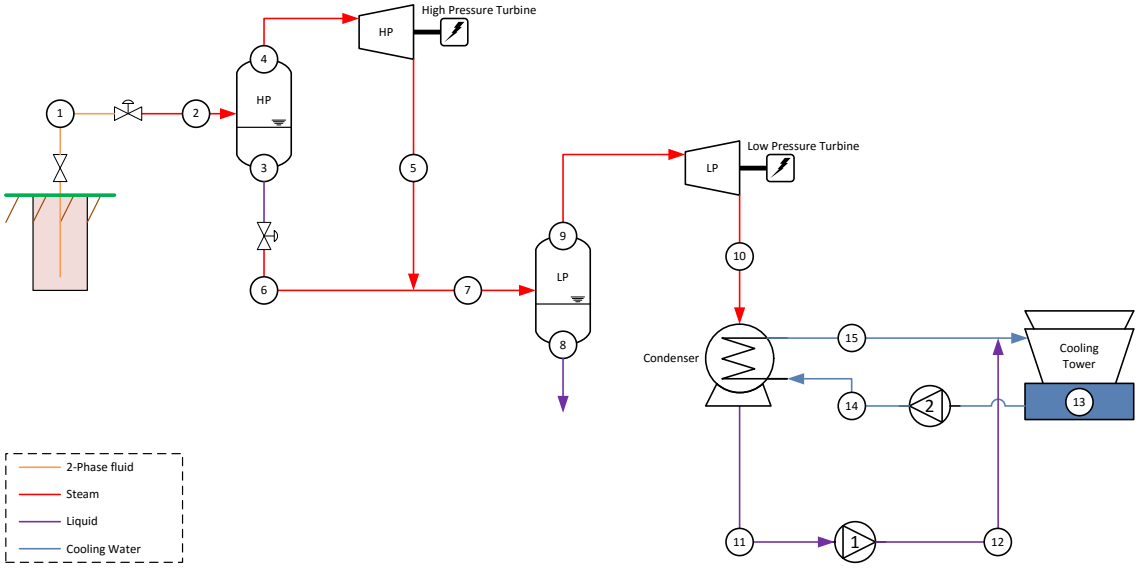

FIGURE 10: Schematic flow diagram, case 2

3.3.4 Topping unit, double flash system, steam mixed, case 3

In this model, the back pressure turbine is installed after the separation station. The brine from the high-pressure separator is then flashed. The steam obtained is mixed with the steam exhausted from the back pressure turbine. The combine steam is finally conveyed to the main steam turbine at an inlet pressure of 6 bara. The schematic flow diagram is shown in the Figure 11.

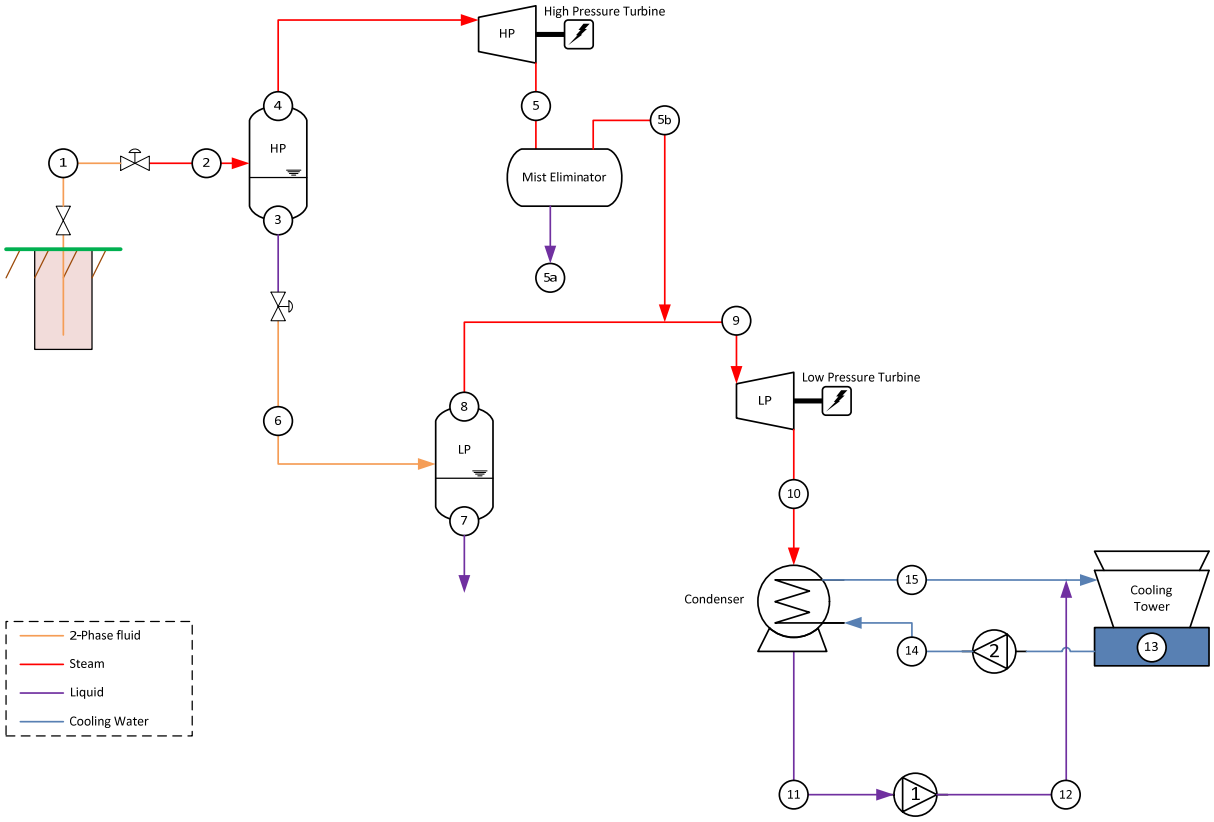

FIGURE 11: Schematic flow diagram, case 3

3.3.5 Topping unit with optimized separation pressures, case 4

In this model, two scenarios are considered for case 2. First scenario is to optimize the high-pressure separator pressure and fix the main inlet turbine pressure. The second case is to optimize for both high-pressure separator pressure and the inlet pressure for the main turbine.

4. THEORETICAL ANALYSIS

4.1 Energy conversion system

Once the steam has been separated and the right dryness fraction is achieved, it is then conveyed to the power plant as dry steam. For this report, a single- flash plant is considered as shown in Figure 12. The turbines are single-pressure units with impulse-reaction blading, either single-flow for smaller units or double-flow for larger units. The condensers can be either direct-contact (barometric or low-level) or surface-type (shell-and-tube). For this report, the condenser is direct contact and is placed directly below the turbine.

The arrangement of equipment above includes: several valves, piping and instruments (pressure and temperature gauges). If wellhead separators are used, the cyclone separator (CS) will be located close to the wellhead on the same pad. For this report, a modular separator station is presented.

The processes undergone by the fluid are shown in Figure 13. The wells produce saturated steam as well as saturated water (or slightly superheated steam), so the starting point (state 1) is located on the saturated vapour curve. If the steam is superheated, point 1 moves slightly to the right. The turbine expansion process 1–2 generates somewhat less power output than the ideal, isentropic process 1–2s. Heat is rejected to the surroundings in the condenser via the cooling water in process 2–3.

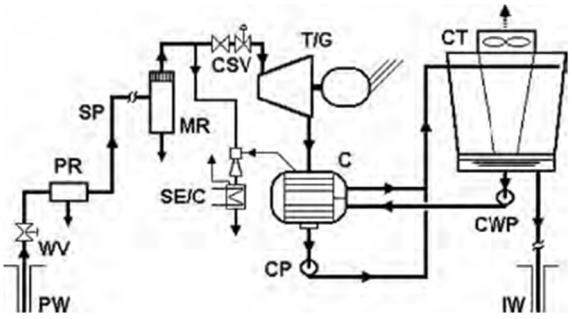

FIGURE 12: Simplified single-flash power plant schematic (DiPippo, 2007)

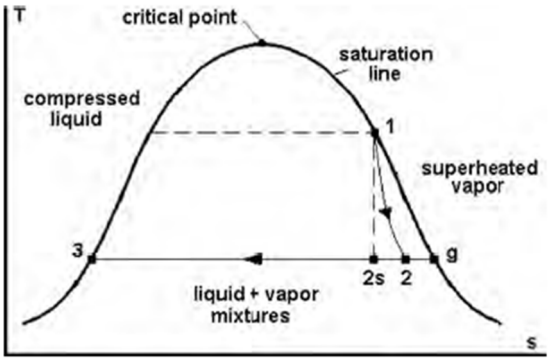

FIGURE 13: Temperature-entropy diagram for a dry steam plant with saturated steam at the turbine inlet (DiPippo, 2007)

4.2 Turbine expansion process

The work produced by the turbine per unit mass of steam flowing through it is given by Equation 1:

$$W_t = h_1 - h_2 \tag{1}$$

where W_t = Work done by the turbine;
h_1 = Enthalpy of steam at turbine entry;
h_2 = Enthalpy of steam at turbine exit.

It is assumed that the turbine is expanding adiabatically thus the changes in kinetic and potential energy of the fluid entering and leaving the turbine are neglected. The maximum possible work would be generated if the turbine operated adiabatically and reversibly, i.e. at constant entropy, that is isentropically.

The isentropic turbine efficiency, η_t, is the ratio of the actual work to the isentropic work, and is given by Equation 2:

$$\eta_t = \frac{h_1 - h_2}{h_1 - h_{2s}} \tag{2}$$

where η_t = Isentropic turbine efficiency;
h_1 = Enthalpy of steam at entry;
h_2 = Enthalpy of steam at exhaust;
h_{2s} = Enthalpy of steam at saturated state.

The power developed by the turbine is given by Equation 3:

$$\dot{W}_t = \dot{m}_s W_t = \dot{m}_s (h_1 - h_2) = \dot{m}_s \eta_t (h_1 - h_{2s}) \tag{3}$$

where $\dot{m}_s$ = Steam mass flow rate

The gross electrical power will be equal to the turbine power times the generator efficiency and is given by Equation 4:

$$\dot{W}_g = \eta_g \dot{W}_t \tag{4}$$

where $\dot{W}_g$ = Gross electrical power;
η_g = Generator efficiency.

The net power is the gross electrical power reduced by all parasitic loads, including condensate pumping power, cooling tower fan power, and station lighting.

Since there is degradation in performance of a wet steam turbine, the Baumann rule as given below is applied:

$$\eta_{tw} = \eta_{td}\, X \left[\frac{1 + X_2}{2}\right] \tag{5}$$

where the dry turbine efficiency, η_{td} may conservatively be taken to be constant at 85%, η_{wd} is the wet turbine efficiency and X_2 is the dryness fraction.

Taking into account that the steam present inside the turbine is not 100% dry then according to the Baumann rule, the enthalpy exiting the turbine is given by Equation 6:

$$h_2 = \frac{h_1 - A\left[1 - \dfrac{h_3}{h_g - h_3}\right]}{1 + \dfrac{A}{h_g - h_3}} \tag{6}$$

where h_3 = Total two-phase flow;
and the factor A is defined as:

$$A = 0.425\ (h_1 - h_{2s}) \tag{7}$$

where the subscript numbers indicate the state points and the associated subscript letters *'g'* and 's' are the steam phase and the isentropic state values, respectively.

4.3 Optimum well head pressure

The scenario of the optimum wellhead pressure for a dry steam plant receiving saturated vapour at the wellhead is considered. It is assumed that the pressure losses in pipelines are negligible. It is also assumed that the pressure of the wellhead can be controlled by means of a throttle valve. Then the well productivity curve can be approximated as an elliptical equation for the mass flow rate of steam as a function of the wellhead pressure as in the Equation 8:

$$\left[\frac{\dot{m}}{\dot{m}_{max}}\right] + \left[\frac{P}{P_{ci}}\right]^2 = 1 \tag{8}$$

where $\dot{m}$ = Total two-phase flow;
$\dot{m}_{max}$ = Maximum observed mass flow rate;
P = Pressure;
P_{ci} = Closed-in wellhead pressure.

Assuming that values for these two parameters are available from well tests, the mass flow rate at any pressure can be calculated from Equation 9, and a plot obtained as shown in Figure 14.

$$\dot{m} = \dot{m}_{max}\sqrt{1 - (P/P_{ci})^2} \tag{9}$$

Opening the wellhead valve will result in lower pressure, and higher flow rates, but the enthalpy of the steam will remain the same since it is a throttling process.

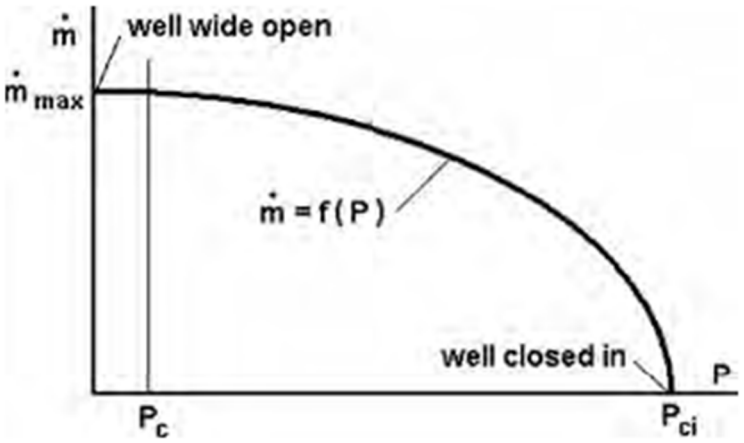

FIGURE 14: Dry steam productivity curve (Dipippo, 2007)

The turbine power is proportional to the product of the steam mass flow rate and the enthalpy drop Δh, as previously shown by the isentropic expansion of the turbine. There are two limits to the wellhead pressure; the closed-in pressure, Pci, for which there is no steam flow, and the condenser pressure, Pc, for which there is no enthalpy drop. Thus the power vanishes at the two extreme positions for the wellhead pressure, indicating there is some wellhead pressure for which the power will be maximum. The power output per maximum steam flow rate is given by Equation 10:

$$\frac{\dot{W}}{\dot{m}_{max}} = \frac{\dot{W}}{\dot{m}} X \frac{\dot{W}}{\dot{m}_{max}} = (h_1 - h_{2s}) X \sqrt{1 - (P/P_{ci})^2} \quad (10)$$

where $h_1 - h_{2s}$ is the isentropic enthalpy drop across the turbine.

4.4 Pressure drops

4.4.1 Pressure drops in pipes

Pressure drop in two-phase geothermal pipelines consists mainly of static pressure drop, momentum pressure drop and frictional pressure drop. Several different methods for calculating the pressure drop in two-phase flow in pipelines have been proposed. Separated flow models are a class of commonly utilized models (Thome, 2006) for calculating the two-phase pressure drop; they employ two artificial pipes, one carrying the gaseous phase and the other the liquid phase. The resulting two-phase pressure drop is then calculated from the single-phase pressure drops. There is no analytical formula for solving the pressure drops of the two-phase flow in the pipe, however studies have shown two methods for calculating pressure drops in a two-phase flow. One is the homogeneous flow model where the two phases are treated as a single fluid and the other is the separate flow model where each phase is treated separately. The formula used for the pressure drop according to the homogeneous flow model is shown in the Equation 11:

$$\Delta P = \frac{2 f_H L \dot{m}^2}{d\, \rho_H} \quad (11)$$

where L = Length of the pipe line;
d = Internal diameter of pipe;
$\dot{m}$ = Total two-phase flow;
f_H = Friction factor;
ρ_H = Homogenous fluid density expressed in terms of the Reynolds number;
$\dot{m}_2$ = Two-phase flow from production well.

The calculations on the two-phase pipe pressure drops in the pipe lines are not been presented in this report.

The location of the proposed topping plant shall be nearer to the separator station within a distance of 50 m. In this report it is assumed that there will be no pressure loss due to long distance piping.

4.4.2 Pressure drop in separators

A separator is a vessel used to separate a mixed-phase stream into gas and liquid phases that are relatively free of each other. They are characterized as either vertical (cyclone) or horizontal (gravity), based on orientation. Recommended inlet velocities should be in the range of 25-40 m/s, the higher the velocity, the better the separation, but it is limited by unacceptable pressure drop. The pressure head is estimated in terms of velocity head as follows (Walas, 1990):

$$\Delta P_{sep} = 4\,\mathrm{P}\frac{V^2}{2g} \tag{12}$$

where V = Inlet velocity;
P = Pressure.

For this report, the separators have been installed and so the actual calculations for the pressure drops are not been presented. However, the pressure drop for the high-pressure separators have been taken to be equal to 0.1 bara. The pressure of 0.1 has be assumed to take care of pressure differential between entry and exit.

5. RESULTS AND DISCUSSIONS

The engineering equation solver (EES) was used to calculate the power output of the back pressure turbine and the existing low-pressure turbine for the six cases considered.

Following assumptions have been made to simplify these calculations:

1. The flow of geothermal fluid is steady which means the mass flow in, equals to the mass flow out, and there are no fluid losses;
2. The turbine is thermally insulated which means there is no heat exchange between the turbine and the surrounding environment;
3. Geothermal fluid has the same thermodynamic properties as pure water;
4. The pressure drops have been ignored as the steam field design is already existing and the location of the back pressure turbine is close to the power plant.

5.1 Presentation of the productivity curves

The well tests data presented in this report are for the Olkaria IV geothermal field. They were reviewed and analysed in order to generate productivity curves for the wells to be considered. Table 4 shows discharge test results. A relationship between wellhead pressure (WHP) and the mass flow of the well commonly known as productivity curves is plotted in Figure 15 and a curve is fitted to the test points to correlate the well flow from the corresponding wellhead pressure. Based on the relationship, a correlation polynomial equation of order 3 was developed, represented by Equation 13 (Valdimarsson, 2011)

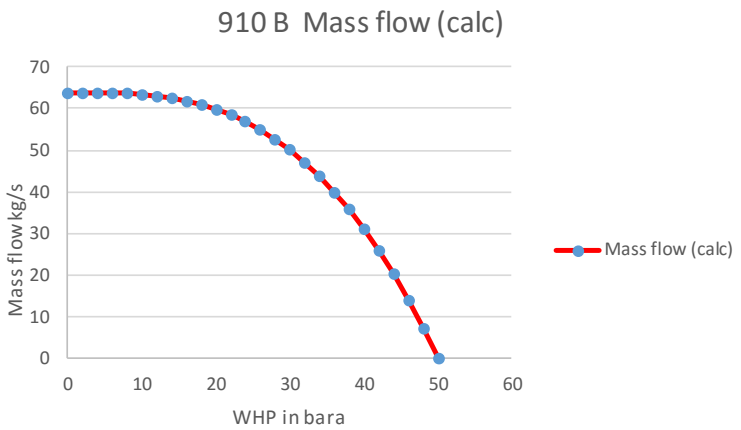

FIGURE 15: Productivity curve for well 910B

$$WHP = a - b * \dot{m}^3 \quad (13)$$

where WHP = wellhead pressure;
a = closed-in pressure;
b = ratio of $^{a}/_{\dot{m}^3}$ when the WHP =0.

TABLE 4: Productivity curves parameters

Well	WHP	Productivity curves parameters	
		a	b
W-4	36	36.1	0.0023
W-14	64	63.9	0.0005
W-13	34	33.9	0.0008
W-12	23	22.5	0.0028
W-3	38	37.5	0.0024
W-7	10	10.0	0.0008
W-8	38	38.1	0.0017
W-9	26	25.8	0.0017
W-17	40	40.3	0.0003
W-18	27	26.9	0.0017

Well	WHP	Productivity curves parameters	
		a	b
W-19	28	27.8	0.0035
W-20	34	33.9	0.0005
W-21	36	35.6	0.0004
W-15	25	25.3	0.0016
W-416	18	18.1	0.0008
W-10	41	40.6	0.0026
W-411	32	32.2	0.0040
W-5	24	23.6	0.0015
W-1	19	19.4	0.0012
W-42	24	23.6	0.0030

5.2 Presentation of wells and steam separation stations

The well data for two separation stations, SD2 and SD3, are presented in Table 5. The steam obtained from these stations is conveyed to each of the steam turbines for power generation. The weighted enthalpy, has been calculated using Equation 14 and mass flow rate is presented in Table 6.

TABLE 5: Mass flow and enthalpy of the wells

Separator station	Well no.	WHP	Two-Ph	Enthalpy	Min h	Max h	Steam	Brine
		bara	t/h	kJ/kg	kJ/kg	kJ/kg	t/h	t/h
SD2A	W-7	14.9	30	2200	2130	2250	21.2	8.8
SD2A	W-8	17.5	115	1420	1380	1470	36.1	78.9
SD2A	W-9	14.7	87	2050	2000	2100	54.9	32.1
SD2C	W-10	12.9	130	2000	1900	2100	78.8	51.2
SD2C	W-11	12.4	100	1820	1700	1870	51.5	48.5
SD2A	W-12	18.3	60	1950	1900	2000	34.8	25.2
SD2B	W-13	18.1	110	2250	2150	2350	80.5	29.5
SD2B	W-14	18.6	210	2000	1700	1900	127.3	82.7
SD3B	W-15	12.6	40	1950	1900	2000	23.2	16.8
SD3B	W-16	12.6	64	2520	2480	2575	55.5	8.5
SD3C	W-17	14.0	130	2475	2425	2550	109.8	20.2
SD3B	W-18	13.4	65	2150	2050	2250	44.3	20.7
SD3A	W-19	16.3	75	2070	1900	2150	48.1	26.9
SD3A	W-20	15.3	110	2450	2375	2525	91.5	18.5
SD3C	W-21	15.4	105	2200	2150	2250	74.1	30.9
	Total		**1431**				**931.7**	**499.3**

$$h_{wg} = \frac{\dot{m}_1 h_1 + \dot{m}_2 h_2}{\dot{m}_1 + \dot{m}_2} \quad (14)$$

where h_{wg} = Weighted enthalpy of two fluids;

h_1 = Enthalpy of fluid 1;
h_2 = Enthalpy of fluid 2;
$\dot{m}_1$ = Mass flow rate of fluid 1;
$\dot{m}_2$ = Mass flow rate of fluid 2.

TABLE 6: Weighted enthalpy and mass flow

Separator stations SD2 and SD3				
	Weighted average	**Minimum**	**Maximum**	**Units**
Enthalpy	2089.9	1980.3	2134.6	kJ/kg
Mass flow	397.5			kg/s

5.3 EES models

Simulation models on EES were made for all the cases considered (see Appendix I for the codes of the selected options). EES results for the current status are shown in Figure 16.

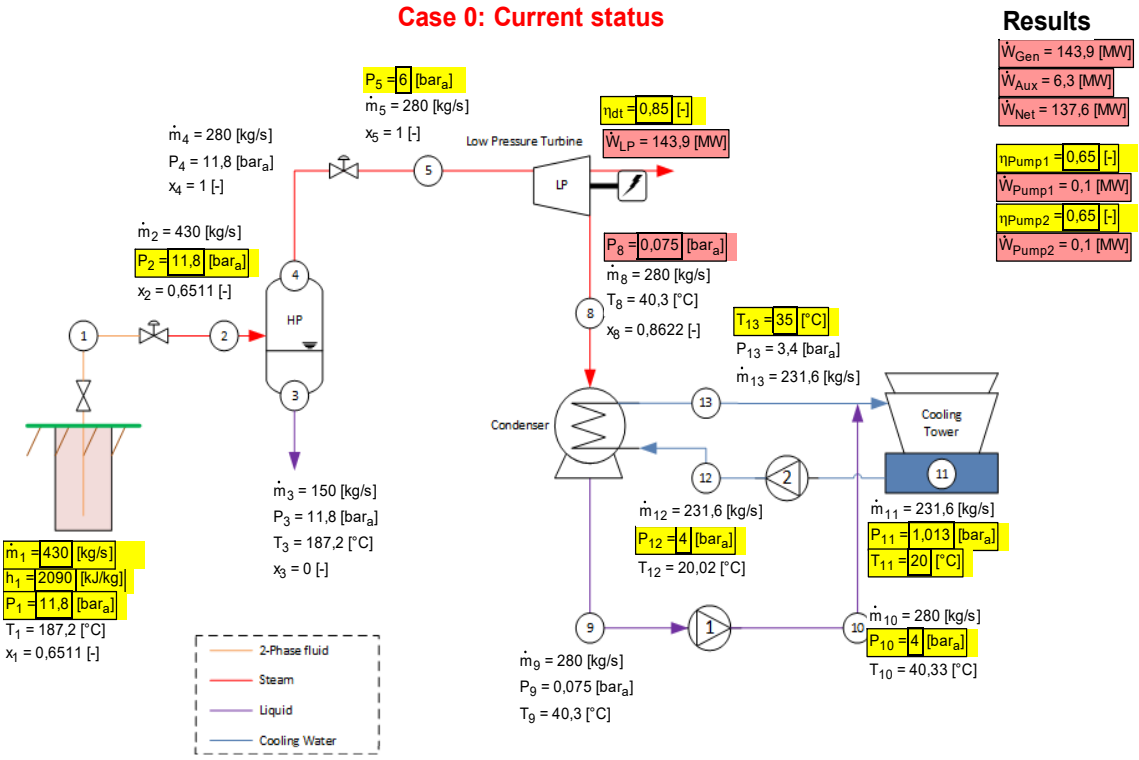

FIGURE 16: EES results for the current status

where $\dot{W}_{Gen}$ = Total power generated;
$\dot{W}_{HP}$ = Total power generated by high-pressure turbine;
$\dot{W}_{LP}$ = Power generated by low-pressure turbine;
$\dot{W}_{Net}$ = Net power generated;
$\dot{W}_{Aux}$ = Auxiliary power.

5.3.1 Case 1

All the wells are separated with 11.8 bara separation pressure and the resulting steam passed through the back pressure turbine to reduce the pressure at the existing inlet turbine. A mist eliminator is installed

after the topping unit to remove the condensed steam created during the expansion process of the back pressure turbine.

Two-phase steam from the steam field with a mass flow rate of 430 kg/s and a weighted enthalpy of 2090 kJ/kg is collected and conveyed to the modular separation station at a pressure of 11.8 bara. From the above results, it is noted that for a mass flow rate of 280 kg/s of steam passed through the back pressure turbine at an inlet pressure of 11.8 bara, the electricity equivalent of 29.7 MW would be generated. The quality of exhaust steam is 96%. The condensed steam is then removed by the mist eliminator and the resulting dry steam passed through the main turbine at a pressure of 6 bara. Electricity amounting to 138.5 MW is generated as shown in Figure 17.

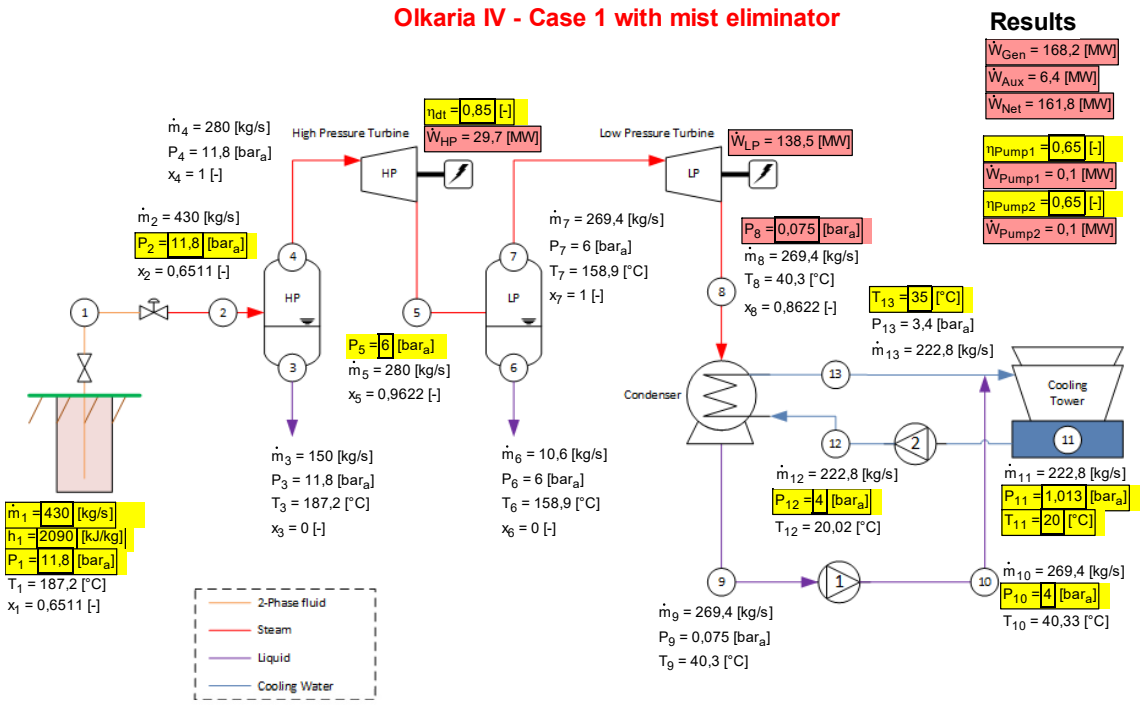

FIGURE 17: EES results of Case 1

5.3.2 Case 2

Two-phase steam from the steam field with a mass flow rate of 430 kg/s and a weighted enthalpy of 2090 kJ/kg is collected and conveyed to the modular separation station at a pressure of 11.8 bara. The brine obtained from the high-pressure separator is then mixed with the exhaust steam at 96% dryness fraction from the back pressure turbine and further flashed at 6 bara. In this case, 29.7 MW of power is obtained from the back pressure turbine and 143.1 MW of power is obtained from the main turbine as shown in Figure 18.

5.3.3 Case 3

Two-phase steam from the steam field with a mass flow rate of 430 kg/s and a weighted enthalpy of 2090 kJ/kg is collected and conveyed to the modular separation station at a pressure of 11.8 bara. The brine obtained from the high-pressure separator is then flashed at a pressure of 6 bara. The steam obtained is then mixed with the exhaust steam from the back pressure turbine. Mist eliminator is installed to remove the condensed water droplets that resulted from the expansion process. The total steam is then conveyed to the main steam turbine at an inlet pressure of 6 bara. In this case, 29.7 MW of power is obtained from the back pressure turbine and 143.1 MW of power is obtained from the main turbine as shown in Figure 19.

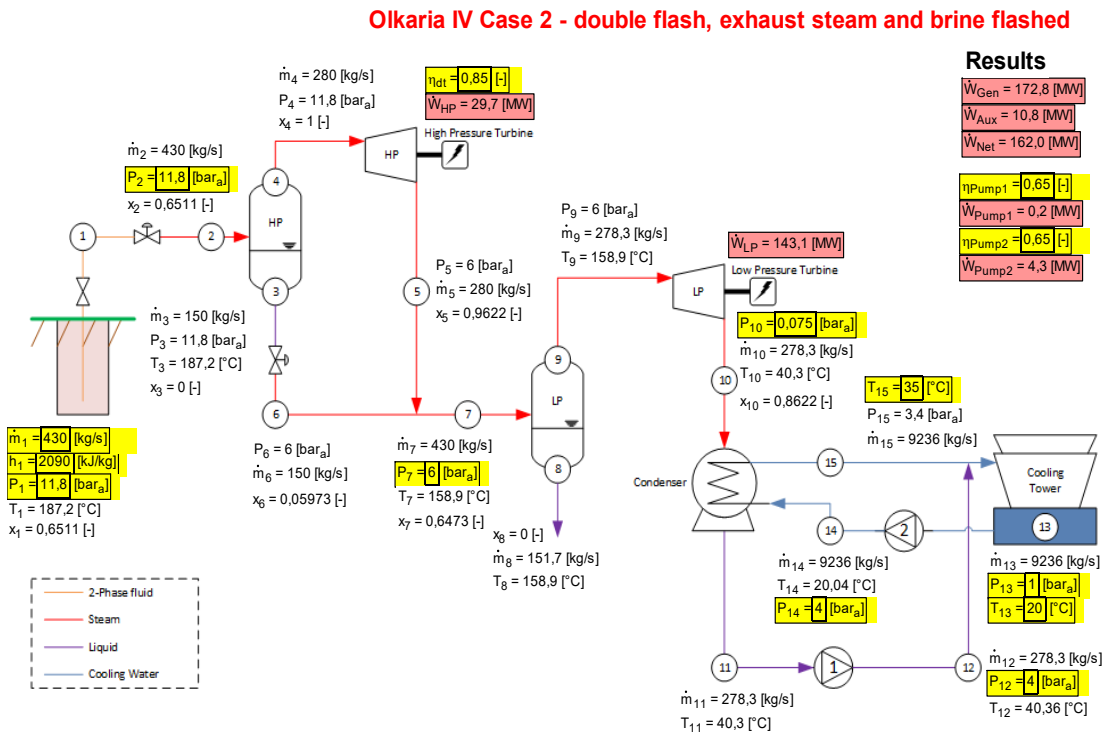

FIGURE 18: EES results of case 2

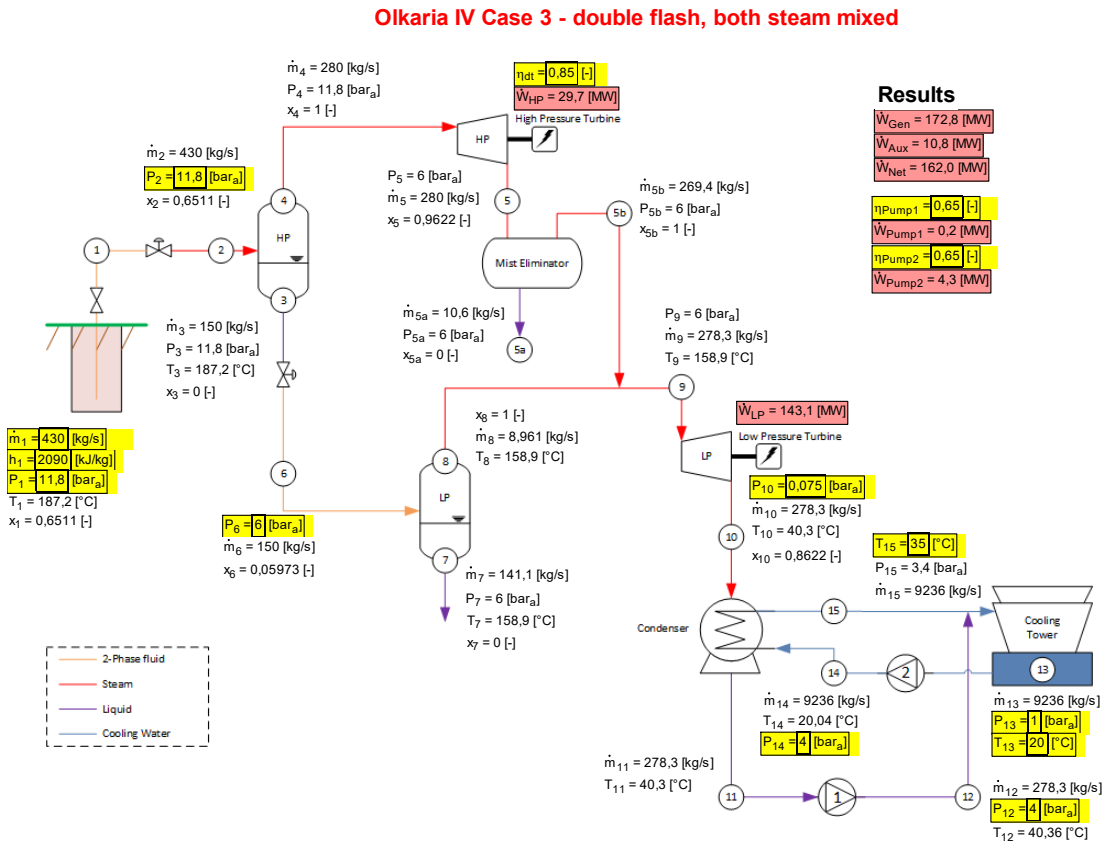

FIGURE 19: EES results of case 3 model

5.3.4 Case 4

Two scenarios were considered here. First, the pressure at the high-pressure separation station is maximized while the pressure at the inlet of the main turbine is fixed at 6 bara. From the results obtained,

the back pressure turbine would generate 16.4 MW of power while the main turbine would generate 150.5 MW of power.

The second scenario is to maximise both the high and low separator pressures. The lower pressure bound pressure would be that of the exhaust pressure of the main turbine. The results obtained for both scenarios are shown in Figure 20 and Figure 21, respectively.

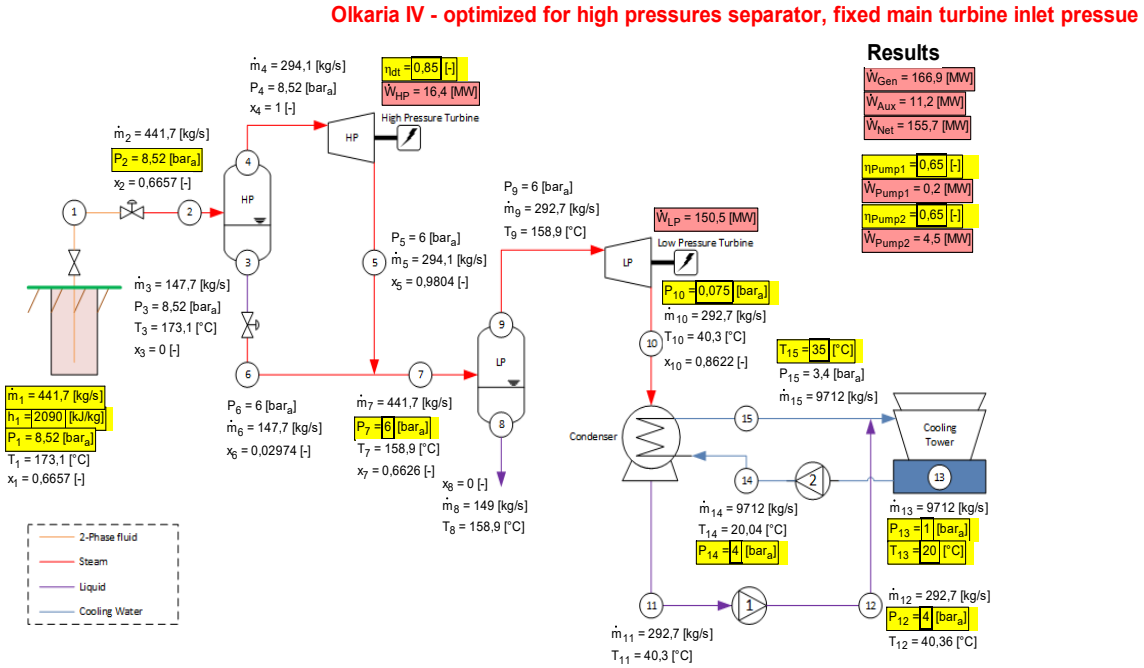

FIGURE 20: EES results of maximized HP separation pressure

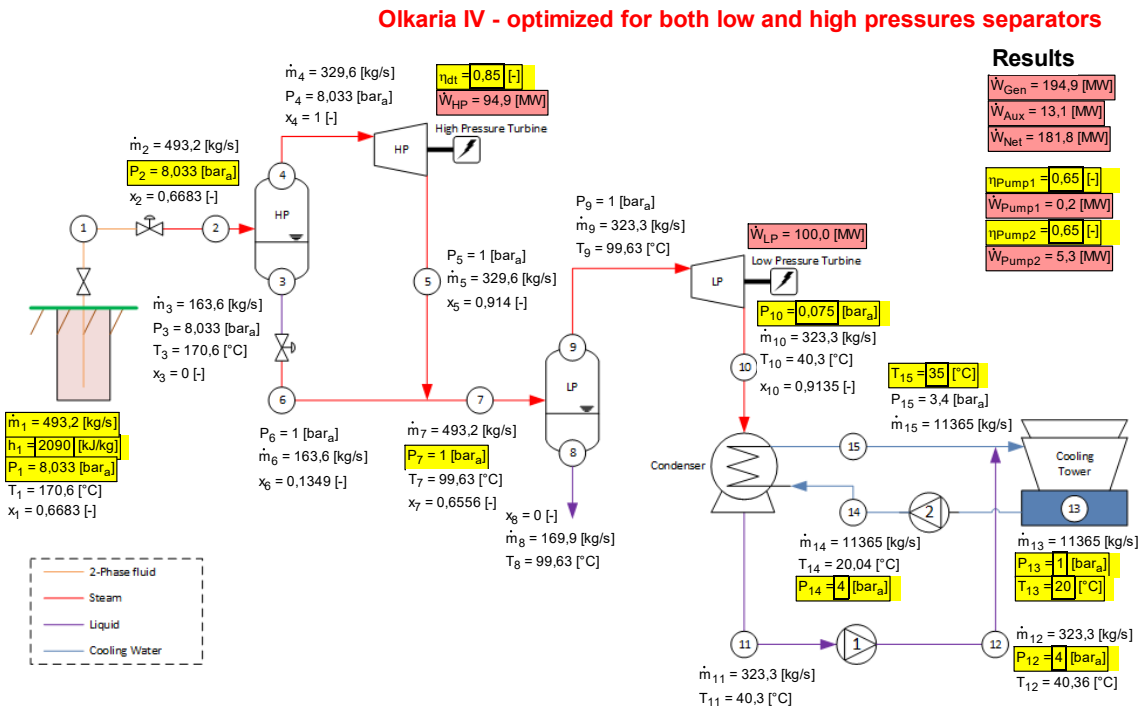

FIGURE 21: EES results of maximized both high and low separation pressure

6. CAPITAL COST OF INSTALLATIONS

From confidential communication with industry participants, it was found that the estimated capital cost of installation of a single flash geothermal power plant with a condensing unit is in the range of USD 3500-4000/kW for smaller units of 5-50 MWe output, and USD 3000-3500/kW for larger units of 50 to 100 MWe. Literature is available on economic comparison between a well-head geothermal power plant and a traditional geothermal power plant (Geirdal, 2013).

These costs include steam field pipelines, steam separators, well connections, civil works, electrical and mechanical installations, switches and controls, generators, evacuation power lines and anything that is needed to make the geothermal power plant operational.

Figures obtained from geothermal developers indicate that the estimated drilling costs for a geothermal well is in the range 4-5 million USD. The average power output of drilled wells in the Olkaria geothermal field, for purposes of this analysis, is assumed to be 6 MWe.

7. CONCLUSIONS AND RECOMMENDATIONS

From the study and the results obtained, the following conclusions and recommendations are made:

1. The total electrical power output that could be generated from the back pressure turbine ranges from 16 to 30 MWe, depending on the option selected, contributing to an increase in gross power of 10 to 20%;
2. It is possible to increase the electrical power by about 5 MW by flashing the brine from the high-pressure separator and adding it back to the main steam line;
3. There is a significant amount of avoided drilling cost, of up to approximately 20 million USD, assuming a conservative cost estimate of 5 million USD per drilled geothermal well;
4. A thorough investigation on the probability of scaling issues in the pipelines during separation should be looked into.

It is recommended to study the economic feasibility of installing a back-pressure turbine, taking into account all the cost of installation and running cost and then compare them with the revenue of selling electricity generated from the back-pressure turbine.

ACKNOWLEDGEMENTS

I would like to express my sincere gratitude to the Government of Iceland, The United Nations University-Geothermal Training Programme (UNU-GTP) and my employer, Kenya Electricity Generating Company, KenGen, for granting me this opportunity to attend this training programme. I owe my sincere appreciation to Mr. Lúdvík S. Georgsson, director of UNU-GTP.

I would also like to thank my supervisors Prof. Páll Valdimarsson and María Sigrídur Gudjónsdóttir from Reykjavik University for their guidance, support and advice during my project period. Many thanks to Mr. Ingimar Haraldsson. Mrs. María S Gudjónsdóttir. Mr. Markús A. G. Wilde and Ms. Thórhildur Ísberg for their assistance during my stay in Iceland.

I give special thanks and heartfelt gratitude to my wife Joyce and the entire family for their unwavering support and encouragement throughout the six months and especially for enduring my absence for six months.

I would also like to thank all 2015 UNU-GTP fellows for an unforgettable time during the six months, especially my group in geothermal utilization for all the discussions and the nice times we had together. Finally, I wish to express my heartfelt gratitude to the almighty God for giving me the strength and good health of the entire period.

NOMENCLATURE

C	=	Condenser
CP	=	Condensate pump
CSV	=	Control and stop valves
CT	=	Cooling tower
CWP	=	Cooling water pump
f	=	Saturated liquid
g	=	Saturated vapour
IW	=	Injection well
MR	=	Moisture remover
PW	=	Production well
SE/C	=	Steam ejector/condenser
SP	=	Steam piping
T/G	=	Turbine/generator
S	=	Specific entropy (kJ/kg-K)
T	=	Temperature (°C)
X	=	Quality
W	=	Power (W)

Greek symbols

η	=	Efficiency (%)
ρ	=	density (kg/m^3)

Abbreviations

CS	=	Cooling system
CWP	=	Circulating water pump
EES	=	Engineering Equation Solver
GES	=	Gas extraction system
MWe	=	Megawatt electricity
NCG	=	Non-condensable gases
NCR	=	Nominal continuous rating
SD	=	Separator station
USD	=	United States dollar
WHP	=	Wellhead pressure

REFERENCES

Brookes, B, Chong, W and De Krester, S. 2011: Olkaria geothermal project: Fast-track geothermal steamfield development using modular steam separator stations. *Proceedings, Kenya Geothermal Conference 2011, Kenyatta International Conference Centre, Nairobi, November 21-22*, 6 pp.

DiPippo, R., 2007: *Geothermal power plants. Principles, aplications, case studies and environmental impact* (2nd ed.). Butterworth Heineman, Elsevier, Kidlingiton, UK, 493 pp.

Geirdal, C.A.C., 2013: *Economic Comparison between a Wellhead Geothermal Power Plant and a Traditional Geothermal Power Plant*. Reykjavík University, Reykjavík, Iceland, MSc thesis, 100 pp.

Kaplan. U. and Schochet. D.N., 2000: Improving geothermal power plant performance with topping and bottoming cycles. Case histories in Iceland, New Zealand, and the Philippines. *Proceedings World Geothermal Congress 2000, Kyushu-Tohoku, Japan*, 2111-2114.

Karingithi, C., 2002: *Hydrothermal mineral buffers controlling reactive gases concentration in the Greater Olkaria geothermal system, Kenya*. University of Iceland, MSc thesis, UNU-GTP, Iceland report 2, 51 pp.

KenGen, 2011: *Olkaria IV 280 MW Geothermal power plant contract document*. KenGen, unpublished internal execution contract document.

KenGen, 2012: *Wells data summary, Olkaria IV Domes*. KenGen, unpublished internal well testing report.

Lagat, J.K., 2004: *Geology, hydrothermal alteration and fluid inclusion studies of the Olkaria Domes geothermal field, Kenya.* University of Iceland, MSc thesis, UNU-GTP, Iceland, report 2, 71 pp.

Lee, K.C., 1996: *Classification of geothermal resources: An engineering approach.* Proceedings of the 21st Workshop on Geothermal Reservoir Engineering, Stanford University, Stanford, Ca, 85-92.

Thain, I.A. and Carey, B., 2008: Fifty years of geothermal power generation at Wairakei. *Geothermics 38*, 48–63.

Thome, J. (ed.), 2006: *Engineering data*. Book III. Wolverine Tube Inc., Lausanne, Switzerland.

Valdimarsson, P., 2011: Geothermal power plant cycles and main components. *Presented at "Short Course on Geothermal Drilling. Resource Development and Power Plants", organized by UNU-GTP and LaGeo, in Santa Tecla. El Salvador*, 24 pp.

Walas, S.M., 1990*: Chemical process equipment, selection and design*. Butterworth-Heinemann, Washington, USA, 755 pp.

APPENDIX I: EES codes for cases selected

EES CODES
Case 0: Current status

```
"Wells"
T[1]=Temperature(Water;P=P[1];h=h[1])
x[1]=Quality(Water;h=h[1];P=P[1])

"State 2"
h[2]=h[1]
m_dot[2]=m_dot[1]
x[2]=Quality(Water;h=h[2];P=P[2])

"State 3"
P[3]=P[2]
x[3]=0 [-]
h[3]=enthalpy(Water;P=P[3];X=x[3])
T[3]=Temperature(Water;P=P[3];x=x[3])
v[3]=volume(Water;h=h[3];P=P[3])
m_dot[3]=(1-x[2])*m_dot[2]
```

"State 4"
P[4]=P[2]
x[4]=1 [-]
h[4]=enthalpy(Water;P=P[4];X=x[4])
T[4]=Temperature(Water;P=P[4];x=x[4])
s[4]=entropy(Water;P=P[4];x=x[4])
m_dot[4]=x[2]*m_dot[2]

"State 5"
h[5]=enthalpy(Water;P=P[5];x=1)
s[5]=entropy(Water;P=P[5];x=1)
T[5]=Temperature(Water;P=P[5];x=1)
x[5]=1
m_dot[5]=m_dot[4]

"State 8"
s_8s=s[5]
h_8s=enthalpy(Water;P=P[8];s=s_8s)
"!Baumann rule"
h_aLP=enthalpy(Water;P=P[8];x=0)
h_bLP=enthalpy(Water;P=P[8];x=1)
A_LP=eta_dt/2*(h[5]-h_8s)
h[8]=(h[5]-A_LP*(1-h_aLP/(h_bLP-h_aLP)))/(1+A_LP/(h_bLP-h_aLP))
s[8]=entropy(Water;P=P[8];h=h[8])
x[8]=Quality(Water;h=h[8];P=P[8])
T[8]=Temperature(Water;P=P[8];h=h[8])
m_dot[8]=m_dot[5]

"State 9"
P[9] = P[8]
x[9] = 0
h[9] = enthalpy(Water;P=P[9];x=x[9])
T[9] = Temperature(Water;P=P[9];x=x[9])
v[9] = volume(Water;P=P[9];x=x[9])
m_dot[9] = m_dot[8]

"State 10"
m_dot[10]=m_dot[9]
h_10s=h[9]+v[9]*(P[10]-P[9])*80
h[10]=h[9]+(h_10s-h[9])/eta_Pump1
T[10]=Temperature(Water;P=P[10];h=h[10])
x[10]=quality(Water;P=P[10];h=h[10])
v[10]=Volume(Water;P=P[10];h=h[10])

"State 11"
m_dot[11] = Q_dot_Condenser*800/(h[2]-h[12])
h[11]=enthalpy(Water;T=T[11];P=P[11])
v[11]=volume(Water;T=T[11];P=P[11])

"State 12"
m_dot[12]=m_dot[11]
h_12s=h[11]+v[11]*(P[12]-P[11])*80
h[12]=h[11]+(h_12s-h[11])/eta_Pump2
T[12]=Temperature(Water;P=P[12];h=h[12])
x[12]=quality(Water;P=P[12];h=h[12])

"State 13"
DELTAP_Condenser=0,6 [bar]
P[13]=P[12]-DELTAP_Condenser
h[13]=enthalpy(Water;T=T[13];P=P[13])
m_dot[13]=m_dot[12]

"Energy calculations"
W_dot_LP = m_dot[5]*(h[5]-h[8])/1000
W_dot_Pump1 = m_dot[9]*(h[10]-h[9])/1000
W_dot_Pump2 = m_dot[11]*(h[12]-h[11])/1000
W_dot_Pumps = W_dot_Pump1+W_dot_Pump2
W_dot_Gen = W_dot_LP
W_dot_Aux = W_dot_Pumps+W_dot_400V+W_dot_CoolingTower+W_dot_GasExtraction+W_dot_T&G+W_dot_Other

W_dot_Net=W_dot_Gen-W_dot_Aux

"Auxiliaries power consumption"
W_dot_400V=3,89*W_dot_Gen/1000
W_dot_T&G=2,3*W_dot_Gen/1000
W_dot_CoolingTower = 4,13*Q_dot_Condenser/1000
W_dot_GasExtraction=4,13*Q_dot_Condenser/1000
W_dot_Other=3,04*W_dot_Gen/1000

"Cooling capacity of Condenser"
Q_dot_Condenser = m_dot[8]*(h[8]-h[9])/1000

Case 1: Topping unit with mist eliminator
"Wells"
T[1]=Temperature(Water;P=P[1];h=h[1])
x[1]=Quality(Water;h=h[1];P=P[1])

"State 2"
h[2]=h[1]
m_dot[2]=m_dot[1]
x[2]=Quality(Water;h=h[2];P=P[2])

"State 3"
P[3]=P[2]
x[3]=0 [-]
h[3]=enthalpy(Water;P=P[3];X=x[3])
T[3]=Temperature(Water;P=P[3];x=x[3])
v[3]=volume(Water;h=h[3];P=P[3])
m_dot[3]=(1-x[2])*m_dot[2]

"State 4"
P[4]=P[2]
x[4]=1 [-]
h[4]=enthalpy(Water;P=P[4];X=x[4])
T[4]=Temperature(Water;P=P[4];x=x[4])
s[4]=entropy(Water;P=P[4];x=x[4])
m_dot[4]=x[2]*m_dot[2]

"State 5"
s_5s=s[4]
h_5s=enthalpy(Water;P=P[5];s=s_5s)
"!Baumann rule"
h_a=enthalpy(Water;P=P[5];x=0)
h_b=enthalpy(Water;P=P[5];x=1)
A=eta_dt/2*(h[4]-h_5s)
h[5]=(h[4]-A*(1-h_a/(h_b-h_a)))/(1+A/(h_b-h_a))
s[5]=entropy(Water;P=P[5];h=h[5])
x[5]=Quality(Water;h=h[5];P=P[5])
T[5]=Temperature(Water;P=P[5];h=h[5])
m_dot[5]=m_dot[4]

"State 6"
P[6] = P[5]
x[6]=0 [-]
h[6]=enthalpy(Water;P=P[6];X=x[6])
T[6]=Temperature(Water;P=P[6];x=x[6])
v[6]=volume(Water;h=h[6];P=P[6])
m_dot[6]=(1-x[5])*m_dot[5]

"State 7"
P[7]=P[6]
x[7]=1 [-]
h[7]=enthalpy(Water;P=P[7];X=x[7])
T[7]=Temperature(Water;P=P[7];x=x[7])
s[7]=entropy(Water;P=P[7];x=x[7])
m_dot[7]=x[5]*m_dot[5]

"State 8"
s_8s=s[7]

```
h_8s=enthalpy(Water;P=P[8];s=s_8s)
"!Baumann rule"
h_aLP=enthalpy(Water;P=P[8];x=0)
h_bLP=enthalpy(Water;P=P[8];x=1)
A_LP=eta_dt/2*(h[7]-h_8s)
h[8]=(h[7]-A_LP*(1-h_aLP/(h_bLP-h_aLP)))/(1+A_LP/(h_bLP-h_aLP))
s[8]=entropy(Water;P=P[8];h=h[8])
x[8]=Quality(Water;h=h[8];P=P[8])
T[8]=Temperature(Water;P=P[8];h=h[8])
m_dot[8]=m_dot[7]

"State 9"
P[9] = P[8]
x[9] = 0
h[9] = enthalpy(Water;P=P[9];x=x[9])
T[9] = Temperature(Water;P=P[9];x=x[9])
v[9] = volume(Water;P=P[9];x=x[9])
m_dot[9] = m_dot[8]

"State 10"
m_dot[10]=m_dot[9]
h_10s=h[9]+v[9]*(P[10]-P[9])*80
h[10]=h[9]+(h_10s-h[9])/eta_Pump1
T[10]=Temperature(Water;P=P[10];h=h[10])
x[10]=quality(Water;P=P[10];h=h[10])
v[10]=Volume(Water;P=P[10];h=h[10])

"State 11"
m_dot[11] = Q_dot_Condenser*800/(h[2]-h[12])
h[11]=enthalpy(Water;T=T[11];P=P[11])
v[11]=volume(Water;T=T[11];P=P[11])

"State 12"
m_dot[12]=m_dot[11]
h_12s=h[11]+v[11]*(P[12]-P[11])*80
h[12]=h[11]+(h_12s-h[11])/eta_Pump2
T[12]=Temperature(Water;P=P[12];h=h[12])
x[12]=quality(Water;P=P[12];h=h[12])

"State 13"
DELTAP_Condenser=0,6 [bar]
P[13]=P[12]-DELTAP_Condenser
h[13]=enthalpy(Water;T=T[13];P=P[13])
m_dot[13]=m_dot[12]

"Energy calculations"
W_dot_HP = m_dot[4]*(h[4]-h[5])/1000
W_dot_LP = m_dot[7]*(h[7]-h[8])/1000
W_dot_Pump1 = m_dot[9]*(h[10]-h[9])/1000
W_dot_Pump2 = m_dot[11]*(h[12]-h[11])/1000
W_dot_Pumps = W_dot_Pump1+W_dot_Pump2
W_dot_Gen = W_dot_HP+W_dot_LP
W_dot_Aux = W_dot_Pumps+W_dot_400V+W_dot_CoolingTower+W_dot_GasExtraction+W_dot_T&G+W_dot_Other
W_dot_Net=W_dot_Gen-W_dot_Aux

"Auxiliarie power consumption"
W_dot_400V=3,89*W_dot_Gen/1000
W_dot_T&G=2,3*W_dot_Gen/1000
W_dot_CoolingTower = 4,13*Q_dot_Condenser/1000
W_dot_GasExtraction=4,13*Q_dot_Condenser/1000
W_dot_Other=3,04*W_dot_Gen/1000

"Cooling capacity of Condenser"
Q_dot_Condenser = m_dot[8]*(h[8]-h[9])/1000
```

Case 2: Topping unit with double flash

```
"Wells"
T[1]=Temperature(Water;P=P[1];h=h[1])
x[1]=Quality(Water;h=h[1];P=P[1])
```

"State 2"
h[2]=h[1]
m_dot[2]=m_dot[1]
x[2]=Quality(Water;h=h[2];P=P[2])

"State 3"
P[3]=P[2]
x[3]=0 [-]
h[3]=enthalpy(Water;P=P[3];X=x[3])
T[3]=Temperature(Water;P=P[3];x=x[3])
v[3]=volume(Water;h=h[3];P=P[3])
m_dot[3]=(1-x[2])*m_dot[2]

"State 4"
P[4]=P[2]
x[4]=1 [-]
h[4]=enthalpy(Water;P=P[4];X=x[4])
T[4]=Temperature(Water;P=P[4];x=x[4])
s[4]=entropy(Water;P=P[4];x=x[4])
m_dot[4]=x[2]*m_dot[2]

"State 5"
P[5] = P[7]
s_5s=s[4]
h_5s=enthalpy(Water;P=P[5];s=s_5s)
"!Baumann rule"
h_a=enthalpy(Water;P=P[5];x=0)
h_b=enthalpy(Water;P=P[5];x=1)
A=eta_dt/2*(h[4]-h_5s)
h[5]=(h[4]-A*(1-h_a/(h_b-h_a)))/(1+A/(h_b-h_a))
s[5]=entropy(Water;P=P[5];h=h[5])
x[5]=Quality(Water;h=h[5];P=P[5])
T[5]=Temperature(Water;P=P[5];h=h[5])
m_dot[5]=m_dot[4]

"State 6"
P[6] = P[7]
h[6] = h[3]
m_dot[6]=m_dot[3]
x[6]=Quality(Water;h=h[6];P=P[6])

"State 7"
m_dot[7] = m_dot[5] + m_dot[6]
h[7] = (h[5]*m_dot[5] + h[6]*m_dot[6])/m_dot[7]
T[7]=Temperature(Water;P=P[7];h=h[7])
x[7]=quality(Water;P=P[7];h=h[7])
v[7]=Volume(Water;P=P[7];h=h[7])

"State 8"
P[8] = P[7]
x[8]=0 [-]
h[8]=enthalpy(Water;P=P[8];X=x[8])
T[8]=Temperature(Water;P=P[8];x=x[8])
v[8]=volume(Water;h=h[8];P=P[8])
m_dot[8]=(1-x[7])*m_dot[7]

"State 9"
P[9]=P[7]
x[9]=1 [-]
h[9]=enthalpy(Water;P=P[9];X=x[9])
T[9]=Temperature(Water;P=P[9];x=x[9])
s[9] = entropy(Water;P=P[9];x=x[9])
m_dot[9]=x[7]*m_dot[7]

"State 10"
s_10s=s[9]
h_10s=enthalpy(Water;P=P[10];s=s_10s)
"!Baumann rule"
h_aLP=enthalpy(Water;P=P[10];x=0)
h_bLP=enthalpy(Water;P=P[10];x=1)

```
A_LP=eta_dt/2*(h[9]-h_10s)
h[10]=(h[9]-A_LP*(1-h_aLP/(h_bLP-h_aLP)))/(1+A_LP/(h_bLP-h_aLP))
s[10]=entropy(Water;P=P[10];h=h[10])
x[10]=Quality(Water;h=h[10];P=P[10])
T[10]=Temperature(Water;P=P[10];h=h[10])
m_dot[10]=m_dot[9]

"State 11"
P[11] = P[10]
x[11] = 0
h[11] = enthalpy(Water;P=P[11];x=x[11])
T[11] = Temperature(Water;P=P[11];x=x[11])
v[11] = volume(Water;P=P[11];x=x[11])
m_dot[11] = m_dot[10]

"State 12"
m_dot[12]=m_dot[11]
h_12s=h[11]+v[11]*(P[12]-P[11])*100
h[12]=h[11]+(h_12s-h[11])/eta_Pump1
T[12]=Temperature(Water;P=P[12];h=h[12])
x[12]=quality(Water;P=P[12];h=h[12])
v[12]=Volume(Water;P=P[12];h=h[12])


"State 13"
m_dot[13] = Q_dot_Condenser*1000/(h[15]-h[14])
h[13]=enthalpy(Water;T=T[13];P=P[13])
v[13]=volume(Water;T=T[13];P=P[13])

"State 14"
m_dot[14]=m_dot[13]
h_14s=h[13]+v[13]*(P[14]-P[13])*100
h[14]=h[13]+(h_14s-h[13])/eta_Pump2
T[14]=Temperature(Water;P=P[14];h=h[14])
x[14]=quality(Water;P=P[14];h=h[14])

"State 15"
DELTAP_Condenser=0,6 [bar]
P[15]=P[14]-DELTAP_Condenser
h[15]=enthalpy(Water;T=T[15];P=P[15])
m_dot[15]=m_dot[14]

"!Energy calculations"

W_dot_HP = m_dot[4]*(h[4]-h[5])/1000
W_dot_LP = m_dot[9]*(h[9]-h[10])/1000
W_dot_Pump1 = m_dot[11]*(h[12]-h[11])/1000
W_dot_Pump2 = m_dot[13]*(h[14]-h[13])/1000
W_dot_Pumps = W_dot_Pump1+W_dot_Pump2
W_dot_Gen = W_dot_HP+W_dot_LP
W_dot_Aux = W_dot_Pumps+W_dot_400V+W_dot_CoolingTower+W_dot_GasExtraction+W_dot_T&G+W_dot_Other
W_dot_Net=W_dot_Gen-W_dot_Aux

"Auxiliarie power consumption"
W_dot_400V=3,89*W_dot_Gen/1000
W_dot_T&G=2,3*W_dot_Gen/1000
W_dot_CoolingTower = 4,13*Q_dot_Condenser/1000
W_dot_GasExtraction=4,13*Q_dot_Condenser/1000
W_dot_Other=3,04*W_dot_Gen/1000

"Cooling capacity of Condenser"
Q_dot_Condenser = m_dot[10]*(h[10]-h[11])/1000
```

Case 3: Topping unit, double flash, both steam mixed

```
"Wells"
P_1_barg = P[1]-1,01325
T[1]=Temperature(Water;P=P[1];h=h[1])
x[1]=Quality(Water;h=h[1];P=P[1])
```

"State 2"
h[2]=h[1]
m_dot[2]=m_dot[1]
x[2]=Quality(Water;h=h[2];P=P[2])

"State 3"
P[3]=P[2]
x[3]=0 [-]
h[3]=enthalpy(Water;P=P[3];X=x[3])
T[3]=Temperature(Water;P=P[3];x=x[3])
v[3]=volume(Water;h=h[3];P=P[3])
m_dot[3]=(1-x[2])*m_dot[2]

"State 4"
P[4]=P[2]
x[4]=1 [-]
h[4]=enthalpy(Water;P=P[4];X=x[4])
T[4]=Temperature(Water;P=P[4];x=x[4])
s[4]=entropy(Water;P=P[4];x=x[4])
m_dot[4]=x[2]*m_dot[2]

"State 5"
P[5] = P[6]
s_5s=s[4]
h_5s=enthalpy(Water;P=P[5];s=s_5s)
"!Baumann rule"
h_a=enthalpy(Water;P=P[5];x=0)
h_b=enthalpy(Water;P=P[5];x=1)
A=eta_dt/2*(h[4]-h_5s)
h[5]=(h[4]-A*(1-h_a/(h_b-h_a)))/(1+A/(h_b-h_a))
s[5]=entropy(Water;P=P[5];h=h[5])
x[5]=Quality(Water;h=h[5];P=P[5])
T[5]=Temperature(Water;P=P[5];h=h[5])
m_dot[5]=m_dot[4]

"State 5a"
P_5a=P[5]
x_5a=0 [-]
h_5a=enthalpy(Water;P=P_5a;X=x_5a)
T_5a=Temperature(Water;P=P_5a;x=x_5a)
v_5a=volume(Water;h=h_5a;P=P_5a)
m_dot_5a=(1-x[5])*m_dot[5]

"State 5b"
P_5b=P[5]
x_5b=1 [-]
h_5b=enthalpy(Water;P=P_5b;X=x_5b)
T_5b=Temperature(Water;P=P_5b;x=x_5b)
s_5b=entropy(Water;P=P_5b;x=x_5b)
m_dot_5b=x[5]*m_dot[5]

"State 6"
h[6] = h[3]
m_dot[6]=m_dot[3]
x[6]=Quality(Water;h=h[6];P=P[6])

"State 7"
P[7]=P[6]
x[7]=0 [-]
h[7]=enthalpy(Water;P=P[7];X=x[7])
T[7]=Temperature(Water;P=P[7];x=x[7])
v[7]=volume(Water;h=h[7];P=P[7])
m_dot[7]=(1-x[6])*m_dot[6]

"State 8"
P[8]=P[6]
x[8]=1 [-]
h[8]=enthalpy(Water;P=P[8];X=x[8])
T[8]=Temperature(Water;P=P[8];x=x[8])
m_dot[8]=x[6]*m_dot[6]

```
"State 9"
m_dot[9] = m_dot_5b + m_dot[8]
P[9] = P[6]
h[9] = (h_5b*m_dot_5b + h[8]*m_dot[8])/m_dot[9]
T[9]=Temperature(Water;P=P[9];h=h[9])
x[9]=quality(Water;P=P[9];h=h[9])
v[9]=Volume(Water;P=P[9];h=h[9])
s[9] = entropy(Water;P=P[9];h=h[9])

"State 10"
s_10s=s[9]
h_10s=enthalpy(Water;P=P[10];s=s_10s)
"!Baumann rule"
h_aLP=enthalpy(Water;P=P[10];x=0)
h_bLP=enthalpy(Water;P=P[10];x=1)
A_LP=eta_dt/2*(h[9]-h_10s)
h[10]=(h[9]-A_LP*(1-h_aLP/(h_bLP-h_aLP)))/(1+A_LP/(h_bLP-h_aLP))
s[10]=entropy(Water;P=P[10];h=h[10])
x[10]=Quality(Water;h=h[10];P=P[10])
T[10]=Temperature(Water;P=P[10];h=h[10])
m_dot[10]=m_dot[9]

"State 11"
P[11] = P[10]
x[11] = 0
h[11] = enthalpy(Water;P=P[11];x=x[11])
T[11] = Temperature(Water;P=P[11];x=x[11])
v[11] = volume(Water;P=P[11];x=x[11])
m_dot[11] = m_dot[10]

"State 12"
m_dot[12]=m_dot[11]
h_12s=h[11]+v[11]*(P[12]-P[11])*100
h[12]=h[11]+(h_12s-h[11])/eta_Pump1
T[12]=Temperature(Water;P=P[12];h=h[12])
x[12]=quality(Water;P=P[12];h=h[12])
v[12]=Volume(Water;P=P[12];h=h[12])

"State 13"
m_dot[13] = Q_dot_Condenser*1000/(h[15]-h[14])
h[13]=enthalpy(Water;T=T[13];P=P[13])
v[13]=volume(Water;T=T[13];P=P[13])

"State 14"
m_dot[14]=m_dot[13]
h_14s=h[13]+v[13]*(P[14]-P[13])*100
h[14]=h[13]+(h_14s-h[13])/eta_Pump2
T[14]=Temperature(Water;P=P[14];h=h[14])
x[14]=quality(Water;P=P[14];h=h[14])

"State 15"
DELTAP_Condenser=0,6 [bar]
P[15]=P[14]-DELTAP_Condenser
h[15]=enthalpy(Water;T=T[15];P=P[15])
m_dot[15]=m_dot[14]

"!Auxilaries"
"Energy calculations"
W_dot_HP = m_dot[4]*(h[4]-h[5])/1000
W_dot_LP = m_dot[9]*(h[9]-h[10])/1000
W_dot_Pump1 = m_dot[11]*(h[12]-h[11])/1000
W_dot_Pump2 = m_dot[13]*(h[14]-h[13])/1000
W_dot_Pumps = W_dot_Pump1+W_dot_Pump2
W_dot_Gen = W_dot_HP+W_dot_LP
W_dot_Aux = W_dot_Pumps+W_dot_400V+W_dot_CoolingTower+W_dot_GasExtraction+W_dot_T&G+W_dot_Other
W_dot_Net=W_dot_Gen-W_dot_Aux

"Auxiliarie power consumption"
W_dot_400V=3,89*W_dot_Gen/1000
W_dot_T&G=2,3*W_dot_Gen/1000
```

```
W_dot_CoolingTower = 4,13*Q_dot_Condenser/1000
W_dot_GasExtraction=4,13*Q_dot_Condenser/1000
W_dot_Other=3,04*W_dot_Gen/1000

"Cooling capacity of Condenser"
Q_dot_Condenser = m_dot[10]*(h[10]-h[11])/1000
```

Case 4a: Topping unit, optimized, fixed pressure for main turbine

```
"Wells"
m1=38-0,0017*P[1]^3                    {OW 908A}
m2=25,8-0,0017*P[1]^3                  {OW 908B}
m3=22,5-0,0028*P[1]^3                  {OW 910}
m4=33,8-0,0008*P[1]^3                  {OW 910A}
m5=63,5-0,0005*P[1]^3                  {OW 910B}
m6=40,3-0,0003*P[1]^3                  {OW 916}
m7=26,9-0,0017*P[1]^3                  {OW 916A}
m8=27,8-0,0035*P[1]^3                  {OW 915}
m9=33,9-0,0005*P[1]^3                  {OW 915A}
m10=35,6-0,0035*P[1]^3                 {OW 915B}
m11=10-0,003*P[1]^3                    {OW 908}
m12=40,5-0,0093*P[1]^3                 {OW 915B}
m13=32,2-0,0145*P[1]^3                 {OW 908}
m14=25,3-0,0058*P[1]^3                 {OW 912}
m15=18,1-0,0029*P[1]^3                 {OW 912A}

m_dot[1]=m1+m2+m3+m4+m5+m6+m7+m8+m9+m10+m11+m12+m13+m14+m15
T[1]=Temperature(Water;P=P[1];h=h[1])
x[1]=Quality(Water;h=h[1];P=P[1])

"State 2"
P[2] = P[1]
h[2]=h[1]
m_dot[2]=m_dot[1]
x[2]=Quality(Water;h=h[2];P=P[2])

"State 3"
P[3]=P[2]
x[3]=0 [-]
h[3]=enthalpy(Water;P=P[3];X=x[3])
T[3]=Temperature(Water;P=P[3];x=x[3])
v[3]=volume(Water;h=h[3];P=P[3])
m_dot[3]=(1-x[2])*m_dot[2]

"State 4"
P[4]=P[2]
x[4]=1 [-]
h[4]=enthalpy(Water;P=P[4];X=x[4])
T[4]=Temperature(Water;P=P[4];x=x[4])
s[4]=entropy(Water;P=P[4];x=x[4])
m_dot[4]=x[2]*m_dot[2]

"State 5"
P[5] = P[7]
s_5s=s[4]
h_5s=enthalpy(Water;P=P[5];s=s_5s)
"!Baumann rule"
h_a=enthalpy(Water;P=P[5];x=0)
h_b=enthalpy(Water;P=P[5];x=1)
A=eta_dt/2*(h[4]-h_5s)
h[5]=(h[4]-A*(1-h_a/(h_b-h_a)))/(1+A/(h_b-h_a))
s[5]=entropy(Water;P=P[5];h=h[5])
x[5]=Quality(Water;h=h[5];P=P[5])
T[5]=Temperature(Water;P=P[5];h=h[5])
m_dot[5]=m_dot[4]

"State 6"
P[6] = P[7]
h[6] = h[3]
```

```
m_dot[6]=m_dot[3]
x[6]=Quality(Water;h=h[6];P=P[6])

"State 7"
m_dot[7] = m_dot[5] + m_dot[6]
h[7] = (h[5]*m_dot[5] + h[6]*m_dot[6])/m_dot[7]
T[7]=Temperature(Water;P=P[7];h=h[7])
x[7]=quality(Water;P=P[7];h=h[7])
v[7]=Volume(Water;P=P[7];h=h[7])

"State 8"
P[8] = P[7]
x[8]=0 [-]
h[8]=enthalpy(Water;P=P[8];X=x[8])
T[8]=Temperature(Water;P=P[8];x=x[8])
v[8]=volume(Water;h=h[8];P=P[8])
m_dot[8]=(1-x[7])*m_dot[7]

"State 9"
P[9]=P[7]
x[9]=1 [-]
h[9]=enthalpy(Water;P=P[9];X=x[9])
T[9]=Temperature(Water;P=P[9];x=x[9])
s[9] = entropy(Water;P=P[9];x=x[9])
m_dot[9]=x[7]*m_dot[7]

"State 10"
s_10s=s[9]
h_10s=enthalpy(Water;P=P[10];s=s_10s)
"!Baumann rule"
h_aLP=enthalpy(Water;P=P[10];x=0)
h_bLP=enthalpy(Water;P=P[10];x=1)
A_LP=eta_dt/2*(h[9]-h_10s)
h[10]=(h[9]-A_LP*(1-h_aLP/(h_bLP-h_aLP)))/(1+A_LP/(h_bLP-h_aLP))
s[10]=entropy(Water;P=P[10];h=h[10])
x[10]=Quality(Water;h=h[10];P=P[10])
T[10]=Temperature(Water;P=P[10];h=h[10])
m_dot[10]=m_dot[9]

"State 11"
P[11] = P[10]
x[11] = 0
h[11] = enthalpy(Water;P=P[11];x=x[11])
T[11] = Temperature(Water;P=P[11];x=x[11])
v[11] = volume(Water;P=P[11];x=x[11])
m_dot[11] = m_dot[10]

"State 12"
m_dot[12]=m_dot[11]
h_12s=h[11]+v[11]*(P[12]-P[11])*100
h[12]=h[11]+(h_12s-h[11])/eta_Pump1
T[12]=Temperature(Water;P=P[12];h=h[12])
x[12]=quality(Water;P=P[12];h=h[12])
v[12]=Volume(Water;P=P[12];h=h[12])

"State 13"
m_dot[13] = Q_dot_Condenser*1000/(h[15]-h[14])
h[13]=enthalpy(Water;T=T[13];P=P[13])
v[13]=volume(Water;T=T[13];P=P[13])

"State 14"
m_dot[14]=m_dot[13]
h_14s=h[13]+v[13]*(P[14]-P[13])*100
h[14]=h[13]+(h_14s-h[13])/eta_Pump2
T[14]=Temperature(Water;P=P[14];h=h[14])
x[14]=quality(Water;P=P[14];h=h[14])

"State 15"
DELTAP_Condenser=0,6 [bar]
P[15]=P[14]-DELTAP_Condenser
```

```
h[15]=enthalpy(Water;T=T[15];P=P[15])
m_dot[15]=m_dot[14]

"!Energy calculations"
"Energy calculations"
W_dot_HP = m_dot[4]*(h[4]-h[5])/1000
W_dot_LP = m_dot[9]*(h[9]-h[10])/1000
W_dot_Pump1 = m_dot[11]*(h[12]-h[11])/1000
W_dot_Pump2 = m_dot[13]*(h[14]-h[13])/1000
W_dot_Pumps = W_dot_Pump1+W_dot_Pump2
W_dot_Gen = W_dot_HP+W_dot_LP
W_dot_Aux = W_dot_Pumps+W_dot_400V+W_dot_CoolingTower+W_dot_GasExtraction+W_dot_T&G+W_dot_Other
W_dot_Net=W_dot_Gen-W_dot_Aux

"Auxiliarie power consumption"
W_dot_400V=3,89*W_dot_Gen/1000
W_dot_T&G=2,3*W_dot_Gen/1000
W_dot_CoolingTower = 4,13*Q_dot_Condenser/1000
W_dot_GasExtraction=4,13*Q_dot_Condenser/1000
W_dot_Other=3,04*W_dot_Gen/1000

"Cooling capacity of Condenser"
Q_dot_Condenser = m_dot[10]*(h[10]-h[11])/1000
```

Case 4b: Topping unit, optimized, fixed pressure for main turbine

```
"Wells"
m1=38-0,0017*P[1]^3                    {OW 908A}
m2=25,8-0,0017*P[1]^3                  {OW 908B}
m3=22,5-0,0028*P[1]^3                  {OW 910}
m4=33,8-0,0008*P[1]^3                  {OW 910A}
m5=63,5-0,0005*P[1]^3                  {OW 910B}
m6=40,3-0,0003*P[1]^3                  {OW 916}
m7=26,9-0,0017*P[1]^3                  {OW 916A}
m8=27,8-0,0035*P[1]^3                  {OW 915}
m9=33,9-0,0005*P[1]^3                  {OW 915A}
m10=35,6-0,0035*P[1]^3                 {OW 915B}
m11=10-0,003*P[1]^3                    {OW 908}
m12=40,5-0,0093*P[1]^3                 {OW 915B}
m13=32,2-0,0145*P[1]^3                 {OW 908}
m14=25,3-0,0058*P[1]^3                 {OW 912}
m15=18,1-0,0029*P[1]^3                 {OW 912A}
m16=30-0,0018*P[1]^3                   {OW 912}
m17=18,1-0,0019*P[1]^3                 {OW 912A}

m_dot[1]=m1+m2+m3+m4+m5+m6+m7+m8+m9+m10+m11+m12+m13+m14+m15+m16+m17

T[1]=Temperature(Water;P=P[1];h=h[1])
x[1]=Quality(Water;h=h[1];P=P[1])

"State 2"
P[2] = P[1]
h[2]=h[1]
m_dot[2]=m_dot[1]
x[2]=Quality(Water;h=h[2];P=P[2])

"State 3"
P[3]=P[2]
x[3]=0 [-]
h[3]=enthalpy(Water;P=P[3];X=x[3])
T[3]=Temperature(Water;P=P[3];x=x[3])
v[3]=volume(Water;h=h[3];P=P[3])
m_dot[3]=(1-x[2])*m_dot[2]

"State 4"
P[4]=P[2]
x[4]=1 [-]
h[4]=enthalpy(Water;P=P[4];X=x[4])
T[4]=Temperature(Water;P=P[4];x=x[4])
```

```
s[4]=entropy(Water;P=P[4];x=x[4])
m_dot[4]=x[2]*m_dot[2]

"State 5"
P[5] = P[7]
s_5s=s[4]
h_5s=enthalpy(Water;P=P[5];s=s_5s)
"!Baumann rule"
h_a=enthalpy(Water;P=P[5];x=0)
h_b=enthalpy(Water;P=P[5];x=1)
A=eta_dt/2*(h[4]-h_5s)
h[5]=(h[4]-A*(1-h_a/(h_b-h_a)))/(1+A/(h_b-h_a))
s[5]=entropy(Water;P=P[5];h=h[5])
x[5]=Quality(Water;h=h[5];P=P[5])
T[5]=Temperature(Water;P=P[5];h=h[5])
m_dot[5]=m_dot[4]

"State 6"
P[6] = P[7]
h[6] = h[3]
m_dot[6]=m_dot[3]
x[6]=Quality(Water;h=h[6];P=P[6])

"State 7"
m_dot[7] = m_dot[5] + m_dot[6]
h[7] = (h[5]*m_dot[5] + h[6]*m_dot[6])/m_dot[7]
T[7]=Temperature(Water;P=P[7];h=h[7])
x[7]=quality(Water;P=P[7];h=h[7])
v[7]=Volume(Water;P=P[7];h=h[7])

"State 8"
P[8] = P[7]
x[8]=0 [-]
h[8]=enthalpy(Water;P=P[8];X=x[8])
T[8]=Temperature(Water;P=P[8];x=x[8])
v[8]=volume(Water;h=h[8];P=P[8])
m_dot[8]=(1-x[7])*m_dot[7]

"State 9"
P[9]=P[7]
x[9]=1 [-]
h[9]=enthalpy(Water;P=P[9];X=x[9])
T[9]=Temperature(Water;P=P[9];x=x[9])
s[9] = entropy(Water;P=P[9];x=x[9])
m_dot[9]=x[7]*m_dot[7]

"State 10"
s_10s=s[9]
h_10s=enthalpy(Water;P=P[10];s=s_10s)
"!Baumann rule"
h_aLP=enthalpy(Water;P=P[10];x=0)
h_bLP=enthalpy(Water;P=P[10];x=1)
A_LP=eta_dt/2*(h[9]-h_10s)
h[10]=(h[9]-A_LP*(1-h_aLP/(h_bLP-h_aLP)))/(1+A_LP/(h_bLP-h_aLP))
s[10]=entropy(Water;P=P[10];h=h[10])
x[10]=Quality(Water;h=h[10];P=P[10])
T[10]=Temperature(Water;P=P[10];h=h[10])
m_dot[10]=m_dot[9]

"State 11"
P[11] = P[10]
x[11] = 0
h[11] = enthalpy(Water;P=P[11];x=x[11])
T[11] = Temperature(Water;P=P[11];x=x[11])
v[11] = volume(Water;P=P[11];x=x[11])
m_dot[11] = m_dot[10]

"State 12"
m_dot[12]=m_dot[11]
h_12s=h[11]+v[11]*(P[12]-P[11])*100
```

```
h[12]=h[11]+(h_12s-h[11])/eta_Pump1
T[12]=Temperature(Water;P=P[12];h=h[12])
x[12]=quality(Water;P=P[12];h=h[12])
v[12]=Volume(Water;P=P[12];h=h[12])

"State 13"
m_dot[13] = Q_dot_Condenser*1000/(h[15]-h[14])
h[13]=enthalpy(Water;T=T[13];P=P[13])
v[13]=volume(Water;T=T[13];P=P[13])

"State 14"
m_dot[14]=m_dot[13]
h_14s=h[13]+v[13]*(P[14]-P[13])*100
h[14]=h[13]+(h_14s-h[13])/eta_Pump2
T[14]=Temperature(Water;P=P[14];h=h[14])
x[14]=quality(Water;P=P[14];h=h[14])

"State 15"
DELTAP_Condenser=0,6 [bar]
P[15]=P[14]-DELTAP_Condenser
h[15]=enthalpy(Water;T=T[15];P=P[15])
m_dot[15]=m_dot[14]

"!Energy calculations"
"Energy calculations"
W_dot_HP = m_dot[4]*(h[4]-h[5])/1000
W_dot_LP = m_dot[9]*(h[9]-h[10])/1000
W_dot_Pump1 = m_dot[11]*(h[12]-h[11])/1000
W_dot_Pump2 = m_dot[13]*(h[14]-h[13])/1000
W_dot_Pumps = W_dot_Pump1+W_dot_Pump2
W_dot_Gen = W_dot_HP+W_dot_LP
W_dot_Aux = W_dot_Pumps+W_dot_400V+W_dot_CoolingTower+W_dot_GasExtraction+W_dot_T&G+W_dot_Other
W_dot_Net=W_dot_Gen-W_dot_Aux

"Auxiliarie power consumption"
W_dot_400V=3,89*W_dot_Gen/1000
W_dot_T&G=2,3*W_dot_Gen/1000
W_dot_CoolingTower = 4,13*Q_dot_Condenser/1000
W_dot_GasExtraction=4,13*Q_dot_Condenser/1000
W_dot_Other=3,04*W_dot_Gen/1000


"Cooling capacity of Condenser"
Q_dot_Condenser = m_dot[10]*(h[10]-h[11])/1000
```

UNITED NATIONS UNIVERSITY
UNU-GTP
Geothermal Training Programme

Orkustofnun, Grensasvegur 9,
IS-108 Reykjavik, Iceland

Reports 2015
Number 19

USE OF GEOTHERMAL ENERGY FOR SEAWATER DESALINATION IN THE GALÁPAGOS ISLANDS, ECUADOR

Andrés Lloret C.
National Institute of Energy Efficiency and Renewable Energy, INER
Av. 6 de Diciembe N33-32 e Ignacion Bossano
ECUADOR
andres.lloret@iner.gob.ec, andreslloret@gmail.com

ABSTRACT

The lack of reliable sources of potable water is a health and social problem in the Galápagos. The presence of geothermal resources in the islands opens a window of opportunity for the development of a geothermal energy-driven desalination system. Analysis on the available research studies on three shield volcanoes located on the western side of Isabela Island, reveals that Alcedo Volcano presents the most active hydrothermal system with a liquid-dominated reservoir. This type of system is suitable to achieve the separation of nearly salt-free fresh water by implementing a Single Stage Flash Geothermal desalination system (SSF-G). The concept implies the use of geothermal brine from a separator unit as the heat input source for desalination, while producing electricity from the steam to power the plant totally detached from the grid. Results from a thermodynamic model and exergy analysis of the system, using Engineering Equation Solver (EES) software, show that the geothermal resource can be successfully coupled to this desalination method. It also reveals that most of the energy received from the well, exits the plant while still containing substantial exergy, which can be used to perform usable work by the system. As a result of irreversibilities, exergy destruction occurs in all the heat exchangers of the desalination process. As the area under study is within a National Park, the impacts of the plant need to be considered especially. An accounting framework that measures social, environmental and financial performance in terms of sustainability was undertaken in this study. It indicates that an improvement in water quality on Isabela Island, using geothermal energy, would have significant positive impacts on these dimensions of performance. Detailed geophysical studies using AC resistivity methods, and an exploratory drilling campaign is needed to achieve more conclusive information about the feasibility of this project. The results, collected from these studies will help obtaining more information regarding the cap rock, host rock, and hydrothermal alteration of the geothermal prospects located in the Island.

1. INTRODUCTION

The Galápagos Islands, located 973 km off the west coast of Ecuador, are known by its unique biodiversity which inspired Charles Darwin´s theory of evolution. They are also considered to be one of the most volcanically active regions on earth. With 25,124 inhabitants (INEC, 2015), the population in the Galápagos is spread out in small towns across 4 of the 18 islands.

Presently, the lack of provision and access to a reliable source of potable water is a health and social problem for the community due to very limited sources of fresh water. Bacteriological contamination of the municipal tap water system (López et al., 2007), along with high concentrations of dissolved salt, force islanders to continuously turn to unregulated private alternatives for fresh water supply (Walsh et al., 2010). Moreover, embedded use of fossil fuels, waste generation and the depletion of existing aquifers, resulting from the current local water supply model, compromises its sustainability when faced with an uncontrolled population increase.

Advances in water desalination technologies have made production of potable water a viable option over the last few years. In 2007, the world´s desalinated water production was 40 million m^3/day (Khawaji et al., 2008). Over the following 7 years it doubled, reaching 81 million m^3/day in 2014 (Ghaffour et al., 2015). According to the Global Water Intelligence (Olsson, 2015), the total global desalination capacity is expected to reach over 100 million m^3/day by the end of 2015.

Water desalination by means of renewable energy has been proven to be technically and economically feasible in remote, isolated, or water scarce locations. Renewable sources such as solar, geothermal and wind have already been researched and tested to work as the main energy input for desalination. Goonsen et al. (2014) provide an overview of pilot Renewable Energy (RE) driven desalinations systems installed around the world.

In this study, the potential use of geothermal energy for seawater desalination in Isabela Island is analysed. A review is done on the existing geothermal activity documented by Geist et al. (1994), Goff et al. (2000), and Naumann et al. (2002), to identify a potential geothermal prospect for the application of a geothermal energy-driven desalination system on the island. A thermodynamic model and exergy analysis of a proposed Single Stage Flash geothermal desalination system (SSF-G) is done using Engineering Equation Solver (EES) software. The model will simulate the distillation of nearly 276 m^3 of seawater per day, using geothermal brine from a separator unit as the heat input source for the desalination process. The inflow of potable water from this process will be sufficient to match the average consumption of water per day in the island (Guyot-Téphany and Liu, 2011). The design will also simulate the use of high enthalpy geothermal steam to produce electricity for a stand-alone operation, enabling the desalination plant to run in an off-grid mode. The study concludes with a simplified Triple Bottom Line (TBL) assessment approach to discuss the economic, social and environmental aspects of a potential geothermal desalination project.

2. JUSTIFICATION

2.1 Overview of the problem

The Province of Galápagos, with a total population of 25,124 is divided into three cantons: Isabela (9%), Santa Cruz (60%) and, San Cristobal (31%) (Figure 1).

Over the last 40 years, the majority of inhabitants from the islands have been supplied brackish water from the municipal service. It is presently the only subsurface source available; it is extracted from basal aquifers and distributed by local municipalities to its citizens. Figure 2 shows the main sources of water on Isabela Island. The resource is composed of rain water from the highlands, and three main aquifers: El Chapin, el Manzanillo, and San Vicente. However, these aquifers cannot sustainan an uncontrolled urbanization growth, which leads to an increase in demand. As a result, water supply restrictions are presently in place, although so far they have not been proven effective and, in some cases, have created other water related issues (Guyot-Téphany et al., 2012). In addition, improvised (and unregulated) private desalination business and, imported bottled water from the mainland, provide the daily supply of freshwater required to sustain domestic and commercial activities in the island.

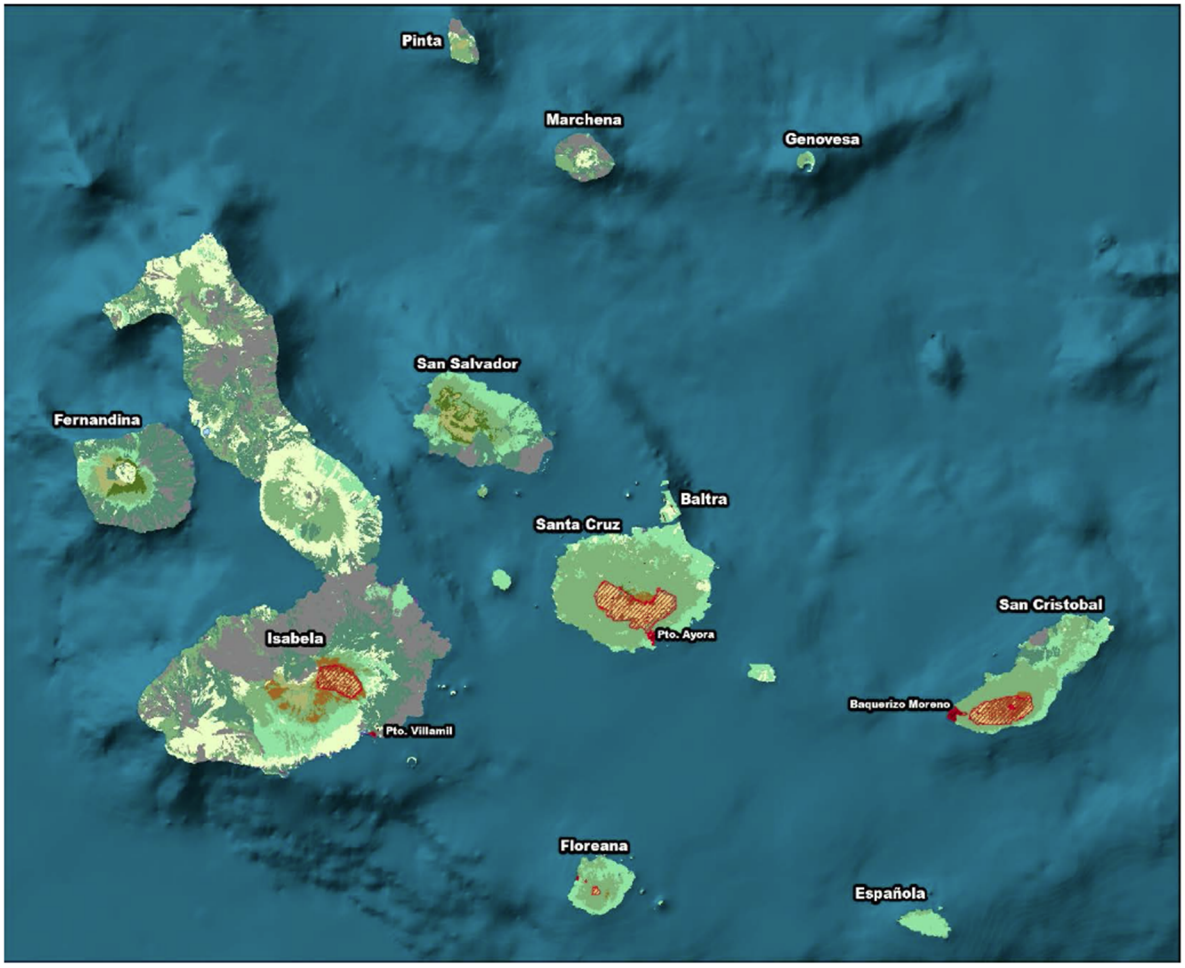

FIGURE 1: Demographic map of the Galápagos Islands
(CEPROEC-IAEN and SENPLADES, 2014)

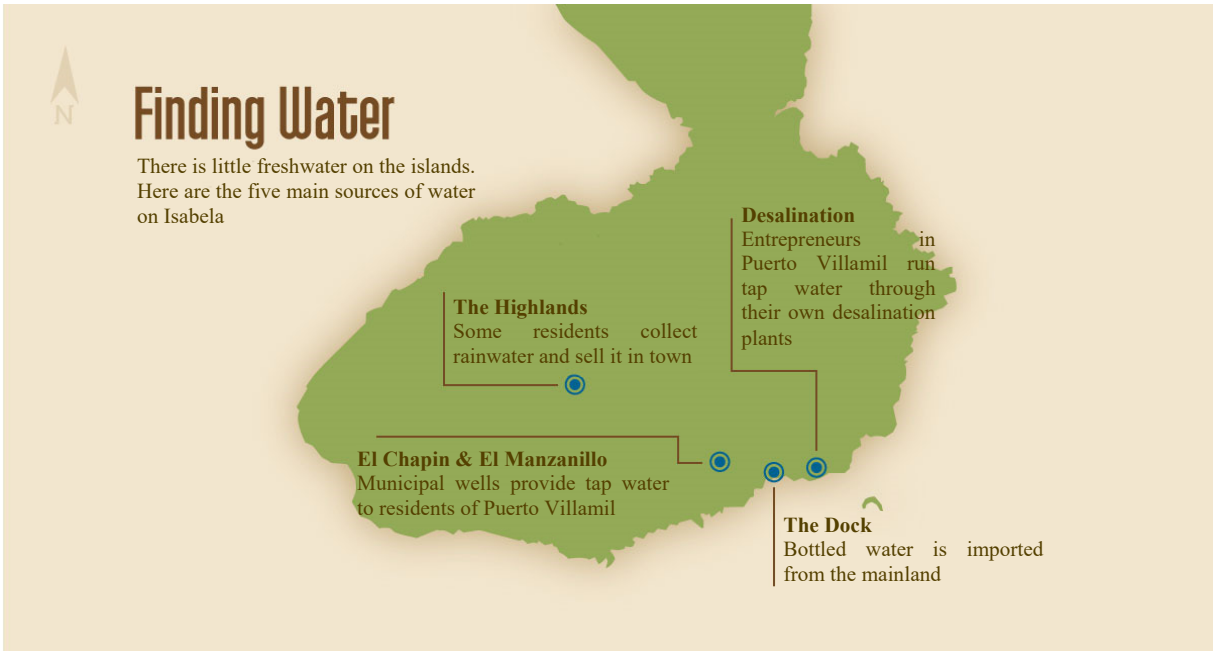

FIGURE 2: Location of the main water sources on Isabela Island (Living Galápagos, 2015)

2.2 Contamination of water supply

Studies on the quality of tap water show evidence of bacteriological and a possible chemical contamination at the municipal extraction locations. This is possibly caused by a lack of sanitation protocols, which causes water to be in contact with contaminated elements along the pipelines (Guyot-Téphany et al., 2012).

Liu (2011) states in her report that despite the presence of pathogens in the water during extraction, the biggest contamination source is the poor storage conditions in households. The absence of chlorine disinfection practices and, not cleansing the reservoirs permanently, causes bacteria in the water to multiply. As a result, the population is vulnerable to an outbreak of stomach and intestinal diseases. An outbreak already occurred in 2006 where water analysis, traced the origin of the infection to inadequate water treatment (Guyot-Téphany et al., 2012).

A third issue is the salinity of the tap water. A study carried out in 2007 by López et al., revealed that the concentration of salt in the municipal tap water systems in Isabela greatly exceeded the level recommended for human consumption Figure 3. For human consumption water must contain less than 1000 mg of salt per litre.

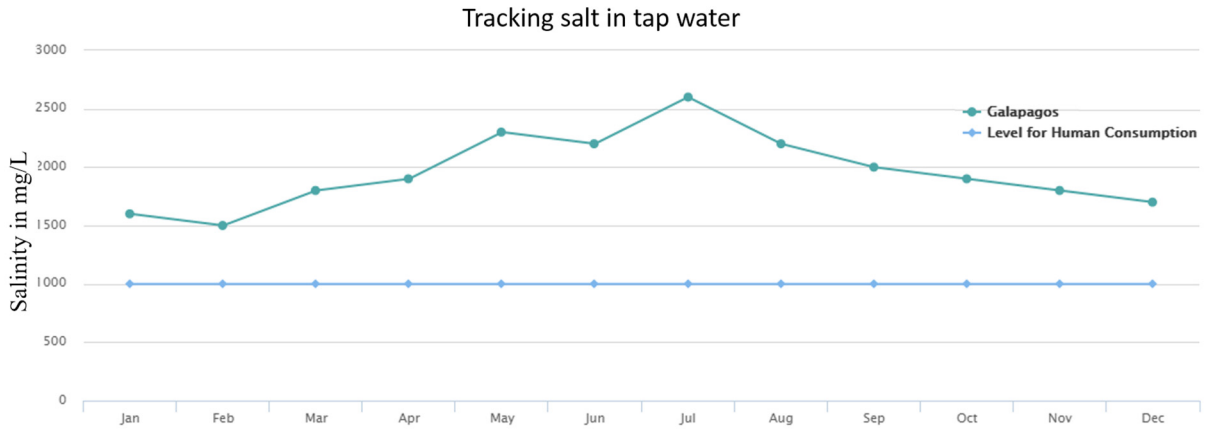

FIGURE 3: Salinity concentration in municipal tap water systems in the Galápagos (Walsh et al., 2010)

2.3 Consequences of the current water supply scheme

In 2009, it was estimated that approximately 70% of diseases in Puerto Villamil resulted from consumption or exposure to contaminated water. Common water-related illnesses include gastrointestinal problems such as diarrhea and gastritis, fungal skin infections and urinary tract infections. Young children (1-4 years of age) are most affected by the effects of tap water and the related health issues, because their immune systems are under-developed, they practice poor hygiene, and tend to experience higher exposures to contaminated sources of water (Walsh et al., 2010). Similar illnesses, which were documented around the world in the past, due to high levels of sodium in drinking-water (WHO, 2003), are likely to happen in the island as a result of the current situation.

In an attempt to prevent this, boiling water is a common practice among the inhabitants. In Isabela, 41% of the population boil the tap water to prevent diseases when using it for drinking and cooking. This is also done in Santa Cruz and San Cristobal, as shown in Figure 4. Household owners also collect rain water from roofs, although this practice has decreased due to the fact that in the past, roofs were typically made of fibercement with asbestos, which are known to cause serious health hazards in humans. A third option is to obtain purified water from a local private water desalination business.

Although this is the preferred option among villagers, it is also the most expensive compared to the previous methods (Guyot-Téphany et al., 2012).

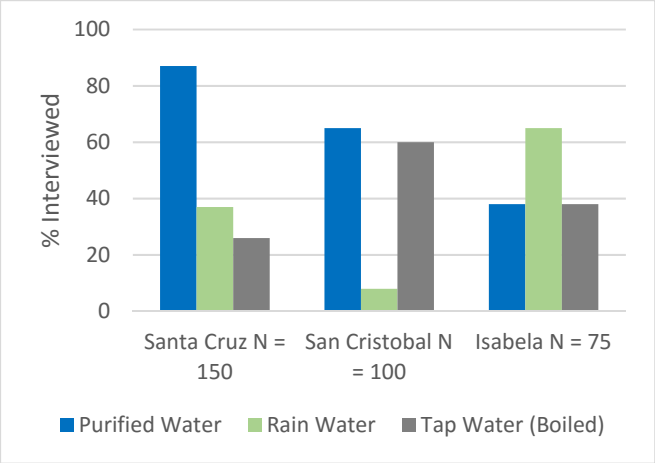

FIGURE 4: Type of water used for human consumption (modified fom Guyot-Téphany et al., 2012)

Contrary to the belief that a limited resource will cause a more responsible use, low quality water creates a culture of wastefulness among the citizens as it has almost no economic value. For example, 61% of interviewed residents who have a tank in Santa Cruz, as well as 47% in San Cristobal and 21% in Isabela, confirm that they allow their tank to overflow once it fills (Guyot-Téphany et al., 2013). In addition, failures in the current supply network are also major causes for water wastage. It is estimated that the volume of water wasted or lost in the system is higher than the volume of water actually consumed (Guyot-Téphany et al., 2012).

Furthermore, activities related to extraction, distribution and use of water resources from aquifers in Isabela rely directly or indirectly on the use of fossil fuels; Gasoline is used in tanker trucks to distribute water to households and, in electric powered storage infraestructures, which were built to bypass the water supply restrictions in the island. In addiion, approximately 5.370 m³ of bottled water is imported annually from the mainland to cover the influx of tourist and supply to local demand (CEPROEC-IAEN and SENPLADES, 2014). Considering that 94% of energy generated in Galápagos comes from fossil fuels (CEPROEC-IAEN and SENPLADES, 2014), the scheme under which the water supply system operates is detrimental in terms of sustainability efforts in the island, and it is certainly in contrast to the government´s plan to eliminate the use of fossil fuels in the Galápagos in the future (MEER, 2015).

3. GEOLOGICAL SETTING OF THE GALÁPAGOS

The Galápagos Islands are an archipelago of 13 main islands, and 48 small islands and islets that belong to the Republic of Ecuador (Neall and Trewick, 2008). They are located on top of a hotspot on the Nazca Plate in the eastern Pacific Ocean, 973 km off the west coast of Ecuador. The Islands are among the most active oceanic volcano groups in the world (Simkin, 1984).

The archipelago is the result of hotspot activity 100 km south of the Galápagos Spreading Center (GSC), a mid-ocean ridge separating the Cocos and Nazca plates (Figure 5). The islands emerge from a broad submarine volcanic platform that marks the western end of the aseismic Carnegie Ridge (Geist et al., 1998). The GSC is migrating north-west away from the hotspot and is thought to have overlain the hotspot around 8 million years ago (Hey, 1977). The proximity of the hotspot and the spreading ridge creates a complex geochemical interaction that strongly affect the composition of lavas from the ridge (Schilling et al., 1976; Verma et al., 1983; in Geist et al, 1998).

Holocene volcanism is present throughout the archipelago. Each major island consists of a single large volcano, which have been active historically, with the exception of the largest island, Isabela, which consists of six volcanoes (Geist et al., 1995). The archipelago has distinct petrologic and volcanologic subprovinces defined by regional differences in the morphologies of the volcanoes (McBirney and Williams, 1969). In general, the lavas tend to be more alkaline and enriched isotopically to the east, north, and south from the central east-west axis of the archipelago, but the central and southern

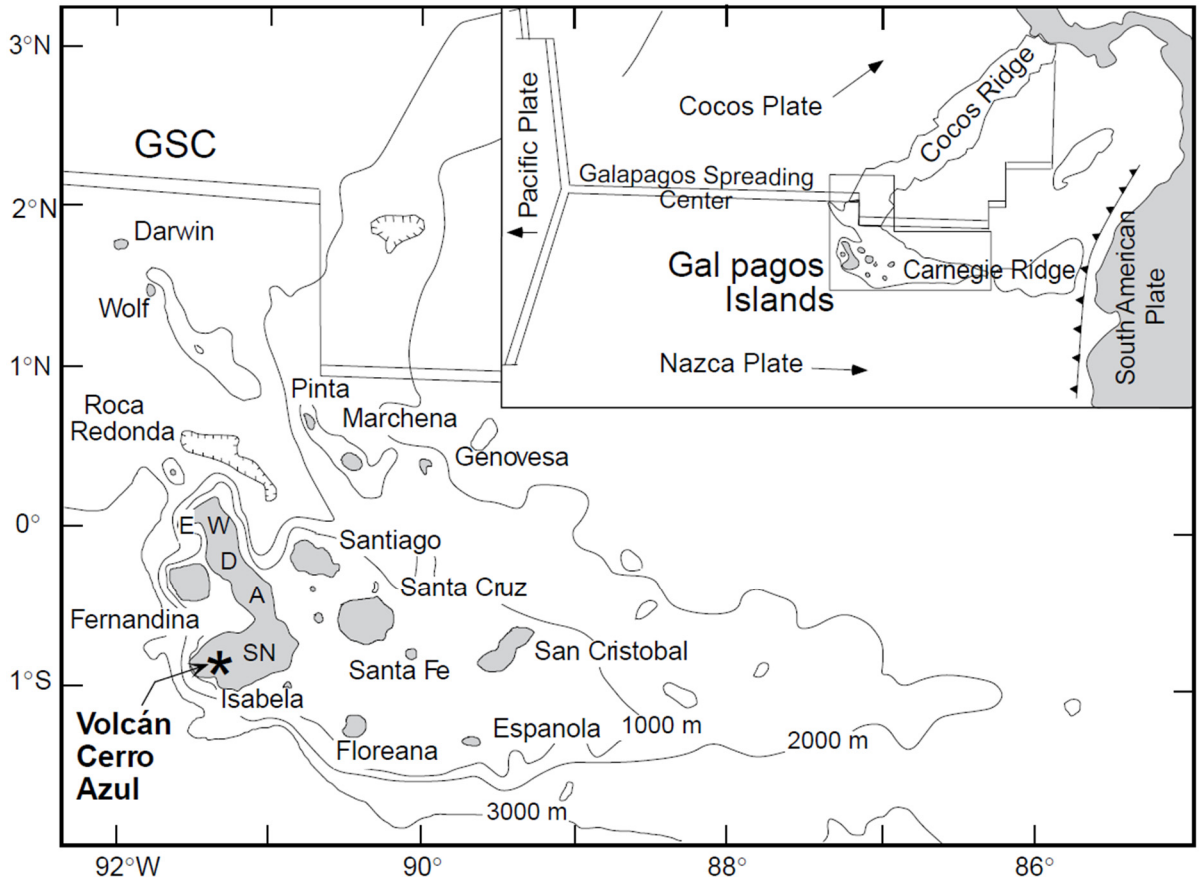

FIGURE 5: Bathymetric map of the Galápagos archipelago. Abbreviations for the six volcanoes of Isabela Island are: E, Ecuador; W, Wolf; D, Darwin; A, Alcedo; SN, Sierra Negra; CA, Cerro Azul. GSC, Galápagos Spreading Centre (Geist et al, 1998)

volcanoes have erupted basalts with unusually great diversity in trace element compositions (Geist, 1992). Chemical and isotopic data indicate that the Galápagos magmas are generated as an undegassed deep mantle plume rises and mixes with magmas derived from relatively depleted asthenospheric mantle (White et al., 1993; Graham et al. 1993). Diffuse hydrothermal phenomena and fumarolic activity occur at several volcanoes throughout the archipelago (Simkin, 1984).

3.1 Isabela

Isabela is the largest island of the Galápagos archipelago with an area of 4,640 km^2 (Figure 6). The hotspot is supposedly centred under the island, which gives origin to six active volcanoes spread across its surface. Along with Fernandina volcano which is located in the neighbouring island with the same name, these two land masses comprise the seven western Galápagos shield volcanoes. The town of Puerto Villamil is located at the southeast point of the island. Autochthonous wildlife and vegetation prevail in the areas around the volcanoes, including the world's largest population of giant tortoises. As is the case

FIGURE 6: Isabela Island view from space (Source: NASA, 1988)

with the rest of the archipelago, almost the entire island is a National Park, subject to environmental regulations and limited public access to maintain its status as a World Natural Heritage site, granted by the United Nations Educational, Scientific and Cultural Organization (UNESCO) in 1978.

Geothermal activity has been documented in the past years around three volcanoes in Isabela: Alcedo, Sierra Negra, and Cerro Azul (Geist et al., 1994; Goff et al., 2000; Naumann et al., 2002). These geothermal prospects shown in Figure 7 were selected based on the available data, and will be discussed in the following sections.

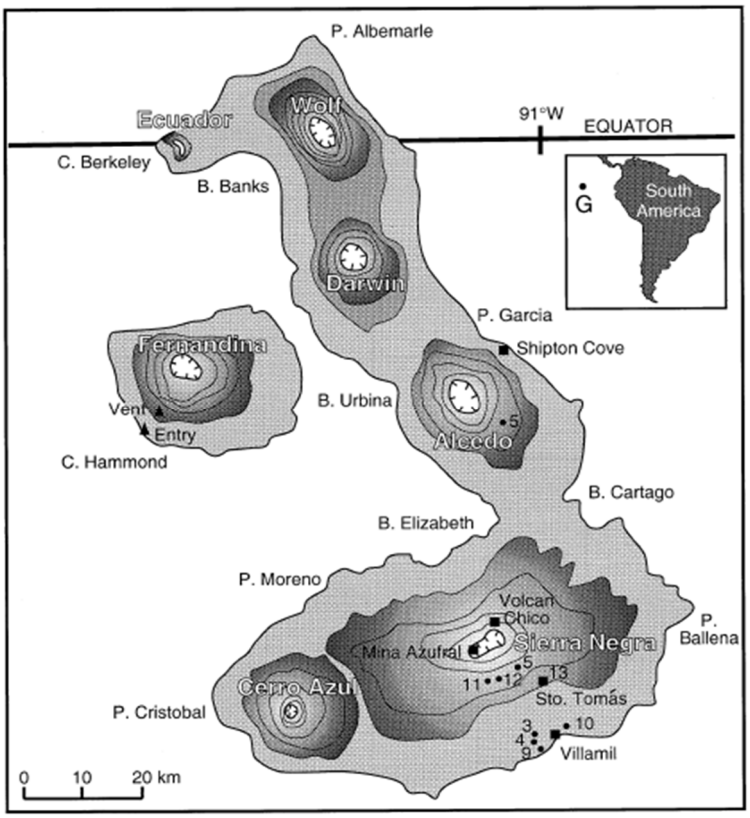

FIGURE 7: Map location of shield volcanoes on Isabela and Fernandina Islands, Galápagos Archipelago. Contour interval is 200 m (Goff et al, 2000)

3.2 Alcedo

Alcedo, located in the centre of Isabela, is the only active Galápagos volcano known to have erupted rhyolite as well as basalt. Its caldera is 7-8 km wide and has a maximum depth of 270 m. This geothermal prospect stands at 1128 m.a.s.l., and its one and only known eruption occurred sometime between 1946 and 1960 from its southern flank, according to aerial photographic evidence (Geist et al., 1994).

The geological setting is characterized by an old basaltic eruptive phase, an intermediate age rhyolite phase, and a young basaltic phase. Several hydrothermal explosion craters followed by fumarolic activity in the eastern zone and, the evidence of subsurface fracture networks, denotes that hydrothermal activity in the area is transient and fault controlled (Goff et al, 2000). Based on surface exploration studies and hydrogeochemical data presented by Goff et al. (2000), Alcedo is likely to host a high-temperature geothermal system. A preliminary conceptual cross-section of the geothermal model is shown in Figure 8.

Reservoir temperatures are estimated between 260 and 320°C, and may circulate as deep as 1 km based on gas geothermometry. The presence of high water content and predominance of reduced sulphur supports the existence of a liquid-dominated system. The reservoir is under a vapour-rich cap and contains neutral-chloride rich fluids. These are composed primarily of local meteoric water infiltrating the caldera and degassed magmatic components from shallow, compound rhyolitic intrusions (Geist et al., 1994; 1995). Permeability is enhanced by a fault controlled system and explosive rhyolitic events. Basaltic eruptions post-dating the rhyolites may add additional heat and magmatic volatiles to the system (Goff et al., 2000). Considering the size of the geothermal anomaly in Alcedo, an estimated power output of 150 MW can likely be obtained if an equivalent volume (15 m^3/s) of flashed steam is generated from geothermal wells at a separation temperature of 180°C (Goff et al., 2000).

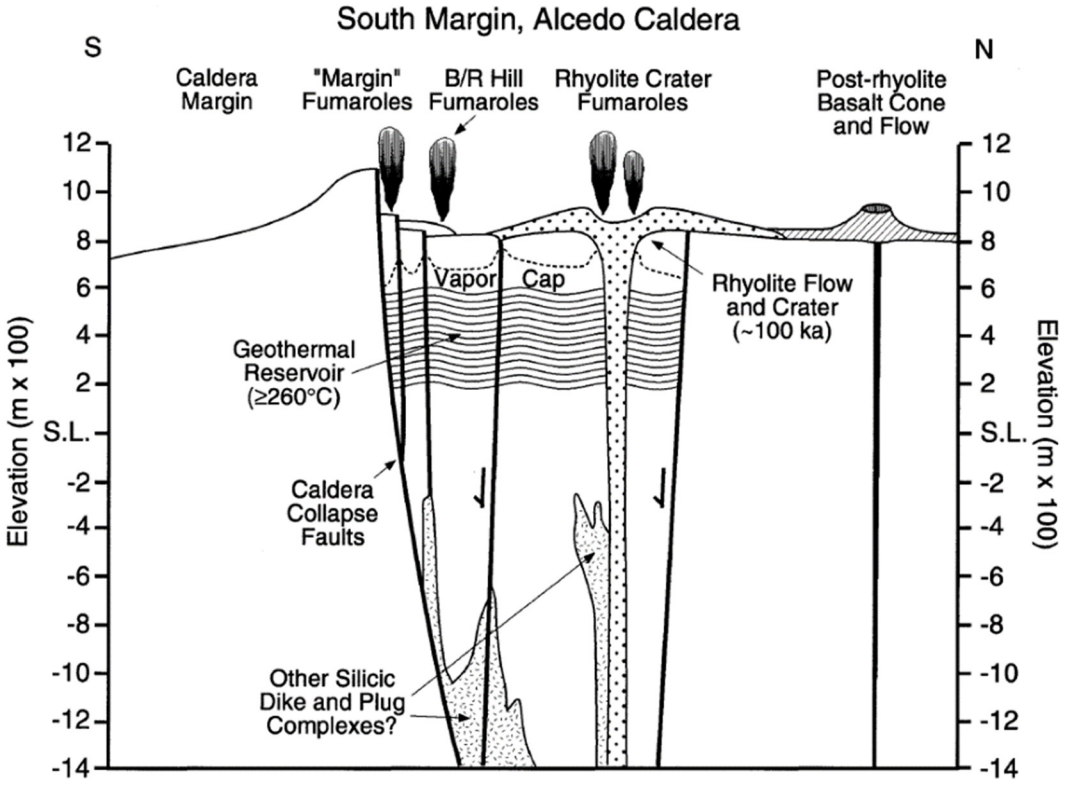

FIGURE 8: Conceptual cross-section of hydrothermal activity in southern sector of Alcedo volcano, Galápagos (Goff et al, 2000)

3.3 Sierra Negra

With a caldera of 7 x 10 km and elevation of 1124 m.a.s.l., Sierra Negra is the largest and most active shield volcano in the archipelago, located at the south eastern end of Isabela Island. It collides with Alcedo to the north and Cerro Azul to the west. The last eruption of Sierra Negra Volcano was registered in October 2005, after 26 years of relative low activity (IGEPN, 2015).

Geothermal manifestations are mainly observed in two particular areas: In a fissure where a parasitic cone named Volcán Chico is located, and in a high temperature fumarole field named Mina Azufral. Activity in this location is mainly fault controlled, creating particular high temperature fumaroles in the range of 110- 210°C, which are associated with sulphur deposits. Both sites were studied by Colony and Nordlie (1973), and Delaney et al. (1973).

Goff et al. (2000) elaborated a conceptual model of hydrothermal activity in the western sector of Sierra Negra based on surface exploration activities and hydrogeochemical data. A conceptual cross-section is shown in Figure 9.

The presence of relatively small basaltic magma intrusions at under 5 km depths are inferred within the conceptual model. The heat from these magmatic bodies may have created a ‘blind geothermal system’ that circulates the western moat, as no surface hydrological evidence such as hot springs is visible to confirm the existence of this theory. Detailed visual reconnaissance of the fumarole field at Mina Azufral suggest that the source of magma and the fault structure has remained relatively unchanged over the last 100 years (Goff et al., 2000).

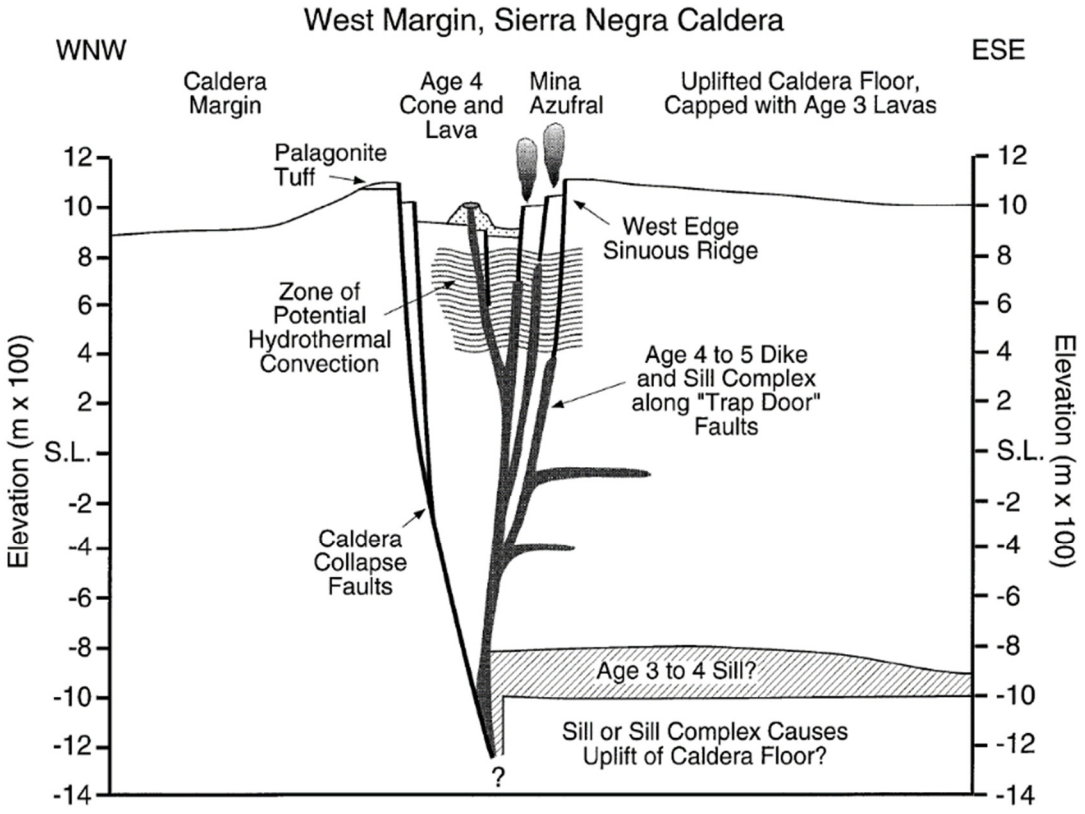

FIGURE 9: Conceptual cross-section of hydrothermal activity in western moat of Sierra Negra volcano, Galápagos (Goff et al, 2000)

Gas geothermometry indicates an apparently shallow decompression of magma. This statement is supported by the presence of high temperature fumaroles and a predominant release of SO_2. Shallow hydrothermal fluids mix with magmatic gases before reaching the surface. Nonetheless, not enough heat is provided by basaltic dikes to sustain a vigorous hydrothermal convection system within the Sierra Negra caldera (Goff et al., 2000).

3.4 Cerro Azul

Cerro Azul Volcano forms the south west end of Isabela Island (Figure 7). It rises up to 1640 m.a.s.l. and is second in elevation only to Wolf Volcano (1710 m.a.s.l.). It is also the second most active volcano after Sierra Negra, with an average of one eruption every 6.5 years (IGEPN, 2015).

Naumann and Geist (2000), and Naumann et al. (2002), provide detailed information on the eruptive history, growth rate, and morphologic development; as well as detailed major, trace and isotopic analyses from Cerro Azul. Clear evidence of explosive hydrovolcanic activity has been documented from Hawaiian-style eruptions in the vents on the caldera floor and southern summit rim (Figure 10).

A cross-section of the caldera denotes an area of 4,2 x 2,2 km, the smallest among the western Galápagos shield volcanoes. Nevertheless, its depth (450 m) almost doubles the one of Alcedo, and extends nearly 4 times Sierra Negra caldera´s depth (Naumann et al., 2002). No geochemical information on hydrothermal fluids that would help to determine the presence or lack of a geothermal system was available when this report was written.

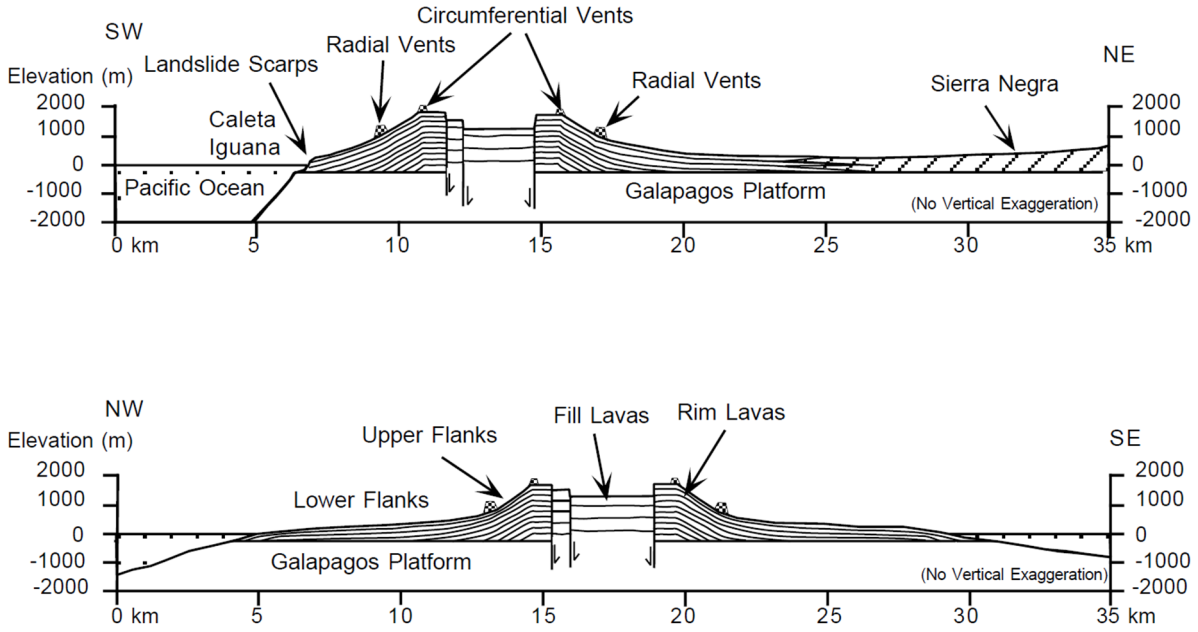

FIGURE 10: Schematic geologic map of Cerro Azul showing cross-sections and internal structure (Naumann et al, 2001)

4. DESALINATION PROCESS

4.1 Overview and current status

The desalination of sea water is the separation of nearly salt-free fresh water from sea or brackish water, where the salts are carried in the rejected brine stream and disposed of back in the sea. A desalination process can be based on thermal or membrane separation methods. The thermal separation techniques consist of evaporation followed by condensation of the formed water vapour, and, freezing followed by melting of the formed water ice crystals. The former process is the most used and nearly in all cases, coupled with power generation units which may be based on steam or gas turbine systems. The evaporation of the brine can be achieved by either boiling or flashing techniques.

Presently, the desalination industry is experiencing a vast expansion around the globe. This is because of an increase in water demand and higher cost of fresh water from natural resources. Although thermal desalination has been increasingly taken over by membrane processes during the last 15 years, it still accounts for 30% of the total desalinated water produced globally (Ghaffour et al., 2015). Multi Stage Flashing (MSF) and Multiple Effect Distillation (MED) technologies dominate the market in thermal desalination.

4.2 Developments in MSF

Since it was first used in 1950, MSF has gone through a series of improvements in its initial design, as the technology advanced and experience was gained from its operation (El-Dessouky and Eltouney, 2002). MSF is derived from Single Stage Flashing (SSF), where seawater is evaporated by reducing the pressure, as opposed to raising the temperature. The latent heat released by the condensing water vapour at each stage gradually raises the temperature of the incoming seawater. The SSF system includes the brine heater and the flashing chamber, which contains the condenser/preheater tubes, the demister, the brine pool, and the collecting distillate tray.

Modifications to the original design, from Single Stage Flashing, to Once Through MSF, to Brine Mixing MSF, and finally to MSF with Brine Recirculation and a Heat Rejection Section, lead to an overall increase of the thermal performance ratio and reliability of the system. Figure 11 shows the most distinctive features and drawbacks of each configuration.

The Three Stage Heat Rejection Brine Circulation (MSF-M) process is currently the industry standard. It combines the previous MSF and MSF-OT features to reduce energy losses and significantly increase the overall system performance (El-Dessouky and Eltouney, 2002). A scheme of MSF-M desalination plant is shown in Figure 12.

Further developments in MSF technology are mainly focused on continuous improvements, such as maximizing the profitability of operation, thermal performance ratio, and optimizing the design and operating parameters. Likewise, replacing non-renewable fossil fuels as energy input in the desalination process, with nuclear energy and renewables in the future.

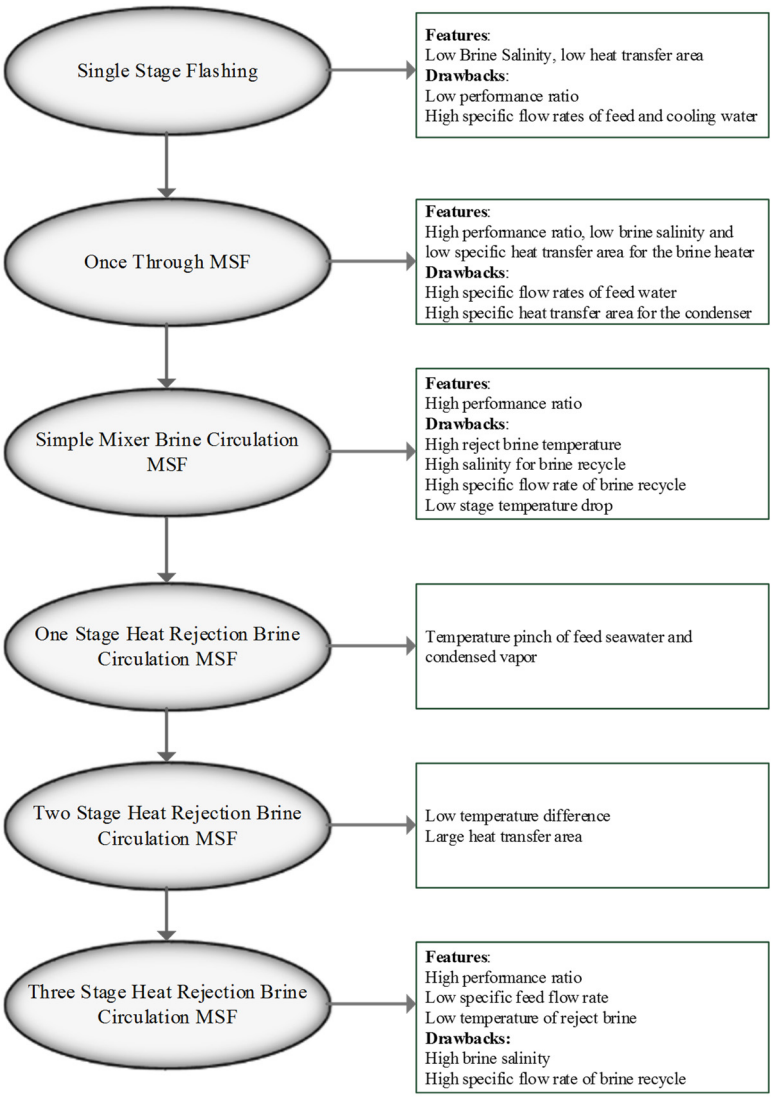

FIGURE 11: Performance summary of various MSF configurations (modified from El-Dessouky and Eltouney, 2002)

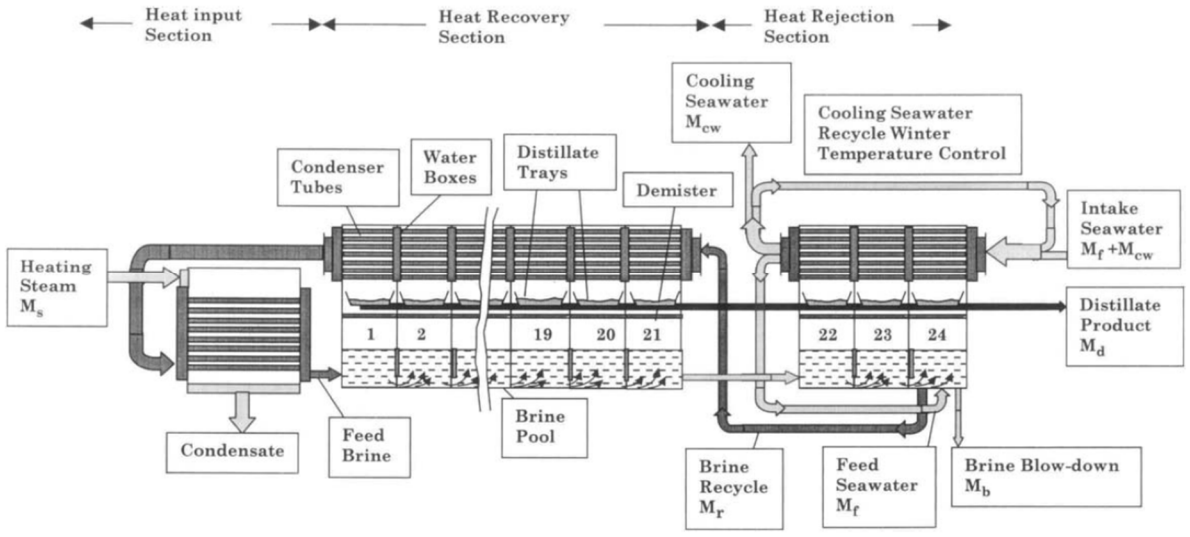

FIGURE 12: Multistage flash desalination with brine recirculation (MSFM) (El-Dessouky et al, 1999)

4.3 RE-driven desalination plants

The present installed desalination capability using RE is negligible compared to the world's total capacity, despite the fact that several small-scale RE-driven desalination plants have been installed worldwide and most of them have been successfully operated under very simple maintenance (Goosen et al, 2014). In the case of geothermal energy, one of the most documented case studies is the Kimolos Geothermal Desalination Project. Built in 1999, a Multiple Effect Distillation unit produced 80 m^3/h of potable water, utilizing geothermal steam at a wellhead temperature of 61°C, for the inhabitants of the Kimolos Island (Karytsas et al., 2004).

Although renewable desalination systems cannot presently compete with conventional technologies in terms of water costs (mostly due to the low price of fuels), they remain applicable for remote and arid areas with limit water access and are likely to represent a feasible solution at a large scale in the near future (Ghaffour et al., 2015).

5. THERMODYNAMIC MODELLING AND EXERGY ANALYSIS

To estimate the feasibility of water desalination through the use of geothermal energy, a thermodynamic model and exergy analysis of a SSF-G desalination system were done to study the physical and chemical behaviour of this particular system configuration. The thermodynamic modelling framework helps to describe and validate available data, and to extrapolate with reasonable confidence outside the range of available data. On the other hand, an exergy analysis will help identifying the causes, locations and magnitude of the system inefficiencies associated with chemical reaction, heat transfer, mixing, and friction. It also provides the true measure of how far the system departs from its equilibrium state (Dincer and Rosen, 2007).

The Single Stage Flash configuration was chosen in this study based on its relative simplicity and the daily demand of fresh water from Isabela Island, which is estimated at 276 m^3. Although, the MSF-M is the most efficient in terms of performance, the overall upfront costs of adding more flashing stages, a recirculation brine system and a heat rejection stage, will most likely compromise the project´s economic feasibility when faced with such a low demand of fresh water. MSF is commonly more suitable for large scale distillate production (over 100.000 m^3).

5.1 Description of work

The main objectives of this project are to:

- Develop a thermodynamic model and exergy analysis of a Single Stage Flash (SSF) desalination system;
- Simulate the separation of nearly salt-free fresh water from sea in Isabela Island using geothermal brine as the primary heat input source;
- Simulate the production of electricity for the operation of the desalination cycle, using geothermal steam from the separator unit;
- Determine the performance parameters of the system, i.e. the total mass and salt balances, rate equations for the heat transfer units, as well as energy balances for the brine heater and the condenser.

The Engineering Equation Solver (EES) software was used for developing and analysing the thermodynamic model of energy and exergy flow. The simulation was based on overall heat transfer coefficients, salt balances and, the following design parameters described below.

5.2 Design parameters

Design parameters for the geothermal single stage flash were selected based on information from the geothermal resource in Alcedo. Normal operating conditions for the geothermal and desalination cycle were obtained from literature reviews. Seawater properties (temperature and salinity) were assumed based on the geographical location. The following parameters were used for the thermal design:

Geothermal input

- Reservoir temperature was estimated at 260°C.
- Flashed steam mass flow was estimated at 15 kg/s.
- Separation temperature was estimated at 180°C.
- All pressure and heat transfer losses were neglected.

Sea water properties and distillate water demand

- Seawater temperature was estimated at 20°C.
- Salinity of seawater was estimated at 42.000 ppm.
- Desalination capacity of the system was set to 276 m^3/day.

Desalination plant

- Constant and equal specific heat for all liquid streams.
- Negligible effect of non-condensable gases on the heat transfer process.
- Negligible effects of the boiling point rise and non-equilibrium losses on the stage energy balance; however, their effects are included in the design of the condenser heat transfer area.
- The distillate product was assumed to be salt-free.
- The maximum attainable concentration of the rejected brine, X_b, was 70.000 ppm. This value was imposed by scale formation limits of $CaSO_4$.

5.3 Process description

The layout for the SSF-G process shown in Figure 13. The main elements include the brine heater and the flashing chamber, which contains the condenser/preheater tubes, the demister, the brine pool, and the collecting distillate tray. The main elements of the geothermal desalination system include the separator to obtain steam and brine, a turbine to produce electricity required by the desalination process, and a condenser to maximize the turbine efficiency. The geothermal fluid can be supplied from a single well in the Alcedo geothermal field. The characteristics in the well are roughly estimated based on the existing data.

The geothermal brine coming from a separator unit at a saturation pressure of 10 bar, and a temperature of 180°C enters the brine heater on G3, while the feed seawater enters the other side in point 2. The geothermal feedwater exits the heater and is injected back into the reservoir. The heat transfer that occurs in the brine heater increases the feed seawater temperature to the top brine temperature in point 4. The hot brine enters the flashing stage at a pressure lower than the saturation pressure of the brine. This allows a free flow of the stream across the system, without the aid of pumping power. As the brine circulates through the flashing chamber, heat is transferred by evaporation of a small portion of the brine inside the evaporator. The remaining brine carrying the gained salinity is returned back to the sea in point 7. The formed vapour flows through the demister pad, which prevents product contamination from brine droplets entrained with the flashed off vapour. In point 5, the vapour releases its heat as it condenses on the seawater condenser/preheater tubes. The condensed vapour, which results in high purity distillate water, is collected in the distillate tray, and then exits the system at stage 6. One of the heat recovery features in the SSF process is that it transfers

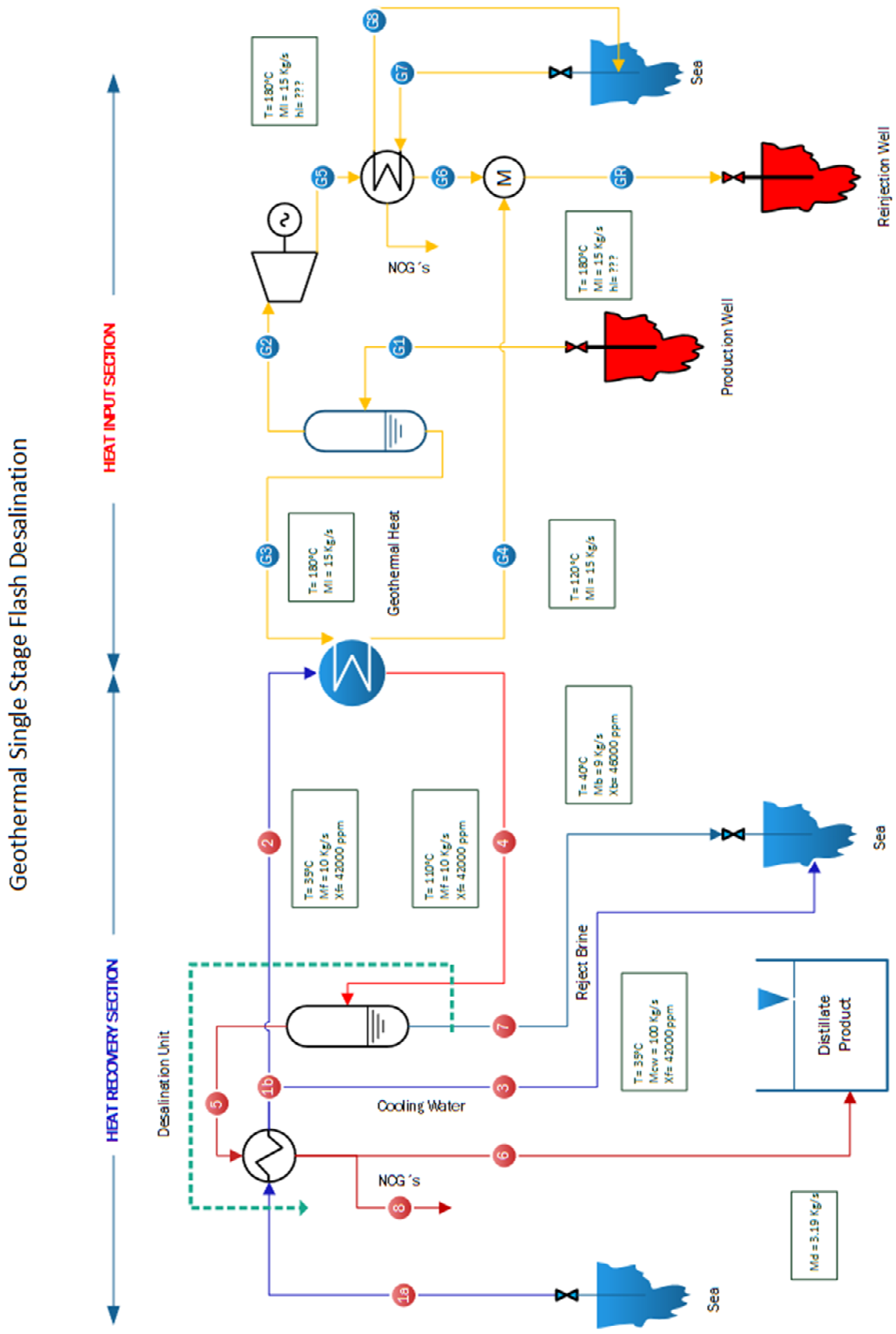

FIGURE 13: Process diagram for the SSF-G system

the heat of condensation to the intake seawater. As a result, seawater is preheated from its natural state to the feed temperature. The cooling seawater removes the excess heat added to the system in the brine heater and is rejected back to the sea after exiting the condenser in point 7.

The feed seawater undergoes a pre-treatment process which includes de-aeration and addition of antiscalant and foaming inhibitors before flashing. The distillate water produced by the SSF plant follow a potabilization process to raise the calcium and bicarbonate contents of the water and adjust the pH to make the product suitable for human consumption. Fresh water from the distillate is stored in tanks or injected directly into the municipal distribution network.

5.4 Thermodynamic modelling

The thermodynamic model for the SSF process is shown in Figure 14, and consists of two main sections: heat input, and heat recovery. In the heat input section, the geothermal liquid phase at T_{G3} enters the brine heater, where it releases its sensible heat to the feed seawater. This energy increases the temperature from T_2 to the top brine temperature T_4. The terminal temperature difference caused by the heat exchange process between the geothermal brine and the effluent sea water brine, is represented by TTD_h. The type of chemical additive that is used to control scale formation dictates the upper limit on T_4. For acid and modern chemical additives, the limit on T_4 is 120°C and for polyphosphate the limit is 90°C (El-Dessouky and Eltouney, 2002). In the heat recovery section, the feed seawater flows into the flashing chamber. This process is represented by the stage temperature drop, ΔT_{st}, where part of the sensible heat is converted into latent heat by the evaporation of the brine pool. The latent heat is released to the intake seawater as the vapour condenses in the seawater condenser/preheater tubes, increasing the temperature from T_{1a} to the feed seawater temperature T_2. The temperature difference of the condensing vapour and the seawater leaving the condenser, is shown as TTD_c.

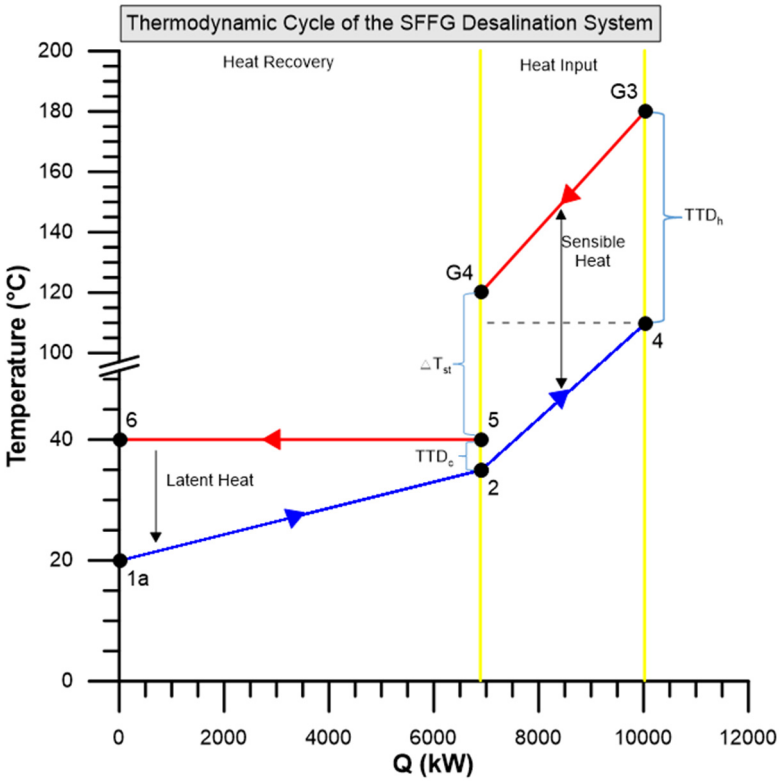

FIGURE 14: Thermodynamic model of the SSF-G system

Recovery of the latent heat by the feed seawater improves the overall efficiency of the desalination process and controls the saturation pressure inside the flashing chamber. Distillation results from the condensation of the feed seawater.

Thermodynamic losses occur during the SSF. These are caused by the boiling point elevation, the non-equilibrium allowance, and the temperature drop corresponding to the pressure drop in the demister pad and during condensation.

5.5 Thermodynamic relations

A simplified thermodynamic model for the Geothermal Single-Stage Flash (SSF-G) process is presented below and will provide a first approach into a more detailed mathematical model to be developed in the future as more accurate data becomes available. The total mass and salt balance equations are given by:

$$\dot{m}_f = (\dot{m}_b + \dot{m}_d) \tag{1}$$

$$X_f \dot{m}_f = X_b \dot{m}_b \tag{2}$$

where $\dot{m}$ is the mass flow rate, X is the salt concentration and the subscripts b, d, and f refer to the brine, distillate, and feed water, respectively.

The brine heater and condenser energy balances are given respectively by:

$$\dot{m}_{G3}(h_{G3} - h_{G4}) = \dot{m}_2(h_4 - h_2) \tag{3}$$

$$\dot{m}_6(h_5 - h_6) = \dot{m}_{1a}(h_{1b} - h_{1a}) \tag{4}$$

where h is the enthalpy of the fluid and the subscripts G3, G4, 1a, 1b, 2, 4, 5 and 6, refer to the stage number.

The heat transfer rate equations for the brine heater is:

$$Q_h = U_h A_h (LMTD)_h \tag{5}$$

where

$$(LMTD)_h = \frac{(T_{G3} - T_4) - (T_{G4} - T_2)}{\ln\big((T_{G3} - T_4/T_{G4} - T_2)\big)} \tag{6}$$

The heat transfer rate equation for the condenser is:

$$Q_c = U_c A_c (LMTD)_c \tag{7}$$

where

$$(LMTD)_c = \frac{(T_5 - T_{1b}) - (T_6 - T_{1a})}{\ln\big((T_5 - T_{1b}/T_6 - T_{1a})\big)} \tag{8}$$

In the above system of equations, A is the heat transfer area, U is the overall heat transfer coefficient, and T is the temperature. The subscripts c and h refer to condenser, and brine heater respectively.

The unit thermal performance ratio, defined as the mass ratio of fresh water produced per unit mass of heating steam, is obtained by:

$$PR = M_6/M_{G3} \tag{9}$$

Single-flash cycle

The flow rate of the steam and brine are defined by mass and heat balance of the separator as follows:

$$\dot{m}_{G1} = \dot{m}_{G2} + \dot{m}_{G3} \tag{10}$$

$$\dot{m}_{G1} h_1 = \dot{m}_{G2} h_2 + \dot{m}_{G3} \tag{11}$$

where $\dot{m}$ and h are the mass flow and enthalpy of the stream. The subscript numbers denote the state position of stream in Figure 13.

The turbine power production is:

$$\dot{W}_{turb} = \dot{m}_{G2}(h_{G2} - h_{G5}) \tag{12}$$

$$\eta_{turb} = \frac{(h_{G2} - h_{G5})}{(h_{G2} - h_{G5s})} \tag{13}$$

where h_{G5} and h_{G5s} are the enthalpy values at the turbine exit states for actual and isentropic processes, respectively. For the condenser, the heat rejected by cooling water is:

$$\dot{Q}_{Cond} = \dot{m}_{G2}(h_{G5} - h_{G6}) \tag{14}$$

The mass flow of cooling water is defined by:

$$\dot{m}_{CW} = \frac{\dot{Q}_{Cond}}{(h_{G8} - hG_7)} \tag{15}$$

where h_7 and h_8 are the enthalpies of cooling water at the inlet and outlet of condenser.

5.6 Exergy analysis

The concept of exergy relates to the maximum work output that could theoretically be obtained from any system relative to given surroundings. It is often referred to the state of the surroundings as the dead state because when fluids are in thermodynamic equilibrium with the surroundings there is no potential for doing work, and the fluid may be considered "dead" (DiPippo, 2004).

Disregarding kinetic and potential energy changes, the specific flow exergy of a geothermal fluid at any stage can be calculated from

$$E = \dot{m}\big(h - h_{dead} - T_{dead}(s - s_{dead})\big) \tag{16}$$

where T_{dead} is the environment (dead state) temperature, h and s are the enthalpy and the entropy of the geothermal fluid at the specified stage, and h_{dead} and s_{dead} are the corresponding properties at the restricted dead state (Kanoglu, 2002).

Exergetic Efficiencies

The definition is used in this report is called rational efficiency and defined by Kotas (1985) as the ratio of the exergy recovered to the exergy supplied to the system or process:

$$\eta_e = \left(E_{desired}/E_{input}\right) \tag{17}$$

$$E_{input} = E_{output} + E_{destroyed} \tag{18}$$

$$E_{output} = E_{desired} + E_{waste} \tag{19}$$

where E_{desired} = Sum of desired exergy outputs (net positive work by the system);
$E_{\text{destroyed}}$ = Exergy rate lost in the system as a result of irreversibility;
E_{waste} = Exergy exiting the system which still has capacity to do work.

When this concept is applied to a power plant as a whole, the overall exergetic efficiency reduces the ratio of the net power output to the exergy of the motive fluid serving as the energy source for the plant (DiPippo and Marcille, 1984). Consequently; the exergetic efficiency for the single flash cycle based on the two phase fluid exergy input to the plant can be calculated as:

$$\eta_{e_overall_SF} = \left(\dot{W}_{net_}SF/E_{G1}\right) \tag{20}$$

where the $\dot{W}_{net_}SF$ is the net power output of single flash cycle and E_{G1} is the exergy rate of two phase geothermal fluid in stage 1.

The exergetic efficiency of the single flash condensing turbine, can be calculated as:

$$\eta_{\varepsilon_SF_Turb} = \left(\dot{W}_{SF_Turb}/E_{G2} - E_{G5}\right) \tag{21}$$

The difference between the numerator and denominator in Eq. (21) gives the exergy destruction in the turbine.

$$I_{SF_Turb} = (E_{G2} - E_{G5}) - \dot{W}_{SF_Turb} \tag{22}$$

The brine heater and condensers in the desalination plant are essentially heat exchangers designed to perform different tasks. The exergetic efficiency of a heat exchanger may be measured by the increase in the exergy of the cold stream divided by the decrease in the exergy of the hot stream (Wark, 1995). Applying this definition to the condenser in single flash cycle, the following equation is obtained:

$$\eta_{\varepsilon_cond_SF} = \frac{E_{G8} - E_{G7}}{E_{G5} - E_{G6}} \tag{23}$$

where the exergy rates are given in Table 1. The difference between the numerator and denominator in Equation 23 gives the exergy destruction in the condenser:

$$I_{cond_SF} = (E_{G5} - E_{G6}) - (E_{G8} - E_{G7}) \tag{24}$$

Nonetheless, the exergy drop of the working fluid across the condenser can be expressed as the exergy destruction in the condenser. That is, the exergy gained by the cooling water is not considered (Kanoglu, 2002).

The exergetic efficiency of the heat exchangers in the desalination cycle is calculated as below:

$$\eta_{\varepsilon_brine_\mathrm{H}} = \frac{E_4 - E_2}{E_{G3} - E_{G4}} \tag{25}$$

$$\eta_{\varepsilon_cond_DS} = \frac{E_{1b} - E_{1a}}{E_5 - E_6} \tag{26}$$

The exergy balance for the desalination and the single flash combined system can be written as:

$$E_{in} = E_{out} + E_{des} + E_{loss} \tag{27}$$

where

$$E_{in} = E_{1a} + E_{G1} + E_{G7} \tag{28}$$

$$E_{out} = \dot{W}_{SF_Turb} \tag{29}$$

$$E_{loss} = E_3 + E_6 + E_7 + E_{G4} + E_{G8} \tag{30}$$

5.7 Results

The results from thermodynamic calculations and exergy analyses of the proposed system were established in the EES software. In Table 1, temperature, pressure, mass flow, enthalpy, entropy and exergy rate data for geothermal fluid, working fluid, and cooling water are given according to their stage numbers specified in Figure 13.

For geothermal fluid, the thermodynamic properties of water were used. The thermodynamic properties of the working fluid, sodium chloride, were obtained from the EES software. The temperature of the sea brine at the exit of the brine heater (stage 4 in the process diagram) was

restricted by the calcium sulphate saturation point and should be in the range 90-110°C to prevent calcium deposition inside the flashing chamber. At the other exit of the brine heater (stage G4 in the process diagram), the temperature was restricted by the silica amorphous saturation point and should be in the range 70-120°C to prevent the silica deposition inside the mixer (El-Dessouky and Eltouney, 2002). The data listed in Table 1 was created by the thermodynamic design model when running it in the EES software.

TABLE 1: Results from thermodynamic calculations and exergy analyses of the proposed system

Stage	**Fluid**	**Phase**	***Salinity***	$\dot{m}$	***T***	***P***	***h***	***s***	***E***
N°			*(ppm)*	*(kg/s)*	*(°C)*	*(bar)*	*(KJ/Kg)*	*(KJ/Kg - K)*	*(kW)*
1a	sea water	liquid	42000	124.4	20	2	84.02	0.296	12.46
1b	sea water	liquid	42000	124.4	35	2	146.8	0.505	209.4
2	sea water	liquid	42000	26.12	35	2	146.8	0.505	43.98
3	sea water	liquid	42000	98.24	35	2	146.8	0.505	165.4
4	sea water	liquid	42000	26.12	110	2	461.4	1.419	1269
5	sea water	vapor	--	3.19	40	0.07	2573	8.255	502.4
6	Distillate	liquid	0	3.19	30	0.07	127.5	0.442	2.191
7	sea water	liquid	47844	22.93	40	0.07	167.5	0.572	61.42
G1	geothermal	two phase	--	25.83	207	18	1200	2.398	12921
G2	geothermal	steam	--	4.26	207	18	2796	6.378	3964
G3	geothermal	liquid	--	21.57	207	18	884.7	2.398	3989
G4	geothermal	liquid	--	21.57	120	18	503.8	1.528	1273
G5	geothermal	steam	--	4.26	46	0.1	2136	6.744	693.1
G6	geothermal	liquid	--	4.26	46	0.1	191.8	0.649	18.98
G7	sea water	liquid	42000	95.1	20	2	83.93	0.296	284.9
G8	sea water	liquid	42000	95.1	41	2	171	0.583	1557
GR	geothermal	liquid	--	25.83	110	18	503.8	1.528	1273

The summary of the exergy analysis for the combined system (geothermal single flash cycle with single stage flash desalination) is presented in Table 2. The results show that the total available exergy in the two phase geothermal fluid produced by the well was 12921 kW. Of this available exergy, 3989 kW existed in the geothermal brine which was available for the desalination cycle; 1269 kW exergy was transferred to the seawater which exited the system through cooling water, reject brine and distillate product; 3964 kW was contained in the steam and connected to the single flash cycle.

TABLE 2: Summary of the exergy analysis for the combined system

Component	**Exergy Input**	**Exergy Output**	**Exergy Destroyed**	**Waste Exergy**	**Exergetic Efficiency**
	(kW)	*(kW)*	*(kW)*	*(kW)*	*(%)*
Geothermal Single Flash Cycle					
Wellhead & separator	12921	3964	4968	3989	31
Turbine	3964	2814	456	694	22
Condenser	693	19	427	247	42
Desalination Single Stage Flash Cycle					
Brine heater	5258	3706	1491	61	45
Preheater/Condenser	705	403	302	0	39
Overall combined cycle	12921	2814	7644	1002	22

As a result of irreversibilities in the system, exergy destruction occurred in all the heat exchangers of the desalination process. The exergy destruction in the combined system was found to be 7644 kW.

The low exergy efficiency in the turbine indicates that most of the exergy was transferred into the desalination cycle through the geothermal brine. The greatest exergy losses occurred in the condenser where part of the exergy was rejected through the cooling water, and the rest was reinjected in the reservoir. The exergy content of the geothermal brine still has potential to perform usable work. The work output developed by the turbine was 2814 kW, at an exergetic efficiency of 22%.

The desired exergy output from combined system in form of electricity was 2814 kW. 1557 kW of the exergy in the form of brine was discarded as waste heat. The large difference in the efficiencies shows that most of the energy received from the well, exits the plant while still containing substantial exergy.

6. TRIPLE BOTTOM LINE ASSESSMENT

The Triple Bottom-Line (TBL) is an accounting framework that incorporates three dimensions of performance: social, environmental and financial (Slaper and Hall, 2011). The purpose of including a TBL in this report is to provide a general estimation of the positive and negative impacts that might arise from the implementation of a RE-driven desalination plant in the Galápagos Islands.

Nine variables were selected based on the parameters that directly affect social, environmental and economic development in the Galápagos. Three levels of impacts were estimated according to their influence on the selected variables. Table 3 shows the variables associated with the three dimensions of performance and their estimated impacts.

TABLE 3: Triple Bottom-Line assessment of a RE-driven desalination project

#	Measures	Cost Unit	Economic		Social		Environmental	
			Positive	Negative	Positive	Negative	Positive	Negative
1	Change in land use (for irrigation)	$/m2	•••	-	••	-	-	•
2	Health-adjusted life expectancy		•	-	•••	-	-	-
3	Resource access and managment	$/m3	••	-	••	-	•••	-
4	Water Quality improvement	$/m3	•••	-	•••	-	••	-
5	Fossil fuel consumption (petrol)	$/gal	•	-	•	-	•	-
6	Electricity consumption	$/kW-h	•	-	•	-	•	-
7	Revenue by sector (contributing to GDP)	$	••	-	•	-	-	-
8	Cost of desalted water	$/m3	-	•	••	-	-	-
9	Renewable energy use	$/kW-h	••	•	••	-	•••	-

Overall, the potential benefits that a RE-driven desalination project could have in the island in terms of economic, social and environmental performance can be expected in the improvement of resource access and management, and in water quality (Table 3). The provision of fresh water through desalination will undoubtedly allow the development of goods and services that are presently conditioned by water restrictions in the island. It will also redirect the use of brackish water from the municipal tap water system so that it can be used for other economic activities such as agriculture. The lack of water for land irrigation has hampered the development of this sector, which has resulted in food imports from the mainland to sustain local demand (Palacios, 2012). This not only increases the risk of invasive species and plagues being introduced in the local ecosystem, but also prevents the sustainable development of local producers, who cannot compete with the food supply from the mainland.

The decrease in brackish water usage from aquifers will enable the natural recharge of the hydrological cycle, making the management of watersheds more sustainable. Also, the reduction of imported bottled water from mainland will reduce the amount of waste generated from plastic bottles.

Fossil fuel consumption by the water tankers that distribute the product, and the electricity consumption, presently needed to operate the water reservoirs in households, would be unnecessary under a more efficient scheme that guarantees a continuous supply of fresh water through improvements in the existing distribution system.

7. CONCLUSIONS AND RECOMMENDATIONS

7.1 Access to fresh water sources

The lack of public potable water services is clearly an ongoing problem in the Galápagos. It poses a risk to the inhabitant's health, and greatly limits the development of economic and agricultural activities linked to the use of the resource. As a result, access to potable water in Galápagos has been taken over by private businesses that operate under weak regulations regarding sanitation protocols, and a lack of permanent inspections (Liu, 2011). The need for a permanent long term solution that provides sufficient potable water, in balance with the fragile ecosystem of the islands, will rely on the innovative use of the natural resources available on site. Moreover, it will allow the local government to regain its responsibility over the provision of public services for its citizens in regards of potable water access, as stated in article 137 of the Ecuadorian Constitution (Asamblea Nacional del Ecuador, 2015).

7.2 Geothermal resources in Isabela Island

An analysis of the available information on Alcedo, Sierra Niegra and Cerro Azul was undertaken via literature reviews. Alcedo presents the most active hydrothermal system with a liquid-dominated reservoir (97% water and 3% non-condensable gases) containing neutral-chloride rich fluids. Geothermometry indicates a meteoric origin and low acidic properties of the fluid. Its proximity to the closest sea shore and its relative low volcanic activity when compared to Sierra Negra and Cerro Azul, can be seen as favourable conditions for further assessment as a potential resource. Therefore, under a preliminary broad context, the characteristics of this high enthalpy resource denote its apparent suitability to be utilized as a main heat input in a desalination process.

Additional variables in terms of location, distance to the closest town, eruptive periods, and environmental factors, will need to be considered for future development and direct use application. Further research is needed to validate the conceptual model and track possible changes in terms of geological and geochemical properties. Suggested studies include a detailed geophysics campaign with AC resistivity methods (TEM, MT, and AMT), a temperature gradient well, and an exploratory drilling campaign to obtain more information on the cap rock, host rock, and hydrothermal alteration.

7.3 Geothermal desalination project costs

A summary of the estimated upfront cost for a geothermal desalination project, including geophysical and exploratory drilling phases is presented in Table 4. The values shown are only indicative of the investment and will vary depending on the availability of the equipment and access to the location.

Desalination based on thermal separation methods is relatively simple, as the process is driven by temperature difference and its thermodynamic states, and no mechanical or moving parts are involved.

Consequently, a great percentage of the operating costs of this technique is not due to the process itself but the energy source. Fossil fuels such as coal or natural gas, are commonly use to heat the seawater for the distillation process. Operating costs can be greatly minimized when renewable energy sources such as geothermal energy is coupled with the desalination process.

The MSF-M is the industry standard and it is more suitable for large scale production ($\geq$ 100.000 m^3/day) in terms of economies of scale, but because the demand for Isabela is under 300 m^3/day and, even considering the total demand of water for the archipelago (4.500 m^3/day), the final cost of the distillate product under this configuration will not be competitive compared to other technologies. Nevertheless, the SSF-G configuration analysed in this report could produce 276 m^3/day of de-salted water from the sea, at a reasonable cost, due to its simpler design.

TABLE 4: Estimated investment costs for the proposed system (adapted from Jónsson, 2015)

Project Investment Cost		
Type	Unit	Total
Exploration cost:		
Surveys (TEM, MT, and AMT)	USD	$650 000
Total	USD	**$650 000**
Confirmation and drilling cost		
Drilling	USD	$6 000 000
Other cost	USD/Project	$20 000
Well test	USD/Well	$140 000
Well test	USD/Field	$100 000
Subtotal	USD	$6 260 000
Administration	USD/Project	$469 500
Compliance reports	USD/Project	$626 000.00
Total	USD	**$7 355 500**
Power Plant and Separators		
Separators	USD/kW	$14 000
Steam turbine	USD/kW	$1 736 000
Condenser	USD/kW	$120 400
Pump/compressor	USD/kW	$14 000
Cooling system	USD/kW	$84 000
Total	USD/kW	**$1 968 400**
Operational and maintenance cost	USD	$199 478.00
Total		**$199 478**
Capital Costs	USD	**$9 973 900**

7.4 Potabilization of distillate water

The distillate product obtained from the SSF-G is of high purity with a very small amount of dissolved salts and minerals. These properties make the water unsuitable for human consumption. Therefore, a potabilization process is required before it can be injected into the pipe distribution network for the inhabitants of Isabela. Typical treatment methods used involve carbon dioxide and hydrated lime injections, and passing carbonated water through limestone bed filters (Khawaji et al., 2008). Interestingly, as a source of carbon dioxide, CO_2 gas can be extracted from non-condensable gases in the geothermal steam and the SSF desalination vent, to be used in either potabilization methods.

7.5 Thermodynamic modelling and exergy analysis

The results from a thermodynamic model and exergy analysis of the system, using Engineering Equation Solver (EES) software, show that the geothermal resource can be successfully coupled to this desalination method. They also reveal that more work can be extracted from the exergy contained in the geothermal brine, meaning that additional low enthalpy uses might increase the project attractiveness. This exergy in the reject brine with a temperature of 40°C can be recirculated in the system, increasing the overall performance ratio of the desalination process.

7.6 Triple Bottom Line assessment

Overall, the TBL assessment denoted that potential savings on its three dimensions of performance can be achieved from the implementation of a renewable energy desalination project. Having a good quality product will reduce the government´s expenditure in treating diseases in public hospitals, which are related to water contamination cases. Consequently, it will generate a positive impact, both in the economic and social aspect.

Although it is the best alternative when compared to traditional desalination processes that use fossil fuels as the energy source, an environmental impact assessment study of the project is needed to assess possible effects that a renewable energy driven desalination system might have on the ecosystem in the Galápagos. Special attention must be placed in controlling the release of brine back into the sea, as well as road construction, CO_2 emissions, noise and disturbances to wildlife and fauna.

ACKNOWLEDGEMENTS

I gratefully acknowledge the support from Páll Valdimarsson, María Gudjónsdóttir, and Málfrídur Ómarsdóttir for their supervision and feedback. I also thank Vijay Chauhan, Lúdvík S. Georgsson and UNU-GTP staff for their support and assistance. This report is dedicated to the memory of Jerko M. Labus.

REFERENCES

Asamblea Nacional del Ecuador, 2015: *Constitución 2008. Dejemos el pasado atrás* (in Spanish). Asamblea Nacional del Ecuador – Ecuadorian Parliament, Quito, Ecuador, 223 pp.

CEPROEC-IAEN and SENPLADES, 2014: *Diagnosis and biophysical analysis for evaluation and formulation of development scenarios in the Galapagos Archipelago* (*Diagnóstico y análisis biofísico para evaluación y formulación de escenarios de desarrollo en el Archipiélago de Galápagos)*. Centro de Prospectiva Estratégica – Instituto de Altos Estudios Nacionales (CEPROEC-IAEN), Quito, Ecuador, 402 pp.

Colony, W.E., and Nordlie, B.E., 1973: Liquid sulfur at Volcano Azufre, Galapagos Islands. *Economic Geology, 68*, 371-380.

Delaney, J.R., Colony, W.E., Gerlach, T.M., and Nordlie, B.E., 1973: Geology of the Volcan Chico area on Sierra Negra volcano, Galapagos Islands. *Geological Society of America Bulletin, 84*, 2455-2470.

Dincer, I., and Rosen, M.A., 2007: *Exergy, energy, environment and sustainable development*. Elsevier, 472 pp.

DiPippo, R., and Marcille, D.F., 1984: Exergy analysis of geothermal power plants. *Geothermal Resources Council Transactions, 8*, 47–52.

DiPippo, R., 2004: Second law assessment of binary plants generating power from low-temperature geothermal fluids. *Geothermics, 33*, 565-586.

El-Dessouky, H.T., and Eltouney, H.M., 2002: *Fundamentals of salt water desalination.* Elsevier Science, Amsterdam, Netherlands, 691 pp.

Geist, D.J., 1992: An assessment of melting processes and the Galapagos hotspot: major and trace element evidence. *Journal of Volcanology and Geothermal Research, 52*, 65-82.

Geist, D.J., Howard, K.A., Jellinek, A.M., and Rayder, S., 1994: The eruptive history of Volcan Alcedo, Galapagos Archipelago: A case study of rhyolitic oceanic volcanism. *Bulletin of Volcanology, 56*, 243-260.

Geist, D.J, Howard, K.A., Larson, P., 1995: The generation of oceanic rhyolites by crystal fractionation: the basalt-rhyolite association at Volcan Alcedo, Galapagos archipelago. *Journal of Petrology, 36*, 965-982.

Geist, D.J., Naumann, T.R., and Larson, P.L., 1998: Evolution of Galápagos magmas: mantle and crustal fractionation without assimilation. *Journal of Petrology, 39*, 953–971.

Goff, F., McMurtry, G.M., Counce, D., Stimac, J., Roldan, A., and Hilton, D., 2000: Contrasting hydrothermal activity at Sierra Negra and Alcedo volcanoes, Galapagos Archipelago, Ecuador. *Bulletin of Volcanology, 62*, 34-52.

Goosen, M.F.A., Mahmoudi, H., and Ghaffour N., 2014: Today's and future challenges in applications of renewable energy technologies for desalination. *Critical Reviews in Environmental Science and Technology. 44*, 929-999.

Guyot-Téphany, J., and Liu, J., 2011: *Hydro resources in the Galápagos Islands (Recursos hídricos en las islas Galápagos).* Charles Darwin Foundation, 32 pp.

Guyot-Téphany, J., Grenier, C., and Orellana, D., 2012: *Scientific Report on survey campaign "Perceptions, use and management of water in the Galapagos"* (*Informe científico de la campaña de encuesta "Percepciones, usos y manejo del agua en Galápagos")*. Charles Darwin Foundation / University of Nantes, 86 pp.

Guyot-Téphany, J., Grenier, C., and Orellana, D., 2013: Uses, perceptions and management of water in Galapagos. In: GNPS, GCREG, CDF, and GC, *Galapagos report 2011-2012*. Galapagos National Park Service, Governing Council of Galapagos, Charles Darwin Foundation, and Galapagos Conservancy, 67-75 pp.

Ghaffour, N., Bundschuh, J., Mahmoudi, H., and Goosen, M.F.A., 2015: Renewable energy-driven desalination technologies: A comprehensive review on challenges and potential applications of integrated systems. *Desalination, 356*, 94-114.

Graham, D.W., Christie, D.M., Harpp, K.S., and Lupton, J.E., 1993: Mantle plume helium in submarine basalts from the Galapagos platform. *Science, 262*, 2023-2026.

Hey, R., 1977: Tectonic evolution of the Cocos–Nazca spreading center. *Geological Society of America Bulletin, 88*, 1401–1406.

IGEPN, 2015: Islas Galápagos. Institute of Geophysics, Polytechnic National School (IGEPN). Website: *http://www.igepn.edu.ec/islas-galapagos*

INEC, 2015: Población y demografía. National Institute of Statistics and Census. Website: *http://www.ecuadorencifras.gob.ec/censo-de-poblacion-y-vivienda/*

Jónsson, M. Th., 2015: *Mechanical design of geothermal power plants - feasibility study cost analysis, economic decision rules, NPV*. UNU-GTP, Iceland, unpublished lecture slides.

Kanoglu, M., 2002: Exergy analysis of a dual-level binary geothermal power plant. *Geothermics, 31*, 709-724.

Karytsas, C., Mendrinos, D., and Radoglou, G., 2004: The current geothermal exploration and development of the geothermal field of Milos Island in Greece. *GHC Quart. Bull., 25-2*, 17-21.

Khawaji, A.D., Kutubkhanah, I.K., and Wie, J., 2008: Advances in seawater desalination technologies. *Desalination, 221*, 47-69.

Kotas, T.J., 1985: *The exergy method of thermal plant analysis*. Butterworhts. London, Great Britain, 293 pp.

McBirney, A.R., and Williams, H., 1969: *Geology and petrology of the Galapagos Islands*. Geological Society of America, Memoir 118, 197 pp.

MEER, 2015: Zero Fossil fuels in Galapagos (Cero combustibles fósiles en Galápagos). Ministry of Electricity and Renewable Energy (MEER). Website: http://www.energia.gob.ec/cero-combustibles-fosiles-en-galapagos-2/

Naumann, T., and Geist, D.J., 2000: Physical volcanology and structural development of Cerro Azul volcano, Isabela Island, Galápagos: Implications for the development of Galapagos-type shield volcanoes. *Bulletin of Volcanology, 61*, 497-514.

Naumann, T., Geist, D.J., and Kurz, M., 2002: Petrology and geochemistry of Volcan Cerro Azul: Petrologic diversity among the western Galapagos volcanoes. *Journal of Petrology, 43*, 859-883.

Neall, V.E., and Trewick, S.A, 2008: The age and origin of the Pacific islands: A geological overview. *Philosophical Transactions of the Royal Society of London B: Biological Sciences, 363*, 3293–3308.

Liu, J., 2011: *Investigation of the microbiological quality of water and water-related diseases in the island Santa Cruz*. (*Investigación de la calidad microbiológica del agua y de las enfermedades relacionadas al agua en la isla Santa Cruz)*. Charles Darwin Foundation, unpublished report, 67 pp.

Living Galápagos, 2015: Dirty water 2013. Website: http://livinggalapagos.org/en/dirty-water/

López, J., Rueda, D., and Nakaya, S., 2007: Water quality monitoring on Isabela Island - annual report. (Monitoreo de calidad del agua en la isla Isabela - Informe annual). Dirección Nacional Parque Galápagos (DNPG) and Japan International Cooperation Agency (JICA), Puerto Ayora, Galapagos, Ecuador, 29 pp.

Olsson, G., 2015: *Water and energy: Threats and opportunities* (2nd ed.). IWA Publishing, London, United Kingdom, 496 pp.

Palacios, P., 2012: *Conceptual analysis of local food chains in the market. Local chains Galapagos Project, Product V. (Análisis conceptual de los encadenamientos locales en el mercado alimenticio. Proyecto Encadenamientos Locales Galápagos, Producto V).* Charles Darwin Foundation, 1-7.

Simkin, T., 1984: Geology of Galapagos. *Biological Journal of the Linnean Society, 21*, 61-75.

Schilling, J.G., Anderson, R.N., and Vogt, P., 1976: Rare earth Fe and Ti variations along the Galápagos spreading centre, and their relationship to the Galápagos mantle plume. *Nature, 261*, 108–113.

Slaper, T.F., and Hall, T.J., 2011: The triple bottom line: What is it and how does it work? *Indiana Business Review, 86*, 4-8.

Verma, S.P., Schilling, J.G., and Waggoner, D.G., 1983. Neodymium isotopic evidence for Galápagos hotspot-spreading center system evolution. *Nature, 306*, 654–657.

Walsh, J., McCleary A., Heumann, B., 2010: Community expansion and infrastructure development: implications for human health and environmental quality in the Galapagos Islands of Ecuador. *Journal of Latin American Geography, 9*, 137-159.

Wark, K.J., 1995: *Advanced Thermodynamics for Engineers*. McGraw-Hill, New York, United States, 326 pp.

White, W.M., McBirney, A.R., and Duncan, R.A., 1993: Petrology and geochemistry of the Galapagos Islands: portrait of a pathological mantle plume. *Journal of Geophysical Research, 98*, 533-563.

WHO, 2003: *Sodium in drinking-water. Background document for development of WHO guidelines for drinking-water quality*. World Health Organization (WHO), Geneva, Switzerland, document WHO/SDE/WSH/03.04/15, 11 pp.

UNITED NATIONS UNIVERSITY
UNU-GTP
Geothermal Training Programme
Orkustofnun, Grensasvegur 9,
IS-108 Reykjavik, Iceland

Reports 2015
Number 20

INTERPRETATION OF GEOCHEMICAL DATA FROM LOW-TEMPERATURE GEOTHERMAL AREA FLJÓTIN, N-ICELAND, COMPARED TO SELECTED GEOTHERMAL SAMPLES FROM RUNGWE TANZANIA

Nyaso Makwaya
Ministry of Energy and Minerals
754/33 Samora Avenue
P. O. Box 2000
Dar es Salaam,
TANZANIA
nyasomakwaya@yahoo.com

ABSTRACT

The chemical analysis of geothermal water requires proper sample collection, analysis, and presentation of the data. The interpretation and evaluation of all available information regarding the geochemistry are accomplished by the methods of Na-K-Mg ternary diagram, Cl-SO_4-HCO_3 ternary diagram, geothermometers, WATCH programme and Suffer 12.6.963 software. Data samples from Fljótin-Iceland are analysed pertaining to their geochemistry surface exploration and compared to selected data from Rungwe geothermal area from Tanzania. The geothermal fields differ according to volcanic activities, rock types and mineral composition. Fljótin are low-temperature geothermal field while Rungwe is classified as high-temperature geothermal field at Ngozi-Songwe (northern system) and a low-temperature field at Kiejo-Mbaka (southern system). The reservoir temperatures at Fljótin are estimated by Na-K-Mg ternary diagram in the range of 120°C -160°C and confirmed with geothermometers with temperature range; 74-136°C (chalcedony) and 64-158°C (Na/K). The mineral saturation stated were calculated by chalcedony temperature where calcite and anhydrite are saturated but not precipitating while amorphous silica is under saturated. The estimated reservoir temperature at the Rungwe volcanic zone are 130-200°C by Na-K-Mg ternary diagram, which is in agreement with quartz and K/Mg geothermometers at a temperature range of 119-154°C and 106-252°C respectively. Detailed study of the Rungwe thermal fluid chemistry is required in order to be satisfied for direct or indirect use, due to its high concentration of CO_2 which can affect the utilization of the fluid, both fields have a potential for geothermal utilization. Fljótin on the other hand can be used directly due to its low total dissolved elements and low-temperature.

1. INTRODUCTION

Global pollution has increased awareness of the detrimental environmental effects that results from burning of fossil fuel for power generation and an increasing global interest is sparked towards using

green renewable energy source such as geothermal energy. Currently, Tanzania has put more efforts towards affordable and sustainable energy by increasing the number of experts for developing the geothermal resource.

Geochemistry studies play an important role in developing geothermal field from the exploration stage, for the purpose of management and monitoring of the field. Normally geochemical exploration provides information of subsurface composition, temperature, contribution to conceptual model which contain origin of geothermal fluid and flow direction, reservoir location and boiling (Arnórsson, 2000). Furthermore, it will provide information required during production phase such as scaling deposition and corrosion which can have negative effect on operation phase as well as on the environment.

Generally, geochemistry deals with geothermal fluid composition (that is aqueous solution and gaseous steam) that reflect the thermal condition at depth which are controlled by equilibrium with minerals in the aquifer rock. Data sampling, analysis and interpretation play paramount importance in geochemistry studies of geothermal fluids.

The major types of geothermal fluid are steam, gas, geothermal waters, mixed waters and steam heated surface waters. However, the types of geothermal fluid can provide different information in the geothermal field, depending on the sampling location. Steam can be useful in calculating the temperature geothermometry and state the origin of the fluid. Gas can provide information about the characteristics of the underlying geothermal system such as reservoir temperature and the direction of subsurface water flow. The geothermal water commonly provides useful information of geothermometry, origin of fluids and production properties. Mixing models are used when the sampled fluids are a mixture of different types and can be used for designing a conceptual model of the system and steam heated surface waters. According to literature, steam heated waters have never been in the deep geothermal system but provide geothermal manifestation and physical condition of geothermal system (Arnórsson, 2000).

My study will focus on data analysis and interpretation of the low-temperature geothermal field in Iceland called the Fljótin and compare it with samples from the geothermal area in the Rungwe volcanic zone, Tanzania.

2. THE ROLE OF FLUID CHEMISTRY IN EXPLORATION

Surface exploration is at its initial stage for locating and outlining geothermal fields, and a successful study will provide enough information for site development. Its achievement depends on collaboration of a team of geoscientists dealing with geological mapping, geochemical and geophysical surveys.

The main purpose of fluid chemistry in surface exploration is to predict the reservoir temperature and give preliminary assessment on the production properties, among other things chemical equilibrium, speciation, and effect of boiling, scaling and corrosion. With fluid chemistry it is also possible to map the up-flow and flow directions, define the surface area of the reservoir, and obtain information on the origin of the fluid (Figure 1). This chapter tells about the role of the fluid chemistry in surface exploration and the tools one can use to obtain this goal.

2.1 Data sampling and quality

The collection of water samples plays an important role in developing the conceptual model for geothermal system as well as for monitoring and environmental control. Therefore, data sampling requires well trained personnel with insight into possible errors and interferences (Arnórsson, 2000). This will be further discussed in Section 5.

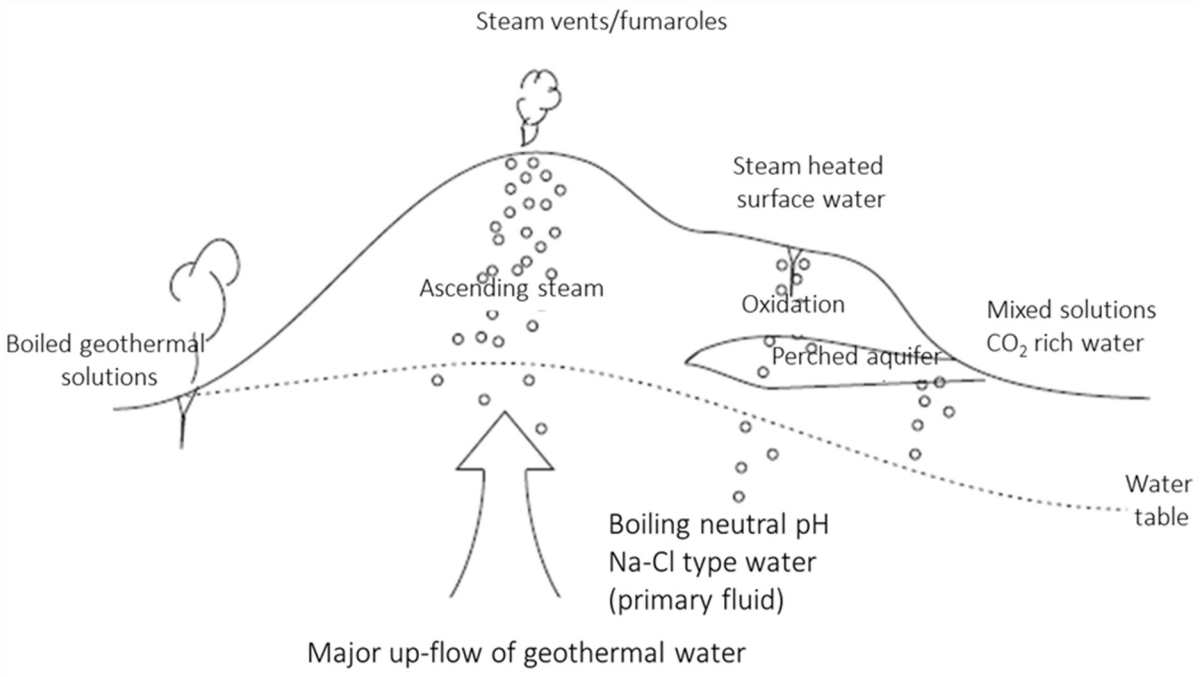

FIGURE 1: Types of geothermal fluids (modified from Arnórsson et al., 2007).

2.2 Water classification

The composition of water in geothermal field have their own characteristics depending on the rock composition, the residence time of the water within the rocks, the rate of leaching of components from the rocks, the fluid flow into the system, the rate of formation of secondary minerals, pressure and temperature. Cooling due to boiling, conduction and dilution as well as degassing, cause the chemistry of surface discharges to deviate from the composition of the thermal water in the reservoir (Arnórsson, 2000).

Ellis and Mahon (1977) has divided water into two categories: subsurface water and geothermal water respectively. Subsurface water is described as meteoric water, ocean water, carbonate water formed in young marine sediments, magmatic water and juvenile water. Geothermal water is described as water formed by reaction between the fluid and the host rock which may contain alkali-chloride water with pH 4-11, acid sulphate water and bicarbonate water.

In geothermal exploration the waters are classified regarding their composition and equilibration with geothermometry (Giggenbach, 1988). Also very useful classification is obtained by plots on ternary diagrams and other methods described below.

2.3 The Na-K-Mg ternary diagram

The nature of geothermal industry contributes many challenges on classifying fluid composition through different methods. Giggenbach (1986) developed the Na-K-Mg ternary diagram which has two areas: full-equilibrium line and "partial equilibrium, dilution or mixing" that contain Na-K-isotherms (T_{Na-K}) which may reflect deeper fluid, effective Na-K-equilibration conditions (Figure 2). The diagram is based on the temperature dependence of the three reactions shown in Equations 1, 2, and 3. Equation 4 shows the calculated sum of a large number of samples simultaneously plotted on the diagram. The area near the Mg-corner) will not apply to reflect fluid-rock equilibrium and only (T_{K-Mg}) can be used as a measure for fluid-rock equilibration temperatures by Equation 5. The Na-K-Mg ternary diagram (Giggenbach,

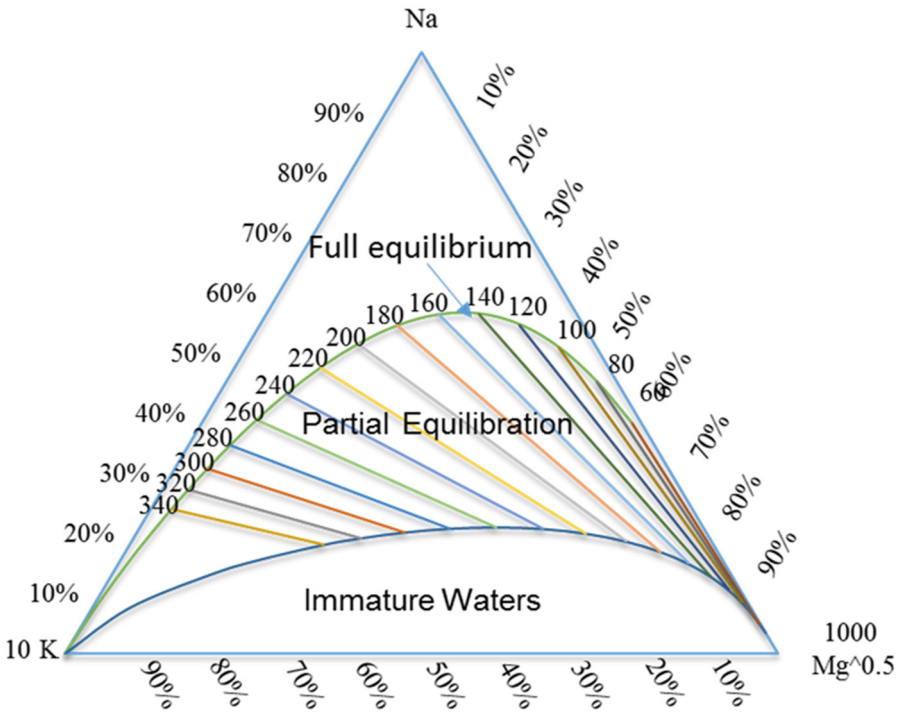

FIGURE 2: Na-K-Mg ternary diagram (Giggenbach, 1986)

1986; 1988) shown in Figure 2 can be used to classify water into equilibrium, partial equilibrium and immature waters (dissolution of rock with little or no chemical equilibrium). The full equilibrium curve is for reservoir water composition corrected for loss of steam owing to decompression boiling. Uncorrected boiled waters will generally plot slightly above the full equilibrium line. The diagram can be used to better clarify the origin of the waters and then determine whether the fluids has equilibrated with hydrothermal minerals and to predict the equilibrium temperatures by $T_{Na\text{-}K}$ and $T_{K\text{-}Mg}$:

$$K - feldspar + Na^{+} = Na - feldspar + K^{+} \quad (1)$$

$$2\,albite + 0.8K - feldspar + 1.6H2O + Mg^{2+} = 0.8mica + 0.2chlorite + 5.4silica + 2Na^{+} \quad (2)$$

$$2.8K - feldspar + 1.6H2O + Mg^{2+} = 0.8mica + 0.2chlorite - 5.4silica + 2K^{2+} \quad (3)$$

A large number of samples can be plotted simultaneously on this diagram, and mixing trends and grouping predicted. The sum is calculated as:

$$S = C_{Na/1000} + C_{K/100} + \sqrt{C_{Mg}} \quad (4)$$

Then the %Na, %K and %Mg, can be calculated as

$$\%Na = \frac{C_{Na}}{10S};\ \ \%K = \frac{C_K}{S}\ \ and\ \ \%Mg = \frac{100\sqrt{C_{Mg}}}{S}$$

where C is in mg/L.

The K-Mg geothermometer equation where calculated by Giggenbach (1991):

$$T_{K-Mg}(°C) = 4410/(14.0 - \log(K^2/Mg) - 273.15 \quad (5)$$

where *K* and *Mg* refer to the concertation's of the respective cations.

Analysis of Na, K and Mg, by using the ternary diagram will give clear distinction between waters suitable or unsuitable for the application of ionic solute geothermometers.

2.4 The Cl-SO_4 -HCO_3 ternary diagram

Giggenbach (1991) proposed a Cl-SO_4 -HCO_3 ternary diagram (Figure 3) for the initial classification of geothermal solutions to identify whether the geothermometers are applicable for the given water sample, as most solute geothermometers work only for neutral water or matured water that is characterized by high Cl and low SO_4 (Sekento, 2012). This diagram is helpful in providing an initial indication of mixing relationships or geographical groupings.

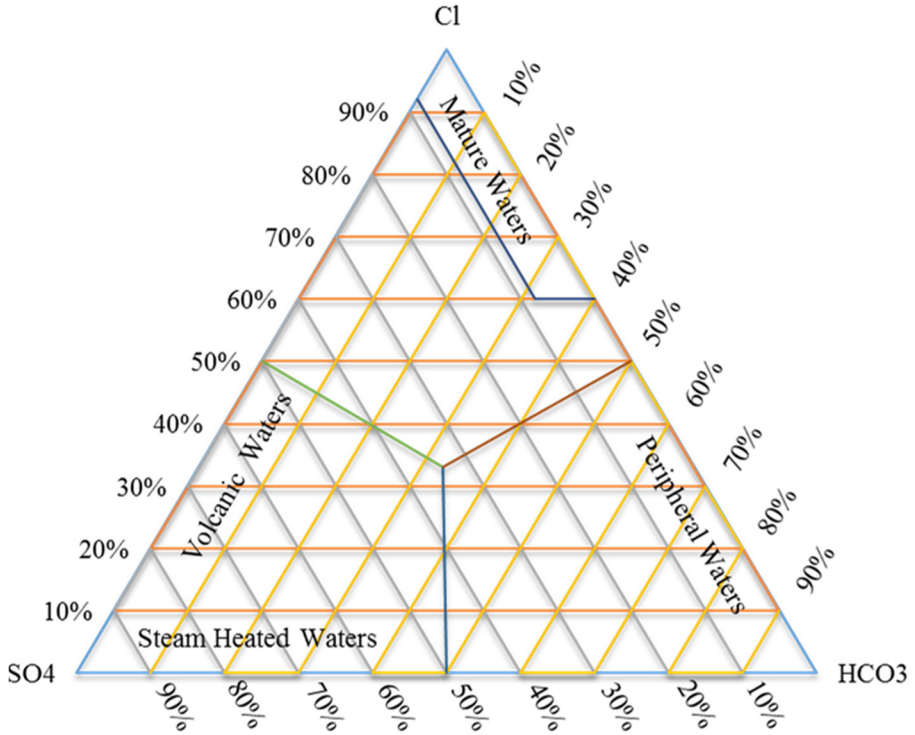

FIGURE 3: Cl-SO4-HCO3 ternary diagram

The position of a data point in such a triangular diagram is obtained by first obtaining the sum S of the concentration of all three constituents involved. In the present case:

$$S = C_{Cl} + C_{SO_4} + C_{CHO_3} \quad (6)$$

The next step consists of the evaluation of %Cl, %SO_4 and %HCO_3 according to the following:

$$\%Cl = 100C_{Cl;}\ \ \%SO_4 = 100C_{SO_4/S;}\ \ \%HCO_3\ = 100C_{HCO_3/S}$$

The degree of separation between data points for high chloride and bicarbonate water gives an idea of the relative degree of interaction of CO_2 charged fluids at lower temperatures and the HCO_3 contents increasing with time and distance travelled. The geothermometer can only be used with close neutral water which contain Cl as major anion.

2.5 Geothermometers

According to Arnórsson (2000), geothermometers have been classified in three groups; water or solute

geothermometer, steam or gas geothermometer and isotope geothermometer where water and steam are termed collectively as a chemical geothermometer. In addition to that, Sekento (2012) reported that equilibrium between minerals, geothermal solutions and vapour phase can affect the chemical composition of geothermal fluids, providing the basis for chemical geothermometer. Chemical geothermometer are normally applied to thermal springs, steam vents and geothermal wells. The effect of boiling and cooling geothermometry is used to elucidate the chemical reaction occurring in the zone of depressurization around wells that result from recharging cold water (Arnórsson, 2000). The most widely used geothermometer are based on silica concentration (quartz and chalcedony), cation ratios (Na/K, K/Mg and Na-K-Ca) based on equilibration on Na-K-Mg. Below I describe and discuss the geothermometers used in this paper/work.

2.6 Silica geothermometers

The silica solubility increases with temperature rise, which tend to control the silica in the geothermal fluid. The common geothermometer temperature predicted by silica are referred as quartz, amorphous silica and chalcedony temperatures. The amorphous silica method is recommended for 25-250°C range, chalcedony for water in the subsurface temperature range of 120°C-250°C, while quartz is recommended above 200°C (Arnórsson, 2000). The basic reaction for the dissolution of silica minerals is:

$$SiO_{2(s)} + 2H_2O = H_4SiO_{4(aq)} \quad (7)$$

At pH levels below 9, nearly all dissolved silica is present in solution as dissociated silicic acid, H_4SiO_2. At higher pH levels, the silicic acid dissociates to form H_3SiO_4, thus effectively increasing the solubility of silica in water in equilibrium with quartz. Therefore, very high pH levels can lead to over-estimation of the reservoir temperature if the aqueous speciation of silica is not considered. However, several geothermometers have been developed as more experimental data has become available (Gunnarsson and Arnórsson, 2000). Verma and Santoyo (1997) have recently developed a new silica geothermometer based on statistical treatment of earlier experimental data. Their new geothermometer is proposed through detecting an outlier and rejecting one sample from the data set of Fournier and Potter, 1982. The quartz geothermometer was tested experimentally over the temperature range from 100°C to 500°C and pressure of 1000 bars, performed well up to 400°C without any effect of fluid composition (Pope et al., 1987). However, Verma (2000) criticized the use of the quartz geothermometer, especially its discrepancy at high temperatures arising from the incoherence between the theoretical and experimental solubility data. The silica geothermometers equations used to calculate the temperature of a reservoir are as follows:

Quartz, 25-900°C (Fournier and Potter, 1982):

$$T(^oC) = -42.2 + 0.28831S - 3.6686x10^{-4}S^2 + 3.1665x10^{-7}S^3 + 77.034logS \quad (8)$$

Chalcedony, 0-250°C (Fournier, 1977):

$$T(^oC) = \frac{1032}{4.69 - logS} - 273.15 \quad (9)$$

Chalcedony (Arnórsson et al., 1983):

$$T(^oC) = \frac{1112}{4.91 - logS} - 273.15 \quad (10)$$

Amorphous silica (Fournier, 1977) for 25-250°C:

$$T(^oC) = \frac{731}{4.52 - logS} - 273.15 \quad (11)$$

where S refers to the concentration of SiO_2 in mg/kg and T is the Temperature.

2.7 Cation geothermometer

Cation geothermometer is commonly used to estimate reservoir temperatures. For the cation geothermometers, the Na-K geothermometer is most widely used, rather than K/Mg and Li-Mg (Kharaka and Mariner, 1989). The geothermometers equations used to calculate the temperature of a reservoir are as follows:

Arnórsson et al. (1983) for 25-250°C:

$$T(^{O}C) = \frac{933}{0.993 + log\frac{Na}{K}} - 273.15 \quad (12)$$

Giggenbach et al. (1988):

$$T(^{O}C) = \frac{1390}{1.75 + log\frac{Na}{K}} - 273.15 \quad (13)$$

Giggenbach et al. (1988):

$$T(^{O}C) = \frac{4410}{14.0\ - \mathrm{og}(\frac{K^2}{Mg})} - 273.15 \quad (14)$$

2.8 Mineral saturation

Mineral saturation is applied in geochemistry to obtain an understanding of various physical features of a geothermal system through specific minerals which are in chemical equilibrium. The saturation index of several minerals is computed as a function of temperature and if the saturation indices of the minerals converge to zero (saturation) at a specific temperature that the temperature is taken to present the reservoir temperature. Using the result of the aqueous speciation calculations, the saturation indices (SI) of minerals in aqueous solutions at different temperatures were computed as in Equation 15:

$$SI = loqQ - logK = log\ Q/K \quad (15)$$

where Q is the calculated ion activity product and K is the equilibrium constant.

The SI value for each mineral is a measure of the saturation state of the water phase with respect to the mineral's phase. Values of SI greater than, equal to, and less than zero represent super saturation, equilibrium and under saturation respectively, for mineral phase with respect to aqueous solution. Equilibrium constants for mineral's dissolution often varies strongly with temperature, that temperature taken to be the reservoir temperature. The WATCH computer program version 2.1A (Arnórsson et al., 1982) is commonly used for calculation of mineral saturation index.

3. ICELAND – GEOLOGICAL BACKGROUND

3.1 Regional geology

Iceland is young volcanic island with the oldest rocks about 16 million year old according to radiometric dating. The volcanic activity in Iceland is high with the eruption frequency of over 20 events per century with a magma output of over 5 km^3 (Hjartarson and Saemundsson, 2014). The lava flows cover more than 2000 km^2. The volcanic activities have been contributed to the complex interaction between the N-Atlantic Ridge system and the Iceland Mantle Plume in the mid oceanic ridge which has generated a complex tectonic situation (Hjartarson and Saemundsson, 2014). The location of Iceland at the

asthenospheric flow under the NE-Atlantic plate boundary interacts and mixes with a deep-seated mantle plume that contributes to volcano activities (Schlitzer et al., 1985) with series division of postglacial (last 9000 to 13000 years), upper Pleistocene (back to 0.7 million years), Plio–Pleistocene (0.7-3.1 million years) and Tertiary rocks older than 3.1 million years (Hjartarson and Saemundsson, 2014).

The buoyancy of the Icelandic plume leads to a dynamic uplift of the Iceland plateau and high volcanoes over the plume produce a relatively thick crust. The Greenland – Faeroe ridge represents the Icelandic plume track through the history of the NE-Atlantic. The two main volcanic belts are connected in central Iceland by the Hofsjökull volcanic system (Hjartarson and Saemundsson, 2014) (Figure 4). The northern end of the eastern main volcanic belt is connected to the crested zone of the Mid Atlantic Ridge by active transverse faults. In southern Iceland this volcanic belt is propagating south; at the same time dilation is dying out in the northern half of the western main volcanic belts. The main volcanic belts in Iceland are displaced relative to the crest zone of the mid Atlantic Ridge because the lithosphere tends to break up above the mantle plume and the plume has been moving east relative to the plate boundary (Saemundsson, 1979).

North and northwest Iceland are composed of tertiary basalt formation, except for the outlying and extinct Skagi volcanic belt which was formed during the Plio – Pleistocene time. The age of the Tertiary basalt formation ranges from about 12 million years in the deepest part of the stratigraphically column at the northern tip of Tröllaskagi to about 7 million years in the region from Blönduós across the central highlands to the bottom of Eyjafjardardalur (Hjartarson and Saemundsson, 2014). The volcanic activities are the major factor in identifying the geothermal system.

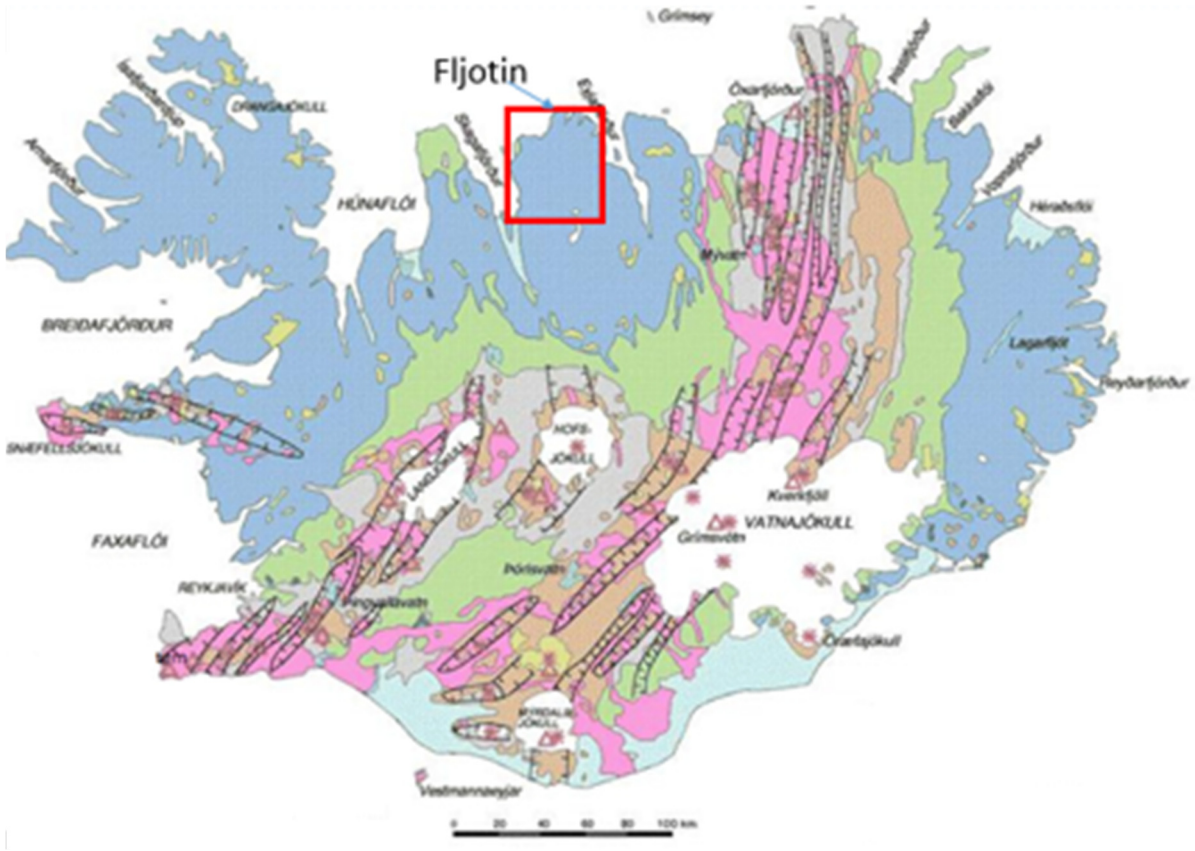

FIGURE 4: A simplified geological map of Iceland showing the volcanic zones, fissures swarms and central volcanoes (Jóhannesson and Saemundsson, 1999). The box represents the study area of Fljótin

3.2 Geothermal systems in Iceland

Several classification schemes have been proposed for geothermal systems. The most used terms are; high-temperature and low-temperature geothermal systems, hot water (liquid dominated) and vapour dominated system and volcanic and non-volcanic systems as described below. High temperature systems are generally volcanic and low-temperature systems non-volcanic.

The first classification is based on the physical state of reservoir fluid, where the geothermal system is classified as liquid-dominated reservoirs when the temperature is at or below boiling point, while water phase controls pressure (hydro-static). Two-phase reservoirs where the fluid temperature and pressure follow the boiling point curve. The second one is based on vapour-dominated reservoirs where the temperature will be at or above boiling point, while steam phase controls pressure (vapour-static) (Nicholson, 1993).

The third classification is based on geological conditions of the system. They can be volcanic systems, which are associated with volcanic activity (hot intrusions/magma), secondly it can be convective fracture controlled systems where hot crust occurs at depth in tectonically active areas, thirdly it can be sedimentary systems where permeable layers occur at great depth or have above average heat flow. Fourthly, geo-pressured systems with stratigraphic sedimentary "traps" and lastly enhanced (EGS) systems where reservoir permeability is enhanced or created, previously "hot dry rock" (HDR) systems. In addition to that, there are shallow resources that are utilized through ground-source heat-pumps (Nicholson, 1993).

Based on geological settings and temperature from geothermal fields, the geothermal areas in Iceland are classified as high- or low-temperature geothermal fields. The high–temperature are located within volcanic belts in the central part of the country whereas most of the low -temperature occur in the quaternary and tertiary formation (Arnórsson, 1995).

3.2.1 Fljótin, N-Iceland

Fljótin (Figure 5) is a district located in north Iceland on the northern part of Tröllaskagi, a mountainous peninsula between two ocean fjords called Skagafjördur to the west and Eyjafjördur to the east. The whole part of Fljótin is covered by basaltic lavas and minor intermediate extrusive rocks and sedimentay horizons (Hjartarson and Saemundsson, 2014). The bedrock in the Fljótin district is tertiary in age, tholeiitic basalts in composition. The lava pile has a westerly dip and the mountainous strata is near totally composed of lavas with only minor sedimentary horizons. Dykes

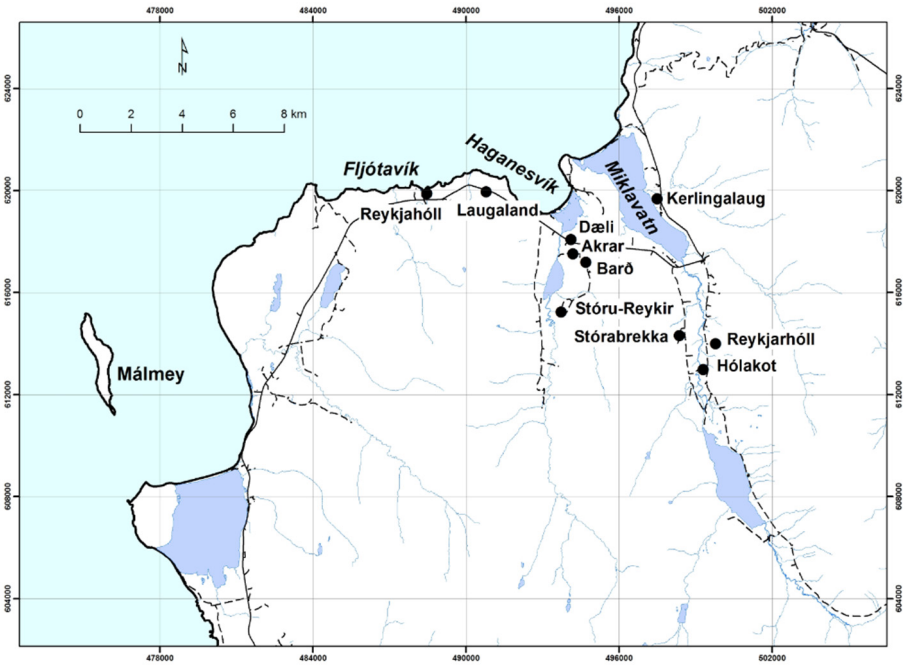

FIGURE 5: Location of the thermal springs in Fljótin used in this project (Map drawn by Jónsdóttir, 2015)

generally trend near N10°E and are rare in Fljótin district but more numerous to the northeast. Large N-S faults are observed north of Miklavatn, and such faults are likely to be present in the western part of Fljótin. The pores in the lavas are mostly filled by deposition reducing the permeability and it is likely that permeability of geothermal systems are largely related to fractures, faults and dykes. The area is low-temperature liquid dominated with widespread distribution of warm springs (25-50°C) and hot springs (50-75°C) of which few are shown in Figure 5 and in Table 1. Fljótin are flat lowlands and covered by green vegetation (Jóhannesson, 1991).

The young rock is the main heat source for the Fljótin low-temperature field. Rainwater from the surrounding high mountainous area, reaching above 1000 m above sea level, seeps through the north-south trending faults down to hot rocks at a temperature around 150°C. Normally rainwater has lower density than cold water, then after being heated by the hot rock it flows up to reach the surface at temperature around 60-70°C (Sæmundsson, pers. comm. 2015). Thermal springs are widespread in the area which is shown in Figure 5 and fluid composition in Table 1.

TABLE 1: Fluid composition from Fljótin (samples collected in October 1985)

Name	Sample No	Temp. surface (°C)	pH/°C	CO_2	H_2S	SiO_2	Na	K	Mg	Ca	Cl	SO_4	F	dO_{18}	Conductivity/ 25°C	Charge balance
Bardslaug (1)	19850276	66.5	9.76/22.0	18.9	0.49	135.7	77.3	1.96	<0.001	1.77	29.23	53.63	0.62	-12.22	385	-0.24
Bardslaug (1*)	19730114	-	9.78/20.0	24.2	<0.10	146.0	75.3	1.9	0.060	1.63	24.80	52.7	0.70	-	-	-4.31
Daelir_(2)	19850277	46.4	9.72/22.0	20.6	0.16	142.2	80.5	2.69	0.005	2.3	29.65	56.5	0.61	-12.43	402	2.49
Akrar_(3)	19850278	61.0	9.7/22.2	20	0.23	147.1	78.7	2.71	0.004	1.77	29.68	56.32	0.63	-12.31	395	-0.08
Reykir (4)	19850279	48.8	10.2/22.5	13.4	0.10	90.4	65.2	0.87	0.001	2.09	22.50	40.15	0.53	-12.31	338	-5.31
Laugaland_(5)	19850280	64.7	9.85/22.3	18.9	<0.10	95.9	61.0	1.08	0.015	0.28	21.48	34.83	0.62	-12.33	304	-0.97
Reykjarhóll á Bökkum - well (6)	19850281	57.5	9.64/22.4	23.6	0.95	147.8	76.2	2.42	<0.001	2.41	29.89	50.79	0.73	-12.11	381	-0.43
Kerlingalaug_(7)	19850282	55.5	9.98/23.0	18.8	0.53	94.2	62.6	0.98	<0.001	1.86	22.45	35.3	0.59	-11.97	321	-3.98
Kerlingalaug (7*)	19690130	49.0	9.45/22.0	18.5	0.58	97.0	76.5	2.37	0.040	1.78	24.20	34.7	0.60	-	-	51.48
Hólakot_(8)	19850283	23.8	10.16/22.5	14.6	0.15	101.5	50.1	0.86	0.063	2.05	8.55	19.69	0.50	-12.21	252	-3.96
Reykjarhóll east (9)	19850284	52.8	10.19/22.7	14.1	0.17	102.8	51.3	0.8	<0.001	1.78	8.78	19.76	0.51	-12.19	255	-5.61
Reykjarhóll east (9*)	19690128	58.0	9.74/22.0	13.5	0.16	107.0	50.0	0.87	0.030	1.66	9.10	20.1	0.60	-	-	50.86
Stóra-Brekka (10)	19850285	88.5	10.21/22.5	8.2	0.13	52.0	74.7	0.32	<0.001	4.53	36.28	72.01	0.42	-12.67	406	-2.62
Stóra-Brekka (10*)	19690131	55.0	9.71/22.0	13	<0.10	87.0	65.5	1.1	0.08	1.94	23.4	38.5	0.40	-	-	36.92

Samples (1, 7, 9, and 10) have Mg value below detection limits therefore author uses 0.001 mg/L in these samples in diagrams
Number in brackets represent the numbers in ternary diagrams. All sample are hot springs except for sample number 6 which is from a well
- Not analysed

4. TANZANIA GEOLOGICAL BACKGROUND

Tanzania is part of East African countries along the Indian Ocean. "The youngest sediments and volcanic are related to the active Cenozoic East African Rift System (EARS). The location of the Cenozoic EARS is strongly controlled by Proterozoic tectonics and Karoo rift geometry with both Eastern and Western branch following the margins of the Archean Tanzania craton" (Ebinger et al., 1989), e.g. Figure 6. The two branches form a junction in southern Tanzania which has been the location of intensive eruption in Holocene time, producing basalt, phonolite and phonolitic trachyte lavas which have erupted from numerous centres and had significant trachytic

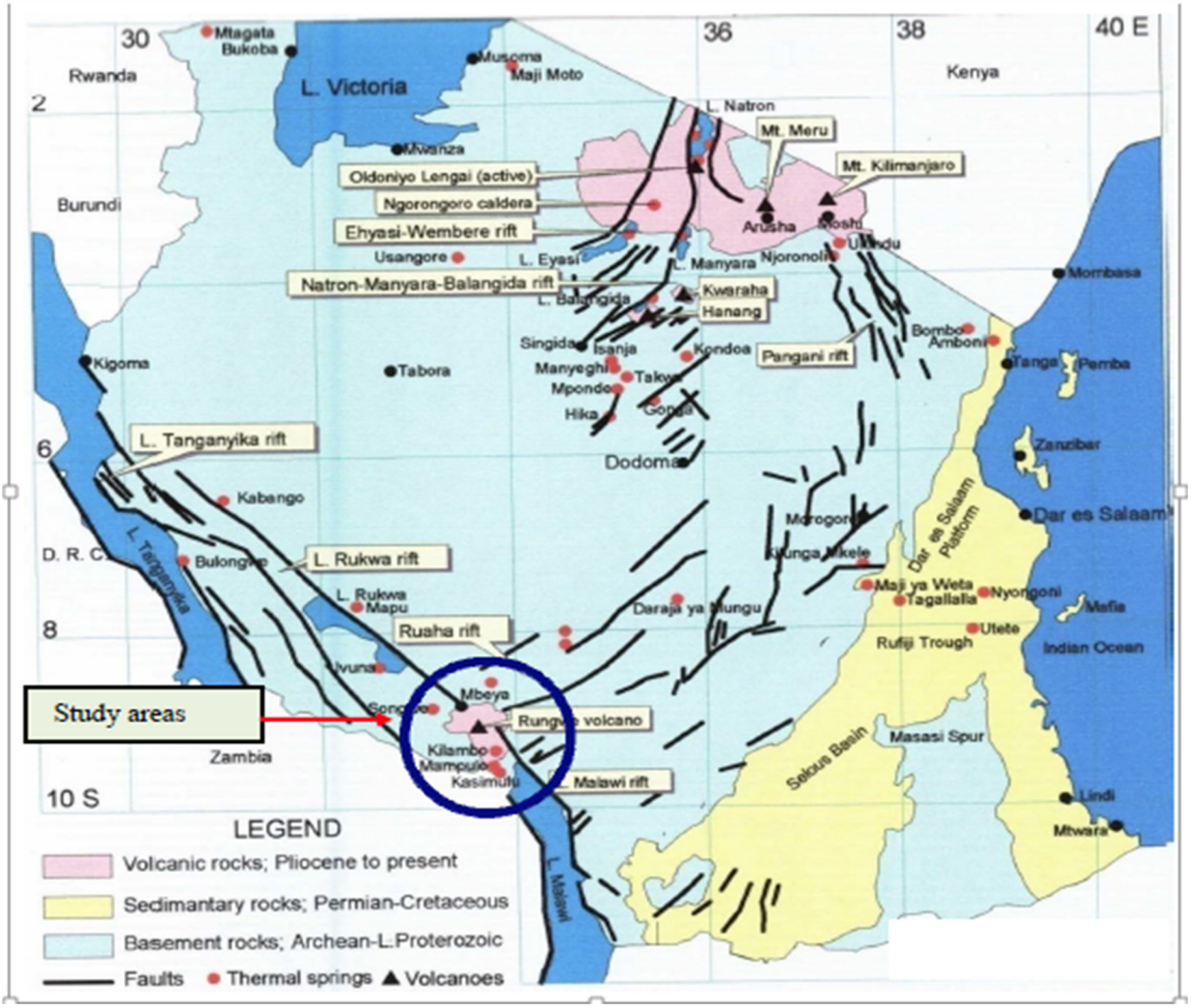

FIGURE 6: Geothermal site, study area and the rifting system in Tanzania. The blue ring represents Rungwe volcanic zone with selected thermal springs used in this report (Mwihava, 2004)

explosive eruptions. Two eruptions were dated ca.10-12 ka (plinian-style eruption: Kitulo Pumice) and < 1ka (Ignimbrite-forming eruption: Ngozi Tuff (Ochmann and Garofalo, 2013).

The geology of Tanzania is dominated by the Archean Craton, a stable continental nucleus, which covers most of central and western Tanzania. Tanzania craton is the Paleoproterozoic Ubendian Belt and the southeast the Paleoproterozoic Usagara Belt, which are dominated by a variety of high to medium grade metamorphic rocks of both sedimentary and igneous origin. Holocene volcanism has taken place in three main large volcanoes of the RVP, Ngozi, Rungwe and Kiejo (Ochmann and Garofalo, 2013).

4.1 Rungwe volcanic zone

The area of investigation belongs to the Rungwe Volcanic Province in Mbeya as shown in Figure 6 and Figure 7. The Mbeya area is located at the intersection between the western and eastern branches of the East African Rift system (EARS) forming a triple junction. The area is characterised by hydrothermal surface manifestations, potential volcanic heat sources, and fault-controlled permeability favouring fluid pathways along faults associated to the East African Rift system. Additionally, there is sufficient recharge in the high elevated area for filling up the naturally lost fluid (Ochmann and Garofalo, 2013). The previous study reveal that almost 10 MW of thermal fluid is lost from Songwe hot springs

(geothermal outflow zone), which is indicating a substantial reservoir in the subsurface. Table 2 represent fluid composition of geothermal water from Rungwe.

TABLE 2: Fluid composition of Rungwe (Collected 2006-2008; Ochmann. and Garofalo, 2013)

Name	Sample number	pH	Temp °C	CO_2	SiO_2	Na	K	Mg	Ca	Cl	SO_4	Al	Fe	Li	Charge balance
Udindilwa (a)	23	7.00	82.40	854.75	72.7	893.0	28.50	3.90	13.40	82.40	247.	0.017	0.100	0.30	0.019
Ibayi (b)	29	6.80	80.20	1269.50	82.3	646.0	40.30	2.30	12.00	116.00	297.00	0.008	0.100	0.30	0.001
Main spring ER (d)	19	6.70	65.70	1441.20	71.8	775.0	95.40	15.60	30.30	197.00	154.00	0.023	0.100	0.70	0.005
Aqua Afia 3 (e)	15	6.90	60.30	1384.20	133.0	106.0	48.70	4.50	12.10	9.00	1.70	0.007	<0.100	20.60	-0.015
Aqua Afia 1 (f)	16	6.70	56.60	1990.80	124.0	100.0	46.90	5.80	15.50	8.20	1.00	0.003	<0.100	17.50	0.009
Ikumbi 2 (g)	26	6.80	54.70	2019.70	125.0	102.0	48.70	4.90	13.50	8.70	1.40	0.004	<0.100	20.60	-0.007
Kandete (h)	9	7.40	56.60	295.02	126.0	1246.0	66.00	13.90	15.50	224.00	252.00	<0.005	0.300	0.40	0.164
Kasimulo (i)	10	7.70	42.40	293.57	105.0	1218.0	68.10	15.80	26.10	204.00	317.00	<0.005	0.200	0.40	0.144
Ilatile 4 (k)	5	8.50	80.20	139.21	70.3	818.0	82.00	8.00	17.10	184.00	143.00	<0.005	0.200	0.80	0.013
Swaya (m)	12	7.20	44.10	295.02	89.5	52.1	80.40	4.80	13.10	12.50	14.00	0.019	0.027	0.00	0.162

Letters in brackets represent the numbers in ternary diagram

The triple junction of the NW-SE trending south Rukwa and North Malawi rift basin intersected by younger NE-SW trending Usangu basin is covered by Rungwe volcanic rocks. There are also a number of Cretaceous carbonatite intrusions in the Mbeya region, including the Panda Hill Carbonatite which is located between Ngozi Volcano and Songwe hot springs. The condition for high enthalpy resources are principally favourable in the Mbeya region due to the presence of active faults which allow fluid flow, young volcanic heat sources (which are sparse in other areas of western branch of the east African system) and the occurrence of surface manifestations, such as hot springs, indicating geothermal subsurface activity (Ochmann and Garofalo, 2013). Figure 7 indicate the hot spring sample selected for Rungwe area.

The Rungwe volcanic zone has been divided into two geothermal fields; Northern geothermal system (Ngozi-Songwe) which is high temperature field (>200°C) and Southern geothermal system which is low-temperature field (<200°C) (Ochmann and Garofalo, 2013).

FIGURE 7: Locations of selected samples form Rungwe area used in this work. The map is from the geothermal site, study area and the rifting system in Tanzania (Source: Google Earth)

5. RESULTS AND DISCUSSION

5.1 The Fljótin geothermal area

5.1.1 The charge balance evaluation

The samples from the Fljótin in north Iceland which are discussed in this report were collected in 1963, 1969, 1973 and 1985 by geoscientists from ISOR (ISOR database). At that time only the major elements were analysed and very limited interpretation been published on these data and all the reports are in Icelandic. The author of the current report calculated speciation, sample quality, and mineral saturation index (Tables 3 and 4) by using the WATCH program (Arnórsson et al., 1982).

The surface temperature indicates low-temperature geothermal field with temperature range of 23.5-88.5°C. The Fljótin data consist of 13 samples from hot springs and one from a borehole (number 6). The ID number for each sample is shown in parenthesis following the name. These are: Bardslaug (1, 1*), Daelir (2), Akrar (3), Reykir (4) Laugaland (5) Reykjarhóll á Bökkum (6) a borehole, Kerlingalaug (7, 7*), Hólakot (8), Reykjarhóll east (9, 9*), and Stóra-brekka (10, 10*). The fluid composition is shown in Table 1. The borehole is only 257.3 m deep and was drilled in February 1985 (ISOR database).

The sample quality is one of the major factors in geochemical data analysis, which could depend on factors such as sampling procedure, storage, sampling point, treatment and transportation and even climate condition. The sample quality can be evaluated by charge balance error (CBE Equation 16), is calculated from the total number of anions and cations in the fluid sample. The CBE value should be less than 5% to be regarded as an acceptable geochemical analysis – the closer to zero the better.

$$CBE(\%) = \frac{\sum Z_{cat} m_{cat} - \sum Z_{an} m_{an}}{\sum Z_{cat} m_{cat} + \sum Z_{an} m_{an}} x100\% \quad (16)$$

Where Z_{cat} and Z_{an} are charge of the cation and the anion, m_{cat} and m_{an} represent concentration of an element.

The charge balance error states the sample quality during collection and total composition of charges anions and cations (Table 1). Five of the samples from Fljótin of seven samples have CBE value in the range > 5 –51. The CBE for Kerlingalaug (7*) is 51.48%, Reykjahóll East (9*) is 50.86% and Stóra-Brekka (10*) is 36.92% which are too high for sample quality analysis. The results for high CBE can be caused by sampling procedure, laboratory error, sample contamination, unfiltered samples, and some samples can precipitate in the container (Basu, 2008). Though the sample quality is beyond the limit value for analysis and interpretation of thermal fluid, it will be used for learning purpose with their inclusive in data analysis and interpretation. Apart from being with high CBE the samples are used due to their minor difference in concentration of major element in the samples such as H_2S, SiO_2, Na, and Cl which differ at a range of 1-5mg/L.

The Mg value for Bardslaug (1), Kerlingalaug (7), Reykjarholl East (9) and Stora Brekka (10) were almost zero value (<0.001 mg/L) or less than the detection limits which meant the sample could not be used for the Na-K-Mg ternary diagram (Giggenbach, 1986). Therefore, Mg concentration for those samples were interpolated as 0.001 mg/L. The low concentration of Mg can be caused by time difference and mixing of sample and/or different analytical methods.

5.1.2 The Na-K-Mg and the Cl-SO_4-HCO_3 ternary diagrams

The samples were plotted on Na-K-Mg ternary diagram shown in Figure 8. The reservoir temperature estimated at a temperature range of 120-160°C. The temperature range is within the range calculated by the geothermometers as shown later. Samples from Reykir (4) and Reykjarhóll á Bökkum (6) the bore hole which are both equilibrated, while Bardslaug (1*), Daelir (2), Akrar (3), Laugaland (5),

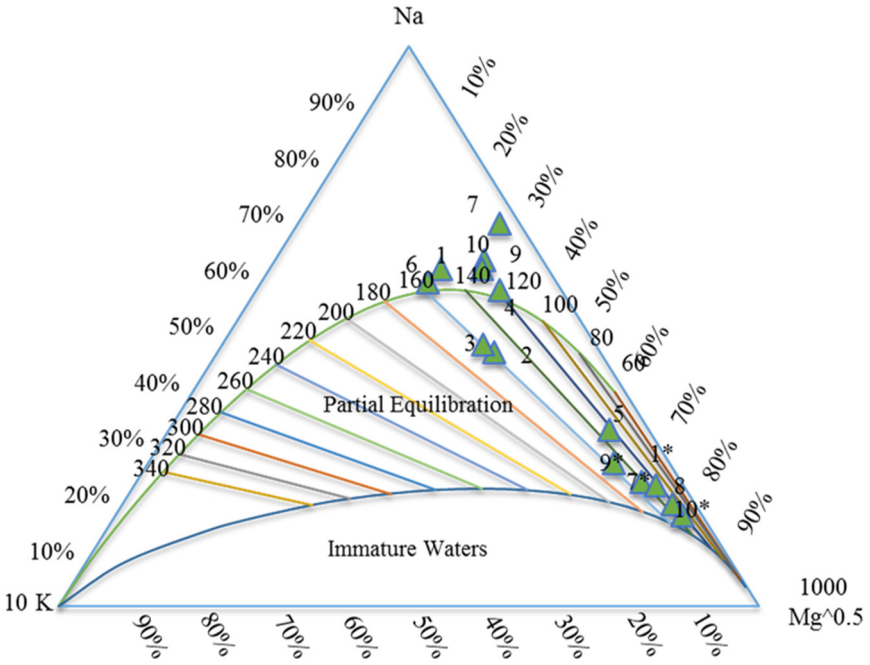

FIGURE 8. Classification of water by Na-K-Mg ternary diagram for the Fljótin samples, numbers are the same as in Table 1

Kerlingalaug (7*), Hólakot, Reykjahóll east (9*) and Stóra-Brekka (10*) are partially equilibrated. On the other hand, Bardslaug (1), Kerlingalaug (7) Reykjahóll east (9), and Stóra-Brekka (10) were beyond the equilibrated line indicated by Giggenbach (1986).

The different results from same sample like no 7 and 7* are likely affected by time difference in sample collection, and technology. The effect can be seen in Na-K-Mg ternary diagram where sample plotted above the equilibrium line and to the corner of Mg (no 7 and 7*). Also seen in Table 1.

The results from same area can give different values as can be seen on the Na-K-Mg ternary diagram (Figure 8) for chalcedony geothermometer Bardslaug (1), and (1*) has an approximate temperature of 130°C and 135°C respectively, Kerlingalaug (7) and (7*) has 107°C and 109°C respectively, Reykjarhóll East (9) and (9*) has an approximate temperature value of 112°C and 115°C respectively, and Stóra-Brekka (10) and (10*) has a temperature 74°C and 102°C respectively. The temperature difference is almost +5 or-5 which is small compared to Stóra-Brekka where difference is ~25°C. Therefore, the duplicated sample for Bardslaug, Kerlingalaug and Reykjarhóll East sampling point are considered to be agreement, where on the other hand Stóra-Brekka does not agree.

On the Cl-SO_4-HCO_3 ternary diagram shown in Figure 9 the Fljótin samples plots in the volcanic waters and close to the center of the diagram. The low concentration of Cl may indicate mixing process with rainwater and/or low Cl concentrations of the Icelandic tholeiitic basalts.

5.1.3 The geothermometers

The geothermometers are selected according to volcanic activities, rock type, and mineral composition and sampling surface temperature. The geothermometer used to calculate the reservoir temperature for Fljótin are: the quartz geothermometer by Fournier and Potter (1982), the chalcedony geothermometer by Arnórsson et al., (1983), the amorphous silica geothermometer by Fournier (1977) and the Na/K geothermometer by Giggenbach (1988). The results of the calculations are shown in Table 3.

The chalcedony geothermometer gives temperature range between 74 and 136°C, the quartz geothermometer temperature range between 104-160°C, the amorphous silica range in 10-38°C and

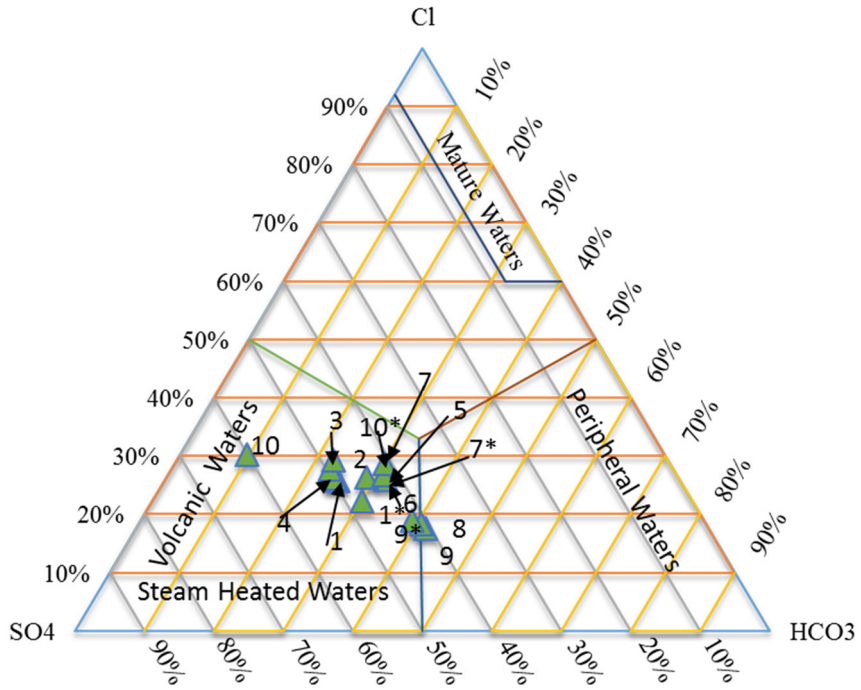

FIGURE 9: Classification of water by Cl-SO_4-HCO_3 ternary diagram for the Fljótin samples; numbers are the same as in Table 1

Na/K geothermometer temperature range was 64-158°C. The amorphous silica geothermometer gives unexpected lower temperature compared to surface temperature for such situation, as amorphous silica will not fulfil the estimation of the reservoir temperature.

The Na/K geothermometer and Na-K-Mg ternary diagram gives similar temperature value for reservoir temperature estimation. Arnórsson (1975) concluded that the Icelandic water are equilibrated with chalcedony at a temperature < 180°C. Therefore, chalcedony geothermometer is considered here to give the most likely reservoir temperature range of 74-136°C.

TABLE 3: Solute geothermometers for Fljótin samples (°C)

Sample name	Surface temperature (°C)	Chalcedony (°C) (1)	Quartz (°C) (2)	Amorphous silica (°C) (3)	Na/K (°C) (4)
Bardslaug (1)	66.5	130	155	33	142
Bardslaug (1*)	-	135	160	37	122
Daelir (2)	64.7	134	158	36	158
Akrar (3)	57.5	136	160	38	159
Reykir (4)	55.5	104	132	12	110
Laugaland (5)	52.8	108	135	15	124
Reykjarhóll á Bökkum, well (6)	88.5	136	161	38	155
Kerlingalaug (7)	48.8	107	134	14	118
Kerlingalaug (7*)	49.0	109	136	15	134
Hólakot (8)	46.4	111	138	18	122
Reykjarhóll east (9)	61.0	112	139	18	118
Reykjarhóll east (9*)	58.0	115	141	20	102
Stóra-Brekka (10)	23.8	74	104	33	64
Stóra-Brekka (10*)	55.0	102	130	10	100

Number in brackets represent the numbers in ternary diagrams

1. Arnórsson et al., 1983; 2. Fournier and Potter, 1982; 3. Fournier, 1977; 4. Giggenbach, 1988

5.1.4 The mineral saturation

According to the theory of mineral saturation, equilibrium is reached when saturation index (SI) is equal to zero, under-saturated when SI is less than zero and supersaturated when the SI is greater than zero. In Fljótin the system is under saturation with higher temperature of chalcedony by considering samples from Bardslaug (1, 1*), Kerlingalaug (7, 7*), Reykjarhóll east (9, 9*), and Stóra-Brekka (10, 10*) as in Table 4. The mineral saturation state of the Fljótin geothermal field are calculated by the chalcedony reservoir temperature by Fournier (1977) which indicate saturation for calcite and amorphous silica while under-saturation for anhydrite as shown in Figure 10. This indicates low mineral precipitation when utilizing the fluid.

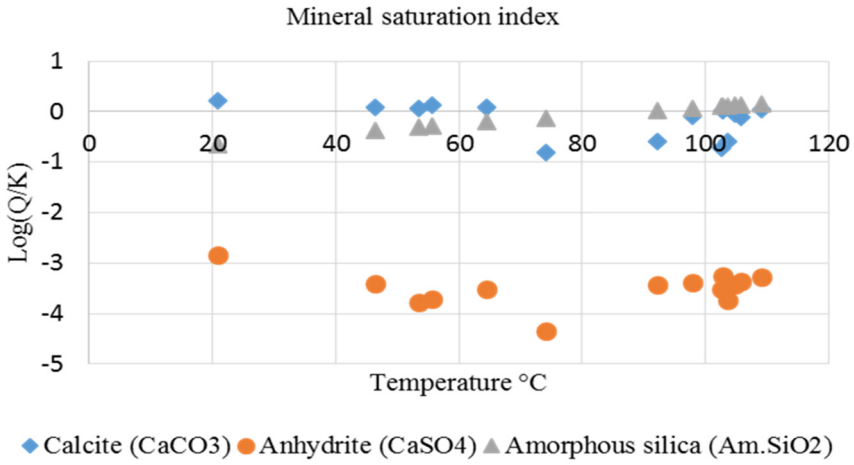

FIGURE 10: Mineral saturation state for Fljótin

TABLE 4: Mineral saturation state for Fljótin. SI index calculated at chalcedony temperature

Hot spring	Surface temperature (°C)	Chalcedony temperature (°C)	Calcite ($CaCO_3$) SI index	Anhydrite ($CaSO_4$) SI index	Amorphous silica ($Am.SiO_2$) SI index
Bardslaug (1)	66.5	97.9	-0.1	-3.38	0.065
Bardslaug (1*)	.	104.8	-0.049	-3.425	0.116
Daelir (2)	64.7	102.8	0.02	-3.25	0.101
Akrar (3)	57.5	105.7	-0.11	-3.36	0.122
Reykir (4)	55.5	46.5	0.09	-3.42	-0.383
Laugaland (5)	52.8	74.2	-0.82	-4.34	-0.125
Reykjarhóll á Bökkum well (6)	88.5	109.1	0.05	-3.27	0.146
Kerlingalaug (7)	48.8	64.5	0.08	-3.52	-0.21
Kerlingalaug (7*)	49	102.6	-0.718	-3.51	0.1
Hólakot (8)	46.4	55.6	0.12	-3.71	-0.293
Reykjarhóll east (9)	61	53.5	0.07	-3.77	-0.313
Reykjarhóll east (9*)	58	103.6	-0.599	-3.74	0.107
Stóra-Brekka (10)	23.8	20.9	0.21	-2.85	-0.664
Stóra-Brekka (10*)	55	92.1	-0.597	-3.423	0.02

Numbers in brackets represent the numbers in ternary diagrams and in Table 1

5.1.5 Component distribution in Fljótin

The distribution of the major elements of geothermal field in the contour map is interpreted with the Surfer 12.6.963 software by Golden Software. The contour map provides useful information for fluid composition distribution and up-flow zone in geothermal field. However, resource management and environment effect will be viable in component distribution map upon utilization of the geothermal field. The selected elements are, SiO_2, CO_2 and Cl. They are selected according to their application in geothermal field where SiO_2 is the indication of heat source, CO_2 describes the size of the reservoir and the major fracture of the geothermal system and Cl indicate the water maturity in the geothermal field.

Component distribution for Fljótin is presented in Figure 11. The SiO_2 concentrations range between 52-148 mg/l in the Fljótin geothermal area. As shown in Figure 11 the concentration of SiO_2 increases from 52 mg/l in the SE (Stóra-Brekka) to NW at Daelir, Bardslaug, Akrar, and Reykjarhóll á Bökkum with SiO_2 concentration range between 136-147 mg/l. The CO_2 concentrations range between 8-24 mg/L increase with the same trend as the silica concentration from SE to NW with the low concentration 8 mg/L at Stóra-Brekka to higher

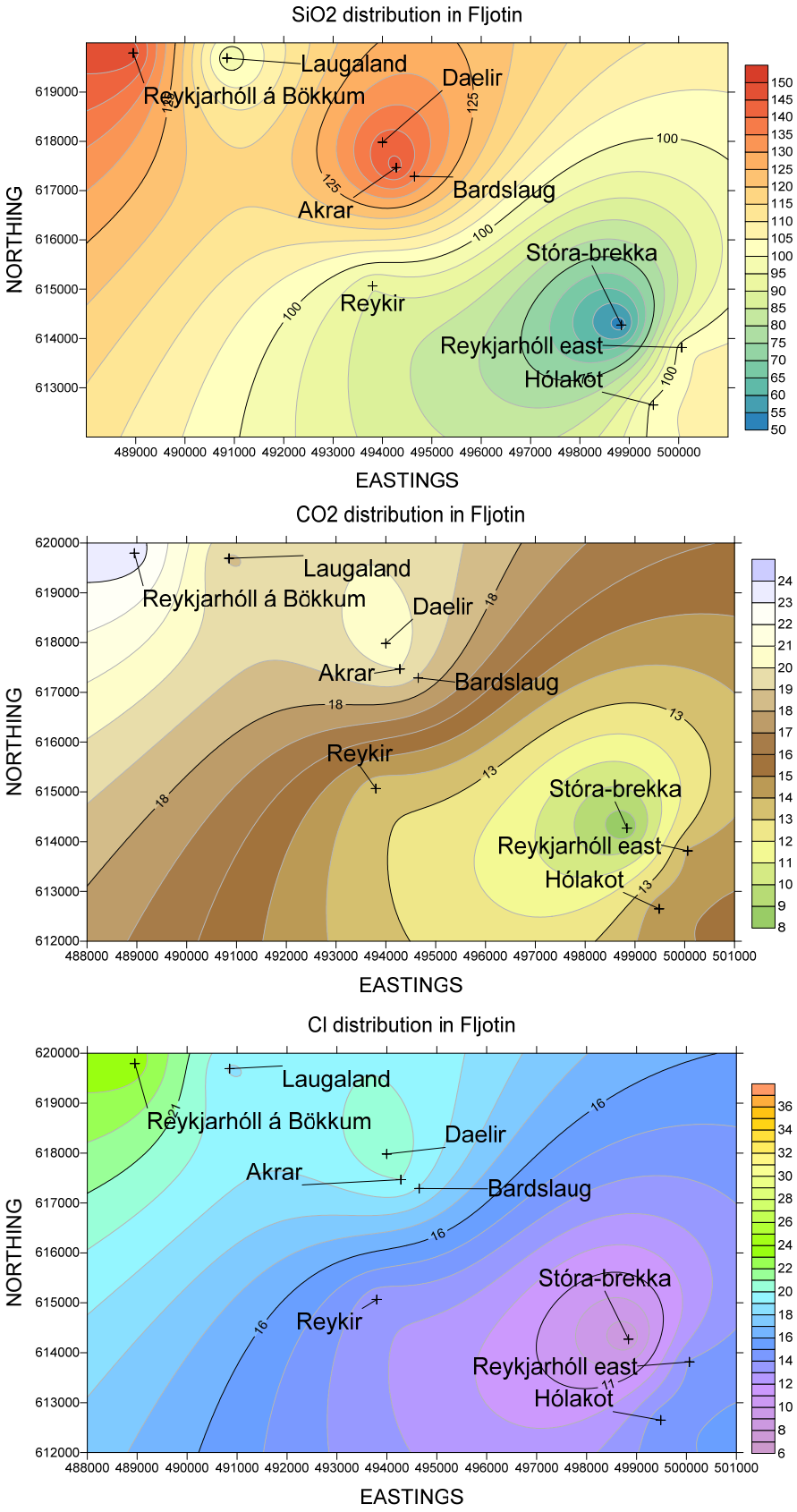

FIGURE 11: Distribution of CO_2, SiO_2, and Cl in Fljótin Iceland

concentration at Reykjarhóll á Bökkum (148 mg/L). The Cl concentration which is very low, range between 9-36 mg/L, increase from 9 mg/L (Reykjarhóll/Hólakot) in the SE towards NW—SE with high concentration of 36 mg/L at Stóra-Brekka and Reykjarhóll á Bökkum.

This SiO_2 concentration is highest between 136-147 mg/l in Daelir, Akrar, Bardslaug and Reykjahóll (the well in the north) which is consistent with the calculated temperature shown in Figure 12.

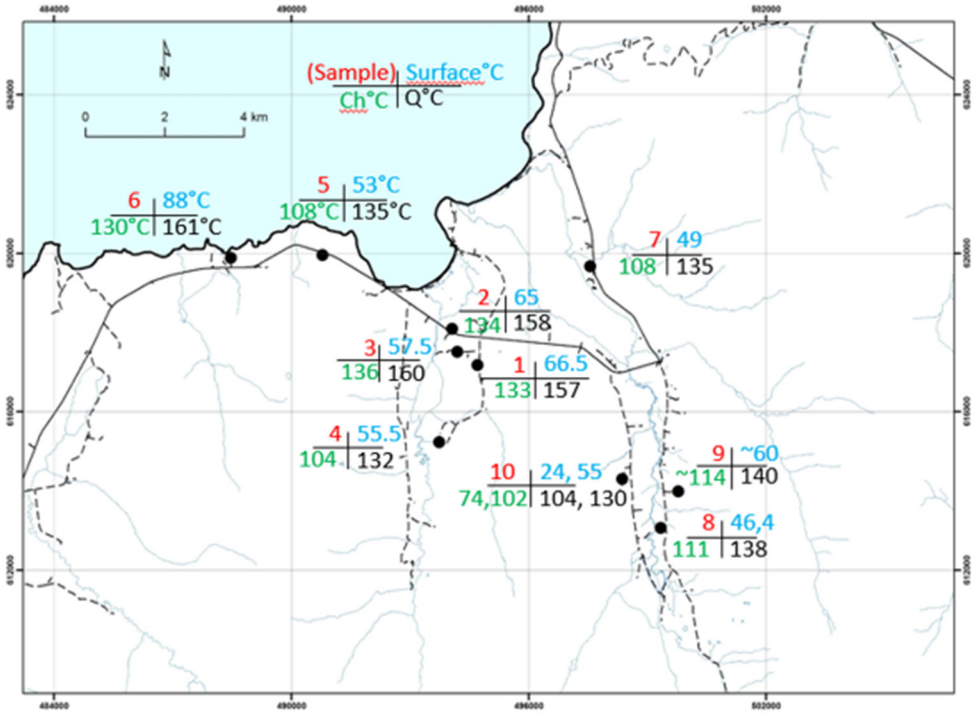

FIGURE 12: Map of Fljótin showing the samples location (number in red) together with measured surface temperature (blue), calculated Chalcedon temperature (green) and calculated quartz temperature

According to geology and chemical analysis of Fljótin, reservoir temperature can be estimated to be 120°C to 160°C. The hot spring is characterized by low temperature geothermal fluid with low enthalpy. Therefore, the area has a potential for direct utilization such as swimming pool, fishing industry, and greenhouses.

5.2 The Rungwe geothermal area

The selected data from Rungwe Tanzania chosen for comparison have been published and interpreted in a report by Ochmann and Garofalo (2013). The selected samples have similar surface temperature as the Fljótin samples. The work on these ten selected samples from the Rungwe volcanic zone (Figure 7) had been done by Bundesanstalt für Geowissenschaften und Rohstoffe (BGR), Sweden Cosultantation Company (SWECO), Icelandic International Development Agency (ICEIDA) and Japan International Cooperation Agency (JICA).

The samples chosen are from the hot springs; Ibayi (a), Ilatile 4 (b), Udindilwa (d), Main Spring (e), Kandete (f), Kasimulo (g), Aqua Afia 3 (h), Aqua Afia1 (i), Swaya (k) and Ikumbi 2 (m). Letters in brackets represent the numbers in ternary diagrams. The samples quality is shown in Table 2, the mineral saturation index is shown in Table 5 and the geothermometers results are shown in Table 6.

The mineral saturation states (index) are expressed by calculated quartz temperature (Fournier and Potter, 1982) where calcite and anhydrite will be saturated while amorphous silica will be supersaturated as is shown Figure 13 and Table 5.

TABLE 5: Mineral saturation state – Rungwe SI index calculated at quartz temperature

Hot spring	Surface temp (°C)	Quartz temp (°C)	Calcite ($CaCO_3$) SI index	Anhydrite ($CaSO_4$) SI index	Amorphous silica (Amr. SiO_2) SI index
Udindilwa (a)	65.7	120.20	-0.980	-2.187	0.017
Ibayi (b)	82.4	126.80	-1.081	-2.152	0.071
Main spring ER (d)	60.3	119.70	-0.758	-2.058	0.012
Aqua Afia 3 (e)	44.1	154.00	-1.100	-4.070	0.28
Aqua Afia 1 (f)	42.4	149.80	-1.250	-4.210	0.249
Ikumbi 2 (g)	44.1	150.20	-1.180	-4.130	0.253
Kandete (h)	56.6	150.50	-0.899	-2.512	0.256
Kasimulo (i)	54.7	139.60	-0.363	-1.840	0.176
Ilatile 4 (k)	80.2	118.60	0.013	-2.256	-0.004
Swaya (m)	44.0	131.20	-0.800	-3.080	0.107

Letters in brackets represent the numbers in ternary diagram and in Table 2

TABLE 6*:* Solute geothertmometers for Rungwe

Sample name	Chalcedony (25-250°C) (1)	Quartz (0-900°C) (2)	K/Mg (°C) (3)
Udindilwa (a)	91.70	120.3	106
Ibayi (b)	98.80	126.8	124
Main Spring (d)	91.00	119.7	121
Aqua Afia 3 (e)	129.00	154.0	120
Aqua Afia1 (f)	124.00	150.0	115
Ikumbi 2 (g)	125.00	150.0	118
Kandete (h)	125.00	150.6	257
Kasimulo (i)	139.90	113.3	252
Ilatile 4 (k)	88.90	117.8	248
Swaya (m)	103.70	131.2	134

Letters in brackets represent the numbers in ternary diagram

1. Arnórsson et al., 1983; 2. Fournier and Potter, 1982; 3. Giggenbach, 1988

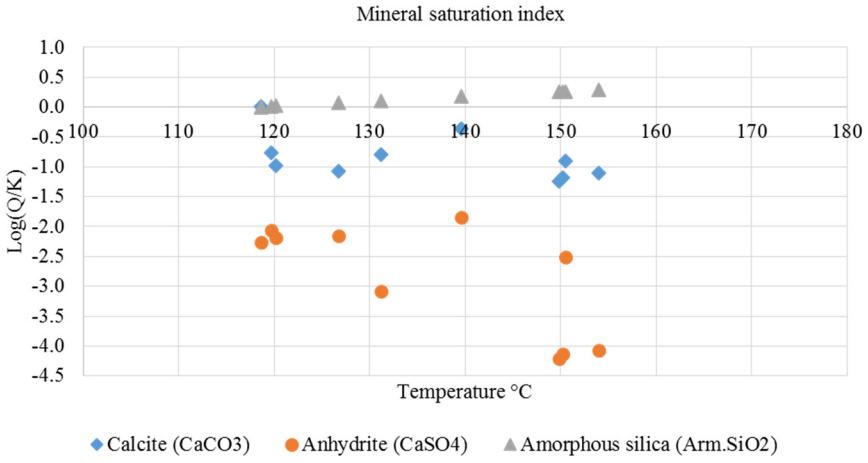

FIGURE 13: Mineral saturation state in Rungwe

The geothermometers used to calculate the reservoir temperature for the Rungwe volcanic zone are quartz, chalcedony, and K/Mg. However, Arnórsson 2000 states that for non-reactive minerals or volcanic system, normally quartz equilibration is used at a temperature less than 100°C. Giggenbach 1986 states that for water with high concentration of Mg, K-M geothermometry will apply for reservoir

estimation temperature. The subsurface temperatures indicate low-temperature geothermal field with confirmation of Na-K-Mg ternary diagram with temperature range of 160-200°C according to geothermometers of quartz and K/Mg with temperature range of 116-154°C and 106-252°C respectively.

5.2.1 Components distribution in Rungwe

The samples were selected in two areas of the geothermal field as indicated in the map: Northern geothermal system (Ngozi-Songwe) and Southern geothermal system (Kiejo-Mbaka) (Ochmann and Garofalo 2013). According to Figure 14 the highest SiO_2 concentration, 105-133mg/l, is in the SE

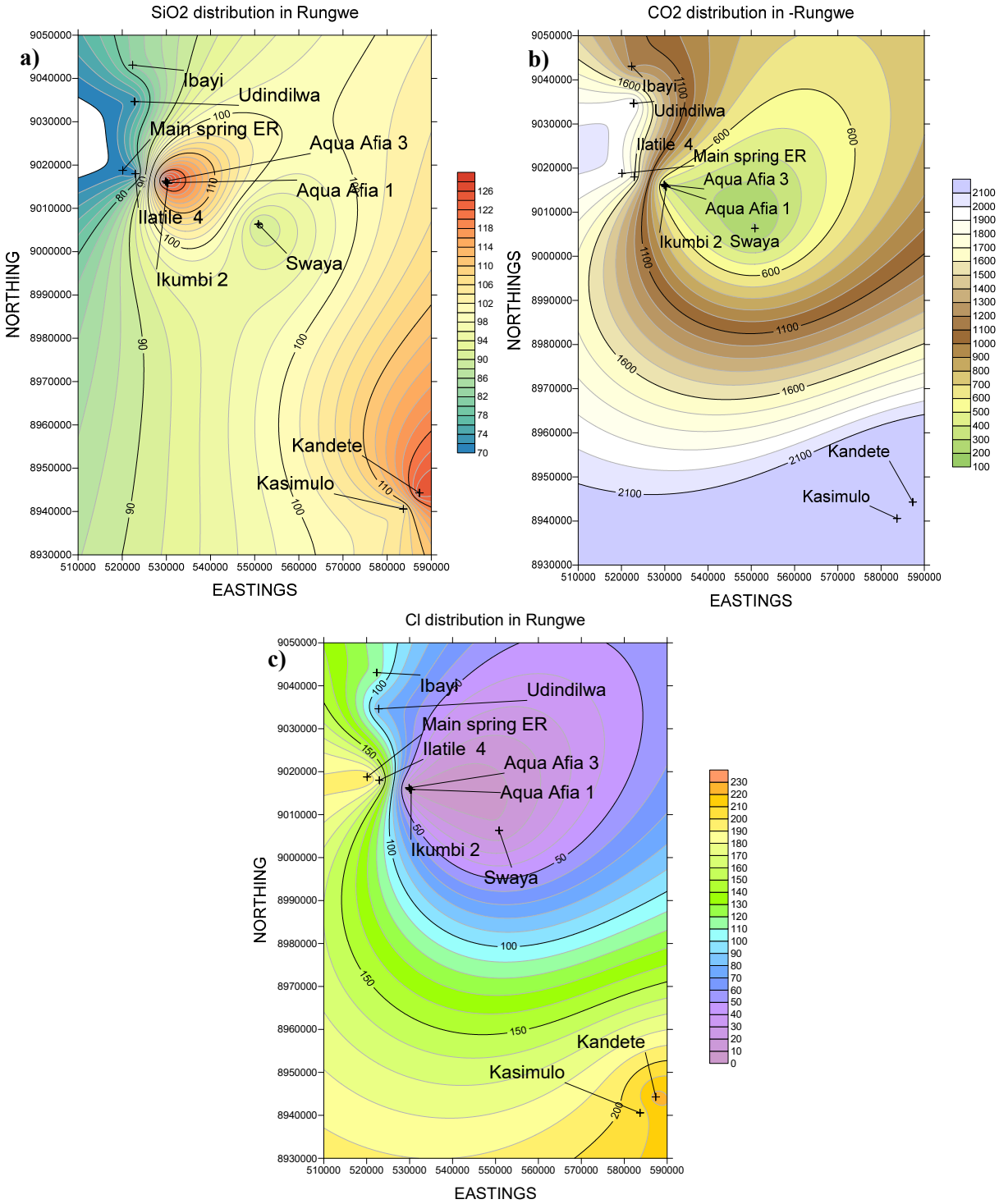

FIGURE 14: Distribution of SiO_2 (a), CO_2 (b), and Cl (c), Rungwe Tanzania

(Kandete and Kasimulo) and in the centre where most of the hot springs are Aqua Afia1, Aqua Afia 3 and Ikumbi 2 locations. In the northern part of the area (Ibayi and Udindilwa), the SiO_2 is lower of ~70-80 mg/l. The trend of CO_2 concentration is increasing towards SE with high concentration of 294mg/l and 295mg/l at Kandete and Kasimulo. The Cl concentration increases on NW-SE direction with high concentration at Main Spring ER, Ilatile 4, Kandete and Kasimulo. From BGR report, Ibayi and Udindilwa have been reported to equilibrate at temperature <200°C (Ochmann and Garofalo 2013).

5.3 Comparison of the Fljótin and the Rungwe geothermal fluids

As written earlier these two geothermal areas are very different both in age and rock composition and therefore the fluid compositions are also very different. The Fljótin a low-temperature geothermal area have estimated reservoir temperature in the range 120°C to 160°C whereas the Rungwe geothermal area reservoir temperature range are in 130°C to 200°C. Rungwe has been divided into two geothermal fields: Northern geothermal system (Ngozi-Songwe) which is high temperature field (>200°C) and Southern geothermal system (Kiejo-Mbaka) which is low-temperature field (<200°C) (Ochmann and Garofalo 2013).

The Fljótin and Rungwe are similar in mineral saturation where both are saturated by amorphous Silica and under saturation calcite and anhydrite are at the estimated reservoir temperature estimated. Fljótin water is classified as low-temperature volcanic water and Rungwe classified as peripheral water with high concentration of HCO_3 as seen in Figure 15. The reservoir temperature for Fljótin can be estimated by chalcedony geothermometer and cation geothermometer in relation with Na-K-Mg ternary diagram. Due to different volcanic activities, rock type and mineral composition (Arnórsson 2000) the chalcedony and Na/K geothermometer has promising result for Fljótin (Table 3), while Rungwe quartz and K/Mg is providing necessary information that compares to other geothermometry (Table 6).

The Fljótin geothermal area and the Rungwe geothermal area are compared on CL-SO_4-HCO_3 ternary diagram shown in Figure 15. According to Ochmann and Garofalo (2013) the selected sample point in Rungwe volcanic zone is classified as low-temperature field (<200) regarding to southern geothermal system with peripheral water characterized by major anion of HCO_3 (blue square) as in Figure 15. The concentration of HCO_3 normally indicate mixing with ground water or mixing of the discharge of CO_2

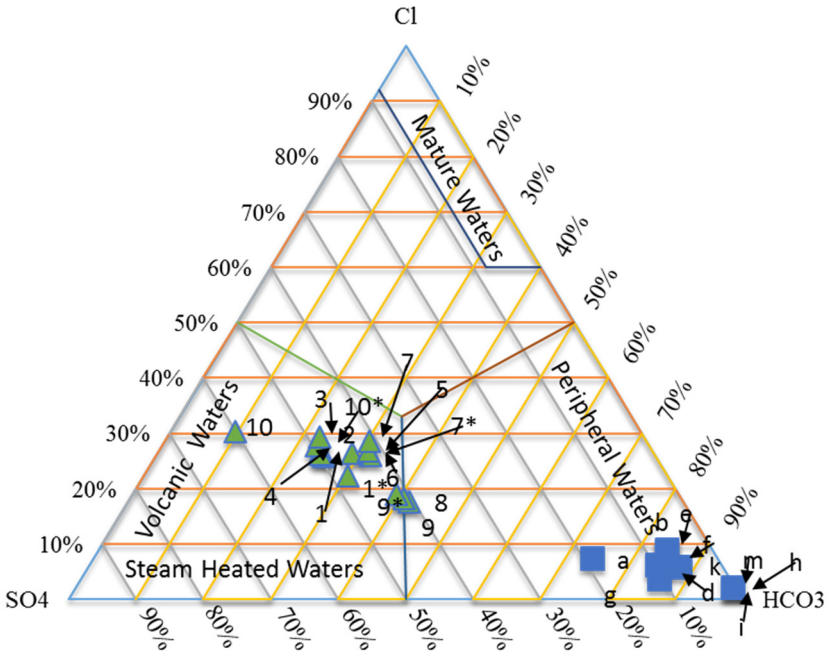

FIGURE 15: Relationship (Comparison) of Fljótin (green triangle) and Rungwe geothermal field samples (blue square) by Cl_SO_4-HCO_3 ternary diagram

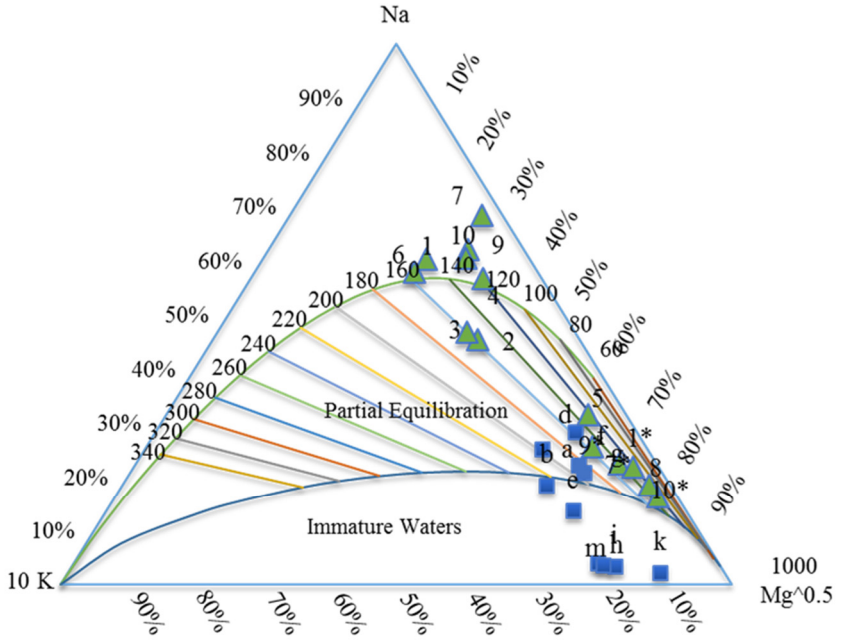

FIGURE 16: Comparisons of the Fljótin samples (green triangle) and the Rungwe samples (blue square) on the Na-K-Mg ternary diagram

from the reservoir interact with ground water fluid at lower temperature (Arnorsson 2000). The Fljótin temperature was estimated at a range of 120°C to 160°C by Na-K-Mg ternary diagram, while in Rungwe volcanic zone the temperature was estimated to be 130°C to 200°C according to the Figure 16 which are confirmed with geothermometers. Geothermometers may provide conclusive information if applied to what is collected as mature water that has reacted with bed rock minerals and reached equilibrium with them.

6. CONCLUSIONS

According to charge balance errors (CBE), sampling collection should be taken by a very keen and skilled person for the purpose of reducing contamination by sampling. The sample quality can contribute to wrong results of geothermal field such as type of fluid, reservoir temperature, size of the reservoir, original of the fluid, the up-flow zone and flow direction.

The Fljótin is a low-temperature geothermal fluid field with low total dissolved elements, low Ca, SiO_2 and CO_2 concentrations, all indicating that the fluid can be used directly without precipitation of calcite and amorphous silica. Fljótin are estimated to have the reservoir temperature range between 120°C-160°C according to chalcedony geothermometer and with temperature range of 64°C-159°C temperature range according to Na/K geothermometer. Which is in agreement with the full equilibrated fluid on the Na-K-Mg ternary diagram. The Fljótin area can be used directly for direct heating, greenhouse industry, aquaculture, fishing industry, tourist attraction like swimming pool and natural bathing.

The Rungwe volcanic zone has been divided into two geothermal fields; Northern geothermal system (Ngozi-Songwe) which is high temperature field (>200°C) and Southern geothermal system (Kiejo-Mbaka) which is low-temperature field (<200°C) (Ochmann and Garofalo 2013). The selected point of thermal water from Rungwe volcanic zone are characterized by Mg-HCO_3 peripheral waters that are partially equilibrated, with estimated reservoir temperature range around 106°C-200°C Although, Rungwe volcanic zone has promising results for a geothermal industry, although Ochmann and Garofalo (2013) report indicate high concentration of CO_2 which will require detailed study in order to reduce the

high operation risk. However, at the moment the field can be used for direct use such as greenhouse, fishing and tourist attraction.

ACKNOWLEDGEMENTS

It gives me great pleasure to extend my sincere gratitude to the UNU-GTP in Iceland and the Ministry of Energy and Minerals, Tanzania. To the UNU-GTP Director Ludvik S. Georgsson, Deputy Director Ingimar G. Haraldsson: thank you for awarding me the opportunity to study in Iceland; Thòrhildur Ísberg, Málfríður Ómarsdóttir and Markús A. G. Wilde: many thanks for facilitating my academic endeavours in Iceland. To all, your ever present support towards the completion of the programme is highly appreciated. To Ministry of Energy and Minerals, my sincere gratitude goes to Permanent Secretary and Commissioner of Energy (CEP) for nominating and granting me permission to attend this vital course. My appreciation to UNU 2015 fellows for laughs and ideas shared during the entire period.

My heartfelt and sincere thanks also go to my supervisor, Dr Vigdís Harðardóttir, for her excellent supervision, fruitful ideas valuable advice and encouragement during the entire project period. Also, my warm thanks go to Gestur Gíslason geochemist at Reykjavík Geothermal, for his constant guidance and knowledge sharing. Appreciation goes to Dr Kristjan Sæmundsson and Dr Halldór Arnórsson for providing useful information for my Project.

Finally, I thank God for keeping health, my lovely kids Clement, Innocent and Eva for the entire period of my study.

REFERENCES

Arnórsson, S., 2000: Mixing processes in upflow zones and mixing models. In: Arnórsson, S. (ed.), *Isotopic and chemical techniques in geothermal exploration, development and use. Sampling methods, data handling, and interpretation*. International Atomic Energy Agency, Vienna, 200-211.

Arnórsson, S., and Andrésdóttir, A., 1995: Processes controlling the distribution of boron and chlorine in natural waters in Iceland. *Geochim. Cosmochim. Acta, 59*, 4125-4146.

Arnórsson, S., Gunnlaugsson, E., and Svavarsson, H., 1983: The chemistry of geothermal waters in Iceland III. Chemical geothermometry in geothermal investigations. *Geochim. Cosmochim. Acta, 47*, 567-577.

Arnórsson, S., Sigurdsson, S. and Svavarsson, H., 1982: The chemistry of geothermal waters in Iceland I. Calculation of aqueous speciation from 0°C to 370°C. *Geochim. Cosmochim. Acta, 46,* 1513-1532.

Arnórsson, S., 1975: Application of the silica geothermometer in low-temperature hydrothermal areas in Iceland. *Am. J. Sci., 275,* 763-783.

Ebinger, C.J., Deino, A.L., Drake, R.E., and Tesha, A.L., 1989: Chronology of volcanism and rift basin propagation: Rungwe volcanic province, East Africa. J. Geophys. Res., 94 B11:15, 785-803.

Ellis, A.J., and Mahon, W.A.J., 1977: *Chemistry and geothermal systems*. Academic Press, New York, 392 pp.

Fournier, R.O., 1977: Chemical geothermometers and mixing model for geothermal systems. *Geothermics, 5,* 41-50.

Fournier, R.O., and Potter, R.W., 1982: An equation correlating the solubility of quartz in water from 25° to 900°C at pressures up to 10,000 bars. *Geochim. Cosmochim Acta, 46*, 1969-1973.

Giggenbach, W.F., 1986: Graphical techniques for the evaluated water/rock equilibration conditions by use of Na, K, Mg and Ca contents of discharge water. *Proceedings of the 8th New Zealand Geothermal Workshop,* 37-43.

Giggenbach, W.F., 1988: Geothermal solute equilibria. Derivation of Na-K-Mg-Ca geoindicators. *Geochim. Cosmochim. Acta, 52*, 2749-2765.

Giggenbach, W.F., 1991: Chemical techniques in geothermal exploration. In: D'Amore, F. (coordinator), *Application of geochemistry in geothermal reservoir development*. UNITAR/UNDP publication, Rome, 119-144.

Gudnason, E.Á., Arnaldsson, A., Axelsson, G., Magnússon, I.Th., Berthet, J.C.C, and Halldórsdóttir, S., 2015: Analysis and modelling of gravity changes in the Reykjanes geothermal field in Iceland, during 2004–2010. *Proceedings of the World Geothermal Congress 2015, Melbourne, Australia*.

Gunnarsson, I. and Arnórsson S., 2000: Amorphous silica solubility and the thermodynamic properties of H_4SiO_4° in the range of 0° to 350°C at P_{sat}. *Geochim. Cosmochim. Acta, 64*, 2295-2307.

Hjartarson, Á. and Sæmundsson, K. 2014: *Geological map of Iceland. Bedrock 1:600 000*. ISOR-Iceland GeoSurvey, Reykjavik.

Jóhannesson, H., 1991: The mountains west of Eyjafjordur, In: *The Icelandic Tourist Association yearbook 1991* (in Icelandic). The Icelandic Tourist Association, Reykjavík, 246 pp.

Kharaka, Y.K., and Mariner, R.H., 1989: Chemical geothermometers and their application to formation waters from sedimentary basins. In: Naesar, N.D. and McCollon, T.H. (editors), *Thermal history of sedimentary basins.* Springer-Verlag, New York, 99-117.

Mwihava, N., 2004: United Republic of Tanzania - Brief on Status of Geothermal Energy. *International Conference "Gethermal Energy Territory" Pemarance, Italy 29-30, Conference Volume* 217-220.

Nicholson, K., 1993: *Geothermal fluids: chemistry and exploration techniques*. Springer-Verlag, Berlin, 268 pp.

Ochmann, N., and Garofalo K., 2013: *Geothermal energy as alternative source of energy for Tanzania.* BGR Final Report.

Pope, L.A., Hajash, A., and Popp, R.K., 1987: An experimental investigation of the quartz, Na-K, Na-K-Ca geothermometers and the effect of fluid composition. *J. Volcanol. Geotherm. Res., 31*, 151-161.

Saemundsson, K., 1979: Outline of the geology of Iceland. *Jökull 29,* 7-28.

Schlitzer, R., Roether, W., Weidmann, U., Kalt, P., and Loosli, H. H., 1985: A meridional 14C and 39Ar section in northeast Atlantic deep water. *Journal of Geophysical Research: Oceans (1978–2012)*, *90*(C4), 6945–6952.

Sekento, L. R.., 2012: Geochemical and isotopic study of the Menengai geothermal field, Kenya. Report 31 in: *Geothermal Training in Iceland 2012*. UNU-GTP, Iceland, 769-792.

Verma, S.P., and Santayo, E., 1997: New improved equations for Na/K, Na/Li and SiO_2 geothermometers by outlier detection and rejection. *J. Volcanol. Geotherm. Res., 79*, 9-23.

Verma, M.P., 2000: Chemical thermodynamics of silica: a critique on its geothermometer, *Geothermics 29*, 323-346.

UNITED NATIONS UNIVERSITY
UNU-GTP
Geothermal Training Programme

Orkustofnun, Grensasvegur 9,
IS-108 Reykjavik, Iceland

Reports 2015
Number 21

PROJECT REVIEW OF GEOTHERMAL SPAS´ CONSTRUCTION IN KENYA AND ICELAND

Peketsa Mwaro Mangi
Kenya Electricity Generating Company Ltd. - KenGen
P.O. Box 785-20117, Naivasha
KENYA
pmangi@kengen.co.ke

ABSTRACT

This study reviews the project management approach that was adopted during the construction of the Blue Lagoon, Mývatn Nature Baths and the Olkaria Geothermal Spa, as well as the brine flow system of the three spas. The level of application of a project management approach in a project is dictated by the uncertainties in the outcome of the project, current and emerging risks, threats and opportunities in the business environment, the scope of the project, the stakeholder environment, cost, objective of the project, quality and the phase of the project. Both the Blue Lagoon and Mývatn Nature Baths project outcomes were well known, based on previous knowledge of the popularity of bathing at the Blue Lagoon, and therefore a strict project management approach with no flexibility in schedule, time, resources and scope was adopted. Meanwhile, the Olkaria Geothermal Spa adopted a flexible project management approach that allowed for scope, design and improvement changes. For direct use projects that have no previous baseline data, phased development is recommended because of the uncertainties associated with the outcome of the project. It is also concluded that management of the brine flow system in a geothermal spa is important in ensuring a quality of service that meets customer expectations.

1. INTRODUCTION

Since 1981, the use of geothermal resources in Kenya was mainly confined to electricity generation. Currently, the total installed capacity in geothermal power plants in Kenya stands at 630 MWe. Out of this, the Kenya Electricity Generating Company, Ltd. (KenGen) contributes 513 MWe. In the late 1990s, direct use applications on a commercial scale were adopted by the Oserian Development Company in the form of greenhouses. Before this, Lake Bogoria Resort used warm water from a nearby spring to establish a spa.

To diversify the use of the geothermal resource in the Olkaria geothermal area, KenGen has constructed a geothermal spa. The construction of the spa started in April 2011 and was completed in June 2013. Currently it receives about 14,000 visitors a year. In Iceland, the first and now world acclaimed Blue Lagoon was opened to members of the public in 1987 and later commercialized in 1994. It utilises brine from the Svartsengi geothermal power plant, which is owned by HS Orka hf. Today, it is one of the greatest tourist attractions in Iceland, with over 700,000 visitors recorded in 2014 (Ragnarsson, 2015).

A second lagoon, Mývatn Nature Baths was constructed in the northern part of Iceland from October 2003 to June 2004 and currently receives about 200,000 visitors a year.

During the construction of the spa in Kenya, project management challenges were encountered which contributed to a delay in the completion of the project. In addition, there were technical challenges in the design of the brine flow system from the reinjection line through the spa to the reinjection well. This created a challenge in the management of the temperature of the brine.

The study objectives are to:

i. Review the level of project management approach that was applied at the Olkaria Geothermal Spa, the Mývatn Nature Baths and the Blue Lagoon during the initiation, planning, implementation and closure, in relation to project management processes of scope, quality, cost, and time control, communication management, stakeholder management, human resource management, risk assessment, procurement and the integration of these areas.
ii. Propose a suitable project development approach for similar geothermal direct use projects.
iii. Review the brine flow system of the three geothermal spas and provide a recommendation for improvement of brine flow control at the Olkaria Geothermal spa and for similar projects.

This paper gives an introduction to the study, a review of literature on direct uses of geothermal energy in order to provide an understanding of the project environment as well as a review of literature on project management principles and techniques. It also includes the background of the study, data collection methods used, a presentation and discussion of the results, and conclusions and recommendations. In the discussion of the results, the level of understanding of project management principles and application or adoption of ten knowledge areas is rated. These are: integration management, scope management, time management, cost management, quality management, human resource management, communication management, risk management, procurement management, and stakeholder management during the initiation, planning, implementation and closure of the three projects.

The standards which describe the ten knowledge areas and which have been used for this study include the Project Management Body of Knowledge (PMBOK) guide, ISO 21500 (ISO, 2012) and the International Project Management Association Competence Baseline –ICB (IPMA, 2006). A rating of 1 to 5 is used where 1 represents least understanding of project management principles and application or adoption of the ten knowledge areas, while 5 represents excellent understanding of project management principles and application or adoption of the ten knowledge areas. Conclusions and recommendations are made on the level and applicability of a project management approach as dictated by uncertainties in several areas, including: project outcomes, emerging opportunities and threats, risks, and stakeholder influence and control, suitable project development approach for direct use projects; and the brine flow system of the three geothermal spas.

Due to the technical nature of the three projects, and in order to understand the project management approach that was adopted, some technical aspects are mentioned within the project management processes. However, specific technical reviews and recommendations, including drawings and technical literature that help to clarify the discussion in the project management approach and which will be used to improve the quality of the Olkaria Geothermal Spa, are referenced and presented in the appendices and do not form the main body of the paper.

2. LITERATURE REVIEW

For centuries, swimming in warm water from hot springs was the widely known direct use of geothermal energy. This provided recreation to many people and improved their quality of life. Today, direct utilisation of geothermal energy is gaining momentum and total installed capacity has increased over

the years. Some of the direct uses of geothermal energy today are geothermal heat pumps, greenhouses, aquaculture, agricultural drying, industrial uses, cooling, snow melting, space heating, bathing and swimming. The total installed capacity, reported at the end of 2014 for geothermal direct utilisation worldwide is 70,329 MWt, a 45.0% increase from 48,493 MWt since 2010, an annual growth rate of 7.7%. The total annual energy use is 587,786 TJ, indicating a 38.7% increase from the 423,830 TJ/yr in 2010, an annual growth rate of 6.8%. The worldwide capacity factor is 0.265 (equivalent to 2,321 full load operating hours per year), down from 0.28 in 2010, 0.31 in 2005 and 0.40 in 2000. The lower capacity factor and growth rate for annual energy use is due to the increase in geothermal heat pump installations which have a low capacity factor, 0.21, worldwide. Total installed capacity for direct uses in Iceland as of 2014 was 2,040 MWt. Total energy use for space heating was in total about 26,700 TJ, which corresponds to 7,417 GWh. Total installed capacity for direct use in Kenya is 82.40 MWt with energy use of 182.62 TJ, corresponding to 50.73 GWh (Lund and Boyd, 2015). Figure 1 shows the global installed direct use geothermal capacity and annual utilisation from 1995 to 2015.

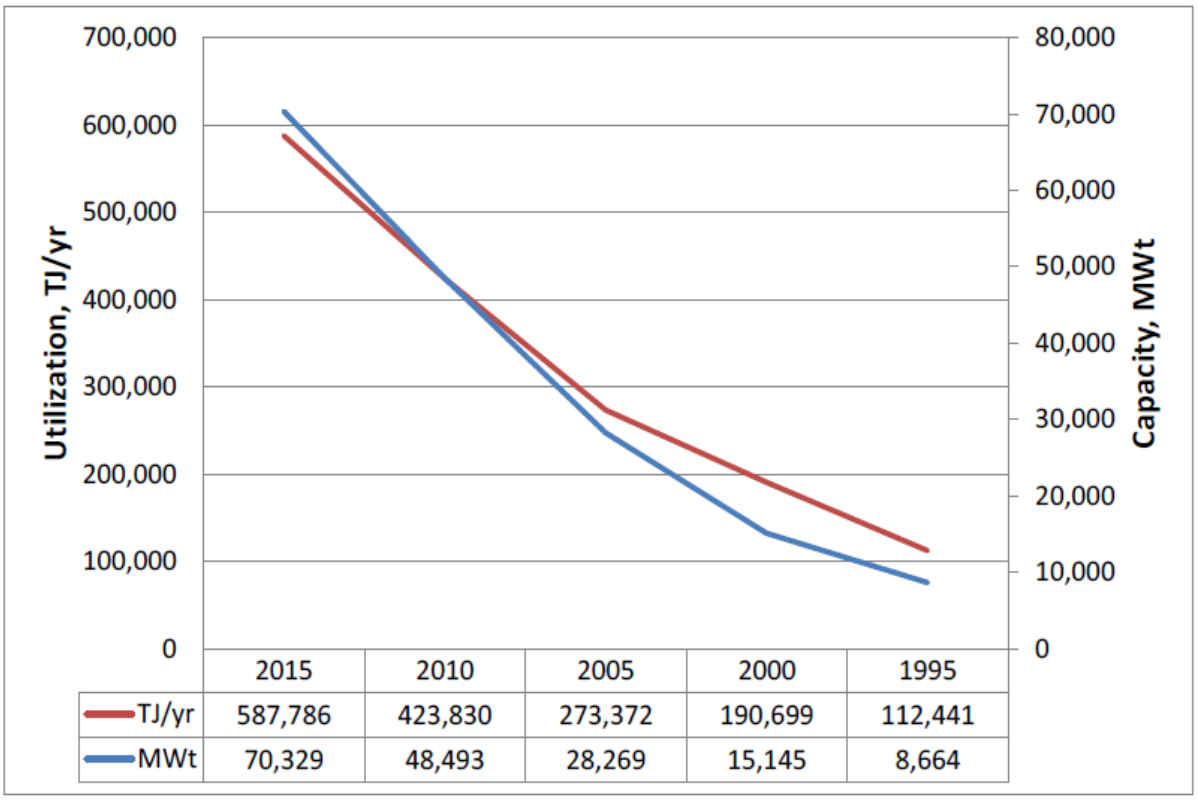

FIGURE 1: Global installed direct-use geothermal capacity and annual utilisation from 1995 to 2015 (Lund and Boyd, 2015)

The above statistics show steady increase in the development of direct use of geothermal energy, and therefore an increase in the number of direct use projects. In Kenya, direct use projects were confined to rudimentary water harvesting from fumaroles for domestic use, mainly in Eburru and to a smaller extent at Olkaria, drying of pyrethrum at Eburru and a spa establishment at Lake Bogoria Resort. In 2003, Oserian Development Company leased a well from KenGen and used geothermal energy to heat their greenhouses at night and as producer of carbon dioxide to increase carbon dioxide levels to further photosynthesis in the plants to promote their growth (Mariita, 2010). To diversify the geothermal utilisation in the Naivasha region, were Olkaria is located, KenGen constructed a geothermal spa in the years 2011-2013, where visitors can enjoy warm bathing and the balneological effects of the brine on their skins.

As the development of direct utilisation of geothermal energy gains momentum, and more and more direct use projects are implemented, there is a need to adopt a project management approach in their

initiation, planning, implementation and closure, so as to increase the number of successful projects. A project management approach reduces the risks, and failure, and increases a timely delivery of project, while at the same time ensuring that quality as well as the project objectives are achieved. This creates a positive impact on the project teams and the client. Burke, 2004, argues that more and more organisations are accomplishing their businesses through projects and that a management by projects approach has been used in engineering, construction, aerospace, and now in other disciplines such as medicine, system development, and energy.

According to PMBOK Guide (PMI, 2013), project management is the application of knowledge, skills, tools, and techniques to project activities in order to meet the stakeholders' needs and expectations from a project. Reiss, 2007, on the other hand, defines project management as a collection of loosely connected techniques, some of which are useful in bringing projects to a successful conclusion. PMBOK identifies ten knowledge areas that are critical in the management of a project. The ten knowledge areas: integration management, scope management, time management, cost management, quality management, human resource management, communication management, risk management, procurement management, and stakeholder management, are described here below. ICB reinforces the importance of the ten knowledge areas in its description of forty-six competence elements that are crucial for a project manager to be able to effectively apply the knowledge, skills, tools and techniques as advocated by PMBOK (PMI, 2013).

Project integration
This process integrates the four main project management processes of initiation, planning, implementation and closure. It involves bringing together inputs from several knowledge areas and ensuring that the inputs are deployed for the success of the project.

Scope management
This includes all the processes that are required to ensure that all the activities and tasks of the project, that are required so as to achieve the deliverables and objectives, are completed. The project manager may be required to identify the activities and tasks that constitute the scope, but also those that are not part of the scope. Scope management constitutes: scope planning, definition, scope change management and scope verification, normally determined during initiation and also during implementation and closure.

Time management
This is the management process that ensures that the project is delivered within the stipulated time and according to schedule. This process is affected by a number of factors, which include scope variations, availability of finances, supplier or contractor management, and poor management of tasks and deliverables. Time management therefore consists of activity definition, activity sequencing, duration estimation, schedule development and time control.

Cost management
This consists of resource planning, cost estimating, cost budgeting, cash flow and cost control. The objective of cost management is to ensure that the project is completed within budget.

Quality management
Quality is a constituent of the inherent characteristics of the project deliverable that meets the expectation of the user or customer or client. The project, therefore, should satisfy the needs for which it was intended. The quality of the project is tied to the design of the project, in line with customer requirements. Quality management includes quality planning, quality assurance, and quality control.

Human resource management
The human resources deployed should be effectively managed so as to deliver value to the project. Management of human resources involves identification of the appropriate talent and skills and deployment of these skills to specific areas of the project. It also involves ensuring that the human

resource remains motivated during the project. The process involves organisation planning, staff acquisition, and team development.

Communication management
This process ensures that project information is collected and disseminated without putting the project in jeopardy. Some information may be sensitive and only to be shared among certain personnel. That means the information dissemination should be based on a clear policy of a need to know basis. Communication management consists of communication planning, information distribution, project meetings, progress reporting and administrative closure.

Risk management
This process involves the identification of risks, risk quantifying and impact, and risk control. In a project, risks exist before a project but can also emerge as the project is in progress. A risk control process must be activated during the project so as to minimise project failure.

Procurement management
Procurement in a project involves the procurement of project materials as well as contractors. It involves the procurement of goods and services from outside the project team, and constitutes procurement planning, source selection, contract administration and contract closeout.

Stakeholder management
This includes the process required to identify and manage the project sponsor, customers and other interested parties that may have impact on or are impacted by the project, either positively or negatively. Before the start of a project, it is important that all the stakeholders of the project are identified and their impact or influence to the project mapped. A stakeholder management plan should then be developed based on their degree of influence or impact.

3. BACKGROUND OF THE STUDY

3.1. Olkaria Geothermal Spa

Occupying an area of 4.5 ha, the spa, shown in Figure 2, is located at the Olkaria geothermal field in Naivasha, in the Kenyan Rift Valley, about 120 km from Nairobi and within the Hell's Gate National Park. The Olkaria geothermal field, one of the high-temperature geothermal fields in Kenya as shown in Figure 3, belongs to the Kenya Electricity Generating Company, Ltd. (KenGen), which has a development licence for the field covering a total area of 204 km^2. KenGen owns a part of the land, and obtained a lease from the Kenya Wildlife Service (KWS) for the part of the land that belongs to KWS. To manage the relationship between KWS and the company, a memorandum of understanding (MoU) on the management of the land was signed. Currently, KenGen operates four geothermal power stations in Olkaria, Olkaria I (45

FIGURE 2: Panoramic view of the Olkaria Geothermal Spa

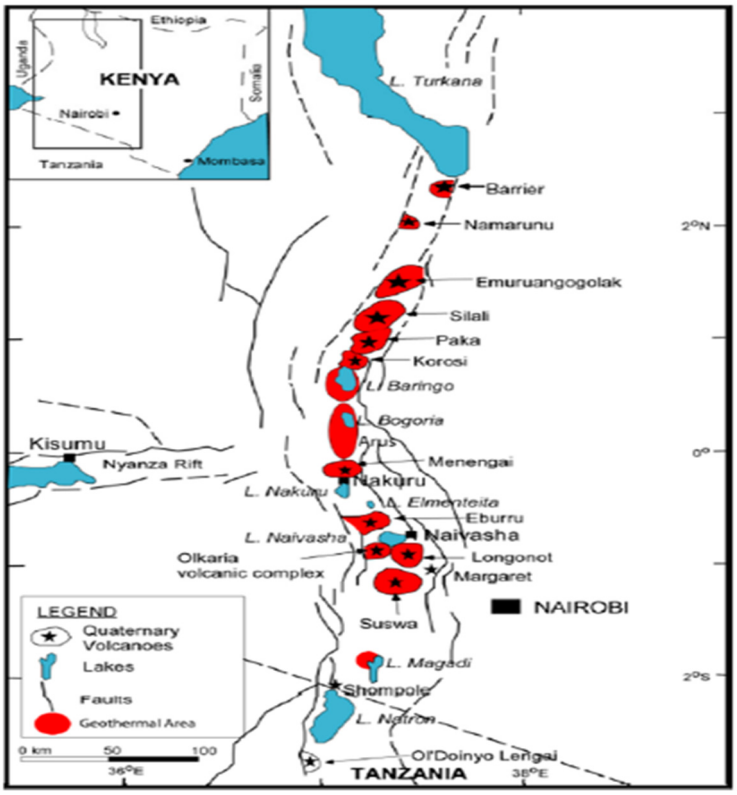

FIGURE 3: Location of Olkaria volcanic complex

MWe), Olkaria II (105 MWe), Olkaria I units 4 & 5 (140 MWe) and Olkaria IV (140 MWe) (Mangi, 2014). In addition to the power plants, KenGen generates a total of 55.6 MWe from nine wellhead units. Alongside the operation of the power plants, KenGen sells steam to Oserian Development Company for the generation of 4 MW from two power plants.

The construction of the geothermal spa is one of the efforts the company is undertaking to diversify the geothermal resource utilisation. The idea to construct the Olkaria Geothermal Spa was first introduced in 2008 and research was thereafter carried out to determine the brine suitability for bathing. Construction of the spa and the facilities started in April 2011 and was completed in July 2013. The construction was undertaken in-house at KenGen and brought together functions across departments that included: civil engineering, reservoir and steamfield and research and consultancy. Initially, the spa was to consist of small size lagoons with the largest being 1,500 m^3 but as the project progressed, the size of the large lagoon was modified to 3,500 m^3 and an administration block was added, which has changing rooms, an exhibition room and a restaurant. Later, an additional pool for children was added. Other services planned alongside the spa are a conference facility, a sauna, a steambath, a cable car, a children's park, and a picnic area.

The spa is located near the main reinjection line to reinjection well OW-708. Total brine flow to well OW-708 is 300 tonnes/hr, of which 140 tonnes/hr is available for the spa. The brine flow system through the spa and to the reinjection well is manually controlled. This has created a challenge in the management of the temperature to the required range. It has also become costly due to overtime payments to personnel. The brine availability and proximity to the reinjection line are some of the factors that determined the location of the spa. Another factor was the topography of the area that allowed gravity flow of the brine from the receiver lagoon. Due to its location in the park and near the geothermal power plants, the spa was expected to benefit from the tourists who visit the park and the many visitors and students who visit the power plants. The short distance of about 120 km from Nairobi, 80 km from Nakuru town and 35 km from Naivasha town was also expected to provide convenience for many people to visit the spa.

Design of the brine flow system

The layout of the spa consists of four cascading blue lagoons. The temperature of the brine is manually regulated. The brine is flashed into the first lagoon at 150°C through a pipe designed and constructed to collect the brine as it bubbles out. A silencer in the first lagoon muffles the noise during the flashing of the brine. The hot water pipe to the first lagoon has two valves for safety reasons, but they are also used to control the flow of the brine. The brine flows into the first lagoon at about 91°C and when it fills up, the brine overflows into the second lagoon at about 85°C through an open tunnel, which is the only entry to the second lagoon. The brine in the second lagoon, which is slightly bigger than the first lagoon, cools to about 84°C before exiting into the third and largest lagoon at about 69°C through a single entry. The

outlet temperature in the largest lagoon is 46°C. These values assume a total flow rate of 140 tonnes/hr in an 8" pipe.

At full flow, the three lagoons, assuming that they were empty at the start, fill up in 23 hours. To manage the temperatures in the large lagoon to between 30 and 35°C, after the initial fill up of the lagoon, the brine was left to cool to the desired temperature. Later on, to maintain the temperature within the desired range, the valve on the brine line at the first lagoon is opened, while at the same time, part of the brine in the third lagoon is drained to the reinjection well OW-R1 through a drain at the base of the lagoon. The hot brine replaces the cooler brine that is drained and heats up the remaining brine. This process is repeated daily with the valve being opened from 0700 hours to 1600 hours, thus heating up and filling the largest lagoon which is used for bathing. The layout of the lagoons and the brine flow system from the reinjection line through the lagoons to the reinjection well are shown in Appendix I, Figures 1 and 2.

3.2 The Blue Lagoon

The Blue Lagoon, shown in Figure 4, is located on the Reykjanes peninsula in SW-Iceland, which is primarily composed of porous lava (Gudmundsdóttir et al. (2010)). The Blue Lagoon was first created when hot brine from Svartsengi power plant was discharged into the adjacent lava field after the installation of the power plant, around 1980. Soon after the lagoon was formed, its healing effects on psoriasis patients were discovered. The Icelandic Psoriasis Foundation built a primitive shelter to make it possible for its members to change clothes and shower after bathing. Later, the members were given an old mortuary, no longer in use, which served its new purpose shelter for changing clothes at the Blue Lagoon for a number of years. In 1987, the first bathing facilities for public opened. Until then the public and people with psoriasis had been bathing in the lagoon and using the primitive available housing. An idea to construct a lagoon on a commercial scale developed and this formed the main objective of constructing the current Blue lagoon.

FIGURE 4: The Blue Lagoon spa facility

The Blue Lagoon, Ltd., was founded in 1992 to develop health-related tourism related to the Blue Lagoon. The company took over the operation of the Blue Lagoon facilities in 1994 and opened a treatment centre for psoriasis patients in cooperation with the Icelandic health authorities the same year. Scientific studies on the healing power of the Blue Lagoon were conducted in 1992-1996. This research provided data essential for the Blue Lagoon to become recognized by the Icelandic health authorities as an official treatment centre for psoriasis (Gudmundsdóttir et al., 2010). According to Haraldsson and Lloret Cordero (2014), the Blue Lagoon contains about 6 million litres of brine and the hydraulic retention time is about 40 hours. The salt content is 2.5%, close to 70% of that of sea water.

The Blue Lagoon also produces skin care products that contain unique natural ingredients, silica, minerals and algae. The number of Blue Lagoon visitors has increased rapidly during the past years and reached 700,000 in 2014, making it one of Iceland's most popular tourist attractions (Ragnarsson, 2015). The initial scope of the project included: the construction of a 5,000 m^3 lagoon as well as a 1,000 m^3 lagoon as part of the treatment centre for psoriasis and other skin ailments which has 35 rooms, the renovation of the existing facilities to include changing rooms, and the construction of the brine flow

system. Other services developed alongside the lagoon were: two cafeterias, a restaurant, laundry services, and a beauty products shop. Blue Lagoon is currently constructing a five-star hotel and expanding the Blue Lagoon by 3,000 m^3, which is the second expansion phase of the project. The expansion will cover an area of 8,500 m^2, in addition to the current areal occupation of 7,500 m^2. The second phase of the Blue Lagoon project will cost about US $47,000,000.

3.2.1 Design of the brine flow system

At the Blue Lagoon, brine used in the lagoons is obtained from the separator station serving the Svartsengi power plant. Part of the separated brine (152°C, 5.5 bars) that goes to a reinjection well flows into a 250 mm (10") diameter brine pipe to the lagoon. The brine pipe is reduced from 10" to 3" and finally to 2", to which 15 mm diameter nozzles are connected, that discharge brine into the lagoon. The pipe is fitted with pneumatic valves, and solenoid valves are fitted on the air control system. The air control system opens the valves along the system so there is a provision for an overflow of the brine in case there is a problem with the reinjection system to the well. Temperature sensors are located in the brine along the edge of the lagoon. When temperatures fall below 40°C, or as otherwise set in the control system, the temperature sensors signal the valves to open. Hot brine flows in through the 15 mm diameter nozzles at high pressure and sucks the cold brine from the bottom of the lagoon, creating a convectional current, and mixes with it until temperature reaches 39-40°C at which point the valves close and the flow stops.

In total, there are eight brine inlets into the lagoon. Due to the inflow of brine into the lagoon during the regulation of the temperatures, there is an overflow to the surrounding lava field. A schematic flow diagram of the brine flow is shown in Appendix II, Figure 1. Along the edge of the lagoon is a waterfall area where the brine is pumped through overhead showers and jutes out in moderated quantity and at certain pressure to massage the muscles of visitors. In the steambath, the brine is pumped through nozzles and temperature sensors regulate the flow of steam through valves. If the temperature drops below the 40-44°C range, or other set temperatures, the sensors signal the valves to open and brine steams out through the nozzles until the temperature range of 40-44°C is achieved, after which the valves close and steam flow is stopped.

3.3 Mývatn Nature Baths

FIGURE 5: Myvatn Nature Baths (Gudmundsson, 2015)

Mývatn Nature Baths, shown in Figure 5, are near the village of Reykjahlíd, which is situated on the shores of Lake Mývatn in N-Iceland. It is far away from Reykjavík (Travelandscape, 2013), and located within the Námafjall geothermal field.

According to an interview with Jóhann F. Kristjánsson, 2015, before 1998, people constructed makeshift structures on fumaroles coming out of cracks on the ground. It was later realised that it was in the interest of the community if more durable material was used to construct a permanent structure where people could enjoy a steambath. In 1999, an interest group constructed a structure in the area to tap the fumaroles for a steambath and an idea to construct nature baths for the area was conceived. A five-year research on the temperatures and chemistry of hot springs in the Mývatn

area was commissioned after the interest group obtained a grant from an innovation fund created by the Icelandic government and the local municipality. After the research, the interest group registered a company with the objective of constructing a lagoon to serve the community and visitors. The Mývatn Nature Baths were constructed from October 2003 to June 2004.

The Mývatn Nature Baths use brine from one of the nearby high-temperature wells drilled in 1976 meant for steam generation for a diatomite factory. The scope of the project included the construction of a 2,550 m^3 lagoon, an administration block that had changing rooms, and a brine flow system. Other services planned alongside the lagoon included a souvenir shop, a cafeteria and laundry. Construction was done by contractors as per the initial design and no major changes were implemented. Initially, the brine flow was managed manually but automatic temperature controls were introduced during operations.

3.3.1 Design of the brine flow system

Two-phase geothermal fluid from the nearby brine well enters a separator where brine is separated from steam. The separated brine at 180°C with a flow rate of 40 l/s flows into a heat exchanger where it heats fresh water for district heating. It exits the heat exchanger at 130°C with a flow rate of 20 l/s. This brine is collected in a reservoir and maintains a top temperature of 98°C. Inside the reservoir, a coil (heat exchanger) carrying fresh water runs through, which heats water that is used in the Mývatn Nature Baths buildings. The reservoir has an overflow which drains excess brine to a reinjection well. The brine from the reservoir flows by gravity to the lagoon and enters at about 80°C. To reduce this temperature to between 38 and 40°C, circulating pumps behind rock formations within the lagoon transfer the cold brine at the bottom of the lagoon and create convectional currents. This mixes the hot and cold brine and thus reduces the temperature to 38-40°C or to different desired temperature.

The brine from the main reservoir enters the lagoon at five points with automatic temperature controls. When temperatures drop, the thermostats signal the valves to open up and allow in more brine from the main reservoir until temperatures of 38-40°C are achieved after which the flow stops. Due to the inflow of brine into the lagoon during this process, there is an overflow to the reinjection well that takes in the excess brine. A schematic flow diagram of the brine flow is shown in Appendix II, Figure 2. Along the edge of the lagoon is a waterfall where the brine is pumped through overhead showers and jutes out in moderated quantity and at a certain pressure thus massaging the muscles of those under the waterfall.

4. METHODOLOGY

The following data collection methods were used:

i. *Documentary sources:*
   Information available on direct uses of geothermal energy, the concept/initiation, planning, construction and closure of geothermal spas in Kenya and Iceland was collected.
ii. *Observation method:*
   The author visited the Blue Lagoon and the Mývatn Nature Baths on 2nd June 2015 and 9th July 2015, respectively, and later visited the Blue Lagoon again on 22nd September 2015.
iii. *Interviews:*
   Interviews were conducted with staff who were involved in the design of the brine flow system for the three geothermal spas and with those who were involved in project management during the construction of the spas. Additionally, for the Blue Lagoon, an interview was conducted with a staff member who is currently involved in the operations of the brine flow system (see interview schedule, Appendix III). For the Olkaria Geothermal Spa, the information presented is based on personal experiences by the author who was the project manager during the initiation, planning, and construction.

iv. Data analysis and presentation:
The data collected was analysed and presented focusing on the project management approach that was adopted during the initiation, planning, implementation and closure of the three projects. The analysis of the level of project management applied is based on the project manager's understanding and application of the ten knowledge areas as described in PMBOK guidelines and ISO 21500 and elaborated in ICB. A review of the design of the brine flow from the well/s, power plant or reinjection line to the geothermal spas and into the reinjection well or disposal system is also presented.

For the discussion of the level of application of project management approach, a rating was determined based on the application of the ten knowledge areas as defined in PMBOK guidelines and ISO 21500 as well as application of the competences as described in the ICB. A rating of 1-5 was adopted, where 1 represents poor understanding and/or lack of application of one or more of the ten knowledge areas and/or competences as described in ICB, while 5 is the highest as described in Table 1. To rate the main phases, the average of the ratings of the knowledge areas or competences was calculated and rounded off to the nearest number. The author, through an objective analysis of the data, determined the rating.

TABLE 1: Rating of project management approach

Grade	Description
1	Poor understanding and adoption of project management techniques, poor application of knowledge areas or technical, behavioural and contextual competences.
2	Fair understanding and adoption of project management techniques, knowledge areas or technical, behavioural and contextual competences.
3	Good understanding and adoption of project management techniques, knowledge areas or technical, behavioural and contextual competences.
4	Very good understanding and adoption of project management techniques, knowledge areas or technical, behavioural and contextual competences.
5	Excellent understanding and adoption of project management techniques, knowledge areas or technical, behavioural and contextual competences.

Conclusions and recommendations were made on the application of the project management approach as dictated by: risks associated with the project, emerging opportunities and threats in the business environment, the size of the project, the objective of the project, the stakeholder environment, cost, business environment, quality and the current phase of the project. In line with this, further recommendation is given on the development approach for direct use projects. Specific technical recommendations on the brine flow system and enhancement of usage of the brine for the Olkaria Geothermal Spa are also given (Appendix I, Figure 3).

5. RESULTS AND DISCUSSION

The problems encountered at the Olkaria Geothermal Spa were partly contributed by an inadequate project management approach that resulted in some key steps in the process being overlooked. This included the design aspects of the brine flow system during planning as well as adequate planning for procurement and identification of alternatives.

The level of application, however, differed from one project to another. From the review and analysis of the information gathered, overall project management approach was adopted at a rating of 3 for Olkaria Geothermal Spa, rating of 4 for Mývatn Nature Baths and rating of 5 for the Blue Lagoon. These results indicate an application of a strict project management approach and project integration at the Blue Lagoon and the Mývatn Nature Baths with no flexibility, or float or buffer provision, for time,

scope and cost. On the other hand, the project management approach at the Olkaria Geothermal Spa was more flexible and did not adhere to strict project management approach as advocated by PMBOK guide and ISO 21500. Details of the application of the project management approach are discussed below in line with the four project life cycles of: concept/initiation, planning, implementation and closure, and the ten knowledge areas as described in PMBOK guide, ISO 21500, and emphasised in ICB. The ratings are presented in Appendix IV.

5.1 Concept and initiation

The Olkaria Geothermal Spa was rated 3 for concept and initiation, Mývatn Nature Baths 4 and Blue Lagoon 4. For both Mývatn Nature Baths and the Olkaria Geothermal Spa, concept development was dictated by necessity while for Blue Lagoon, the concept was driven by a commercial agenda. Mývatn Nature Baths intended to provide a bathing facility for the community while for the Olkaria Geothermal Spa, there was a need to diversify the geothermal resource utilisation. On the other hand, the Blue Lagoon realised an opportunity to expand the bathing facility arising from reports of people getting healed of psoriasis and skin ailments after taking baths in the area.

For the Olkaria Geothermal Spa, the objectives of the construction of the spa were not specific, measurable, achievable, realistic, nor time bound and this affected the rating, while objectives for the Mývatn Nature Baths and the Blue Lagoon objectives were to construct lagoons and were therefore specific to the projects.

Concept and initiation of the Olkaria Geothermal Spa took two years of research while it took five years for the Mývatn Nature Baths and more than five years for the Blue Lagoon. To avoid project failure, adequate planning is necessary. All aspects of a project must be taken into account, including the project risks and viability. In the case of a direct use project like geothermal spas, assessment of brine availability and suitability is critical because unavailability or unsuitability of the brine may kill the project. Adequate time must be provided for research.

Olkaria Geothermal Spa rated poor at 1 on ethics analysis because no ethics analysis was done, nor were project rules and regulations made clear to the project team. The Mývatn Nature Baths and the Blue Lagoon rated fair at 2, because project rules and regulations were made clear to the project team. The importance of ethics analysis is best described by Jónasson and Ingason (2013), who argue that ethics govern the conduct of the individual, the team, and the organisation in a project, define the relationships, and sets out behaviour and expectations. Definition of project ethics helps to reduce conflict, and where it arises, helps the project manager to deal with conflict without prejudice or bias.

Project charter
For the Olkaria Geothermal Spa, a proposal based on a payback period financial model was submitted and therefore it rates fair at 2, while the Blue Lagoon prepared a project charter and therefore rates excellent at 5. Mývatn Nature Baths rates good at 3 because while no project charter was done, a business plan that captured aspects of a charter such as the risks, stakeholders, project costs and business focus was done. A project charter presents a refining of the business case for a project on which the board or management of the company makes a decision on whether to proceed with the project or not. A project charter also provides the project plan in terms of: project team composition, refined design and a simulation of options, refined quality management plan and refined objectives in view of any changes in the market, refined stakeholder management plan, refined project controls, schedules, and resource requirements including cost. Without a project charter, the project becomes exposed to risk of being no longer relevant due to a changing business environment.

Project team
The Olkaria Geothermal Spa rated 4 for project team while both Mývatn Nature Baths and the Blue Lagoon rated 5. The Olkaria Geothermal Spa had a project manager who supervised three subproject

managers in charge of lagoon construction, building construction and the brine line. For Mývatn Nature Baths, the project had an overall project manager with three subproject managers in charge of lagoon, brine line and outside works; groundwork; and construction of the building. The project manager had authority to make decisions except those that entailed additional costs. For the Blue Lagoon, the project manager had authority to make decisions except those that involved large additional costs, and supervised contractors who were responsible for construction of the lagoon, construction of the treatment centre and renovation of the building; and the brine line.

Identification of stakeholders
Olkaria geothermal Spa rated 2 for stakeholder identification while both Mývatn Nature Baths and the Blue Lagoon rated 5. Olkaria Geothermal Spa did not identify and list the stakeholders but only made an assumption. Some of the stakeholders like Kenya Wildlife Service (KWS), senior management, staff, customers, local authorities, Ministry of Health and NEMA were only assumed. On the other hand, the Blue Lagoon identified contractors, HS Orka, Grindavík municipality, the Chief Executive Officer of the Blue Lagoon, members of the public, and environmental activists as stakeholders. Stakeholders for Mývatn nature Baths included Landsvirkjun - National Power Company, shareholders, landowners, environmentalists, members of the public, tourists, and local authorities.

5.2 Planning

Planning for the Olkaria Geothermal Spa was rated at 3 while both Mývatn Nature Baths and the Blue Lagoon were rated at 4. Ratings of processes under planning are presented below.

Time, scope, work breakdown structure, and activities
All the three projects identified the scope, work breakdown structure and carried out scheduling and determined the time that would be required. They all rated excellent at 5. According to schedule, the construction of the Olkaria Geothermal Spa was to take 4 months (see Table 2).

Meanwhile the construction time for the Mývatn Nature Baths was 7 months and 1½ years for the Blue Lagoon. The initial scope of the Olkaria Geothermal Spa included three cascading lagoons, an administration block and the brine line. The administration block has changing rooms, exhibition room and a restaurant and the brine line and reinjection system. Later, a fourth lagoon for children was added. Other services planned alongside the spa were a conference facility, sauna, steambath, cable car, a children's park, and a picnic area. The project was broken down into the construction of the lagoon, the building and the brine line and reinjection system.

Mývatn Nature Baths consist of a 2,550 m^3 lagoon, an administration block that has changing rooms, and the brine flow system. The building has a museum, a cafeteria and laundry. The project was broken down into three main functions, namely groundworks, lagoon and outside works, and the construction of the building. For the Blue Lagoon, the works were also broken down into three areas, namely, construction of the lagoon, construction of the treatment centre and renovation of the building, and construction of the brine line. All three projects sequenced, scheduled activities and estimated durations using MS project.

Resource estimation and project organisation
For Olkaria Geothermal Spa, 100 workers were required for the three components of the projects, and the project implementation team consisted of 16 staff from various departments of KenGen. Rough estimation of the requirements, both financial and labour, was done and for human resources, relevant competences were identified and deployed. For the Mývatn Nature Baths and the Blue Lagoon, detailed bills of quantities were done and cost estimated and the contractors provided personnel for the project. The projects were divided into functional areas that were headed by subproject managers. In addition,

the subproject managers had supervisory role over the individual sub project implementation team (PIT). In all the three projects, there was an overall project manager who had an overseeing role.

TABLE 2: Activities and schedules at Olkaria Geothermal Spa

Task name	Duration	Start	Finish	Prede-cessors	Resource names
Lagoons	**76 days**	**12.4.11**	**25.7.11**		
Excavations	50 days	12.4.11	17.6.11		Civil Technician (1)
Hardcore Fills	20 days	27.4.11	23.5.11		Unskilled Labour (7); Masons (2)
Concrete Works	20 days	24.5.11	20.6.11	4	Unskilled Labour (7); Masons (2); Carpenter (1)
Footpaths & Parking	20 days	21.6.11	18.7.11	5	Unskilled Labour (7); Masons (2)
Finishes	25 days	21.6.11	25.7.11	5	Unskilled Labour (4); Masons (2)
Building	**125 days**	**18.4.11**	**5.10.11**		
Substructure	**25 days**	**18.4.11**	**19.5.11**		
Excavations for Foundations	5 days	18.4.11	22.4.11		Unskilled Labour (8); Masons (2); Carpenter (1)
Foundation concrete works	10 days	7.5.11	19.5.11	10	Masons (2); Unskilled Labour (8); Carpenter (1)
Superstructure	**100 days**	**20.5.11**	**5.10.11**	**9**	
Walling	30 days	20.5.11	30.6.11		Masons (2); Carpenter (2); Unskilled Labour (8)
Roofing	20 days	1.7.11	28.7.11	13	Masons (2); Carpenter (2); Unskilled Labour (8)
Fitting & Fixtures	20 days	29.7.11	25.8.11	14	Masons (2); Carpenter (2); Unskilled Labour (8)
Finishes	30 days	26.8.11	5.10.11	15	Masons (2); Carpenter (2); Unskilled Labour (8)
Services	**102 days**	**7.5.11**	**25.9.11**		
Mechanical	**90 days**	**24.5.11**	**25.9.11**		**Mechanical technician (1); Plumbers (2)**
Plumbing & drain. for Lagoon	30 days	24.5.11	4.7.11		Mechanical technician (1); Plumbers (2)
Plumbing & drain. for Building	90 days	24.5.11	25.9.11		Mechanical technician (1); Plumbers (2)
Mechanical ventilat.	14 days	29.7.11	17.8.11		Mechanical technician (1); Plumbers (2)
Electrical	**90 days**	**7.5.11**	**8.9.11**		
Conduiting	40 days	7.5.11	30.6.11		Electrical Technician (1); Electrician (1)
Wiring & Fit-Out	30 days	29.7.11	8.9.11	14	Electrical Technician (1); Electrician (1)
External Lighting	20 days	19.7.11	15.8.11	6	Electrical Technician (1); Electrician (1)

Cost

Initial project cost for the Olkaria Geothermal Spa was estimated at US$300,000 but increased to US$500,000. No detailed bill of quantity was done. This cost excludes additional US$500,000 that was spent on equipment and electrical works. The project was fully funded by KenGen. Financing of the project was planned in line with the annual budgeting cycle of the company.

Both Mývatn Nature Baths and the Blue lagoon prepared detailed bills of quantities and the cost was US$1,000,000 for Mývatn Nature Baths. The two projects were financed by shareholders.

Risk identification and assessment

In risk analysis, both Mývatn Nature Baths and Blue Lagoon rate very good at 4. Olkaria Geothermal Spa rates fair at 2 because risks were not adequately addressed through a comprehensive business plan and the risk analysis that was undertaken was not exhaustive. Some of the risks that were identified were brine availability, reinjection system, brine chemical composition, safety risks, and approvals. The chemical composition of the brine was analysed and found to be suitable for bathing. Regarding safety, the spa is 1-1.5 m deep and warning signs were erected and rules and regulations published. Lifeguards are on site and visitors are not allowed into the spa past 18:00 hours. There are first aid kits and fire

extinguishers available in the building. Financial risk, customer availability and sustainability were not analysed and this exposed the project to financial loss.

For Mývatn Nature Baths, risk analysis was undertaken on the financial success, brine availability, reinjection system, brine chemical composition, and safety. A detailed financial and business plan was done which provided an assessment of the viability of the project. The brine is obtained from one of the wells drilled in the area, initially meant for a diatomite factory. The brine was analysed and found to be suitable for bathing. No reinjection system was designed for the project until 2014 when a 100 m depth reinjection well was drilled. Some of the safety measures taken include recruitment of lifeguards, limiting depth of the lagoon to a maximum of 1.5 m, availability of first aid and life-saving equipment and erecting warning signs. Environmental scoping licence and building designs approvals were obtained. However, Mývatn Nature Baths get inadequate brine to heat up the entire baths uniformly because the heat exchanger is not able to supply enough brine at the desired exit temperature of 130°C.

Some of the risks analysed for the Blue Lagoon project included financial risk and profitability, brine availability, and brine chemical composition. A lot of time was spent on designing a temperature management system that ensured the visitors' safety, since from previous experience, visitors to the lagoon got burnt during bathing when the brine from the separator flowed into the lagoon without notice. The brine was analysed and found to be suitable for bathing. Some of the safety measures taken were recruitment of lifeguards, lagoon depth limited to maximum of 1.5 m, availability of first aid and life-saving equipment and erecting warning signs. No environmental scoping was done because it was not required at that time. Approvals were obtained for the building designs and the use of brine for treatment of psoriasis and other skin ailments.

Quality
Olkaria Geothermal Spa rated 1 because there was no quality plan put in place while Mývatn nature Baths and the Blue Lagoon rated 4 and 5, respectively, because of developed quality plans. Methods used in the quality planning included regular inspection of works as per design and regular meetings.

Procurement
Olkaria Geothermal Spa rated poor at 1 on procurement plan while Mývatn Nature Baths and Blue Lagoon rated excellent at 5. The delay in completion of the Olkaria Geothermal Spa was mainly caused by procurement hiccups, scope change that impacted procurement and human resource unavailability. Such delays were not experienced at the Mývatn Nature Baths and the Blue Lagoon because contractors who were selected through restricted tendering were responsible for the supply of materials and labour. For Mývatn Nature Baths, 5% of the contract amount was levied to a contractor for every day of non-delivery or delay.

Communications
Olkaria Geothermal Spa rated poor at 1 on communication plan because no communication plan was developed. However, during the implementation of the project, the project manager was the point of communication. Mývatn Nature Baths and the Blue Lagoon rated at 5 because they had comprehensive communication plans and the project managers were the contacts for the projects. All the three projects used emails, status and progress reports, and verbal communication through telephones, telephone texts, as well as daily, weekly and monthly meetings.

Design of the brine flow system
The initial designs of the brine flow at the Olkaria Geothermal Spa and the Mývatn Nature Baths provided for manual control of temperature. This caused difficulty in managing the temperature of the brine to the required range of between 38 and 40°C for Mývatn Nature Baths and between 30 and 35°C for the Olkaria Geothermal Spa. Mývatn Nature Baths later automated the temperature control system when funds became available. Manual temperature control at the Olkaria Geothermal Spa is becoming expensive and untenable and this necessitates the need to install an automatic temperature control system.

Brine at Mývatn Nature Baths is being reinjected into a 100 m depth well. At the Blue Lagoon, there is no effective reinjection system for the used brine and brine overflows to the surrounding lava.

5.3 Implementation

Project management approach on implementation rated 4, 3, and 5 for Mývatn Nature Baths, Olkaria Geothermal Spa and Blue Lagoon, respectively. The ratings were affected by the level of application of the various knowledge areas or processes as described below.

During implementation, close supervision was required. Some project components ran concurrently and these required to be supervised, monitored, controlled and delivered within schedule and in adequate quality. Some of the methods that were used to monitor and control the scope and time included: regular meetings with supervisors and teams, daily, weekly, and monthly progress reports that were submitted to senior management, proper stage management, and identifying the need for and obtaining approvals for variations in good time.

Stakeholder management
Stakeholder management was rated fair at 2 for the Olkaria Geothermal Spa, and 4 and 5 for Mývatn Nature Baths and Blue Lagoon, respectively.

Olkaria Geothermal Spa rates at 2 on stakeholder management because there was no stakeholder management plan. Both Blue Lagoon and Mývatn Nature Baths had stakeholder management plans and this enabled them to obtain most of the initial funding of the projects from shareholders. They, therefore, rate 5 and 4 respectively. For the Olkaria Geothermal Spa, lack of stakeholder management plan resulted in inadequate engagement with stakeholders such as KWS, especially on visitors' entry charges. This has continued to be a problem as visitors are charged at the KWS-gate for entry into the Hell's Gate National Park as well as for entry at the spa.

Mývatn Nature Baths and Blue Lagoon had stakeholder management plans that enabled the companies to get initial financing for the projects. The importance of having a stakeholder management plan is best explained by PMBOK Guide (PMI, 2013), which states that identifying stakeholders, understanding their relative degree of influence on a project, and balancing their demands, needs, and expectations are critical to the success of the project. Failure to do so can lead to delays, cost increases, unexpected issues, and other negative consequences including project cancellation. Example of an unexpected issue that ought to have been resolved earlier is that visitors to the Olkaria Geothermal Spa pay entry fees at the KWS gate and also at the spa, which is costly.

Project team development
Before the start of a project, it is important to have a team building session during which project expectations, ethics, rules and regulations, and project objectives are made clear to the team. The team should also be trained on how to conduct quality inspections and supervision, so that the project is delivered to the client's expectations and within schedule. The PIT at Olkaria Geothermal Spa was not trained on interpersonal skills, supervisory skills, project scheduling, project controls, and quality auditing. No team building sessions were held nor were ground rules set. However, staff were given Key Performance Indicators (KPIs) upon which they were evaluated based on delivery and timelines. Olkaria Geothermal Spa, therefore, rates at 2 while PITs at Mývatn Nature Baths and the Blue Lagoon rated 4 because the various subproject managers had experience in project management.

Risk treatment and control
On risk treatment and control, Olkaria Geothermal Spa rated 2 while both Mývatn nature Baths and Blue lagoon rated 3. Risks identified during the implementation of the projects were addressed. For example, during the construction of the Olkaria Geothermal Spa, coarse finishing was done on the floor of the lagoon to make it less slippery. Stairs into the lagoon were modified to 4" to make them less deep. For

the Blue Lagoon, no reinjection system was designed for the project. However, shallow wells were later drilled to take in the brine. These got easily clogged up with silica and so as to the date of publication there is no effective brine reinjection system and the used brine is spreading into the lava field surrounding the lagoon. This is becoming untenable to the environment and can have an impact on stakeholder relationships.

Quality control
Olkaria Geothermal Spa rates at 3, Mývatn Nature Baths 4 and Blue Lagoon 5 on quality control. For Olkaria Geothermal Spa, the rating was affected by, among others, inadequate control of scope due to lack of change request forms despite the significant changes witnessed, and quality control on inadequate specifications especially on the brine flow system. This resulted in a manual temperature control system, while the Mývatn Nature Baths and the Blue Lagoon use automatic temperature control systems. However, all the three projects implemented quality control in line with specifications through on-site inspections, quality checks against design, consultations and regular meetings. Schedule and time control methods adopted by the three projects included regular meetings, taking daily records of the activities, and review of schedules against work delivered. Any corrective actions needed were recorded in notebooks and carried out so as to ensure quality as per design. Regular meetings were also held to identify areas of focus or corrections. At the Olkaria Geothermal Spa, time and schedule control was affected by poor selection of suppliers and a change of scope and this delayed the project by 1 year and 11 months. This was not the case for Mývatn Nature Baths and the Blue Lagoon where scope changes were minimal and contractors supplied the materials and a strict project management approach was adopted.

Supplier selection
The Blue Lagoon and Mývatn Nature Baths rated 5 on supplier selection because both projects procured contractors through restricted tendering. The contractors were responsible for supply of materials and labour during construction. On the other hand, Olkaria Geothermal Spa rated fair at 2. Suppliers of project materials were selected based on specifications and cost. Delay in procurement of materials delayed the construction of the Olkaria Geothermal Spa by 1¾ years. Some of the suppliers did not deliver materials, while obtaining approval for procurement of some of the items was sometimes deferred. Any deferment or non-delivery of materials increased the procurement timeline for any single item by six months which is the normal procurement cycle.

Information distribution
All the three projects rated 4 on information distribution. Information was distributed on a need to know basis. Methods used to distribute information included meetings, memos, letters, emails, mobile texts, verbal communication, and status reporting.

Scope control
On scope management, Olkaria Geothermal Spa and Mývatn Nature Baths rated at 3 and 4, respectively, while Blue Lagoon rated at 5. For both the Mývatn Nature Baths and the Blue Lagoon, no major changes were made to the original designs. Mývatn Nature Baths and Olkaria Geothermal Spa did not develop change request forms while the Blue Lagoon had change request forms which are critical for managing scope, cost, scheduling and accountability.

During the construction of the Olkaria Geothermal Spa, the source of the brine was changed. Initially, brine was tapped from the reinjection line from well OW-710 that connects to the main reinjection line to well OW-708. The construction was done from 1st June 2013 to 6th June 2013. After tapping the brine from the reinjection line from well OW-710, it was realised that the brine flow was cyclic and not adequate. A new brine line was constructed from 10th June to 30th June 2013 to tap brine from the main reinjection line to well OW-708. Furthermore, an additional lagoon for children was constructed. Changes at the Olkaria Geothermal Spa represent a flexible project management approach because the outcomes were not certain. If scope control was strictly adhered to, the children's lagoon would not have been added, nor would the size of the largest lagoon have been increased from 1,500 m^3 to 3,500 m^3.

Time control
On schedule and time control, Mývatn Nature Baths and Blue Lagoon rated excellent at 5 and Olkaria Geothermal Spa fair at 2. Construction of Mývatn Nature Baths took 7 months, the Blue Lagoon 1 ½ years, and Olkaria Geothermal Spa 2¼ years, while the original schedule was 125 days. For the Olkaria Geothermal Spa, this delay was caused mainly by procurement bureaucracy and non-delivery of some critical materials and occasional human resource unavailability. Supervisors ensured that work was assigned to teams as per the schedule and stage of works, with measured targets in terms of time and quality expectations, and getting concurrence from the supervisors and the foremen regarding the daily Key Performance Indicators (KPI). Alongside the KPIs, resource requirements were provided (if available) to ensure that no team stopped work due to lack of resources. The foremen, through their supervisors, submitted daily reports of their KPIs and these were reviewed against the schedule and required quality. For the Mývatn Nature Baths and the Blue Lagoon, construction was done by contractors as per the initial design and no major changes were done. The project management approach adopted at the Olkaria Geothermal Spa was flexible so as to accommodate any changes in scope or delays caused by quality improvement and procurement hiccups.

Cost control
Olkaria geothermal Spa rates 3 on cost control while Mývatn Nature Baths and Blue Lagoon rate excellent at 5. For the Olkaria Geothermal Spa, the cost was controlled through the recording of daily activities, daily material movements and inventory control, and review of actual costs against budget provision for specific components of the project. Inventory of the materials was reviewed daily to ensure no materials were lost or to determine if there was any additional requirement that needed to be provided for. At Mývatn Nature Baths and the Blue Lagoon, the contractors were directly responsible for the construction and the work was evaluated per deliverables to ensure that there was no cost overrun.

5.4 Closure

Project management approach on closure was rated excellent at 5 for the Mývatn Nature Baths, the Olkaria Geothermal Spa and the Blue Lagoon. The Olkaria Geothermal Spa is still being tested and therefore has not yet been closed. The project has now been handed over to a management board and an operations committee. The management board is responsible for resource mobilisation, marketing, talent management, and strategic planning for the facility, including any improvements to the spa operation, while the operations committee is responsible for the day to day running of the spa. Outstanding works include a conference facility, cottages and a cable car, as well as remedial works on the brine flow system and temperature management. After the construction of the spa and the administration building was completed, the PIT was retained but with minimum activity as it awaits the next phase of development. In line with partial closure of the project, all the documentation related to the project was collated and kept and a final project report was prepared, detailing the total cost of the project and outstanding works. During the test run, a number of challenges have been experienced that need to be addressed. These include: inadequate business planning resulting in fewer visitors now at 14,000 per year, and inadequate stakeholder management. Lessons learnt in the three projects include the following:

i. Documentation of all aspects of a project. This is normally overlooked and it can become a subject of auditing. All transactions including procurement and payments must be recorded and evidence kept.
ii. Projects of such magnitude should be contracted out. This will reduce time wasting on obtaining approvals for every single purchase which delays project delivery.
iii. All members of the project team must be officially released from their day to day duties so as to focus on the project.
iv. The project leader should learn to motivate teams to be able to perform under difficult circumstances.
v. Open communication by the project manager to the teams and other interested parties is essential for project success.
vi. Support from senior management is important for the success of any project.

vii. Regular updates to management are important so that the stakeholder does not lose interest in the project.
viii. A project that takes a long time to be completed can fatigue management and runs the risk of being abandoned.

6. CONCLUSIONS AND RECOMMENDATIONS

From the discussion of the results, it can be concluded that the type and level of project management approach in projects depends on the risks associated with the project, the size of the project, the stakeholder environment, cost, business environment, the objective of the project, quality and the current phase of the project. These factors and their level of influence on the project management approach in relation to the type of project are discussed below and appropriate recommendations made.

Risk analysis
Where the viability of the project, risks and opportunities are not clear, as in the case of the Olkaria Geothermal Spa, it is recommended that the project starts small and expands later, depending on the business growth. This, therefore, requires a different project management approach that allows scope change, more focus on stakeholder management, a communication plan and business strategy, review of business environment, continuous review and assessment of risks and opportunities, and development and execution of marketing strategy. On the other hand, Mývatn Nature Baths had a fairly clear indication of the visitors' numbers and the popularity of bathing in the brine arising from the experiences at the Blue Lagoon, and therefore they could start with a big project. For the Blue Lagoon, there was a clear indication of the number of visitors, based on previous use of the lagoon and this formed a benchmark from which the Blue Lagoon could expand with a clear and strict project management approach that provided little change for scope change, cost and schedule variations. The application of project management approach for the Blue Lagoon was thus different from the Mývatn Nature Baths and the Olkaria Geothermal Spa.

Marketing strategy
For a project with uncertain immediate outcome, opportunities and risks like the Olkaria Geothermal Spa, it is recommended that a marketing strategy be developed during the planning stage but executed only when adequate data has been collected on the potential opportunities, risks and threats available as well as quality of services. This requires that the project starts in small phases and uses trial and error as the quality of service is improved. A one-year test run period is thus recommended during which baseline data is collected about the customers, the usability and usage of the brine, improvement of the services is undertaken and stakeholders are managed. Olkaria Geothermal Spa is still on a test run although it was opened to the public in August 2014. A marketing strategy will be developed and executed once all required services have been established. Mývatn Nature Baths launched a marketing strategy after it was ensured that the quality of the service had been improved, mainly through installation of an automatic temperature control system. The test run and corrective action period took nine months.

Cost and scope
Due to the uncertainty of the project requirements and how the project would evolve, being the first project of its kind ever undertaken by the KenGen company, it was difficult to obtain a near actual cost estimate for the Olkaria Geothermal Spa. The scope changed during project implementation and this increased the cost. Strict cost and scope control could not be applied because the outcome and requirements were not clear and therefore could not be established accurately. It is, therefore, recommended that a strict scope and cost control as a project management approach should only be applied in a project where the outcomes are certain, for example, a power plant, or any expansion project that already has information on business viability and known requirements for the project. This means

the financing and scope plans should have a buffer or float provision that allows changes, provided the project is still under control.

Quality
For projects with uncertain outcomes and whose risks or opportunities are difficult to ascertain, the quality is impaired by little information on design, arising from a lack of adequate knowledge as well as little knowledge about customer expectations. Quality, though managed through the design specifications, cannot easily be guaranteed because the design could be based on inadequate consideration of customer needs or a lack of adequate knowledge. It is recommended that for such projects, the quality plan be flexible so as to allow some aspects of quality to be addressed as the project progresses. The quality plan should allow for trials and test runs to determine the functionality of the product. Due to the uncertainty of the functionality of the lagoons, the first lagoon that was constructed at Olkaria Geothermal Spa was test run and it was realised that it could not hold the brine as intended and thus had to be reconstructed. A strict project management approach that does not allow for cost variation and rescheduling is not applicable in such a project.

Time
During the construction of the Olkaria Geothermal Spa, time could not be managed in a strict project management sense although this was the initial intention. The completion time was delayed due to unanticipated procurement delays and non-delivery of items. Time control is difficult in a project that has uncertain processes controlled by other factors beyond the direct authority of the project manager. During scheduling, the plan should provide flexibility so that issues are addressed as they arise. This can be applied for trial and experimental projects whose outcomes, risks and opportunities are uncertain. However, for projects that are to be delivered within an inflexible timeframe, it is recommended that processes which are not in direct authority of the project manager, and which can impact the completion time of the project, be outsourced. In such a case, a contractor should be procured to undertake the construction.

Procurement plan
For projects that have strict timelines, especially those that have been tested and proved viable such as expansion projects, it is recommended that contractors be procured to undertake the construction. This will ensure that the project is delivered within time and as per specification. For pilot or small direct use projects, however, in-house capacity, if available, can be used to initiate, plan and implement the project.

Stakeholder management
A comprehensive stakeholder management plan that allows for constant engagement with the stakeholders is required for a project that has uncertain outcomes, opportunities or risks. This is true of the Olkaria Geothermal Spa that required a comprehensive stakeholder management plan to manage stakeholders such as KWS. Inadequate engagement of KWS is, at the time of writing, posing a threat to the number of visitors to the spa because of what visitors think is a double charge as they pay entry fees at both the KWS-gate and the spa. Engagement with KWS can provide additional opportunity for increasing the number of visitors to the spa through waiver of entry fees and also by making the spa one of the destinations while visiting the park.

Choice of project development approach
It is recommended that due to the uncertainties associated with the risks and outcomes, as well as emerging opportunities and threats, direct use projects adopt a phased development approach. This allows a review of the functionality of the project, and reassessment of opportunities and threats which change as the project is being implemented. Table 3 shows a proposed two-phased development of a geothermal spa or another direct use project. During phase one, the project is developed small and test run for one year. The test run period is used to collect baseline data about the customers, as well as a constant review of the risks and opportunities and stakeholder environment. During this period, the marketing strategy is executed once it is clear that the project is functioning as per design expectations. Any improvements to the project that enhance use of the brine are noted and executed during phase one

and lessons learnt recorded. Phase two is an expansion phase that is premised on adequate data and therefore strict project management approach on scope, quality and cost control is adopted.

TABLE 3: Proposed phased development of geothermal spa or direct use project

	Duration (Years)													
PHASE 1	**1**		**2**		**3**		**4**		**5**		**6→**			
Concept/ Initiation														
Research on brine availability and suitability														
Project charter														
Stakeholder identification														
Planning														
Define scope														
Work breakdown structure														
Define and sequence activities														
Define project organisat.														
Estimate costs														
Develop budget														
Approvals														
Internal														
Abridged business plan														
Environmental scoping/ EIA														
Financing plan														
Develop market. strategy														
Risks identification and assessment														
Plan quality														
Plan procurements														
Plan communication														
Design Approvals														
Implementation														
Procurement of contractor														
Construction of lagoons														
Test run														
Execution market. strategy														
PHASE 2: REDEVE-LOPMENT														
Planning														
Implementation														
Closure														
Operations														

In line with these recommendations, the Olkaria Geothermal Spa should spend about 7½ months developing and executing a marketing strategy, as well as analysing opportunities in enhancing and increasing services from the geothermal fluid as shown in Table 4 and further described in Appendix I, Figure 3 and in Appendix V.

As part of stakeholder and communication management, Mývatn Nature Baths should drill a deeper reinjection well, obtain adequate supply of brine especially during winter and provide safety briefs to visitors. Similarly, the Blue Lagoon should find ways of disposing the used brine and also provide safety briefs to visitors.

TABLE 4: Schedule of activities for Olkaria Geothermal Spa

	Duration (months)															
	1		**2**		**3**		**4**		**5**		**6**		**7**		**8**	
Activity																
Research on algae																
Algae composition and management																
Partnership with Ministry of Health																
Contact ministry																
Research on health benefits of brine																
Research on beautification products																
Use of products																
Business plan development																
Marketing strategy developm.																
Marketing strategy execution																
Other services																
Steambaths																
Swim suits for hire																
Restaurant services																
Massage services																
Installation of hot water system																
Procurement of steel coil, pipes and connections																
Installation																
Automatic temp.control system																
Specifications																
Procurement of contractor																
Design of the system																
Installation of the system																
Closure																

ACKNOWLEDGEMENTS

I thank my supervisors, Mr. Yngvi Gudmundsson and Mr. Jóhann F. Kristjánsson for the professional guidance, support and encouragement during the research project. Without their support, it would not have been possible to complete the work. I am grateful to the UNU-GTP Director, Mr. Lúdvík S. Georgsson for enabling me to attend the course and the Deputy Director, Mr. Ingimar G. Haraldsson and all the UNU-GTP staff for providing the much needed support that made it possible for me to undertake the course. Special thanks go to the management of KenGen – the Kenya Electricity Generating Company, Ltd. for the sponsorship. Forever, I will be indebted. To my family for giving me support during this long duration of stay in Iceland when they needed me most and especially my daughter Patience Kadzo Peketsa who was preparing for her form IV examination the same year.

REFERENCES

Burke, R., 2004: *Project management: Planning and control techniques* (4th ed.). John Wiley & Sons, West Sussex, 509 pp.

Gudmundsson, Á., 2015: *Námafjall high temperature area*. UNU-GTP, Iceland, unpublished lecture notes.

Gudmundsdóttir M., Brynjólfsdóttir Á., Albertsson A., 2010: The history of the Blue Lagoon in Svartsengi. *Proceedings of the World Geothermal Congress 2010. Bali, Indonesia,* 6 pp.

Travelandescape, 2013: *Location of Mývatn Nature Baths in North Iceland*. Travelandescape, webpage: *www.travelandescape.ca/2013/09/blue-lagoon-vs-Mývatn-baths/.*

Haraldsson, I.G., and Lloret Cordero, A., 2014: Geothermal baths, swimming pools and spas: Examples from Ecuador and Iceland. *Paper presented at Short Course VI on Utilisation of Low- and Medium-Enthalpy Geothermal Resources and Financial Aspects of Utilisation, organized by UNU-GTP and LaGeo, in Santa Tecla, El Salvador,* 14 pp.

IPMA, 2006: *Competence baseline* (version 3). International Project Management Association, Nijkerk, The Netherlands, 212 pp.

ISO, 2012: *ISO 21500:2012. Guidance on project management*. International Organization for Standardization, Geneva, 36 pp.

Jónasson, H.I., and Ingason, H.Th., 2013: *Project ethics*. Gower Publishing Ltd., Surrey, 142 pp.

Lund, J.W., and Boyd, T.L., 2015: Direct utilisation of geothermal energy 2015, worldwide review. *Proceedings of the World Geothermal Congress 2015, Melbourne, Australia,* 31 pp.

Mangi, P., 2014: Geothermal direct use application: A case of the Geothermal Spa and Demonstration Centre at the Olkaria geothermal project, Kenya. *Paper presented at Short course IX for Geothermal Exploration, organized by UNU-GTP, KenGen and GDC, Naivasha, Kenya,* 12 pp.

Mariita, N., 2010: An update on applications to direct-uses of geothermal energy development in Kenya. *Proceedings of the World Geothermal Congress 2010, Bali, Indonesia, 5* pp.

PMI, 2013: *A guide to the project management body of knowledge* (5th ed.). Project Management Institute, 5 pp.

Ragnarsson, Á., 2015: Geothermal development in Iceland 2010-2014. *Proceedings of the World Geothermal Congress 2015, Melbourne, Australia,* 15 pp.

Reiss, G., 2007: *Project management demystified* (3rd ed.) Taylor & Francis, London, 210 pp.

APPENDIX I: Lagoon layout and brine flow system at the Olkaria Geothermal Spa

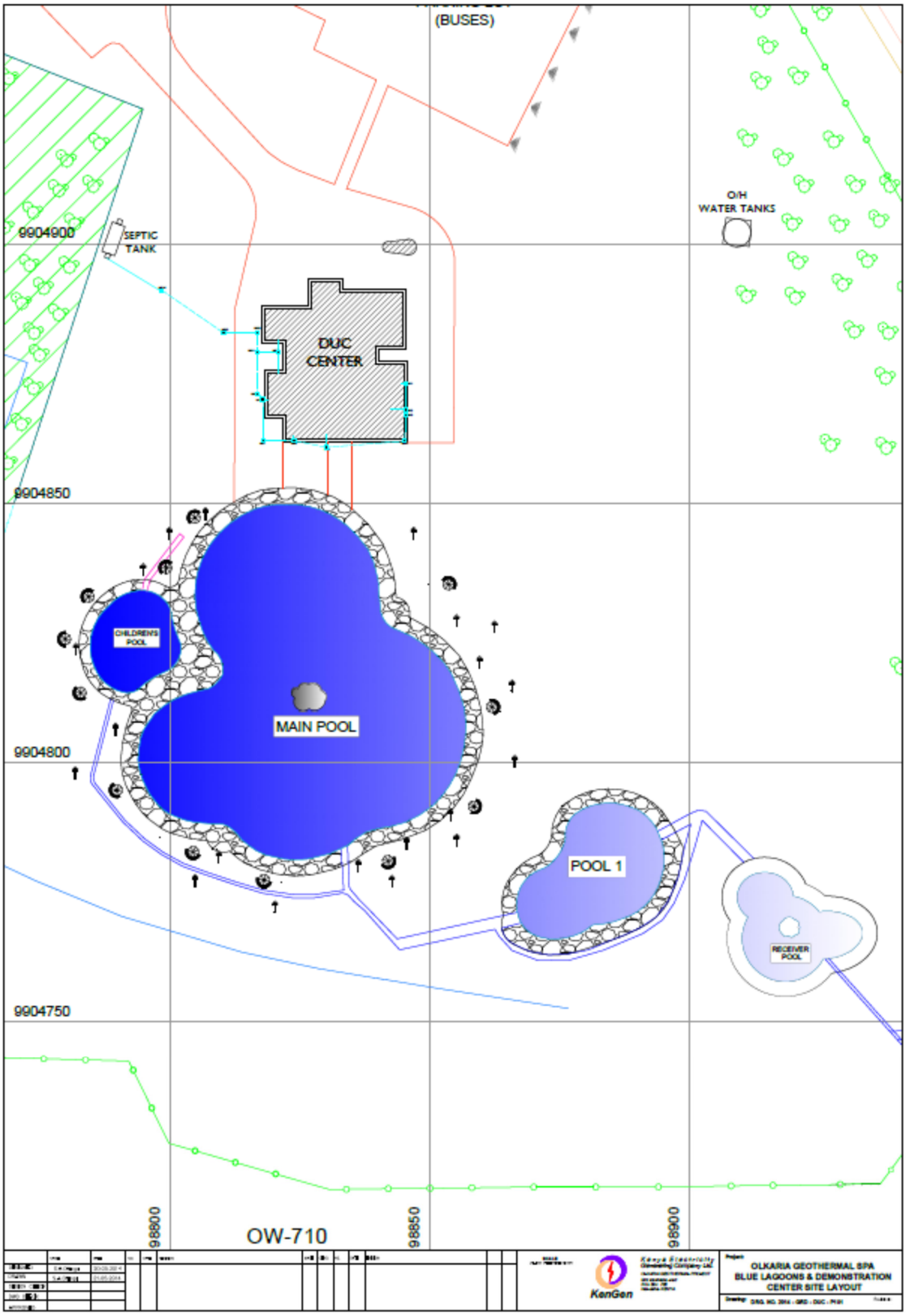

FIGURE 1: Lagoon layout

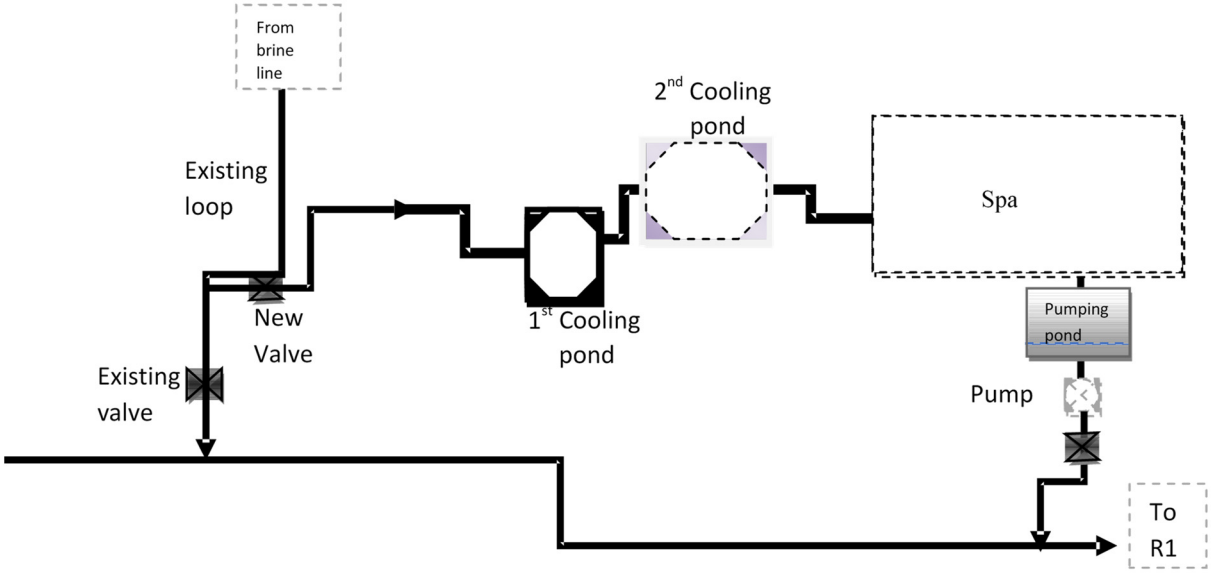

FIGURE 2: Brine flow system

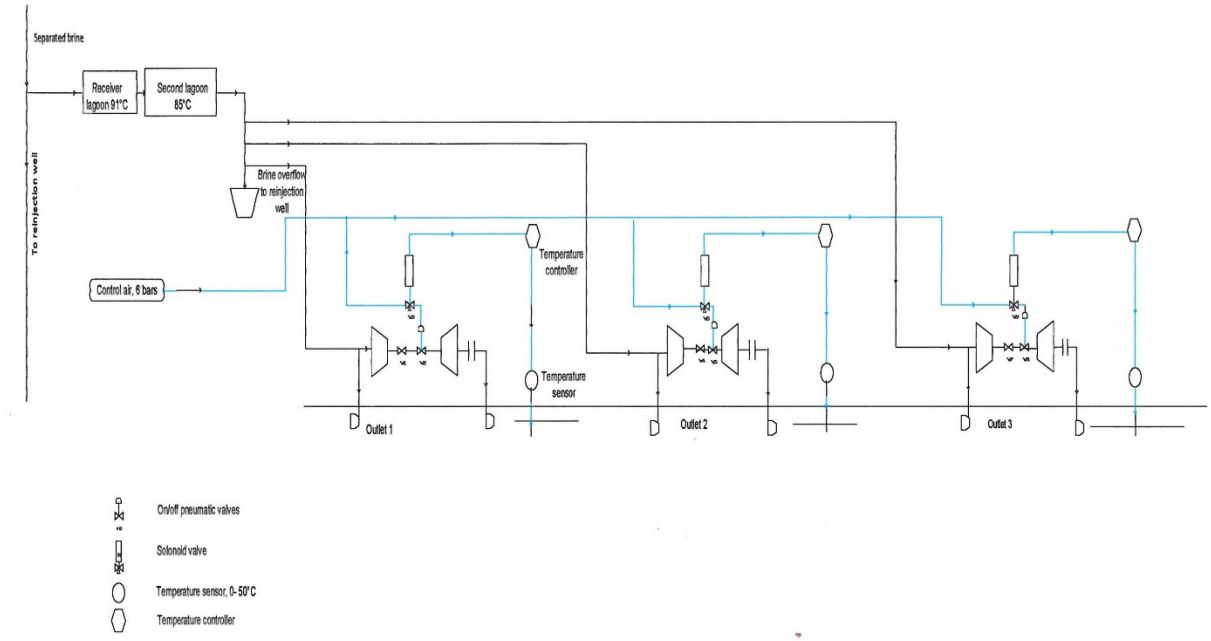

FIGURE 3: Proposed brine flow and temperature control system for Olkaria Geothermal Spa

APPENDIX II: Blue Lagoon and Mývatn Nature Baths brine flow systems

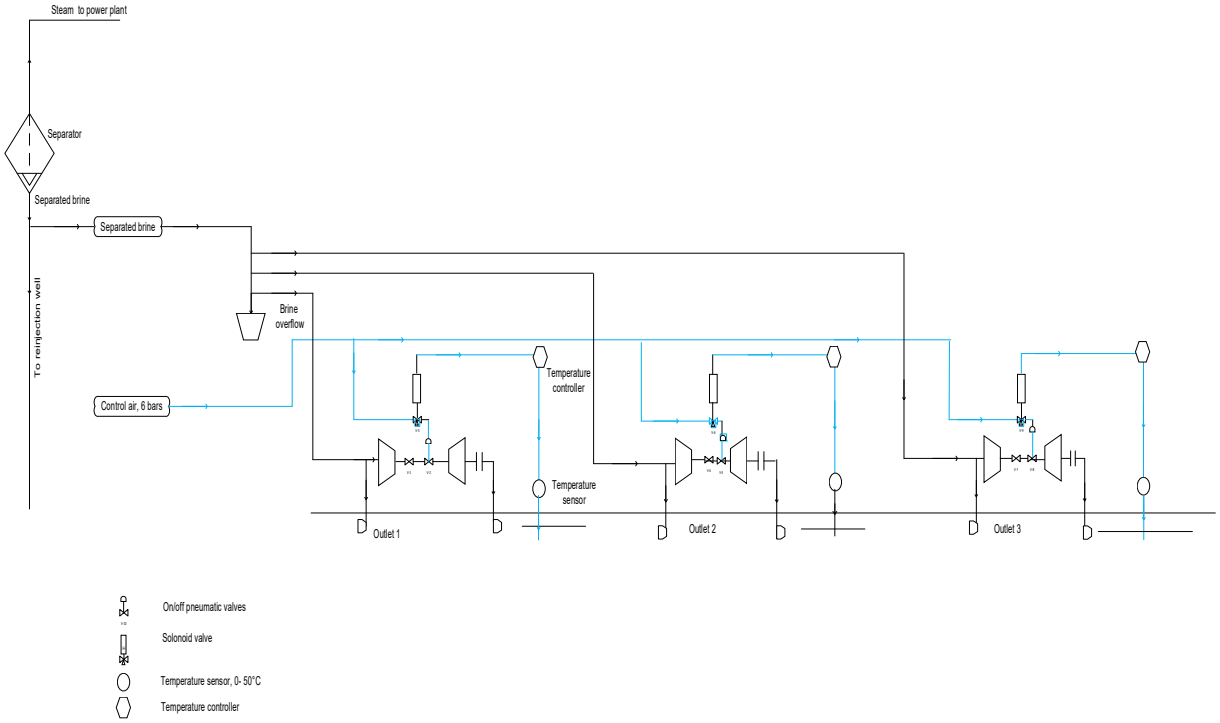

FIGURE 1: Brine flow and temperature control system at Blue Lagoon

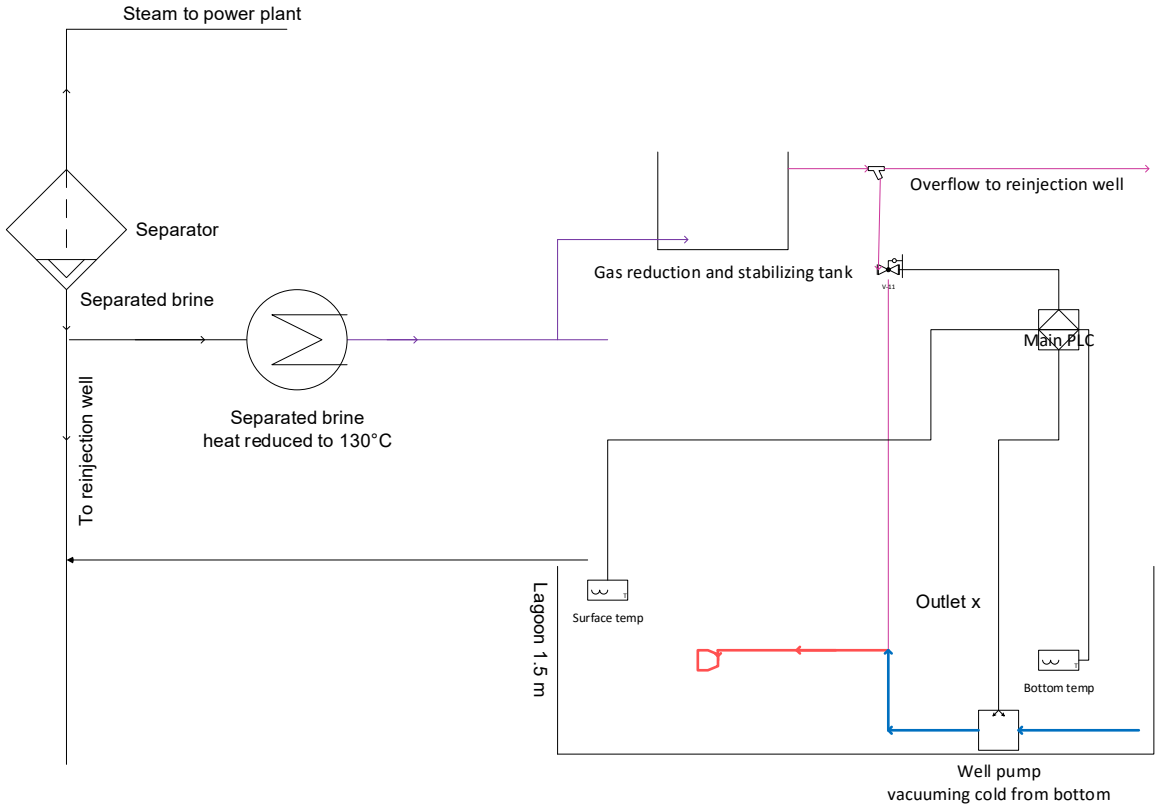

FIGURE 2: Mývatn Nature Baths brine flow system

APPENDIX III: Interview schedule

Introduction
Name of Interviewer: Peketsa Mangi
Pursuing Geothermal Project Management and Finances course at UNU-GTP
Purpose: Undertaking project as part of requirement for award of certificate in geothermal technology
Confidentiality: Information will be treated with confidentiality
Interviewee: Identified as one of the officers involved in the initial design of the Blue Lagoon
Thanking interviewee for time and agreeing to be interviewed

Introduction by Interviewee:

Name:
Position in organisation
Areas of interviews

DESIGN OF THE BRINE FLOW SYSTEM

What is the source of the brine?

What is the minimum and maximum depths of the lagoon?
Minimum depth _____ Maximum depth _____

How is the brine flow from the separator to the lagoon controlled?
Use of automatic valves; Controlled manually using valves; Brine flows into a reservoir

Temperature of the brine from the source?

How is temperature regulated to the desired temperature in the lagoon?

Where is the brine overflow from the lagoon disposed?
In the nearby lava formation; In a reinjection well; Flows to the sea through a pipe

How many brine entry points are there in the lagoon?

Please indicate if brine flow is automatic or manual
Manually controlled; Automatic controlled by use of thermostat

What is the average temperature of the brine in the lagoon?

PROJECT MANAGEMENT

Project initiation

During construction of a project with such complexity as the Blue Lagoon, project management techniques are deployed so as to ensure success of the project.

What was the objective of constructing the Blue Lagoon?

Was a project manager appointed for the project?

If a project implementation team was appointed, was it released officially to undertake the project work?

If yes, was the project manager involved in the appointment of the project team?

Was the project manager granted authority to make decisions regarding the project

Before project kick off, one of the requirements is production of a Project Initiation Document (PID) that summarises project viability, and refines the scope, duration, resources and project team composition and business environment review. Was a PID issued before start of the project?

Project ethics analysis and agreement on the project ethics is useful in managing teams and creating a moral standing for the project. Did you undertake a project ethics analysis before start of the project?

Did you prepare a project charter that captured the costs, tasks, schedules, and deliverables of the project with the team?

During the initiation, did you identify all the stakeholders of the project?

Please tick if the following were some of your stakeholders
HS Orka; Grindavik town; The CEO of Blue Lagoon; Tourists; Members of the public; Environmental activists; Any other?

If yes, who among these posed risk to the project?
HS Orka; Grindavik; The CEO of Blue Lagoon; Tourists; Members of the public; Environmental activists; Any other?

Who among these presented the biggest opportunities to the project?
HS Orka; Grindavik; The CEO of Blue Lagoon; Tourists; Members of the public; Environmental activists; Any other?

Was a business case developed for the project?

PLANNING

Project plan

Did you develop an overall project plan for the project?

Scope and work breakdown structure

What was the scope of the Blue Lagoon during the initial implementation?
Lagoon; Washrooms; Restaurant; Administration building; Cafeteria; Souvenir shops; Steambaths; Sauna.

Was a work breakdown structure that gives the main works done for the project?

How many contractors were involved in the construction of the project, if any?

How many workers in total were involved in the construction of the Blue Lagoon?

Sequence of activities, Activity duration and schedule

What planning tools did you use to schedule activities?
MS project; Excel sheet; MS Word; Any other

What time estimation did you make for the entire project?

How long did you take to complete the project?

Based on the total time taken to complete the project, how would you apportion the time taken:
During planning stage; During construction; During closure of the project

Cost estimates and budget
What budget estimate was done for the initial scope of the project?

Projects have different components that may require financing at different times. Please indicate the breakdown of the budget in line with the various components
Blue Lagoons; Buildings; Electrical installations; Equipment and furniture.

Finances for the project were provided by
Owner; Loans; Shareholders; Any other

What was the total cost of the project?

Identification and assessment of risks
During the planning of the project, project risks have to be considered. Please indicate if risk assessment was undertaken regarding the following and indicate the action taken as a risk mitigation:
Brine disposal system; financial risk; Brine availability; Brine chemical composition; Environmental Impact assessment; Safety; Any other risks not mentioned above.

Indicate if the following approvals were required for the project:
Building designs; Brine chemical composition; Environmental impact assessment licence; Safety standards; Health certificate for restaurant services; Provision of health products; Provision of health services for psoriasis.

Did you develop a quality plan for the project?

If yes, please tick if any of the following was part of your quality plan
Regular inspection in line with standards; Quality review meetings; Review of construction in line with specifications and design; Project audits; Assigning personnel for quality review; Correction Action plans; Any other/s.

Procurement
Was a procurement plan for the project developed?

What procurement methods were used to procure the contractor or materials?
International competitive tendering; National competitive tendering; Selective tendering; Direct procurement.

Who was responsible for procurement of materials for the project?

What procurement bottlenecks did you experience, if any?
Delay in delivery of materials; Unavailability of materials; Lack of finances; Substandard materials; Change of prices; Any other, please specify.

Please give the methods of marketing you adopted (many can apply)
Linkage with local tour agents; Attending local Travel fairs; Attending international travel fairs; Incentives to local tour guides; Linkage and incentives to local hotels; Linkage and incentives to local tour bus drivers; Incentives to bus drivers; Schools visits; Brochures; Coupons distribution to hotels, travel agents, excursion companies; Distribution of brochures to schools, tour agencies, trade fairs, excursion buses, Advertisement in the media; Any other?

Did you develop a communication plan for the project, i.e. who will be responsible for communication and methods of communication?

If yes, which methods were used?
Daily meetings; Weekly meetings; Monthly meetings; Emails; Progress reports; Verbal – telephone, face to face; Memos and letters; Any other, please specify.

IMPLEMENTATION, MONITORING AND CONTROL

Directing and controlling the project
What project control activities were undertaken?
Regular meetings with the supervisors; Regular progress reports; Recording of daily activities; Daily materials movements control as part of cost management; Taking inventory of materials on a daily basis; Scheduling of activities; Daily scheduling of activities; Review of schedules against deliverables; Regular inspection of works; Any other, please specify.

During project implementation, the scope of the project may change. Please indicate if any of these actions were put in place.
Change request forms prepared; Approval required for any change; Scope definition done.

Manage stakeholders
What methods were used to manage the stakeholders?
Profiled stakeholder according to level of influence, level of impact to the project; Meetings with stakeholders were held; Regular updates were sent to stakeholders; The project sponsor was regularly updated on the progress of project; Quality reviewed in line with expectations of customers and project sponsor; Shareholders updated on progress of construction

Develop project team
Was the project team trained on quality assessment, project control techniques, and supervision?

If no, was that because the know-how was already in place within the team?

Risk treatment
Were risks identified during the project?

Were corrective actions put into place and acted upon to deal with project risk?

Quality assurance
What methods were used to ensure quality?
Regular inspections of works at site undertaken; Regular meetings were held with supervisors; Construction was reviewed against design; Any other method?

Information distribution
What methods were used to distribute information to the project team, stakeholders and contractors?
Daily meetings; Weekly meetings; Monthly meetings; Emails; Progress reports; Verbal – telephone, face to face; Memos and letters; Any other, please specify.

Was information distributed on the need to know basis?

Team management
Indicate which of the methods best describes how conflict was managed in the project team
Stage management with supervisors; Discussion with teams; Removal of non-complying team members; Counselling; Negotiation with members.

How would you describe the morale of the team during implementation of the project?

Manage stakeholders
Did you have a plan of how to manage the various stakeholders?

CLOSURE OF THE PROJECT

During handing over of the project, what are some of the activities that you undertook so as to bring the project to a closure?
Meeting held; Documentation done; Final project report written; Lessons learnt recorded; Database of lessons learnt kept; Project handed over.

APPENDIX IV: Rating of project management approach in geothermal spas construction

On a scale of 1-5, rating how best the items in the matrix were addressed during the planning and execution of the project. 1- Poor and 5 is best						
Grade	**Description**					
1	Poor understanding and adoption of project management techniques, poor application of knowledge areas or poor application of technical, behavioural and contextual competences					
2	Fair understanding and adoption of project management techniques, knowledge areas or technical, behavioural and contextual competences					
3	Good understanding and adoption of project management techniques, knowledge areas or technical, behavioural and contextual competences					
4	Very good understanding and adoption of project management techniques, knowledge areas or technical, behavioural and contextual competences					
5	Excellent understanding and adoption of project management techniques, knowledge areas or technical, behavioural and contextual competences					
REVIEW OF PROJECT MANAGEMENT APPROACH						
Phases and subjects	**Olkaria Geothermal Spa**	**Rating**	**Blue Lagoon**	**Rating**	**Mývatn Nature Baths**	**Rating**
Concept/ initiation		**2**		**4**		**4**
Clarity of objectives	Not project objective but corporate objective. Objectives clear to team.	3	Objective clear to team	5	Objective clear to team	5
Project charter	Not prepared. Simple payback period done in a proposal	2	Prepared	5	Not prepared. Business plan done	3
Project ethics analysis	Not done	1	Rules and regulations were made clear	2	Rules and regulations were made clear	2
Stakeholder identification	Stakeholders not listed	2	Stakeholders identified	5	Stakeholders identified	5
Establish project team	PIT established with project manager. Team not officially released	4	PIT established with project manager	5	PIT established with project manager	5
Planning		3		5		5
Project plan						
Scope, WBS, Define activities	Scope identified, WBS done and activities defined	5	Scope identified, WBS done and activities defined	5	Scope identified, WBS done and activities defined	5
Resource estimate, project organisation	Resource estimate done. Casual labour restrictions	3	Resource estimates done. Contractor labour	5	Resource esti-mates done. Contract. labour	5
Sequence activities, activity duration, schedule	Done on MS Project	5	Done on MS Project	5	Done on MS Project	5
Cost estimate, budget	Done	3	Done	5	Done	5
Identify and assess risk	Not all risks identified and assessed	2	Risks identified and assessed	3	Risks identified and assessed	3
Plan Quality	No plan done	1		**5**		4
Procurement plan	No plan done	1		**5**	**Plan done**	5
Plan communication	No plan done	1	Plan done	5	Plan done	5
Implementation		**3**		**5**		**4**
Direct project work	Done		Done		Done	

Manage stakeholders	No stakeholder management plan. Management on ad hoc basis	2	Identified as HS Orka, the CEO, Grindavik	5	No stakeholder management plan. Management on ad hoc basis	4
Develop project team	Team not trained on project controls, supervision. Meetings used	2	Team trained on project management aspects	4	Team trained on project management aspects	4
Treat risk	Risks mitigation identified and applied	2	Risks mitigation identified and applied	3	Risks mitigation identified and applied	3
Quality assurance	Quality requirements reviewed against controls	4	Quality requirements reviewed against controls	5	Quality requirements reviewed against controls	4
Select suppliers	Suppliers selected. Procurement beaurocracy delayed delivery of project materials	2	Contractors procured. Procurement of materials by contractors	5	Contractors procured. Procurement of materials by ontractors	5
Distribute information	Need to know basis	4	Need to know basis	4	Need to know basis	4
Team morale & motivat.	Team morale high and low	3	Team morale was high	4	Team morale was high	4
Leadership style adopted	Participatory	4	Participatory	4	Participatory	4
Monitoring and control						
Control project work and project changes	Done				Done	
Control scope	No change requests forms. Significant changes	2	Change request forms. No major change	5	No change request forms. No major change	3
Control resources, manage team	Done - inventories and stock control, cost versus deliverables, team supervised	3	Contractor role. Consultation	5	Contractor role. Consultation	5
Control schedule	Poorly executed. No adequate materials and labour	2	Done	5	Done	5
Control cost	Done	3	Done	5	Done	5
Control risk	Risks mitigated. Financial and stakeholder risks mitigation not done	3	Risks mitigated except brine reinjection	4	Risks mitigated except for inadequate brine during winter	4
Quality control	Continuous inspection was done by supervisors per specificat.	3	Continuous inspection was done by supervisors	5	Done	4
Administration	Done	4	Done	4	Done	4
Manage communications	Done through meetings, reports, emails on a need to know basis	4	Done through meetings, reports, emails on a need to know basis	5	Done through meetings, reports, emails on a need to know basis	5
Closure		5		5		5
Close project phase or project	Done	5	Done	5	Done	5
Lessons learned	Project success and failures were recorded	4	Project success and failures were recorded	5	Project success and failures were recorded	5
SUMMARY RESULTS	**Olkaria Geothermal Spa**	**3**	**Blue Lagoon**	**5**	**Mývatn Nature Baths**	**4**

APPENDIX V: Activities for Olkaria Geothermal Spa

i. *Installation of automatic temperature control system*
Olkaria Geothermal Spa can adopt the design of the temperature control system that was installed at the Mývatn Nature Baths. At least five entries for the brine should be created at the Olkaria Geothermal Spa, controlled by valves and temperature sensors that allow brine flow when the temperature drops below 30°C or as may be desired (a proposed design layout is shown in Appendix I, Figure 3)

ii. *Hot water supply to the building*
This system can adopt the Mývatn Nature Baths method that has a coil carrying cold fresh water running through the hot reservoir and onwards to the building. At the Olkaria Geothermal Spa, the receiver lagoon that has temperature of between 91 and 86°C can be used to heat the fresh water. The heated fresh water can then be supplied to the building.

iii. *Business plan and a marketing strategy development*
The business plan should assess the project plans in terms of visitors, identify project risks, define a marketing strategy, review the products and services range, define the business environment, market trends, competitors, strengths and weakness, opportunities and threats.

iv. *Silica mining*
Use of silica for beautification of the skin has become popular at the Blue Lagoon. This product can also be used to popularise the Olkaria Geothermal Spa.

v. *Research on algae*
Green algae grow at the Olkaria Geothermal Spa after months of use. Algae growth was once experienced at some portion of the Mývatn Nature Baths where fresh water used to drip. This problem at the Mývatn Nature Baths stopped when the fresh water line was removed. The algae growth at the Olkaria Geothermal Spa needs to be investigated in line with the existence of a certain microalgae species at the Blue Lagoon that is partly attributed to skin beautification effects.

vi. *Establishment of linkage with Ministry of health officials on the health benefits of the brine*
The Blue Lagoon has gained prominence and is recognised as an alternative treatment centre for psoriasis due to the brine chemical composition. This has helped to market the lagoon. Possibility of linkage with the Ministry of Health should be explored and pursued.

vii. *Manage stakeholders*
The relationship with Kenyan Wildlife Service (KWS) who are one of the stakeholders should be managed adequately. A better managed relationship will ensure that tourists visiting the park will also visit the spa. Fees charged to visitors when they visit the spa may also be waived.

viii. *Introduce additional services such as steambath, massage, restaurant, and swim suits for hire*

ix. *Undertake the tasks shown in Table 3 within a period of 7½ months*
This will enhance quality of service, guarantee increased number of visitors, and enhance project viability and sustainability. This should be initiated immediately so as to leverage on the advantage of being the only geothermal spa in Africa and therefore a special tourist destination.

UNITED NATIONS UNIVERSITY
UNU-GTP
Geothermal Training Programme

Orkustofnun, Grensasvegur 9,
IS-108 Reykjavik, Iceland

Reports 2015
Number 22

EVALUATION OF STRUCTURAL PERMEABILITY IN MAHANAGDONG GEOTHERMAL FIELD, PHILIPPINES USING SOIL GASES (^{220}Rn, ^{222}Rn, CO_2 FLUX)

Jigo W. Mismanos
Geosciences and Reservoir Engineering Group
Energy Development Corporation – EDC
38/F One Corporate Centre, Julia Vargas corner Meralco Avenue
OrtigasCenter, Pasig City 1605
PHILIPPINES
mismanos.jw@energy.com.ph

ABSTRACT

The use of soil gases as a geologic tracer has long been elaborately demonstrated in several volcanic, seismic, and geothermal studies. Carbon dioxide (CO_2) is an abundant geothermal gas while radon (^{222}Rn) and thoron (^{220}Rn) are radioactive gases with a half-life of 3.8 days and 55 seconds, respectively. In theory, anomalous radon, thoron, and CO_2 gas emissions can be indicative of rapid vertical transport through permeable structures that serve as pathways of degassing. These gas anomalies can indicate structures, reservoir changes and processes. The application of soil gas mapping to permeability exploration was tested in production, reinjection, and undeveloped areas in Mahanagdong Geothermal Field, Leyte, Philippines. Most soil gas anomalies were observed at structural intersections and segments that were reported by drilling to exhibit good permeability. The concurrence of soil gas anomalies at fault traces indicated the presence of highly permeable structures that can be targeted for drilling exploration or make-up/replacement wells.

1. INTRODUCTION

The Leyte Geothermal Field, the world's largest liquid-dominated geothermal system, is situated in Leyte Island in central Philippines (Figure 1). The field consists of two distinct convection systems: the Mahiao-Sambaloran-Malitbog-Tongonan system and the Mahanagdong system, separated by a cold (<200°C) impermeable block (Seastres Jr. et al., 1996). The exploration and development of the geothermal field began in the late 1970s and currently has an installed capacity of more than 700 MWe, supplying electricity to the nearby islands and Luzon.

The geothermal system is related to Quaternary volcanism spawned by the subduction of the Philippine Sea Plate under the Philippine Mobile Belt. The geothermal reservoir is composed of Miocene-Pleistocene volcano-sedimentary units intruded by microdioritic dikes (Ward, 1979). The northwest-southeast oriented left-lateral strike-slip Philippine Fault, which transects the island, forms splays across the geothermal system. Parallel splays of the Philippine Fault within the Leyte Geothermal Field are complimented by conjugate faults oriented northeast-southwest (Delfin and Tebar, 1986). This dense,

interconnected structural network is the main source of permeability in the geothermal reservoir (Caranto and Jara, 2015). Conventional geologic mapping can be surmised to be successful in mapping these permeable fluid-bearing structures, as evidenced by the calculated encounters with highly productive intercepts and zones, but now other methods that can corroborate permeability are also being considered, such as geophysical imaging and soil gas mapping.

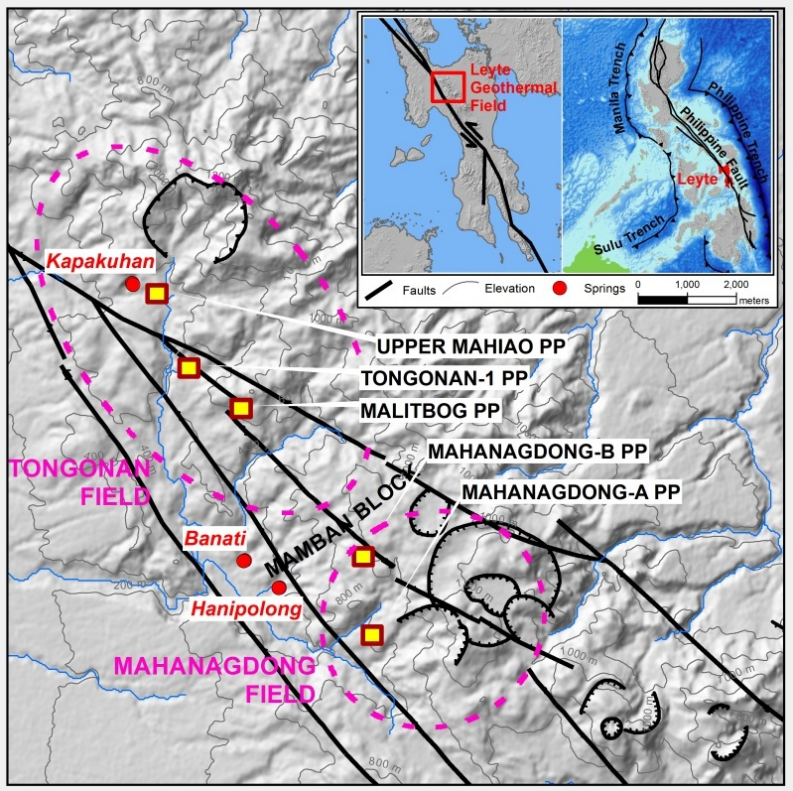

FIGURE 1: Location map of Mahanagdong Geothermal Field, Leyte island, Philippines

Soil gases have long been studied for various geoscientific and environmental applications. Surveys employing soil gases are anchored on the principle that gases from a deep source (e.g. a degassing magma body, decay of radioactive minerals) are also released through permeable pathways, or diffuse soil emanations aside from concentrated point sources such as volcanic vents and fumaroles (Allard et al., 1991). Previous works demonstrated interest in the fluctuations of soil gas concentrations as a function of volcanic/seismic activity (Brusca et al., 2004; Heiligmann et al., 1997) or meteorological variability (Hinkle, 1991; Rinaldi et al., 2012). In geothermal applications, mapping soil gas anomalies has been used to delineate a geothermal system (Cox, 1980; Lewicki and Oldenburg, 2004; Voltattorni et al., 2010) and map permeable structures (Jolie et al., 2015; Padrón et al., 2003; Rodríguez et al., 2008), or aid in field monitoring in the advanced phases (Fridriksson et al., 2006; Bergfeld et al., 2001). Usually, one or a combination of soil gases are considered in a study, but perhaps the most commonly used gases are carbon dioxide and radon. Beside their innate physicochemical properties as geologic tracers, detection of these gases in the field can be achieved with adequate accuracy.

Carbon dioxide (CO_2) is the second most abundant gas in volcanic emissions, accounting for 10% to 40% of total molar gas content after water, which normally comprises more than 60% of the vapour phase (Delmelle and Stix, 1999). In geothermal systems, carbon dioxide generally constitutes 80% w/w of all gases excluding steam (Mahon et al., 1980). Elevated carbon dioxide fluxes in soil have been measured above geothermal resources, typically at hot grounds and faults/structures (Chiodini et al., 1998; Klusman et al., 2000) but anomalous CO_2 fluxes have also been encountered above main upflow zones (Werner and Cardellini, 2006). In developed geothermal fields, elevated soil CO_2 fluxes have been associated with the onset of or continuous fluid extraction, resulting in the expansion of the steam zone and increased heat flow to the surface (Bergfeld et al., 2001; Hinkle, 1991; Óladóttir and Fridriksson, 2015).

Radon is a radioactive noble gas formed from the decay of uranium. ^{222}Rn (radon), the most abundant isotope, is a part of the ^{238}U decay series and has a half-life of only 3.8 days. Another isotope of radon, ^{220}Rn, occurs as an intermediate step in the ^{232}Th (thorium) decay series, thereby acquiring the name thoron. It has a much shorter half-life of only 55.6 seconds. Parent nuclides of ^{222}Rn and ^{220}Rn (^{238}U to ^{224}Ra and ^{232}Th to ^{226}Ra, respectively) occur naturally in trace concentrations in most rock types (Parker,

1967). Thus, the emanation of radon gas from rock matrix to reservoir pore volume ensures a steady and constant influx of radon to the geothermal fluids (Semprini and Kruger, 1983).

In sub-terrestrial settings, radon can migrate by diffusion and/or convection (Tanner, 1980). Because of the short half-life of radon, diffusion can only facilitate short distances of transportation before significant decay takes place (McCarthy and Reimer, 1986). Rapid extraction of large amounts of radon from deeper origins is generally made possible by convection (Witcher, 1991; Cox, 1980). Since thoron has a much shorter half-life, its diffusive length is extremely limited to orders of centimetres (Fleischer and Mogro-Campero, 1978). Thus, it is useful only in areas where convective flow is considerable. Permeable vertical conduits such as faults and fractures provide pathways of rapid bulk transport from depth to surface, where they can occur at levels higher than background (Voltattorni and Lombardi, 2010). In some studies, the different half-lives of ^{222}Rn and ^{220}Rn are used to estimate the depth of origin of gases, *i.e.*, a relatively deep source for ^{222}Rn, and shallow source for ^{220}Rn (Giammanco et al., 2009; Yang et al., 2005). For example, low radon/thoron ratios in soil gases over a fault trace have been inferred as indicative of shallower gas source (Yang et al., 2005).

In 2013, a soil radon survey campaign was conducted in Mahanagdong to investigate the correlation of soil radon anomalies with the permeability of structures that were intersected by wells (Mismanos and Vasquez, 2013). High radon anomalies were observed above surface traces of proven permeable structures. Based on this preliminary work, soil gas prospecting is seen as a potential method in identifying and locating permeable structures which can be targeted for drilling exploration or make-up and replacement wells in new or producing geothermal fields in the Philippines, or in Mahanagdong at least.

This study aims to investigate the relationship between radon and other soil gases and subsurface permeability in Mahanagdong geothermal field, specifically by examining the correlation of soil radon, thoron, and CO_2 flux anomalies with permeability reported from drilling of geothermal wells, in pursuance of the positive results of the initial radon survey. Moreover, this study seeks to assess the potential of soil gas exploration in delineating permeable structures or structural segments in undeveloped areas within a geothermal field, *i.e.*, sectors with no geothermal wells drilled yet.

2. METHODS

2.1 Study area

The soil gas surveys were conducted in selected sites in Mahanagdong Geothermal Field (Figure 2), using the same stations occupied by an initial radon survey campaign executed from February in May 2013 (Mismanos and Vasquez, 2013). The measurement stations are grid-spaced roughly 150 m from each other. The grid areas, having a combined area of 5.9 km^2, are (1) Area A, a production sector located inside an old flank collapse feature, where production wells have been drilled; (2) Area B, a reinjection sector where reinjection wells have been drilled; and (3) Area C, an unexploited area immediately southeast of Area B, which will be investigated for permeability. The survey campaign was carried out from February to March 2015 to coincide with the local dry season. In most cases, sampling stations are located in regions of thick vegetation and steep terrain.

As none of the stations manifested thermal anomalies, i.e. soil temperatures were never greater than ambient, measurements were also taken at three hot spring/fumarole areas located around Leyte geothermal field (Figure 1), namely Kapakuhan, Banat-i, and Hanipolong to characterize soil gas concentrations and fluxes in grounds with elevated temperature.

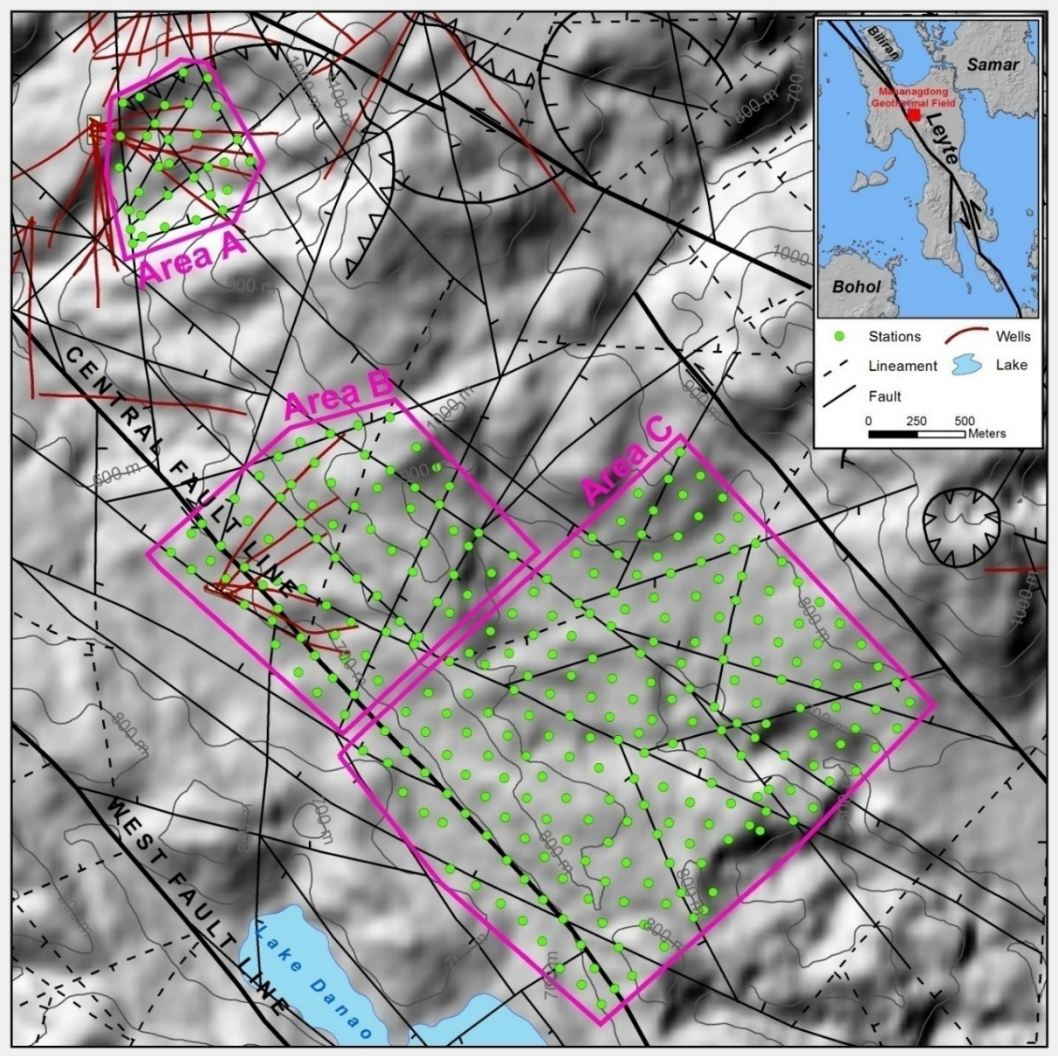

FIGURE 2: Soil gas grid surveys (enclosed in pink rectangles) at Mahanagdong geothermal field. From northwest to southeast: Area A, Area B, and Area C

2.2 Soil gas measurements

For each station, radon and thoron in soil gas and soil CO_2 flux were measured (Figure 3). In addition, GPS coordinates, soil air temperature and barometric pressure were recorded by the instruments, and observations on soil characteristics and prevailing weather were collected during the survey. Radon and thoron were measured using a radon detector with a pump and a steel probe (Figure 3). The instrument uses a solid-state alpha detector, which is a semiconductor material that converts alpha radiation directly to an electrical signal. The daughter isotopes of radon and thoron have different alpha energies and produce different strength signals in the detector, which is then identified through alpha emission spectroscopy. The steel probe is inserted vertically in the soil, down to 1 m depth and connected to the detector. Soil gas is pumped inside the detector chamber, where emissions are counted in five, 5 minute cycles. For radon, the first two cycles are disregarded to account for the response of its progeny, ^{218}Po (half life of 3.1 minutes). Radon and thoron concentrations are reported in the SI units becquerels per cubic meter (Bq/m^3), with 1 Bq/m^3 equivalent to one radioactive disintegration per second happening in one cubic meter of space. In contrast, the 2013 survey used a different instrument which operates using a diffusion chamber. It also relies on alpha spectroscopic detection, but instead of pumping the soil gas directly into the detection chamber, soil gases were allowed to diffuse through a silica membrane, thereby requiring a measurement duration longer than 60 minutes. Using the instrument with a diffusion

chamber to collect samples also introduces more soil perturbation because it requires a 4"-diameter-wide borehole, unlike the ¼" steel probe used in this survey which can easily be inserted in the ground.

FIGURE 3: Soil gas sampling for ^{222}Rn and ^{220}Rn using a radon detector with a soil gas probe (left) and CO_2 flux using an accumulation chamber (right) at Mahanagdong, Leyte

Soil CO_2 flux is measured using the accumulation chamber method (Figure 3). This technique is the most commonly used approach in soil respiration investigations as it is relatively inexpensive and adaptable to a wide range of field conditions and objectives (Rochette and Hutchinson, 2005). With this technique, flux is calculated from the rate of increase in CO_2 concentration observed within an inverted chamber placed on a soil surface. The instrument used is an accumulation chamber connected to an infrared gas analyzer for quantifying CO_2. One flux reading is taken in each station. A measurement takes 90 to 180 seconds until a flux curve with a good regression coefficient is attained. Soil CO_2 flux is initially measured as $mol \cdot m^{-2} \cdot d^{-1}$ and later converted to $g \cdot m^{-2} \cdot d^{-1}$ by multiplying the value with the molecular weight of CO_2 (44.01 g/mol).

2.3 Partitioning of anomalous soil gas populations

In order to identify possible threshold values of anomalous soil gas concentration and flux, the soil gas data was evaluated using probability plots following the graphical procedure of Sinclair (1974). The idea is to partition a polymodal data set into separate populations by identifying inflection points in a probability plot of soil gas data. In turn, these natural breaks in the data set can distinguish the anomaly of interest from the background signal. This method has been widely used in geochemical data sets, especially in soil gas studies where it is used to separate soil gases of hydrothermal or deep origin from soil gases of background processes or superficial origin.

2.4 Logistic regression

Whereas a good estimation of a soil gas anomaly threshold using partitioning is reliant on experiential visual perception of a probability graph (Sinclair, 1991), logistic regression depends on the correlation of soil gases with a parameter approximated by the anomaly. Logistic regression is suitable for predicting a dependent categorical/discrete variable from one or more independent predictors which can either be continuous or a mix of continuous and categorical variables. The general form of the logistic regression equation is:

$$P(y = 1|x_1, \dots x_i) = \frac{1}{1 + e^{-(\beta_0 + \beta_1 x_1 + \cdots \beta_i x_i)}} \quad (1)$$

where $P(y = 1|x_1, \dots x_i)$ = Probability of the desired outcome (*i.e.* dependent variable, y)
β_0 = Coefficient of the intercept
$\beta_1 \dots \beta_i$ = Coefficient of $x_1 \dots x_i$
$x_1 \dots x_i$ = Independent variable or predictor

The desired outcome is to predict “highly permeable” areas based on soil gas concentration values measured at the surface, with the assumption that vertical permeability is continuous. Using the derived model, a threshold value for soil gas concentration/flux can be calculated and used to assess the occurrence of structural permeability in unexploited areas. The database is populated with stations from the production and reinjection sectors that correspond to surface expressions of the intercept between drilled wells and faults. Based on evaluations of permeability from drilling, geology and completion tests, a value of "1" was set for stations positioned at intercepts with reported good permeability and "0" for stations located on intercepts with reported poor permeability. The input database for the model consists of the continuous variables (radon and thoron concentration, CO_2 flux), and discrete variable (permeability). Upon generation of a logistic regression model, a cut-off point shall be chosen based on balanced values of sensitivity and specificity and a robust overall percentage of correct classification (PCC). Sensitivity describes the proportion of positives that are correctly classified as positives, while specificity represents the proportion of negatives that are correctly classified as negatives. Meanwhile, the value of PCC takes into account the effect of both specificity and sensitivity. The cut-off point corresponding to the most optimized values of these three factors can be substituted to P in Equation 1 to get a threshold of the predictor. Based on the model, this “permeability threshold” is the borderline soil gas concentration differentiating between good permeability and poor permeability structures. In evaluating the best model, inspection of the AIC (Akaike Information Criterion) can aid the comparison between different models. The AIC is a measure of the probability of loss of information from the model, and deals with the compromise between the goodness of fit and the complexity of the model. A smaller AIC means that there’s a higher chance for the model to minimize loss of information. The R software was used to execute the logistic regression codes and build the regression model based on the generated parameters for each variable pair.

2.5 Soil gas maps

Interpolation of values between measurement nodes was done using sequential Gaussian simulation (sGs), which is a suitable tool to model soil diffused degassing (Frondini et al., 2004). The sGs method uses the dataset to generate a great number of equiprobable representations or realizations of the spatial distribution of soil gases. The sampled attribute is simulated at each unsampled location by random sampling of a Gaussian conditional cumulative distribution defined on the basis of the original data. The desired number of the equiprobable realizations is then generated and used in drawing a map representing the average of all simulations. The WinGslib software of Statios was used to process the interpolation of soil gas data. For each dataset, 100 realizations are calculated on a model grid with a 5 m grid spacing using the sGs code by Deutsch and Journel (1998), and the average value for each grid cell is presented on maps.

3. RESULTS

A total of 32, 75, and 207 soil gas measurements were collected from grid surveys at Area A, Area B, and Area C, respectively. A summary of the measurements, along with the radon measurements from 2013 is presented in Table 1.

For all three areas, radon concentrations measured in 2013 only amounted to less than half the value of the recent radon gas measurements. The difference is explained by the different instruments employed in these surveys. Analysis of the 2013 readings indicated that the counting duration could not have been optimized for the diffusion chamber instrument, despite the 90-minute duration of measurement, and/or that the soil perturbation from sampling induced compaction and reduction of soil permeability (Mismanos and Vasquez, 2013).

TABLE 1: Summary of soil gas measurements at Mahanagdong

	Year	Units	Area A	Area B	Area C
N			32	75	207
Radon (^{222}Rn)	2013	Bq/m^3	200–13300	80–21000	200–13400
Radon (^{222}Rn)	2015	Bq/m^3	136–31100	0–45300	0–45900
Thoron (^{220}Rn)	2015	Bq/m^3	0–16000	0–14900	0–23400
CO_2 Flux	2015	g·m^{-2}·d^{-1}	7.81–31.58	4.98–82.69	4.90–79.04

N = number of points

3.1 Soil gases in thermal areas

Soil gas measurements from Kapakuhan (KAP), Banat-i (BAN), and Hanipolong (HAN) thermal areas are shown in Table 2 below. Kapakuhan is an extensive thermal ground sprawled along a stream valley in Tongonan. Boiling mudpools, hot springs, and fumaroles are littered throughout this thermal area. Banat-i is situated at the northwestern edge of the Mahanagdong field and is characterized by 2 to 3 large vigorously boiling springs with disseminated hot grounds within less than a 100 m^2 area beside a stream. Hanipolong is located several hundred meters from Banat-i, and is characterized by large altered grounds and a mud pool. All measurements were taken at a certain distance from active manifestations where the substrate is not rocky or water-saturated.

TABLE 2: Soil gas concentrations and fluxes measured at thermal grounds

Name	Soil Temp *°C*	Radon *Bq/m^3*	Thoron *Bq/m^3*	^{222}Rn/^{220}Rn	CO_2 Flux *g·m^{-2}·d^{-1}*
KAP1	31.9	781	105	7.44	3.70
KAP2	40.2	2467	0.00	0.00	154.5
BAN1	31.3	205333	3033	67.69	23.42
BAN2	32.5	4417	4370	1.011	28.44
HAN1	31.6	19633	778	25.25	52.68
HAN1	32.2	16233	805	20.17	77.11

The measurements taken from the thermal areas show a wide range of values. In fact, the highest radon (205,333 Bq/m^3) and CO_2 flux (154.5 g·m^{-2}·d^{-1}) read in the whole survey came from Banat-i and Kapakuhan, respectively. While thermal areas are manifestations of permeability and obviously mark the presence of convective forces and abundant carrier gases, small and localized environments may exist that can exert control on the diffuse emanation of trace gases. For one, clay alterations can hold water and plug pores and fractures. In some instances, the high flux rate of carrier gas overwhelms the trace gases being detected by the instrument (Giammanco et al., 2009).

3.2 Soil gas anomaly threshold

Partitioning was done for each set of radon, thoron, and CO_2 flux data from the 2015 grid surveys. In general, the soil gas data are not normally distributed and highly skewed to the right. To assimilate a normal distribution, logarithmic transformation is applied to CO_2 flux and radon/thoron ratios, while cube root transformation is applied to radon and thoron data sets. These transformations were chosen to correct the positive skew of the data and take on a Gaussian-shaped distribution. At least two inflection points have been observed in most data sets (see Appendix I). A summary of the partitioned populations is also presented in Appendix II.

Populations representing the background are combined into a single group and presented in Table 3. Since the anomaly of interest is caused by unusual enrichment of gases or gas flux in soil, the populations

in the upper extremes are considered. These anomalous populations are thus defined from the inflections occurring at the uppermost quantiles of the data, with most of the anomalies generally occurring above the 80th percentile. From the table, different anomalies have been generated from each area due to the different characteristics of each data set.

TABLE 3: Partitioned populations from probability curves of Mahanagdong soil gas data sets

Gas	Characteristic	Area A			Area B			Area C		
		N_i	f_i (%)	Range	N_i	f_i (%)	Range	N_i	f_i (%)	Range
^{222}Rn	Anomaly	3	11.2%	11467–31100	9	12.8%	23300–45300	15	7.5%	25367–45900
	Background	29	88.8%	136–11467	66	87.2%	0–23300	192	92.5%	0–25367
^{220}Rn	Anomaly	3	11.2%	8510–11600	10	14.1%	9923–14900	21	10.4%	13000–23400
	Background	29	88.8%	0–8510	65	85.9%	0–9923	186	89.6%	0–13000
^{222}Rn/ ^{220}Rn	Anomaly	4	15.3%	2.32–3.74	7	10.6%	6.19–20.77	21	11.0%	4.17–61.03
	Background	26	84.7%	0.38–2.32	65	89.4%	0.27–6.19	175	89.0%	0.08–4.17
CO_2 Flux	Anomaly	3	11.2%	24.34–31.58	4	6.1%	32.1–82.69	7	3.7%	40.78–50.57
	Background	29	88.8%	7.81–24.34	71	93.9%	4.98–32.1	200	96.3%	4.90–40.78

N_i = size of population
f_i = proportion of population

3.3 Logistic regression and permeability threshold

The database for logistic regression was composed by projecting the well-fault intersection to its surface trace and matching it with the soil gas measurement at the corresponding station. Since faults are projected down to a range of dips, occasionally this approach gets crude when the well track is sub-parallel to the fault trace. Due to the close spacing of wells, there are instances where different well-fault intercepts share the same soil gas data. A summary of the data is presented in Table 4 below. The mean and the range (enclosed in parentheses) of good and poor permeability groups are shown in each field. Although there is a significant overlap between the two groups, the means can be considerably distant, e.g. radon, radon/thoron ratio.

TABLE 4: Summary of soil gas data used for logistic regression

Permeability	*N*	Radon (Bq/m^3)	Thoron (Bq/m^3)	Radon/Thoron	CO_2 Flux(g·m^{-2}·d^{-1})
Good (1)	20	13721 (1021-45300)	5717 (80-11667)	4.13 (1.03-15.13)	17.96 (4.98-38.24)
Poor (0)	34	5988 (591-25967)	5059 (0-16133)	1.19 (0-2.80)	16.19 (7.81-29.30)

Four models were considered in the logistic regression as a predictor of permeability. As shown in Table 5 below, these models are: a) Model A with permeability explained by radon concentration, b) Model B with permeability explained by thoron, c) Model C with permeability explained by the isotopic ratio of radon over thoron, and d) Model D with permeability explained by CO_2 flux. The parameters of the fitted models (β_0,β_1,AIC) generated using the R software, are also presented in Table 5 below.

TABLE 5: Generated parameters for the logistic regression models

Model	Definition	β_0	β_1	AIC	Cut-off	Sp	Se	PCC
A	P ~ ^{222}Rn	4.643×10^{-1}	6.031×10^{-5}	66.4	0.72	0.51	0.53	0.51
B	P ~ ^{220}Rn	4.032×10^{-1}	1.095×10^{-4}	66.6	0.70	0.64	0.40	0.57
C	P ~ ^{222}Rn/^{220}Rn	6.090×10^{-1}	1.775×10^{-1}	66.3	0.70	0.64	0.40	0.57
D	P ~ FCO_2	9.793×10^{-1}	-1.410×10^{-3}	67.8	0.70	1.00	0.00	0.72

AIC = Akaike Information Criterion; Sp = Specificity; Se = Sensitivity
PCC = Percent correct classification

For each model, the optimal cut-off and corresponding specificity, sensitivity, and PCC are also described. The values achieved by the model on these checks are below the rule-of-thumb value of 0.70. While Model A roughly balances sensitivity with specificity, Models B and C favour specificity. Model D, on the other hand, rates poorly on sensitivity. It is impossible to choose a good cut-off for Model D because it changes from strictly specific to strictly sensitive in just a small change in cut-off. For this reason, this model is not evaluated further in threshold estimation.

Substituting the parameters β_0, β_1, and selected cut-offs for each model to Equation 1 yields a threshold value of 7,962 Bq/m^3 for radon, 4,055 Bq/m^3 for thoron, and 1.34 for radon/thoron ratio (Table 6). The corresponding proportion of the population above the permeability threshold is also shown in Table6 above. Compared to the anomaly threshold obtained from partitioning, the permeability thresholds are much lower and in most cases encompass more than half of the population. As a result, this threshold estimation method is not narrowing down or pinpointing specific structures or structural segments for further investigation. For the succeeding sections, more focus shall be given to the anomaly threshold (from partitioning) in defining structural zones of interest.

TABLE 6: Calculated thresholds from the logistic regression models

Model	Definition	Threshold	% Population		
			Area A	Area B	Area C
A	P ~ ^{222}Rn	7962	25%	72%	53%
B	P ~ ^{220}Rn	4055	53%	64%	61%
C	P ~ ^{222}Rn/^{220}Rn	1.34	50%	88%	63%
D	P ~ FCO_2	-	-	-	-

4. DISCUSSION

The mapped soil gas concentrations and fluxes interpolated using sGs are shown in the succeeding figures. For each map, the anomaly threshold (AT) is represented as a contour line bounding the high values. Color scale ranges have been standardized for each soil gas across different areas to aid comparisons.

4.1 Soil gas anomalies in Area A

Overall, the gas anomalies in Area A fit spatially well together (Figure 4). In this sector, the highest radon (AT=11,467 Bq/m^3) and thoron concentrations (AT=8,510 Bq/m^3) were measured in the northern portion of the area, particularly at points along the Mahanagdong Flank Crater and its intersection with the North Mamban and Mantugop faults (No. 1 and 2 in Figure 4, respectively), which is consistent with the results of the 2013 radon survey. The north-south trending North Mamban Fault was intersected by production wells targeted to the east. Both well A-36 and A-27 indicated good permeability characteristics, *i.e.* shearing/veining, mud circulation losses, and faster rates of penetration in its intersection at this fault (Esperidion and Bien, 2004; Vicedo, 1996), while wells A-5, A-18, and A-34 reported tight or poor permeability in their intersection with this structure (Tebar, 1983; Alincastre, 1994; Palma and Bien, 2003).

High radon/thoron ratios (AT=2.32), on the other hand, are only evident on the juncture of the northeast-southwest trending Mantugop faults with the Mahanagdong flank crater (No. 2, Figure 4). This can denote a deeper gas source emanation along this structural intercept. The thoron anomaly also extends southwest following the Mantugop-D fault, which appears to be the favored degassing zone in this area. CO_2 flux anomalies (AT=24.34 g·m^{-2}·d^{-1}) also appear along the Mantugop faults and manifest strongly

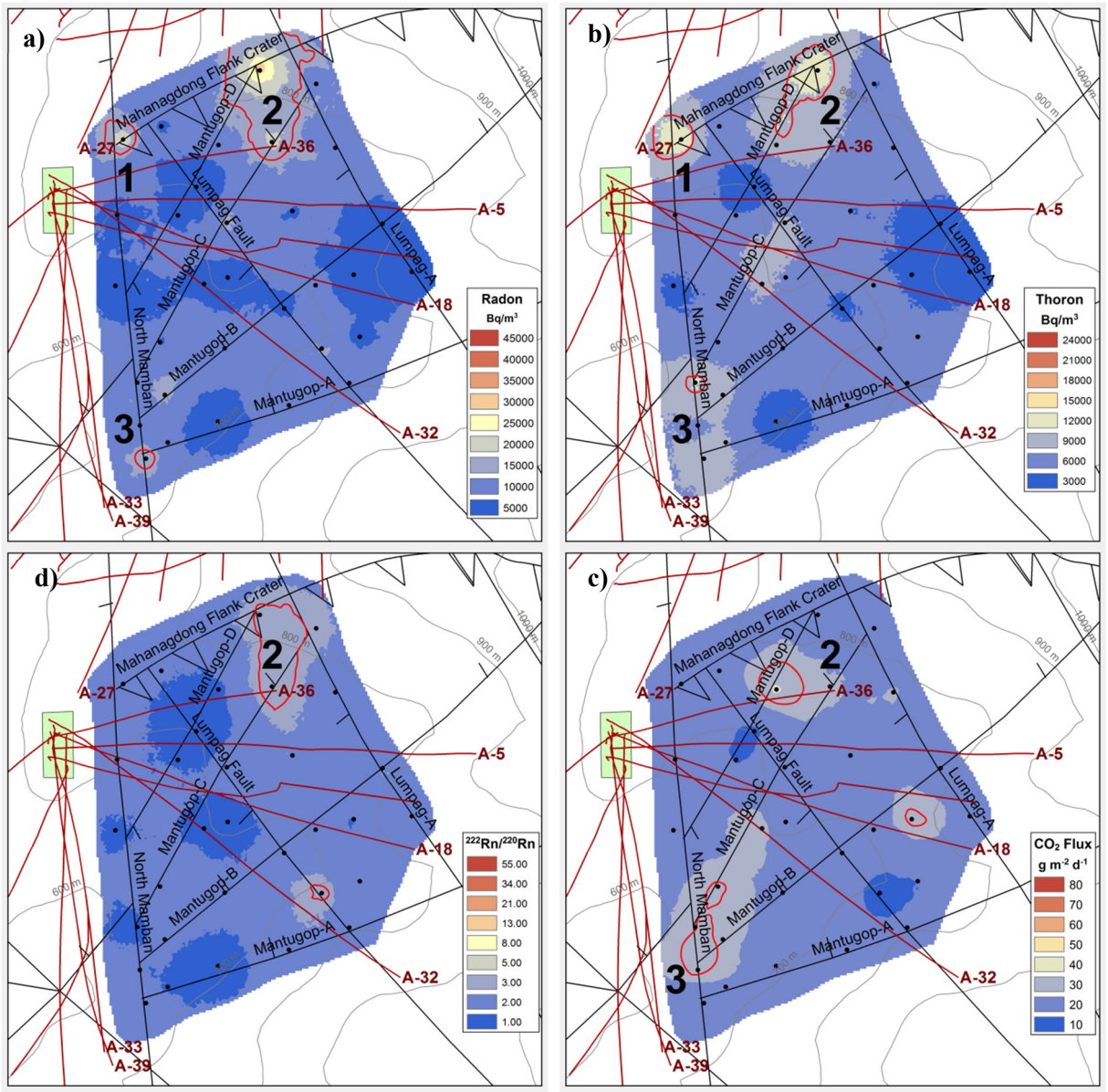

FIGURE 4: Soil gas anomaly maps in Area A. Clockwise from top left: radon (a), thoron (b), CO_2 flux (c), and radon/thoron ratio (d). Anomalies enclosed in red contours

in the closely-spaced intersections of the Mantugop faults with the North Mamban fault (No. 3 in Figure 4). Equivalently, wells A-33 and A-39 have good permeable zones attributable to this segment of the North Mamban fault (Herras, 1997; Bien and Contemplacion, 2007). The agreement of the anomalies in the production sector indicates that radon and thoron is carried mostly by CO_2 through these structures/structural segments.

4.2 Soil gas anomalies in Area B

Unlike Area A, in Area B the most discernible anomalies of each soil gas are absent in the other (Figure 5). For the related soil gases radon and thoron, the general trends are still similar despite variations in the highlighted anomaly.

A prominent radon anomaly (AT=23,300 Bq/m^3) can be seen bounded by the Central Fault Line, Cabalonan-A fault, and the parallel northeast trending Kinuhaan West and Kinuhaan-C Faults (No. 1 in Figure 5), with its highest reading at the Cabalonan-A fault. This is in agreement with good permeabilities encountered by wells B-7 (Leynes, 1996a) and B-8 (Bien, 1996) through Cabalonan-A

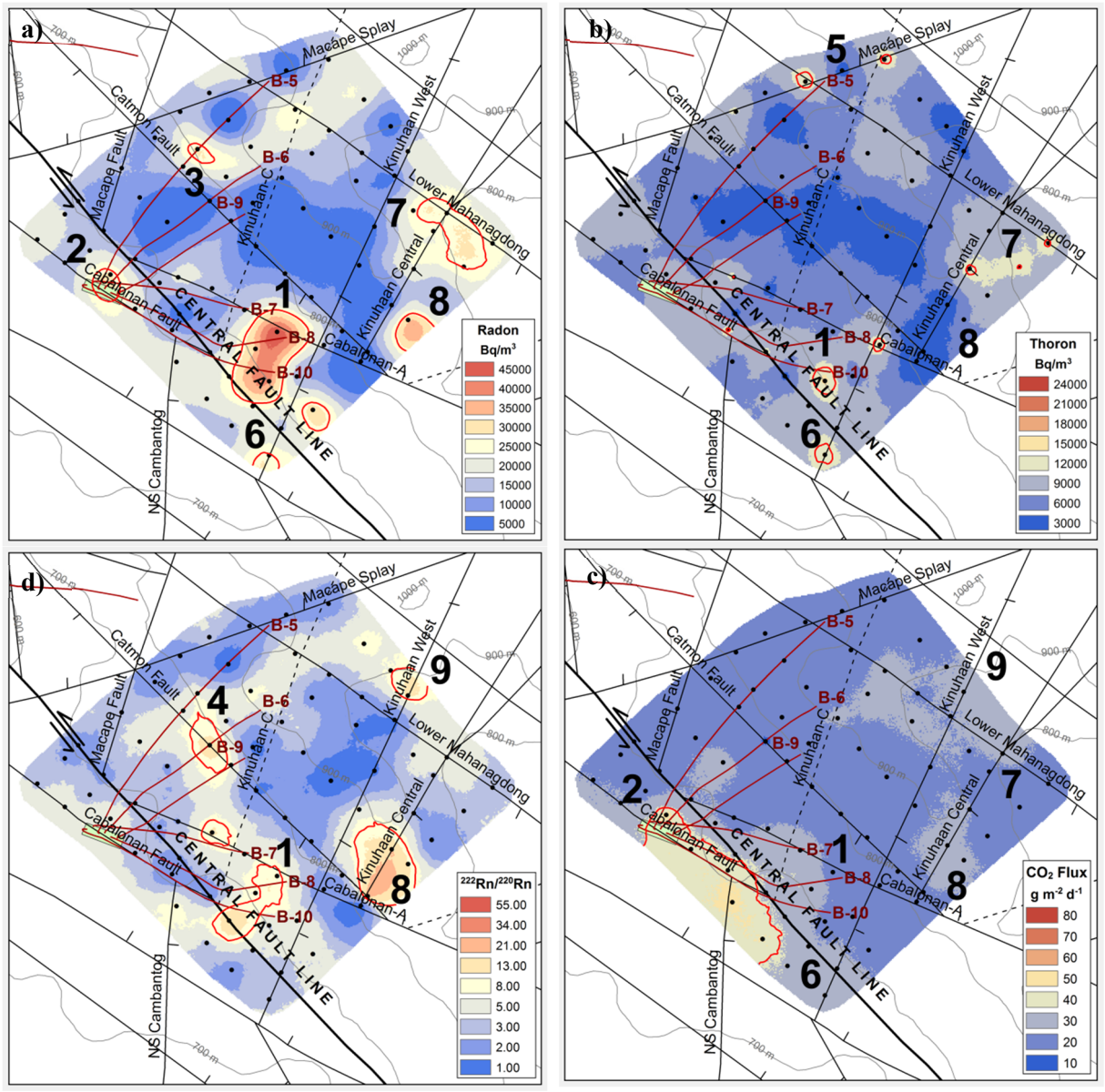

FIGURE 5: Soil gas anomaly maps in Area B. Clockwise from top left: radon (a), thoron (b), CO_2 flux (c), and radon/thoron ratio (d). Anomalies enclosed in red contours

fault. Kinuhaan-C fault is also described as one of the markedly permeable structures intersected by well B-10 (Bien and Palma, 2005).The existence of thoron activity (AT=9,923 Bq/m^3) and radon/thoron ratio(AT=6.19) anomalies also affirm that this area is a major degassing zone.

A contiguous CO_2 flux anomaly (AT=32.1 g·m^{-2}·d^{-1}) exists west of the Central Fault Line (No.2 in Figure 5). This anomaly follows the trace of the Cabalonan fault. A small radon anomaly is also present along this structure and around the well pad. This is consistent with the results of 2013 radon survey. Well B-10, whose track is parallel to the Cabalonan fault, had some indications of permeability at this structure, *i.e.*, intense argillization, influx of hematite and goethite, drusy veins and shearing, and circulation losses (Bien and Palma, 2005). The Central Fault Line, a splay of the Philippine Fault, is a regional structure running the whole length of the geothermal field. It is believed that this structure sets the western boundary of the shear zone, and consequently of permeability, in Leyte geothermal field (Caranto and Jara, 2015). Most of the wells drilled west of this structure reported poor permeability. In particular, all wells in Area B encountered weak shearing and minimal circulation losses through this structure. Even so, measurements along this structure are not distinctively low.

Wells B-5, B-6 and B-9 attribute their most productive zones to the east-northeast trending Catmon fault (Vicedo and Medrano Jr., 1995; Vicedo, 1997; Leynes, 1996b), and this was seen as high radon anomalies in 2013.However, distinct anomalies were not encountered, except for one or two high radon and thoron readings. A radon anomaly close to Catmon fault (No. 3, Figure 5) may be a manifestation of degassing. The anomaly along Catmon fault seen at the ratio map (No. 4, Figure 5) is caused by low radon and very low thoron values. It is therefore important to scrutinize anomaly distributions further because radon/thoron ratio anomalies can yield erroneous deductions, unless corroborated by radon or thoron. Well B-5 also has a permeable zone attributable to the overlap of Macape Splay and Lower Mahanagdong fault (Vicedo and Medrano Jr., 1995), which is also affirmed by a thoron anomaly (No. 5, Figure 5) in the same fault intersection.

Anomalies located along faults and fault intersections are also distributed throughout Area B (Nos. 6, 7, 8, 9 in Figure 5). No. 6 located in Kinuhaan West has consistent radon and thoron anomalies, and elevated CO_2 flux. No. 7 is a large radon anomaly in the intersection of Lower Mahanagdong and Kinuhaan West faults, with minor thoron anomalies and elevated CO_2 fluxes along the Lower Mahanagdong fault. These anomalies are indicative of degassing zones and good vertical permeability.

A radon anomaly south of Kinuhaan Central (No. 8, Figure 5) also has an elevated CO_2 flux. Despite the presence of ratio anomalies and elevated CO_2 flux along the western terminus of Kinuhaan fault, the radon concentrations are very low, and thus minimal vertical permeability is presumed for the structure. Same deduction can be made for a ratio anomaly and elevated CO_2 flux at the eastern segment of Kinuhaan West (No. 9, Figure 5), without accompanying high radon readings.

4.3 Soil gas anomalies in Area C

In Area C, it is important to look at the relationships and concurrence of anomalies to discern the degassing structures. Radon and thoron patterns (and their ratio) can suggest dynamics with regards to the depths of origin of these gases. However, the connotation of a deep or shallow source is not of a quantified depth, but rather referring only to the relative vertical distances that can be traveled by radon and thoron considering their short half-lives. For the radon (AT=25,367 Bq/m^3), thoron (AT=13,000 Bq/m3), and radon/thoron ratio maps (AT=4.17), there are four principal patterns. First is the observed persistent anomaly of both radon and thoron, occurring along the north-northeast trending Concepcion fault (No. 1, Figure 6), the northern terminus of the north-northwest-trending Cabalonan-B fault (No. 2, Figure 6), a probable extension of Catmon fault (No. 3, Figure 6), and a fault west of the Central Fault Line with an apparent extension east of the Central Fault Line (No. 4, Figure 6).The presence of a very high radon concentration, coupled with a high thoron concentration indicates very good conduction of deep gases through continuously permeable vertical channels. A CO_2 flux anomaly (AT=40.78 $g \cdot m^{-2} \cdot d^{-1}$) has been observed along No. 1, while elevated flux values correspond to Nos. 2, 3, and 4.

The second case is the occurrence of radon anomalies accompanied by radon/thoron ratio anomalies, such as No. 5, located on Lower Mahanagdong and its intercepts with NE-Janagdan, Pangog, and EW Cabalonan faults, and No. 6, west of Central Fault Line, at Imelda North Fault. The anomaly at No. 5 is supported by a sizeable area of elevated CO_2 flux, while at No. 6 there is a high CO_2 flux trend following the Central Fault Line. These radon anomalies have also been encountered in the previous radon survey. The presence of high radon in all these structures may indicate good permeability from deep sources, but slower transport in soil or at the shallower depths resulted in lower thoron values being measured, and thus higher ratios being observed.

The third observation is the occurrence of thoron anomalies only, found at the EW Cabalonan fault (No. 7, Figure 6) and the Cabalonan-A fault (No. 8, Figure 6). In almost all cases, anomalous thoron is accompanied by a fairly high radon concentration. CO_2 flux anomalies do not coincide with thoron anomalies but high concentrations are located in these spots. The abundance of thoron can be explained by the presence of structures with good permeability but restricted at shallower depths.

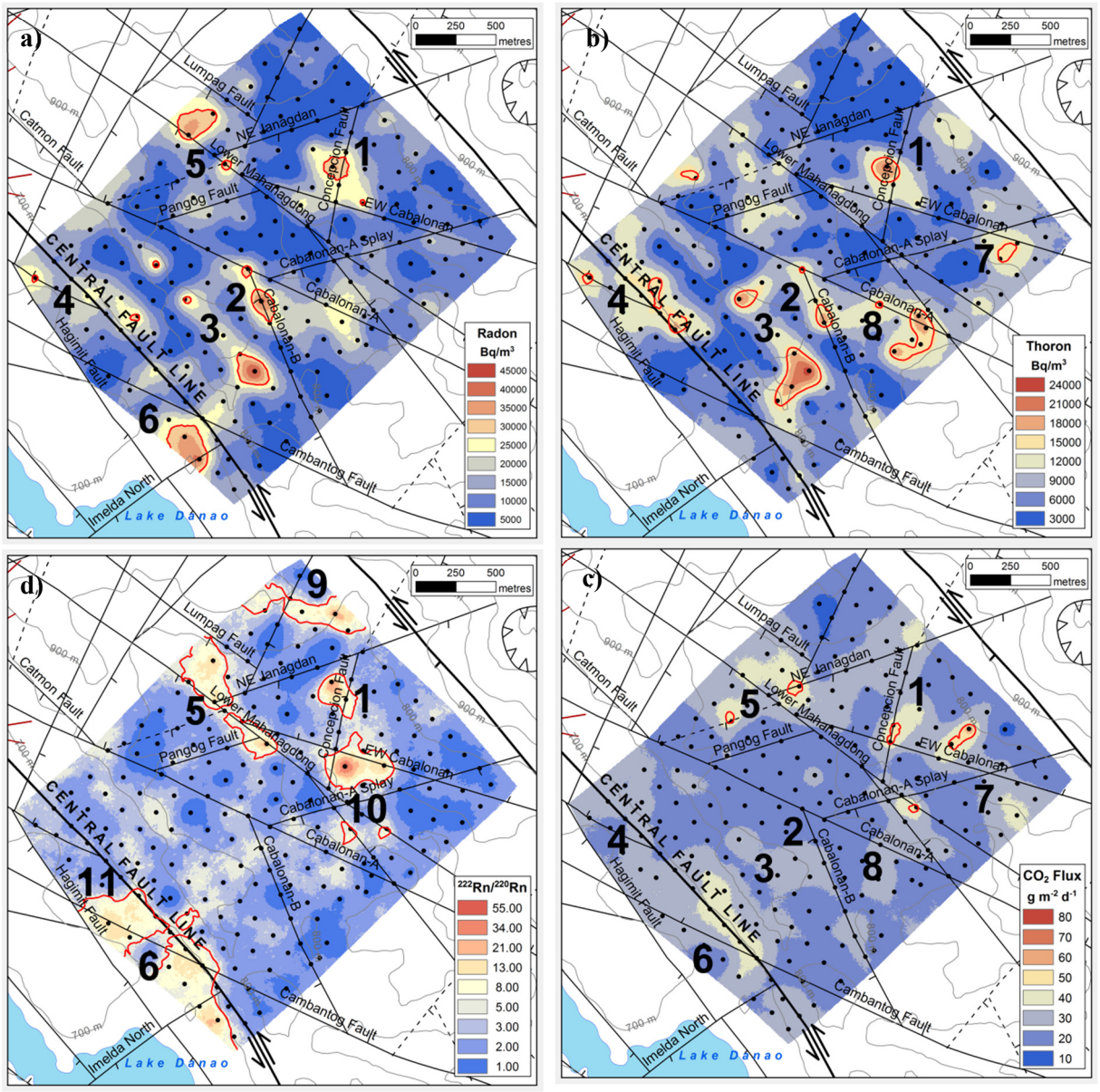

FIGURE 6: Soil gas anomaly maps in Area C. Clockwise from top left: radon (a), thoron (b), CO_2 flux (c), and radon/thoron ratio (d). Anomalies enclosed in red contours

The fourth case is the occurrence of only ratio anomalies. Such stations occur at the north-northeast trending NW Janagdan splay (No. 9, Figure 6), the west-southwest trending EW Cabalonan fault (No. 10, Figure 6), and the area east of the Central Fault Line along Cambantog fault (No. 11, Figure 6). Closer inspection shows that these anomalous ratios are reflections of low values for radon and much lower ratios for thoron. Since no radon or thoron anomalies are present, these “false anomalies” may not signify the presence of good vertical permeability. This kind of anomaly may also denote very poor soil permeability. For example, the area east of the Central Fault is a stream valley and several spots are swampy year-round. In this area have low radon values and almost zero thoron values were measured, likely due to water saturation of underlying strata.

5. CONCLUSIONS

The soil gas survey conducted in Mahanagdong geothermal field showed that soil gas anomalies can be correlated to the permeability characteristics of structures. It is possible to model the relationship between soil gases and permeability using logistic regression and obtain a permeability threshold, although this resulted in broad general anomalies. Certainly, improvements can be done with the sample size by the addition of measurements from well-fault intersections to further evaluate the models. Nonetheless, delineating structural zones of interest can be done with a partitioning method. This resulted in compact anomalies that in most cases can be associated with a structural feature.

Very high values of radon, thoron and CO_2 flux has been measured in soil close to thermal areas, confirming that convecting geothermal fluids are enriched in these gases. However, small and localized environments may exist at near surface that can exert control on the diffuse emanation of trace gases, which can lead to low measurements as well.

Radon, thoron, and radon/thoron ratio can be useful in the inference of the gas source depth. Concurrence of radon and thoron anomalies suggests very good conduction of gases from deep sources through continuously permeable vertical conduits. A high radon and radon/thoron ratio can indicate good permeability and advection from deep sources, while a high thoron will indicate a shallow gas source and good permeability only at shallow depths.

The CO_2 flux anomalies are not in strong agreement with the anomalies of the radioactive gases, but elevated CO_2 fluxes are still observed in most instances. Nevertheless, the occurrence of high fluxes with high radon and thoron measurements will indicate that CO_2 functions as the major carrier gas of radon and thoron. In several cases it has also been demonstrated that gases may follow a favorable degassing zone. In turn, this offers an alternative assumption for the logistic regression model that vertical permeability may not always be continuous.

ACKNOWLEDGEMENTS

I am extremely indebted to the United Nations University – Geothermal Training Programme, for providing us the opportunity to learn from geothermal experts and further our knowledge in this field. My deepest gratitude goes out to the people who foster this institution, the director, Lúdvík S. Georgsson, deputy director, Ingimar G. Haraldsson, and staff, Thórhildur Ísberg, María S. Gudjónsdóttir, Málfrídur Ómarsdóttir, and Markús A.G. Wilde, for all their help in almost every aspect of living here in Iceland and for ensuring that we maximize our experience and learning. I would also like to express my appreciation to the staff of ÍSOR, Orkustofnun, and our lecturers for sharing their knowledge and expertise with us fellows, especially to Finnbogi Óskarsson for his guidance during our specialized training. I am very thankful for my advisor, Audur Agla Óladóttir for giving good counsel along the course of the project work and for imparting helpful thoughts and ideas that shaped this report. My participation in this programme would not have been possible if not for the grace and vision of Energy Development Corporation (EDC), through Mr. Manuel S.Ogena, Ka Noel D. Salonga, Mr. Francis M. Sta. Ana, Mr. Joeffrey A. Caranto, and Ms. Rosella G. Dulce. Thank you for this opportunity. A million thanks also to Atoz A.Vasquez, who has been the other half of this study, for his valuable reviews, and for his dedication to this project. I would also like to thank my colleagues at EDC, whom I find pleasure working with, for job-related assistance and much needed encouragements. I am very grateful to the 2015 UNU Fellows for sharing this awesome learning and life experience with them. In the future, I hope to meet these amazing people as experts in their respective fields. And to all the friends I've made here in Iceland, thank you for the kindness and friendship. Trust that we will meet again in the future. To my housemates at Fýlshólar, Lee, Jason, and Bryan, I can never be grateful enough for the friendship and all the good times. Lastly, I wish to thank my loving mom, my brother and sisters, relatives and friends back home, who have been very supportive and proud of my endeavours. This is dedicated to all of you.

REFERENCES

Alincastre, R.S., 1994: *Geology of well MG-18D.*Philippine National Oil Company – Energy Development Company, Taguig City, Philippines, internal report, 28 pp.

Allard, P., Carbonnelle, J., Dajlevic, D., Le Bronec, J., Morel, P., Robe, M.C., Maurenas, J.M., Faivre-Pierret, R., Martin, D., and Sabroux, J.C.,1991: Eruptive and diffuse emissions of CO_2 from Mount Etna. *Nature*, *351*, 387–391.

Bergfeld, D., Goff, F., and Janik, C.J., 2001: Elevated carbon dioxide flux at the Dixie Valley geothermal field, Nevada; relations between surface phenomena and the geothermal reservoir. *Chemical Geology*, *177*, 43–66.

Bien, O.C., 1996: *Geology of MG-8RD*. Philippine National Oil Company – Energy Development Company, Taguig City, Philippines, internal report, 52 pp.

Bien, O.C., and Contemplacion, R.D., 2007: *Geology of well MG39D.*Philippine National Oil Company – Energy Development Company, Taguig City, Philippines, internal report, 30 pp.

Bien, O.C., and Palma, R.R., 2005: *Geologic report of well MG-10RD.*Philippine National Oil Company – Energy Development Company, Taguig City, Philippines, internal report, 27 pp.

Brusca, L., Inguaggiato, S., Longo, M., Madonia, P., and Maugeri, R., 2004: The 2002-2003 eruption of Stromboli (Italy): Evaluation of the volcanic activity by means of continuous monitoring of soil temperature, CO_2 flux and meteorological parameters. *Geochemistry, Geophysics, Geosystems*, *5*, 14 pp.

Caranto, J.A., and Jara, M.P., 2015: Factors controlling reservoir permeability at the Leyte geothermal field, Philippines.*Proceedings of the World Geothermal Congress 2015, Melbourne, Australia,* 8 pp.

Chiodini, G., Cioni, R., Guidi, M., Raco, B., and Marini, L., 1998: Soil CO_2 flux measurements in volcanic and geothermal areas. *Applied Geochemistry*, *13*, 543–552.

Cox, M.E., 1980: Ground radon survey of a geothermal area in Hawaii. *Geophysical Research Letters*, *7*, 283–286.

Delfin, F.G., and Tebar, H.J., 1986: Geologic structures at the Mahiao, Sambaloran and Malitbog sectors of the Tongonan geothermal field, Leyte, Philippines.*Proceedings of the 8th New Zealand Geothermal Workshop*, 129–134.

Delmelle, P., and Stix, J., 1999: Volcanic gases. In Sigurdsson, H.,Houghton, B.,Rymer, H.,Stix, J., and McNutt, S. (eds.), *Encyclopedia of Volcanoes.*Academic Press, 803–816.

Deutsch, C.V., and Journel, A.G., 1998: *GSLIB: Geostatistical software library and user's guide*. Oxford University Press, New York, NY, United States, 384 pp.

Esperidion, J.A., and Bien, O.C., 2004: *Well MG-36D geology report.*Philippine National Oil Company – Energy Development Company, Taguig City, Philippines, internal report, 30 pp.

Fleischer, R.L., and Mogro-Campero, A., 1978: Mapping of integrated radon emanation for detection of long-distance migration of gases within the Earth: Techniques and principles. *Journal of Geophysical Research: Solid Earth*, *83*, 3539–3549.

Fridriksson, Th., Kristjánsson, B.R., Ármannsson, H., Margrétardóttir, E., Ólafsdóttir, S., and Chiodini, G., 2006: CO_2 emissions and heat flow through soil, fumaroles, and steam heated mud pools at the Reykjanes geothermal area, SW Iceland. *Applied Geochemistry*, *21*, 1551–1569.

Frondini, F., Chiodini, G., Caliro, S., Cardellini, C., Granieri, D., and Ventura, G., 2004: Diffuse CO_2 degassing at Vesuvio, Italy. *Bulletin of Volcanology*, *66*, 642–651.

Giammanco, S., Immè, G., Mangano, G., Morelli, D., and Neri, M., 2009: Comparison between different methodologies for detecting radon in soil along an active fault: The case of the Pernicana fault system, Mt. Etna (Italy). *Applied Radiation and Isotopes*, *67*, 178–185.

Heiligmann, M., Stix, J., Williams-Jones, G., Lollar, B.S., and Gustavo Garzón, V., 1997: Distal degassing of radon and carbon dioxide on Galeras volcano, Colombia. *Journal of Volcanology and Geothermal Research*, *77*, 267–283.

Herras, E.B., 1997: *Geology of well MG-33D.*Philippine National Oil Company – Energy Development Company, Taguig City, Philippines, internal report, 24 pp.

Hinkle, M.E., 1991: Seasonal and geothermal production variations in concentrations of He and CO_2 in soil gases, Roosevelt Hot Springs known geothermal resource area, Utah, U.S.A. *Applied Geochemistry*, *6*, 35–47.

Jolie, E., Klinkmueller, M., and Moeck, I., 2015: Diffuse degassing measurements in geothermal exploration of fault controlled systems. *Proceedings of the World Geothermal Congress 2015, Melbourne, Australia*, 8 pp.

Klusman, R.W., Moore, J.N., and LeRoy, M.P., 2000: Potential for surface gas flux measurements in exploration and surface evaluation of geothermal resources. *Geothermics*, *29*, 637–670.

Lewicki, J.L., and Oldenburg, C.M., 2004: *Strategies for detecting hidden geothermal systems by near-surface gas monitoring.* Lawrence Berkeley National Laboratory, Berkeley, CA, United States,report no. LBNL-56895, 76 pp.

Leynes, R.D., 1996a: *Geology of well MG-7RD.*Philippine National Oil Company – Energy Development Company, Taguig City, Philippines, internal report, 35 pp.

Leynes, R.D., 1996b: *Geology of Well MG-6RD*. Philippine National Oil Company – Energy Development Company, Taguig City, Philippines, internal report, 42 pp.

Mahon, W.A.J., McDowell, G.D., and Finlayson, J.B., 1980: Carbon dioxide: its role in geothermal systems. *New Zealand Journal of Science*, *23*, 133–148.

McCarthy, J.H., and Reimer, G.M., 1986: Advances in soil gas geochemical exploration for natural resources: Some current examples and practices. *Journal of Geophysical Research: Solid Earth*, *91*, 12327–12338.

Mismanos, J., and Vasquez, A., 2013: *Soil radon gas survey in Mahanagdong, Leyte: integrated final report.* Energy Development Corporation, Pasig City, Philippines,internal report, 64 pp.

Óladóttir, A.A., and Fridriksson, Th., 2015: The evolution of CO_2emissions and heat flow through soil since 2004 in the utilized Reykjanes geothermal area, SW Iceland: Ten years of observations on changes in geothermal surface activity. *Proceedings of the World Geothermal Congress 2015, Melbourne, Australia*, 10 pp.

Padrón, E., López, D.L., Magaña, M.I., Marrero, R., and Pérez, N.M., 2003: Diffuse degassing and relation to structural flow paths at Ahuachapán geothermal field, El Salvador. *Geothermal Resources Council Transactions*, *27,* 325–330.

Palma, R.R., and Bien, O.C., 2003: *Geology report of well MG-34D.*Philippine National Oil Company – Energy Development Company, Taguig City, Philippines, internal report, 23 pp.

Parker, R.L., 1967: Composition of the earth's crust. In: Fleischer, M. (ed.), *Data of geochemistry* (6th ed.). United States Government Printing Office, Washington D.C., United States, D1-D19.

Rinaldi, A.P., Vandemeulebrouck, J., Todesco, M., and Viveiros, F., 2012: Effects of atmospheric conditions on surface diffuse degassing. *Journal of Geophysical Research*, *117*, 14 pp.

Rochette, P., and Hutchinson, G.L., 2005: *Measurement of soil respiration in situ: chamber techniques.* University of Nebraska, Lincoln, NE, United States, 40 pp.

Rodríguez, A., Torres, Y., Chavarría, L., and Molina, F., 2008: Soil gas radon measurements as a tool to identify permeable zones at Las Pailasgeothermal area, Costa Rica. *Presented at the "30th Anniversary Workshop", organized by UNU-GTP, in Reykjavik, Iceland*, 7 pp.

Seastres Jr., J.S., Salonga, N.D., and Saw, V.S., 1996: Hydrology of the greater Tongonangeothermal system, Philippines and its implications to field exploitation. *Geothermal Resources Council Transactions*, *20,* 713–720.

Semprini, L., and Kruger, P., 1983: Simulation of radon transport in geothermal reservoirs. *Proceedings of the 9th Workshop on Geothermal Reservoir Engineering,*Stanford University, Stanford, CA, United States, 261-268.

Sinclair, A.J., 1974: Selection of threshold values in geochemical data using probability graphs. *Journal of Geochemical Exploration*, *3*, 129–149.

Sinclair, A.J., 1991: A fundamental approach to threshold estimation in exploration geochemistry: probability plots revisited. *Journal of Geochemical Exploration*, *41*, 1–22.

Tanner, A.B., 1980: Radon migration in the ground: a supplementary review. *Natural Radiation Environment III*, *1*, 5–56.

Tebar, H.J., 1983: *Well MG-5D preliminary geologic report.*Philippine National Oil Company – Energy Development Company, Taguig City, Philippines, internal report, 10 pp.

Vicedo, R.O., 1996: *Geology of well MG-27D.*Philippine National Oil Company – Energy Development Company, Taguig City, Philippines, internal report, 25 pp.

Vicedo, R.O., 1997: *Geology of well MG-9RD.*Philippine National Oil Company – Energy Development Company, Taguig City, Philippines, internal report, 21 pp.

Vicedo, R.O., and Medrano Jr., R.A., 1995: *Geology of well MG-5RD.*Philippine National Oil Company – Energy Development Company, Taguig City, Philippines, internal report, 39 pp.

Voltattorni, N., and Lombardi, S., 2010: Soil gas geochemistry: significance and application in geological prospectings. In: Potocnik, P. (ed.), *Natural Gas*. Sciyo, 183-204.

Voltattorni, N., Sciarra, A., and Quattrocchi, F., 2010: The application of soil gas technique to geothermal exploration: study of "hidden" potential geothermal systems. *Proceedings of the World Geothermal Congress 2010, Bali, Indonesia*, 7 pp.

Ward, C.W., 1979: The geology and hydrothermal alteration of the Tongonan geothermal field. *Proceedings of the New Zealand Geothermal Workshop,* 113–125.

Werner, C., and Cardellini, C., 2006: Comparison of carbon dioxide emissions with fluid upflow, chemistry, and geologic structures at the Rotorua geothermal system, New Zealand. *Geothermics*, *35*, 221–238.

Witcher, J.C., 1991: Radon soil-gas surveys with diffusion-model corrections in geothermal exploration. *Geothermal Resources Council Transactions*, *15*, 301–308.

Yang, T.F., Walia, V., Chyi, L.L., Fu, C.C., Chen, C.H., Liu, T.K., Song, S.R., Lee, C.Y., and Lee, M., 2005: Variations of soil radon and thoron concentrations in a fault zone and prospective earthquakes in SW Taiwan. *Radiation Measurements*, *40*, 496–502.

APPENDIX I: Probability plots of data sets from Areas A, B, and C

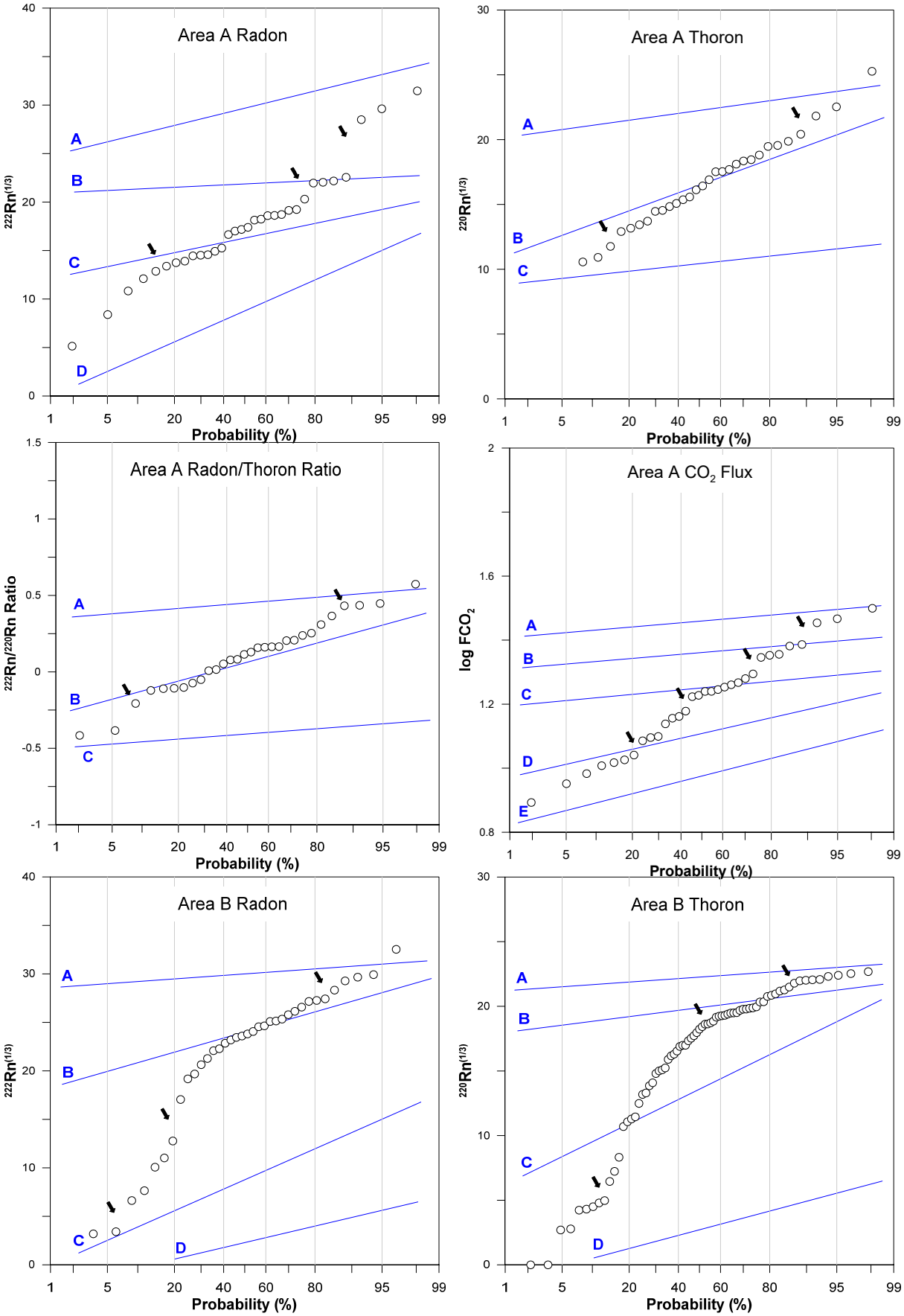

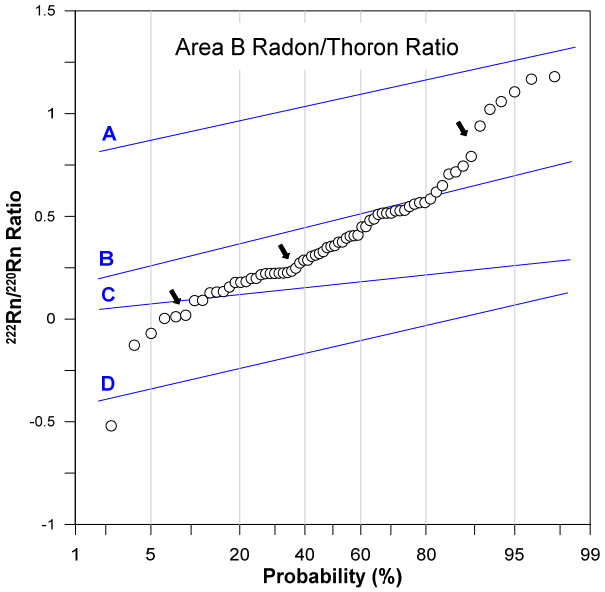
Area B Radon/Thoron Ratio
222Rn/220Rn Ratio
Probability (%)
A
B
C
D

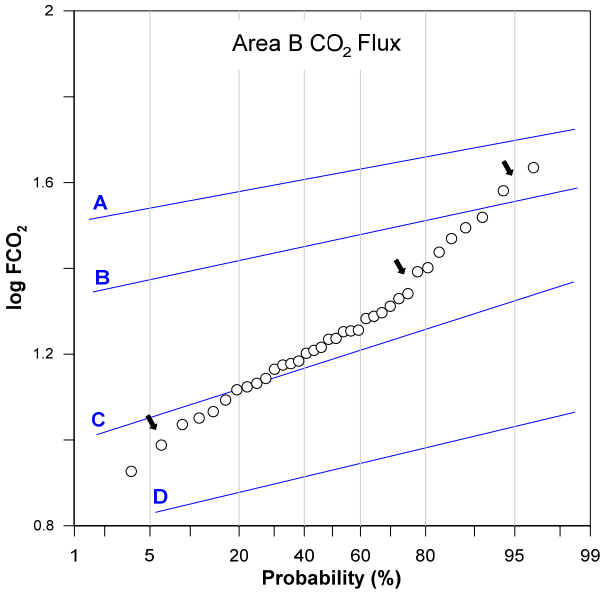
Area B CO2 Flux
log FCO2
Probability (%)
A
B
C
D

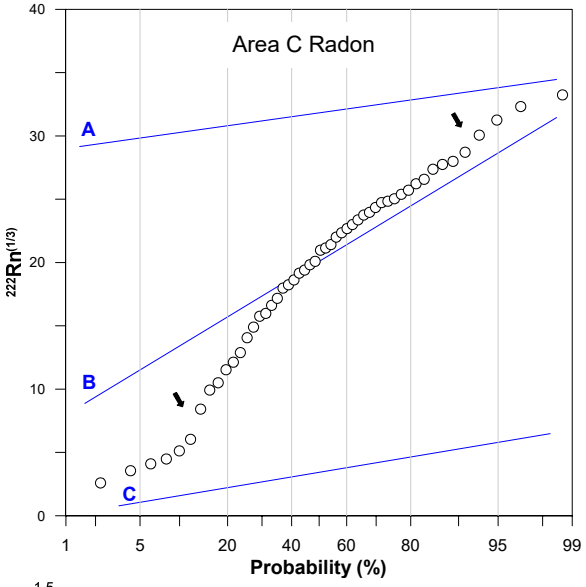
Area C Radon
222Rn(1/3)
Probability (%)
A
B
C

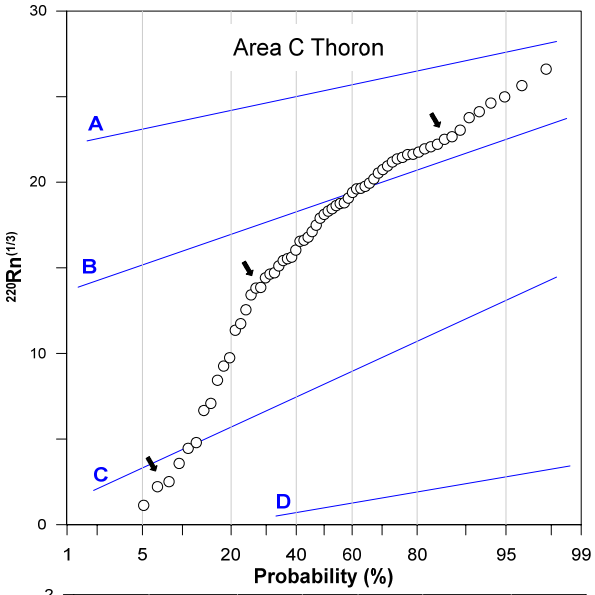
Area C Thoron
220Rn(1/3)
Probability (%)
A
B
C
D

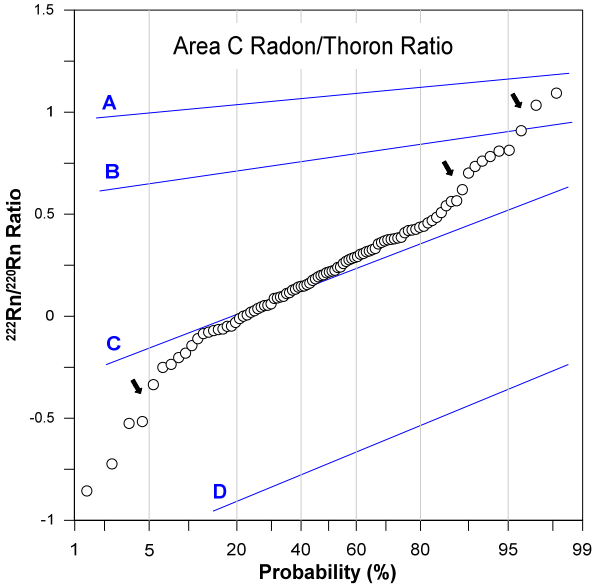
Area C Radon/Thoron Ratio
222Rn/220Rn Ratio
Probability (%)
A
B
C
D

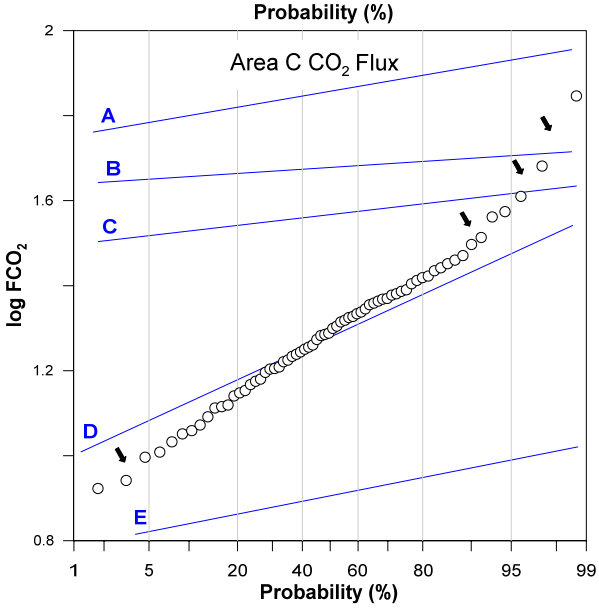
Area C CO2 Flux
log FCO2
Probability (%)
A
B
C
D
E

APPENDIX II: Results of the partitioning of populations

	Area A		Area B		Area C		Characteristic
	N	range	*N*	range	*N*	range	
Radon Bq/m^3	3	11467–31100	9	23300–45300	15	25367–45900	Anomaly
	4	8367–11467	49	4957–23333	167	220–25367	Background
	21	1770–8363	13	30–4957	25	0–220	Background
	4	136–1770	4	0–33			Background
Thoron Bq/m^3	3	8510–11600	10	9923–14900	21	13000–23400	Anomaly
	24	1627–8510	27	6057–9923	132	2457–13000	Background
	5	0–1627	29	110–6057	37	16–2457	Background
			9	0–110	17	0–16	Background
Radon/ Thoron					6	8.22-61.03	Anomaly
	4	2.32-3.74	7	6.19-20.77	15	4.17-8.22	Anomaly
	24	0.41-2.32	40	1.68-6.19	165	0.31-4.17	Background
	2	0.38-0.41	18	1.04-1.68	10	0.08-0.31	Background
			7	0.27-1.04			Background
CO_2 Flux g·m^{-2}·d^{-1}					4	50.57–79.04	Anomaly
	3	24.34–31.58	4	32.1–82.69	3	40.78–50.57	Anomaly
	5	19.70–24.34	13	22.64–32.1	10	32.61–40.78	Background
	10	15.07–19.70	53	9.73–22.64	181	9.72–32.61	Background
	8	10.62–15.07	5	4.98–9.73	9	4.90–9.72	Background
	6	7.81–10.62					Background

UNITED NATIONS UNIVERSITY
UNU-GTP
Geothermal Training Programme

Orkustofnun, Grensasvegur 9,
IS-108 Reykjavik, Iceland

Reports 2015
Number 23

MICROGRAVITY SURVEY IN 2009-2010 AROUND BACMAN GEOTHERMAL FIELD, PHILIPPINES - GRAVITY CORRECTIONS AND INTERPRETATIONS

Jonathan Lee C. Monasterial
Energy Development Corporation - EDC
38/F One Corporate Centre Building
Julia Vargas corner Meralco Avenue
OrtigasCenter, Pasig City, 1605
PHILIPPINES
monasterial.jc@energy.com.ph

ABSTRACT

A microgravity survey was conducted in 2009-2010 around the Bacman geothermal field, Philippines. The observed gravity readings were subjected to the standard reduction process such as tidal, instrumental drift, latitude, and terrain corrections using Gravos, Gnet, Terra and Terrb reduction programs. Free-air and Bouguer corrections were calculated by using the Bouguer program. After these corrections, the optimum reduction density was determined analytically by using the Parasnis method. To enhance the local anomalies, the regional trend in the Bouguer maps was removed. The regional field was estimated to be planar.

Positive anomalies in the central part of the field are within the Bacman Fault Zone. These are interpreted to be dense, intrusive rocks such as diorite which are present beneath this area based on core samples. In addition, these anomalies extend to the western and northern regions of the field near Mts. Tikolob and Kayabon and may be related to the resistivity anomaly seen in the western part of the field. Negative anomalies represent the sedimentary formations and collapse features in the south-eastern and northern parts of the area, respectively.

Using limiting depth analysis, the dense intrusive rock was approximated as a spherical body and its centre was found to be at a depth of around 900 m. In addition, an irregularly shaped body was assumed to be present beneath the western parts of the field and a depth to the top of this body was found to be about 1750 m.

1. INTRODUCTION

Geothermal energy has become increasingly important around the world for the past few decades. This renewable energy has been utilized for electricity generation in 24 countries. In total globally, around 12.35 GWe of installed capacity are projected for this year, which is an increase of 16% compared to 2010. USA, Philippines, Indonesia, Mexico and New Zealand are among the leading countries in terms of installed electrical power capacity (Bertani, 2015). Moreover, this clean energy is also used directly

in 82 countries worldwide for ground-source heat pumps, bathing and swimming pools, space heating, greenhouses, etc. Globally, the total installed thermal power is around 70.329 GWth, an increase by 45% compared with the data gathered in 2010 (Lund and Boyd, 2015). Countries with the largest installed capacities include China, USA, Sweden, Turkey and Iceland. In terms of primary energy supply available, geothermal energy is very small compared to other sources such as oil, coal, and natural gas which comprise 31.4%, 29.0%, and 21.3%, respectively, of the total primary energy supply worldwide (IEA, 2014). More geothermal energy development is needed in order to increase the supply coming from this green and clean energy. However, geothermal energy development, like any other energy development, needs to start with scientific investigation and exploration. Effective methods of exploration are crucial for the successful development of geothermal resources due to the complexity of subsurface geothermal systems. In general, geothermal exploration should be done with a multidisciplinary approach which focuses on geology, geochemistry and geophysics. Geological exploration methods include mapping of tectonic structures, stratigraphy and hydrothermal alteration, as well as geological history. Geochemical studies on surface manifestations such as hot springs and fumaroles are done to evaluate fluid properties and estimate reservoir temperature. Geophysical surveys are used to detect and image subsurface structures related to geothermal systems and estimate the reservoir size and properties and together with other observations to locate possible drilling targets (Flóvenz et al., 2012).

Most geophysical methods are passive, i.e. they are based on natural changes. These include magnetotelluric (MT), seismic, magnetic, and gravity methods. The seismic methods use natural seismicity to obtain information that may be related to fluid movement within geothermal systems, as well as information on velocity structures. In the magnetic method, which is a potential method, spatial variations in the earth's magnetic field strength are measured. Magnetic maps are then generated which represent the variations of magnetic properties of subsurface features. The gravity method, which is also a potential method, is used in a similar way. These methods are used to identify structures such as faults, dykes and intrusions by measuring spatial variations in gravitational acceleration and magnetic intensity due to lateral changes of density and susceptibility of the earth. The field variations can, in many cases, be interpreted by using analytical modelling and thereby give an idea about the depth, geometry and density or susceptibility causing them (Mariita, 2007). On the other hand, active methods do not rely on natural changes but use artificial signal sources, such as in seismic refraction and reflection and transverse electromagnetic (TEM) methods.

The gravity method is the main objective of this report. This report focuses particularly on the microgravity survey conducted at the Bacman geothermal field (BGF) in the provinces of Albay and Sorsogon of the Philippines in 2009 and 2010. Previous and most recent geophysical surveys in the area are briefly presented. Microgravity data processing, analysis and interpretation are discussed in detail in this report.

2. GRAVITY CONCEPTS AND PRINCIPLES

Newton's law of gravitation states that the attractive force F between two bodies is directly proportional to the product of the masses and inversely proportional to the square of the distance between the centres of mass of the bodies. It is given by:

$$F = G\frac{m_1 m_2}{r^2} \tag{1}$$

where G = Universal gravitational constant [Nm^2/kg^2] in SI units;
m_1 = Mass of the first body [kg];
m_2 = Mass of the second body [kg];
r = Distance between the centres of masses of the particles [m].

Based on Newton's Second Law of Motion, which states that force is the product of mass and acceleration, Equation 1 can be rearranged into:

$$F = m_1 G \frac{m_2}{r^2} = m_1 g_2 \quad (2)$$

where g_2 = Acceleration due to gravitational force of the second body of mass m_2 on unit mass of the first body [m/s^2].

In Equation 2, if m_1 is free to move, it will be drawn towards m_2 at a speed which constantly increases with acceleration g_2 (Hunt, 2001). For the case of Earth, g_2 becomes the acceleration of gravity g_e on the surface of the earth and is given by:

$$g_e = G \frac{M_e}{{R_e}^2} \quad (3)$$

where R_e = Radius of the Earth [m];
M_e = Mass of the Earth [kg].

The force of gravity is a derivative of a potential field which has no gaps or discontinuities. The gravitational force at a point can be presented by a vector whose magnitude and direction is the sum of the attraction of all bodies in the universe. In general, the force of gravity at any point on the Earth's surface is mainly due to the Earth itself with minor contributions from the sun and moon (Hunt, 2001).

The acceleration of gravity due to Earth was first measured by Galileo Galilei in his famous experiment at Pisa. Two equivalent SI units can be used for acceleration which is metres per second squared (m/s^2) and Newton per kilogram (N/kg). The value for the acceleration of the earth is 9.8 m/s^2 on the average but varies with latitude and elevation. In geophysics, the most commonly used unit of gravity is Gal, named after Galileo, 1 Gal = 1cm/s^2 = 10^{-2} m/s^2. In gravity measurements, 1 milligal (mgal) = 10^{-5} m/s^2 and 1 microgal (μgal) = 10^{-8} gal. Furthermore, a commonly used unit is gravity unit (gu) which is equivalent to 0.1 mgal.

The Earth´s gravitational potential is defined as:

$$U = G \frac{M_e}{r} \quad (4)$$

where U = Gravitational potential [J/kg];
r = Distance from the centre of mass of Earth [m].

In Equation 4, the gravitational potential field U is a scalar quantity and its first derivative in any direction gives the acceleration of gravity in that direction. Equipotential surfaces on earth are surfaces where U is constant. The sea-level surface, or the geoid, is the most easily recognized equipotential surface. It is horizontal, that is at a right angle to the gravitational acceleration (Kearey et al., 2002). An approximation of the geoid is the WGS 84 ellipsoid, which is a geocentric equipotential ellipsoid of revolution (NIMA, 1997).

3. GRAVITY FIELD OF THE EARTH

The gravitational field at any point on the earth's surface is composed mainly of gravitation due to the mass of the earth and a centrifugal component due to the rotation of the earth. Furthermore, the gravity fields of the sun and the moon are significant on the surface of the earth.

As the earth is not a perfect sphere, and due to its rotation, the acceleration of gravity is not constant on its surface. Due to that and the variable centrifugal effect, the gravity on the earth's surface varies with

latitude. The non-spherical shape of the earth and local variations of density within the earth (Hunt, 2001) also cause variations. The rotation of the earth and its equatorial bulge produce an increase of gravity with latitude as the centrifugal component of the gravity field is at maximum at the equator and zero at the geographic poles, and the distance from the surface to the centre of mass decreases.

Atmospheric pressure changes also contribute to earth's temporal gravity variation directly by a gravitational effect and indirectly by a deformation effect. Groundwater level, rainfall amount and soil moisture content changes through time add directly to gravitational variations and for large loads, indirect deformation effects are involved (Torge, 1989).

4. GRAVITY SURVEYING AND CORRECTIONS

4.1 Gravity surveying

Regional reconnaissance surveys can have measurements at points several kilometres apart, preferably with uniform distribution, but usually measurement points are along roads. Regional surveys can provide information about major rock unit distribution and deep crustal features of the area covered. To increase the resolution, detailed surveys with denser station distribution are carried out. For survey areas with rapidly changing gravity fields, a denser station spacing is needed, as accurate measurement of gravity gradients is often critical in the subsequent interpretation (Kearey et al., 2002). The necessary interval between stations is dependent on the assumed depth and size of geological features that are expected to create gravity anomalies such as dykes or intrusions, geological contacts, discontinuities and faults.

Accurate measurements of elevation are necessary for corrections of the measurements. An accuracy of station elevation of ±1 cm is needed to achieve accuracies of a few μGals in the gravity values. This precision can be achieved by optical levelling surveys and by the use of differential global positioning system (GPS) surveys (Seigel, 1995). Uncertainty in the elevations of gravity stations probably accounts for the greatest errors in the corrected gravity values on land. Accuracy of the horizontal position of gravity stations on the other hand is far less critical so the latitude of the station should be known to ±10 m (Kearey et al., 2002). In addition, it is important to note that the same reading procedure must be used at every survey point, during each survey. Measurements should preferably not be made during rainy or windy days.

The standard procedure for conducting gravity surveys follows the loop technique. In this technique, a daily field survey starts by measuring at a base or reference gravity station with a known absolute gravity value and ends by measuring at the same base station. In between these measurements, new or previously occupied gravity stations are visited. After the survey is finished, all observed gravity readings are subjected to a reduction or correction process.

Difference in elevations leads to variations in gravity because the gravitational force of the Earth varies with the square of the distance of the survey-point from the centre of the Earth. The higher the elevation h, the smaller gravitational acceleration would be measured (Telford et al., 1990). It is also important to note that the differences in elevation are caused by topographic changes on the earth's surface. Topography also leads to changes in the gravitational acceleration. If a mountain is near the measuring point, it has an upward component of gravity. If a valley is present, a mass is lacking, assuming a correction for a Bouguer plane has been made. This is similar for correction for the sea or bathymetry. Consequently, topographic corrections are always positive or increase in gravity (Lichoro, 2014). A schematic diagram depicting these situations is shown in Figure 1.

Local density variations within the earth affect the gravity as well and cause the anomalies that are the purpose of the surveys. The effect depends on the nature and depth of the material or entity causing these lateral density contrasts. In order to know and explain these variations physically, other factors of

known origin which contribute to changes in the gravitational field should be removed. After they are removed, the anomalies may be interpreted. An example of a gravity anomaly for a hypothetical dense body beneath the surface is shown in Figure 2.

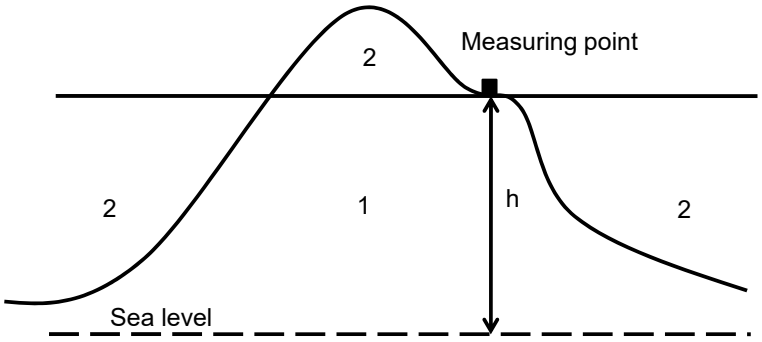

FIGURE 1: The gravity observed at the measuring point (square) of height *h* above the sea level is affected by presence of the hill nearby and valleys on both sides (2) and by the mass underneath it (1)

4.2 Gravity reduction

Gravity reduction is a process used to correct for variations in time and space of the earth's gravitational acceleration, that are not caused by local density differences in the rocks underneath the Earth's surface. The result is reduced gravity readings whose values are on a datum surface such as the geoid or sea-level surface. The corrections are to be made after the observed readings are calibrated based on the calibration factor of the gravimeter used.

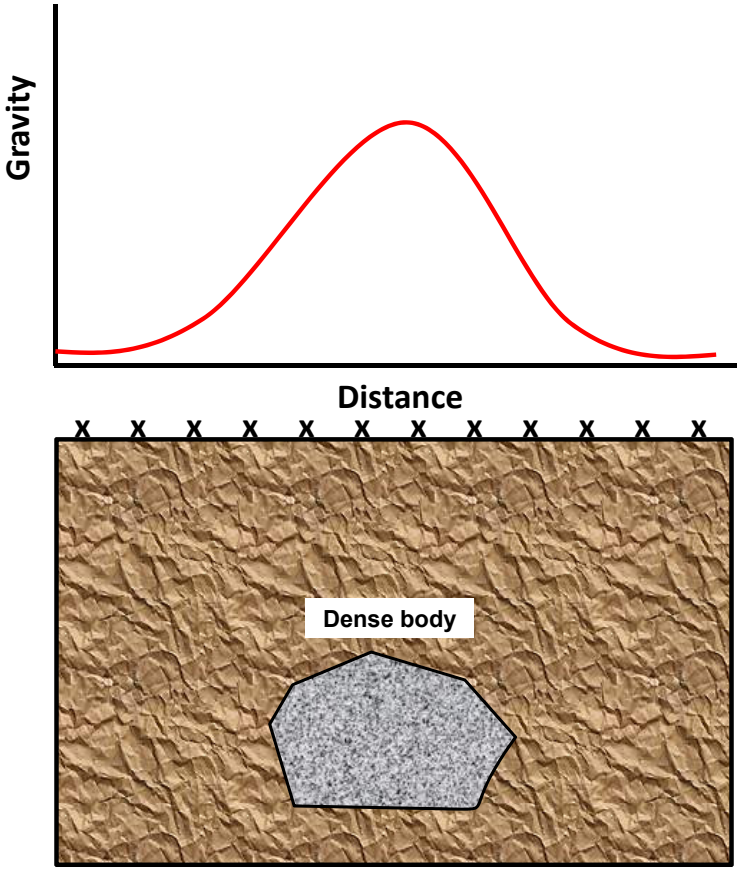

FIGURE 2: Gravity anomaly caused by a buried dense body (modified from Mariita, 2007)

Instrumental drift refers to a change in measured value with time, observable when the gravimeter is left in a fixed location or a measurement is repeated. This phenomenon is due to the imperfect elasticity of the springs inside the gravimeter that undergo creep with time. This can also be caused by temperature variations that, unless counteracted in some way, cause expansion or contraction of the spring and thus give rise to changes in measurements which are unrelated to variations in gravity (Kearey et al., 2002). In order to compensate for the gravimeter drift, repeated measurements at a certain base station are done throughout the day. A drift curve in Figure 3 shows the meter reading at one station against recording time. The drift is assumed to be linear between consecutive base station measurements.

Tidal forces are the direct gravitational forces of the sun and the moon and contribute to the observed gravity field variations of values in the range of about 0.3 mGal and a minimum period of about 12 hours. Tidal correction is made before the instrumental drift is estimated.

As previously mentioned, the non-spherical nature of the Earth's shape contributes to the latitude variation of its gravitational field. Also, as it rotates, a centrifugal acceleration is produced which causes

the gravity to decrease from its poles to the equator. Therefore, any point near the equator is farther from the centre of mass of the Earth and experiences lesser gravitational pull than if it were near the poles. The difference of the gravitational attraction is by some 5.19 mGal. The latitude correction is to be subtracted from the observed gravity readings.

Another correction needed to be accounted for is related to any measurement taken at a certain elevation. As the gravitational acceleration is inversely proportional with the square of the distance, the observed gravity value at a certain height needs to be corrected to a datum sea-level surface. This is resolved by a free-air correction using the formula:

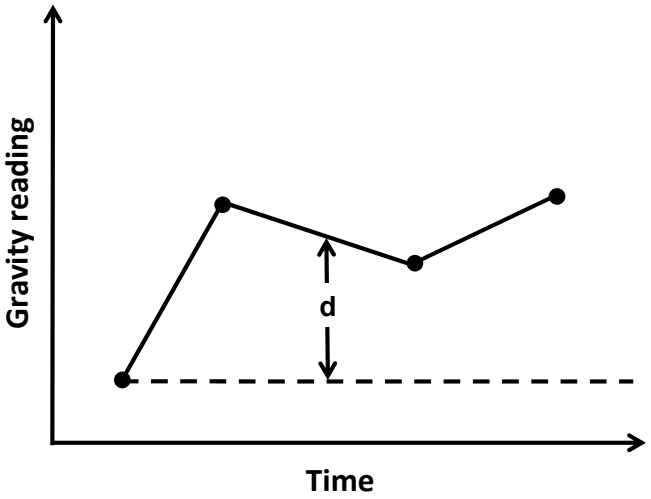

FIGURE 3: Gravimeter drift behaviour (adapted from Kearey et al., 2002)

$$g_{FC} = 0.3086\, h\, mGal \qquad (5)$$

where h = Height of the station measured relative to sea-level [m].

The calculated g_{FC} is then usually added to the observed gravity reading since most of the measurements are above the reference sea-level surface.

Bouguer correction accounts for the mass between the gravity station and the reference level. An infinite horizontal slab is assumed to represent the rock layer beneath the observation point and its thickness is equal to the elevation difference between the observation point and the reference level. The value calculated (Equation 6) will be subtracted from the observed gravity reading at elevation h.

$$g_{BC} = 2\pi G\rho h = 0.04191\, \rho h\, mGal \qquad (6)$$

where ρ = Density of infinite horizontal slab [kg/m^3].

Accounting for effects of topography is important and critical in the gravity reduction process. Hills or mountains reaching above the gravity station exert an upward force on the gravimeter. Valleys are a mass deficit and therefore the Bouguer correction is greater than it should be. In both cases, a correction for these effects is called terrain correction and it is a positive number. One method to account for this correction is the Hammer chart. This is a circular graticule which consists of radial and concentric lines defining several sectors, where the outermost zone extends to 22 km or even farther, beyond which the terrain effects are usually negligible. This transparent graticule is laid out over a topographic map with its centre on the gravity station being observed and the average terrain elevation of each sector is determined. Gravitational effect of each sector is determined and the summation of the gravitational contribution of all sectors contribute to the terrain correction value to be added to the value of the observed gravity (Kearey et al., 2002).

Today, digital maps have been made for many areas. Terrain corrections based on these maps are made by a computer. It is also important to emphasize that in areas of rugged topography, terrain effects are large, being at a maximum in steep-sided valleys, at the base or top of cliffs and at the summits of mountains. This can contribute significant errors as it may be difficult to account correctly for the topographic effect (Kearey et al., 2002). It is therefore advisable to avoid gravity measurements in these areas, if possible.

Atmospheric gravity correction is necessary if the datum level used for reference is the WGS 84 ellipsoid

since this reference ellipsoid encloses the whole mass of the Earth, including atmosphere. With this, the theoretical or normal gravity can be computed at the ellipsoid surface and in space without having to consider atmospheric density differences (NIMA, 1997). The equation for this correction is shown in Equation 7, and it is to be added to the observed gravity reading value:

$$g_A = 0.87e^{-0.116\,h^{1.047}} \tag{7}$$

where h = Elevation with respect to sea level (m).

To summarize, the free-air (g_F) and Bouguer (g_B) gravity anomalies are given by the following:

$$g_F = g_C - g_L + g_A + g_{FC} \tag{8}$$

$$g_B = g_F + g_{TC} - g_{BC} \tag{9}$$

where g_C = Tide and drift corrected gravity values (mGal);
g_L = Normal gravity value with latitude correction (mGal);
g_A = Atmospheric air correction (mGal);
g_{FC} = Free-air correction (mGal);
g_{TC} = Terrain correction (mGal);
g_{BC} = Bouguer correction (mGal).

5. APPLICATIONS OF GRAVITY SURVEYS TO GEOTHERMAL PROSPECTING

Gravity surveys shed light on the structure and physical properties of geothermal fields. The gravity anomalies observed may be due to subsurface geologic features such as lithological contacts, boundaries, faults, dikes, intrusions, and calderas. They can also be due to a change in the physical conditions such as the existence of steam cap (Nordquist et al., 2010). Furthermore, change in gravity because of extraction of fluid can be observed (Eysteinsson, 2000).

Subsurface faults that have no evidence on the surface were delineated and other faults were confirmed in a gravity survey using horizontal gradient analysis of the gravity data collected in the Ungaran Volcano geothermal field in Indonesia (Setyawan et al., 2015). Regional faults were delineated in Hohi geothermal area, Japan, using horizontal gradient interpretation of gravity data (Salem et al., 2005). First and second horizontal gradient methods applied to gravity data from Cipinas geothermal prospect, Indonesia (Martakusumah et al., 2015) also revealed lateral boundaries of density contrasts that may be related to relatively deep faults or geological boundaries within the subsurface.

Dense intrusions and dikes in the Hengill geothermal field have been inferred by correlating gravity anomaly maps with MT resistivity maps. These geological features, perceived to be deep conductors, are reflected as regions with high gravity values (Hersir et al., 2009). Analysis of gravity maps and magnetic maps have also revealed dike intrusions which may serve as heat sources, such as in the Olkaria geothermal field, Kenya (Mariita, 2011).

Geothermal reservoirs of existing geothermal fields are also being monitored by conducting microgravity surveys. These surveys aim to quantify temporal gravity changes associated with continuous exploitation. These temporal variations of gravity values may be caused by mass changes in the geothermal reservoir, vertical ground movements such as subsidence or inflation and groundwater level variations (Hunt, 2001). Mass changes due to liquid drawdown and saturation level changes in the two-phase zone were reported to be the possible reason for the decreased gravity values measured at Tongonan geothermal field, Philippines (Apuada and Olivar, 2005). Subsurface fluid dynamics such as in geothermal reservoirs were also studied in Semarang alluvial plain in Indonesia (Sarkowi et al., 2005) and in Ogiri geothermal power plant, Japan (Nishijima et al., 2015) by time-lapse four-dimensional and hybrid microgravity measurements. Refinement of a geothermal reservoir model was also accomplished by calibrating it against repeated microgravity data (Pearson et al., 2015).

6. MICROGRAVITY SURVEY IN BACMAN GEOTHERMAL FIELD

A microgravity survey was conducted in 2009 and 2010 around the Bacman geothermal field, Philippines. This survey covered a network of 101 gravity stations (Figure 4), using the looping method. Using this method, the daily survey began and ended by doing measurements at the base station. In between, measurements were carried on other gravity stations. Some stations were measured more than once on a trip and in some cases on different trips (Figure 5). At each station, at least three readings were done with difference in dial not exceeding ± 0.3. In this survey, station 77 was used as a base station. The gravity value at station 77 was derived from station 71 where the absolute gravity value is known. Precise levelling survey was conducted in tandem with the gravity survey to determine the elevations of all gravity stations. Appendix I shows location of gravity stations, gravity values and anomalies.

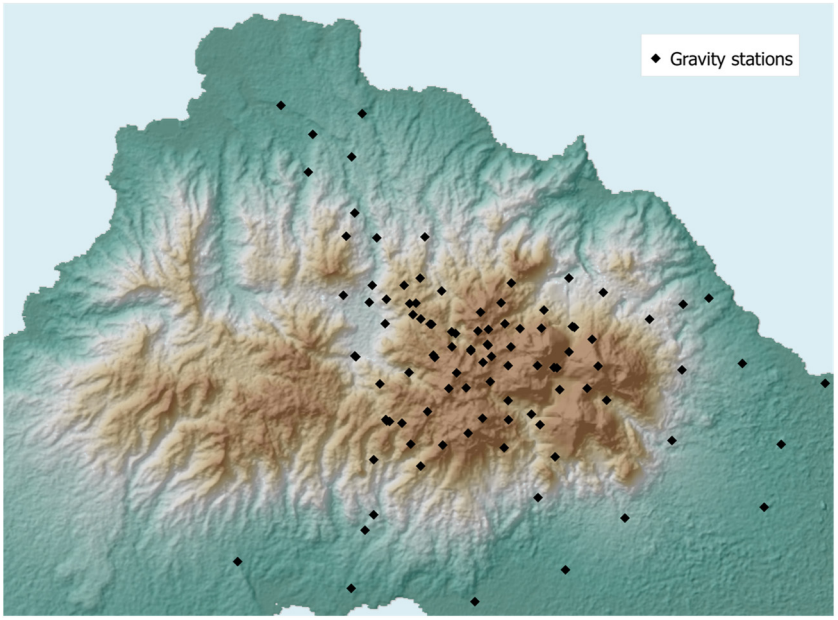

FIGURE 4: Microgravity survey conducted in 2009 and 2010 covering 101 gravity stations in and around the Bacman geothermal field

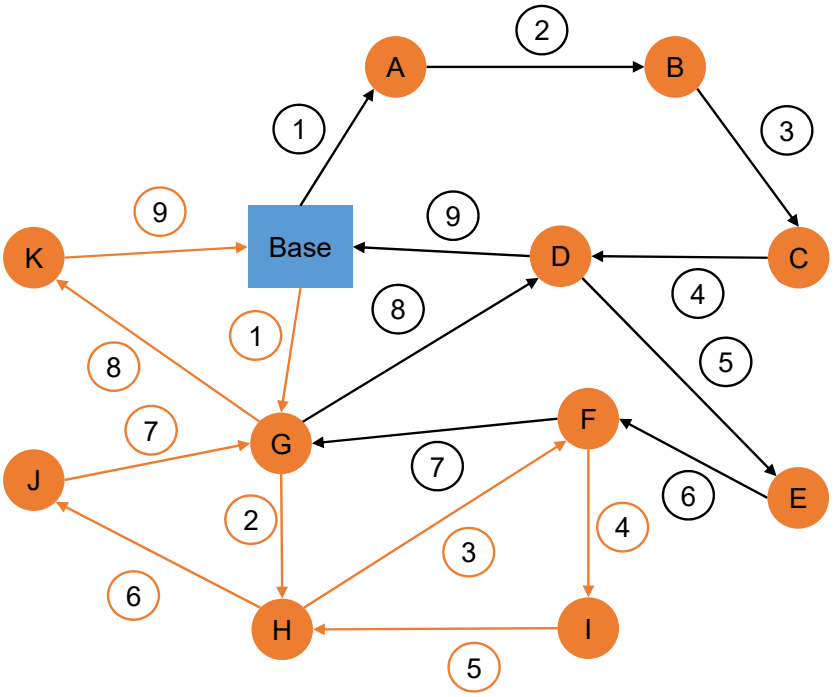

FIGURE 5: A network of gravity stations (orange circles) for two different one-day survey trips; these trips always started and ended at the base station (blue square)

6.1 Microgravity survey data processing

6.1.1 Drift reduction using Gravos reduction program

The Gravos reduction program by Iceland GeoSurvey (ISOR) converts the observed gravity readings of the gravimeter to gravity values. This program calculates the tide correction using the Longman Formula (Longman, 1959). To compensate for the drift of the gravimeter, the drift correction is then calculated for each survey trip. Input parameter files included the summary of the observed gravity readings at each station of each survey trip, the instrument calibration table, the base station with known absolute gravity value, and the gravity stations' coordinates and their corresponding elevations. The output of this will be used for the Gnet reduction program which adjusts the gravity values in a network of gravity stations.

6.1.2 Gravity network adjustment using Gnet program

The Gnet program by ISOR is used to calculate new gravity values of tied or redundant stations measured at least twice by different survey trips. Due to the redundancy of some observations, the gravity measurements need to be adjusted since they may contain gross, random, and systematic errors. These systematic errors are a result of instrument drift, and instrument reading unmodelled calibration factors. In addition, gross errors considered as outliers may be hidden in the data and failure in detecting them may result in false gravity values (Hwang et al., 2002). The Gnet program also calculates the gravity values of all other stations in order to compensate for the newly computed gravity values of tied stations. The program does the calculation by either setting a station with a fixed value as a constraint, or by using no fixed value. The output file of the Gravos reduction program, which corresponds to individual loop drift corrections, will be an input file for the Gnet program. Other input files include the calibration scale factor of the gravimeter used, the observed station readings for the entire survey, the observed station coordinates and elevation. The results of this network adjustment will then be subjected to terrain and elevation corrections.

6.1.3 Latitude, atmospheric air, free-air and Bouguer corrections using Gravity and Bouguer programs

Latitude and atmospheric air corrections are calculated using the Gravity program by ISOR while the free-air and Bouguer corrections were computed via the Bouguer program. The values for these corrections are to be subtracted and added to the observed gravity value, respectively.

6.1.4 Terrain corrections using Terra and Terrb reduction programs

The Terra and Terrb reduction programs by ISOR are used to calculate terrain and bathymetric corrections, respectively. These corrections consider the effect of masses related to land and sea topographic reliefs within the field and several kilometres away from it. However, the program has a limitation in calculating the terrain correction for each gravity station. The program computes the correction by using the Hammer method which divides the area into several zones, but skips the first two zones near and around the observed station, as it assumes the area is relatively flat within 20 m or there is no topographic relief within that distance. The terrain correction is to be added to the observed gravity value. The output of this program will be used to calculate the free-air and Bouguer corrections.

6.1.5 Reduction density estimation

The Parasnis method (Parasnis, 1952) is used to estimate the reduction density ρ. Generally, this method assumes that the free-air correction is only affected by elevation changes, thus, it will increase linearly with elevation. In addition, the Bouguer anomaly is considered to be a random error of mean value zero. Therefore, the plot of free-air anomaly values against the difference between the product of a constant and elevation values and terrain correction per unit density T for all gravity stations, should follow a straight line (Telford et al., 1990).

7. BACMAN GEOTHERMAL FIELD

7.1 Geologic and tectonic setting

Bacman geothermal field, hereafter referred to as BGF, straddles the boundary between the provinces of Albay and Sorsogon, Region V, Philippines (Figure 6). The geothermal field is within two municipalities; Manito town in Albay and Bacon District in Sorsogon. To the northwest is the Mayon Volcano and to the southeast is Mt. Bulusan. The geothermal field is located within a series of Pliocene to recent andesitic and basaltic volcanoes collectively known as Pocdol Mountains and Pocdol volcanic complex.

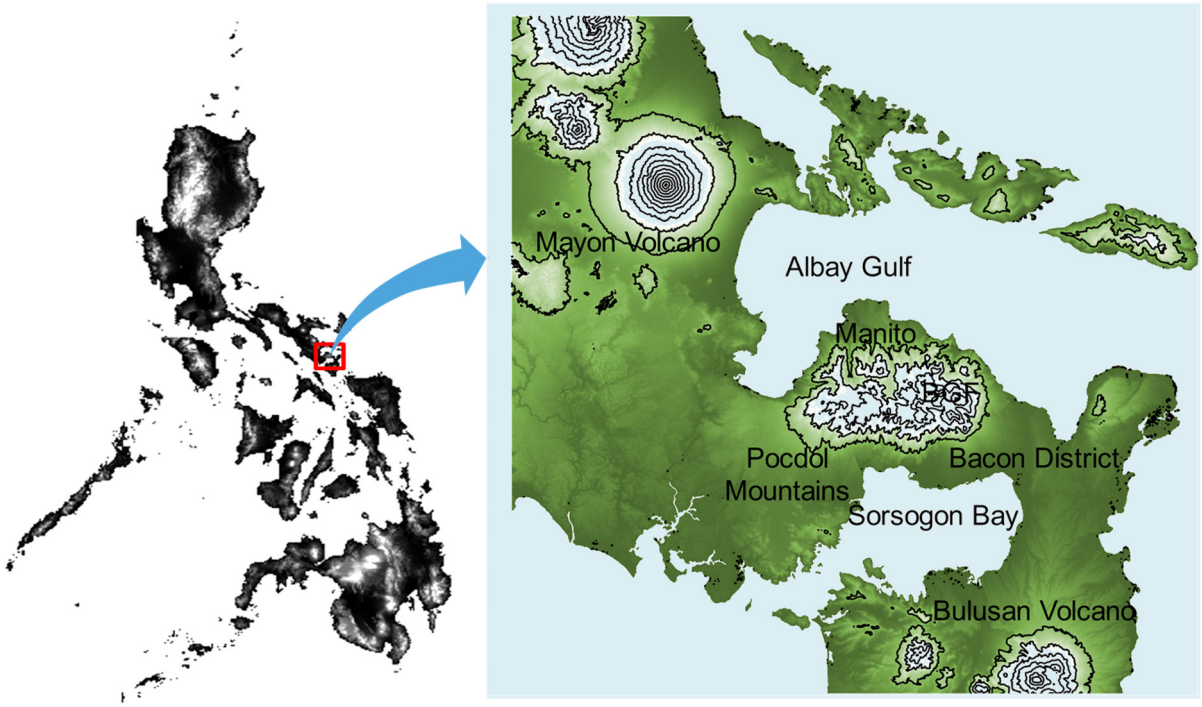

FIGURE 6: Geographical location of Bacman geothermal field, Philippines

The Pocdol volcanic complex is a part of NW-SE trending volcanic chain termed "Bicol Volcanic Belt" which includes Mt. Labo, Mt. Isarog, Mt. Iriga, Mt. Mayon and Mt. Bulusan, as seen in Figure 7. Bicol Volcanic Belt is located between two active tectonic regions. To the east is the Philippine Trench, a subduction zone resulting from the ongoing convergence of the Philippine Sea Plate and the Eurasian Plate, and to the west is the prominent Philippine Fault which runs through the country in a NW-SE orientation. Bacman Fault Zone (BFZ), oriented east-southeast, is a major splay fault of the Philippine Fault, but both faults are active (Lagmay et al., 2005) which affects the geodynamics in the BGF (Figure 8). In the BGF there is extensive faulting, forming graben structures. The geology of the BGF is characterized by volcanic domes and cones, heavily dissected by faults whose attributes and distribution are mainly controlled by the BFZ. In addition, the BGF also contains prominent, eroded collapse features and scarps due to landslides in the western part. The geothermal activities of the BGF appear to be constrained within the BFZ (Braganza, 2014).

Three major lithological formations comprise the BGF. These are: Pocdol volcanics formation (PVF), Gayong sedimentary formation (GSF), and Cawayan intrusive complex (CIC):

- PVF is a sequence of volcanic units composed of lava flows and pyroclastic deposits from numerous volcanic centres of Pliocene to Recent age. PVF is also characterized as slightly to intensely altered andesite lavas and tuff breccias with minor pyroxene basalt.

FIGURE 7: NW-SE alignment of volcanoes locally known as "Bicol Volcanic Belt" (modified from Google Earth, 2015)

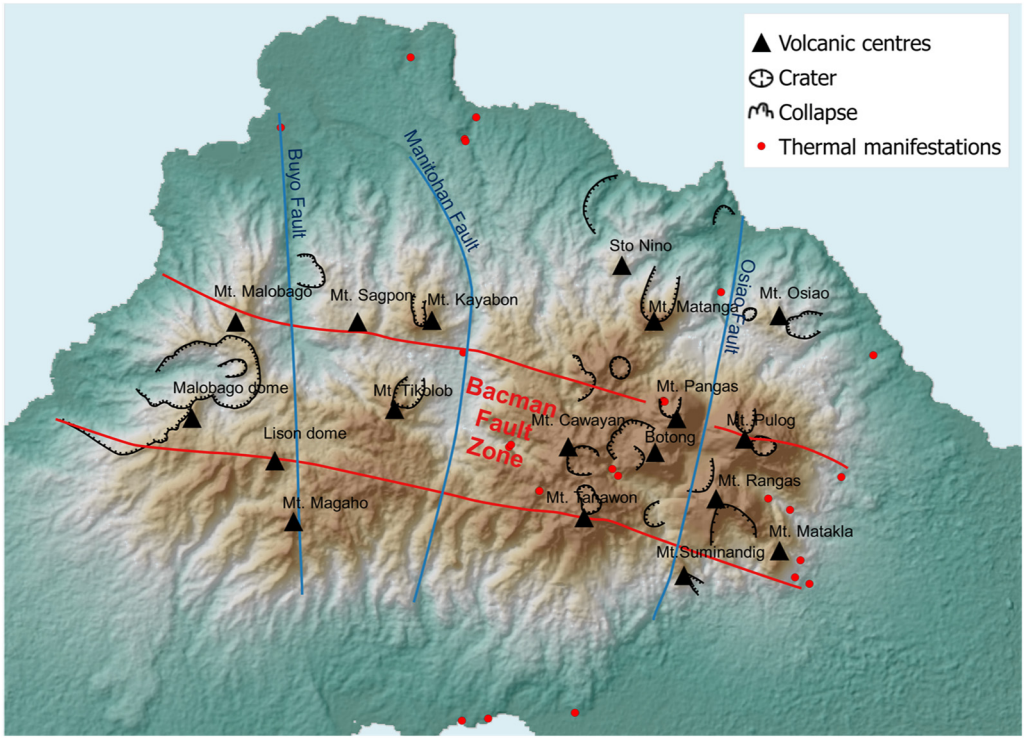

FIGURE 8: Bacman geothermal field elevation map with major tectonic structures, volcanic centres, collapses, craters, and thermal manifestations (modified from Braganza, 2014)

- Beneath the PVF is GSF which is generally described as multi-lithologic units composed of calcareous and fossiliferous sedimentary breccias with volcanic clasts, and dark fossiliferous uniformly-grained and impervious siltstones.
- CIC on the other hand is composed of porphyritic microdiorite, diabase and pyroxene-andesitic rocks and intrudes both PVF and GSF (Santos and Dimabayao, 2011).

7.2 Previous geophysical surveys

Several geophysical surveys have been conducted in Bacman geothermal field since 1970. Regional Schlumberger resistivity traversing (SRT) surveys were conducted in the 1970s into early 1980s and vertical electrical sounding (VES) surveys were done in 1982-1985. In 1996, regional, microgravity, and precise levelling surveys were conducted within and outside the geothermal field, covering a total of 162 temporary and 80 permanent gravity stations. Results from these surveys (Figure 9) show a large positive gravity anomaly across BGF (Tugawin et al., 2015). Several magnetotelluric (MT) and transient electromagnetic (TEM) surveys were carried out in this field from 1999 to 2012. These surveys were conducted in different areas of the geothermal field. The most recent MT survey was done in 2014 covering 75 stations in the eastern part of the field.

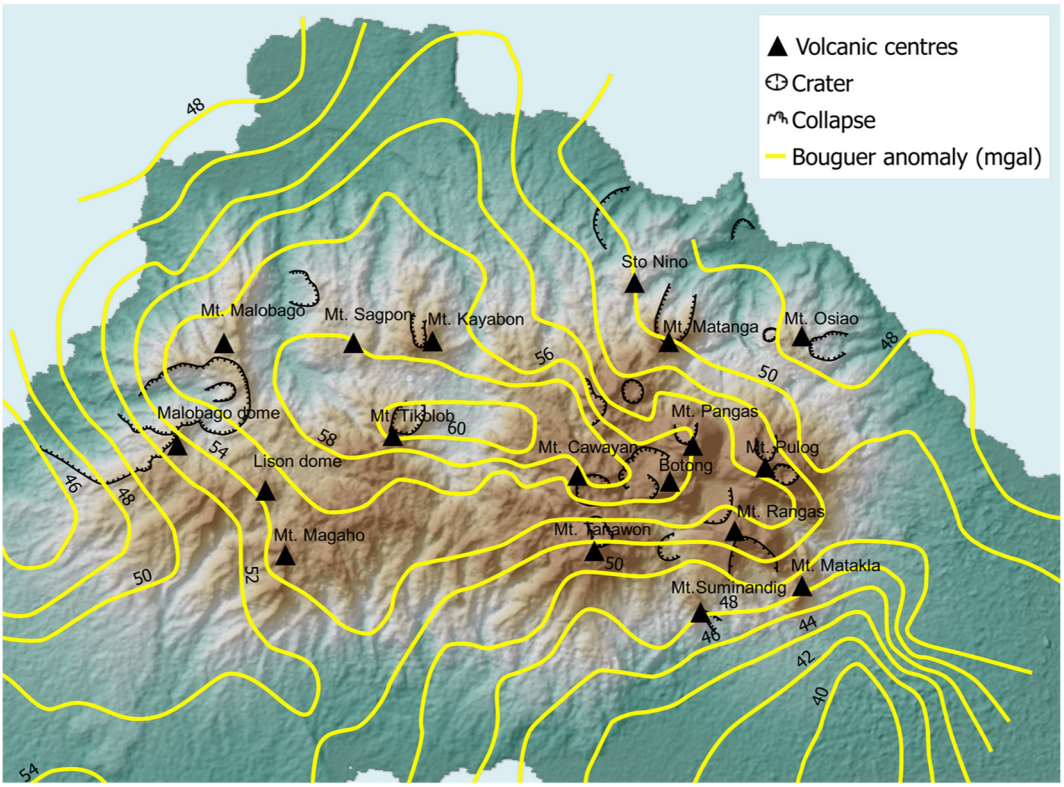

FIGURE 9: Bouguer anomaly map of Bacman geothermal field based on the 1997 regional and microgravity surveys (modified from Tugawin et al., 2015)

8. RESULTS, ANALYSIS AND INTERPRETATION

8.1 Reduction density estimation

A plot (Figure 10) based on Parasnis method shows how the gravity values are distributed. The best fitting line is 2.67 g/cm^3 and this value was computed using the trend1d function of Generic Mapping Tools (GMT) in Linux. The slope is the density that will be optimal in Bouguer and terrain corrections.

Another method of estimating this is by using the Nettleton method (Nettleton, 1939). A SW-NE profile across a prominent topographic feature of the area is generated (Figure 11). Various reduction densities were used to calculate the Bouguer anomalies and are plotted with the topography (Figure 12). By visual inspection, the gravity profile with the least correlation to topography would represent optimal density. The density of 2.67 g/cm^3 is the best choice as in the case of the Parasnis method.

The density of surface rocks can also be measured by collecting samples in the area and measuring the density using laboratory techniques. However, these samples may be eroded due to weathering which can generate a different estimated density values. Also, the density of rocks at depth is different from the rocks at the surface due to variability in water content and compaction (Parasnis, 1986).

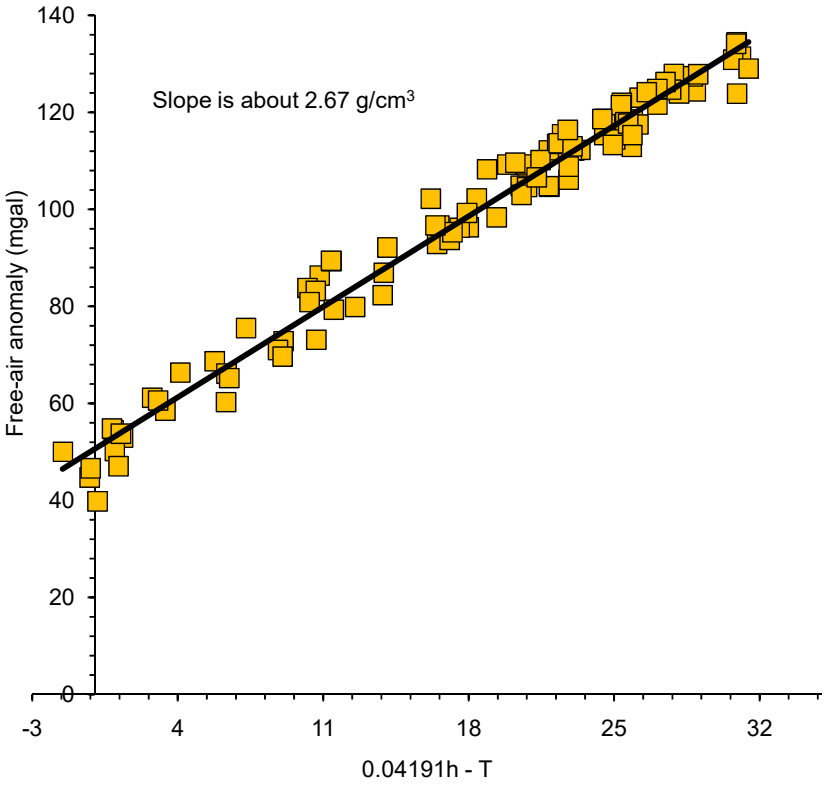

FIGURE 10: Parasnis method to determine the optimum reduction density

8.2 Free-air and Bouguer maps

Free air and Bouguer anomaly maps (Figures 13 and 14) were generated. As seen in Figure 13, relatively high contour values for the free-air anomalies generally correlate with the high topographic reliefs such as the volcanic centres in the middle and relatively low values correspond with low topographic reliefs like plain landforms of the area.

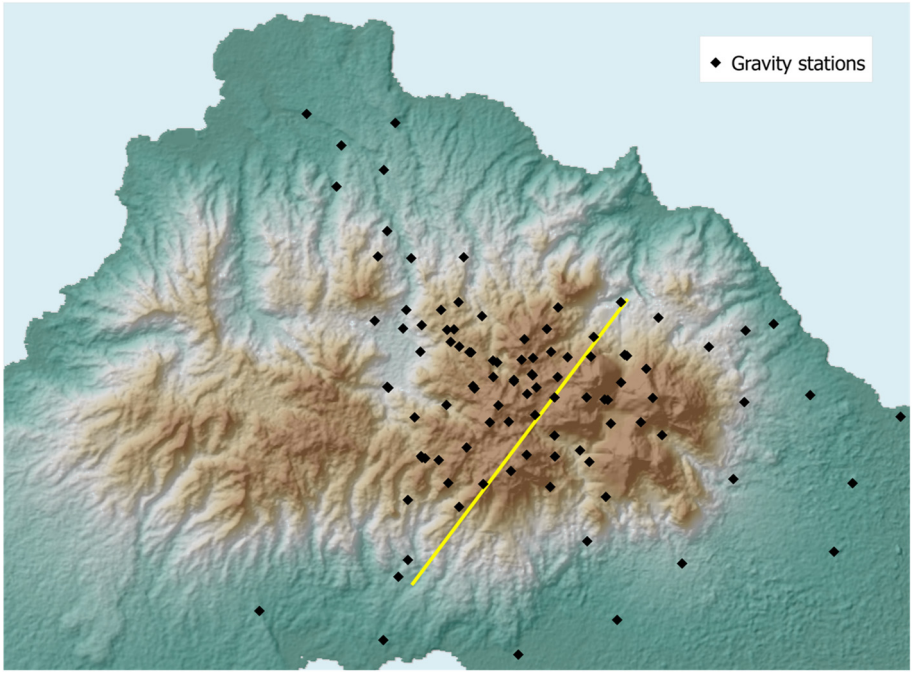

FIGURE 11: Profile (yellow line) used for the Nettleton method

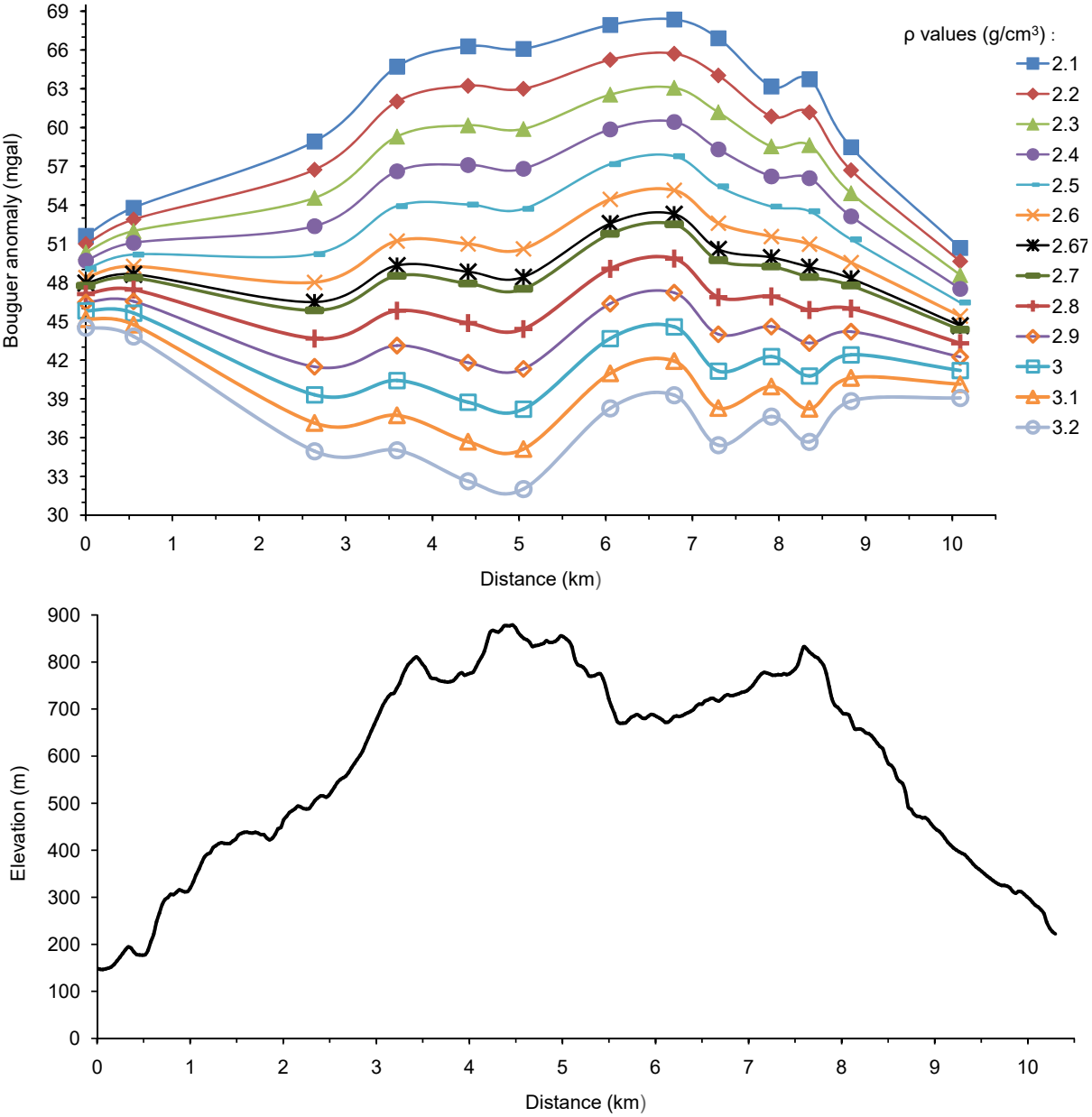

FIGURE 12: Plots of calculated Bouguer anomalies using various reduction densities ρ (top) are compared with the cross-section of the topographic profile (below)

On Figure 14, a relatively high Bouguer anomaly is prominent at the centre of the area near Mts. Cawayan and Botong, and is oriented in the E-W direction. It is also evident that this gravity high is within the BFZ (red lines). The BFZ is actually a main shear zone related to the Philippine Fault and it has many hydrothermal manifestations, caldera structures and volcanic cones (Braganza, 2014). An extension of this broad gravity anomaly extends to the north near Mts. Kayabon and Tikolob. Relatively low gravity values are observed in the southeast region of the area as well as in the northern parts.

8.3 Residual anomaly map

The residual field (Figure 15) is generated by removing the regional field in the Bouguer field. A planar polynomial surface was generated to represent the regional gravity field and the difference between it

and the Bouguer values is the residual field. Higher order polynomials were also tested to model the regional field. It turned out that higher order polynomial planes did not change the residual much. Since there is always a danger of higher order polynomials following the local anomalies, it was decided that planar region field was the most robust and safe. This calculation was done using the Generic Mapping Tool (GMT) grdtrend function in Linux.

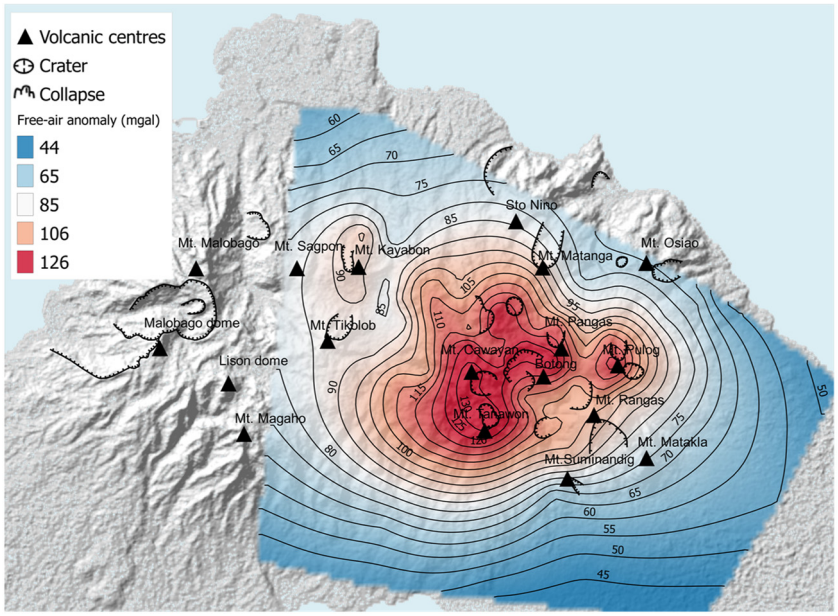

FIGURE 13: Free-air anomaly map of the Bacman geothermal field; the red regions represent high gravity values and the blue regions have low values

Various positive gravity anomalies are observed in the area particularly in the central and western parts. Broad negative gravity anomalies are situated in the northern and south-eastern regions of the field.

The positive anomalies in the central part of the field coincide with the several active hydrothermal manifestations such as solfataras, altered ground, and hot springs. These anomalies are within the BFZ and are near Mts. Botong and Cawayan.

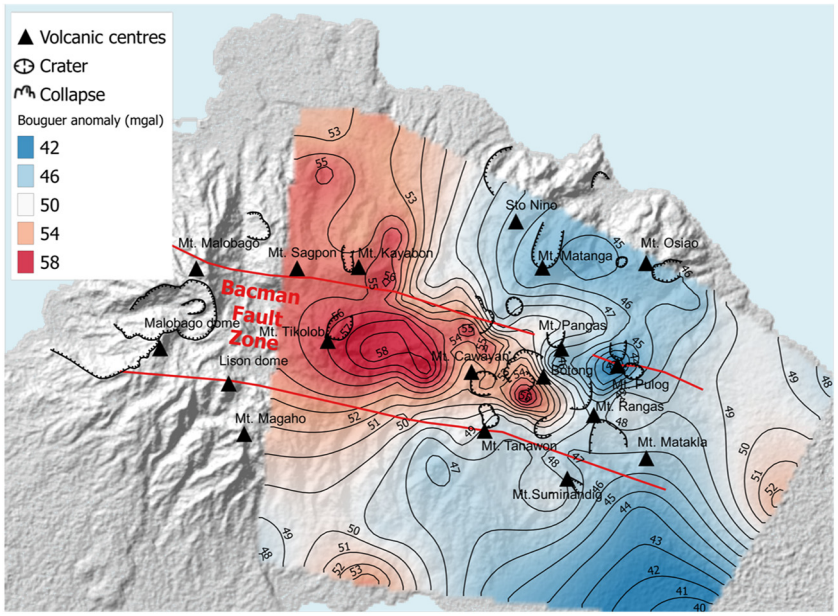

FIGURE 14: Terrain-corrected Bouguer anomaly map of Bacman geothermal field; the red regions correspond high gravity values while the blue regions represent low values

It is also inferred that an upflow zone exists below this area (Ramos and Santos, 2012). Dense intrusive rocks such as diorites are present beneath this area, based on core samples. In addition, positive anomalies also extend to the western and northern parts near Mts. Kayabon and Tikolob and they may be related to the resistivity anomaly seen in the western part of the field (Tugawin et al., 2015). It is also important to note that the high positive anomalies in the central region of the field are separated from the high positive anomalies in the western and northern regions by a narrow zone of lower gravity.

The negative anomalies indicated by blue regions in Figure 15 represent the sedimentary formations and collapse features in the south-eastern and northern parts of the area, respectively. These sedimentary formations are reported to be present particularly in the vicinity of Mt. Rangas (Braganza, 2014).

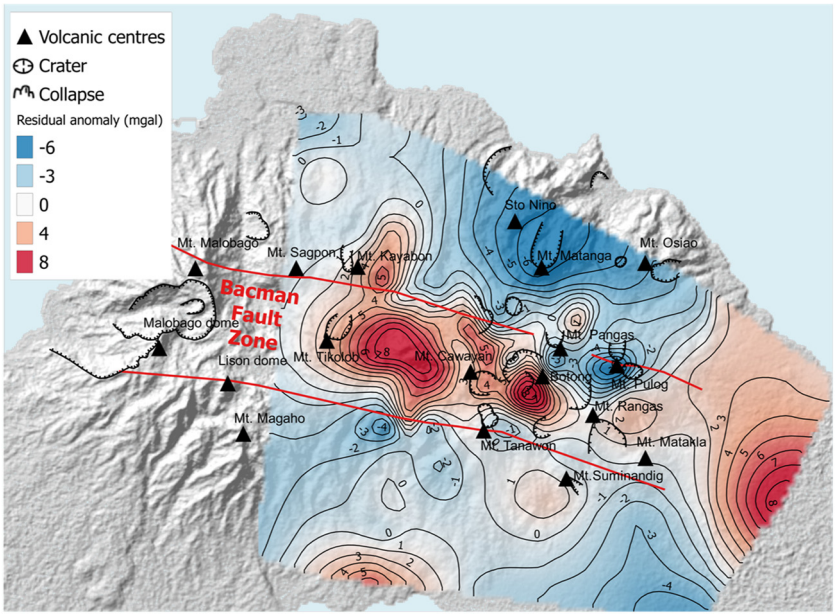

FIGURE 15: Residual anomaly map of the Bacman geothermal field; the red regions correspond to relatively positive numbers while the blue regions represent relatively negative values

9. LIMITING DEPTH ANALYSIS

In order to quantitatively interpret the anomalies, the limiting depth analysis of any dense regular body, can be used, such as the half-width method. This method was applied to the gravity anomaly (Figure 16) at the central part of the field where the dense intrusive rock lies beneath. Assuming this intrusive rock to be a buried regular sphere, the limiting depth z is calculated by:

$$z = 1.302 \times x_{1/2} \tag{10}$$

where $x_{1/2}$ = Horizontal distance from the anomaly maximum to the point at which the anomaly has reduced to half of its maximum value [m].

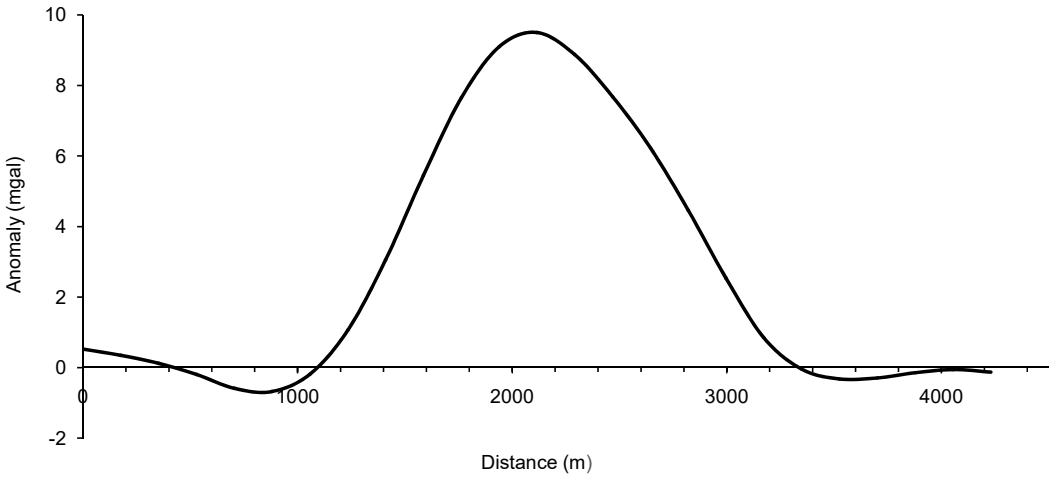

FIGURE 16: Gravity response of a dense body beneath the central part of the Bacman geothermal field

Using Equation 10, the calculated limiting depth is about 900 m. Note that this depth is the distance from the surface to the centre of mass of the buried sphere. Using a simple shape such as a sphere is useful as a first approximation for cases of three-dimensional bodies which are almost symmetrical (Telford et al., 1990).

Meanwhile, for a buried dense body which is assumed to be irregularly shaped, a maximum depth to the top of the body z is computed by the gradient-amplitude ratio method which is:

$$z \leq 0.86 \times \left({}^{A_{max}}/_{A'}\right) \tag{11}$$

where A_{max} = Peak height of the anomaly [mgal];
A' = Maximum slope of anomaly [mgal/m].

This method was applied to an anomaly at the western part of the field wherein an unknown dense body might be present (Figure 17). Assuming it to be irregularly shaped, the maximum depth to the top of this unknown dense body was computed to be about 1750 m.

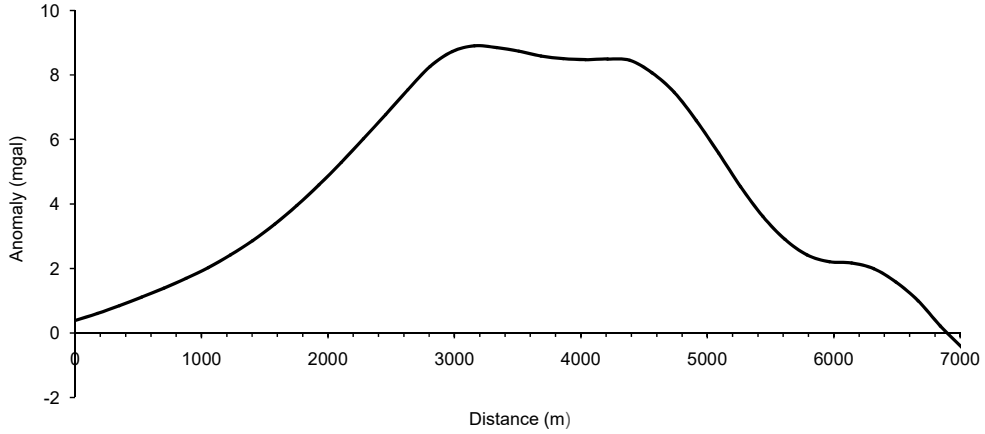

FIGURE 17: Gravity response of a dense body beneath the western part of the Bacman geothermal field

It is important to note that interpretation of gravity anomalies suffers from a non-uniqueness problem, as all geophysical methods. This means that a gravity anomaly can be interpreted by many models. Also, this problem is additional to other uncertainties arising from lack of, or poor quality of data, or interference from other anomalies. Even though the anomaly due to any specified body can be calculated uniquely, one cannot obtain a unique model from an anomaly (Mussett and Khan, 2000). Thus, it is always important to keep in mind that the assumption of the shapes of these dense bodies must be geologically plausible and all available data is needed for a better and accurate modelling. In reality, the shapes of these dense bodies are not simple and symmetrical so more complex modelling tools are required for finer and more precise interpretation.

10. CONCLUSIONS

Microgravity data from the Bacman geothermal field was processed, including tidal and instrumental drift corrections, latitude corrections, atmospheric air, free-air, Bouguer and terrain corrections, and carried out in a Linux environment. Parasnis and Nettleton methods were utilized to estimate the optimum reduction density which was used in the calculations of Bouguer anomalies. Free-air and Bouguer maps were produced. Residual anomaly maps were also generated by removing the regional trend in the terrain-corrected Bouguer maps using a planar polynomial model. Positive anomalies in the central part of the field are within the Bacman Fault Zone. These are interpreted to be dense intrusive rocks such as diorite which are present beneath this area based on core samples. In addition, these anomalies extend to the western and northern regions of the field near Mts. Kayabon and Tikolob. They may be related to the resistivity anomaly found in the western part of the field. Negative anomalies represent the sedimentary formations and collapse features in the south-eastern and northern parts of the area, respectively.

To quantitatively interpret these anomalies, a limiting depth analysis using the half-width and gradient-amplitude ratio methods was done. A sphere model was used for the dense intrusive rock beneath the central region of the field and the computed depth to its centre was around 900 m. Also, the anomaly in the western part of the field was modelled as an irregularly shaped body and the calculated depth to its top was about 1750 m. Note that these methods are very crude in interpretation since they only use simple shapes to represent the anomalies.

ACKNOWLEDGEMENTS

I would like to express my utmost gratitude to the UNU-GTP staff for making this six-month training interesting and more enjoyable. This training was quite a memorable experience for me and my co-fellows. The additions of the project management topic in the Introductory Lectures and group project work in the training were a bit of a surprise for us but we are proud to be the first to have them. A sincere thank you is due to Mr. Lúdvík S. Georgsson, current director of UNU-GTP, for sharing his knowledge, experience, and ideas to us in achieving our objectives in this training. Keep up the good work! It is inevitable to appreciate the dedication and hard work of my supervisors Mr. Kristján Ágústsson and Mr. Ingvar Thór Magnússon. Thank you for your patience in teaching me the basics and complexities of gravity data processing and interpretation. I really learned a lot about gravity corrections using your programs and Linux. You both really pushed me to use Linux and I am thankful for that. Special thanks also to Mr. Gylfi Páll Hersir, the MT method expert, for your patience and guidance to me and my co-geophysicists fellows. You are a good teacher and a great person. Thank you for the home-made ice cream and blueberry cake! It has been a great pleasure as well to work with Mr. Knútur Árnason, the TEM method expert, for sharing his expertise in this method and in Linux as well. To the lecturers from ISOR and other companies of the Introductory Courses and Specialized Trainings, I tip my hat to you all, thanks for the knowledge and experience.

To the UNU-GTP staff Ingimar, Markús, Thorie, and Frída, “takk fyrir” for being patient to us UNU Fellows during our stay in school and fieldtrips. To my co-geophysicist Fellows Ali of Comoros, Amali, and Getenesh, thank you for sharing your ideas and experiences. Of course, most importantly, thanks for your friendship and kindness. I hope we will see each other someday. To the other Fellows, namely Fredrick, Antonio, Hamda, Patrick, Davar, Nyaso, John, Ruth, Anthony, Ali of Djibouti, Fridah, Elizabeth, Aloysius, Pedro, Tingting, Andres, Nuno, Reuben, Fardaneh, Kondwani, Peketsa, Shammah, and Kasu, thank you for the memories and experiences together.

To my colleagues at EDC and co-Fellows, my brothers, Jason, Jigo and Bryan, I am thankful to have experienced this six-month training with you guys. I am proud of you all. To my supervisor Mr. Carlos Emmanuel Los Baños, thank you for giving me this opportunity to go and be trained in Iceland. To Sir Domie also, I know you are in Heaven, thanks for believing in me. To the GREG management namely Mr. Manny Ogena, Mr. Francis Sta. Ana, Mr. Noel Salonga, and Mr. Jeff Caranto, thank you for the support you gave for this training. To my co-EDC employees, thanks are due to all of you for the support and assistance before and during this training: Boyie, Mike, Ado, Randy, Jepoy, David, Gab, Verge, Rocelle, Rod, Suzette, Grace, Bea, Lei, Menchie, and Isay. To all the Filipinos who we met in Iceland, thank you very much for your kindness, for sharing your home with us, and for giving us moral support during this training. I will cherish our good times and bad times together and I will never forget you all.

I am also very thankful to my family, my mother Elena, sister Janine, brothers James and Jay, thank you for your love and care. Most especially, I thank my wife Jenny and daughter Jenny Lee, for the never ending love and support for me in the entirety of this training. You are my motivation and strength to go on. I love you all very much.

Finally and foremost, I would like to dedicate this report to God. Without Him, everything is possible... Glory to God always…

REFERENCES

Apuada, N.A., and Olivar, R.E.R., 2005: Repeat microgravity and leveling surveys at Leyte geothermal production field, North Central Leyte, Philippines. *Proceedings of the World Geothermal Congress 2005, Antalya, Turkey*, 9 pp.

Bertani, R., 2015: Geothermal power generation in the world 2010-2014 update report. *Proceedings of the World Geothermal Congress 2015, Melbourne, Australia*, 19 pp.

Braganza, J.S., 2014: *Volcano-tectonic evolution of the Bacon-Manito geothermal project, Sorsogon, Philippines*. University of Auckland, MSc thesis, 202 pp.

Eysteinsson, H., 2000: Elevation and gravity changes at geothermal fields on the Reykjanes peninsula, SW Iceland. *Proceedings of the World Geothermal Congress 2000, Kyushu-Tohoku, Japan,* 6 pp.

Flóvenz, Ó.G., Hersir, G.P., Saemundsson, K., Ármannsson, H., and Fridriksson, Th., 2012: Geothermal energy exploration techniques. In: Sayigh, A. (ed.), *Comprehensive renewable energy, vol.7.* Elsevier, Oxford, United Kingdom, 51-95.

Google Earth, 2015: *Map of Bicol volcanic belt.* Google Earth.

Hersir, G.P., Árnason, K., and Steingrímsson, B., 2009: Exploration and development of the Hengill geothermal field. *Presented at "Short Course on Surface Exploration for Geothermal Resources", organized by UNU-GTP and LaGeo, Ahuachapan and Santa Tecla, El Salvador*, 12 pp.

Hunt, T.M., 2001: *Five lectures on environmental effects of geothermal utilization.* UNU-GTP, Iceland, report 1-2000, 109 pp.

Hwang, C., Wang, C.G., and Lee, L.H., 2002: Adjustment of relative gravity measurements using weighted and datum-free constraints. *Computers & Geosciences, 28*, 1005–1015.

IEA, 2014: *Key world energy statistics 2014*. OECD Publishing, Paris, France, 80 pp.

Kearey, P., Brooks, M., and Hill, I., 2002: *An introduction to geophysical exploration* (3rd ed.). Blackwell Publishing, Massachusetts, USA, 262 pp.

Lagmay, A.M.F., Tengonciang, A.M.P., and Uy, H.S., 2005: Structural setting of the Bicol basin and kinematic analysis of fractures on Mayon Volcano, Philippines. *J. Volcanology and Geothermal Research, 144,* 1-14.

Lichoro, C.M., 2014: Gravity and magnetic methods. *Presented at "Short Course IX on Exploration for Geothermal Resources", organized by UNU-GTP, GDC and KenGen, Lake Bogoria and Lake Naivasha, Kenya*, 8 pp.

Longman, 1959: Formulas for computing the tidal accelerations due to the moon and the sun. *J. Geophysical Research Atmospheres, 12,* 2351-2355.

Lund, J.W., and Boyd, T.L, 2015: Direct utilization of geothermal energy 2015 worldwide review. *Proceedings of the World Geothermal Congress 2015, Melbourne, Australia*, 31 pp.

Mariita, N.O., 2007: The gravity method. *Presented at "Short Course II on Surface Exploration for Geothermal Resources", organized by UNU-GTP and KenGen, Lake Naivasha, Kenya*, 9 pp.

Mariita, N.O., 2011: Exploration history of Olkaria geothermal field, by use of geophysics. *Presented at "Short Course VI on Exploration for Geothermal Resources", organized by UNU-GTP, GDC and KenGen, Lake Bogoria and Lake Naivasha, Kenya*, 13 pp.

Martakusumah, R., Srigutomo, W., Suryantini, Pratama, A.B., Trimadona, and Haans, A., 2015: Gravity analysis for hidden geothermal system in Cipanas, Tasikmalaya Regency, West Java. *Proceedings of the World Geothermal Congress 2015, Melbourne, Australia*, 9 pp.

Mussett, A.E., and Khan, M.A., 2000: *Looking into the Earth: An introduction to geological geophysics*. Cambridge University Press, UK, 492 pp.

Nettleton, L.L., 1939: Determination of density for the reduction of gravimeter observations. *Geophysics, 4*, 176-183.

NIMA, 1997: *World Geodetic System, 1984, its definition and relationships with local geodetic systems* (3rd ed.). National Imagery and Mapping Agency (NIMA), Department of Defence, Washington DC., US, Techn. Report TR 8350.2.

Nishijima, J., Oka, D., Higuchi, S., Fujimitsu, Y., Takayama, J., and Hiraga, N., 2015: Repeat microgravity measurements using absolute and relative gravimeters for geothermal reservoir monitoring in Ogiri geothermal power plant, South Kyushu, Japan. *Proceedings of the World Geothermal Congress 2015, Melbourne, Australia*, 5 pp.

Nordquist, G.A., Acuña, J., and Stimac, J., 2010: Precision gravity modeling and interpretation at the Salak geothermal field, Indonesia. *Proceedings of the World Geothermal Congress 2010, Bali, Indonesia*, 8 pp.

Parasnis, D.S., 1952: A study of rock density in the English Midlands. *Mon. Not. R. Astron. Soc. Geophysics. Suppl., 6*, 252-27.

Parasnis, D.S., 1986: *Principles of applied geophysics* (4th ed.). Chapman and Hall, NY, US, 402 pp.

Pearson, S.C.P., Franz, P., and Clearwater, J., 2015: Strategy of 4D microgravity survey for the monitoring of fluid dynamics in the subsurface. *Proceedings of the World Geothermal Congress 2015, Melbourne, Australia*, 7 pp.

Ramos, S.G., and Santos, B.N.E.A., 2012: Updated hydrogeological model of the Bacon-Manito geothermal field, Philippines. *Proceedings of the 37th Workshop on Geothermal Reservoir Engineering, Stanford University, Stanford, CA, US,* 4 pp.

Salem, A., Furuya, S., Aboud, E., Elawadi, E., Jotaki, H., and Ushijima, K., 2015: Subsurface structural mapping using gravity data of Hohi geothermal area, Central Kyushu, Japan. *Proceedings of the World Geothermal Congress 2015, Melbourne, Australia*, 6 pp.

Santos, B.N.E.A., and Dimabayao, J.J.T., 2011: Paleoenvironment reconstruction of the Gayong sedimentary formation, BacMan geothermal field, Philippines. *Proceedings of the 33rd New Zealand Geothermal Workshop, Auckland, New Zealand*, 7 pp.

Sarkowi, M., Kadir, W.G.A., and Santoso, D., 2005: Strategy of 4D microgravity survey for the monitoring of fluid dynamics in the subsurface. *Proceedings of the World Geothermal Congress 2005, Antalya, Turkey*, 5 pp.

Seigel, H.O., 1995: *A guide to high precision land gravimeter surveys* (2nd ed.). Scintrex, Ltd., Ontario, Canada, 122 pp.

Setyawan, A., Yudianto, H., Nishijima, J., and Hakim, S., 2015: Horizontal gradient analysis for gravity and magnetic data beneath Gedongsongo geothermal manifestations, Ungaran, Indonesia. *Proceedings of the World Geothermal Congress 2015, Melbourne, Australia*, 6 pp.

Telford, W.M., Geldart, L.P., and Sheriff, R.E., 1990: *Applied geophysics* (2nd ed.). Cambridge University Press, Cambridge, United Kingdom, 770 pp.

Torge, W., 1989: *Gravimetry.* Walter de Gruyter and Co., Berlin, Germany, 465 pp.

Tugawin, R.J., Rigor, D.M., Los Baños, C.E.F., and Layugan, D.B., 2015: Resistivity model based on 2D inversion of magnetotelluric sounding data in Bacon-Manito, Southern Luzon, Philippines. *Proceedings of the World Geothermal Congress 2015, Melbourne, Australia*, 6 pp.

APPENDIX I: Gravity stations: Location, gravity values and anomalies

Gravity station	Latitude	Longitude	Elevation (m)	Calculated gravity value (mgal)	Free-air anomaly (mgal)	Bouguer anomaly (mgal)
1	13.06225	123.923517	611.02	978218.878	111.75	51.21
2	13.05965	123.942067	836.05	978161.943	124.33	47.12
3	13.056361	123.949056	720.89	978191.597	118.59	49.47
4	13.049861	123.95075	850.94	978160.054	127.42	50.59
5	13.047194	123.945167	806.35	978174.139	127.86	50.35
6	13.054367	123.9413	809.91	978170.109	124.64	49.78
7	13.029567	123.91475	600.87	978221.13	112.17	50.54
10	13.062133	123.921717	552.01	978232.944	107.62	51.95
11	13.057817	123.9249	571.56	978231.329	112.21	53.87
12	13.056367	123.927617	584.59	978228.574	113.53	54.13
15	13.054167	123.933783	546.65	978235.887	109.23	56.24
17	13.049183	123.939267	613.13	978221.51	115.55	55.53
18	13.045517	123.942733	700.39	978201.969	123.07	53.09
19	13.0506	123.944017	662.58	978209.44	118.68	53.12
20	13.0548	123.9443	764.34	978183.442	123.9	48.81
21	13.054972	123.953389	639.14	978210.481	112.32	49.95
22	13.060167	123.960278	506.72	978235.562	96.35	48.31
23	13.055528	123.968389	480.04	978240.173	92.91	48.95
25	13.04839	123.96741	637.65	978203.062	104.7	46.27
26	13.04389	123.96393	721.43	978186.853	114.51	45.84
28	13.046967	123.928917	669.39	978210.55	122.03	54.33
30	13.03822	123.93289	895.87	978152.823	134.51	52.02
37	13.0309	123.956567	509.07	978239.641	102.31	53.21
38	13.038117	123.972567	725.78	978183.692	112.92	43.93
40	13.063383	123.91505	444.66	978255.148	96.66	52.4
41	13.056517	123.914667	316.2	978284.23	86.39	57.5
42	13.047233	123.906233	321.05	978285.336	89.36	58.94
44	13.04275	123.921467	456.5	978256.203	102.19	59.03
45	13.039583	123.9131	545.22	978235.834	109.31	53.96
46	13.028533	123.919383	644.53	978210.806	115.35	49.92
48	13.06915	123.96745	308.86	978273.775	73.17	44.68
49	13.067817	123.950933	636.89	978205.545	106.18	45.27
52	13.067317	123.911	290.62	978289.993	83.84	56.51
53	13.080667	123.91235	226.87	978301.872	75.52	56.09
54	13.103517	123.905233	155.79	978317.913	68.73	53.29
55	13.11565	123.908283	78.6	978334.672	61.2	53.79
56	13.11805	123.885	32.72	978342.14	54.42	51.98
58	13.018267	123.911233	463.64	978247.109	96.27	49.38
59	13.016433	123.9247	601.25	978213.156	104.83	46.5
60	13.002783	123.911183	248.66	978289.428	72.89	48.64
61	13.00744	123.95836	219.7	978291.801	66.14	49.2
62	13.0016	123.98326	174.95	978299.55	60.32	43.43
63	13.02335	123.99682	252.74	978287.087	70.99	47.44
64	13.063333	124.007583	73.83	978325.823	52.96	49.31
65	13.099267	123.892783	125.82	978324.655	66.4	55.41
66	12.98975	123.872133	55.31	978325.877	50.21	47.65
67	12.99845	123.90867	180.37	978302.701	65.27	47.96
68	12.98211	123.90466	6.39	978340.529	50.07	54.17
69	12.97825	123.94015	7.59	978334.64	44.71	45.33

Gravity station	Latitude	Longitude	Elevation (m)	Calculated gravity value (mgal)	Free-air anomaly (mgal)	Bouguer anomaly (mgal)
70	12.9871	123.96615	41.52	978326.855	47.04	44
71	12.9711	124.00146	8.54	978329.154	39.8	39.42
72	13.0045	124.02319	33.12	978337.902	54.81	52.58
73	13.02215	124.02814	38.14	978335.993	53.75	50.36
74	13.03926	124.04083	2.13	978340.639	46.61	47.12
75	13.044936	124.017099	100.02	978322.597	58.54	49.44
77	13.02917	123.91499	596.12	978222.677	112.27	50.98
81	13.059033	123.92265	565.72	978231.171	110.2	52.94
82	13.047617	123.9285	666.91	978210.861	121.56	53.92
83	13.056283	123.928067	585.82	978228.357	113.69	54.07
85	13.06929	123.92475	570.64	978224.488	104.63	49.08
86	13.08087	123.92617	370.65	978268.99	86.98	49.86
87	13.06565	123.93095	475.9	978248.26	99.32	51.47
88	13.050317	123.9442	663.61	978209.036	118.61	53.39
89	13.03838	123.93787	743.09	978193.401	127.96	53.56
90	13.02981	123.94254	902.76	978147.317	131.47	48.44
91	13.02563	123.93839	959.24	978129.125	130.86	48.85
92	13.029017	123.915817	598.45	978222.682	113	51.63
93	13.022317	123.9311	839.72	978156.613	121.61	49.33
94	13.055267	123.969	491.47	978237.447	93.72	48.1
95	13.03475	123.949883	543.67	978235.127	108.32	57.93
96	13.048767	123.939267	622.84	978219.33	116.38	55.6
97	13.053667	123.9349	550.55	978235.045	109.61	55.58
98	13.03175	123.92675	745.98	978189.016	124.73	50.68
99	13.0426	123.93515	892.39	978153.693	134.14	51.75
100	13.049933	123.93385	759.56	978187.121	126.3	52.99
101	13.02935	123.949967	701.88	978195.743	117.95	49.8
102	13.0215	123.9487	636.51	978206.451	108.8	47.91
103	13.0401	123.944783	735.26	978192.798	124.87	52.57
104	13.044583	123.949933	723.85	978195.829	124.21	53.3
105	13.022617	123.921867	696.17	978193.73	114.44	47.57
106	13.062267	123.947983	719.8	978191.109	117.54	47.7
107	13.055083	123.959533	748.28	978182.252	117.75	49.2
108	13.0519	123.97405	736.54	978181.278	113.28	46.73
109	13.065067	123.9773	377.38	978261.666	82.36	45.37
110	13.044017	123.963083	733.62	978183.926	115.34	46.27
111	13.03779	123.96469	584.33	978217.39	103	48.18
112	13.044567	123.95835	902.66	978145.529	129.06	45.07
113	13.044367	123.975733	1017.14	978105	123.85	41.34
114	13.03475	123.978133	522.84	978228.515	95.28	49.3
115	13.027933	123.959017	576.64	978223.009	106.64	49.84
116	13.018883	123.9633	526.56	978229.846	98.39	46.73
117	13.047483	123.905933	322.17	978285.092	89.46	59.06
118	13.062533	123.910133	288.84	978289.7	83.19	54.8
119	13.06455	123.9027	369.87	978273.742	92.14	54.56
120	13.087733	123.90605	281.72	978290.648	80.94	53.31
121	13.08115	123.903583	473.91	978246.907	96.74	52.97
122	13.10988	123.8941	85.64	978331.715	60.64	52.5
123	13.0432	123.999783	328.01	978273.017	79.35	48.64
124	13.06165	124.000183	263.35	978284.029	69.69	45.56
125	13.057483	123.990533	353.02	978266.424	79.91	46.47

UNITED NATIONS UNIVERSITY
GEOTHERMAL TRAINING PROGRAMME
Orkustofnun, Grensasvegur 9,
IS-108 Reykjavik, Iceland

Reports 2015
Number 24

GEOTHERMAL MAPPING IN MIDDALUR FIELD, HENGILL AREA, SW-ICELAND

Patrick Kant Muanza
Geological Survey (CRGM)
44 Av. de la Démocratie (Ex-Huileries), Gombe township
Kinshasa, P.O. Box 898
D. R. CONGO
patrick_kant@yahoo.fr

ABSTRACT

Middalur area is a part of the Hengill volcanic massif located in the western branch of the volcanic rift zone in SW-Iceland. It is a high-temperature geothermal field endowed with impressive geothermal manifestations which include warm and hot springs, mud pools, steam vents (fumaroles), warm grounds, hot grounds and clay alterations.

The geothermal exploration carried out in the area involved mapping surface geothermal manifestations and shallow soil temperature measurements around the active manifestations to delineate the warm (>15°C) and hot (>50°C) isotherms within which many hot springs, mud pools, steam vents and warm springs occur. The results indicate that tectonic features control geothermal activity in the area. Eight faults, inferred faults and fracture were mapped based on aerial photographs, field studies and alignment of the geothermal manifestations. The trends of the geothermal manifestations are N-S, NE-SW and E-W. Most of hot springs precipitate calcite. The proposed geothermal model of the area shows the geothermal activity associated with active faults and fractures.

1. INTRODUCTION

1.1 Background

The Democratic Republic of Congo is located in the western branch of the East African Rift System, referred to as the Albertine Rift. It is one of those developing countries which suffers from a serious shortage of electricity. Only about 30% of the country has electricity coverage. Frequent power cuts also cause problems. In order to improve the electrical supply, the government wants to utilize its sustainable energy resources by 2030. Geothermal energy is one of the priority energy sources given the volcanic chain presence in the eastern part of the country that contains at least six volcanoes, two of which are active (Nyamulagira and Nyiragongo).

The purpose of this report is to stress the contribution of geothermal mapping in geological exploration. The first step of geothermal resource development is geological exploration, which includes geological mapping, structural mapping and hydrothermal mapping. A hydrothermal map should include

phenomena like hot and warm grounds, hot and warm springs, steam vents, mud pits and any kind of surface thermal manifestation. For practical purposes a geothermal map should also include faults, major fractures and young volcanic features like volcanic craters, eruptive fissures etc., as a link is often found to exist between tectonic features and the distribution of geothermal manifestations.

This study is a part of a six-month training course at the UNU-GTP in Iceland in 2015 which commenced in April. The first 2-3 months were used for course work, field excursions and practical training in various geothermal disciplines. The remaining 3 months were used for practical training in geothermal exploration, the results of which are described in this report. The objective of the study was to provide the author with training in geothermal mapping, using the Middalur field, part of the Hengill volcanic complex in SW-Iceland as a study area. This is a high-temperature geothermal field and the author was trained in exploring such an area and how to analyse, interpret and present the data which were gathered.

1.2 Previous work

Reconnaissance geological mapping (1:25,000 scale) of the Hengill area was carried out in the mid-sixties by Saemundsson (1967). Björnsson and Hersir (1981) summarized the results of geophysical reconnaissance studies of the Hengill area using DC-resistivity soundings, aeromagnetic measurements, MT-surveys and seismicity. A low-resistivity anomaly at 400 m below sea level, covering 110 km^2, was found to delineate the high-temperature geothermal area. The aeromagnetic map that was produced shows negative anomalies caused by hydrothermal alteration. K. Saemundsson and a team of geologists (G.I. Haraldsson, G.Ó. Fridleifsson and S. Snorrason) re-mapped the Hengill area during several summers mainly in the nineties resulting in detailed geological and geothermal maps of the Hengill area on a scale of 1:50,000 and 1:25,000, respectively (Saemundsson, 1995a and b). In the present study, the existing geological map was used exclusively while the geothermal activity and faults of the Middalur field were mapped in more detail, as digital mapping and GPS positioning accuracy enables and simplifies the mapping exercise.

2. GENERAL GEOLOGY AND TECTONIC OF ICELAND

Iceland is located in the North Atlantic Ocean between Greenland and Norway at 63°23'N to 66°30'N. It is a large land mass that is part of a much larger entity situated on the junction of the submarine Mid-Atlantic Ridge and the Greenland-Iceland-Faeroes Ridge. The Mid-Atlantic Ridge defines the constructive plate boundary between the American and the Eurasian plates. From magnetic anomalies to the north and south of Iceland, the spreading rate has been estimated as 2 cm/year symmetrically. The whole region is drifting slowly to the northwest with respect to the Iceland plume (Hardarson et al., 2008) (Figure 1). The Greenland-Iceland-Faeroes Ridge is thought to

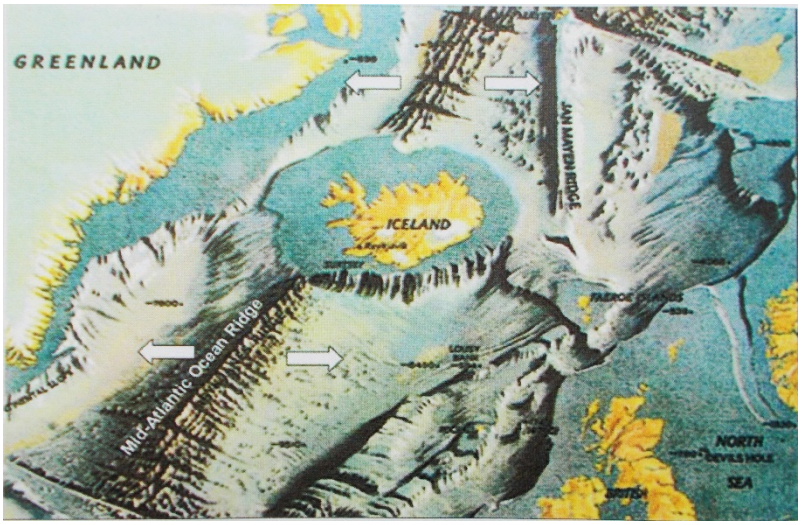

FIGURE 1: Iceland's location in relation to the Mid – Atlantic ridge

be the trail of the Icelandic hot spot which has been active from the time of the opening of the North Atlantic Ocean 60 million years ago.

Iceland is a geologically young island, known as the Icelandic basalt plateau, which rises more than 3000 m above the surrounding ocean floor and covers about 350,000 km^2, thereof about 103,000 km^2 being above sea level (Thordarson and Höskuldsson 2002).

Icelandic rocks are mainly composed of Tertiary plateau lavas, 3.3-16 Ma old (Moorbath et al., 1968; Watkins and Walker, 1977; McDougall et al., 1984; Hardarson et al., 1997), Plio-Pleistocene lavas (0.78-3.3 Ma) and hyaloclastites (0.01-0.78 Ma) formed subglacially and Holocene lavas (< 0.01 Ma) (Hardarson et al., 2008) (Figure 2). Approximately 85-90 % of the volume of Iceland above sea level is igneous rocks while some 10-15 % is consolidated sediments. Due to the shallow erosion level of the volcanic pile volcanic rocks predominate. Less than 0.5 % of the surface is intrusive and plutonic rocks (Saemundsson, 1980; Jóhannesson and Saemundsson, 1998).

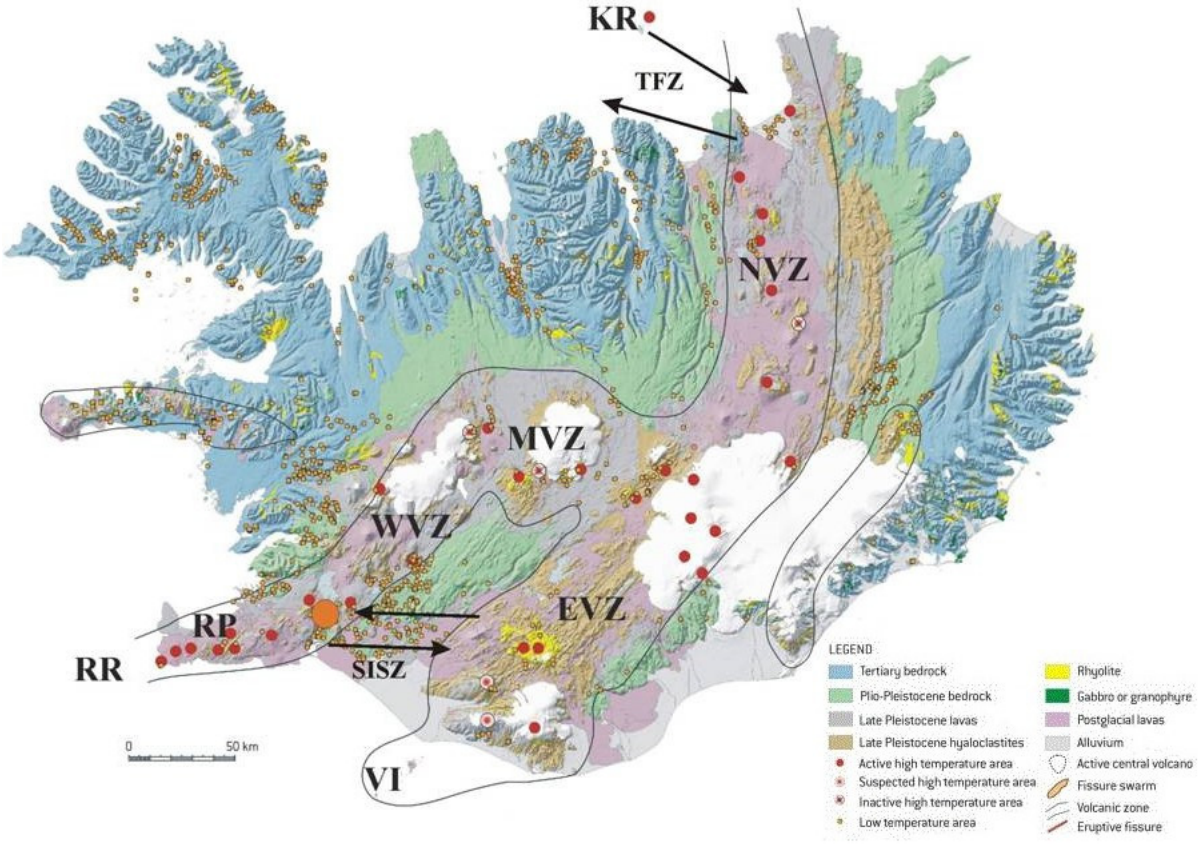

FIGURE 2: Geological map of Iceland showing the location of the active volcanic zones and transforms discussed in this paper. RR = Reykjanes Ridge; RP = Reykjanes Peninsula; WVZ = Western Volcanic Zone; MVZ = Mid-Iceland Volcanic Zone; NVZ = Northern Volcanic Zone; EVZ = Eastern Volcanic Zone; VI = Vestmanna Islands; SISZ = South Iceland Seismic Zone; TFZ = Tjörnes Fracture Zone. Red dots indicate high-temperature areas. Orange circle represents the approximate location of the Hengill volcanic system (from Hardarson et al., 2010)

Iceland owes its existence to the uprising Icelandic mantle plume and crustal accretion at the diverging American and Eurasian lithospheric plates. The movement of the lithospheric plate boundary in relation to the stationary mantle plume is responsible for the complicated tectonic and volcano-stratigraphic structure of Iceland, compared to the Mid Atlantic Ridge to the north and south of the country, and for the eastward shifting of the volcanic belts in Iceland (Ward and Björnsson, 1971; Saemundsson, 1974; Jóhannesson, 1980; Óskarsson et al., 1985; Einarsson, 1989; Hardarson et al., 1997). It is believed that

the general tectonic trends in Iceland as seen today have remained the same for at least 24 Ma (Saemundsson, 1980).

According to Vink (1984), the Mid Atlantic Ridge axis moved on top of the mantle plume and then gradually west during Anomaly 6 (24–19 Ma ago). However, as the spreading ridge system in Iceland continues to drift NW with respect to the plume, it is periodically recaptured by the plume through the process of rift relocation or ridge jumping. This plume-ridge interaction has been a dominant process in the formation and tectonic evolution of Iceland (Hardarson et al., 1997, 2008). The volcanic belts in Iceland run SW-NE trending across the country (Figure 2). The plate spreading across the island is accommodated by several volcanic rift zones and two main transcurrent slip zones. In the south of the island, the Reykjanes segment of the Mid Atlantic Ridge comes on shore at the Reykjanes peninsula as an oblique rift zone and branches into the Western Volcanic Zone (WVZ) and the E-W trending South Iceland Seismic Zone (Saemundsson, 1978).

Plate spreading across South Iceland in the WVZ and the Eastern Volcanic Zone (EVZ) is accommodated by left-lateral E-W transform motion across the South Iceland Seismic Zone (SISZ) which connects two volcanic zones. The EVZ extends northward and continues as the Northern Volcanic Zone (NVZ) (Árnadóttir et al., 2008, see Figure 2).

These main fault structures, volcanic zones and belts that lie within these zones are called volcanic rift zones and are characterised by intense volcanic, seismic and high temperature geothermal activity (Gudmundsson and Jacoby, 2007; Thordarson and Larsen, 2007).

2.1 Geothermal aspects of Iceland

Geothermal activity in Iceland, which is related to the tectonic setting of the country, is mainly classified into high- and low-temperature fields and this classification is based on the geological setting and on temperature data from drill holes (Bödvarsson, 1961). Low-temperature areas are classified by their temperatures which are less than 150°C at 1 km depth while the high-temperature areas reach temperatures above 200°C at the same depth (Fridleifsson, 1979). The areas within the active rifting zones (Figure 2) are considered high-temperature fields, characterized by active volcanoes and fissure swarms. Their heat sources are cooling intrusions or other significant magma bodies. Low-temperature areas are mainly found outside the volcanic rift zones, such as in Quaternary and Tertiary formations. They are often fracture dominated systems and derive their heat from the hot crust conducted and pushed upwards along structures such as faults, fractures and dykes. Away from the fractures, the bedrock is less permeable and heat transfer is dominated by conduction. Few Icelandic geothermal fields have reservoir temperatures in the obvious temperature gap in the definition above which are sometimes called medium-temperature fields (Saemundsson et al., 2009).

3. HENGILL AREA

The Hengill area hosts one of the largest high temperature geothermal fields in Iceland. It is located around 30-50 km away from the city of Reykjavik. It hosts three main volcanic centres which are, listed from SE to NW and decreasing age, Graendalur (0.3–0.5 Ma), Hrómundartindur (Ölkelduháls) on the decline and Hengill at the peak of activity.

3.1 Geology and tectonics

The Hengill High-temperature area is located in the southern end of the western volcanic zone (WVZ) of Iceland in the Hengill volcanic complex which rises about 500 m above the surroundings. It is located

at the triple junction of the WVZ, the Reykjanes Peninsula (RP) which is the landward extension of the Reykjanes spreading ridge and the South Iceland Seismic Zone (SISZ) which is a transform zone, transferring a part of the crustal spreading from the WVZ to the eastern volcanic zone (Figures 2 and 3).

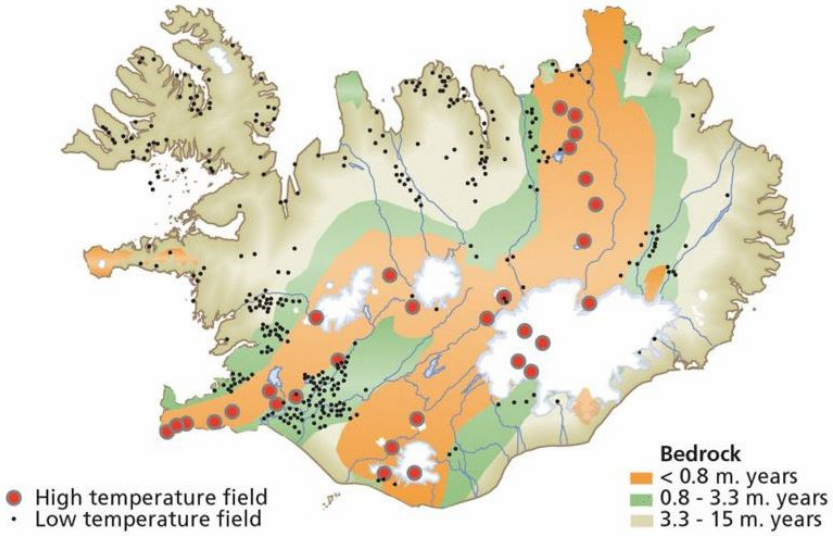

FIGURE 3: Locations of high- and low-temperature geothermal fields in Iceland (Orkustofnun, 2009)

The geology of the Hengill area is intersected by a fissure swarm over 3–5 km wide and 50 km long, trending N 30° E which has a structure of nested grabens. In addition to the major NE-SW fissure swarm and faults, there are some eruptive fissures transecting the centre of Hengill in a NW-SE direction, perpendicular to the main tectonic trend. This area is almost entirely built up of volcanic rocks. Subglacially formed hyaloclastites together with pillow basalts constitute the main rock types (Saemundsson, 1967). Basaltic hyaloclastite forms when magma quenches during an eruption into the base of a glacier and piles up above their orifices as pillow basalts, breccias and tuffs. Some interglacial and postglacial lava flows are also present, the most recent activity being 2500 and 5500 years old (Saemundsson, 1995a).

3.2 Geothermal activity

Geothermal surface manifestations in the Hengill area are connected to the volcanic system (Figure 3). The main heat source of the Hengill geothermal area is considered to be cooling magma intrusions within the upper crust and deep circulation of groundwater in highly fractured rocks transports the heat upwards (Franzson et al., 2010). The CO_2 gas geothermometer shows three upflow zones and the temperature seems to decrease to the southeast (Ívarsson, 1998) (Figure 4).

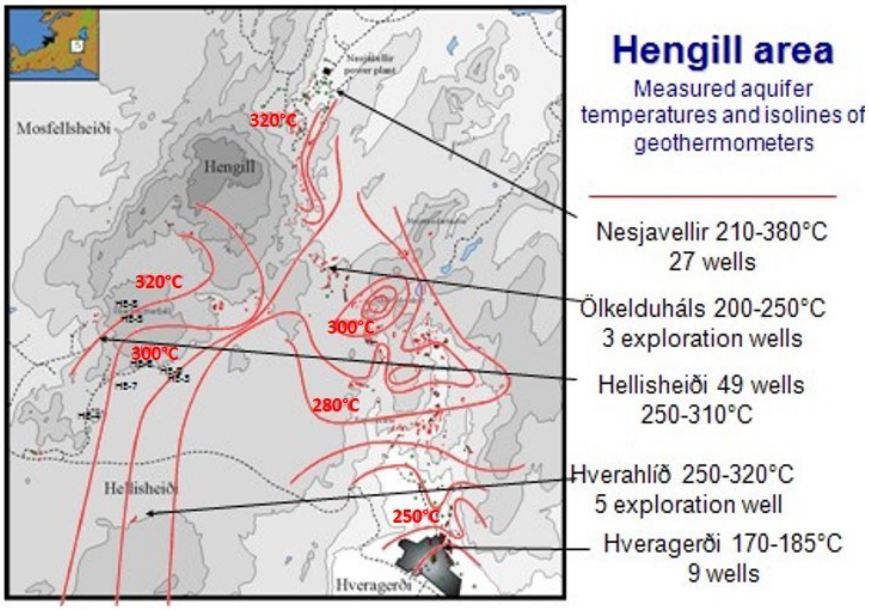

FIGURE 4: Measured aquifer temperatures and isolines of CO_2 gas geothermometers (mod. from Ívarsson, 1998). Geothermal surface manifestations are shown as red dots. Numbers of wells and average temperature in wells for the five known main subfields is shown

3.3 Geophysics

When resistivity surveys conducted in the Hengill area are compared to lithology, alteration mineralogy and temperature they show that the resistivity is high in the surrounding cold unaltered rocks. This high resistivity delineates a 50 km^2 area that represents the hottest central part of the Hengill area (Björnsson and Hersir, 1981). The DC resistivity soundings show a low-resistivity geothermal anomaly at 400 m below sea level which is about 110 km^2 in size. Aeromagnetic measurements carried out in the area indicate negative anomalies, probably caused by hydrothermal breakdown of magnetic minerals within the active high-temperature system (Björnsson and Hesir, 1981). At temperatures of 50-100°C pronounced geothermal alteration sets in with smectite and zeolites as the dominant alteration minerals and the rocks become conductive. At higher temperature in the range of 220-240°C smectite and zeolites are gradually replaced by chlorite as the dominant alteration mineral in the so-called mixed layered clay zone (Kristmannsdóttir, 1979) and the resistivity increases again. At still higher temperatures epidote becomes abundant. The smectite and the zeolites have loosely bound cations that make these minerals conductive, whereas in the chlorites all ions are bound in a crystal lattice (Deer et al., 1962) and are therefore more resistive. Árnason et al., (2000) related the resistivity structures to variations in hydrothermal alteration which appear to be of greater importance than the temperature variation. The low-temperature clay rich outer margin of a high-T reservoir is characterized by low-resistivity and the underlying, higher resistivity is associated with the formation of chlorite and a less water-rich alteration mineral assemblage (Árnason et al., 2000; Árnason and Magnússon, 2001) (Figure 5).

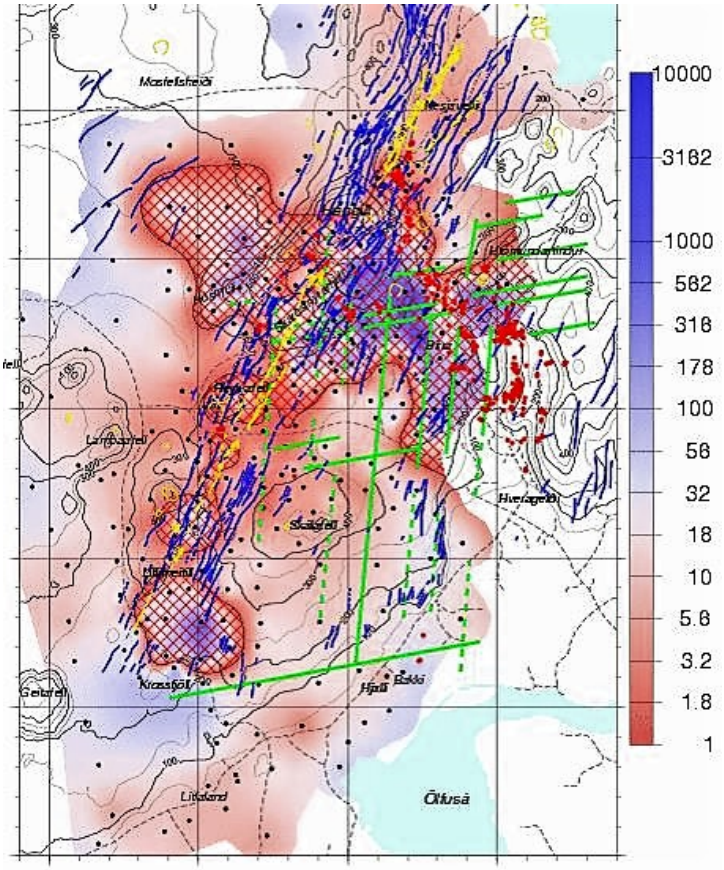

FIGURE 5: A resistivity map of the Hengill central volcano at 850 m b.s.l. showing variations in resistivity. The cross-hatched areas define high resistivity cores below low resistivity and are interpreted as alteration temperatures of over 230°C (Árnason, 2006)

The high temperature from CO_2 might be caused by another system lying deeper, capped by a horizontal dyke (Árnason and Magnússon, 2001).

The Hengill area has been covered with 280 TEM soundings and 148 MT soundings. 1D joint inversion of 148 TEM/MT sounding pairs, correcting for the static shift of the MT curves which can be severe, has revealed the resistivity subsurface structure (Árnason et al., 2009). The inversion showed a conductive cap underlain by a resistive core, both of them being directly related to the geothermal reservoir. At a greater depth (several km) another low resistivity layer was found, the same layer that is found under most of Iceland (Árnason et al., 2010).

The resistive core in Hengill area is trending WNW-ESE, the same orientation as a zone where E-W oriented faults, inferred from seismicity, meet N-S oriented “seismic” faults and indicates alteration temperatures of over 230°C (Árnason et al., 2010) (Figure 5).

The region, where the resistive core rises highest coincides with the area where the seismicity was most intense in the years 1991 to 2001 and where the centre of uplift was located according to InSAR measurements (Feigl et al., 2000).

The MT 3D inversion in this area shows that the low-resistivity ridge to the NW and SE of Hengill extends to the Graendalur central volcano (Figure 5), coinciding with the geothermal surface manifestations and is bordered by high resistivity to the SW and NE (Árnason, 2006). Both inversion approaches of the TEM/MT resistivity soundings reveal a shallow resistivity layer reflecting conductive alteration minerals at temperatures from 100 to 240°C. They also delineate a deep conductor at 3-10 km depth. Deep conductors are believed to reflect hot solidified but ductile magmatic intrusions that are heat sources for geothermal systems (Árnason et al., 2010).

4. GEOTHERMAL EXPLORATION

Geothermal surface exploration invariably entails a multi-geoscientific process which is holistically aimed at defining the geometry and characteristics of the geothermal system prior to drilling. The scientific disciplines commonly involved are geology, geochemistry and geophysics. The geological approach generally aims for understanding the various lithologies, volcanological evolution, structural controls and hydrological regimes of the system. Geochemical exploration relies mostly on sampling and analysis of water, steam and gas from thermal manifestations in order to characterize the fluids, estimate equilibrium reservoir temperature, determine the origin, evaluate mixing scenarios, determine the suitability of the fluids for the intended use and locate recharge areas and direction of fluid flow. Geophysical exploration makes use of methods such as resistivity, gravity and magnetic measurements and help to determine the geometry (shape, size and depth) of the heat sources, reservoir and cap rocks.

Geological studies invariably start at the incipient reconnaissance stage which entails preliminary mapping of the lithologic units and structures, mapping of thermal surface manifestations and possibly relate to the structures and or volcanism in the prospect of interest. This part is the concern of the work presented here.

The Middalur area is composed of surface deposits in the valley, hyaloclastite tuffs and pillow basalts which were probably formed during the second last glacial period (up to 200,000 years old). Part of the geological map is shown in Figure 6. In the map, there is also a section of Hagavikurhraun and Hellisheidarhraun lava which formed about 5500 years ago (Saemundsson, 1995a). The Hagavíkurhraun erupted postglacially in Innstidalur and ran down to Middalur valley. Other bedrock formations shown on the geological map in Figure 6 (and tabulated in Table 1) are mostly composed of hyaloclastite formations of different age.

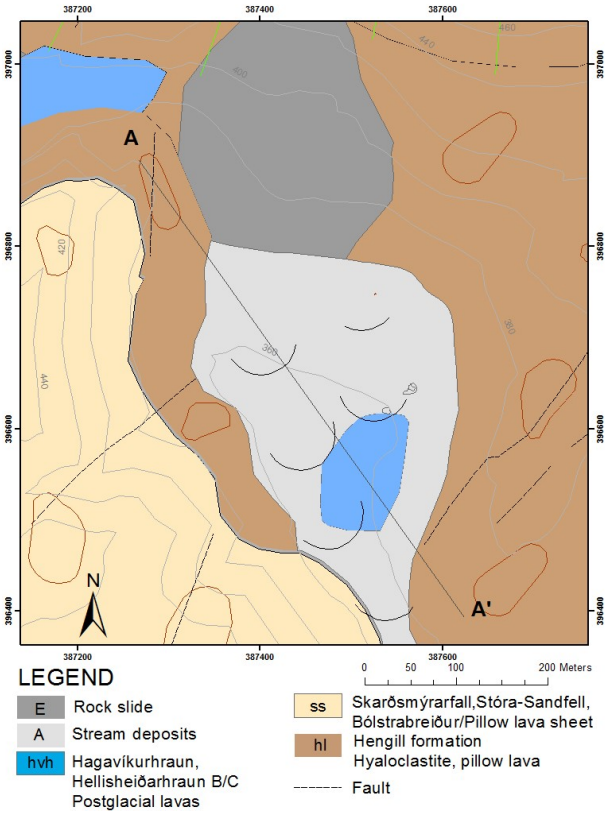

FIGURE 6: A geological map of the Hengill area, modified from Saemundsson (1995a). The volcanic accumulation consists of hyaloclastites from glacial times and interglacial lava flows

Tables 1 and 2 (see also Figure 6) show more a detailed description of the lithological units. Beginning with the youngest to the oldest, i.e. from the Hagavíkurhraun lava (hvh) down to Hengill formation (hl) and some superficial deposits such as major landslides (marked E) and major stream deposits (marked A).

TABLE 1: Bedrock lithology of the present study

No.	Unit (acronym)	Name	Description of rock type	Age
3	hvh	Hagavíkurhraun, Hellisheidarhraun B/C	Postglacial lavas	5500 years
2	ss	Skardsmýrarfall, Stóra-Sandfell, Bólstrabreidur	Pillow lava sheet	< 200,000 years
1	hl	Hengill formation	Hyaloclastite, pillow lava	< 200,000 years

TABLE 2: Superficial deposits of Holocene age

No	Unit (acronym)	Name	Description
1	E	Rock slides	Composed of brecciated hyaloclastite and lava blocks
2	A	Stream deposits	River gravels and other steam deposits

4.1 Structures

The characterization of tectonic structures is very important in geothermal exploration because the geothermal manifestations are often directly related to the presence of these structures. One of objectives of this work was to re-evaluate the distribution of tectonic structures such as faults and fractures.

In Middalur area, being located in a valley covered by soil, it is difficult to map tectonically structures but on either side of the valley in the hyaloclastites, the tectonic structures are visible through aerial photographs and in the field. Two fault/fracture patterns, trending NE–SW and N–S, were identified.

Faults: Three N-S faults (Figure 7) and one NE-SW fault are visible in the field. One fracture NE-SW manifests itself with an opening of 13 cm (Figure 8). It is connected perpendicular to the NW-SE fault which lies it outside of the geothermal map.

FIGURE 7: Fault direction N-S

FIGURE 8: Fracture direction N 30°E with around 13 cm opening

Inferred faults: Based on the preferred alignment of the geothermal manifestations, aerial photo line features and the orientation of 50°C isotherms, the author inferred eight faults pattern, trending NE–SW, N-S and E-W (Figure 9 and 10). The alignments of geothermal manifestations in the valley form six lines that could present faults (Figure 10). They all appear to be normal faults cutting through the hill, disappearing towards Middalur valley. They can be traced on aerial photographs covering the area.

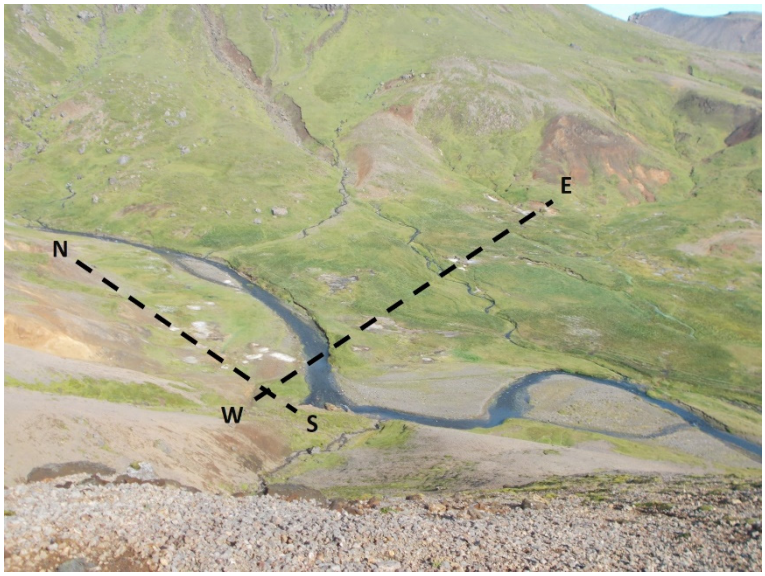

FIGURE 9: Distribution of aligned geothermal manifestations

Faults, inferred faults and fractures visible on the ground and air photographs were mapped with reasonable accuracy. Most of these structures show a NE-SW trend which is the general direction of tectonic structures in the Hengill area.

5. GEOTHERMAL MAPPING OF THE STUDY AREA

The geothermal mapping takes into account the spatial representation of different types of geothermal manifestations that occur in the study area such as hot springs, steam vent, mud pool, hot ground, warm ground, cold spring and clay alteration.

Soil temperature measurements at 50 cm of depth were executed using a digital thermometer. GPS positioning was used to map different temperature sampling points and geothermal manifestations.

The collected data were downloaded to a computer and edited with the ArcGIS software. The end result is a geothermal map with a scale of 1:2500 showing the temperature distribution in the valley, geothermal manifestations and tectonic structures (Figure 10).

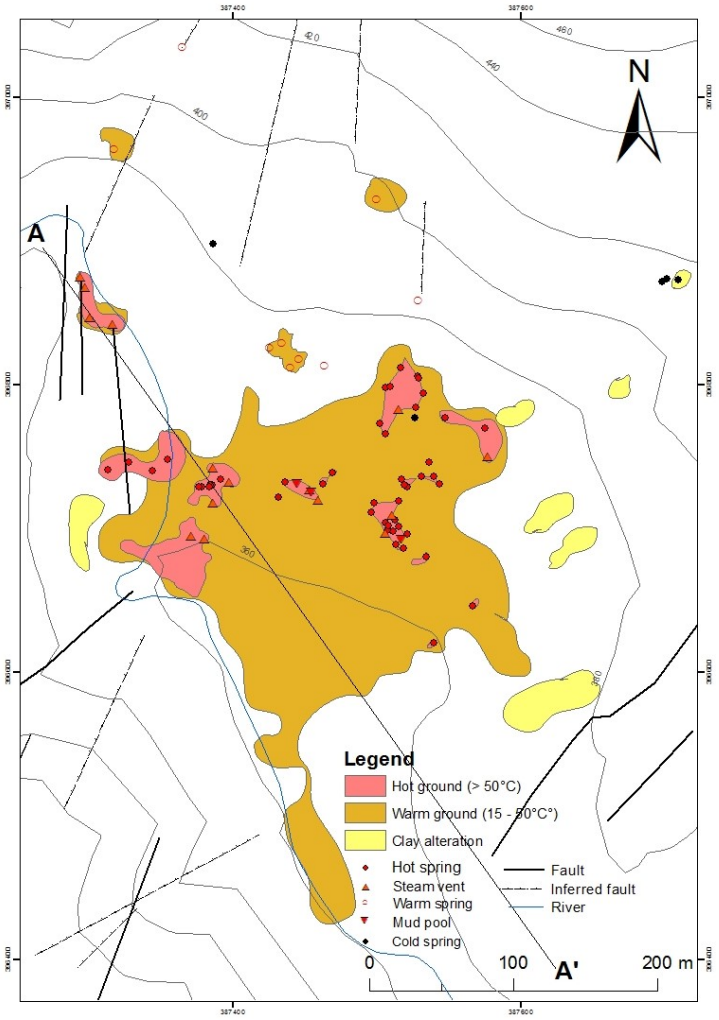

FIGURE 10: Geothermal map of Middalur high–temperature area

5.1 Geothermal manifestations

Geothermal manifestations found in the study area include hot springs, steam vents, mud pools, hot grounds, warm grounds and clay alteration (Table 3). They generally have the characteristics of being highly active.

In the valley (low altitude) one finds manifestations such as hot springs, steam vents, mud pool and hot and warm grounds. At higher altitudes, active geothermal manifestations present are warm and cold springs, steam vents and clay alteration. There appears to be a close relationship between the level of groundwater (water table) and geothermal manifestations in the study area. The cold springs have the same temperature as the groundwater temperatures in Iceland which is about 4°C (Hjartarson and Sigurdsson, 1993).

Figure 10 shows the distribution of geothermal manifestations and temperature in the Middalur area. The manifestations are aligned from east to west, indicating a fault which is, however, not visible on the surface (Figure 9). This possible E-W fault is cut by other faults trending N-S and NE-SW that are also not visible on the surface but can be concluded from the alignment of manifestations (Figure 10). All of these faults are covered with surface deposits.

5.1.1 Hot springs

Hot springs are abundant in the study area (Table 3). In this work, hot springs are classified as having temperatures above 50°C. Most are colourless, brown (due to clay particles) or whitish (due to the abundance of calcite). They can mostly be found on the middle of valley. Most of the springs are boiling but others are simply hot. The temperatures of the hot springs vary between 50 and 97.5°C. Most of these hot springs are surrounded by deposits and dark clay. Some emit CO_2 gas bubbles. Table 3 lists 46 hot springs. The total run off flow was estimated to be about 2-3 l/s.

TABLE 3: Manifestations mapped in Middalur

Manifestation	Total number
Boiling springs	3
Hot springs	46
Warm springs	9
Cold springs	5
Mud pools	3
Steam vents	15
Hot grounds	42

5.1.2 Warm springs

According to the characterization of the springs in this work, those having temperatures between 15°C and 50°C were classified as warm springs. They occur at somewhat higher altitudes than the hot springs. They could be fed by meteoric waters circulating in the faults and fractures where they get heated by circulating steam or cooled maybe by clay alterations and scaling, or by diminishing geothermal activity.

5.1.3 Cold springs

In the present study, cold springs are classified as having temperatures below 15°C. They are colourless and generally have temperatures between 4°C and 5°C. According to Hjartarson and Sigurdsson (1993), the average temperature of groundwater in the SW Iceland is about 4°C. The cold springs found in the area are groundwater fed. The majority of cold springs are located at slightly higher altitudes compared to the valley floor (Figure 10).

5.1.4 Warm grounds

Warm grounds have temperatures between 15 and 50°C. They are widely distributed in the study area (Figure 10). The vegetation colour typically changes from green to yellowish colour with increasing

temperature. In areas not covered by vegetation soils, warm grounds are easily identifiable because they have a whitish or cream-white colouration due to calcite precipitation and they have surfaces wet of smooth clay.

5.1.5 Hot grounds

Hot grounds are those with temperatures above 50°C. They are typical manifestation of high geothermal activity. They are isolated, of whitish brown colour with silica, calcite and aragonite deposits that make them easy to recognize from afar. In the study area, the highest temperature measured in the area was 97.7°C.

FIGURE 11: Mud pool

5.1.6 Mud pools

The mud pools usually occur near hot springs (Figure 10). They are formed in high temperature geothermal areas with surface water deficiency. They are characterized by greyish boiling mud in a basin (Figure 11). Only three mud pools were mapped in the research area (Table 3). In the study area, one of the boiling mud pools is at around 1 m depth. The temperatures of the mud pools vary between 94 and 97.3°C.

5.1.7 Steam vents

Steam vents mainly occur in hot grounds especially in the valley floor or side hill slopes where the water table is low (Figure 10). Most of them produce a whistling sound indicating that boiling water is at relatively shallow depths below the surface. The steam vents in Middalur valley are silent. Sulphur deposits are visible around them. The temperatures of the steam vents are around 97.5°C (Figure 12).

FIGURE 12: Steam vent with sulphur deposit in the fault N-S

5.1.8 Clay alterations

Clay alteration patches are formed by surface modification processes and are observed around mud pools areas but also as cold clay (“Extinct clay alterations”) in which the clay is altered to different degrees. One can easily see the iron oxide stains and precipitates, mud rich in silica alumina or reddish light colour, usually located close to active manifestations. In the study area, the clay alterations are cold, most clearly visible on the hillsides and they are located outside of the resent active areas (Figure 13).

FIGURE 13: Extinct clay alteration

5.2 Geothermal model of the Middalur field

The geothermal model developed for the study area (Figure 14) is calculated along the cross-section line A-A' on the basis of geological and geothermal maps (Figures 6 and 10). This cross-section is used to show schematically geothermal conduits to surface manifestations.

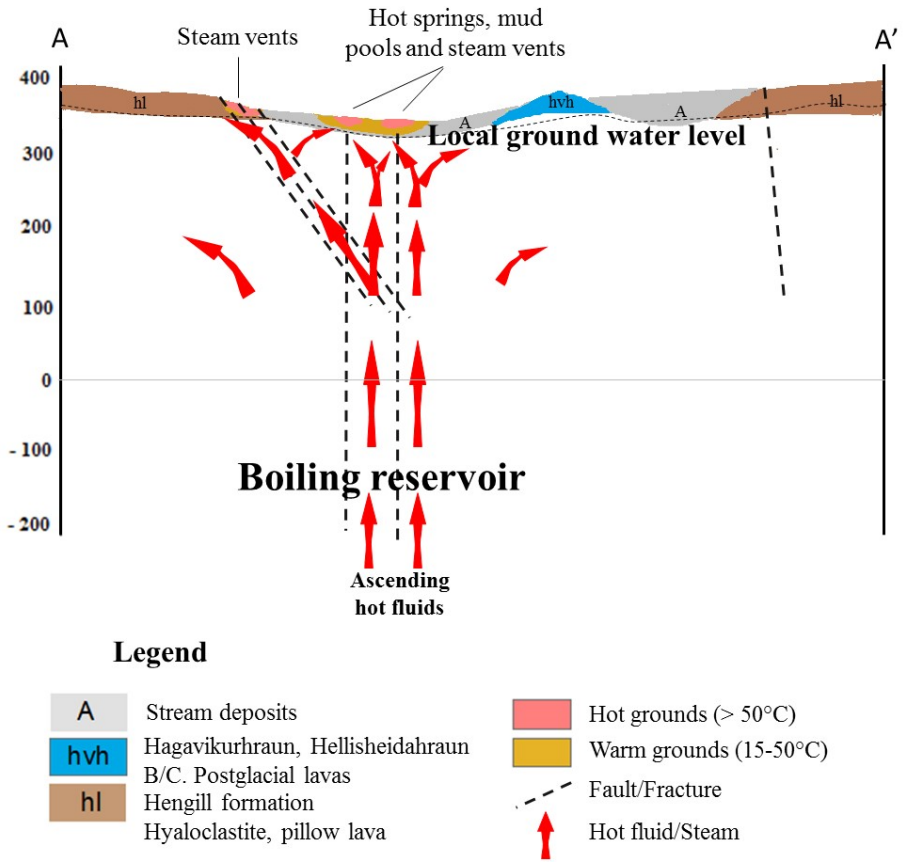

FIGURE 14: Geothermal model of the Middalur area

In the absence of well data to complete the lithology and other in-depth information, we think that the hot water ascends upwards due to buoyancy which offsets further infiltration of cold water from the regional deep-seated groundwater source.

This model assumes a boiling geothermal reservoir at depth. The NE-SW faults and fractures in the region act as upflow zones from which the hot geothermal manifest-tations emerge to the surface. The N-S striking faults intersect the NE-SW trending faults or fractures which are the principal heat conductors in this area and channel the upward flow.

Local groundwater is heated by steam, subsequently flowing upwards and out through fractures as warm springs. The hot springs and mud baths appear in places where the groundwater reaches the surface through the fault or fractures. The hot grounds and the steam vents occur only at relatively low groundwater levels along the N-S trending faults in the hyaloclastites.

6. CONCLUSIONS

During this work, geothermal mapping was carried out in the Middalur valley. The types of geothermal manifestations found are hot springs, mud pools, steam vents and extinct clay alteration. These manifestations were correlated with tectonic structures in the region. On the map, the manifestations are aligned in the directions E-W, N-S and NE-SW that could represent faults or fractures. The isotherms of >15°C and of >50°C delineate warm and hot ground.

The geothermal model assumes a boiling geothermal reservoir at depth. The upward flow occurs along faults and fractures oriented in NE-SW direction. These faults are connected to the N-S and E-W fault trend, and channel the upward flow which leads to the expression of the thermal manifestations.

This upward flow heats or mixes with local groundwater and the surface water systems.

In summary, this work concludes that:

- Most of the geothermal manifestations are related to structural features like faults indicating that the upflow in the area is mostly controlled by those faults;
- Geothermal manifestations and temperature distribution indicate faults/fractures trending in approximately NE-SW, E-W and N-S directions. These faults are probably controlling the movement of the geothermal water of the area. Heat sources are believed to be cooling intrusions underneath (Hengill central volcano);
- Most of hot springs precipitate deposit and the occurrence of sulphur implies a high-temperature geothermal field;
- The local groundwater level determines the occurrence of hot springs and steam vents in the area. If groundwater level lowers, hot springs regress to mud pools and eventually change to steam vents.

7. RECOMMENDATIONS

For the development of geothermal energy in the Democratic Republic of Congo the following recommendations should be considered:

- The training of more people in various fields of geothermal exploration and development, such as geology, geochemistry, geophysics, drilling and reservoir engineering;
- The awareness of decision makers on the importance of geothermal energy as a clean renewable energy source;
- The mobilization of funds for a detailed geothermal resource assessment in the country.

ACKNOWLEDGEMENTS

My sincere thanks go to UNU-GTP and Government of Iceland for granting me the opportunity to take part in this important course and for financing it. For this first participation from Congo D.R. my special thanks go to Mr. Lúdvík S. Georgsson for giving me the opportunity to participate in this course and all the staff of UNU Geothermal Training Programme, Mr. Ingimar G. Haraldsson, Ms. Frída Ómarsdóttir, Mr. Markús A.G. Wilde and Ms. Thórhildur Ísberg, for their organisation and endless efforts to assist me in every way during the entire period. Big thanks also to María S. Gudjónsdóttir. for organization of group project. I am grateful to the entire ÍSOR and Orkustofnun (National Energy Authority of Iceland) staff for sharing their knowledge and experience. The Geological Survey of Congo D.R. is acknowledged for granting me permission to take part in this course.

My heartfelt gratitude goes to my supervisors, Dr. Björn S. Hardarson and Sigurdur G. Kristinsson of ÍSOR for experience they shared with me. Really, I am much honoured to have been your student and to learn more in the field of applied geothermal geology. It was interesting and fun being supervised by you.

My deepest gratitude goes to my family and friends for their unconditional support and best wishes during my stay in Iceland. Thanks to the 2015 UNU Fellows for all the ideas we shared and exchanged during the entire period and for making my entire stay in Iceland fun. It was a pleasure meeting and interacting with all of you. Finally, I thank the almighty father for granting me good health and the grace to start and finish this course.

REFERENCES

Árnadóttir, T., Geirsson, H., and Jiang, W., 2008: Crustal deformation in Iceland: Plate spreading and earthquake deformation. *Jökull, 58, 67*.

Árnason, K., 2006: *TEMTD, a program for 1D inversion of central-loop TEM and MT data. Short manual*. ÍSOR – Iceland GeoSurvey, Reykjavík, Iceland, internal report, 17 pp.

Árnason, K., Eysteinsson, H., and Hersir, G.P., 2010: Joint 1D inversion of TEM and MT data and 3D inversion of MT data in the Hengill area, SW Iceland. *Geothermics*, *39*, 13-34.

Árnason, K., Karlsdóttir, R., Eysteinsson, H., Flóvenz, Ó.G., and Gudlaugsson, S.Th., 2000: The resistivity structure of high-temperature geothermal systems in Iceland. *Proceedings of the World Geothermal Congress 2000*, *Kyushu-Tohoku, Japan,* 923-928.

Árnason, K., and Magnússon, I.Th., 2001: *Geothermal activity in Hengill and Hellisheidi. Results of resistivity surveys.* Orkustofnun, Reykjavík, Iceland, report OS-2001/091 (in Icelandic), 250 pp.

Björnsson, A., and Hersir, G.P., 1981: Geophysical reconnaissance study of the Hengill high-temperature area, SW-Iceland. *Geothermal Resources Council Transactions, 10*, 205-210.

Bödvarsson, G., 1961: Physical characteristics of natural heat resources in Iceland. *Jökull*, *11*, 38 pp.

Deer, W.A., Howie, R.A., and Zussman, J., 1962: *Rock-forming minerals, Vol. 3. Sheet Silicates*. Longmans, Green and Co. Ltd., London, United Kingdom, 270 pp.

Einarsson, P., 1989: Earthquake focal depth in Iceland and conclusions on crustal structure and temperatures. *Abstracts from the Conference of the Icelandic Geological Society on the Crust of Iceland, Reykjavík* (in Icelandic), 7 pp.

Feigl, K.L., Gasperi, J., Sigmundsson, F., and Rigo, A., 2000: Crustal deformation near Hengill volcano, Iceland 1993-1998: Coupling between magmatic activity and faulting inferred from elastic modelling of satellite radar interferograms. *J. Geophys. Res., 105,* 25,655-25,670.

Franzson H., Gunnlaugsson E., Arnason K., Saemundsson K., Steingrímsson B. and Hardarson B.S., 2010: The Hengill geothermal system, conceptual model and thermal evolution. *Proceedings of the World Geothermal Congress 2010, Bali, Indonesia,* 9 pp.

Fridleifsson, I.B., 1979: Geothermal activity in Iceland. *Jökull, 29*, 47-56.

Gudmundsson, M.T., and Jacoby, W., 2007: Hotspot Iceland: An introduction. *J. Geodynamics, 43-1*,1-5.

Hardarson, B.S., 2014: Geothermal exploration of the Hengill high-temperature field. *Paper presented at "Short Course IX on Exploration for Geothermal Resources", organized by UNU-GTP, GDC and KenGen, Lake Bogoria and Lake Naivasha, Kenya,* 9 pp.

Hardarson, B.S., Einarsson, G.M., Gunnarsson, G., Helgadóttir, H.M., Franzson, H., Árnason, K., Ágústsson, K., and Gunnlaugsson, E., 2010: Geothermal reinjection at the Hengill triple junction, SW Iceland. *Proceedings of the World Geothermal Congress 2010, Bali, Indonesia,* 7 pp.

Hardarson, B.S., Fitton, J.G., and Hjartarson, Á., 2008: Tertiary volcanism in Iceland. *Jökull, 58,*161-178.

Hardarson, B.S., Fitton, J.G., Ellam, R.M., and Pringle, M.S., 1997: Rift relocation – a geochemical and geochronological investigation of a paleo-rift in northwest Iceland. *Earth Planet. Sci. Lett., 153,* 181-196.

Hjartarson, Á., and Sigurdsson, F., 1993: *Hydrogeological map, Vífilsfell 1613 iii SA-V, 1:25,000.* Iceland Geodetic Survey, Orkustofnun, Reykjavík, Iceland.

Ívarsson, G., 1998: Fumaroles gas geochemistry in estimating subsurface temperatures at Hengill in south-western Iceland. *Proceedings of the 9th Symposium on Water-Rock Interaction, Taupo, New Zealand*, 459-462.

Jóhannesson, H., 1980: Structure and evolution of volcanic zones in W-Iceland. *Náttúrufraedingurinn*, *50*, 13-31 (in Icelandic).

Jóhannesson, H., and Saemundsson, K., 1998: *Geological map of Iceland 1:500.000* (2nd ed.). Náttúrufraedistofnun Íslands and Landmaelingar Íslands, Reykjavík, Iceland.

Kristmannsdóttir, H., 1979: Alteration of basaltic rocks by hydrothermal activity at 100-300°C. In: Mortland, M.M., and Farmer, V.C. (editors), *International Clay Conference 1978*. Elsevier Scientific Publishing Co., Amsterdam, Netherlands, 359-367.

McDougall, I., Kristjánsson, L., and Saemundsson, K., 1984: Magnetostratigraphy and geochronology of northwest Iceland. *J. Geophys. Res., 89,* 7029-7060.

Moorbath, S., Sigurdsson, H., and Goodwin, R., 1968: K-Ar ages of oldest exposed rocks in Iceland. *Earth Planet. Sci. Lett., 4*, 197-205.

Orkustofnun, 2009: *Geothermal areas in Iceland, high-temperature fields*. Orkustofnun – National Energy Authority, Reykjavik, website: *www.os.is/jardhiti/jardhitasvaedi-a-islandi/hahitasvaedi/* (in Icelandic)

Óskarsson, N.S., Steinthórsson, S., and Sigvaldason, G.E., 1985: Iceland geochemical anomaly: origin, volcanotectonics, chemical fractionation, and isotope evolution of the crust. *J. Geophys. Res., 90*, 10,011-10,025.

Saemundsson, K., Axelsson, G., and Steingrímsson, B., 2009: Geothermal systems in global perspective. *Presented at "Short Course on Surface Exploration for Geothermal Resources", organized by UNU-GTP and LaGeo, Santa Tecla, El Salvador*, 16 pp.

Saemundsson, K., 1967: Vulkanismus und Tektonik des Hengill-Gebietes in Sudwest-Island. *Acta Nat. Isl., II-7* (in German), 195 pp.

Saemundsson, K., 1974: Evolution of the axial rifting zone in northern Iceland and Tjörnes fracture zone. *Geol. Soc. Am. Bull., 85*, 495-504.

Saemundsson, K., 1978: Fissure swarms and central volcanes of the neovolcanic zones of Iceland. *Geol. J., Sp. Issue, 10*, 415-432.

Saemundsson, K., 1980: Outline of geology of Iceland. *Jökull, 29*, 28.

Saemundsson, K., 1995a: *Geological map of the Hengill area 1:50,000*. Orkustofnun, Reykjavík, Iceland.

Saemundson, K., 1995b: *Geological map of the Hengill area, 1:25,000.* Orkustofnun, Reykjavík, Iceland.

Thórdarson, T., and Höskuldsson, A., 2002: *Iceland.* Terra Publishing, Reykjavik, 200 pp.

Thórdarson, T., and Larsen, G., 2007: Volcanism in Iceland in historical time: Volcano types, eruption styles and eruptive history. *J. Geodyn., 43*, 118-152.

Vink, G.E., 1984: A hotspot model for Iceland and the Voring Plateau. *J. Geophys. Res., 89,* 9,949-9,959.

Ward, P., and Björnsson, S., 1971: Micro earthquakes, swarms and the geothermal areas of Iceland. *J. Geophys. Res., 76*, 953-982.

Watkins, N.D., and Walker, G.P.L., 1977: Magnetostratigraphy of Eastern Iceland. *Am. J. Sci., 277,* 513-584.

UNITED NATIONS UNIVERSITY
UNU-GTP
Geothermal Training Programme

Orkustofnun, Grensasvegur 9,
IS-108 Reykjavik, Iceland

Reports 2015
Number 25

MINERAL SCALING POTENTIAL OF GEOTHERMAL FLUIDS IN WELL MW 01A IN MENENGAI, KENYA

John Kiplagat K. Mundui
Geothermal Development Company, Ltd. – GDC
P.O. Box 1453 – 20117
Naivasha
KENYA
jmundui@gdc.co.ke

ABSTRACT

The Menengai geothermal field was drilled in 2011. Some of the wells that have been discharging have recorded a decrease in productivity over time. In this study, geothermal water was sampled from well MW 01A in Menengai to determine the scaling potentials of calcite, amorphous silica, and anhydrite to understand the possible areas where scaling could occur. Simulations for fluids' scaling potential was done for the reservoir fluid, discharge and reinjection by adiabatic boiling and conductive cooling by use of the WATCH program. Two conceptual models for these minerals' saturation in the fluids are used. The results of simulations shows that calcite is expected to cause some scaling problems at the well during initial boiling and does not cause any problem at production, utilization, and reinjection. Amorphous silica may deposit during utilization especially if the water lowered below 100°C during discharges and reinjection. Anhydrite has no possibility of scaling in both boiling and cooling at any stage. Measures should be taken to avoid calcite mineral scaling at the well and amorphous silica deposition by saturated water at temperatures < 150°C during utilization.

1. INTRODUCTION

The Menengai geothermal field, having a capacity of 700 MWe (Muchemi, 2010), is one of three geothermal fields in Kenya undergoing development for steam production for electricity generation and direct uses. The other developed fields are Olkaria and Eburru that are undergoing expansion.

Geothermal Development Company (GDC) is currently drilling for steam at the Menengai caldera for 105 MWe production in phase one while heat energy is extracted for direct uses. Currently 29 wells have been drilled as of September 2015, of which eight wells are directional wells. Reservoir temperatures up to 400°C at 2,000 m have been encountered in several wells making it the hottest geothermal system in Kenya. The average temperature gradient of Menengai caldera is approximately 120°C/km. Steam production from the wells varies from relatively small to greater than 10 MWe. Currently 80 MWe of steam equivalent is on the wellhead and full steam production for the planned 105 MWe power plants is expected before the end of 2014. Three companies have been licensed for 20 years to operate 35 MWe modular plants each, which are due to be commissioned within 2015 (Omenda and Simiyu, 2015).

To maximize on energy efficiency, GDC is in the process of establishing a 'Direct Use Energy Park' where the main source of energy is heat in the brine from various discharging wells, collected and piped to various industrial applications at the park. Well MW 03 (depth of 2101.5 m) with a mass flow rate of 16 kg/sec is dedicated for demonstration of direct uses having varied temperature requirements and was commissioned in August 2015.

2. BACKGROUND

2.1 Study area

The Menengai geothermal field is a ring like crater that is located 10 km to the North of Nakuru town with the caldera measuring approximately 90 km^2. It is one of the 14 geothermal prospects that spread along the east rift system (Figure 1). The caldera is bound by the UTM coordinates 157000 E to 185000 E and 9966000 N to 0 (equator) (Mungania et al., 2004). The field is within a geothermal system consisting of the Ol'Rongai volcanic field to the North West, Ol'banita plains and Solai graben to the North of the Menengai volcano. The volcano is geologically categorized as one of seven late Quaternary caldera volcanoes that occurred along the Kenya rift valley about 200,000 years ago. It is one of the volcanic complexes located along the East African Rift System that has a high thermal gradient due to shallow magmatic bodies. Surface manifestations in Menengai are fumaroles, altered grounds/rocks, and existence of *Fimbristylis exilis* 'geothermal grasses' associated with hot grounds. Others manifestations outside the caldera are warm springs, gas boreholes, hot/warm water boreholes, solfatara deposition and silica and or chalcedonic deposition at the fumaroles' vents (Mungania, 2004).

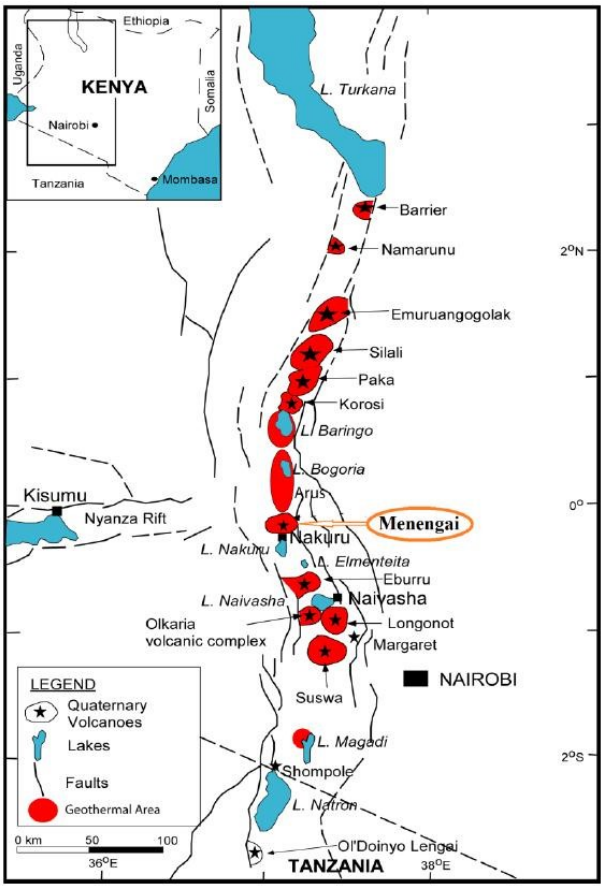

FIGURE 1: A map showing location of Menengai geothermal field and other high-temperature geothermal fields in Kenya (adapted from Onyango, 2012)

2.2 General settings and geology

The surface of Menengai volcano is covered by volcanic rocks mostly erupted from centres within the area. The geology and tectonic map of the Menengai geothermal system is represented by Figure 2. Most of the area is covered by pyroclastics that have erupted from centres associated with the volcano. The syn-caldera rocks are spread around the Menengai caldera and comprise the ignimbrite and pumice/ash deposits (Mbia, 2014). It forms part of the central Kenya peralkaline province, a unique assemblage of peralkaline salic magmatic systems (Macdonald and Baginski, 2009; MacDonald and Scaillet, 2006). These magmatic systems have been described by MacDonald et al. (2011) as composed largely of silica-oversaturated, peralkaline trachytes, with subordinate volumes of metaluminous trachytes and pantelleritic rhyolites. Leat (1983) described the geology Menengai volcano. Briefly, a shield-building phase (K–Ar dated at 0.18±0.01 Ma) erupted lavas and interbedded fall deposits with an estimated volume of 29 km^3. This was followed by two caldera-forming events (at 29 ka and 8 ka, respectively), each accompanied by eruption of an ash-flow tuff with a volume of 20–30 km^3. Post-

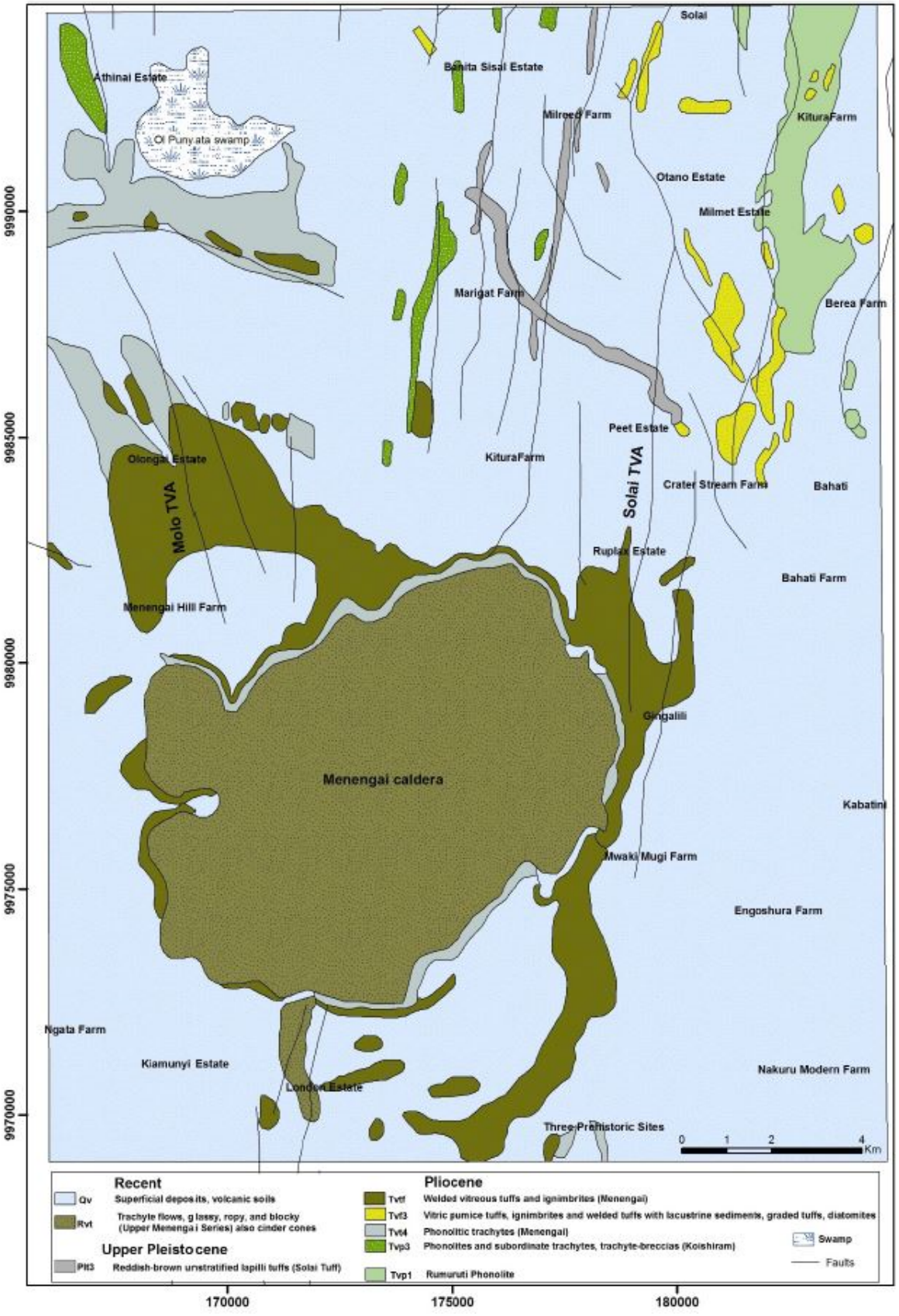

FIGURE 2: Geological and structural map of Menengai (adapted from Sekento, 2012)

caldera activity has largely been restricted to inside the second caldera and produced mainly lavas (at least 70 flows), sheet-forming fall pumice deposits and strombolian cinder cones.

The volcano is built of Trachyte lavas and associated intermediate pyroclastics. Most of the pyroclastics activity accompanied caldera collapse. Post caldera activity (<0.1 Ma) mainly centred on the caldera floor with eruption of thick piles of trachyte lavas from various centres (Simiyu, 2010). The caldera and ring faults, Ol' Rongai and Molo TVA trending NW- SE, and the Solai TVA trending N-S axis forms the three structures.

The regional TVA's in Menengai geothermal system are an important conduit of deep fluids thus an important geothermal controlling feature in the area (Lagat, 2011). These faults/fractures at the rift floor resulting from continental rifting joining the Molo and Solai scarps, allow water to recharge the aquifers below Menengai, where the water is heated up by intrusion of mantle-derived magma. Menengai has subsurface fractures and ring caldera faults that facilitate recharge of the aquifer with permeable zone observed between 1000 and 1600 m in three wells, MW-1, MW-2 and MW-3. The existence of these faults penetrated by well one (MW-01) was supported by Mibei and Lagat (2011) that lithological contacts indicated by high penetration rates, pH loss and chloride gains. These structures are therefore important controls in the Menengai geothermal field. Petrography and mineral chemistry of the basaltic and trachytic end members of the Menengai rocks indicate that two or more distinct magma types were involved in the formation of the volcano (Mbia et al., 2015). The mineral alteration resulting from longer residence time between geothermal fluids and rocks is evidenced by high concentration of dissolved solids. This is in concurrence with Mbia (2014) that at sea level high resistivity dominates almost the entire caldera, which could be attributed to alteration due to high temperature alteration minerals which are resistive. Drilling for steam in Menengai was targeted at a region with high permeability and MW 01 was the best target for exploration well and MW 01 A was drilled as a production well.

2.3 Geochemistry of Menengai fluids

When a caldera geothermal field is drilled into, geothermal fluids (having dissolved solids in varying proportions) have their sources from geothermal reservoirs at different depths reflecting the subsurface thermal, chemical, and rock mineral properties. Those can then be used to predict subsurface temperatures, fluid flow, and the types of the reservoir fluids. Gas geothermometer temperatures for well MW 01, which lies adjacent to the well in study, indicate high values in excess of 300°C compared to the Na/K and quartz equilibrium temperatures of about 190°C and 220°C respectively (Kipng'ok, 2011). According to Kanda and Suwai (2013), well MW 01 geothermometry studies indicate that there exists a fairly shallow aquifer (i.e. ~1050 -1100 m) hosting predominantly liquids at temperatures about 190°C - 223°C as confirmed by Na/K and Quartz equilibrium geothermometers, and relatively deeper aquifer (~1800- 2050 m) hosting temperatures that exceed 300°C as indicated by gas geothermometers (Kanda and Suwai, 2013). This is in agreement with Mbia (2014) and GDC (2013) reports on 7 wells in Menengai geothermal field where quartz equilibrium and Na/K geothermometer temperatures are around 200°C indicating that the water is from relatively cold feed zones and therefore inferred to be shallow.

Fluids encountered from 7 wells are of sodium bicarbonate type with HCO_3 concentrations as high as 8,200 ppm (calculated as CO_2) and average ~5,000 ppm (GDC, 2013) with near neutral pH, and close to equilibrium with respect to calcite (Malimo, 2013). Some of the boreholes drilled in the area have production capacity >20 m^3/hr, with some on the northern sides having temperatures >30°C. Geochemical analyses indicate high CO_2 values (>1.2%), especially along the fractured zones, with absolute values of Rn-222 indicating a NW-SE trend anomaly. These areas apparently coincide with high Rn-222 absolute values (anomalous values in the range of 2002-3700 cpm) in the caldera and to the north and northwest out of the caldera (GDC, 2010).

2.4 Mineral deposition chemistry

Chemical equilibria between alteration minerals and solution is generally attained in geothermal systems for all major components except chloride (Arnórsson, 1983). Upon fluid ascent the equilibrium conditions may be disturbed, resulting in mineral over- or under-saturation. In this study, the saturation state of calcite, amorphous silica and anhydrite were investigated.

2.4.1 Silica

In reservoirs, aqueous silica concentrations are commonly controlled by quartz solubility (Arnórsson, 1975; Arnórsson and Stefánsson, 1999). Reservoir fluids are saturated with respect to quartz but under-saturated with amorphous silica and exists as a reactive monomeric form H_4SiO_4 (aq) as shown by equation below:

$$SiO_2(s) + 2H_2O = H_4SiO_4^0(aq) \quad (1)$$

Within the reservoirs, aqueous silica may dissociate to form silicic acid according to the reaction

$$H_4SiO_4(aq) = H_3SiO_4^- + H^+ \quad (2)$$

The solubility of silica minerals (quartz and amorphous silica) increases with an increase of pH and temperature.

During steam production, utilization or discharges, three important factors affect silica solubility: CO_2 and H_2S partitions to vapour phase resulting in increased solution pH of the boiled liquid phase increasing the solubility of amorphous silica in solution; a pressure decrease causing temperature drop in separated water and decreasing silica solubility; and silica is concentrated in the separated water due to above two factors.

The solubility of quartz, chalcedony and amorphous silica is shown in Figure 3A.

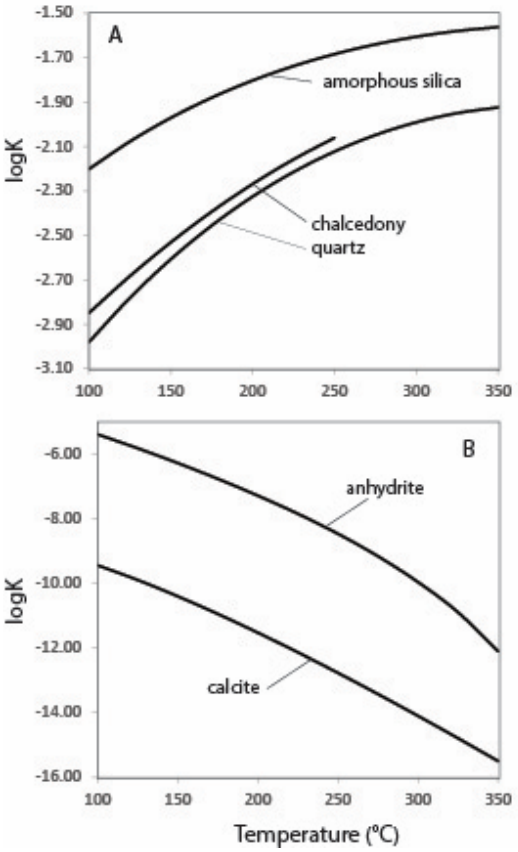

FIGURE 3: Minerals solubility in geothermal water

2.4.2 Calcite

Calcite is another mineral commonly observed to be in equilibrium with respect to reservoir geothermal fluids. Calcite reaction may be described by the reaction,

$$CaCO_3 = Ca^{2+} + CO_3^{2-} \quad (3)$$

Calcite solubility decreases with increasing temperature. It also depends on the speciation of dissolved inorganic carbon in solution with the major species being CO_2 (aq), HCO_3^- and CO_3^{2-} and linked through the ionization constants,

$$CO_2(aq) + H_2O = H^+ + HCO_3^- \quad (4)$$

$$HCO_3^- = H^+ + CO_3^{2-} \quad (5)$$

With increasing pH, HCO_3^- and CO_3^{2-} become progressively important, respectively. CO_2 (aq) may also partition into the vapour phase through the reaction,

$$CO_{2\,(aq)} = CO_{2\,(g)} \quad (6)$$

It follows that upon boiling, dissolved inorganic carbon of the liquid phase decreases upon degassing of CO_2 (aq), resulting in increased pH of the boiled water and increased relative concentration of CO_3^{2-}. This may lead, at least in some cases, to calcite formation upon boiling (Simmons and Christenson, 1994). The solubility of calcite silica is shown in Figure 3B.

2.4.3 Anhydrite

Anhydrite is often observed to be close to equilibrium with respect to geothermal fluids, particularly associated with reservoir fluids with elevated sulphate concentration. Anhydrite forms according to the reaction:

$$CaSO_4(s) = Ca^{2+} + SO_4^{2-} \quad (7)$$

The solubility of anhydrite does not depend on aqueous speciation, as Ca^{2+} and SO_4^{2-} are the dominant species under most conditions, but rather temperature and salinity. However, boiling may lead to calcite super-saturation through loss of liquid water to the vapour phase and consequently increase in elemental concentrations in the boiled liquid water including Ca^{2+} and SO_4^{2-}. In geothermal operations, anhydrite deposition has not been a major problem. However, anhydrite deposition in a number of production wells in Bacman in Philippines develops in the wellbore when the high SO_4 fluid mixes with up flowing deep fluid and as the mineral deposits grow, this progressively isolates the hotter, neutral, deeper fluids until the discharge fluid becomes acidic, dilute and cooler (Espartinez and See, 2015).

The solubility of anhydrite with temperature is shown in Figure 3B and shows decreased in solubility with increasing temperature.

3. METHODS

3.1 Sampling and analysis of geothermal fluids

In this study discharge fluids from the MW 01A well were collected in October 2014 and March 2015. The well was drilled at an inclination 11° and azimuth N85°E in 2014 to 2200 M and is adjacent to a vertically drilled well MW 01 (2195 m).

Collection, treatment and preservation of steam condensate and non-condensable gases and residual gases from a high temperature two phase well was done and later taken for laboratory analysis. Webre separator samples were collected according to procedures described by Arnórsson et al. (2006). The Webre separator was fixed at 1.5 m away from the T-junction of the horizontal and the vertical pipes, where the fluids are assumed to be homogenous.

The Webre separator was allowed to stabilize with the pressure inside and the pipe's discharge flow with adequate care taken to ensure boiling does not occur in the separator. The dry steam containing non condensable gases (CO_2 and H_2S) and other volatiles are passed through a 500 ml evacuated gas sampling bottle containing 50 ml of 40% w/v NaOH to absorb these gases as the bottle is continuously cooled while the residual gases Ar, N_2, CH_4, and O_2 are collected into the gas space in the bottle. Steam passed through the Webre separator and was cooled using a stainless steel coil immersed in a cold water bath to condense the steam and then collected as condensate.

The collected samples are labelled according to the treatment, and the nature of the analysis to be done. 500 ml of raw untreated samples were stored in clean polyethylene bottles for CO_2, pH, total dissolved solids (TDS), Cl, F, B, total carbonate carbon analysis, and conductivity measurement. Samples for laboratory analysis of SiO_2 were collected in 150 ml bottles in triplicate, diluted in the ratio 1:10 to prevent polymerization. Samples for cations and SO_4 analysis were filtered through 0.45 µm millipore membrane and acidified using 1 ml Conc. HNO_3 to 250 ml of the sample bottle. To the sample for SO_4 determination 2 ml of 0.2M Zn-acetate was added to fix the dissolved sulphide. Continuous sampling

and analysis was done for the entire period between October 2014 and March 2015 to assess the well performance to understand the reservoir conditions.

Immediate analysis in the laboratory is done for pH, conductivity and total dissolved solids (TDS). Chloride concentrations we reanalysed by argentometric titration method. Major element concentrations were diluted to recommended limits followed by analysis of Na, K, and Ca using Inductively coupled plasma mass spectrometry (ICP-MS). Dissolved silica, B, and SO_4 are done using UV-Vis spectrophotometer. Fluoride and NH_3 were analysed using ion selective electrodes. Concentrations of CO_2 and H_2S were determined on site using modified alkalinity titration and Hg-precipitation titration, respectively. For steam samples, the concentrations of CO_2 and H_2S were measured in the steam condensate using the previously mentioned analytical method whereas the concentrations of non-condensable gases CH_4, N_2, H_2, and O_2 were analysed using gas chromatography.

3.2 Reservoir fluid composition

The reservoir fluid composition was calculated from the samples of two-phase well discharges collected at surface. Comparison of wellhead and deep water calcium concentrations has been found the most useful method of predicting the extent of deposition (Ármannsson, 1989). In addition, the effects of depressurization boiling were simulated in a similar manner from the reservoir to 100°C and from the well head temperatures to 100°C. The calculations were carried out using the WATCH program (Arnórsson et al., 1982; Bjarnason, 2010) assuming conservation of enthalpy and mass. The calculations involve three steps: (i) assessment of the steam fraction at sampling and in the reservoir, (ii) assessment of reservoir fluid temperatures and (iii) reconstruction of the reservoir steam and liquid water composition from chemical data on steam and liquid water well discharges.

The steam fraction is obtained assuming conservation of enthalpy:

$$h^t = h^s X^s + h^{lq} X^{lq} = h^s X^s + h^{lq}(1 - X^s) \quad (8)$$

and

$$X^s = \left(h^t - h^{lq}\right)/\left(h^s - h^{lq}\right) \quad (9)$$

where h^t = is the enthalpy of the total fluid, h^s is the enthalpy of steam, h^{lq} is the enthalpy of liquid and X^s and X^{lq} are the steam and liquid fractions with $X^s+X^{lq} = 1$.

Similarly, for the conservation of mass:

$$m_i^t = m_i^s X^s + m_i^{lq}(1 - X^s) \quad (10)$$

where m_i^t is the concentration of the i-th component in the total fluid, m_i^s is the concentration of the i-th component in the steam phase and m_i^{lq} is the concentration of the i-th component in the liquid water phase.

For non-volatile components that do not enter into the steam phase upon boiling:

$$m_i^t = m_i^{lq}(1 - X^s) \quad (11)$$

For volatile components only partition into the steam phase:

$$m_i^t = m_i^s X^s \quad (12)$$

Some components partition both into the steam and liquid water phase, like CO_2 and H_2S. The concentration ratios between the phases is given by:

$$D_s = n_i^s / n_i^{lq} \quad (13)$$

where D_s is the distribution coefficient for the i-th component between the steam (s) and the liquid (lq) phase.

To calculate the reservoir fluid composition one needs to know the reservoir fluid temperature. In the present study, the reservoir fluid temperature was calculated assuming equilibrium with quartz, i.e. using the quartz geothermometry temperature. The enthalpy of the total fluids may be either obtained from measurements of well discharge at surface, i.e. $h^t=h^{measured}$, or assuming liquid only aquifer and taken the enthalpy of liquid at the reservoir temperature, i.e. $h^t = h^{lq}_{T^{qtz}}$. Here, the former is measured to as calculated enthalpy or model 1 and the latter as measured enthalpy or model 2.

3.3 Aqueous speciation and mineral saturation

Aqueous speciation and mineral saturation were calculated with the aid of the WATCH program (Arnórsson et al., 1982; Bjarnason, 2010)

The mineral saturation is expressed in terms of the mineral saturation index (SI) of a particular mineral, defined as the logarithm of the ratio of the reaction quotient (Q) to the equilibrium constant (K):

$$SI= \log(Q/K) \tag{14}$$

where Q is defined as:

$$Q = \prod a_i^v \tag{15}$$

where a_i is the activity of aqueous species to the stoichiometric power v for the reaction, negative for reactants and positive for products.

The three mineral reactions considered here were amorphous silica, calcite and anhydrite. The dissolution of these minerals is defined according to:

$$SiO_2(s) + 2H_2O = H_4SiO_4(aq) \tag{16}$$
$$CaCO_3(s) = Ca^{2+} + CO_3^{2-} \tag{17}$$
$$CaSO_4(s) = Ca^{2+} + SO_4^{2-} \tag{18}$$

The reaction quotients for these reactions are:

$$Q_{SiO_2(s)} = a_{H_4SiO_4(aq)} \tag{19}$$
$$Q_{CaCO_3(s)} = a_{Ca^{2+}} a_{CO_3^{2-}} \tag{20}$$
$$Q_{CaSO_4(s)} = a_{Ca^{2+}} a_{SO_4^{2-}} \tag{21}$$

The equilibrium solubility of amorphous silica was taken from Gunnarsson and Arnórsson (2000) and the equilibrium solubility of calcite and anhydrite was taken from Arnórsson et al. (1982) represented by the equations:

$$\log K_{am.silica} = -8.476 - 485.24 * T^{-1} - 2.268 * 10^{-2} + 3.068 * \log T \tag{22}$$
$$\log K_{calcite} = +10.22 - 0.0349T - \frac{2476}{T} \tag{23}$$
$$\log K_{anhydrite} = +6.20 - 0.0229\,T - \frac{1217}{T} \tag{24}$$

From the activities of the respective aqueous species and the mineral solubility constants, the mineral saturation state was assessed. At equilibrium, SI = 0, whereas if SI > 0 the fluid is supersaturated and the mineral can precipitate (i.e. form mineral scales) whereas if SI<1 the fluid is under-saturated with respect to the mineral and will no form and/or dissolve.

3.4 Boiling and cooling and mineral scaling

The potential scaling of amorphous silica, calcite and anhydrite were assessed in the steps: (i) from the reservoir to the well head by boiling, (ii) from the wellhead to 100°C, both assuming the liquid and steam phases to be separated and coexisting upon boiling and cooling and (iii) upon reinjection of the geothermal wastewater.

The chemistry of the reservoir fluids was obtained both by assuming liquid only reservoir (model 1) and two-phase reservoir (model 2). These were boiled to 100°C and 1 bar and the mineral scaling potential assessed.

The chemistry of the well discharge was obtained directly from the chemical analysis of the well head steam and liquid water phases. These were boiled and cooled to 100°C in order to simulate potential mineral scaling potential upon production and utilization.

The boiled water at 100°C was then heated up to reservoir conditions and the mineral scaling potentials assessed upon re-injection of wastewater into the geothermal reservoir.

4. RESULTS

4.1 Sampled fluid composition

Samples of discharge fluids from well MW 01A were collected October 2014 and March 2015. The discharge chemical composition was plotted against time to determine when stable discharge fluid composition had been achieved. Based on this analysis, selected samples of discharge fluid composition were selected for further study. Average composition of these selected analyses is listed in Table 1 together with an example of one sample.

4.2 Reservoir fluid composition

The composition of the reservoir fluid composition for selected well discharges was calculated with the aid of the WATCH speciation program. The temperatures were calculated assuming equilibrium with quartz, i.e. the quartz geothermometry temperatures were used. The fluid discharges of well MW 01A display excess enthalpy, the cause being: two-phase liquid and vapour reservoir fluids and/or phase segregation upon depressurization boiling in the system (Arnórsson et al., 2007). Here two different approaches were selected to calculate the reservoir fluid composition: Model 1 assumes liquid only reservoir and model 2 assumes two phase reservoirs, liquid and vapour. For model 1, the reservoir enthalpy is calculated based on the reservoir temperatures and corresponding liquid enthalpy at that temperature whereas for model 2, the measured discharge enthalpy was selected. The results of the two models for a representative sample are listed in Table 1.

The two models to calculate reservoir fluid composition differ mostly in respect to volatile composition. When assuming liquid only reservoir, all the volatiles in the sampled vapour phase are dissolved into the liquid phase including CO_2 and H_2S, resulting in higher liquid concentrations of these elements and lower pH values. However, when assuming reservoir liquid and vapour, large fraction of volatiles like CO_2 and H_2S are present in the reservoir vapour phase, hence the reservoir liquid exhibit lower CO_2 and H_2S concentration and higher pH (more alkaline). With respect to non-volatile concentrations the difference is less between the two models.

5. DISCUSSION

Utilization of geothermal fluids for electricity production and for direct use poses several problems, among these being scaling. Scaling is the precipitation and growth of minerals from the fluids that can coat the surfaces of equipment during geothermal utilization, from the casing of the well, in the steam gathering systems, separation stations, other pipelines and upon reinjection. Scaling inside wells lead to decreased productivity with time. Scaling within surface infrastructure can also lead to flow-problems and corrosion. I n Figures 4, 5 and 6, the grey and black symbols represents model 1 (liquid phase

TABLE 1: Average chemical composition and physical properties of the well MW 01A stabilised

	Well discharge [a]	**Well discharge**	**Reservoir fluid model 1 [b]**	**Reservoir fluid model 2 [c]**
#	Average	2015-0238	2015-0238	2015-0238
Sampling p (bar-g)	13,6	13,1		
t °C		192	276	230
Enthalpy (kJ/kg)	2419	2429	1218	2429
Liquid phase (ppm)				
pH/T	9,43/23	9,20/22	7,51/276	8,44/230
CO_2	2513	2333	7668	2157
H_2S	184	156	181	175
B	0,27	0,29	0,23	0,25
SiO_2	757	762	607	670
Na	2286	2443	1945	2146
K	198	173	138	152
Ca	0,049	0,030	0,02	0,03
F	352	342	272	300
Cl	963	899	716	790
SO_4	127	75	59,7	65,9
NH_3	21,1	13,7	13,3	0,44
Vapor phase (mmol/kg condensate)				
CO_2	768	648		668
H_2S	11,4	8,2		8,2
H_2	59,4	62,9		65,0
CH_4	4,08	4,30		4,43
N_2	2,30	0		0
O_2	0,54	0		0

[a] Average compostion of well discharge fluids
[b] Liquid only reservoir, i.e. enthalpy of the reservoir fluid is calculated
[c] Liquid and vapour reservoir, i.e. the measured discharge enthalpy is taken to represent reservoir enthalpy

reservoir) and model 2 (two-phase reservoir) respectively. The potential of scaling during production of well MW 01A was examined in this report.

5.1. Mineral saturation within the reservoir

The mineral saturation state of potential minerals forming scaling including calcite, amorphous silica and anhydrite were assessed for the two models applied for calculation of reservoir fluid composition.

5.1.1 Calcite saturation state

The saturation state of the reservoir fluids with respect to calcite is shown in Figure 4. The results of both models are shown. Somewhat higher temperatures were calculated assuming liquid only reservoirs compared to two phase reservoirs or in the range 252-301°C and 198-250°C, respectively. The cause of this has to do with the

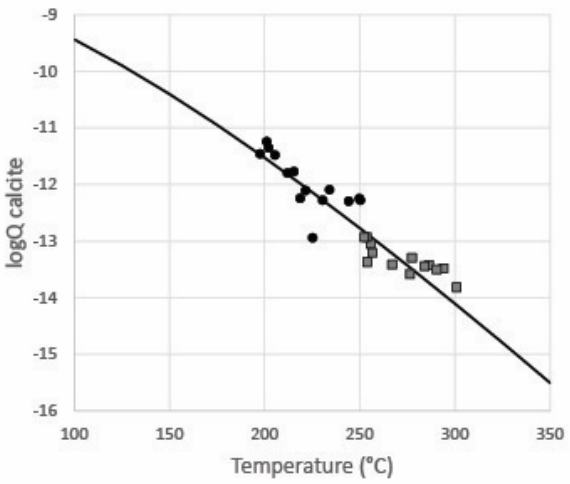

FIGURE 4: Calcite saturation state at reservoir conditions

fraction of vapour in the reservoir to the surface. Independent of the model selected for calculation of reservoir fluids shows calcite saturation.

5.1.2 Amorphous silica state

The saturation state of the reservoir fluids with respect to amorphous silica is shown in Figure 5. In all cases, the fluids are observed to be under-saturated. However, it should be pointed out that the temperatures were calculated assuming equilibrium with respect to quartz, and hence amorphous silica will be calculated to be under-saturated as amorphous silica is more soluble than quartz at all temperatures.

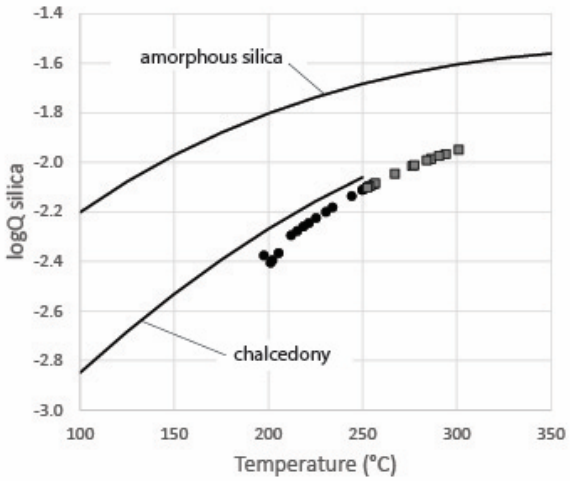

FIGURE 5: Amorphous silica saturation state at reservoir

5.1.3 Anhydrite

The saturation state of the reservoir fluids with respect to anhydrite are shown in Figure 6. In all cases and for both models 1 and 2, the fluids were observed to be under-saturated with respect to anhydrite. This is in accordance with low Ca and SO_4 concentrations in the reservoir fluids and well discharges of well MW 01A.

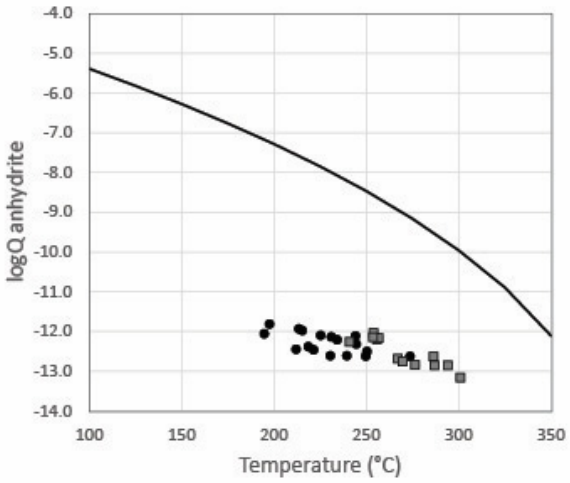

FIGURE 6: Anhydrite saturation state at the reservoir conditions

5.2 Scaling potentials upon cooling and boiling of reservoir fluids

The mineral saturation state of potential minerals forming scaling including calcite, amorphous silica and anhydrite were assessed for the two models applied for calculation of reservoir fluid composition upon conductive cooling and adiabatic boiling from the reservoir conditions to 100°C and 1 bar. In this way, potential mineral scaling within the well and in surface pipelines and infrastructure in a closed system was assessed.

5.2.1 Calcite

The saturation of the fluids with respect to calcite upon cooling and boiling of the reservoir fluids is shown in Figure 7 A and 7 B. One sample was used to represent the reservoir fluid composition, #2015-0238. The results demonstrate that both upon adiabatic boiling and conductive cooling of the fluids form the reservoir temperature to 100°C and 1 bar, calcite is under-saturated, suggesting that calcite scaling will not occur. The only exception of this is initial boiling of reservoir fluids when assuming liquid only reservoir. In this case, slight calcite supersaturation is observed upon the first boiling, possibly resulting in calcite formation.

The saturation state of calcite (logQ) is observed to increase both in the case of boiling and cooling. This is despite the fact that dissolved CO_2 is lost upon boiling into the vapour phase. The reason for this has to do with speciation of Ca and CO_2 in the water phase upon temperature decrease and boiling. Firstly, possible ion association to form various Ca^{2+} and CO_3^{2-}. Ion pairs decrease with decreasing temperature, leading to increased activity of Ca^{2+} and CO_3^{2-}. Secondly, boiling and loss of volatiles including CO_2 and H_2S results in increased pH value (more alkaline) of the boiled liquid water, leading

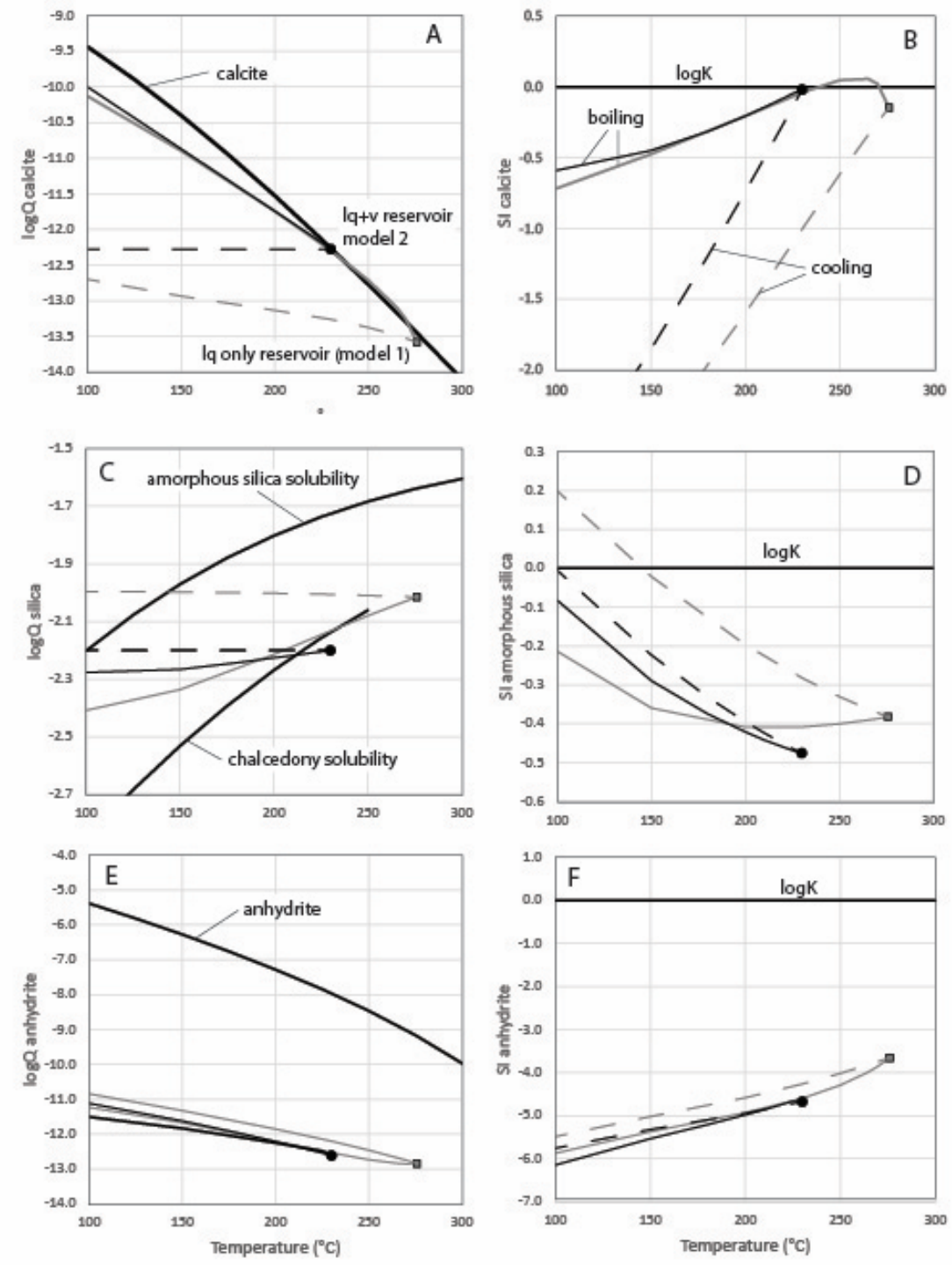

FIGURE 7: Mineral saturation upon boiling of reservoir fluids to 100°C and 1 bar

to ionization of CO_2 (aq) to HCO_3^- to CO_3^{2-}. As a result, despite decreased total dissolved carbon concentration, the activity of CO_3^{2-} may increase, at least initially, upon boiling.

5.2.2 Amorphous silica

The saturation of the fluids with respect to amorphous silica upon cooling and boiling of the reservoir fluids is shown in Figure 7 C and 7 D. Upon boiling, the amorphous silica saturation (loqQ) was found to decrease. This is due to pH decrease of the boiled liquid water discussed previously, resulting in ionization of H_4SiO_4 (aq) to $H_3SiO_4^-$ and hence decrease in the activity of H_4SiO_4. Cooling, on the other

hand results in less changes of the liquid water pH value, eventually resulting in amorphous silica super-saturation independent of the model applied to calculate the reservoir fluid composition. However, it should be pointed out that the sampling pressures were 13.1 bar corresponding to 192°C.

For the temperature interval from the reservoir to the well discharge, silica scaling is not expected according to the results presented in Figure 7C and 7D.

5.2.3 Anhydrite

The saturation of the fluids with respect to amorphous silica upon cooling and boiling of the reservoir fluids is shown in Figure 7E and 7F. In all cases, the fluids are observed to be under-saturated at all conditions for both models 1 and 2 and for boiling and cooling. This indicate that cooling and boiling of reservoir fluids to 100°C and 1 bar will not result in anhydrite scaling.

5.3 Scaling potentials upon cooling and boiling of liquid well discharges

The mineral saturation state of potential minerals forming scaling including calcite, amorphous silica and anhydrite were assessed after separation of the vapour and liquid phase at the well-head conditions to 100°C and 1 bar. In this way, potential mineral scaling within surface pipelines and infrastructure in a closed system after vapour separation is assessed.

5.3.1 Calcite

The saturation of the fluids with respect to calcite upon cooling and boiling of the liquid only phase from well head conditions at 192°C to 100°C and bar is shown in Figure 8A. As observed, upon conductive cooling and boiling of the well head liquid the value of logQ increases, yet the fluids are always observed to be under-saturated with respect to calcite, hence limited if any calcite scaling is expected.

5.3.2 Amorphous silica state

The saturation of the fluids with respect to amorphous silica upon cooling and boiling of the liquid only phase from well head conditions at 192°C to 100°C and bar is shown in Figure 8B. As observed, upon boiling the fluids become progressively more under-saturated. The reason for this is the alkaline pH values formed with increasing boiling resulting in quantitative ionization of H_4SiO_4 (aq) to $H_3SiO_4^-$. In contrast, cooling has limited effects on the fluid pH value,

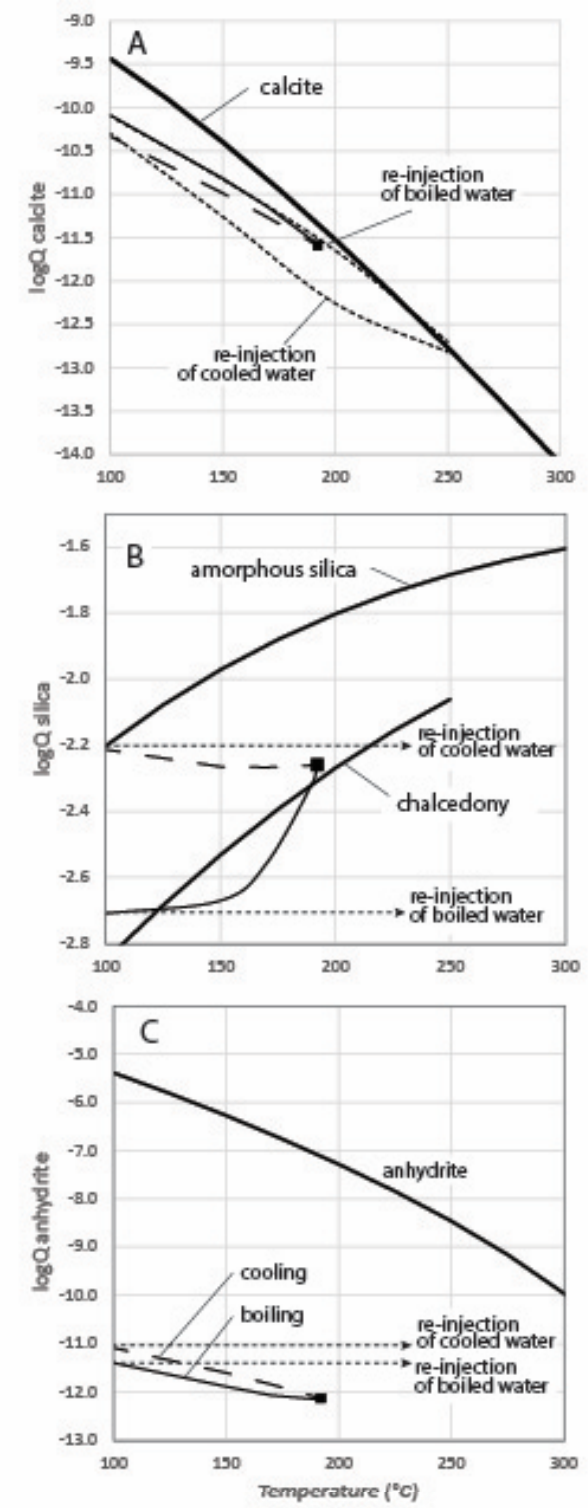

FIGURE 8: Mineral saturation upon boiling and cooling of liquid at well discharges

hence, the fluids become close to saturation with respect to amorphous silica at 100°C, possibly resulting in scaling formation. Cooling to temperatures <100°C would most likely result in formation of amorphous silica.

5.3.3 Anhydrite

The saturation of the fluids with respect to anhydrite upon cooling and boiling of the liquid only phase from well head conditions (192°C) to 100°C and 1 bar is shown in Figure 8 C. In all cases, considerable under-saturation is observed with respect to anhydrite indicating no potential risk of anhydrite scaling upon cooling and boiling of well head liquid phase.

5.4 Scaling potentials upon reinjection of waste water

The scaling potential upon reinjection of waste water, i.e. liquid phase that has been cooled or boiled to 100°C and re-injected into the reservoir. Such calculations affectively involve heating up the 100°C liquid phase to the reservoir temperatures of ~250°C. Such type of scaling may be significant due to decreased solubility of minerals like calcite and anhydrite with increasing temperature, and changes in aqueous speciation with temperature.

5.4.1 Calcite

The saturation of the fluids with respect to calcite upon re-injection and subsequent heating of waste water from 100°C to the reservoir temperature of ~250°C is shown in Figure 8 A. The fluids display under-saturation at all temperatures to 250°C, whereas they become close to the saturation state of the reservoir fluids. This suggest that calcite scaling upon reinjection will most likely not be a major problem, except possibly at >200°C.

It should be pointed out, however, that the calculations are very sensitive to the aqueous speciation and possible ion pair formation of Ca^{2+} and CO_3^{2-}, something that is not well constrained at high temperatures (Stefánsson et al., 2014).

5.4.2 Amorphous silica

The saturation of the fluids with respect to amorphous silica upon re-injection and subsequent heating of waste water from 100°C to the reservoir temperature of ~250°C is shown in Figure 8 B. The fluids display under-saturation with respect to amorphous silica at all temperatures to 250°C. However, they become saturated with both chalcedony and quartz with increasing temperature, possible resulting in silica scaling down-hole.

5.4.3 Anhydrite

The saturation of the fluids with respect to anhydrite upon re-injection and subsequent heating of waste water from 100°C to the reservoir temperature of ~250°C is shown in Figure 8 C. In all cases, considerable under-saturation is observed with respect to anhydrite indicating no potential risk of anhydrite scaling upon re-injection.

6. CONCLUSIONS

Well MW 01A poses a great risk to calcite scaling upon initial boiling for both single and two phase reservoir and this could lead to decrease in productivity of the well. Amorphous silica saturation is expected to occur for fluids cooled to temperatures below 150°C and especially at <100°C. Direct use applications that require temperatures below 100°C may become a problem in utilising this water. Care should be taken to ensure heat energy is extracted from separated water at temperatures that do not

favour oversaturation and deposition of amorphous silica at the equipment. Anhydrite is not found to be a problem from the reservoir through to reinjection. All the minerals under study will not be a problem upon fluid re-injection

ACKNOWLEDGEMENTS

I wish to acknowledge the United Nations University, the Icelandic government and UNU Geothermal Training Programme Director Dr. Lúdvík S. Georgsson for giving me the opportunity to attend 2015 UNU geothermal training program. The author is much indebted to other UNU-GTP staff: Ms. Thórhildur Ísberg, Mr. Ingimar G. Haraldsson, Mr. Markús A.G. Wilde, Ms. Málfrídur Ómarsdóttir.

Special thanks to Prof. Andri Stefansson for his guidance, encouragement and advice in writing this report. Many thanks to the staff of Orkustofnun, University of Iceland, University of Reykjavik, Reykjavik energy who taught us and those who participated in one way or another towards the success of this course. I am grateful to my colleagues in the 2015 UNU GTP program. I thank my employer, Geothermal Development Company (GDC) for granting me the opportunity for this training.

Special thanks also go to my dear wife June, and my children Lindy and Gabriel for the moral support and prayers during my stay in Iceland

REFERENCES

Ármannsson, H., 1989: Predicting calcite deposition in Krafla boreholes. *Geothermics, 18*, 25-32.

Arnórsson, S., 1975: Application of the silica geothermometer in low hydrothermal areas in Iceland. *Am J. Sci, 275*, 763-784.

Arnórsson, S., 1983: Chemical equilibria in Icelandic geothermal systems. Implications for chemical geothermometry investigations. *Geothermics, 12,* 119-128.

Arnórsson, S., Bjarnason, J.Ö., Giroud, N., Gunnarson, I., and Stefánsson, A., 2006: Sampling and analysis of geothermal fluids. *Geofluids 6,* 203-216.

Arnórsson, S., and Stefánsson, A., 1999: Assessment of feldspar solubility constants in water in the range 0 degrees to 350 degrees C at vapor saturation pressures. *Am J. Sci, 299*, 173-209.

Arnórsson, S., Sigurdsson, S. and Svavarsson, H., 1982: The chemistry of geothermal waters in Iceland I. Calculation of aqueous speciation from 0°C to 370°C. *Geochim. Cosmochim. Acta, 46*, 1513-1532.

Arnórsson, S., Stefánsson, A., and Bjarnason, J.Ö., 2007: Fluid-fluid interaction in geothermal systems. *Rev. Min. Geochem. 65,* 259-312.

Bjarnason, J.Ö., 2010: *The speciation program WATCH, version 2.4*. ÍSOR, Reykjavík, Iceland, 7 pp.

Espartinez, C.M.R., and See, F.S., 2015: The BacMan geothermal field, Philippines: Geochemical changes and challenges after twenty years of operation. *Proceedings of the World Geothermal Congress 2015, Melbourne, Australia*, 8 pp.

GDC, 2010: *Menengai geothermal prospect; an investigation for its geothermal potential*. Geothermal Development Company (GDC), unpublished report.

GDC., 2013: *Menengai geothermal project; Data integration report*. Geothermal Development Company (GDC), unpublished report.

Gunnarsson, I., and Arnórsson, S., 2000: Amorphous silica solubility and the thermodynamic properties of $H_4SIO^{\circ}_4$ in the range of 0° to 350 °C at Psat. *Geochim. Cosmochim. Acta, 64*, 2295-2307.

Kanda, I., and Suwai, J., 2013: Hydrogeochemistry of shallow and deep water aquifers of Menengai geothermal area, Kenya Rift Valley. *GRC Transactions, 37*, 403-410.

Kipng'ok, J.K., 2011: Fluid chemistry, feed zones and boiling in the first geothermal exploration well at Menengai, Kenya. Report 15 in: *Geothermal training in Iceland 2011*. UNU-GTP, Iceland, 281-302.

Lagat J., 2011: *Geothermal surface exploration approach: Case study of Menengai geothermal field, Kenya*. Proceedings of the Kenya Geothermal Conference 2011, Nairobi, Kenya, 10 pp.

Leat, P.T., 1983: *The structural and geochemical evolution of Menengai caldera volcano, Kenya Rift Valley*. PhD thesis, University of Lancaster, Lancaster, United Kingdom, 482 pp.

Macdonald, R., and Baginski, B., 2009: The central Kenya peralkaline province: a unique assemblage of magmatic systems. *Mineralogical Magazine, 73*, 1-16.

Macdonald, R., and Scaillet, B., 2006: The central Kenya peralkaline province: insights into the evolution of peralkaline salic magmas. *Lithos, 91*, 59-73.

Macdonald, R., Baginski, B., Leat, P.T., White, J.C., and Dzierzanowski, 2011: Mineral stability in peralkaline silicic rocks: Information from trachytes of the Menengai volcano, Kenya. *Lithos, 125*, 553-568.

Malimo, S.J., 2013: Fluid chemistry of Menengai geothermal wells, Kenya. *GRC Transactions, 37*, 425-430.

Mbia, P.K., 2014: *Sub-surface geology, petrology and hydrothermal alteration of menengai geothermal field, Kenya*. University of Iceland, MSc thesis, UNU-GTP, Iceland, report 1, 87 pp.

Mbia, P.K., Mortensen, A.K., Óskarsson, N., and Hardarson, B.S., 2015: Sub-surface geology, petrology and hydrothermal alteration of the Menengai geothermal field, Kenya: Case study of wells MW-02, MW-04, MW-06 and MW-07. *Proceedings of the World Geothermal Congress 2015, Melbourne, Australia*, 20 pp.

Mibei, G., and Lagat, J., 2011: Structural controls in Menengai geothermal field. *Proceedings of the Kenya Geothermal Conference 2011, Kenya*, 5 pp.

Muchemi, G., 2010: Current status of the geothermal development in Kenya. *Proceeding of ARGEO C-3 third East African Rift Geothermal Conference, Djibouti, 2010* 8pp.

Mungania, J., 2004: *Geological studies of Menengai geothermal prospects*. Kenya Electricity Generating Company Ltd. (KenGen), internal report, 18 pp.

Mungania, J., Lagat, J., Mariita, N.O., Wambugu, J.M., Ofwona, C.O., Kubo, B.M., Kilele, D.K., Mudachi, V.S., Wanjie, C.K., 2004: *Menengai prospect: Investigations for its geothermal potential*. The Government of Kenya and Kenya Electricity Generating Company Ltd., internal report, 91 pp.

Omenda, P., and Simiyu, S., 2015: Country update report for Kenya 2010-2014. *Proceedings of the World Geothermal Congress 2015, Melbourne, Australia*, 11 pp.

Onyango S. O., 2012: Preliminary design of the Menengai phase I steam gathering system. Report 26 in: *Geothermal training in Iceland 2012.* UNU-GTP, Iceland, 601-641.

Sekento L. R., 2012: Geochemical and isotopic study of the menengai geothermal field, Kenya. Report 31 in: *Geothermal training in Iceland 2012.* UNU-GTP, Iceland, 769-792.

Simiyu, S.M., 2010: Status of geothermal exploration in Kenya and future plans for its development. *Proceedings of the World Geothermal Congress 2010, Bali, Indonesia*, 11 pp.

Simmons, S.F., and Christenson, B.W., 1994: Origins of calcite in a boiling geothermal system. *American Journal of Science, 294*, 361-400.

Stefánsson, A., Bénézeth, P., and Schott, J., 2014: Potentiometric and spectrophotometric study of the stability of magnesium carbonate and bicarbonate ion pairs to 150°C and aqueous inorganic carbon speciation and magnesite solubility. *Geochim. Cosmochim. Acta, 138*, 21–31.

UNITED NATIONS UNIVERSITY
UNU-GTP
Geothermal Training Programme

Orkustofnun, Grensasvegur 9,
IS-108 Reykjavik, Iceland

Reports 2015
Number 26

BOREHOLE GEOLOGY AND HYDROTHERMAL ALTERATION MINERALOGY OF WELL MW-19A, MENENGAI GEOTHERMAL FIELD, KENYA

Fredrick M. Mutua
Geothermal Development Company – GDC
P.O Box 17700-20100
Nakuru
KENYA
fmutua@gdc.co.ke / fredmachokaa@gmail.com

ABSTRACT

Well MW-19A in Menengai is a directional well drilled to the north at an azimuth of 339.92° and inclination of 20.19° to a measured depth (MD) of 2355 m. The aim of drilling this well was to tap steam from NNW-SSE trending structures associated with the Molo Tectono-Volcanic Axis (TVA) and also to confirm the extent of the resource to the north inside the Menengai caldera. Comprehensive binocular and petrographic analyses of cuttings from the well indicate that the lithology of the well comprises five rock units i.e. pyroclastics, tuffs, trachytes and intrusions of syenitic and basaltic composition. Trachyte forms the main reservoir rock and it is the dominant rock below 504 m. These rock units host secondary hydrothermal mineral assemblages which are dependent on temperature, permeability, rock type and the chemistry of the circulating fluid. Hydrothermal alteration patterns show prograde alteration with increase in temperature and depth, as observed from alteration minerals in veins and vesicles. Five alteration zones were identified: unaltered zone (0-120 m), zeolite zone (120-502 m), chlorite-smectite zone (502-1100 m), quartz-illite-epidote zone (1100-1358 m) and quartz-illite-epidote-wollastonite-actinolite zone (1358-2355). Appearance of epidote at 1202-1760 m and actinolite at 1358-1882 m indicates that alteration temperatures have reached 230°C and 290°C respectively at these depths. Correlation of fluid inclusion analyses, alteration and formation temperature indicates two geothermal episodes; one of a high temperature geothermal system below 600 m depth and a recent second phase of cooling between 1140 and 1400 m. The well is also very permeable as observed from the intensity of alteration, oxidation, veining, in addition to circulation losses and the abundance of calcite and pyrite. Eight permeable locations were identified which were further grouped into four major aquifers deduced from temperature logs, and their locations correlate with the cutting data. The major feed zone below 1400 m is considered the dominant one in the well. Alteration mineral correlation of MW-19A with neighbouring wells of MW-22 and MW-11 suggests that the well is nearer to an up flow zone than the latter wells while the stratigraphic correlation between the wells reveals the existence of normal faults between MW-19A / MW-22 and MW-22 / MW-11.

1. INTRODUCTION

1.1 General information

Menengai is a high-temperature geothermal field situated north of Lake Nakuru and south of Lake Bogoria on the floor of the central Kenyan Rift (Figure 1). It encompasses the Menengai volcano, the Ol'Rongai volcanoes, Ol'Banita plains and parts of the Solai graben to the northeast. It is located at the triple junction between the main Kenya rift and the less prominent Nyanza rift. Deep geothermal wells have been drilled in the Menengai caldera and proved the existence of a geothermal resource. Currently, 28 deep wells of depths varying from 2,100 to 3,200 m have been drilled. Well MW-19A is the fourth directional well to be drilled in the Menengai geothermal field. The well is located at the dome area on the floor of the caldera and shares the same well pad with production well MW-19. It is defined by the UTM coordinates E 172629.35, N 9977723.82 at an elevation of 2072 m a.s.l. The well was aimed at tapping from the NNW-SSE trending structures associated with the Molo TVA. The specific objectives for drilling the well were to increase steam production for the planned 105 MWe Menengai power plant and establish the resource extent to the NW as well as providing additional information on sub-surface geology, hydrothermal alteration, and the chemical characteristics of the reservoir. The well was drilled to a depth of 2354 m from 16th October, 2014, to 6th January, 2015, i.e. for 87 days.

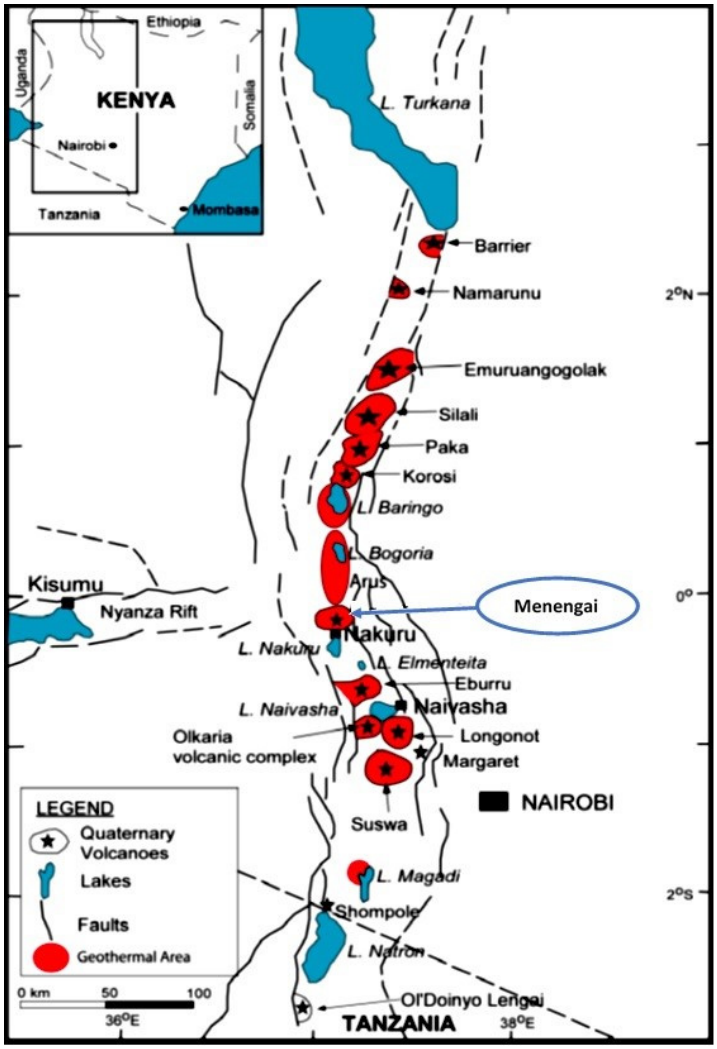

FIGURE 1: Location of the Menengai field within the Kenyan Rift Valley (modified from GDC, 2010)

1.2 Purpose of the project

The aim of this project is to study the borehole geology of MW-19A by analysing drill cutting samples taken in the well at 2 m intervals in order to identify the sub-surface lithology, determine the alteration and hydrothermal mineralogy, locate aquifers/feed zones, and try to conceptualize the geothermal system(s) and temperatures in the Menengai field.

1.3 Previous work

Menengai geothermal field has previously been studied by various geoscientists for various purposes/objectives including academically based research, regional geological mapping for government institutions and regional mapping with interests in natural resources, including geothermal. McCall was the first geologist to describe the Menengai volcano and the surrounding area. In his reports

(McCall, 1957a, 1957b, 1964, 1967) he provides a comprehensive account of many aspects of the geology of the area. Jones and Lippard (1979), Jones (1985), Griffith (1980), and Griffith and Gibson (1980) published reports on the geology of Menengai and the surrounding areas. Leat (1983, 1984) studied the structural and geochemical evolution of Menengai Caldera. In his reports, he described the volcano as being solely composed of peralkaline and silica oversaturated rocks.

Geotermica Italiana (1987) was the first group to carry out research focused solely on the assessment of the geothermal potential of Menengai. The project was coordinated and financed by UNDP and the Government of Kenya. It resulted in a detailed geological description of the area.

Another detailed geoscientific survey was conducted by KenGen and the Kenyan Ministry of Energy in 2004. The study involved geological, geophysical and geochemical surveys. The results from this survey indicated the existence of a hot, ductile, and dense body centred beneath the Menengai caldera. The study estimated that the high-temperature part of the resource covers an area of about 48 km^2 (KenGen, 2004).

In 2010, GDC conducted a comprehensive study in the Menengai prospect to confirm all geological observations recorded in previous work that might be associated with development and occurrences of a geothermal resource. Findings from this study point to the existence of exploitable geothermal resources within the Menengai caldera, Ol-Rongai and Ol-Banita calderas to the northwest of the Menengai caldera (Figure 2). This is evidenced by active strong surface manifestations and young lavas, signifying an active heat source. From this study, MT resistivity distribution at 2000 m b.s.l. shows a conductive body of less than 5 ohm-m under the caldera floor with a westward extension. Seismology indicates seismic wave attenuation at <6 km depth underneath Menengai caldera and Ol'rongai, suggesting the occurrence of shallow magma bodies which would be the heat sources for the geothermal system. (Simiyu and Keller, 1997).

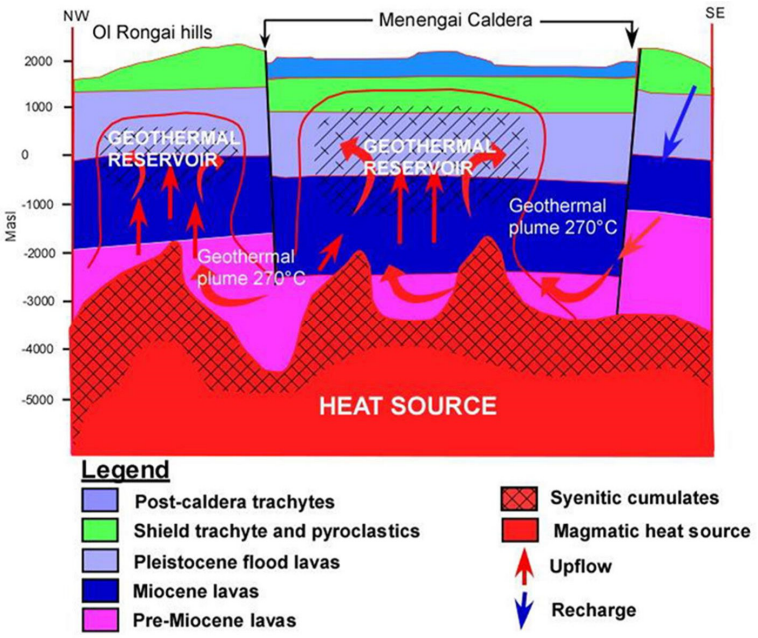

FIGURE 2: Menengai geothermal model (GDC, 2010)

Previous studies have led to the development of a geothermal conceptual model (currently being developed) with a hot magmatic body beneath the caldera floor with an up-flow under the caldera and an outflow to the north (Figure 2). In addition, gas geothermometry, based on H2S and CO2, indicates that the reservoir temperatures are greater than 250°C. Following these encouraging results, three exploratory wells were sited and a decision to commence drilling was reached.

Exploration drilling commenced in February 2011 and currently production drilling is underway and a total of 28 deep wells of depths varying from 2,100 m to 3,200 m have been drilled. Reservoir temperatures of up to 400°C at 2,000 m have been encountered in several wells making it the hottest geothermal system in Kenya. Steam production from the wells varies from small to greater than 10 MWe.

Borehole geological studies on completed wells (Omondi, 2011, Mibei, 2012; Kipchumba, 2013; Lopeyok, 2013; Mbia, 2014; Kahiga, 2014) have also been done to further re-evaluate the geothermal system. Further structural mapping has recently been carried out (Strecker et.al, 2013), with the aim of studying the young structural evolution of the greater Menengai area north of Nakuru in light of the ongoing geothermal exploration and structural assessment of this sector of the central Kenya Rift.

Currently 132.5 MW of steam equivalent is on the wellheads and full steam production for the planned 105 MWe power plants is expected before the end of 2015 (GDC, 2015). Three Independent Power Producers (IPPs) have been licensed for 20 years to operate 35 MWe modular plants each. In addition, GDC has recently successfully piloted four projects on the direct utilization of steam in a move aimed at diversifying geothermal use apart from power generation in Menengai. These are: geothermal powered dairy unit, geothermal powered laundry, geothermal heated aquaculture ponds and geothermal heated green houses.

2. GEOLOGY AND STUCTURAL SETTING

2.1 Regional geology

The East African Rift is an active continental rift zone in eastern Africa that appears to be a developing divergent tectonic plate boundary where rift tectonism is accompanied by intense volcanism. The rift is a narrow zone in which the African plate is in the process of splitting into two new tectonic plates (McCall, 1967). It runs from the Afar Triple Junction in the Afar depression southward through eastern Africa. The East African Rift System consists of two main branches; the Eastern Rift Valley and the Western Rift Valley. These resulted from the actions of numerous normal (dip-slip) faults which are typical of all tectonic rift zones (Strecker et al., 1990).

The Kenya Rift Valley comprises 14 geothermal prospects (Figure 1) starting from Barrier in the north to Lake Magadi in the south (Omenda, 2000). It forms a classic graben with an average width of 40-80 km, dotted by several Tertiary volcanoes. The rift floor is comprised mainly of the eruptive materials from these volcanoes (McCall, 1957). Most of the volcanic centres have gone through one or more explosive phases including a caldera collapse. Some centres are dotted with hydrothermal activity and are envisaged to host extensive geothermal systems which are driven by hot magma at shallow depths in the crust (Dunkley et al., 1993, Suwai, 2011).

The Menengai geothermal prospect is located within an area characterized by complex tectonic activity associated with a rift triple junction. This is a zone at which the failed rift arm of the Nyanza rift joins the main Kenyan rift. The Kenyan rift is characterized by extensional tectonism where the E-W tensional forces resulted in block faulting, which includes tilted blocks as evident in both the floor and scarps of the rift (KenGen, 2004). Narrow scarps that show little effect of movement have been eroded resulting in gentle scarps characterize the western margin. The eastern margins, however, depict wider belts with sharp scarps, implying recent active movements. The rift trough is cut by numerous normal faults that clearly represent continued extensive tectonism under the rift floor (Gichira, 2012; KenGen, 2004).

2.2 Geology of Menengai volcano

The Menengai geothermal field region comprises Menengai volcano, the Ol'rongai volcanoes, the Olbanita plains, and parts of the Solai TVA to the northeast (GDC, 2010) covering an area of approximately 950 km² (Figures 3 and 4). Menengai is one of the Quaternary volcanoes formed on the axis of the Kenyan Rift (Figure 1). It is a trachytic central volcano that is underlain by a shallow magma chamber. The activity in the volcano started 0.2 Ma ago with the formation of a broad low angle trachytic

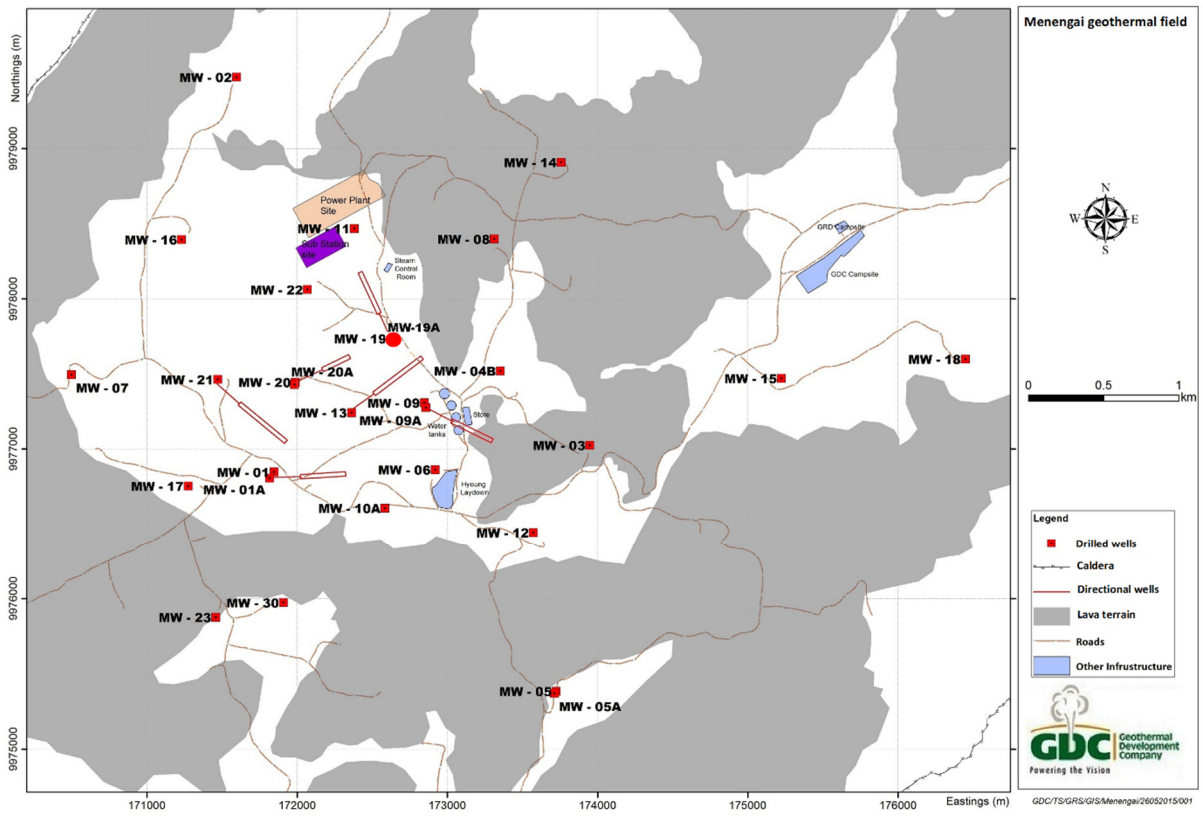

FIGURE 3: Location of well MW-19A, highlighted in a red circle (GDC, 2015)

lava shield (Leat, 1984). The activity continued in the Pleistocene, with the formation of a caldera, to more recent activity that has given rise to the flows on the caldera floor (Macdonald et al., 1970).

The surface geology is dominated by recent (post caldera) lavas, especially within the caldera, pyroclastics and ignimbrite sheets on the northern flanks and alluvial sediments on the surrounding rift floor (Figures 3 and 4). The geology and evolution of the Menengai caldera is intricately tied to the volcanology of the Kenyan Central Rift Valley and can be divided into three main phases: pre-caldera volcanics, syn-caldera activity, and post-caldera activity.

The first phase, the pre-caldera phase, is associated with the

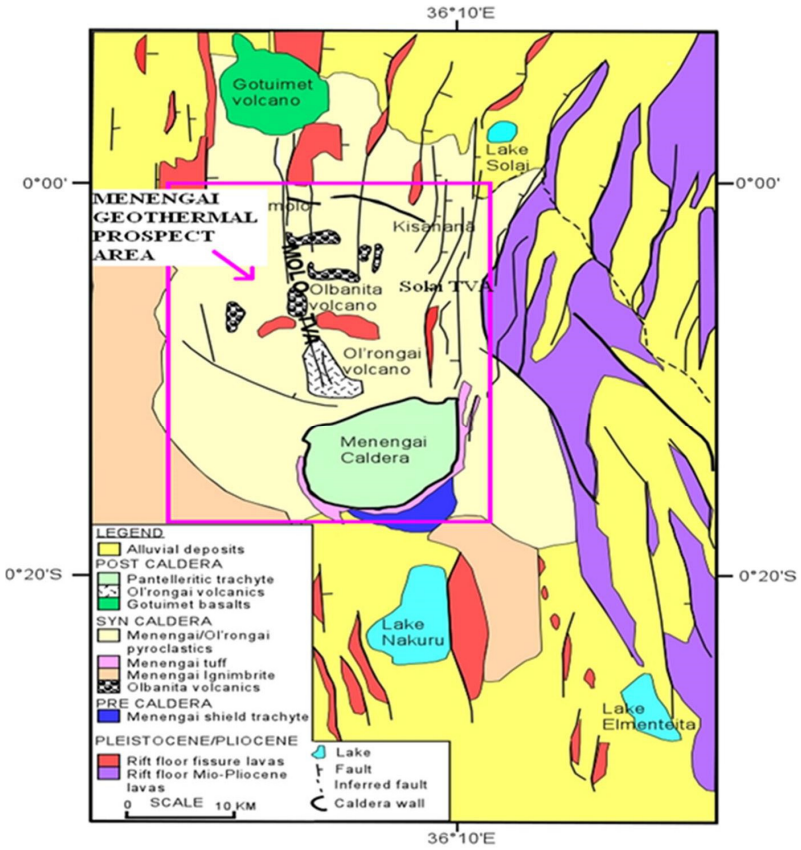

FIGURE 4: Simplified geological map and extent of the Menengai field (GDC, 2010)

formation of the shield and the eruption of lavas that preceded the collapse of the caldera. Pre-caldera volcanics now form low hills which slope away from the rim of the caldera. The rocks formed during this period are not visible on the caldera floor owing to mantling by thick syn-and post-caldera volcanics. There are, however, good exposures of these rocks at the caldera wall, especially at the Lions Head cliff (view point). The only other outcrop away from the caldera wall is the ballast quarry off the Nakuru-Bahati road. The height of the caldera wall, and thus the exposed thickness of the volcanics, varies dramatically around the caldera. The total throw of the caldera wall at the Lion´s Head Cliff is about 300 m, where almost the entire 235 m pre-caldera succession is composed of simple trachyte lavas, most of which are dark grey and slightly fissile. The mean thickness of the flows is 23 m, varying between 11 m and 60 m. Tops of lavas are blocky, transitional to a crude, vesicular pahoehoe; no well-developed ropy tops are seen. Air- fall pumice deposits make up only about 1% of the thickness of the Lions Head section, and there are no pre-caldera ash flows. Almost constant thickness of reddened soil horizons separating many lavas suggests that eruptions took place at regular intervals. These lavas are all trachytic with the groundmass being composed of mainly sanidine crystallites. Some riebeckite/ arfvedsonite are also present. Large (up to a meter) to small lithic inclusion of syenitic rocks are common. The pre-caldera lavas have been dated at 0.18±0.01 My (Leat, 1983) and, therefore, the shield volcano is estimated to be around this age.

The second phase, the syn-caldera activity, is associated with the caldera collapse. The incremental caldera collapse is believed to have occurred in two episodes (Leat, 1984; Macdonald and Scaillet, 2006). The formation of the 11.5×7.5 km large caldera was accompanied by the eruption of two ash flow tuffs. Each of the tuff layers is underlain by a pumice deposit and separated by a thin layer of sediments, indicating a short quiescence period between the eruptions (Leat, 1984). The collapse is mainly associated with the second ash flow eruption. The syn-caldera rocks are spread around the Menengai caldera and comprise ignimbrite and pumice/ash deposits. They are exposed both at the upper parts of the caldera rim (east and northern rim), where the rim resembles an agglomerate deposit, which is rich in poorly sorted angular lithic and glassy/semi-pumiceous material. The syn-caldera rocks show flow texture (rheomorphic) indicative of a pyroclastics flow mode of emplacement. This is the proximal phase indicating that the source was at the caldera and its rim. Other exposures away from the caldera rim include extensive mantling of the ground in the north and west (Kampi Ya Moto, El Bonwala and Ol‘rongai areas) where there is a slight transition due to distance of transportation before deposition occurred. Here the ignimbrite resembles welded tuff with numerous collapsed pumice fiamme depicting eutaxitic texture´. This is a distal facies of deposition. Further away to the north and east, this formation is thin (few centimetres to meters) and occurs as ash tuff, representing the distal facies. The age of the syn-caldera pyroclastics has been published by many researchers, e.g. Leat (1983) published an age of 29,000±300 years for the older eruptives and 12,850 years for the younger ones. Geotermica italiana Srl (1987) published an age of 14,900±900 years based on carbon dating of palaeosoils between the syn-caldera eruptives.

The third phase, the post-caldera activity, mainly involved eruptions of recent lavas and ash deposits from vents within the caldera. This eruption episode probably occurred contemporaneously both inside the caldera floor and at Ol‘rongai. Several distinct lava flows can be identified on the caldera floor, with most of the eruption centres emitting the flows located in the central and western parts. These lavas have built a huge pile inside the caldera rising to 2160 m a.s.l. and estimated to be about 300 m thick. The lowest part of the caldera floor, which is also in-filled with the same lavas, stands about 1700 m a.s.l.

During the post-caldera era, lava and ash eruptions continued with most of the activity being concentrated within the caldera summit. Several vents and eruption centres like “Mlima punda” can be identified within the summit area. Mlima punda is one of the cinder cones formed by an explosive eruption emitting scoria due to the high amounts of volatiles in the magma. Generally, all rock formations and cinder cone structures seen on the caldera floor are of the post-caldera stage. The lavas are dark in colour, holocrystalline, glassy and vesicular (Mibei 2012).

The ropy flow texture, which is still intact, indicates a young age and the low viscosity of the lavas. Samples from the thicker part (non-vesicular) show that they are trachytes with the groundmass exhibiting a strong trachytic flow texture. The groundmass is mainly made up of sanidine feldspar laths and occasional riebeckite crystallites. An age of 1,400 yrs for the post-caldera lava is published by Jones and Lippard (1979). The apparent lack of disturbance in the thin flow tubes in the ropy texture indicates that some of these lava flows are younger than the specified age (Leat, 1984).

Other post- caldera lithological units are the lake sediments in the northeast near the gate barrier. This formation is evidence of a palaeo intra-caldera lake presumed to be from 8,000-10,000 yrs. BP as proposed by Leat (1984) and could have formed minor components of the recharge to the Menengai geothermal system. The lake was formed as a result of subterranean outflow of Lake Nakuru through structures and faults associated with the Solai system. The diatomaceous deposits associated with this Palaeo-lake are overlain by post-caldera volcanics.

2.3 Structural geology

Menengai Geothermal field is located within an area characterized by complex tectonic activity associated with the rift triple junction. This is a zone at which the Nyanza half-graben (failed rift) joins the main Kenyan rift (KenGen 2004, Burke and Dewey, 1973). The floor of the Menengai caldera depicts extensional tectonics with the main trough trending N-S north of Menengai and NNW-SSE south of Menengai. Menengai is therefore set at a point where the Kenyan Rift abruptly takes a sharp change in direction. This change is associated with the contact between the Tanzanian craton and orogenic belts (Simiyu and Keller, 1997). The floor of the Menengai area depicts extensional tectonics with spatial variation in the stress regime, indicated by different styles in the orientation of faults north of the caldera. The structures associated with Ol'rongai system are oriented to the NW-SE and are related to the NW-SE Menengai pre-caldera shield orientation (Figure 5) (Leat, 1984). On the other hand, faults associated with the Solai system have a NE-SW orientation, also assumed by the Menengai caldera. Therefore, the faults appear to have influenced the caldera's formation. Most structures in the Solai system can be extrapolated and cut into the caldera rim, indicating that some of these faults are in fact younger than the caldera. The variation in the orientation styles of the old NW-SE structures and the younger NE-SW structures could be due to a change or a shift in the crustal stresses. Generally, the main structures in the Menengai field (Figure 6) can be divided into three main groups, namely:

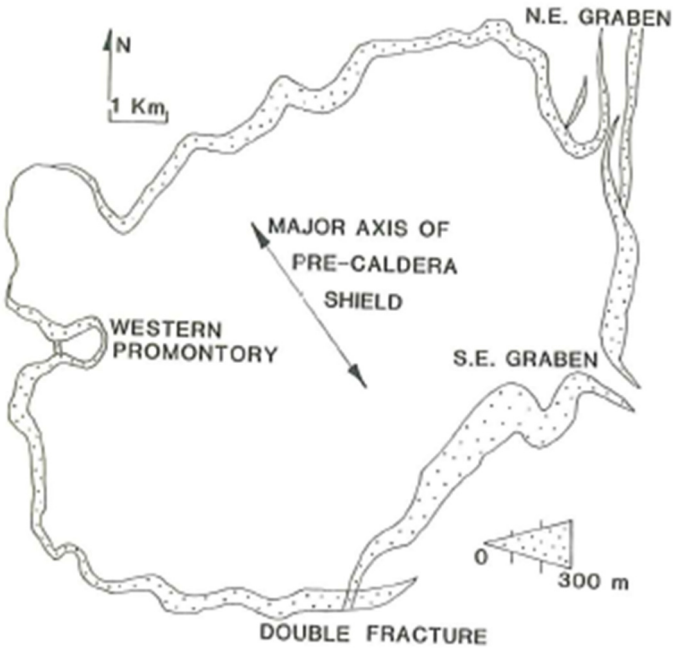

FIGURE 5: Topography of Menengai caldera (Leat, 1984)

a. The Menengai caldera and ring faults;
b. Ol'rongai and the Molo Tectono-volcanic axis TVA;
c. The Solai structural system.

2.3.1 The Menengai caldera and ring faults

The Menengai caldera is an elliptical depression with minor and major axes measuring about 11.5 km and 7.5 km, respectively (GDC, 2010). The circular rim of the caldera ring fault is well preserved with vertical cliffs at some places measuring up to about 400 m. The ring structure has been disturbed only by the Solai graben faults on the northeast end and another fracture at the south-southwest end of the caldera wall extending southwards (Figure 6).

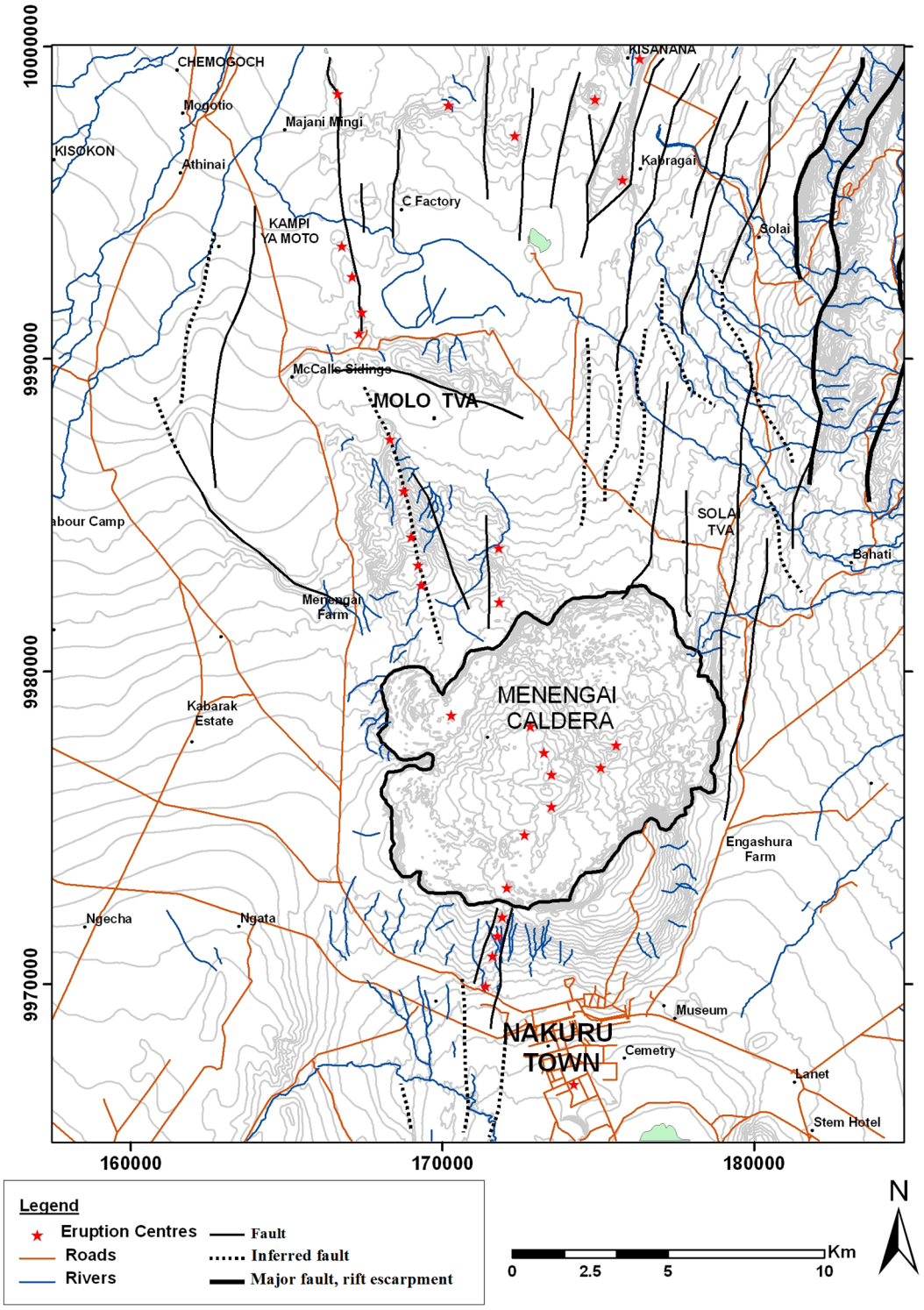

FIGURE 6: The main geological structures in the Menengai geothermal field (GDC, 2010)

Other disturbances at the southeast and northwest ends may be grabens that existed before the caldera collapse. Two large fragments of caldera wall have remained in a partially collapsed condition since the caldera formation (McCall 1957a, 1967, Leat, 1984). The most striking feature is the Western promontory which location can be seen in Figure 5. This block dropped only 60 m and was tilted 8º to the S during the collapse. Some minor (1 m) post caldera movements have taken place on the fault which separates the Promontory from the main part of the caldera wall. This movement disturbed early post caldera tephra beds and dropped the Promontory further into the caldera. The other partial collapse feature, the Double Fracture (Figure 5) consists of a tilted block.

Leat (1984), described the presence of the fault-bounded sector graben and the partially collapsed features suggest that the portions of the adjacent caldera wall also represents surface expressions of faults, and the embayment's in the caldera wall are not the back-walls of landslips but are the surface expressions of an embayed ring fracture. Also, some post caldera vents occur close to the caldera wall, perhaps marking the position of a major fault. The presence of embayment's in the ring fracture and the partial collapse features suggest that the cauldron block foundered as dislocated pieces, not as a simple piston. The random arrangement of some post-caldera vents is further evidence that the cauldron block is fractured. The caldera floor is covered with post-caldera lavas such that tectonic structures are hardly seen. However, most of the caldera infill lavas are fissure eruptions that billowed out of the fracture openings (Leat, 1984). Mibei (2012) suggests that most structures can be extrapolated into the caldera, based on evidence in and around the caldera walls as well as using the flow direction of lavas and hotspots mapped by infrared spectroscopy by Schwonke, (2009). At the central part of the caldera, a fissure with a NW-SE orientation has been mapped; this fissure may have resulted from transform faulting. A portion of the post-caldera lavas appears to have erupted from this fissure in a sub-plinian style. Strecker and Melnick (2013), mapped numerous linear features oriented either ESE-WNW or E-W, in the central area of the Menengai caldera. They attributed this to the central doming which is associated with magma intrusions. Additionally, these features are characterized by numerous fractures with aligned fumaroles, some of which are active and sulphurous.

2.3.2 The Molo Tectono-volcanic axis (TVA)/ Ol'rongai structural system

The Molo Tectono-volcanic axis (Geotermica Italiana, 1987) is a very prominent volcanic feature represented on the surface by a zone with a concentration of faults and fractures with a NW-SE orientation and along which volcanic eruptions have taken place (Figure 6) that resulted in the formation of a NNW trending ridge, referred to as the Ol'rongai volcano.

On a regional scale, the Ol'rongai system extends northwards through Lomolo to as far as Gotuimet volcanic centre (Figure 6). Over the Ol'rongai area, the structure is marked by intense volcanic activity including explosive (pumice issuing) craters. This part of the structure is adjacent to the Menangai caldera and possibly extends into the caldera. Although obscure on the surface, the structure probably extends into the Menengai caldera system and beyond, giving rise to the Makalia fault system, which pass through the western part of Nakuru Town. The apparrent intense volcanism indicated by numerous eruption centres in the western part of the Menengai caldera is probably due to the intersection of the caldera structures and the Molo TVA/ Ol'rongai freacture system (KenGen 2004). Leat (1984) argued that the Menengai pre-caldera shield had the same orientation as the described NW-SE structures and was probably influenced by these faults.

2.3.3 The Solai structural system

The Solai structural system, referred to as the Solai graben (4 km on average), includes structures that run in a N-S direction from the eastern end of Menengai caldera, through Solai (Figure 6). It is comprised of numerous faults/fractures all trending in a N-S direction. The eastern boundary of the graben probably extends to the foot of Marmanet escarpment. This is the only system that has cut the Menengai pyroclastics. On the northern end, it also cuts through the Pleistocene trachyphonolites of the Lake Bogoria suite NW of Kisanana out of the Menengai field. Its southern extension under the Menengai

volcanic pile is an important hydrogeological control and a possible permeability enhancement of brittle lava formations underlying the Menengai eruptives (KenGen, 2004).

2.4 Hydrogeology and surface drainage systems

The surface drainage system is largely from the east and the western scarps. On the rift floor, the drainage is mainly from Menengai caldera northwards with the exception of the drainage from the southern rim, or slopes of Menengai caldera, into Lake Nakuru (Kuria and Woldai, 2003). The N-S, NE-SW, and NW-SE trending fault/fracture systems provide underground channels resulting in stream water disappearing underground (Suwai, 2011). The hydrogeology of the area is mainly inferred from data obtained from water boreholes. Information on aquifer properties and groundwater flow patterns is provided by interpretation of data from these boreholes, the majority of which were drilled to 100-200 m depth. However, on the caldera floor, greater reliance is placed on indirect methods of assessing recharge, e.g. surface hydrological information due to a paucity of borehole data. The relative yields of the boreholes may be matched with the petro-physical properties of the feeder formations, which range from dry and thermally anomalous boreholes to very high yield boreholes (>20 m^3/h). The dry and elevated temperature boreholes are distributed along the Molo TVA that extends from the Menengai caldera northward through the Ol'Rongai volcano, Lomolo and Gotuimet volcano. The high yield boreholes are located to the east of the caldera and are bound by the Bahati and Marmanent scarps which are relatively wetter and on higher grounds. Earlier studies have shown that these areas are fed by channels along the rift scarp faults (Kipng'ok, 2011).

3. SAMPLING AND ANALYTICAL METHODS

3.1 Sampling

Samples for this project were obtained from well MW-19A in the Menengai geothermal field. Drill cuttings were sampled at a 2 m interval during drilling after which preliminary analysis was performed at the rig site through binocular microscopy. No cores were recovered from this well and therefore, all the descriptions and interpretations are solely based on cutting samples. The main objective was to identify the lithology, alteration minerals, feed zones and possible foreign materials in the cuttings, such as bit fragments. The aim was to develop a preliminary lithostratigraphy and estimate the down-hole temperatures based on alteration mineralogy. This helped in the determination of casing depths and also to foresee possible imminent problems that might occur during drilling operations due to geological factors. The samples were then processed further by washing and drying in preparation for thin-section and XRD analyses. In the present study, however, a more detailed analyses of the samples from well MW-19A were carried out at the ISOR (Iceland GeoSurvey) geological laboratories.

3.2 Analytical methods

With the aim of characterizing the borehole geology and the hydrothermal alteration mineralogy of well MW-19A, several analytical methods were employed in this study. These include; binocular microscope analysis, petrographic microscope analysis, X-ray Diffractometer analysis (XRD) and fluid inclusion analysis. A brief description of these analytical techniques is provided below:

3.2.1 Binocular microscope analysis

Samples were analysed at a 2 m interval using a binocular microscope. The samples were carefully washed with clean water to remove impurities and dust to enhance visibility of samples and obscure features such as finely disseminated sulphides e.g. pyrite and chalcopyrite. The aim of this analysis was to identify the lithology, texture, alteration mineralogy, degree of alteration, fracturing and probable aquifers. The samples were analysed using an *Olympus SZX12* binocular microscope and the properties

noted include: the colour of the rock, grain size, texture, vein filling if present, alteration mineralogy, and degree of alteration; from these observations, the rock types and their properties were identified. Dilute HCl was used to identify the presence of calcite; caution was taken at depths where foreign material from cement plugging or cementing of casing was suspected. Samples of interest were selected for XRD analysis. In addition, calcite and quartz grains from different depths in MW-19A were picked for fluid inclusion geothermometry analysis.

3.2.2 Petrographic microscope analysis

Based on preliminary binocular analysis performed at the rig site, representative samples from different depths and lithologic units from MW-19A were selected for petrographic analysis. A total of 26 thin sections were prepared at the GDC laboratory. The thin sections were analysed using a Leitz Wetzler petrographic microscope at ISOR, Icelandic GeoSurvey laboratories. The purpose for this analysis was to confirm the rock types and the hydrothermal alteration minerals and any other additional minerals that were not observed under the binocular microscope. The analysis also aimed at identifying the paragenetic sequence and patterns of the alteration minerals in veins and vesicle fillings.

3.2.3 X-ray diffractometer analysis

This technique is mainly used for the identification of clay minerals and zeolites. Clay minerals are known to have diverse mineralogy and crystal structures, thus, are not easily distinguishable by microscopic analysis. A total of 18 samples were selected and prepared for XRD analysis. Here, untreated, glycolated and heated samples were run. The main aim of the analysis was to identify clay alteration mineralogy with depth and further deduce the temperature regime in the system.

Small portions of cuttings from selected samples were scooped and mixed with water in test tubes. The mixtures were shaken for 4-5 hours to dissolve and extract clay from the cuttings. A few drops of water from each of the dissolved drill cutting samples were placed on separate glass slides which had been washed previously with an organic solvent, acetone, and dipped in a glycol solution for 24 hours. The samples in the test tubes were left to settle for 12 hours. The clay samples were first run in the X-ray diffractometer (Bruker AXS, D8 Focus Diffractometer) and the peaks recorded. The glycolated samples were subsequently run in the X-ray diffractometer and the peaks were recorded. The clay samples were heated to 550°C before performing the third run in the X-ray diffractometer and the peaks were recorded. For each sample, three peaks, each from the corresponding runs, were recorded. Results of the XRD analysis for MW-19A are summarized in a Table 2 while some graphical presentations of some results are displayed in Appendix I.

3.2.4 Fluid inclusion analysis

Fluid inclusion analysis is the study of fluids trapped in vacuoles inside mineral grains during growth or recrystallization. The trapped fluids, termed as fluid inclusions, give an approximate temperature from the time when the fluid was trapped in the mineral grain. This is measured by heating the crystal until the fluid inclusion reaches the homogenization temperature (Th). In this study, calcite and quartz grains from different depths in the well were hand-picked for fluid inclusion geothermometry analysis. Since the crystals were not clear enough, they were polished to enhance their transparency. Upon confirmation by use of the petrographic microscope of the presence of clear fluid inclusions, the grains were slowly heated, each at a time, on a Linkam THSMG 94 heating and freezing stage until the fluid homogenized in a single phase (i.e. bubbles disappeared) and the temperature of homogenization (T_h) was measured. Fluid inclusion geothermometry, when compared with results from alteration mineralogy and measured temperatures from the well, provide important information on the thermal history of the geothermal system. It provides evidence as to whether a geothermal system is heating up, cooling or is in equilibrium. The data acquired from all of the above analyses was intergrated using LogPlot 7 from RockWare Inc., a software which is very useful in correlating and interpreting geological and geotechnical data.

4. BOREHOLE GEOLOGY

4.1 Drilling of well MW-19A

Well MW-19A was spudded on 19th October, 2014 at 1715 hours and completed on 14th January, 2015 after which the rig was released for demobilization. It took 87 days to complete. MW19A is a directional well drilled to the north at an azimuth of 339.92° and inclination of 20.19° to a measured depth (MD) of 2355 m CT. The drilling was conducted in the following four main stages (Figure 7):

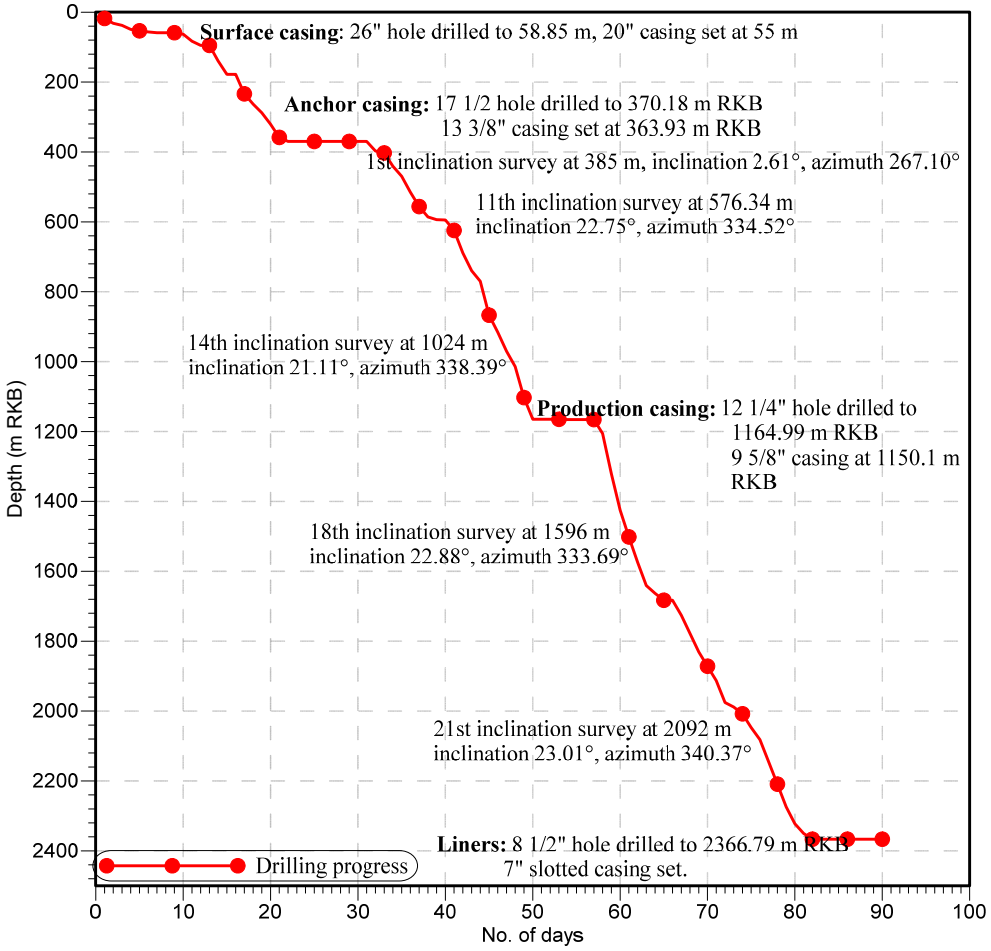

FIGURE 7: Well MW-19A drilling progress

Stage one (drilling of 26" hole): The 26″ hole was drilled to a depth of 58.85 m with intermittent losses experienced. This section was drilled with water complemented by mud gel sweeps. The 20″ casing was run in hole with the shoe set at 55 m. A total of 5 casing joints were run in where primary and secondary cementing was done. One backfill cement job was done in this section with a total of 19.02 tons of cement slurry being used to bond the 20" OD 94 lb/ft BTC casing.

Stage two (drilling of 17½" hole): The 17½″ hole was drilled to a depth of 370.18 m with the 13⅜″ casing being set at a depth of 363.93 m. A total of thirty-one 54.5 lb/ft casing joints were run in the hole. Three plug jobs and eleven backfill cement jobs were done in this section with a total mass of 333.32 tons of cement being used for both the casing and plugging jobs.

Stage three (drilling of 12¼" hole): The third drilling stage for the production casing was drilled with varied BHA. This is because the well was directional and it is at this section that the kick-off angle is built. To attain the kick-off angle, a rat hole at 400 m was drilled using slick BHA. POOH to change

from slick to kick off BHA followed. Drilling continued using aerated water and foam with returns being received on the surface. At 593.78 m the drill string was pulled out to change kick off BHA to lock up BHA and drilling of the 12¼" hole with aerated water and foam continued with partial returns received on the surface. Total loss of circulation was experienced at 902 m. Drilling blindly continued down to 970 m where POOH was done to change bit. After bit change, the hole was drilled with aerated water and foam with full returns received to casing depth of 1154 m CT. POOH to shoe to do wiper trip was done and 9⅝" casings run in. A total of 100 casings were run in. Casing shoe was set at a depth of 1150.1 m RKB. Primary cementing and three backfills were completed before returns were received on the surface. A volume of 109.81 tons of cement was consumed in this section for both casing and one plug job.

Stage four (drilling of 8½" hole): The 8½" hole section started on the 55th day of drilling with backing off of 9⅝" landing joint. Top of cement was tagged at 1116 m. Drilling out cement using slick BHA and water commenced with returns received on surface down to a depth of 1155 m. An integrity test of the shoe was done but the shoe failed. It was decided to cement plug. Mule shoe was placed 11m above the shoe and 1.3m^3@ 1.8 g/cm^3 cement slurry pumped. After WOC, top of cement was tagged at 1139.94 m using mule shoe and slick BHA run in to DOC. DOC continued up-to 1165.15m where the slick BHA was pulled out of hole to change to pendulum BHA. An obstruction was tagged at 1124.98 m when running in the pendulum assembly and the hole was reamed. Drilling in formation using aerated water and foam with returns received on the surface continued to a depth of 1309.9 m where a gyro-survey was done. Drilling on bottom continued to a depth of 1663.2 m where POOH was done to change bit. On RIH with new bit, fill was tagged at 1650 m and the hole was reamed with aerated water and foam. Drilling then continued to a depth of 1683.10 m with 60% returns received on the surface. At this depth drilling was due to high torque and the hole reamed down from 1680 to 1683 m. Encountered consistent torque and fill at 1681m and decided to POOH to change BHA (remove SSTB2) and extract bit nozzles. After BHA change, drilling continued blindly to a depth of 1688.50 m where circulation was regained. Drilling on bottom with aerated water and foam continued to a depth of 1779.34 m with returns received on the surface. Circulation was done at this depth to clean hole after experiencing high torque before continuing to drill to a depth of 1988.32. POOH was then done to inspect the bit. It was discovered that the bit bearings were completely worn out. New bit was run in and drilling continued to a depth of 2081.80 m where TLC was experienced. Drilling blindly was then done from 2081.80 to 2146 m. From 2146 to 2322 m drilling was done using aerated water and foam with partial and intermittent returns received on the surface. TLC was experienced at this depth and blind drilling continued to TD of 2366.79 m. Wiper trip and POOH was done and 7" liners run in. This was followed by well completion test; the well was capped with a 10" class 900 master valve and completed on the 87th drilling day.

4.2 Stratigraphy

Based on both binocular stereo microscope observations and petrographic analysis five types of rock formations were found to form the litho-stratigraphy of MW-19A. These include: pyroclastics, tuff, trachyte, syenite and basalt. The lithology of the well is shown in Figure 8, in addition to alteration mineral distribution and alteration zonation.

Pyroclastics

Pyroclastic fragments are found on the surface and occasionally as highly oxidized thin layers intercalating with trachyte lavas in Menengai. They form conspicuous thin lenses in the upper 450 m of the stratigraphy well column, signifying several pyroclastic eruptions in the post-caldera stage. The pyroclastics appear as brownish to grey, loose unconsolidated deposits composed of ash and vesicular fragments of pumice lapilli particles, obsidian, glass and lithics of trachytic composition. Oxides and some calcite are the main alteration minerals found in this formation however, zeolites and chalcedony are also found infilling vesicles.

Tuffs
Tuffs were rare in this well and occur as thin intercalations at 368-372 m, 388-400 m, 492-504, and at 836-842 m. They are generally reddish brown to grey, commonly composed of non-welded, poorly crystalline and vitrified volcanic ash with vesicular texture. The tuffs were observed often altering to clays along contact boundaries. Four major tuff marker horizons were identified in MW-19A, which possibly demarcate the post, syn- and the pre-caldera volcanics. These markers are defined by tuffs encountered at 368-372 m, 388-400 m, 492-504 m and 836-842 m.

Trachyte
Trachyte is the most dominant rock encountered in the well right from top to the bottom of the well where it occurs alternating with tuff, pyroclastics, basalt and syenite. The rock is light grey to dark grey in colour, fine grained and feldspar phyric composed of mainly feldspars, quartz, pyroxenes and mafic minerals. The rock has large feldspar phenocrysts (e.g. sanidine) surrounded by minute dark minerals, some exhibiting trachytic texture. Pyroxenes and minor amphiboles are the main mafic minerals present in this rock unit. The matrix consists of flow oriented feldspar microlites in a fine grained to glassy groundmass. The rock generally shows weak to moderate intensity of alteration except where the formation is fractured; when high intensity of alteration occurs the grey lava transforms either into a light greenish colour or appears bleached giving the rock a mottled texture.

In an endeavour to characterize different episodes of lava eruptions, trachyte in this study was classified into three groups based on its grain sizes; these are: fine-grained, medium-grained and coarse-grained trachytes. Although the chemistry of these rocks may vary slightly, textural classification was preferred.

Basalts
First occurrence of basalt was at 1672-1674 m, and then at 1770-1802 m. The rock is dark grey to almost black in colour, with holocrystalline groundmass composed of plagioclase laths and anhedral clinopyroxenes and magnetite. It is porphyritic with phenocrysts of augite, plagioclase and olivine.

Syenite intrusions
Menengai caldera is hosted in a spreading zone, hence, fresh magma pulses from the main magma chamber are readily injected into the overlying formations, forming dikes and other intrusions. These magma injections are facilitated by faults and fractures resulting from the tectonics associated with a divergent plate setting (Mibei, 2012). In MW-19A, syenite intrusions were encountered at 1418-1584 and 1920-1952 m depths. These intrusions are relatively fresh, grey coarse- to medium-grained, porphyritic with phenocrysts of feldspars, clinopyroxene (e.g. augite) and amphiboles. A summarized description of each of the lithologic units encountered in well MW-19A is given in Appendix II and plotted in Figure 8.

5. HYDROTHERMAL ALTERATION

In well MW-19A, hydrothermal alteration minerals appear both as replacement of the primary minerals, as well as fillings in vesicles, vugs and fractures. The distribution and abundance of the hydrothermal minerals (Figure 8) were obtained from binocular, petrographic and XRD studies of drill cuttings samples taken after every 2 m from the well.

The distribution and abundance of any kind of mineral assemblages present in hydrothermal systems is influenced by several factors, which include, permeability, rock and water composition, temperature, pressure and duration of hydrothermal alteration (Browne and Ellis, 1970). These factors are largely independent, but the effects of one or more of the factors can exert a dominant influence on the location and extent of hydrothermal alteration. Permeability in rocks plays a crucial role in the access of thermal fluids, which cause hydrothermal alteration of the rocks and precipitation of secondary minerals in open spaces. Rocks, which possess very restricted permeability or are completely impervious to fluid, will only be slightly altered or show no alteration at all.

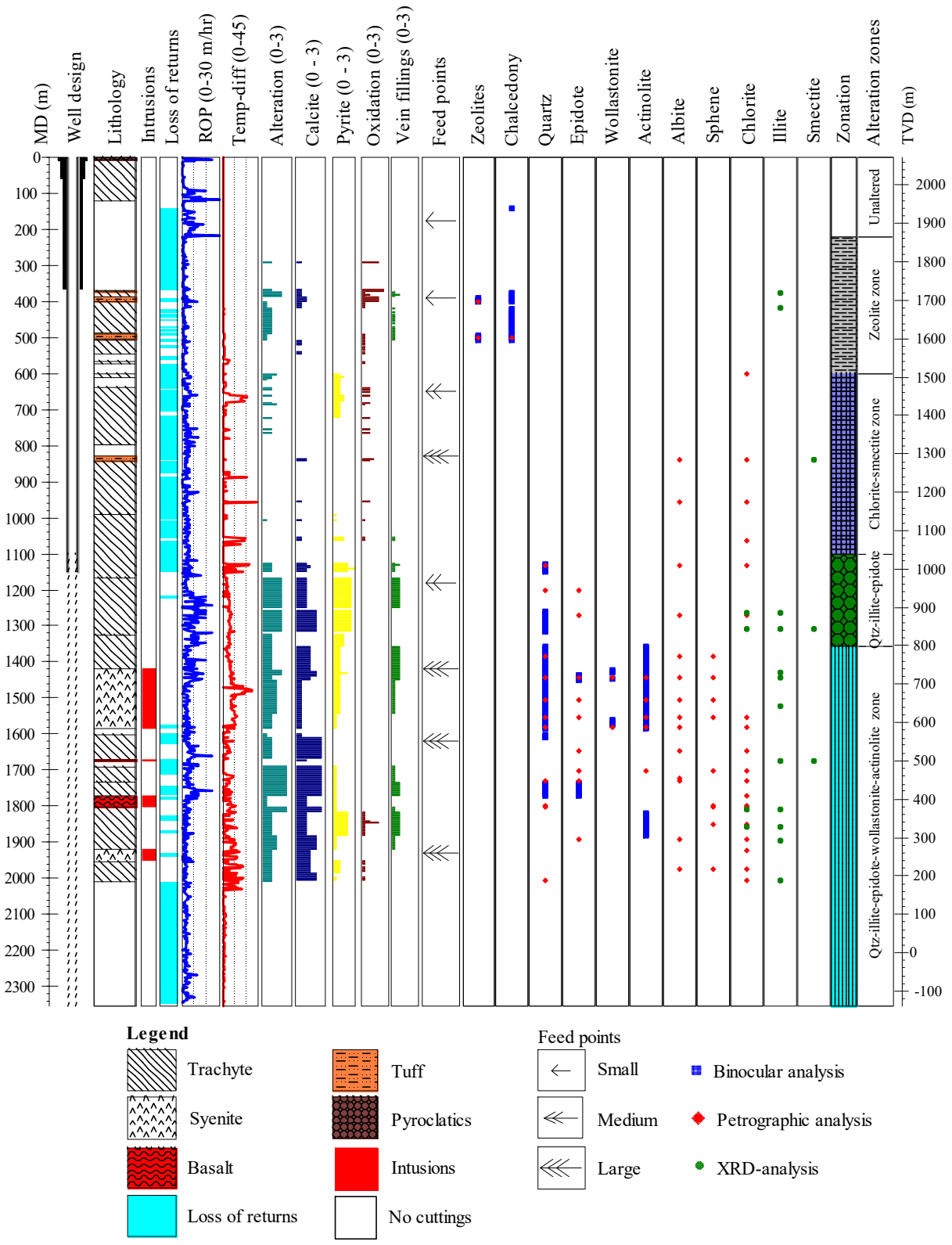

FIGURE 8: Lithology, distribution of hydrothermal alteration minerals, mineral zonation and location of aquifers in well MW-19A

Crystallinity of the host rock is of importance because glass is more easily altered than crystalline rock. The chemical composition of the host rock determines the availability of components to form alteration minerals as well as possible fugitive components from the presumed magmatic heat source. Temperature is the most significant factor in hydrothermal alteration because most of the chemical reactions require elevated temperatures and also minerals are thermodynamically stable at high temperatures (Lagat et al., 2005) Pressures at the depths penetrated by well MW-19A drill hole, like any other geothermal fields elsewhere in the world are not sufficient to greatly affect hydrothermal alteration minerals transformation (Browne and Ellis, 1970; Lagat et al., 2005).

The main hydrothermal minerals in Menengai geothermal field are calcite, zeolites (e.g. scolecite), chlorite, chalcedony, epidote, actinolite, wollastonite, secondary iron oxides (e.g. magnetite), sulfides (e.g. pyrite and chalcopyrite) and quartz. Mineral associations in vesicles are common and consist of two or more of the alteration minerals with the paragenetic sequence varying with depth and from one well to another.

5.1 Alteration of primary minerals

Most of the primary rock forming minerals are unstable in a geothermal environment and are, therefore susceptible to replacement by new minerals that are either stable or at least metastable under the new conditions. Although hydrothermal alteration has changed the primary minerals in different ways and magnitude, often the original textures of the minerals are still recognizable. The primary minerals found in MW-19A include volcanic glass, quartz, olivine, pyroxene, amphibole, feldspars, and opaque minerals (FeTi-oxides). Glass shows little alteration at shallow depths but is completely altered down the well, whereas quartz apparently shows little or no alteration at all. Feldspars, pyroxenes, and iron oxides show a greater resistance to alteration compared to glass and olivine. Sanidine and plagioclase are the main feldspars in this well. In thin sections, the sanidines appear fine grained and elongated, exhibiting the trachytic texture. It also occurs both in the groundmass and as phenocrysts exhibiting porphyritic textures. The sanidine phenocrysts were readily identified by low relief and simple twinning. At shallow depths, the feldspars are relatively unaltered but become progressively altered with depth into albite and occasionally to clays, calcite, and epidote. Albite, epidote and sphene are observed to partly replace plagioclase below 800 m. Olivine is rare in this wells and occurs as greenish anhedral crystals with polygonal outlines. It is distinguished by its poor/lack of cleavage and high birefringence under the petrographic microscope. Olivine shows alteration to oxides and clays. In most cases it is completely altered and its presence is revealed by the outline of the alteration product. Fe-Ti Oxides are the most abundant opaques in this well and are relatively resistant to alteration. These oxides occur as magnetite and mostly alter to sphene. Table 1 below summarizes the order of replacement of the primary minerals and their alteration products in the well.

TABLE 1: Order of replacement of primary minerals and their alteration products (modified from (Browne, 1984)

Primary minerals		Replacement products
Volcanic glass	Increasing order of replacement ↓	Zeolites, quartz, calcite, clays
Pyroxenes, amphiboles, olivines		Chlorite, illite, quartz, pyrite, calcite
Sanidine, orthoclase, microcline		Calcite, adularia, chlorite, illite,
Ca-plagioclase		Calcite, albite, adularia, chlorite, illite, sphene, quartz, epidote
Iron oxides		Pyrite, sphene, secondary oxides

5.2 Description and distribution of hydrothermal alteration minerals in well MW-19A

The distribution of hydrothermal minerals in well MW-19A is shown in Figure 8. At shallow depths, low temperature minerals are seen to dominate with mainly zeolites, chalcedony, amorphous silica, calcite, oxides, clays (smectite and chlorite) and sulphides being the minerals present. In the deeper parts of the well, hydrothermal alteration is seen to range from moderate to high. Quartz, epidote, pyrite, calcite, wallastonite, albite, sphene, illite, chlorite and actinolite are the alteration minerals here.

Generally, the hydrothermal alteration pattern shows prograde alteration with increase in temperature and depth with the low temperature mineral assemblages disappearing as the high temperature assemblages appear. However, actinolite, which is a high temperature alteration mineral was observed at 1358 m depth where the current measured formation temperature is 226°C. This mineral now exists where the present temperature is much lower than its expected thermal stability range (>290°C) indicating that the temperatures at this section at one time must have been higher than the present temperatures and therefore the mineral is considered relict. Below is a brief description of the hydrothermal alteration minerals encountered in MW-19A.

Zeolites were observed at 142, 402 m and between 494-506 m depths in this well. Two types of zeolites were observed, scolecite and mesolite. They occur as densely packed fibrous aggregates often in hemispherical forms radiating from several sources along vesicle walls, especially in tuff layers. Zeolites are generally thermodynamically metastable at 60-110 °C (Kristmannsdóttir, 1979).

Chalcedony is noted from 142 m to around 450 m. It is translucent, often milky or greyish cryptocrystalline form of silica which occurs at temperatures below 120ºC mostly in vesicles, vein fillings or fractures. It is characterized by smooth, almost perfectly circular morphology. At greater depths where temperatures are high, chalcedony in vesicles is seen transforming or is completely transformed into quartz but the chalcedonic outline is still preserved.

Calcite is ubiquitous in this well and occurs from around 300 m, through to the bottom of the well and is most abundant from 1120 m. This is attributed to increased boiling as a result of high formation temperatures. Calcite presence is associated with carbon dioxide activity in the reservoir which clearly indicates active magmatism. The mineral occurs as deposition vesicles, veins and disseminated in the groundmass where it replaces sanidine feldspar. Crystal morphology of calcite is variable and ranges from individual thin-bladed crystals to equant or needle like crystals.

Quartz is colourless to white in colour and occurs in euhedral to subhedral crystals. Quartz is identified both as open space (vesicle) fillings and vein filling mineral. The mineral was first seen at 1128 m depth and persists almost to the bottom of the well with varying intensities. It was easily identified in cuttings by its typical euhedral shape, transparency and forming a regular hexagonal pyramid form. Some of the euhedral grains of quartz were noted growing in clusters while others grew individually. At shallow depths, it was seen replacing chalcedony while at deeper depths it deposited in vesicles, veins and fractures. Its presence in a geothermal system indicates temperatures of above 180°C. (Franzson, 1998).

Epidote is one of the main hydrothermal index minerals which often shows a systematic textural development with increasing depth. The first occurrence of epidote in this well is indicated by its greenish colouration forming fine-grained aggregates and later fully develops into yellowish-pale green idiomorphic, tabular, radiate to fibrous crystals. Epidote was first seen in the petrographic microscope at 1202 m. It is found filling fractures, vesicles, and replacing primary plagioclase and pyroxene. In most cases epidote forms mineral associations with mainly quartz, chlorite and sometimes calcite and pyrite. The presence of well-crystallized epidote indicates temperatures above 250°C.

Wollastonite is an alteration mineral often associated with contact metamorphism and, therefore, its occurrence is probably related to the numerous intrusions in the caldera summit area (Mibei, 2012).

Wollastonite was observed at 1270 m and was seen to diminish below 1574 m in this well. It is colourless and fibrous under the binocular microscope and indicates temperatures of ≥270°C.

Pyrite is fairly abundant in MW-19A in comparison to other wells drilled in Menengai and was obseved to occur between 600 to 720 m and 1100 to the bottom of the well with varying intensities. It occurs as euhedral cubic crystals with brassy yellow luster in reflected light. Very small cubic pyrite crystals were deposited in fractures, vesicles and veins and as disseminations in the groundmass. Appearance of this mineral is taken to indicate enhanced permeability within the reservoir.

Actinolite is green to greyish green in colour, forms radiating fibres or acicular crystals and also massive to granular aggregates in the groundmass and has a moderate birefringence. It's produced as a result of high degree of water rock interaction. Where it occurs alteration is strongest especially near micro-fractures and veins that were interpreted to be the main fluid conduits. In this well actinolite was encountered between 1358 and 1882 m where intense alteration was also noted. The presence of actinolite indicates temperatures between 280 and 350ºC.

Albite is a secondary mineral which occurs as an alteration mineral from feldspars. Albitization in this study is referred to replacement of primary K-feldspar and plagioclase phenocryst by hydrothermal albite. Albitized K-feldspar has a low refractive index and shows no zoning but typical microcline-like twinning. Albite alteration occurs at around 800 m but extensive albitization is noted at 1400 m in this well. Below 1,900 m, clear euhedral albite crystals were identified.

Sphene (titanite) was observed only in petrographic microscope. In thin section, it was easily identified by its distinct yellow-brown colour, very high relief and its common diamond shape often seen replacing opaque minerals.

Oxides form readily in the surface or near surface environment, where oxygen from the atmosphere is more readily available and at the baked contact between the cold and the hot rock. The most common ones to form are mainly iron oxides, but many different types can form, depending on the metal cations present. Sulphide minerals often weather easily because they are susceptible to oxidation and replacement by iron oxides. In this well oxidation was noted from the surface to around 1000 m depth and from 1800 to 2000 m although in minute quantities.

Clay minerals have proved very useful mineral geothermometers in the study of many geothermal systems around the world. Mixed-layer clays (illite, smectite and chlorite), kaolin group (two-layer clays) smectite group (three-layer, expanding lattice), illite group (three-layer, non-expanding) and the chlorite group (three-layer with interlayer cations). Typically, clay minerals form microscopic to sub-microscopic crystals (in some cases, crystallinity is totally limited); hence, it becomes a bit complicated to study these minerals under a microscope. In order to compliment petrographic and binocular analysis, X-ray diffraction analysis for 18 samples in well MW-19A was carried out (Table 2). In this analysis the samples were prepared and subjected to three XRD treatments; air-dried, glycolated and then heated. Three types of clay were identified; these are: smectite, chlorite and illite.

Smectite is a low-temperature clay and its occurrence is an indication of temperatures lower than 200°C. Smectite is not common in MW-19A. It was positively identified in the XRD analysis at 838-840 m, 1308-1310 m and 1672-1674 m depth (Table 2). It showed peaks commonly occurring between 12.8 and 15 Å when untreated, 13 to 17 Å when treated with glycol and collapsing to 10.3 Å when heated (Figure 1 in Appendix I). The appearance of smectite at 1308-1310 m can therefore be attributed to the temperature reversal observed (see chapter 5.7 in Figure 13b) between 1100 and 1400 m depth in this well while its appearance at greater depths is against the norm where it is found existing where the present formation temperature is much higher than its thermal stability range of 50-200°C. This may indicate several regimes of geothermal activity or evidence of reduced permeability in this section of the well where it occurs.

TABLE 2: Results of clay minerals identified from XRD analysis

Sample ID	Depth (m)	Untreated (Å)	Glycolated (Å)	Heated (Å)	Type of clay
1	374-376	10.21	10.21	10.21	Illite?
2	416-418	10.21	10.21	10.21	Illite?
3	500-502				No clay
4	540-542				No clay
5	838-840	15.53	17.32	10.02	Smectite
6	992-994				No clay
7	1128-1130				No clay
8	1262-1264	12.70	12.70	7.57	Smectite?
	1262-1264	10.30	10.30	10.30	Illite?
9	1308-1310	12.70	12.70	10.30	Smectite
	1308-1310	10.30	10.30		Illite
	1308-1310	12.70	12.70		Chlorite
10	1426-1428	10.40	10.40	10.26	Illite
11	1440-1442	10.40	10.40	10.26	Illite
12	1522-1524	10.40	10.40	10.26	Illite
13	1602-1604				No clay
14	1672-1674	15.26	17.48	10.26	Smectite
	1672-1674	10.26	10.26	10.26	Illite
15	1808-1810	14.67	7.20		Unstable chlorite
	1808-1810	10.26	10.26	10.26	Illite
16	1856-1858	12.24	12.24	10.19	Smectite?
	1856-1858	10.32	10.32	10.19	Illite
17	1894-1896	10.40	10.40	10.20	Illite
18	2004-2006	10.37	10.37	10.19	Illite

Chlorite occurs below 438 m to the bottom of the well. The mineral shows a wide distribution and a big variability in colours, form and textures. It varies in colour from light-to-dark green, has low birefringence and occasionally shows anomalously blue, brown or purple interference colours and presents two different forms. In the upper section of the well, chlorite appears in small intergranular patches whereas at the deepest levels, chlorite is idiomorphic, forming radial aggregates in vein-lets and vugs in association with quartz, calcite, epidote and pyrite. Within veins, chlorite occurs as micro-spherules enclosed within epidote, but it may also replace primary pyroxene, and the matrix. In the study well, chlorite was first identified in the petrographic microscope at 580 m depth and was seen to occur intermittently to the bottom of the well. It exhibits characteristic unchanged peaks of 14.50 and 7.28 Å when untreated and glycolated, and completely collapses after being heated to 550°C. Occurrence of chlorite indicates formation temperatures of over 220°C (Reyes, 2000).

Illite is the most common clay mineral group in well MW-19A. In the study well, illite first occurred at 400 m, becomes rare and reappears again from 1444 m to the bottom of the well. It displayed peaks between 10.19-10.40 Å in untreated, glycolated and heated samples (Figures 2, 3 and 4 in Appendix I). Occurrence of illite indicates temperatures greater than 200°C.

5.3 Mineral paragenesis

The paragenetic sequences in hydrothermal systems are identified from cross-cutting relationship in veins and mineral fillings in vugs and vesicles. This gives a clear picture on the way the geothermal system has evolved over time as well as predicting its future. The mineral deposition sequence in well MW-19A was rarely observed. However, a few sequences were noted. At shallow depths, zeolites were seen to deposit in vesicles, which later disappeared at around 550 m. Chalcedony on the other hand

which is a low temperature mineral was seen to form in vesicles and later transforming into quartz with depth. At greater depths of 1308 m, well developed quartz crystals were seen overlying calcite in vesicles, but at some instances quartz was observed to form first and calcite deposited later. At around 1748 m, actinolite was seen to form on top of epidote an indication that the system is evolving to higher temperature conditions. This is also evidenced by the measured formation temperatures of 319°C at the same depth.

5.4 Hydrothermal mineral zonation

Hydrothermal conditions found in the reservoir could easily be inferred from a closer look at the hydrothermal mineral assemblages. Occurrence of alteration minerals, whose formation temperatures are known, are useful geothermometers to predict formation temperatures, although some minerals may represent past conditions. In this well the hydrothermal minerals used to determine the zonations are zeolites, smectite, chlorite, quartz, illite, epidote, wollastonite and actinolite. Each zone is characterized by a definite assemblage of hydrothermal minerals and is defined by the first appearance of its index mineral. Based on this study five hydrothermal alteration zones were identified (Figure 8), although there could be a possibility of one or two more sub-zones. Below is a brief description of each of the zones.

Unaltered zone which consists mainly of pyroclastics and trachytes showing a high level of oxidation. The rocks in this zone show little or no alteration at all.

Zeolite zone: This zone extends from around 220 m to about 502 m. Presence of circulation losses in this section of the well makes it difficult to determine the exact boundaries of the zone. This zone is marked by the presence of chalcedony, calcite, smectite and zeolites and the temperature range is less than 200°C.

Chlorite-smectite zone: This zone is made up of an assemblage of clay minerals. It ranges from around 502 m to 1100 m when quarts starts to appear, and characterises a temperature interval of about 180-230°C. Clays are found to occur in a wide temperature range, however, chlorite and illite show a wide temperature range mainly in intermediate to acidic rocks which seems to be the case in this well.

Quartz-illite-epidote zone: This zone is marked by the appearance of quartz, illite, smectite, albite, chlorite, calcite, epidote and wollastonite and ranges from 1100 to 1358 m. This zone indicates an alteration temperature of more than 230°C.

Quartz-illite-epidote-wollastonite-actinolite zone: It is defined by the appearance of quarts, illite, epidote, wollastonite and actinolite from 1358 m, and persists to the bottom of the well. The appearance of actinolite at this zone reveals formation temperatures of above 280°C (Reyes, 2000).

5.5 Fluid inclusion geothermometry

Fluid inclusion geothermometry is a powerful tool for outlining changes in temperature regimes in a geothermal system (Roedder, 1972). Fluid inclusions are tiny bubbles of liquid and vapour that are formed when fluids are trapped in crystals and subsequently cooled due to differential thermal contraction of fluid and host mineral. Primary inclusions are formed during primary crystal growth, often concentrated along the first order of growth discontinuity or occur as isolated inclusions distributed within the crystal. Secondary inclusions are formed after primary growth, often along healed micro-structures (Roedder, 1984). The inclusions in any given sample are seldom of only one generation. In some minerals from hydrothermal deposits, the primary inclusions are sparse and randomly distributed and relatively large, but the secondary inclusions in the same sample are small, very numerous and in planar arrays (Roedder, 1984).

In the present study fluid inclusion micro-thermometric measurements were done on inclusions trapped in a quartz crystal from 1406 to 1408 m depth and calcite crystal from 1748-1758 m depth range in MW-19A, to determine the temperature at which the inclusions were formed. They were heated using a Linkam THSMG 94 freezing and heating stage and the temperatures at which the inclusions reached homogenisation temperature and the bubbles disappeared were noted. The temperature measurements were done in three phases; the first heating phase was done at a rate of 20°C/minute up to 100°C, while the second phase of heating was done at a rate of 10°C/minute up to 200°C and the last heating phase was done at a rate of 5°C /minute until the bubbles disappeared, care being taken to avoid blowing up the inclusions.

In this well a total of 30 inclusions were analysed, 14 and 16 inclusions from quartz and calcite, respectively. The homegenization temperatures obtained from the quartz crystal ranged from 293 to 305°C (Figure 9) with an average value of 298°C while those from calcite ranged from 265 to 310.7°C (Figure 10). The results obtained from calcite varied widely showing two populations. The first population ranged from 265 to 277°C with an average value of 272°C while the second population ranged from 287 to 310.7°C with an average value of 297.7°C. The low temperature values from the first population are therefore assumed to be from secondary inclusions, whilst the higher values from the second population are assumed to be from primary incluisions. The results from this analysis are presented on histograms in Figures 9 and 10.

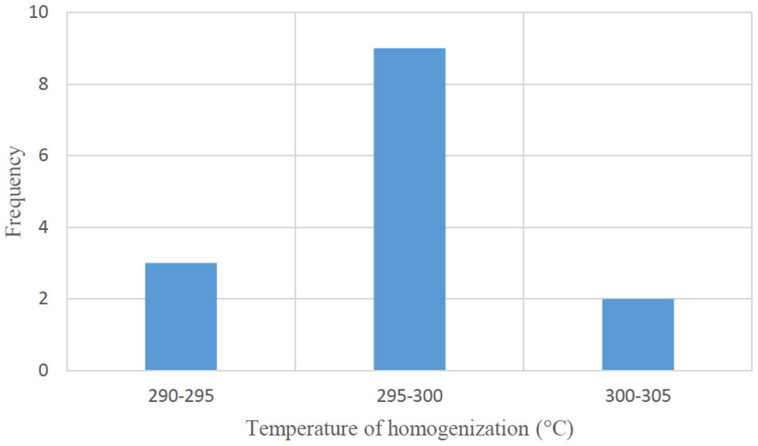

FIGURE 9: Fluid inclusion measurements from quartz crystal (1406-1408 m depth)

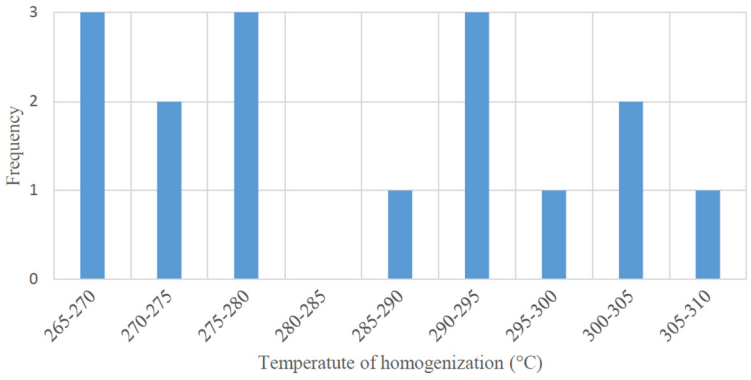

FIGURE 10: Fluid inclusion measurements from calcite crystal (1748-1758 m depth)

The T_h values from inclusions hosted in the quartz crystal gave an average value of 298°C whereas, the measured formation temperature at the same depth is 226°C. The lowest T_h value of 293°C is 67°C higher than the measured formation temperature and the highest T_h value (305°C) is 75°C above the measured formation temperature. The average value for inclusions in the quartz crystal is 298°C and is 72°C above the measured formation temperature.

In the calcite crystal, the lowest T_h value of 266°C from the first population is 53°C lower than the measured formation temperature (319°C) and the highest T_h value (277°C) from the same population is 42°C lower than the measured formation temperatures. The average value (272°C) of the first population from the calcite crystal is 47°C below the measured formation temperature. In addition, the lowest T_h values in the second population from the calcite crystal is 32°C lower than the measured formation temperature and the highest T_h value (310.7°C) is 8.3°C below the measured formation temperature (319°C). The average Th value for the inclusions from the second population is 21.3°C below the measured formation temperature. These measurements indicate that the inclusions in the quartz

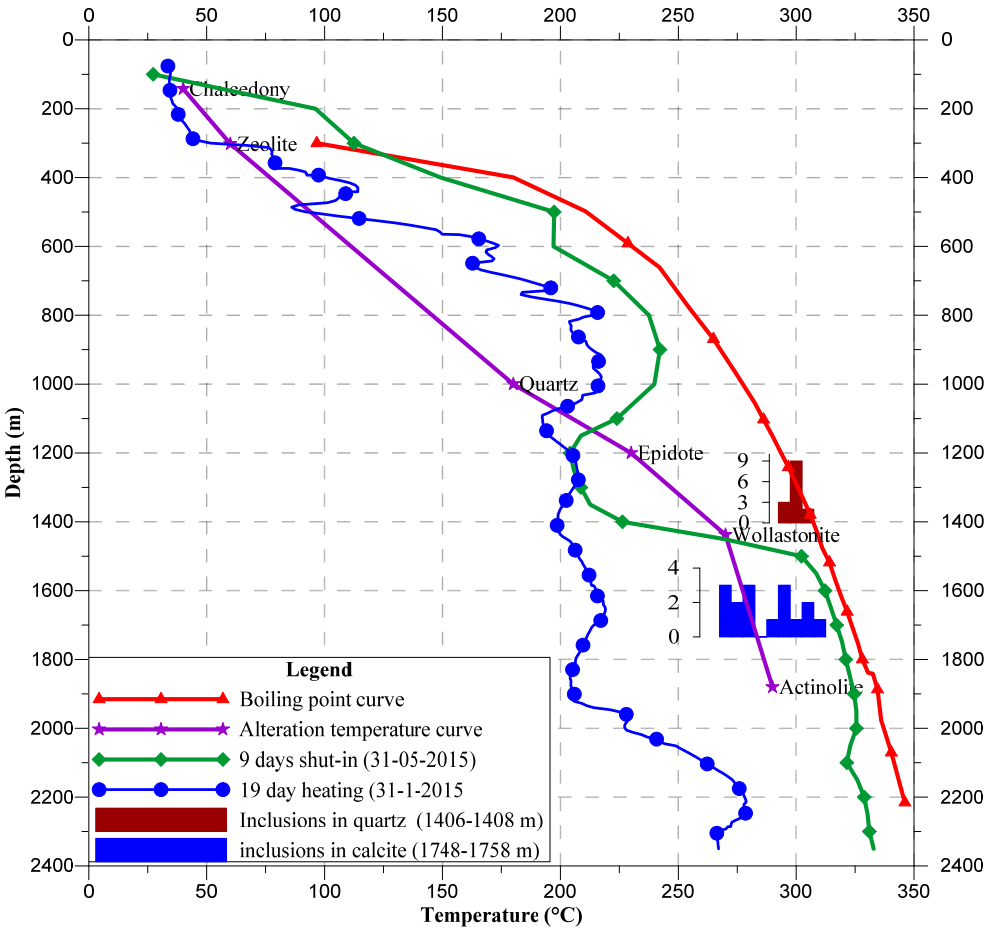

FIGURE 11: Boiling point curve and correlation between measured, interpreted hydrothermal alteration minerals and fluid inclusion temperatures with depth of well MW-19A

precipitated from a hotter fluid implying a much hotter conditions in the past. Moreover, the inclusions in the first population from calcite indicate that the fluids in these inclusions were trapped from a much cooler fluid at a later stage whereas the fluid from the second population from the calcite crystal indicate that the fluid in this inclusions were trapped in a more or less the same temperatures as the current formation temperatures hence the system at this point is either heating up or at equilibrium. Generally, the fluid inclusion analysis indicate an increase in temperature with depth.

Results from fluid inclusions from well MW-19A were integrated together with the measured, alteration and boiling point temperature curves (Figure 11), so as to understand how the geothermal system has evolved with time. The correlation between the alteration temperature, measured formation temperature and fluid inclusions in this well indicate cooling between 1100 and 1400 m with hydrothermal minerals occurring below their stability range. For example, actinolite was seen to form before wollastonite (Figure 8) where the formation is below its temperature stability range indicating it is relict. Below 1400 m and to the bottom of the well, the measured formation temperature is greater than both the alteration and fluid inclusions temperature and almost close to the boiling point curve. Therefore, it appears that the system is heating up, or possibly approaching equilibrium, with the mineral assemblages in this zone occurring within their temperature stability ranges.

5.6 Aquifers / permeable zones

For a hydrothermal system to exist, permeable formations or structures should exist to allow hot water to percolate through. These permeable zones form the aquifers (Lagat, 2004). Typically, aquifers are

located at the intersection of faults, fractures, intrusions and lithological contacts. In a geothermal system, aquifers can either be cold or hot. The cold aquifers, which are usually encountered in the upper parts of the wells, are cased off and carefully cemented to prevent them from cooling the hot aquifers in the deeper part of the wells. Permeable zones in MW-19A were interpreted based on various parameters, which include; the rate of penetration (ROP), loss of circulation, differential temperature in the circulation fluid during drilling, lithological contacts and hydrothermal alteration mineralogy patterns as well as temperature logs.

Indicators of high permeability in MW-19A, apart from high alteration intensity and sheared rocks (fractures), include the presence of abundant pyrite and calcite. These minerals are commonly found in or adjacent to aquifers penetrated by the well and occur as alteration of the rocks as well as in veins, often as coarse grains. Low permeability on the other hand, apart from absence of the above minerals, is indicated by relatively fresh rock indicating low water rock interaction and presence of blocked veins. However, based on the above mentioned parameters, MW-19A is a very permeable well and eight possible permeable locations were identified at 150-200, 388-400,620-680, 836-842, 960, 1460-1500, and 1920-1980 m depths (Figures 12). Table 3 below gives a brief summary of the possible permeable zones identified in the well.

Minor loss or gain in circulation could not be established because the volume of circulation fluid coming out of the well-bore was not being measured during drilling, therefore small aquifers could not be identified. Circulation losses recorded at shallow depths above the groundwater table were attributed to blocky trachytic lavas but most of these zones, including the unwanted cold aquifers, were cased off. Generally, the identified permeable locations can be grouped into four major aquifers (Figure 12). Production casing in this well was positioned at 1150.1 m RKB depth. Therefore, the upper two aquifers were cased off to avoid quenching of the deeper hot aquifers. However, the second aquifer was partly cased as evidenced by the temperature reversal from the temperature logs (Figure 13b).

TABLE 3: Interpreted permeable zones and aquifers/feed zones based on geological observations and fluid circulation temperature measurements

Depth	Evidence from geological observations, drilling observations and temperature monitoring profiles (logs)
150-200	Major circulation loss, high rate of penetration, increase in measured temperature
388-400	Primary permeability in tuff, circulation loss, increase in alteration intensity and oxidation, increase in measured temperature
620-680	Circulation loss, relatively high penetration rates, increase in alteration intensity and oxidation, increase in measured temperature, abundance of pyrite
800-860	Primary permeability in tuff, major circulation loss, increase in measured temperature
1110-1300	Major circulation loss, abundance of calcite and pyrite, decrease (reversal) in measured temperature
1460-1500	Lithological contact between trachyte and syenite, increase in alteration intensity, increase in measured temperature, abundance of calcite and pyrite, fractured formation
1770-1800	Lithological contact between trachyte and basalt, increase in alteration intensity, increase in measured temperature, abundance of calcite and pyrite, fractured formation
1920-1980	Lithological contact between trachyte and syenite, increase in alteration intensity, increase in measured temperature, abundance of calcite and pyrite,

5.7 Correlation of MW-19A and other wells (MW-19, MW-22 and MW-11)

A lithologic cross-section across wells MW-19A, MW-22 and MW-11 is presented in Figure 12a below. The section reveals to some extend the subsurface geology and the structural system of the north western part of the caldera and partly part of the area around the caldera summit. The lithology of MW-19A shows some similarity to that of some previously studied wells in Menengai. The top most section is

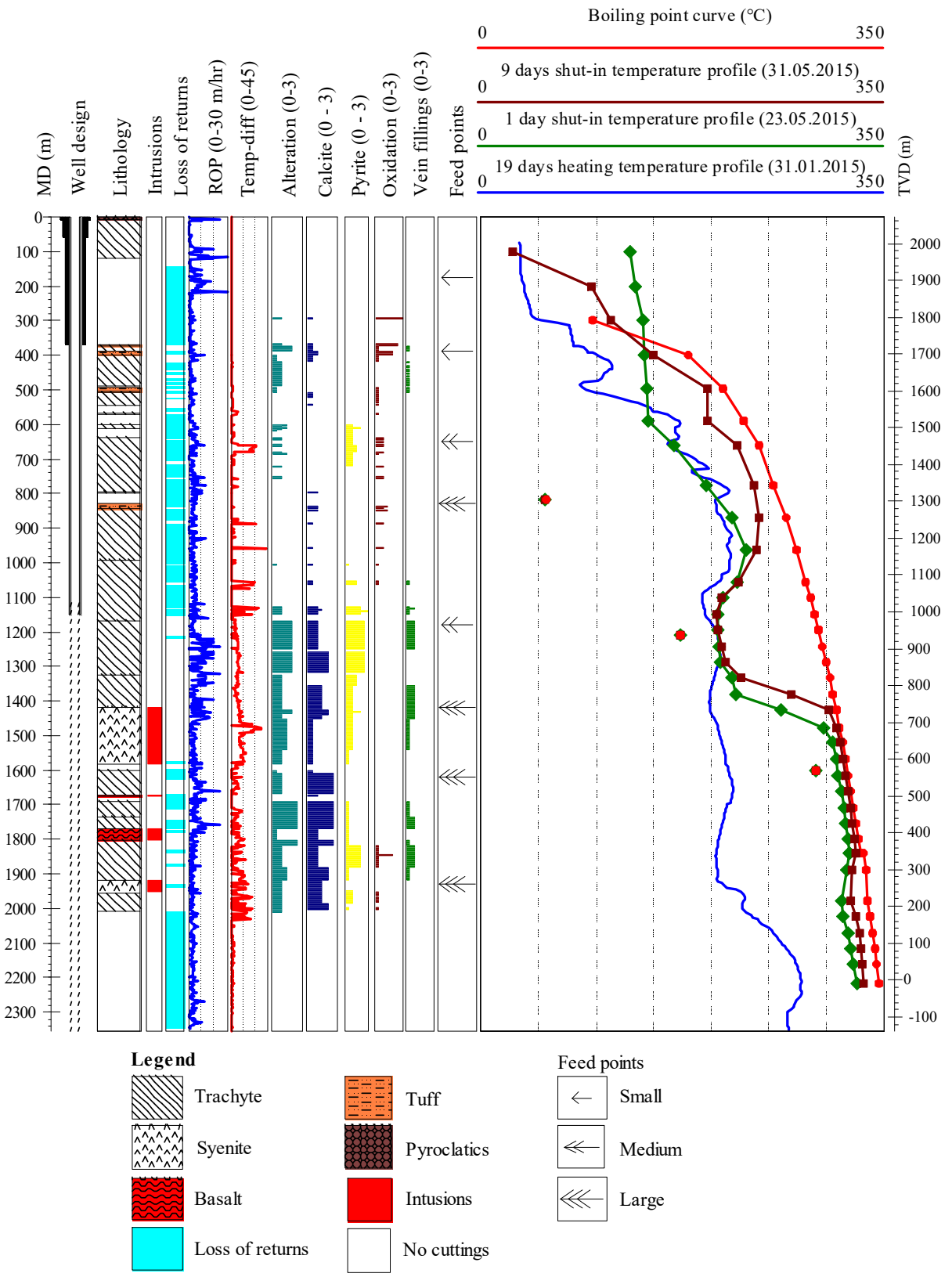

FIGURE 12: Lithology, selected alteration minerals and temperature logs in correlation with aquifers in well MW-19A

mostly composed of mainly unconsolidated pyroclastics. The pyroclastic unit is seen to thin towards the caldera summit area and this can be associated with erosion since the area is topographically high but thickens towards well MW-11.

Four major tuff marker horizons were identified in MW-19A (Figure 13a), which possibly demarcate the boundaries between post-, syn- and pre-caldera volcanics. These markers are defined by tuffs encountered at 368-372 m, 388-400 m, 492-504 m and 836-842 m in MW-19A.

These markers were also encountered in well MW-11, but only one marker horizon was encountered in well MW-22. This is attributed to the total circulation loss experienced in the well, hence no samples were recovered making a correlation difficult. The first two tuff markers are believed to have been emplaced during the syn-caldera activity whilst the other two were emplaced during the pre-caldera phase in tandem with what Leat (1984) reported. Basalt on the other hand was intersected in both wells MW-19A and MW-11, but it was not intersected in MW-22. Kipchumba (2013) presumed that the basaltic intrusions were linked to the Pliocene and Pleistocene subordinate basalts overlying the Miocene phonolites, resting on the Precambrian basement, described by Leat (1984). Syenite was only intersected in well MW-19A and MW-22. MW-11 is a shallow well therefore syenite was not intersected in the well. Syenite in MW-19A was encountered at a shallower depth compared to MW-22. This could possibly be interpreted to have been caused by complex intrusive activity that resulted to the doming underneath the central part of the caldera at 2 km depth (GAB, 2013, Mbia, 2014). From lithologic correlation we can infer the possibility of the existence of normal faults between these three wells.

From the temperature logs (Figure 13b), cold inflow is observed in all the three wells. In well MW-19A it is noted between 1100 and 1380 m, while in MW-22 and MW-11 the cold inflow is seen to occur at

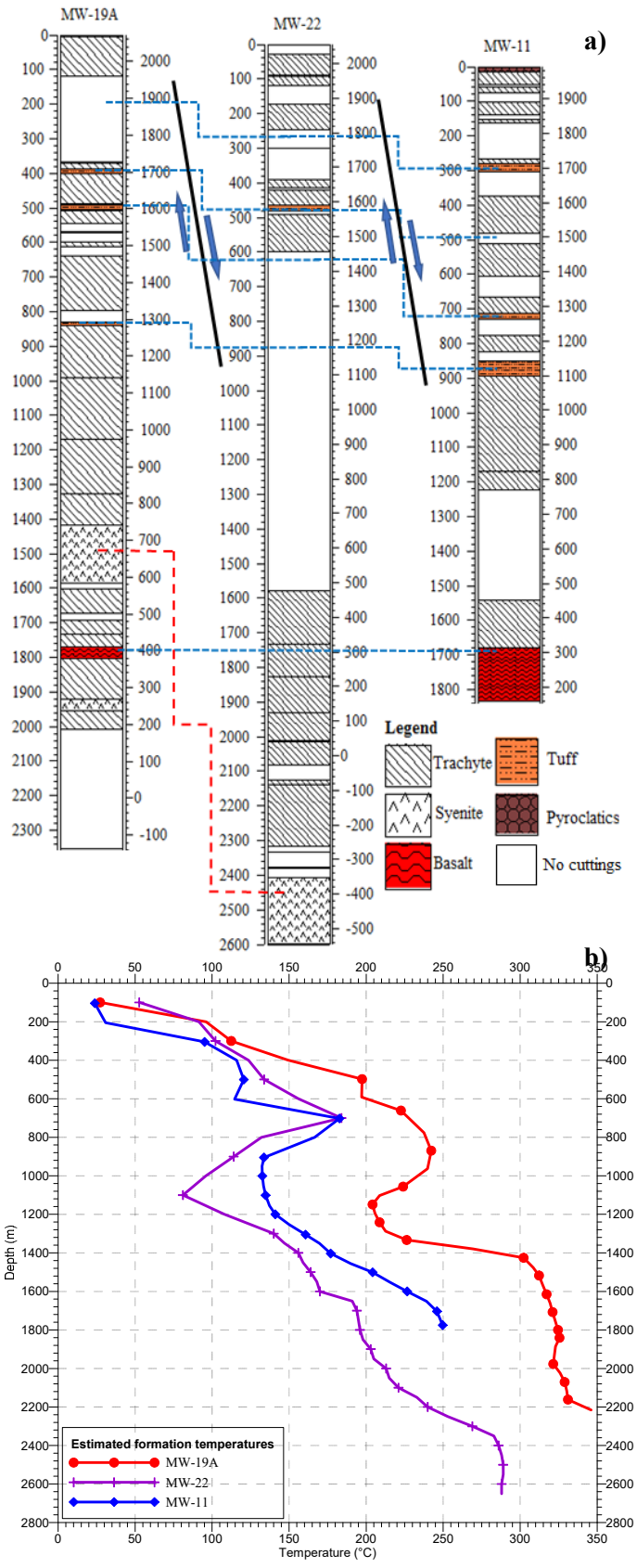

FIGURE 13: Comparison plots of lithologic cross-section (a) and estimated formation temperatures of wells MW-19A, MW-22 and MW-11 (b)

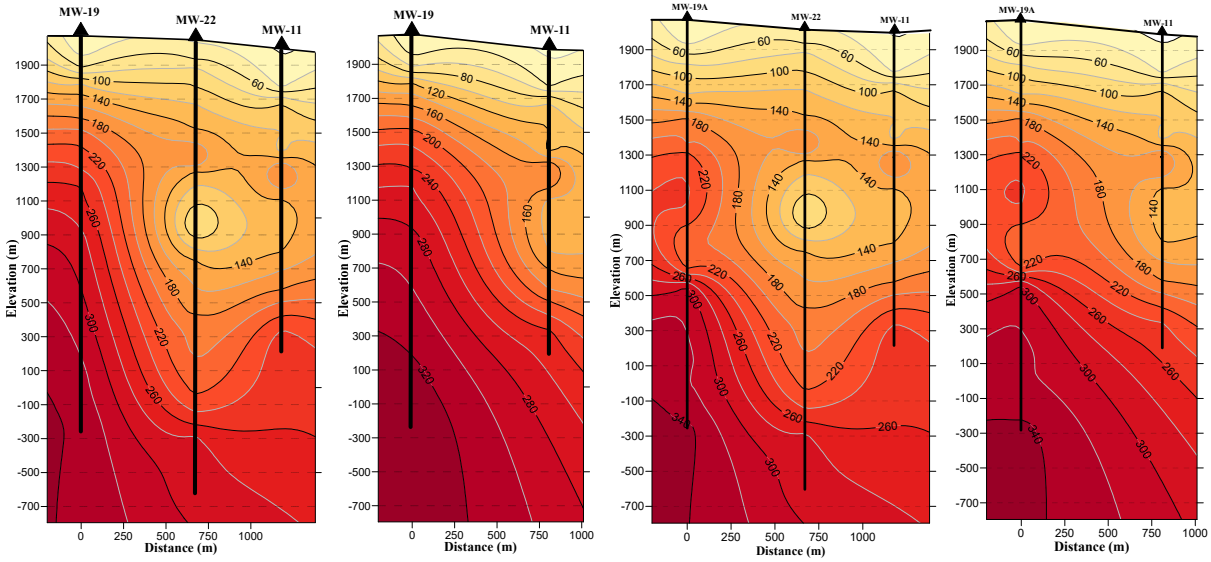

FIGURE 14: Correlation of estimated formation temperatures between wells MW-19, MW-19A, MW-22 and MW-11

almost the same depth but at a shallower depth as compared to MW-19A. This could be attributed to the occurrence of a young underlying structure which could be channelling cold water into the wells.

In an attempt to understand better the sub-surface structural controls in this part of the caldera, a correlation was completed (Figure 14) between the measured formation temperatures in the three wells. From Figures 14a and 14c it is clear that a structure exists between well MW-22 and MW-11 which correlates very well with lithologic interpretation in addition to the persistent loss of circulation experienced in this section of the wells. The cross-section between the vertical well MW-19 and MW-11 (Figure 14a) also confirms the existence of same structure since the cold inflow is seen occurring near well MW-11, while in Figure 14d the effects of the cold inflow in the study well MW-19A drilled towards MW-11 is also seen to occur confirming that a structure is controlling this cold incursion. Therefore, the cold inflow in this wells can be attributed to the extrapolated E-W trending structure (Figure 15) mapped by Strecker et.al. (2013) on the surface near well MW-8 and seems to extend

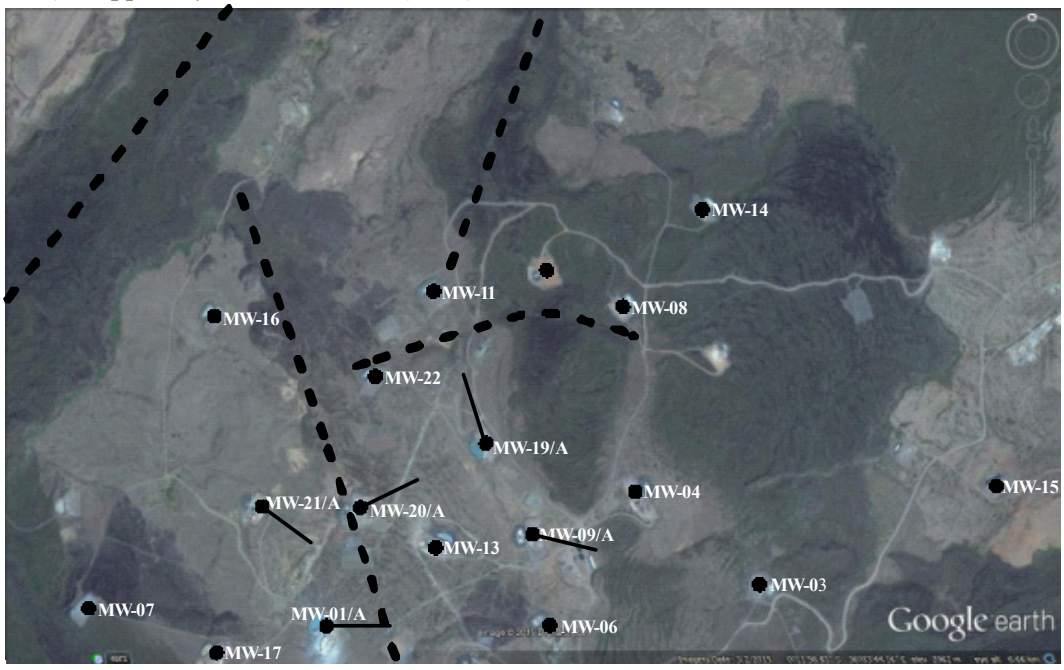

FIGURE 15: Inferred faults north of MW-19/A

towards well MW-11. In the present study, this structure has been extrapolated to form an arc like fissure towards well MW-22 following the topography assumed by the lavas which emanated from the same structure. Another structure that can be associated with the cold inflow is the N-S trending structure north of well MW-11. Since the two structures seem to converge somewhere between well MW-22 and MW-11 it can interpreted that the structures here act as a trap of cold surface water which in turn finds its way to the nearby wells. This is supported by the inferred faults in the lithologic cross-section although more data is deemed necessary to validate the exact positions and the occurrence of these faults. In this light, it is recommended that deeper production casing of the wells around this area need to be considered in future to prevent the cold inflow.

6. DISCUSSION

The lithology of MW-19A was interpreted by analysing the drill cuttings from the well using binocular and petrographic microscopes. From these analyses, five main rock types, pyroclastics, tuffs, trachytes, basalts and syenite were encountered in the well. Pyroclastic rocks form the uppermost 6 m while the underlying formation is formed by trachyte, which is the dominant rock alternating with pyroclastics, tuff, basalt and syenite. The trachyte showed varied textures in the well column, which could indicate different episodes of lava eruptions during the pre-caldera volcanic phase, an observation made by Mibei (2012) and Kipchumba (2013). Four major tuff marker horizons were identified in MW-19A, which possibly demarcate the post, syn- and the pre-caldera volcanics.

Hydrothermal alteration minerals are observed in veins, vugs and vesicles and as a replacement of primary minerals. Their distribution pattern shows prograde alteration with increasing temperature and depth. The hydrothermal alteration minerals observed in this well include, zeolites, chalcedony, calcite, chlorite, pyrite, quartz, epidote, albite, sphene, wollastonite and actinolite. The study of the hydrothermal distribution pattern shows five distinct alteration zones with the first appearance of index alteration minerals coinciding with the upper boundary of each zone. These are: the unaltered zone (0-220 m) that has no alteration related to geothermal activity, suggesting temperatures of <40°C. The second zone (zeolite zone) that extends from 220 to 502 m is the lowest grade mineral alteration zone indicating alteration temperatures of <200°C. It is characterised by high oxidation, chalcedony, calcite and zeolites. The third zone (chlorite-smectite zone), which is marked by the first appearance of chlorite, occurs between 502 and 1100 m. This zone is highly fractured as evidenced by loss of circulation during drilling and is characterised by high oxidation and the presence of pyrite and calcite, suggesting the zone is highly permeable. Quartz-illite-epidote zone is the fourth zone, extending from 1100 to 1358 m. The top depth is marked by the first appearance of quartz, and it is characterised by high intensity of alteration, veining, abundance of pyrite and calcite, indicating that the zone is also highly permeable. The appearance of epidote in this zone indicates that the alteration temperature at 1202 m and below could be above 230°C. Other minerals present in this zone include albite, chlorite, illite, pyrite and calcite. The fifth zone extends from 1358 m to bottom of the well. It is marked by first appearance of actinolite at 1358 m, indicating temperatures above 290°C below this depth. It is characterised by the mineral assemblage of actinolite, wollastonite, epidote and quartz. Other minerals in this zone include pyrite, calcite, chlorite, illite, albite, sphene and oxides.

Observations made from the distribution of hydrothermal alteration minerals, alteration intensity, oxidation trends, veining and temperature logs in well MW-19A indicate that the well is highly permeable and that this permeability acts as fluid flow channels in the rock formations. The presence of abundant calcite and pyrite in the well indicates high past or present permeability. Eight permeable locations were identified in MW-19A and were further grouped into four major aquifers. Circulation losses also play an important part in positioning of the aquifers. The aquifers in well MW-19A are mainly associated with high intensity of alteration, lithological boundaries, highly fractured rocks and associated underlying structures.

Correlation of fluid inclusion analyses, alteration and formation temperatures indicate two geothermal episodes; one of a high temperature geothermal system below 600 m depth to the bottom of the well and a recent second phase of cooling between 1100 and 1400 m. A reversal in formation temperatures is observed between this depth range indicating an incursion of cold fluids. A similar observation is observed in both well MW-22 and MW-11. However, observations made from hydrothermal alteration mineralogy and mineral deposition sequence do not show temperature reversal hence signs of cooling are not evident. This probably implies that the cooling phase observed in this part of the well is a relatively recent event.

7. CONCLUSIONS

The following conclusions can be drawn from the present study on well MW-19A:

I. The lithology of well MW-19A is composed of five different rock units; trachyte, tuff, pyroclastics, basalt and syenite, trachyte being the most dominant.
II. Hydrothermal alteration mineral assemblages and their distribution in the well are mainly controlled by temperature, rock type, fluid composition and permeability. The shallow section of the well is characterized by low-temperature hydrothermal alteration minerals which evolve to form high-temperature ones at greater depths.
III. Five alteration zones were identified, based on hydrothermal mineral assemblages. These include; unaltered zone, zeolite zone, chlorite-smectite zone, quartz-illite-epidote zone and quartz-illite-epidote-wollastonite- actinolite zone.
IV. Well MW-19A is very permeable. Eight permeability zones were identified; these were further grouped to form four main aquifers. Aquifers in this well show close association with circulation losses, temperature logs, fractured formations, lithological contacts between formations and intrusions at depth. High past and present permeability in this well is indicated by the high abundance of pyrite and calcite, high alteration intensity, oxidation, fracturing and occurrence of veins.
V. Stratigraphic correlation of wells MW-19A, MW-22 and MW-11 indicates the possibility of existence of a normal faulting between MW-19A and MW-22, and MW-22 and MW-11.
VI. Comparison between fluid inclusion, alteration, and formation temperature indicate evidence of two geothermal phases in the proximity of the well; the first phase of elevated temperatures succeeded by a cooling phase between 1100 and 1400 m CT. Production casing in this well was positioned at 1150.1 m RKB depth. Therefore, deeper production casing of the wells around this area is recommended to be considered in future to prevent the cold inflow.
VII. Observations made from hydrothermal alteration mineralogy and mineral deposition sequence do not show temperature reversal hence signs of cooling is not evident. This could may imply the cooling of area around the well is a recent event.

ACKNOWLEDGEMENTS

I would like to express my gratitude to the Government of Iceland and the United Nations University Geothermal Training Programme (UNU-GTP) for giving me the opportunity to take part in the six months course. I would also like to thank Geothermal Development Company (GDC) for granting me the oppotunity and time to undertake this noble training.

I am so grateful to the entire UNU-GTP staff: Mr. Lúdvík S. Georgsson, Director, Mr. Ingimar G. Haraldsson, Deputy director, Ms. Málfrídur Ómarsdóttir, Ms. Thórhildur Ísberg and Mr. Markús A. G. Wilde for their guidance, time and help in various capacities that made the whole training successful. I am greatly indebted to my supervisor Dr. Björn S. Hardarson for his patience and time to guide me

throughout the project period. My deep and sincere gratitude to the entire Iceland GeoSurvey (ÍSOR) staff, in particular Dr. Hjalti Franzson, Mr. Sigurður S. Jónsson, Ms. Signý and not forgetting Dr. Eniko Bali of the University of Iceland, for taking time off from their busy schedules to share their skills and knowledge with me. Special thanks also go to Ms. Rósa S. Jónsdóttir, for availing literature material at a time when I needed them.

I would finally like to thank the 2015 UNU-GTP fellows most specifically the geothermal geologists (António Luis Peixoto Franco, Patrick Kant Muanza, Davar Ebrahimi, and Hamda Hassan Wais) for the memorable moments, and continuous support with information and ideas whenever needed.

Special thanks to my entire family and friends back home in Kenya for their encouragement and prayers. My deepest appreciation goes to my wife, Juliet, my son, Ethan for their patience, sacrifice, support and for enduring my long absence.

Lastly, I give thanks to God for his sufficient grace, divine favour and blessings upon my life.

REFERENCES

Browne, P.R.L., 1984: Subsurface stratigraphy and hydrothermal alteration of the eastern section of the Olkaria geothermal field, Kenya. *Proceedings of the 5th New Zealand Geothermal workshop, Auckland, New Zealand,* 33-41.

Browne, P.R.L., and Ellis, A.J., 1970: The Ohaki-Broadlands hydrothermal area, New Zealand: mineralogy and related geochemistry. *Am. J. Sci., 269,* 97-131.

Burke K., and Dewey J., F. 1973: Plume generated triple junctions: Key indicators in applying plate tectonics to old rocks. *J. Geol., 81*, 406-433.

Dunkley, P.N., Smith, M., Allen, D.J. and Darling, W.G., 1993*: The geothermal activity and geology of the northern sector of the Kenya Rift Valley*. British Geological Survey Research Report SC/93/1.

Franzson, H., 1998: Reservoir geology of the Nesjavellir high-temperature field in SW-Iceland. *Proceedings of the 19th Annual PNOC-EDC Geothermal Conference, Manila*, *Philippines*, 13-20.

GAB, 2013: *Geothermal Advisory Board (GAB) report*. Geothermal Development Company (GDC), internal report, 67 pp.

GDC, 2010: *Menengai geothermal prospect, an investigation for its geothermal potential*. Geothermal Development Company (GDC), Nakuru, Kenya, Geothermal Resource Assessment Project, internal report, 44 pp.

GDC, 2015: *Geothermal Development Company (GDC) - A Brief*. Geothermal Development Company (GDC), internal report, 1 pp.

Geotermica Italiana Srl., 1987: *Geothermal reconnaissance survey in the Menengai-Bogoria area of the Kenya Rift Valley.* UN (DTCD)/Government of Kenya, report.

Gichira, J.M., 2012: Joint 1D inversion of MT and TEM data from Menengai geothermal field, Kenya. Report 11 in: *Geothermal training in Iceland 2011.* UNU-GTP, Iceland, 137-167.

Griffith, P.S., 1980: Box fault systems and ramps: A typical association of structures from the eastern shoulder of the Kenya rift. *Geol. Mag., 117,* 579-586.

Griffith, P.S., and Gibson, I.L., 1980: The geology and the petrology of the Hannington trachyphonolite formation, Kenya Rift Valley. *Lithos, 13,* 43-53.

Jones, W.B., 1985: Discussion on geological evolution of trachytic caldera and volcanology of Menengai volcano, Rift Valley, Kenya. *J. Geol. Soc. London, 142,* 711-712.

Jones, W.B., and Lippard, S.J., 1979: New age determination and geology of Kenya rift – Kavirondo rift junction, west Kenya. *J. Geol. Soc. London, 136*, 63 pp.

Kahiga, E. W., 2014: Borehole geology and hydrothermal alteration mineralogy of well MW-13, Menengai geothermal field, Kenya. Report 16 in: *Geothermal training in Iceland 2014*. UNU-GTP, Iceland, 261-294.

KenGen, 2004: *Menengai volcano: Investigations for its geothermal potential.* Kenya Electricity Generating Company (KenGen), Kenya, Geothermal Resource Assessment Project, unpublished report.

Kipchumba, J. L., 2013: Borehole geology and hydrothermal alteration of wells MW-08 and MW-11, Menengai geothermal field, Kenya. Report 10 in: *Geothermal training in Iceland 2013*. UNU-GTP, Iceland, 143-176.

Kipng'ok, J., 2011: Fluid chemistry, feed zones and boiling in the first geothermal exploration well at Menengai, Kenya. Report 15 in: *Geothermal training in Iceland 2011*. UNU-GTP, Iceland, 281-302.

Kristmannsdóttir, H., 1979: Alteration of basaltic rocks by hydrothermal activity at 100-300°C. In: Mortland, M.M., and Farmer, V.C. (editors), *International Clay Conference 1978*. Elsevier Scientific Publishing Co., Amsterdam, 359-367.

Kuria, Z.N., and Woldai, T., 2003*: Groundwater exploration: A case study of the location of well field north of Nakuru town, Rift Valley Province, Kenya*. Unpublished report, 15 pp.

Lagat, J.K., 2004: *Geology, hydrothermal alteration and fluid inclusion studies of the Olkaria Domes geothermal field, Kenya.* University of Iceland, MSc thesis, UNU-GTP, Iceland, report 1, 79 pp.

Lagat, J.K., Arnórsson, S., Franzson, H., 2005: Geology, hydrothermal alteration and fluid inclusion studies of Olkaria Domes geothermal field, Kenya. *Proceedings of the World Geothermal Congress 2005, Antalya, Turkey*, 14 pp

Leat, P.T., 1983: *The structural and geochemical evolution of Menengai caldera volcano, Kenya Rift Valley.* University of Lancaster, UK, PhD thesis, 482 pp.

Leat, P.T., 1984: Geological evolution of the trachytic caldera volcano Menengai, Kenya Rift Valley. *J. Geol. Soc. London, 141,* 1057-1069.

Lopeyok, T.P., 2013: Borehole geology and hydrothermal mineralization of wells MW-09 and MW-11, Menengai geothermal field, Kenya. Report 15 in: *Geothermal training in Iceland 2013*. UNU-GTP, Iceland, 289-324.

MacDonald, R., and Scaillet, B., 2006: The central Kenya peralkaline province: insights into the evolution of peralkaline salic magmas. *Lithos, 91*, 59-73.

MacDonald, R., Bailey, D. K., and Sutherland, D., 1970: Oversaturated peralkaline glassy trachyte from Kenya. *J. Petrology, 11*, 507-517.

Mbia, P.K., 2014: *Sub-surface geology, petrology and hydrothermal alteration of Menengai geothermal field, Kenya*. University of Iceland, MSc thesis, UNU-GTP, Iceland, report 1, 96 pp.

McCall, G.J.H., 1957a: The Menengai caldera, Kenya Colony. *20th International Geological Congress, section 1,* 55-69.

McCall, G.J.H., 1957b: *Geology and groundwater conditions in the Nakuru Area.* Ministry of Water, Hydraulic Branch, Nairobi, technical report 3, 36 pp.

McCall, G.J.H., 1964: Froth flows in Kenya. *Geol. Runsch., 54*, 1148-1195.

McCall, G.J.H., 1967: *Geology of the Nakuru-Thomson's Falls-Lake Hannington area.* Geological Survey of Kenya, report 78, 122 pp.

Mibei, G., 2012: Geology and hydrothermal alteration of Menengai geothermal field. Case study: Wells MW-04 and MW-05. Report 21 in: *Geothermal training in Iceland 2013.* UNU-GTP, Iceland, 442-448.

Omenda, P.A. (editor), 2000: *Ranking of the geothermal prospects in the Kenya Rift Valley*. Contributions from: Lagat, J., Mungania, J., Mariita, N., Onacha, S., Simiyu, S., Opondo, K., Kubo, B.P., Ouma, P., Wetangula, G., and Kollikho, P., KenGen – Kenya Electricity Generating Company, Kenya, internal report, 121 pp.

Omondi, C., 2011: Borehole geology and hydrothermal mineralisation of wells MW-01 and MW-02, Menengai geothermal field, Central Kenya Rift valley. Report 30 in: *Geothermal training in Iceland 2011*. UNU-GTP, Iceland, 737-773.

Reyes, A.G., 2000: *Petrology and mineral alteration in hydrothermal systems. From diagenesis to volcanic catastrophes.* UNU-GTP, Iceland, report 18-1998, 77 pp.

Roedder, E., 1972: Composition of fluid inclusions. In: Fleischer, M. (technical editor), *Data of geochemistry.* Geological survey of America, Washington DC, United States, 199 pp.

Roedder, E., 1984: *Fluid inclusions*. Mineral. Soc. Am., Rev. Mineral., 12, Washington, DC, 7 pp.

Schwonke, F., 2009: *High-resolution airborne thermal infrared remote sensing for geothermal site characterization. Geothermal exploration at* Menengai-*Olbanita prospect, Republic of Kenya*. Bundesanstalt für Geowissenschaften und Rohstoffe (BGR), Germany, 1 pp.

Simiyu, S.M., and Keller, G.R., 1997: Integrated geophysical analysis of the East African plateau from gravity anomalies and recent seismic studies. *Tectonophysics, 278,* 291–314.

Strecker, M.R., Blisniuk, P.M., and Eisbacher, G.H., 1990: Rotation of extension direction in the Central Kenyan Rift. *Geology, 18,* 299.

Strecker, M.R., and Melnick, D., Riedl, S., Njue, L., Mibei, G., Mutonga, M., 2013: *Structural characteristics of Menengai caldera, central Kenya Rift, Republic of Kenya: preliminary assessment of the structural characteristics of Menengai caldera and regions farther north, Nakuru, Kenya.* GDC, Kenya, unpublished report.

Suwai, J.J., 2011: Preliminary reservoir analysis of Menengai geothermal field exploration wells. Report 32 in: *Geothermal training in Iceland 2011*. UNU-GTP, Iceland, 799-826.

APPENDIX I: Characteristic XRD patterns for the clay minerals of well MW-19A

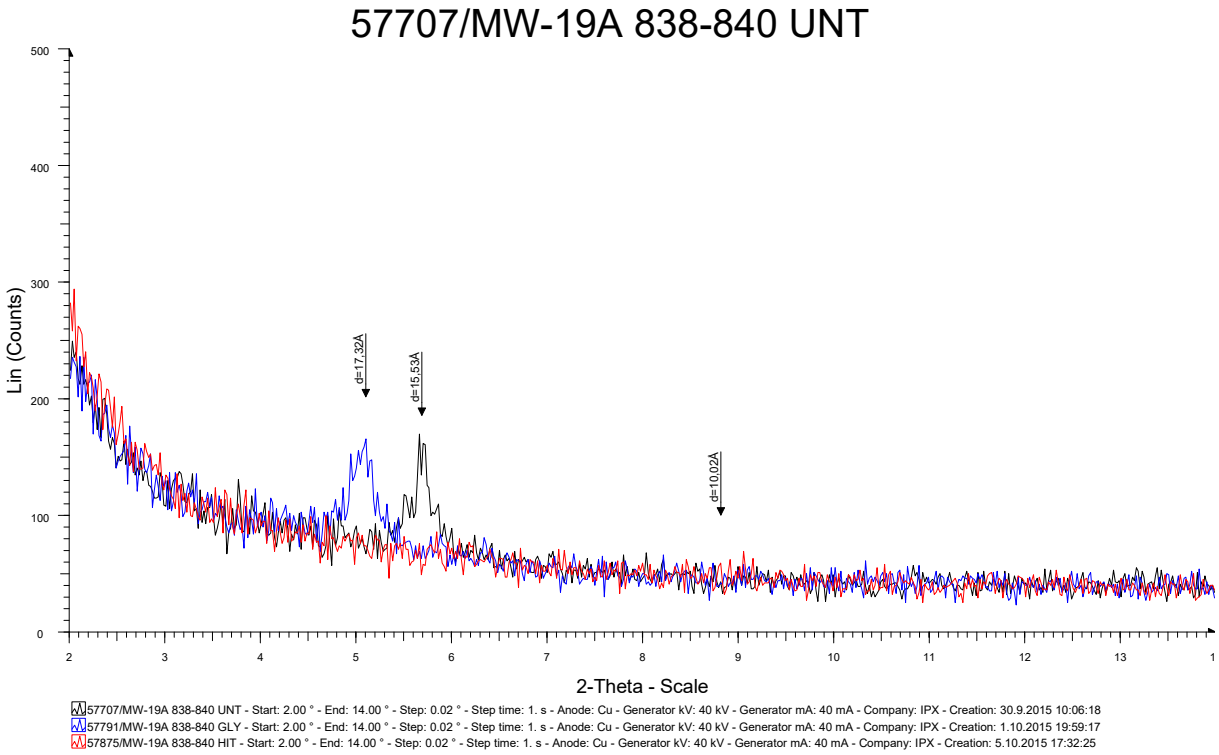

FIGURE 1: Smectite at 838-840 m depth in well MW-19A

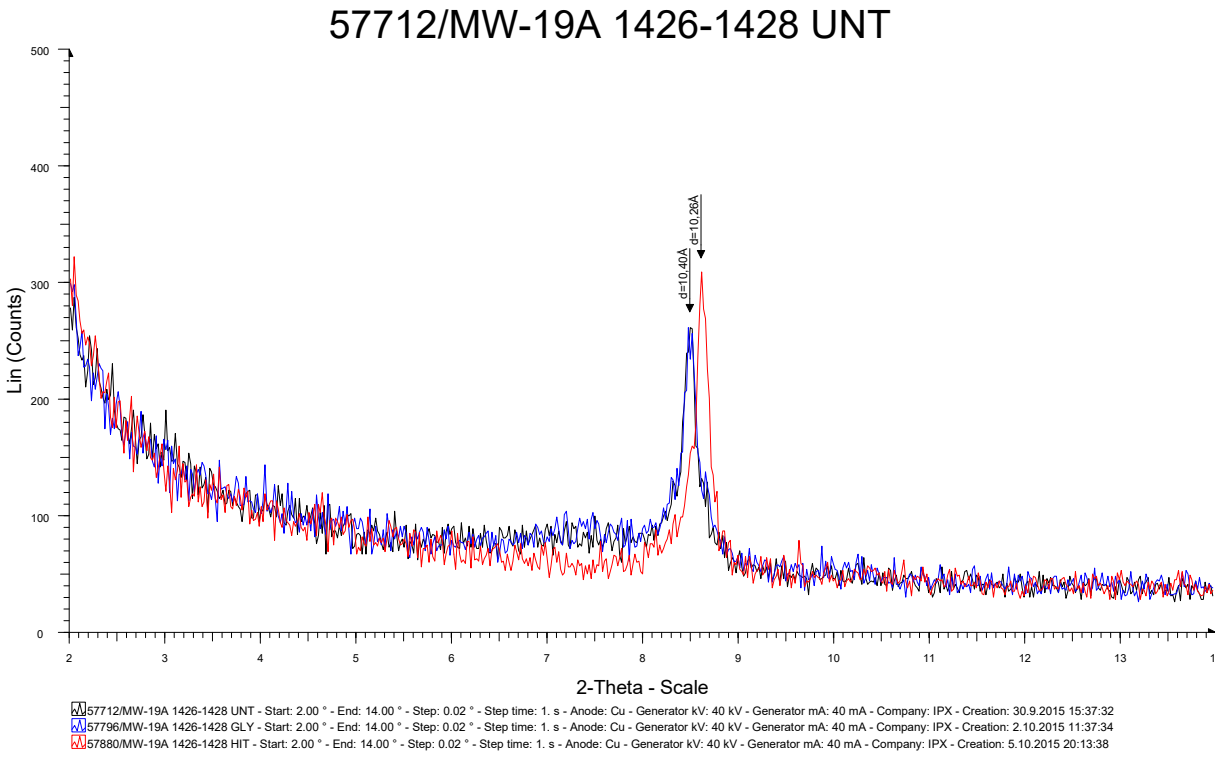

FIGURE 2: Illite at 1426-1428 m depth in well MW-19A

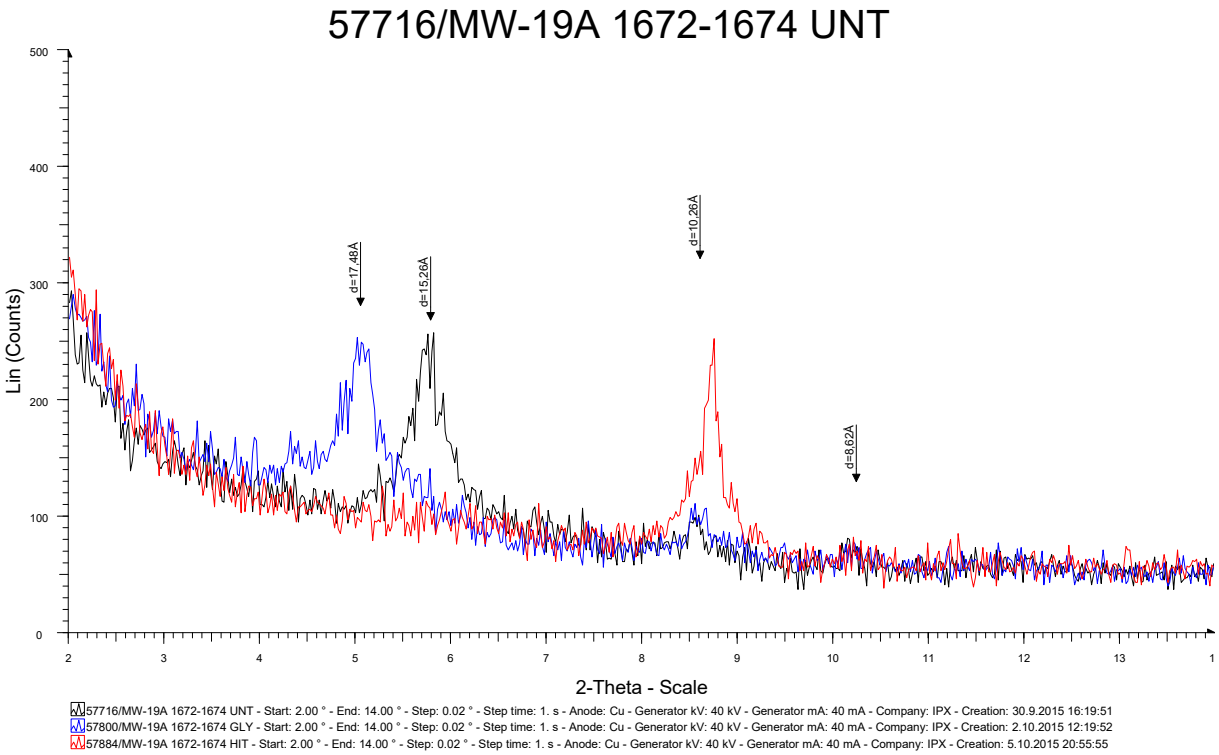

FIGURE 3: Smectite, illite and amphiboles at 1672-1674 m depth in well MW-19A

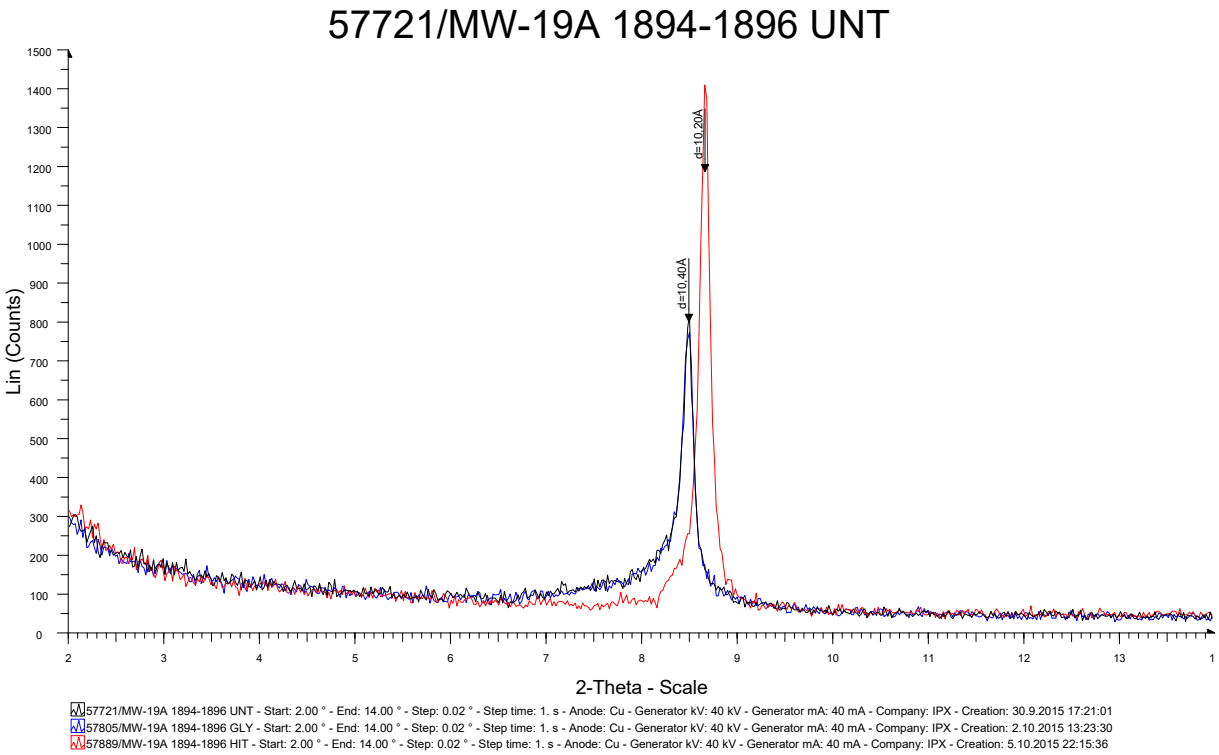

FIGURE 4: Illite at 1894-1896 m depth in well MW-19A

APPENDIX II: Lithology of MW-19A

Post caldera volcanics

0-6 m: *Pyroclastics. G*rey to brownish grey, loose unconsolidated deposits composed of ash and vesicular fragments of pumice lapilli particles, obsidian, glass and lithics of trachytic composition. The alteration minerals observed are oxides (opaques), some calcite and clays, indicating an interaction due to precipitation.

6-120 m: *Fine- to medium-grained trachyte*. Dark grey to greenish grey, fine-to medium-grained porphyritic rock fragments mixed with brownish grey, fine-grained vesicular rock fragments. Chalcedony is observed infilling vesicles while iron oxide is observed to precipitate at the margins and interstices of mafic minerals.

120-368 m: *Loss of returns.*

Possible syn-caldera volcanics

368-372 m: *Tuff.* Reddish brownish fine-grained vesicular rock mixed with dark grey fine-grained rock fragments.

372-388 m: *Fine-grained trachyte.* Dark grey fine-grained equi-granular rock mixed with reddish brown fine-grained vesicular rock fragments. Chalcedony and zeolite (scolesite) are seen infilling veins and vesicles. Iron-oxide precipitates are also evident.

388-400 m: *Tuff.* Reddish brown to grey fine-grained vesicular rock. Chalcedony and zeolite (scolesite) are seen infilling veins and vesicles. Loss of circulation at 388-390 m therefore no cuttings were recovered.

400-488 m: *Fine- to medium-grained trachyte*. Light grey to dark grey fine- to medium-grained equi-granular trachytic lava. Chalcedonic lining is observed on the rock surface and as vein fillings. The formation is moderately fractured and shows low degree of alteration. Loss of returns at 420-422, 426-428, 434-436 and 448-450 m.

488-492 m: *Loss of returns.*

Possible pre-caldera volcanics

492-504 m: *Tuff*. Brownish grey fine-grained vesicular rock. Scolecite and chalcedony linings are observed on the rock surfaces and also infilling vesicles.

504-508 m: *Loss of returns.*

508-544 m: Fine-grained trachyte. Light grey to dark grey fine-grained weakly porphyritic lava. The formation is slightly oxidized and mixed with few tuff fragments.

544-568 m: *Loss of returns.*

568-572 m: *Fine-grained trachyte* Dark grey to greenish grey fine-grained porphyritic lava. The rock shows moderate alteration to greenish clays. Sanidine phenocrysts are seen embedded in the rock matrix.

572-600 m: *Loss of returns.*

600-612 m: *Fine-grained trachyte.* Mixed cuttings composed of brownish grey fine-grained vesicular rock fragments and dark grey to greenish grey porphyritic lava.

612-638 m: *Loss of returns.*

638-796 m: *Fine-grained trachyte.* Light grey fine-grained porphyritic lava. The rock is slightly altered into greenish clays. Feldspathic fragments are also evident (640-642), this could probably be interpreted as a micro-vein. Iron oxide is observed to precipitate at the margins and interstices of mafic minerals. Intermittent returns received in this section. Loss of returns experienced at 644-658, 662-682, 684-686, 688-700, 702-722, 724-752, 766-778, and 780-796 m.

796-798 m: *Fine-grained trachyte.* Dark grey fine-grained rock formation. The rock shows medium intensity of alteration and bleaching effects. Mafic minerals are slightly altered to reddish oxides. Chlorite and abundant calcite dominate this section.

798-836 m: *Loss of returns.*

836-842 m: *Tuff.* Brownish grey fine-grained poorly crystalline vesicular rock. The rock is moderately altered into greenish clays and slightly oxidized.

842-992 m: *Fine-grained trachyte.* Mixed cuttings of brownish grey poorly crystalline rock and light grey fine-grained porphyritic rock fragments. Persistent loss of returns experienced at 842-848, 850-886 and 888-954 m; Partial returns experienced at 954-958, 992-994 m respectively. Therefore, the rock formation here cannot be defined with certainty due to the high rate of mixing.

992-1168 m: *Fine-grained trachyte.* Brownish grey moderately altered fine-grained feldspar rich lava. Phenocrysts of alkali feldspars (sanidine) and possibly quartz are seed embedded in the rock groundmass. Effects of bleaching are evident in some zones. Pyrite cubes seen disseminated on the rock surface indicative of permeability. Loss of circulation experienced at 994-1004, 1008-1054, 1064-1070, 1074-1126 and 1150-1168 m.

1168- 1326 m: *Fine- to medium-grained trachyte*. Dark grey to greenish fine- to medium-grained lava. The formation shows high intensity of alteration. Well-formed pyrite cubes are seen disseminated on the rock groundmass; it is also seen filling veins and vesicles. Quartz grains were first observed at 1202 m, but well developed crystals were noted at 1308 m forming in vesicles. Calcite is also abundant in this section. Loss of circulation at 1250-1258 m, 1316-1326 m.

1326-1418 m: *Fine-grained trachyte.* Light grey to greenish grey fine-grained porphyritic rock showing moderate to high intensity of alteration. Phenocrysts of plagioclase feldspars and pyroxenes are seen embedded in a fine groundmass. High temperature minerals characterize this formation; these include quartz, actinolite, wollastonite, chlorite and epidote. Pyrite is also seen disseminated on the rock surface. Actinolite and epidote are first seen to appear at 1418 and 1436 m respectively.

1418-1584 m: *Syenite intrusion.* Whitish grey medium- to coarse-grained porphyritic rock showing low degree of alteration. The rock also shows some mixing with slight oxidation noted between 1542 and 1584.

1584-1602 m: *Loss of returns*.

1602-1672 m: *Fine-grained trachyte.* Greenish grey to dark grey fine-grained rock showing moderate alteration. The formation shows a bleaching effect giving the rock a mottled texture. Calcite is abundant in this section. Bluish fine-grained rock fragments were observed and were handpicked for further analysis with XRD. Loss of circulation at 1668-1672 m.

1672-1674 m: *Fine-grained basalt.* Dark grey to almost black fine-grained unaltered rock.

1674-1692 m: *Loss of returns*.

1692-1734 m: *Fine-grained trachyte.* Greenish grey to whitish fine-grained porphyritic lava. The rock appears bleached exhibiting a mottled texture with abundant calcite. Pyrite is seen disseminated in the groundmass.

1734-1770 m: *Fine-grained trachyte.* Mixed cuttings composed of greenish grey to whitish fine-grained moderately altered lava with dark grey to black fine-grained rock fragments. Epidote colouration is observable starting at 1750 m and is seen to persist with depth.

1770-1802 m: *Fine-grained basalt*. Dark grey to black fine-grained hypocrystalline rock. Between 1778 and 1780 the rock appears finer. Calcite and pyrite specs characterize this section.

1802-1920 m: *Fine-grained trachyte.* Greenish grey to whitish fine-grained feldspar rich rick. The formation shows high intensity of alteration with abundant calcite and exhibiting a mottled texture. At 1844-1846 the formation is slightly oxidized.

1920-1952 m: *Syenite.* Light grey fine- to medium-grained lava showing low to medium degree of alteration. Loss of circulation experienced 1924-126, 1928-1930 and 1946-1952.

1954-2008 m: *Fine-grained trachyte.* Brownish to greenish grey fine-grained lava. The rock is fractured and shows effects of bleaching into whitish clays. The rock exhibits low intensity of alteration and has abundant calcite. Major loss zones encountered at 1954-1956, 1960-1962, 1966-1972, 1974-1986, 1988-1992 and 1994-2004 m.

2008-2354 m: *Loss of returns*.

UNITED NATIONS UNIVERSITY
UNU-GTP
Geothermal Training Programme

Orkustofnun, Grensasvegur 9,
IS-108 Reykjavik, Iceland

Reports 2015
Number 27

PRELIMINARY ENVIRONMENTAL COST ACCOUNTING FOR OLKARIA IV GEOTHERMAL PROJECT

Elizabeth Mwangi-Gachau
Kenya Electricity Generating Company Limited
P.O. Box 785
20117 – Naivasha.
KENYA
ewmwangi7@gmail.com

ABSTRACT

Environmental impact is one of the most significant considerations in the evaluation of economic development projects, yet it is a difficult factor to measure and to monetize. Regularly, decisions are made by governments on new development proposals that have significant economic and environmental implications, yet the economics of environmental impacts are frequently ignored. Decision-making in the areas of energy and environment calls increasingly for a better evaluation of the possible impacts of any envisaged policy and measure. In such decision-making, the benefits of geothermal energy are made explicit, while the ensuing environmental impacts are merely identified and qualitatively described. This paper underscores the importance of valuing and monetizing environmental impacts that are associated with the development of geothermal energy. A preliminary economic accounting of the common environmental impacts of Olkaria IV geothermal project was conducted. The results of this study recommend that a comprehensive economic valuation study be carried out on all the environmental impacts that are associated with the development of the larger Olkaria geothermal project.

1. INTRODUCTION

Environmental impact is one of the most significant considerations in the evaluation of economic development projects, yet it is a difficult factor to measure and to monetize. The idea of sustainable development has led to a search for ways in which development projects can be assessed, accounting simultaneously for project outputs and environmental effects. This search recognizes the fact that there are trade-offs between economic development and the goods and services provided by the environment (Dixon and Hufschmidt, 1986). Nevertheless, many environmental cost assessments seriously understate the economic value of environmental impacts, a problem that has yet to be fully resolved (Callan and Thomas, 2013). In order to assess and ultimately determine if a project should proceed, and if so under what conditions, methods are required that allow comparisons of the direct project inputs and outputs and environmental effects (Dixon and Hufschmidt, 1986). Development of geothermal energy at Olkaria is currently accelerated, in order to meet the nation's ever increasing demand for power. Inevitably, this development is occurring against a backdrop of ecologically sensitive ecosystems; the Hell's Gate National Park and Lake Naivasha, which is a Ramsar site. Olkaria IV geothermal power plant was commissioned in October 2014 and it has an installed capacity of 140 MW.

It was selected for this study because of its relatively isolated location from the other power plants, making it ideal to identify, quantify and value its specific environmental impacts.

The aim of this study was to reveal the hidden costs of the environmental impacts that are associated with the development of Olkaria IV geothermal project, in order to broaden decision making in the application of the appropriate mitigation measures.

2. ECONOMIC VALUATION OF ENVIRONMENTAL IMPACTS

2.1 The concept of total economic value

2.1.1 Ecosystems and economic values

According to MNRE (2008), a general premise that underlies economic valuation of environmental impacts of projects is that the environment (or ecosystems) produce(s) multiple goods and services of a large variety of nature, which are 'valued' by human beings as they contribute to human welfare and well-being. Changes in the flow of goods and services provided by the environment are occasionally triggered by natural events, e.g. tropical storms, and may adversely impact the flow of agricultural outputs. Such changes may also be triggered by human actions, e.g. development policies and projects, which may positively or negatively impact the flow of goods and services produced by the environment. In such cases, the main issue is to identify and quantify the changes in the flow of goods and services produced by the environment, which are impacted by a development project, and then to monetize these changes into costs or benefits.

2.1.2 Total economic value and its components

Currently, the generally recognized suitable framework for guiding the economic valuation of environmental impacts is the concept of total economic value. Total economic value of ecosystem goods and services is made of different types of economic values, each corresponding to the respective use that is made of the environment. Figure 1 is an illustration of total economic value and its components.

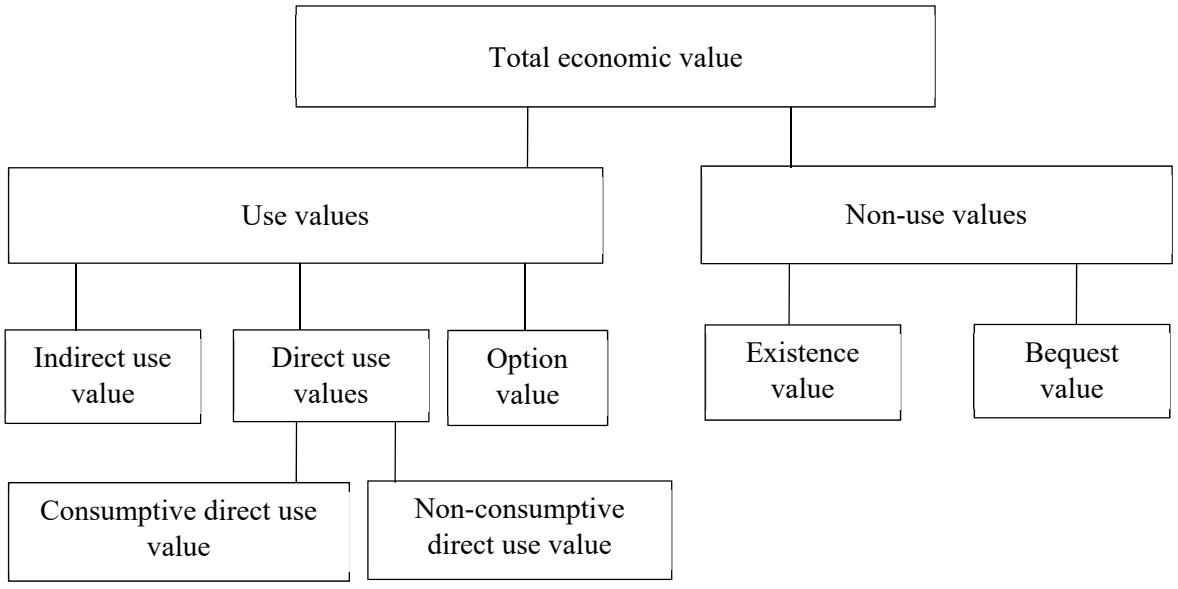

FIGURE 1: Total economic value and its components
(MNRE, 2008)

The distinction between use and non-use values is described below (MNRE, 2008; Goulder and Kennedy, 2009).

Use values
They relate to the actual use of the good or service produced by the environment. Use values are sub-divided into direct use values, indirect use value, and option value (MNRE, 2008). Direct use values are further sub-divided into consumptive direct use value and non-consumptive direct use value.

Consumptive direct use value
Refers to the economic value of those goods and services produced by the environment which are actually extracted for the purpose of consumption. Examples of consumptive direct use include:

- Harvesting of fish either for commercial or recreational purposes;
- Extracting of timber or non-timber forest products;
- Harvesting of fruits from fruit trees;
- Abstracting surface water or groundwater for domestic, agricultural, or industrial purposes.

Non-consumptive direct use value
Refers to the economic value of those goods and services produced by the environment without actual extraction or abstraction taking place. Examples of non-consumptive direct use include:

- Using surface waters for purpose of transportation;
- Recreational swimming;
- Bird watching in a protected area;
- Hydro-power production (in cases where the water is not diverted).

The sum of consumptive and non-consumptive direct use values defines the direct use value of the environment.

Indirect use value
Results from the use of services provided by the environment and ecosystems. Examples of indirect use of services include:

- Storm and flooding protection services provided by mangrove swamps;
- Water purification services provided by wetlands;
- Watershed protection services provided by forests;
- Carbon sequestration services provided by forests.

Option value
Refers to the benefit of potentially using a resource at a later point in the future. For instance, protected areas may be set aside for conservation purposes not only for the direct and indirect values they may currently generate, but also for keeping the option possible (in the future) to conduct these or other activities.

The sum of direct, indirect, and option values defines the use value of the environment, as shown in Figure 2 below:

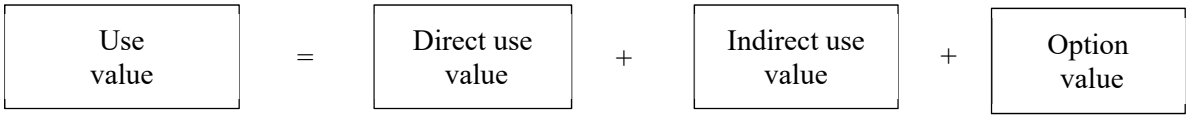

FIGURE 2: Use value (MNRE, 2008)

Non-use or passive use values
Refer to the fact that some individuals in our societies obtain satisfaction (welfare) simply from knowing that the existing flow of goods and services produced by the environment is maintained as it currently is, even if there is no current or potential use of these goods and services by themselves (EV, 2000). These values are divided into what is called existence value and bequest value.

Existence value
It is the non-use value that people place on simply knowing that something exists, even if they will never see it or use it.

Bequest value
It is the value that people place on knowing that future generations will have the option to enjoy something.

The sum of bequest and existence values defines the non-use value of the environment as displayed in Figure 3 below:

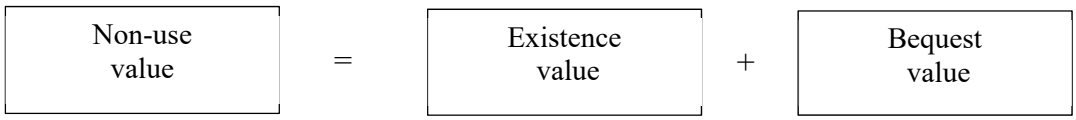

FIGURE 3: Non-use value (MNRE, 2008)

The sum of use and non-use values defines the total economic value of the goods and services produced (delivered) by the environment, Figure 4 below:

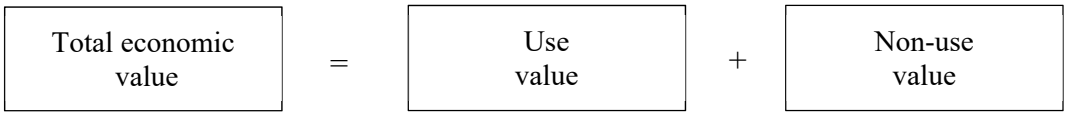

FIGURE 4: Total economic value (MNRE, 2008)

2.2 Economic valuation methods and techniques

Economic valuation of environmental goods and services or ecosystem services is quite difficult and fraught with uncertainties. Every day through the choices we make, we implicitly value environmental goods and services. However, as ecosystem goods and services are in most cases non-market goods that value is very low (Costanza et al., 1997, Field and Field, 2002). Traditional project appraisals consisted of economic evaluations accompanied by environmental impact statements, where the environmental impact was not monetized. In the recent past though, new economic approaches have been devised that place monetary values on some environmental effects and place them in the overall balance of benefits and costs, enabling a more comprehensive assessment of a project's net benefits (Dixon and Hufschmidt, 1986). Nevertheless, many environmental cost assessments seriously understate the value of environmental impacts, a problem that has yet to be fully resolved (Callan and Thomas, 2013). Since the impact of economic development on ecosystem services is, in many cases, affecting goods and services that are not traded in markets (Pearce et al. (2006), the economic assessment of ecosystem services necessitates creating hypothetical markets. To do so, economists try to identify people's willingness-to-pay (WTP) for those services or willingness-to-accept (WTA) compensation for losing these services in artificial markets (Munda, 1996).

Different economic valuation techniques are used to undertake the economic valuation of environmental impacts (EV, 2000; Pearce et al., 2006; MNRE, 2008). The following methodologies are presented and described below:

- Revealed preference methodologies;
- Stated preference methodologies;
- Benefit-transfer methodology.

2.2.1 Revealed preference methodologies

The methods entail the valuation of non-market impacts by observing actual behaviour, particularly purchases made in actual markets. The economic costs associated with this behaviour may *reveal* the extent to which individuals respond to a change in environmental quality (MNRE, 2008). The methods considered to fall under this category include: market price, productivity, hedonic pricing, travel cost, averting or defensive behaviour, cost of illness, as well as damage cost avoided/replacement cost/and substitute cost methods. The market price method estimates the economic value of ecosystem products or services that are bought and sold in commercial markets. The market price method can be used to value changes in either the quantity or quality of a good or service. The productivity method, also referred to as the net factor income or derived value method, is used to estimate the economic value of ecosystem products or services that contribute to the production of commercially marketed goods. It is applied in cases where the products or services of an ecosystem are used, along with other inputs, to produce a marketed good, e.g. water quality affects the productivity of irrigated agricultural crops. The hedonic pricing method is used to estimate economic values for ecosystem or environmental services that are directly associated with specific market prices. Mostly, it is applied to variations in housing prices that reflect the value of local environmental attributes like a scenic beach or mountain view (EV, 2000). Travel cost methodology attempts to estimate the economic value of sites which are essentially used for recreation purposes (such as beaches, coral reefs, or protected areas). The basic premise of the method is that the time and travel cost expenses that people incur to visit an unpriced recreation site represent the willingness to pay for that recreational site. Averting or defensive behaviour methods are based on the notion that individuals and households can defend themselves from a non-market bad, such as pollution or noise by selecting costlier types of behaviour e.g. installation of double-glazed windows in houses to avoid exposure to noise from road traffic or airports (Pearce et al., 2006; MNRE, 2008). Cost of illness methodology relies on estimating expenditure associated with treating illnesses and diseases necessitated by changes in environmental quality e.g. respiratory diseases due to dust emissions. Damage cost avoided, replacement cost, and substitute cost methods are related methods that estimate values of ecosystem services based on either the costs of avoiding damages due to lost services, the cost of replacing ecosystem services, or the cost of providing substitute services. For example, valuing storm protection services of coastal wetlands by measuring the cost of building retaining walls (EV, 2000).

2.2.2 Stated preference methodologies

Stated preference methods offer a direct survey approach to estimate willingness-to-pay for changes in provision of (non-market) goods. They seek to estimate economic values by directly asking individuals to *state* such willingness-to-pay, based on a hypothetical scenario. It is only stated preferences methodologies that can be used to assess non-use economic values (EV, 2000; MNRE, 2008). There are two types of stated preferences methodologies: the contingent valuation methodology and the choice modelling methodology. The contingent valuation method involves directly asking people, in a survey, how much they would be willing to pay for, or amount of compensation they would be willing to accept to give up, specific environmental services. It is called "contingent" valuation, because people are asked to state their willingness to pay, *contingent* on a specific hypothetical scenario and description of the environmental service. Choice modelling methodology estimates economic values for virtually any ecosystem or environmental service. It is based on asking people to make trade-offs among sets of ecosystem or environmental services or characteristics. It does not directly ask for willingness to pay,

this is inferred from trade-offs that include cost as an attribute (EV, 2000). Choice modelling is a useful stated preference method where an environmental problem is complex or multidimensional, and proposed policy options are numerous and also provide different combinations of these multiple dimensions (Pearce et al., 2006; MNRE, 2008).

2.2.3 Benefit-transfer methodology

Benefit-transfer is the adaptation and use of economic information derived from a specific site(s) under certain resource and policy conditions to a site with similar resources and conditions. The site with data is typically called the "study" site, while the site to which data are transferred is called the "policy" site. Benefit transfer is a practical way to evaluate management and policy impacts when primary research is not possible or justified because of budget constraints, time limitations, or resource impacts that are expected to be low or insignificant (Rosenberger and Loomis, 2001).

2.3 Economic valuation of environmental impacts

Decision-making in energy and environment calls increasingly for a better evaluation of the possible impacts of any envisaged policy and measure, such as a renewable electricity target or internalisation of external costs. The consideration of the external costs caused by energy production and consumption, i.e. the monetary quantification of its social-environmental damage, is one way of re-balancing social and environmental dimensions with purely economic ones. An external cost, or an externality, arises when the social or economic activities of one group of persons have an impact on another group and when that impact is not fully accounted, or compensated for, by the first group (EC, 2013). Many types of environmental impacts are multidimensional in character. Consequently, an environmental asset that is affected by a proposed project or policy often will give rise to changes in component attributes, each of which command distinct valuation techniques (Pearce et al., 2006).

Economic valuation of environmental impacts can be viewed as a four-step exercise as shown in Figure 5. First, the most important environmental effects need to be identified. Next, the effects have to be quantified. The quantified changes must then be valued and monetary values placed on them. The last step is the actual economic analysis. Thus, economic valuation of a project's environmental impacts can only be as good as the identification and physical quantification of its resultant impacts on the environment (Dixon and Hufschmidt, 1986; MNRE, 2008).

2.4 Environmental impacts of geothermal projects

Maintaining the natural environment and the integrity of underlying ecosystems is an important consideration for any significant development project. Fundamentally, the concepts of environmental and social sustainability are now widely recognized by policymakers, development institutions, and the society at large (ESMAP/WB, 2012). Shortall, et al. (2015) emphasize the need to monitor all the environmental, social and economic impacts of developing geothermal energy in order to ensure its sustainability. Geothermal energy is generally accepted as being an environmentally benign energy source, especially in comparison to fossil fuel energy sources (Hunt, 2001). Nevertheless, like any infrastructure development, it has its own environmental impacts and risks that have to be assessed, mitigated and managed, in order to advance its utilisation (ESMAP/WB, 2012). Environmental effects vary considerably from one geothermal field and power plant to another, due to the influence of geology and structure of the underground, the nature of the reservoir, as well as the type of utilization (Kristmannsdóttir, H. and Ármannsson, H., 2003). According to Thayer (1980), geothermal plants are unique among thermal power plants since all steps of the fuel cycle are localized at the site of production facilities. A sustainable geothermal energy development is described as one that generates positive impacts to the society, is environmentally benign, demonstrates economic and financial viability, is

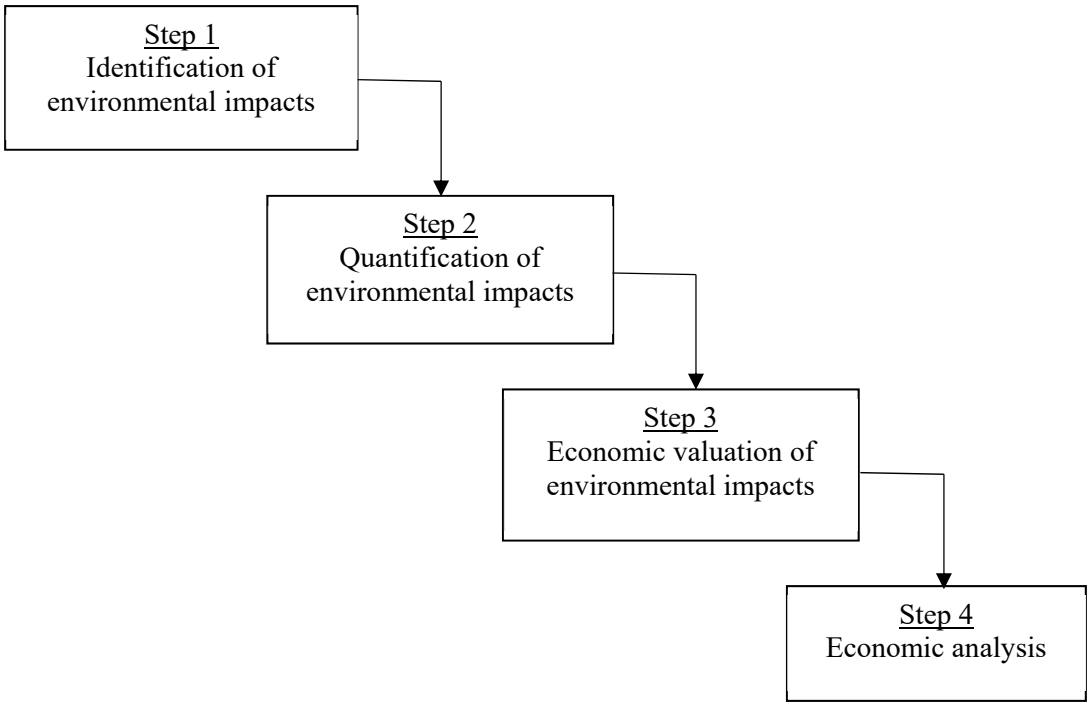

FIGURE 5: Steps of economic valuation of environmental impacts (modified from MNRE, 2008)

efficiently generated and utilised, as well as equitably distributed (Shortall, et al. 2015). The common environmental impacts that are associated with exploitation of geothermal energy are discussed below.

2.4.1 Landscape impacts

Power plants are built on the site of geothermal reservoirs, since long fluid transmission pipes would be expensive and result in pressure and temperature losses. Land is required for well pads, steam pipelines, power plants, cooling towers and electrical switchyards. Geothermal fields are often situated in places of outstanding natural beauty like national parks and forests, where tourism and historic interest are important. The presence of drilling activity, pipelines, transmission lines and electric generating facilities introduce forms, shapes, and colours that are inconsistent with the natural landscape. Installed pipelines can disrupt natural habitats and the surface morphology. Removal of vegetative cover and exposure of raw soil in unnatural land forms causes visual aesthetic loses. This implies that recreation areas may have to yield to extractive activities as well as electric generation plants and transmission lines, all of which could have a negative impact on the outdoor recreation experience. Development of a geothermal reservoir could therefore impose aesthetic damages upon the visitors to the region (Thayer, 1980; Hunt, 2001; Kristmannsdóttir and Ármannsson, 2003; ESMAP/WB, 2012, Mwangi-Gachau, 2012).

2.4.2 Mass withdrawal

Large-scale exploitation of liquid-dominated high temperature geothermal systems involves withdrawal of large volumes of geothermal fluids. This can lead to the degradation, disappearance, shift or transformation of thermal, and common touristic and cultural features like hot springs, hot pools, mud pools, fumaroles and sinter terraces. Surface subsidence can also result from the reduction in formation pore pressure due to a compaction in rock formations that have high compressibility. Such subsidence can compromise the stability of pipelines, drains and well casings in a geothermal field, as well as residential buildings (Hunt, 2001; Kristmannsdóttir and Ármannsson, 2003).

2.4.3 Air pollution

Geothermal fluids (steam and hot water) usually contain gases like carbon dioxide (CO_2), hydrogen sulphide (H_2S), ammonia (NH_3) and methane (CH_4), which contribute to global warming, acid rain and nuisance smells if released into the atmosphere. They also contain trace amounts of mercury (Hg) and boron (B). The emissions are mainly from the gas exhausters of power plants that are discharged through the cooling towers. The impacts of H_2S discharge depend on local topography, wind patterns and land use. The gas can be highly toxic, causing eye irritation and respiratory damage in humans and animals, and has an unpleasant odour. Ammonia can cause irritation of the eyes, nasal passages and respiratory tract at concentrations of 5 to 32 ppm. Ingesting or inhaling mercury can cause neurological disorders. Boron irritates the skin and mucus membranes, and is also phytotoxic at relatively low concentrations. The metals may be deposited on soils and if leached, they may cause groundwater contamination (Hunt, 2001; ESMAP/WB, 2012).

2.4.4 Disposal of waste fluids

Discharge of waste geothermal fluids is a potential source of chemical and thermal pollution. Waste water from cooling towers has a higher temperature than ambient water, therefore constitutes a potential thermal pollutant when discharged to nearby streams or lakes. Untreated waste geothermal fluids lead to chemical poisoning of fish, birds and animals living near the water since toxic substances bio-accumulate through the food chain. Surface disposal of large volumes of waste geothermal fluids may cause soil erosion and contamination of groundwater sources (Hunt, 2001; ESMAP/WB, 2012).

2.4.5 Noise pollution

Noise pollution accompanies industrial development and has a potential impact of instigating a loss of natural silence and opportunity for solitude. The noise associated with operating geothermal electricity power plants could be a problem to humans and animals living nearby. High noise levels are normally generated from drilling and well testing activities (Thayer, 1980; Hunt, 2001; ESMAP/WB, 2012), as illustrated below:

- Air drilling – 120 dBa (85 dBa with appropriate muffling);
- Discharging wells – 120 dBa;
- Well testing – 70-110 dBa (with silencers);
- Earth moving machinery during construction – 90 dBa;
- Well bleeding – 85 dBa (65 dBa with rock muffler);
- Mud drilling – 80 dBa;
- Diesel engines – 45-55 dBa (with suitable muffling).

2.4.6 Landslides

Earth moving activities in areas of high relief and steep terrain could potentially cause landslide hazards. Landslides may also be triggered naturally by heavy rain or earthquakes. Landslides are dangerous in that they may place constraints on the placement of wells and other constructions (Ármannsson and Kristmannsdóttir 1992; Hunt, 2001).

2.4.7 Induced seismicity/earthquakes

The majority of high-temperature geothermal systems lie in tectonically active regions with high stress levels in the upper parts of the crust, which are manifested by active faulting and numerous earthquakes. High wellhead reinjection pressures increase the pore pressure in deep existing fractures, allowing a sudden release of stress that results in an earthquake (Hunt, 2001). Enhanced geothermal system projects are perceived to induce some earthquakes through the “fracking” process, i.e. creation of an artificial underground reservoir by re-injecting highly pressured cold water (ESMAP/WB, 2012).

3. DEVELOPMENT OF OLKARIA GEOTHERMAL PROJECT

3.1 Olkaria geothermal power project

The Kenya Electricity Generating Company Limited (KenGen) is a state corporation that supplies the bulk of the power, about 80%, to the national electricity grid. The company's power generation mix comprises hydro, thermal, geothermal and wind resources (KenGen, 2010). Currently, KenGen operates four power plants and nine wellhead units at Olkaria geothermal field, generating a total of 485.6 MW. The Olkaria I (commissioned between 1981 and 1985) and Olkaria II (commissioned in 2003 and 2010) power stations generate 45 and 105 MW of electricity, respectively. The Olkaria III geothermal power station, which generates 102 MW of electricity, belongs to an independent power producer (IPP), Orpower 4 Limited. In addition, the new Olkaria IV and Olkaria I Units 4 and 5 power plants were commissioned in 2014, with an installed capacity of 140 MW each. Olkaria I, II and III and three wellhead units are situated inside Hell's Gate National Park. The park was gazetted in 1984, three years after the commissioning of Olkaria I power plant. The Park is known for its scenery and wide variety of wildlife, including the common zebra (*Equus burchelli*), Masai giraffe (*Giraffa camelopardalis*), Thomsons gazelle (*Gazella thomsonii*), leopard (*Panthera pardus*), Klipspringer (*Oreotragus oreotragus*), African buffalo (*Syncerus caffer*), common eland (*Taurotragus oryx*), various raptors i.e. Ruppell's vulture (*Gyps rueppellii*), white backed vulture (*Gyps africanus*), among other species of wildlife. The beautiful scenery includes the Fischer's Tower and Central Tower columns and Hell's Gate Gorge. The most common vegetation types include *Hyperrhenia, Digitaria, Themeda* grasses and *Tarchonanthus* and *Acacia* shrubs (Mwangi-Gachau, 2012).

Olkaria IV power plant is located on KenGen's land, about 7 km from the Olkaria I power station, Figure 6. This land constitutes an important dispersal area for wildlife from Hell's Gate National Park. Furthermore, KenGen utilizes water for its drilling and domestic activities from the nearby Lake Naivasha, which is a wetland of international importance according to the Ramsar Convention on Wetlands. KenGen is implementing plans to increase geothermal power production within the Greater Olkaria Geothermal Area (GOGA) by optimizing the current potential of the Olkaria Domes and Olkaria East area. These plans will lead to the establishment of new power plants to be named Olkaria V and Olkaria I Unit 6 power stations, with an estimated total installed capacity of 210 MW (KenGen, 2010).

FIGURE 6: Olkaria IV power plant

3.2 Common environmental impacts of Olkaria geothermal project

The common environmental impacts which are associated with the development of Olkaria IV geothermal project and their respective mitigation measures are discussed below:

3.2.1 Impact on flora

Clearing of vegetation was inevitable to allow for construction of the required infrastructure to support the Olkaria IV power plant. This led to a disturbance of the significant ecosystem that provides the habitat, feeding and breeding grounds for fauna within the park. To minimize the impact, clearing of vegetation was done selectively and was strictly controlled and limited to what was absolutely necessary. Disturbed areas were later re-vegetated with indigenous vegetation that include *Hyperrhenia, Digitaria,*

Themeda grasses, *Tarchonanthus* shrubs, and *Acacia* trees. Furthermore, directional drilling that provides for multiple wells on the same pad was implemented to reduce the surface area of cleared vegetation. Drilling multiple wells on a single pad significantly minimizes the total cleared surface area. One of the pads with multiple wells include OW-915, which has three wells comprising one vertical and two directional wells as shown in Figure 7.

FIGURE 7: Olkaria well-915 pad with three wells

3.2.2 Impact on fauna

The project lies within Hell's Gate National Park and Olkaria domes field. Both areas are environmentally significant for biodiversity conservation, the latter being an important wildlife dispersal area. The environmental impact results from loss of habitat due to vegetation clearing and bush fires; loss of migratory corridors through the installation of structures such as elevated steam pipes and power plants; use of fences to restrict animal movement; and potential drowning of animals in brine ponds. Consequently, the following mitigation measures were implemented to reduce the stated impacts:

- Animal census and animal migratory route studies are conducted regularly by KenGen and Kenya Wildlife Service (KWS) to determine the wildlife population as well as map their respective movement routes. The studies generate information that is used to locate and design animal friendly steam pipes to avoid interfering with the animals' routes in search of water and a habitat for breeding, feeding and hiding. Figures 8 and 9 show existing giraffe and buffalo/zebra pass loops, respectively;
- Clearing of vegetation is reduced to what is absolutely necessary and rehabilitation is carried out immediately on the affected areas to restore the vegetation;
- Fences and other enclosures that reduce the grazing range and restrict the movement of wild animals have been installed to secure only critical operational areas such as power plants, offices, and temporary brine holding ponds, to avoid restricting the animals too much.

FIGURE 8: A giraffe pass loop

FIGURE 9: A buffalo and zebra pass loop

3.2.3 Exposure to high noise and vibration levels

Emission of uncontrolled noise is a danger to human health and causes damage to the environment. The maximum permissible noise level for residential areas near such a construction site is 60 dBa during the

day (6a.m. – 6p.m.) and 35 dBa at night (6p.m. – 6a.m.) (NEMA, 2009). Noise modelling was conducted to assess the impacts of the proposed development on noise levels. The model considered the effect of noise from a combination of the existing Olkaria I & II, the proposed Olkaria IV & I Units 4 & 5 power stations, and OW 38 that was on discharge testing at the time (Gibb, 2010a). Discharge testing of wells takes about three months in order to determine the well flow characteristics and establish the power output at different wellhead pressures. The exercise is carried out all year round to test wells that are being drilled on a continuous basis. Monitoring of noise levels is carried out on all working days, and information is circulated immediately if the noise level exceeds the recommended limit. Workers in and visitors to the relatively noisy areas are provided with personal protective equipment (PPEs) that comprise ear muffs and ear plugs. Furthermore, staff working in the power plants and drilling sites operate in 12 hour shifts to prevent prolonged exposure periods to high noise levels. Information and warning signs are clearly displayed in the national, and in some instances the local, language, in areas where it is mandatory for the PPEs to be worn. During discharge testing, noise levels at wells can reach a high of 125 dBa, but decline to a low of 90 dBa when fitted with temporary silencers. Figure 10 shows OW-909 that is discharging and is fitted with four silencers to reduce noise levels. The permanent separator stations at Olkaria IV, as illustrated in Figure 11, are made of concrete and rock mufflers that substantially reduce noise to negligible levels.

FIGURE 10: Discharging OW-909

FIGURE 11: Olkaria IV steam venting station

3.2.4 Exposure to hydrogen sulphide gas emissions

Geothermal wells and power plants emit substantial quantities of hydrogen sulphide (H_2S) gas. Air dispersion modelling was conducted to assess the impact of the proposed development on H_2S levels. The model considered the effect of H_2S emissions from a combination of the existing Olkaria I & II, the new Olkaria IV & I Units 4 & 5 power stations (Gibb, 2010a and 2010b). Currently, the World Health Organization (WHO) 24-hour guidelines are being used to assess the impacts, since there are no ambient air quality criteria for H_2S gas in force in Kenya. The guidelines recommend an average exposure limit of 0.10 ppm concentrations for a period of 24 hours (WHO, 1987). Monitoring of H_2S gas levels is carried out on all working days and information is circulated immediately if the levels exceed the recommended limit. Information and warning signs are clearly displayed in the national, and in some instances the local, language, in areas where high gas emissions are recorded. The new power plant was fitted with cooling towers that are similar to those at the relatively new Olkaria II to provide greater plume rise and achieve better dispersion than in the older Olkaria I power plant. Workers operate in 12 hour shifts to prevent prolonged exposure to the H_2S gas emissions. They are also regularly trained on the dangers of exposure to hydrogen sulphide gas.

3.2.5 Water utilization and waste water disposal for the geothermal wells

The Olkaria IV power plant is currently utilising 2,500 m^3 of fresh water for the cooling towers initially, up to a duration of about three years. Thereafter, only a small quantity will be required for top up. More water is utilised for drilling of geothermal wells, for household use at KenGen staff housing quarters, and to supply to local communities for their domestic and livestock use. This water is extracted from a single source, the nearby Lake Naivasha, which is a Ramsar Site. The total amount of lake water drawn by the existing and the proposed geothermal project development on its own does not impact significantly on the lake water level. Nevertheless, historical data shows that the Lake Naivasha water level fluctuates significantly, and is likely to continue to do so over the expected 30-year life span of the power plant. This can significantly scale down the power plant's operations. The fluctuation is mainly attributed to prolonged periodic droughts as experienced in 2009 and the beginning of 2010, and subsequent over-extraction by competing users, such as the flourishing horticulture farming and domestic water use by the increasing population in the area. The mitigation measures being implemented include: continued monthly monitoring of the lake level; re-use of drilling water by conserving it in temporary circulation ponds; rainwater harvesting facilities installed in the newer buildings; monitoring and immediate repair of accidental pipe leakages and bursts; and use of brine for drilling.

Brine is the main waste water from geothermal wells and power plants. Substantial quantities of brine from production wells are separated from the steam that is used to drive the turbines that generate electricity in the power plant. Inappropriate disposal of the brine may cause soil erosion, as well as the contamination of soils, water, and vegetation. The most appropriate brine disposal method is hot and cold re-injection from the wells and power plant, respectively. Re-injection plays an important role of recharging the reservoir and minimizing land subsidence. Several wells are being used for re-injection, like OW-R5 and OW-901. In addition, brine is held temporarily in ponds that are lined with high density polyethylene (HDPE) to prevent percolation and surface flow that can cause contamination of soils, water and vegetation. Small rocks are laid on the HDPE layer to provide a grip to small crawling animals like lizards, snakes and rodents, against the slippery lining. Alternatively, brine is being used as drilling fluid, in order to supplement the fresh water that is abstracted from Lake Naivasha. A pumping station that is located at OW-903 supplies brine for drilling wells that provide steam to Olkaria IV power plant.

3.2.6 Impact on recreation and aesthetics

Construction of power plants and their associated infrastructure, that is comprised of the traversing steam gathering pipelines, transmission lines, and road network, affects the aesthetics of the area. The existence of these diverse structures has facilitated degradation of the surrounding environment through intrusion on the view of the natural landscape and the imposition of an image of economic and industrial nature within and in the vicinity of Hell's Gate National Park. In an attempt to reduce the impact of visual intrusion, the steam pipes were initially painted in a single beige or green colour so as to blend with the natural environment, as shown in Figures 8 and 9 above. Nevertheless, due to the increasing number of power plants, the associated infrastructure and the changing climatic conditions, the beige-painted pipes are now quite conspicuous during the wet season, which is dominated by a lot of green vegetation; in contrast, the green-painted pipes are highly visible during the dry season when the prevalent vegetation and soil cover is mainly grey and brown. In an attempt to address this problem, a new method of camouflaging the steam pipes with alternating patterns of beige and various shades of green so that the pipes are not as conspicuous during either season was adopted, as illustrated in Figure 12.

FIGURE 12: Camouflaged green and beige steam pipes

4. PRELIMINARY ENVIRONMENTAL COST ACCOUNTING FOR OLKARIA IV GEOTHERMAL PROJECT

The assessment below describes the economic costs associated with the environmental impacts of the Olkaria IV geothermal power project. The cost assessment reveals the WTP for environmental impacts as shown by the company's mitigation methods, but not the WTP as shown by societal actions. Consequently, this assessment accounts only for the environmental costs that are borne by the company.

Environmental costs arise at different points in time, some in the near future, and others in a more distant future. Consequently, time is a critical parameter in any calculation that involves monetary values (MENR, 2008). Since the overall cost of a particular mitigation measure is a combination of costs that occur at different points in time, discounting is therefore undertaken. Discounting is a mechanism whereby benefits and costs that occur at different points of time can be measured in a common unit (Dixon and Hufschmidt, 1986; MNRE, 2008). The monetary unit applied in the economic valuation is the US dollar ($) which is equivalent to 103 Kenya Shillings (KES). Equation 1 has been applied to calculate the levelized annual costs of mitigation measures of the respective environmental aspects and is applied to any capital cost that is incurred (Harris and Roach, 2002):

$$U = P\left[\frac{i}{1-(1+i)^{-n}}\right] \quad (1)$$

where U = Uniform series amount
P = Present value
i = interest rate for the capital investment
n = number of time periods capturing the economic lifetime of the investment

The total levelized costs then consist of the sum of capital costs converted to annual costs of capital by Equation 1, and operation and maintenance costs that may include labour, transport and subsistence costs. The total levelized costs incurred by the company indicate its willingness-to-pay (WTP) for mitigating the environmental impacts of its activities.

Table 1 shows the five significant environmental aspects of Olkaria IV geothermal project, their respective associated effects and impacts, applied mitigation measures, as well as valuation methods and cost elements.

4.1 Economic valuation of the impact on flora

Economic valuation of the impact on flora was undertaken using replacement cost and defensive expenditure methodologies. Both methodologies rely on assessing the costs of undertaking activities aimed at offsetting changes in environmental quality. Replacement cost methodology applies when changes in environmental quality have an impact on productivity, while defensive expenditure methodology is applied when changes in environmental quality have an impact on the ecosystem or human health and actions have been taken to defend against that impact (Hufschmidt et al., 1983; MNRE, 2008). The replacement cost methodology was applied to assess the costs of restoring vegetation (rehabilitating) in ten well sites that supply steam to the Olkaria IV power plant. Defensive expenditure methodology was applied to assess the costs of controlling invasive species in the same well sites, as they have an impact on the health of the vegetation due to competition for nutrients. To calculate the levelized annual capital cost, Equation 1 was used with P = $174,194.20, n = 5, and i = 0.06 as shown in Table 2. Capital cost is the expenditure that was incurred to purchase tools and implements to undertake the rehabilitation activities. Capital cost of controlling invasive species is not included since the activity entails manual removal. Operational cost represents labour and subsistence expenditure. An average rate of 6% was applied for discounting for five years, the period that the restoration investment is estimated to last before being carried out again. The total levelized annual cost was then obtained from a sum of the levelized annual capital and operational costs.

TABLE 1: Valuation of common environmental impacts of Olkaria IV Geothermal Project

Environmental aspect	**Environmental effects**	**Environmental impacts**	**Mitigation measures**	**Valuation technique and cost elements**
1. Flora				Cost of replacement/ defensive expenditure
	i) Disturbance of vegetation by clearing	i) Degraded Park	i) Rehabilitate disturbed areas with indigenous vegetation	i) Cost of rehabilitation
	ii) Growth of opportunistic and invasive species	ii) Reduced wildlife habitat	ii) Control growth of opportunistic and invasive species	ii) Cost of removing invasive species
	iii) Loss of biodiversity and habitat			
2. Fauna				Defensive expenditure
	i) Loss of migratory corridors	i) Reduced wildlife habitat	i) Wildlife friendly steam pipe designs	i) Cost of wildlife accessible pipe design
	ii) Increased human activity	ii) Increased bush fires	ii) Erect humps to reduce speed limits	ii) Cost of installing speed humps
	iii) Loss of dispersal areas	iii) Reduced wildlife population	iii) Install firebreaks	iii) Cost of firebreaks
	iv) Risk of drowning in brine ponds		iv) Monitor wildlife population	iv) Cost of participation in wildlife census
			v) Fencing off well sites	
3. Air quality				Defensive expenditure
	i) Dust emissions	i) Discomfort and nuisance	i) Use of dust masks by the workers	i) Cost of dust masks for the workers
	ii) H_2S gas emissions		ii) Daily monitoring of H_2S gas concentrations	ii) Cost of monitoring H_2S gas concentrations
	iii) Noise and vibrations		iii) Daily monitoring of noise levels	iii) Cost of monitoring noise levels
			iv) Use of ear muffs by the workers	iv) Cost of ear muffs for the workers
			v) Installation of concrete vent stations/silencers	v) Cost of concrete vent stations
4. H_2S gas and noise	i) H_2S gas emissions	i) Discomfort and nuisance	i) Resettlement action plan	Contingent valuation/cost of replacement
	ii) Noise and vibrations			i) Cost of resettling project affected persons
5. Water	i) Water pollution	i) Reduced water quality	i) Re-injection of brine	Defensive expenditure
				ii) Cost of re-injection wells
	ii) Water resources' depletion	ii) Reduced water quantity	ii) Monitoring of Lake Naivasha levels	
				iii) Cost of monitoring of Lake Naivasha water levels
			iii) Rainwater harvesting	iv) Cost of rainwater harvesting reservoirs
			iv) Use of brine for drilling	v) Cost of brine pumping station

TABLE 2: Valuation of annual cost of protecting flora

No.	Applied mitigation measures	Capital cost (USD)	Levelized annual capital cost (USD)	Operational cost (USD)	Total levelized annual cost (USD)
1.	Rehabilitate well sites (10)	174,194.20	41,353.08	2,158.25	43,511.33
2.	Control invasive species (10)	*n/a	n/a	29,667.50	29,667.50
				Total	**73,178.83**

*n/a – not applicable

4.2 Economic valuation of the impact on fauna

Defensive expenditure methodology was used to assess the costs of mitigation measures aimed at protecting the wildlife and its habitat. The mitigation measures include providing wildlife access loops, fencing around well sites, erecting speed bumps and firebreaks. The cost of carrying out semi-annual wildlife census to monitor the population was also included. Operational cost represents labour and subsistence expenditure. The total levelized annual cost was then obtained from a sum of the levelized annual capital and operational costs shown in Table 3.

TABLE 3: Valuation of annual cost of protecting fauna

No.	Applied mitigation measure	Capital cost (USD)	Levelized annual capital cost (USD)	Operational cost (USD)	Total levelized annual cost (USD)
1.	Wildlife access loops	29,126.21	2,278.45		2,278.45
2.	Fence well sites (10)	31,768.90	7,541.82	45,436.90	52,978.72
3.	Erect speed bumps (10)	8,427.20	3,152.70	2,528.20	5,680.90
4.	Establish firebreaks	*n/a	n/a	16,370.87	16,370.87
5.	Conduct wildlife census	n/a	n/a	3,200.00	3,200.00
				Total	**80,508.94**

*n/a – not applicable

Wildlife access loops
The levelized annual capital cost of wildlife access loops was derived from Equation (1) with P = $ 29,126.21, n = 25, and i = 0.06. A period of twenty-five years was applied, being the economic life of the power plant.

Fencing around well sites
The levelized annual capital cost of fencing around ten well sites whose wells supply steam to Olkaria IV power plant was derived from Equation (1) with P = $ 31,768.90, n = 5, and i = 0.06. The fencing materials are given a lifetime of five years before being replaced.

Erect speed bumps
The levelized annual capital cost of erecting ten speed bumps on roads leading to Olkaria IV power plant was derived from Equation (1) with P = $ 8,427.20, n = 3, and i = 0.06. The speed bumps are given a duration of three years before being replaced for wearing out.

4.3 Economic valuation of noise control

The defensive expenditure methodology was used in an attempt to measure the cost of mitigation measures to avoid the impact of exposure to excessive noise and vibrations. Operational cost represents labour and subsistence expenditure, as well as the annual cost of purchasing ear muffs and ear plugs.

The operational costs of well test silencers and concrete separator stations are not included. The total levelized annual cost was obtained from a sum of the levelized annual capital and operational costs as shown in Table 4.

TABLE 4: Valuation of annual cost of noise control

No.	Applied mitigation measure	Capital cost (USD)	Levelized annual capital cost (USD)	Operational cost (USD)	Total levelized annual cost (USD)
1.	Monitor noise levels (2)	9,374.56	2,225.49	30,249.12	32,474.61
2.	Well test silencers (5)	242,718.45	43,479.37	missing data	43,479.37
3.	Concrete separator station	105,950.47	8,288.16	missing data	8,288.16
4.	Ear muffs and ear plugs	*n/a	n/a	7,893.20	7,893.20
				Total	**92,135.34**

*n/a – not applicable

Monitoring of noise levels
The levelized annual capital cost of monitoring noise levels using two integrated sound level meters was derived from Equation (1) with P = $ 9,374.56, n = 5, and i = 0.06. A life span of five years is assumed for the integrated sound level meters.

Well test silencers
The levelized annual capital cost of installing five twin well test silencers was derived from Equation (1) with P = $ 242,718.45, n = 7, and i = 0.06. A period of seven years was applied, being the economic life of the silencers.

Concrete separator station
The levelized annual capital cost of installing a concrete separator station was derived from Equation (1) with P = $ 105,950.47, n = 25, and i = 0.06. A period of twenty-five years was applied, being the economic life of the power plant...

4.4 Economic valuation of air quality

The defensive expenditure methodology was applied to obtain the mitigation measures applied to avoid exposure to the degraded ambient air quality resulting from the emission of hydrogen sulphide gas, particulate matter and dust. The mitigation measures include monitoring of hydrogen sulphide gas and particulate matter, as well as the procurement of dust masks. Operational cost represents labour and subsistence expenditure, as well as the annual cost of purchasing dust masks. The total levelized annual cost was obtained from a sum of the levelized annual capital and operational costs as shown in Table 5.

TABLE 5: Valuation of annual cost of improving air quality

No.	Applied mitigation measure	Capital cost (USD)	Levelized annual capital cost (USD)	Operational cost (USD)	Total levelized annual cost (USD)
1.	Monitor H_2S gas (2)	39,471.84	5,362.96	30,249.12	35,612.08
2.	Monitor particulate matter (2)	29,732.04	4,039.63	30,249.12	34,288.75
3.	Dust masks	*n/a	n/a	611.65	611.65
				Total	**70,512.48**

*n/a – not applicable

Monitor H_2S gas concentration levels
The levelized annual cost of monitoring H_2S gas concentration levels using two H_2S gas analysers was derived from Equation (1) with P = \$ 39,471.84, n = 5, and i = 0.06. A life span of five years is assumed for the integrated sound level meters.

Monitor particulate matter level
The levelized annual cost of monitoring particulate matter levels using two particulate matter level meters was derived from Equation (1) with P = \$ 29,732.04, n = 5, and i = 0.06. A life span of five years is assumed for the integrated sound level meters.

4.5 Economic valuation of H_2S gas and noise emissions' control

Defensive expenditure methodology was applied to measure the costs of resettling the seventy-five families that would have been affected by exposure to H_2S gas and noise emissions from the operations of the power plant. To calculate the levelized annual capital cost, Equation (1) was used with P = \$ 4,126,213.59, n = 25, and i = 0.06. The total levelized annual cost was obtained from a sum of the levelized annual capital and operational costs as shown in Table 6. A period of twenty-five years was applied, being the economic life of the power plant. Capital cost is the expenditure that was incurred to construct the project affected persons' residential houses and social amenities. The resettlement cost represents the company's willingness-to-pay to acquire the land for development of Olkaria IV power plant on one hand, and the project affected persons' willingness-to-accept compensation for the loss of their land and livelihoods, on the other hand.

TABLE 6: Valuation of annual cost of H_2S gas and noise emissions' control

No.	Applied mitigation measure	Capital cost (USD)	Levelized annual capital cost (USD)	Operational cost (USD)	Total levelized annual cost (USD)
	Resettlement	4,126,213.59	322,780.15	missing data	322,780.15

4.6 Economic valuation of water quality and quantity

The defensive expenditure methodology was used in an attempt to measure the cost of mitigation measures applied to avoid contamination of water sources by brine. The methodology was also used to assess the costs of preventing depletion of water from Lake Naivasha as shown in Table 7. Capital costs of monitoring activities are not included. Operational cost represents labour and subsistence expenditure to conduct the monitoring activities.

Brine re-injection
Brine from Olkaria IV power plant is re-injected into nine wells to prevent soil erosion, as well as contamination of soils, water, and vegetation. The nine comprise of seven hot and two cold re-injection wells, respectively. The levelized annual capital cost was derived from Equation 1 with P = \$ 49,500,000.00, n = 25, and i = 0.06. A period of twenty-five years was applied, being the economic life of the power plant.

Monitor soil, vegetation & brine
Monitoring of soil, vegetation, brine and rain chemistry is conducted four times a year to establish if there is any pollution associated with the geothermal development.

Brine sump pond
Brine is held temporarily in ponds that are lined with high density polyethylene (HDPE) to prevent percolation and surface flow that can cause contamination of soils, water and vegetation. The levelized

annual cost of installing fifteen sump ponds that hold brine from Olkaria IV was derived from Equation (1) with P = $ 48,543.70, n = 25, and i = 0.06. A period of twenty-five years was applied, being the economic life of the power plant.

Brine pump station
Brine is being utilised for drilling in order to supplement the fresh water that is abstracted from Lake Naivasha. The levelized annual capital cost of installing a brine pump station was derived from Equation (1) with P = $ 93,203.88, n = 25, and i = 0.06. A period of twenty-five years was applied, being the economic life of the power plant.

Rainwater harvesting reservoir
Rainwater is harvested in order to supplement the fresh water that is abstracted from Lake Naivasha. The levelized annual capital cost of installing a rainwater harvesting reservoir was derived from Equation (1) with P = $ 29,126.21, n = 25, and i = 0.06. A period of twenty-five years was applied, being the economic life of the power plant.

Monitor Lake Naivasha water level
Monitoring of Lake Naivasha water level is conducted on a monthly basis to establish if the water level changes are associated with extraction for the development of geothermal energy at Olkaria.

TABLE 7: Valuation of annual cost of conserving water quality and quantity

No.	Applied mitigation measure	Capital cost (USD)	Levelized annual capital cost (USD)	Operational cost ($)	Total levelized annual cost ($)
1.	Brine re-injection (9)	49,500,000.00	3,872,222.55	missing data	3,872,222.55
2.	Monitor rain chemistry	missing data	missing data	594.23	594.23
3.	Monitor soil, vegetation & brine	missing data	missing data	885.49	885.49
4.	Brine sump pond (15)	48,543.70	3,797.41	missing data	3,797.41
5.	Brine pump station	93,203.88	7,291.03	missing data	7,291.03
6.	Rainwater harvesting reservoir	29,126.21	2,278.45	missing data	2,278.45
7.	Monitor Lake Naivasha water level	missing data	missing data	1,151.07	1,151.07
				Total	**3,888,220.24**

5. DISCUSSION

Results of a preliminary economic valuation of the common environmental impacts of Olkaria IV geothermal project in separate categories of the key significant environmental aspects have been presented. A summary of the economic valuation that provides the total levelized annual cost of mitigating the common environmental impacts of Olkaria IV geothermal project is shown in Table 8. The estimated total levelized annual environmental cost is $ 4,534,362.13, from a possible annual net revenue of $ 52,545,108, amounting to 8.6% of the total annual revenue. A large proportion of this cost, 85.40%, is the expenditure on re-injection wells. As stated before, these costs reflect the company's WTP to mitigate against the adverse impacts of its development activities to the environment.

TABLE 8: Summary of economic valuation of environmental impacts of Olkaria IV geothermal project

Environmental aspect	Valuation technique and elements	Total levelized annual cost (USD)
1. Flora	**Cost of replacement & defensive expenditure**	
	i) Cost of rehabilitation	43,511.33
	ii) Cost of removal of invasive species	29,667.50
	Sum	**73,178.83**
2. Fauna	**Defensive expenditure**	
	i) Cost of wildlife accessible pipe design	2,278.45
	ii) Cost of installing speed bumps	52,978.72
	iii) Erection of speed bumps	5,680.90
	iv) Cost of firebreaks	16,370.87
	v) Cost of participation in wildlife census	3,200.00
	Sum	**80,508.94**
3. Noise	**Defensive expenditure**	
	i) Monitoring noise levels	32,474.61
	ii) Well test silencers	43,479.37
	iii) Concrete separator station	8,288.16
	iv) Ear muffs and ear plugs	7,893.20
	Sum	**92,135.34**
3. Air quality	**Defensive expenditure**	
	i) Monitoring H_2S gas	39,619.59
	ii) Monitoring particulate matter	37,307.40
	iii) Dust masks	611.65
	Sum	**77,538.64**
4. H_2S gas and noise	**Cost of replacement**	
	i) Cost of resettling project affected persons	322,780.15
	Sum	**322,780.15**
5. Water	**Defensive expenditure**	
	i) Cost of re-injection wells	3,872,222.55
	ii) Monitoring rain chemistry	594.23
	iii) Monitoring soil, vegetation & brine	885.49
	iv) Brine sump pond (15)	3,797.41
	v) Drilling brine pump station	7,291.03
	vi) Rainwater harvesting reservoir	2,278.45
	vii) Monitoring lake water level	1,151.07
	Sum	**3,888,220.24**
	Total	**4,534,362.13**

The main shortcomings in this study are threefold. First, the missing costs and associated uncertainties. For instance, by including the missing values of operational, maintenance and regulatory costs, as well as using different values of *p, n* and *i* in Equation 1 for the different mitigation measures could significantly affect the total levelized annual costs. Consequently, additional information is required to arrive at a more precise valuation. Secondly, the valuation focused only on the common environmental impacts. As a result, there is a need to value other environmental impacts, such as solid waste disposal, visual intrusion and lost aesthetics among others, in order to complete the economic valuation. Third, as the assessment only looked at WTP for environmental impact as shown by the company further economic valuation on societal WTP for ecosystem services is recommended for impacts on:

- Biodiversity in Hell's Gate National Park;
- Recreation activities in Hell's Gate National Park;
- Lost carbon sequestration due to cleared vegetation;

- Corrosion of structures and equipment by hydrogen sulphide gas;
- Extraction of water from Lake Naivasha.

Such assessment would illustrate the economic impact on society due to the environmental impact of economic development. The assessment would rely on economic valuation methods such as travel cost and contingent valuation to establish the society's WTP, e.g. to retain the services of recreation in Hell's Gate National Park, carbon sequestration or the existence of Lake Naivasha.

6. CONCLUSION

Despite the highlighted caveats, this report presents a practical example of how an economic valuation of environmental impacts of geothermal development can be conducted. Economic valuation as described in this report, helps to identify, quantify and monetise the environmental impacts that are associated with the development of geothermal projects, as borne by the company. By clearly identifying all possible environmental impacts and by placing monetary values on them where possible, a more realistic economic analysis of geothermal development projects can be achieved, by uncovering the usually hidden environmental costs that are associated with development activities. This provides significant opportunities for making informed decisions on minimising costs, through the application of economically efficient, environmentally friendly and socially acceptable mitigation measures, in order to achieve sustainable development.

ACKNOWLEDGEMENTS

It gives me pleasure to thank the Government of Iceland and the United Nations University Geothermal Training Programme for awarding me a scholarship to study the Six Months Course. I would like to appreciate the management of KenGen for granting me an opportunity to undertake this vital training. Further, my gratitude goes to my colleagues at Olkaria Geothermal Project who provided me with the required data as well as photos.

I am greatly indebted to Dr. Lúdvík S. Georgsson, the UNU-GTP director, Mr. Ingimar G. Haraldson, Ms. Málfrídur Ómarsdóttir, Mr. Markús A.G. Wilde, Ms. Thórhildur Ísberg and Ms. María S. Gudjónsdóttir for guidance and support in their respective capacities, throughout the training period. I thank all the UNU-GTP lecturers and 2015 Fellows for sharing their invaluable knowledge during the training, and Ms. Rósa S. Jónsdóttir for swiftly availing to me the required study materials.

My warmest regards go to my supervisor, Prof. Brynhildur Davídsdóttir, for her apt guidance and making me comfortable in a subject that was relatively new to me. I am very thankful to Mr. David Cook for his valuable comments and ideas on my project work.

I would like to sincerely thank my dear family and friends, for their invaluable support as well as enduring my long absence. I am forever indebted to God for His faithfulness in my life.

NOMENCLATURE

m^3	= Cubic metres
dB	= Decibels absolute
L	= Lake
MW	= Megawatts
%	= per cent
ppm	= parts per million
$/USD	= United States Dollar
WTA	= Willingness-to-accept
WTP	= Willingness-to-pay

REFERENCES

Ármannsson, H., and Kristmannsdóttir, H., 1992: Geothermal environmental impact. *Geothermics, 21-5/6,* 869-880.

Callan, S.J. and Thomas, J.M., 2013: *Environmental economics & management: Theory, policy, and applications* (6th ed.). Cengage Learning, South-Western, USA, 624 pp.

Costanza, R., d'Arge, R., de Groot, R., Farber, S., Grasso, M., Hannon, B., Naeem, S., Limburg, K., Paruelo, J., O'Neill, R.V., Raskin, R., Sutton, P., and van den Belt, M., 1997: The value of the world's ecosystem services and natural capital. *Nature 387*, 253–260.

Dixon, J.A. and Hufschmidt, M.M. (eds.), 1986: *Economic valuation techniques for the environment*. Johns Hopkins University Press, Baltimore, USA, 203 pp.

EC, 2013: *External costs: research results on socio-environmental damages due to electricity and transport*. European Commission, Luxemburg, Belgium, 24 pp.

ESMAP/WB, 2012: *Geothermal handbook: Planning and financing power generation*. The World Bank Group, Washington DC, USA, 164 pp.

EV, 2000: *Ecosystem Valuation*, website: *www.ecosystemvaluation.org/.*

Field, B.C., and Field, M.K., 2002: *Environmental economics: an introduction.* McGraw-Hill, USA, 510 pp.

Gibb, 2010a: *Environmental and Social Impact Assessment study report for Olkaria 1 Units 4 and 5, Geothermal Project, KenGen.* Gibb Africa Ltd., Nairobi, Kenya.

Gibb, 2010b: *Environmental and Social Impact Assessment Study Report for Olkaria IV (Domes) Geothermal Project, KenGen.* Gibb Africa Ltd., Nairobi, Kenya.

Goulder, L.H., and Kennedy, D., 2009. Interpreting and estimating the value of ecosystem services. In Daily, G.C. (ed.) *Nature's services: societal dependence on natural ecosystems*. Island Press, W*ashington, DC,* 23-47.

Harris, J.M. and Roach, B., 2002: *Environmental and natural resource economics: A contemporary approach*. Houghton Mifflin Company, USA.

Hufschmidt, M. M., James, D. E., Meister, A. D., Bower, B.T., and Dixon, J. A., 1983: *Environment, natural systems and development: An economic valuation guide*. Johns Hopkins University Press, Baltimore, USA.

Hunt, T.M., 2001: *Five lectures on environmental effects of geothermal utilization.* UNU-GTP, Iceland, report 1-2000, 109 pp.

Kristmannsdóttir, H., and Ármannsson, H., 2003: Environmental aspects of geothermal utilization. *Geothermics, 32,* 451-461.

MNRE, 2008: *Guidelines on the economic valuation of the environmental impacts for EIA projects*. Ministry of Natural Resources and Environment, Putrajaya, Malaysia.

Munda, G., 1996: Cost-benefit analysis in integrated environmental assessment: Some methodological issues. *Ecological Economics*, *19,* 157-168.

Mwangi-Gachau, 2012: Expansion of geothermal development in environmentally significant areas: A case of Olkaria geothermal project in Hell's Gate National Park, Kenya. *Proceedings of the ArGeo-C4, Nairobi, Kenya,* 10 pp.

NEMA, 2009: *Environmental management and coordination (noise and excessive vibrations) regulations.* NEMA, Government Printer, Nairobi, Kenya, 30 pp.

Pearce, D., Atkinson, G., and Mourato, S., 2006: *Cost benefit analysis and the environment: Recent developments*. OECD Publishing, Paris, 318 pp.

Rosenberger R.S., Loomis, J.B., 2001: *Benefit transfer of outdoor recreation use values: A technical document supporting the Forest Service strategic plan (2000 revision).* U.S. Department of Agriculture, Forest Service, Rocky Mountain Research Station, Fort Collins, CO, Gen. Tech. Rep. RMRS-GTR-72, 59 pp.

Shortall, R., Davídsdóttir, B. and Axelsson, G., 2015: Geothermal energy for sustainable development: A review of sustainability impacts and assessment frameworks. *Renewable and Sustainable Energy Reviews*, *44,* 391-406.

Thayer, M. 1980: Contingent valuation techniques for assessing environmental impacts: Further evidence. *J. Environmental Economics & Management, 8,* 27-44.

WHO, 1987: *Air quality guidelines for Europe.* World Health Organisation, Regional Office Copenhagen, Denmark.

UNITED NATIONS UNIVERSITY
UNU-GTP
Geothermal Training Programme

Orkustofnun, Grensasvegur 9,
IS-108 Reykjavik, Iceland

Reports 2015
Number 28

GEOTHERMAL WELL DESIGN USING THE NEW 2015 NEW ZEALAND STANDARD AND 1991 STANDARD: A CASE OF MW-20A IN MENENGAI, NAKURU COUNTY, KENYA

Anthony Ng'ang'a Ngigi
Geothermal Development Company - GDC
P.O. Box 100746-00101, Nairobi
KENYA
anganga@gdc.co.ke

ABSTRACT

The design of geothermal wells is an important task in well construction, as this allows the effective conveyance of geothermal fluids from deep depths to the surface for utilization. The New Zealand design code NZS 2403:1991 has been used for the last two decades to design geothermal wells, but in 2015 it was replaced by a new design code NZS 2403:2015.

This report presents the design of a geothermal well using the two design codes for comparison purposes. The well was designed using exact reservoir conditions in Menengai geothermal field in Kenya, using MW-20A as a reference well. After determining the reservoir pressure, the minimum casing depth for the different casing strings was determined from the codes. In addition, the design premises were established and it was found that the worst case for design was when the well was considered to be filled with steam from bottom to surface. Design calculations were carried out given this condition using the two codes and the best casing strings were determined. The design computations showed that a 20" 94 lb/ft casing, 13⅜" 54.5 lb/ft casing and 9⅝" 47 lb/ft casing were adequate to be run in hole for surface, anchor and production strings respectively. Further calculations showed that the weight of the production casing could be reduced to 36 lb/ft and still be within the minimum design factors, but to account for corrosion during the life of the well, the 47 lb/ft production casing was selected. Due to high stresses when the production casing rises into the wellhead, the weight of the upper two joints of the anchor casing string was changed to 72 lb/ft from 54.5 lb/ft.

Several design considerations have changed between the codes, that include the following: The 2015 code gave deep minimum casing depths compared to the 1991 code. Temperature reduction factors for yield were reduced in the 2015 code when checked against the 1991 code. Minimum design factors for thermal expansion of anchor casing into wellhead and compressive stress in liners were reduced to 1.4 and 1.0 in the 2015 code from 1.5 and 1.2 in the 1991 code, respectively. The 2015 code considers fracture pressure for maximum pressure boundary while determining minimum casing depth while the 1991 code considers the overburden. The 1991 code does not allow the thermal expansion of the casing to exceed minimum yield, while the 2015 code acknowledges the use of strain based design in such cases. It is recommended that to avoid the introduction of tensional stresses into the well, cold fluids should not be pumped into a hot well.

1. INTRODUCTION

Hole (2008a) describes the geothermal well design process as a think through process where the engineer has to consider; the purpose and objective of the well, conditions likely to be encountered downhole during drilling, identification of material and equipment required, and safe drilling procedures that will ensure successful well completion and thereafter a satisfactory design life of the well. A sound design is required to achieve a satisfactory well drilling process, and to obtain the integrity and desired life of the well. Part of the design is the selection of casing depths and specification of the material weights and connections. The course taken in casing design and determining the right specification embraces the knowledge of the prerequisite services of the casings, proper setting depths and scrutinizing potential modes of failure.

Typically, geothermal wells are constructed from several concentric steel casings, with cement in the annulus between the casing walls and the hole. It is essential to achieve structural integrity of the casings, especially for high temperature wells which are normally characterised by high temperature and pressure. Failure of casings in such wells may lead to reduced energy output from the well or making it difficult to operate the well and in worst cases cause unsafe conditions outside the well such as blow outs (Kaldal et al., 2013).

The New Zealand 1991 code of practice for deep geothermal wells (NZS 2403:1991) has been used as a guideline for designing geothermal wells since it was released. Since the inception of this design code, many deep geothermal wells have been drilled worldwide providing additional design information and challenges necessitating the revision of the code. Therefore, the NZS 2403:1991 code has been undergoing review and in 2015 it was replaced by NZS 2403:2015 code of practice for deep geothermal wells. The NZS 2403:2015 code has incorporated the knowledge and experiences gained by geothermal drilling experts from years of designing geothermal wells.

This study will use the new and old New Zealand code of practice (NZS 2403:2015) and (NZS 2403:1991) to design a 2000 m deep well for the reservoir conditions already identified at the Menengai geothermal area in Kenya. The reference high temperature geothermal well MW-20A, is a directional well already drilled in the Menengai geothermal field to a depth of 2219 m. The design will be limited to 2000 m since the codes are limited to that depth.

The report will describe the well design process, list all equations, and then follow it with calculated examples. First, the objectives and criteria are established for drilling the well, and then the expected loads are estimated on each casing string (surface, anchor and production casing) during well drilling, heating up (static) and flowing (dynamic). Based on the calculated loads the casing design will be made according to API, ISO and New Zealand norms. The results, based on the two New Zealand standards, will be compared to well MW-20A as it was drilled in Menengai, Kenya in 2014.

2. LITERATURE REVIEW

2.1 Background of geothermal well design

Many authors have documented the importance of the casing design of geothermal wells for the production life of the wells. The authors have considered the presence of high temperatures and pressures in deep geothermal wells and therefore recommended a proper evaluation of loads that arise from this kind of downhole environment. The goal is to come up with the best casing design that will ensure safe operation and a reasonable well life. Below are thoughts from different scholars and authors putting into perspective their understanding of the proper or acceptable casing design procedures. Inherently they agree that a well is only a well when the casing design has been done properly and to such an extent that the desired life of the well can be met.

Finger and Blankenship (2010) mention that the design of casings has a substantial impact on the well cost. Geothermal wells utilise large diameter casings, and as a result the casing and cementing can represent more than 40% of the total well cost. Eliminating one string of casing in the design can result in the lowering of costs of up to 20%. The idea of saving must, however, be balanced against the risk of reducing the safety during drilling and later during operation. All these factors depict the importance of a thorough consideration of the casing program. While drilling at various depths below the surface, successive separate casing strings are set and cemented as the well gets deeper. Each casing depth is determined by several factors which include, but are not limited to: rock properties (fracture gradient, sloughing, swelling, unstable or unconsolidated formation), formation fluids and well control considerations, and the need to conform to any regulatory requirements.

They explain that in most drilling operations, onshore or offshore oil and gas, geothermal, or even minerals exploration, the following parameters will determine the casing requirements:

- Design production rate from the well;
- Depth of the production zone;
- Expected temperature distribution in the reservoir;
- Chemistry of the fluid being produced;
- Whether the completion will be open-hole or with a slotted liner;
- Well trajectory i.e. vertical, directional or multi-leg;
- Kick off point for directional wells;
- Necessity for special casing material or connections;
- Length of individual casing strings.

Further, Finger and Blankenship (2010) expound that the above criteria may be further complicated by the possibility of unforeseen events in the process of making the well, which would imply running extra strings of casing to remedy downhole problems, leading to more cost. After selecting the required casing profile for the well, there are normally five distinct parameters that describe the casing, namely; weight (lb/ft), diameter (inches), connections, length range (I-III) and steel grade. The outside diameter does not include the couplings, which have larger diameter than the casing body. Weight is expressed in weight units per unit length and is a measure of the wall thickness of the casing. A heavier casing suggests that it has a smaller inside diameter, as the outside diameter remains constant for a given size of casing. The casing grade is related to the material's tensile strength, however there are other metallurgical properties which are geared to bear certain specific effects such as corrosion and sulphide stress cracking that emanates from the chemistry of the fluid being discharged. Engineers carrying out casing design to be run in hole should understand that the casings have to withstand several kinds of loading in different scenarios. The most important design criterion is for collapse pressure, burst pressure and axial tension. The casing steel grade is essential as it determines strength against burst pressure and axial tensile strength, while the wall thickness of the casing defines the collapse resistance. Collapse is governed by the material's elastic behaviour and geometry, as well as its tensile strength.

Teodoriu and Falcone (2009) maintain that during the design life of a geothermal well, the casing string is generally subjected to external loads that are either static or quasi-static. Design standards such as those by American Petroleum Institute (API) reflect the casing string load to be static, whereas it can be subjected to varying loads due to temperature changes or internal pressure. Casing cementing ensures, or aims at, permanently holding the casing in place and therefore restricting its movement.

Further ideas put forward by Karlsson (1978) outline that various loading scenarios may occur on a casing string during the running of the casing, during cementing, during drilling or after the completion of a well. Occurrence of these loads may be in the axial direction of the casing or in the radial direction, inwards or outwards. From the possible load combinations acting on the casing string, the most critical is caused by the internal and external pressure and by thermal expansion. The maximum pressure to be expected in the well therefore dictates the minimum depth to which each casing string will be set, as is described in the NZ standards.

Material properties, such as the yield strength, vary with temperature, meaning that at elevated temperatures the yield strength of a casing is lower than at ambient temperature (Lari, 1997 in Teodoriu and Falcone, 2009). Southon (2005) postulate that in a casing that is cemented in place, it is inevitable that hoop, radial and axial stresses will build up as the well heats up. When carrying out the design calculations, the reference temperature, also known as "neutral temperature", is the temperature that the cement sets in and locks the casing in place. This temperature varies along the casing and usually will increase with depth, trying to match the adjacent formation temperature, but does not reach it due to the short heating time. It is important to note the reference temperature to be able to compute the temperature change (ΔT) for design purposes. It is worth to note that sometimes the heat of hydration of cement slurry may actually influence the reference temperature.

According to Teodoriu and Falcone (2009) when the well experiences temperature variations, thermal stresses are induced in the casing string to a level that may exceed the yield strength of the casing material. As a result, fatigue failure of the casing material can occur during the life cycle of a well and can be termed as low cycle fatigue (LCF). Low cycle fatigue is a common form of failure occurring when the applied loads induce high stresses in the material that often surpass the material yield strength. The number of cycles may range from 10 to 100 cycles, where the connections are most sensitive to failure. They further show that the fatigue resistance of connections can be as low as 10 cycles. Geometry variations in the casing body, for instance the connection threads, will magnify the local stresses, thereby reducing the LFC resistance of the casing. A large number of cycles will be required for high cycle fatigue failure to occur, normally a minimum of 10^6 cycles. To avoid catastrophic failure, fatigue resistance should be sufficient for metallic components.

According to Vollmar et al., (2013) the overall aim or intent of drilling is to construct a well in the safest way, following laid out standards and procedures to economically recover the resource out of the reservoir. In geothermal, the resource is in the form of heat from hot, fractured, intrusive, volcanic or hard sedimentary rocks. The design of a well is a bottom up process. The depth of the production zone and the required flow determine the optimum well geometry. Thereafter the well profile above the production zone is set by iteration of the larger casing strings, as geological considerations and drilling demand. To affirm the mechanical strength of the casing, it is advisable to consider the density and thickness of the formation being drilled. The density and thickness of the formation result in overburden pressure. Formations being drilled through are of different densities, and therefore the overburden may differ from region to region. While setting the casing depths, the overburden pressure at the selected depth should be high enough to accommodate the highest anticipated pressure in the well.

They continue to remark that the three mechanical failures of the casing that influence the design of the casing string are:

- Maximum burst loads;
- Axial stress during well control operations, well integrity testing and cementing;
- Highest collapse pressure occurs during well cementing operations and when kicks are experienced.

Hole (2008a) directs that when choosing setting depths for a geothermal well the following information should be considered:

- *Surface and conductor casing strings* are the largest casings and are set at shallow depths to bridge loose or unconsolidated shallow material from collapsing into the well. In addition, these casing strings are used to support the preliminary drilling wellhead and also to handle the circulating drilling fluid. Geological evaluation is usually used to decide the casing setting depth, but other conditions encountered during drilling may change the determined depth. For instance, if during drilling a thermal zone is intercepted, then the casing may be required to contain hot fluid under pressure.
- *Anchor or intermediate casing* strings are run in hole to support successive wellheads, and in most cases the permanent wellhead as well. They are intermediate in setting depth and diameter and

are used to contain drilling and formation fluids at a fairly elevated temperature and pressure. Choice of depth is guided by the anticipated rock and fluid characteristics to assure a stable anchorage and also to eliminate problems arising during drilling, and especially during blowouts.

- *Production casing* is a smaller casing in diameter compared to the previous casings. The main function is solely to convey steam and water to the surface. It also enables drilling to total depth, while at the same time preventing undesirable seepage of fluids into or out of different aquifers.

The main conduit for geothermal production fluids from the reservoir is the production casing. This casing string is subjected to extreme stress conditions which are introduced thermally, and also constant contact with formation fluids which may cause adverse effects on the inside or outside of the casing (Hole, 2008b). If a production casing collapses, the cross section area is decreased and hence the well will produce less compared to an intact well. This suggests that the well output is proportional to the cross sectional area of the casing (Thórhallsson, 2006). Proper design should be done to avoid any chances of collapsed casings in the well.

Thórhallsson, (2008) states that in geothermal well drilling and design the objective is to safely drill into the geothermal reservoirs and to allow production of geothermal fluid. The open hole for these wells is usually over 1000 m long and supported by a slotted liner, or in rare cases a screen, allowing reservoir fluids into the well bore. Several casing strings, one inside the other, are found in geothermal wells and may range from –two to five cemented casing strings. The production casing diameter selection for most high-temperature geothermal wells is between 9⅝" and 13⅜", while the slotted liners are either 7" or 9⅝", and for the upper section of the well, the surface casing, 13 3/8", 18⅝" or 20". As explained, these casing strings are of the American Petroleum Institute (API) oilfield tubular diameter standard and there is an API recommended practice for the combination of casing sizes and drill bit diameters (Figure 1). Temperature and pressure versus depth should be known to establish the minimum casing depth for each casing string in a high temperature well to be drilled. In a new field where actual information is not available the 'worst case scenario' for casing design is the Boiling Point Depth curve (BPD).

He continues to discuss that when the reservoir conditions are not known, two methods are available to determine the minimum casing depth as discussed below:

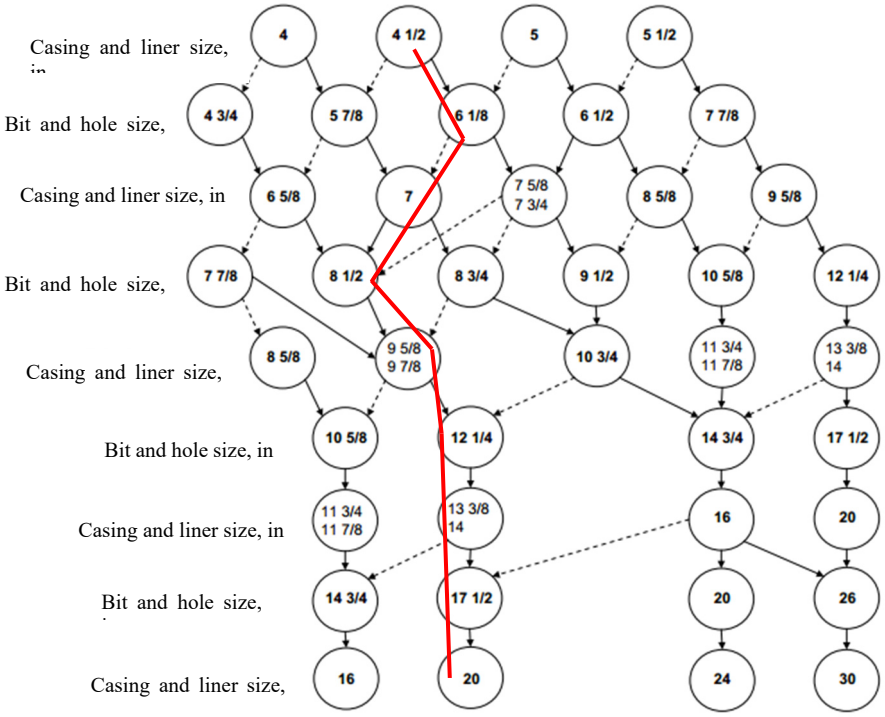

FIGURE 1: Casing selection chart (Thórhallsson, 2015); drawn line shows common path for geothermal wells

- The New Zealand Standard NZS 2403:1991 assumes that the bottom hole pressure is conveyed up the hole through a steam column, that is the well is steam filled, and that this pressure should not exceed the overburden pressure at the respective casing shoe depth. However, in the NZS 2403:2015 revision it is replaced by the fracture gradient of the formation, where the casings shoe is being set;
- A method mainly used in Iceland assumes the same bottom-hole pressure from the Boiling Point Depth curve. This pressure profile is taken to be that of an adiabatically boiling column of water. The rationale behind this is to be able to kill the well with mud with the specific gravity of 1.4 in the worst possible case, but possibly and preferably with water alone.

In addition, Thórhallson points out that geothermal wells are usually associated with H_2S gas from the formation fluids, and for this case the best casing material is to be chosen if a desirable design life of the well is to be achieved. For this matter, the casing steel grades commonly used are API K55 or N80, as they are known to be less susceptible to sulphide cracking and perform better in such conditions. Casing connections that have been found to be adequate are API Buttress, however proprietary connections are sometimes selected, such as WAM, Geocon, Tenaris Blue. Welded casing connections are sometimes selected for large diameter casings.

When the casings are successfully cemented in place to the various sections, the well is not complete in most cases and further drilling is done to the required depth for the next section. Drilling to the required depth is normally guided by the reservoir conditions encountered down hole. After the well has reached total depth, a liner is run in the hole and the well is capped with a wellhead. The wellhead flange is mounted on the anchor casing and therefore has an influence on the design of the anchor casing.
Wellheads sustain quite a range of temperatures and pressure depending on the well characteristic or the geothermal system below, and if the well is flowing or shut in. The range is 10-100 bars and 0-300°C. Operating pressures for the well heads are from 5 to 20 bars, but when the well is shut the well head pressure can rise to pressures between 80 and 100 bars, either from steam or when gases build up at the top of the production casing (Ólafsson, 2011).

3. DESIGN METHODOLOGY

3.1 Well design using NZS 2403:1991 and NZS 2403:2015 considering the exact reservoir conditions of well MW-20A

To establish the design premises with the exact reservoir conditions for well MW-20A, the temperature and pressure logs for different heating and shut-in periods were plotted and studied. The objective is to obtain the minimum casing depths based on the maximum temperature and pressure for the well in the static condition. In addition, valuable information on the well enthalpy, mass flow and well head pressure was obtained from the discharge tests, and thereby enabling the usage of the Hola program at Icelandic Geosurvey-ISOR to simulate the dynamic conditions for MW-20A.

After MW-20A was capped with Class 900 master valve the well was allowed to heat for 11 days before a temperature and pressure logging run was done (Figure 2). After 11 days of heating, the well was discharged for 103 days and shut-in for six days. Logging was done and the results obtained are shown in Figure 3. Note that the pressure log was unsuccessful as the clock failed.

Further two more logs were done after eight days and 21 days of shut in, as shown in Figures 4 and 5, respectively.

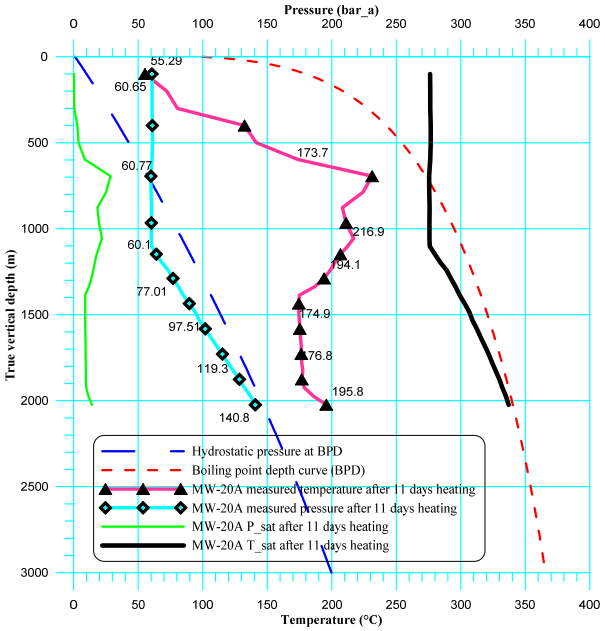

FIGURE 2: MW-20A temperature and pressure profiles 11 days after well capping

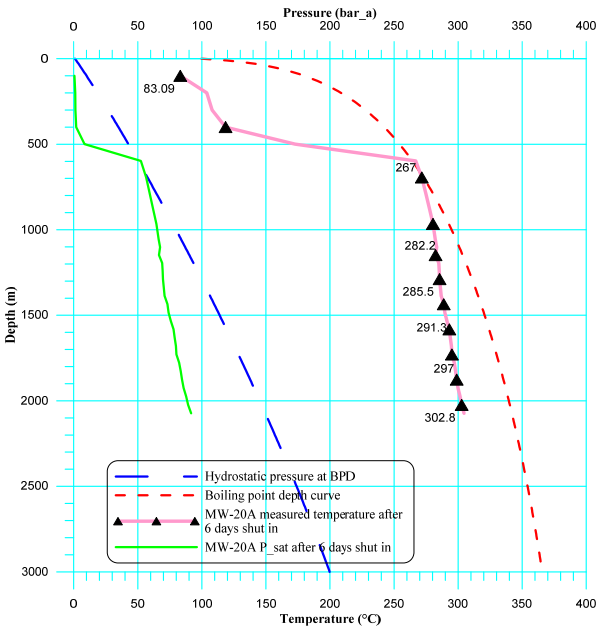

FIGURE 3: MW-20A temperature and pressure profiles after 103 days of flowing and six days of shut-in

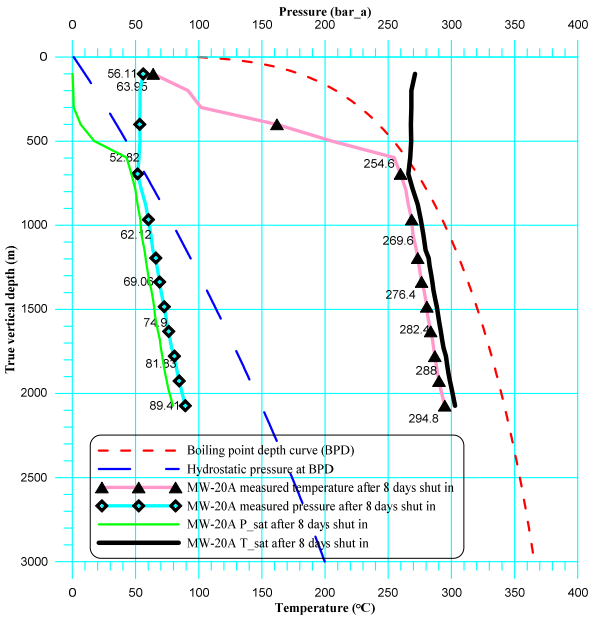

FIGURE 4: MW-20A temperature and pressure profiles after 103 days flowing and eight days of shut-in

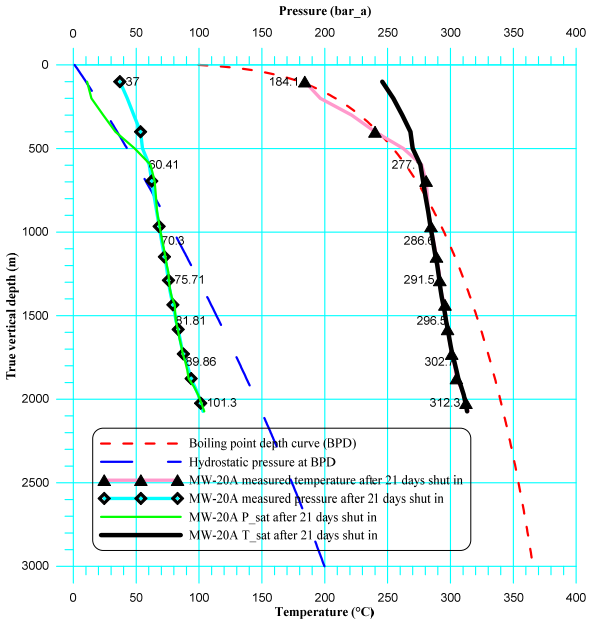

FIGURE 5: MW-20A temperature and pressure profiles after 103 days flowing and 21 days of shut-in

From the above logs, the pressure pivot point/depth was determined by plotting all the pressure logs. As shown in Figure 6 the pivot was at 95 bars at 1500 m. This is the point where the pressure in the well remained unchanged for the different logging periods, and is the basis for the design.

After the pivot point was determined, the hydrostatic pressure curve at boiling was shifted to pass through this point, and similarly the BPD curve was shifted to show the corresponding temperatures for the hydrostatic pressure curve as shown in Figure 7.

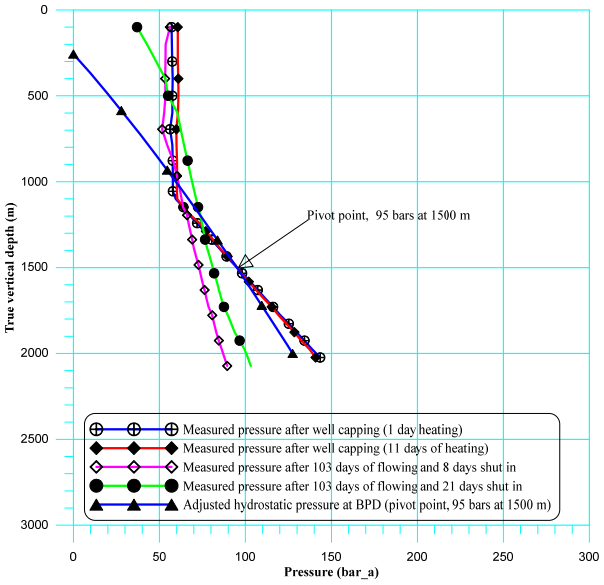

FIGURE 6: MW-20A pressure profiles

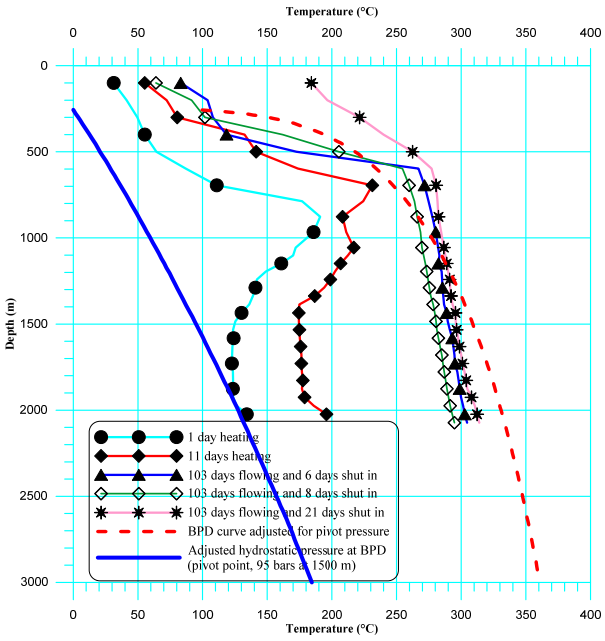

FIGURE 7: MW-20A temperature profiles, adjusted BPD curve and adjusted hydrostatic pressure at BPD

The adjusted hydrostatic pressure at the BPD curve represents the boiling pressures in the well. This pressure curve acts as the lower margin for the determination of minimum casing depth according to both NZS 2403:1991 and NZS 2403:2015. The upper boundary for NZS 2403:1991 is the pressure from the underlying bedrock known as the overburden and is calculated using Equation 1; in this case the overburden is composed of trachyte rocks with minor intrusions of tuff and syenite. The 2015 New Zealand code of practice (NZS 2403:2015) has replaced the use of overburden with the effective containment pressure (fracture pressure) for minimum casing depth determination and is computed using Equation 2, Eaton Formula (for definitions of parameters, see Nomenclature at end):

$$S_v = \rho \times g \times h \tag{1}$$

$$P_{frac} = P_f + \frac{v}{1-v}(S_v - P_f) \tag{2}$$

Figure 8 and Figure 9 show the minimum casing determination for Menengai using NZS 2403:1991 and NZS 2403:2015 respectively. It is evident from the two Figures that the new New Zealand code of practice NZS 2403:2015 gives deeper depths for the production casing and subsequent casings that follow compared to the earlier code NZS 2403:1991. The NZS 2403:2015 code gives minimum depth of the production casing as 740 m and NZS 2403:1991 gives the minimum depth as 450 m.

From the various wells drilled in Menengai geothermal field, many logs and measurements have been done to create the conceptual model of this field. It has been deduced in the process that in many wells there are cold flows beyond 1000 m depth, which was initially considered to be the best depth for the production casing. Due to this finding, a decision was made to place the production casing shoe between 1150 m and 1200 m to case off these cold inflows.

For this reason, the production casing will be set at 1200 m and the preceding casing string depths recalculated. Figures 10 and 11 show the adjusted production casing depth to 1200 m and the minimum depths for the preceding casing strings, anchor and surface casings, for NZS 2403:1991 and NZS 2403:2015, respectively. The results from NZS 2403:1991, after adjusting the production casing shoe to 1200 m, place the minimum anchor casing depth at 290 m and the surface casing minimum depth at 20 m.

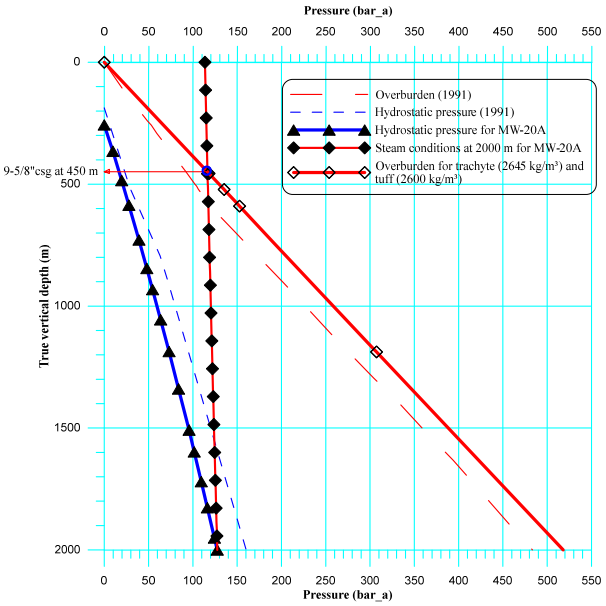

FIGURE 8: Minimum casing depth determination using NZS 2403:1991; the solid lines are for the conditions in Menengai and the dotted ones for the example shown in the standard

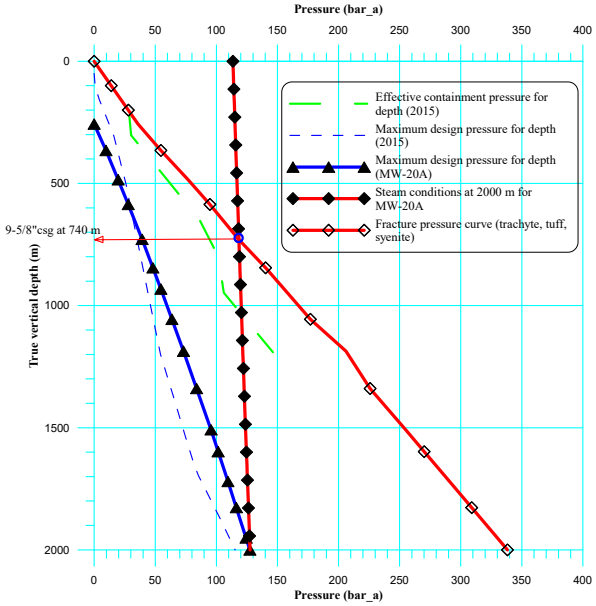

FIGURE 9: Minimum casing depth determination using NZS 2403:2015; the solid lines are for the conditions in Menengai and the dotted ones for the example shown in the standard

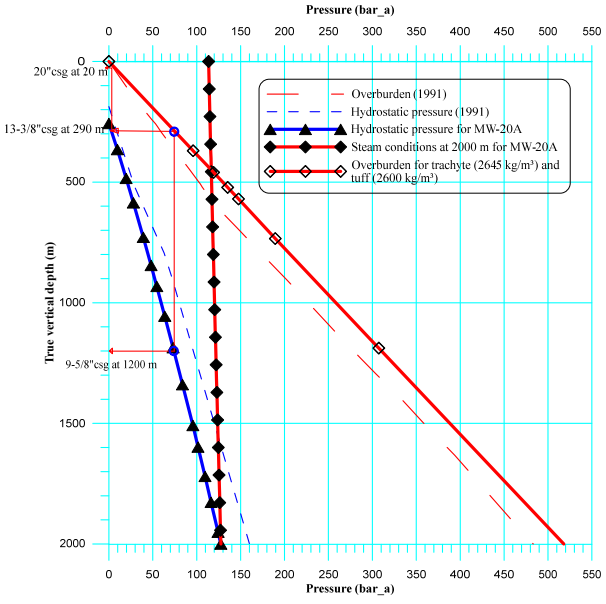

FIGURE 10: Adjusted production casing depth to 1200 m in NZS 2403:1991; the solid lines are for the conditions in Menengai and the dotted ones for the example shown in the standard

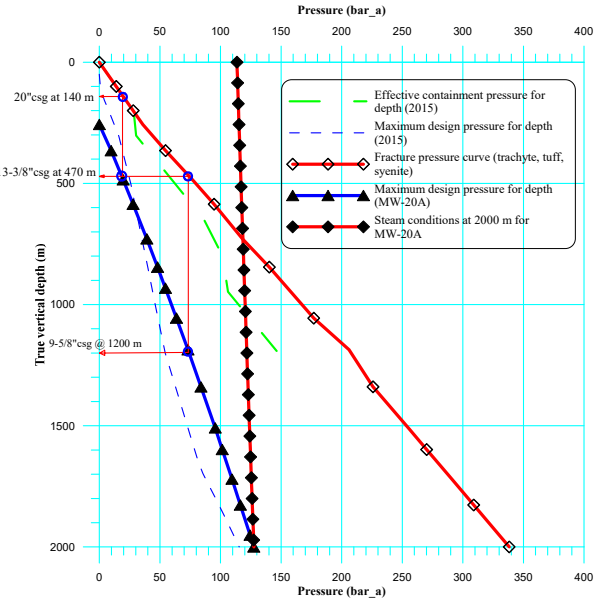

FIGURE 11: Adjusted production casing depth to 1200 m in NZS 2403:2015; the solid lines are for the conditions in Menengai and the dotted ones for the example shown in the standard

These depths are shallow, given that the water table in Menengai is expected to be at 300 m. Therefore, the depths for the anchor and surface casing are adjusted to 350 and 80 m, respectively. Using NZS 2403:2015, after adjusting the production casing shoe depth to 1200 m, the minimum shoe depths for the surface and anchor casings are relatively deep at 140 and 470 m, respectively, and these depths have been used for the design.

3.2 Design premises

Three design premises were considered to find the worst case scenario and the design for it. The three cases considered were: static (shut-in) condition, dynamic (flowing) condition and the third case is that the well is full of steam from bottom to surface. These conditions are displayed in Figures 12, 13 and 14. For the shut-in condition, the temperatures are very low since this is when there is an accumulation of gases in the production casing, suppressing the fluid level in the well.

The worst case scenario was found to be when the well was full of steam from bottom to surface, as is the design premise in the NZ standards. With this condition, the maximum pressure and temperature at the bottom of the well is 127.3 bars and 329.2°C, respectively.

For the shut in condition it is assumed that cold gases have accumulated at the top of the well depressing the water level to the depth of the casing shoe. For the gas filled well the temperatures are very low within the casing.

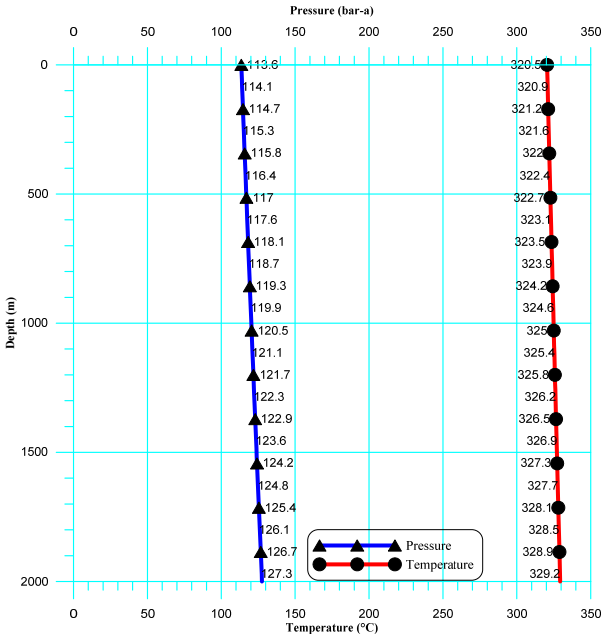

FIGURE 12: Steam conditions in MW-20A

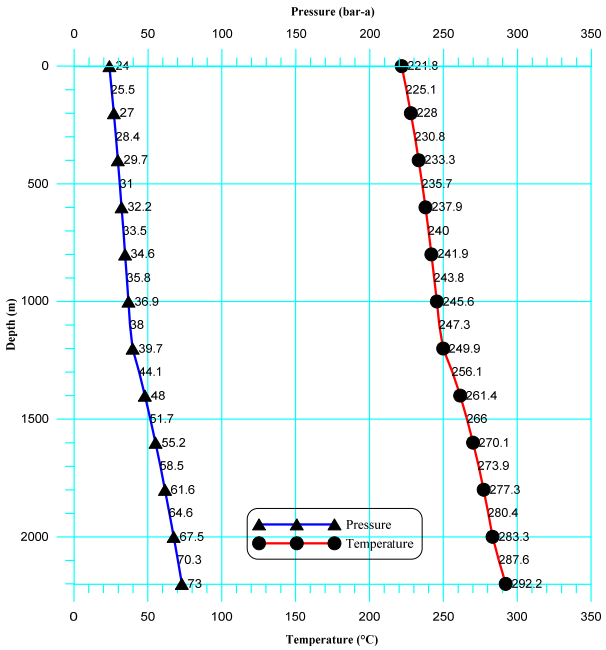

FIGURE 13: Flowing TP conditions in MW-20A

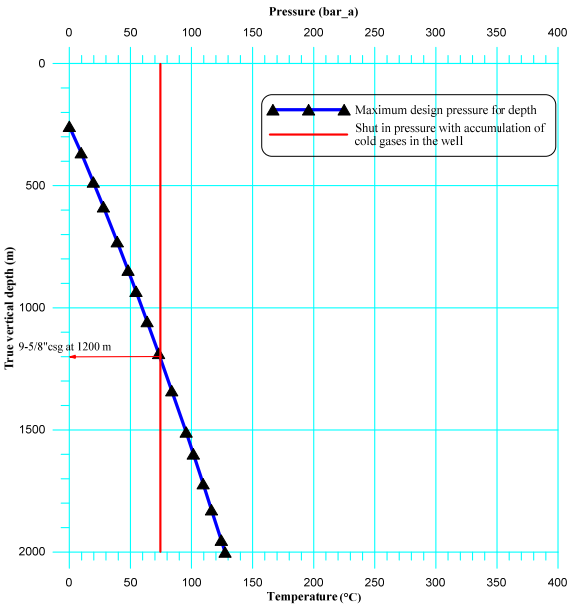

FIGURE 14: Shut in condition with accumulation of cold gases at the top of the well

4. DESIGN CALCULATIONS

4.1 Introduction to design calculations

After establishing the minimum casing depths for the different casing strings from the NZS 2403:1991 and NZS 2403:2015 design codes, the best casing weights, diameter and grade were calculated. The diameter of the casing is known, since the well is a regular well. A regular well casing string constitutes a 30" conductor casing, 20" surface casing, 13⅜" anchor casing, 9⅝" production casing and 7" slotted liners (Thórhallsson, 2015). The chosen grade for all the casing strings is K55, which has resistance to H_2S and has been approved as it conforms to ANSI/NACE MR 0175/ISO 15156 (NZS 2403:2015). The casing grade is essential as it determines the burst pressure and axial tensile strength, while the wall thickness (weight) of the casing defines collapse (Finger and Blankenship, 2010). Design for burst, axial stress and collapse was done for a steam filled well as this was the worst case scenario.

4.2 Design calculation equations of well MW-20A with NZS 2403:1991 considering exact reservoir conditions

Below are the equations used to calculate different casing loads and stresses using the NZS 2403:1991 code of practice for deep geothermal wells. For definition of parameters, see Nomenclature.

4.2.1 Axial loading before and during cementing

$$F_p = L_z \times W_p - \left[\frac{L_f \times A_p}{n \times 10^3}\right] \times g \times 10^{-3} \tag{3}$$

4.2.2 Maximum bending stress in crooked wells

$$F_b = 0.582 \times E \times q \times D \times 10^{-3} \tag{4}$$

The calculated bending stress applies to a 9⅝"casing string which is run in the deviated part of the well.

$$Design\ Factor = \frac{minimum\ tensile\ strength}{maximum\ tensile\ load} \geq 1.8 \tag{5}$$

4.2.3 Axial loading after cementing

While calculating this loading it should be understood that a static force F_p, which is the tensile force at the surface from casing weight, is normally present and will be used to calculate the resultant force.

a. Compressive force due to temperature rise with a partial longitudinal and lateral constraint

$$F_c = 2.4 \times (T_2 - T_1) \times A_p \times 10^{-3} \tag{6}$$

The resultant force is therefore,

$$F_r = F_c - F_p \tag{7}$$

$$Design\ Factor = \frac{minimum\ compressive\ strength}{maximum\ compressive\ force} \geq 1.2 \tag{8}$$

b. Tension due to temperature reduction when cool fluid is circulated from the surface during drilling, testing or reinjection

$$F_t = 2.4 \times (T_1 - T_3) \times A_p \times 10^{-3} \tag{9}$$

Resultant force at every depth,

$$F_r = F_p + F_t \tag{10}$$

$$Design\ Factor = \frac{minimum\ tensile\ strength}{maximum\ tensile\ load} \geq 1.8 \tag{11}$$

4.2.4 Tension at top of any string anchoring a wellhead against lifting force by fluid in the well

$$F_w = \left(\frac{\pi}{4} \times P_w \times d^2 \times 10^{-3}\right) - F_m \tag{12}$$

$$Design\ Factor = \frac{minimum\ tensile\ strength}{maximum\ tensile\ load} \geq 1.8 \tag{13}$$

4.2.5 Design factor for the anchor casing thermal expansion into wellhead

As the production casing expands thermally, a tensile force is applied to the anchor casing. To protect the anchor casing and the well head the following design factor is used.

$$Design\ Factor = \frac{anchor\ casing\ tensile\ strength}{rising\ casing\ compressive\ strength} \geq 1.5 \tag{14}$$

4.2.6 Extreme fibre compressive stress in an uncemented liner due to axial self-weight and helical buckling (axial loading with buckling and bending)

When the liners are run in hole after drilling to the final depth, they can either hang in the production casing or be left to rest at the bottom of the well. When the liners are left to rest at the bottom, compressive stresses are initiated due to axial self-weight and helical buckling. These stresses are calculated as below, in Equation 15:

$$f_c = L_z \times W_p \times g \left[\frac{1}{A_p} + \frac{D\ e}{2I_p}\right] \tag{15}$$

The design factor should not be less than 1.2 and R_j should be equal or less than 1:

$$Design\ Factor = \frac{minimum\ yield\ strength \times R_j}{total\ compressive\ stress} \geq 1.2 \tag{16}$$

4.2.7 Maximum differential burst pressure of string near shoe or stage cementing ports

$$P_i = \left(L_f \times G_f \times g \times 10^{-3}\right) - P_z \tag{17}$$

$$Design\ Factor = \frac{internal\ yield\ strength}{differential\ burst\ pressure} \geq 1.5 \tag{18}$$

4.2.8 Maximum differential burst pressure will occur at the surface after cementing and two cases need to be considered:

i. With steam at the wellhead, when the design factor is:

$$Design\ Factor = \frac{minimum\ yield\ strength \times R_i}{wellhead\ steam\ pressure} \geq 1.8 \tag{19}$$

ii. With cold gas at the wellhead, the stress corrosion tensile limit of the steel should be used to determine the appropriate yield strength.

4.2.9 Biaxial stress if the wellhead is fixed on casing being considered (combined effects of axial and circumferential tension)

$$f_t = \frac{\sqrt{3}}{2} \times \left(\frac{P_w \times d}{D - d}\right) \tag{20}$$

$$Design\ Factor = \frac{steel\ strength}{maximum\ tensile\ stress} \geq 1.5 \tag{21}$$

The steel strength is the lesser of the yield and the sulphide stress corrosion limit.

4.2.10 Hoop stressing (collapse)

$$P_z = L_f \times g \left[G_f - \frac{1}{n}\right] \times 10^{-3} \tag{22}$$

$$Design\ Factor = \frac{pipe\ collapse\ strength}{net\ external\ pressure} \geq 1.2 \tag{23}$$

4.2.11 Design for thermal expansion of a trapped liquid (inner casing string collapse resistance should exceed burst strength of outer string)

$$Design\ Factor = \frac{production\ casing\ collapse\ strength}{outer\ casing\ burst\ strength} \geq 1.2 \tag{24}$$

4.3 Design calculation equations of well MW-20A with NZS 2403:2015 considering exact reservoir conditions

The following equations were used to calculate the different loading and stress scenarios using the NZS 2403:2015 code of practice for deep geothermal wells as described below. For definition of parameters, see Nomenclature.

4.3.1 Axial loading before and during cementing

$$F_{hookload} = F_{csg\ air\ wt} + F_{csg\ contents} - F_{displaced\ fluids} \tag{25}$$

$$F_{csg\ air\ wt} = L_z \times W_p \times g \times 10^{-3} \tag{26}$$

$$F_{csg\ contents} = \sum \rho_{if} \times L_{if} \times \frac{\pi d^2}{4} \times g \times 10^{-6} \tag{27}$$

$$F_{displaced\ fluids} = \sum \rho_{ef} \times L_{ef} \times \frac{\pi D^2}{4} \times g \times 10^{-6} \tag{28}$$

4.3.2 Maximum bending stress in non-vertical or curved wells

Bending stress for casings run in non-vertical or curved wells is given by:

$$F_b = 0.291 \times E \times q \times D \times 10^{-6} \tag{29}$$

$$Design\ Factor = \frac{minimum\ tensile\ strength}{maximum\ tensile\ load} \geq 1.8 \tag{30}$$

4.3.3 Axial loading after cementing

While calculating this loading it should be understood that a static force F_p (hookload) which is the tensile force at the surface from casing weight is normally present and will be used to calculate the resultant force.

a. Change in axial force (with tension as positive) due to a temperature rise in situations of partial longitudinal and lateral constraint

$$F_c = E \times a \times (T_1 - T_2) \times A_p \times 10^{-3} \quad (31)$$

The resultant force is therefore:

$$F_r = F_P + F_c \quad (32)$$

b. Tension due to temperature reduction when cold fluid is circulated from surface during drilling, testing or reinjection

$$F_T = E \times a \times (T_1 - T_3) \times A_p \times 10^{-3} \quad (33)$$

Resultant force at every depth, except close at the wellhead:

$$F_r = F_P + F_T \quad (34)$$

4.3.4 Tension at the top of any string anchoring a wellhead against lifting force by fluid in the well

$$F_w = \left(\frac{\pi}{4} \times P_w \times d^2 \times 10^{-3}\right) - F_m \quad (35)$$

$$Design\ Factor = \frac{minimum\ tensile\ strength}{maximum\ tensile\ load} \geq 1.8 \quad (36)$$

4.3.5 Extreme fibre compressive stress in an uncemented liner due to axial self-weight and helical buckling (axial loading with buckling and bending)

$$f_c = L_z \times W_p \times g \left[\frac{1}{A_p} + \frac{D\ e}{2I_p}\right] \quad (37)$$

$$Design\ Factor = \frac{minimum\ yield\ strength \times R_j}{total\ compressive\ stress} \geq 1.0 \quad (38)$$

R_j should be equal or less than 1.0.

4.3.6 Maximum differential burst pressure of string during cementing near shoe or stage cementing ports

$$\Delta P_{internal} = \left(L_z \rho_c - L_f \rho_f\right) \times g \times 10^{-3} \quad (39)$$

$$Design\ Factor = \frac{internal\ yield\ pressure}{differential\ internal\ pressure} \geq 1.5 \quad (40)$$

4.3.7 Maximum differential burst pressure at the surface (after cementing), two cases need to be considered:

i. With steam at the wellhead, when the design factor is:

$$Design\ Factor = \frac{internal\ yield\ pressure\ \times\ R_i}{wellhead\ pressure} \geq 1.8 \quad (41)$$

ii. With cold gas at the wellhead, when the stress corrosion tensile limit of the steel should be used to determine the appropriate yield strength.

4.3.8 Biaxial stress if wellhead is fixed on the casing being considered (combined effects of axial and circumferential tension)

$$f_t = \frac{\sqrt{5}}{2} \times \left(\frac{P_w \times d}{D - d}\right) \quad (42)$$

Design factor should not be less than 1.5:

$$Design\ Factor = \frac{steel\ yield\ strength}{maximum\ tensile\ stress} \geq 1.5 \quad (43)$$

4.3.9 Hoop stressing (collapse) during casing cementing operations

$$\Delta P_{external} = \left(L_z\,\rho_c - L_z\,\rho_f\right) \times g \times 10^{-3} \quad (44)$$

$$Design\ Factor = \frac{pipe\ collapse\ pressure}{differential\ external\ pressure} \geq 1.2 \quad (45)$$

4.3.10 Hoop stressing (collapse)-during production operations, annulus is at formation pressure

$$P_z = P_f$$

$$Design\ Factor = \frac{pipe\ collapse\ pressure}{differential\ external\ pressure} \geq 1.2 \quad (46)$$

4.4 ISO/TR 10400

The above equations from the two design codes were used to calculate casing loads assuming a well full of steam from bottom to surface. To check the burst, collapse and axial stress adequacy of the chosen casing strings, the ISO/TR 10400 technical report was used to calculate the allowable limits by computing the design factors and checking against the minimum design factors in the design codes (ISO/TR 10400, 2007). The formulas below from ISO/TR 10400 technical report were used to calculate the conformity. For definition of parameters, see Nomenclature.

4.4.1 External pressure resistance (collapse)

Collapse is dependent on the D/t ratio of the casing. For K55 casing grade, the ratio delineates the type of collapse that is going to occur, thereby giving the equation to be used to calculate the collapse limit for the casing. Table 1 below shows the various D/t ratio ranges for K55 and the type of collapse in that range.

TABLE 1: D/t ratio ranges for K55

D/t ratio	14.81	and less	Yield strength collapse
	14.81	25.01	Plastic collapse
	25.01	37.21	Transition collapse
	37.21	and greater	Elastic collapse

a. Yield strength collapse equation

$$PY_p = 2f_{ymn}\left[\frac{(D/t)-1}{(D/t)^2}\right] \quad (47)$$

b. Plastic collapse equation

$$P_P = f_{ymn}\left[\frac{A_c}{D/t} - B_c\right] - C_c \quad (48)$$

c. Transition collapse equation

$$P\,\mathrm{T} = f_{ymn}\left[\frac{F_c}{D/t} - G_c\right] \quad (49)$$

d. Elastic collapse equation

$$P_E = \frac{46.95 \times 10^6}{[D/t\,(D/t-1)^2]} \quad (50)$$

4.4.2 Triaxial yield of pipe body (Burst, yield)

a. Capped-end conditions - axial, radial and hoop stress: evaluated at the inner diameter

$$P_{iYLc} = \frac{f_{ymn}}{\left(\frac{(3D^4 + d_{wall}^4)}{(D^2 - d_{wall}^2)^2} + \frac{d^4}{(D^2-d^2)^2} - \frac{2d^2d_{wall}^2}{(D^2-d^2)(D^2-d_{wall}^2)}\right)^{1/2}} \quad (51)$$

b. Zero axial load - radial and hoop stress: evaluated at the inner diameter

$$P_{iYLo} = f_{ymn}\left(D^2 - d_{wall}^2\right)/\left(3D^4 + d_{wall}^4\right)^{½} \quad (52)$$

c. Historical, one-dimensional yield pressure design equation (the Barlow Equation for pipe yield)

$$P_{iYAPI} = \left[2f_{ymn}(k_{wall}t)/D\right] \quad (53)$$

4.4.3 Bending stress

$$\sigma_b = \pm M_b r/I = \pm E \cdot c \cdot r \quad (54)$$

5. RESULTS

5.1 Design using NZS 2403:1991 with exact reservoir conditions from MW-20A

The design results of MW-20A using NZS 2403:1991 are presented below in Tables 2 - 12.

5.1.1 Collapse and burst

Below in Tables 2 and 3 collapse and burst pressures for the different casing sizes are shown and the calculated design factors. Collapse has been calculated considering the annulus is filled with 1.85 kg/l of cement slurry, and water of mean specific volume of 0.988 l/kg at 50°C.

TABLE 2: Collapse pressure using NZS 2403:1991

CASING GRADE K55		COLLAPSE					
		Depth	1991 Code (MPa)	Collapse resistance (MPa)	Calculated design factor	Minimum design factor	lb/ft
Production casing (9⅝")	Top	10	0.08	26.84	326.51	1.20	47
	Middle	600	4.93	26.84	5.44	1.20	
	Shoe	1200	9.86	26.84	2.72	1.20	
Anchor casing (13⅜")	Top	10	0.08	7.89	95.94	1.20	54.5
	Middle	170	1.40	7.89	5.64	1.20	
	Shoe	350	2.88	7.89	2.74	1.20	
Surface Casing (20")	Top	10	0.08	3.53	42.94	1.20	94
	Middle	40	0.33	3.53	10.74	1.20	
	Shoe	80	0.66	3.53	5.37	1.20	

TABLE 3: Burst pressure using NZS 2403:1991

CASING GRADE K55		BURST					
		Depth	1991 Code (MPa)	Internal yield pressure (MPa)	Calculated design factor	Minimum design factor	lb/ft
Production casing (9⅝")	Top	10	0.10	32.40	326.32	1.5	47
	Middle	600	5.96	32.40	5.44	1.5	
	Shoe	1200	11.91	32.40	2.72	1.5	
Anchor casing (13⅜")	Top	10	0.10	18.91	190.44	1.5	54.5
	Middle	170	1.69	18.91	11.20	1.5	
	Shoe	350	3.48	18.91	5.44	1.5	
Surface Casing (20")	Top	10	0.10	14.48	145.82	1.5	94
	Middle	40	0.40	14.48	36.46	1.5	
	Shoe	80	0.79	14.48	18.23	1.5	

Calculations for burst pressure consider a cement slurry density of 1.85 kg/l inside the casing and hot water of mean specific volume of 0.988 l/kg at 50°C in the annulus.

5.1.2 Axial loading before and during cementing

During running of casing strings and cementing, casing axial tensile forces develop and act on the casing string, the calculated forces and design factors are shown in Table 4. Where the well is deviated for directional wells, stress due to bending is added to the hook load (tensile load). The bending stress in this case will be considered maximum at the kick off point (400 m), where the highest bending of the casing is expected. Bending stress will be added to the tensile load at the kick off depth. The casing string that is in the deviated section is the production casing (9⅝ casing). The maximum dog leg severity has been taken as 3° per 30 m.

TABLE 4: Tensile forces on casings before and during cementing

CSG GRADE K55		**Length (m)**	**Hook load, F_p (kN)**	**Min. tensile strength (kN)**	**Calculated design factor**	**Minimum design factor**	**lb/ft**
20" Csg	Surface	80	**95.99**	11374.73	**118.50**	1.8	**94**
13⅜ Csg	Surface	350	**243.69**	6555.90	**26.90**	1.8	**54.5**
9⅝ Csg	Surface	1200	**719.05**	5735.18	**7.98**	**1.8**	**47**
	Kick Off Point (KOP) at 400 m	400	239.68		**5.81**		
	Bending		747.58				
	Stress at KOP +Bending stress		**987.27**				

5.1.3 Axial loading after cementing

Axial loading after cementing may arise due to a rise in temperature in the well or when cold fluids are pumped in to the well. This results in compressive and tensional forces which are calculated as shown below in Section (a) and (b). In addition to these forces, bending stress from deviated sections of the well should be added to the calculated compressive and tensional forces. The bending stress is calculated at the kick off point where the stress is considered maximum, with a dog leg severity of 3° per 30 m. The deviated casing string is the production casing.

a. Compressive force due to temperature rise where there is partial longitudinal and lateral constraint

When cementing has been done, temperatures in the well may rise introducing compressive forces as shown in Table 5. The bottom hole setting temperature for the production, anchor and surface casings was taken as 75, 50 and 30°C, respectively. A temperature of 120°C has been selected to be the maximum expected temperature in the well after cementing. The change in temperature is 45, 70 and 90°C for the production, anchor and surface casing, respectively.

TABLE 5: Compressive force due to temperature rise

	Compressive force, F_c (kN)	**Minimum compressive strength (kN)**	**Calculated design factor**	**Minimum design factor**
20" Csg	**3751.06**	11374.73	3.03	1.2
13⅜ Csg	**1681.51**	6555.90	3.90	1.2
9⅝ Csg	945.65		3.39	1.2
Bending at kick off	747.58			
(400 m)	**1693.23**	5735.18		

b. Tension due to temperature reduction when cool fluid is circulated from the surface during drilling, testing or reinjection

Table 6 shows tension as a result of cool fluid being circulated during drilling, testing or reinjection. It was assumed that the cold fluid introduced was an ambient temperature of 25°C. The bottom hole setting temperature after cementing for the production, anchor and surface casings was taken as 75, 50 and 30°C, respectively. The change in temperature was therefore 50, 25 and 5°C for the production, anchor and surface casing strings, respectively.

TABLE 6: Tension when cool fluid is circulated in the well

Casing string	Tension force, F_t (kN)	Minimum tensile strength (kN)	Calculated design factor	Minimum design factor	lb/ft
20" Csg	**177.13**	11374.73	64.22	1.8	94
13⅜ Csg	**510.46**	6555.90	12.84	1.8	54.5
9⅝ Csg	893.11	5735.18	3.50	1.8	47
Bending at kick off (400 m)	747.58				
	1640.69				

5.1.4 Tension at the top of any string anchoring a wellhead against a lifting force by fluid in a well

The anchor casing holds the wellhead after the well has been completed. Lifting force by fluid in the well may introduce tension at the top of the anchor casing. The tension forces are calculated as shown in Table 7. The maximum well head pressure is 11.36 MPa from the worst case scenario where the well is assumed to be filled with steam from bottom to surface. The weight of the selected master valve, Class 900 manufactured by Alfa Oil, is 2 tonnes.

TABLE 7: Tension on anchor casing due to lifting force by fluid in the well

Casing string anchoring w/head	F_w (Tension at top) (kN)	Min. tensile strength (kN)	Calculated design factor	Min. design factor	lb/ft
13⅜ Csg	896.42	87775.69	97.92	1.80	**72**

5.1.5 Design factor for anchor casing thermal expansion into wellhead

During the operation of the well the production casing may rise into the wellhead, introducing stresses onto the anchor casing. Table 8 shows the design factor for this situation and how the best casing string is arrived at.

TABLE 8: Design factor for anchor casing thermal expansion into wellhead

lb/ft	Anchor casing tensile strength (kN)	Rising casing (prod. casing) compressive strength (kN)	Calculated design factor	Minimum design factor	
54.5	6555.90	5735.18	1.14	1.50	
61	7389.71	5735.18	1.29	1.50	
68	8216.98	5735.18	1.43	1.50	
72	8775.69	5735.18	1.53	1.50	Adequate

5.1.6 Extreme fibre compressive stress in an uncemented liner due to axial self-weight and helical buckling

Slotted liners are run in hole after drilling to the determined depth. The slotted liners allow the steam into the well and up to the surface through the production casing. The liners may hang using a liner hanger or they may be rested at the bottom of the well. When rested at the bottom, as is the practice in Menengai, compressive forces due to axial self-weight and helical buckling need to be considered. The slots in the liner are 20 mm in diameter and there are eight slots around the circumference of the liner.

The distance in between the rows along the axial direction is 60 mm, resulting in 16 rows of slots for every 1 m of the liner. Due to the slotting, the liner cross section area and the moment of inertia is reduced and were calculated as 4,520.91 mm^2 and 16,238,393 mm^4. The joint strength for the liner was 2,832.64 kN with a joint efficient of 0.96 required for this calculation. The compressive stress calculated is shown in Table 9.

TABLE 9: Compressive stress in uncemented liner due to axial self-weight and helical buckling

		Depth of liner	Compressive stress (MPa)	Calculated design factor	Minimum design factor
7" Csg 26 lb/ft	Top	10.00	1.63	**223.03**	**1.20**
	Middle	640.00	104.40	**3.48**	**1.20**
	Bottom	830.00	135.40	**2.69**	**1.20**

5.1.7 Maximum differential burst pressure at the surface after cementing

The maximum differential burst pressure occurs at the surface after cementing with steam or cold gas at the well head. The design factor calculation for this case is shown in Table 10 with the minimum design factor from the 1991 code for comparison. The casing string considered here is the anchor casing as it supports the wellhead.

TABLE 10: Design factor for maximum differential burst pressure at surface after completion

lb/ft	Well head Press (MPa)	Well head Temp. (°C)	Temp. reduction factor on yield strength	Internal yield strength (anchor) (MPa)	Calculated design factor	Minimum design factor	
54.5	11.36	320.5	0.95	18.91	1.58	1.8	
72	11.36	320.5	0.95	25.5	2.13	1.8	Adequate

5.1.8 Biaxial stress if the wellhead is fixed on the casing being considered (combined effects of axial and circumferential tension)

After drilling is completed a wellhead is placed on the anchor casing, introducing biaxial stress. The calculation of this stress is based on the upper casing joints interacting with the well head. The well head pressure used for this calculation is the maximum expected pressure of 11.36 MPa. Table 11 displays the calculation of biaxial stress and the design factor comparison.

TABLE 11: Biaxial stress on anchor casing

	Biaxial stress, f_t (MPa)	Yield strength (MPa)	Calculated design factor	Minimum design factor	lb/ft
13⅜ Csg	163.32	379	2.32	1.5	72

5.1.9 Design for the thermal expansion of a trapped liquid (inner casing string collapse resistance should exceed burst strength of outer string)

The 1991 design code instructs that a sacrificial casing is needed if there is trapped liquid within a cemented annulus. The design is such that if the trapped fluid expands, the outer casing should burst rather than the production casing collapse. To allow this, then the collapse resistance for the production casing should be higher than the burst of the outer casing. The weight of the 13⅜" casing and 9⅝"

casing is 54.5 and 47 lb/ft, respectively. In Table 12 the calculated design factor is compared with the desired design factor.

TABLE 12: Design factor for thermal expansion of a trapped liquid

	Prod. csg collapse (MPa)	**Anchor csg burst (MPa)**	**Calculated design factor**	**Minimum design factor**
13⅜ Csg 9⅝ Csg	26.84	18.91	1.42	1.2

5.2 Design using NZS 2403:2015 with reservoir conditions from MW-20A

The design results of MW-20A using NZS 2403:2015 are presented below in Tables 13-23.

5.2.1 Collapse and burst

The collapse and burst pressure for the three casing strings are shown in Tables 13 and 14 with the design factors also being compared. Collapse has been calculated considering the annulus is filled with 1.85 kg/l of cement slurry and water of mean specific volume of 0.988 l/kg at 50°C. Calculations for burst pressure consider a cement slurry density of 1.85 kg/l inside the casing and hot water of mean specific volume of 0.988 l/kg at 50°C in the annulus.

TABLE 13: Collapse pressure using NZS 2403:2015

CSG GRADE K55		**COLLAPSE**					
		Depth	**2015 Code**	**ISO/TR 10400**	**Calculated design factor**	**Minimum design factor**	**lb/ft**
Production casing (9⅝")	Top	10	0.08	26.84	317.36	1.20	47
	Middle	600	5.07	26.84	5.29	1.20	
	Shoe	1200	10.15	26.84	2.64	1.20	
Anchor casing (13⅜")	Top	10	0.08	7.89	93.25	1.20	54.5
	Middle	240	2.03	7.89	3.88	1.20	
	Shoe	470	3.97	7.89	1.99	1.20	
Surface casing (20")	Top	10	0.08	3.53	41.74	1.20	94
	Middle	70	0.59	3.53	5.98	1.20	
	Shoe	140	1.18	3.53	2.99	1.20	

TABLE 14: Burst pressure using NZS 2403:2015

CSG GRADE K55		**BURST**					
		Depth	**2015 Code**	**ISO/TR 10400**	**Calculated design factor**	**Minimum design factor**	**lb/ft**
Production casing (9⅝")	Top	10	0.08	32.40	383.15	1.5	47
	Middle	600	5.07	32.40	6.39	1.5	
	Shoe	1200	10.15	32.40	3.19	1.5	
Anchor casing (13⅜")	Top	10	0.08	18.91	223.61	1.5	54.5
	Middle	240	2.03	18.91	9.32	1.5	
	Shoe	470	3.97	18.91	4.76	1.5	
Surface Casing (20")	Top	10	0.08	14.48	171.22	1.5	94
	Middle	70	0.59	14.48	24.46	1.5	
	Shoe	140	1.18	14.48	12.23	1.5	

5.2.2 Axial loading before and during cementing

During the running of casing strings and before cementing, axial forces develop and act on the casing string. The fluid in the well is either hot water or drilling mud, but in this case the fluid considered is hot water of mean specific volume of 0.988 l/kg at 50°C. Where the well is deviated for directional wells, stress due to bending is added to the hook load (tensile load). The bending stress in this case will be considered maximum at kick off point (500 m) where the highest bending of the casing is expected.

Bending stress will be added to the weight of the casing at the kick off point i.e. 500 m. The casing string that is in the deviated section is the production casing (9⅝ casing**)**. The maximum dog leg severity has been taken as 3° per 30 m. Axial forces before and during cementing from NZS 2403:2015 are presented in Table 15.

TABLE 15: Axial forces on casings before and during cementing

CSG GRADE K55		$F_{csg\ air\ wt}$ **(kN)**	$F_{csg\ contents}$ **(kN)**	$F_{displaced\ fluids}$ **(kN)**	$F_{hookload}$ (F_p) **(kN)**	**Min. tensile strength (kN)**	**Calcul. design factor**	**Min. design factor**	**lb/ft**
20" Csg	Surface (140 m)	192.12	251.44	275.06	**168.50**	11374.73	**67.51**	1.8	**94**
13⅜" Csg	Surface (470 m)	373.95	367.33	412.92	**328.36**	6555.90	**19.97**	1.8	**54.5**
9⅝" Csg	Surface (1200 m)	823.38	444.19	546.15	**721.42**	5735.18	**7.95**	1.8	**47**
	Kick Off Point (KOP) at 500 m	343.07	185.08	227.56	300.59		**8.28**		
	Bending				392.48				
	Stress at KOP + Bending stress				**693.07**				

5.2.3 Axial loading after cementing

Axial loading after cementing may arise due to a rise in temperature in the well or when cold fluids are pumped into the well. This results in compressive and tensional forces which are calculated as shown below in Section (a) and (b). In addition to these forces, bending stress from deviated sections of the well should be added to the calculated compressive and tensional forces. The bending stress is calculated at the kick off point where the stress is considered maximum with a dog leg severity of 3° per 30 m. The deviated casing string is the production casing.

a. Change in axial force due to temperature rise in situations of partial longitudinal and lateral constraint

When cementing has been done the temperature in the well may rise, introducing axial loads in the casings as shown in Table 16. The negative symbols show that the forces experienced are compressive. The bottom hole setting temperature for the production, anchor and surface casing was taken as 75, 50 and 30°C, respectively. A temperature of 120°C has been selected to be the maximum expected temperature in the well after cementing. The change in temperature is 45, 70 and 90°C for the production, anchor and surface casing, respectively.

TABLE 16: Axial force due to temperature rise

	Compressive force, F_c (kN)	**Resultant force, F_r (kN)**	**Minimum yield strength (kN)**	**lb/ft**
20" Csg	**-4266.83**	**-4317.88**	6581.71	**94**
13⅜" Csg	**-1912.72**	**-1939.86**	3793.41	**54.5**
9⅝" Csg	-1075.67	-1223.23	3318.52	**47**
	Bending at kick off (500 m)	-392.48		
		-1615.71		

b. Tension due to temperature reduction when cold fluid is circulated from surface during drilling, testing or reinjection

Table 17 shows tension as a result of cool fluid being circulated, during drilling, testing or reinjection. It was assumed that the temperature of the cold fluid introduced was at an ambient temperature of 25°C. The bottom hole setting temperature after cementing for the production, anchor and surface casings was taken as 75, 50 and 30°C, respectively. The change in temperature was therefore 50, 25 and 5°C for the production, anchor and surface casing strings, respectively.

TABLE 17: Tension when cool fluid is circulated in the well

	F_T (kN)	**Resultant force F_r (kN)**	**Minimum yield strength (kN)**	**lb/ft**
20" Csg	237.05	185.99	6581.71	94
13⅜" Csg	683.11	655.97	3793.41	54.5
9⅝" Csg	1195.19			
Bending at kick off (500 m)	392.48	1832.60	3318.52	47
	1587.67			

5.2.4 Tension at the top of any string anchoring a wellhead against the lifting force by fluid in well

The anchor casing holds the wellhead after the well has been completed. The lifting force by the fluid in the well may introduce tension at the top of the anchor casing. The tension forces are calculated as shown in Table 18. The maximum well head pressure is 11.36 MPa from the worst case scenario where the well is assumed to be filled with steam from bottom to surface. The weight of the selected master valve, Class 900 manufactured by Alfa Oil, is 2 tonnes.

TABLE 18: Tension on anchor casing due to lifting force by fluid in the well

Casing string anchoring w/head	**F_w (Tension at the top) (kN)**	**Minimum tensile strength (kN)**	**Calculated design factor**	**Minimum design factor**	**lb/ft**
13⅜ Csg	896.42	87775.69	97.92	1.80	72

5.2.5 Design factor for the anchor casing thermal expansion into wellhead

During operation of the well the production casing may rise into the wellhead introducing stresses onto the anchor casing. Table 19 shows the design factor for this situation and how the best casing string is arrived at.

TABLE 19: Design factor for anchor casing thermal expansion into wellhead

lb/ft	Anchor casing tensile strength	Rising casing (Prod. csg) compressive strength	Calculated design factor	Minimum design factor	
54.5	6555.90	5735.18	1.14	1.50	
61	7389.71	5735.18	1.29	1.50	
68	8216.98	5735.18	1.43	1.50	
72	8775.69	5735.18	1.53	1.50	Adequate

5.2.6 Extreme fibre compressive stress in an uncemented liner due to axial self-weight and helical buckling

Slotted liners are run in hole after drilling to the determined depth. The slotted liners allow geothermal fluid into the well and up to the surface through the production casing. The liners may hang with the help of a liner hanger or they may be rested at the bottom of the well. When rested at the bottom, as is the practice in Menengai, compressive forces due to axial self-weight and helical buckling need to be considered. The slots in the liner are assumed to be 20 mm in diameter and with eight slots around the circumference of the liner. The distance between the rows along the axial direction is 60 mm resulting in 16 rows of slots for every 1 m of the liner. Due to the slotting, the liner cross section area and the moment of inertia are reduced and were calculated as 4520.91 mm^2 and 16238393mm^4. The joint strength for the liner was 2832.64 kN with a joint efficient of 0.96 required for this calculation. The compressive stress calculated is shown in Table 20.

TABLE 20: Compressive stress in uncemented liner due to axial self-weight and helical buckling

		Depth of liner	Compressive stress (MPa)	Calculated design factor	Minimum design factor
7" Csg 26 lb/ft	Top	10.00	1.63	223.03	1.0
	Middle	640.00	104.40	3.48	1.0
	Bottom	830.00	135.40	2.69	1.0

5.2.7 Maximum differential burst pressure at the surface (after cementing)

The highest differential burst pressure is expected to occur at the surface after cementing. The calculated design factor for this case is compared with the calculated design factor in Table 21. The anchor casing is considered here as it supports the well head.

TABLE 21: Design factor for maximum differential burst pressure at surface after cementing

lb/ft	Well head press. (MPa)	Well head temp. (°C)	Temp. reduction factor	Internal yield strength (anchor) (MPa)	Calculated design factor	Min. design factor	
54.5	11.36	320.5	0.8	18.91	1.33	1.80	
72	11.36	320.5	0.8	25.5	1.80	1.80	Adequate

5.2.8 Biaxial stress if wellhead is fixed on casing considered (combined effects of axial and circumferential tension)

Biaxial stresses are introduced on the casing string anchoring the wellhead. The biaxial stress is calculated below in Table 22 for a 13⅜" casing string considering the upper casing joints interacting with the well head. The calculated design factor is then compared with the minimum design factor from the design code. The well head pressure used for this calculation is the maximum expected pressure of 11.36 MPa.

TABLE 22: Biaxial stress on anchor casing

	Biaxial stress, f_t (MPa)	**Yield strength (MPa)**	**Calculated design factor**	**Min. design factor**	**lb/ft**
13⅜ Csg	210.85	379	1.80	1.5	72

5.2.9 Hoop stressing (collapse)-during production

The worst case scenario for the design has been chosen to be when the well is filled with steam from bottom to surface during production. Considering this case, collapse is computed at the production shoe so as an appropriate casing string can be provided. The differential collapse pressure is shown in Table 23 and the design factor calculated. The fluid inside the casing is steam and therefore the density is assumed to be zero.

TABLE 23: Collapse during production

Differential external pressure $\Delta P_{external}$	**Production casing collapse pressure at 1200 m**	**Calculated design factor**	**Min. design factor**
21.7782	26.83	1.23	1.20

5.3 Joint strength

The selected casing strings need to be checked for strength at the connections, or at the joints. The chosen type of connection is a buttress and Table 24 shows the strength of the joints for each casing string and the joint efficiency. According to the society of petroleum engineers it is imperative during casing design to appreciate that the API joint-strength values are a function of the ultimate tensile strength (SPE, 2015).

TABLE 24: Joint strength and efficiency

Casing	**lb/ft**	**Joint strength (kN)**	**Pipe body strength (kN)**	**Joint efficiency**
20	94	6576.49	11374.73	0.58
13⅜	54.5	4612.96	6555.90	0.70
9⅝	47	4444.00	5735.18	0.77
7"	26	2832.64	2961.20	0.96

6. DISCUSSION

The design of a well drilled to 2000 m using the two New Zealand design codes was done using the high temperature and pressure geothermal well MW-20A in Menengai as a reference well to estimate the reservoir pressure to be used in the design. The casing loads were evaluated for collapse, burst and axial stresses and the best casing size suggested. The casing strings were selected from the drilling data handbook (Gabolde and Nguyen, 2014) and were as follows:

- Production casing was 9⅝" with a weight of 47 lb/ft (see further discussion in section 6.12);
- Anchor casing was 13⅜" with a weight of 54.5 lb/ft, however, due to thermal expansion of the casing into well head, calculations showed that the upper part of the string was to be replaced with 2 joints of 72 lb/ft as will be explained later in this chapter, assuming that it was the minimum rise of the production casing that causes this stress;

- The surface casing that was found to be adequate was 20” with 94 lb/ft.

All the calculations for the casing loads have been based on these casing strings and the results are discussed herein.

6.1 Collapse and burst

Collapse pressure for the production casing at 1200 m from NZS 2403:1991 at the shoe was 9.86 MPa with a design factor of 2.72 while for the same depth the collapse from NZS 2403:2015 was 10.15 MPa and a design factor of 2.64. The minimum design factor from both codes is 1.2 hence the design was adequate.

Burst pressure at the shoe for the production casing at 1200 m calculations from NZS 2403:1991 showed a pressure of 10.15 MPa and a design factor of 3.19. NZS 2403:2015 calculations for burst resulted to a pressure of 10.15 MPa and a design factor of 3.19. The minimum design factor for burst was 1.5 from both codes showing that the provided production casing string was sufficient.

The collapse pressure at the shoe for the anchor casing was 2.88 MPa and a design factor of 2.74 as given by NZS 2403:1991 at a shoe depth of 350 m. The NZS 2403:2015 calculations give a collapse pressure of 3.97 MPa and a design factor of 1.99 at a shoe depth of 470 m. Both design codes provide a minimum design factor of 1.5 and thus this design is sufficient.

The burst pressure for the anchor casing at the shoe was calculated as 2.96 MPa with a design factor of 6.39 using the NZS 2403:1991 design code at a shoe depth of 350 m. From NZS 2403:2015 the burst at 470 m shoe depth was found to be 3.97 MPa and design factor of 4.76. The minimum design factor is 1.5 for the two codes and thus the choice of the casings was appropriate.

The surface casing was set at 80 m using the NZS 2403:1991 code and the collapse pressure at this depth was 0.66 MPa with a design factor of 5.37. The NZS 2403:2015 design code placed the surface casing shoe at 140 m and the collapse pressure was 1.18 MPa with a design factor of 2.99. The minimum design factor for collapse from the two codes is 1.5 concluding that the selected casing string was satisfactory.

Burst pressure for the surface casing (20” casing) was also computed considering the two different codes. At a shoe depth of 80 m and using the NZS 2403:1991 code the burst pressure was 0.68 MPa and the design factor was 21.4. The 2015 New Zealand code, NZS 2403:2015 gives a burst pressure of 1.18 MPa and a design factor of 12.23. The minimum design factor for burst from the two design codes is 1.5 and so the design is correct.

6.2 Axial loading before and during cementing

Axial loads before and during cementing were calculated from both codes. The computed axial load for the surface casing (20”) using NZS 2403:1991 was 95.99 kN and the design factor was 118.5. Results from NZS 2403:2015 showed an axial load of 168.5 kN. The design factor for this case was 67.51 and the minimum design factor was 1.8 for the two codes. Given the computed design factors the design was found to be sound and safe.

For the anchor casing the NZS 2403:1991 design standard provided an axial load of 243.69 kN and design factor of 26.9 while the 2015 NZS 2403:2015 showed an axial load of 328.36 kN and a design factor of 19.97. It was deduced from the calculated design factors that the design was adequate as the minimum design factor from the design codes was 1.8.

The production casing string axial load was computed from NZS 2403:1991 as 719.05 kN from the shoe and the calculated design factor was 7.98 without considering bending. However, it should be noted that this casing string is placed in the deviated part of the well and bending stresses need to be accounted for by adding the stress to the tensile load at the kick off depth. The bending stress calculated at the kick off point (400 m) was 747.58 kN and the tensile load at the kick off depth was calculated as 239.68 kN; the resultant was 987.27 kN with a design factor of 5.81.

Similarly the NZS 2403:2015 was used to calculate the axial loading on the production casing and the results showed that the load was 721.42 kN from the shoe without considering bending with a design factor of 7.95. The bending force was calculated as 392.48 kN and was added to the casing weight (tensile load) at the kick off (500 m) computed as 300.59 kN. The resultant load was 693.07 kN and a design factor of 8.28 was calculated. When compared against the minimum design factor of 1.8 from the two codes, the design was found to be safe.

6.3 Axial loading after cementing

After casing cementing has been done, the temperature variations in the well will introduce stresses in the casing. A rise in temperature will result in compressive stresses in the well and if the temperature is lowered in the well, especially during drilling, testing or reinjection, then tension stresses are introduced in the casings. The calculated stresses from the rise or reduction of temperature should be added to the axial loading before and during cementing in clause 6.2 as it exists as a static force to arrive at a resultant force on the casing string.

6.3.1 Compressive forces after cementing due to a rise in temperature in situations of partial longitudinal and lateral restraint

After cementing is done and the bottom hole setting temperature has been noted the formation may start to heat up, leading to an increase in temperature, and the result is that compressive forces will build up on the casing. The bottom hole setting temperature for the production, anchor and surface casing was 75, 50 and 30°C, respectively. A temperature of 120°C was chosen to be the maximum expected temperature in the well after cementing.

Design computation for axial loading after cementing from NZS 2403:1991 for the production casing portrayed a compressive force of 945.65 kN, and adding the additional compressive force of 747.58 kN from bending the resultant force was 1693.23 kN and the design factor was 3.39 compared to the minimum design factor of 1.2. The anchor casing computation of the force due to rise in temperature showed a compressive force of 1681.51 kN and a design factor of 3.9 compared to the minimum design factor of 1.2. More so using the same design code the calculated surface casing compressive force was 3751.06 kN and a design factor of 3.03 whereas the minimum design factor was 1.2. Given the calculated design factors it is evident that they are all above the minimum design factor of 1.2 and this confirms that the design adequate.

Resultant compressive forces from NZS 2403:2015 were obtained as follows; the production casing had a force of 1615.71 kN including a bending force of 372.48 kN, and for the anchor casing the force was 1939.86 kN and the surface casing had 4317.88 kN. Using the design code guides to check for the design adequacy, the resultant forces have to be checked against the minimum yield strength of each of the casing strings. The minimum yield strength for the production, anchor and surface casing was computed as 3318.52, 3793.41 and 6581.71 kN, respectively. Doing a comparison of the calculated compressive forces and the minimum yield strength of the different casing strings, the design was found to be appropriate.

6.3.2 Tension due to temperature reduction when cold fluid is circulated from surface

After cementing there is a need to continue drilling or to do a test on the well, while in other cases the well might be used for reinjection. In such cases, cold fluids are introduced into the well, lowering the existing temperature. Lowering of the temperature introduces tension forces into the casings and this may become significant if very cold fluids are used.

The following are results for tension induced forces due to cooling in the well. It was assumed that the temperature of the cold fluid introduced is 25°C. The bottom hole setting temperature for the production, anchor and surface casing was taken as 75, 50 and 30°C, respectively

Using NZS 2403:2015 the tension forces on the surface casing were found to be 177.13 kN and the calculated design factor was 64.22, the tension on the anchor casing was 510.46 kN with a design factor of 12.84 and the tension on the production casing, including tension of 747.58 kN due to bending, was 1640.69 kN with a design factor of 3.5. The design was checked against the minimum design factor of 1.8 and hence found to be safe.

The NZS 2403:2015 design code showed a tension of 185.99 kN on the surface casing, 655.97 kN on the anchor casing and 1832.6 kN on the production casing, including a bending tensional force of 392.48 kN. Given the yield strength of the surface, anchor and production casing as 6581.71, 3793.41 and 3318.52 kN, respectively, the design showed that the chosen casing weights were adequate.

6.4 Tension at the top of a casing string anchoring a wellhead against the lifting force by fluid in the well

Tension forces do occur at the top of the casing string that holds the well head. This force needs to be calculated so that the best anchor casing can be chosen. In this case the casing holding the well head is the 13⅜”casing with a weight of 72 lb/ft. The calculation for this force is the same from the two standards and the force calculated is 857.95 kN with a design factor of 102.31. This design is appropriate as the minimum design factor for this case is 1.8.

6.5 Design factor for anchor casing thermal expansion into wellhead

The production casing, which is cemented inside the anchor casing, may in some instances rise and elongate at the free end up at the wellhead and this is where it is advised to have an expansion spool at the wellhead. The design factor required for a successful design is 1.5 for NZS 2403:1991 and 1.4 for NZS 2403:2015. The previously chosen anchor casing weight of 54.5 lb/ft could not provide an adequate design. This necessitated the changing of the design of the top two joints of the anchor casing by increasing their weight to 72 lb/ft for the design to hold. After calculations using the 72 lb/ft anchor casing a design factor of 1.53 was obtained against a minimum design factor of 1.5 and 1.4 for NZS 2403:1991 and NZS 2403:2015 respectively hence this design criterion holds for the two New Zealand codes.

6.6 Maximum differential burst pressure at the surface after cementing

After the casing cementing the maximum differential burst pressure will occur at the surface and the anchor casing has to be sufficient enough to hold the pressure. The design calculation from the two New Zealand standards is the same, however the temperature reduction factors for yield are different. The NZS 2403:2015 design code has revised the reduction factors downwards, and for example in this case considering a temperature of 320.5°C at the wellhead the reduction factor for yield strength from NZS 2403:2015 is 0.8 while the one from NZS 2403:1991 is 0.95. Calculated design factor from NZS

2403:1991 is 2.13 and the one from NZS 2403:2015 is 1.8. The minimum design factor is 1.8 hence the design is adequate.

6.7 Biaxial stress if wellhead is fixed on casing being considered

Considering that the wellhead will be fixed on the anchor casing, biaxial stress is bound to occur and therefore needs to be incorporated into the design. The biaxial stress is a combined effect of axial and circumferential tension.

Biaxial stress calculated from NZS 2403:1991 was 118.21 MPa with a calculated design factor of 3.21 while the NZS 2403:2015 design code gave a biaxial stress of 152.61 MPa with a design factor of 2.48. The minimum design factor from the two codes is 1.5, hence the design is appropriate.

6.8 Hoop stressing (Collapse during production) NZS 2403:2015

During production operations the annulus is at the formation pressure, meaning that the external fluid pressure at the production casing shoe is equal to the pore pressure. To take care of this collapse NZS 2403:2015 provides a minimum design factor of 1.2. The calculated design factor for the production casing at the shoe is 1.23 and thus the design is adequate.

6.9 Design for thermal expansion of a trapped liquid NZS 2403:1991

NZS 2403:1991 design code provides a minimum design factor of 1.2 for the thermal expansion of trapped fluids. The thermal expansion of trapped fluids results in pressures exceeding the strength of casing strings in either collapse or burst. The code therefore provides a design of a production casing which has a higher collapse resistance than the burst resistance of the outer casing so that the integrity of the production casing is preserved, in case there is an occurrence of expansion of trapped fluids. The calculated design factor in this scenario is 1.42 and the minimum design factor is 1.2 and thus the design is safe.

6.10 Extreme fibre compressive stress in an uncemented liner due to axial self-weight and helical buckling

After drilling to total depth a well may be completed by running a liner, screen or left barefoot that is without a liner or a screen. Where liners are run in hole they can hang on the liner hanger or left to rest at the bottom of the well, which is the practice in Menengai. When liners are left to rest at the bottom of the well there will be compressive forces on the liner due to self-weight and helical buckling. The liner will tend to buckle in the well as the well diameter is larger than the diameter of the well. Due to this the liner should be checked so it does not exceed its minimum yield.

Calculations for the compressive stress are the same from the two New Zealand codes and the maximum stress is 195.76 MPa at the bottom of the liner with a design factor of 2.69. The minimum design factor from NZS 2403:1991 and NZS 2403:2015 is 1.2 and 1.0, respectively and therefore the design is adequate.

6.11 Connection/joint strength

The casing connection that was chosen for the casing strings was a buttress. The joint strength for surface, anchor, production and slotted liner was calculated as 6576.49, 4612.96, 4444 and 2832.64 kN,

respectively. The connection efficiency was 0.58, 0.7, 0.77 and 0.96 for the surface, anchor, production and slotted liners, respectively.

6.12 Corrosion

NZS 2403:1991 and NZS 2403:2015 design codes recognize the effect of corrosion which reduces the cross section area of casings. The production casing is the main conveyor of geothermal fluid to the surface and into the wellhead. This casing will be prone to corrosion where conditions for corrosion are favourable. From the design that has been carried out, the production casing string selected is 9⅝" 53.5 lb/ft. Closer examination shows that the weight of this casing can be reduced to 36 lb/ft and the design will still be adequate as the collapse design factor will be 1.23, compared to a minimum design factor of 1.2. However, due to corrosion effects during the life time of the well reducing the thickness would compromise the anticipated well life. Corrosion is regarded to be acceptable for material used at a rate of 0.1 mm per year from studies conducted in Iceland on wells across the country (Thorbjornson, I., pers.comm., September, 2015); this translates to 2 mm in 20 years. If the weight of the production casing is reduced from 53.5 to 36 lb/ft the thickness is reduced by 3 mm. Hence if corrosion is to be considered the chosen casing of 53.5 lb/ft is adequate during the life of the well estimated to be 20 years.

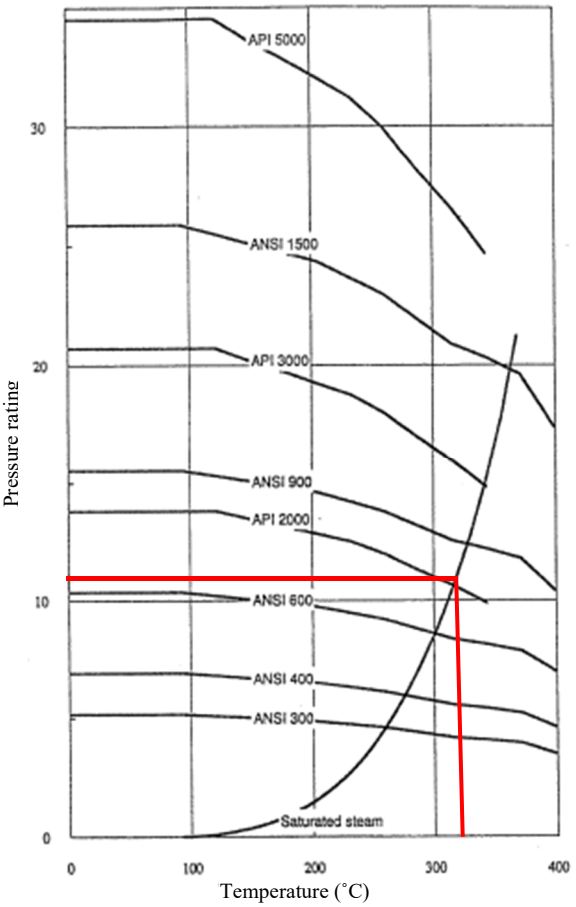

FIGURE 15: Wellhead working pressure de-rating for flanges and valves conforming to ANSI/ASME B16.5 and to API Spec 6A (New Zealand Standard, 2015)

6.13 Well head selection

The design premise adopted for designing the considered well was the steam filled condition as this presented the worst case scenario. The expected pressure and temperature at the wellhead in this condition is 11.36MPa and 320.5°C as shown in Figure 15. The most suitable wellhead from Figure 15 is an ANSI 900 or Class 900 master valve.

7. CONCLUSIONS AND RECOMMENDATION

The two New Zealand design codes have been used to design a 2000 m well, although in principle the two codes differ as will be detailed here. NZS 2403:1991 uses the overburden of the underlying formation as the maximum pressure boundary while determining the minimum casing depth, whereas the 2015 code, NZS 2403:2015 adopts the fracture pressure as the maximum boundary for minimum casing determination.

Increase in temperature reduces the yield strength, modulus of elasticity and tensile strength of steel and therefore reduction factors have been provided for various temperature ranges, quite notable is that the reduction factors in the 2015 design have been reduced compared to the ones previously found in the 1991 design code. For example, the temperature reduction factor for yield strength at a temperature of 300°C is 0.8 in the 2015 design code whereas in the 1991 code the reduction factor is 0.95.

Some of the minimum design factors have been reduced in the 2015 design code, for instance the minimum design factor for anchor casing expansion into the well head and compressive stress due to liner self-weight and helical buckling are 1.4 and 1.0, respectively, while in the 1991 code the minimum design factors are 1.5 and 1.2 respectively. The 1991 code accounts for the thermal expansion of fluids trapped within the casing by providing an outer casing with a lower burst pressure resistance than the collapse resistance of the inner casing and provides a minimum design factor of 1.2. On the other hand the 2015 design code recognizes the effect of high pressures generated by expansion of trapped fluids and stipulates that an adequate safety margin against yield arising from this case is taken into account while designing for collapse. Thermal expansion of the casing is not allowed to exceed the minimum yield in the 1991 design code, while in the 2015 design code this is allowed and it is advised that when this is anticipated, the strain based design should be considered.

While determining the minimum casing depth it was noted that the 2015 code gave deeper minimum casing depths compared to the 1991 code. The two design codes provide guidance of minimum casing determination up to 2000 m. More light needs to be shed for wells that are to be drilled deeper than 2000 m. Generally from the calculations obtained during the design process there was no significant variation between the two design codes that was noted.

The author recommends that after the casing cementing has been done and drilling has to continue, then if possible the drilling fluid temperature should be elevated close to the bottom hole setting temperature of the casing to avoid introduction of tensional forces in the well. Similarly during reinjection activities, cold fluid should not be pumped into the wells.

ACKNOWLEDGEMENTS

I wish to take this opportunity to thank the government of Iceland and UNU-GTP for the UNU Fellowship award. My special regards goes to ÍSOR – Iceland GeoSurvey and Orkustofnun - the Icelandic National Energy Authority for their wonderful and knowledgeable teaching staffs that was available throughout the training period; their kindness was overwhelming. Much appreciation goes to my company Geothermal Development Company for giving me the opportunity and believing that I deserved this chance to study here in Iceland.

I am highly indebted to UNU-GTP director Mr. Lúdvík S. Georgsson, Ms. Málfrídur Ómarsdóttir, Mr. Markús A. G. Wilde, Ms. María S. Gudjónsdóttir, Ms. Thórhildur Ísberg and Mr. Ingimar G. Haraldsson for their outstanding support and smooth facilitation of the entire training programme lasting six months.

I would like to extend my sincere and heartfelt gratitude to my supervisors Mr. Sverrir Thórhallsson, Mr. Ingólfur Örn Thorbjörnsson and Mr. Gunnar Skúlason Kaldal for their support and invaluable advice during the preparation of this report; I have now become a knowledgeable drilling engineer. Without your close supervision this report would not have been of this quality. Thanks to Mr. Björn Már Sveinbjörnsson who took his time to take me through drilling technology lectures and field trips to the drilling rig. I appreciate in a special way my colleagues back in Kenya who assisted me with data for this project, Janet Suwai, Isaac Makuk, Moses Chemeitoi, Francis Wanjohi and Simon Njuguna, may you be blessed abundantly for your assistance.

Special regards to my fellow colleagues under the training programme for the good times we have shared together during the six months, and to Fardaneh and Nuno for reminding me every time “no mercy” as a push button to finish my project report, to all of you thank you and God bless you.

I am grateful to my family for the moral support and understanding they have provided me with, God bless you. And finally, last but not least to the Almighty God for the health, for the care and for the divine protection.

NOMENCLATURE

A_C = Empirical constant in the historical API collapse equation
A_p = Cross-sectional area of pipe/casing wall (mm^2) allowing for any slotting
a = Coefficient of thermal expansion ($°C^{-1}$)
B_C = Empirical constant in the historical API collapse equation
C_C = Empirical constant in the historical API collapse equation
c = Tube curvature, the inverse of the radius of curvature to the centre line of the pipe
D = Pipe outside diameter (mm)
d = Pipe inside diameter (mm)
d_{wall} = Inside diameter based on $K_{wall}\,t$, $d_{wall} = D - 2K_{wall}\,t$
E = Young's modulus of elasticity (MPa)
e = Eccentricity (mm) = actual (not nominal) hole diameter minus D
F_b = Maximum stress due to bending (MPa)
F_C = Empirical constant in the historical API collapse equation
F_c = Compressive force due to heating / Change in axial force within casing body due to heating (kN)
$F_{csg\ air\ wt}$ = Air weight of casing (kN);
$F_{csg\ contents}$ = Weight of internal contents of casing (kN)
$F_{displaced\ fluids}$ = Weight of fluids displaced by casing (kN)
$F_{hookload}$ = Surface force suspending casing that is subjected to gravitational & static hydraulic loads (kN)
F_m = Net downward force applied by wellhead (kN) due to its own mass and any pipework reactions
F_P = Axial force within casing body at cement set (kN)
F_p = Tensile force at surface from casing weight (kN)
F_r = Resultant axial force within casing body combining the force at cement set and subsequent thermal forces (kN)
F_T = Change in axial force within casing body due to cooling (kN)
F_t = Tensile force due to cooling (kN)
F_w = Lifting force due to wellhead pressure (kN)
f_c = Total extreme fibre compressive stress due axial and bending forces (MPa)
f_t = Maximum tensile stress (MPa)
f_{ymn} = Minimum yield strength
G_C = Empirical constant in the historical API collapse equation
G_f = Cement slurry density (e.g. 1.8 kg/l)
g = Gravitational acceleration (9.81 m/s^2
h = Depth below liquid level (m)
I = Moment of inertia of the pipe cross section, $I = \pi/64(D_4 - d_4)$
I_p = Net moment of inertia of the pipe section (mm^4) allowing for any slotting/perforations
K_{wall} = Specified manufacturing tolerance of pipe wall, e.g. tolerance of 12.5% = 0.875
L_{ef} = Vertical length of a section of fluid having the same density within the external annulus (m)
L_f = Total vertical length of a fluid column in an annulus / depth below liquid level (m)
L_{if} = Vertical length of a section of fluid having the same density within the casing (m)
L_z = Total vertical length of liner or casing below any level (m)
M_b = Bending moment
n = Mean specific volume of hot fluid (l/kg)
P_E = Pressure for elastic collapse (MPa)
P_f = Pore pressure (MPa)
P_{frac} = In situ fracture pressure of a formation (MPa)
P_i = Differential internal yield pressure (MPa)
P_{iYAPI} = Internal pressure at yield for a thin tube (MPa)
P_{iYLc} = Internal pressure at yield for a capped-end thick tube (MPa)
P_{iYLo} = Internal pressure at yield for an open-end thick tube (MPa)
P_p = Pressure for plastic collapse (MPa)
P_T = Pressure for transition collapse (MPa)

P_w = Maximum well head pressure (MPa)
P_z = External fluid pressure at casing shoe (MPa)
PY_p = Pressure for yield strength collapse (MPa)
q = Curvature (degrees per 30 m);
R_i = Temperature reduction factor (ratio)
R_j = Joint/connection efficiency in compression (joint strength / pipe body strength)
r = Radial coordinate $d/2 \leq r \leq D/2$
S_V = Overburden pressure (vertical pressure due to weight of overlying formations (MPa)
T_1 = Neutral temperature (i.e. temperature of casing at time of grout/cement set) (°C)
T_2 = Maximum expected temperature (°C)
T_3 = Minimum temperature after cooling well (°C)
t = Pipe wall thickness
W_p = Nominal unit weight of casing in air (kg/m)

$\Delta P_{external}$= Differential pressure on casing during cementing (MPa)
$\Delta P_{internal}$= Differential pressure on casing during cementing (MPa)
ρ = Density of the underlying bedrock (kg/m^3)
ρ_c = Cement slurry density (kg/l)
ρ_{ef} = Density of a section of fluids with constant density within an annulus (kg/l)
ρ_f = Density of fluid -usually water- in the well bore or annulus (kg/l)
ρ_{if} = Density of a section of fluids with constant density within a casing (kg/l)
σ_b = Bending stress
v = Poisson's ratio

REFERENCES

Finger, J. and Blankenship, D., 2010: *Handbook of best practices for geothermal drilling.* Sandia National Laboratories, Albuquerque, website: *artikel-software.com/file/geothermal%20drilling%20handbook.pdf.*

Gabolde G. and Nguyen, J.P., 2014: *Drilling data handbook* (9th edition). Edit. Technip, Paris, 576 pp.

Hole, H., 2008a: Geothermal well design – casing and wellhead. In: *Petroleum Engineering Summer School, Dubrovnik, Croatia, Workshop, 26,* website: *www.geothermal-energy.org/pdf/IGAstandard/ISS/2008Croatia/Hole02.pdf*

Hole, H., 2008b: Geothermal well completion tests. In: *Petroleum Engineering Summer School Dubrovnik, Croatia Workshop, 26*, 9-13.

ISO/TR 10400, 2007: *Petroleum and natural gas industries - Equations and calculations for the properties of casing, tubing, drill pipe and line pipe used as casing or tubing*. Technical report, ISO/TR 10400, 229 pp.

Kaldal, G.S., Jónsson, M.Th., Pálsson, H. and Karlsdóttir, S.N., 2013: Collapse analysis of the casing in high temperature geothermal wells. *Proceedings of the 38th Workshop on Geothermal Reservoir Engineering, Stanford University, Stanford, CA*, 10 pp.

Karlsson, Th., 1978: Casing design for high temperature geothermal wells. *Geothermal Resources Council, Transactions, 2,* 355-358.

Lari, I., 1997: Rezistenta coloanelor de bulrane tubate in sondele supuse procesului de injectioe de abur. ICPT internal Report, Campina, Romania, 55 pp.

New Zealand Standard, 1991: *Code of practice for deep geothermal wells*. Standards Association of New Zealand, Wellington, NZ, 93 pp.

New Zealand Standard, 2015: *Code of practice for deep geothermal wells*. Standards New Zealand, Wellington, NZ, 102 pp.

Ólafsson, A., 2011: *Structural and stress analysis of a high temperature geothermal wellhead.* University of Iceland, Reykjavik, MSc thesis, 92 pp.

Southon, J.N., 2005: Geothermal well design, construction and failures. *Proceedings of the World Geothermal Congress 2005, Antalya, Turkey,* 6 pp.

Teodoriu, C., and Falcone, G., 2009: Comparing completion design in hydrocarbon and geothermal wells: The need to evaluate the integrity of casing connections subject to thermal stresses. *Geothermics, 38-2*, 238-246.

Thórhallsson, S., 2015: *Well designs and geothermal drilling technology.* UNU-GTP, Iceland, unpublished lectures, 379 pp.

Thórhallsson, S., 2008: Geothermal drilling and well pumps. *Proceedings of Workshop for Decision Makers on Direct Heating Use of Geothermal Resources in Asia, organized by UNU-GTP, TBLRREM and TBGMED, in Tianjin, P.R. China,* UNU-GTP SC-06, 11-18.

Thórhallsson, S., 2006: New developments in geothermal drilling. *Proceedings of Workshop for Decision Makers on Geothermal Projects in Central America" organized by UNU-GTP and LaGeo in San Salvador, El Salvador, UNU-GTP SC-02,* 8 pp.

Vollmar, D., Wittig, V., and Bracke, R., 2013: *Geothermal drilling best practices: The Geothermal translation of conventional drilling recommendations - main potential challenges.* International Geothermal Association, IGA Academy Report 0104-2013.

SPE 2015: *Casing and tubing.* Society of Petroleum Engineers, Petrowiki, website: *petrowiki.org/Casing_and_tubing#Connection_design_limits.*

UNITED NATIONS UNIVERSITY
UNU-GTP
Geothermal Training Programme

Orkustofnun, Grensasvegur 9,
IS-108 Reykjavik, Iceland

Reports 2015
Number 29

TEMPERATURE AND PRESSURE ANALYSIS OF WELLS NJ-13 AND NJ-28 IN THE NESJAVELLIR GEOTHERMAL SYSTEM, SW-ICELAND

Aloysius Tunu Otmar
Mineral Resources Authority
Mining Haus, Poreporena Freeway, P O Box 1906,
Port Moresby 121, National Capital District
PAPUA NEW GUINEA
aotmar@mra.gov.pg

ABSTRACT

Temperature and pressure analysis of geothermal wells is one of the vital steps in evaluating a geothermal reservoir during exploration, production and monitoring the wells. By analysing temperature and pressure logs from the warm up period of a well, the formation temperature and initial pressure can be deduced. Injection well testing is usually done at the end of drilling to find out physical parameters of the well and the reservoir surrounding it and get information on the connection of the well to the reservoir.

Well NJ-13 is a 1609 m deep vertical production well drilled in 1985. It is located in the Nesjavellir high-temperature geothermal field of the Hengill geothermal system located in SW-Iceland. The total enthalpy of well NJ-13 is around 2500 kJ/kg. At well head pressure (P_0) of 16 bar-g, the power output for well NJ-13 is 15 MWe, as estimated from the original production test data.

Well NJ-28 is a directional well drilled from the same well pad as NJ-13 in May-June 2015 as a makeup well to a depth of 1301 m with respect to the platform. The intended depth of this well was 2100 m but the drilling was stopped at 1301 m after several attempts to continue when the drill string repeatedly got stuck due to intrusions at the bottom of the well. The total enthalpy of well NJ-28 is around 2600 kJ/kg. At a well head pressure (P_0) of 20 bar-g, the power output of well NJ-28 is 5 MWe estimated from production test data from September 2015. Well NJ-28 has lower transmissivity and injectivity than well NJ-13 which might explain why NJ-28 is a poor producer compared to NJ-13.

1. INTRODUCTION

This paper is written as a final project report of the six-month training at the United Nations University Geothermal Training Programme in 2015. The report presents analysis of temperature and pressure logs from wells NJ-13 and NJ-28 from the Nesjavellir geothermal field. The available pressure and temperature logs from their warm up periods were used to deduce the formation temperature and initial

pressure in the wells. Additionally, injection and production well tests were analysed to find relevant parameters of the geothermal reservoir around the wells.

The Nesjavellir geothermal field is situated at the northern margin of the Hengill geothermal system in SW-Iceland (Figure 1A). There are several other high-temperature geothermal fields within Hengill geothermal system, such as Hellisheidi and Hverahlíd which lie further towards the south (Figure 1B), Gráuhnúkar towards the southwest and Bitra towards the south east. The data analysed and presented in this report is from Orka Náttúrunnar (ON Power), which operates the Nesjavellir geothermal field. The Nesjavellir geothermal power plant's output is 120 MWe and 300 MWt (2014).

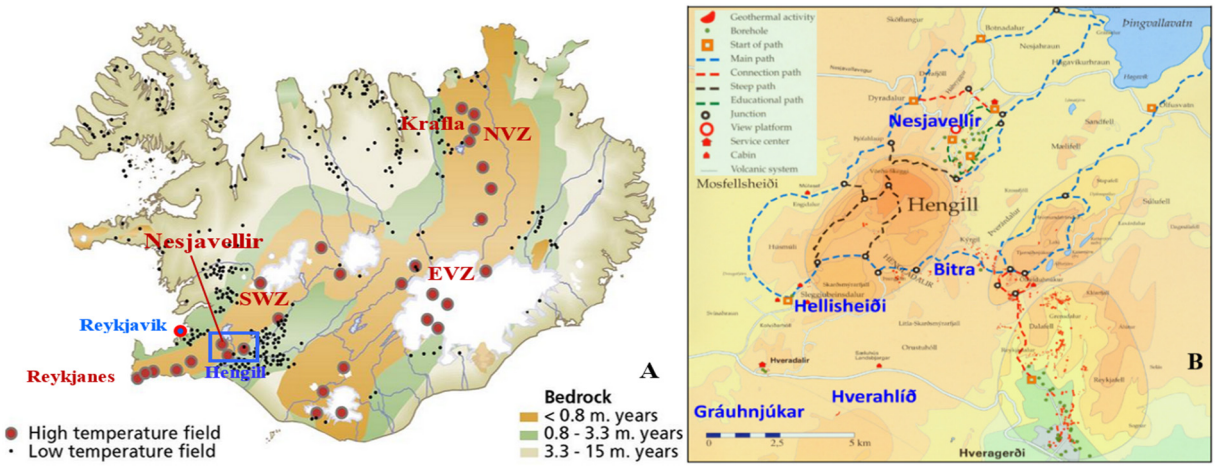

FIGURE 1: A) Geological map of Iceland, with geological zones, low- and high-temperature geothermal fields, and main volcanic zones (modified after Jóhannesson and Saemundsson, 1999), NVZ – Northern Volcanic Zone, EVZ – Eastern Volcanic Zone, SWZ – Southwestern Volcanic Zone; B) Hengill volcanic system, SW-Iceland and its geothermal fields (Gíslason and Gunnlaugsson, 2003)

2. BACKGROUND

2.1 Regional geology

With about thirty active volcanic systems and numerous geothermal systems, the island of Iceland is located on the northern part of the diverging Mid-Atlantic Ridge between the North American and Eurasian plate (Saemundsson, 1979). The two plates are moving away from each other at a rate of 15 mm/year (Árnadóttir et al. 2008). The active spreading of the ridge and the Icelandic mantle plume enhance magma flow from the earth's interior to the surface or as intrusions at shallow levels, which react with groundwater resulting in the formation of the highly prospective geothermal systems in Iceland.

Iceland can be divided into three (3) main geological zones depending on the age of the basaltic rocks. These three main active volcanic zones of Iceland, as identified by Níelsson and Franzson (2010), are: the south-western volcanic zone (SWZ), which includes the Hengill and Reykjanes volcanic systems, the eastern volcanic zone (EVZ) and the northern volcanic zone (NVZ) as shown in Figure 1A.

Most of the high-temperature geothermal fields of Iceland are located inside the volcanic zones, which are covered with late Quaternary basalts (less than 0.8 million years old) and hyaloclastites trending NE-SW. Low-temperature geothermal fields are mainly scattered on the peripheries of these areas and further away, indicated by the black dots in Figure 1A.

2.2 Geology of Hengill geothermal area

The Nesjavellir high-temperature geothermal field is ~30 km ESE of Reykjavík on the northern margin of the Hengill area, which hosts one of the largest high-temperature geothermal systems in Iceland, extending over 50 km^2 and located in the south western volcanic zone (Figure 1A). The tensional stress that has developed as a result of the structural activity in the area has opened up NE-SW trending vertical fractures creating permeable zones for the outflow of thermal fluids (Franzson and Sigvaldason, H., 1985). These thermal fluids are heated through shallow crustal magma at temperatures of approx. 1200°C (Bödvarsson et al., 1990).

The Hengill area is comprised entirely of late Quaternary and Postglacial volcanic rocks mostly of basaltic flows and hyaloclastites and minor deposits of rhyolites. Árnason et al. (1967) stated that the Nesjavellir field features a 10 km broad graben trending NE-SW.

2.3 Surface geophysical exploration of Hengill area

Surface geophysical exploration studies of the Hengill area have been undertaken since 1964, including Nesjavellir and other geothermal fields in the Hengill area. The most advanced and informative exploration methods used to image the Hengill geothermal system as well as other geothermal areas in Iceland prior to drilling are resistivity measurements. Recent studies include TEM and MT electromagnetic soundings, which were integrated through a joint inversion, in order to construct a comprehensive map of resistivity from the surface down to over 15 km depth (Árnason et al., 2010).

Figure 2 shows the resistivity at 850 m below sea level and the density of seismic events in the Hengill geothermal system. A joint inversion of TEM and MT data from 148 sounding stations in the Hengill area reveals a resistivity structure consisting of a shallow low-resistivity layer in the upper most 2 km, underlain by high resistivity.

The resistivity structures are related to variations in hydrothermal alteration which appear to be of greater importance than the temperature variation. The low-temperature clay-rich outer margin of a high-temperature reservoir is characterized by low resistivity while the underlying higher resistivity is associated with the formation of chlorite (formation temperature >230°C) and less water-rich alteration mineral assemblages (Árnason et al. 2010). At greater depth a second low-resistivity layer is observed in most parts of the area, again underlain by higher resistivity. The depth to this second low-resistivity layer varies over the Hengill area. It is seen at its shallowest depth (about 3 km) under and around Mount Hengill. The nature of the second low-resistivity layer is not well known.

Figure 3 shows a cross-section of the alteration zones of Nesjavellir high-temperature geothermal system and the main permeability structures.

2.4 The Nesjavellir geothermal field

Exploration drilling of the Nesjavellir geothermal field started in 1964 and drilling was continued with intervals until 1986, when a total of eighteen wells had been drilled. Construction of the Nesjavellir power plant was started in 1987. The power plant was officially opened on the 29th September 1990 (Gunnarsson et al., 1992).

In October 2015, a total of 28 wells have been drilled. In May-June 2015, a new makeup well, NJ-28, was drilled from the same well pad as production well NJ-13. Thirteen of these wells are commercial producers with an output of 120 MWe and 300 MWth (2014). The rest of the wells are either used for re-injection, or are shut-in or abandoned wells (Franzson and Steingrímsson, 2015).

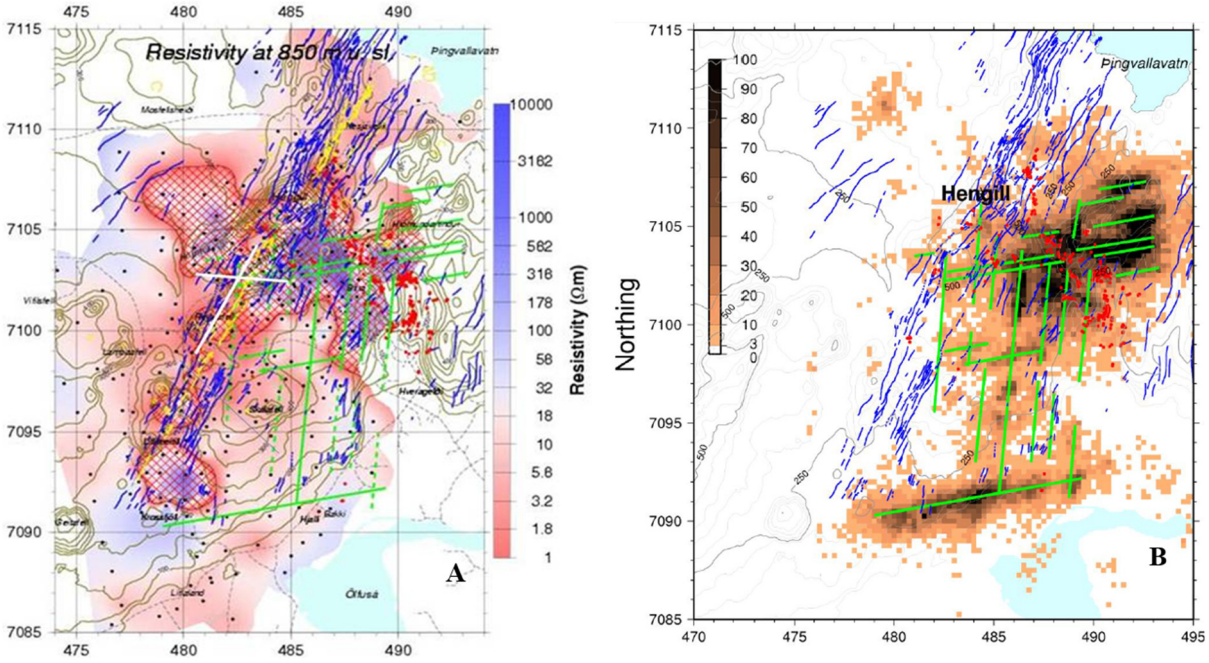

FIGURE 2: A) Resistivity map of Hengill and surroundings at 850 m b.s.l. based on inversion of TEM and MT data; low resistivity (<10Ω) is red and high is blue, while the cross-hatched areas define high resistivity bodies below the low resistivity indicating alteration temperatures of over 230°C. Geothermal manifestations are marked by red dots, TEM and MT stations by black dots, mapped and inferred faults or fractures are blue and green respectively and volcanic craters and fissures are marked yellow (from Árnason et al., 2010). B) Seismicity of the Hengill central volcano from 1991 to 2001; inferred faults and fractures are symbolized by green straight lines (Árnason et al., 2010, modified from Árnason, and Magnússon, 2001)

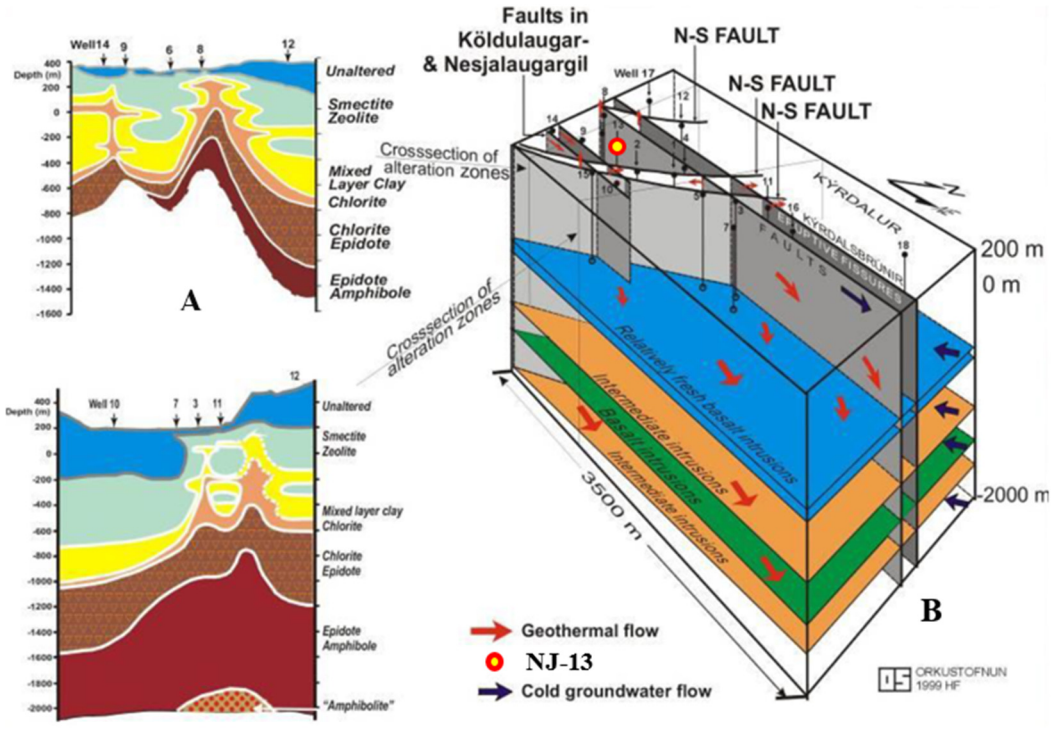

FIGURE 3: A) Cross-section of alteration zones in the Nesjavellir high-temperature system; B) Main permeability structure (Franzson and Steingrímsson, 2015)

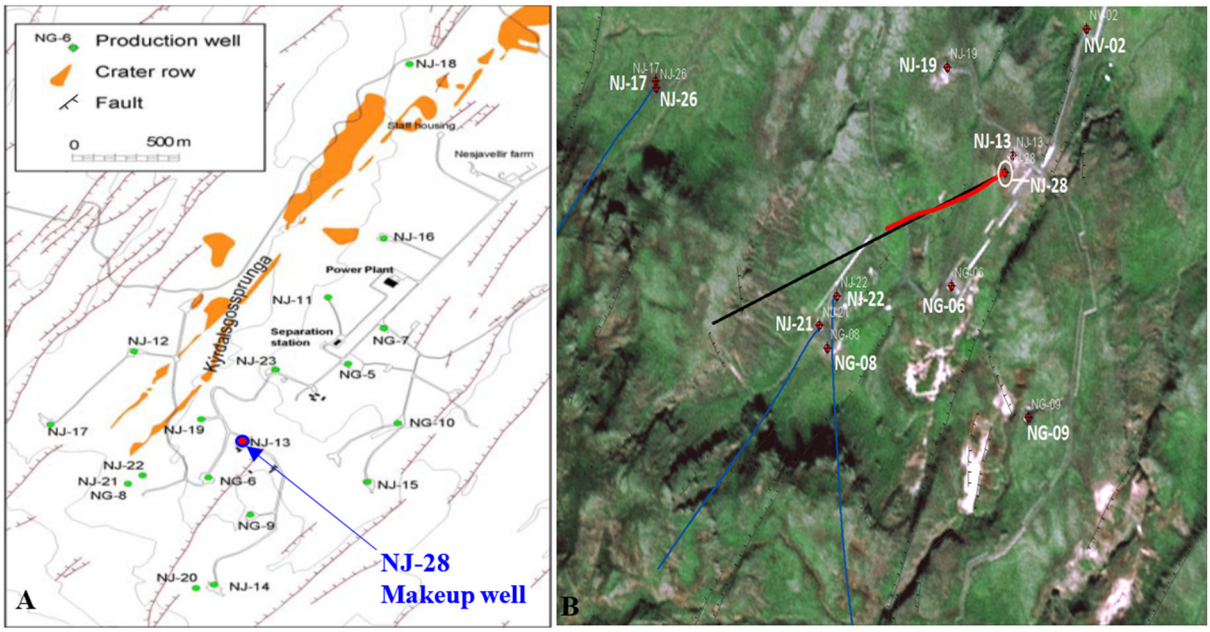

FIGURE 4: A) Nesjavellir geothermal field (Gíslason, 2000); B) Trajectory of well NJ-28 projected on the surface is indicated by a red line (Gunnarsdóttir et al., 2015)

A map of the Nesjavellir geothermal field with the locations of wells NJ-13 and NJ-28 is shown in Figure 4. It also shows the trajectory of well NJ-28 towards the west-southwest (Gunnarsdóttir et al., 2015).

3. ANALYSIS OF FORMATION TEMPERATURE AND INITIAL PRESSURE

Formation temperature and initial pressure are important information for each well and they are deduced from well logs during warm up. During drilling, injection of cold water cools the surrounding formations and then the well is left for a few months to recover to the initial temperature and pressure condition of the surroundings. This recovery period is known as the 'warm-up' period. Measurements of temperature and pressure are done during drilling, warm-up period and as a part of regular reservoir monitoring. Temperature logs during drilling and warm-up are analysed to provide information on the location of feed zones, relationship between these zones and the relative size (permeability) of the individual feed zones.

Different methods are used to estimate the formation temperature and initial pressure of the formation. For the formation temperature estimation, two methods are commonly used as an aid in determining the formation temperature, i.e. the Horner plot and the Albright methods.

The Horner plot method, which is incorporated in the BERGHITI of the ICEBOX (Arason et al., 2004) software, was used in this project and is described below. After defining the formation temperature, the corresponding initial pressure was estimated using the PREDYP programme of the ICEBOX software.

3.1 The Horner plot method

The Horner plot uses an empirical equation to estimate the formation temperature for relatively long recovery periods, usually ranging from weeks to months (Dowdle and Cobb, 1975). This method

assumes a straight line between the maximum wellbore temperature and the natural logarithm of the relative time, τ or *Horner time*, as described in Equation 1 below:

$$\tau = \left(\frac{t_0 + \Delta t}{\Delta t}\right) \text{ Horner time} \quad (1)$$

where Δt = Time passed since last circulation stopped;
t_0 = Circulating time.

Equation 1 is incorporated into the BERGHITI software and is used to find the formation temperature at a selected depth as a function of $\ln(\tau)$ and then plot a straight line through the temperature measurements (t,T) in which the formation temperature is estimated by extrapolation to $\tau = 1$ (Helgason, 1993). Figure 1 in Appendix I shows an example of how the formation temperature is determined using the BERGHITI software. The dots are temperature readings taken at different dates and the green line joins the two later temperature values where the formation temperature is determined from the y-axis at the top right hand corner.

3.2 Initial pressure - introduction

Initial pressure is the reservoir pressure estimated from data obtained during the recovery period of the well. The warm-up pressure profiles are plotted to determine their intersection known as the 'pivot point' which is the initial or reservoir pressure for the dominating feed zone. For two or more dominating feed zones, the pivot point represents the average pressure condition between these feed zones. If the formation temperature and pivot point pressure is known, the PREDYP program from ICEBOX (Arason et al., 2004) which computes pressure in a static water column, can be used to calculate the initial pressure in the well, depending on the corresponding formation temperature, by adjusting the depth-pressure-curve to the known pressure at the pivot point.

3.3 Temperature and pressure profiles

The temperature and pressure conditions of wells NJ-13 and NJ-28 are analysed and interpreted with the purpose of understanding their formation temperature and initial pressure. Temperature and pressure measurements for NJ-13 and NJ-28 taken during warm up and end of drilling and presented by Steingrímsson et al., (1986), and Gunnarsdóttir et al., (2015), respectively, are analysed in this report. The temperature and pressure profiles for both wells are presented in this section. Table 1 shows the borehole dimensions of both NJ-13 and NJ-28.

TABLE 1: Borehole dimensions for wells NJ-13 and NJ-28

Borehole No	Year drilled	Total depth w.r.t. platform (m)	Section	Casing diameter (in)	Casing depth w.r.t. platform (m)	ISN 93 coordinates (X, Y, Z)
NJ-13	1985	1609	Surface 1 2 3	18 5/8 13 3/8 9 5/8 7	63 277.55 816.85 1595.9	389319, 401490, 287
NJ-28	2015	1301	Surface 1 2 3	18 5/8 13 3/8 9 5/8 7	98.3 316.9 801.2 1290.6	389319, 401490, 287

3.3.1 Well NJ-13

Well NJ-13 is a vertical well, drilled in 1985, to a measured depth of 1609 m with respect to the drilling platform. Hyaloclastites and lava flows were dominant down to 500 m. Intrusions are rather common below 700 m depth where most of the feed points are located similar to other wells at Nesjavellir (Steingrímsson et al., 1986). Loss of circulation was observed in feed points high up in the well, but little or no loss at 300-800 m depth where the system seems to be over-pressurized. The top pressure in the production zone from 800 m down was on the other hand under-pressurized. When the well was closed the pressure was around or above 85 bar, so the well was left open, constantly blowing for a period of time. It was also shut in for a short while when well NJ-28 was connected to the pipe system.

Figure 5 shows temperature and pressure logs as well as the formation temperature and initial pressure. According to Steingrímsson et al. (1986), several feed points were identified in NJ-13 from the temperature logs measured during and after drilling. The feed points identified from these T-logs are at 940, 1070, 1120, 1150, 1190, 1363, 1500 and 1540 m depth. The largest feed point detected was at 940 m but the one at 1120 m also showed rapid warm-up. The main feed point where total loss of circulation was noticed during drilling is at 1363 m depth. This does not appear on the temperature log but it is worth mentioning that the well was cooled down to 1300 m depth while logging the temperature before finishing the drilling.

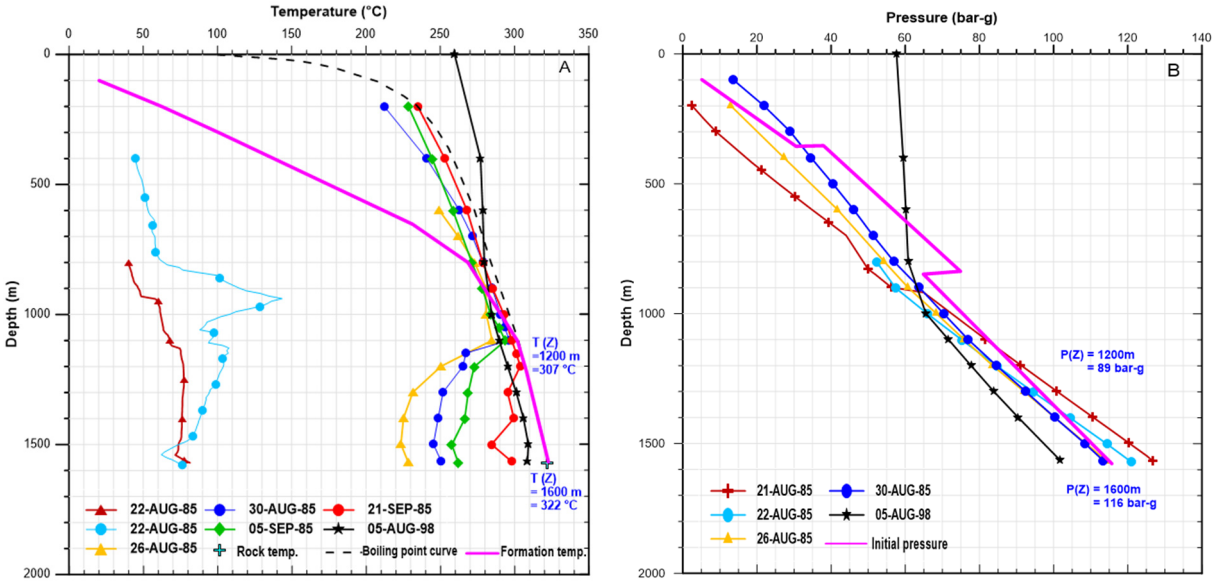

FIGURE 5: A) Temperature logs, boiling point curve and formation temperature; and B) Pressure logs, boiling point pressure and initial pressure from well NJ-13

The inversed temperature profiles from 1100-1500 m indicate cooling due to water circulation during drilling. The BERGHITI software was used to determine the formation temperature by inserting the temperature values at selected depths from the four warm-up measurements on 26th August to 21st September 1985 and reading from the Horner plots. The measurements from 5th August 1998 were not used for this analysis but for comparison. The formation temperatures estimated using BERGHITI are 307°C at 1200 m and 322°C at 1600 m depth.

3.3.2 Well NJ-28

Well NJ-28 is a directional well drilled from the same well pad as NJ-13 in May-June 2015 to a measured depth of 1301 m with respect to the drill platform which corresponds to 1160 m vertical depth from the surface. Hyaloclastites are dominant down to 1044 m followed by lava flows down to 1280 m, underlain by another lava flow formation to the bottom of the well.

The intended depth of this well was 2100 m but the drilling was stopped after several attempts to continue when the drill string reportedly got stuck. This is believed to be due to an intrusion at the bottom of the well. Circulation loss was first detected at 1086 m depth and at the end of drilling it was 25 l/s, but increased up to 80 l/s during the process of trying to release the drill string.

Figure 6 shows the temperature and pressure logs for NJ-28. Only two (2) temperature and pressure logs were measured during warm-up on the 10th July and 04th August 2015. These two measurements were used to determine the formation temperature and initial pressure of well NJ-28. The main feed zone of well NJ-28 is located at the bottom of the well. Though it wasn´t possible to precisely locate the largest feed point(s), several smaller feed points were observed at 820, 900, 1020 and 1060 m depth (Gunnarsdóttir et al., 2015).

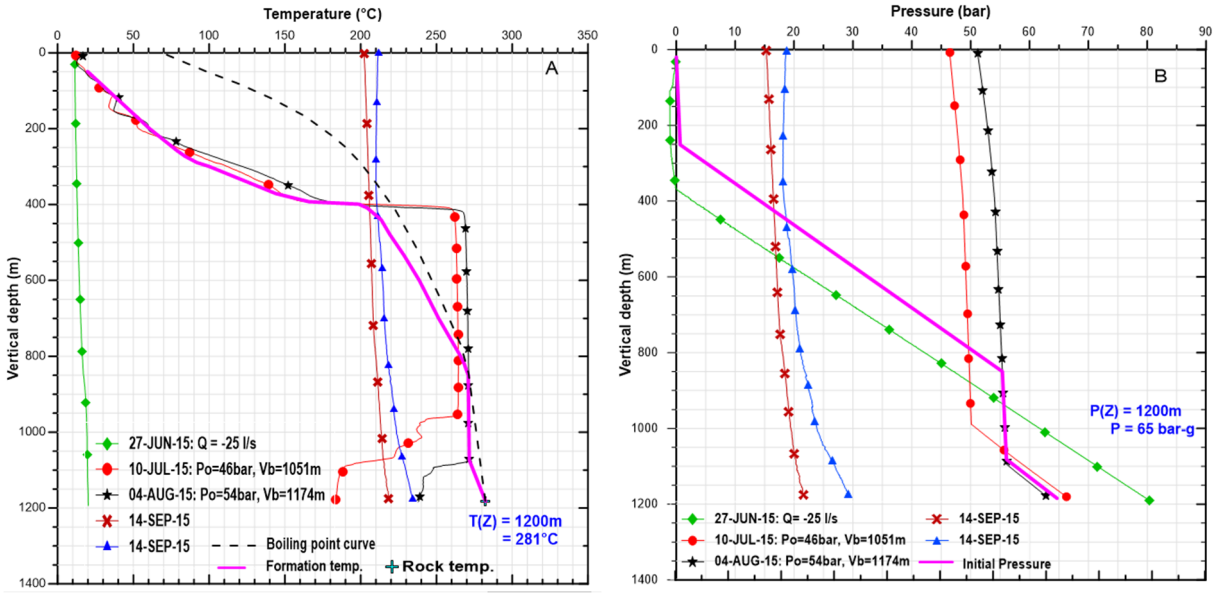

FIGURE 6: A) Temperature logs, boiling point curve and formation temperature;
B) Pressure logs, boiling point pressure and initial pressure from well NJ-28

The inversed temperature profiles from 950 m indicate cooling due to circulation during drilling. The temperature logs for NJ-28 are most likely affected by other nearby production wells including NJ-13 and NG-6 which is located 300 m southwest of NJ-13. Since there were only two measurements done during warm-up, the formation temperature could not be determined using BERGHITI. It was deduced by assuming that the initial pressure value at 1200 m depth was between those given by the two pressure profiles measured on the 10th July and the 04th August 2015. The initial pressure is estimated to be 65 bar-g with corresponding boiling point temperature of 281°C estimated from the steam table. These values are 24 bar-g and 26°C less than that of NJ-13 at the same depth of 1200 m.

The great pressure difference between the estimated initial pressures of the wells is due to utilization of geothermal energy from NJ-13 and the other wells nearby. The difference is both caused by drawdown in the reservoir (production response) and by the fact that nearby wells (NJ-13 and NG-6) are in production at the same time as the well is measured. It is recommended to do some additional measurements during its warm-up period to fully understand the characteristics of well NJ-28.

The well is at boiling conditions from the bottom up to 1075 m, then there is a steam cap up to a depth of 850 m with a pressure of 56 bar-g and a corresponding temperature of 271°C. The corresponding boiling point temperatures from the steam tables for each initial pressure value at the respective depths were plotted to determine the formation temperature curve. Figure 6 shows the temperature and pressure logs for NJ-28, including the estimated formation temperature and initial pressure. The temperature and pressure profiles measured on the 14th September 2015 during production obviously indicate boiling down the well (Figure 6).

4. WELL INJECTION TEST

4.1 Theoretical overview of injection well testing

The main aim of injection well tests is to investigate the physical parameters of the well and the reservoir that control the response of the reservoir with respect to pressure changes caused by the injection. During injection well testing, fresh water is injected gradually into the well to change the water level until a steady height is reached. The pressure response is recorded as a function of time.

The pressure diffusion equation forms the basis of all models in well testing theory that are used to calculate the pressure response in the reservoir at a certain distance (r) from the well after a given time (t) with constant injection (or production). The three main laws that are used in deriving the pressure diffusion equation are conservation of mass, conservation of momentum (Darcy´s Law) and fluid compressibility equation which describes the state of the reservoir fluid. Each of these laws is described below.

i) *Law of conservation of mass*:

Mass in – Mass out = Rate of change of mass, or

$$\left(\rho Q + \frac{\partial(\rho Q)}{\partial r} dr\right) - \rho Q = 2\pi r dr \frac{\partial(\rho \varphi h)}{\partial t} \tag{2}$$

where ρ = Density of fluid (kg/m^3);
Q = Mass flow (kg/s);
h = Reservoir thickness (m);
φ = Porosity (ratio, $0<\varphi<1$);
r = Distance from the centre of the well to the cylindrical shell; and
dr = Thickness of the shell.

ii) Law of conservation of momentum (Darcy´s Law)

$$Q = \frac{2\pi r h k}{\mu} \frac{\partial p}{\partial r} \tag{3}$$

where k = Permeability (m^2);
μ = Fluid viscosity (Pa s); and
$\frac{\partial p}{\partial r}$ = Pressure gradient (Pa/m);.

iii) *Compressibility (relative volume change as a response to pressure)*

$$C_t = \varphi C_w + (1 - \varphi) C_r \quad where \quad C_r = \frac{1}{1-\varphi} \frac{\partial \varphi}{\partial p} \quad and \quad C_w = \frac{1}{\rho} \frac{\partial \rho}{\partial p} \tag{4}$$

where C_r = Rock compressibility (Pa^{-1});
C_w = Water compressibility (Pa^{-1}); and
C_t = Total compressibility (Pa^{-1}).

Depending on the boundary and initial conditions, different solutions to the pressure diffusion equation can be obtained. Assumptions are established through knowledge gained on the reservoir system including the boundary and the initial conditions. Horne (1995) suggested several assumptions, given below for simplification leading to the diffusion equation:

- Horizontal radial flow;
- Application of Darcy's law;
- Homogeneous and isotropic reservoir;
- Isothermal conditions;
- Uniform thickness of reservoir, *h;*

- Single-phase flow;
- Small pressure gradients;
- Small and constant compressibility, c_t;
- Constant porosity, φ;
- Constant fluid viscosity, μ; and
- Constant permeability, k.

Furthermore, some assumptions are made to get the Theis solution:

- *Initial conditions*
  Pressure throughout the reservoir is equal to the initial pressure P_0:

$$P(r,t) = P_0 \qquad \text{for } t = 0, \text{ all } r > 0 \tag{5}$$

- *Boundary conditions*
  i. Outer boundary
  Pressure is equal to the initial pressure at infinity:

$$P(r,t) = P_0 \qquad \text{for } r \to \infty,\ t > 0 \tag{6}$$

  ii. Inner boundary
  Well flow at a constant rate Q (m^3/s):

$$Q = \frac{2\pi kh}{\mu} \lim_{r \to \infty} \left(r \frac{\partial p}{\partial r} \right) \quad \text{for } r \to 0,\ t > 0 \tag{7}$$

Given the above assumptions, the three equations for the three laws are combined to give the diffusion equation as follows:

$$\frac{1}{r}\frac{\partial}{\partial r}\left(r \frac{\partial p}{\partial \rho} \right) = \frac{\mu C_t}{k}\frac{\partial p}{\partial t} = \frac{S}{T}\frac{\partial p}{\partial t} \ or \ \frac{\partial^2 p}{\partial r^2} + \frac{1}{r}\frac{\partial p}{\partial r} = \frac{\mu C_t}{k}\frac{\partial p}{\partial t} = \frac{S}{T}\frac{\partial p}{\partial t} \tag{8}$$

using $$S = c_t h \qquad \text{and} \qquad T = \frac{kh}{\mu} \tag{9}$$

where S = Storativity ($m^3/Pa.m^2$)); and
T = Transmissivity ($m^3/(Pa\ s)$).

The Theis (1935) solution of the radial pressure diffusion equation for these condition (initial and boundary in Equations 5-7) given above is then given by:

$$\Delta P = P(r,t) - P_0 = \frac{Q}{4\pi T} W\left(\frac{Sr^2}{4Tt} \right) = \frac{Q\mu}{4\pi kh} W\left(\frac{-\mu C_t r^2}{4kt} \right) \tag{10}$$

where W(u) is known as the "well function"; and $u = \frac{Sr^2}{4Tt}$, or:

$$W(u) = E_i(-u) = -\int_u^\infty \frac{e^{-x}}{x} dx \tag{11}$$

If $u < 0.01$, Equation 11 can be approximated by: $W(u) \approx -In(u) - \gamma \approx -In(u) - 0.5772$, with γ known as the Euler constant.

Equation 10 for $t > 25\frac{Sr^2}{T}$ gives:

$$\Delta P = \frac{2.303Q}{4\pi T}\left[\log\left(\frac{Sr^2}{4Tt} \right) + \frac{\gamma}{2.303} \right] \tag{12}$$

Figure 7 shows the different types of boundaries with their expected responses of the reservoir where pressure is a function of log time. The Theis behaviour describes an infinitely large reservoir with absence of boundary effects. However, the boundary effects will appear in every reservoir (Bödvarsson and Whiterspoon, 1989).

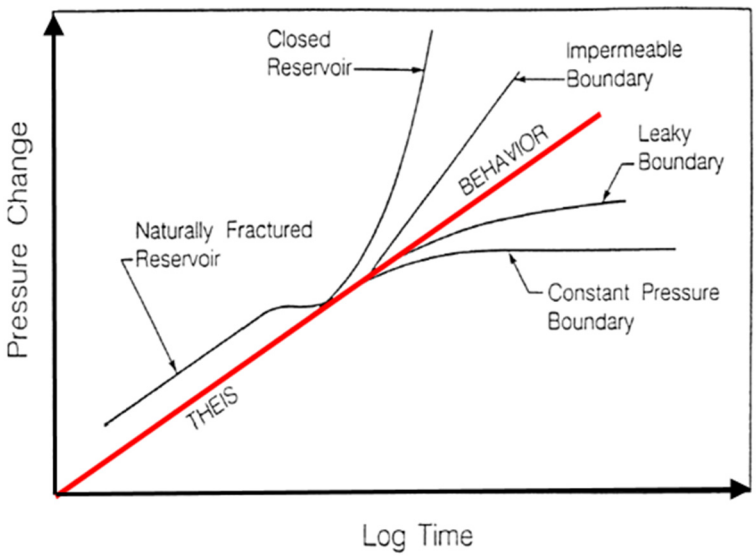

FIGURE 7: Typical pressure responses indicating different reservoir boundaries over log-time (Bödvarsson and Whiterspoon, 1989)

The injection data is analysed and a model is selected including the reservoir boundary properties, reservoir characteristics such as *transmissivity, storativity, wellbore skin* and *wellbore storage.*

The Well Tester software (Júlíusson et al., 2007) is used to simulate the data using the selected model and iterating to an acceptable solution. Each of these characteristics and parameters are explained mostly word by word in automatic reports made by Well Tester (Júlíusson et al., 2007).

The *storativity* (Equation 9) defines the volume of fluid stored in the reservoir per unit area per unit increase in pressure. It has a great impact on how fast the pressure is transmitted within the reservoir. Because of fluid compressibility, storativity varies significantly between reservoir types; liquid-dominated, two-phase or dry steam. Typical storativity values for liquid-dominated geothermal reservoirs are around 10^{-8} m^3/ (Pa.m^2) while for two-phase reservoirs the values might be in the order of 10^{-5} m^3 / (Pa.m^2).

The *transmissivity* (Equation 9) describes the ability of the reservoir to transmit fluid which affects the pressure gradient between the well and the reservoir. The transmissivity can vary depending on certain geological factors but typical values from injection testing in Icelandic geothermal reservoirs are in the order of 10^{-8} m^3 / (Pa.s).

The *injectivity index* (*II*) is an estimated value which describes the connectivity of the well to the surrounding reservoir. It is given in units of (l/s)/bar and is defined as the change in injection flow rate divided by the change in stabilized reservoir pressure:

$$II = \frac{\Delta Q}{\Delta P} \tag{13}$$

where II = Injectivity index (l/s)/bar;
ΔQ = Change of flow rate l/s; and
ΔP = Change in pressure bar.

The *skin factor* is a variable describing the permeability of the volume surrounding the well where the permeability is not the same as in the reservoir (Figure 8). The skin zones are often affected by drilling operations such as fracture blockage from the cuttings or mechanically induced fractures. For damaged wells, the *skin factor* is positive and for stimulated wells it is negative.

The skin factor in Icelandic geothermal reservoirs is typically around -1, however values may range from about -5 to 20. When $s < 0$, the well reacts like a wider well or as a stimulated well, if $s > 0$, the well seems narrower and acts like a damaged well (Hjartarson, 1999).

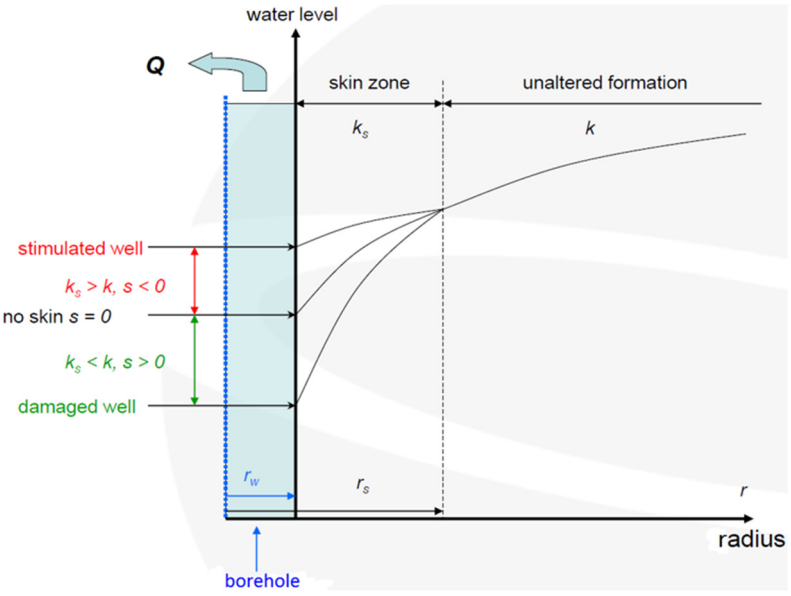

FIGURE 8: Schematic diagram showing pressure changes in the vicinity of a well due to a skin effect where: *rw* = well radius and *rs* = radius of skin (modified from Hjartarson, 1999)

The *wellbore storage* C is a property that accounts for the difference between the wellhead flow rate and the "sand face" flow rate (i.e. the flow into or out of the actual formation). Wellbore storage effects can occur in several ways but most commonly by changing the liquid level and fluid expansion. In injection testing the most dominant cause for wellbore storage is a change in liquid level. The storage effect is caused by the volume in the wellbore itself being emptied or filled. Fluid expansion is caused by fluid flow from the well. When the well is first opened to flow, the pressure in the wellbore drops and the fluid in the wellbore expands, providing the initial production volume (Horne, 1995). Typically, under single-phase liquid conditions the wellbore storage is negligible because of fluid expansion. However, in a geothermal well where the wellbore fluid changes from a single-phase liquid to a two-phase steam-water mixture the expansion effect can be very significant.

4.2 Well injection test analysis and interpretation for NJ-13 and NJ-28

Well injection tests were performed in wells NJ-13 and NJ-28 after the completion of their drilling. All the well test analyses and interpretations were done using Well Tester software (Júlíusson et al., 2007). The software is designed to analyse well test data with respect to the reservoir models selected and the best response is usually selected by comparing the best simulated response, i.e. the generally lowest coefficient of variation C_v, which by Júlíusson et al. (2007): "is defined as the ratio between the standard deviation σ and the mean value μ for the particular parameter in the model:

$$C_v = \frac{\sigma}{\mu}$$

It gives an indication on the spread in the parameter estimate in relation to the estimated parameter value."

The data manipulation is done by dividing the test into several simple processes that range from setting initial conditions to modelling and giving a final report (Júlíusson et al., 2007). Table 2 shows the well testing model used for all steps for the analysis of both NJ-13 and NJ-28.

TABLE 2: Model selected for both wells NJ-13 and NJ-28

Reservoir	Homogenous
Boundary	Constant pressure
Well	Constant skin
Wellbore	Wellbore storage

4.2.1 Well injection test of NJ-28

An injection test at well NJ-28 was performed on the 27th June 2015. The temperatures and pressures were measured from 20 to 1290 m depth at an initial constant injection rate of 21 l/s after which the sensor was left for a short while to measure the stabilized pressure before starting the first step. Injection at step 1 started with 35 l/s, step 2 with 50 l/s and step 3 with 25 l/s. After the step test, the temperatures and pressures were measured again from the bottom at 1290 m up to 30 m at a constant rate of 25 l/s. Figure 9 shows the pressure responses during each of the three steps.

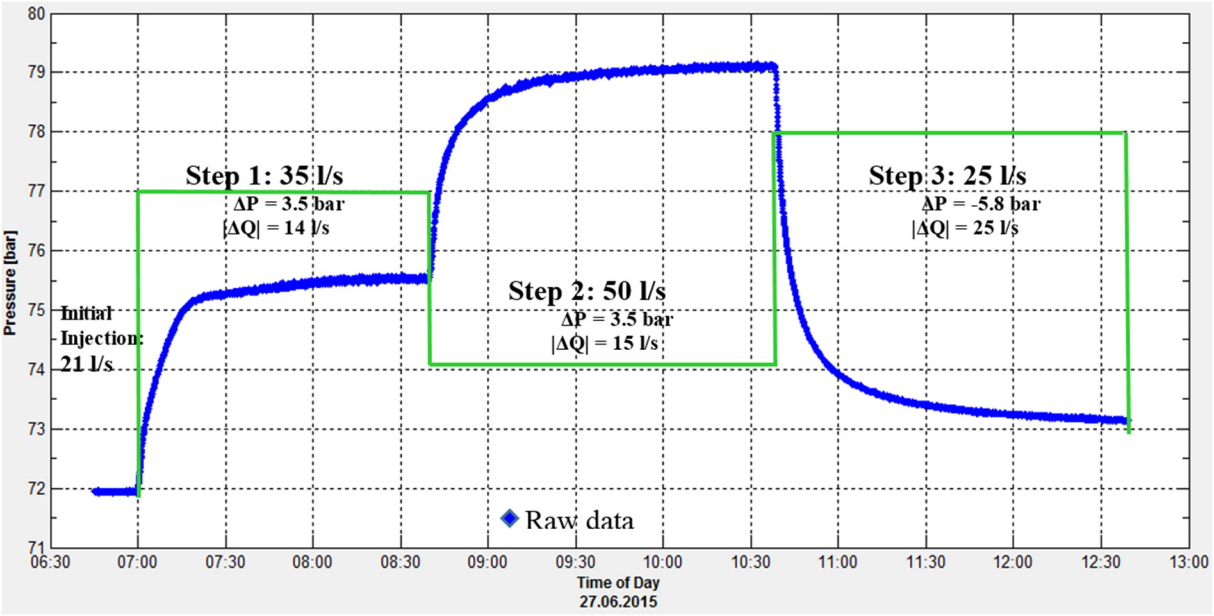

FIGURE 9: Pressure and injection as a function of time in well NJ-28 during injection well test with 3 steps

The initial parameters that were used to calculate the estimated reservoir pressure using Well tester are given in Table 3.

TABLE 3: Summary of initial parameters of well NJ-28

Parameter name	Value	Unit
Estimated reservoir temperature T	280	°C
Estimated reservoir pressure P	75	bar
Wellbore radius r_w	0.12	m
Porosity φ	0.1	-
Dynamic viscosity of reservoir fluid μ	9.39×10^{-5}	Pa·s
Compressibility of reservoir fluid c_w	2.17×10^{-9}	Pa^{-1}
Compressibility of rock matrix c_r	2.44×10^{-11}	Pa^{-1}
Total compressibility c_t	2.39×10^{-10}	Pa^{-1}

Each of the steps was separately simulated through a non-linear regression analysis and their respective parameters were estimated using Well Tester software (Table 4).

For comparison, the same data from well NJ-28 was also simulated by selecting a *dual porosity, constant pressure boundary, constant skin* and *wellbore storage.* Table 5 shows the results simulated by a non-linear regression analysis for a *dual porosity* model.

TABLE 4: Summary of the results from the non-linear regression parameter estimation using injection test data from well NJ-28 for a homogenous model

	Step 1	**Step 2**	**Step 3**	**Unit**
Transmissivity *T*	3.7×10^{-8}	4.3×10^{-8}	3.5×10^{-8}	$m^3/(Pa.s)$
Storativity *S*	2.0×10^{-8}	4.4×10^{-8}	8.6×10^{-8}	$m^3/(Pa.m^2)$
Skin factor *s*	-0.6	-0.4	-0.9	-
Wellbore storage *C*	1.7×10^{-5}	1.4×10^{-5}	9.8×10^{-6}	m^3/Pa
Injectivity Index *II*	4.0	4.3	4.3	(l/s) / bar
Permeability thickness *kh*	3.4×10^{-12}	4.1×10^{-12}	3.3×10^{-12}	$m.m^2$

TABLE 5 Summary of results from the non-linear regression parameter estimation using injection test data from well NJ-28 for a dual porosity model

	Step 1	**Step 2**	**Step 3**	**Unit**
Transmissivity *T*	3.3×10^{-8}	3.7×10^{-8}	3.5×10^{-8}	$m^3/(Pa.s)$
Storativity *S*	6.3×10^{-8}	2.4×10^{-8}	8.4×10^{-9}	$m^3/(Pa.m^2)$
Skin factor *s*	-1.1	-1.35	-2.05	-
Wellbore storage *C*	1.9×10^{-5}	1.5×10^{-5}	1.0×10^{-5}	(m^3/Pa)
Injectivity Index *II*	3.9	4.3	4.2	(l/s) / bar
Permeability thickness *kh*	3.4×10^{-12}	4.1×10^{-12}	3.3×10^{-12}	$m.m^2$

Step 1 is selected to illustrate the results of the data simulations. They are plotted using Well Tester output figure. The simulated results from Table 4 and 5 were compared and all 3 steps of well NJ-28 turned out to give the best response for the selected model of a *homogenous reservoir*, *constant pressure boundary*, *constant skin* and *wellbore storage*. Figure 10 shows the simulated model, collected data and selected data for step 1 for the homogenous reservoir model.

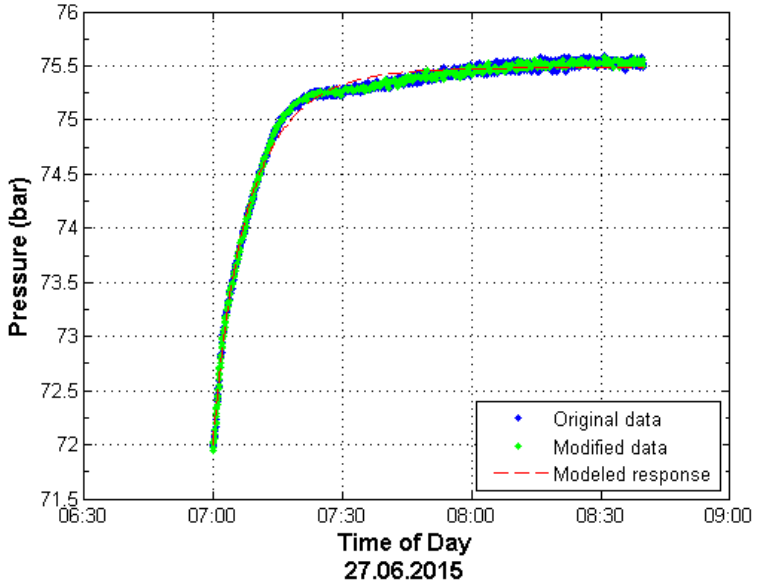

FIGURE 10: Well NJ-28. Simulated model (red line), selected data (green) and collected data (blue) for step 1

Figure 11 shows additional plots of the same data on a log-time scale and linear pressure scale (A), and a log-log scale with the modelled response of the data (B). This is used to determine which type of model is most applicable for each step.

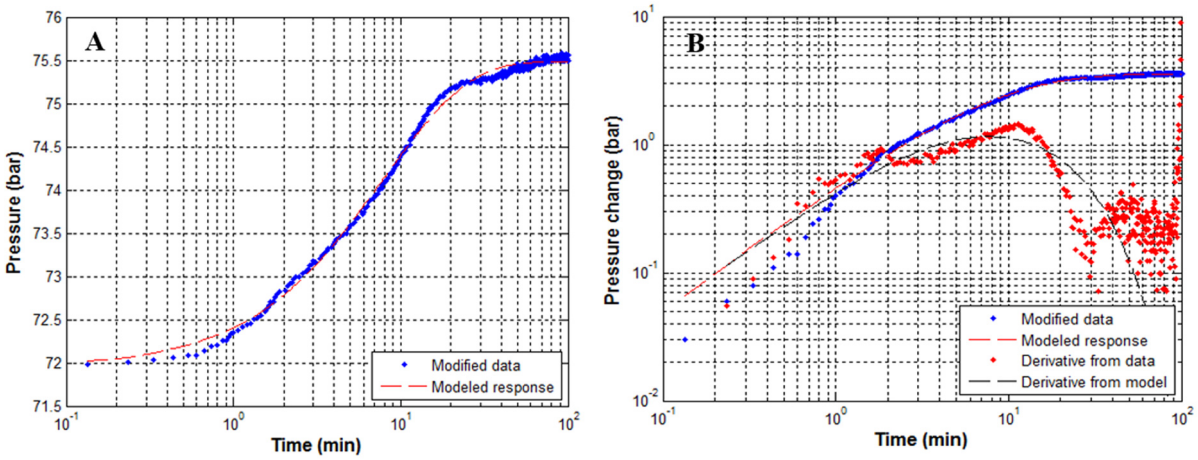

FIGURE 11: Well NJ-28. A) Simulated model, and collected data for step 1 using log-time scale; and B) On a log-log scale showing the derivatives of the same step (1) from a homogenous

4.2.2 Well injection test of NJ-13

The injection test at well NJ-13 consisted of 5 steps and was performed from the 21st – 22nd August 1985. The initial injection was constant with an injection rate of 26 l/s to stabilize the pressure in the well. The measurements of the pressure and temperature during the steps were performed at 1570 m depth which was believed to be close to the main feed zone of the well. Injection in step 1 started with 10 l/s, step 2 with 20 l/s, step 3 with 30 l/s, step 4 with 45 l/s and in step 5 with 0 l/s. Figure 12 shows the injection (Q) and the pressure (P) responses as well as their changes (ΔQ and ΔP) for each step.

In step 1, at around 01:10, the pressure dropped probably due to instable injection, but increased again before starting step 2. Steps 2, 3, and 4 show an increase in pressure at the respective injection rates and the injectivity index increased from 3.11 – to 5.11 (l/s)/bar. At 07:56 on the second day of the injection test, step 5, the final step in the test which was a fall off step was conducted.

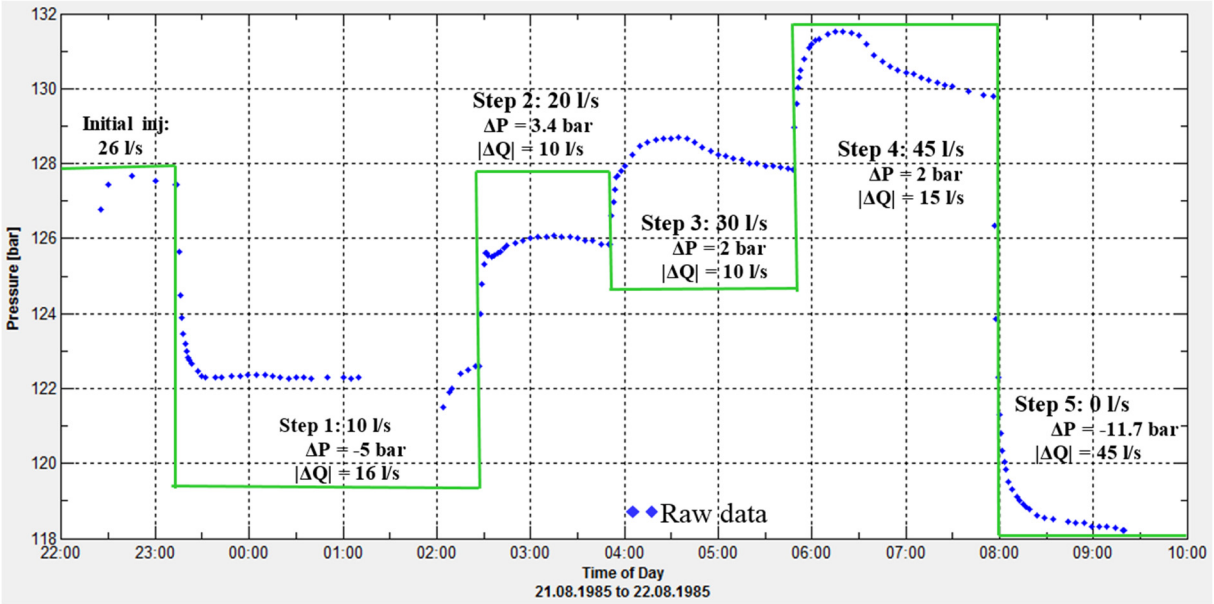

FIGURE 12: Pressure and injection as a function of time in well NJ-13 during the injection well test

The Well Tester software requires the input of some initial parameters and deduces the estimated reservoir pressure from the input data file. Table 6 shows all the initial parameter values of the reservoir that were used for this analysis.

Each of the steps was simulated using non-linear regression analysis separately and their respective parameters were estimated using Well Tester software (Table 7). Comparing the simulated results from Well Tester, steps 2, 3 and 4 in well NJ-13 turned out to give the best response for the selected model of *homogenous reservoir*, *constant pressure boundary*, *constant skin* and *wellbore storage*.

TABLE 6: Summary of initial parameters of well NJ-13

Parameter name	Value	Unit
Estimated reservoir temperature T	280	°C
Estimated reservoir pressure P	126	bar
Wellbore radius r_w	0.12	m
Porosity	0.1	-
Dynamic viscosity of reservoir fluid μ	9.55×10^{-5}	Pa·s
Compressibility of reservoir fluid c_w	1.97×10^{-9}	Pa^{-1}
Compressibility of rock matrix c_r	2.44×10^{-11}	Pa^{-1}
Total compressibility c_t	2.19×10^{-10}	Pa^{-1}

TABLE 7: Summary of the results from the non-linear regression parameters estimated using injection test data from well NJ-13

	Step 1	Step 2	Step 3	Step 4	Step 5	Unit
Transmissivity T	3.0×10^{-8}	3.1×10^{-8}	4.0×10^{-8}	4.9×10^{-8}	7.3×10^{-8}	$m^3/(Pa.s)$
Storativity S	3.6×10^{-9}	4.6×10^{-9}	2.2×10^{-9}	1.6×10^{-9}	2.1×10^{-9}	$m^3/(Pa.m^2)$
Skin factor s	-0.8	-0.6	-1	-0.4	3.4	-
Wellbore storage C	3.7×10^{-6}	3.0×10^{-6}	6.6×10^{-6}	6.2×10^{-6}	5.7×10^{-6}	m^3/Pa
Injectivity Index II	3.2	2.9	5	7.5	4	(l/s) / bar
Permeability thickness kh	2.7×10^{-12}	2.9×10^{-12}	3.9×10^{-12}	4.3×10^{-12}	7.2×10^{-12}	$m.m^2$

In the report by Steingrímsson et al., 1986, the model used to simulate the injection test for well NJ-13 calculated *dual porosity*, *infinite pressure boundary*, *constant well skin* and *wellbore storage*. However, the simulated values of the parameters attained in this injection analysis assuming a homogenous reservoir and constant pressure boundary (Table 7) do not defer much from the values given in the old report.

5. PRODUCTION WELL TESTING

5.1 Theoretical overview of production well testing

Production well tests for high-enthalpy geothermal wells are conducted after the well has been left to warm up for 2-4 months after completion to determine the energy content and production capacity and to analyse the flow characteristics of a well (Grant and Brixley, 2011). Furthermore, a production test may be necessary for developers of geothermal projects so that better utilization schemes can be proposed for each production well and to get information on how the reservoir should be managed in the future for better sustainability.

During the warm-up period, the well conditions become those of the surrounding rocks, so production test calculations after warm-up reflect the true energy status of the reservoir. However, it is also vital to bear in mind that other nearby wells may be affecting the results. Production well tests are done by

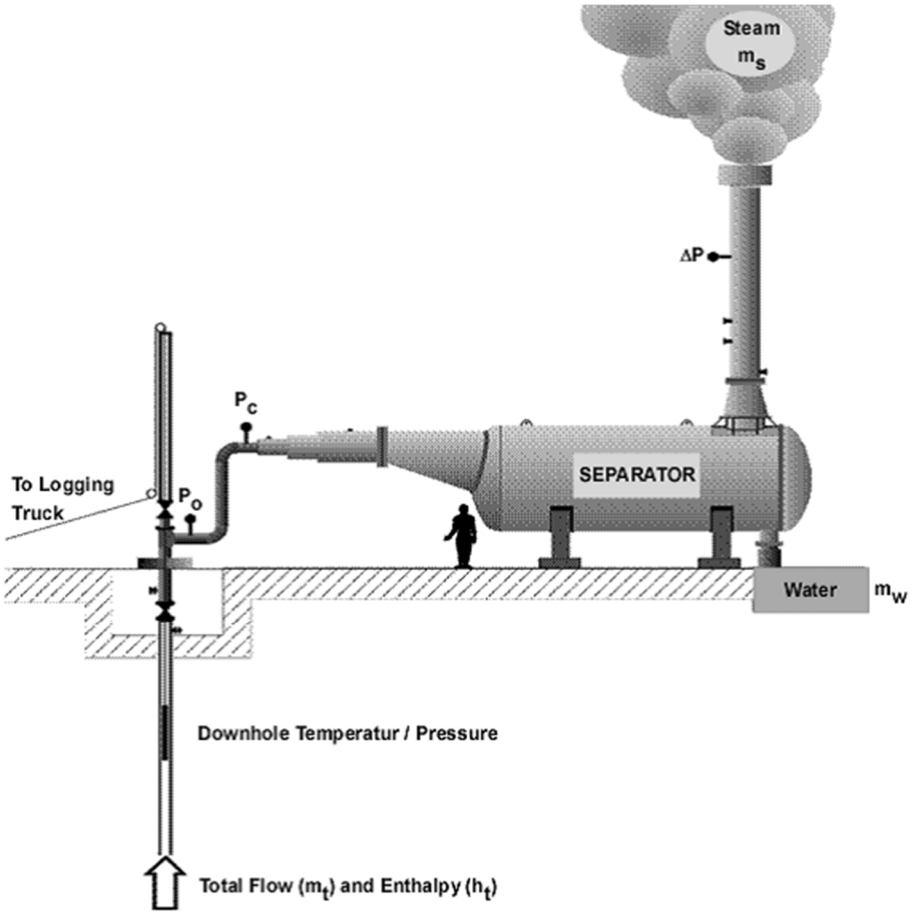

FIGURE 13: Production well test setup for flow and enthalpy measurements with a horizontal separator (Björnsson, et al., 1998)

measuring the fluid flow from a discharging well at different wellhead pressures. The fluid flow is discharged into a silencer or separator which is designed to reduce the noise level resulting from the discharge and it separates the fluid into steam and water at atmospheric pressures.

A typical setup for production well testing which is commonly used in Iceland is shown in Figure 13. The separator and equipment are connected to the well which is to be monitored. The lip pressure is measured at the end of the discharge pipeline as it enters the silencer and water discharged from the silencer or separator is collected in a V-notch weir box for measurements while the steam is discharged into the atmosphere. For well NJ-28 at Nesjavellir, a vertical steam separator was used but in Figure 13 a horizontal separator is shown.

The relation between mass flow, enthalpy, cross-sectional area of the discharge pipe and lip pressure is described by the Russell James´s empirical formula below (Grant and Brixley, 2011):

$$Q_t = KA\,\frac{P_c^{0.96}}{H^{1.102}} \tag{14}$$

where Q_t = Total mass flow (kg/s);
K = 183.5 when A is given in (cm^2), i.e. K is not dimensionless;
H = Total enthalpy (kJ/kg);
A = Cross-section area of the pipe (cm^2); and
P_c = Lip pressure (bar-a).

Mass ratio of steam to the total flow and total enthalpy as a function of enthalpy of steam and water can be written as:

$$X = \frac{Q_s}{Q_t} \quad \text{and} \quad H = XH_s + (1 - X)H_w \tag{15}$$

where X = The steam mass fraction;
Q_s = Mass flow of steam (kg/s);
H_s = Enthalpy of steam (kJ/kg); and
H_w = Enthalpy of water (kJ/kg).

The separated water flow Q_w describes the water separated at atmospheric pressure from the total well flow with enthalpy H. Therefore:

$$Q_t = Q_w \frac{H_s - H_w}{H_s - H} \tag{16}$$

where Q_w = Mass flow of water (kg/s).

Combining Equations 14 and 16 gives:

$$\frac{Q_w}{AP_c^{0.96}} = \frac{183.5}{H_t^{1.102}} \frac{H_s - H}{H_s - H_w} \tag{17}$$

The enthalpies of steam H_s and water H_w are found from steam-tables for corresponding well head pressure or temperature. The lip pressure P_c is measured during the production test. Figure 13 shows the set up. The total flow Q_t and the total enthalpy H can be calculated with algorithms solving non-linear equations.

The *LIP* programme from the ICEBOX software uses the Russell James equation (Equation 14) to find properties of two-phase geothermal wells. This programme was used to calculate the flow rates of both steam and water and their enthalpy.

5.2 Production well testing of NJ-13

A total of fourteen production test manual readings and measurements exist from 23rd September – 10th October 1985 during the production testing of well NJ-13. Table 8 shows the measurements from the production tests taken using a lip pipe diameter of 16.05 cm.

TABLE 8: Measurements of pressure at different times and water heights in well NJ-13

Date	Time	Water height *W* (cm)	Well head pressure *Po* (bar-g)	Critical pressure *Pc* (bar-g)
23-Sep-85	20:20	23.4	17.0	3.40
23-Sep-85	20:25	23.6	16.0	3.80
23-Sep-85	21:15	23.6	15.5	3.70
23-Sep-85	23:20	23.3	15.0	3.60
24-Sep-85	13:00	21.3	16.5	4.10
24-Sep-85	17:00	20.8	16.7	3.80
26-Sep-85	15:00	9.2	20.5	4.40
27-Sep-85	11:45	11.3	16.2	4.18
29-Sep-85	15:00	10.3	15.8	4.40
30-Sep-85	22:00	10.2	16.2	4.50
05-Oct-85	11:20	8.9	16.3	4.50
07-Oct-85	11:35	7.7	16.4	4.70
10-Oct-85	14:00	8.0	16.3	4.50
10-Oct-85	18:35	8.2	16.7	4.40

The water height in the weir box W over the V-notch, well head pressure P_0 and the critical pressure P_c were manually entered into the Lip programme of the Icebox software to calculate the flow rates of steam Q_s and water Q_w. The total enthalpy H was calculated assuming the separator pressure to be 1 bar-g and 7 bar-g which are the separator pressure for the steam separator during testing and assumed separator pressure for the Nesjavellir power plant, respectively. The total flow rate Q_t is the sum of Q_s and Q_w.

Table 9 shows the results obtained using the Lip programme and the energy value calculated using a constant total steam flow rate of 2 kg/s for the production of 1 MWe. In general, the amount of steam needed for production of 1 MWe varies between 1.6 and 2.2 kg/s for different power plants. For a well head pressure P_0 of 16.4 bar-g the steam flow rate is 31 kg/s with a power output of 15 MW of electricity.

TABLE 9: Results of flow rate and enthalpy for well NJ-13

Date	Time	At 1 bar-a separator pressure				Enthalpy	Q_s at 7 re	Power
		Q_w (kg/s)	Q_s (kg/s)	Q_t (kg/s)	X (%)	H (kJ/kg)		(MW_e)
23-Sep-85	20:20	37.4	20.5	57.9	35	1285	15.9	8.0
23-Sep-85	20:25	38.2	22.6	60.9	37	1324	17.9	9.0
23-Sep-85	21:15	38.2	22.1	60.3	37	1311	17.4	8.7
23-Sep-85	23:20	37.0	21.7	58.7	37	1318	17.1	8.6
24-Sep-85	13:00	29.7	25.6	55.3	46	1523	21.7	10.8
24-Sep-85	17:00	28.0	24.1	52.2	46	1524	20.4	10.2
26-Sep-85	15:00	4.1	30.6	34.6	88	2447	29.2	14.6
27-Sep-85	11:45	6.5	29.1	35.5	82	2305	27.5	13.8
29-Sep-85	15:00	5.3	30.4	35.7	85	2382	28.9	14.5
30-Sep-85	22:00	5.2	31.0	36.1	86	2393	29.5	14.8
05-Oct-85	11:20	3.8	31.1	34.9	89	2467	29.8	14.9
07-Oct-85	11:35	2.8	32.3	35.1	92	2531	31.1	15.5
10-Oct-85	14:00	3.0	31.2	34.2	91	2512	30.0	15.0
10-Oct-85	18:35	3.2	30.7	33.8	91	2500	29.4	14.7

5.3 Well NJ-28 production well testing

Measurements of temperature and pressure logged in the well during the production testing in September 2015 were not available when this report was finalised. A total of nine manual readings and measurements were carried out on the 14th September 2015 during the production test of well NJ-28.

Table 10 shows the manual measurements from the production test using a lip pipe diameter of 10 cm, the results obtained using the *LIP* programme and the energy value calculated using a constant total flow rate of 2 kg/s for the production of 1 MWe. From these results, it is estimated that NJ-28 could produce up to 5 MW_e for a wellhead pressure P_0 of 20 bar-g at a flow rate of 9.4 kg/s for 1 bar-a separator pressure. Table 10 shows that the mass fraction X of steam Q_s to the total flow Q_t calculated using Equation 15 is greater than 96 %. This indicates that the well produces mostly dry steam, hence it is not necessary to calculate the power output at 7 bar-a separator pressure.

The steam enthalpy H_s at 1 bar-a separator pressure and measured as 2675 kJ/kg, is slightly lower than at 7 bar-a separator pressure where it is 2762.7 kJ/kg. Calculations have shown that the power output (MWe) is slightly less at 7 bar-a separator pressure than at 1 bar-a separator pressure. However, this does not change the results significantly and the well is estimated to produce mostly dry steam at well head pressures between 18-21 bar-g and could produce up to 5 MWe at 7 bar-a, which is the assumed separator pressure for the Nesjavellir power plant.

TABLE 10: Manual production test measurements taken on 14th September 2015 and results of flow rate and enthalpy for well NJ-28 at flow rate of 2 kg/s for production of 1 MWe at 1 bar-a separator pressure

Time	Water height W (cm)	P_0 (bar-g)	P_c (bar-g)	Q_w (kg/s)	Q_s (kg/s)	Q_t (kg/s)	X (%)	Enthalpy H (kJ/kg)	Power MW_e
13:50	1.4	21.2	2.10	0.1	7.1	7.2	98	2665	3.5
13:55	3.0	20.1	3.20	0.4	9.4	9.8	96	2625	4.7
14:00	3.1	20.2	3.00	0.4	9.0	9.4	96	2618	4.5
14:05	3.0	19.5	2.20	0.3	7.6	7.9	96	2610	3.8
14:10	1.0	18.8	2.00	0.1	6.8	7.0	98	2671	3.4
14:15	0.8	18.4	2.00	0.1	6.8	7.0	98	2673	3.4
14:20	0.5	17.8	2.00	0.1	6.9	7.0	99	2675	3.4
14:25	1.4	18.0	2.60	0.2	8.2	8.3	98	2666	4.1
14:30	3.0	18.0	2.50	0.3	7.9	8.3	96	2615	4.0

6. CONCLUSIONS AND DISCUSSIONS

The main aim of this study was to analyse available temperature and pressure data and well tests from wells NJ-13 and NJ-28 in the Nesjavellir geothermal field in SW-Iceland. Well NJ-28 is a directional makeup well drilled from the same well pad as well NJ-13. Analysis of temperature and pressure profiles to find the formation temperature and initial pressure as well as analysis of injection and production well tests were the main methodologies applied to characterise various physical parameters of these two wells and the reservoir in their vicinity. The following conclusions have been made from the analysis of the two wells.

The formation temperature and initial pressure of NJ-13 at 1600 m depth, determined using BERGHITI, are 322°C and 116 bar-g, respectively. The formation temperature lies right on the boiling curve indicating a two-phase well. This is not far from conclusions of the previous analysis of well NJ-13 by Steingrímsson et al. (1986). For well NJ-28, the estimated initial pressure and the corresponding boiling point temperature are 65 bar-g and 281°C, respectively, at 1200 m vertical depth. The difference in the estimated initial pressure and formation temperature is 24 bar and 26°C, respectively, at the same depth (1200 m). The drawdown in the reservoir due to production cannot be estimated based on this difference because nearby wells, including well NJ-13, were in production when the warmup measurements were conducted.

Injection well test data from 5 steps in NJ-13 was simulated using Well Tester. The selected model was that of a *homogenous reservoir*, *constant pressure boundary*, *constant skin* and *wellbore storage* and showed that steps 2, 3 and 4 gave the best results.

The transmissivity in well NJ-13 generally increases with increasing injection rate in steps 2, 3 and 4. The injectivity index also increases from 2.9 to 7.5 (l/s)/bar in these 3 steps. This was explained by Steingrímsson et al. (1985) who believed this to be caused by more feed points becoming active when pressure was increased, especially from 900-1150 m depth.

All three steps for well NJ-28 were simulated using Well Tester and the best fit between modelled and measured data was obtained when using a *homogenous reservoir, constant pressure boundary, constant skin* and *wellbore storage*. The transmissivity and storativity were within the normal range of values in high-temperature reservoirs in Iceland. The injectivity index was slightly increasing in the step test from 4.0 to 4.3 (l/s)/bar, indicating a small opening up of the surroundings of the well during the test.

The older production well, NJ-13, drilled in 1985, has a power output of 15 MW_e estimated from the original production test data in September and October 1985. The recent well, NJ-28, which was directionally drilled from the same well pad in 2015, only has a power output of 5 MW_e estimated from production test data measured in September 2015. The mass fraction X of steam Q_s to the total flow Q_t calculated using Equation 15 is greater than 96% (Table 10). This indicates that the well produces mostly dry steam.

In general, the reservoir characteristics concluded from the interpretation of the injection tests of both wells NJ-13 and NJ-28 are fairly similar. However, well NJ-13 has both a higher transmissivity ranging from 4 to 5×10^{-8} m^3/Pa.s, and an injectivity ranging from 5 to 7.5 (l/s)/bar compared to well NJ-28 which has a transmissivity ranging from 3 to 4×10^{-8} m^3/Pa.s and an injectivity of ~4 l/s/bar. This might explain why the recent well, NJ-28, is a poor producer compared to the older well NJ-13.

ACKNOWLEDGEMENT

I would like to sincerely appreciate and thank my supervisors Dr. Svanbjörg Helga Haraldsdóttir, Saeunn Halldórsdóttir and Benedikt Steingrímsson for imparting their knowledge and experience in temperature and pressure, injection and production tests analysis and the applicable software used for each analysis. It is due to their tireless guidance and efforts that has led me through to the successful completion of this report.

Special thanks to the Orka nátturúnnar (ON) and Iceland GeoSurvey (ISOR) for providing the well data of NJ-13 and NJ-28 which were used in this report.

I would also like to extend my special thanks to all the staff members of UNU-GTP under the stewardship of director Mr. Lúdvík S. Georgsson for the training opportunity, care and all the other associated privileges during the six months training programme. Extended appreciation to all the lecturers involved for imparting their knowledge and experiences through their presentations. Finally, I would like to appreciate and thank all the UNU-GTP Fellows for the moments we shared together.

NOMENCLATURE

A = Cross section area of the pipe (cm^2)
C = Wellbore storage (m^3/Pa)
C_r = Rock compressibility (Pa^{-1})
C_t = Total compressibility (Pa^{-1})
C_w = Water compressibility (Pa^{-1})
dr = Thickness of shell/well (m)
h = Reservoir thickness (m)
H_s = Enthalpy of steam (kJ/kg)
H_t = Total enthalpy (kJ/kg)
H_w = Enthalpy of water (kJ/kg)
II = Injectivity index ((l/s)/bar))
K = 183.5 for A in cm^2 at Reykjanes
k = Permeability (m^2)
P = Pressure (bar)
P_c = Lip pressure (bar-a)
P_0 = Initial pressure or top-pressure (bar)
Q = Mass flow (kg/s)
Q_s = Mass flow of steam (kg/s)
Q_t = Total flow rate (kg/s)

Q_w = Mass flow of water (kg/s)
r = Radius (m)
r_w = Wellbore radius (m)
S = Storativity ($m^3/Pa.m^2$)
S = Skin factor (-)
T = Transmissivity ($m^3/(Pa.s)$)
W = Water height in weigh box (cm)
X = Steam mass fraction
ρ = Density of fluid (kg/m^3)
φ = Porosity
τ = Horner time (-)
μ = Fluid viscosity (Pa.s)
γ = Euler constant

REFERENCES

Arason, Th., Björnsson, G., Axelsson, G., Bjarnason, J.Ö., and Helgason, P., 2004: *The geothermal reservoir engineering software package Icebox, user´s manual.* Orkustofnun, Reykjavík, report, 53 pp.

Árnadóttir, T., Geirsson, H., and Jiang, W., 2008: Crustal deformation in Iceland: Plate spreading and earthquake deformation. *Jökull, 58*, 59-74.

Árnason, B., Theodórsson, P., Björnsson, S., and Saemundsson, K., 1967: Hengill, a high-temperature thermal area in Iceland. *Bull. Volcanologique, XXXIII-1*, 245-260.

Árnason, K., and Magnússon, I.Th, 2001: *Geothermal activity at Hengill and Hellisheidi. Results of electromagnetic soundings*. Orkustofnun, Reykjavik, Iceland, report OS-2001/091 (in Icelandic), 250 pp.

Árnason, K., Eysteinsson, H., Hersir, G.P., 2010: Joint 1D inversion of TEM and MT data and 3D inversion of MT data in the Hengill area, SW Iceland. *Geothermics, 39*, 13–34.

Björnsson, G., 2004: Reservoir conditions at 3-6 km depth in the Hellisheidi geothermal field, SW-Iceland, estimated by deep drilling, cold water injection and seismic monitoring. *Proceedings of the 29th Workshop on Geothermal Reservoir Engineering, Stanford University, Stanford, CA, US,* 8 pp.

Björnsson, G., Bjarnason, J.Ö., and Thórdarson S., 1998: *Discharge measurements in Svartsengi and Eldvörp in 1996-1997.* Orkustofnun, Reykjavík, Iceland, report OS-98008 (in Icelandic), 57 pp.

Bödvarsson, G.S., Björnsson, S., Gunnarsson, Á., Gunnlaugsson, E., Sigurdsson, Ó., Stefánsson V., and Steingrímsson, B., 1990: The Nesjavellir geothermal field, Iceland. Part 1. Field characteristics and development of a three-dimensional numerical model. *J. Geotherm. Sci. and Tech., 2-3,* 189-228.

Bödvarsson, G.S., and Witherspoon, P.A., 1989: Geothermal reservoir engineering, part 1. *Geotherm. Scie & Tech, 2-1,* 1-68.

Dowdle, W.L., and Cobb, W.M., 1975: Static formation temperature from well logs – an empirical method. *J. Petrol. Tech.*, *27*, 1326-1330.

Franzson, H. and Sigvaldason, H., 1985: *Nesjavellir well NG-8, geology, alteration, logging and aquifers.* Orkustofnun, Reykjavík, report OS-85120/JHD-16 (in Icelandic), 33 pp.

Franzson, H., and Steingrímsson, B., 2015: *The Hengill geothermal system – exploration, drilling, monitoring and modelling.* UNU-GTP, unpublished lecture notes, 102 pp.

Gíslason, G., 2000: Nesjavellir co-generation plant, Iceland. Flow of geothermal steam and non-condensable gases. *Proceedings of the World Geothermal Congress 2000, Kyushu-Tohoku, Japan*, 585-590.
Gíslason, G., and Gunnlaugsson, E., 2003: Preparation for a new power plant in the Hengill geothermal area. *IGA News, 51,* 4-5.

Grant, M.A., and Bixley, P.F., 2011: *Geothermal reservoir engineering* (2nd edition). Academic Press, NY, US, 359 pp.

Gunnarsdóttir, S., Helgadóttir, H.M., Tryggvason, H., Sigurgeirsson, M.Á., Egilson, Th., Stefánsson, H.O., 2015: *Nesjavellir – Well NJ-28; third stage: Drilling of production zone to 1301 m depth*. ÍSOR – Iceland GeoSurvey, Reykjavík, report ÍSOR-2015/033 (in Icelandic), 103 pp.

Gunnarsson, Á. Steingrímsson, B.S., Gunnlaugsson, E., Magnússon, J., and Maack, R., 1992: Nesjavellir geothermal co-generation power plant. *Geothermics, 21*, 559-583.

Helgason, P., 1993: *Step by step guide to BERGHITI. User's guide*. Orkustofnun, Reykjavík, Iceland, 17 pp.

Hjartarson, Á., 1999: *Analysis of reservoir data collected during reinjection into the Laugaland geothermal system in Eyjafjördur, N-Iceland*. MSc. thesis, University of Iceland and Orkustofnun, Reykjavík, 107 pp.

Horne, R.N., 1995: *Modern well test analysis, a computer aided approach* (2nd ed.). Petroway Inc., Palo Alto, CA, United States, 257 pp.

Jóhannesson H., and Saemundsson, K., 1999. Geological map 1:1.000.000, Icelandic Institute of Natural History.

Júlíusson, E., Grétarsson, G., Jónsson, P., 2007: *Well tester 1.0b, user´s guide*. ÍSOR – Iceland GeoSurvey, Reykjavik, Iceland, report ÍSOR-2008/063, 27 pp.

Níelsson, S., and Franzson, H., 2010: Geology and hydrothermal alteration of the Hverahlíd HT-system, SW-Iceland. *Proceedings of the World Geothermal Congress 2010, Bali, Indonesia*, 6 pp.

Saemundsson, K., 1979: Outline of the geology of Iceland. *Jökull 29,* 7-28.

Steingrímsson, B., Gudmundsson, Á., Sverrisdóttir, G., Sigvaldason, H., Sigurdsson, Ó., Gunnlaugsson, E., 1986: *Nesjavellir, well NJ-13: Drilling, exploration and production characteristics.* Orkustofnun, Reykjavík, Iceland, report OS-86027/JHD-07, 145 pp.

Theis, C.V., 1935: The relation between the lowering of the piezometric surface and the rate and duration of discharge of a well using ground-water storage. *Transactions, American Geophysical Union, 16-2,* 519-524.

APPENDIX I: Estimation of formation temperature of well NJ-13

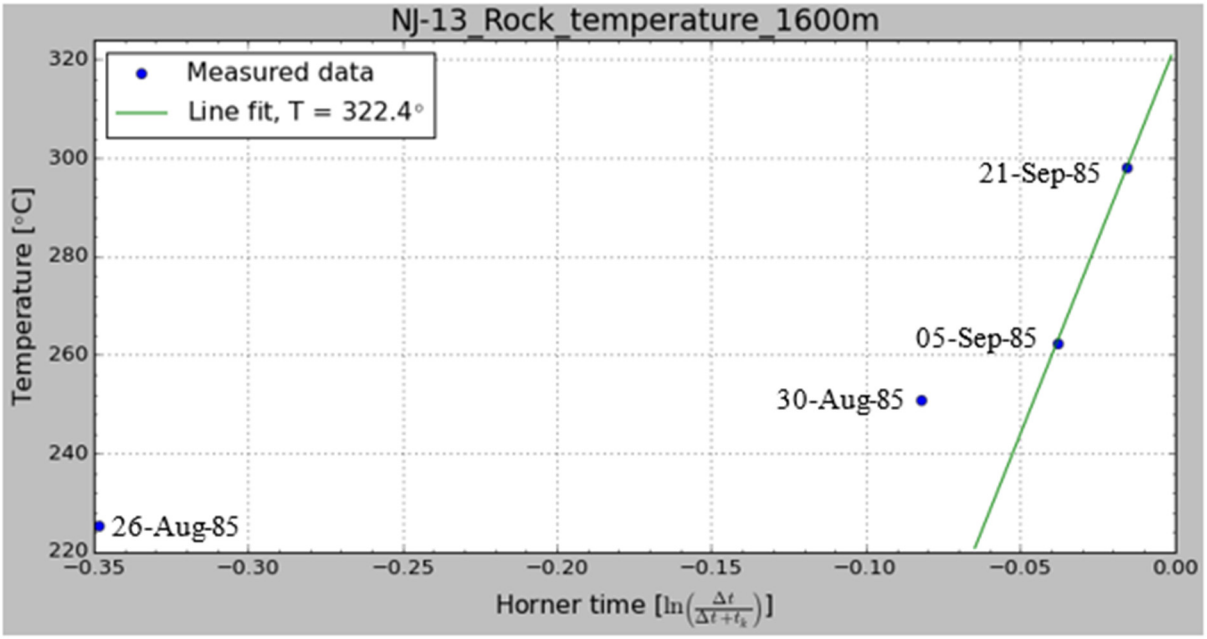

FIGURE 1: Estimation of formation temperature of well NJ-13 at 1600 m depth using BERGHITI

UNITED NATIONS UNIVERSITY
UNU-GTP
Geothermal Training Programme

Orkustofnun, Grensasvegur 9,
IS-108 Reykjavik, Iceland

Reports 2015
Number 30

WELL DATA ANALYSIS AND VOLUMETRIC ASSESSMENT OF THE SOL DE MAÑANA GEOTHERMAL FIELD, BOLIVIA

Pedro Rómulo Ramos Sullcani
Empresa Nacional de Electricidad – ENDE
Av. Ballivián N° 503, Cochabamba
BOLIVIA
pedro.ramos@ende.bo, pedro.ramos.1985@gmail.com

ABSTRACT

Bolivia is located in South America, where the subduction of the Nazca Plate under the South American Plate generates the Andes volcanic chain that crosses Bolivia. In 1976, ENDE and the Ministry of Energy and Hydrocarbons, with funds from the United Nations Development Programme (UNDP), began evaluating the geothermal potential of 42 hydrothermal manifestations, and the Laguna Colorada area was considered the most prospective. Geo-volcanological mapping indicates the existence of an extensive ignimbrite unit that almost completely covers the area, and overlies an andesitic-dacitic lava sequence and possibly ignimbrites of Neogene origin. The structural geology shows two orthogonal tectonic systems, NNW-SSE and NNE-SSW, and this structural system has caused secondary deep fracturing that allows hot water to rise up through faults and fractures to reach the surface in hydrothermal alteration zones. The temperature obtained from geothermometers are in agreement with the measured reservoir temperature of around 250°C. Geophysical studies carried out in the exploration stage identified important gravimetric and resistive anomalies. When correlated with MT data, this information allows the identification of the possible reservoir extension.

Six wells were drilled between 1989 and 1994 in the Sol de Mañana geothermal field, confirming high temperature (250-260°C). Temperature cross-section allows better understanding of the reservoir characteristics. Results of well testing show similar characteristics for wells SM-01 and SM-02 and better connection between these two wells than other wells in the field. These results correlated with the structural geology, indicate that wells SM-01 and SM-02 could intersect the same fault. Based on temperature measurements and well test analysis, an initial resource assessment is done using the volumetric method considering two scenarios. The most likely value obtained for the production capacity of the Sol de Mañana geothermal field, is 75 MW_e for 25 years.

1. INTRODUCTION

1.1 Location and project history

Bolivia is located in South America and covers 1,980,581 km^2, it is bordered by Chile and Peru in the west, by Brazil in the east and north and by Argentina and Paraguay in the south. The subduction of the

Nazca Plate under the South American Plate generates the Andes volcanic chain and the Andes crosses Bolivia with two branches: Cordillera Occidental and Cordillera Oriental, the Altiplano plateau is located between these branches.

The Bolivian National Electricity Company (ENDE) and the Bolivian Geological Survey (GEOBOL) started the geothermal development in Bolivia in 1970s in the Cordillera Occidental by studying 42 geothermal manifestations and concluding that there is significant potential in this region.

In 1976, ENDE and the Ministry of Energy and Hydrocarbons, with funds from the United Nations Development Programme (UNDP) based on the study by GEOBOL (GEOBOL, 1976), began evaluating the geothermal potential in; Volcan Sajama, Valle de rio Empexa, Salar de Laguna, Volcan Ollague-Cachi, Laguna Colorada, Laguna Verde and Quetena, Three of the seven fields were considered the most prospective: Laguna Colorada, Sajama and Valle de rio Empexa located along the Occidental Cordillera (GEOBOL, 1976). Figure 1 shows the Laguna Colorada area and the location of the geothermal field. Laguna Colorada is the name of the area where ENDE has its geothermal project, but Sol de Mañana is the name of geothermal field.

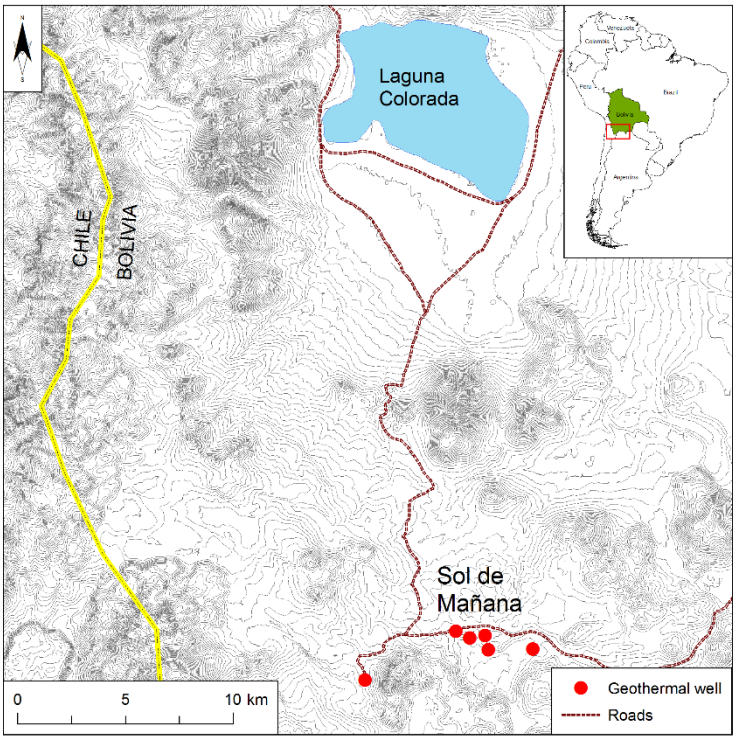

FIGURE 1: Location of the Sol de Mañana geothermal field

In 1980, ENDE carried out a prefeasibility study, and in the period 1988-1994 six deep wells were drilled confirming a reservoir temperature of 250-260°C. The drilling was carried out by the Bolivian Oil Company (YPFB) and the Italian government through the Italian Electricity Company (ENEL). Production tests performed on the wells indicated a potential of 40-50 MW_e, with possible extension up to 100-150 MW_e (ENEL, 1991). Unfortunately, due to a change in political situation the project was suspended in 1994.

In 1997, the Mexican Electricity Company (CFE) carried out an interference test, well testing and resource assessment certificating a geothermal potential of 120 MW_e for 25 years (CFE, 1997). In 2008, Japan External Trade Organization (JETRO) with West Japan Engineering Consultants, Inc. (West JEC) carried out a feasibility study for a 100 MW_e geothermal plant (JETRO, 2008). Following that study in 2010, the government of Bolivia started the planning for the financing of the construction of a 50 MW_e geothermal power plant in the Sol de Mañana field. In 2013, Japan International Cooperation Agency (JICA) with West JEC carried out well testing and resource assessment confirming the potential of 100 MW_e for 30 years in the Sol de Mañana field (JICA, 2013).

1.2 Goals of the study

The main objectives of this study are to:

- Review the available information from the Laguna Colorada Geothermal Project and literature related to geothermal assessment and modelling from the area;

- Review and collect information of preliminary studies and digitize relevant information from temperature and pressure logs, production tests, injection tests, interference tests and resource assessment;
- Review preliminary conceptual models carried out previously in order to obtain the reservoir properties;
- Analysis of temperature and pressure characteristics;
- Estimate the resource capacity using the volumetric method.

2. SOL DE MAÑANA GEOTHERMAL FIELD

2.1 Geological setting

The study area is located in southwest Bolivia, around 4900 m a.s.l. This area is comprised of Miocene-Pleistocene rock of the Andes volcanic arc extending in N-S direction generally parallel to the Pacific coast, and overlies marine and terrestrial sediments of Cenozoic-Paleogene age. The volcanic arc products are of calc-alkaline composition and vary between rhyodacites and andesite, and consists of lavas, tuffs and ignimbrites. The regional structure has two directions: N-S parallel to the magmatic arc and another NW-SW with long alignments along the recent volcanism.

The geo-volcanological mapping indicates the existence of an extensive ignimbrite unit that almost completely covers the area, and overlies an andesitic-dacitic lava sequence and possibly ignimbrites from the Neogene. The structural geology shows two orthogonal tectonic systems NNW-SSE and NNE-SSW, the first system is more pronounced and also affects the most recent formations and determines the formation of small horsts and grabens. This system is related to seismic events whose effects are still recognizable (ENEL, 1991). Figure 2 shows the stratigraphy and structural geology of the area.

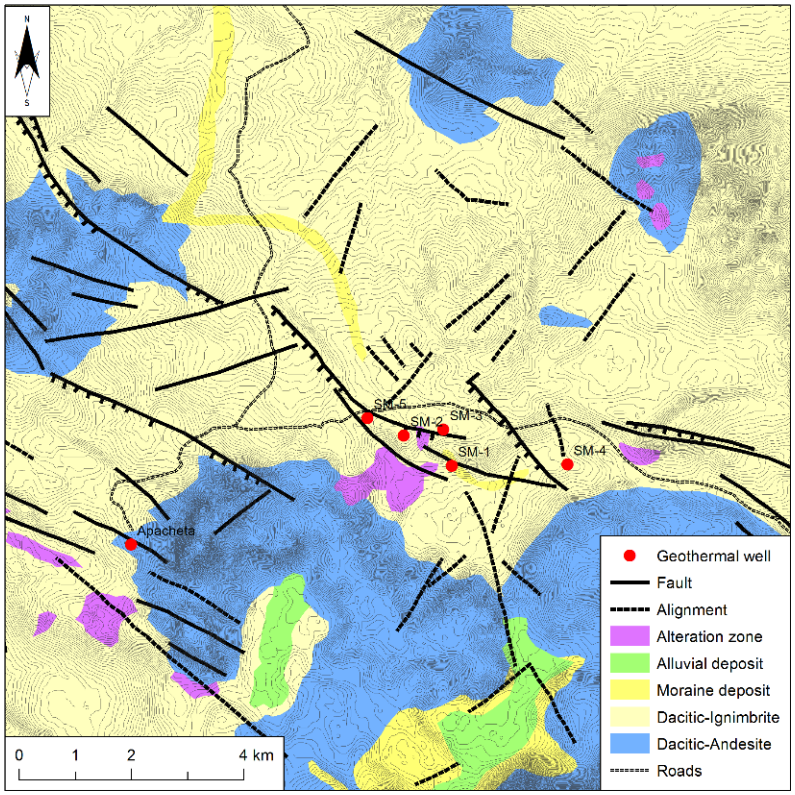

FIGURE 2: Stratigraphy and structural geology map (modified from JETRO, 2008)

The geological information suggests the existence of magmatic chambers located below the volcanic axis, indicating important heat sources in the west part of the manifestation areas (ENDE, 1986).

The structural system has caused secondary deep fracturing, which allows the hot water to rise up resulting in a heat exchange with shallower aquifers. Part of the geothermal fluid rises as vapour through

faults and fractures to reach the surface in springs, resulting in hydrothermal alteration zones (CFE, 1997).

2.2 Chemistry

According to Cl-SO_4-HCO_3 ternary diagram, the fluid could be classified as a mature water of neutral pH with a relatively high concentration of chloride. The Na-Ka-Mg ternary diagram indicates a fully equilibrated reservoir fluid with a reservoir temperature of 280°C, however liquid from hot springs in the area show signs of mixing with cold groundwater. The temperature obtained from Na/K, H_2S, H_2S/Ar and H_2S/H_2 geothermometers are in agreement with the measured reservoir temperature (Villarroel, 2014).

2.3 Geophysics

The structural mapping is based on gravimetric and resistivity data, and the possibility that those anomalies are related to hydrothermal alterations rather than the primary rock characteristics. According to laboratory results, the rock density for ignimbrites and lavas are 2-2.7 g/cm^3, but there is not a significant difference between these two rock types. The low resistivity layer corresponds to high argillic alteration, and the circulation fluid pattern that alters the rocks is related to fracturing system (ENEL, 1991).

Recently, a magneto telluric survey (MT) was carried out in order to connect better the gravimetric and resistivity anomalies that have been identified in the exploration stages. Figure 3 shows the gravimetric and resistivity anomalies and resistivity map modified from JECTRO (2008) at 3500 m a.s.l., displaying two boundaries inferred by the data. According to the resistivity data, the reservoir could be inside these two boundaries. A comparison was made between surface resistivity and drilling data with the lithology and temperature logs in well SM-3. The main conclusion is that the cap rock would be associated with resistivity of around 30 ohmm (Ramos, 2014).

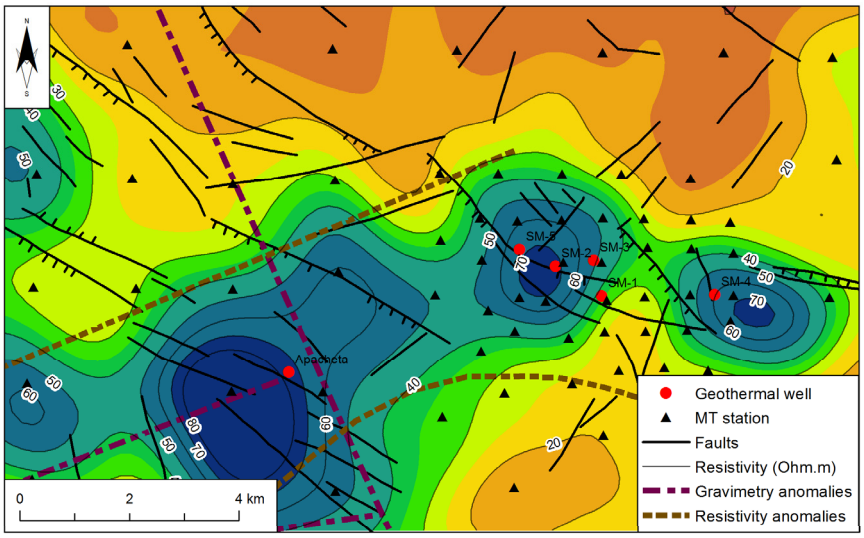

FIGURE 3: Gravimetric and resistivity anomalies and resistivity map at 3500 m a.s.l. (modified from JETRO, 2008)

According to preceding reports, the geothermal resource would be divided into two fields: Sol de Mañana and Apacheta (ENEL, 1991; JETRO, 2008). In this study the main focus will be on the Sol de Mañana field, due to better information availability.

2.4 Description of the wells in Sol de Mañana field

The deep drilling began in 1987 in the Cerro Apacheta zone, but due to discouraging results from that well the drilling continued at the Sol de Mañana field (ENEL, 1991), where five wells (Figure 4) were

drilled between 1989 and 1994. The well depths vary between 1180 and 1726 m, and all the wells are vertical (see also Table 1). Only the reinjection well has a slotted liner due to a collapse at the bottom. The section A-A' (Figure 4) is described in Chapter 3.3.

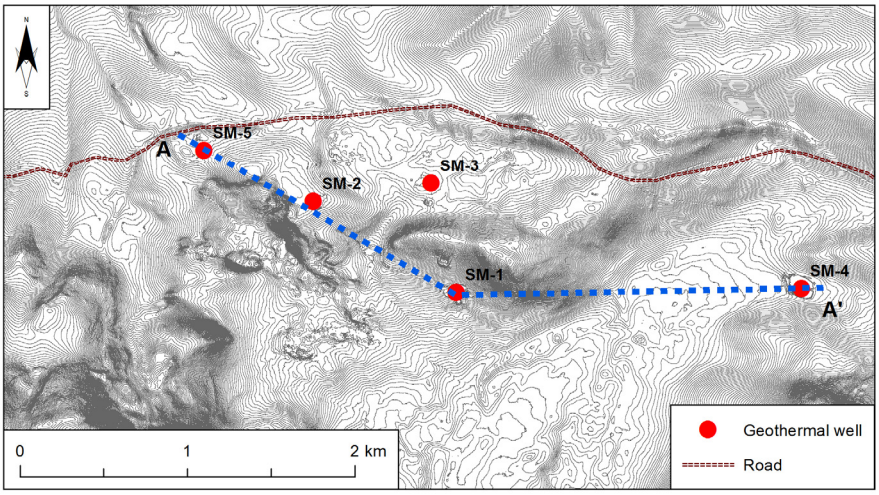

FIGURE 4: Well locations in the Sol de Mañana field

During the drilling of the wells several temperature logs were performed in order to determine the formation (undisturbed) temperature. Most of the logs were successful, except in zones with a loss of circulation, particularly in well SM-02. Temperature and pressure logs were also performed in static and dynamic conditions. However, the tests carried out at different times were not performed in all the wells. Well SM-03 was opened to production after almost 23 years.

TABLE 1: Description of wells in Sol de Mañana field

Well	**Elevation** (m a.s.l.)	**Drilled depth** (m)	**Casing depth** (m)	**Liner**	**Type of well**
SM-1	4859	1180	737	Open hole	Production
SM-2	4906	1486	608	Open hole	Production
SM-3	4885	1406	765	Open hole	Production
SM-4	4841	1726	1307	Slotted	Reinjection
SM-5	4904	1705	900	Open hole	Production
AP-1	5023	1602	780	Open hole	Production

In this report, the work carried out after the drilling by ENEL and ENDE in the period 1989-1994, and the well testing by CFE in 1997 and JICA in 2013, will be addressed.

3. ANALYSIS OF TEMPERATURE AND PRESSURE CHARACTERISTICS

Wells are vital components in both geothermal research and utilization, since they provide essential access for both energy extraction and information collection. A geothermal well is connected to the geothermal reservoir through feed-zones in the open section or intervals. The feed-zones are either open fractures, or permeable aquifer layers. In volcanic rocks the feed-zones are often fractures or permeable layers, such as layers between different rock formations. In some instances, a well is connected to a reservoir through a single feed-zone, while in other cases several feed-zones may exist in the open section, but often one of these is the dominant one (Axelsson, 2013).

The temperature and pressure logs are carried out during the drilling of wells, during heat-up after drilling, and during flow tests. The biggest challenge in analysing these logs is to define the temperature and pressure reservoir conditions, by determining the formation temperature profile for each well and the pressure potential of permeable zones intersected by the wells. When several wells have been drilled in an area, maps can be drawn to show the formation temperature and the pressure distribution in the geothermal reservoir. Early in the development, these maps will show the initial reservoir conditions

prior to utilization. Later, when production from the field commences, the mass withdrawal from the reservoir will lead to pressure drawdown and sometimes also temperature changes in the geothermal reservoir. Temperature and pressure logs are then used to monitor the changes and map the long term response of the reservoir to the utilization (Steingrímsson, 2013).

Determining the temperature and pressure distribution in a geothermal system is a fundamental requirement in the resource assessment. The temperature distribution indicates the resource quality and the feed-zones. A cross-section map shows how the temperature and pressure varies within the reservoir horizontally and vertically. Contour plots and vertical cross-sections can then be prepared at selected depths and locations to show how the temperature varies within the reservoir either horizontally or vertically. These plots are useful for showing how hot and cold fluids interact within the geothermal system and are important in the formulation of the system model (Abdollahzadeh Bina, 2009).

According to Steingrímsson (2013), the boiling point depth curve (BPD curve) is often plotted as a reference as this curve defines the maximum possible formation temperature for a hydrothermal system. If the temperature logs do not accurately define the formation temperature, further analyses, interpretation, assumptions or pure guesses are necessary in order to estimate the formation temperature for the well.

3.1 Formation temperature tests

After the drilling of a geothermal well is completed, the well is usually allowed to recover in temperature (heat up) from the cooling caused by drilling fluid circulation and cold water injection. The heat up of a well can take from a period of few hours to a few months, but it usually takes a few months. The principal reservoir engineering research conducted during this period is repeated temperature and pressure logging. The temperature data collected during heat up is used to estimate the undisturbed system temperature, often called the formation temperature, as wells usually do not recover completely during the recovery period. The method most often applied for this estimation is the Horner method. The pressure data collected is used to estimate the reservoir pressure with the intersection of several warm-up pressure profiles, defining the pivot point. If a single feed-zone dominates a well, the pivot point defines the reservoir pressure at the feed-zone depth. If two or more feed-zones exist in a well, the pivot point defines average conditions instead (Axelsson and Steingrímsson, 2012).

3.2 Interpretation of temperature and pressure profiles

Temperature and pressure logs carried out in Sol de Mañana field were collected at different stages and by different companies:

- In 1989-1994 by ENEL and ENDE, after drilling in all the wells under static conditions;
- In1997 by CFE in all the wells under static conditions;
- In 2013 by JICA through West JEC in wells: SM-01, SM-02, SM-03 and SM-04 under static and dynamic conditions.

Unfortunately, the same measurements were not performed in all the wells, and in some cases the information was not detailed enough about the state of the wells before and during the logging of the wells. However, it was possible to digitize records of temperature and pressure logs in order to plot data from individual wells on a single graph, for better understanding and comparison.

The first logs from 1989 to 1997 were performed with mechanical tools while the last records from 2013 were performed with electronic tools, making the last logs more detailed.

3.2.1 Well SM-01

The production well SM-01 was drilled in the period 08.09.1989-13.11.1988 to 1180 m depth, and has an open interval from 737 m depth to the well bottom. During the drilling, a partial loss of circulation was identified at 762-977 m depth, and finally total loss of circulation occurred at 977-1180 m depth. The main well rock type is ignimbrite of dacite composition of variable colour, which consists of quartz crystals, plagioclase, biotite and hornblende immersed in a vitreous matrix with chaotic texture. Study on secondary minerals revealed three zones of hydrothermal alteration:

- Zone of heulandite: 0 to 400 m depth;
- Zone of quartz and chlorite: 400 to 780 m depth;
- Zone of epidote: 780 to 1180 m depth.

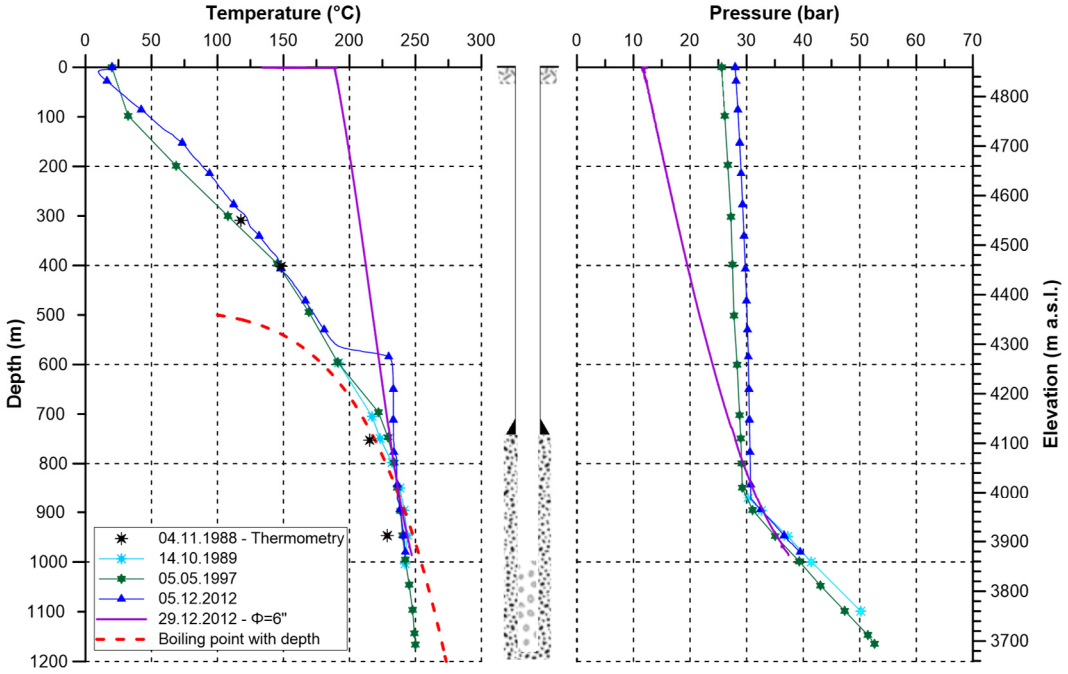

FIGURE 5: Temperature and pressure logs in well SM-01 in static and dynamic conditions

Figure 5 shows the temperature and pressure logs performed in the well. During the drilling of the well, some thermometry tests were carried out at different depths in order to assess the stabilized temperature using the Horner method. Finally, after the heating period, the well was opened to production for about 14 days (ENEL, 1989a).

The temperature gradient is around 300°C/km down to 700 m depth. This gradient could indicate an impermeable layer acting as a cap rock for the reservoir. The reservoir temperature is 240-250°C. In the interval of 860-1180 m depth the well is liquid compressed. There is a possibility that the well is in a two phase zone from 600-960 m depth, but above this depth and up to the surface the well has a gas column. In all cases, the temperature and pressure logs were carried out after a long time of heating up. The wellhead pressure in static conditions is around 28-30 bar (gas column), that allows the well to discharge without pressurization (ENEL, 1991).

3.2.2 Well SM-02

The production well SM-02 was drilled in the period 19.12.1989-17.02.1989 to 1486 m depth and has an open interval from 617 m depth to the well bottom. There was a partial loss circulation while drilling down to 920 m depth, but a total loss of circulation occurred while drilling in the interval 920-1486 m

depth. As the for well SM-02, this one is characterized in the upper part by dacitic ignimbrites, followed by dacitic lavas and dacitic ignimbrites at the bottom of the well. The study of secondary minerals showed four hydrothermal alteration zones:

- Zone with clay minerals: 0 to 400 m depth;
- Zone with wairakite: 525 to 800 m depth;
- Zone with wairakite and epidote: 800 to 950 m depth;
- Zone with epidote and adularia: 950 to 1486 m depth.

Figure 6 shows the temperature and pressure logs performed in the well. The thermometry carried out to different depths were analysed using the Horner method, however the tests were affected by the loss in circulation (ENEL, 1989b).

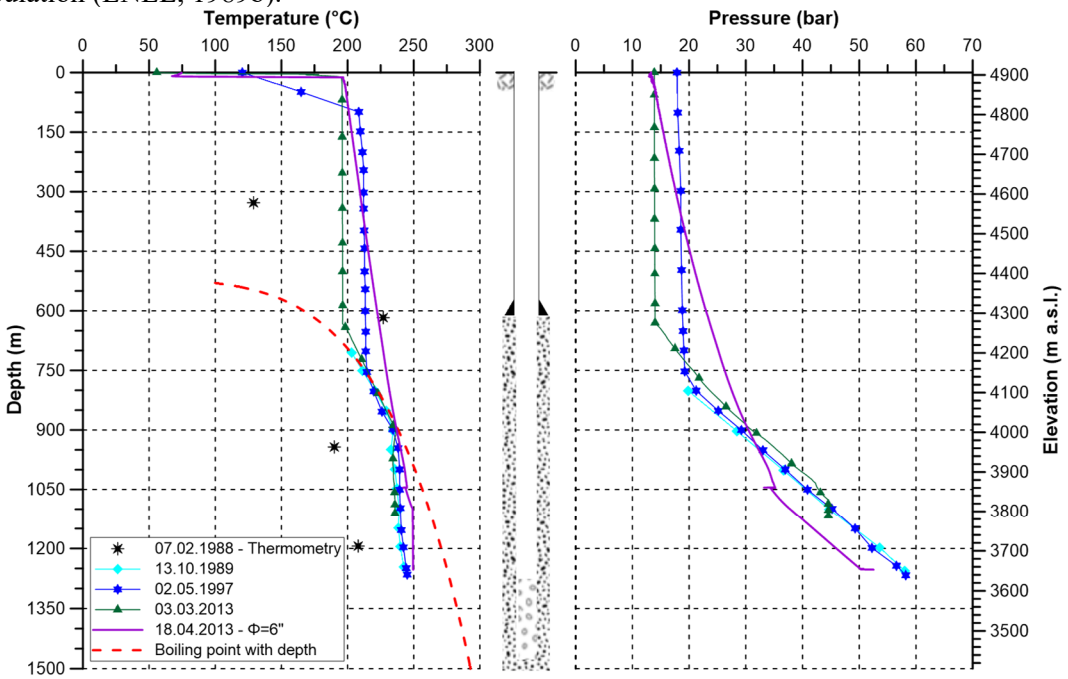

FIGURE 6: Temperature and pressure logs in well SM-02 in static and dynamic conditions

A high thermal gradient around 275°C/km is observed in the well down to 700 m depth, where the heat is transferred by conduction. Possibly there are two phase conditions in the depth range of 700-900 m depth and a low thermal gradient with temperatures within 230-242°C in the bottom section, 900-1250 m depth. The reservoir temperature is estimated about 245°C. According to the temperature logs below 900 m depth the system is liquid compressed, within 750-900 m depth it is two-phase and above this depth there is a gas column in the well.

The closed well has enough wellhead pressure (15-30 bar) to produce without stimulation. The well was open to production at the end of drilling, in 1997 and again in 2013.

3.2.3 Well SM-03

The production well SM-03 was drilled in the period 21.04.1989-05.10.1989 to 1406 m depth and has an open interval from 736 m depth to the well bottom. The drilling operation stopped after around 90 days. The drilling penetrated through impermeable formations to 900 m depth, below this depth the drilling continued with total loss circulation down to 1406 m depth. The layers are characterized by formations of dacitic ignimbrites to 970 m depth. No cuttings were returned from below that depth due to total loss circulation and it was not possible to distinguish ignimbrite in the upper layer followed by andesite (ENEL, 1990).

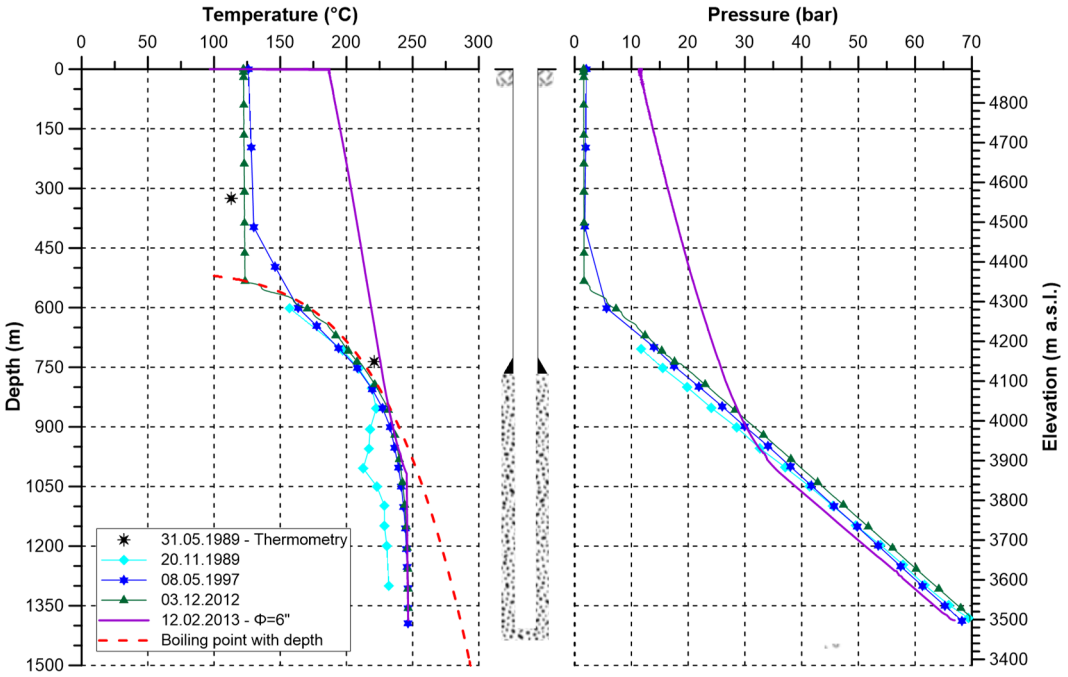

FIGURE 7: Temperature and pressure logs in well SM-03 in static and dynamic conditions

Figure 7 shows the temperature and pressure logs performed in the well. Two temperature recovery measurements were carried out at different depths and were analysed using the Horner method.

A high thermal gradient around 300°C/km in the uppermost 750 m depth of the well was identified and the first temperature log after drilling shows that the well was still heating up. According to the temperature logs below 900 m depth, the well is liquid compressed, within 600-900 m depth it is two-phase and above 600 m depth there is a gas column in the well. The reservoir temperature is close to 250°C.

3.2.4 Well SM-04

The well SM-04 was designed as a reinjection well, and was drilled in the period 31.10.1989-23.12.1989 to 1474 m depth. Due to low permeability, the injectivity index was only around 1 m^3/h/bar. The well was deepened in the period 02.12.1991-17.12.1991 to 1726 m depth (ENDE, 1994a). The well has a slotted liner from 1307 m depth to the well bottom. The well crossed impermeable formations down to 1300 m depth, but below, partial and total circulation losses were observed during drilling. The lithology penetrated was dacitic ignimbrites, andesitic lavas and dacitic ignimbrites in the bottom section of the well. The study of secondary minerals shows the following hydrothermal alteration zones:

- Zone with clay minerals: 0 to 650 m depth;
- Zone with sericite and chlorite: 650 to 1474 m depth;
- Zone with sericite, chlorite and epidote: 1474 to 1726 m depth.

Figure 8 shows the temperature and pressure logs performed in the well. The stabilized temperature log shows a constant gradient around 150°C/km down to 1400 m depth, displaying typical character for impermeable rocks with heat transfer by conduction (ENEL, 1991).

The well is liquid compressed from the surface down to the well bottom, without wellhead pressure. The thermometry indicates that the area around the well had not reached equilibrium temperature below 800 m depth (ENDE, 1994a), but the thermometry (1989) suggests a much higher temperature at 1200 m depth than was measured (2012, 1997 and 1993). The temperature measurement from 2012 is very similar to the one from 1997 indicating undisturbed temperature, except if the well had been cooled

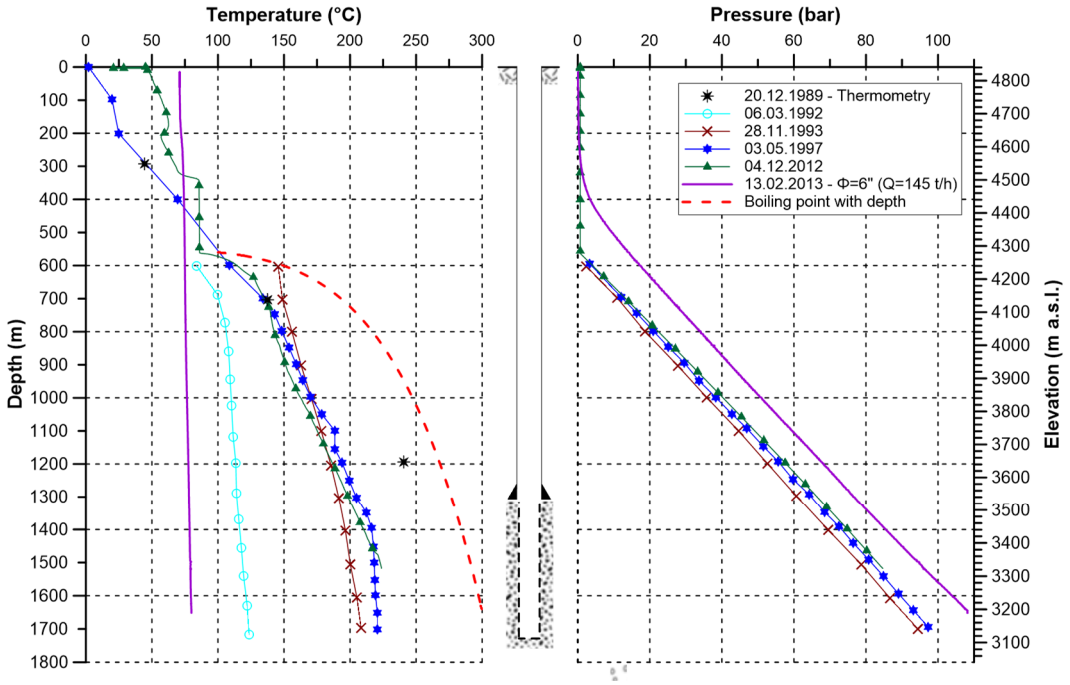

FIGURE 8: Temperature and pressure logs in well SM-04
in static and dynamic conditions

down for some reason before the last temperature measurement in 2012. The reservoir temperature would then be about 225°C.

3.2.5 Well SM-05

The production well SM-05 was drilled in the period 03.04.1992-04.11.1992 to 1705 m depth and has an open interval from 900 m depth to the bottom of the well. The drilling operations stopped for about four months due to winter conditions. The well penetrated relatively impermeable formations down to 900 m depth, with partial circulation losses. The well was drilled with total circulation loss from that depth down to the bottom. The strata are characterized by dacitic ignimbrite down to 700 m depth, continuing with andesitic pyroxene to 920 m depth and finally dacitic ignimbrite on the bottom of the well. The study of secondary minerals shows three hydrothermal alteration zones:

- Zone with clay minerals: 0 to 420 m depth;
- Zone with epidote and adularia: 420 to 900 m depth;
- Zone with epidote and orthoclase: 900 to 1700 m depth.

Figure 9 shows the temperature and pressure logs performed in the well. The temperature logs revealed gradients around 225°C/km to 1000 m depth where the heat transfer was by conduction, and below this depth by convection with reservoir temperatures around 250°C at the well bottom. The pressure log after drilling showed a decrease due to gas accumulation in the upper zone (ENDE, 1994b).

The logs also showed that below 900 m depth the well is compressed liquid, from 600 to 900 m depth in two-phase and gas exists in the upper part. During the well testing in 1997, two logs in static conditions were carried out before and after the well testing. In the last log there was an increase in temperature and it was by heating of the well after drilling (CFE, 1997).

3.3 Temperature and pressure distribution

Contour maps, both cross-sections and contour plans, show how the temperature varies within the reservoir and at the reservoir boundary. Such maps indicate the locations of conductive and convective

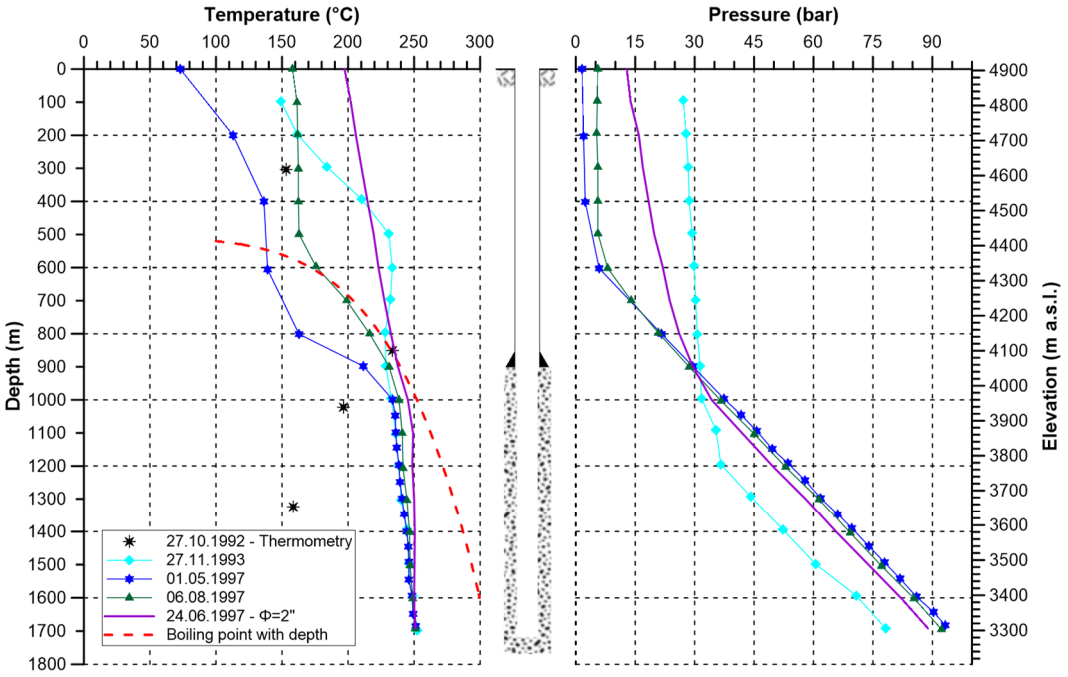

FIGURE 9: Temperature and pressure logs in well SM-05 in static and dynamic conditions

zones in the geothermal system and divide it into recharge areas, up flow zones and out flow areas. The formation temperatures maps, drawn before any exploitation starts from the reservoir, define the natural thermal state of the reservoir but maps based on temperature data from the reservoir under exploitation will reveal temperature changes caused by the production through pressure drawdown, induced fluid recharge and boiling. Temperature maps are very important in the development of conceptual models of geothermal reservoirs (Axelsson and Steingrímsson, 2012).

Figure 10 shows a vertical cross-section from the profile line A-A' presented in Figure 4 (Chapter 2.4). The profile line A-A' crosses through wells SM-05, SM-02, SM-01 and SM-04 (direction W-E), and the geological structure in the Sol de Mañana field.

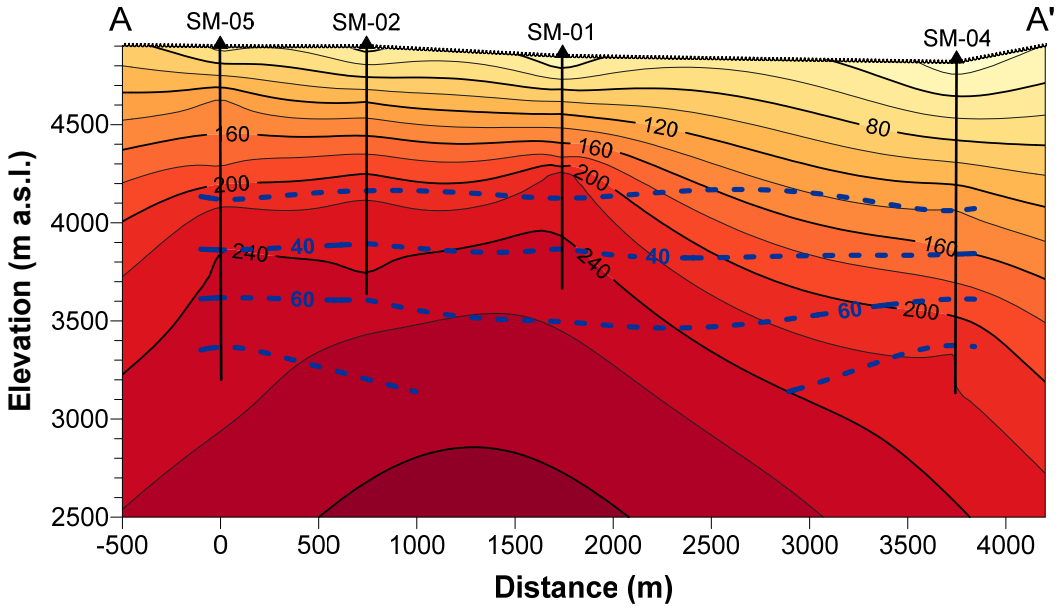

FIGURE 10: Temperature (°C) and pressure (bars) cross-section in Sol de Mañana field through wells SM-05, SM-02, SM-01 and SM-04

According to the temperature cross-section, the up flow is likely close to wells SM-01 and SM-02, and cooling is evident from well SM-04 towards the production wells. According to the pressure data, the pressure is almost constant along the same cross-sections, as presented in blue on the temperature cross-section.

Interpretation of sub-surface pressures is generally more difficult than sub-surface temperatures, because the pressure profile within the wellbore does not generally reflect the pressure profile with depth in the surrounding formation. The well pressure is often in equilibrium with the formation pressure only in the major feed zone. If there are two or more significant permeable zones, then the depth of the equilibrium will lie between these zones (Abdollahzadeh Bina, 2009).

4. WELL TESTING IN SOL DE MAÑANA FIELD

During a well test, the response of a reservoir to changing production (or reinjection) conditions is monitored. Since the response is, to a greater or lesser degree, characteristic of the reservoir properties, it is possible in many cases to infer reservoir properties from the response. Well test interpretation is therefore an inverse problem in that model parameters are inferred by analysing model response to a given input. The objectives of a well test usually fall into three major categories: reservoir evaluation, reservoir management and reservoir description (Horne, 1995).

4.1 Production well tests

Production well tests are conducted to determine the energy content (deliverability), and to analyse the flow characteristics of a well, the tests are done by measuring the fluid flow from a discharging well at different wellhead pressures (Afeworki, 2010).

During the production well test, the total flow, enthalpy and fluid chemistry are measured. Grant and Bixley (2011) refer to different methods to estimate these variables.

The first production test was carried out after drilling wells SM-01 and SM-02, the total flow and enthalpy were estimated using the Russel James method (ENEL, 1989c; ENEL, 1991). The second production test was carried out in 1997 in the wells SM-02 and SM-05, the total flow and enthalpy were estimated using the Russel James method (CFE, 1997). Finally, the last production test was carried out in 2013 in the wells SM-01, SM-02 and SM-03, the total flow and enthalpy was calculated using the Russel James method and tracer flow test method (TFT) (Villarroel, 2014).

The productivity of geothermal wells is often presented through a simple relationship between mass flow rate or production, and the corresponding pressure change. In general, the productivity of geothermal wells is a complex function of the well and reservoir parameters (Axelsson, 2013).

The most important result of a production test is the characteristic well curve. Figure 11 shows the well curve for the wells in Sol de Mañana field. It shows that the characteristic curves are similar for wells SM-01 and SM-02 for the production tests (1989, 1997 and 2013), while the wells SM-03 and SM-05 show different characterises, but they were open to production only once.

According to Axelsson (2013), the characteristic well curve for the well SM-01 and SM-02 could be consistent with two-phase inflow, and the characteristic well curve for the wells SM-03 and SM-05 are similar to liquid-phase wells.

Wells that exhibit reduction in mass flow with increasing wellhead pressures, indicate that the well is wellbore controlled. The output is said to be wellbore controlled if the wellbore size limits the production. This is normally observed in areas where the permeability is very high (Sarmiento, 2011).

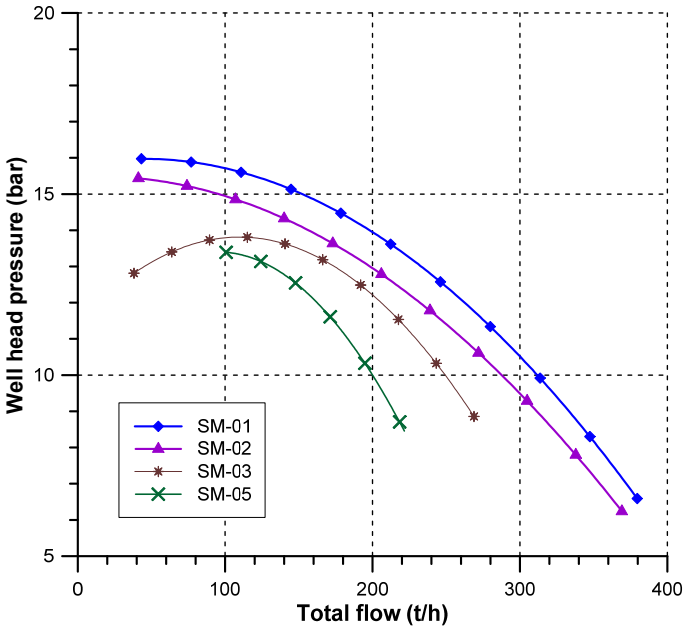

FIGURE 11: Characteristic well curves of the Sol de Mañana field

4.2 Injection well tests

An injection test is conceptually identical to a drawdown test, except that flow is into the well rather than out of it. Injection rates can be often controlled more easily than production rates, however analysis of the test results can be complicated by multiphase effects, unless the injected fluid is the same as the original reservoir fluid (Horne, 1995).

The injectivity index is defined as the change in the injection flow rate, divided by the change in the stabilized reservoir pressure. The injection tests were carried out in all the wells after drilling and several times in well SM-04. Table 2 summarizes the different injectivity tests.

TABLE 2: Injectivity index (II) at different depths in the Sol de Mañana field

Tests	**Wells injectivity index [m^3/h/bar] / (depth [m])**				
	SM-01	**SM-02**	**SM-03**	**SM-04**	**SM-05**
Tests 1 (*1989*)	2.8 (*1030 m*)	4 (*1198 m*)	13 (*1254 m*)	3 *(1413 m)*	2 (*1035 m*)
Tests 2 (*1989*)	>70 (*1180 m*)	67 (*1486 m*)	27 (*1406 m*)	2 *(1473 m)*	4 (*1350 m*)
Tests 3 (*2013*)	---	---	---	13.5 (*1500 m*)	---
Tests 4 (*2013*)	---	---	---	27.3 (*1500 m*)	---

The deeper injectivity tests in the wells SM-01, SM-02 and SM-03 give higher injectivity indexes, indicating that the wells have intersecting fracture zones with high permeability. Well SM-05 on the other hand shows only slight increase with depth. The injectivity index in well SM-04 is low compared with the wells SM-01, SM-02 and SM-03, even in the last injection test from 2013.

4.3 Interference well tests

In an interference test, one well is produced and pressure is observed in a different well (or wells), i.e. the pressure changes in the reservoir at a distance from the original producing well are monitored. An interference test may be useful to characterize reservoir properties over a greater length scale than during single well tests. Pressure changes at a distance from the producing well are smaller than in the producing well itself, so interference tests require sensitive pressure recorders and may take a long time to carry out (Horne, 1995).

In order to obtain additional information about the reservoir characteristics several interference tests were carried out, Table 3 summarizes the different interference well tests.

TABLE 3: Summary of interference tests at different stages

Year	Production well	Production period	Monitoring well	Observation period	Distance (m)	Observation
1989	SM-02	~167 days	SM-01	100 days	1000	- Interruption due to technical problems.
			SM-03	167 days	700	- Capillary tubing method.
1997	SM-02	~60 days	SM-01	5 logs recording for 24 hours	1000	- Pressure tool was recording alternatively for 24 hours.
			SM-03	4 logs recording for 24 hours	700	- It is suggested to perform this test with other equipment.
2013	SM-01	~23 days	SM-03	~36 days	670	- Capillary tubbing method.
	SM-03	~38 days	SM-01	~90 days	670	
	SM-02	~22 days	SM-03	~48 days	700	- Problems due to gas leakage.

4.3.1 Interference tests by ENEL 1989

An interference test was performed during the period 15.10.1989-22.05.1990 (with interruptions due to technical problems) by producing from well SM-02 but monitoring the pressure response in wells SM-01 (at 1050 m depth) and SM-03 (at 995 m depth). Figure 12 shows the production in well SM-02 and the pressure in wells SM-01 and SM-03 corrected at 3750 m a.s.l. during the tests.

Well SM-01: The observation in well SM-01 started after opening well SM-02, unfortunately the pressure values in the first 34 days (15.10.1989 to 18.11.1989) are not reliable since oscillation around ± 1 bar was observed in the pressure, reflecting problems with the measurement equipment. During the second period of 97 days (05.12.1989 to 12.03.1990), the measurement equipment worked correctly and the data reflected actual reservoir variations showed in Figure 12. There is no explanation about the oscillation during the period 75-100 days, as well as for the tendency in the well SM-01 to show increases in pressure before the well SM-02 was closed. Finally, during the third period of 57 days (19.03.1990 to 17.05.1990), the data is not usable due to equipment problems.

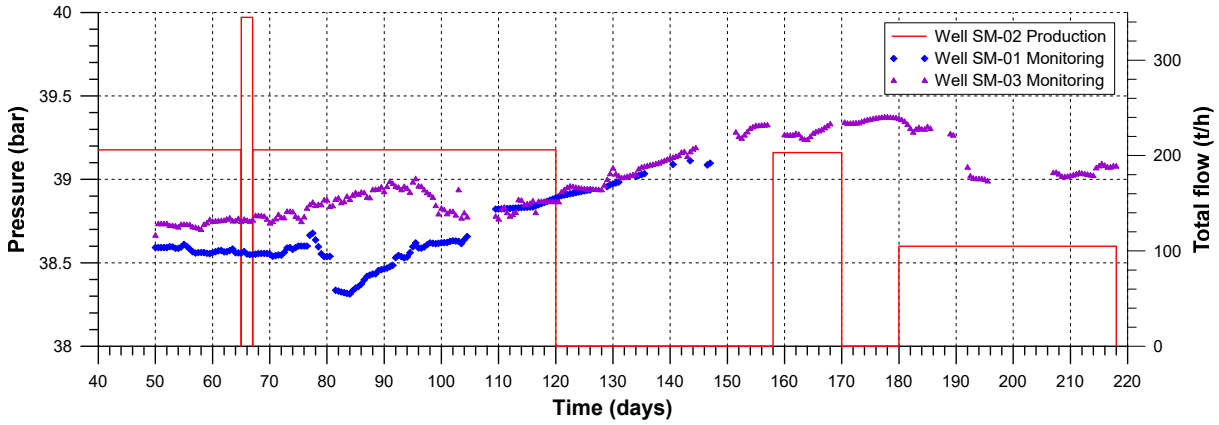

FIGURE 12: Corrected pressure monitoring at 3750 m a.s.l. (modified from ENEL, 1991)

Well SM-03: The data quality throughout the measurement period was satisfactory, except some values after about 200 days of recording (Figure 12) were possibly affected by the gas loss in the equipment, and also the data shows an oscillation during the period of 75-125 days of recording. There is a pressure increase in wells SM-01 and SM-03 during the period 130-150 days when the well SM-02 is closed.

In the period 120-150 days the wells SM-01 and SM-03 show a parallel trend where there is an increase in pressure, possibly as a response to the closure of the well SM-02, even though this trend starts in both wells before well SM-02 is closed, making it difficult to draw any definite conclusions. In the last period, after150 days of measuring, the data is hardly interpretable. The data from well SM-01 in the period 50-80 days is most promising for a quantitative interpretation (ENEL, 1991). The pressure changes in both wells is very small and could be non-related to the production from well SM-02, especially since the behaviour does not correspond in time with changes in production.

4.3.2 Interference tests by CFE 1997

Well SM-02 was opened to production for approximately four months, in this period pressure logs were performed in wells SM-01 and SM-03 aiming to observe interference between the wells, the operation basically consisted in lowering the pressure probe at 1160 m depth (SM-01) and at 1380 m depth (SM-03) and record the pressure change by 24 hours. The results in the wells show a typical liquid compressed reservoir with good permeability and an apparent connection between the wells observing an immediate response to the operation change in well SM-02 (CFE, 1997). Figure 13 shows the different pressure logs carried out in order to observe the interference between wells SM-01, SM-02, and SM-03.

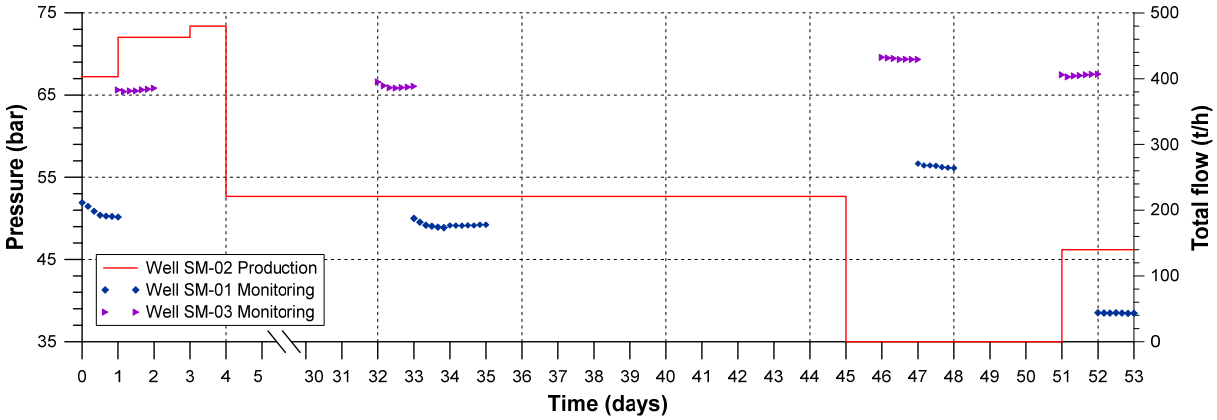

FIGURE 13: Interference tests between wells SM-01, SM-02, and SM-03 (modified by CFE, 1997)

According to the interference tests shown in Figure 13 when well SM-02 is open to production, there is an interference in well SM-01 and well SM-03. After closing well SM-02 there is an increase in pressure in both wells but it is more evident in well SM-01 than in well SM-03. Finally, when well SM-02 is opened to production the interference is higher in well SM-01 than in well SM-03. Therefore, there is a better connection between wells SM-02 and SM-01 than between wells SM-02 and SM-03.

4.3.3 Interference test by JICA 2013

The last interference test was performed using more accurate equipment in wells SM-01, SM-02, and SM-03 than in previous tests in 1989 and 1997. In the first stage, well SM-01 was opened to production and the pressure was monitored in well SM-03. In the second stage, well SM-03 was opened to production and the pressure was monitored in well SM-01. Finally, when well SM-02 was opened to production, wells SM-01 and SM-03 were monitored, but in this last stage the monitoring was stopped due to equipment problems, when well SM-02 was still producing (JICA, 2013). Figure 14 shows the production and pressure during the tests.

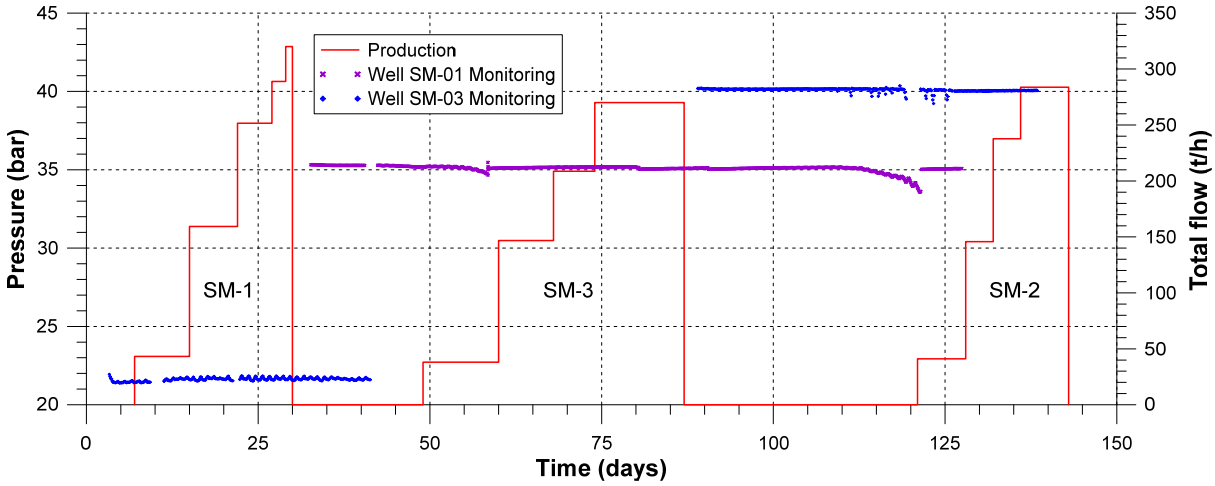

FIGURE 14: Production and pressure monitoring during the interference well testing (modified from JICA, 2013)

The pressure changes between wells SM-01 and SM-03 shown in Figure 14 are very small in relation to production of well SM-02 during the interference tests, it could be related to reservoir extension.

The different interference tests show more connection between wells SM-01 and SM-02 than wells SM-01 and SM-03, and also the geological structure map in Figure 2 (Chapter 2.1) shows a fault that crosses wells SM-05, SM-02 and between the wells SM-01 and SM-03. Therefore, the interference test confirms the geological connection between the wells SM-01 and SM-02.

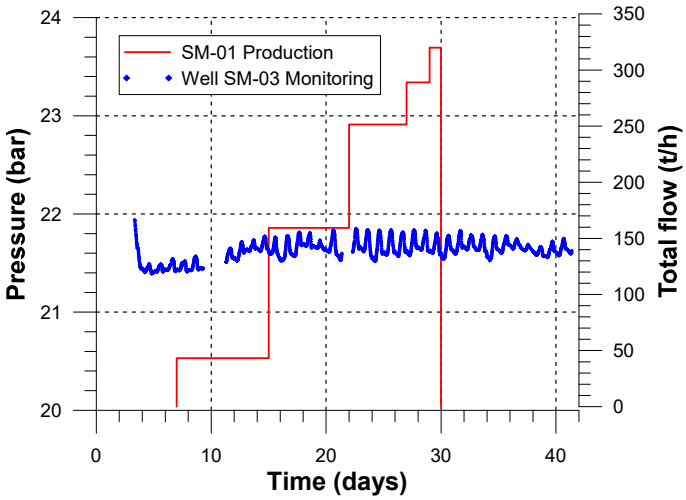

FIGURE 15. Production and pressure monitoring in the well SM-01 and SM-03 (modified from JICA, 2013)

During the production from well SM-01 the monitoring in well SM-03 showed atypical patterns as can be seen in Figure 15. The data shows a cyclical performance with one day periods. Grant and Bixley (2011) make references to changes in barometric pressure and the Earth tides that could apply here for well SM-03. The pressure changes are relatively small and most likely not connected to the production from well SM-01. Barometric pressure changes usually cause long-period pressure changes in wells that have aquifers that are connected to the atmosphere.

Leaver (1986) mentions that the increased use of sensitive quartz crystal gauges for pressure measurements has meant greater emphasis on filtering out earth tide and barometric effects to obtain a clean interference pressure response. The response of reservoirs to barometric pressure, earth and oceanic tides and rainfall has long been observed with the magnitude of the pressure response depending on the fluid viscosity, permeability, porosity and total compressibility. Barometric variations can produce reservoir responses of more than 8 kPa while earth tide responses in the reservoir are usually less than 1 kPa.

5. RESOURCE ASSESSMENT USING VOLUMETRIC METHOD

Geothermal resource assessment is a process of evaluating surface discharge and downhole data, and integrating it with other geoscientific information obtained from geological, geophysical and geochemical measurements. An assessment of geothermal resources can be made during the reconnaissance and exploratory stage prior to drilling of wells, taking into account the extent and characteristics of the thermal surface discharges and manifestations, geophysical boundary anomaly, the geological setting and subsurface temperatures obtained from geothermometers. An updated resource assessment can be made after drilling a number of wells and after the wells have been put into production, to forecast the future performance of the field. The use of simple volumetric calculations in initially committing a power plant capacity has proven that it can reliably predict the minimum commitment for a field (Sarmiento and Björnsson, 2007).

5.1 Thermal energy calculation

The volumetric method refers to the calculation of thermal energy in the rock and the fluid which could be extracted based on specified reservoir volume, reservoir temperature, and reference or final temperature. This method is patterned from the work applied by the USGS to the Assessment of Geothermal Resources of the United States (Muffler, 1979). In their work, the final or reference temperature is based on the ambient temperature, following the exhaust pressures of the turbines for electrical generation (Sarmiento et al., 2013).

The equation used in calculating the thermal energy for a liquid dominated reservoir is as follows:

$$Q_T = Q_r + Q_w \tag{1}$$

and

$$Q_r = Ah\left[\rho_r C_r (1-\varphi)\left(T_i - T_f\right)\right] \tag{2}$$

$$Q_w = Ah\left[\rho_w C_w \varphi\left(T_i - T_f\right)\right] \tag{3}$$

where: Q_T = Total thermal energy (kJ/kg);
Q_r = Heat in rock (kJ/kg);
Q_w = Heat in water (kJ/kg);
A = Area of the reservoir (m^2);
h = Average thickness of the reservoir (m);
C_r = Specific heat of rock at reservoir condition (kJ/kg°K);
C_w = Specific heat of liquid at reservoir condition (kJ/kg°K);
φ = Porosity;
ρ_r = Rock density (kg/m^3);
ρ_w = Water density (kg/m^3);
T_i = Average temperature of the reservoir (°C); and
T_f = Final or rejection temperature (°C).

If the reservoir has a two-phase zone existing at the top of the liquid zone, it is prudent to calculate the heat component of both the liquid and the two-phase or steam dominated zone of the reservoir. However, a comparison made by Sanyal and Sarmiento (2005) indicates that if merely water were to be produced from the reservoir, only 3.9% of the stored heat is contained in the fluids; whereas, if merely steam were to be produced from the reservoir, only 9.6% of the stored heat is contained in the fluids. If both water and steam were produced from the reservoir, the heat content in the fluids is somewhere between 3.9 and 9.6%. Conclusively, majority of the stored heat is contained in the rock and it does not matter whether one distinguishes the stored heat in water and steam independently (Sarmiento et al., 2013).

The possible size of a new power plant that could be supported by the resource in question is based on the following equation:

$$P = \frac{Q_T R_f C_e}{P_f t} \tag{4}$$

where: P = Power potential (MW_e);
R_f = Recovery factor;
C_e = Conversion efficiency;
P_f = Plant factor; and
t = Time in years (economic life).

The *recovery factor* (R_f) refers to the fraction of the stored heat in the reservoir that could be extracted to the surface. It is dependent on the fraction of the reservoir that is considered permeable and on the efficiency by which heat could be swept from these permeable channels. Figure 16 shows a correlation between recovery factor and porosity proposed by Muffler (1979).

The *conversion efficiency* (C_e) takes into account the conversion of the recoverable thermal energy into electricity. More accurately, the conversion can be estimated in two stages; first the conversion of the thermal energy into mechanical energy and later the conversion of the mechanical energy into electrical energy. This is not considered necessary, in view of all the uncertainties involved in the volumetric assessment method, so applying a single thermal-mechanical-electrical efficiency is considered sufficiently accurate. Figure 17 shows the correlation between thermal conversion efficiency and reservoir temperatures presented by Nathenson (1975) and Bödvarsson (1974).

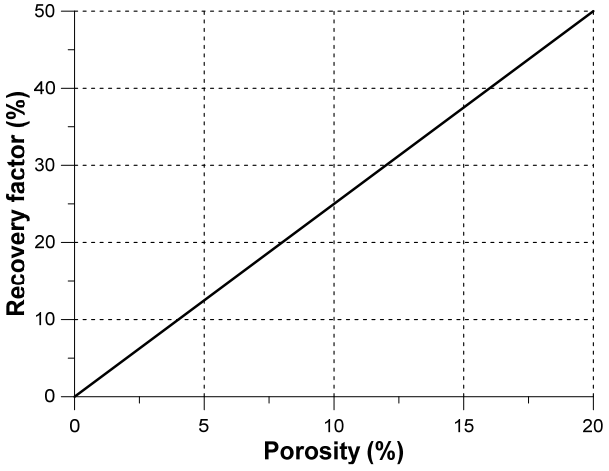

FIGURE 16: Correlation between recovery factor and porosity (From Muffler, 1979)

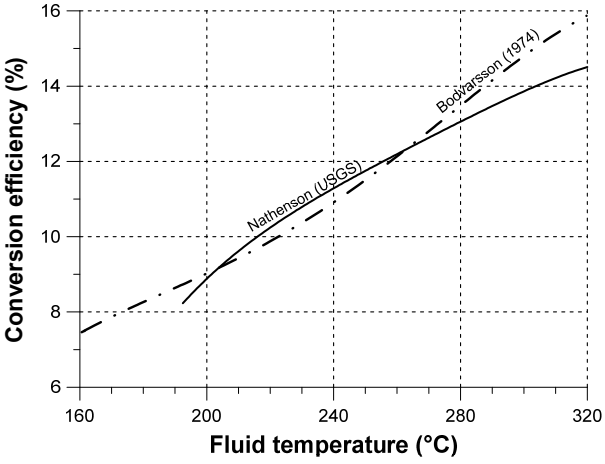

FIGURE 17: Correlation between thermal conversion efficiency and reservoir temperatures (From Nathenson, 1975 and Bödvarsson, 1974)

The *economic life* (t) of the project is the period it takes the whole investment to be recovered within its target internal rate of return. This is usually 25-30 years.

The *plant factor* (P_f) refers to the plant availability throughout the year taking into consideration the period when the plant is scheduled for maintenance, or whether the plant is operated as a base-load or peaking plant. The good performance of many geothermal plants around the world places the availability factor between 90 and 97% (Sarmiento et al., 2013).

5.2 Parameters estimated

The parameters required for the volumetric assessment were estimated following the guidelines of Sarmiento et al. (2013), based on earlier studies in conceptual model and resource assessment by ENEL (1989), CFE (1997), JETRO (2008), JICA (2013), Ramos (2014) and Villarroel (2014).

Surface area of the geothermal system: The size of the Sol de Mañana field is not yet fully known, therefore defining the extension of the reservoir can be difficult, even when many wells have been drilled (Grant and Bixley, 2011). Information on the extent of a geothermal system is usually assumed from the resistivity measurements. In Ramos (2014) a correlation was made of geophysical anomalies with drilling data to obtain a possible reservoir extension. Figure 18 shows the surface area limits for two scenarios. Scenario I which considers geophysical anomalies from the exploration reports for the Sol de Mañana field in 1989, and scenario II which considers geophysical anomalies including the Apacheta field. Table 4 summarizes the surface estimated for both scenarios.

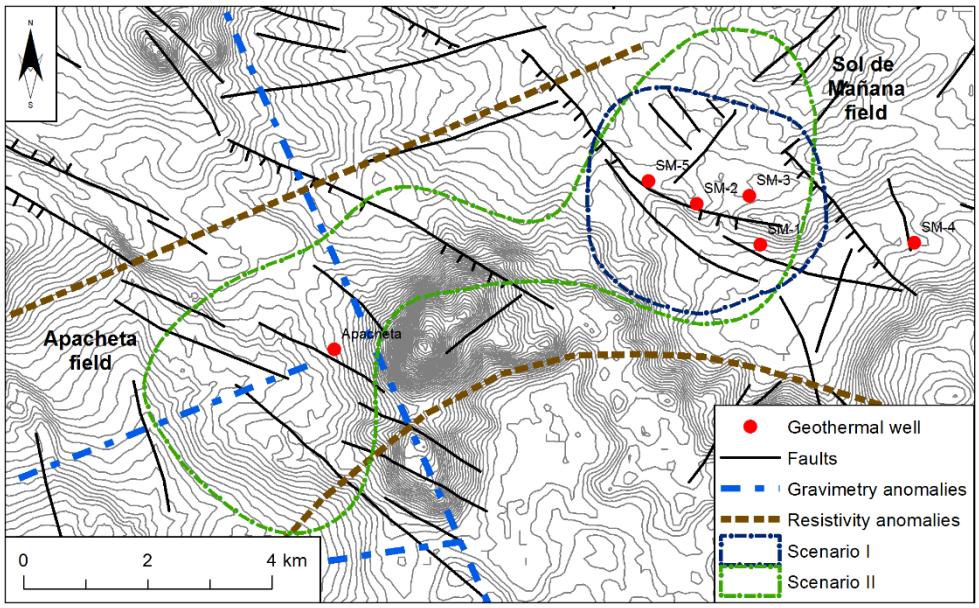

FIGURE 18: Reservoir boundaries considering two scenarios

TABLE 4: Parameter used to estimate probability distribution for Monte Carlo simulation

Input parameters	Units	Minimum	Most likely	Maximum	Type of distribution
Surface area (scenario I/II)	km^2	5/5	7/20	13/45	Triangular
Thickness	m	1000	1500	2000	Triangular
Rock density	kg/m^3		2600		Single value
Porosity	%	5	8	10	Triangular
Rock specific heat	J/kg°C		850		Single value
Temperature	°C	230	250	280	Triangular
Fluid density	kg/m^3	827	814	750	f(temp)
Fluid specific heat	J/kg°C	4683	4770	5286	f(temp)
Recovery factor	%	13	20	25	Triangular
Conversion efficiency	%	10	12	14	Triangular
Plant life	years		25/50		Single value
Reinjection temperature	°C		150		Single value

Reservoir thickness: The reservoir thickness was estimated from the temperature profiles, the depth to the reservoir was considered to be where the temperature data becomes almost constant. The lower depth is more difficult to estimate since none of the wells completely penetrates the reservoir. The minimum thickness is therefore assumed to be to the bottom of the deepest well.

Reservoir temperature: The minimum and most likely reservoir temperatures were estimated from the temperature profiles and the maximum temperature from chemistry studies.

Recovery factor and conversion efficiency: In both cases were estimated using the relations showed in Figure 16 and Figure 17.

Rock and fluid parameters: The rock properties were obtained from exploration reports in 1989. The fluid parameters are functions of thermodynamic tables.

Table 4 summarizes the parameters obtained according to the available information from the reports mentioned in the text above. Scenarios I and II are evaluated for different exploitation period.

5.3 Results

The thermal energy or the plant capacity is usually plotted using the relative frequency histogram and the cumulative frequency distribution. The relative frequency of a value or a group of numbers (intervals or bins) is calculated as a fraction or percentage of the total number of data points (the sum of the frequencies). The relative frequencies of all the numbers or bins are then plotted (Sarmiento et al., 2013). Results obtained for scenario I (maximum surface area of 13 km^2), calculated for a period of 25 years through the Monte Carlo simulation are displayed in Figure 19.

The results for the first scenario shows that the most likely value for the power production capacity is 75 MW$_e$ for a plant life of 25 years. Also, from the 80% acceptance range, the results of the simulations are that the estimated power production will be in the range of 57-124 MW$_e$ for 25 years (Figure 19a). Furthermore, the cumulative frequency, with 90% probability, shows that the resource capacity will be at least 57 MW$_e$ for 25 years (Figure 19b).

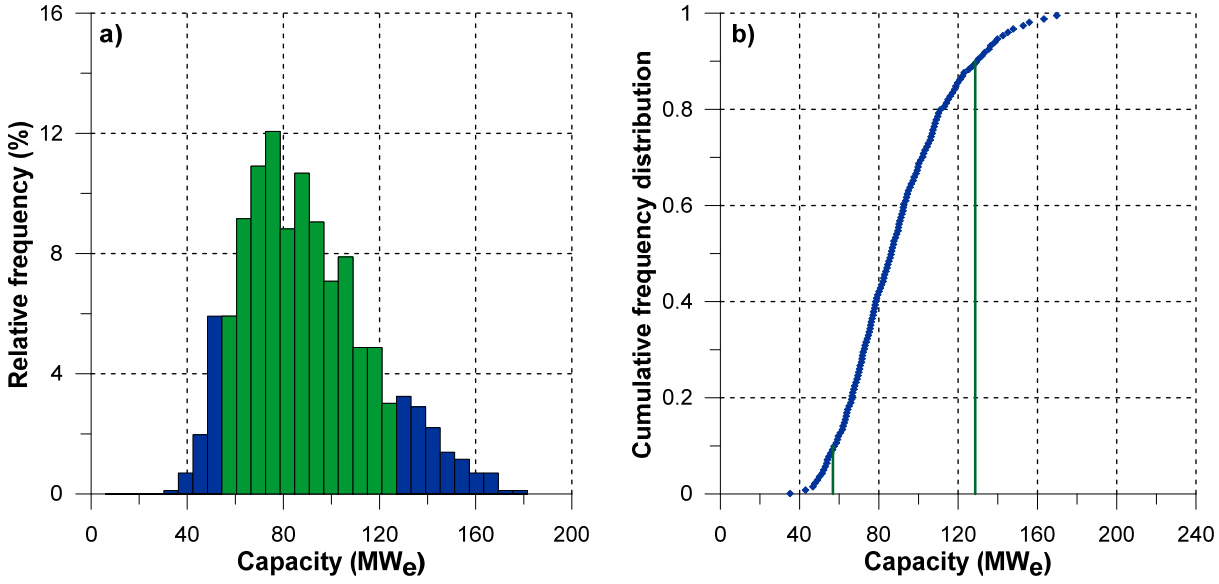

FIGURE 19: Simulation results for scenario I (13 km^2 maximum area), calculated for 25 years:
a) relative frequency of the power production capacity
b) cumulative frequency of the power production capacity

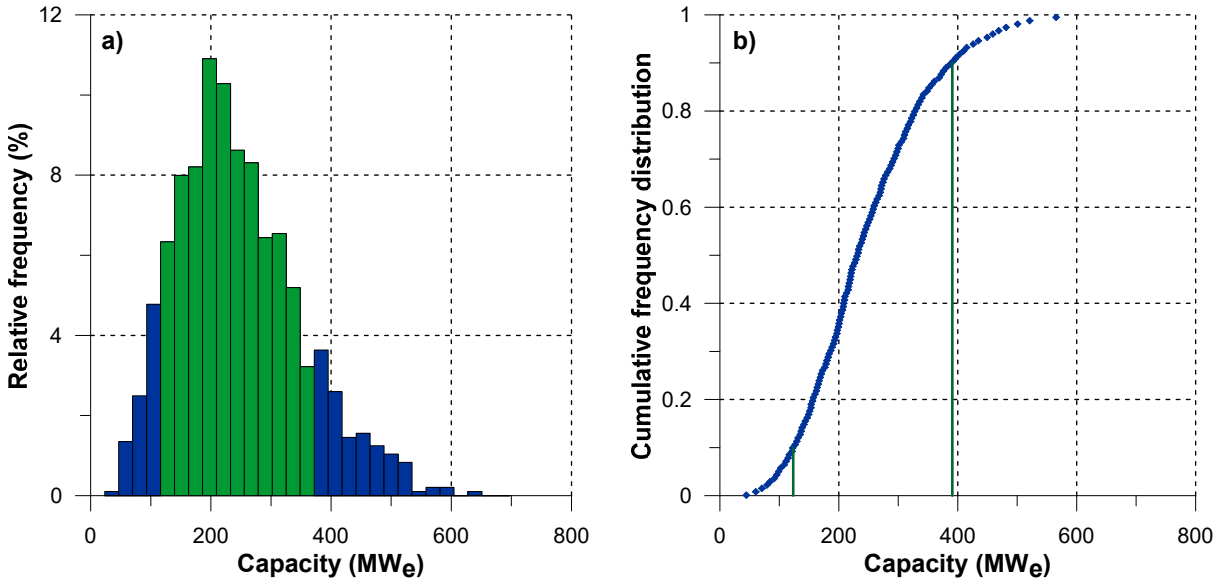

FIGURE 20: Simulation results for scenario II (45 km^2 maximum area), calculated for 25 years:
a) relative frequency of the power production capacity
b) cumulative frequency of the power production capacity

Results obtained for scenario II (maximum surface area of 45 km^2), calculated for 25 years, through the Monte Carlo simulation are displayed in Figure 20.

Similarly, results for this second scenario shows that the most likely value of the power production capacity is 214 MW$_e$ for a plant life of 25 years. Also, the estimated power production will be in the range of 125-394 MW$_e$ (80% acceptance range, Figure 20a) and the cumulative frequency shows that the resource capacity will be at least 125 MW$_e$ (with 90 % probability, Figure 20b).

Finally, Table 5 summarizes the simulation results for scenarios I and II. As was expected, scenario I is more conservative than scenario II. The difference between the two scenarios lies in the estimated surface area. The first considers only the Sol de Mañana field but the second considers the Apacheta field as well, but the results of the geophysical exploration indicate that the resource might be extended to that area.

TABLE 5: Monte Carlo simulation results

Most likely parameters	**Scenario I**		**Scenario II**	
	25 years	**50 years**	**25 years**	**50 years**
Electric power (MW$_e$)	75	38	214	107
Monte Carlo simulation results				
90% above (P10 MW$_e$)	57	28	125	62
90% below (P90 MW$_e$)	124	64	394	196

6. CONCLUSIONS AND RECOMMENDATIONS

The main conclusions of the project are as follows:

- The review of the all available data on the Sol de Mañana geothermal field has revealed the relevance and quality of the data in order to evaluate and suggest further studies on the field.

- The general geological setting of the Sol de Mañana geothermal field is well defined, as is the structural geology, heat source and the local stratigraphy.
- Geophysical data along with temperature and pressure logs were used to outline the size of the geothermal area, giving two possible scenarios for the surface extension of the area of 5-13 km^2.
- The temperature logs indicate a reservoir temperature of about 250°C and over 1000 m thickness of the reservoir.
- The characteristic curves for the wells show similar characteristics in wells SM-01 and SM-02 (two-phase inflow) that are different from wells SM-05 and SM-03 (liquid-phase inflow).
- The high injectivity index in wells SM-01 and SM-02 indicates that these wells intersect highly permeable zones that correlate with geological structure in the area.
- The interference test shows less connection between wells SM-02 and SM-03 than wells SM-02 and SM-01.
- The review of conceptual models that exist for the area helped getting the reservoir parameters in order to use them for the resource assessment.
- The resource assessment using the volumetric method with the exploration data and well logs have allowed to obtain the most likely potential of 75 MW_e for 25 years for the Sol de Mañana geothermal field.

The main recommendations for this project are as follows:

- To continue with the analysis of relevant information in order to improve and update the conceptual model and continue with the resource assessment using numerical methods.
- To expand the geophysical survey to confirm the anomalies identified in the exploration stage, in order to define the reservoir limits in the Apacheta field.
- To work on a well testing plan in order to obtain better quality data in the following project stages.
- To calibrate equipment for next well tests.
- In order to outline the reservoir extension, it is necessary to expand the drilling area, especially southwest of the Sol de Mañana field.

ACKNOWLEDGEMENTS

I want to extend my sincere gratitude to the Government of Iceland and specially the United Nations University Geothermal Training Programme (UNU-GTP) for giving me the opportunity to take part in the six months training. My profound gratitude goes to Mr. Lúdvik S. Georgsson and Mr. Ingimar Gudni Haraldsson for giving me the opportunity and support in this training. I also thank very much Mr. Markús A.G. Wilde, Ms. Thórhildur Ísberg and Ms. Málfrídur Ómarsdóttir for their help and guidance during these six months and for making me feel welcome in Iceland.

Sincere thanks to my supervisors, Ms. Helga Tulinius and Ms. Saeunn Halldórsdóttir from ÍSOR – Iceland GeoSurvey for being excellent guides in the development of this final project. Also I wish to give my thanks to all presenters in the introductory course for sharing their knowledge and experience.

Thanks so much to all UNU-GTP Fellows for their support during this time and for this great experience in Iceland.

Thanks to all my family. And finally, I want to thank God for giving me strength and knowledge to be able to finish my final project.

REFERENCES

Abdollahzadeh Bina, F., 2009: Geothermal resource assessment of the NW-Sabalan field, Iran, through well testing. Report 6 in: *Geothermal training in Iceland 2009*. UNU-GTP, Iceland, 15-44.

Afeworki, O.M., 2010: Analysis of temperature and pressure characteristics of the Hverahlíd geothermal field in the Hengill geothermal system, SW-Iceland. Report 6 in: *Geothermal training in Iceland 2010*. UNU-GTP, Iceland, 1-28.

Axelsson, G., and Steingrímsson, B., 2012: Logging, testing and monitoring geothermal wells. *Presented at "Short Course on Geothermal Development and Geothermal Wells", organized by UNU-GTP and LaGeo, Santa Tecla, El Salvador*, 20 pp.

Axelsson, G., 2013: Geothermal well testing. *Presented at "Short Course V on Conceptual Modelling of Geothermal Systems", organized by UNU-GTP and LaGeo, Santa Tecla, El Salvador*, 30 pp.

Bödvarsson, G.S., 1974: Geothermal resources energetics. *Geothermics, 3*, 83-92.

CFE, 1997: *Potential certification of Sol de Mañana geothermal field*. Comisión Federal de Electricidad (CFE), internal report submitted to ENDE (in Spanish), 225 pp.

ENDE, 1986: *Geothermal feasibility study in Laguna Colorada area, geoscientists surface studies.* Empresa Nacional de Electricidad (ENDE), Cochabamba, Bolivia, internal report (in Spanish), 98 pp.

ENDE, 1994a: *Laguna Colorada geothermal project, expansion of geothermal drilling, well SM-04 deepening*. Empresa Nacional de Electricidad (ENDE), Cochabamba, Bolivia, internal report (in Spanish), 35 pp.

ENDE, 1994b: *Laguna Colorada geothermal project, expansion of geothermal drilling, well SM-05 report.* Empresa Nacional de Electricidad (ENDE), Cochabamba, Bolivia, internal report (in Spanish), 58 pp.

ENEL, 1989a: *Geothermal feasibility study in Laguna Colorada area, SM-01 well report.* ENEL, internal report submitted to ENDE (in Spanish), 111 pp.

ENEL, 1989b: *Geothermal feasibility study in Laguna Colorada area, SM-02 well report.* ENEL, internal report submitted to ENDE (in Spanish), 179 pp.

ENEL, 1989c: *Geothermal feasibility study in Laguna Colorada area, SM-01 and SM-02 well testing report.* ENEL, internal report submitted to ENDE (in Spanish), 108 pp.

ENEL, 1990: *Geothermal feasibility study in Laguna Colorada area, SM-03 well report.* ENEL, internal report submitted to ENDE (in Spanish), 163 pp.

ENEL, 1991: *Geothermal feasibility study in Laguna Colorada area, feasibility final report.* ENEL, internal report submitted to ENDE (in Spanish), 395 pp.

GEOBOL, 1976: *Geothermal resource evaluation for Bolivia.* Servicio Geológico de Bolivia (GEOBOL), internal report submitted to ENDE (in Spanish), 78 pp.

Grant, M.A., and Bixley, P.F., 2011: *Geothermal reservoir engineering* (2nd ed.). Academic Press, 359 pp.

Horne, R.N., 1995: *Modern well test analysis, a computer-aided approach* (2nd ed.). Petroway Inc., Palo Alto, CA, United States, 257 pp.

JETRO, 2008: S*tudy of feasibility for construction of the Laguna Colorada geothermal plant Potosi, Bolivia.* Japan External Trade Organization (JETRO), internal report submitted to ENDE (in Spanish), 269 pp.

JICA, 2013: *Project preparation for the Project Construction of Laguna Colorada geothermal plant*. Japan International Cooperation Agency (JICA), internal report submitted to ENDE (in Spanish), 185 pp.

Leaver, J.D., 1986: *A technical review of interference testing with application in the Ohaaki geothermal field*. Stanford University, Stanford, CA, United States, report SGP-TR-95, 184 pp.

Muffler, L.P.J. (editor), 1979: *Assessment of geothermal resources of the United States - 1978*. USGS Circular 790, Arlington, VA, United States, 163 pp.

Nathenson, M., 1975: *Physical factors determining the fraction of stored heat recoverable from hydrothermal convection systems and conduction dominated areas*. U.S. Geological Survey, Menlo Park, CA, United States, open-file report 75-525, 51 pp.

Ramos, P., 2014: *Updating the conceptual model and resource assessment - Laguna Colorada Geothermal Project*. Programa Regional de Entrenamiento Geotermico (PREG), University of El Salvador, San Salvador, El Salvador, final report (in Spanish), 39 pp.

Sanyal, S.K., and Sarmiento, Z.F., 2005: Booking geothermal energy reserves. *Geothermal Resources Council Transactions, 29*, 467-474.

Sarmiento, Z.F., and Björnsson, G., 2007: Geothermal resource assessment – volumetric reserves estimation and numerical modelling. *Presented at "Short Course on Geothermal Development in Central America – Resource Assessment and Environmental Management", organized by UNU-GTP and LaGeo, Santa Tecla, El Salvador*, 13 pp.

Sarmiento, Z.F., 2011: Application of well testing in assessing geothermal resources. *Presented at "Short Course on Geothermal Drilling, Resource Development and Power Plants", organized by UNU-GTP and LaGeo, Santa Tecla, El Salvador*, 13 pp.

Sarmiento, Z.F., Steingrímsson, B., and Axelsson, G., 2013: Volumetric resource assessment. *Presented at "Short Course V on Conceptual Modelling of Geothermal Systems", organized by UNU-GTP and LaGeo, Santa Tecla, El Salvador*, 15 pp.

Steingrímsson, B., 2013: Geothermal well logging: temperature and pressure logs. *Presented at "Short Course V on Conceptual Modelling of Geothermal Systems", organized by UNU-GTP and LaGeo, Santa Tecla, El Salvador*, 16 pp.

Villarroel, D., 2014: Geochemical studies of geothermal fluid and evaluation of well test results from wells SM-01, SM-02 and SM-03, Sol de Mañana field, geothermal project, Laguna Colorada, Bolivia. Report 32 in: *Geothermal training in Iceland 2014*. UNU-GTP, Iceland, 697-720.

UNITED NATIONS UNIVERSITY
UNU-GTP
Geothermal Training Programme

Orkustofnun, Grensasvegur 9,
IS-108 Reykjavik, Iceland

Reports 2015
Number 31

A STUDY ON OPERATION AND MAINTENANCE OF FLASH STEAM GEOTHERMAL POWER PLANTS: REYKJANES POWER PLANT

Fardaneh Ravazdezh
Renewable Energy Organization of Iran
Dademan Blvd., Shahrak-e Ghods
P.O.Box 1468611387, Tehran
IRAN
fardaneh.ravazdezh@gmail.com

ABSTRACT

For a geothermal power plant to operate prosperously, series of activities starting from optimum design and installation to efficient monitoring of operation and maintenance (O&M) should be carried out precisely. Experience acquired during real O&M of a geothermal power plant gives a practical insight into observing the quality of material and equipment, optimal repair and replacement, troublemaking factors affecting the power plant's performance and management of failure incidents by utilizing suitable devices.

In this report operation and maintenance procedures of Reykjanes power plant in SW-Iceland is analysed. Most maintenance practice done in this power plant is preventive maintenance done on basis of routine and annual outage period maintenance. Efficient planning of outage minimizes tasks and time needed for scheduled and forced activities and consequently maximizes the reliability and availability of the power plant. The O&M team running both Svartsengi and Reykjanes power plants have gained valuable know-how to maintain reliability, availability, maintainability, and other critical performance factors at a satisfactory level so that electricity productivity and economic profitability of the power plants are guaranteed.

This study presents common problems occurring in the running of a geothermal power plant and their solutions, as well as analysis of outage period including required actions for each component of the power plant, manpower and cost breakdowns.

1. INTRODUCTION

It is a fact that geothermal energy plays a significant role in the Icelandic energy sector, generating 68% of the primary energy and 29% of the total electricity in the country. The first geothermal power plant started operation in 1969 and since then seven power plants with a total capacity of 663 MWe have been installed and operated, making Iceland one of the leaders in the geothermal sector (Ragnarsson, 2015). Developing a geothermal power plant and producing electricity is costly. For a power plant to be prosperous in a competitive energy market, innovatory steps should be adopted. The best way to lower

the costs is to reduce the amount of losses in the process of generating energy in the power plant, i.e. electricity, which is achieved by boosting reliability and availability of the power plant through optimal O&M procedures.

The development of a trustworthy O&M plan relies on optimizing the methods and practices based on specific characteristics and requirement of the operating geothermal power plant.

The term maintenance refers to any activities carried out on an asset in order to ensure continuous performance of its intended functions, repairing any equipment that has failed, to keep the equipment running or to restore it to a favourable condition (Kachru, 2007). There are different methods how maintenance tasks can be planned and scheduled. These methods have been categorized in various manners according to different sources. However, main procedures are classified as *Corrective Maintenance* (also referred to as reactive) that aims to take corrective action when a failure occurs, *Preventive Maintenance* that includes activities to avoid failures based on a specific time-based routine, *Predictive Maintenance* that in some studies is considered as an independent type while in others has been seen as a subcategory of Preventive Maintenance using techniques to predict failures and problems based on equipment condition, and lastly *Reliability Centred Maintenance* (Proactive view) which allocates priorities to components and focuses on mitigating the need for maintenance (root-cause finding) (see Sullivan et al., 2010; Kahn, 2006).

Emphasis on allocating financial and human resources in O&M has been drastically increased in power plants by growing awareness on its importance. For example, in most geothermal power plants over a quarter of the total workforce in the process industry is dedicated to maintenance work (Adale, 2009). However, not many studies have been carried out regarding O&M of geothermal power plants. Studies in this field could accumulate unrecorded experience of Icelandic geothermal operators and maintenance experts to assist new generation of operators predicting probable failure modes and reduce or stop potential troubles and damages which might occur during the design and various operation stages.

Methodology of this study was to collect secondary data from related reports and papers, documents from the Dynamic Maintenance Management (DMM) used at the Reykjanes power plant, SW-Iceland, as well as conduct interviews with power plant managers and make several visits during the annual outage activities, recording procedures. The operation of the major equipment and maintenance undertaken in Reykjanes flash steam power plant is reviewed as a case study. Furthermore, analysis of operation indexes is carried out. Major problems that the equipment may encounter as well as the effective maintenance processes to prevent or correct those problems are investigated. Finally, all activities in an annual outage maintenance period are recorded and categorized. An analysis of actions, manpower and cost breakdowns are presented. The data of the Icelandic geothermal power plant gathered in this study can be used to improve the O&M procedures in other geothermal power plant all around the world.

2. BASIC GEOTHERMAL CYCLE

Geothermal systems can be grouped into several categories. The main source of geothermal energy production are hydrothermal systems that are driven by natural flow of hot water. Other systems include enhanced geothermal systems (EGS) and hot, dry rock (HDR) (DiPippo, 2008).

Geothermal power conversion systems are typically divided into three basic systems:

- Flashed steam/dry steam condensing systems in which resource temperature range from about 320 to 230°C.
- Flashed steam back pressure systems in which resource temperature range from about 320 to 200°C.
- Binary or twin-fluid systems (based on the Kalina or the Organic Rankine cycle) in which resource temperature range between 190 and about 120°C or less.

In addition to three basic power conversion systems mentioned above, so-called hybrid systems are in use which are in fact a combined system comprising two or more of the above basic types in series and/or in parallel (Elíasson, et al., 2011).

2.1 Geothermal power plants worldwide

In 2014, 612 power plants worldwide with a capacity of 12.8 gigawatt (GWe) produced 74 terawatt-hours (TWh) electricity (Bertani, 2015). At the end of 2014, top 5 countries with the largest amounts of geothermal electric generating capacity were the United States (3.5 GW), the Philippines (1.9 GW), Indonesia (1.4 GW), Mexico (1.0 GW), and New Zealand (1.0 GW). The majority of installed capacity (7.8 GW) and 63% of the global geothermal generation is represented by 237 flash steam plants. The main geothermal field/plant operators in 2014 were US-based Chevron and Calpine (1.3 GW each), followed by EDC of the Philippines (1.2 GW), the Mexican state utility CFE, Italy's Enel Green Power (1 GW each), and the US-based Ormat (0.9 GW) (Bertani 2015).

Capital cost of a typical condensing flash geothermal power plant with 1–100 MW size and capacity factor of 60–90% has been estimated to be 1900-3800 USD/KW (Ren21, 2015). In Figure 1, the percentage of each type of geothermal power plant in electricity production is shown.

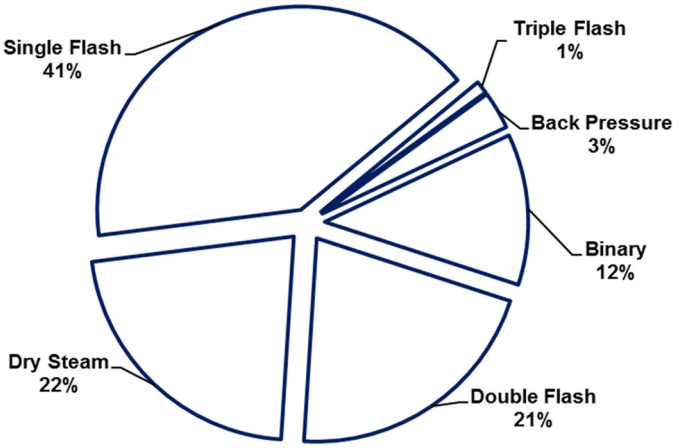

FIGURE 1: Share of each type of geothermal power plants in global electricity production

2.2 Geothermal flash steam power plants

DiPippo (2008) defines single-flash power plants as power plants that utilize the flow of steam between two pressure levels to generate electricity by rotating a turbine. The term flash refers to the pressurized liquid that is flashed into a steam and liquid mixture by reducing the pressure of the liquid below the saturation pressure of water for a given temperature. In double flash cycle, the design differs in a way that a flasher has been added resulting in a low pressure steam line to the turbine, in addition to the high pressure line from the separator.

Flashing can occur in the reservoir, in the production well, in the gathering pipes leading to a steam separator or at the separator inlet. With extended exploitation of the reservoir over the power plants lifetime, reservoir pressure drops, causing the flashing to "move back" and occur in the production well or the reservoir itself. To maintain reservoir pressure, re-injection of fluid into the reservoir is common.

2.3 General description of Reykjanes power plant

Geologically, Reykjanes geothermal area is the landward extension of the mid-Atlantic spreading ridge. There is a history of episodic hot spring activities from early times (Fridriksson et al., 2010). The geological succession depicts a steady build-up of volcanic strata within a submarine environment (Franzson, 2004). Exploration of the area started in 1956 when the first well was drilled. The field was investigated extensively in the years 1968-1970 when 7 exploration wells were drilled (Gudmundsson and Hauksson, 1981).

FIGURE 2: Svartsengi power plant

Reykjanes power plant (Figure 2) is located 55 km away from Reykjavik city at the southwest tip of the Reykjanes peninsula. The geothermal area is one of the hottest in use for power production in Iceland, with downhole temperatures reaching up to 320°C. The geothermal fluid in the Reykjanes reservoir is a 32,000 ppm of total dissolved solids (TDS) (Thórólfsson, 2005). Drilling for power production commenced in 1998. Until today 34 wells have been drilled in total and 18 of them are contributing to steam provision with an average temperature of 290°C down the wells.

This single-flash condensing type geothermal power plant was commissioned in 2006 with a total capacity of 100 MW and with approximately 96 MW net electrical output to the grid. Design of the power plant has two major unique features; one is having one of the highest turbine inlet steam pressure in the world (18 bar) in order to impede the silica scaling in exposed components. Another specific feature of the plant is the use seawater for cooling excluding cooling towers.

Both Reykjanes and Svartsengi power plant are run by HS Orka, hf. This is a privately owned company who has developed geothermal and other renewable energy applications since 1975. This company is responsible for the production and sale of electricity and heat in the Reykjanes Peninsula area. Future plans for developing the power plant include adding 30-80 MWe to the capacity in two phases, a 50 MW double flow condensing unit and a 30 MW low pressure turbine.

3. OPERATION AND MAINTENANCE

In general terms, operation and maintenance are the decisions and actions taken regarding the control and upkeep of property and equipment. These are inclusive but not limited to the following:

1) Actions focused on scheduling, procedures, and work/systems control and optimization; and
2) Performance of routine, preventive, predictive, scheduled and unscheduled actions aimed at preventing equipment failure or decline with the goal of increasing efficiency, reliability, and safety (Sullivan et al., 2010).

Focusing on the operation aspect, the performance status of any kind of power plant and working equipment in their cycle of electricity production can be evaluated by inspecting current states of key parameters such as separator inlet pressure, turbine inlet pressure, steam flowrate, non-condensable gas content and others in a geothermal power plant. By means of using various instruments, compiling all detailed performance recorded in control systems and precisely analysing the gathered data, operators can determine the power plant functionality.

Today, almost all geothermal plants are using the SCADA (Supervision, Control and Data Acquisition) system for plant operation control. The following parameters are vital for plant operation (Woodworth, 1988):

a) *Operator training:* The operation personnel should understand the operating system. Especially if modern power plants are remotely controlled, the ability and knowledge of the operators determine the smooth operation of the machinery.
b) *Technology*: Nowadays a plant can be controlled and operated remotely with a few well-trained personnel using a SCADA system. The plant should update its equipment on a regular basis to the latest technology for better production.

c) *Operation manual:* A manual is a guidebook for an operator. It gives full information and necessary steps about the operating and control systems of the plant including start-up, normal operation, shut-down and emergency procedures.

To investigate a flash steam geothermal power plant operation performance, it is necessary to recognize basic elements of the cycle.

3.1 Basic equipment of a geothermal flash steam power plant

3.1.1 Steam production, collection and transmission

High-temperature wells, wellhead valves, controls and piping system are key elements to provide steam for the power plant. Pipelines transport the fluids that will be used to generate electricity and convey the waste fluids to their destinations. The main factors involved in pipeline design are pressure drop due to flow in the pipeline, heat losses to the environment as well as structural strength of the pipeline systems (Pálsson, 2010).

3.1.2 Separator

A steam separator, either vertical or horizontal installed depending on design specification or owners´ experience of the power plant, is a device used to separate water from steam in a two-phase flow so that only steam is sent to run the turbine.

The earliest method to separate steam and water is passing the mixture into a large drum, called a *knock out drum*. Flashing occurs due to the drop in the fluid pressure and the less dense steam will rise up while the denser water will fall down to the bottom of the drum.

Currently, the *cyclone separator* is the most popular design. Separation process is carried out by generating centrifugal force on the mixture entering the separator by using a tangential or spiral inlet to the cyclone. As the fluid rotates, the liquid with higher density will move outward and downwards while the steam which has lower density will move inward and upward. Finally, a stream of steam flows through turbine and water stream (brine) will be utilized or disposed in later steps (Zarrouk and Purnanto, 2015).

3.1.3 Steam turbine and auxiliaries

Steam turbines are turbo-machines that transform the thermal energy of steam into mechanical energy. In the first step the thermal energy of the steam is converted into kinetic energy by letting the steam expand, and secondly by momentum exchange to transform the kinetic energy into mechanical energy, through turning of the turbine wheels.

The basic components of a steam turbine are rotor blades, stator blades (nozzles), diaphragms, seals, bearings and casing. Bearings support the moving part of the turbine, i.e. rotor and seals are used to prevent leakage of the turbine. Stator blades are located on diaphragms which transform thermal energy of the steam into kinetic energy. The rotor supports the moving blades that convert the kinetic energy to mechanical energy. The casing holds the diaphragms, seals the rotor and protects the whole turbine from the environment.

There are two different types of steam turbines, so-called *Impulse* and *Reaction* turbines. In Impulse turbines pressure drop occurs only across the stator blades and not through the rotor blades whereas in reaction turbines, pressure drop is divided between both stator and rotor blades.

Moreover, steam turbines can be categorized as *Condensing* and *Back-pressure* turbines. In condensing turbines, a condenser is used to create a vacuum in the outlet of the turbine, steam expands until pressure drops to values lower than the atmospheric pressure. Back-pressure turbines, on the other hand, let the steam down to atmospheric pressure or higher. This allows to release steam directly to the atmosphere (Gunnarsson, 2013).

3.1.4 Gas extraction system

In geothermal steam there are always traces of non-condensable gases (NCG). The amount is usually in the range of 0-3% of the separated steam flow. Since the gas is non-condensable it must be removed out of the condensers, otherwise it will simply build up there, blocking the heat exchange between the cooling water and the steam. The purpose of the gas extraction system is to collect the NCG from the condenser and release to an exhaust at atmospheric pressures. Steam ejectors and liquid ring vacuum pumps are the most common types of equipment used in gas extraction systems though their selection depends mostly on the gas content in the steam (Teke, 2011).

3.1.5 Condenser

After flowing through the turbine, the steam continues its pathway to the condenser. One of the functions of the condenser is to reduce the pressure at the turbine outlet and thus extract more energy from the steam flowing from the turbine. In order to create water circulation from the condenser and reduce the pressure, pumps are used which are equipment of major electrical internal consumption. There are 2 types of condensers available: *Surface condenser systems* in which vapour condenses on coolant pipes and *direct-contact condensers* which mix cooling water with the utilized steam in an open chamber (NREL, 2010).

3.1.6 Cooling system

A cooling water system is composed of the cooling tower, the main circulation water pumps, the cooling pumps and the system of auxiliary pumps.

Cooling systems can be: 1. *Once-through* systems that take water from nearby sources (e.g., rivers, lakes, aquifers or the ocean), circulate it through pipes to absorb heat from the steam in the condensers and discharge the now warmer water to the local sources or 2. *Wet-recirculating (closed-loop)* systems that reuse cooling water in a second cycle rather than immediately discharging it back to the original water source or 3. *Dry-cooling* systems that use air instead of water to cool the steam exiting the turbine. A cooling tower is a specialized heat exchanger in which two fluids (air and water) are brought into direct contact with each other to accelerate the heat transfer.

There are two basic types of cooling towers, *Direct (open)* and *Indirect (closed)*. Direct (open) cooling tower exposes the cooling water directly to the atmosphere whereas Indirect (closed) cooling tower circulates the water through tubes located in the tower with no contact to the atmosphere (Sullivan et al., 2010, Union of Concerned Scientists, 2015).

3.1.7 Silencer

The main purpose of silencers is the reduction of noise level in the environment. Silencers are comprised of a chamber for receiving the spent fluid in the power plant and a lower outlet for the brine flows. The chamber has an upper outlet to release the geothermal vapour (Thórólfsson, 2010).

3.1.8 Electrical system

The electrical system is a complex unit of the power plant consisting of generator, transformer, transmission line, circuit breakers, switchgear/substation, instrumentation system, protection system, and control system (Kebede, 2002).

Generator & transformer
The generator of a geothermal power plant converts mechanical energy to electrical energy, comprising a stationary part: stator windings, as well as the moving part: the rotor with its field winding and excitation system and the prime mover with its associated auxiliaries. Step-up transformers are utilized to bring the low voltage level generated in the generator to the voltage level of the transmission lines.

Control system
To make sure the power plant is operating at optimum performance, the control system collects signals from connected units, analyses them and makes them transparent by visualization systems such as state-of-the-art SCADA systems either on site or in the control room.

The control system configuration of a modern power plant is based on advanced electronics. Some key components are the SCADA system, computers, modem, transmitter, receiver, programmable controllers etc. which are interconnected by fiber optic cables. In addition to the plant system, other systems such as the, fire protection, compressors, etc. can be integrated into the control system (Magnússon and Gunnarsson, 1989). Figure 3 shows one of the SCADA screens of Reykjanes power plant.

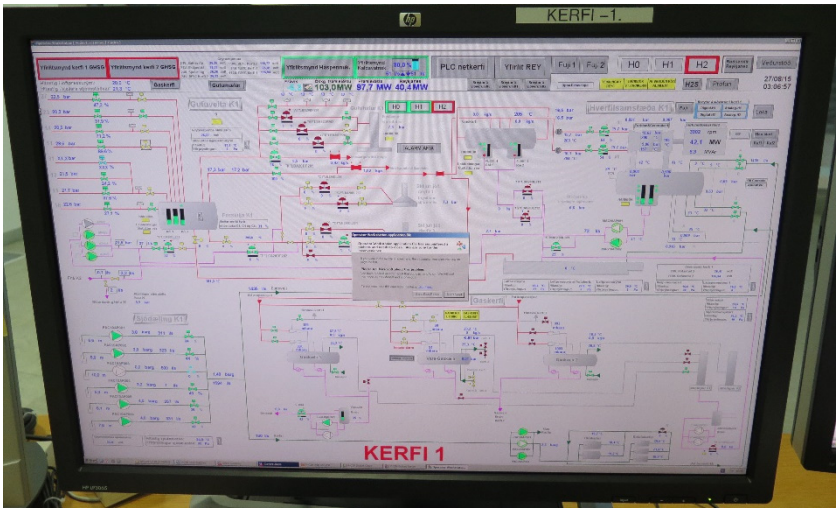

FIGURE 3: A SCADA screen in Reykjanes power plant

The most controlled parameters encountered in the flash steam cycle are flow, level and pressure. Level is measured as a distance or as a difference in pressure by the transmitter and the output of the controller is a position command to the control valve, the final acting element (Avilés, 2011).

Protection system
The protection system of a geothermal power plant ensures that all mechanical and electrical parts of the system are working flawlessly. It is designed to minimize damages due to any fault or error in the performance of the power plant. Electrical protection equipment reduces the consequences of electrical failures and plant damages. Based on the type of equipment and its importance, different types of protection relays can be used. Relays are designed to carry the fault current without damage and withstand the voltage without damage to the insulation. Nowadays, microprocessors based protection relays are becoming popular. A microprocessor-based relay also provides back-up protection. Hence it is more reliable, accurate and fast responding (Kebede, 2002).

Safety devices which trigger the stoppage of parts of the installation or modify the operating regime according to abnormalities in certain parameters are among others:

- Automatic valves at wellheads for closure in case of sudden pressure loss;
- Safety valves on the geothermal circuit to limit the effect of an unexpected pressure increase;
- Circuit breaker in case of an electrical fault in a pump.

Other equipment partly protecting the geothermal loop are settlers and filters removing solid particles.

3.1.9 Reinjection system

Initially, the purpose of re-injection had been simply to dispose the low temperature water from the power plant after the energy extraction by returning some or all of it back into the geothermal system. This process also provides additional recharge which increases the production capacity, lowers the impact on the environment, reduces pressure decline due to mass extraction, enhances thermal extraction from reservoir rocks, offsets surface subsidence etc. The reinjection system usually includes water collection pipelines, injection pumps, injection pipelines, injection wells and a control system (Axelsson, 2008). Figure 4 illustrates a typical configuration of a single-flash geothermal power plant (Moon and Zarrouk, 2012).

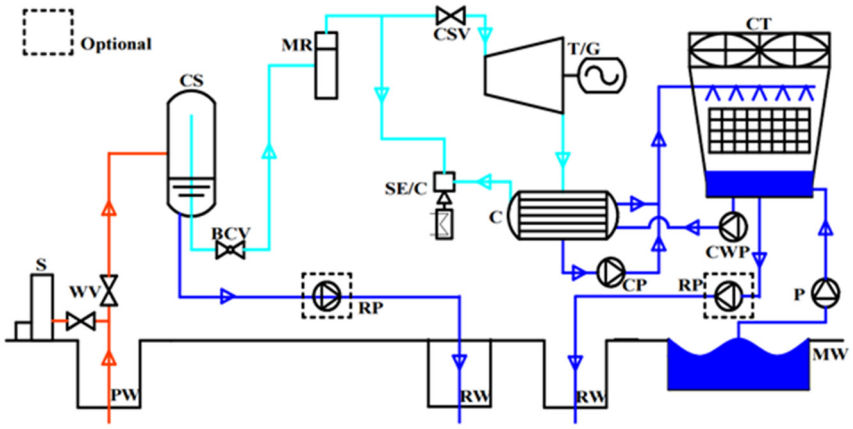

PW	Production well	**WV**	Wellhead valve	**S**	Silencer
CS	Cyclone separator	**BCV**	Ball check valve	**MR**	Moisture remover
CSV	Control / stop valve	**T/G**	Turbine / generator	**SE/C**	Steam ejector/condenser
C	condenser	**CT**	Cooling tower	**CWP**	Cooling water pump
CP	Condensate pump	**RP**	Reinjection pump	**RW**	Reinjection well
P	Pump	**MW**	Make-up water		

FIGURE 4: Typical configuration of single-flash geothermal cycle (Moon and Zarrouk, 2012)

3.2 Operation of the Reykjanes power plant

Reykjanes power plant generates electricity during the whole year except for annual outage maintenance (one week for each 50 MW unit) and during 0 to 10 hour stops due to failures. Thus, with 100 MW of nominal capacity, an average of 815 GWh of electricity is produced annually. Electricity demand is not variable or seasonal due to a base-load contract with the aluminium smelter industry.

The local weather is characterised by high humidity, rain and salinity from the ocean. Three types of fluids are available in this power plant, high temperature geothermal fluid, seawater and fresh water. Originally, the fresh water supply was intended for a cooling tower which was never installed. It is now used for fresh water supply of the power plant facilities.

As shown in Figure 5 electricity production is subject to strong fluctuations in the past 5 years which are a result of major overhauls of unit 1 in 2011 and for 5 weeks in unit 2 in 2012. There was also a decrease in power of the geothermal wells during 2013 and 2014. In 2010, the production was maximal.

Two single-flash steam condensing units of 50 MW are working independently with one separator, one moisture separator, and one condenser each. Flashing process usually happens inside the production wells below 1000 m depth. Two-phase geothermal fluid (steam and mineral-rich brine) with 22-40 bar wellhead pressure and average temperature of 290°C is gathered and directed by 6000 m pipelines toward two horizontal separators (Figure 6) with inlet pressure of around 18 bar, 210°C and 25% steam quality. Density difference and gravity lead the steam and brine into different chambers in the separator.

Steam flows from the separator station to the moisture separator station located 1200 m away. Pipes which transport the steam from the separator to the moisture eliminator perform the role of a second separator. Pressure drop along the way to the turbine unit is around 1 bar. Fine droplets of water that might have formed in the pipelines are removed when the steam passes through the moisture separator. The saturated steam (18 bar and 207-208°C) is expanded and runs with a flowrate of 80.3 kg/s into each of the two double flow, top exhaust reaction turbines.

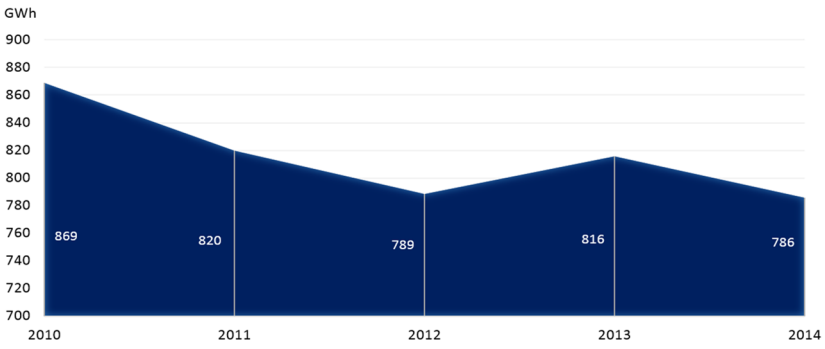

FIGURE 5: Annual electricity production trend in Reykjanes power plant

FIGURE 6: Horizontal separators the power plant

The steam enthalpy at the turbine inlet is about 2,800 kJ/kg and steam passes through the 14 stages of the turbine and leaves it with a pressure of 0.1 bar and 42°C. This significant expansion is accompanied by a decline in enthalpy of about 627 kJ/kg and hence this energy is transformed into shaft work by the rotating turbine blades which move with a speed of 3000 rpm. The turbine efficiency has been calculated to be about 80%. At the turbine exhaust, the steam enthalpy is found to be around 2.170 kJ/kg and wetness is about 18%. Rotor and stationary blades are made from alloy Steels and the outer casing is made of welded Carbon Steel plates.

The turbines are directly coupled to the 3-phase horizontal cylindrical revolving field synchronous Fuji generators with a brushless exciter (62.5 MVA) and totally enclosed water-air-cooled (TEWAC). Air is recirculated into the TEWAC machine by air to water heat exchangers. It generates 16.5 kV voltage with a power factor of 0.8. Output voltage is increased by step-up transformers in substation inside the power plant with switchgears (circuit breakers) to connect it to grid (16.5 to 132/230 kV).

A surface condenser is connected to the exit of each of the turbines and 1600 l/s of cold seawater is pumped into the condenser coming from 4 boreholes of 50-60 m depth. Lava layers are used as natural filters to purify the cold sea. The more vacuum pressure in the condenser the more efficient is the turbine. Eventually the condensate leaves the unit toward a mixing vessel with a remaining temperature of 38°C. Seawater used for cooling, condensate and most part of the brine from the separator are collected in the mixing vessel to be released into the ocean. The mixed fluid in the mixing vessel has a flow rate of 1900 l/s, atmospheric pressure and a temperature of 55-60°C. Auxiliary coolers of the turbine-generator are also cooled by seawater. The heat-exchangers tubes are all made of titanium.

On the other side of the condenser, the NCG is vacuumed to gas ejectors in the gas extraction system which is connected to the outlet of the condenser in order to discharge them to the atmosphere. Pressure of the NCG when leaving the condenser is low and requires 2 stages of steam ejectors (totally 3 steam

FIGURE 7: Silencers of the power plant

ejectors: one ejector for each turbine and one spare) to increase its pressure to 1200 mbar before being vented through the chimney to the atmosphere. After each steam ejectors the steam remaining in the NCG is condensed by a cooling system. Small parts of brine are transported to the silencers shown in Figure 7 and the power plant has the permit to release the brine into the sea.

A part of the brine from separator is mixed with the condensate in order to reduce the brine temperature and dilute it before reinjection to reduce the risk of scaling in the reinjection well.

The level of brine in the separator is controlled. When the level of brine is too high, brine mixes with the steam which is critical for the turbine performance and if the level of brine is too low, steam exists in the brine that causes bubble collapse and eventually a water hammer or a wave shock in the pipelines.

In a normal operation, the valve in the silencer is slightly open and if the level of brine exceeds a specific level this valve will open more and increase the flow of the brine towards the silencers. The power plant flashing brine silencers are large basins with aluminium tops, constructed from concrete with epoxy coated rebar. The aluminium top separates the brine drops from the steam in order to minimize brine carry-over. The brine in the basin boils and the aluminium top is a lid with vent holes. The basins are designed to enable a maximum flow of 300 kg/s.

The reason for not reinjecting all brine is that only one reinjection well exists on the power plant. This well had not been used for reinjection at first but due to its position close to other production wells it became a reinjection well because it could not produce. In a few months 4 new reinjection wells will be on operation which allows the reinjection of more fluid back into reservoir as well as decreasing the risk of pressure drawdown. The new reinjection wells are located 2000 m away from production area and are around 2500 m deep which is about 900 m deeper than the old reinjection well.

A lubrication system is located in the basement adjacent to each of the two units. This system supplies oil to the turbines and generator bearings for lubrication and contains a tank, a pump, a cooler, filters, and accumulators.

The power plant is equipped with centrifugal water and oil pumps which range in size from 270 kW to 1.0 kW. Each unit has three auxiliary cooling water pumps and 3 hot well pumps (only 1 is working). The auxiliary oil pump (AOP) and emergency oil pump supply oil to the turbine bearings and control oil. The AOP supplies oil during unit start-up when the turbine speed is low and during unit shut-down. The emergency oil pump is a DC motor-driven pump used to supply oil during power black-outs.

The power plant has 4 valve houses (A, B, C, and D), two of them (1 for each unit) next to the separation station containing steam control valves. Two other valve houses are next to the silencers containing

valves to control the brine. Steam pressure control valves let the steam be released to the atmosphere if the pressure is above a set point but other regulatory of pressure is controlled by the turbine itself. The most critical valves in the power plant are:

- *Turbine main stop valve (MSV):* is open during normal operation and closed under stop and failure conditions; closes very quickly if it receives trip signal and closes automatically stopping the turbine from over-speed.
- *Main control valve (GV):* is for speed and power control of the turbine. This valve is regulated by the governor of the turbine and power settings intervene if the speed of the turbine is not within the correct range to be synchronized with the grid.
- *Pressure or Vent control valves:* is a steam pressure regulatory valve regulating the exact amount of steam needed by the turbine control valves.

The most significant control equipment used in Reykjanes power plant consists of:

- *In the steam gathering system:* wellhead control valve that opens remotely during the start-ups and lets two- phase fluid from the wells flow through the control valves to the silencers where steam is vented to the atmosphere. Additionally, each well has pressure and flow sensors;
- *In the separator:* a level control sensor that prevents brine from mixing into the steam pipe;
- *In the turbine:* valves MSV and GV which were mentioned earlier are controlling steam flow and load;
- *In the generator:* an automated voltage regulator (AVR) adjusts the voltage, the frequency and the current to operational limits;
- *In the condenser:* condenser basin level control to keep level of condensate in the condenser within a specific range.

In Figure 8 a process flow diagram of the power plant is shown presenting important operating parameters and components.

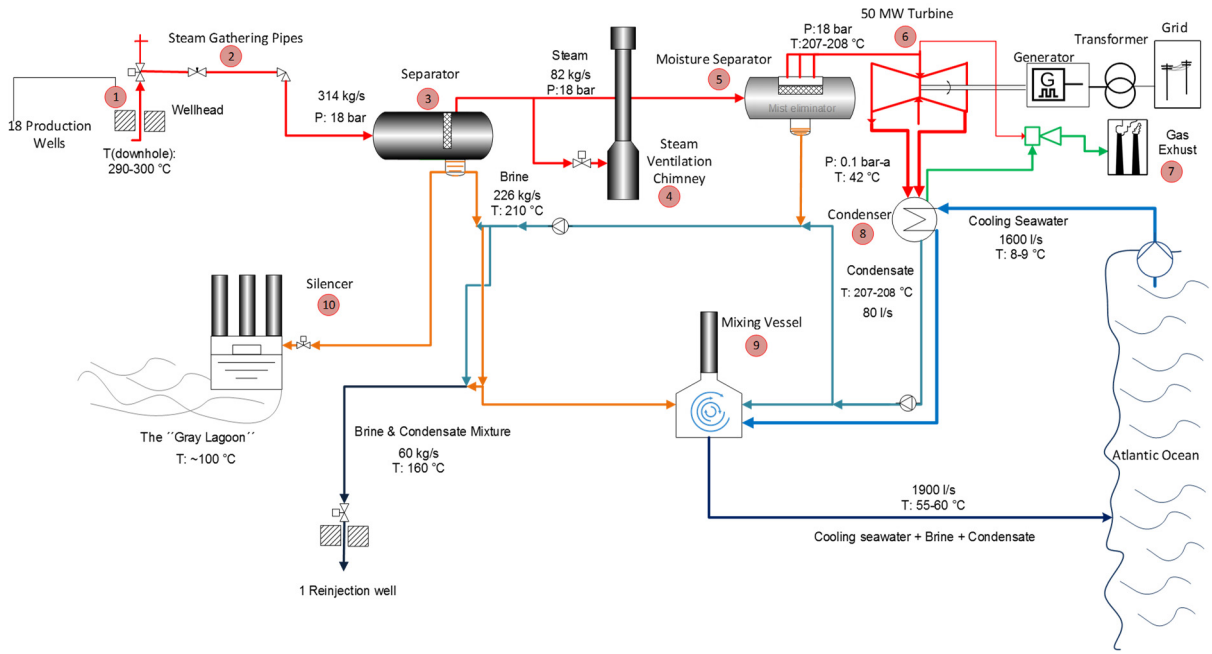

FIGURE 8: Process flow diagram of Reykjanes power plant

Number of major equipment in the Reykjanes power plant is shown in Table 1.

TABLE 1: Total number of components

Total wells	Exploration wells	Production wells	Reinjection wells	Separators	Moisture separators	Turbines	Generators	Transformers	Condensers	Gas ejectors	Cooling towers	Pumps	Motors	Valve houses
34	12	18	4 (new) 1 (old)	2	2	2	2	2 Main 6Auxiliary	2	3	-	~30	~30	4

4. MAINTENANCE PROCESS

According to the Oxford dictionary maintenance is defined as the process of keeping something in good condition. To narrow down the concept, maintenance refers to all actions that should be taken to prevent a device or component from failing or to repair normal equipment degradation experienced with the operation of the device to keep it in proper working order.

In the design life of most equipment, they require periodic maintenance. Belts need adjustment, shaft alignment needs to be maintained, proper lubrication of rotating equipment and replacement of non-functioning elements are required and so on. In addition to waiting for a piece of equipment to fail (corrective maintenance), preventive maintenance, predictive maintenance or reliability-centred maintenance are utilized (Sullivan et al., 2010; Tessema, 2002).

4.1 Maintenance methods and procedures

Maintenance methods have been categorized variously by different studies. In almost all the papers and studies, corrective, preventive and predictive maintenance have been identified. Although in all sources first type of maintenance is referred to as corrective or reactive maintenance, they differ in categorizing preventive and predictive maintenance. Some scholars regard predictive maintenance as a subcategory of preventive maintenance while others see predictive maintenance as an independent category. Nevertheless, the definition of these procedures is almost the same (Sullivan et al., 2010; Adale, 2009; López, 2008; PECI, 1999; Bore, 2008; Márquez, 2007).

4.1.1 Corrective (reactive) maintenance

Maintenance which is classified as corrective is performed only when the equipment or system fails to function. The damaged equipment will then be repaired or replaced.
Corrective action can either be deferred or immediate. Deferred maintenance is delayed for any reason and is assumed to have little impact on system performance, immediate action is executed as soon as a failure has been detected.

At first sight, this method seems the most cost effective because the manpower and their associated costs are minimal especially for new equipment. But in real practice, when equipment fails, labour costs associated with repair will probably be higher than normal because the failure will most likely require more extensive repairs or if it is a critical piece of equipment that needs to be back on-line quickly, maintenance overtime costs will have to paid. Lost revenues due to non-production, safety issues for equipment and for staff caused by failures can be added to pitfalls of this method.

4.1.2 Preventive maintenance

Preventive maintenance, as the name indicates, includes activities for prevention of failures. Inspecting and diagnosing breakdowns before occurrence aiming to preserve and enhance equipment reliability to prolong lifetime of the power plant components closer to design are considered as preventive maintenance. Preventive maintenance activities include equipment checks, partial or complete overhauls at specified periods, oil changes, lubrication and so on. In addition, workers can record equipment deterioration so they know when to replace or repair worn parts before they cause system failure.

Some scholars have divided preventive maintenance to time-based (periodic) and conditioned-based procedures (predictive) maintenance assuming predictive maintenance as a subcategory of preventive procedures. Time-based preventive maintenance refers to procedures done based on calendar intervals, after a specified number of operating cycles or a certain number of operating hours while conditioned-based maintenance consists of programmes measuring equipment condition on a regular basis, track the measurements over time and take proper action when measurements are about to exceed the equipment operating limits.

4.1.3 Predictive maintenance

Seeing predictive maintenance as a main category and third type of maintenance, it is defined as the establishment of a baseline performance data, monitoring performance criteria over a period of time and observing changes in performance so that failure can be predicted. Basically, predictive maintenance differs from preventive maintenance by basing maintenance need on the actual condition of the machine rather than on some schedule (Sullivan, et al., 2010). On the down side, to initially start predictive maintenance is not inexpensive and needs training of in-plant personnel to effectively utilize predictive maintenance technologies. Common predictive technologies are as follow:

Infrared thermography (IR): Process of generating visual images that represent variations in IR radiance of surfaces of objects. The primary value of IR is thermographic inspections of equipment to locate problems so that they can be diagnosed and repaired such as transmission lines or rotating equipment problems. Thermography can be used to define temperature profiles indicative of equipment operational faults or failure.

Oil analysis is used to define three basic machine conditions related to the machine's lubrication or lubrication system. Firstly, it is the condition of the oil, secondly lubrication system condition and finally the machine condition itself (machine wear).

Ultrasonic analysis or ultrasounds are defined as sound waves of a frequency above 20 kHz which are used to detect airborne ultrasound. Most rotating equipment and many fluid system conditions will emit sound patterns in the ultrasonic frequency spectrum. Changes in these ultrasonic wave emissions are reflective of equipment condition such as component wear or leaks.

Vibration analysis used for vibration detection of rotating equipment via sensors to quantify the magnitude of vibration or how rough or smooth the machine is running.
Motor analysis provides all the answers required to properly characterize motor condition electrically or mechanically.

Performance trending maintenance activities by utilizing already provided instrumentation to determine the health/condition of the related component.

In Table 2 Common predictive technology applications in different components of a power plant are been shown (Sullivan et al., 2010)

TABLE 2: Common predictive technology applications

Technologies	Applications	Pumps	Electric Motors	Diesel Generators	Condensers	Heavy Equipment/ Cranes	Circuit Breakers	Valves	Heat Exchangers	Electrical Systems	Transformers	Tanks, Piping
Vibration Monitoring/Analysis		X	X	X		X						
Lubricant, Fuel Analysis		X	X	X		X					X	
Wear Particle Analysis		X	X	X		X						
Bearing, Temperature/Analysis		X	X	X		X						
Performance Monitoring		X	X	X	X				X		X	
Ultrasonic Noise Detection		X	X	X	X			X	X		X	
Ultrasonic Flow		X			X			X	X			
Infrared Thermography		X	X	X	X	X	X	X	X	X	X	
Non-destructive Testing (Thickness)					X				X			X
Visual Inspection		X	X	X	X	X	X	X	X	X	X	X
Insulation Resistance			X	X			X			X	X	
Motor Current Signature Analysis			X									
Motor Circuit Analysis			X				X			X		
Polarization Index			X	X						X		
Electrical Monitoring										X	X	

4.1.4 Reliability centred maintenance (proactive)

Basically, Reliability Centred Maintenance (RCM) methodology deals with some key issues that are not taken into consideration by other maintenance programs allocating priorities to components considering financial and personnel limitations as well as importance of the equipment. It recognizes that equipment design and operation differs and that different equipment will have a higher probability to undergo failures from varying degradation mechanisms. RCM sometimes is seen as an umbrella term of proactive maintenance which aims to emphasize on proper installation and precision rebuild Failed-parts analysis such as Root-cause failure analysis, Reliability engineering, Rebuild certification/verification, Age exploration and Recurrence control to extend machinery life (Chalifoux and Baird, 1999).

Table 3 presents results of a case study comparing costs of different maintenance strategies (Sullivan et al., 2010):

TABLE 3: Case study comparison of four maintenance programs

Maintenance method	**Cost ($/Horsepower/year)**
Reactive maintenance (breakdown or run-to-failure maintenance)	18
Preventive maintenance (time-based maintenance)	13
Predictive maintenance (condition-based maintenance)	9
Reliability centred maintenance (proactive)	6

4.1.5 Optimum maintenance strategy

To decide which of the methods discussed above should be employed by a power plant maintenance team (Figure 9) could be based on criticality/impact and vulnerability/risk analysis. Corrective maintenance should be the strategy of choice only if the risk of failure is very low and if the consequences of failure are fairly mild or where preventive maintenance measures are not available.

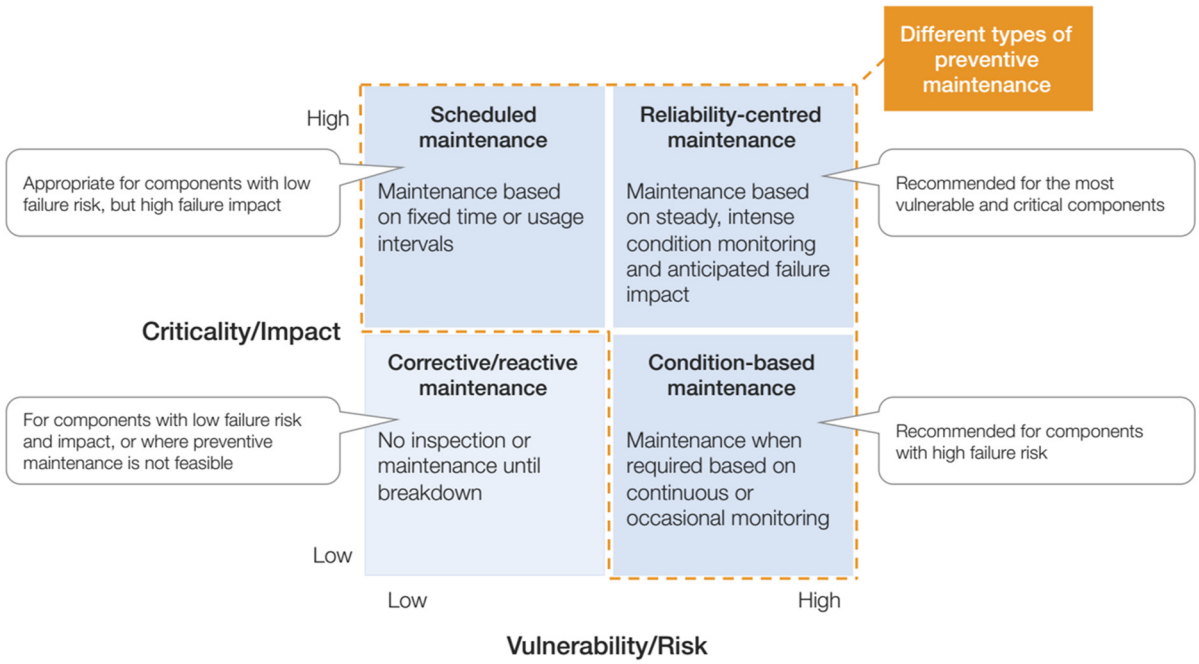

FIGURE 9: Selection of optimum maintenance methods (World Economic Forum, 2014)

Scheduled (time-based) maintenance is the strategy of choice when failures are costly or safety is critical and when the failure rate is fairly low but tends to increase over time.

Condition-based or predictive maintenance is a strategy that triggers maintenance activity when the asset's condition falls below a certain threshold. The aim is to time the maintenance work optimally so that it is not performed more often – and hence more expensively – than necessary and in a way that it can be undertaken at a convenient time when the service will be disrupted the least.

Reliability-centred maintenance considers not only the asset's current condition but also the likely consequences of failure. The main aim of this strategy is to reduce the overall risk and impact of unexpected failures i.e. to ensure high reliability. To put in a nutshell, maintenance methods need to be customized for each asset and correct combination of strategies should be applied for each component of the power plant (World Economic Forum, 2014).

4.2 Overhauls (outages)

Unit overhaul is carried out annually or after every two, four, five etc. years of continuous operation depending on maintenance management of the power plant. This maintenance usually takes some weeks to complete depending on which unit is being maintained. For this type of maintenance, it is necessary to optimize time and costs and to plan all steps in advance including preparing tools, possible spare parts and hiring external personnel to carry out the work if needed, because downtime affects plant operational availability, reliability and eventually prosperity of power plant regarding produced electricity.

4.3 Dynamic maintenance management (DMM)

In order to arrange a maintenance schedule, a maintenance management programme is used to help define coordination, control, planning, implementing and monitoring of the necessary activities required for each component of the plant. For this purpose, CMMS (Computerized Maintenance Management Systems) have been developed to fulfil all maintenance tasks flawlessly. DMM software is one of the CMMS methods that have the following common functions: Machine history, preventive maintenance

schedules, work orders, condition monitoring, condition based flagging, time accounting, fault reports, improved safety, expense tracking, procurements, trending and performance reports (Adale, 2009).

4.4 Geothermal power plant maintenance system

Geothermal power plants can make substantial savings by practising effective maintenance of equipment. Annual O&M cost is estimated to be 1-4% of the capital cost of a typical geothermal power plant with 50 MW capacity.

However, the maintenance process is very case-dependant, considering the nature of the geothermal system in the area, chemical and state properties of fluid, geographical setting such as weather, age of power plant etc.

Most maintenance activities are done in a geothermal power plant targeting and combating scaling in pipelines, cracking in metal parts or pipes, corrosion, erosion and failure in component pipes due to nature of the geothermal fluid result in damage in equipment, plugging in pipes, more pressure drop due to friction and less energy to be converted in the turbines (Elísson, 2013).

4.5 Maintenance of Reykjanes power plant

In this section, maintenance activities carried out for each component in Reykjanes power plant are described. Methods to gather information on operation and maintenance of the Reykjanes power plant in this report have been analysis of secondary data from related reports and papers, documents from the Dynamic Maintenance Management (DMM) of the power plant as well as interviews with power plant staff in addition to visits during the annual outage activities and recording maintenance procedures in one-week outage of one unit of the plant. So all accumulated data were utilized to have a general overview of how the operation and maintenance of Reykjanes power plant is accomplished.

The maintenance team of Reykjanes power plant uses a DMM software since the commission of the power plant. The DMM software is interconnected to SCADA screens to control all procedures. SCADA screens present Process Flow Diagram (PDF) including piping, instrumentation, utility connections and power layout with equipment identification including pumps, valves, ancillary fittings as well as measurements and control of points and loops. Maintenance actions are triggered by equipment condition, run time or a fixed schedule (Tessema, 2002). The DMM software interface consist of following tabs: logbooks, availability of unit, documents (manuals), reports of O&M, equipment with KKS (Kraftwerk Kennzeichen System) for coding all components, work orders, green book (reports on wastes of the plant), Gantt charts and instruments in each of which comprehensive data on operation and maintenance have been embedded.

In Figure 10 recorded work orders in the DMM system of Reykjanes power plant during the year 2014 have been categorized. Table 4 shows performance and cost data on Reykjanes power plant that will be used in the next sections.

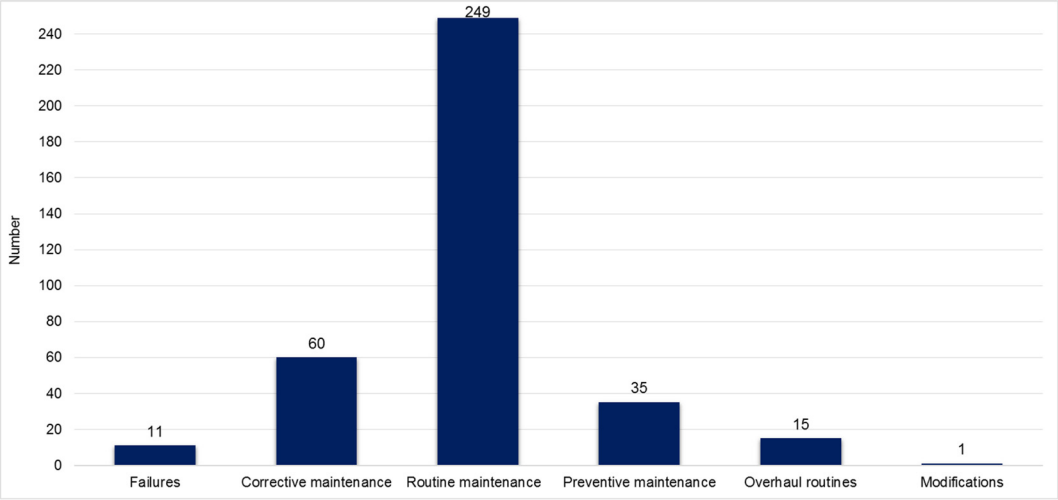

FIGURE 10: Total work orders in DMM system in 2014

TABLE 4: Data gathered of Reykjanes power plant

Total number of stops	15	(time)
Total stop (outage) time (unavailable time)	336	(hours)
Scheduled outage time	224	(hours)
Unscheduled outage time	112	(hours)
Total routine (day) maintenance time (For one unit: 50 MW)	2300	(hours)
Total maintenance overtime (For one unit: 50 MW)	440	(hours)
Net electrical output	96	(MW)
Total electricity generated	786000	(MWh)
Electricity price	3	(ISK/KWh)
Total sold electricity (income)	235.8	(Million ISK)
Total cost of lost production	27	(Million ISK)

4.5.1 Maintenance staff

The O&M team of the power plant consists of 12 (marine) engineers working in shifts at both Svartsengi and Reykjanes power plants. Routine inspections, preventive and predictive maintenance activities are done during the daily maintenance shifts. Work that might involve considerable scheduling effort like overhauling the plants and well workovers is done in cooperation with the in-house team. Some tasks are outsourced to local contractors.

In normal operation time during a month, operators work as dayshift operators in the plant for one week, one week as part of the maintenance team and have one week off.

Three operators who work during the dayshift have different responsibilities. Two of the operators monitor the power plant and investigative protection and safety and the third one is responsible for minor maintenance, lubrication etc. The first two operators stay at Svartsengi power plant at night for emergency maintenance.

4.5.2 Power plant RAM (Reliability, Availability, Maintainability)

It is true that a power plant is a system of interdependent subsystems and that, if one of the subsystems fails, the entire power plant may be at risk of shutting down. Reliability is used to express and quantify

the unplanned maintenance needs of a power plant measuring how often a plant is available in comparison to the total number of hours the plant would be available with no unexpected maintenance. Reliability of an ideal power plant is 100%.

By means of Equation 1 and data presented in Table 4, reliability of the Reykjanes Power plant in 2014 has been calculated to 98.7%.

$$Reliability = \left(1 - \frac{hours\ unavailable\ caused\ by\ unscheduled\ outages}{total\ hours}\right) \times 100 \quad (1)$$

Availability is a measure of how often a unit is capable of providing service. In most cases, equipment must be shut down for maintenance to be performed. It may be extremely reliable but it is unavailable during the time it is shut down. Availability can be improved by maximizing uptime (reliability supplemented or enhanced by redundancy) and minimizing downtime (high maintainability). Availability considers both scheduled and unscheduled maintenance and compares to an ideal situation with no maintenance outages at all. By means of Equation 2 as well as data from Table 4 availability of Reykjanes power plant in 2014 has been calculated to be: 96.1% which is higher than average availability of geothermal power plants reported to be 90% (EERE, 2015).

$$Availability\ = \left(1 - \frac{hours\ of\ unscheduled\ outages + scheduled\ hours}{total\ hours}\right) \times 100 \quad (2)$$

Maintainability is used to express the cost of maintenance. This includes the cost for parts and servicing. Material management in Reykjanes power plant is maintained within the accounting system and regular status checks are made on the inventory. This system has proven to be working well so there is no plan for changing inventory system (Figures 11 and 12).

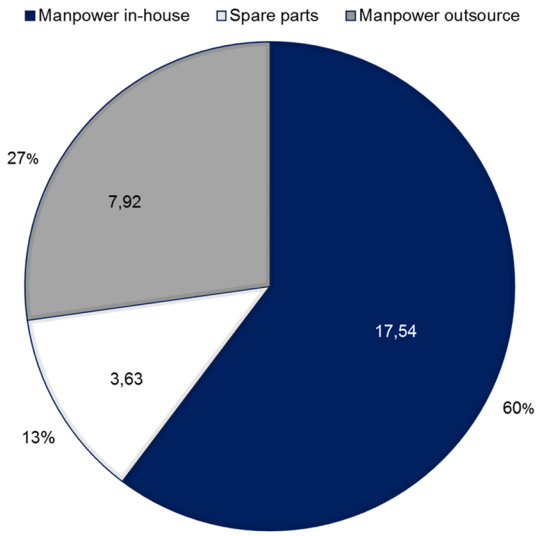

FIGURE 11: O&M annual cost breakdown for 50 MW unit (Million ISK) (2014)

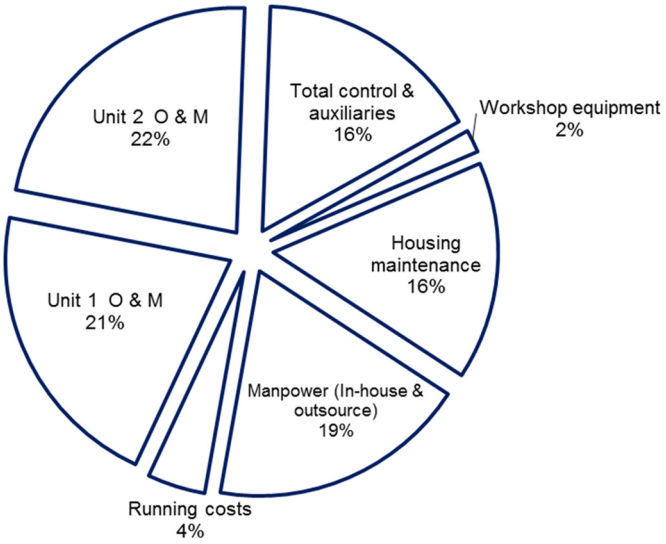

FIGURE 12: Annual O&M and Control cost of total 100 MW (2014)

Combining these considerations, RAM looks at how often you can use the equipment and how much it costs to keep it in operating condition (HPAC Engineering, 2013; Michael Curley, 2013; Marini, 2006). Other important parameters based on IEEE 762 Standard from the power plant have been calculated.

By means of Equation 3 as well as data from Table 4 the Net Capacity Factor (NCF) of Reykjanes is calculated to be 89.7% which is higher than the average worldwide capacity factor of single-flash dry-steam plants (80,1%) (Moon and Zarrouk, 2012).

$$Net\ Capacity\ Factor(NCF) = \frac{Actual\ Energy\ Generated}{Maximum\ Possible\ Energy\ could\ have\ generated} \quad (3)$$

By means of Equation 4 as well as data from Table 4 the Scheduled Outage Rate (SOR) of Reykjanes is calculated to be 2.55%. The lower this index is, the better. It is worth mentioning that from the total of 15 times of the plant stops, 8 times have been caused by steam supply failures, 4 times by maintenance work and 3 times by transmission lines and grid failures.

$$Scheduled\ Outage\ Rate(SOR) = \frac{Total\ hours\ unit\ is\ out\ of\ service\ due\ to\ scheduled\ maintenance}{Total\ hours} \quad (4)$$

And finally by means of Equation 5 as well as data from Table 4 Forced Outage Rate (FOR) of Reykjanes is calculated to be 1.2%. This indicator should be as low as possible and is supposed to be less than the SOR.

$$Forced\ outage\ Rate(FOR) = \frac{Total\ hours\ unit\ is\ out\ of\ service\ due\ to\ unexpected\ failures}{Total\ hours} \times 100 \quad (5)$$

4.5.3 Maintenance procedure for each component

Most maintenance procedure in Reykjanes power plant involves preventive maintenance although corrective actions are sometimes inevitable. It has been tried to prioritise corrective steps, especially regarding the price of electricity since during a power plant stop, the power plant owner is required to purchase and provide electricity for contracted sales (aluminium industry) and if the timing is not suitable, electricity could have to be bought for higher prices than necessary.

Maintenance is carried out weekly, monthly and annually. Inspection of power plant component (preventive and predictive maintenance) is the main activity during annual outage. Each unit of 50 MW takes one week outage per year and the time between outages of each unit is at least one week to do necessary preparations. Major activities done during this period will be discussed step by step by following the steam route flow from the wells to the powerhouse equipment.

Steam gathering and pipes

Each wellhead is equipped with a control valve in order to regulate the flow from the wells to meet the power plants' requirements. The valve actuator is a hydraulic cylinder. This valve has been designed by engineers of the power plant and are set up as a large needle valve (choke valve) which does not stick due to scaling and does not suffer from erosion. They are remotely controlled although position of the valves does not change regularly.

Drain valves are open during warm-up of pipeline in the start-up process and are closed before taking the full pressure. Besides, these valves are used during tracer test flow measurement and for collecting the fluid samples. Figure 13 shows the repairing process of brine pipelines (cleaning).

FIGURE 13: Pipeline and valve maintenance

Scaling problems however, are prominent in the level-control valves for the brine in the separators. The scaling in wells and wellheads of Reykjanes power plant consists mostly of metal sulphides but not silica (Figure 14). Silica scaling can be found downstream in separators and brine pipes.

FIGURE 14: Cleaning scaling in pipes

In the past, brine valves were prone to get stuck and valve stems wore down too quickly but both problems were solved by modifying the control valves.

In the annual outage maintenance period, valves are taken out, opened and depending on their condition they are cleaned, repacked and reinstalled or they are replaced if needed.

Other main maintenance tasks in outage period is stopping the leakage in steam pipes which can be caused by different reasons, but mainly by H_2S cracking and bad quality of steel or improper welding. Regarding maintenance of the pipe insulations, they are changed only if they are damaged due to leaks from the steam pipes.

Separator

Horizontal separators have been installed in Reykjanes power plant which are considered to be safer regarding earthquakes. In the first years of operation they faced scaling problems. The scaling was gradually reduced by pressure drop and a change in the chemistry of the geothermal system. Moreover, some minor cracks have been observed only in the upper part of some pipes while in the separator vessel itself no cracks have been identified. Generally, inlet pipes that connect to the separator are a critical point affected by high manganese content in the steel (Thórólfsson and Einarsson, 2015).

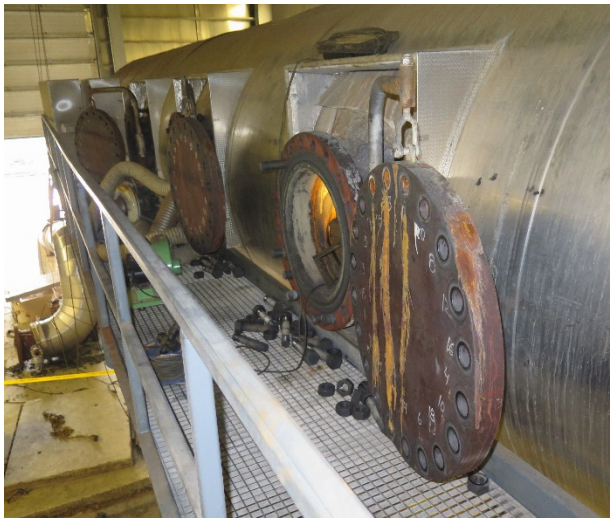

FIGURE 15: Separator inspection during outage

In the annual outage maintenance periods, the separator is cooled down by an air pump to allow visual inspections, taking pictures of the centre chamber and steam outlet, checking for stuck valves and scaling (Figure 15).

In general, maintaining high pressure in the separator inlet reduces scaling in the vessels. In addition, corrective procedures are done if necessary such as repairing or replacing. For instance, in the 2015 outage, a leakage in the brine outlet pipe from the separator caused by a faulty welding was fixed. Also as droplets of brine fall down to the bottom in two rows of the chevrons inside the separators, they needed cleaning.

Moisture separator

Steam from separators flows towards a moisture separator unit, passing through the stainless steel mist eliminator pads.

The moisture separator is a unit highly prone to cracks. About 400 kg of condensate is drained through the moisture separator per hour, carrying about 1 kg/h of dissolved solids compared to 80 kg/s of condensate from the condenser that carries only 0.1 kg/s of solids (Thórólfsson and Einarsson, 2015).

A recent incident was related to the mist eliminator which is made of 316 Stainless Steel. It had deteriorated and cracked caused by pressure fluctuation due to an electricity grid failure. The cut mesh pieces went into the steam line and into the steam inlet strainer, broke the strainer and into the turbine. It was not realized at the time and after 3 years of operation the maintenance team found the damage of

the turbine blades during an overhaul. Eventually one row of turbine blades was replaced. The wire mesh was improved from 316 to duplex Stainless Steel which lasts for 3 to 4 years. During the maintenance outage period the mist eliminator pads are inspected visually and pulled by hand to check if they are deteriorated as shown in Figure 16.

FIGURE 16: Moisture separator inspection during outage

Steam turbine

As the most significant part of the geothermal power plant, the turbine is also the most complicated and sensitive equipment in terms of operation and maintenance. Thus, in addition to periodic inspections in routine maintenance procedure, a specific overhaul period is assigned just for the turbine and its auxiliaries. Main components of the turbine that are monitored in the maintenance procedure are the rotor, stationary blades (nozzles), lubrication system, sealing, packing and casing parts, bearings, steam traps and steam strainers. The turbines in Reykjanes power plant have been designed for easy and fast maintenance, blade carriers are bolted into the turbine casing so they can be removed quickly for cleaning.

The turbines have built-in protection systems against vibration, over-speed, eccentricity, axial movements and differential expansion as well as control of lubrication oil temperature, bearings temperature and turbine gland (seal) pressure. Sensors are installed in all bearings to monitor vibrations in the turbine. A portable vibration meter is available to record the vibration of pumps and smaller rotating units.

In the last stage of the turbine, there is 18% moisture at the end of the blades where they are exposed and hit by liquid drops. The blades have a strip made of a special hard metal, Stellite, which is a cobalt-chromium alloy designed for wear resistance.

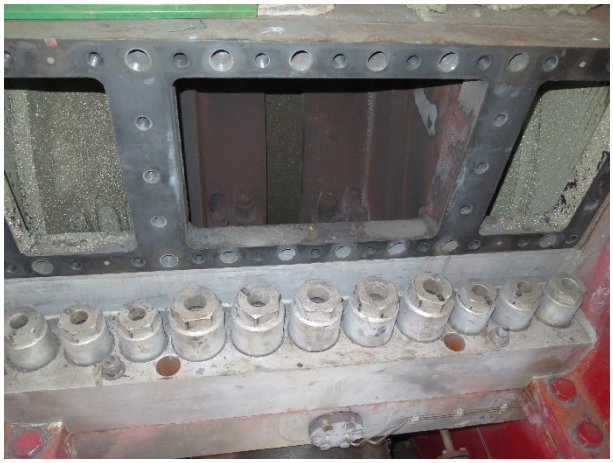

FIGURE 17: Visual inspection of inlet nozzles of turbine for scaling

In the annual outage, turbine maintenance involves a visual inspection of scaling in the inlet chamber and the inlet nozzles of turbine. Photos are taken and compared to photos taken in previous years to decide on a date of the next major overhaul (Figure 17). Also the pressure in the head of the nozzles is measured to track how the inlet pressure increases with time due to scaling. In 2012, damaged blades of the rotor were changed which were broken due to the incident in the mist eliminator, that was mentioned above (Figure 18).

During the 5-year major overhaul, that takes 5 weeks' time, turbines are dismantled, bolts are loosened, casings are opened, all parts are cleaned, scaling is removed, and blades are repaired if necessary. If blades are damaged they can be replaced with spare turbine rotors.

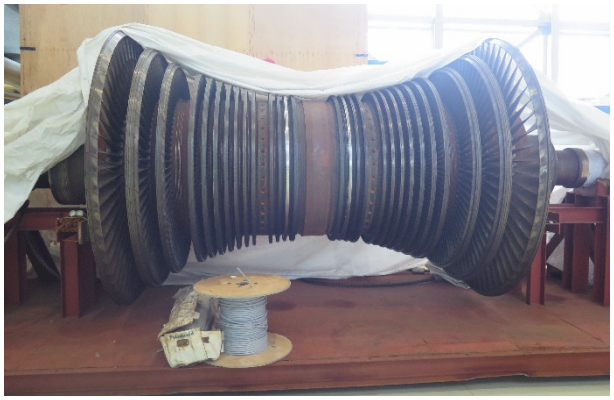

FIGURE 18: A repaired steam turbine rotor

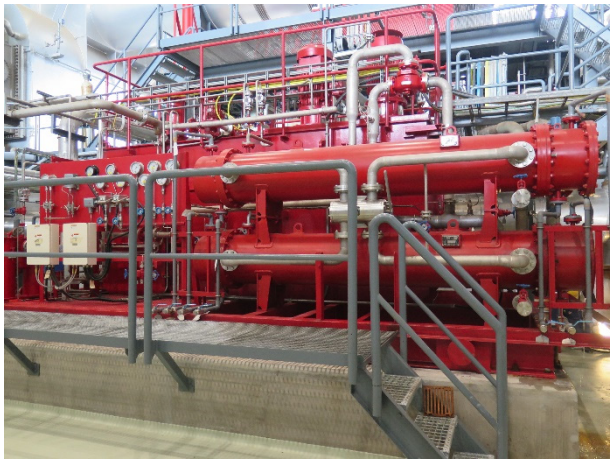

FIGURE 19: Lubrication system of the Reykjanes power plant

Turbine auxiliaries

Steam traps are automatic valves that drain condensed steam (condensate) from a steam space while preventing the loss of live steam. Droplets are formed by heat transfer especially during start-up time when pipes are still cold. Number of steam traps for one unit is 22.

Excluding design problems, two of the most common causes of trap failure are under-sizing and dirt. Under-sizing increases the work load on single traps. In some cases, this can result in blowing of live steam. Dirt is always being created in a steam system and excessive build-up can cause plugging. Steam traps are periodically checked to avoid failures.

Steam strainers are another turbine auxiliary that captures any foreign materials like rocks at the inlet of the turbine. Maintenance procedure in outage involves opening and taking out the foreign material.

Lubrication system as one of auxiliary systems of the turbine. It has pumps, motors, tanks, filters and pipes and circulates oil through all components that need lubrication (Figure 19). The turbine and generator rotors weigh 28 and 15 tonnes, respectively, rotating at 3000 rpm. Normally, circulating oil does not require frequent replacement, instead samples of oil are taken for analysis every 2 or 3 months. Separators in the oil system and micro filters as they are installed in lubrication system of Reykjanes power plant are not very common in geothermal power plants but, since engineers of this power plant are marine engineers, they used the same equipment applied in lubrication system on ships. However, this extra equipment is beneficial for the system in a way that oil can be used for 10 to 15 years. When the turbine starts to work, the first component that starts is the auxiliary oil pump and the jacking oil pump that lifts the rotor in the bearings. So when the turbine reaches working speed they can stop, and the main oil pump, mounted on the turbine shaft, takes over.

Generators

Prevalent failures of the generator and electrical systems can be rotor vibration, loose stator coils, arcing of switch gears, failure of motors and failure of transformers (Bore, 2008). Yet, these failures have occurred rarely in Reykjanes power plant. The only experienced failure has been a house load transformer which broke down due to defective manufacturing.

Plant generators are one of the least problematic equipment in the power house, working since 2006 without breakdown. They do not require complex maintenance, only the bearing system is constantly monitored and lubricated. The hydrodynamic bearings are also reliable pieces. Preventive maintenance of generators involves controlling and protecting it against any failure caused by internal factors of the power plant or from the grid.

In major overhauls, the disassembly and internal inspection of mechanical components of the generator is necessarily carried out according to the manual. Electrical tests consist of insulation condition assessment, cleaning and testing.

Generator grounding and its fault protection, excitation system, thermal and fault protection of stator of generator, rotor field protection, breaker failure protection, protection against loss of fields, over-excitation, unbalanced currents, motoring overvoltage, fluctuation in frequencies etc. are common protection considerations of generators (Aguirre, 2010).

Condenser and cooling system

The surface condenser used in this power plant is much more expensive than direct contact condensers, although it is less vulnerable to scaling. In addition, with having the clean condensate from the surface condenser which is used to dilute the brine for reinjection, less scaling problems occur in the reinjection pipes. There are six condensate pumps, three for each unit that increase the pressure of the condensate from 2 to 20 bar. To protect the unit, the water level inside the condenser as well as the pressure and temperature of the steam exhaust of the turbine is controlled.

The maintenance process of the condenser has been proactive to begin with by considering the fluid salinity of the area during the design phase and by choosing the surface condenser type. Visual inspection for foreign objects in the condenser and cleaning scaling in the pipes is usually not carried out annually. This is usually done on a biannual basis or only in the major 5-year overhaul (Figure 20). The steam condensate is corrosive because of its low pH. However, when it is mixed with brine no corrosion occurs anymore. Oxygen in the condensate is the cause of corrosion which does not happen in surface condensers. By selecting the type 316 Stainless Steel for condensate pipes and vessels, this problem is also prevented. The seawater pipes, transporting cooling water, are made by fibre glass or composite and the tubes in the condensers are titanium which is more expensive yet more reliable in cycles using seawater.

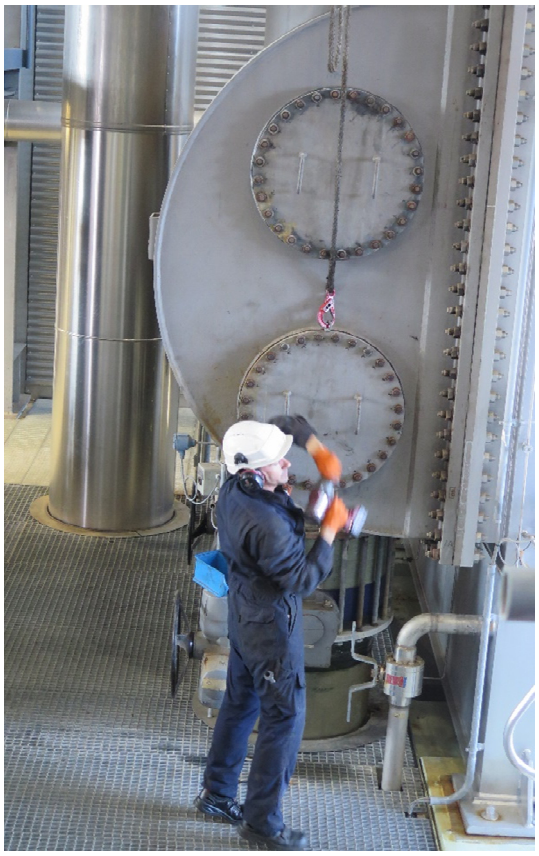

FIGURE 20: Inspection of the condensers

Temperature sensors in the low temperature side of the condenser last many years but in the high temperature (steam) side the sensors should be replaced after 4 or 5 years and need more frequent calibration during the annual overhaul.

Common problems of cooling towers such as scale deposits or clogged spray nozzles, that require maintenance, do not exist in Reykjanes power plant because of the usage of a once-through cooling system that takes water from the sea. Cooling water supply for condenser is not directly taken from the sea but from ashore wells. Regarding cooling water, generally no trouble has occurred in condenser performance due to cooling water so far. Biological bacteria and sea animals could gradually plug up the pipes of the condenser. Inspection, cleaning and effective filtration are actions that should be done.

Gas extraction systems

Currently 0.7% of the steam consists of NCG in Reykjanes power plant of which 98% is CO_2 and 2% H_2S. Comparing to other geothermal power plants, this amount of NCG is very low. However, even very little amounts of H_2S in the system can cause huge problems for the equipment. After the separation of steam and brine, the proportion of NCG increases in the steam and high partial pressure of H_2S causes cracks in vulnerable pipes (Carbon Steel pipes).

FIGURE 21: Steam ejector

FIGURE 22: Cleaning pipes of silencers by hydro-blast pumps

FIGURE 23: Power plant pumps

Since steam ejectors have no moving parts and due to their simple construction, this is a relatively low-cost component, easy to operate and low in maintenance efforts (Green and Perry, 2008).

Typical steam ejectors components are nozzles, intercoolers, control valves, and isolating valves. During outage maintenance only nozzles and control valves are disassembled to check for cracks (Figure 21). Outlets of the moisture separator and the main steam line between the moisture separator and the turbine are most vulnerable to cracks because of the high temperature and high H_2S concentration. Significant part of the 2015 annual outage corrective maintenance procedure consisted of repairing at least 4 steam leaks in pipes caused by H_2S corrosion.

Silencers

Silencers in Reykjanes power plant take a part of the brine from the separator depending on the status of the level controls in the separator. Inside the silencers the flow is directed downwards through vertical pipes into a water tank inside the silencer vessel 3 m below water level. In systems including brine, the main problems coming up in silencers relate to scaling and corrosion. During annual outage the silencers pipes are washed by hydro blast pumps to prevent or clear blockage (Figure 22).

Pumps and motors

One of the special design features of Reykjanes power plant is that brine flows through the system by utilizing the separator pressure as well as taking advantage of gravity, so that no pumps are needed for brine circulation and problems of scaling in brine pumps, which is a common problem that does not occur in this power plant. Two condensate pumps, three auxiliary cooling water pumps for oil, and the generator in main power house are shown in Figure 23.

Maintenance of pumps and motors by minimizing the vibration plays a vital role in the performance of the whole system and also influences the lifetime of their related auxiliaries like bearings, couplings and others. Shaft alignment of the pumps is done by a laser alignment tool.

Motors, if bearings are lubricated properly, can work for a long time without any mechanical problems. On the other hand, there is a number of common electrical failures in motors that need protective actions

by monitoring critical parameters of motor performance such as phase overcurrent, negative sequence, ground fault, stall or locked rotor, over-temperature of stator winding and vibrating sensors (Aguirre, 2010).

Air cleaning room

This unit serves for removing any trace of H_2S from all electrical rooms by filtering H_2S from the air to avoid corrosion of electrical components such as computers, electronic and low voltage electrical systems. Hydrogen sulphide combined with humid air corrodes copper. All sensitive equipment has to be kept in a room where H_2S gas has been cleaned from the ambient air.

FIGURE 24: Air cleaning room

This room consists of drawers that are filled with chemical air purifier material, based on potassium permanganate, providing optimum adsorption and oxidation of a wide variety of gaseous contaminants (Figure 24). The air flows through drawers and ventilators and then to the electrical rooms and then circulates again. There are six filtering units for six electrical rooms, each of which works with an electrical blower to circulate the air. Maintenance of the ventilation system is rather straightforward including replacement of the air purifier material when its colour changes and reshuffling the drawers. The more H_2S in the air in a power plant, the faster the deterioration of the air purifier material will be.

Electrical rooms

Electrical rooms contain PLC units, electrical protection systems (breaker system), optical fibre connections, power breakers for generator and Earthing system, cable room, batteries for DC systems, backup for power cut and generally all the devices and circuits required for automatic control. There is a copper plate hanging in each electrical room to monitor if there is any stain of corrosion on it in order to make sure that the ventilation system is working properly (Figure 25).

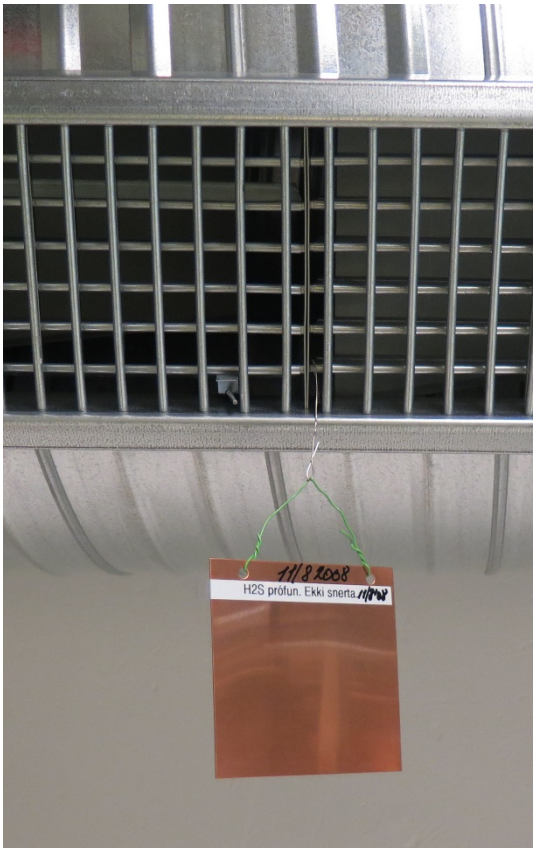

FIGURE 25: Copper plate for monitoring corrosion

In the 2015 annual overhaul, some minor modifications were made for this unit and basically all tests needed in the electrical system, such as load test of DC system, were carried out. Cables are long lasting components and do not need any specific maintenance.

Control system and instrumentation

The control system of Reykjanes power plant is an open system, i.e. the SCADA system, which is used for monitoring the operation. In the control room there are direct boards of switches for manual control of all components and parameters of two turbine units and turbo-generators such as opening and closing of valves, motors, pumps, temperature and pressure control, trip switches etc. (Figure 26).

FIGURE 26: Main control room

All control panels are supplied by the turbine manufacturer since it is common practise to purchase turbines together with their control system. Although it might look outdated and bulky, no corrective maintenance has been required since the commissioning of unit. Computers in the main control room consist of SCADA screens for all station sections for alarm handlings. Therefore, operators can check the parameters constantly.

However, sometimes the control system can be problematic because it is a PC based system which uses a Windows operation system that can freeze, so during the 2015 outage, the control unit was replaced with a safer alternative. The SCADA system is being replaced after 8 years of power plant operation.

Maintenance of instrumentation is carried out during the turbine operation, whereas during an outage of power plant, cleaning, scaling, and recalibrating is done. In the past, a differential pressure measuring device has been used to measure the water level in equipment such as the separator and condenser, but currently radar measurement equipment is used and appears to be more reliable. Besides the radar sensors in the condenser, there is an indicator of water level and Vegaswing instruments, which are vibrating level switches sensitive to liquid level, used for extra safety in case radar measurements fail as shown in Figure 27.

FIGURE 27: Radar and Vegaswing sensors for water level control

Radar sensors can also control pumps or pump valves. If high levels are measured then the pump starts if it is not running yet, and at low level the pump stops, pumping condensate, and the highest level trips the turbine.

The three level-controls of the separators are working independently, one is spare and can be taken out of service and repaired while two of them are operating (triple redundancy), checking the level of brine in the separator. Temperature sensors should be calibrated at least once a year during the annual overhaul and changed if necessary. By means of efficient safety and backup systems as well as periodic calibration of the instruments, wrong control signals, which are one of the most frequent risks in power plants, can be prevented.

Emergency alarms

The control system has a warning system classified into three categories:

Category 1: immediate attendance required, beeper of operator 1 is activated and if it is needed other operators are called to take care of the emergency incident. However, emergencies usually happen during day time.

Category 2: operators have to take care of this category, checking control room to see what caused the alarm, yet no need for immediate repair. Usually category 2 is a warning for upcoming category 1.
Category 3: it is only an alarm for an event. No failure has happened and operator only gets reports on screen.

Valve houses
Valves are closed during outage for maintenance of pipes but normally valves themselves do not need maintenance annually unless cleaning is necessary in case of blockage.

Reinjection systems
Reinjection systems include series of pipes that take condensate to be added to the brine from the separator before reinjection. They also include connection pipes used for mixing a little part of condensate to the main brine pipe, between the separator station and the mixing vessel at the power plant. This is done in order to use the pressure of the separator to pump the brine so that boiling due to pressure drop and elevation changes is killed in the pipe line. Brine temperature should be reduced by 5-10 degrees. During outage, inspection of the pipes and, if necessary cleaning, is done as well as calibration of the instruments as for example the temperature sensors. Figure 28 shows the repairing process of a brine pipeline.

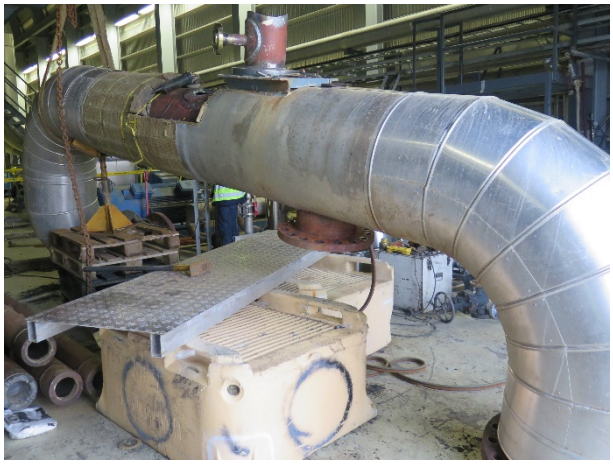

FIGURE 28: Repairing of pipes

4.5.4 Analysis of maintenance procedures

In Table 5, most common failures in Reykjanes power plant which require maintenance based on type of components, as well as required action in each type of maintenance method, have been classified. It explains what should be done to prevent or predict the problem, and if it failed, what action should be done to correct it.

TABLE 5: Summary of problems and solutions in Reykjanes power plant

Main system	Component	Most common problems in Reykjanes PP	Maintenance procedure: Preventive/predictive/proactive action	Maintenance procedure: Corrective action
Steam supply systems	Wellhead valves and control units	Scaling	Keeping fluid temperature high	Cleaning
	Separator	Scaling	Designing high separator working pressure	Cleaning
	Moisture eliminator	Cracks on carbon steel	Considering H_2S partial pressure and condensate pH during design	Repairing or Replacing in 5-year interval
			Efficient welding process and possibly post weld heat treatment to reduce hardness and internal stresses in the high-temp. pipe	
			Using drawn steel pipes with a manganese content less than 1%	
			Changing steel type from welded pipes to seamless,	
			Using higher alloy metals	

Main system	Component	Most common problems in Reykjanes PP	Maintenance procedure: Preventive/predictive/proactive action	Maintenance procedure: Corrective action
			Material crack test of mist eliminator pads	
	Reinjection systems	Minor scaling	Mixing condensate with brine	Cleaning
	Silencers	Scaling	Designed to be cleaned easily	Cleaning
Mechanical components	Turbine	Scaling on stator blades	Constant monitoring of steam pressure	Changing worn out parts, cleaning
			Visual inspection in outage	
			Suspecting cracks with magnetic particle testing, also referred to as MPI testing and Magnaflux Testing that identifies surface flaws in metal parts in turbine major overhaul period (every 5 years)	
	Condenser	Minor scaling	Choosing surface condenser avoiding scaling and corrosion	Cleaning
			Bringing cold water not directly to system from the sea but by wells and filtering	
	Gas extraction system	Cracks	Improving material (Using higher alloy metals)	Cleaning, or changing low-quality material, or grinding welds and re-welding or welding a patch over cracked parts
			Checking operating pressures of steam ejectors	
	Cooling system	Leakage of stuffing box in submersible pumps between pump and motor so seawater enters motor and destroys it	Redesigning of stuffing box with mechanical seal	Replacing or repairing faulty motors via rewinding the coils of motor in electrical shop
	Pumps and Motors	-Failure (seldom) -Leaking stuffing box -Erosion on pump impellers	Monitoring current and power of motor	Rewinding the coil or replacing the bearings
			Vibration monitoring	
			Improving quality of stuffing box like double mechanical shaft seals	
			Improving quality of impellers like duplex Stainless Steel	
	Lubrication system	Almost no problems	Using extra filters	-
			Using Centrifuge oil separators	
	Valves	Sticking by scaling (inevitable especially in brine lines)	Periodically operating valves (opening, closing)	Cleaning
	Ventilation system	-	Changing filters	-
	Air compressors	Failure in PLC controlling the unit	-	Repairing the PLC

Main system	Component	Most common problems in Reykjanes PP	Maintenance procedure: Preventive/predictive/proactive action	Maintenance procedure: Corrective action
Electrical components	Generator	Almost no problems	-	-
	Control system and instrumentation	-Wrong control signal, faulty trips -Failures in sensors and transducers	Redesigning control system	Replacing (renewing) defective components
			Checking the air by copper in electrical rooms	
			Using triple redundancy for critical sensors like separator level	
			Recalibrating equipment in outage	
	Transformer	Failure	Checking transformer oil for moisture or dirt	Replacing
	Protection systems	-Failure of relays -Faulty programming -Wrong connection between components -Wrong instrum.	Ensuring correct design	Redesigning protection system or reprogramming of system
			Checking instrument calibration in outage	

Analysis of maintenance procedures of the power plant regarding predictive technologies are shown in Table 6:

TABLE 6: Predictive maintenance technologies application in Reykjanes power plant

Technologies	Vibration Monitoring/Analysis	Lubricant, fuel Analysis	Wear Particle Analysis	Bearing, Temperature/Analysis	Performance Monitoring	Ultrasonic Noise Detection	Ultrasonic Flow	Infrared Thermography	Non-destructive Testing (Thickness)	Visual Inspection	Insulation Resistance	Motor Current Signature Analysis	Motor Circuit Analysis	Polarization Monitoring	Electrical Monitoring
Reykjanes Power Plant	✓	✓	-	✓	✓	-	-	✓	✓	✓	✓	-	-	-	✓
Application	Routine operation	Routine & outage	-	Is Monitored in SCADA	Routine operation & after overhauls	-	-	Routine operation & outage	(Only if necessary)	Routine operation& outage	Routine operation	-	-	-	Is Monitored in SCADA

In Table 7, a number of metrics that can be used to evaluate an O&M program have been presented. Not all of these metrics can be used in all situations. However, a maintenance program should make use of as many metrics as possible to better define deficiencies that can be used as a guide for tracking and trending metrics against industry benchmarks. Based on available data gathered from Reykjanes power plant in Table 4, some of these metrics have been calculated and results can be seen in Table 8 (Sullivan et al., 2010).

Understandably, based on available data only some of the metrics could be evaluated. Only the maintenance overtime factor of Reykjanes power plant is above expected range and other indicators are in an acceptable range.

TABLE 7: Industry O&M metrics and benchmarks (Sullivan et al., 2010)

Metric	Variables and Equation	Benchmark
Equipment Availability	% = Hours each unit is avaialbe to run at capacity / Total hours during the reporting time period	> 95%
Schedule Compliance	% = Total hours worked on scheduled jobs / Total hours scheduled	> 90%
Emergency Maintenance Percentage	% = Total hours worked on emergency jobs / Total hours worked	< 10%
Maintenance Overtime Percentage	% = Total maintenance overtime during period / Total regular maintenance hour during period	< 5%
Preventive Maintenance Completion Percentage	% = Preventive maintenance actions completed / Preventive maintenance actions scheduled	> 90%
Preventive Maintenance Budget/Cost	% = Preventive maintenance cost / Total maintenance cost	15% – 18%
Predictive Maintenance Budget/Cost	% = Preventive maintenance cost / Total maintenance cost	10% – 12%

TABLE 8: Evaluation for Reykjanes power plant O&M program

Metric	Benchmark	Reykjanes Power Plant
Power plant availability	>95%	96.1%
Schedule compliance	>90%	~99%
Emergency maintenance percentage	<10%	N/A
Maintenance overtime	<5%	16%
Preventive Maintenance completion	>90%	~100%
Preventive maintenance Cost	15%-18%	NA
Predictive maintenance Cost	10%-12%	NA

4.5.5 Annual outage analysis (2015)

As mentioned before, to carry out this study, maintenance procedure of one of the Reykjanes power plant units in 2015 outage period has been observed during several days. All maintenance activities have been recorded and categorized based on the maintenance schedule of the 7 days' outage, based on the required maintenance of each component, on maintenance methods and on workforce needed to carry out the maintenance. A prepared schedule containing all maintenance actions in detail is presented in Appendix I. In the following sections, results achieved from collected data of the outage maintenance will be presented. A total of 81 actions have been completed during the 12-hour day 7 days' outage period.

In Figure 29, the share of components in activities during the outage period of the power plant is presented. Maintenance has been performed for all components. The turbine and its auxiliaries had the highest number of maintenance work processes while the generator and reinjection system have been the least effected with the lowest number of maintenance activities required. The maintenance activities carried out for each component have been classified based on the maintenance method applied. Both the highest corrective and preventive/predictive maintenance tasks have been connected to the turbine and its auxiliaries implying that these components are more sensitive and therefore need more attention during routine maintenance than others.

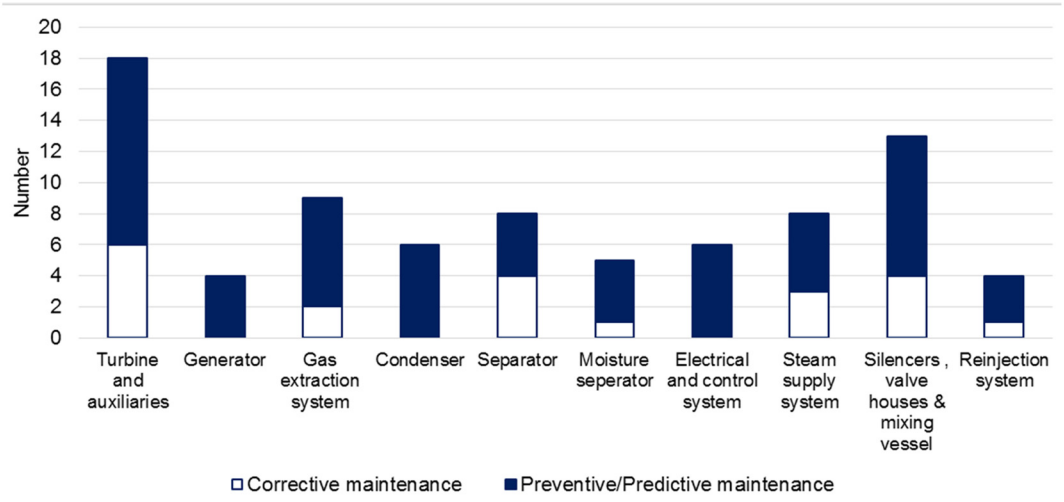

FIGURE 29: Shares and methods of maintenance used for components in the 2015 annual outage

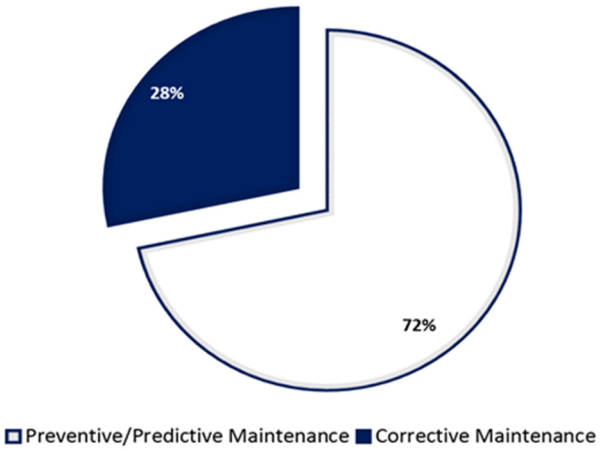

FIGURE 30: Maintenance methods used in the 2015 outage

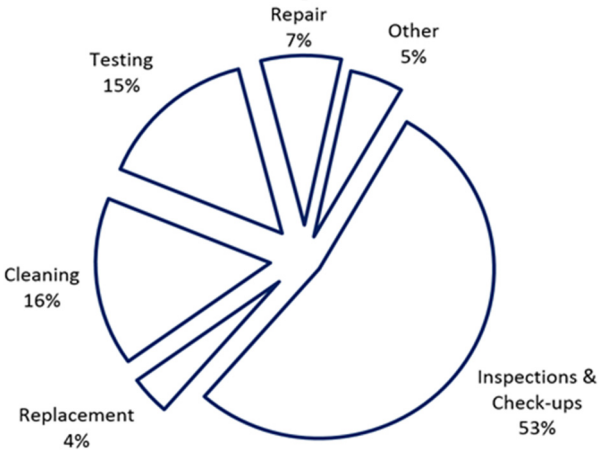

FIGURE 31: Maintenance activities share in annual outage cost 2014

Figure 30 presents a pie chart of the percentage of each maintenance method of the maintenance activities carried out during the outage maintenance period 2015. In addition, Figure 31 shows a pie chart of the percentage of cost categories in 2014 since cost data of the 2015 outage had not gathered completely yet.

Outage manpower:
Outage maintenance is organized and performed by the operation and maintenance team at Reykjanes and Svartsengi power plants. In addition, some activities are outsourced to local contractors and workshops, providing manpower to assist in performing outage maintenance actions. In Figure 32, the percentage of power plant staff and contractors in outage maintenance activities has been illustrated.

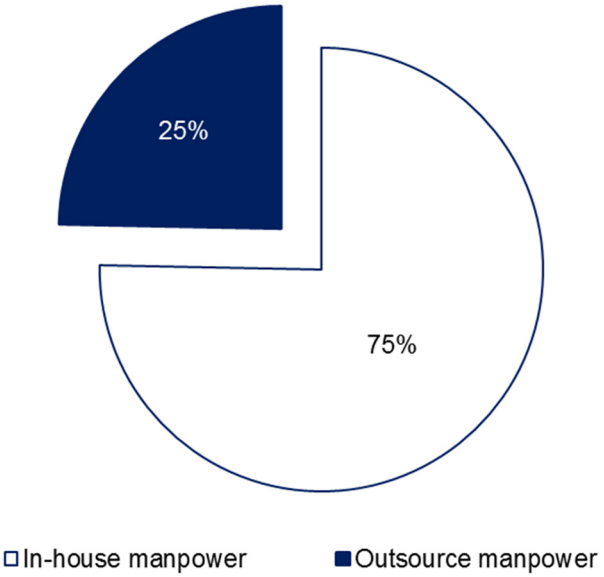

FIGURE 32: Manpower share in the 2015 outage

In Figure 33, an organizational chart of the outage period and number of personnel in each subcategory is been presented.

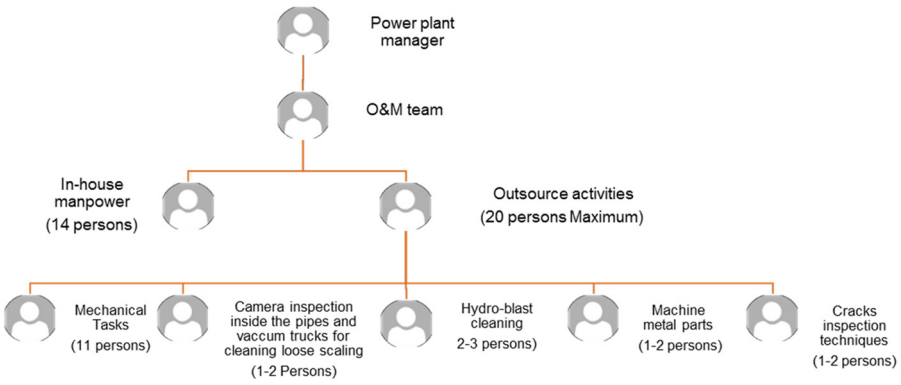

FIGURE 33: Annual outage manpower organizational chart of 2015

Outage cost

Performing effective maintenance has a great influence in reducing O&M costs as well as decreasing outage days and eventually lowering the costs for lost electricity. In Figure 34, electricity production during 2014, and the production drop due to stoppage time, has been illustrated. The total loss of electricity production for the 96 MW net power plant output was 820 MWh costing about 84 Million ISK. If days of outage period can be reduced by one day (24 hours), approximately 7 Million ISK cost due to lost production will be avoided, according to Table 3.

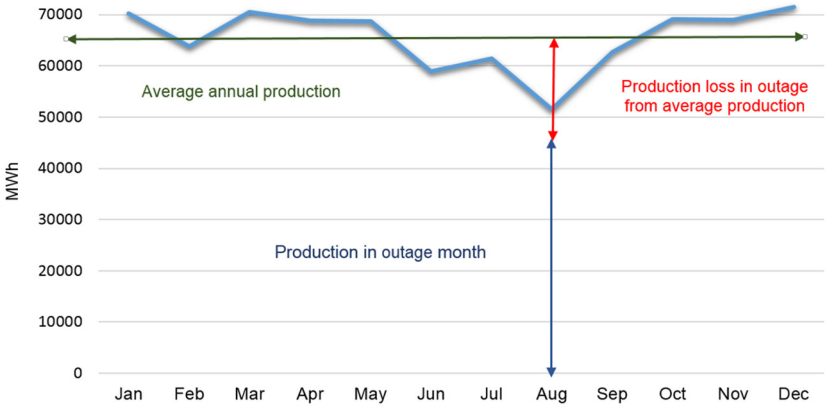

FIGURE 34: Electricity production loss during the annual 2014 outage

Finally, Figure 35 shows a cost breakdown of the outage maintenance carried out in 2014. Major costs of outage are allocated to manpower cost (77%), most of it power plant personnel.

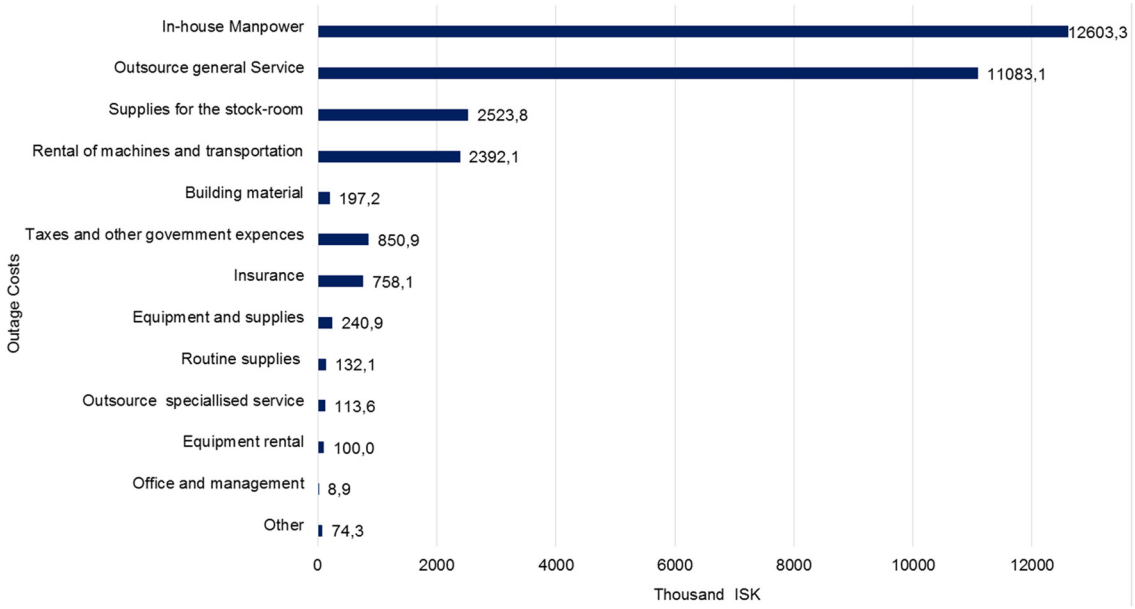

FIGURE 35: Breakdown of annual outage maintenance cost of 2014

5. CONCLUSIONS

From the preceding study the following can be concluded and recommended:

- Experienced operators of Reykjanes geothermal power plant have been able to run the power plant smoothly and have minimized the time and cost caused by outages by optimizing preventive and proactive maintenance, i.e. considering root-cause failures and efficient redundancies of components in a design phase, and constantly inspecting and testing equipment.
- As common in geothermal power plants, dealing with high temperature fluid and special chemical traits, the main source of problems in Reykjanes power plant is due to chemical compositions of geothermal fluids.
- The most common problem of the plant is scaling which basically has been prevented by maintaining high separation pressure of fluid and keeping the wells hot. Also cracks in steam pipes ought to be avoided since steam leaks in piping or components, leading to failures.
- Analysing metrics of IEEE 762 Standard, based on available data, indicates that the power plant performance is above the benchmark range. Nevertheless, there are many other performance indicators or benchmarking worth investigating to keep track of the power plant performance or developing a comprehensive set of indicators based on Reykjanes power plant requirements.
- To enhance the quality of O&M performance, inspecting procedures based on related available standards, such as API 571, are used and their requirements met. Thus, damage mechanisms affecting fixed equipment in the refining and petrochemical industries can be avoided. For specifying equipment, standards such as ANSI NACE MR0175/ISO 15156, can be used for equipment such as separators, to find corrosion cracking resistant material.
- By employing modern computerized systems, i.e. DMM system, comprehensive record of events and incidents for managers and operators are accumulated. The system is kept up to date and options such as expense tracking into the system are added, generating automated breakdown of costs of operating years in detail. Applying different categorizations would give great insight for power plant managers and operators.
- It would be beneficial to organize a database of work orders of DMM systems, and have a documentation of operation and critical maintenance data from operators, available when needed. Instructing contractors to prepare a documentation and reports for the O&M team to evaluate their performance regarding quality, time, cost, record of equipment and material contractor utilized etc. would be of great value. It provides the team with valuable data for comparing past and current conditions of the equipment and system performance.
- Utilizing tools and technologies of predictive maintenance that have not been applied before such as Wear Particle Analysis, Ultrasonic Noise Detection, and Ultrasonic Flow etc. presented in Table 6, can help detecting abnormalities of performance in early stages.
- Establishing an assessment system to investigate all steps and activities done according to the schedule (Gantt charts), especially during outage period when timing is critical.
- The turbine and auxiliaries had to have the most corrective, as well as preventive maintenance actions, while generators are the most reliable part of the power plant. Considering the fact that the steam turbine has its own major overhaul, it is understandable that the turbine and its auxiliary are the most critical components of the power plant and require more attention and maintenance care to decrease probability of failures.

ACKNOWLEDGEMENTS

I would like to express my sincere gratitude to the staff of the United Nations University, Geothermal Training Programme (UNU-GTP), led by Mr. Lúdvík S. Georgsson, for giving me the opportunity to participate in this course. Special thanks to Mr. Ingimar Gudni Haraldsson, Mr. Markús A.G. Wilde, Ms. Málfrídur Ómarsdóttir and Ms. Thórhildur Ísberg for their support, guidance and assistance during the training. I am so grateful to my supervisor, Mr. Geir Thórólfsson, for his guidance to complete my

project report, as well as Mr. Hreinn Halldórsson and all the operation and maintenance team of Reykjanes power plant.

I also want to thank all 2015 UNU Fellows; special thanks go to my dear friends, Amali and Tingting for an unforgettable friendship and memorable moments during these six months. Thanks to my utilization fellows especially Nuno Vieira for his support during the course and reviewing my report with valuable comments.

I extend my appreciation to the Director of the Geothermal Department in Renewable Energy Organization of Iran, Dr Soheil Porkhial for allowing me to participate in this programme.

My deepest thanks go to my family my parents and sisters for their support during the Six Month Programme. And above all, I would like to thank the almighty God for all his help.

REFERENCES

Adale, M.A., 2009: *Evaluation of maintenance management through benchmarking in geothermal power plants.* University of Iceland, MSc thesis, UNU-GTP, report 3, 52 pp.

Aguirre. L.A., 2010: Main considerations in the protection system design for a geothermal power plant. Report 7 in: *Geothermal training in Iceland 2010*. UNU-GTP, Iceland, 29-52.

Avilés, V.M., 2011: Instrumentation appraisal in single and double flash. Report 17 in: *Geothermal training in Iceland 2011*. UNU-GTP, Iceland, 67-83.

Axelsson, G., 2008: Importance of geothermal reinjection. *Presented at the "Workshop for Decision Makers on Direct Heating Use of Geothermal Resources in Asia", organized by UNU-GTP, TBLRREM and TBGMED, in Tianjin, China*, 16 pp.

Bertani, R., 2015: Geothermal power generation in the world 2010-2014 update report. *Proceedings of the World Geothermal Congress 2015, Melbourne, Australia,* 19 pp.

Bore, C.K., 2008: *Analysis of management methods and application to maintenance of geothermal power plant*. University of Iceland, MSc thesis, UNU-GTP, report 5, 52 pp.

Chalifoux, A., and Baird, J., 1999: *Reliability centred maintenance (RCM) guide: Operating a more effective maintenance program.* US Army Corps of Engineers, Construction Engineering Research Laboratories, CERL Technical Report 99/41, 99 pp.

Curley, G.M., 2013: *Reliability analysis of power plant unit outage problems*. Generation Consulting Services, presentation, 87 pp. Website: *famos.scientech.us/PDFs/2013_Symposium/Reliability_ Analysis_of_Power_Plants_Curley.pdf.*

DiPippo, R., 2008: *Geothermal power plants. Principles, applications, case studies and environmental impact*. Elsevier Ltd., Kidlington, UK, 493 pp.

EERE, 2015: *Geothermal FAQS*. Office of Energy Efficiency & Renewable Energy (EERE), Washington D.C., United States. Website: *energy.gov/eere/geothermal/geothermal-faqs*

Elísson, A., 2013: *Indicators for maintenance in geothermal power.* University of Iceland, Reykjavík, Iceland, MSc thesis, 88 pp.

Elíasson, E.T., Thórhallsson, S. and Steingrímsson, B., 2011: Geothermal power plants. *Presented at* "*Short Course on Geothermal Drilling, Resource Development and Power Plants", organized by UNU-GTP and LaGeo, in Santa Tecla, El Salvador,* 16 pp.

Franzson, H., 2004: *The high temperature system at Reykjanes.* ÍSOR – Iceland GeoSurvey, report ÍSOR-2004/012 (in Icelandic), 68 pp.

Fridriksson, Th., Saemundsson, K., Óladóttir, A.A., Einarsson, G.M., Kristinsson, S.G., Ármannsson, H., and Eyjólfsdóttir, E., 2010: *Environmental monitoring of the Reykjanes geothermal field.* ÍSOR – Iceland GeoSurvey, report ÍSOR-2010/100 (in Icelandic), 78 pp.

Green, D.W., and Perry, R., 2008: *Chemical engineers' handbook* (8th ed.). McGraw Hill, 2640 pp.

Gudmundsson, J.S., and Hauksson, T.J., 1981: The Reykjanes geothermal field in Iceland: Subsurface exploration and well discharge characteristics. *Proceedings of the Seventh Workshop on Geothermal Reservoir Engineering, Stanford University, Stanford, CA, United States*, 61-69.

Gunnarsson, A., 2013: *Maintenance of steam turbines at Hellisheidi power plant.* University of Iceland, Reykjavík, Iceland, MSc thesis, 81 pp.

Kachru, U., 2007: *Production and operations management*. Excel Books, New Delhi, India, 810 pp.

Kahn, J.D., 2006: Applying six sigma to plant maintenance improvement programs. *Proceedings MARCON 2006 - 3rd International Marketing Congress, Lahore, Pakistan*, 19 pp.

Kebede, H., 2002: Study of geothermal power plant electrical and control system with emphasis on reliability aspects. Report 7 in: *Geothermal training in Iceland 2011.* UNU-GTP, Iceland, 77-96.

López. G.A., 2008: Maintenance systems of Ahuachapán power plant, El Salvador and Svartsengi power plant, Iceland: Comparison and optimization proposal for the Ahuachapán maintenance system. Report 22 in: *Geothermal training in Iceland 2008*. UNU-GTP, Iceland, 365-386.

Magnússon, T.J., and Gunnarsson, Á., 1989: Design of an automatic control system for the Nesjavellir geothermal power plant. *International Symposium on District Heating Simulation, Reykjavik, Iceland*.

Marini, B., 2006: Turbine system economics and reliability, availability & maintainability (RAM). In: Dennis R. (ed.), *The gas turbine handbook*. U.S. Department of Energy, Office of Fossil Energy, National Energy Technology Laboratory, website: *www.netl.doe.gov/research/coal/energy-systems/turbines/publications/handbook*

Márquez A.C., 2007: *The maintenance management framework: models and methods for complex systems maintenance.* Springer-Verlag, London, United Kingdom, 333 pp.

Moon, H., and Zarrouk, J.S., 2012: Efficiency of geothermal power plants: A world review. *Proceedings of the New Zealand Geothermal Workshop 2012, Geothermal Institute, Auckland, New Zealand,* 1-13.

NREL, 2010: Advanced condenser boosts geothermal power plant output. National Renewable Energy Laboratory (NREL), Golden, CO, United States. Website: *www.nrel.gov/docs/fy11osti/49152. pdf*

Pálsson, H., 2010: *Flow in pipelines.* UNU-GTP, Iceland, unpublished lecture notes, 14 pp.

Ragnarsson, Á., 2015: Geothermal development in Iceland 2010-2014. *Proceedings of the World Geothermal Congress 2015, Melbourne, Australia,* 15 pp.

PECI, 1999: *Fifteen O&M best practices for energy efficient buildings*. Portland Energy Conservation, Inc. (PECI), Portland, OR, United States, 42 pp.

Ren21, 2015: *Renewables 2015 – Global status report*. Renewable Energy Policy Network for the 21st Century, Paris, France, 32 pp.

Sullivan, G.P., Pugh, R., Melendez, A.P., Hunt, W.D., 2010: *Operations & maintenance - Best practices. A guide to achieving operational efficiency*. Pacific Northwest National Laboratory, Richland, WA, United States, release 3.0 prepared for the Federal Energy Management Program (FEMP), 321 pp.

Teke, M.A., 2011: *Guidelines for optimum gas extraction system selection*. University of Iceland, Reykjavík, Iceland, MSc thesis, 54 pp.

Tessema, M., 2002: Geothermal binary plant operation and maintenance systems with Svartsengi power plant as a case study. Report 15 in: *Geothermal training in Iceland 2002*. UNU-GTP, Iceland, 287-306.

Thórólfsson, G., 2005: Maintenance history of a geothermal plant: Svartsengi Iceland. *Proceedings of the World Geothermal Congress 2005, Antalya, Turkey*, 7 pp.

Thórólfsson, G., 2010: Silencers for flashing geothermal brine, thirty years of experimenting. *Proceedings of the World Geothermal Congress 2010, Bali, Indonesia*, 4 pp.

Thórólfsson, G., and Einarsson, A., 2015: The influence of the manganese content of mild steel on the rate of crack formation in geothermal steam pipes at the Reykjanes power plant in Iceland. *Proceedings of the World Geothermal Congress 2015, Melbourne, Australia,* 7 pp.

Union of Concerned Scientists, 2015: *How it works: Water for power plant cooling*. Union of Concerned Scientists, website: *www.ucsusa.org*

Woodworth, M.R., 1988: Operation and maintenance manuals. *Geothermal Resources Council Transactions, 12,* 429-434.

World Economic Forum, 2014: *Strategic infrastructure steps to operate and maintain infrastructure efficiently and effectively.* World Economic Forum, Geneva, Switzerland, 86 pp.

Zarrouk, J.S., and Purnanto, M.H, 2015: Geothermal steam-water separators: Design overview. *Geothermics, 53*, 236-254.

APPENDIX I: Schedule containing all maintenance actions in detail

Maintenance outage schedule of the power plant - August 2015	Type of maintenance: Corrective(C) preventive/ predictive (P)	Contractor
Turbine and auxiliaries		
Inspecting turbine through open manhole	P	In-House
Inspecting turbine steam strainer	P	In-House
Checking cooling water valves for lubrication oil cooler	P	In-House
Inspecting return oil filter in lubrication system	P	In-House
Turbine borescope inspection	P	In-House
Overhauling steam traps(Cleaning clogged traps from corrosion)	C	In-House
Overhauling steam traps on main steam pipe in basement of plant	C	In-House
Inspecting the "bypass valve": automatic drain valve on drain pipe from steam lines	P	In-House
Opening stuck valves and cleaning	C	In-House
Inspecting stuffing box inside the valves, changing old rings inside it made of carbon fibre and carbon that got hard when they wear out and lose their elasticity	P	In-House
Inspecting and replacing worn parts of gate valve in in front of the turbine steam traps	P	In-House
Testing all the control valves from the control centre , resetting	P	In-House
Reviewing and verifying the measurements of turbine instrumentation according to the list, recalibrating instruments	P	In-House
Inspecting and cleaning steam ejectors for turbine gland connected to the shaft	P	In-House
Cleaning main lubrication 2 filters (called Sister Filters one working one cleaned in outage in normal operation while in outage 2 of them cleaned)	C	In-House
Checking cleanness of oil filters	P	In-House

Maintenance outage schedule of the power plant - August 2015	Type of maintenance: Corrective(C) preventive/ predictive (P)	Contractor
Fixing leaks in the seawater piping system in seawater cooling system.	C	Out-Source (Mec.Contr.)
Repair the stainless steel piping from the vacuum drain tank and inspect the tank	C	OS (MC)
Generator:		
Inspecting of generator according to manual	P	In-House
Testing pressure of the generator cooling components	P	In-House
Inspecting the cooling water pipes toward air-coolers	P	In-House
Maintaining the generator heating on during the down time/outage	P	In-House
Gas extraction system		
Removing and inspecting the second stage ejector nozzle for inspection (crack inspection)	P	In-House
Cleaning filters in the drains of condensate from coolers that condense steam in NCG after ejectors	C	In-House
Inspecting of steam input valve of ejectors and checking stuffing box	P	In-House
Inspecting the steam traps on the steam lines to ejectors	P	In-House
Checking Interlocks of ejectors and verifying their functionality in control system	P	In-House
Cleaning Vegaswing sensors (level detection sensor) in the 2 drain systems (vacuum and atmospheric tank)	C	In-House
Testing and confirming of all warnings systems/messages	P	In-House
Checking main stop valve, adjusting operation limit of the valve	P	In-House
Inspecting control valves, changing if necessary	P	In-House
Condenser		
Testing vacuum pressure switch (bad vacuuming result in high pressure in outlet of turbine)	P	In-House
Examining and evaluating of rubber coating in the water compartments.	P	In-House
Inspecting all the measuring equipment, pipe connections and pressure and temperature sensors (If time permits)	P	In-House
Inspecting leakage of nipples and measurement equipment in the seawater system around the condenser.	P	In-House
Inspecting leaks and packaging of manholes	P	In-House
Inspecting expansions compensators in the pipe connected to the condensate pump	P	In-House
Moisture separator		
Opening and examining the moisture filters	P	OS (MC)
Removing and cleaning Vegaswing sensors	C	In-House
Examining gate valve around nuts/bolts of the moisture separator.	P	In-House
Checking for leaks on manholes moisture separator	P	In-House
Checking for leakage in the steam pipes connected to this station	P	In-House
General-, electrical-, control-, and machinery.		
Testing all control valves	P	In-House
Testing all remotely controlled stop-valves	P	In-House
Testing all alarms, parameters, confirming the messages in SCADA	P	In-House
Testing batteries and recharging units , also capacity test of battery system	P	In-House
Testing all remote controls from SCADA	P	In-House
Testing all status indicators , switches, valves and etc.	P	In-House
Steam Supply		
Examining the "well flow control valve" , replacing if necessary	P	In-House
Lubricating all the valves in the well basements	P	In-House
Examining all the measuring nozzles on the wells.	P	In-House
Examining all the drain valves	C	In-House
Replacing measuring valves on 12 , 25, 26 , 28 wells	C	In-House
Cleaning the drain pots and valves	C	OS (MC)

Maintenance outage schedule of the power plant - August 2015	**Type of maintenance: Corrective(C) preventive/ predictive (P)**	**Contractor**
Camera inspection of the pipelines(decide which pipelines should be inspected)	P	OS (Camera & Vacuum)
Changing the surface material (gravel) under the pipes outside separator station	C	OS
Separator station		
Cleaning main Separators	C	OS (C & V)
Examining all the measuring equipment and the water level controls of separator	P	In-House
Testing all the stop valves from the control room.	P	In-House
Cleaning steam trap in steam pressure control valves (in normal operation closed)	C	In-House
Cleaning diffuser in inlet of steam chimney next to separator station (downstream to pressure c.v.)	C	OS (MC)
Checking the condition of optical glasses and cleaning if necessary	P	OS (MC)
Checking and cleaning all check valves	P	OS (MC)
Repairing leak in steam pressure control	C	OS (MC)
Silencers – C valve house		
Empting water chamber from silencer, pump out the water with the diesel pump for cleaning	C	In-House
Inspecting valves in valve house	P	In-House
Checking butterfly valves ahead of the control valves in the valve house	P	In-House
Cleaning the nozzles on the silencer in the valve house	C	OS (Hydro-blasting)
Checking Thickness Measuring DN600 pipes in C valve house for corrosion from inside	P	OS (Crack Inspection)
Removing valve to the testing steam station and clean.	P	OS (MC)
Repair the end flange of the header from the base for the C valve house to the nozzles	C	OS (Metal Mac.)
Mixing vessel –D Valve house.		
Empty collection chamber with the diesel pump and well pump	P	In-House
Inspecting Valve house D	P	In-House
Examine butterfly valve in front of and behind the D - valve.	P	In-House
Cleaning the measuring pipe for connection pipes to pressure sensor	C	In-House
Inspecting outlet compartment D valve house	P	OS (MC)
Inspecting the reducer behind latter butterfly valve. (Cavitation)	P	OS (MC)
Reinjection		
Inspecting the check valve	P	OS (MC)
Removing butterfly valve for cleaning and examine pipelines from separator to mixing chambers	P	OS (MC)
Replacing ball valve for sampling	C	OS (MC)
Checking the control valve	P	OS (MC)

UNITED NATIONS UNIVERSITY
UNU-GTP
Geothermal Training Programme

Orkustofnun, Grensasvegur 9,
IS-108 Reykjavik, Iceland

Reports 2015
Number 32

SEISMIC MONITORING OF GEOTHERMAL FIELDS: A CASE STUDY OF HELLISHEIDI GEOTHERMAL FIELD

Shashika Amali Samaranayake
National Institute of Fundamental Studies
Hantana road, Kandy
SRI LANKA
samaranayakerusl@gmail.com

ABSTRACT

The study of induced seismicity in geothermal fields can be used to understand the physics of the ongoing processes in the reservoir. Microseismic activity in reservoirs can result from brittle deformation of reservoir rocks due to mass extraction and reinjection. Careful installation of monitoring stations is the initial step of all monitoring procedures. Information gained from seismic monitoring forms the basis of mitigating risk associated with induced seismicity. Mitigation procedures can be divided into three steps: understanding the background seismicity to identify whether events are natural or induced; install a permanent, stand-alone surface-based seismic network; and implement risk management procedures.

Seismic activity connected with reinjection of waste water at the Hellisheidi power plant is considered for this case study, and the seismic events recorded during a seismic swarm in 21 -22 April 2012 are analysed. Successful methodologies and processing methods that can be used to monitor geothermal field are discussed and compared with global scenarios.

1. INTRODUCTION

Geophysics is a branch of physics and one of the most powerful ways to explore the interior of the earth. It is an interdisciplinary science composed of physical principles that allow us to determine the physical contrast of formations and processes in the deep via remote sensing manners. Geophysics integrate the observations, hypotheses and theories of geology with the techniques and principles of physics to understand the composition, nature, structure and processes of the earth. There are many methods involved in geophysical exploration and the techniques differ with the objective.

Geophysical methods are widely used in geothermal resource exploration and monitoring. It provides basic information about the reservoir and necessary information to demarcate the resource periphery. Magnetotellurics (MT), Time Domain Electromagnetics (TDEM), gravity and magnetic techniques are prominent in geothermal exploration and seismic methods are mostly involved in the monitoring stage. Large scale mass extraction for a long time period can lead to internal changes of the subsurface and continuous monitoring of the reservoirs and its vicinity becomes inevitable (Evans et al., 2011). Fluid re-injection has been introduced for mass balancing, preventing possible subsidence at extraction sites

and recharging the geothermal system (Halldórsson et al., 2012). These measures can induce or trigger microseismic activity at the geothermal sites, causing concern among people living in the vicinity.

Nowadays, studies on induced seismicity are one of the major topics in the geothermal field because of the public concerns (Halldórsson et al., 2012). Induced seismicity can be defined as earthquake activity resulting from human activity that causes a rate of energy release, or seismicity recorded beyond its normal level. A number of activities can cause induced seismicity. It is common in relation with production in geothermal fields, in connection with reservoir impoundment, waste injection and oil and gas exploration. The seismicity is thought to take place when the effective stress is decreased so that the rock can no longer withhold the stress and it is released in an earthquake. The effective stress can either be reduced by increasing the pore pressure or decreasing the surrounding stress. Hydraulic fracturing is also associated with induced seismicity. In that case water is injected into the sub surface under high pressure, creating new fractures effectively linking existing fractures together. This activity creates additional permeability in the subsurface (LBNL, 2015).

There are global examples where public objections against induced seismicity have either delayed, altered or altogether cancelled proposed geothermal projects (Evans et al., 2011). Therefore, induced seismicity is an important and practical issue that should be handled very carefully when developing geothermal projects (Halldórsson et al., 2012). Icelandic induced seismic activities are not normally considered as risk elements and are focused on widening the micro fractures to enhance the effective permeability (Gunnarsson et al., 2015). Continuous and thorough monitoring of seismicity assists in making decisions, in order to avoid negative side-effects and possible risks on the community due to induced seismicity. It is important to follow an appropriate methodology to obtain a clear picture of subsurface processes. The methodology proposed here is location specific, yet with common features and infrastructure that can be applied in any area.

2. OBJECTIVE

Detecting underground fractures is very important for geothermal reservoir exploration and micro earthquakes are very good indications for the existence of such fractures. Many developing geothermal fields maintain a small earthquake monitoring system, but the systems are not fully used for geothermal exploration. The main objective of this study is to discuss the procedures of installing, maintaining, acquiring and processing seismic data for sustainable maintenance of geothermal resources. A case study was done in the Húsmúli area in Iceland which relates to one of Iceland´s largest high-temperature geothermal fields and the largest power plant.

3. BACKGROUND OF CASE STUDY AREA

The Hellisheidi field is located in the southern part of the Hengill volcanic system and is a naturally seismic area. The area is characterized by NE-SW oriented fissure swarms and hyaloclastite formations as shown in Figure 1. The geothermal system in Hellisheidi is located in fractured bedrock. The Hellisheidi power plant started operations in 2006 and has a 303 MWe installed electrical capacity and a thermal capacity of 133 MWth, which is utilized for district heating. The major challenge of the power plant operation is re-injection, since injecting all the brine into the geothermal reservoir is a primary requirement and a legal obligation. This is quite difficult because of the temperature dependant performance of the injection wells and the increased level of seismicity immediately following the start of re-injection. (Gunnarsson, 2013). Hellisheidi power plant has two re-injection zones. The previous zone was at Gráuhnúkar, situated on the southern edge of the Hellisheidi geothermal field. Gráuhnúkar has a very high formation temperature and it has been suggested as a possible production zone. The current injection site is at Húsmúli at the northern edge of the field. It has a comparably low formation

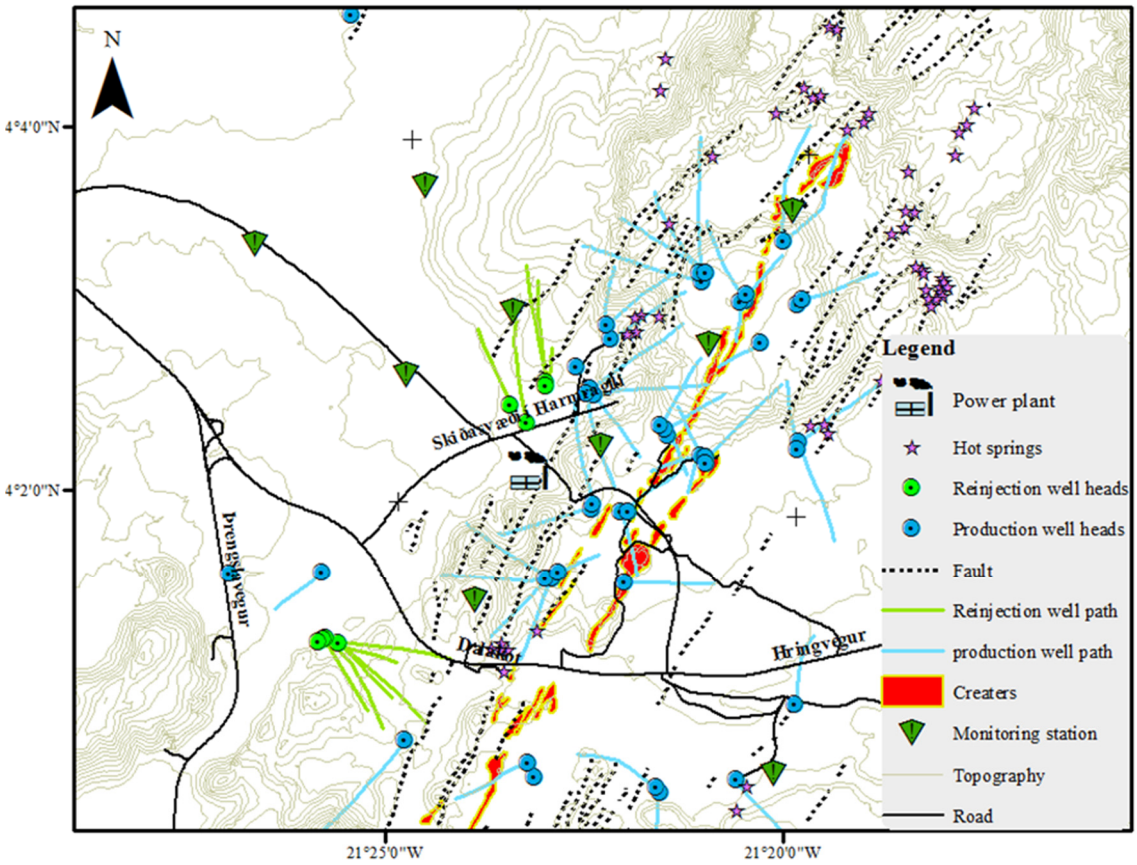

FIGURE 1: Topographical map of the Hellisheidi geothermal field with related faults, craters, surface manifestations, production wells, injection wells and seismic monitoring stations

temperature and the zone re-injectivity depends on the re-injection temperature. The injectivity at Húsmúli is higher for cold water, which can be explained by the changing aperture of fractures due to thermal expansion and contraction, which has a major effect on permeability and outweighs the effects of viscosity. It can be described simply as fracture-dominated permeability. Seven wells have been drilled in the Húsmúli zone. Five directional wells are used as re-injection wells, one is impermeable and one shallow well is used as an observation well. The drilling targets of the Húsmúli re-injection wells are the fault zones associated with the Húsmúli area. Re-injection was started in September 2011 and was followed by a swarm of induced seismicity culminating in two ~4.0 M events on October 15th, 2011 (Gunnarsson et al., 2015). This was an unexpected situation but as proposed the seismicity gradually decreased with continued operations. The decrease of seismic activity with time can be explained by the release of natural stress built up in the crust due to crustal movements.

Most mapped faults in the Hengill formation follow a NE-SW direction and are normal faults. There are some N-S trending faults recorded in post seismic monitoring and it has been suggested that there is a relationship between those faults and the South Iceland Seismic Zone (SISZ). N-S trending faults with a strike-slip behaviour are a typical feature of the SISZ (Gunnarsson et al., 2015) and the Hengill formation marks the western boundary of the SISZ.

A local seismic network was operated in the Hengill area by Uppsala University, MIT and ISOR during the induced seismic activities following the reinjection in Húsmúli. It was a part of a larger network operated from 2009 to 2013 ranging from the western part of the Reykjanes Peninsula to the eastern part of the Hengill volcanic system. Currently the closest station is ~10 km away. It is a part the Icelandic Meteorological Office's regional network.

4. THEORY

4.1 Elasticity and seismic wave

Earthquake seismology is a subject that evaluates ground motion produced by an energy source within the earth. In this case it is assumed that the ground returns to its initial position except at the vicinity of the source. This type of vibrations leads to small scale elastic deformations or strains in response to the initial forces in the rock or *stresses*. Using the theory of elasticity, we can explain the behaviour of earthquake waves mathematically. Energy that originates from an earthquake travels through the medium as different kinds of waves, mainly as body waves and surface waves. There are two kinds of body waves, called P waves and S waves. P waves involve compressional motion and volumetric changes as the wave disturbances passes through the continuum. S waves involve shearing motions without volume change (see Figure 2).

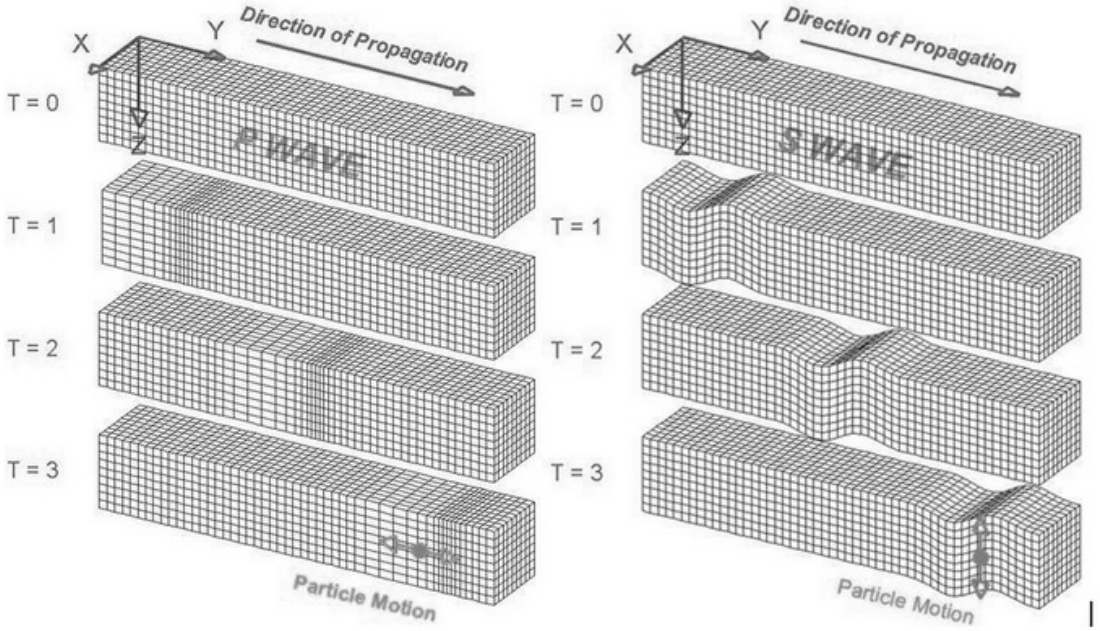

FIGURE 2: P and S wave propagation. (Seale et al., 2011)

Helmholtz's theorem can be used to derive mathematical equations for P and S waves. It states that any vector field $\boldsymbol{U}$ can be represented in terms of a vector potential $\boldsymbol{\Psi}$ and a scalar potential ϕ by,

$$\boldsymbol{U} = \boldsymbol{\nabla}\phi + \boldsymbol{\nabla} \times \boldsymbol{\Psi} \tag{1}$$

where $\boldsymbol{\nabla} \cdot \phi$ = Curl free scalar potential field $(\boldsymbol{\nabla} \times \phi = 0)$ for non-shearing motion; and
$\boldsymbol{\nabla} \times \boldsymbol{\Psi}$ = Divergence less vector potential field $(\boldsymbol{\nabla} \cdot \boldsymbol{\Psi} = \boldsymbol{0})$ involves no changes in volume.

Equation of a motion gives force balance on a cubic element in a continuum that is undergoing internal motions:

$$\rho\left(\frac{\partial^2 u_i}{\partial t^2}\right) = f_i + \frac{\partial \sigma_{ij}}{\partial x_j} \tag{2}$$

where, ρ = Density of the continuum;
u = Displacement;
f_i = Component of body force per unit volume;
σ_{ij} = Stress component;
i - Corresponds to the direction normal to the plane being acted on force;

j - Direction of the force.

When no body-forces are considered, we get the homogeneous equation of motion as follows:

$$\rho\left(\frac{\partial^2 u_i}{\partial t^2}\right) = \frac{\partial \sigma_{ij}}{\partial x_j} \tag{3}$$

The most general form of a constitutive law for linear elasticity is Hooke's law. It states that the stress and strain are linearly related and is given by:

$$\sigma_{ij} = C_{ijkl}\varepsilon_{kl} \tag{4}$$

where C_{ijkl} = Elastic moduli defining the material properties of the medium;
ε_{kl} = Strain tensor.

The elastic properties for many materials and material composites in the Earth are independent of direction or orientation of the sample. Isotropic elastic substances have only two independent elastic moduli called the Lamé constants, λ and μ. The relationship between those and Hooke's law is given by:

$$\sigma_{ii} = \lambda\theta + 2\mu\varepsilon_{ii} \text{ (Figure 3)}$$
$$\sigma_{ij} = 2\mu\varepsilon_{ij} \tag{5}$$

where θ = Trace of the strain tensor:$\left(\frac{\partial u_1}{\partial x_1} + \frac{\partial u_2}{\partial x_2} + \frac{\partial u_3}{\partial 3}\right)$.

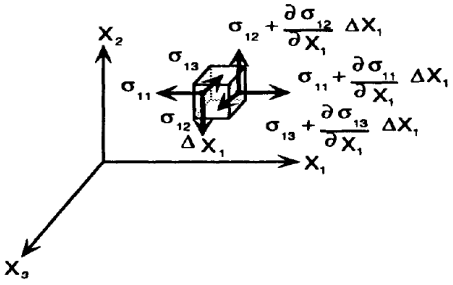

FIGURE 3: A cubic element in the continuum bounded by faces paralleling the coordinate planes. Balancing the stresses on each face acting in a given direction leads to the equation of equilibrium. Only the stresses acting on $\pm x_1$ face are shown. Similar stress terms act on the other four faces (Lay and Wallace, 1995)

This relationship gives following statements (Equation 6):

$$\sigma_{11} = \lambda\left(\frac{\partial u_1}{\partial x_1} + \frac{\partial u_2}{\partial x_2} + \frac{\partial u_3}{\partial 3}\right) + 2\mu\frac{\partial u_1}{\partial x_1}$$

$$\sigma_{12} = 2\mu\varepsilon_{12} = \mu\left(\frac{\partial u_1}{\partial x_2} + \frac{\partial u_2}{\partial x_1}\right) \tag{6A}$$

$$\sigma_{13} = \mu\left(\frac{\partial u_1}{\partial x_3} + \frac{\partial u_3}{\partial x_1}\right)$$

where angular distortion between segments in the x_1 and x_2 directions gave:

$$\varepsilon_{12} = \frac{1}{2}\left(\frac{\partial u_1}{\partial x_2} + \frac{\partial u_2}{\partial x_1}\right) \tag{6B}$$

Using the above relationships in Equation 3 we can rewrite things as follows:

$$\rho\left(\frac{\partial^2 u_i}{\partial t^2}\right) = \lambda\frac{\partial\theta}{\partial x_i} + \mu\frac{\partial}{\partial x_i}\left(\frac{\partial u_1}{\partial x_1} + \frac{\partial u_2}{\partial x_2} + \frac{\partial u_3}{\partial x_3}\right) + \mu\left(\frac{\partial^2 u_i}{\partial x_1^2} + \frac{\partial^2 u_i}{\partial x_2^2} + \frac{\partial^2 u_i}{\partial x_3^2}\right) \text{ or}$$
$$\rho\left(\frac{\partial^2 u_i}{\partial t^2}\right) = (\lambda + \mu)\frac{\partial\theta}{\partial x_i} + \mu\nabla^2 u_i \tag{7}$$

We can write all three components of above equations in the equivalent vector format as follows:

$$\rho\ddot{\boldsymbol{u}} = (\lambda + \mu)\boldsymbol{\nabla}(\boldsymbol{\nabla}\cdot\boldsymbol{u}) + \mu\nabla^2\boldsymbol{u} \tag{8}$$

Using the vector identity:

$$\nabla^2 \boldsymbol{u} = \boldsymbol{\nabla}(\boldsymbol{\nabla} \cdot \boldsymbol{u}) - (\boldsymbol{\nabla} \times \boldsymbol{\nabla} \times \boldsymbol{u}) \tag{9}$$

we can rewrite Equation 8 as follows:

$$\rho \ddot{\boldsymbol{u}} = (\lambda + 2\mu)\boldsymbol{\nabla}(\boldsymbol{\nabla} \cdot \boldsymbol{u}) - (\mu \boldsymbol{\nabla} \times \boldsymbol{\nabla} \times \boldsymbol{u}) \tag{10}$$

Substituting Equation 1 in to Equation 10, we get;

$$\boldsymbol{\nabla} \underbrace{\left[(\lambda + 2\mu)\nabla^2 \phi - \rho \ddot{\phi}\right]}_{0} + \boldsymbol{\nabla} \times \underbrace{\left[\mu \nabla^2 \boldsymbol{\Psi} - \rho \ddot{\boldsymbol{\Psi}}\right]}_{0} = \boldsymbol{0} \tag{11}$$

which can be satisfied if each term in the brackets goes to zero as indicated:

$$\begin{aligned} &\textbf{(i)} \quad \left[(\lambda + 2\mu)\nabla^2 \phi - \rho \ddot{\phi}\right] = 0; \text{ Scalar wave equation} \\ &\nabla^2 \phi - \frac{1}{\alpha^2} \ddot{\phi} = 0; \alpha = \sqrt{\frac{\lambda + 2\mu}{\rho}} \text{ (P wave velocity)} \\ &\textbf{(ii)} \quad \left[\mu \nabla^2 \boldsymbol{\Psi} - \rho \ddot{\boldsymbol{\Psi}}\right] = 0; \text{ Vector wave equation} \\ &\nabla^2 \boldsymbol{\Psi} - \frac{1}{\beta^2} \ddot{\boldsymbol{\Psi}} = 0; \beta = \sqrt{\frac{\mu}{\rho}} \text{ (S wave velocity)} \end{aligned} \tag{12}$$

For most materials both λ and μ are positive, therefore α is always higher than β and the P wave is always the first wave arriving from an earthquake.

4.2 Data processing

The primary objective of observational seismology is to locate seismic sources. The hypocentre and the source origin-time are the parameters which need to be solved for in seismic processing. The major factors that are required to determine the origin of an earthquake are the identification of seismic phases, measuring their travel time, and the velocity structure between source and seismic station. Both forward and inverse modelling can be used to solve the seismic problem addressing the above parameters (see Figure 4). Inverse modelling is the most used method for processing seismic data as well as other geophysical data.

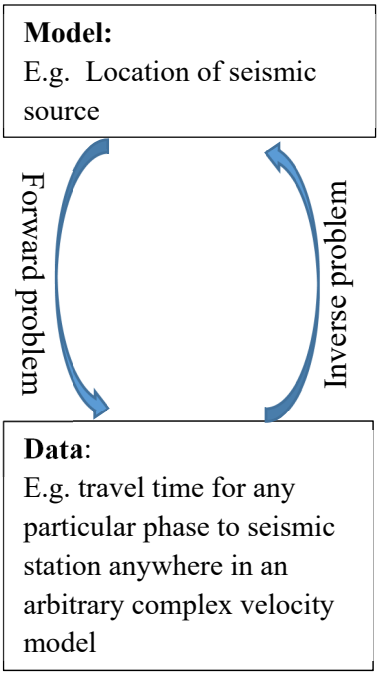

FIGURE 4: Forward and inverse problem

4.2.1 Forward algorithm

The number of stations that collect raw data for an event is a crucial factor to locate seismic activity accurately. In theory, even a single station is adequate to locate an earthquake, however, practically only a very crude estimation can be obtained. When several stations are available, an accurate location can be determined by using P and/or S wave arrival times. If the event is local, close to the stations, the two principle phases on the seismogram are P and S. The Wadati diagram is a technique that is used to find the origin time of the earthquake (Figure 5). In this case, time difference between S and P waves (t_s-t_p) are plotted against the absolute arrival time of the P wave. Since (t_s-t_p) goes to zero at the hypocentre, a straight line fit on Wadati diagram provides an approximate origin time (T_{origin}) of the event (Lay and Wallace, 1995).

4.2.2 Calculation of epicentre of the event by graphical method

It is possible to calculate the P wave travel time by using T_{origin} and the P travel time of the ith station. By using the P wave travel time and the P wave velocity (α), the epicentral distance for the ith station (D_i) can be easily calculated.

$$D_{focal} = \sqrt{D_i^2 - D_{prop.}^2} \tag{13}$$

A possible location of the earthquake lies on the circumference of circle with the radius D_i. The epicentre should be located at the intersection of circles drawn for each station. The focal depth $D_{focal,}$ according to the ith station, can be determined by Equation 13, where $D_{prop.}$ is the distance along the surface to the epicentre.

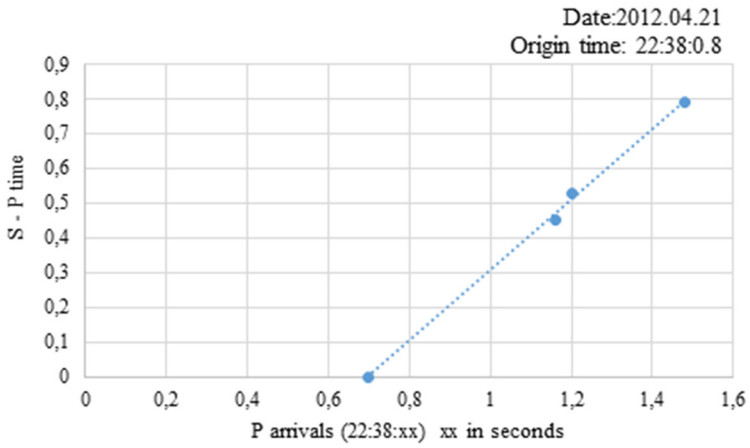

FIGURE 5: An example of the Wadati diagram method for determining the origin time. The intersection with the P wave arrival time axis gives the origin time (event related in case study site)

More observations always make complications, since they give more intersections. Our primary target is to determine four unknowns: X, Y, Z and origin time. We can assume a solution and calculate expected P-wave arrival times. Comparing this prediction with the real observation, the difference between calculated and observed arrival times can be determined. Shifting predicted parameters according to the deviations, a new model can be recalculated with an improvement. The procedure continues until an acceptable difference between calculated and observed arrivals are obtained. This is the procedure of forward modelling.

4.2.3 Inverse modelling

The model data that is approximately similar to the observed data can be mathematically described as follows. Introduce function *f*, which calculates the arrival time as a function of location (x_i, y_i, z_i) and velocity (v):

$$t_{i(predicted)} = f(x_i, y_i, z_i, v) = t_{i(observed)} \tag{14}$$

If we have n number of stations, our data (observation) vector is $\boldsymbol{d} = (t_1, t_2, \dots, t_i, \dots, t_n)$ where t_i is observed P arrival time on the ith station. The model parameters come in vector $\boldsymbol{m}$ and it has four components for location and origin time:

$$\boldsymbol{m} = \left(x, y, z, t_{i(predicted)}\right) \tag{15}$$

$$\overline{\boldsymbol{F}}(\boldsymbol{m}) = \boldsymbol{d} \tag{16}$$

$\overline{\boldsymbol{F}}$ is a matrix called the data kernel.

If we can divide $\overline{\boldsymbol{F}}(\boldsymbol{m}) = \boldsymbol{d}$, by some operator $\overline{\boldsymbol{F}}^{-1}$ to give $\boldsymbol{m}$ directly, we are solving the problem inversely. In a homogeneous half space, consider the Cartesian coordinates of the true hypocentre (x, y, z) and the coordinates of the ith station (x_i, y_i, z_i). Then the arrival time of the ith station can be written as follows:

$$t_i = t_{origin} + \frac{\sqrt{(x_i - x)^2 + (y_i - y)^2 + (z_i - z)^2}}{v} \quad (17)$$

where t_i = Arrival time of the i[th] station;
v = Velocity.

Ideally, only one unique set of parameters fits with the observed values. According to $\overline{\boldsymbol{F}}(\boldsymbol{m}) = \boldsymbol{d}$, we can write $\overline{\boldsymbol{F}}(x, y, z, t) = \boldsymbol{d}$. The equation for $\boldsymbol{d}$ is nonlinear, so we must linearize the problem and iteratively improve the solution (model parameters). This can be done with a Taylor series approximation. This links the needed changes in hypocentral location with the difference in observed and predicted travel time. We define the partial derivative matrix of our problem as G_{ij} with respect to the i^{th} station's j^{th} model parameter as:

$$G_{ij} = \frac{\partial d_i}{\partial m_j} \quad (18)$$

Then we can rewrite our problem as $\Delta\boldsymbol{d} = \boldsymbol{G}\Delta\boldsymbol{m}$ or $\boldsymbol{d} = \boldsymbol{G}\boldsymbol{m}$. This is the linearized form of the problem. If we have 4 stations we have $\boldsymbol{n}=\boldsymbol{m}$ type problem and Gaussian elimination can be used to solve it. Once $\delta x, \delta y, \delta z$ and δt are calculated, we can modify the parameters using the equation $m_j^1 = m_j^0 + \delta m_j^0$. This iterative process can be continued until $\Delta\boldsymbol{d}$ becomes acceptably small. This method is known as Geiger's method. Its disadvantages are that the final model totally depends on the initial guess and the process does not guarantee convergence (Lay and Wallace, 1995).

$\boldsymbol{d} = \boldsymbol{G}\boldsymbol{m}$ gives $\boldsymbol{G}^{-1}\boldsymbol{d} = \boldsymbol{m}$.

Solution of this equation is quite easy. However, as seismology data has several errors and the velocity model can be changed, it means the equations are inconsistent making it impossible for us to use this simple equation. With many observations ($\boldsymbol{n}>\boldsymbol{m}$), as in the case of earthquake location problems, we can obtain an overdetermined solution, which is the best fit to an average of the data.

4.3 Theory of induced seismicity

Induced seismicity is earthquake activity resulting from human activity that causes an increased rate of energy release, or seismicity, which exceeds the normal level of background seismic activity. In order to discern the induced seismicity from the natural seismicity, surveys of the regional background activity should be conducted before operations are started. Berlin in El Salvador, is a good example of a geothermal field with high levels of recorded background seismicity (Majer et al., 2007).

Induced seismicity has been recorded in a number of operating geothermal fields worldwide. In most of these cases thousands of small events have been recorded annually (Majer et al., 2007). Drilling, mass extraction and reinjection are all capable of inducing seismicity in the related area. Notable cases are: Rangely, CO, injection experiments (M4.9, 1995), 1945-1995; Rocky Mountain Arsenal (M5.3, 1967), fluid injection; Gazli, Uzbekistan, gas recovery (M7.2), 1976-1984; Lake Mead (M5), reservoir impoundment; Geysers geothermal field (M4.6), injection-enhanced production; Youngstown, Ohio (M4.0), fluid injection, 2011. It is important to identify the causes of the induced seismicity to be able to take precautions for the future sustainability of the project.

There are several different mechanisms that have been proposed to explain the occurrence of induced seismicity in geothermal areas (See Figure 6). Stress is the major factor that affects induced seismicity. Some of the major mechanisms of induced seismicity in geothermal environments are categorized as follows (Majer et al., 2007):

1. Pore pressure increase

Increased fluid pressure can decrease static friction and facilitate seismic slip in the presence of a deviatoric stress field. Sometimes seismicity is driven by the local stress field, but triggered on an

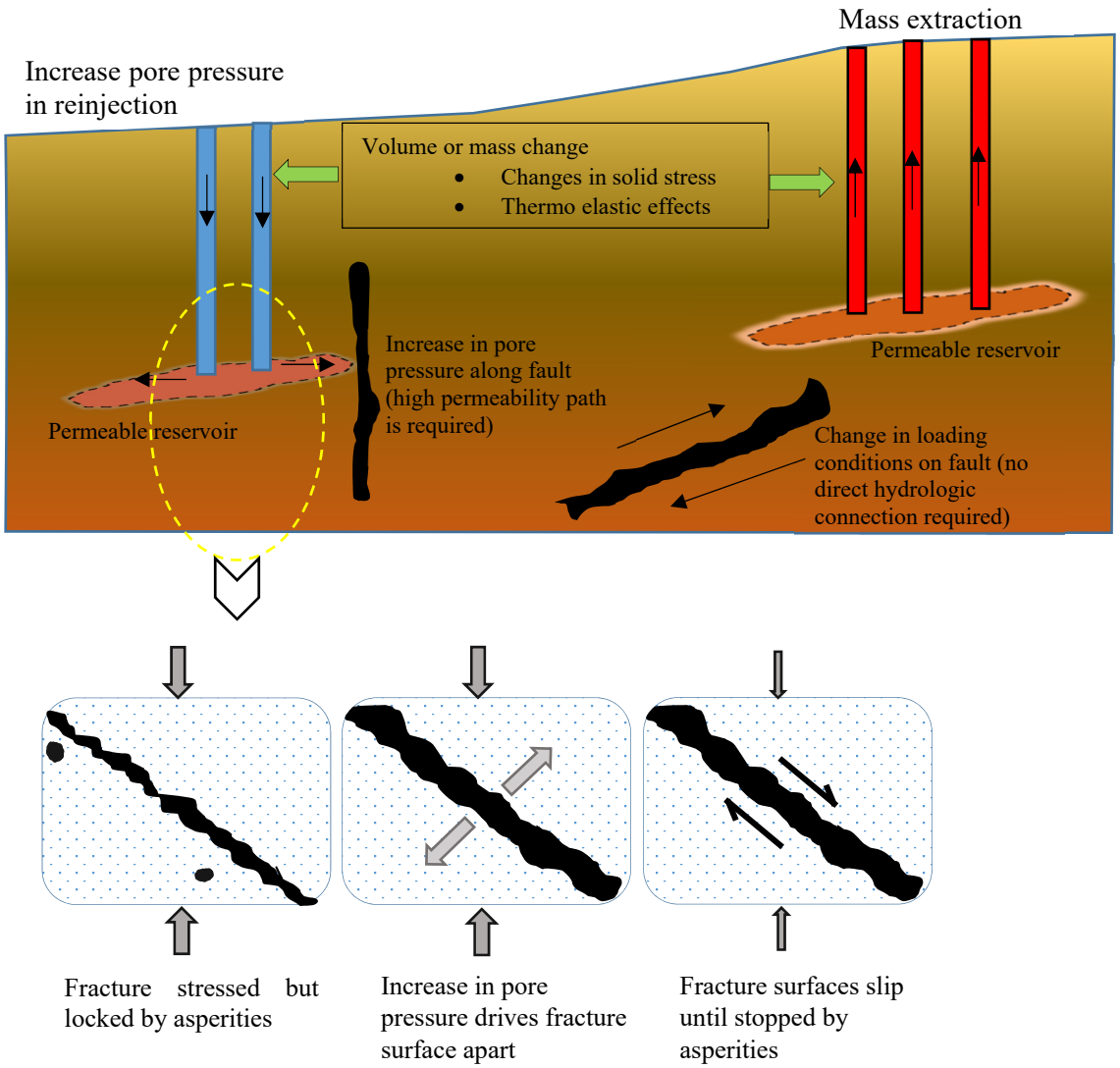

FIGURE 6: Earthquake course explained by mass extraction and re injection (after Nordquist (2005) and Ellsworth (2013))

existing fracture by increasing pore pressure. The pore pressure increase required can in some cases be very low. Many seismic events occur as the pressure migrates away from the wellbore in the direction of principle stress. Fluid injection in geothermal fields obviously increases the pore pressure in that area, resulting in high seismic activity around the injection well, provided that there are local regions of low permeability. High-pressure fluid injection can exceed the rock strength and create new fractures in the rocks (Majer et al., 2007).

2. Temperature decrease

When cool fluid is injected into the sub surface it interacts with the hot rock which can cause contraction of the fracture surface. Cool fluid and hot rock interaction can also create fractures and seismicity directly with the thermal contraction (Majer et al., 2007).

3. Volume change due to mass extraction and reinjection

Fluid level changes (reduction or increase) will affect the reservoir rock. It can compact or be stressed. The volume changes cause a perturbation in the local stress conditions, which can lead to a slip on a fault that is close to failure. This is common in geothermal fields as they are often situated within faulted regions under high stress, and will cause a seismic slip within or around the reservoir (Majer et al.,2007).

4. Chemical alteration of fracture surfaces

Injecting non-native fluid can change the chemical composition in the reinjection area. It may cause geochemical alteration of fracture surfaces and cause a change in the coefficient of friction on those surfaces (Majer et al., 2007). One or more of the phenomenon mentioned above can be involved in the onset of earthquakes.

5. METHODOLOGY

5.1 Seismographs

Seismographs are generally composed of two major components: A sensor to measure the ground motion, known as a seismometer, and a recording system. Most seismometers are three-component devices that measure the ground motion along three orthogonal directions. These components are normally aligned to N-S, E-W (horizontal plane) and vertical directions. Modern seismometers can be categorized according to their dynamic range. *Long period seismometers* record very low frequencies and are usually designed to measure seismic signals with frequencies in the range 0.01 Hz - 0.10 Hz. *Short period seismometers* have a very short natural period and a correspondingly high resonant frequency which is higher than most frequencies of a seismic wave. They are usually designed to respond to frequencies in the range of 1 Hz-10 Hz. *Broadband seismometers* are highly sensitive over a wide range, typically between 0.1 Hz and 50 Hz.

Selecting a proper frequency range is very important for successful data gathering and achieving objective(s). In geothermal monitoring, the expected signal has a high frequency. Therefore, seismometers with dynamic range of 1-10 Hz (short period seismometers) are in order. To be able to detect the low magnitude events some magnification might be necessary in the digitizer (recording system).

5.2 Deployment of seismometers

When deploying seismic stations, we must consider the number of required stations, distance to expected activity and coverage angle of the network. The deployment has to be thoroughly planned to ensure the detection of possible unrest due to geothermal related activities. The geology of the area is one of the prime concerns in selecting locations for seismometers in close proximity to the production and re-injection wells. During the drilling period additional seismic stations may add to the system to detect possible induced seismicity changes due to drilling operations. Before deploying the seismometer, we should have a good idea of the target event area. Figure 7 shows a seismometer network and two seismic events, A and B. Both events are covered by the same number of stations. However, event B is detected by stations covering a 360° angle around the event while event A is only covered by stations on one side. Azimuthal coverage greatly influences the location accuracy of seismic events. Installing a station close to the epicentre can greatly improve the determination of depth.

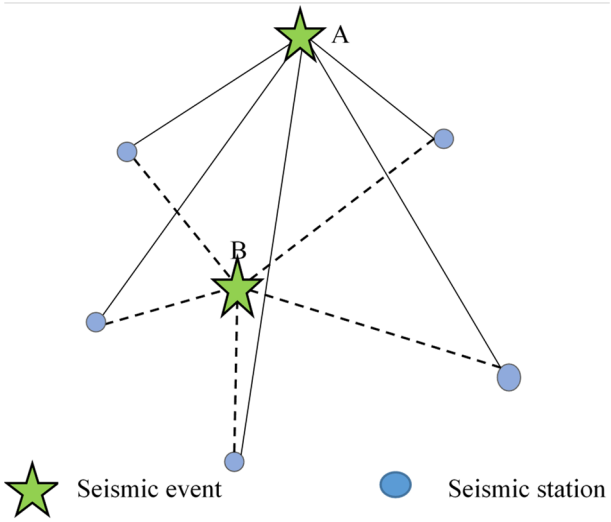

FIGURE 7: Simulated seismic array for detecting earthquakes

5.3 Installation of a seismic station

The classification of seismometers additionally depends on the environment in which they are deployed. Two major types of classifications are inland and ocean bottom seismometers. The installation procedures of these two types are quite different.

5.3.1 Inland seismometer

Inland seismometers are the most available type and simpler to deploy. They can either be a part of a real time monitoring system or a post processing system. Initial procedures are identical for the two systems and additional components are added to the real time monitoring system. Environmental factors are of great importance in the installation of a seismic station. The sensor needs to be well protected from environmental noise, such as temperature fluctuation, turbulent air flow around walls and human activity. This can be done by selecting a suitable site, and placing the sensor in a protective enclosure. For the best possible results, a seismometer should be installed in a specially built vault, where conditions are near perfect. Different kinds of techniques are used to achieve this near perfect status. Some of them are:

- Standing the sensor on a concrete cylinder which is perfectly coupled to solid bed rock;
- Use only a little extra mass to create the concrete cylinder;
- Use rock wool or other insulators for insulation;
- Shield from wind and rain;
- Isolate area from human activity etc.;
- Suitable distance from sensor to mast;
- Clearing the floor of the hole of all loose material.

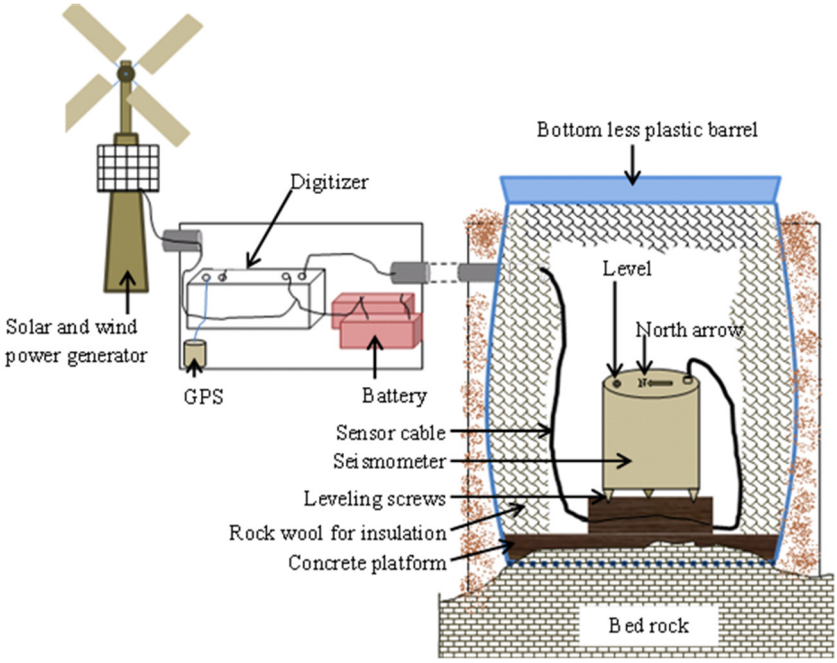

FIGURE 8: Schematic diagram of an inland seismometer

The setup of a protective enclosure is the first step of installation, as described in Figure 8, as well as the whole system of an inland seismic station.

There are two factors that need to be considered when a sensor is installed in the protective enclosure: 1) align the sensor to true north, and 2) level the sensor. Optimally we should use a gyro compass to find true north, because it is not affected by the surrounding rock's magnetic properties (Figure 9). It is convenient to draw the N-S line in the surface of the concrete cylinder. Before placing the sensor on the line it is recommended to connect the cable, because once the sensor is

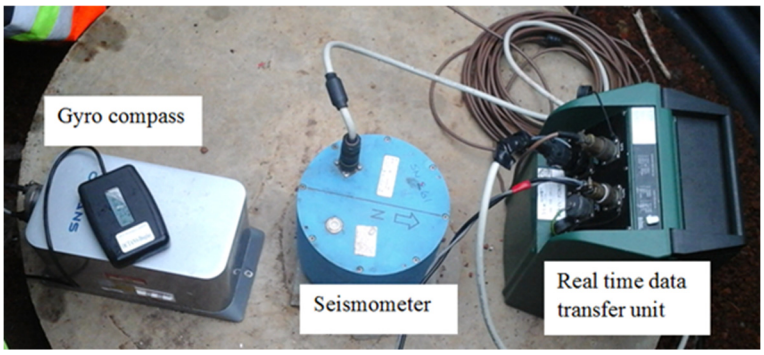

FIGURE 9: Setup of a gyro compass survey at Reykjanes peninsula

properly aligned, connecting cables may disrupt the sensor position. Then the sensor is placed on the line to align the sensor to the true north direction. To facilitate this, sensors often have a steel pointer on the instrument which shows the north axis of the sensor. Then the sensor is levelled by adjusting each of the three screws on the bottom of the instrument, until the bubble in the spirit level lies entirely within the inner circle (Figure 10). As the final step, the sensor is connected to the seismic recording system. There are different types of energy sources used for seismic stations, such as battery, solar power, wind power etc. In post processing systems, data is recorded on flash memory cards which are collected routinely. Real time monitoring systems data recorders are linked to a communication tower which transmits directly to the working station.

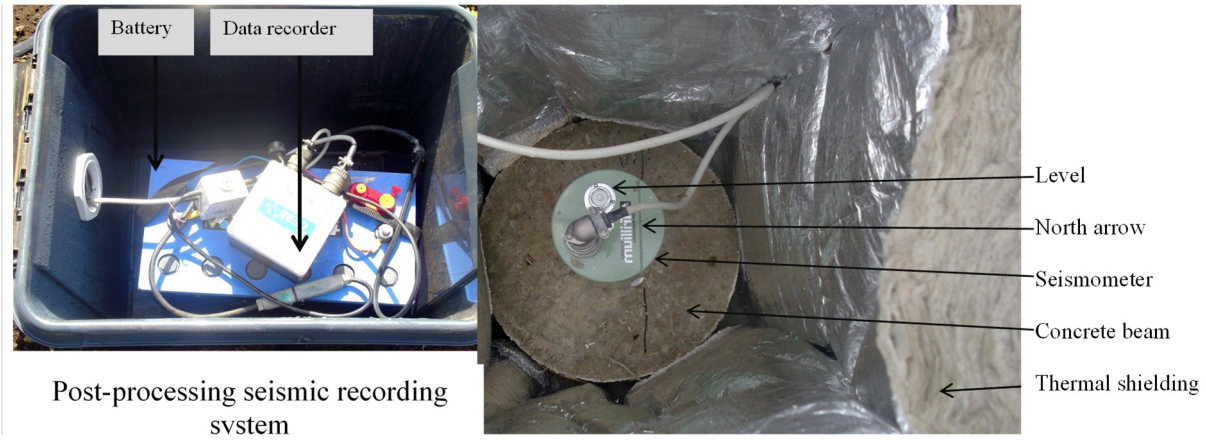

FIGURE 10: Parts of the seismic monitoring stations

5.3.2 Ocean bottom seismometers (OBS)

This is not a prominent method in geothermal projects; because most geothermal projects are away from the ocean and deploying procedures are very complicated. OBS record distant arrivals from large earthquakes and local swarms of smaller tremors. These arrivals can be used to provide information relating to the source mechanisms and subsurface structures, if enough stations record the arrivals. An OBS needs to be designed to be able to carry and deploy a heavy and large sensor package with a dynamic range of 0.01 Hz to about 30 Hz, and to operate autonomously for up to one year. Because of the longer deployment durations, a long-lasting internal clock is required with high precision for accurate time stamping of raw data.

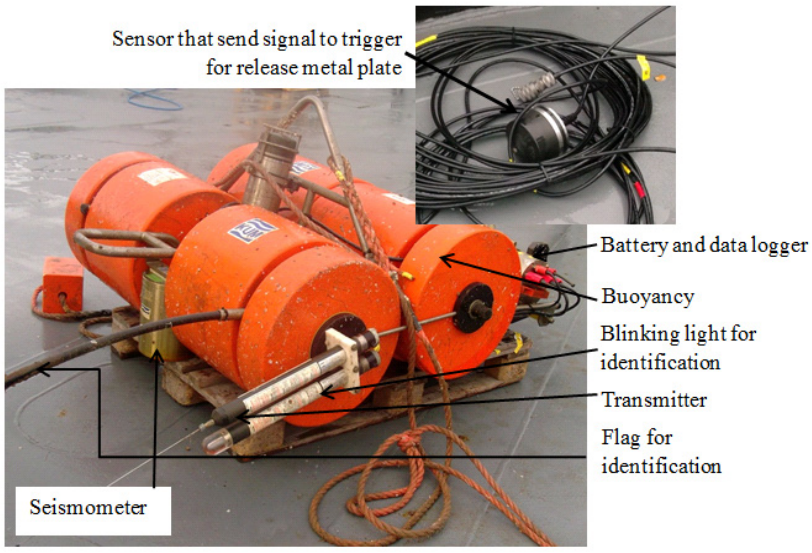

FIGURE 11: Ocean bottom seismometer

The advantage of OBSs for recording on the seabed rather than using towed arrays to record in the water column is that OBSs can record seabed shear waves directly as a vector using three component geophones, thus providing useful additional information for the interpretation process.

The major components of the OBS are shown in Figure 11. The system attaches to a heavy metal plate and is dropped to the sea bottom and

is retrieved after a specific period, most commonly one year. In the retrieval process, a trigger is used to detect the OBS system and a signal is sent to release the system from the attached platform, the metal plate. A buoyancy mechanism activates and the OBS is brought to the surface for safe retrieval.

There are several methods to determine the angle between the sensor north in the OBS and true north. One way is to take known large scale earthquakes within the measuring period and calculate the Rayleigh wave behaviour, enabling us to find the angle between sensor north and true north. Another technique is triggering a blast in a known location at known depth. The wave path of the incoming signals of the controlled source enables us to detect the angle. In the OBS data processing stage, waveforms are rotated by the angle obtained from the above methods.

5.4 Data processing

Several software has been developed to process passive seismic data in real time and post processing approaches. Some are developed with graphical user interfaces (GUI) to process data in an easy manner. In the study of Hellisheidi, a software called SeisComP3 (Seismological Communication Processor) was used, which was originally developed for the GEOFON program, and is maintained by the GEOFON software development group at GFZ Potsdam. This is an open source, freely available software and it consists of acquisition, picking and analysing facilities. The software can be configured to accommodate different projects and site characteristics, in order to locate earthquakes accurately and reliably.

Figure 12 explains the front page view of the software. The map (A) can be used to view the suspected area and enter the initial guess (location of the earthquake and origin time). After entering the initial guess, we can pick P and S waves.

Using the picking tool in the picker window shown in Figure 13, we can pick the P and S wave arrival times for all the stations within a certain distance. Available data are displayed in the bottom of the window. Depending on our objectives, we can apply different filters to enhance the signal. In the case study area, a 4-10 Hz bandpass filter was used. After picking all the stations, the data is sent to the locater and the main window appears. By returning to the main window, different methods and velocity models can be chosen to relocate the earthquake.

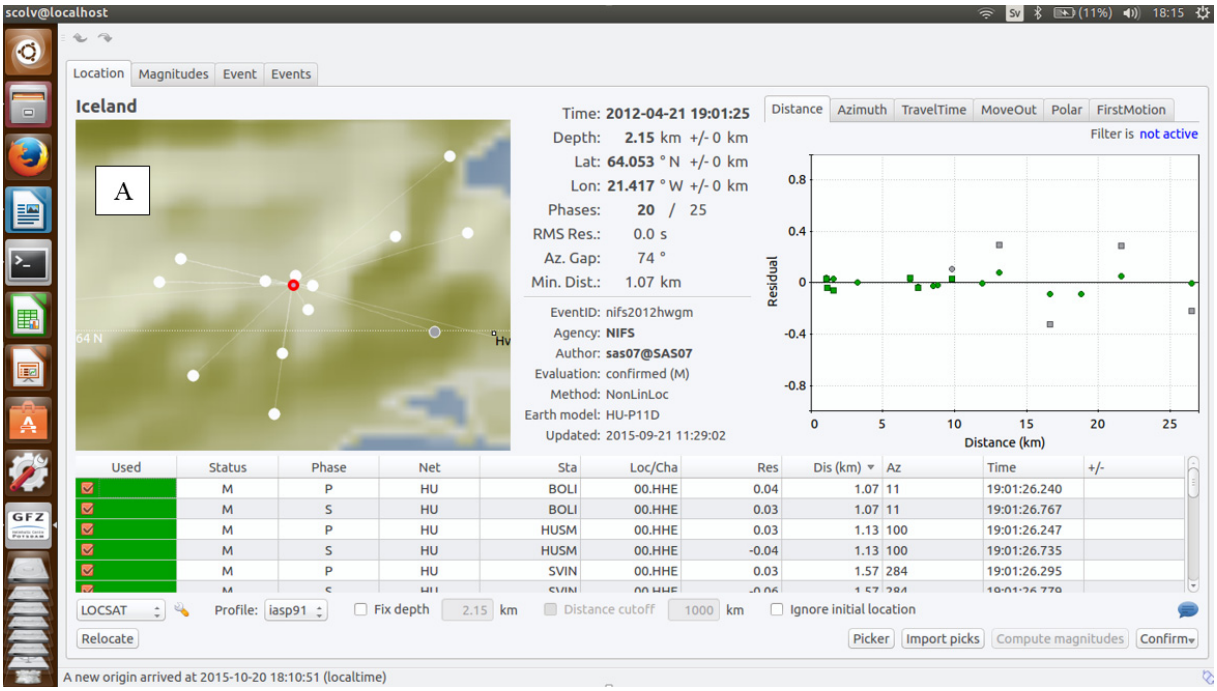

FIGURE 12: Front view of the SeisComP3 software

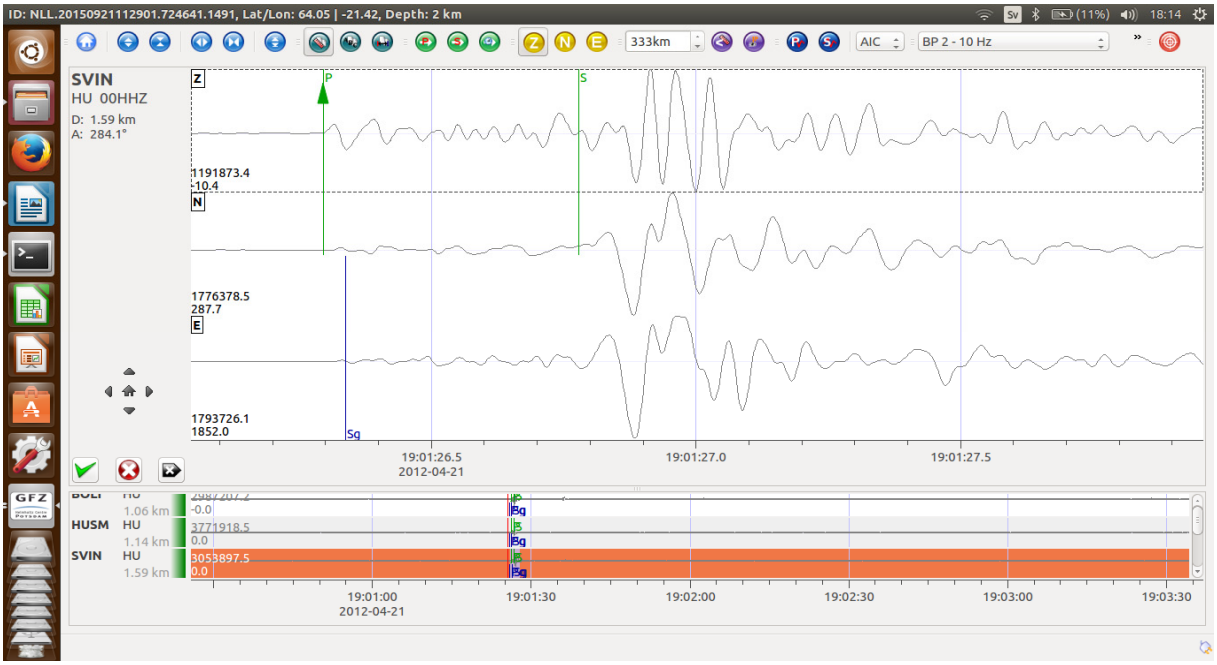

FIGURE 13: Picker window in the SeisComP3 software showing P and S waves from an event in Hellisheidi

5.5 Velocity model

The velocity model is one of the most important parts of processing passive seismic data. The accuracy of the location always depends on the accuracy of that model. Constructing velocity models is not an easy task. Data collected from vertical seismic profiling and drill holes are mainly used to construct the model. Depending on the data gathered, the velocity can be modelled as a 1D, 2D or 3D model. 1D models, in which the velocity changes only in the z direction and is constant in the X and Y directions, is the most available model. 2D and 3D models are more accurate than 1D, but are harder to obtain.

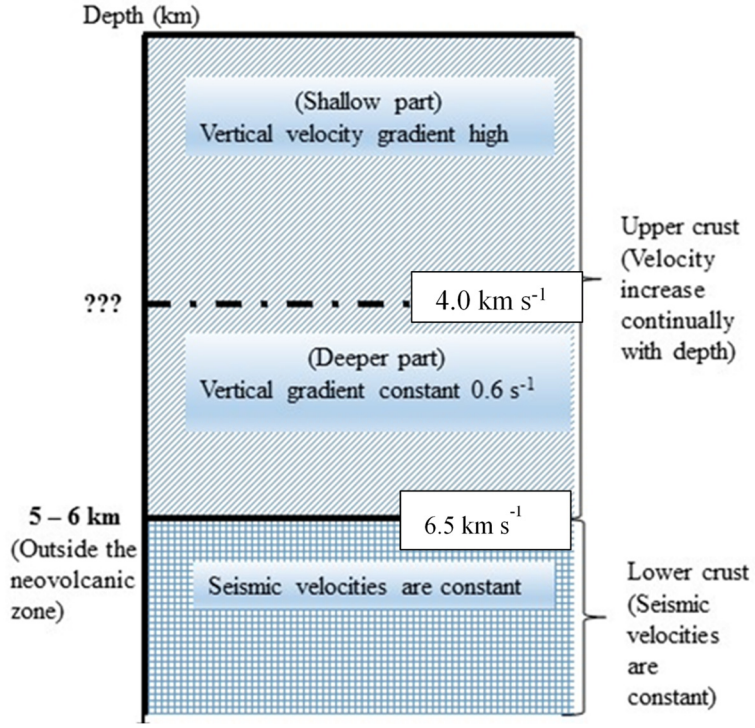

FIGURE 14: Icelandic crustal structure according to Flóvenz (1980)

5.5.1 Average one-dimensional crustal structure of Iceland

The general tomographic inversion of Iceland was done by Flóvenz in 1980 (Foulger and Toomey, 1989) and it represents the general velocity depth structure. In this structure the Icelandic crust is divided into two main divisions, upper crust and lower crust. Details of the velocity model interpretation can be seen in Figure 14. (Foulger and Toomey, 1989)

5.5.2 Velocity of the Hengill triple junction volcanic system

Three major principle high-velocity bodies are recognized in the Hengill area, which correlate with three extinct volcanic systems. These bodies can be explained as dense, intrusive, solidified, shallow crustal magma reservoirs. Grensdalur and Ölkelduháls are still hot and host the geothermal field while Húsmúli is cold.

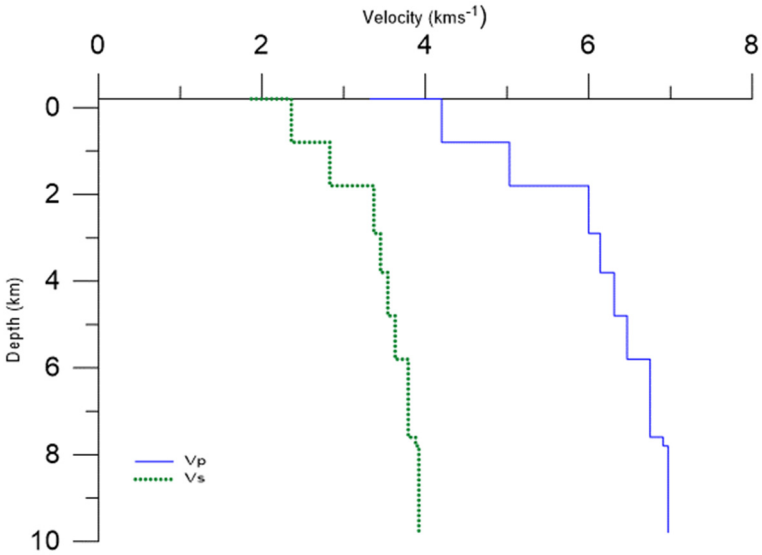

FIGURE 15: Velocity model used to process the Hellisheidi seismic data

The velocity model that we used for the Hellisheidi area is given in Figure 15. The density of the layers are constant in that model at 2.5 kg m^{-3}. P and S wave velocities that have significant difference and velocity changes are very small compared to depth. Locating earthquakes is a non-linear problem and inverse modelling is used to solve the problem. All these features are included in the NonLinLoc procedure, which is available as a plugin for the SeisComP3 software (Lomax, et al., 2015).

6. RESULTS AND DISCUSSION

6.1 Seismic monitoring in Hellisheidi area (Case study)

Waste water from the Hellisheidi power plant is reinjected into the system through wells in Húsmúli. It started in September 2011 and in the period of 2011-2012 a large number of induced earthquake activities were recorded in the area. One of the earthquake swarms recorded in that series was used to demonstrate the processing steps. The seismic events took place in Húsmúli in a two-day period in 2012, from April 21st to April 22nd. It was picked and located with the SeisComP3 software. The events had a magnitude range from -1 to 3, and the evolution of the swarm is shown in Figure 16. It follows a typical earthquake swarm behaviour. The activity started around 17:00 on the 21st April and reached a peak around midnight. After that it slowly decays until it fades out at midnight of 22nd April.

6.1.1 Event distribution and depth variation

Figure 17 shows the depth distribution of the seismic events located in the swarm. It shows that most of the events are in the range of 1.61-2.61 km. Figure 18 shows the seismic event density in map view and Figure 19 shows NS and EW profiles. It clearly shows that the recorded swarm delineates a N-S striking vertically dipping fault.

Figure 20 shows that the seismic events concentrate some distance from the reinjection zone. Figure 21 shows the overall seismic activities in that area in the 2011-2012 period and clearly shows that the activity moves westward with time, away from the injection site. It is one of the most interesting observations in the Húsmúli area.

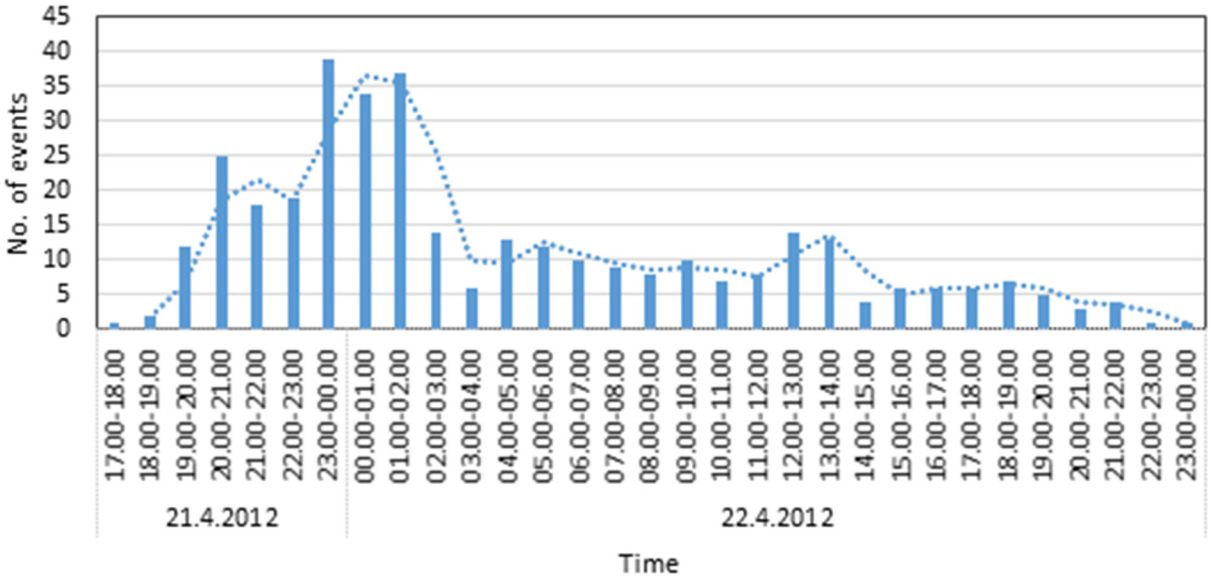

FIGURE 16: Frequency distribution of swarm

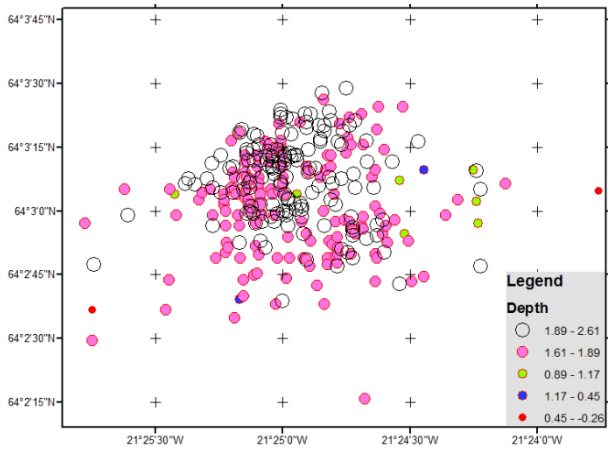

FIGURE 17: Events depth distribution in map view

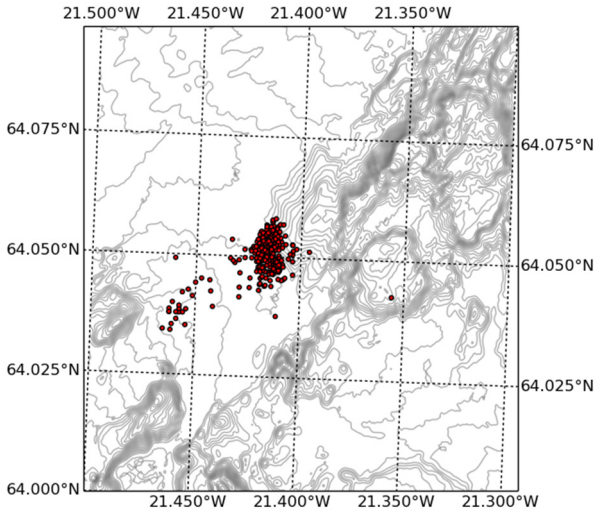

FIGURE 18: Event distribution of the located swarm, 360 earthquake events were located in the range of -1 to 3 M during 2012.04.21 – 2012.04.22

6.2 Review of seismic monitoring in geothermal projects in comparison with case study site

Learning from the mistakes and successes of past geothermal projects allows us to enhance the quality of the monitoring of our own projects. Here, world geothermal case histories will be compared with the Hellisheidi seismic monitoring.

According to environmental laws, geothermal power companies are obliged to reinject waste water back into the aquifer, below the ground water table. With injection comes a high probability of inducing seismic activity in the area. Long term monitoring is very important for identifying both prior and post states of the project area. The Geysers in northern California, USA, is a good case study for this point of view (Majer, 2007) (Figure 22). The area is one of the world's largest geothermal fields and can partly

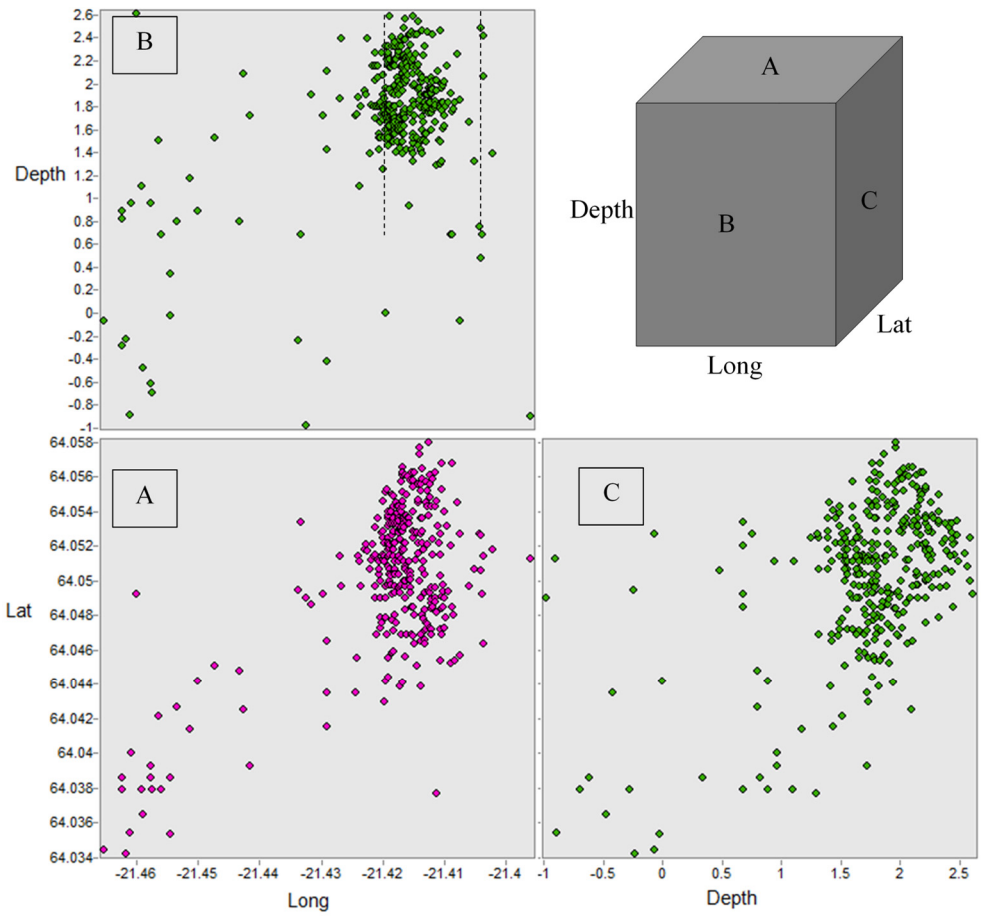

FIGURE 19: Cross-sectional view of the seismic activities; A) shows the seismicity as viewed from above, B) is an E-W cross-section and C) is a N-S cross-section

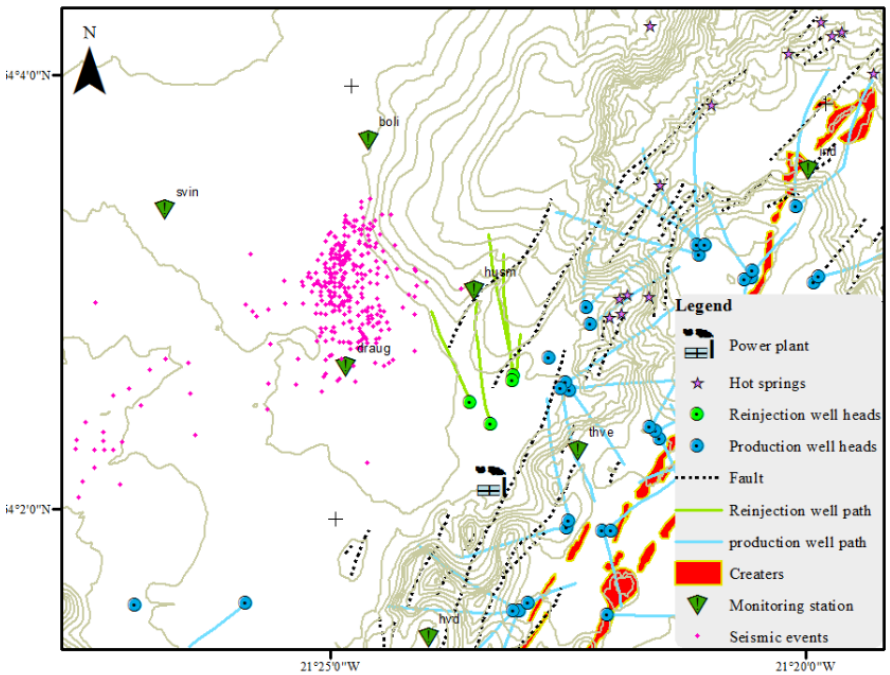

FIGURE 20: Location of the seismic swarm (pink diamonds) in relation with the location of the injection wells (green lines)

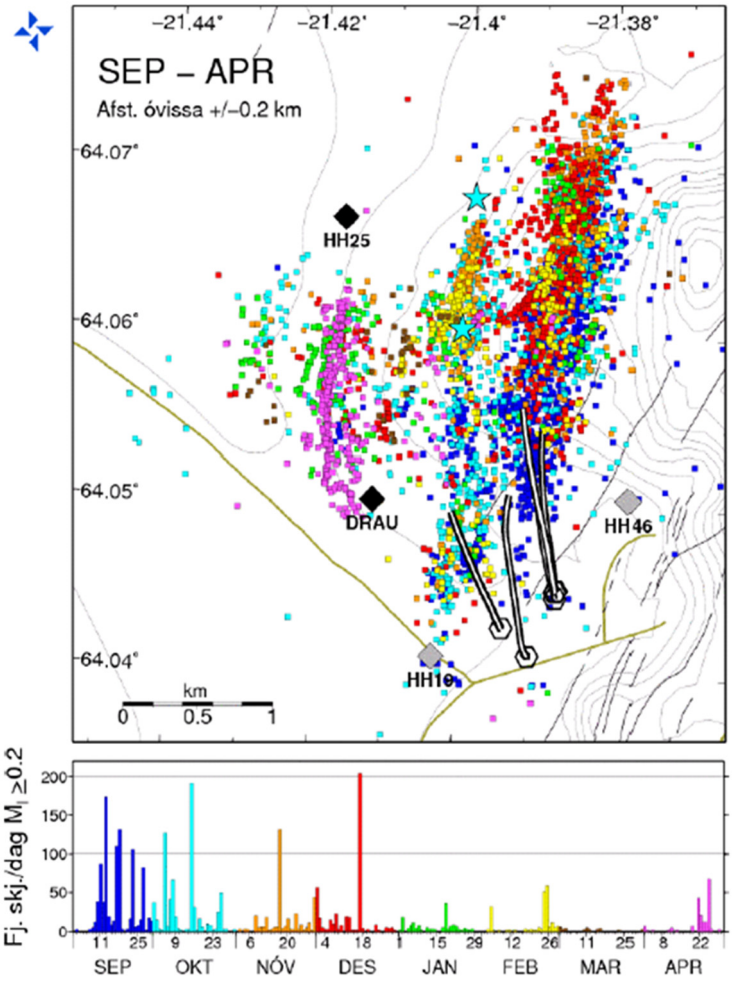

FIGURE 21: Overall seismic activity in the Húsmúli area during 2011-2012 (Bessason, et al. 2012)

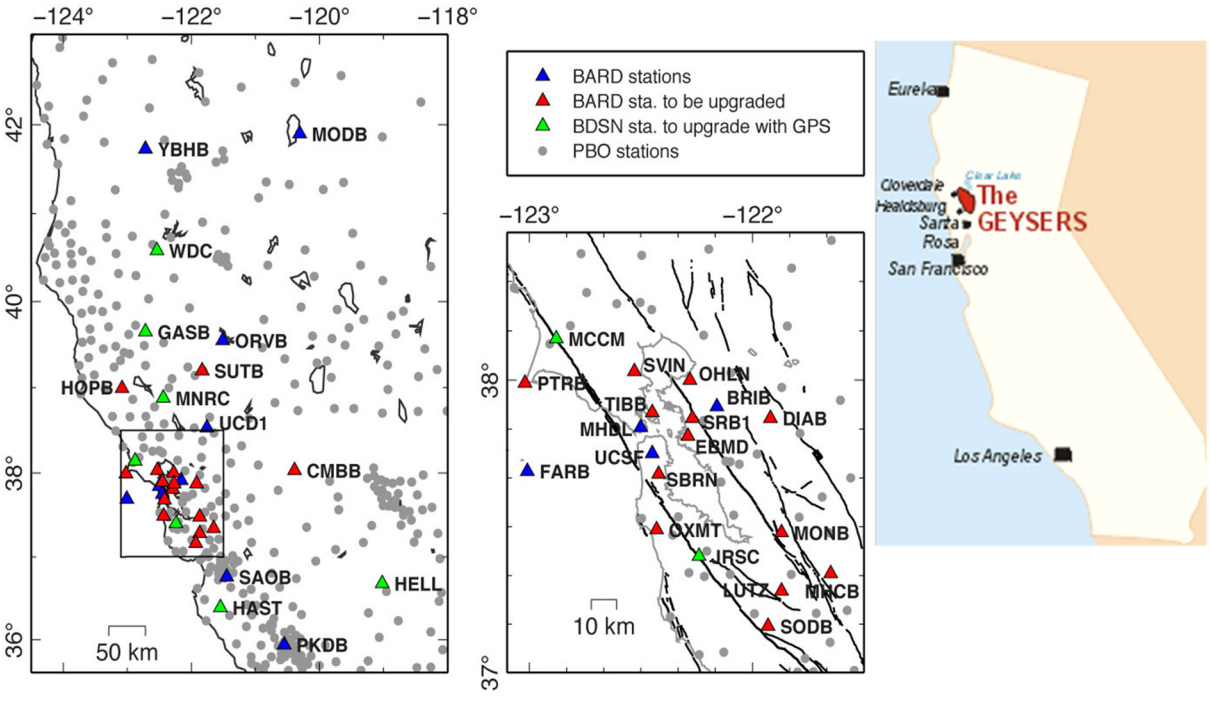

FIGURE 22: Seismic monitoring system related to The Geysers system, USA (BSL, 2015)

be identified as an enhanced geothermal system. As in Hellisheidi, seismic activities have been recorded in relation with mass extraction and reinjection of the geothermal field. The field has been monitored continually for a number of years. The wide coverage of the seismic network, including the injection and production areas, as well as neighbouring areas, has enabled scientists to examine the field-wide response to injection. Currently, the nearest station to Hellisheidi is located nearly 9 km away from the event site. It shows the importance of increasing the number of stations in the network for better evaluation.

When reinjection started in the Cooper Basin field in Australia, the number of earthquakes in the area drastically increased. Fortunately, the project is located in a remote area, minimizing negative effects on local population. There are some benefits to locating geothermal projects close to communities: it reduces the cost of transmitting electricity or opens new avenues for the use of hot water for various purposes. However, strong community oppositions can lead to the termination or postponing of energy projects. Three events larger than M 3.0, induced during the development stages of an enhanced geothermal system in Basel, Switzerland, led to the suspension of the project (Majer, 2007). In the Hellisheidi area, the nearest community lies around 10 km away from the operation area. This is a comparably large distance, but the events with a magnitude larger than M 3.0 could be felt in the community (Bessason et al., 2012).

Careful monitoring of seismic activity is a valuable tool to get a better idea about subsurface activities, which otherwise would go unnoticed.

Controlling risk associated with induced seismicity is the ultimate goal of continuous monitoring. This is twofold. *Reducing the risk of the power project*; thorough research of the subsurface activities reduces the uncertainty of the effects of the mass extraction and reinjection. *Increasing safety;* safety issues are major factors that any project should consider at all stages. Taking precaution strategies against seismic events is important for the operation of the power plant, as well as the neighbouring community. The Berlin, El Salvador, project has a built-in warning system for monitoring, quantifying and controlling the risk associated with induced seismicity (Majer, 2007). When a destructive event takes place, it is very important to identify whether it is an induced event or a natural seismic event for the decision making process. The gap that exists today between acquired knowledge and the real situation needs to be bridged. A field like Berlin, which has a high degree of natural earthquakes, could serve as a test site for further development of mitigation processes. Figure 23 describes the traffic light system that is used in Berlin for maintaining the field. A real time monitoring system is essential for this system and should be located in the injection and production zones.

A detailed description of the traffic light system can be expressed as follows:

Green; ground shaking below the general detectability. Operation proceeds according to plan.
Amber; everyone can feel ground shaking but damages are very unlikely. Injection continues with caution and, depending on the situation, flow rate can be reduced and observations intensified.
Red; lower main boundary (thick line) indicates that events have crossed the safety level. In this stage ground shaking can be experienced and very light damage can be expected. When it crosses the upper minor boundary (dashed line) weak structures may be damaged and injection is suspended immediately. Beyond the upper minor boundary is where high levels of damage are expected.

A risk management plan like this is essential in monitoring of all active sites. In the Hellisheidi geothermal field induced seismicity is controlled by keeping the injection rate steady. The seismic monitoring system could be improved, as was suggested by Bessason et al. (2012). Active communications with the public is a valuable social tool to increase awareness and acceptance of geothermal power projects.

As a final step, filling gaps of existing knowledge is most important for future decisions. Access to funds and data for researchers is imperative to reach this goal. Active participation in the international science community is the key to finding new solutions to dealing with induced seismicity.

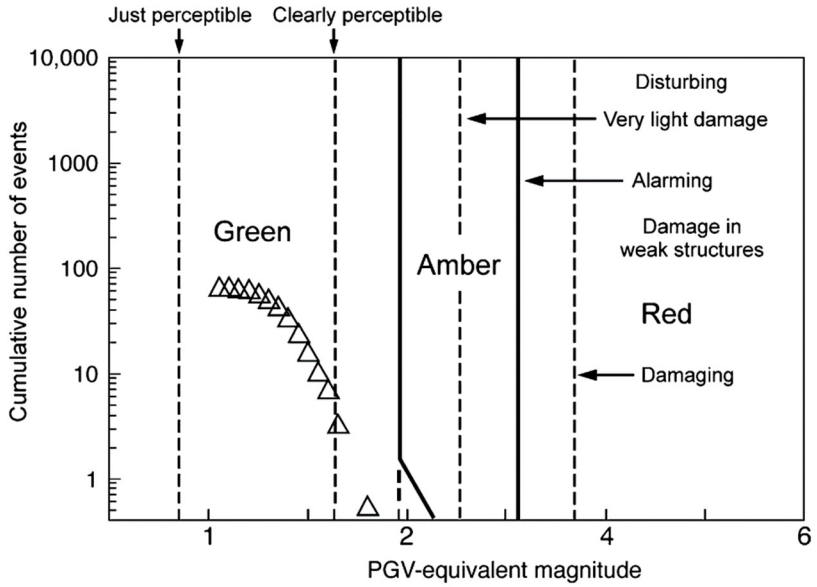

FIGURE 23: "Traffic light" boundaries superimposed on event recurrence defined in terms of magnitudes adjusted to produce the epicentral Peak Ground Velocity (PGV) if their focal depths were exactly 2 km. Triangles represent the cumulative recurrence data from the three episodes of fluid injection (totalling 54 days of pumping) normalized to a period of 30 days in The Geysers, USA. (Majer, 2007)

7. CONCLUSIONS

The ultimate goal of seismic monitoring in geothermal fields is to find the best methodologies to minimize negative impacts of induced seismicity and increase the positive aspects for the sustainable use of resources. A major element of this is close and continuous monitoring of the geothermal field. Following successful methodologies in the initial stages gives more reliable results and helps to make more reliable decisions. A case study was done in Hellisheidi geothermal field, which is one of the monitored geothermal fields in Iceland. One earthquake swarm was analysed and results show that the recorded swarm delineates a N-S trending vertically dipping fault. The swarm was a part of a larger sequence of induced earthquakes taking place in the area in connection with reinjection of geothermal waste water. Detailed study of the overall seismicity has shown that the activity moves to the west with time, away from the injection well. Seismic study is a powerful tool for the monitoring of geothermal fields and having these kinds of observations are invaluable for decision makers.

ACKNOWLEDGEMENTS

I would like to express my gratitude to the Government of Iceland and the United Nations University Geothermal Training Programme for granting me the opportunity to be a fellow in this excellent programme. Special thanks goes to family of UNU-GTP, Director Lúdvík S. Georgsson, Deputy Director Ingimar G. Haraldsson, Ms. Málfrídur Ómarsdóttir, Ms. Thórhildur Ísberg and Mr. Markús A.G. Wilde for their assistance and guidance through these six months. I would also like to acknowledge my supervisor Ms. Sigríður Kristjánsdóttir for her support and patience, helpful discussion and useful advice. I also thank Gylfi Páll Hersir for his guidance and encouragement. ISOR has generously supported me in this work, for which I am very thankful.

Last but not least, I am forever grateful for the effort of my institute (National Institute of Fundamental Studies) in Sri Lanka which was always available for advice and support.

REFERENCES

Bessason, B., Ólafsson, E.H., Gunnarsson, G., Flóvenz, Ó.G., Jakobsdóttir, S.S., Björnsson, S., and Árnadóttir, Th., 2012: *Working procedures due to induced seismicity in geothermal systems*. Reykjavík Energy, Reykjavík, internal report (in Icelandic), 10 pp.

BSL, 2015: *Map of Bay area regional deformation network sites*. University of California, Berkeley Seismological Laboratory, Berkeley, CA, US. Website: *http://seismo.berkeley.edu/ bard/map.html*

Ellsworth, B., 2013: *Injection-induced seismicity.* U.S. Geological Survey, Earthquake Science Center seminars, lecture notes, 75 pp. Website: *http://earthquake.usgs.gov/regional/nca/seminars/2013-12-02/*

Evans, K.F., Zappone, A., Kraft, T., Deichmann, N., and Moia, F., 2011: A survey of the induced seismic responses to fluid injection in geothermal and CO_2 reservoirs in Europe. *Geothermics, 41*, 30-54.

Flóvenz, Ó.G., 1980: Seismic structure of the Icelandic crust above layer three and the relation between body wave velocity and the alteration of the basaltic crust. *J. Geophys. 47,* 211-220.

Foulger, G.R., and Toomey, D.R., 1989: Structure and evolution of the Hengill-Grensdalur volcanic complex, Iceland: Geology, geophysics, and seismic tomography. *J. Geophysical Research: Solid Earth*, *94*, 17511-17522.

Gunnarsson, G., Kristjánsson, B.R., Gunnarsson, I., and Júlíusson, B.M., 2015: Reinjection into a fractured reservoir – induced seismicity and other challenges in operating re-injection wells in the Hellisheidi field, SW-Iceland. *Proceedings of the World Geothermal Congress 2015, Melbourne, Australia*, 9 pp.

Gunnarsson, G., 2013: Temperature dependent injectivity and induced seismicity – managing re-injection in the Hellisheidi field, SW-Iceland. *Geothermal Resources Council, Transactions, 37*, 1019-1025.

Halldórsson, B., Rupakhety, R., and Sigbjörnsson, R., 2012: On the effects of induced earth quakes due to fluid injection at Hellisheidi geothermal power plant, Iceland. *Proceedings of the 15th World Conference on Earthquake Engineering, Lisboa, Portugal*, 10 pp.

LBNL, 2015: *Induced seismicity*. Lawrence Berkeley National Laboratory (LBNL), Berkeley, CA, United States. Website: *http://esd1.lbl.gov/research/projects/ induced_seismicity/primer.html#defined*

Lay, T., and Wallace, T.C., 1995: *Modern global seismology*. Academic Press, San Diego, CA, United States, 521 pp.

Lomax, A.A., Michelini, A.C., and Curtis, A., 2009: Earthquake location, direct, global-search methods. In: Meyers, R.A. (ed.), *Encyclopedia of complexity and system science*. Springer, NY, US, 2449-2473.

Majer, E.L., Baria, R., Stark, M., Oates, S., Bommer, J., Smith, B., and Asanuma, H., 2007: Induced seismicity associated with enhanced geothermal systems. *Geothermics, 36-3*, 185-222.

Nordquist, G., 2005: Microearthquake monitoring and applications. *WPRB/INAGA Bali Seminar 2008, Bali, Indonesia*, 27 pp.

Seale, S., Vincent, H., and NEES EOT, 2011: *Everything important about earthquakes (and other assorted information)*. The George E. Brown Network for Earthquake Engineering Simulation (NEES). Website: *https://nees.org/resources/3936*

APPENDIX I: The temporary seismic networks operated in Reykjanes - Hellisheidi area

Name of station	Latitude	Longitude
GRV	63.8572	-22.4558
KAS	64.0229	-21.8520
KRI	63.8781	-22.0765
NYL	63.9737	-22.7379
RNE	63.8168	-22.7056
VOG	63.9697	-22.3929
VOS	63.8528	-21.7036
BJA	63.9459	-21.3026
HEI	64.1998	-21.2360
KRO	64.0981	-21.1198
KUD	64.3206	-21.8747
SAN	64.0560	-21.5701
SOL	63.9290	-20.9436
HUSM	64.0513	-21.3938
BOLI	64.0626	-21.4133
HIMN	64.0490	-21.3524
THVE	64.0393	-21.3744
DRAUG	64.0451	-21.4158
LYKL	64.0823	-21.5450
SVIN	64.0566	-21.4485
BUG	63.9045	-21.4376
ELB	63.8582	-21.9872
ENG	64.0879	-21.4105
GEI	63.9482	-21.5307
HAH	63.9286	-22.6386
HDV	63.8699	-21.8839
HOV	63.9530	-22.0830
HVD	64.0245	-21.3995
HVV	64.1118	-21.2158
ISS	63.8629	-22.3029
LAG	63.9052	-22.4888
LAT	63.8583	-22.1869
LHL	63.9792	-21.8320
LME	63.9742	-21.4291
LSK	64.0350	-21.2960
MOH	63.9200	-22.0596
NUP	63.9989	-21.2536
SEL	64.1336	-21.2383
SOG	63.9927	-21.1496
STH	63.9863	-22.2652
SVH	63.8779	-21.5515
TRH	64.0608	-21.1798
ASH	63.9871	-22.1361
BIT	64.0573	-21.2577
BLF	63.9737	-21.6489
FAF	63.9064	-22.2148
GUD	64.0198	-21.1885
HRG	63.9606	-21.9779
HVH	64.0097	-21.3356
IND	64.0616	-21.3358
KLV	63.9112	-21.9582
LHA	64.0241	-21.0489
LSF	63.9222	-22.3722
SEA	63.8434	-22.1112
SHR	64.0240	-21.5016
SKD	64.1079	-21.2988
VSV	63.8737	-22.5881

APPENDIX II: Seismic events recording during 21 April – 22 April 2012

Date	Time	Latitude	Longitude	Depth (km)	RMS	d_lat (km)	d_lon (km)	d_dep (km)	M	Picking mode
21.4.2012	00:17:11.405	63.9755	-21.4565	0.8	0.061	0.88	1.58	1.31	1.95	manual
22.4.2012	00:00:10.751	64.0435	-21.4291	-0.42	0.063	2.33	2.42	2.01	1.71	manual
22.4.2012	00:00:17.382	64.0379	-21.4575	-0.69	0.002	1.49	1.66	1.47	1.73	manual
22.4.2012	00:04:07.650	64.0513	-21.396	-0.9	0.009	1.44	1.61	1.42	1.61	manual
22.4.2012	00:05:08.967	64.0455	-21.4241	1.73	0.042	0.52	0.75	0.6	1.22	manual
22.4.2012	00:09:30.012	64.0545	-21.4142	1.95	0.053	0.35	0.34	0.33	1.18	manual
22.4.2012	00:16:37.096	64.0538	-21.419	2.27	0.06	0.22	0.2	0.3	1.33	manual
22.4.2012	00:18:58.644	64.0485	-21.4101	1.84	0.047	0.21	0.25	0.26	1.21	manual
22.4.2012	00:19:23.297	64.0454	-21.4082	1.83	0.029	0.22	0.26	0.27	1.03	manual
22.4.2012	00:20:22.247	64.0471	-21.4132	1.84	0.041	0.46	0.59	0.58	1.17	manual
22.4.2012	00:20:42.945	64.0536	-21.4137	1.79	0.035	0.35	0.35	0.34	1.07	manual
22.4.2012	00:21:25.978	64.0353	-21.4545	-0.02	0.023	0.78	0.92	0.88	0.97	manual
22.4.2012	00:22:01.687	64.0485	-21.4087	0.68	0.042	1.65	1.7	1.56	1.53	manual
22.4.2012	00:22:38.801	64.0557	-21.4129	1.8	0.035	0.63	0.71	0.62	1.1	manual
22.4.2012	00:28:54.953	64.0448	-21.4433	0.8	0.021	1.76	2.01	1.82	1.68	manual
22.4.2012	00:29:54.934	64.0425	-21.4427	2.09	0.007	1.59	2.25	1.07	2.39	manual
22.4.2012	00:33:51.693	64.0494	-21.4126	1.84	0.02	0.26	0.25	0.3	1.06	manual
22.4.2012	00:33:10.526	64.0386	-21.4576	-0.62	0.002	1.5	1.71	1.51	1.73	manual
22.4.2012	00:35:52.173	64.0525	-21.415	2.59	0.057	0.23	0.18	0.32	1.36	manual
22.4.2012	00:37:13.345	64.0551	-21.4195	1.96	0.049	0.25	0.23	0.25	1.07	manual
22.4.2012	00:34:39.365	64.0386	-21.4544	0.34	0.008	1.47	1.67	1.46	1.72	manual
22.4.2012	00:37:35.487	64.0563	-21.4152	2.19	0.039	0.29	0.22	0.36	1.14	manual
22.4.2012	00:35:16.805	64.0527	-21.4138	1.51	0.01	1.47	1.75	1.51	1.69	manual
22.4.2012	00:39:35.802	64.0456	-21.4164	1.78	0.037	0.59	0.82	0.68	1.17	manual
22.4.2012	00:40:09.126	64.04	-21.4609	0.96	0.014	1.57	1.84	1.57	1.64	manual
22.4.2012	00:40:32.358	64.0492	-21.4296	1.72	0.003	1.48	1.77	1.54	1.76	manual
22.4.2012	00:47:48.375	64.0529	-21.4173	2.24	0.043	0.26	0.22	0.35	1.18	manual
22.4.2012	00:49:40.772	64.054	-21.417	2.33	0.052	0.18	0.18	0.27	1.29	manual
22.4.2012	00:50:04.750	64.0496	-21.4122	1.9	0.022	0.19	0.21	0.26	1.15	manual
22.4.2012	00:52:17.680	64.0415	-21.4291	1.43	0.042	0.45	0.68	0.6	1.03	manual
22.4.2012	00:55:14.944	64.0365	-21.459	-0.48	0.005	1.36	1.63	1.42	1.7	manual
22.4.2012	00:55:46.814	64.0354	-21.4611	-0.89	0.015	1.16	1.19	1.46	0.86	manual
22.4.2012	01:03:22.857	64.0522	-21.4108	1.5	0.033	0.23	0.25	0.39	2.33	manual
22.4.2012	00:59:33.738	64.0531	-21.4169	2.41	0.033	0.27	0.26	0.41	1.01	manual
22.4.2012	00:59:55.386	64.0518	-21.423	1.94	0.008	0.63	0.68	0.66	1.01	manual
22.4.2012	01:00:21.193	64.0506	-21.404	0.48	0.013	1.44	1.59	1.4	1.68	manual
22.4.2012	01:01:16.804	64.0492	-21.4039	0.68	0.017	1.45	1.57	1.39	1.56	manual
22.4.2012	01:04:48.339	64.0527	-21.4074	-0.07	0.007	1.52	1.72	1.52	1.72	manual
22.4.2012	01:05:26.341	64.052	-21.409	0.68	0.017	1.54	1.73	1.5	1.92	manual
22.4.2012	01:05:48.811	64.0414	-21.4514	1.17	0.036	1.64	1.92	1.68	1.63	manual
22.4.2012	01:06:27.479	64.0465	-21.429	2.11	0.007	0.85	1.12	0.83	2.45	manual
22.4.2012	01:06:42.872	64.0442	-21.4501	0.89	0.022	1.79	2.06	1.81	1.8	manual
22.4.2012	01:07:19.986	64.0494	-21.4101	1.98	0.038	0.18	0.23	0.25	1.03	manual
22.4.2012	01:09:39.072	64.0511	-21.4197	1.87	0.013	0.88	1.16	0.87	2.18	manual
22.4.2012	01:10:30.618	64.0514	-21.427	1.87	0.003	2.28	2.99	2.11	0.88	manual
22.4.2012	01:13:48.511	64.0471	-21.4182	1.65	0.008	1.53	1.14	1.43	1.7	manual
22.4.2012	01:14:46.681	64.0451	-21.4473	1.53	0.03	1.18	1.65	0.93	2.51	manual
22.4.2012	01:16:12.309	64.0497	-21.4268	2.39	0.004	1.28	2.42	0.93	1.68	manual
22.4.2012	01:18:59.821	64.0532	-21.4095	2.15	0.041	0.25	0.23	0.34	1.05	manual
22.4.2012	01:20:29.692	64.0536	-21.4165	2.05	0.05	0.25	0.2	0.33	1.53	manual
22.4.2012	01:22:41.511	64.0393	-21.4577	0.96	0.003	1.42	1.72	1.48	1.87	manual
22.4.2012	01:24:46.703	64.0545	-21.4078	2.26	0.045	0.27	0.3	0.3	1.27	manual
22.4.2012	01:25:00.006	64.0514	-21.424	1.88	0.027	0.49	0.59	0.42	1.49	manual
22.4.2012	01:25:39.632	64.0533	-21.4165	2.02	0.03	0.23	0.23	0.26	1.42	manual
22.4.2012	01:26:15.656	64.0561	-21.4123	1.83	0.05	0.26	0.28	0.27	1.11	manual
22.4.2012	01:27:13.908	64.0551	-21.4167	2.17	0.069	0.23	0.24	0.27	1.28	manual
22.4.2012	01:27:54.419	64.0492	-21.4601	2.61	0.001	2.54	2.98	2.02	0.88	manual
22.4.2012	01:28:09.465	64.0379	-21.4624	0.89	0.003	1.9	2.45	1.56	2.31	manual
22.4.2012	01:30:35.885	64.0551	-21.4195	1.81	0.05	0.27	0.25	0.31	1.08	manual
22.4.2012	01:31:21.673	64.0386	-21.4624	0.82	0.011	1.48	1.79	1.5	1.79	manual
22.4.2012	01:33:50.233	64.0379	-21.4559	0.68	0.008	1.45	1.69	1.45	1.66	manual

Date	Time	Latitude	Longitude	Depth (km)	RMS	d_lat (km)	d_lon (km)	d_dep (km)	M	Picking mode
22.4.2012	01:35:42.383	64.0558	-21.4155	1.74	0.047	0.42	0.42	0.69	1.19	manual
22.4.2012	01:36:12.585	64.0379	-21.4591	1.1	0.012	1.47	1.7	1.47	1.62	manual
22.4.2012	01:36:52.746	64.0521	-21.4228	1.9	0.033	0.47	0.54	0.39	1.16	manual
22.4.2012	01:42:18.270	64.0486	-21.4316	1.9	0.052	0.6	0.71	0.57	1.03	manual
22.4.2012	01:49:35.434	64.0377	-21.4113	1.29	0.04	0.93	0.5	0.67	1.59	manual
22.4.2012	01:50:12.866	64.0427	-21.4535	0.8	0.03	1.56	2.39	1.04	1.88	manual
22.4.2012	01:51:48.086	64.0497	-21.4236	1.8	0.014	0.55	0.67	0.58	0.94	manual
22.4.2012	01:52:54.938	64.0393	-21.4416	1.72	0.001	1.4	1.53	1.38	1.72	manual
22.4.2012	01:54:45.896	64.0435	-21.4243	1.72	0.025	0.77	0.92	1	0.92	manual
22.4.2012	01:55:23.084	64.0455	-21.4192	1.66	0.05	0.58	0.8	0.69	0.99	manual
22.4.2012	02:07:36.815	64.0546	-21.42	1.8	0.041	0.51	0.58	0.42	2.46	manual
22.4.2012	02:11:53.766	64.0379	-21.4624	-0.28	0.01	1.54	1.83	1.55	1.67	manual
22.4.2012	02:16:32.808	64.0553	-21.4193	2.21	0.042	0.56	0.73	0.6	1.25	manual
22.4.2012	02:19:41.234	64.0527	-21.4106	1.3	0.004	1.51	1.76	1.51	1.74	manual
22.4.2012	02:20:07.228	64.0479	-21.4098	1.8	0.049	0.24	0.3	0.29	1.1	manual
22.4.2012	02:22:48.634	64.0543	-21.4122	1.76	0.065	0.19	0.18	0.27	2.04	manual
22.4.2012	02:24:43.157	64.0485	-21.4153	2.45	0.078	0.21	0.19	0.28	1.29	manual
22.4.2012	02:30:07.096	64.0527	-21.4042	0.75	0.008	1.47	1.69	1.46	1.73	manual
22.4.2012	02:33:42.677	64.0505	-21.4159	2.14	0.042	0.2	0.19	0.25	1.13	manual
22.4.2012	02:34:59.703	64.0563	-21.4115	1.79	0.058	0.23	0.23	0.26	1.16	manual
22.4.2012	02:36:51.954	64.0568	-21.4104	1.83	0.037	0.29	0.33	0.39	1.18	manual
22.4.2012	02:44:37.402	64.0517	-21.4224	2.39	0.073	0.33	0.39	0.36	1.27	manual
22.4.2012	02:48:30.139	64.0558	-21.4151	1.98	0.061	0.22	0.21	0.26	1.21	manual
22.4.2012	02:50:55.959	64.048	-21.4136	1.71	0.033	0.22	0.2	0.24	1.27	manual
22.4.2012	03:00:44.670	64.0543	-21.4174	1.96	0.037	0.28	0.24	0.37	1.26	manual
22.4.2012	03:36:35.796	64.0543	-21.4128	1.9	0.05	0.58	0.93	0.55	1.33	manual
22.4.2012	03:47:50.721	64.0535	-21.4161	2.03	0.034	0.34	0.38	0.32	1.07	manual
22.4.2012	03:55:09.478	64.0504	-21.4173	2.28	0.061	0.19	0.19	0.28	2.24	manual
22.4.2012	03:49:15.852	64.0496	-21.4114	1.79	0.03	0.25	0.26	0.3	1.09	manual
22.4.2012	03:57:13.788	64.0505	-21.4155	2.43	0.06	0.25	0.28	0.31	1.25	manual
22.4.2012	04:00:13.168	64.05	-21.4188	2.59	0.014	0.68	0.79	0.68	0.91	manual
22.4.2012	04:03:37.498	64.0344	-21.4653	-0.07	0.017	1.47	1.79	1.49	1.74	manual
22.4.2012	04:04:49.525	64.0342	-21.4616	-0.23	0.019	1.06	1.3	1.01	0.98	manual
22.4.2012	04:04:57.091	64.049	-21.4212	2.15	0.052	0.27	0.26	0.25	1.15	manual
22.4.2012	04:19:58.207	64.0504	-21.4132	2.32	0.01	1.01	1.31	1.1	1.54	manual
22.4.2012	04:22:57.340	64.0514	-21.4037	2.42	0.036	0.77	1.24	0.9	1.66	manual
22.4.2012	04:24:20.929	64.0421	-21.4563	1.51	0.001	1.5	1.81	1.55	1.85	manual
22.4.2012	04:36:17.601	64.0556	-21.4123	1.95	0.06	0.19	0.22	0.27	1.42	manual
22.4.2012	04:39:25.035	64.0487	-21.4121	2.05	0.038	0.41	0.64	0.34	1.21	manual
22.4.2012	04:49:33.743	64.0568	-21.4088	1.76	0.033	0.33	0.34	0.41	1.19	manual
22.4.2012	04:53:39.953	64.0546	-21.4112	1.94	0.029	0.5	0.86	0.91	1.13	manual
22.4.2012	04:57:20.732	64.0556	-21.4143	2.1	0.038	0.19	0.21	0.26	1.62	manual
22.4.2012	04:59:06.814	64.0552	-21.4127	2.03	0.033	0.21	0.22	0.27	1.21	manual
22.4.2012	05:06:44.867	64.0501	-21.4158	2.22	0.035	0.21	0.23	0.25	1.16	manual
22.4.2012	05:06:11.574	64.0559	-21.4119	2.02	0.032	0.25	0.29	0.3	1.21	manual
22.4.2012	05:02:05.915	64.0507	-21.4181	1.66	0.012	0.71	0.46	0.83	2.55	manual
22.4.2012	05:07:35.817	64.0504	-21.4181	2.15	0.025	0.64	0.41	0.42	3.43	manual
22.4.2012	05:09:48.370	64.0503	-21.4154	2.21	0.052	0.17	0.17	0.18	1.35	manual
22.4.2012	05:25:37.595	64.0498	-21.417	2.14	0.051	0.17	0.15	0.17	1.15	manual
22.4.2012	05:26:55.491	64.0498	-21.419	2.15	0.054	0.19	0.16	0.19	1.22	manual
22.4.2012	05:27:48.574	64.0501	-21.4154	2.24	0.057	0.2	0.19	0.19	1.44	manual
22.4.2012	05:34:25.030	64.0536	-21.4207	2.15	0.017	0.6	0.61	0.81	2.67	manual
22.4.2012	05:34:50.285	64.05	-21.4166	2.22	0.054	0.19	0.15	0.18	1.21	manual
22.4.2012	05:42:04.737	64.0473	-21.4204	1.81	0.032	0.29	0.31	0.35	1	manual
22.4.2012	05:53:16.032	64.0517	-21.4168	2.22	0.051	0.4	0.23	0.25	1.05	manual
22.4.2012	06:08:00.690	64.0522	-21.4166	1.7	0.011	0.46	0.67	0.92	2.51	manual
22.4.2012	06:09:29.373	64.0522	-21.418	2.36	0.027	0.19	0.19	0.18	1	manual
22.4.2012	06:36:48.914	64.0504	-21.4189	1.77	0.005	0.39	0.64	0.81	1.74	manual
22.4.2012	06:42:13.924	64.0518	-21.4134	2.25	0.013	0.29	0.72	0.4	0.88	manual
22.4.2012	06:30:07.036	64.0472	-21.413	1.56	0.01	0.29	0.41	0.82	2.52	manual
22.4.2012	06:37:16.451	64.0525	-21.4199	1.25	0.04	0.97	0.93	1.04	2.37	manual
22.4.2012	06:43:22.034	64.0504	-21.4205	1.8	0.01	0.37	0.38	0.77	2.63	manual
22.4.2012	06:54:53.869	64.0513	-21.4169	1.72	0.04	0.41	0.61	0.77	2.45	manual

Date	Time	Latitude	Longitude	Depth (km)	RMS	d_lat (km)	d_lon (km)	d_dep (km)	M	Picking mode
22.4.2012	06:51:22.227	64.0442	-21.4195	0	0.02	0.9	1.08	0.91	2.47	manual
22.4.2012	07:16:42.131	64.0476	-21.4202	1.73	0.033	0.41	0.7	0.6	1.92	manual
22.4.2012	06:59:59.653	64.049	-21.4139	2.08	0.027	0.6	0.59	0.92	2.38	manual
22.4.2012	07:18:40.202	64.0507	-21.4181	1.63	0.012	0.36	0.54	0.82	2.53	manual
22.4.2012	07:09:40.265	64.0504	-21.4181	1.56	0.005	0.76	0.75	0.9	2.19	manual
22.4.2012	07:22:36.701	64.0503	-21.4106	1.81	0.046	0.17	0.18	0.17	1.17	manual
22.4.2012	07:24:58.700	64.0553	-21.4105	1.77	0.01	0.4	0.39	0.6	2.43	manual
22.4.2012	07:26:39.603	64.0452	-21.409	1.91	0.038	0.15	0.19	0.19	1.09	manual
22.4.2012	07:30:29.866	64.0497	-21.4172	1.7	0.024	0.38	0.64	0.5	2.59	manual
22.4.2012	07:42:27.506	64.0536	-21.4183	1.8	0.006	0.58	1.24	0.95	2.58	manual
22.4.2012	07:52:09.565	64.0495	-21.4337	-0.24	0.017	1.55	1.89	1.71	2.47	manual
22.4.2012	08:02:39.751	64.0473	-21.41	2.02	0.035	0.17	0.18	0.19	1.14	manual
22.4.2012	08:20:18.642	64.0483	-21.4131	1.56	0.01	0.31	0.42	0.78	2.52	manual
22.4.2012	08:26:05.952	64.0472	-21.4122	1.6	0.016	0.29	0.43	0.83	2.38	manual
22.4.2012	08:34:50.960	64.0554	-21.4151	2.21	0.044	0.16	0.15	0.17	1.11	manual
22.4.2012	08:45:32.232	64.0525	-21.4191	1.66	0.009	0.57	1.19	0.94	2.41	manual
22.4.2012	08:49:22.623	64.0529	-21.4151	1.56	0.01	0.37	0.37	0.71	2.66	manual
22.4.2012	08:52:23.175	64.0488	-21.4114	1.85	0.038	0.16	0.16	0.17	1.27	manual
22.4.2012	08:57:25.571	64.0498	-21.4103	1.61	0.061	0.15	0.17	0.15	1.63	manual
22.4.2012	09:02:53.455	64.0464	-21.4037	2.06	0.007	1.97	1.71	1.48	2.45	manual
22.4.2012	09:04:31.320	64.0522	-21.4142	1.46	0.015	0.35	0.36	0.71	2.57	manual
22.4.2012	09:04:52.282	64.0525	-21.415	1.53	0.018	0.38	0.47	0.81	2.7	manual
22.4.2012	09:05:32.125	64.0525	-21.415	1.32	0.012	0.34	0.46	0.81	2.53	manual
22.4.2012	09:20:32.668	64.0525	-21.415	1.39	0.018	0.36	0.39	0.74	2.68	manual
22.4.2012	09:24:45.083	64.0511	-21.4157	0.94	0.033	0.46	0.38	1	2.62	manual
22.4.2012	09:32:58.675	64.0469	-21.4105	1.32	0.029	0.27	0.38	0.87	2.47	manual
22.4.2012	09:40:10.096	64.0532	-21.4191	1.49	0.04	0.44	0.45	0.84	2.54	manual
22.4.2012	09:53:44.505	64.049	-21.4195	1.6	0.007	0.33	0.38	0.82	2.53	manual
22.4.2012	09:50:11.786	64.0439	-21.4139	1.41	0.004	1.33	0.97	1.33	2.31	manual
22.4.2012	10:03:31.993	64.0444	-21.4192	1.77	0.007	0.72	1.17	1.14	1.75	manual
22.4.2012	10:04:11.395	64.0469	-21.4137	1.42	0.007	0.28	0.37	0.84	2.48	manual
22.4.2012	10:10:55.801	64.0458	-21.4185	1.7	0.014	0.3	0.41	0.83	2.52	manual
22.4.2012	10:11:45.588	64.0511	-21.4237	1.11	0.024	0.35	0.38	0.89	2.35	manual
22.4.2012	10:12:07.471	64.049	-21.4324	-0.98	0.025	0.35	0.77	1.04	2.61	manual
22.4.2012	10:20:26.825	64.0543	-21.4168	1.49	0.023	0.4	0.33	0.67	2.63	manual
22.4.2012	10:53:11.324	64.0533	-21.4177	2.05	0.024	0.44	0.48	0.45	2.42	manual
22.4.2012	11:16:00.572	64.0469	-21.4121	1.97	0.045	0.17	0.2	0.21	1.2	manual
22.4.2012	11:24:38.658	64.0522	-21.419	1.56	0.016	0.39	0.47	0.82	2.34	manual
22.4.2012	11:26:43.859	64.0529	-21.4183	1.8	0.017	0.32	0.36	0.44	2.58	manual
22.4.2012	11:35:57.493	64.043	-21.4198	1.73	0.027	0.39	1.12	1.17	2.47	manual
22.4.2012	11:40:45.056	64.0522	-21.4182	1.6	0.008	0.55	0.51	0.88	2.52	manual
22.4.2012	11:42:19.509	64.0511	-21.4181	1.6	0.031	0.39	0.35	0.73	2.47	manual
22.4.2012	11:49:19.525	64.0514	-21.4198	1.53	0.015	0.37	0.36	0.81	2.49	manual
22.4.2012	11:55:31.180	64.0549	-21.4183	2.17	0.062	0.24	0.24	0.25	1.14	manual
22.4.2012	12:02:20.078	64.0507	-21.4221	1.39	0.004	1.78	1.99	1.78	2.51	manual
22.4.2012	12:14:17.730	64.0561	-21.4164	2.05	0.052	0.25	0.19	0.19	1.1	manual
22.4.2012	12:18:06.294	64.0559	-21.4135	2.02	0.048	0.18	0.15	0.17	1.31	manual
22.4.2012	12:21:29.221	64.0536	-21.4175	1.9	0.015	0.47	0.51	0.76	2.59	manual
22.4.2012	12:18:53.235	64.0479	-21.4203	1.84	0.024	0.35	0.66	0.66	2.73	manual
22.4.2012	12:23:34.463	64.0547	-21.4142	2.17	0.047	0.23	0.3	0.26	2.17	manual
22.4.2012	12:31:09.450	64.0561	-21.4168	2.14	0.038	0.19	0.19	0.19	1.17	manual
22.4.2012	12:33:03.849	64.0565	-21.4136	2.03	0.056	0.22	0.19	0.19	1.13	manual
22.4.2012	12:34:20.547	64.0539	-21.4176	1.49	0.016	0.38	0.35	0.7	2.63	manual
22.4.2012	12:36:17.007	64.056	-21.416	2.07	0.061	0.16	0.15	0.15	1.21	manual
22.4.2012	12:51:21.034	64.0475	-21.4128	1.9	0.068	0.17	0.19	0.18	1.32	manual
22.4.2012	12:48:57.794	64.0539	-21.4176	1.94	0.017	1.66	1.2	1.88	2.41	manual
22.4.2012	12:57:29.877	64.0563	-21.4148	2	0.04	0.22	0.18	0.18	2.39	manual
22.4.2012	12:49:18.197	64.0518	-21.4166	1.63	0.033	0.48	0.74	0.9	2.38	manual
22.4.2012	13:10:00.165	64.0514	-21.419	1.63	0.011	0.45	0.53	0.86	2.52	manual
22.4.2012	13:01:38.308	64.0514	-21.4182	1.7	0.016	0.37	0.55	0.8	2.49	manual
22.4.2012	13:13:17.146	64.0469	-21.4153	1.42	0.022	0.43	0.52	1.02	2.66	manual
22.4.2012	13:23:19.971	64.0514	-21.4182	1.49	0.004	0.36	0.36	0.76	2.41	manual
22.4.2012	13:03:32.329	64.0536	-21.4191	1.46	0.024	0.4	0.43	0.82	2.31	manual

Date	Time	Latitude	Longitude	Depth (km)	RMS	d_lat (km)	d_lon (km)	d_dep (km)	M	Picking mode
22.4.2012	13:14:33.943	64.0536	-21.4167	1.39	0.037	0.39	0.39	0.72	2.51	manual
22.4.2012	13:19:56.750	64.0529	-21.4135	1.39	0.008	0.51	0.41	0.95	2.45	manual
22.4.2012	13:28:35.008	64.0478	-21.4134	1.51	0.011	0.37	0.53	0.9	2.4	manual
22.4.2012	13:36:28.799	64.0468	-21.4151	1.48	0.026	0.21	0.3	0.29	2.32	manual
22.4.2012	13:43:36.745	64.0457	-21.4074	1.86	0.085	0.16	0.17	0.18	1.73	manual
22.4.2012	13:47:28.270	64.0468	-21.4151	1.98	0.035	0.27	0.33	0.36	2.49	manual
22.4.2012	13:57:01.874	64.0466	-21.4131	1.79	0.014	0.38	0.47	0.47	1.89	manual
22.4.2012	13:58:25.105	64.0451	-21.4144	1.53	0.008	0.26	0.41	0.88	2.07	manual
22.4.2012	14:15:05.882	64.048	-21.4148	1.81	0.037	0.17	0.17	0.19	1.15	manual
22.4.2012	14:26:59.925	64.0515	-21.4212	2.27	0.035	0.31	0.25	0.25	2.65	manual
22.4.2012	14:50:40.139	64.0511	-21.4133	1.66	0.008	0.35	0.4	0.72	2.76	manual
22.4.2012	14:57:59.536	64.049	-21.4099	1.63	0.015	0.35	0.65	0.57	2.51	manual
22.4.2012	15:01:58.050	64.0543	-21.4176	1.6	0.026	0.41	0.35	0.66	2.6	manual
22.4.2012	15:16:04.767	64.0545	-21.4178	1.4	0.019	0.38	0.34	0.71	2.75	manual
22.4.2012	15:18:28.918	64.0566	-21.4168	2.07	0.078	0.19	0.17	0.17	1.22	manual
22.4.2012	15:24:32.321	64.0557	-21.4169	1.6	0.003	0.79	0.73	0.92	2.5	manual
22.4.2012	15:25:45.079	64.0543	-21.4182	2.15	0.031	0.18	0.16	0.18	1.19	manual
22.4.2012	15:37:08.974	64.0529	-21.4167	1.56	0.024	0.39	0.34	0.69	2.69	manual
22.4.2012	15:49:15.174	64.0573	-21.414	1.86	0.045	0.19	0.17	0.16	1.11	manual
22.4.2012	15:56:50.085	64.0577	-21.4141	1.96	0.043	0.22	0.18	0.18	1.15	manual
22.4.2012	16:19:05.334	64.0533	-21.4185	2.41	0.041	0.22	0.21	0.21	1.29	manual
22.4.2012	16:21:55.546	64.054	-21.419	2.33	0.031	0.23	0.18	0.2	1.02	manual
22.4.2012	16:31:52.455	64.058	-21.4125	1.96	0.045	0.27	0.31	0.23	1.02	manual
22.4.2012	16:34:12.474	64.0459	-21.4183	1.66	0.041	0.28	0.45	0.46	1.05	manual
22.4.2012	16:41:04.486	64.0534	-21.4332	0.68	0.008	1.44	1.87	1.43	1.76	manual
22.4.2012	16:42:14.211	64.0496	-21.4154	2.34	0.061	0.16	0.17	0.17	1.87	manual
22.4.2012	17:02:23.959	64.0541	-21.4172	1.44	0.033	0.4	0.4	0.69	2.66	manual
22.4.2012	17:30:16.840	64.0492	-21.4184	1.58	0.008	0.53	0.42	0.88	2.56	manual
22.4.2012	17:34:41.847	64.0473	-21.4124	1.93	0.055	0.18	0.19	0.19	1.2	manual
22.4.2012	17:36:29.302	64.0487	-21.4121	1.74	0.02	0.28	0.4	0.39	2.43	manual
22.4.2012	17:46:33.938	64.0439	-21.4171	1.82	0.025	0.44	0.41	0.56	2.53	manual
22.4.2012	17:59:10.006	64.0485	-21.4119	1.78	0.016	1.83	1.29	1.11	2.5	manual
22.4.2012	18:11:20.370	64.0508	-21.4191	1.81	0.027	0.35	0.43	0.5	2.7	manual
22.4.2012	18:12:32.371	64.05	-21.4204	1.53	0.031	0.65	0.9	0.95	2.58	manual
22.4.2012	18:29:03.429	64.0441	-21.4167	1.94	0.027	0.41	0.38	0.46	2.57	manual
22.4.2012	18:32:45.225	64.0476	-21.4178	2.21	0.027	0.52	0.78	1.02	2.61	manual
22.4.2012	18:39:10.182	64.0522	-21.4198	1.77	0.002	0.68	1.33	1.01	1.75	manual
22.4.2012	18:40:44.213	64.0529	-21.4199	1.9	0.007	0.56	0.54	0.82	2.62	manual
22.4.2012	18:49:47.901	64.0518	-21.4021	1.39	0.029	1.98	1.67	1.63	2.31	manual
22.4.2012	19:02:35.848	64.055	-21.4185	2.32	0.029	0.2	0.18	0.18	2.48	manual
22.4.2012	19:04:59.700	64.0531	-21.4213	2.03	0.023	0.35	0.41	0.43	2.61	manual
22.4.2012	19:12:35.031	64.0472	-21.4106	1.49	0.016	0.33	0.7	0.97	2.4	manual
22.4.2012	19:44:53.121	64.0454	-21.4106	1.79	0.044	0.21	0.26	0.27	1.25	manual
22.4.2012	19:51:33.698	64.0536	-21.4207	2.15	0.025	0.38	0.74	0.44	1.83	manual
22.4.2012	20:28:42.808	64.0515	-21.4188	1.95	0.035	0.21	0.2	0.21	1.21	manual
22.4.2012	20:40:51.415	64.0469	-21.4162	1.42	0.021	0.33	0.67	1.02	2.54	manual
22.4.2012	21:14:09.577	64.0566	-21.4168	2.1	0.05	0.21	0.16	0.17	1.22	manual
22.4.2012	21:15:36.712	64.0563	-21.4168	2.17	0.055	0.17	0.16	0.16	1.28	manual
22.4.2012	21:16:31.777	64.0525	-21.4191	1.63	0.014	0.39	0.54	0.8	2.69	manual
22.4.2012	20:41:15.650	64.0507	-21.4052	1.32	0.038	0.41	0.43	0.82	2.39	manual
22.4.2012	21:18:49.135	64.048	-21.4084	1.78	0.043	0.15	0.2	0.17	1.4	manual
22.4.2012	22:51:33.509	64.0425	-21.3559	-0.24	0.007	1.25	1.64	1.26	1.77	manual
22.4.2012	23:22:04.832	64.0464	-21.4131	1.9	0.046	0.16	0.18	0.18	1.25	manual
21.4.2012	22:59:11.807	64.0552	-21.4139	2.03	0.054	0.19	0.17	0.16	2.12	manual
21.4.2012	23:29:03.038	64.0532	-21.4175	1.63	0.013	0.39	0.36	0.7	2.45	manual
21.4.2012	23:30:28.728	64.0507	-21.4205	1.56	0.008	0.38	0.54	0.89	2.36	manual
21.4.2012	23:30:36.994	64.0464	-21.4149	1.72	0.007	1.79	2.07	1.82	2.46	manual
21.4.2012	23:30:54.330	64.0479	-21.4195	2.32	0.053	0.68	0.61	0.88	2.71	manual
21.4.2012	23:31:06.387	64.0493	-21.4132	1.77	0.049	0.18	0.23	0.19	1.26	manual
21.4.2012	23:33:16.175	64.0532	-21.4111	2.11	0.068	0.2	0.19	0.19	1.48	manual
21.4.2012	23:35:15.798	64.0469	-21.417	1.63	0.034	0.36	0.36	0.38	1.13	manual
21.4.2012	23:36:44.461	64.0511	-21.4165	1.77	0.034	0.38	0.36	0.75	2.74	manual
21.4.2012	23:41:37.929	64.0529	-21.4151	1.66	0.018	0.6	0.45	0.94	2.47	manual

Date	Time	Latitude	Longitude	Depth (km)	RMS	d_lat (km)	d_lon (km)	d_dep (km)	M	Picking mode
21.4.2012	23:39:19.333	64.0476	-21.413	1.49	0.016	0.3	0.37	0.83	2.58	manual
21.4.2012	23:44:11.232	64.054	-21.41	1.72	0.054	0.17	0.15	0.14	1.69	manual
21.4.2012	23:45:03.713	64.0484	-21.4121	1.95	0.036	0.18	0.17	0.19	1.38	manual
21.4.2012	23:46:42.852	64.0503	-21.4187	2.14	0.051	0.17	0.15	0.19	1.37	manual
21.4.2012	23:47:25.671	64.0493	-21.4123	1.77	0.004	2.54	1.47	2.03	2.74	manual
21.4.2012	23:48:14.810	64.0514	-21.4214	1.8	0.038	0.29	0.29	0.31	1.72	manual
21.4.2012	23:53:03.895	64.0528	-21.4145	2.43	0.048	0.18	0.19	0.16	1.27	manual
21.4.2012	23:54:30.250	64.0485	-21.4151	1.85	0.047	0.22	0.2	0.25	1.14	manual
21.4.2012	23:57:01.086	64.0511	-21.4181	1.7	0.007	0.41	0.5	0.83	2.62	manual
21.4.2012	23:57:53.063	64.0471	-21.4182	1.72	0.006	0.37	0.68	1.03	2.67	manual
21.4.2012	23:58:06.941	64.0536	-21.4135	1.6	0.006	0.53	0.43	0.91	2.73	manual
21.4.2012	23:00:57.823	64.0545	-21.413	1.9	0.032	0.18	0.16	0.16	1.32	manual
21.4.2012	23:02:29.945	64.0489	-21.4121	1.91	0.045	0.17	0.17	0.17	1.39	manual
21.4.2012	23:03:53.785	64.0491	-21.4105	2	0.036	0.16	0.17	0.17	1.96	manual
21.4.2012	23:05:12.553	64.0554	-21.4151	2.14	0.05	0.26	0.21	0.21	1.15	manual
21.4.2012	23:06:17.066	64.0533	-21.4189	2.14	0.056	0.24	0.23	0.24	1.19	manual
21.4.2012	23:06:35.378	64.0518	-21.4182	1.77	0.01	0.37	0.37	0.71	2.68	manual
21.4.2012	23:07:50.754	64.0518	-21.4166	1.56	0.01	0.36	0.37	0.73	2.51	manual
21.4.2012	23:09:07.745	64.0546	-21.4168	1.73	0.024	0.41	0.35	0.67	2.72	manual
21.4.2012	23:10:25.279	64.0483	-21.4163	1.7	0.009	0.32	0.39	0.78	2.64	manual
21.4.2012	23:13:38.756	64.0494	-21.4093	1.84	0.042	0.15	0.16	0.16	1.67	manual
21.4.2012	23:14:59.083	64.0493	-21.4154	1.78	0.02	0.24	0.31	0.32	2.39	manual
21.4.2012	23:18:29.576	64.0522	-21.4136	2.46	0.072	0.19	0.17	0.15	1.35	manual
21.4.2012	23:26:27.402	64.0548	-21.4124	1.85	0.068	0.18	0.17	0.15	1.34	manual
21.4.2012	22:36:40.340	64.0515	-21.4119	1.95	0.066	0.19	0.18	0.24	3.62	manual
21.4.2012	22:38:00.501	64.0511	-21.4165	1.73	0.014	0.36	0.4	0.72	5.11	manual
21.4.2012	22:41:26.248	64.0511	-21.4197	1.53	0.009	0.35	0.36	0.78	2.66	manual
21.4.2012	22:40:29.377	64.0514	-21.4182	1.73	0.008	0.36	0.38	0.71	2.87	manual
21.4.2012	22:45:20.210	64.0529	-21.4169	2	0.024	0.21	0.18	0.19	1.21	manual
21.4.2012	22:47:21.825	64.0482	-21.4112	2.03	0.041	0.16	0.17	0.17	2.27	manual
21.4.2012	22:55:27.018	64.0507	-21.4135	2.05	0.041	0.19	0.16	0.18	1.26	manual
21.4.2012	19:08:16.131	64.048	-21.4181	1.98	0.034	0.2	0.22	0.24	1.28	manual
21.4.2012	18:59:11.941	64.0536	-21.4159	2.28	0.068	0.2	0.18	0.17	1.54	manual
21.4.2012	18:59:35.714	64.0528	-21.4201	2.27	0.046	0.22	0.19	0.2	1.64	manual
21.4.2012	19:01:25.516	64.0531	-21.4169	2.15	0.043	0.24	0.16	0.18	1.51	manual
21.4.2012	19:04:24.962	64.0512	-21.4147	2.26	0.056	0.17	0.18	0.17	1.92	manual
21.4.2012	19:06:46.228	64.0528	-21.4145	2.14	0.068	0.19	0.16	0.18	1.71	manual
21.4.2012	19:10:39.627	64.0528	-21.4149	2.43	0.05	0.17	0.18	0.15	1.97	manual
21.4.2012	19:17:01.348	64.0498	-21.4186	2.14	0.043	0.18	0.17	0.21	1.3	manual
21.4.2012	19:26:14.012	64.0508	-21.4163	2.57	0.03	0.33	0.39	0.42	2.66	manual
21.4.2012	19:30:37.337	64.0512	-21.4199	2.07	0.029	0.3	0.39	0.35	2.3	manual
21.4.2012	19:34:17.942	64.05	-21.4188	1.77	0.01	0.35	0.4	0.77	2.68	manual
21.4.2012	19:37:43.933	64.055	-21.4161	2.18	0.056	0.2	0.15	0.18	1.93	manual
21.4.2012	19:46:28.573	64.0519	-21.4188	2.21	0.033	0.29	0.2	0.22	1.22	manual
21.4.2012	19:47:16.211	64.0519	-21.4168	2.09	0.043	0.18	0.19	0.19	1.81	manual
21.4.2012	19:50:44.831	64.0529	-21.4175	2.01	0.028	0.25	0.33	0.3	1.84	manual
21.4.2012	19:48:56.707	64.0469	-21.421	1.8	0.031	0.28	0.44	0.44	1.3	manual
21.4.2012	19:55:51.920	64.0521	-21.4192	2.19	0.04	0.21	0.18	0.19	1.39	manual
21.4.2012	20:00:46.370	64.0507	-21.4189	1.63	0.016	1.15	1.59	1.3	2.49	manual
21.4.2012	20:02:02.968	64.0522	-21.4164	2.22	0.042	0.35	0.39	0.42	2.75	manual
21.4.2012	20:03:27.575	64.0526	-21.4185	2.17	0.048	0.25	0.25	0.25	1.2	manual
21.4.2012	20:07:23.305	64.0515	-21.4107	2.46	0.044	0.19	0.2	0.16	1.22	manual
21.4.2012	20:11:57.615	64.0512	-21.4207	2.05	0.028	0.28	0.3	0.32	2.44	manual
21.4.2012	20:13:06.621	64.0514	-21.4192	2.24	0.026	0.24	0.24	0.25	1.19	manual
21.4.2012	20:16:08.507	64.0533	-21.4181	2.21	0.035	0.23	0.22	0.24	1.16	manual
21.4.2012	20:16:28.417	64.054	-21.415	2.09	0.032	0.2	0.19	0.18	1.2	manual
21.4.2012	20:22:33.017	64.0511	-21.4205	1.42	0.014	0.35	0.35	0.81	2.64	manual
21.4.2012	20:08:25.863	64.0514	-21.4174	1.66	0.015	0.37	0.57	0.78	2.53	manual
21.4.2012	20:23:58.275	64.0496	-21.4174	2.27	0.042	0.2	0.17	0.18	1.18	manual
21.4.2012	20:25:12.599	64.0492	-21.4184	1.92	0.003	1.92	1.17	1.83	2.36	manual
21.4.2012	20:25:44.248	64.0524	-21.4172	2.38	0.037	0.21	0.21	0.2	1.72	manual
21.4.2012	20:30:42.246	64.0526	-21.404	2.48	0.042	0.23	0.29	0.24	1.23	manual
21.4.2012	20:31:15.164	64.0497	-21.406	1.66	0.016	0.32	0.43	0.69	2.53	manual

Date	Time	Latitude	Longitude	Depth (km)	RMS	d_lat (km)	d_lon (km)	d_dep (km)	M	Picking mode
21.4.2012	20:33:08.788	64.0504	-21.4181	1.66	0.008	0.35	0.37	0.77	2.53	manual
21.4.2012	20:34:37.022	64.0528	-21.4173	2.02	0.028	0.24	0.22	0.24	1.07	manual
21.4.2012	20:38:16.661	64.0477	-21.4184	1.78	0.029	0.37	0.52	0.51	2.32	manual
21.4.2012	20:39:57.876	64.0556	-21.4139	1.9	0.072	0.25	0.18	0.19	1.32	manual
21.4.2012	20:41:15.937	64.0521	-21.4188	1.81	0.019	0.32	0.3	0.33	1.03	manual
21.4.2012	20:42:43.944	64.0535	-21.4165	2.48	0.051	0.27	0.24	0.23	1.27	manual
21.4.2012	20:48:06.118	64.0504	-21.4189	1.7	0.017	0.36	0.57	0.83	2.43	manual
21.4.2012	20:49:28.608	64.0538	-21.4162	2.22	0.042	0.19	0.17	0.18	1.17	manual
21.4.2012	20:58:44.179	64.0511	-21.4173	1.6	0.01	0.36	0.38	0.77	2.62	manual
21.4.2012	20:59:09.918	64.0535	-21.4173	2.33	0.061	0.17	0.15	0.16	1.44	manual
21.4.2012	21:01:27.417	64.0518	-21.4182	1.56	0.011	0.35	0.36	0.74	2.58	manual
21.4.2012	21:09:28.999	64.054	-21.4186	2.14	0.043	0.19	0.15	0.17	1.26	manual
21.4.2012	21:11:11.952	64.0497	-21.4164	2.11	0.04	0.4	0.39	0.6	2.64	manual
21.4.2012	21:13:21.243	64.0524	-21.412	2.43	0.055	0.28	0.24	0.23	1.18	manual
21.4.2012	21:15:43.010	64.0515	-21.42	1.69	0.032	0.33	0.34	0.47	2.72	manual
21.4.2012	21:17:02.763	64.0507	-21.4163	2.38	0.043	0.23	0.22	0.22	1.25	manual
21.4.2012	21:21:37.443	64.0536	-21.4157	2.22	0.066	0.25	0.27	0.26	1.28	manual
21.4.2012	21:30:48.484	64.0518	-21.419	1.53	0.009	0.41	0.5	0.84	2.59	manual
21.4.2012	21:31:08.254	64.0497	-21.4212	1.7	0.006	0.42	1	1.1	2.56	manual
21.4.2012	21:35:36.605	64.0511	-21.4181	1.56	0.012	0.39	0.53	0.85	2.68	manual
21.4.2012	21:36:11.477	64.0507	-21.4205	1.53	0.015	0.42	0.52	0.9	2.7	manual
21.4.2012	21:41:03.002	64.0497	-21.418	1.8	0.01	0.93	1.26	1.28	2.56	manual
21.4.2012	21:42:07.145	64.049	-21.4115	1.66	0.005	0.36	0.96	1.01	2.84	manual
21.4.2012	21:42:53.390	64.0511	-21.4165	2.49	0.053	0.39	0.41	0.43	2.21	manual
21.4.2012	21:43:49.646	64.0535	-21.4165	2.12	0.056	0.19	0.16	0.18	1.32	manual
21.4.2012	21:46:13.969	64.0469	-21.4194	1.7	0.011	0.36	0.5	0.88	2.41	manual
21.4.2012	21:52:00.242	64.0533	-21.4165	2.38	0.062	0.17	0.16	0.16	1.77	manual
21.4.2012	21:56:02.714	64.0533	-21.4181	2.33	0.055	0.19	0.17	0.18	1.28	manual
21.4.2012	22:00:35.767	64.0521	-21.4128	2.45	0.05	0.19	0.19	0.16	1.61	manual
21.4.2012	22:01:04.792	64.0516	-21.4143	2.54	0.051	0.17	0.16	0.15	1.73	manual
21.4.2012	22:02:08.413	64.049	-21.4163	2.21	0.045	0.4	0.26	0.24	1.59	manual
21.4.2012	22:03:55.246	64.0493	-21.418	1.9	0.018	0.43	0.51	0.83	2.56	manual
21.4.2012	22:05:48.816	64.049	-21.4204	1.66	0.014	0.38	0.45	0.85	2.67	manual
21.4.2012	22:05:17.703	64.0497	-21.4196	1.73	0.013	1.06	1.48	1.28	2.57	manual
21.4.2012	22:08:26.533	64.0521	-21.4216	2.15	0.036	0.34	0.36	0.37	2.33	manual
21.4.2012	22:08:59.090	64.0531	-21.4165	2.24	0.035	0.28	0.29	0.28	1.91	manual
21.4.2012	22:09:05.044	64.0512	-21.4219	1.81	0.032	0.32	0.32	0.41	3.65	manual
21.4.2012	22:20:39.027	64.05	-21.414	1.8	0.009	0.35	0.4	0.7	2.52	manual
21.4.2012	22:27:26.902	64.0533	-21.4157	2.43	0.059	0.17	0.18	0.15	1.3	manual
21.4.2012	22:22:36.668	64.0504	-21.4189	1.63	0.013	0.35	0.39	0.77	2.54	manual
21.4.2012	17:17:58.550	64.05	-21.4164	2.01	0.012	0.43	0.72	0.94	2.44	manual
21.4.2012	23:34:21.582	64.0493	-21.4172	1.97	0.011	0.35	0.4	0.73	2.48	manual
21.4.2012	23:51:35.127	64.0465	-21.4137	1.42	0.02	0.35	0.46	0.96	2.58	manual
21.4.2012	22:59:38.053	64.0543	-21.4114	1.81	0.024	0.33	0.2	0.2	3.23	manual
21.4.2012	23:00:10.961	64.0538	-21.4125	1.74	0.022	0.29	0.35	0.28	2.89	manual
21.4.2012	23:11:24.318	64.0514	-21.4174	1.63	0.013	0.41	0.46	0.82	2.62	manual
21.4.2012	23:20:01.232	64.0484	-21.4105	1.96	0.064	0.16	0.16	0.17	1.63	manual

UNITED NATIONS UNIVERSITY
UNU-GTP
Geothermal Training Programme

Orkustofnun, Grensasvegur 9,
IS-108 Reykjavik, Iceland

Reports 2015
Number 33

STEAM AND BRINE GATHERING SYSTEM DESIGN FOR CACHAÇOS-LOMBADAS NEW PRODUCTION WELLS IN RIBEIRA GRANDE GEOTHERMAL FIELD

Nuno Vieira
EDA Renováveis
Rua Francisco Pereira Ataíde, 1,
9504-535, Ponta Delgada, Açores
PORTUGAL
nunvieira@eda.pt

ABSTRACT

The aim of this study is the development of a conceptual design of a steam and brine gathering system for the Cachaços-Lombadas new production wells and the separation station equipment. The typical configuration in Ribeira Grande geothermal field, consisting of a vertical steam separator and a brine accumulator tank for each well, is evaluated and compared to a single horizontal gravity separator serving all wells.

This study establishes design criteria for the pipe and separation station equipment sizing to try to solve some operational difficulties of existing wells in the field. The steam and brine design flow rates are assumed to be similar to the last make up well drilled in Cachaços-Lombadas, CL7, which is the most productive well of the field, having the expected total production of around 120 ton/h of saturated steam and 450 ton/h of brine. Aiming to minimize steam and brine gathering system piping pressure losses, a maximum velocity criterion of 30 m/s for steam and 1 m/s for brine was established. It was found that the gathering system nominal pipe sizes are DN 700 for steam and DN 400 for brine. The calculated pressure loss in the estimated 1400 m pipe route from the well pad to the plant is 0.7 bar in the steam line and 0.6 bar in the brine line. Some of the wells in Cachaços-Lombadas sector are subject to wellhead pressure fluctuations which results in flow rate changes that cannot be managed by the separation station equipment, namely the brine accumulator tank. Therefore, each accumulator tank is sized to act as a buffer to accommodate possible fluctuations coming up in the well. It has also been noticed that the steam quality decreases at the outlet of the steam separators in the well field, maybe due to undersize. To minimize this occurrence, the separator annular cross section area is sized to keep the upward steam velocity below 2 m/s and so enhance the gravity role in the separation efficiency.

The common horizontal gravity separator for the three wells is sized accordingly to the criteria' established by Verkís for Icelandic geothermal power plants. Its higher volume is better suited to accommodate possible fluctuations while its efficiency is less dependent on the fluid inlet velocity which allows to operate the three wells in any combination possible. The overall project cost is estimated to be € 6,100,000

while differences between installing three individual vertical separator stations and one single horizontal gravity separator is about € 92,500, which is not relevant or decisive in the overall estimated cost but the evaluation of technical matters between both types of separation shall be developed in a later stage of the project.

1. INTRODUCTION

1.1 Project background

The Azores archipelago is an autonomous region of Portugal, located in the Atlantic Ocean, about 1,600 km from the mainland (Figure 1). The island group consists of 9 individual islands with asymmetric small-scale independent power distribution systems which makes an interconnection between islands technically unfeasible (Rangel et al., 2011).

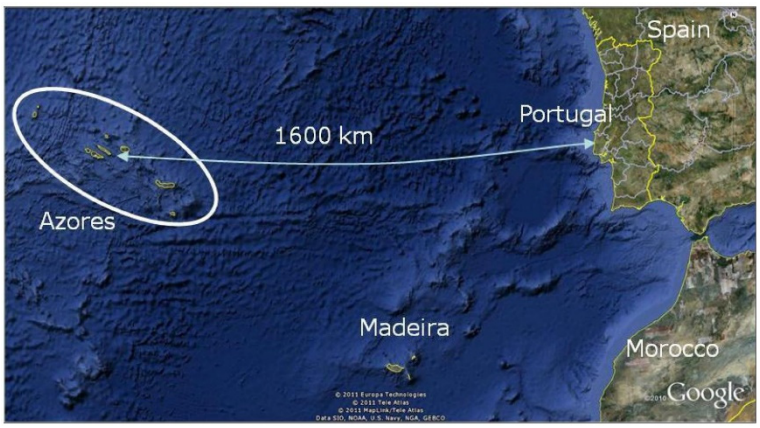

FIGURE 1: Location of Azores archipelago in the Atlantic Ocean (Google Earth)

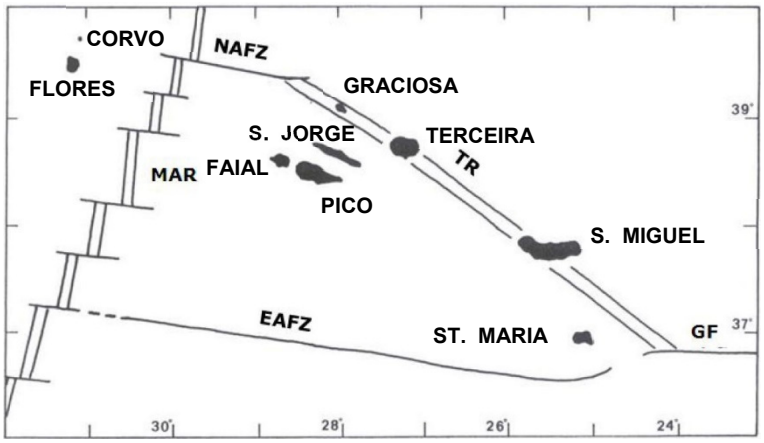

FIGURE 2: Main tectonic structures in Azores region: MAR – Mid Atlantic Ridge; NAFZ – Northern Azores Fault Zone; EAFZ – Eastern Azores Fault Zone; TR – Terceira Rift; GF - GLÓRIA Fault (Rangel et al., 2011)

The Azores islands are aligned following a WNW-ESE trend and emerge above the sea in the North Atlantic Ocean from a submarine topographic high designated as the "Azores Plateau" which is marked by the bathymetric line of 2,000 metres. The archipelago lies where the American, Euro-Asian and African lithospheric plates meet at the "Azores Triple Junction" (Figure 2). As result of this complex geotectonic setting, seismic and volcanic activity is frequent in the region (Rangel et al., 2011).

In six of the nine islands of the archipelago geothermal resources are available. However, due to the existing asymmetries between the islands in terms of population and energy demand, especially noticing that the population of São Miguel and Terceira is about 80% of the total population of the Azores, which is approximately 250,000 inhabitants, only in the largest islands the utilization of the geothermal resource for electricity production is economically feasible.

The power utility company of the Azores is Electricidade dos Açores (EDA) which manages all the production, transportation and distribution of electricity in the region. The archipelago is dependent on fossil fuel for electricity production. In 2014, the energy mix in the archipelago was 64% from fossil fuels (fuel oil and diesel) and 36% from renewable resources (geothermal, hydro, wind and biogas) of

which geothermal energy has the highest percentage with 23% of the total energy production (EDA, 2014).

EDA Renováveis is a subsidiary company of EDA and exploits the Ribeira Grande geothermal field located on the north flank of the Fogo volcano in Ribeira Grande city, São Miguel Island (Figure 3) for electricity production. The Ribeira Grande high temperature geothermal field is liquid-dominated with a maximum measured reservoir temperature of up to 245°C. It is composed by three sectors: Pico Vermelho, Cachaços-Lombadas and Caldeiras.

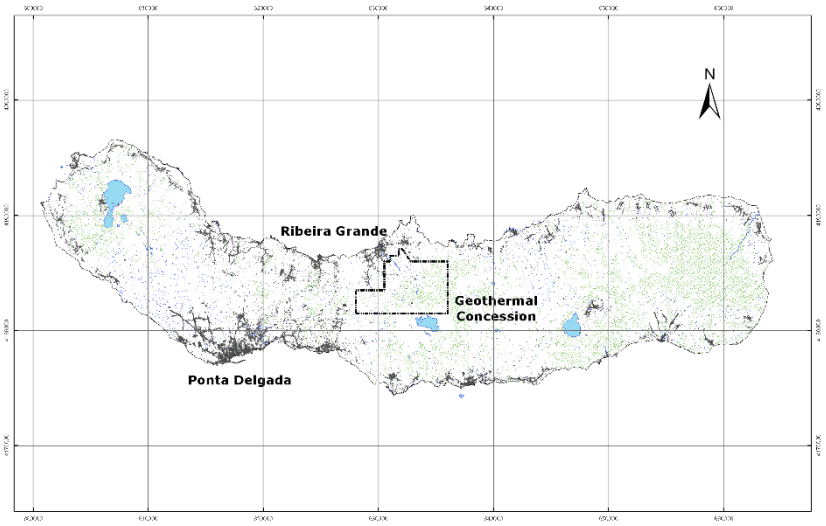

FIGURE 3: São Miguel Island (provided by EDA Renováveis)

The exploitation of the Ribeira Grande geothermal field dates back to 1980 in Pico Vermelho sector and presently only Cachaços-Lombadas and Pico Vermelho sectors are being exploited for electricity production. The concession area for the exploitation of the geothermal resource is identified in Figure 4 as a dotted line.

FIGURE 4: Ribeira Grande geothermal field

In the Cachaços-Lombadas sector, at the Ribeira Grande geothermal power plant, four two-phase binary units with a total rated gross power of 14.5 MWe at the generators terminals are installed which are supplied by steam and brine from 4 production wells, while all condensate and cooled brine is returned to the geothermal reservoir using 2 injection wells. After the deactivation of a back-pressure steam turbine of 3 MWe in the Pico Vermelho sector which was used from 1980 until 2005, a new two-phase binary cycle power plant was installed with one generator unit of 13 MWe gross power at the generators terminals. The steam and brine are supplied by 5 production wells and the condensate and cooled brine is completely reinjected using 3 injection wells.

The combined electrical production of Pico Vermelho and Ribeira Grande plants in 2014 was 183 GWh which represented 44% of São Miguel electrical grid demand. (EDA Renováveis, 2014). These high geothermal penetration values, added to a share of 10% from wind and hydro power plants in operation in São Miguel (EDA, 2014), is an evidence of the strategy of the Regional Government to increase the contribution of renewables sources in the energy mix, while minimizing the dependency on fossil fuel and acting on the sustainable development of the Azores.

1.2 Project motivation

The Ribeira Grande geothermal plant platform is located in an area bounded by two creeks. This geographical feature has been restraining the locations for drilling make-up wells. In fact, only two production wells were drilled from 2005 until present and consequently the power plant has not been able to run continuously at the rated gross power of 14.5 MWe. Therefore, due to the lack of geothermal fluid available, the Ribeira Grande geothermal power plant has been generating energy at an average net power of 9 MWe (based on the unit's operating hours).

The present area of interest, the so-called "Mata do Botelho", has been identified as a potential upflow zone of the geothermal field in which a well pad sized to drill up to 3 make up wells is now planned to be constructed, following EDA Renováveis decision to go forward with the evaluation of this site in order to put the plant operating at the rated gross power.

To access this new drilling site important preliminary civil works have to be executed such as building a new access road to allow the mobilization of the drilling rig and all auxiliary equipment. The project includes the drilling and testing of one production well and, if found productive, two more wells will be drilled. In the second case, a bridge of 6 m width and a length of 70 m will be required to overpass a 57 m deep creek. In addition, a new access road will be constructed to access the power plant platform terrain.

The final stage of the project will be the establishment of a connection of the make-up wells to the plant's steam and brine headers, the design of the separation stations and the gathering system with optimized alternative solutions. Here the already existing solutions implemented by the plant's original designer, in terms of piping material specifications and pipe supports criteria should be kept in mind.

1.3 Project objectives

The aim of this study is the development of a conceptual design of the gathering piping systems and separation station. The project objectives are the following:

- Configuration study of the separation station and gathering piping system;
- Preliminary design of the separation station(s);
- Selection of two-phase flow and steam and brine single flow pipe diameters;
- Preliminary calculation of pipe loads, pipe supports distances and expansion loops;
- Calculation of steam and brine piping pressure losses;
- Sizing of the brine booster pumps; and
- Cost estimation of the project.

The well pad for the new production wells is expected to be located at 430 m a.s.l., while the power plant platform is at 524 m a.s.l., resulting in an elevation difference of 94 m. Figure 5 shows the location of power plant, all existing wells and the "Mata do Botelho" area of interest for drilling the new production wells.

The project objectives shall consider the rated values at the power plant steam and brine headers as follows:

- Steam: 4.1 bar(g)
- Brine: 4.6 bar(g)

The new wells' productivity and operational parameters are assumed to be similar as for well CL7 under normal operation conditions. CL7 is the most recent make-up well which was drilled in 2010 and has demonstrated a stable and productive operation regime. The well operation parameters are as follows:

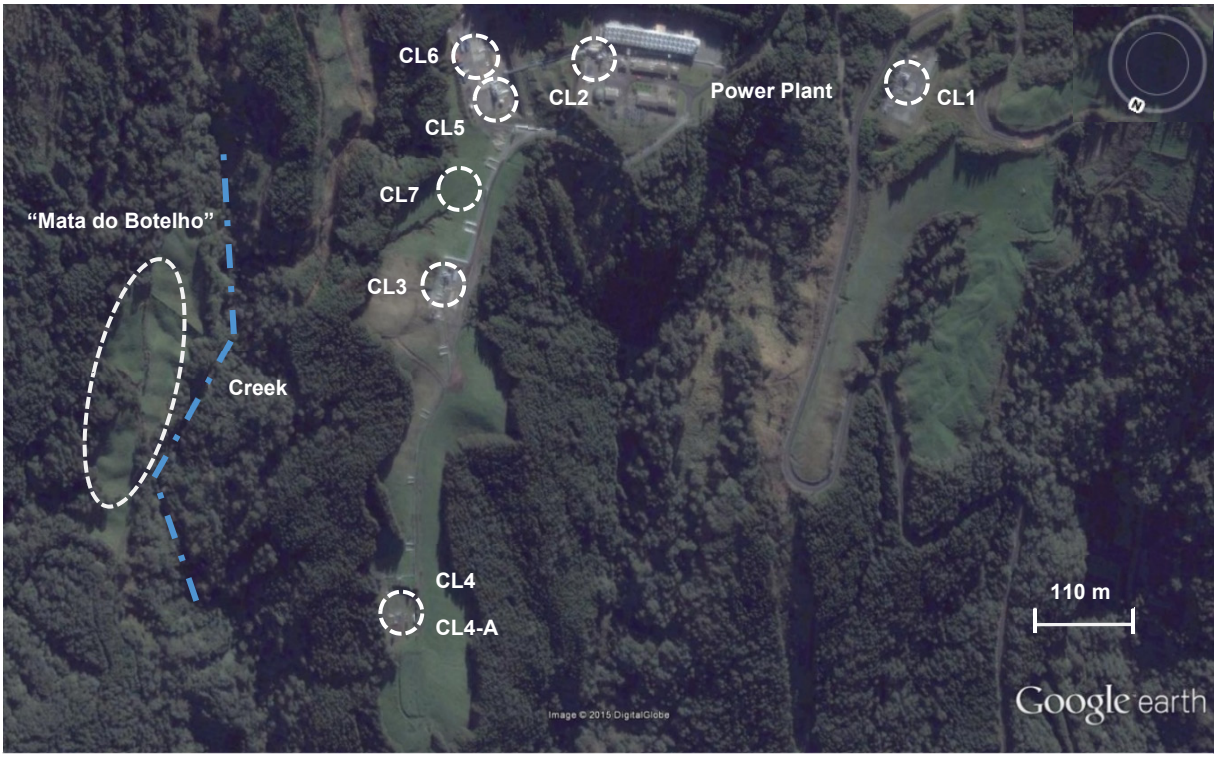

FIGURE 5: "Mata do Botelho" location (Google Earth)

- Wellhead pressure: 11 bar(g)
- Enthalpy: 1070 kJ/kg
- Steam flow rate: 11 kg/s (40 ton/h)
- Brine flow rate: 42 kg/s (150 ton/h)

The production parameters are considered to be ambitious since no other well drilled in Cachaços-Lombadas has such high production parameters as CL7.

This work presents two configurations of the separation station and gathering system piping, focused on minimizing steam and brine flow pressure losses. All the relevant sizing tasks that are to be developed in the scope of this work will be configured in order to be easily adjustable in case of varying production parameters, in the course of the testing of the first drilled well.

2. SYSTEM DESCRIPTION AND CONFIGURATIONS

Two alternative configurations for the wells' separation station and gathering system were studied and are presented in Figures 6 and 7. In both configurations, the separation will be at the well pad.

Configuration A
The solution is typical for the Ribeira Grande geothermal field wells. Each well is served by a vertical steam separator and a brine accumulator tank connected to a steam and brine header, the later through a booster pump. From the headers, one steam and one brine pipeline transports the geothermal fluids to the power plant. This configuration assures the least interference between wells and minimizes operational difficulties that may arise if the production characteristics of the wells are different while a control valve at each wellhead will allow to adjust the well to the required common separation pressure.

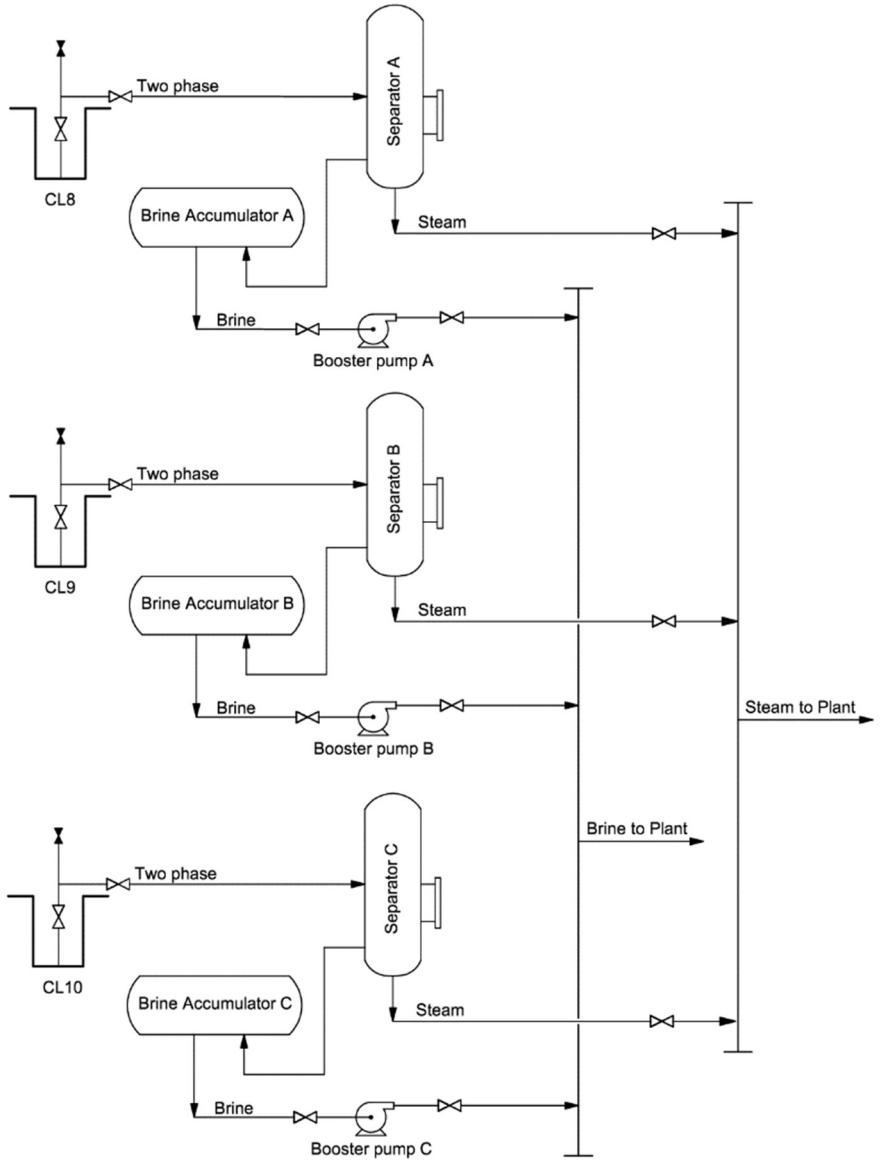

FIGURE 6: Separation station - Configuration A

The brine booster pumps principle of operation is to control the brine level in the accumulator, maintaining a buffer volume in case of sudden changes in the well operation. An important feature is the possibility to maintain continuous monitoring of the production of each well, adding flow measuring devices in each of the steam and brine lines, to satisfy the Ribeira Grande geothermal reservoir management strategy.

Configuration B

The studied solution considers the installation of one horizontal gravity separator as an alternative to the vertical cyclone separator. The operation of the wells should not have any limiting condition and be independent of each other. For a configuration that gathers the two-phase flow from the wells, the horizontal separator offers a more effective operation. It is not dependent on the flow velocity at the separator inlet compared to the vertical separator, for an efficient separation of the vapour and liquid phases.

In comparison to Configuration A, this solution lowers the materials requirements and minimizes the area required for the separation station and piping layout. The control of the separator liquid level can also be performed by the pumps although this requires a careful definition of the operation levels according to the combination of open wells. The main disadvantage of this configuration is that it does not allow a continuous monitoring of the steam and brine flow rates produced from each well. Thus it requires alternative ways to measure the flows such as chemical tracing in the two-phase piping from each well and establishing an admissible period of measurement. Flow measuring devices should also be installed after the separator in the steam and brine piping to measure the combined total flow.

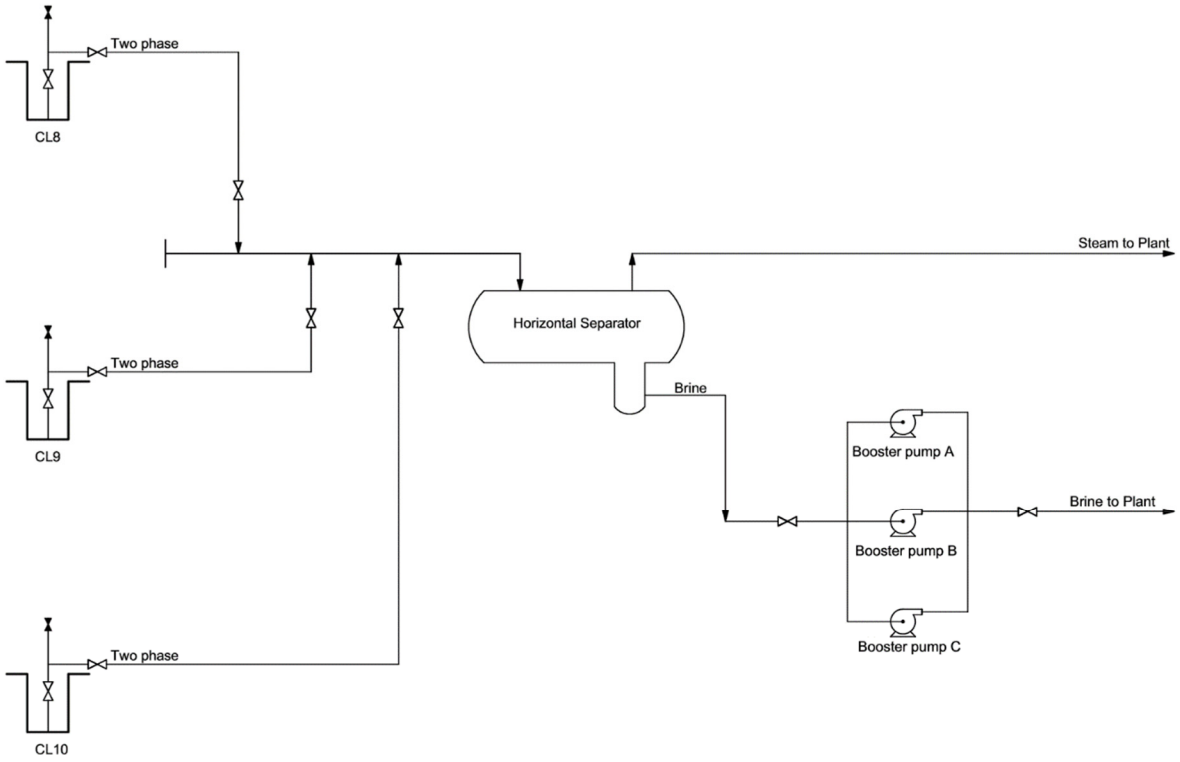

FIGURE 7: Separation station - Configuration B

3. PIPING DESIGN

3.1 Piping route selection

The steam and gathering piping route will follow the access road and bridge to connect the well pad, located at the creek's north margin, to the power plant platform at the south margin. The access road starts at an initial elevation of 430 m a.s.l. at the well pad, has a short downhill section to 428 m until it reaches the bridge section (70 m length). The next section is uphill, with two slopes of 10% and 19%, before the road ends at the final elevation of 462 m.

The steep slope and the expected high liquid fraction in the two-phase flow make it impracticable to run a two-phase flow pipe from the well pad along the access road to minimize total pipe length. Therefore, the two-phase flow will be separated at the well pad and separate steam and brine piping will transport the geothermal fluids to the power plant. From the south margin of the creek, the steam and brine pipes will follow a corridor of existing gathering system piping, duplicating the existing piping flexibility solutions until reaching the power plant platform for the final connection to the headers.

3.2 Piping specifications

The Ribeira Grande geothermal power plant piping specifications require that steam and brine piping material is carbon steel according to ASTM A106 Grade B or equivalent. The pipe thickness is according to ANSI Pipe Schedule STD with thicknesses of all fittings matching the pipe.

Piping
According to ASME B31.1 (ASME, 2007), the required properties of ASTM A106 Grade B steel pipe for the design temperature of 175ºC are presented in Table 1.

Pressure vessels
For the separation station pressure vessels construction, the material required is ASTM A516 Grade 70. According to ASME B31.1, the basic allowable stress for the design temperature of 175°C is shown in Table 2.

TABLE 1: A106 Grade B pipe properties

Properties	Values
Modulus of elasticity (E_h) (1)	193 GPa
Basic allowable stress (S_h)	118 MPa

(1) For carbon steels: C ≤ 0.3 %

TABLE 2: A516 Grade 70 plate properties

Properties	Values
Basic allowable stress (S_h)	138 MPa

3.3 Design conditions

The original design conditions both for the separated steam and brine gathering system piping, which are considered initial conditions in the scope of this study, are the following:

- Design pressure: 7.5 bar(g)
- Design temperature: 175°C
- Pressure class: 150#

The design conditions may be changed according to the calculated results that will define a preliminary separation pressure and the pump head required to boost the brine from the well pad platform to the power plant.

3.4 Pressure loss and pipe diameter selection

One of the main concerns in the design of the gathering system is the pressure losses in the steam piping from the wellhead to the power plant. The steam pressure drop is a function of the diameter, length and configuration of the steam piping as well as the density and mass flow rate of the steam. Of these, the most critical variable is the pipe diameter (DiPippo, 2007).

Two-phase flow piping
Since the separation will be done at the well pad, the length of the two-phase flow piping is reduced and therefore the expected friction losses were not considered relevant in the pipe diameter calculation. The two-phase flow pipe diameter selection was done based on the expected production of the wells, on the steam superficial velocity that should be kept around 30 m/s and on the recommended design parameters for geothermal vertical separators by Lazalde-Crabtree (Lazalde-Crabtree, 1984).

Separation station single-flow piping
The pressure loss in the single-flow piping from the separation station could not be determined at this time. However, due to its expected short length the pressure loss is not expected to be significant. The pipe diameter calculation will consider only the recommended maximum values for the steam and brine velocities.

Gathering system single-flow piping
For the gathering system single-flow piping, the diameter selection was made in a way to minimize friction losses to establish a low velocity criterion for the steam and brine flows. Also, it was evaluated how the reduction of the pipe diameter penalizes the friction losses, allowing the selection of the final diameter. The pipe length from the well pad to the power plant platform is found to be about 1410 m with 90 bends including expansion loop legs.

In this scenario, a first calculation of the pipe diameters and friction losses for several steam and brine flow velocities was carried out and two alternatives of pipe diameters were identified for steam and brine. In order to calculate the friction head losses, either fluid velocity or pipe diameter should be chosen, using Equations 1 or 2:

$$v = \frac{4\dot{Q}}{\pi d^2} \tag{1}$$

where v = Fluid velocity (m/s);
$\dot{Q}$ = Volumetric flow rate (m^3/s);
d = Inside diameter of pipe (m).

or

$$v = \frac{4\dot{m}}{\pi \rho d^2} \tag{2}$$

where $\dot{m}$ = Mass flow rate (kg/s);
ρ = Fluid density (kg/m^3).

The friction head loss (h_{loss}) in straight pipes, expressed in meter of fluid height, is calculated by the Darcy-Weisbach which is introduced as Equation 3:

$$h_{loss} = \frac{fL}{d}\frac{\bar{v}^2}{2g} \tag{3}$$

where f = Friction factor;
L = Pipe length (m);
$\bar{v}$ = Average fluid velocity (m/s);
g = Gravitational constant (m/s^2).

The friction factor is dependent on the Reynolds number which distinguishes the laminar or turbulent nature of the flow.

The Reynolds number is defined in Equation 4:

$$Re = \frac{\rho v d}{\mu} \tag{4}$$

where μ = Fluid dynamic viscosity (kg/(m s)).

The flow is considered to be laminar when $Re \leq 2100$ and turbulent when $Re > 5000$. The friction factor can then be calculated by the relations given by Equations 5 and 6.

Laminar flow

$$f = \frac{64}{Re} \tag{5}$$

Turbulent flow
The friction factor for turbulent flow is calculated by the Colebrook-White equation:

$$\frac{1}{\sqrt{f}} = -2\log_{10}\left(\frac{\epsilon}{3.7d} + \frac{2.51}{Re\sqrt{f}}\right) \tag{6}$$

where ϵ = Pipe absolute roughness (m);
= 0.005 (m).

Pipe fittings like bends and connections, valves and others induces friction head losses that are added to Equation 3, resulting in Equation 7:

$$h_{loss} = \frac{fL}{d}\frac{\bar{v}^2}{2g} + \sum_{i=1}^{n} n_i k \frac{\bar{v}^2}{2g} \tag{7}$$

where k = Loss coefficient of each type of pipe fittings and valves;
n = Number of pipe fittings and valves.

In this study it was not considered relevant to add valves and connections such as t-joints and others for the evaluation of the head loss because of its low number compared to the existing bends. The loss coefficient considered for 90° bends is 0.15 (Krex, 1986).

The recommended steam and brine flow velocities should be according to the following:

v_{steam} ≤ 30 m/s
v_{brine} ≤ 1 m/s

The selected diameters where then used to perform a more detailed analysis of the steam pressure loss. The variation of the steam density caused by the pressure drop on the way from the separation station to the plant steam header is analysed, allowing also a prediction of the separation pressure for each steam gathering system pipe diameter.

3.5 Brine booster pumps

Due to the 94 m elevation difference between the well pad and the power plant, pumps are required to boost the brine from the accumulator tank at the well pad to the header at the power plant platform. The pump power *P* is calculated using the Equation 8:

$$P = \frac{\rho g H Q}{\eta} \tag{8}$$

where H = Head (m);
Q = Volumetric flow rate (m^3/s);
η = Overall efficiency of pump and motor = 0.70.

The pump head can be estimated by applying the Bernoulli Equation between the pump inlet at 1 and the plant brine header at 2, resulting in Equation 9, expressed in height of fluid:

$$\frac{p_1}{\rho g} + \frac{v_1^2}{2g} + z_1 + H - h_{loss_{1-2}} = \frac{p_2}{\rho g} + \frac{v_2^2}{2g} + z_2 \tag{9}$$

where p = Static pressure (Pa);
z = Elevation (m).

The term $\left(\frac{v_2^2}{2g} - \frac{v_1^2}{2g}\right)$ is comparably small because the velocities are similar and can be neglected. Thus Equation 9 can be simplified, resulting in Equation 10:

$$H = \left(\frac{p_2 - p_1}{\rho g}\right) + (z_2 - z_1) + h_{loss_{1-2}} \tag{10}$$

3.6 Pipe thickness

The minimum wall thickness t_m of the gathering system piping for straight pipe is determined under internal pressure in accordance with Equation 11:

$$t_m = \frac{P D_0}{2(SE + Py)} + A \tag{11}$$

where P = Internal design gauge pressure (Pa);
D_0 = Outside diameter of pipe (m);
S = Basic allowable stress (Pa);
E = Weld joint efficiency factor;
y = Temperature coefficient dependence;
A = Additional thickness (m).

For ferritic steels and temperatures of 482°C or below, the *y* coefficient value is 0.4. The weld joint efficiency factor E is included in the allowable stress values given by ASME B31.1 and presented in Tables 1 and 2. Table 1 is applied for a seamless pipe. The additional thickness for corrosion is 3 mm.

The pipe nominal thickness t_n should be chosen according to the power plant piping specifications with a wall thickness corresponding to the STD schedule for each pipe diameter selected.

3.7 Pressure vessel thickness

The thickness of the pressure vessels with internal pressure will also be evaluated through Equation 11. The temperature dependent coefficient y is 0.4, taking the steel and the design temperature in consideration. The weld joint efficiency factor E is assumed to be 1 and the additional thickness for corrosion is 3 mm.

4. SEPARATION STATION DESIGN

4.1 Separation station design

As presented in the possible configurations for the separation station, there are two types of separators, the vertical Webre separator and the horizontal gravity separator. One of the identified operational difficulties of the wells at the Cachaços-Lombadas sector are the fluctuations caused by different inflow zones with different enthalpies. These fluctuations cause changes in the steam and brine flow that has to be dealt by the separation station equipment. The main concern is to avoid dumping brine from the vessels to the surroundings during high peak production periods of brine. The design of the vessels is studied in order to accommodate these excesses and provide the control system the time for the brine booster pumps to react accordingly to the fluctuations.

4.2 Webre separator

Most geothermal fields in the world, like the Ribeira Grande field, are water dominated, producing liquid and steam. The steam can be separated and removed from the mixture before feeding the power plant equipment such as steam turbines where the steam is expanded, or two-phase binary plant heat exchangers.

The most popular steam-water separator is the Webre type. The Webre steam-water separator design is widely used in New Zealand, Philippines, Indonesia, Kenya and elsewhere in the world. It has been very successful with a separation efficiency claimed to be as high as 99.97% (Foong, 2005). In 1961, Bangma ran a series of experiments with a spiral inlet separator. By progressively increasing the inlet velocity of the separator, he demonstrated that the separation efficiency increases until a breakdown velocity is reached. Above this velocity the efficiency deteriorates rapidly. His spiral inlet separator achieves the highest efficiency

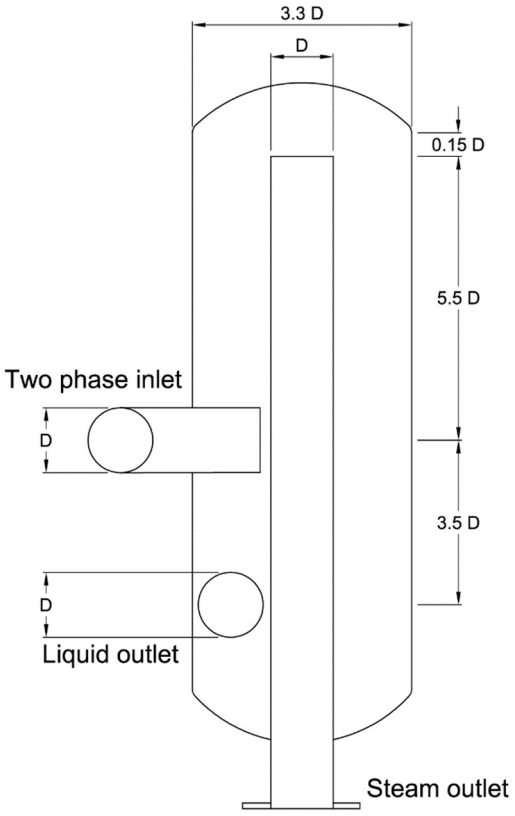

FIGURE 8: Webre separator design parameters (Lazalde-Crabtree, 1984)

when the steam inlet velocity is between 30 and 40 m/s. The breakdown velocity is approximately 45 m/s (Foong, 2005). The Webre type separator is also used in both Pico Vermelho and Ribeira Grande geothermal power plants since 1980.

Lazalde-Crabtree recommended several design parameters for geothermal separators as guidelines. Both geometrical and flow parameters are shown in Figure 8 and Table 3.

TABLE 3: Recommended design parameters for geothermal separators (Lazalde-Crabtree, 1984)

Parameter	Value
Maximum steam velocity at inlet of two-phase inlet pipe	45 m/s
Recommended range of steam velocity at the two-phase inlet pipe	25-40 m/s
Maximum annular upward steam velocity inside cyclone	4.5 m/s
Recommended range of upward annular steam velocity inside cyclone	2.5-4.0 m/s

From operation experience of the Ribeira Grande geothermal field power plants, it was verified that the design of the vertical separator differs from the design parameters recommended by Lazalde-Crabtree. These are the vessel diameter, promoting a lower annular upward steam velocity and the distance between the two-phase inlet and liquid outlet nozzles which are higher in practice.

Based on the experience of operation of the installed separators and considering its more recent design, the parameters for the vertical separators for the new Cachaços-Lombadas wells were adjusted according to Figure 9. The separator general design was according to the following criteria:

1. The inside diameter of the separator is optimized for the annular upward steam velocity inside the cyclone and does not exceed 2 m/s;
2. The brine outlet diameter is selected in order to keep the free flow from the separator to the accumulator in the velocity range from 0.3 to 0.4 m/s. It is calculated for a full cross-sectional flow, thus providing the additional cross-section area for peak brine flow due to well fluctuations.

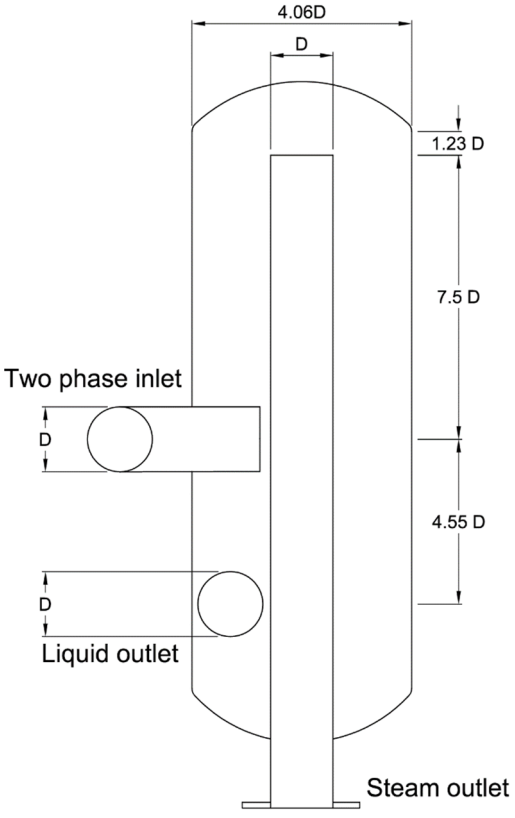

FIGURE 9: Webre separator design parameters for Cachaços-Lombadas

4.3 Brine accumulator tank

The task of the brine accumulator tank is to receive the liquid phase of the mixture after separation, including all salts and other solids of the fluid. In the Ribeira Grande geothermal field, the brine is pumped to the plant main header to feed the binary unit's preheaters. The use of a brine accumulator promotes a stable flow, acting as a buffer to accommodate wells fluctuation to a certain extent. By maintaining its level, it keeps the accuracy of the control of the process within certain limits.

The sizing of the brine accumulator tank, respectively, its approximate volume and initial inside diameter, should be chosen according to the following guidelines:

1. The tank normal operation level corresponds to 120 s of the well brine flow when connected to a single well;

2. The high level of operation is defined as 85% of the full tank height filler. The time required to fill the vessel from normal to high level should be at least 180 seconds;
3. The length of the tank is $L = 4D$, where D is the inside diameter.

4.4 Submergence of pumps and outflow diameter selection for water from a tank with a free surface

The minimum level of brine in the accumulator tank for safe pump operation can be found by the submergence depth S. Submergence of pumps is one parameter which may affect the swirl entering the pump and is certainly important with regard to the formation of strong vortices. The criterion to calculate the minimum submergence depth generally involves the parameter F_B, according to Equation 12, which is akin to the Froude number based on the bell mouth diameter D_B (Clark, 2002):

$$F_B = \frac{V_B}{\sqrt{gD_B}} \qquad (12)$$

where V_B = Average velocity through the plane of the bell mouth (m/s).

The bell mouth diameter corresponds to the brine outlet nozzle inside diameter. The minimum submergence depth to satisfy the criterion is presented in Equation 13:

$$\frac{S}{D_B} > 2.3F_B + 1.0 \qquad (13)$$

4.5 Horizontal gravity separator

A typical illustration of a horizontal gravity separator is shown in Figure 10. The main principle of separation here is gravity, augmented by a set of vane baffle plates fitted to the bottom of the vessel and a horizontal perforated droplet removal plate, or wire mesh screens, at the entrance to the steam exit chamber. The design of the horizontal gravity separator, represented in Figure 11, should be done according to the following requirements given by Jóhannesson and Gudmundsson (2014).

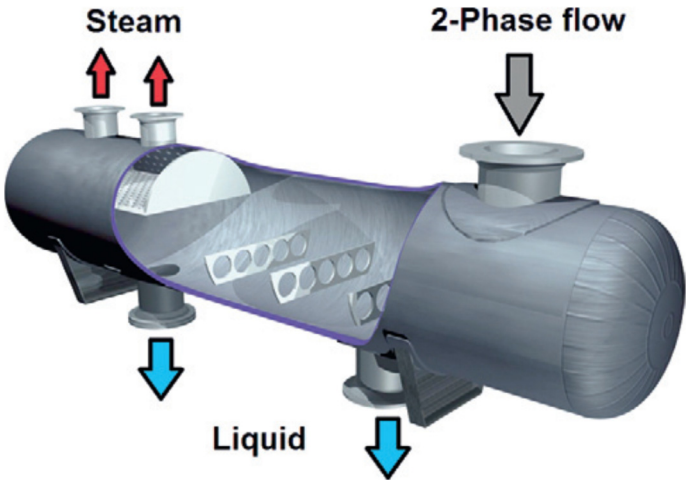

FIGURE 10: Horizontal gravity separator (DiPippo, 2007)

The main design requirements of the horizontal gravity separator are the Chevron type filter cross-section and the vessel bottom brine section. The separated steam will be channelled to the vessel outlet through a Chevron type filter. The filter cross-section area and the steam velocity through the filter are calculated according to Equations 14 and 15:

$$K_f = U_d \sqrt{\frac{\rho_g}{(\rho_l - \rho_g)}} \qquad (14)$$

where K_f = Souders-Brown velocity (m/s) – (0.18 - 0.2 m/s for FLEXCHEVRON);
U_d = Steam velocity through filter (m/s);
ρ_g = Density of the steam phase (kg/m^3);
ρ_l = Density of the liquid phase (kg/m^3).

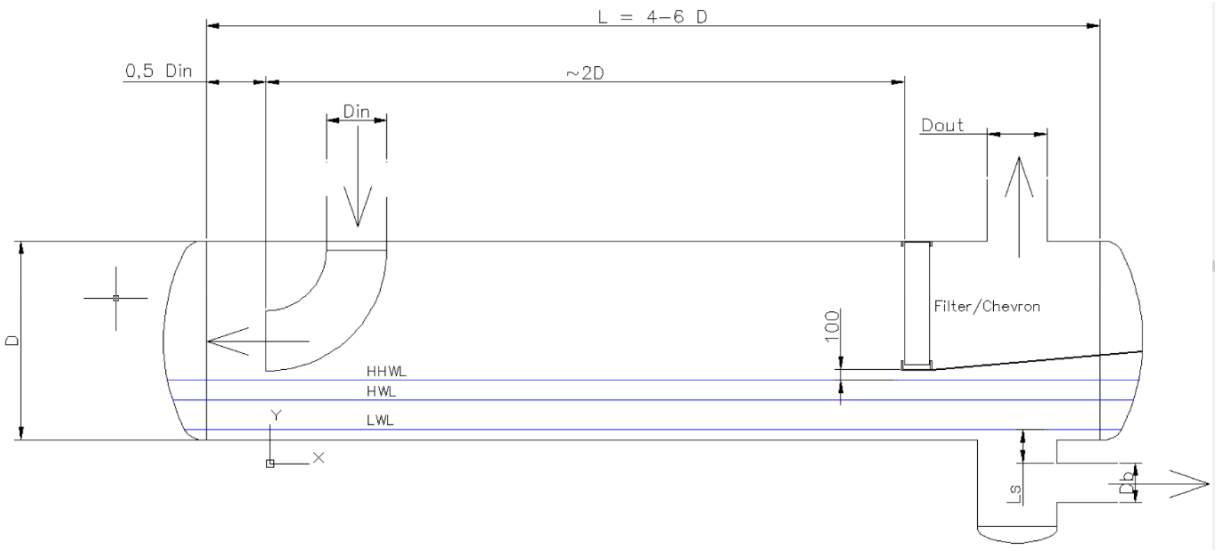

FIGURE 11: Horizontal gravity separator design requirements
(Jóhannesson and Gudmundsson, 2014)

$$\dot{V}_g = A_s U_d \tag{15}$$

where ($\dot{V}_g$) = Volumetric steam flow rate (m^3/s);
A_s = Cross-section area of the filter (m^2).

The design of the separator should comply with the following requirements:

1. A_s = 50-60 % of the total cross section;
2. $L = 4 - 6D$;
3. The level of the brine section allows a stable level control. The volume corresponds to the amount of fluid equivalent to 40-120 s of the brine flow, depending on how many wells are connected to the separator. For this study the selected time is 120 s.
4. The high tank should be kept at least 100 mm below the filter section assembly;
5. The time required to fill the vessel from normal to high level should be at least 60 s;
6. Low brine level should correspond to the submergence depth;
7. Brine outflow drip leg diameter should not be less than D/4.

Horizontal separator nozzle schedule
The definition of the horizontal separator nozzles diameters will be done by calculating the inlet and outlet inside diameters that satisfy the established criteria for the maximum steam and brine velocities. Rewriting Equation 2 as a function of the inside diameter, results in Equation 16:

$$d = \sqrt{\frac{4\dot{m}}{v\pi\rho}} \tag{16}$$

The steam and brine velocities should be according to the following:

v_{steam} ≤ 30 m/s
v_{brine} ≤ 1 m/s

4.6 Flow measurements

In the Ribeira Grande geothermal field, the steam and brine flows are continuously monitored by the power plants *Scada* control system. The flow measurement is done by a *pitot tube* type sensor inserted in each well's steam and brine line after the separator. This condition is also satisfied during a

simultaneous operation of the wells since each well has its individual separation station. Vortex flowmeters have been found giving good results in the brine service in the Ribeira Grande geothermal power plant. They are considered a valid alternative to the *pitot tube* type which is sensitive to solids that are present in the geothermal fluids.

In the case of a single separator which can be found in all of the wells, the measurement of the steam and brine flow from each well is not possible, only the combined measurement for all wells can be done. Nevertheless, this situation can be surpassed if temporarily only a single well is in operation what allows the measurement of flows produced by this well.

Flow tracer testing can also be an alternative for measuring the steam and brine flows of each well.

5. MECHANICAL STRESS ANALYSIS

5.1 Loads acting on piping

The loads and stresses acting on the piping are separated into two types depending on their duration. The first type is called sustained loads, or loads which can be expected to be present virtually at all times of the plant's operation. Examples would be weight and pressure loadings associated to the piping normal operating conditions. The second type is called occasional loads, or loads which are present during only a small period of the piping system operating time. Examples of occasional loads are high winds, fluid hammer, relief valves discharge, earthquakes and high-energy pipe break (Smith and Van Lann, 1987). The sustained loads to be considered in the frame of this work are the pipe medium and insulation weights. As representatives of the occasional loads wind and seismic activity are analysed.

Most of the formulas presented in this chapter are from Jónsson (2015): *Mechanical design of geothermal power plant*, unless referenced otherwise.

5.1.1 Sustained loads

According to ASME B31.1, the sum of the longitudinal stresses (S_L) due to pressure, weights and other sustained loads does not exceed S_L, as seen in Equation 17:

$$S_L = \frac{PD_0}{4t_n} + \frac{0.75iM_A}{Z} \leq 1.0S_h \tag{17}$$

where t_n = Selected nominal wall thickness (m);
M_A = Sustained bending resulting moment (Nm);
S_h = Basic material allowable stress at maximum (hot) temperature (Pa);
i = Stress intensity factor (the product 0.75i shall never be taken less than 1);
Z = Section modulus m^3 = π/32 (D_0^4-d^4)/D_0.

Vertical sustained loads
The vertical sustained loads are designated as q_{vs} and calculated by Equations 18, 19, 20 and 21:

$$q_{vs} = q_p + q_e + q_v \tag{18}$$

$$q_p = \pi g \rho_s \left(\frac{D_0^2 - d^2}{4}\right) \tag{19}$$

$$q_e = \pi g \rho_e \left(\frac{D_e^2 - d^2}{4}\right) \tag{20}$$

$$q_v = \pi g \rho_v \left(\frac{d^2}{4}\right) \tag{21}$$

where q_p = Pipe weight (N/m);
q_e = Insulation weight and cladding (N/m);
q_v = Medium weight (N/m);
ρ_s = Density of steel (kg/m^3) = 7850 kg/m^3 for carbon steel;
ρ_e = Density of thermal insulation (kg/m^3) = 100 kg/m^3 for mineral stone wool;
D_e = Outside diameter of insulation (m).

The insulation thickness to be considered is 100 mm.

5.1.2 Occasional loads

As per ASME B31.1, the effects of pressure, weight, other sustained loads, and occasional loads must meet the following requirement in Equation 22.

$$\frac{PD_0}{4t_n} + \frac{0.75iM_A}{Z} + \frac{0.75iM_B}{Z} \leq kS_h \quad (22)$$

where M_B = Occasional bending resulting moment (Nm);
k = 1.15 for occasional loads acting no more than 8 hours at any time and no more than 800 hour/year;
= 1.20 for occasional loads acting far no more than 1 hour at any one time and no more than 80 hour/year;
= 1.00 in other cases.

The k factor considered is 1.

The occasional loads acting on the pipe can be divided in vertical and horizontal:

Vertical occasional loads
The vertical occasional load q_{vo} is calculated according to Equations 23, 24 and 25.

$$q_{vo} = q_s + q_{sv} \quad (23)$$
$$q_{sv} = 0.5eq_g \quad (24)$$
$$q_g = q_v + q_p + q_e \quad (25)$$

where q_s = Snow weight (N/m);
q_{sv} = Seismic load (N/m);
e = Seismic factor = 0.30

Snow weight q_s is not a load that needs to be considered at the Ribeira Grande geothermal power plant site. So, the vertical occasional load consists only of seismic load q_{sv}.

Horizontal occasional loads
The horizontal occasional load q_{ho} is the maximum value of wind and seismic load calculated through Equations 26-29.

$$q_{ho} = max[q_w, q_{sh}] \quad (26)$$
$$q_w = CpD_e \quad (27)$$
$$p = \frac{v_w^2}{1.6} \quad (28)$$
$$q_{sh} = eq_g \quad (29)$$

where q_w = Wind load (N/m);
q_{sh} = Seismic load (N/m);
C = Form factor, C=0.6 for round pipe;
p = Wind pressure (N/m^2);
v_w = Wind speed (m/s) = 36 m/s (130 km/h).

The seismic factor and wind speed v_w are empirical values based on recent geothermal power plant projects in São Miguel Island by EDA Renováveis.

5.2 Bending moments

The bending moments of the pipeline are calculated making the assumption that the pipe is a simple supported beam with a length L_s between supports and with uniform load over the entire span. This will give us a conservative figure for distance evaluation between supports. In this case, the bending moment is maximal in the middle of the pipeline and so the resulting sustained and occasional moments are according to Equations 30 and 31 (Krex, 1986).

$$M_A = \frac{1}{8} q_{vs} L_s^2 \tag{30}$$

This study does not consider the existence of sustained concentrated loads between supports such as valve weight that should be analysed case by case in a later more detailed design stage. Nevertheless, the installation of valves increases the resultant sustained bending moment M_A, therefore the length between supports should be reduced in the sections where valves are installed.

$$M_B = \frac{1}{8} \sqrt{q_{vo}^2 + q_{ho}^2}\, L_s^2 \tag{31}$$

where L_s = Length between supports (m).

5.3 Deflection criteria

The length between supports can also be determined by the deflection criterion of the pipeline. For a simple supported beam with the support distance L_s the maximum deflection δ is in the middle of the beam and it is given by Equation 32.

$$\delta = \frac{5}{384} \frac{q L_s^4}{EI} \tag{32}$$

where q = Uniform load (N/m) = q_g;
E = Modulus of Elasticity (Pa);
I = Moment of Inertia (m^4) = $\pi/64\ (D_0^4 - d^4)$.

The maximum deflection should be less than $L_s/500$ (Jóhannesson, Th., personal communication) for both steam and brine piping.

5.4 Length between supports L_s

The length between supports L_s is calculated for sustained and occasional loads according to the deflection criterion and the minimum result is selected. For the sustained and occasional loads, the length between supports is the maximum solution of Equations 17 and 22. The final length between supports can be then defined according to the designer criteria and the final sum of the longitudinal stresses S_L can be recalculated.

The calculated length corresponds to a maximum value that satisfies the criteria and the designer is free to choose shorter lengths.

5.5 Thermal expansion of pipeline

Geothermal gathering systems pipelines carry high temperature fluids such as brine and steam. Due to

the temperature variations that occur in the piping between installation and operation, materials will be subject to expansion and contraction, designated in general terms as thermal expansion. The expansion ΔL (m) in a pipe with a length L (m) due to a temperature change is given by Equation 33:

$$\Delta L = \alpha L \Delta T \tag{33}$$

where α = Thermal expansion coefficient (1/°C)
ΔT = Temperature variation (°C);

According to ASME B31.1, the thermal expansion coefficient for carbon and low alloy steels in the temperature range of 20-175ºC is 12.5 × 10^{-6} (1/ºC). A temperature variation of 165ºC is considered, assuming an installation temperature of 10ºC.

Since every piping system has restrictions that prevent free expansion, thermal expansions will always create stresses but, if the system if flexible enough, the expansion may be absorbed without creating undue stresses that may damage the piping system, the supports and the equipment to which the pipes are connected (Smith and Van Lann, 1987). It is then necessary to design a piping system with enough flexibility to absorb the thermal expansion, adding solutions like changes of direction and U shape pipe loop which comprises the expansion loops.

5.6 Flexibility and expansion loops

In the scope of this work two types of expansion loops will be considered that assure the required gathering system piping flexibility, a change in direction and U shaped loops. According to ASME B31.1, all piping should meet the following requirements with respect to flexibility:

1. The piping system duplicates a successfully operating condition or replaces a system with a satisfactory service record;
2. The piping system can be adjudged adequate by comparison with previously analysed systems;
3. The piping system is of uniform size, has not more than two anchors and no intermediate restraints, is designed for essentially noncyclic service (less than 7,000 total cycles), and satisfied the following criterion (Equation 34):

$$\frac{D_0 Y}{(L-U)^2} \leq 208.3 \tag{34}$$

where Y = Resultant displacement between the anchors to be absorbed by the piping (mm);
L = Developed length of pipe along the longitudinal axis (m);
U = Anchor distance (straight line between the anchors) (m).

The gathering system piping of the new wells can be divided into two sections in respect to the flexibility analysis. The first section is new and has a length of almost 400 m. It is located between the well pad and the south margin, where the second section starts in a corridor of existing gathering system piping. The first section meets requirement 3 and the second section meets requirement 1, meeting the empirical values of the existing piping system.

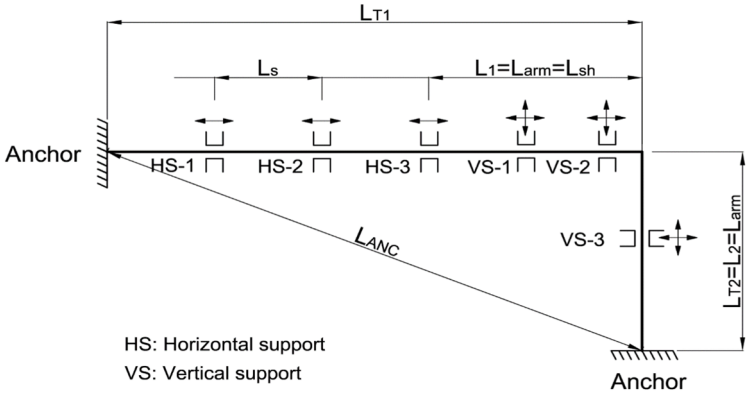

FIGURE 12: Change of direction expansion loop

Change of direction expansion loop
The change of direction expansion loop is exemplified in Figure 12 and meets the requirements of Equation

39 with respect to the arm length. In Jónsson, (2015), the variables of Equation 34 are calculated as follows:

$$Y = \alpha \Delta T \sqrt{L_{T1}^2 + L_{T2}^2} \tag{35}$$

$$L_{ANC} = \sqrt{L_{T1}^2 + L_{T2}^2} \tag{36}$$

$$L = L_1 + L_2 \tag{37}$$

$$U = \sqrt{L_1^2 + L_2^2} \tag{38}$$

Assuming $L_1 = L_2 = L_{arm}$ and substituting the above variables in Equation 34 results in:

$$L_{arm} \geq \sqrt{\frac{D_0 \alpha \Delta T L_{ANC}}{71.48}} \tag{39}$$

The criterion is applied assuming a distance L_{ANC} between the anchors calculated from the expansion arm length L_{arm}.

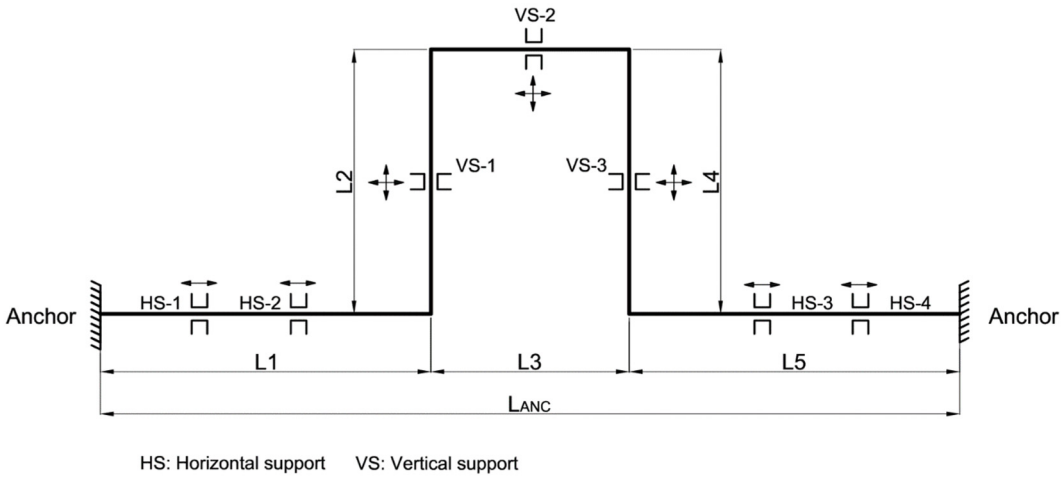

FIGURE 13: U-shape expansion loop

U-shape expansion loop

U-shape expansion loop as shown in Figure 13 can be positioned either vertically or horizontally, depending on the land topology and land use restraints, in the second case for instance, to give passage to animals in the neighbouring pastures. According to Jónsson (2015), U-shape loop sizing can be according to Equation 40:

$$L_2 = \sqrt{\frac{3ED_0\Delta}{S_A}} \tag{40}$$

where Δ = Resultant displacement between anchors (m);
S_A = Allowable stress range (Pa).

Also:

$$L_3 = L_2 \text{ or } L_3 = \frac{L_2}{2}$$

And:

$$S_A = f(1.25S_c + 0.25S_h) \tag{41}$$

where f = cyclic stress range factor ($f \leq 1$), assumed 1;
S_c = Basic material allowable stress at the minimum metal temperature expected (Pa);
S_h = Basic material allowable stress at the maximum metal temperature expected (Pa).

As per ASME B31.1, when S_h is greater than S_L, the difference between them may be added to the term $0.25S_h$ in Equation 41. In this case, the allowable stress range S_A is calculated by Equation 42:

$$S_A = f(1.25S_c + 1.25S_h - S_L) \quad (42)$$

However, this was not considered here.

From Equations 39 and 40 it can be concluded that larger diameter pipes require longer arm loops to accommodate the expansion stresses between anchors, indicating that it is the steam pipe that defines the geometry of the piping system. Typically, vertical loops are limited by the bend leg length since long loops are subject to undesirable wind loads and therefore the distances between anchors have to be shorter. Horizontal loops, if not limited by the land topography and use, have longer bend legs, requiring more supports but allowing longer distance between supports which reduces the total number of loops required.

6. COST ESTIMATE OF IMPLEMENTATION

In the following, the cost estimate of implementation of the steam and brine gathering system piping and separation stations, considering three vertical separators and accumulator tanks or one common horizontal gravity separator, will be presented. All prices presented are in Euro (€). Since the gathering system piping is part of both alternatives, the difference in total cost is the result from the cost of the pressure vessels. We compare three vertical separators and brine accumulator tanks or one horizontal gravity separator.

The cost estimate is based on unit prices of piping, valves and pumps, indicators for steel construction, piping and equipment erection works at site as well as anticorrosion protection using paint coating and thermal insulation works, including aluminium cladding. All prices and indicators are those of Portugal mainland materials suppliers and mechanical contractors for the construction and erection works.
Civil works for foundations of piping and equipment were estimated based on the associated mechanical works. In the total combined costs of mechanical and civil works, the mechanical works corresponds to 70% while civil works reflect only 30%, including steel hardware for pipe supporting (Jóhannesson, Th: personal communication). The electrical, control and instrumentation works were estimated to be 15% of the referred combined costs.

Detailed design and supervision works are empirical values based on EDA Renováveis' experience in similar projects in the past and are assumed to be 7.5% of the referred combined costs.

6.1 Materials

Piping
The most representative piping for the separation stations and gathering systems were pipes with 28", 16" and 10" diameter. The unit prices of pipe and 90° long radius bends are presented in Table 4.

The 28" pipe is not seamless but longitudinal welded.

TABLE 4: Piping and bends unit prices

Material description	Unit price
28" pipe API 5L Gr. B ERW Sch. STD	275 €/m
16" pipe A106 Gr. B 16" Sch. STD	150 €/m
10" pipe A106 Gr. B 16" Sch. STD	90 €/m
28" long radius bend A234 WPB Sch. STD	1055 €/EA
16" long radius bend A234 WPB Sch. STD	285 €/EA
10" long radius bend A234 WPB Sch. STD	105 €/EA

Valves
The valves considered for the estimate are the 28", 16" (for the gathering system piping) and 8" (for the separation station brine piping) in diameter and their costs are presented in Table 5.

TABLE 5: Valves unit prices

Material description	Unit price
28" A216 WCB gate valve Trim 5	10,000 €/EA
16" A216 WCB gate valve Trim 5	5000 €/EA
8" A216 WCB gate and check valves Trim 5	1750 €/EA

Pumps
The unit price for a brine booster centrifugal pump including duplex stainless steel impeller and casing, double mechanical seal shaft sealing, coupling and a 60 kW electrical motor, with pump and motor installed in a steel frame, is estimated to be € 35,000.

6.2 Mechanical construction and erection works

The delivery time of the project was calculated to be between 8 and 9 month or about 200 days. It is important to mention that the climatic conditions at the construction site are very variable, with wind and precipitation typically influencing the works execution, causing the extension of the delivery time.

Piping
In past projects at the Ribeira Grande geothermal power plant, an experienced welder could completely execute two 12" Sch. STD pipe weldings during a work day. The estimated time for the 28", 16" and 10" weldings were evaluated based on this indicator and on the pipe diameter. In these conditions, it was calculated that a total of 5 welders are required to execute both the setup of the separation station and gathering the system piping within the delivery time of 200 days.

The cost of the supporting team of welders and other workers required is estimated to be 5,300 €/day, based on prices from similar projects of EDA Renováveis. For erection works, a crane is needed, a forklift and also scaffolding for the final painting and insulation works of piping and separation station equipment. These costs, based on the Portuguese market, can be considered to be around 1.8 €/kg.

Separators and accumulator tanks
For separators and accumulator tanks steel fabrication works and erection a unit price of 5.5 €/kg is estimated.

6.3 Anticorrosion protection, insulation and cladding

The anticorrosion protection by paint coating and the insulation and cladding works unit prices are as follows. For anticorrosion protection by paint coating (high-temperature specification):

- 20 €/m^2 for shop painting;
- 15 €/m^2 for final painting and touch up at site.

For insulation and cladding:

- 150 €/m^2 for separators and accumulators;
- 100 €/m^2 for piping.

7. RESULTS

The results presented in this section were obtained utilizing *Engineering Equation Solver* software (F-Chart Software, 2015) and *Excel*. The drawings were produced by Autodesk's *AutoCad LT 2013* software unless mentioned otherwise.

7.1 Pipe diameter results

This section presents the results for the nominal pipe size selection for the separation station piping, the two-phase flow and the gathering system single flow piping. The pressure values presented herein are bar absolute (bar) unless stated otherwise.

Separation station single flow piping
For the expected steam and brine flow rates and the defined maximum flow velocities for each fluid, the calculated inside pipe diameters are presented in Table 6.

TABLE 6: Pipe inside diameter for maximum velocity

Fluid	Flow rate (kg/s)	Maximum velocity (m/s)	d (mm)
Steam	11	30	390.1
Brine	42	1	242.4

Selecting the next nominal diameter pipe from ANSI pipe schedule with a thickness corresponding to schedule STD, the final results are presented in Table 7.

TABLE 7: Calculated velocity for nominal pipe size

Fluid	Flow rate (kg/s)	Nominal pipe size (inch)	Nominal pipe size (mm)	d (mm)	Calculated velocity (m/s)
Steam	11	18”	457.00	437.94	23.80
Steam	11	16”	406.40	387.34	30.42
Brine	42	10”	273.10	254.56	0.91

The brine nominal pipe size selected is 10” (DN 250) while for steam it is 16” (DN 400), exceeding marginally the velocity of 30 m/s. Due to the reduced length, there is no decisive advantage in choosing the next pipe size (18”).

Two-phase flow piping
For the expected total production of a well, considering the maximum superficial steam velocity established and observing the recommendations of Lazalde-Crabtree for the vertical separator design, the two-phase flow nominal pipe size selected is 16” (DN 400).

Gathering system single flow piping
The gathering system piping initial pipe diameter analysis, pressure loss and fluid velocity calculations are presented in Tables 8 and 9 for steam and brine total flows:

- Total steam flow rate: 33 kg/s (120 ton/h);
- Total brine flow rate: 126 kg/s (450 ton/h).

TABLE 8: Calculated steam pressure loss and flow velocity for nominal pipe sizes

Option	Nominal pipe size (inch)	Nominal pipe size (mm)	d (mm)	Steam velocity (m/s)	Pressure loss, line (bar)	Pressure loss, bends (bar)	Total pressure loss (bar)
1	30"	762.0	742.94	24.8	0.32	0.13	0.45
2	28"	711.0	691.94	28.6	0.47	0.17	0.64
3	24"	610.0	590.94	39.2	1.07	0.32	1.39
4	20"	508.0	488.94	57.3	2.87	0.68	3.55

TABLE 9: Calculated brine pressure loss and flow velocity for nominal pipe sizes

Option	Nominal pipe size (inch)	Nominal pipe size (mm)	d (mm)	Brine velocity (m/s)	Pressure loss, line (bar)	Pressure loss, bends (bar)	Total press. loss (bar)
1	18"	457.0	437.94	0.9	0.25	0.05	0.30
2	16"	406.4	387.34	1.2	0.48	0.08	0.57
3	14"	355.6	336.54	1.6	1.01	0.15	1.15
4	12"	323.9	304.84	1.9	1.69	0.22	1.91

From the calculated values, two nominal pipes sizes are selected to develop a detailed pressure loss analysis comparison for the transport from the well pad to the plant, which are the 28” (DN 700) and 24” (DN 600) pipe. The 28” pipe keeps the steam velocity below 30 m/s, minimizing the pressure losses while the 24” exceeds that value and results in a pressure drop 2 times higher than the 28” pipe.

The brine pump’s technical characteristics are presented in Table 10 for each nominal pipe size evaluated.

TABLE 10: Brine pump technical characteristics

Option	Pump head (m)	Pump discharge pressure (bar)	Pump driver power (kW)
1	97	14.7	172
2	100	15.0	177
3	107	15.5	189
4	115	16.3	204

For these results, the separation pressure is considered to be 5.8 bar. The 18” and 16” nominal pipe sizes minimize the pressure losses and the pump driver power, noticing that there is only a 5 kW difference between both nominal pipe sizes, hence not presenting a decisive operational cost. Option 2 marginally exceeds the velocity of 1 m/s but the value of 1.2 m/s is acceptable. Considering also the economic benefit of selecting a smaller pipe diameter and maintaining the pumps operational costs low, the selected nominal pipe size for the brine gathering system is 16” (DN 400). The calculated pump driver electrical power is required to boost the total brine flow of the three wells. Therefore, the electrical power to drive one pump is 60 kW for the selected pipe size.

Pressure loss along the pipe route

The steam pressure drop along the pipe route from the well pad to the plant header can be better evaluated by pipe sections for 24” and 28” nominal pipe sizes. The analysis allows evaluating the separation pressure for each pipe size considering that the steam plant header pressure should be kept at 5.1 bar. The results are presented in Tables 11-14 for 24” and 28” nominal pipe sizes, respectively. Section 0 corresponds to the well pad location and separation pressure while Section 10 is at the plant platform and plant steam header pressure.

The estimated separation pressure for the 24” steam pipe gathering system is 6.6 bar while for 28” it is 5.8 bar, assuming the same steam header pressure at the plant. The average flow velocity is 30 m/s in the 28” pipe and 40 m/s in the 24” pipe.

Brine piping design pressure

The pump discharge pressure lies above the original brine piping design pressure; therefore, it should be increased. It is not in the scope of this work to simulate transient flow regimes to characterize the maximum pressure reached in the piping system caused for example by closing a valve upstream the pump discharge or a sudden increase of flow. To account for the transient regimes a design pressure of 20 bar(g) was selected.

TABLE 11: Pressure loss pipe route for 24” nominal pipe size

Section	Pipe length (m)	No. bends	p (bar)	v (m/s)	Pressure loss, line (bar)	Pressure loss, bends (bar)	Pressure loss, total (bar)
0	0	1	6.60	35.8	0.102	0.003	0.106
1	141	20	6.49	36.4	0.104	0.068	0.172
2	282	8	6.32	37.3	0.107	0.028	0.134
3	423	6	6.19	38.0	0.109	0.021	0.130
4	564	10	6.06	38.8	0.111	0.036	0.147
5	705	9	5.91	39.7	0.114	0.033	0.147
6	846	6	5.76	40.7	0.116	0.023	0.139
7	987	9	5.63	41.6	0.119	0.035	0.154
8	1128	11	5.47	42.8	0.122	0.044	0.166
9	1269	10	5.31	44.0	0.126	0.041	0.166
10	1410	-	5.14	-	-	-	-

TABLE 12: Average velocity and total pressure loss values for 24” nominal pipe size

Average velocity (m/s)	Pressure loss, line (bar)	Pressure loss, bends (bar)	Pressure loss, total (bar)
39.5	1.13	0.33	1.46

TABLE 13: Pressure loss along pipe route for 28” nominal pipe size

Section	Pipe length (m)	No. bends	p (bar)	v (m/s)	Pressure loss, line (bar)	Pressure loss, bends (bar)	Pressure loss, total (bar)
0	0	1	5.80	28.6	0.047	0.002	0.049
1	141	20	5.75	28.8	0.047	0.038	0.085
2	282	8	5.67	29.2	0.048	0.015	0.063
3	423	6	5.60	29.6	0.048	0.012	0.060
4	564	10	5.54	29.9	0.049	0.020	0.068
5	705	9	5.47	30.2	0.049	0.018	0.067
6	846	6	5.41	30.5	0.050	0.012	0.062
7	987	9	5.35	30.9	0.050	0.018	0.069
8	1128	11	5.28	31.3	0.051	0.023	0.074
9	1269	10	5.20	31.7	0.052	0.021	0.073
10	1410	-	5.13	-	-	-	-

TABLE 14: Average velocity and total pressure loss values for 28” nominal pipe size

Average velocity (m/s)	Pressure loss, line (bar)	Pressure loss, bends (bar)	Pressure loss, total (bar)
30.1	0.49	0.18	0.67

Flange class rating

The pump and valves flange pressure rating class needs to be increased. The design temperature of 175ºC is limited to 14 bar(g) for 150# class carbon steel flanges so 300# class flanges should be selected.

7.2 Pipe thickness

The gathering system steam and brine pipe minimum thickness t_m and nominal thickness t_n results are presented in Table 15.

TABLE 15: Steam and brine pipe thickness

Fluid	Nominal pipe size (inch)	Design pressure (bar(g))	t_m (mm)	t_n (mm)
Steam	28”	7.5	5.25	9.53
Brine	16”	20	6.42	9.53

7.3 Mechanical stress analysis

The results of the mechanical stress analysis are resumed in Table 16. For the calculation of the applied loading, the brine density was considered to be 1000 kg/m^3 which represents the worst case scenario. The load due to the steam weight is negligible.

TABLE 16: Sustained and occasional loads

Fluid	Vertical sustained load (N/m)				Vertical occasional load (N/m)			Horizontal occasional load (N/m)		
	q_p	q_e	q_v	q_{vs}	q_s	q_{sv}	q_{vo}	q_{sh}	q_w	q_{ho}
Steam	1617	250	0	1867	0	327	327	654	443	654
Brine	915	156	1156	2227	0	390	390	779	295	779

The results for pipeline length between supports are presented in Table 17. It shows that 16” brine piping requires shorter lengths between supports due to the higher sustained load, resulting from the greater medium weight when compared to the 28” steam pipe.

TABLE 17: Length between supports

Pipe size	L_s (m)		
	Sustained loads	Sustained and Occasional loads	Deflection criteria
28” (steam)	40	35	27
16” (brine)	20	17	15

7.4 Flexibility and expansion loops

The results from the expansion loops calculations are presented in Tables 18 and 19.

TABLE 18: U-shape expansion loop design

Pipe size	L_{ANC} (m)	Δ (mm)	L_2 (m)	L_3 (m)	L_1 (m)	S_A (MPa)
28”	30	62	12	6	12	177
16”	30		9	5	13	

U-shape expansion loop
It is evaluated that 7 horizontal expansion loops are required for the new pipeline section of 400 m length.

TABLE 19: Change of direction expansion loop design

Pipe size	L_{ANC} (m)	L_{arm} (m)	L_{T1} (m)	L_{T2} (m)
28”	32	27	23	27
16”	32	20	29	20

Change of direction expansion loop
At least two changes of direction expansion loops should be considered for the new section piping according to the results of this study.

The topography of the area must be included later in the design, taking advantage of the natural opportunities provided by the land elevation for change of direction loops to minimize the number of U-shape loops. The bridge section should be analysed better since an anchor point is typically placed in the middle of the bridge which allows the pipe to expand in both directions.

The main objective of the flexibility analysis was to estimate a maximum number of expansion loops for the new section, to calculate the additional length of pipeline and the number of bends required, to estimate the gathering system piping pressure drop and select the pipe diameter for steam and brine flow. The method used for the flexibility analysis of the new pipe section is conservative and should not be considered final for the implementation of the gathering piping system. Therefore, computer stress analysis should be done in the final piping design which is a normal procedure at EDA Renováveis.

The expected pipe route between the well pad and the power plant platform is included in Appendix I.

7.5 Separation station results

This section presents the design results of the separation station with three vertical separators and brine accumulators, and one single horizontal gravity separator serving the three wells.

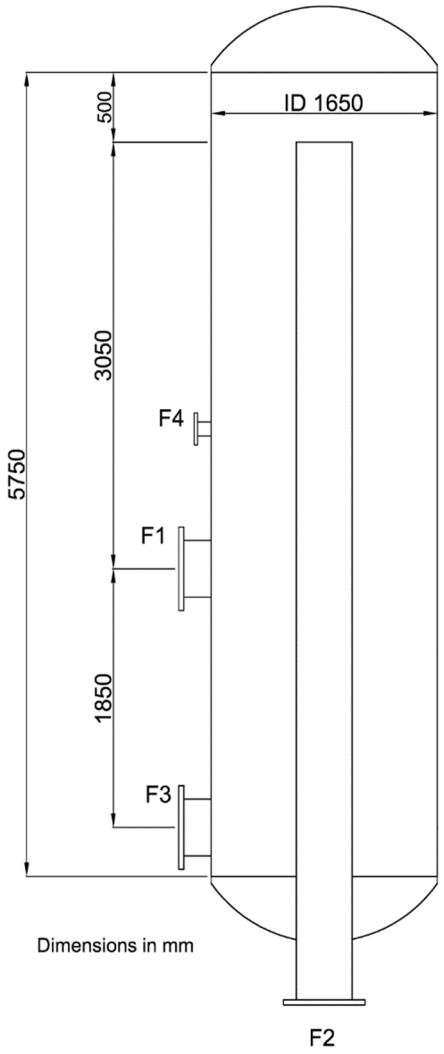

FIGURE 14: Vertical separator design

Vertical separator

The conceptual design of the vertical separator is presented in Figure 14 and the general characteristics and main design parameters of the separator are presented in Tables 20-22. All calculated values, with the exception of the separator inside diameter, which is a design assumption, should be considered approximate values. An additional nozzle is identified in the drawing which is the balance pipe. The balance pipe allows gas which forms by degassing of the brine to be vented to the separator, keeping the pressure of the two vessels balanced.

TABLE 20: Separator general parameters

Parameter	Value
Volume	13.5 m^3
Inside diameter	1650 mm
Vessel weight	4415 kg
Height between head welds	5750 mm
External surface area	40 m^2
Calculated thickness	7.6 mm
Nominal thickness	14 mm

TABLE 21: Separator nozzles schedule

Nozzles schedule		
No.	**Description**	**Size**
F1	Two-phase flow inlet	16”
F2	Steam outlet	16”
F3	Brine outlet	16”
F4	Balance pipe	4”

TABLE 22: Steam and brine design velocities

Parameter	Value
Steam velocity at two-phase inlet pipe (approximate)	30.4 m/s
Annular upward steam velocity inside cyclone	1.8 m/s
Brine outlet velocity	0.4 m/s

Brine accumulator tank

The design of the brine accumulator tank is presented in Figure 15, while the general characteristics of the brine accumulator tank are presented in Tables 23-24.

All calculated values, with the exception of the accumulator tank inside diameter, which is a design assumption, should be considered as approximate values. Low level for safe pump operation is considered to be 35%.

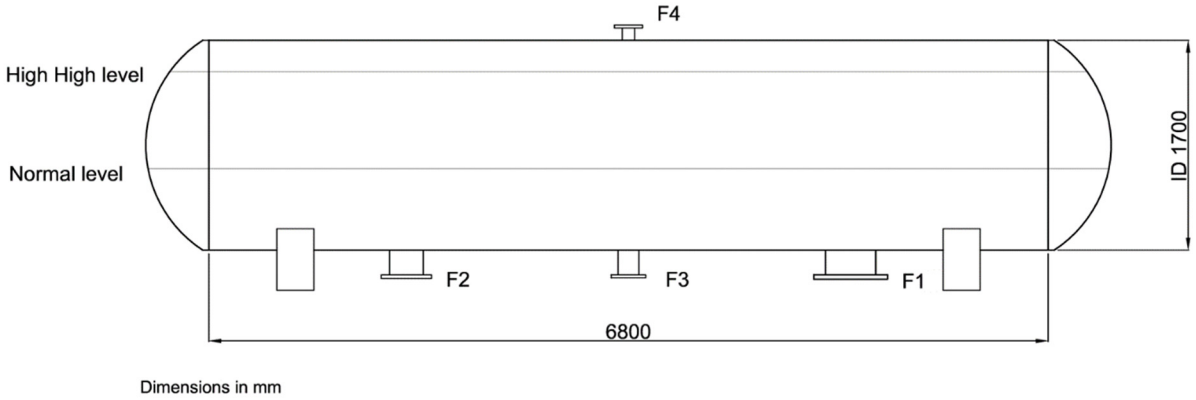

FIGURE 15: Brine accumulator tank

TABLE 23: Accumulator tank general parameters

Parameter	Value
Volume	16.7 m^3
Inside diameter	1700 mm
Vessel weight	5281 kg
Length between head welds	6800 mm
External surface area	47 m^2
Calculated thickness	7.7 mm
Nominal thickness	14 mm
Submergence depth (low level %)	600 mm (35%)
Brine outlet velocity	0.91 m/s

TABLE 24: Accumulator tank nozzles schedule

Nozzles schedule		
No.	**Description**	**Size**
F1	Brine inlet	16”
F2	Brine outlet	10”
F3	Brine drain outlet	6”
F4	Balance pipe	4”

The brine accumulator main nozzles control a brine drain outlet which in case of brine excess flow caused by operational reasons such as a pump failure, can be diverted and disposed adequately.

Horizontal gravity separator

The design of the horizontal gravity separator is presented in Figure 16. The general characteristics of the horizontal gravity separator are presented in Tables 25-27.

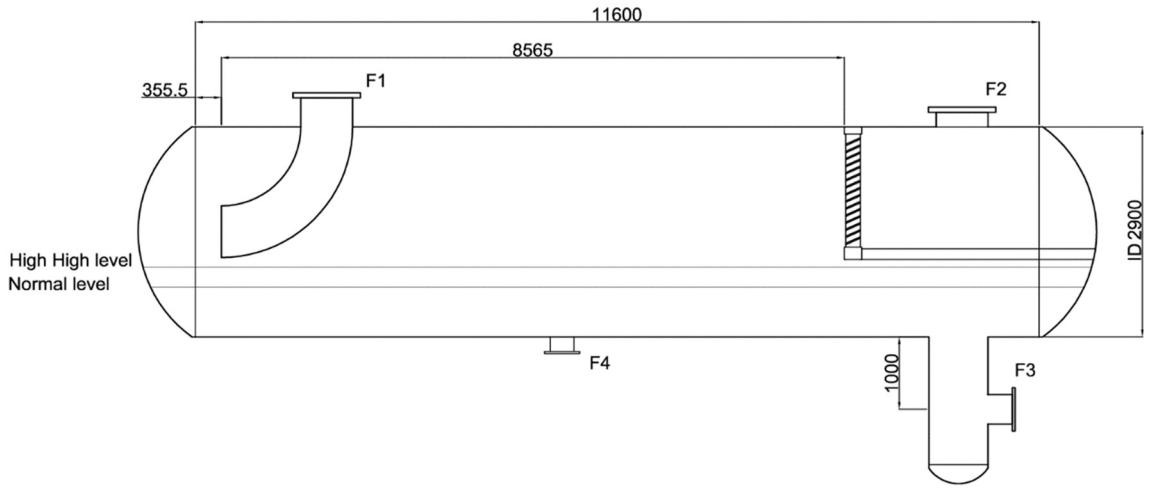

FIGURE 16: Horizontal gravity separator

TABLE 25: Horizontal separator general parameters

Parameter	Value
Volume	76.6 m^3
Inside diameter	2900 mm
Vessel weight	15,270 kg
Length between head welds	11,600 mm
External surface area	135 m^2
Calculated thickness	11 mm
Nominal thickness	14 mm

TABLE 26: Horizontal separator nozzles schedule

Nozzles schedule		
No.	**Description**	**Size**
F1	Two-phase flow inlet	28”
F2	Steam outlet	28”
F3	Brine outlet	16”
F4	Brine drain outlet	12”

TABLE 27: Horizontal separator design values

Parameter	Value
Sounders-Brown velocity K_f	0.182 m/s
Steam trough filter velocity U_d	3.13 m/s
Filter cross section area A_s	3.44 m^2
Brine outflow drip leg diameter	762 mm
Volumetric steam flow rate $\dot{V}_g$	10.8 m^3/s
Steam velocity at two-phase inlet pipe (approximate)	28.6 m/s
Submergence depth	1000 mm
Brine outlet velocity	1.2 m/s

The Sounders-Brown velocity K_f is within the design range of 0.18 to 0.2; the cross-section area of the filter type Chevron selected is 60% of the vessel cross section area. The steam velocity is below 30 m/s and the brine outlet velocity is slightly above 1 m/s. The brine outflow drip leg diameter is 725 mm and the next nominal diameter is 762 mm which corresponds to 30”. The calculated submergence depth relative to the central line of the brine outlet nozzle was 925 mm, which is increased to 1000 mm.

The results from each separation station type are resumed in Table 28, considering three vertical separators and accumulator tanks and one horizontal gravity separator, showing the most significant parameters for a cost evaluation.

TABLE 28: Separation station type parameters comparison

Type	Volume (m^3)	Weight (kg)	External surface area (m^2)
Vertical separators and accumulator tanks	90.6	29,100	261
Horizontal gravity separator	76.6	15,270	135

Selected thickness for pressure vessels
The selected thickness for all pressure vessels is 14 mm, allowing a direct comparison between the vertical and horizontal separators. It is also in accordance with the existent pressure vessels in the Ribeira Grande and Pico Vermelho power plants.

7.6 Cost estimate of the project

The estimated overall breakdown cost of the project is presented in Table 29 for Configuration A and in Table 30 for Configuration B of the separation stations.

TABLE 29: Configuration A project estimated breakdown cost

Activity description	Cost (€)
Design and supervision works	377,200
Gathering system piping	
Piping materials	747,000
Construction and erection works	1,744,500
Anticorrosion protection by painting coating	188,500
Thermal insulation and cladding	538,500
Pumps and valves	165,750
Vertical separators and accumulator tanks	
Construction and erection works	160,000
Anticorrosion protection by painting coating	9,135
Insulation and cladding	39,150
Equipment and piping foundations	1,468,500
Electrical, control and instrumentation	754,500
Total	**6,192,735**

TABLE 30: Configuration B project estimated breakdown cost

Activity description	Cost (€)
Detailed design and supervision works	369,700
Gathering system piping	
Piping materials	747,000
Construction and erection works	1,744,500
Anticorrosion protection by painting coating	188,500
Thermal insulation and cladding	538,500
Pumps and valves	165,750
Horizontal gravity separator	
Construction and erection works	90,900
Anticorrosion protection by painting coating	4,725
Insulation and cladding	20,250
Equipment and piping foundations	1,428,850
Electrical, control and instrumentation	739,300
Total	**6,037,975**

The overall estimated cost of the project is found to be about € 6,100,000. The total costs of Configuration A separation station is € 208,285 while for Configuration B it is €115,875, making the difference € 92,500. In the overall estimated cost of the project this is not decisive and the evaluation and pondering of technical matters have to be considered at a later stage of the engineering detailed design. The percentage of the costs of each project activity is summarised in Table 31.

TABLE 31: Cost weight per project activity

Activity description	Cost weight per activity
Design and supervision works	6%
Gathering system piping	53%
Pumps and valves	3%
Separation station equipment's	3%
Equipment and piping foundations	24%
Electrical, control and instrumentation	12%

The break-down cost per project activity shows that the gathering piping system works is about half of the overall project costs while the civil works for equipment and piping foundations is about a quarter.

8. CONCLUSIONS AND RECOMMMENDATIONS

The main conclusions and recommendations of this study are the following:

- Two configurations of the separation station for the new Cachaços-Lombadas sector wells CL8, CL9 and CL10 were evaluated. Configuration A comprises the installation of individual vertical separators, associated with brine accumulator tanks for each well; Configuration B considers the installation of a single common horizontal gravity separator, receiving the total flow of the three wells. In either of the alternatives, the separation of the two-phase flow is done at the well pad.
- The gathering system pipe sizes selected are 28" (DN 700) for steam and 16" (DN 400) for brine, considering the expected total flow of 33 kg/s (120 ton/h) of steam and 126 kg/s (450 ton/h) of brine. However, 24" can be considered an economical choice, penalizing the piping pressure drop and requiring to operate the wells at a higher separation pressure and therefore at lower wellhead pressure.
- The total electrical power required to boost the three wells brine flow from the well pad to the plant brine header is 177 kW.
- The two-phase flow pipe size should be 16" (DN 400) for each well, considering the steam superficial velocity of 30 m/s and following Lazalde-Crabtree (1984) design criteria; the vertical separator steam and brine outlets are 16" in diameter.
- The vertical separator preliminary design assures that the annular upward steam velocity is below 2 m/s.
- The brine accumulator tank was designed to offer a reasonable buffer volume to accommodate well fluctuations. The volume corresponds to a total of 300 s of the nominal brine flow, 120 s for nominal normal level while 180 s corresponds to the difference from normal to high level.
- In using a single vertical separator in a cluster of wells, the design needs to consider that all wells are operating at the design steam flow rate conditions, otherwise the steam inlet velocity will be lower, reducing the efficiency and therefore the quality of the outlet steam. It is improbable that in coming years the new Cachaços-Lombadas wells will operate simultaneously, therefore a single vertical separator to separate the wells combined two-phase flow is not the best technically solution at the present time, as it can be offered by the horizontal gravity separator.
- The advantage of operation of a horizontal gravity separator serving multiple wells, in contrast to the individual separation station, is that its performance is less dependent of the two-phase inlet flow rate and, due to its large volume, is better adjusted to serve as a buffer to compensate the fluctuations of the wells.
- The flexibility analysis was carried out to estimate a maximum number of expansion loops for the new pipeline section, establishing the additional length of pipe and number of bends required to calculate the gathering system piping pressure losses and to select the pipe diameter for steam and brine flow.
- The method used for the flexibility analysis of the new pipe section from the well pad to the existing piping corridor is conservative and should not be considered final for the implementation of the gathering piping system. Therefore, computer stress analysis should be done in the final piping design what is normal procedure in EDA Renováveis.
- The cost estimate of the project is about 6.1 m€.
- The cost of Configuration A separation station is € 208,285 while for Configuration B it is € 115,875, differing about 92,500 €, which in the overall estimated cost of the project is not relevant. It is recommended that the evaluation and pondering of technical matters between both configurations should be developed at a later stage of the project engineering detailed design.

ACKNOWLEDGEMENTS

I would like to express my appreciation to Mr. Lúdvík S. Georgsson, director of the United Nations University Geothermal Training Programme (UNU-GTP) for the opportunity to participate in this enriching training. I would also like to thank all UNU-GTP staff, namely Mr. Ingimar G. Haraldsson, Ms. Maria Gudjónsdóttir, Ms. Málfrídur Ómarsdóttir, Ms. Thórhildur Ísberg and Mr. Markús A.G. Wilde for their support and for the good hints and advices during my stay in Iceland. My sincere thanks to my supervisor Mr. Thorleikur Jóhannesson from Verkís for the supervision and experienced suggestions in the preparation of this project.

A special word of appreciation is addressed to the 2015 UNU Fellows for the enjoyable moments in this journey that made things much easier.

Finally, thanks to EDA Renováveis for giving me the opportunity to attend this 6-month training in Iceland.

REFERENCES

ASME, 2007: *ASME B31.1-2007. Power piping. ASME code for pressure piping, B31*. The American Society of Mechanical Engineers (ASME), 336 pp.

Clark, P.B., 2002: Some observations on the hydraulics of pumping stations. *Proceedings of the 2nd International Conference on Water and Wastewater Pumping Station Design, Cranfield, United Kingdom*, 9-22.

DiPippo, R., 2007: *Geothermal power plants. Principles, applications, case studies and environmental impact* (2nd edition). Butterworth Heineman, 493 pp.

EDA, 2014: *Demand and supply of electricity.* Electricidade dos Açores (EDA), *PLCOR (Planeamento, Controlo, de Gestão e Regulação)* Ponta Delgada, São Miguel, Azores, Portugal, internal report (in Portuguese), 36 pp.

EDA Renováveis, 2014: Annual Report. EDA Renováveis, Ponta Delgada, São Miguel, Azores, Portugal, (in Portuguese), 103 pp.

F-Chart Software, 2015: *EES, Engineering Equation Solver*. F-Chart Software internet website, *http://www.fchart.com/ees/ees.shtml.*

Foong, K.C., 2005: Design concept for a more efficient steam-water separator. *Proceedings of the World Geothermal Congress 2005, Antalya, Turkey,* 7 pp.

Jóhannesson, Th., and Gudmundsson, Y., 2014: *Mechanical design of geothermal power plants. Lecture 2: Drilling and gathering systems*. Reykjavík University, Reykjavík, Iceland, 82 pp.

Jónsson, M.T., 2015: *Mechanical design of geothermal power plant*. UNU-GTP Iceland, unpublished lecture notes, 25 pp.

Krex, H.E., 1986: *Maskin ståbi* (6th ed.). Nyt Teknisk Forlag, Cph, Denmark, 472 pp.

Lazalde-Crabtree, H., 1984: Design approach of steam water separators and steam dryers for geothermal applications. *Geothermal Resources Council, Bulletin, 13*, 11-20.

Rangel, G., Franco, A., Cabeças, R., Bicudo da Ponte, C., 2011: Use of geothermal resources in the Azores Islands: A contribution to the energy self-sufficiency of a remote and isolated region. *Geothermal Resources Council, Transactions, 35,* 1209-1214.

Smith. P.R., and Van Lann. T.J., 1987: *Piping and pipe support systems*. McGraw-Hill Book Company, New York, NY, US, 334 pp.

APPENDIX I: Gathering system pipe route

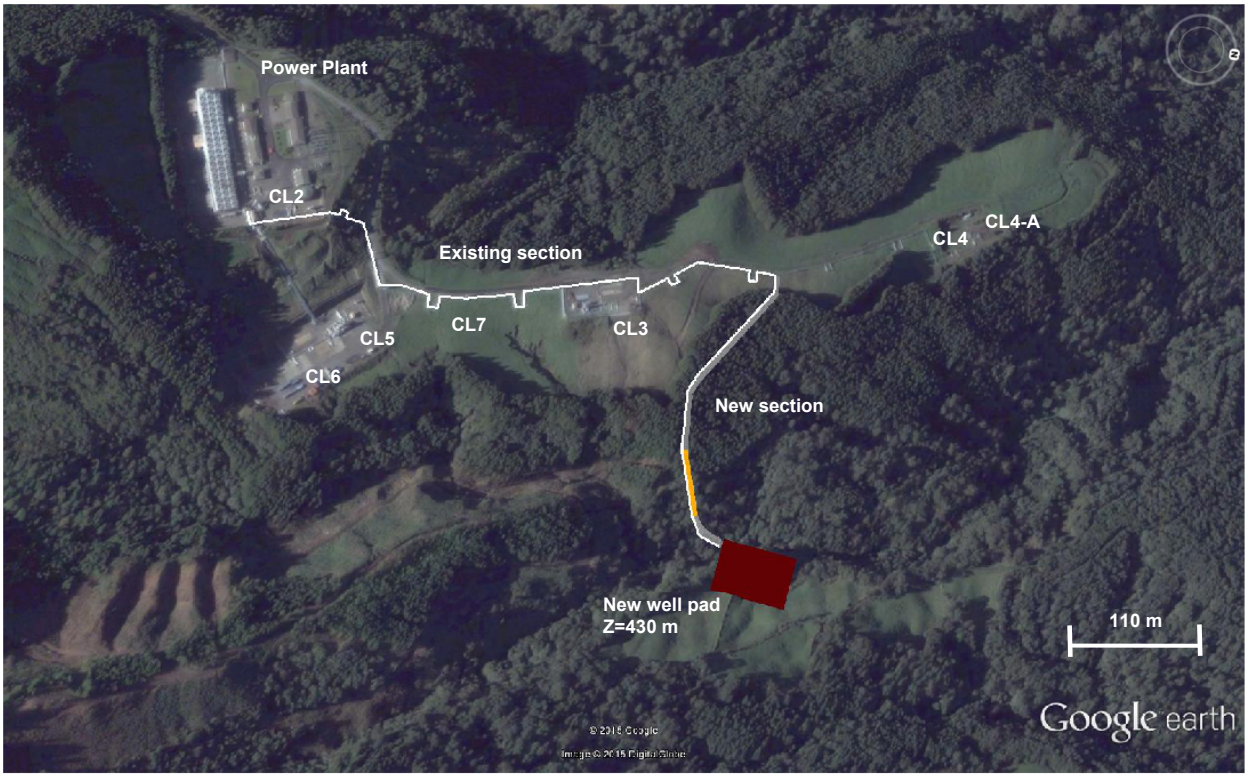

FIGURE 1: Gathering system pipe route from well pad to the plant (Google Earth)

UNITED NATIONS UNIVERSITY
UNU-GTP
Geothermal Training Programme

Orkustofnun, Grensasvegur 9,
IS-108 Reykjavik, Iceland

Reports 2015
Number 34

EVALUATION OF FACTORS CONTROLLING THE CONCENTRATION OF NON-CONDENSIBLE GASES AND THEIR POSSIBLE IMPACT ON THE PERFORMANCE OF WELLS IN OLKARIA, KENYA

Ruth Nelima Wamalwa
Kenya Electricity Generating Company - KenGen
P.O. Box 785-20117
Naivasha
KENYA
wamalwarn2000@gmail.com, rwamalwa@kengen.co.ke

ABSTRACT

The Olkaria geothermal field is located in the Kenyan Rift valley about 120 km from Nairobi. Development of geothermal resources in a high temperature field in the Olkaria area started in the early 1950s. In the following years numerous developments have been made with additional power plants being installed. These include a binary plant at Olkaria South West (Olkaria III) in 2000, a condensing plant at Olkaria North East (Olkaria II) in 2003, another binary plant at Olkaria North West (Oserian) in 2004 and finally two more condensing plants in the year 2014 within the East production field (EPF) and Olkaria Domes (OD) areas. The total generation from the field is about 730 Mw.

In this study samples from four producing wells located in three fields in the Olkaria geothermal area (OW-44 in the Olkaria East, OW-724A in the Olkaria North East and OW-914, and OW-915 in the Olkaria Domes field) were studied. The chemical analysis was carried out using SOLVEQ. The equilibrium state of the system was determined, the reservoir temperatures and the total moles were run through the CHILLER program. The CHILLER runs analysed the processes that have been proven to be occurring in the Olkaria field, i.e. boiling and condensing processes, fluid-fluid mixing rocks and titration resulting from water-rock interaction. The effects on gas evolution were evaluated based on the recalculated gas pressures.

The results indicate that the gas species are not in equilibrium with the mineral assemblages. The CHILLER evaluation shows boiling as the major process leading to evolution of gases. Well OW-44 had the smallest gas concentrations resulting from the reservoir processes in question due to degassing and near surface boiling. Gas breakout is most likely in well OW-914 and least likely in well OW-44. The study proposes different reservoir management strategies for the different parts of the Olkaria geothermal field. The first would be by increasing hot reinjection in the eastern sector around well OW-44. In the part of the reservoir around well OW-914, the wells should be operated at a minimum flow rate, or chemical inhibitors to prevent calcite scaling could be used.

1. INTRODUCTION

Evaluation of gas concentrations in Olkaria geothermal field revealed that on average gases are highest in the Domes, intermediate in Northeast production field and lowest in East production field (West JEC, 2009). West JEC (2009) considers three possible causes for the variations: i) CO_2 is accumulated in the water at great depth in the Northeast production field and Domes waters as a result of volcanic degassing below these areas, this process is less dominant in the East production field; ii) CO_2 addition at depth is similar in all three areas but water of the East production field loose CO_2 during the boiling process in the reservoir which escapes to fumaroles west and south of the East production field iii) cap-rock conditions in the Northeast production field and Domes are more restrictive than in the East production field, leading to more entrapment of CO_2 that has been released by boiling at shallower depths. Gases, in particular CO_2, H_2S, H_2, and CH_4, are natural components of volcanic geothermal systems such as Olkaria (Kenya), Mahanagdong (Philippines) and Nesjavellir, Hellisheidi and Krafla in Iceland (Arnórsson et al., 2010; Angcoy, 2010).

The gas concentration in unexploited systems is generally controlled by temperature dependent equilibria with various mineral buffers (Giroud and Arnórsson, 2005). Giroud and Arnórsson, (2005) also stated that for geothermal systems with average reservoir temperatures between 230-300°C the CO_2 buffer is considered to be clinozoisite, prehnite, quartz, and calcite whereas that for H_2S the main buffer minerals are pyrite, pyrrhotite, epidote, and prehnite. In highly saline waters, the H_2S mineral buffer consists of pyrite, magnetite and hematite. The gas ratios such as the H_2S/H_2 activity ratio correspond closely to the equilibrium of the mineral pairs pyrite/pyrrhotite and pyrite/magnetite which are generally undersaturated with respect to the individual minerals. These findings agree with the study of the Olkaria field by Karingithi (2002) which found that the activity of aqueous H_2 and H_2S gases generally corresponds closely to the equilibrium of the mineral buffer pyrite, pyrrhotite, and magnetite. The activities of these two gases also correspond closely to the equilibrium of the mineral buffer pyrrhotite, prehnite, epidote, and pyrite. The H_2S/H_2 activity ratio corresponds closely to the equilibrium of the mineral pairs pyrite/pyrrhotite and pyrite/magnetite.

The concentration of gases in exploited geothermal fields are higher than of the parent fluid (Akin et al., 2015). The value is frequently in the range of 50-300 and 2-20 mmoles/kg of steam for CO_2 and H_2S respectively (Giroud and Arnórsson, 2005). The variation is dependent on the concentration in the geothermal parent fluid, the steam fraction, the steam separation pressure, and the boiling processes. According to Giroud and Arnórsson, (2005), long-term utilization of geothermal reservoirs can lead to a decline of CO_2 and H_2S concentrations in the steam. This decline may be caused by recharge of cold water into producing aquifers and/or progressive boiling of water retained in the aquifer by capillary forces. Enhanced boiling, which is a consequence of reservoir pressure draw down and steam separation during lateral flow into production wells, may cause the well discharge to become depleted of gas. In case of a boiling reservoir, the gas concentrations tend to be higher compared to concentrations at a particular temperature. The formation of steam caps in the reservoir is observed more frequently and/or an enhance in fumarolic activity. Karingithi (2002) also notes that gas samples from marginal wells whose discharge fluid are mixed with non-geothermal fluid show low H_2 and H_2S values with respect to the equilibrium with the buffer mentioned above.

The gases are among the factors that affect the reservoir pressure in the deep liquid-dominated geothermal reservoirs (Haizlip et al., 2012). Haizlip et al. (2012) further added that under static conditions, pressure in most producing aquifers around the world ranges between 130 to 230 bars at depths between 1700 to 2800 m. The temperatures at this depth range from 219 to 242°C. The effect of the gas pressures on well performance is evaluated by the gas breakout pressure i.e. the pressure below which the fluids begin to transform into two phases. According to Haizlip et al. (2012) gas breakout pressure is the sum of the gas pressure and water pressure at the reservoir temperature. Due to pressure drop, thermal fluids start to boil when rising in the wellbore and CO_2 is released. In bicarbonate type of waters, the fluid becomes saturated with calcite due to a reaction of CO_2 and calcium.

For an exploited field such as the Olkaria area, changes in the gas content of well discharges over time help providing valuable information about the response of the reservoir to the production load (Karingithi, 2002). These changes are a consequence of various processes such as cold recharge resulting to fluid-fluid mixing, volcanic degassing, and enhanced boiling (Gudmundsson and Arnórsson, 2002; Ármannsson, 2003). In this study, an evaluation of reaction processes controlling the concentration of prevalent reactive gases CO_2, H_2S, H_2, CH_4, and N_2 in Olkaria well discharges, is made. The procedure involves the calculation of the equilibrium state between fluids and rocks using the software package SOLVEQ followed by the determination of reaction processes in aqueous-mineral-gas systems using the software package CHILLER (Reed et al., 2012a, b). The software packages SOLVEQ and CHILLER, have been chosen because of their applicability for studying multiphase systems as well as undergoing boiling and mixing processes (Bienkowski et al., 2003). This is relevant for the long-term release of gases from geothermal power plants and makes it interesting for predicting a possible decline in gas emissions. Eventually the results are compared to the measured pressures through the downhole temperature and pressure surveys to determine if there are chances of gas breakout occurrence.

2. GENERAL SETTING OF THE STUDY AREA

The Olkaria Geothermal area is located within the Olkaria central volcanic complex in the central sector of the Kenyan Rift Valley. The complex is located south of Lake Naivasha, approximately 120 km from the capital Nairobi. It is bordered by other geothermal prospect areas like Suswa, Longonot, and Eburru (Figure 1).

The Olkaria geothermal area covers approximately 140 km^2 and is divided into seven fields: Olkaria East, Olkaria Northeast, Olkaria Central, Olkaria Northwest, Olkaria Southwest, Olkaria Southeast, and Olkaria Domes (Figure 2). The fields are in different stages of development. Olkaria East, Olkaria Northeast and Olkaria Southwest are fully explored while Olkaria-Domes is the most recent of them where exploitation started in 2014. Olkaria Southwest is yet to be developed.

The Olkaria East Field is located on the East of the Olkaria hill (Figure 3) and has been under steam exploitation since 1985. The Olkaria 1 power plant is served by 31 wells connected to the steam gathering system. At the end of 2014, the steam of only 22 wells was utilized. 9 wells had become non-commercial producers because of a decline in output. Two of these wells, OW-6 and OW-3, are used as reinjection wells whereas OW-11 was

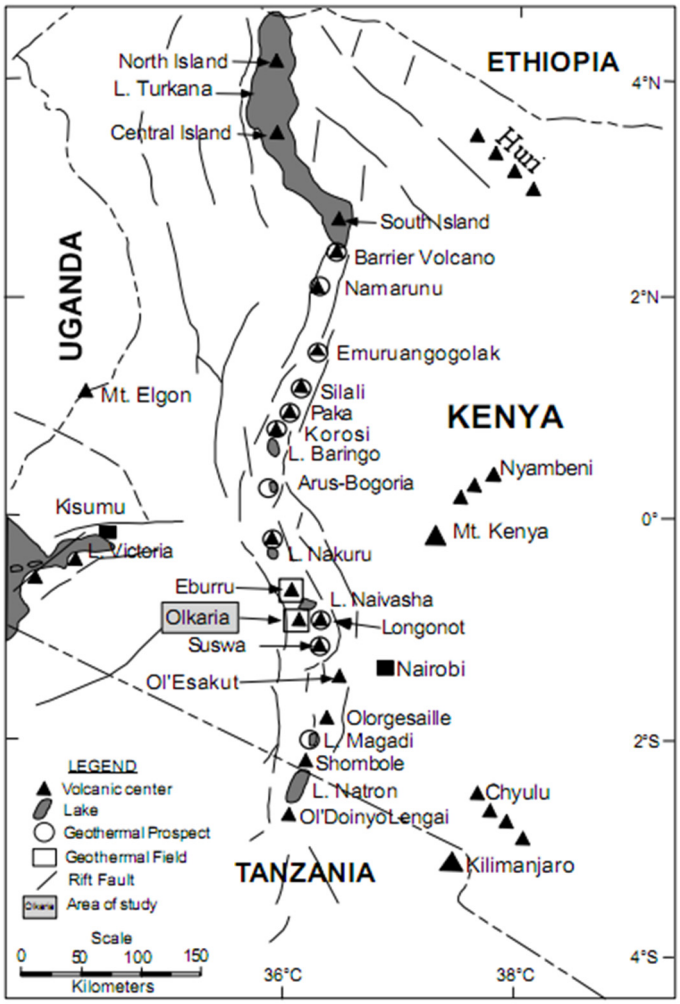

FIGURE 1: Map of the Kenya rift showing the location of Olkaria geothermal field and other Quaternary volcanoes along the rift valley (Lagat, 2005)

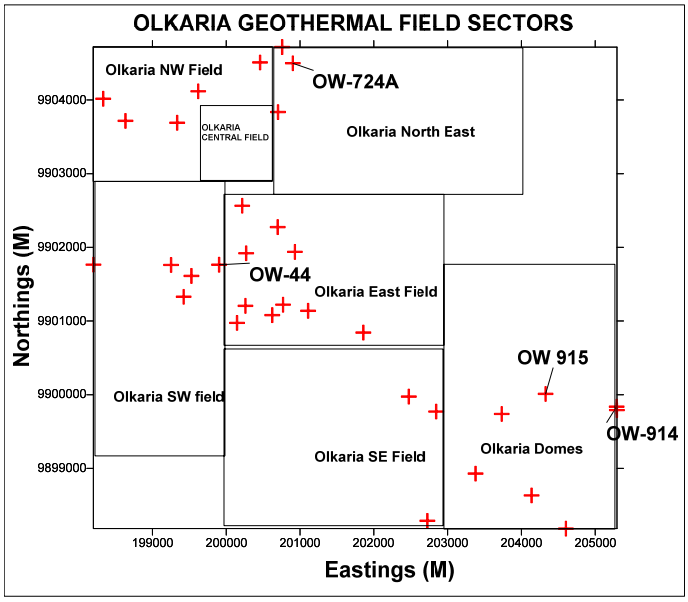

FIGURE 2: Geothermal fields within the Greater Olkaria geothermal area (KenGen, 1999); the red crosses indicate the location of wells; labelled wells are the ones used in this study

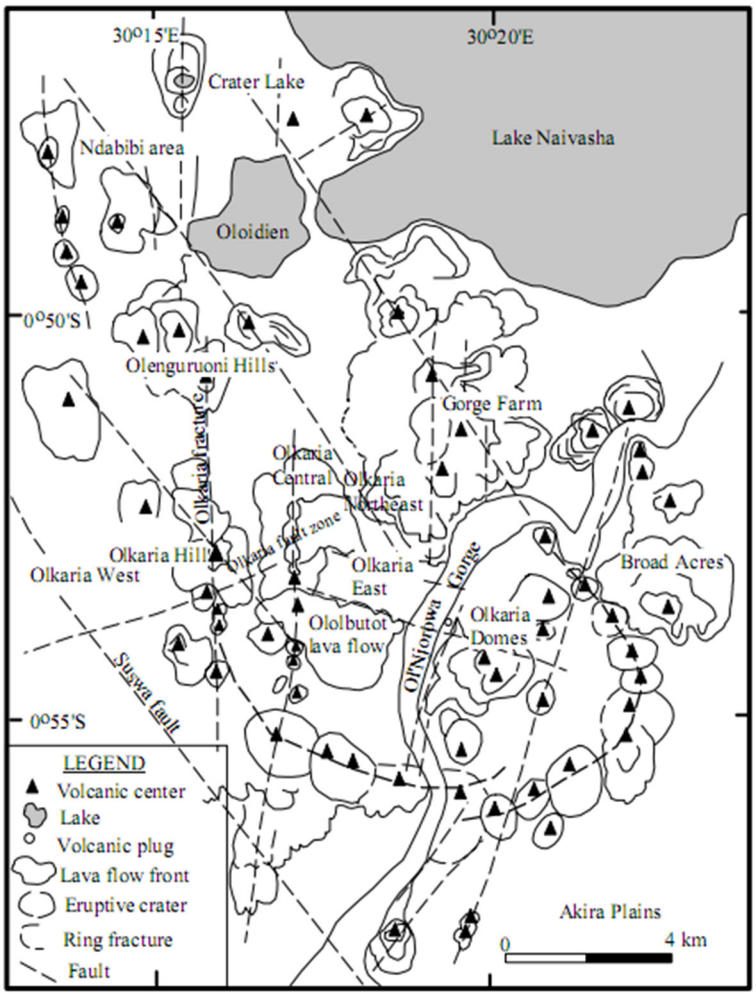

FIGURE 3: Volcano-tectonic map of the Greater Olkaria volcanic complex (modified after Clarke et al., 1990)

recently commissioned to take low pressure (LP) brine from OW-2. The field also hosts newly drilled wells like OW-35, OW-36A OW-37A, OW-38, OW-38A, OW-41, OW-42A, OW-44, OW-44A, and OW-44B for the Olkaria1 unit IV and V power plant. This power plant was commissioned in October, 2014. OW-37A, OW-43, and OW-43A are connected to wellhead generators.

The Olkaria North East has been used for power generation since October 2003. It has a total of 20 wells that are connected to the steam gathering system. Of the twenty, 6 wells (OW-709, OW-710, OW-712, OW-713, OW-718, and OW-721) have individual separators while the other 14 wells (OW-701, OW-727, OW-705, OW-725, OW-706, OW- 711, OW-707, OW-715, OW-714, OW-716, OW-719, OW-726, OW-720, and OW-728) share separators. Four wells are used for hot re-injection (OW-R2, OW-R3, OW-703, and OW-708). Wells OW-704, OW-717, OW-723, and OW-724 are non-producers and are currently used for pressure monitoring (Figure 2).

Olkaria-Domes field lies to the west of Longonot Volcano and on the SE of the Olkaria hill (Figure 3). It was the last of the seven sectors at which test drillings for exploration purposes were carried out. Three deep exploration wells were drilled in 1998 and 1999. Drilling was halted for about eight years due to shortage of funding but resumed in June 2007. This led to realization of a 140 MWe power plant commissioned in October, 2014 using wells OW-910, OW-910A, OW-910B, OW-908, OW-908A, OW-908B, OW-909, OW-915, OW-915A, OW-915B, OW-916, and OW-912.

2.1 Geological features and physical characteristics of the reservoir

2.1.1 Geology of Olkaria volcanic complex

Olkaria volcanic complex does not have a clear caldera association (Naylor, 1972; Virkir, 1980; Clarke et al., 1990; Mungania, 1992). However, Lagat et al., (2005) concluded that the presence of a ring of domes in the east, south and southwest can be used to infer the presence of a buried caldera. The downhole geology in geothermal wells in Olkaria field has helped to reveal the lithostratigraphy of the area (Omenda, 2000). In this study, the regional geology has been divided into six main lithostratigraphy groups: proterozoic "basement" formations, pre-Mau volcanics, Mau tuffs, plateau trachytes, Olkaria basalt and Upper Olkaria volcanics. The basement rocks contain Proterozoic gneises of amphibolite facies-grade, schists, marbles, and quartzites of the Mozambique group (Shackleton, 1986; Smith and Mosley, 1993). The Mau tuffs are the oldest rocks that outcrop on the surface in the Olkaria area. Omenda (1994, 2000) concluded that this might be the surface manifestation of an east dipping high angle normal fault that is cutting through Olkaria Hill. The Upper Olkaria volcanics are overlain by Olkaria basalt in the area to the east of Olkaria Hill while the formation is absent west of it. This formation consists of basalt flows, minor pyroclastics and trachytes and varies in thickness from 100 m to 500 m (Omenda, 2000). The Upper Olkaria formations comprise of mainly lavas and ashes from Suswa and Longonot volcanoes (Thompson et al., 1963; Ogoso-Odongo, 1986; Clarke et al., 1990; Omenda, 2000).

2.1.2 Structural setting of the Olkaria volcanic complex

Structures in the Olkaria geothermal area include a ring structure, the Ol'Njorowa gorge, the Gorge Farm fault, the ENE-WSW Olkaria fault and NW-SE trending faults (Figure 3). Faults are prominent in the East, Northeast and West Olkaria fields unlike in the Olkaria Domes area where they are most likely covered by thick pyroclastic rocks (Clarke et al., 1990). The NW-SE trending faults are considered to be the oldest and are associated with the development of the rift and the presence of hot chloride-rich fluids. An exception is the Gorge farm fault, which bounds the geothermal fields in the north eastern part and extends to the Olkaria Domes area. The most recent structures are the NNE-SSW faults. They are thought to be young and carry cold fluids low in chlorite.

Dike swarms exposed in the Ol'Njorowa gorge trend in a NNE direction confirming the reactivation of recent faults of similar orientation. The development of the Ol'Njorowa gorge is thought to have been initiated by faulting along the orientation of the gorge but the feature as it appears today resulted from a catastrophic outflow of Lake Naivasha during its high stands (Clarke et al., 1990). The volcanic plugs (necks) and felsic dikes along the gorge are another evidence that the fault controls the development of this feature. Subsurface faults have been encountered in most Olkaria wells (KenGen, 1999). They are witnessed mostly in wells where drilling problems were encountered when these faults were dissected. The problems included collapse, and loss of drilling fluids and cement. The cuttings recovered from these zones are mainly fault breccias.

3. RESERVOIR CHARACTERISTICS

3.1 Reservoir pressure and temperature characteristics

Studies on the temperature and pressure distribution in the Olkaria field indicate that fluid movement in the geothermal system is tectonically controlled (Ofwona, 2002). The reservoir temperatures reach as high as 380°C at 3400 metres depth in well OW-49 in Olkaria East. The Olkaria East and North East consist of a two-phase reservoir (reservoir with a steam and water mixture feed zone) at least to the depth that is penetrated by the deepest wells. On the other hand, the Olkaria Domes consist of a liquid-dominated reservoir without a steam cap (Ambusso and Ouma, 1991; KenGen 1999).

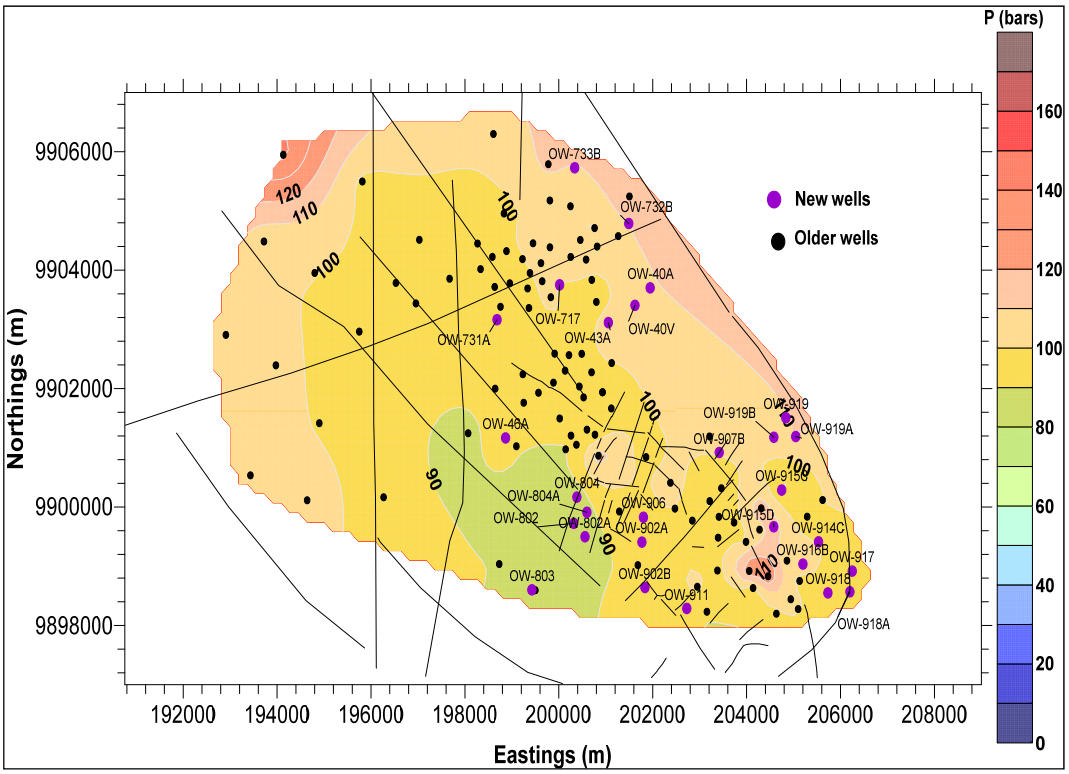

FIGURE 4: Measured pressure variations for the Olkaria geothermal field

Pressure decreases both eastwards and westwards from respective peaks towards Olkaria Central (Figure 4). Within the Olkaria Central and North East, pressures decline southwards towards both well OW-401 and Olkaria East (Ouma, 1999).

As shown in the profiles in Figure 5, well OW-44 was drilled to 3000 m in early 2011. It has a high injectivity index of 164 l pm/bar and downhole temperatures of about 300°C. Major feed zones are observed at around 760 m and 2250 m while minor ones have been localized at 1500 and 1750 m depth. Well OW-724A just like well OW-44 was drilled to a depth of 3000 m in early 2012. It has a slightly higher injectivity index of about 180 l pm/bar. The major feed zone in this well is at 1800 m and minor ones are observed at 1400, 1750, 2000, and 2550 m depths as seen in the heat up temperature profiles. The pressure profiles indicate that the water rest level was at 550 m depth prior to the injection. A pivot point has been observed in around 1800 m depth hence the major feed zone is in around 1800 m depth.

The temperature profile taken at well OW-915 in the Olkaria Domes field indicates minor feed zone between 1200 m and 1500 m and a major feed zone at 2300 m metres depth. The pre-injection data shows a water rest level at approximately 300 m depth. The well has with 145 l pm/bar a low injectivity index compared to wells OW-44 and OW-724A.

3.2 Reservoir fluid chemistry

The Olkaria wells discharge fluids with enthalpy ranging from 1000 kJ/kg to 2750 kJ/kg (Karingithi, 2002). Wells in the eastern production field have excess discharge enthalpy. This implies that the enthalpy of discharged fluid is higher than that of steam-saturated water at the respective aquifer temperatures. The water discharged from wells in the Olkaria field is poor in dissolved solids compared to fluids from most other high-temperature geothermal fields in the world with chloride concentrations in liquid ranging between 50 and 1100 ppm (Karingithi, 2000). The water of wells in Olkaria East and Northeast (Figure 2) tends to be highest in chloride with about 1000 ppm. According to Karingithi

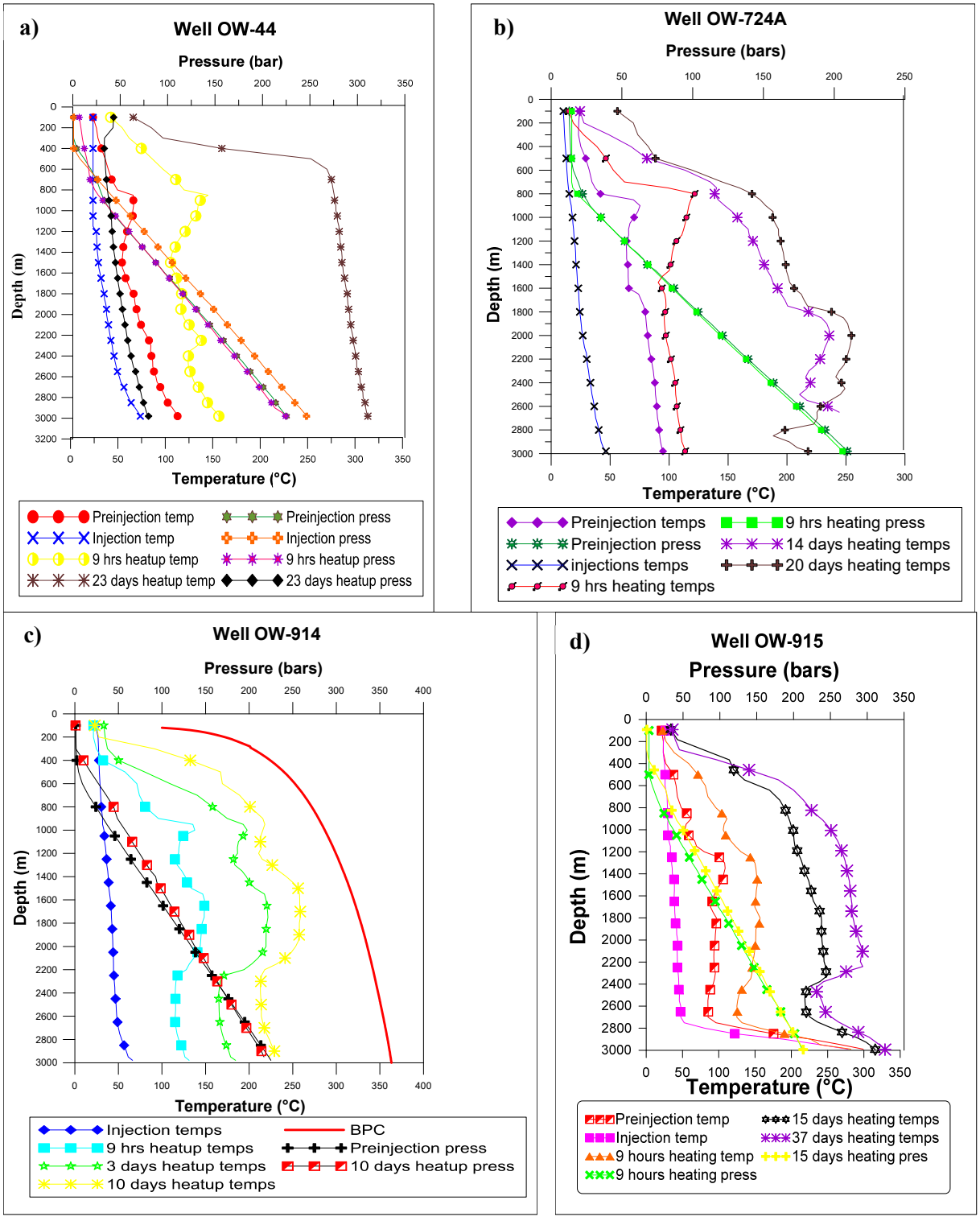

FIGURE 5: Downhole temperature and pressure profiles for wells OW-44 (a), OW-724 (b), OW-914 (c), and OW-915 (d) BPC stands for boiling point curve

(2002) the high chloride content could be as a result of up-flow of high-temperature geothermal fluid, although progressive boiling by heat flow from the rock may also be a contributing factor.

A study by Wambugu (1995) found that in Olkaria West field the chloride concentrations are quite low with about 350 ppm except for well OW-305 which discharges water similar to that of the wells in the Olkaria East and Olkaria Northeast fields. Well OW-305 is therefore thought to be tapping of the up-

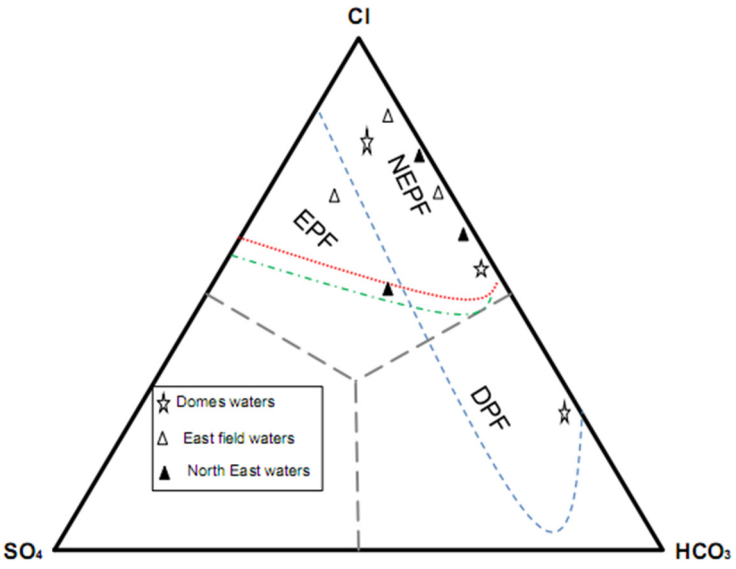

FIGURE 6: Cl-SO_4-HCO_3 ternary diagram for the Olkaria geothermal field. FPF stands for East production field, NEPF for North East production field while DPF for Domes production field

flow fluid for Olkaria West field. The relative abundance of chloride, sulfate and bicarbonate show that wells in the Olkaria East production field and in Olkaria North East discharge sodium-chloride type water while the Olkaria Domes fields discharge a mixture of chloride and bicarbonate end-member water (Figure 6) (KenGen, 2014). The liquid from Olkaria wells is slightly to moderately alkaline (pH 8.1-9.9 as measured at 20°C) and is relatively high in bicarbonate (Wambugu, 1995). The bicarbonate concentration is in the range of 90-13000 ppm with the highest carbon dioxide content found in the Olkaria West field followed by the Olkaria Domes. Wambugu (1995) added that this could be a consequence of CO_2 supply to the geothermal fluid and a subsequent reaction between the carbonic acid and minerals of the rock leading to evolution of CO_2 gas.

3.3 Geochemical conceptual model

The geochemical data identifies upflow zones in the areas around wells OW-701, OW-711, and OW-705 in the Olkaria North East field, around wells OW-38, OW-32, OW-35A, and OW-39A in the Olkaria East field and in the Olkaria Domes area in wells OW-908, OW-908A, and OW-911A (Figure 7). These

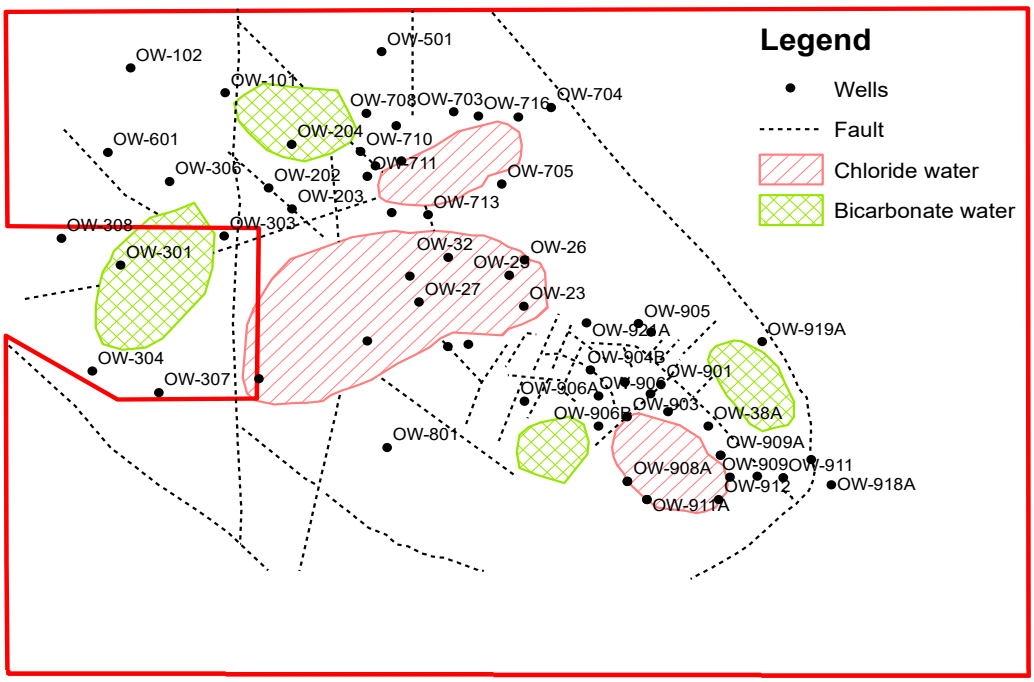

FIGURE 7: Distribution of two water types in the Olkaria geothermal area (KenGen, 2014)

areas are characterized by chloride-dominated fluids. Areas around wells OW-914 and OW-902 have peripheral waters and are thus thought to be on the margins of the reservoir.

The influence of structures is also apparent with the NW-SE trending faults being associated with high temperatures and chloride-rich waters. The NE-SW trending faults tend to carry cold waters that have led to a decline in enthalpies in the wells OW-719, OW-32, and OW-16 where they cut through (Wamalwa et al., 2014). Wamalwa et al., (2014) added that the faults within the Ol Njorowa gorge (between the Olkaria East and Olkaria Domes) carry cold, less mineralized water that tend to dilute the wells in the shallow depths as can be seen in the cases of wells OW-21, OW-22, and OW-23.

4. METHODOLOGY

4.1 Sampling and analysis

This study comprises samples from four producing wells of three fields out of seven in the Olkaria geothermal area (Table 1). The sampling and analysis was carried out by KenGen staff using methods as described by Arnórsson et al. (2006) and Stefansson et al. (2007). The liquid and vapour phases were separated using a Webre separator connected to a pipeline. Care had to be taken to make sure that no condensation occurred as the fluid cools while running through the pipeline on its way in and out of the separator. After the setup, vapour samples were collected into pre-evacuated gas bulbs (100 ml) containing 40% NaOH. CO_2, and H_2S were absorbed in the NaOH solution while the non-condensable

TABLE 1: Geochemical data from the studied wells

	OW-44	**OW-724A**	**OW-914**	**OW-915**
WHP (bar-g)	14	10	11	11.58
SP (bar-g)	14	9	10	10
pH at 20°C	7.91	9.43	9.91	9.93
Enthalpy (KJ/Kg)	2500	1698	2111	2034
Cond (µΩ/cm)	6130	2770	7482	2690
TDS (ppm)	3064	1660	3742	1345
SiO_2 (ppm)	487	610	636	682
B (ppm)	14.41	3.783	2.37	3.17
Cl (ppm)	1203	452.7	431.54	480.64
F (ppm)	79	35.8	244.28	187.41
SO_4 (ppm)	143.1	201.6	68.5	16.1
CO_2 (ppm)	88.22	321.86	1520.6	246.62
H_2S (ppm)	0.15	7.14	6.3	17.88
Li (ppm)	1.83	1.42	2.547	0.671
Na (ppm)	827	508.7	1455	653.5
K (ppm)	245.9	70.95	445.9	189.8
Ca (ppm)	1.266	2.159	0.01	2.672
Mg (ppm)	0.54	0.033	1.282	0.047
Fe (ppm)	1.37	0.265	1.35	1.35
CO_2 (mmol/100moles.H_2O)	88.4	261.3	498.1	329.8
H_2S (mmol/100moles.H_2O)	10.26	4.66	0.91	5.03
CH_4 (mmol/100moles.H_2O)	0.29	0.03	0.61	0.25
H_2 (mmol/100moles.H_2O)	12.91	9.62	12.26	19.5
N_2 (mmol/100moles.H_2O)	21.21	12.15	18.05	2.58
O_2 (mmol/100moles.H_2O)	0	0	0	0.35

WHP = well head pressure
SP = sampling pressure

gases, i.e. H_2, N_2, O_2, Ar and CH_4, became more concentrated in the gas-head of the gas bulb. The non-condensable gases were then analysed inside the head space of the gas bulbs using gas chromatography (GC) while the concentrations of CO_2 and H_2S were analysed in the alkaline condensate by titration. The liquid phase samples were cooled down using a stainless steel spiral that was connected to the Webre separator and immersed into a bucket of water. Samples used for major cation determination were filtered through 0.2 µm filters into polypropylene bottles and acidified with 0.5% HNO_3 and later analysed using an ion chromatography photometer (ICP). Samples used for major anion and CO_2 determination were also filtered through 0.2 µm filters into polypropylene and amber glass bottles and then analysed using ion chromatography (IC). The quality of the sampling and chemical analysis was ensured by using well-known standard solutions for calibration, running reference samples before starting the analysis and evaluation of charge balance for the analyses. The samples had a charge balance between -5 and +5%.

4.2 Data analysis

The chemical data was first run through SOLVEQ to determine the equilibrium state of the system and then through CHILLER analysing the processes that typically occur in most high-temperature fields (Reed et al., 2012a). These processes include boiling and condensing processes, fluid-fluid mixing and rocks titration (hydrothermal alteration of the mineralogy of a well as a result of hot fluids and rocks interaction).

4.2.1 Equilibrium evaluation

The equilibrium constants were determined using mineral assemblages that potentially control the concentrations of H_2S, H_2, and CO_2 in the aquifer fluid by using reactions as shown in Table 2 and temperature equations for the equilibrium constants in Table 3. These include thermodynamic data on oxide and silicate minerals as given by Holland and Powell (1990), data on sulfide minerals were adapted from a study published by Robie and Hemingway (1995). The thermodynamic properties of the dissolved gases were based on the solubility constants by Fernandez-Prini et al., (2003) and the standard Gibbs energies of the ideal gases given by Robie and Hemingway (1995). Considering the limited pressure range, the specific volume of minerals was assumed to be independent of temperature and pressure.

Activities of end-members in the epidote (epidote and clinozoisite), garnet (grossular and andradite), and prehnite (Al-prehnite and Fe-prehnite) solid solutions were used. The values were 0.8 and 0.2 for epidote and clinozoisite respectively as well as for Al and Fe-prehnite. Other minerals were used to have unit activity.

TABLE 2: Reaction equations for the equilibrium constants (Arnórsson et al., 2010)

1 H_2S:	$^1/_3$ pyrite + $^1/_3$ pyrrohtite + $^2/_3$ prehnite + $^2/_3$ H2O = $^2/_3$ epidote + H2S (aq)
2 H_2S:	$^2/_3$ grossular + $^1/_3$ pyrite + $^1/_3$ pyrrohtite + $^2/_3$ quartz + $^4/_3$ H2O = $^2/_3$ epidote + $^2/_3$ wollastonite + H2S (aq)
3 H_2S:	2 grossular + $^1/_4$ pyrite + $^1/_2$ magnetite + 2 quartz + 2H2O = 2 epidote + 2 wollastonite + H2S (aq)
4 H_2S:	$^1/_4$ pyrite + $^1/_2$ pyrrohtite + H2O = $^1/_4$ magnetite + H2S (aq)
5 H_2:	$^4/_3$ pyrrohtite + $^2/_3$ prehnite + $^2/_3$ H2O = $^1/_4$ magnetite + H2S (aq)
6 H_2:	$^2/_3$ grossular + $^4/_3$ pyrrohtite + H2O = $^1/_4$ magnetite + H2S (aq)
7 H_2:	6 grossular + 2 magnetite + 6 quartz + 4 H2O = 6 epidote + 6 wollastonite + H2 (aq)
8 H_2:	$^3/_2$ pyrrohtite + H2O = $^3/_4$ pyrite + $^3/_4$ magnetite + H2 (aq)
9 CO2:	$Clinozoisite + Calcite + {}^3/_2\ quartz + H2O = {}^3/_2\ prehnite + CO2\ (aq)$
10 CO2:	$^2/_5$ Clinozoisite + Calcite + $^3/_5$ quartz = $^3/_5$ Grossular + $^1/_5$ H2O + CO2 (aq)

TABLE 3: Log K-temperature equations for the reactions given in Table 2 above (Arnórsson et al., 2010)

1 $log\ H_2S$	$13.608 + \frac{592324}{T^2} - \frac{9346}{T} - 0.043552T + 0.000029164T^2 + 5.139logT$
2 $log\ H_2S$	$13.659 + \frac{555082}{T^2} - \frac{9256.6}{T} - 0.043608T + 0.000028613T^2 + 5.148logT$
3 $log\ H_2S$	$-0.836 - \frac{216659}{T^2} - \frac{2847.3}{T} - 0.008524T + 0.00002366T^2 + 0.152logT$
4 $log\ H_2S$	$13.589 + \frac{590215}{T^2} - \frac{9024.5}{T} - 0.044882T + 0.000029780T^2 + 5.068logT$
5 $log\ H_2$	$-1.640 - \frac{124524}{T^2} - \frac{777.19}{T} - 0.0005501T + 0.00007756T^2 + 0.565logT$
6 $log\ H_2$	$-1.544 - \frac{151109}{T^2} - \frac{752.389}{T} - 0.0005868T + 0.00007080T^2 + 532logT$
7 $log\ H_2$	$1.444 - \frac{273812}{T^2} - \frac{3962.1}{T} - 0.002401T + 0.00001304T^2 + 0.979logT$
8 $log\ H_2$	$-1.654 - \frac{95456}{T^2} - \frac{621.84}{T} - 0.001257T + 0.00007569T^2 + 0.600logT$
9 log CO2	$-0.890 - \frac{7251.5}{T^2} - \frac{1710.6}{T} - 0.004188T + 0.00002683T^2 + 0.640logT$
10 log CO2	$-1.449 - \frac{40536}{T^2} - \frac{2135.9}{T} - 0.0065639T + 0.00002725T^2 + 0.193logT$

T = Temperature in Kelvin

4.2.2 Evaluation of gas concentrations versus the reservoir processes

a. Gas concentrations as a result of boiling and condensing processes

The calculations were done according to Reed et al., (2012a, b). As an input the reservoir temperatures as calculated by the SOLVEQ software were used. CHILLER was run using the specified reservoir temperatures TEMP and a limit SLIM was set in a way that no temperature increments take place. The fluid pressures (PFLUID) in the pickup file was set lower than the saturation pressures while the temperature increments (STEP INCREM) for temperatures were set to -10 (decreasing temperatures). It must be noted that the oversaturated minerals as read out with SOLVEQ were suppressed to minimize their masking of the convergence of the equations. CHILLER was then executed. The programme equilibrated using the gas phase and started boiling following STEP INCREM temperature drop and adjusted PFLUID. Considering that the enthalpy (ENTH) was set at zero, CHILLER sets the current ENTH to be equal to the enthalpy of the aqueous phase at the given temperature. To ensure that the boiling process remained iso-enthalpic, the starting total enthalpy SENTH was set to zero and CHIM sets SENTH equal to the current total enthalpy ENTH. From the output (CHIMOUT.DAT, at full equilibration) the gas saturation was determined.

b. Fluid-fluid mixing ('Coolbrew' calculations)

This study first considered the mixing of aqueous solution inside a high temperature reservoir with enthalpy constraint scenario (Reed et al., 2012b). CHILLER computed the enthalpy balance between the boiling solution and the mixer solution. The change of composition of the system TOTAL MOLES was calculated as TOTAL MOLES + STEP INCREM * MIXER TOTAL MOLES while the total current enthalpy of the system was also changed from ENTH to ENTH + STEP INCREM * MIXER TOTAL MOLES * ENTHW (enthalpy of the mixer solution). The mixing first resulted in condensation of the gas phase at a constant temperature. As in the boiling evaluation, oversaturated minerals as read out with SOLVEQ were suppressed. According to Reed et al., (2012b) once the gas phase was condensed, CHILLER proceeded in computing fluid-fluid mixing and temperature change by setting TEMPC to a non-zero value. This allowed CHILLER to titrate a mixer solution of composition given by MIXER TOTAL MOLES into the current solution of a composition given by TOTAL MOLES. The composition of the mixer solution was in moles, except for water where MIXER TOTAL MOLES, was given in kilograms.

c. Water-rock interaction (MINSOLV option)

The water-rock interaction option in CHILLER option was enabled with MINSOLV being set to a non-zero value and allowing SiO_2, Fe_2O_3, FeO, MgO, CaO, Na_2O, FeS, and NaCl as reactants. CHILLER

then read the names and amounts of reactants specified in the CHIMRUN file and their stoichiometries from the MINOX data file (Reed et al., 2012b). At the start of a reaction calculation, the TOTAL MIXER was set to zero while the composition of the system changed from TOTAL MOLES to TOTAL MOLES + STEP INCREM * WTPC * 0.01 * SPEC/MVOX, where SPEC is the molar amount of a given component species in the reactant NOMOX. MVOX is the molecular weight of reactant NOMOX. For increments in moles, TOTAL MOLES are changed to TOTAL MOLES + STEP INCREM*WTPC*0.01*SPEC.

4.2.3 Evaluation of depth of gas breakout or bubble point

Gas breakout or two-phase conditions occur at a depth at which the gas pressure plus water pressure exceeds the total pressure, i.e. bubble point depth (Haizlip et al., 2012). In this case, the gas pressure is given in the output files of the CHIM programme whereas the water pressures were estimated using steam tables as follows:

$$P_{liq} = P_{wateratsatT} \quad (1)$$

$$P_{tot} = P_{gas} + P_{liq} \quad (2)$$

Where P_{liq} = pressure of the liquid phase in the well
$P_{wateratsatT}$ = pressure of the saturated water at a given temperature
T = temperature in kelvin
P_{gas} = pressure of the gas phase in the well
P_{tot} = total pressure

The temperature values were taken from the SOLVEQ output files and assigned to the major feed zones as determined from the downhole temperature and pressure profiles of each well as shown in Table 4.

5. RESULTS

The results are categorized into two parts. In part one the evaluation of the equilibrium states of the fluids in the wells is presented. In part 2 the processes leading to gas evolution are discussed. The results are visualized in gas pressure (bars) vs temperature graphs.

5.1 The equilibrium state of the fluids

The logH_2 vs temperature curve (Figure 8) is defined by Equations 5, 6, 7 and 8 in Table 2. The studied wells closely correlate mineral assemblages in Equation 5 which are pyrrohtite, prehnite, epidote, and pyrite, and 8 with magnetite, pyrite and pyrrohtite (Table 4). Wells OW-44 and OW-914 appear to be closest to equilibrium. Wells OW-915 and OW-724A are in equilibrium as they plot far from the top most curve (Equation 5). These results agree with those by Arnórsson et al., (2010) where some wells in the field plotted close to the mineral assemblages in 5 and 8 indicating equilibrium with the minerals while others were scattered hence showing non-equilibrium. The gas concentration is low, ranging between -2.0 moles/kg in well OW-915 and -2.5 moles/kg in well OW-914 which closely corresponds to a range between -3 moles/kg to -5.5 moles/kg (Arnórsson et al., 2010).

In the log H_2S vs temperature graph there are mineral curves for 1, 2, 3 and 4 (Figure 9). The wells range between 300°C and 330°C, except for well OW-724A that lies at 250°C. Well OW-724A seems to be in equilibrium with mineral assemblage in Equation 1 which describes the ratio of pyrite, pyrrohtite, prehnite and epidote and 4 (pyrite, pyrrohtite and magnetite). Well OW-44, on the other hand, fits to the mineral assemblages grossular, pyrite, pyrrohtite, quartz, epidote and wollstonite (Equation 2) and grossular, pyrite, magnetite, quartz, epidote and wollastonite (Equation 3). Wells OW-

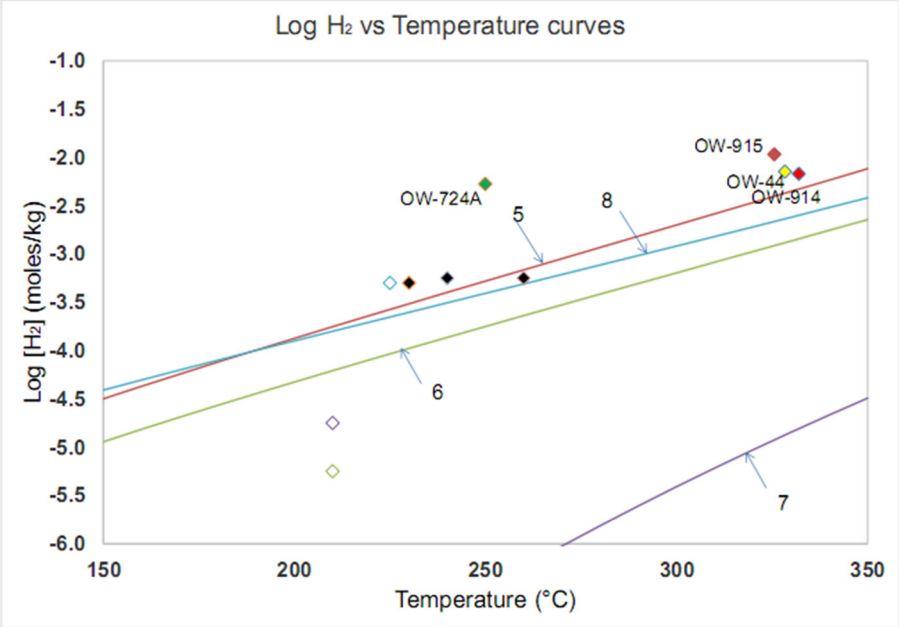

FIGURE 8: Calculated concentrations of H_2 in the total aquifer fluid of wells OW-44, OW-724A, OW-914, and OW-915. White and black symbols are data from Arnórsson et al., (2010) of the Olkaria Domes and Olkaria Central field respectively. The numbers on the curves refer to the reactions in Table 2

915 and OW-914 seems not to be in equilibrium with any of the mineral assemblages. The results still hold for Arnórsson et al., (2010) with the exception of well OW-914 which seemed depleted with H_2S, an indication of steam loss and therefore gas loss. The log CO_2 graph (Figure 10) is defined by two mineral assemblages 9 and 10. Two wells, i.e., OW-914 and OW-915 are in equilibrium with mineral assemblage given by Equation 10. Well OW-44 plots way below the mineral assemblage in Equation 9 whereas well OW-724A plots above the mineral assemblage in Equation 10. This is an indication that

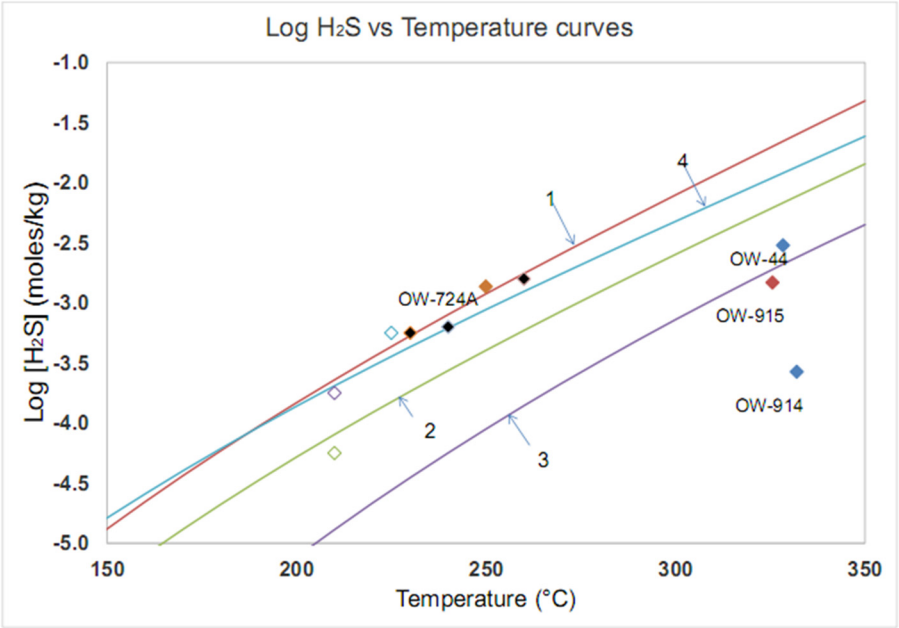

FIGURE 9: Calculated concentrations of H_2S in the total aquifer fluid of wells OW-44, OW-724A, OW-914, and OW-915. White and black symbols are Arnórsson et al., (2010) data from Olkaria Domes and Olkaria Central field respectively. The numbers on the curves refer to the reactions in Table 2

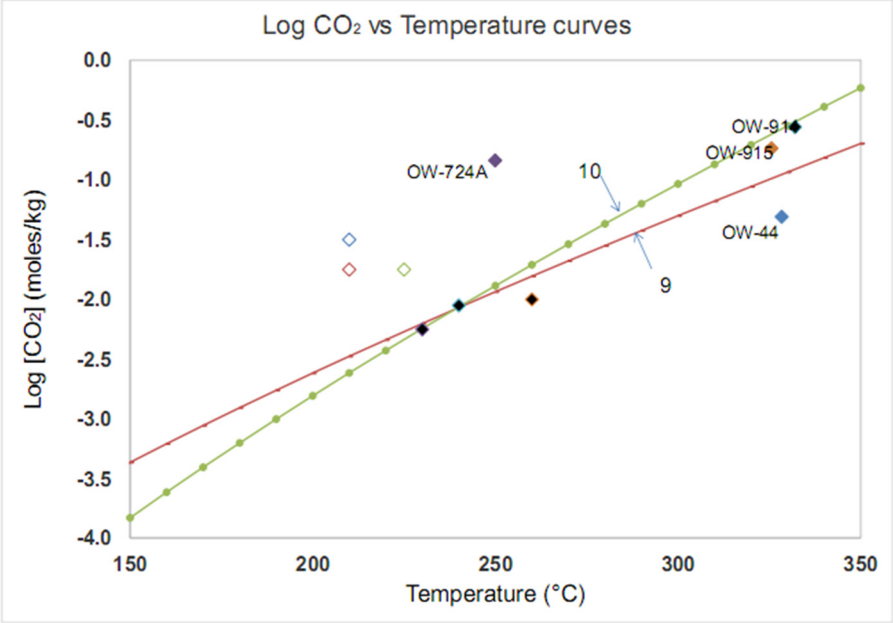

FIGURE 10: Calculated concentrations of H_2 in the total aquifer fluid of wells OW-44, OW-724A, OW-914, and OW-915. White and black symbols are Arnórsson et al., (2010) data from Olkaria Domes and Olkaria Central field respectively. The numbers on the curves refer to the reactions in Table 2

well fluids in OW-724A and OW-44 are not in equilibrium with the mineral assemblages. The values of concentration also suggest that well OW-44 has the smallest amount of gas whereas well OW-914 has the highest. The findings concur with Arnórsson et al., (2010) where the Domes Sector has the highest CO_2 concentration what is likely caused by the high flux of it from the heat source.

5.2 Gas concentrations and the reservoir processes in the wells

The analysed reservoir processes are boiling, fluid-fluid mixing and titration (Figures 11-14). The plots for well OW-44 indicate that boiling is the major process leading to evolution of gases. The gas pressures increased with temperature, steadily rising from 2.4 to 50 bars. The mixing process is the second most dominant. Unlike the boiling process, the curve remains stable up to about 200°C before starting to increase. The curve on titration has almost similar trend but smaller values ranging between 0 and 2.4 bars (Figure 11).

For well OW-724A, just like well OW-44 boiling is the major process leading to gas evolution (Figure 12). Between 100°C and 120°C the gas pressure is constant at about 0.1 bars before steadily rising up to 37 bars. The mixing curve also experiences no change in the gas pressures at low temperatures but later increases. The recorded values are with 0.1 and 17 bars smaller than those related to the boiling processes. The titration process start with a linear increase in the gas pressures up to around 180°C. The curve then shows a decline in the gas pressures between 180°C and 220°C.

Caused by boiling, the resulting gas pressures in well OW-914 are ranging between 10 and 92 bars Figure 13). The values of the mixing curve range between 0 and 50 bars. The titration curves show almost no increase between 100°C and 200°C. This is followed by a slight increase to about 2.5 bars at 300°C. In well OW-915 just like in OW-914 the gas pressures reach a maximum pressure of 85 bars as a consequence of the boiling process (Figure 14). The mixing curve shows a slight increase in gas pressure with temperature, the values lie between 0 and 10 bars. The titration curve shows similar trends as well OW-724A. The curve starts with an increase in gas pressures up to a temperature of 170°C, plateaus until 210°C before starting to increase again to 5 bars.

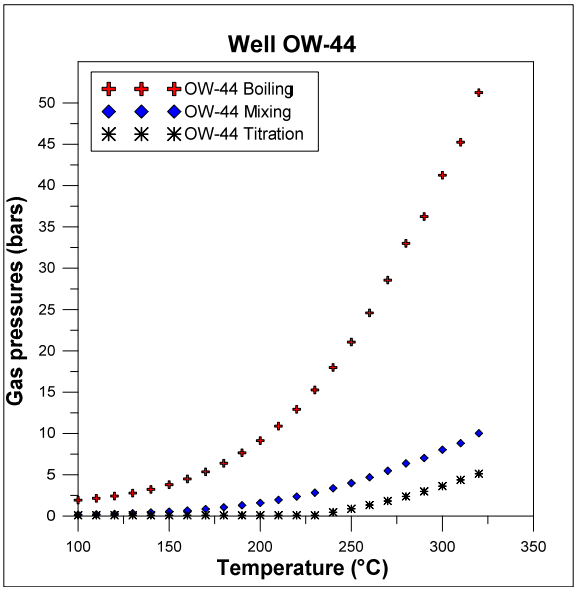

FIGURE 11: Gas pressures against the reservoir processes in well OW-44

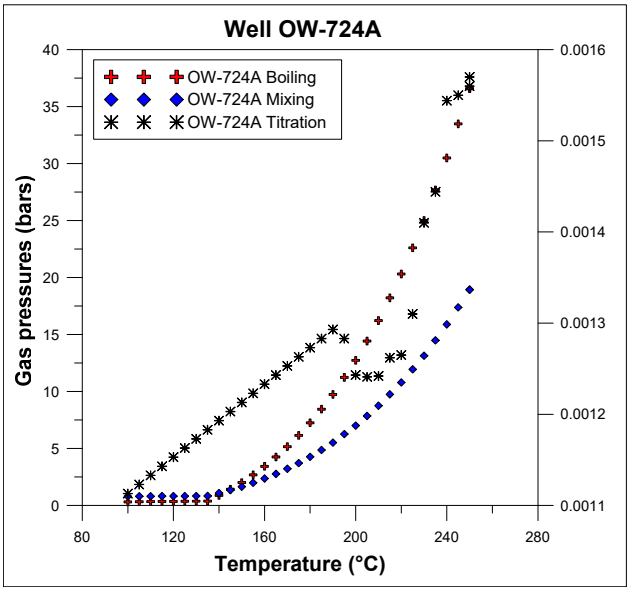

FIGURE 12: Gas pressures against the reservoir processes in well OW-724A. The titration curve has been plotted on the secondary axis

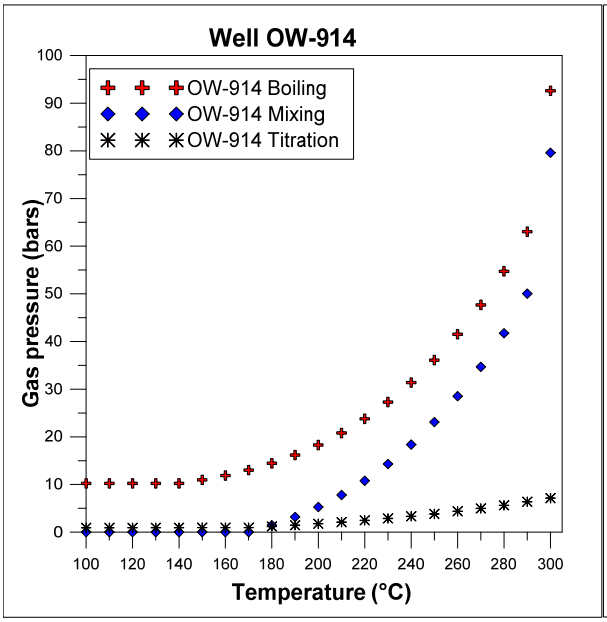

FIGURE 13: Gas pressures against the reservoir processes in well OW-914

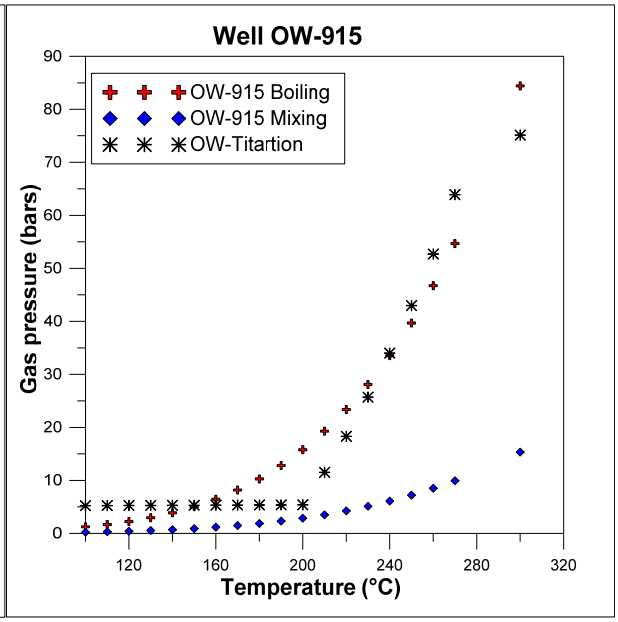

FIGURE 14: Gas pressures against the reservoir processes in well OW-915

The process comparison curves (Figure 15) indicate boiling processes to be the most dominant process in well OW-914 followed by OW-915 and OW-724A. Well OW-44 has the smallest gas pressures generated. Gas evolution caused by mixing processes on the other hand, seems high in well OW-914 followed by OW-724A, OW-915, and OW-44. Titration processes as well as mixing processes produce higher values in OW-914. Well OW-915 comes in second followed by OW-44 and OW-724A.

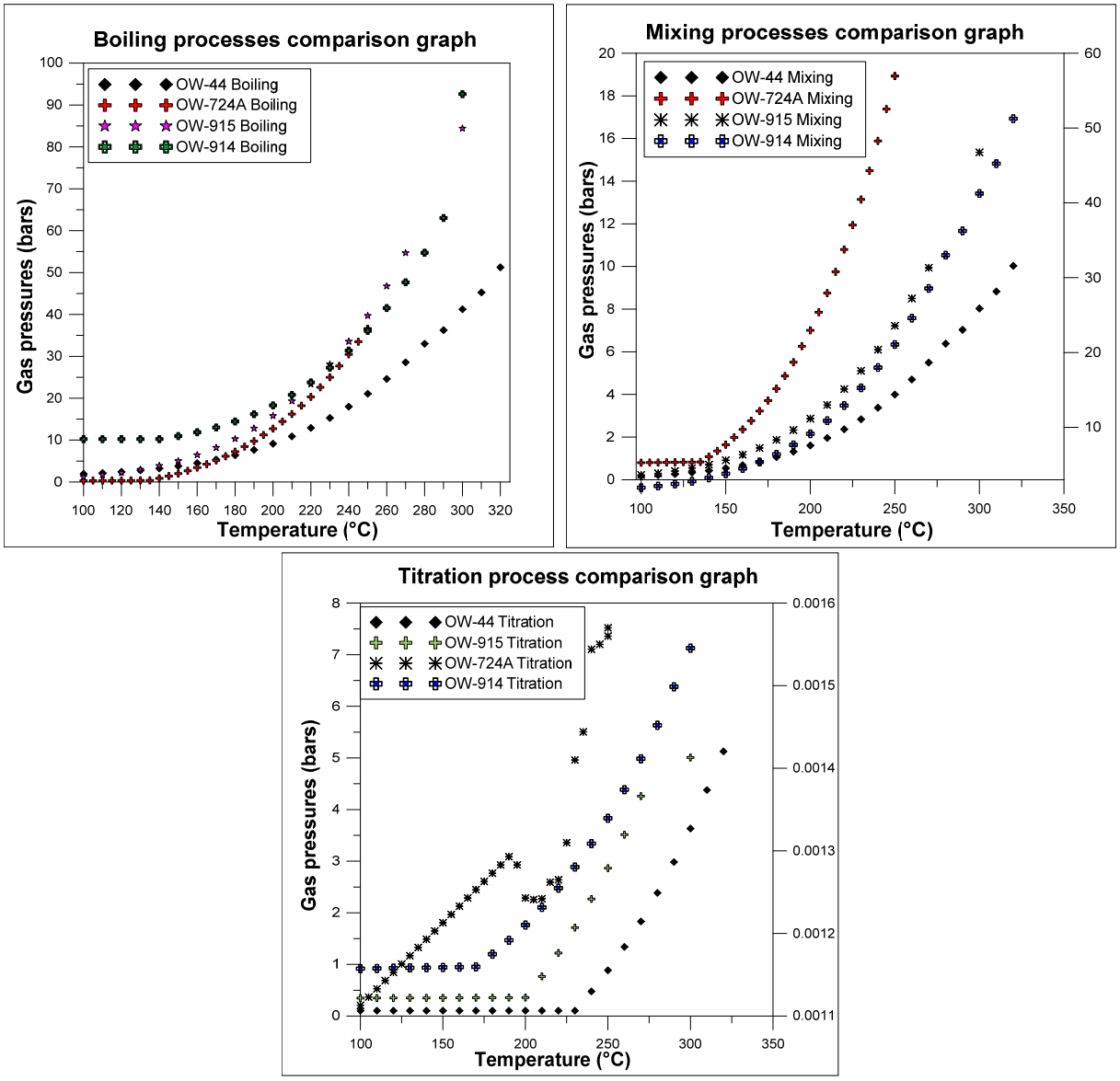

FIGURE 15: Reaction processes comparison graphs. The titration curve in well OW-724A has been plotted on the secondary axis

5.3 Depth of gas breakout or bubble point

The measured pressures at the major feed zones reach the highest values with 175 bars in well OW-44 followed by OW-915 with 150 bars, OW-914 with 100 bars and OW-724A with 90 bars (Table 4). Using steam tables, liquid and gas pressure (P_{liquid} and P_{gas} from CHIM) are added. The total values range between 52 bars in OW-44 and 92 bars in the OW-914. Well OW-914 has a total pressure close to the pressure measured downhole, indicating higher probability of gas break out at its major feed zone. Well OW-44 had the smallest probability, as its total pressure is with 52 bars much lower than the 175 bars that were measured.

TABLE 4: A comparison between measured and calculated pressures in the main feed zones

Well name	Depth of major feed zone (m)	Measured pressure (bars)	Calculated liquid pressure (bars)	Calculated gas pressure (bars)	Total calculated pressure (bars)
OW-44	2250	175	0.105	52	52
OW-724A	1700	90	0.002	36	36
OW-914	1500	100	0.025	92	92
OW-915	2300	150	0.035	84	84

6. DISCUSSION OF THE RESULTS

6.1 The equilibrium state of the fluids

This study and the one of Arnórsson et al., (2010) agree that the H_2 and H_2S gas concentrations are low in the Olkaria geothermal field. This is indicated by small concentration values ranging between -2 to -3.5 moles/kg (Figure 8 and 9) indicating that the aquifer vapour fraction is insignificant. Arnórsson et al., (2010) attribute these low concentrations to steam loss resulting from the boiling of fluid flowing into these wells. Well OW-724A shows values way above the mineral assemblage curves of H_2 whereas well OW-914 is below the H_2S graph. According to Arnórsson et al., (2010), non-equilibrium distributions of gas species in a high temperature field like Olkaria arises from processes like boiling, condensation and mixing.

The CO_2 plot indicates that the calculated aquifer fluid CO_2 concentrations are in equilibrium with mineral assemblages as seen in the case of well OW-914 and OW-915. Well OW-44, apart from being in non-equilibrium with the mineral assemblages, has the smallest concentration (Figure 10). According to Arnórsson et al., (2010), the low CO_2 values as found in well OW-44 are due to an insufficient supply of the gas into the fluid preventing it from saturating with calcite. This shows that the aquifer fluid CO_2 concentration is externally controlled indicating, that the flux into the geothermal fluid originates either from degassing magma or from fluid- and/or fumaroles-rock interaction. This is opposite to the case of well OW-724A which is higher than the equilibrium curves. It supports the possibility that the non-equilibrium in well OW-724A maybe a result of a volcanic degassing process underneath these areas but with minor gas loss compared to OW-44.

6.2 Gas concentrations and the reservoir processes in the wells

The results point to boiling being the major process which leads to evolution of gases (Figures 11-14). Simsek et al., (2009) who were studying the Kizildere geothermal field in Turkey stated that the increase in gases is a result of elevated enthalpy. This is thought to be a consequence of flow or gravity segregation of water. The percentage of water in the reservoir increases either due to a decrease of steam which flows to the well or enhanced vaporization boiling when there is heat flow from the rock into the fluid. The former process describes a scenario of boiling in the area around the well while the second becomes dominant if the water has cooled by adiabatic boiling as a result of pressure drop which leads to steam and gas generation (Simsek et al., 2009). From the graph, it is notable that the intensity of the processes increases with temperatures in the wells in question. Temperature act as catalyst for reactions leading to evolution of the gases (Haizlip et al., 2012).

A comparison of magnitude of these processes indicates that the impacts of the processes are highest in well OW-914 and lowest in OW-44 (Figure 15). This trend in well OW-914 is attributed to the high temperature values of about 325°C in a way that chain reactions similar to those discussed in the mixing processes take place. This is further supported by the fact that this well has high injectivity index of

about 315 l pm/bar, an indication of high permeability in the rock surrounding the well. In streaming fluids react with the mineral assemblages in the aquifer rocks that leads to the evolution of gases.

Well OW-44 had the smallest gas concentrations resulting from the analysed reservoir processes despite the fact that it has high downhole temperatures of about 300°C and considerably high injectivity index. Hazil et al, (2012) attribute this to loss of gas from the deep fluid as a consequence of degassing and near surface boiling. Besides that, NH_3, H_2, and H_2S can be removed from the steam, released by boiling, by processes such as wall-rock interactions and solution into steam condensate. Depending on how far the well is from the recharge zone, gases in the reservoir fluid tend to enter the vapour phase whenever possible (Simsek et al., 2009). Therefore, when boiling sets in, the initially formed steam contains a majority of the dissolved gases while the residual liquid is highly depleted in dissolved gases and later stages of steam separation will contain significantly lower concentrations of gases. Steam formed in the early stages of boiling is characterized by a higher gas content.

6.3 Depth of gas breakout or bubble point

One aim of this study is to determine the potential impacts of gases on the performance of the wells. The results (Table 4) indicate that the probability of a gas breakout is highest in well OW-914 and lowest in OW-44. This is an indication that well OW-914 is likely to experience calcite scaling at its major feed zone at 1500 m depth, considering the type of waters feeding the well. This finding agrees with a dynamic survey carried out in OW-914 well in 2014 (Figure 16) where a calcite scaling potential in the depths between 1200 and 1800 m was indicated. According to Akin et al. (2015), thermal fluids rising in a wellbore experience boiling and degassing of CO_2 as a consequence of pressure drop.

When the initial gas bubbles are formed, CO_2 exsolution affects the pH together with the carbonate species leading to the thermal fluid becoming saturated in respect to calcite.

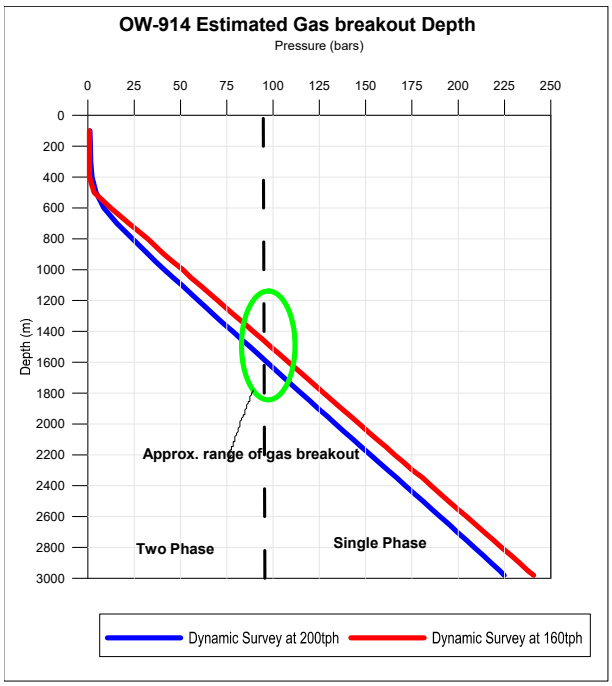

FIGURE 16: Estimated gas breakout depth in well OW-914 from the dynamic surveys

7. POSSIBLE RESERVOIR MANAGEMENT OPTIONS

Continuous exploitation tends to increase the concentration of non-condensable gases in the reservoir (Moya and Yock, 2005). The same study emphasizes the need to establish a program for detailed monitoring of the non-condensable gases at each well in order to determine the principal causes of the increase. The best injection and production strategies have to be found to improve the existing operating conditions.

This study points to the conclusion that the principal cause of the increase in non-condensable gases is a pressure decline in the reservoir consequently leading to depressurization boiling. In order to minimize this tendency, two different strategies for the different parts of the Olkaria geothermal field were considered (Figure 17). Firstly, a reinjection programme which will help to increase the volume of fluids injected in the eastern sector (suitable for example for well OW-44). The immediate response here would be a decrease in the enthalpy of the wells and gases evolution.

For wells with similar chemistry as well OW-914, two options are applicable. The first is the operation of the wells at a flow rate near the minimum. According to Moya and Sanchez (2005) this will minimise pressure drop and consequently non-condensable gas evolution due to depressurization boiling. This will consequently lead to a lowered scaling potential and/or reduced numbers of work overs in case scaling occurs. The second option will be to rethink the chemical dosage. According to Haizlip et al., (2012) successful scale mitigation in the wellbore requires that the inhibitor is injected into the flowing well through capillary tubing at depths 10-50 m below the estimated gas breakout depth preferably within the casing. The inhibitors prevent the growth of scale.

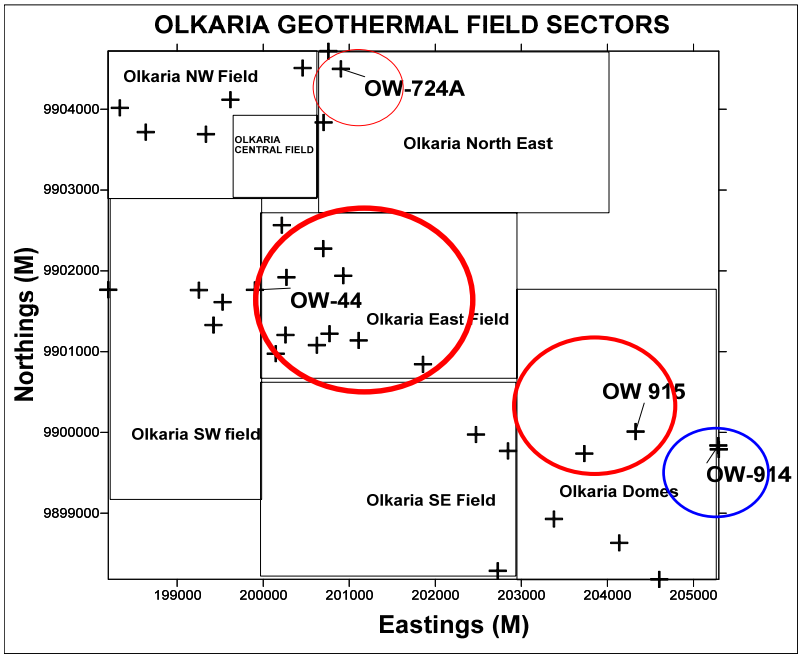

FIGURE 17: Management options for different parts of the field.; red eclipses stand for reinjection while the blue one is for reduced flow from wells and inhibition

8. CONCLUSIONS

The study concludes that:

- The gas species are not in equilibrium with the mineral assemblages due to processes of boiling, condensation, and mixing. The wells OW-914 and OW-915 are exceptions which are in equilibrium with mineral assemblages given by Equation 10;
- The CHILLER evaluation shows boiling as the major process leading to the evolution of gases;
- Well OW-44 had the smallest gas concentrations arising from the considered reservoir processes due to degassing and near surface boiling;
- Gas breakout is most likely in well OW-914 and least in OW-44;
- Different strategies for the management of different parts of the Olkaria geothermal field can be used. One option is increased volume of fluids injected in the eastern sector (for example in well OW-44). The second option, which is suitable for OW-914, is to operate the wells at a minimum flow rate or the use of chemical inhibitors.

ACKNOWLEDGEMENTS

Completion of this work is attributed to support received from various sources which I wish to sincerely thank. First and foremost, to my Almighty God for his grace, faithfulness and guidance that enabled me to cope with challenges of academic life. Sincere gratitude to the entire UNU-GTP fraternity and more so to my supervisor Tobias Weisenberger for his continuous guidance throughout the research. I am greatly indebted to the Kenya Electricity Generating Company LTD (KenGen) for supporting my entire study through finances, lab facilities and permission to use the data. I wish to acknowledge the contributions made by the Geochemistry team through data collection.

REFERENCES

Akin, T., Guney, A., and Kargi, H., 2015: Modeling of calcite scaling and estimation of gas breakout depth in a geothermal well by using PHREEQC. *Proceedings of the Fortieth Workshop on Geothermal Reservoir Engineering, Stanford University, Stanford, CA, United States*, 8 pp.

Ambusso, W.J. and Ouma, P.A., 1991: Thermodynamic and permeability structure of Olkaria Northeast field: Olkaria fault. *Geothermal Resource Council, Transactions, 15,* 237-242.

Angcoy, E.C., 2010: *Geochemical modelling of the high-temperature Mahanagdong Geothermal Field, Leyte, Philippines.* University of Iceland, MSc thesis, UNU-GTP, Iceland, report 1, 71 pp.

Arnórsson, S., Angcoy, E.C., Bjarnason, J.Ö., Giroud, N., Gunnarsson, I., Kaasalainen, H., Karingithi, C., and Stefánsson, A., 2010: Gas chemistry of volcanic geothermal systems. *Proceedings of the World Geothermal Congress 2010, Bali, Indonesia*, 12 pp.

Arnórsson, S., Bjarnason, J.Ö., Giroud, N., Gunnarsson, I., and Stefánsson, A., 2006: Sampling and analysis of geothermal fluids. *Geofluids, 6,* 203-216.

Ármannsson, H., 2003: CO_2 emission from geothermal power plants. *Proceedings of the International Geothermal Conference IGC-2003 "Multiple Integrated Uses of Geothermal Resources" Reykjavík, Session 12*, 56-62.

Bienkowski, R., Torres-Alvarado, I.S. and Hinderer, M., 2003: *Genese hochsaurer Fluide im Geothermalfeld von Los Humeros, Zentral-Mexiko*. Institut für Angewandte Geowissenschaften, Technische Universität Darmstadt, Diplomarbeit (MSc thesis in German), 89 pp.

Clarke, M.C.G., Woodhall, D.G., Allen, D., and Darling, G., 1990: *Geological, volcanological and hydogeological controls of the occurrence of geothermal activity in the area surrounding Lake Naivasha, Kenya*. Ministry of Energy, report, 138 pp.

Fernandez-Prini, R., Alvarez, J.L., and Harvey, A.H., 2003: Henry´s constants and vapor-liquid distribution constants for gaseous solutes in H_2O and D_2O at high temperatures. *J. Phys. Chem. Ref. Data, 32*, 903-916.

Giroud, N., and Arnórsson, S., 2005: Estimation of long-term CO_2 and H_2S release during operation of geothermal power plants. *Proceedings of the World Geothermal Congress 2005, Antalya, Turkey,* 6 pp.

Gudmundsson, B.T., and Arnórsson, S., 2002: Geochemical monitoring of the Krafla and Námafjall geothermal areas, N-Iceland. *Geothermics, 31*, 195-243.

Haizlip, J.R., Guney, A., Tut Haklidir, F.S. and Garg, S.K., 2012: The impact of high non condensable gas concentrations on well performance – Kizildere geothermal reservoir, Turkey. *Proceedings of the 37th Workshop on Geothermal Reservoir Engineering, Stanford University, Stanford, CA, US*, 6 pp.

Holland, T.J.B., and Powell, R., 1990: An enlarged and updated internally consistent thermodynamic dataset with uncertainties and correlations: K_2O-Na_2O-CaO-MgO-MnO-FeO-Fe_2O_3-Al_2O_3-TiO_2-SiO_2-C-H_2-O_2. *J. Metamorphic Petrology, 8,* 89-124.

Karingithi, C.W., 2000: Geochemical characteristics of the Greater Olkaria geothermal field, Kenya. Report 9 in: *Geothermal training in Iceland 2000*. UNU-GTP, Iceland, 165-188.

Karingithi, C.W., 2002: *Hydrothermal mineral buffers controlling reactive gases concentration in the Greater Olkaria geothermal system, Kenya.* University of Iceland, MSc thesis, UNU-GTP, Iceland, report 2, 51 pp.

KenGen, 1999: *Conceptualized model of the Olkaria geothermal field.* Kenya Electricity Generating Company Ltd. (KenGen), internal report no. 10, 46 pp.

KenGen, 2014: *Revised geochemical model of the Olkaria geothermal field*. Kenya Electricity Generating Company Ltd. (KenGen), internal report no. 1, 23 pp.

Lagat, J., Arnórsson, S. and Franzson, H., 2005: Geology, hydrothermal alteration and fluid inclusion studies of Olkaria Domes Geothermal Field, Kenya. *Proceedings of the World Geothermal Congress 2005, Antalya, Turkey*, 14 pp.

Moya, P., and Sánchez, E., 2005: Non-condensable gases at the Miravalles geothermal field. *Proceedings of the 30th Workshop on Geothermal Reservoir Engineering, Stanford University, Stanford, CA, United States*, 11 pp.

Moya, P., and Yock, A., 2005: First eleven years of exploitation at the Miravalles geothermal field. *Proceedings of the Thirtieth Workshop on Geothermal Reservoir Engineering, Stanford University, Stanford, CA, United States*, 8 pp.

Mungania, J., 1992: *Preliminary field report on geology of Olkaria volcanic complex with emphasis on Domes area field investigations*. Kenya Power Company, internal report 11, 37 pp.

Naylor, W.I., 1972: *The geology of the Eburru and Olkaria geothermal projects*. United Nations Development Programme, report no. 01, 52 pp.

Ofwona, C.O., 2002: *A reservoir study of Olkaria East geothermal system, Kenya*. University of Iceland, MSc thesis, UNU-GTP, Iceland, report no. 1, 74 pp.

Ogoso-Odongo, M.E., 1986: Geology of Olkaria geothermal field. *Geothermics, 15*, 741-748.

Omenda, P.A., 1994: Geological control on the reservoir characteristics of Olkaria West Geothermal Field, Kenya. *Proceedings of the Nineteenth Workshop on Geothermal Reservoir Engineering, Stanford University, Stanford, CA, United States*, 125-129.

Omenda, P.A., 2000: Anatectic origin for comendite in Olkaria geothermal field, Kenya Rift; Geochemical evidence for syenitic protholith. *African J. Science and Technology*, *1*, 39-47.

Ouma, P.A., 1999: *Reservoir engineering report for Olkaria Domes field*. Kenya Electricity Generating Company Ltd. (KenGen), internal report 14, 54 pp.

Reed, M.H., Spycher, N.F., and Palandri, J., 2012a: *SOLVEQ-XPT: A computer program for computing aqueous-mineral-gas equilibria*. University of Oregon, Department of Geological Sciences, Eugene, OR, United States, 43 pp.

Reed, M.H., Spycher, N.F., and Palandri, J., 2012b: *Users guide for CHIM-XPT: A program for computing reaction processes in aqueous-mineral-gas systems and MINTAB guide (Ver 2.43)*. University of Oregon, Department of Geological Sciences, Eugene, OR, United States, 73 pp.

Robie, R.A. and Hemingway, B.S., 1995: *Thermodynamic properties of minerals and related substances at 298.15 K and 1 bar (105 Pascals) pressures and at higher temperatures.* U.S. Geological Survey Bulletin, 2131, 461 pp.

Shackleton, R.M., 1986: Precambrian collision tectonics in Africa. In: Coward, M.P. and Ries, A.C. (editors), *Collision Tectonics*. Geological Society, London, United Kingdom, special publications 1986 -19, 329-349.

Simsek, S., Parlaktuna, M. and Akın, S., 2009: *Data gathering and evaluation of Kizildere geothermal field*. Report for Zorlu Energy, 13 pp.

Smith, M. and Mosley, P., 1993: Crustal heterogeneity and basement influence on the development of the Kenya rift, East Africa. *Tectonics, 12*, 591-606.

Thompson, A.O. and Dodson, R.G., 1963: *Geology of the Naivasha area*. Geological Survey Kenya, report no. 55, 88 pp.

Virkir, 1980: *Geothermal development at Olkaria*. Virkir Consulting Group, report no. 09 prepared for Kenya Power Company, 40 pp.

Wamalwa, R., Nyamai, C.M., Ambusso, W. and Mulwa, J., 2014: Structural controls on the chemistry and output of the wells in the Olkaria geothermal field, Rift Valley, Kenya. *Proceedings of the 5th African Rift Geothermal (ARGeo-C5), Arusha, Tanzania*, 11 pp.

Wambugu, J.M., 1995: *Geochemical update of Olkaria West geothermal field*. Kenya Power Company Ltd., internal report no. 5, 40 pp.

West JEC, 2009: *The Olkaria optimization study (Phase II) – Final reservoir analysis report.* West Japan Engineering Consultants Inc., 301 pp.

UNITED NATIONS UNIVERSITY
UNU-GTP
Geothermal Training Programme

Orkustofnun, Grensasvegur 9,
IS-108 Reykjavik, Iceland

Reports 2015
Number 35

ASSESSMENT OF THE URBAN DEZHOU SANDSTONE GEOTHERMAL RESERVOIR IN NORTH CHINA

Zheng Tingting
Shandong Provincial Institute of Geology and Mineral Resources
No.13632 Jingshi Road, Lixia District
Jinan 250014, Shandong Province
CHINA
zttshandong@126.com

ABSTRACT

Sedimentary geothermal reservoirs are one of the two main types of low-temperature reservoirs in China, with productive wells. The reservoirs are characterized by infinite extent, homogeneous aquifers and are heated by heat conduction. This report presents the results of reservoir assessment of the Urban Dezhou Guantao formation sandstone geothermal reservoir in Shandong Province of North China.

As a consequence of large-scale production, water level decline problems have occurred in the Urban Dezhou reservoir. Therefore, reinjection tests were undertaken and the results show that 100% of the production water can be reinjected during a space heating period (120 days) without significant cooling in the reservoir. A tracer test model was set up to predict the geothermal temperature changes, they predict the temperature to remain stable for 50 years. Thermal breakthrough is calculated by another simple model to give an idea of the safe distance between reinjection wells and production wells. Monte Carlo volumetric assessment is undertaken to estimate the total recoverable energy in the Urban Dezhou reservoir. The lifetime of the Urban Dezhou reservoir is estimated based on the current production rate and the recoverable energy. Using the long-term monitoring water level depth data, the sustainable yield of the Urban Dezhou reservoir is estimated based on a two-tank closed lumped parameter model. The prerequisite is a maximum allowable water level depth of 150 m in 50 years' time. The estimated sustainable yield without reinjection is 25% of the current production rate, which cannot meet the demands of the city. To keep the current production rate, the reinjection rate should be more than 75% of the production rate. By keeping the maximum reinjection rate, which is 80% of the production, the sustainable yield becomes 25% more than the current production rate. Therefore, the sustainable yield with reinjection cannot only meet the demands of the city but also gives potential for more development of the reservoir. Further study of temperature and chemistry changes in the Urban Dezhou reservoir should be undertaken to complete the reservoir assessment.

1. INTRODUCTION

Sedimentary geothermal reservoirs are one of the two main types of low-temperature reservoirs in China. They are mostly of high potential with quite productive wells, heated by heat conduction from depth

and are characterized by infinite extent and homogeneous aquifers. The geothermal resources contained in the major sedimentary basins of China are estimated to be about 2.5×10^{22} J (Zheng et al., 2015). The North China sedimentary basin is one of the most important sedimentary basins in China. There are numerous urban areas in the basin, including Beijing, Tianjin, the Hebei Province and the Shandong Province. In Beijing, about 400 geothermal wells had been drilled by 2008, and the annual geothermal water production has been 7-9 million m^3. The temperature is in the range of 38-103°C, mostly 40-70°C (Huang, 2012). In Hebei, there are about 1000 geothermal wells in the sedimentary basin area and the annual geothermal water production has been around 50 million m^3 (Zhang et al., 2013).

This report presents the results of an assessment of the Urban Dezhou reservoir in the Shandong Province of North China. The report gives an overview of the reservoir properties and status and different methods are used to assess its properties and potential for utilization and development. The Urban Dezhou reservoir has a long production history. Water level decline became the main problem for the reservoir for which reinjection is the most effective solution. Reinjection is considered an important part of comprehensive geothermal resource management as well as an essential part of sustainable and environmentally friendly geothermal utilisation (Axelsson, 2012). The first reinjection test in Dezhou City took place in 2006. After 8-years of experiments, substantial improvements in injection, drilling and well construction have been achieved. In 2012, a reinjection test without artificial pressure successfully took place in Pingyuan County, Dezhou City. The first tracer test in the Urban Dezhou reservoir was undertaken in 2015 to predict the cooling in the reservoir and to get more information about reservoir properties.

2. THE URBAN DEZHOU SANDSTONE GEOTHERMAL RESERVOIR

Dezhou is a city in the north-western part of Shandong Province, 400 km from Beijing, in northeast China (Figure 1). The Urban Dezhou sandstone geothermal reservoir is in the north-western Shandong Depression which is part of the North China sedimentary basin located in the Yellow River alluvial plain (Figure 2). It is a low-temperature sedimentary reservoir, where 83 production wells have been successfully drilled since 1997, yielding water with temperatures between 52 and 59°C. The main geothermal development has been in the area of direct-utilization, such as for space heating, swimming pools and balneology (Kang, 2000).

FIGURE 1: Location of Dezhou city, Shandong, China (Kang, 2000)

2.1 Geological setting and hydrogeological conditions

The north-western Shandong Guantao formation sandstone geothermal reservoir is located in a large and continuous sedimentary basin and there are no obvious impermeable boundaries between different parts of the Guantao formation reservoir. For the purposes of this assessment, the reservoir studied is

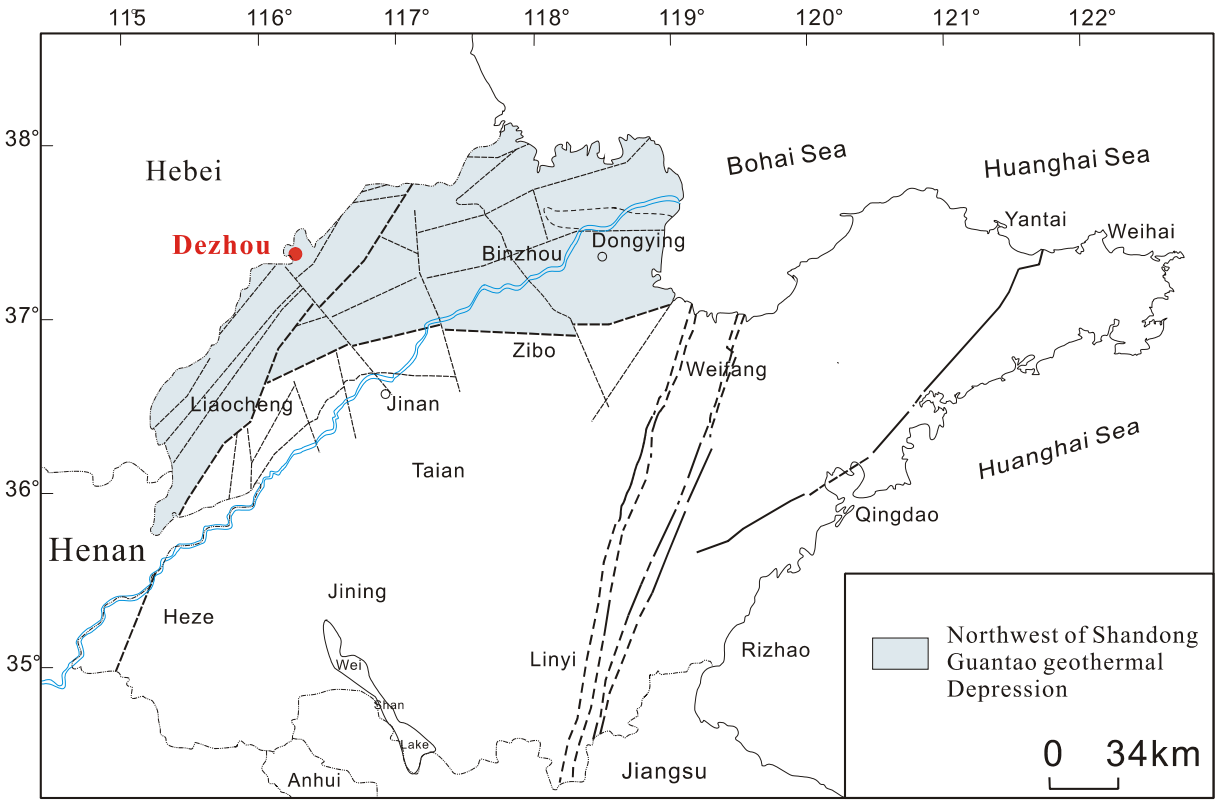

FIGURE 2: Location of the Dezhou geothermal field in the north-western Shandong Guantao geothermal depression

the Guantao formation sandstone aquifer from the Neogene age in the urban area of Dezhou City. The full name of the reservoir should be the Urban Dezhou Guantao formation sandstone geothermal reservoir. Later in this report, the term "the Urban Dezhou reservoir" will be used as an abbreviation for this specific reservoir.

The Dezhou depression area (Figure 3) is considered to correspond to the Urban Dezhou reservoir, with an area of about 169 km^2. The boundaries of the reservoir are permeable faults and tectonic zones, named the Bianlinzhen fault on the east side, the Cangdong fault on the west side, the Xiaoyuzhuang tectonic zone on the south side, and the Xisongmen tectonic zone on the north side. As a low-temperature water-dominated conduction controlled reservoir, the reservoir

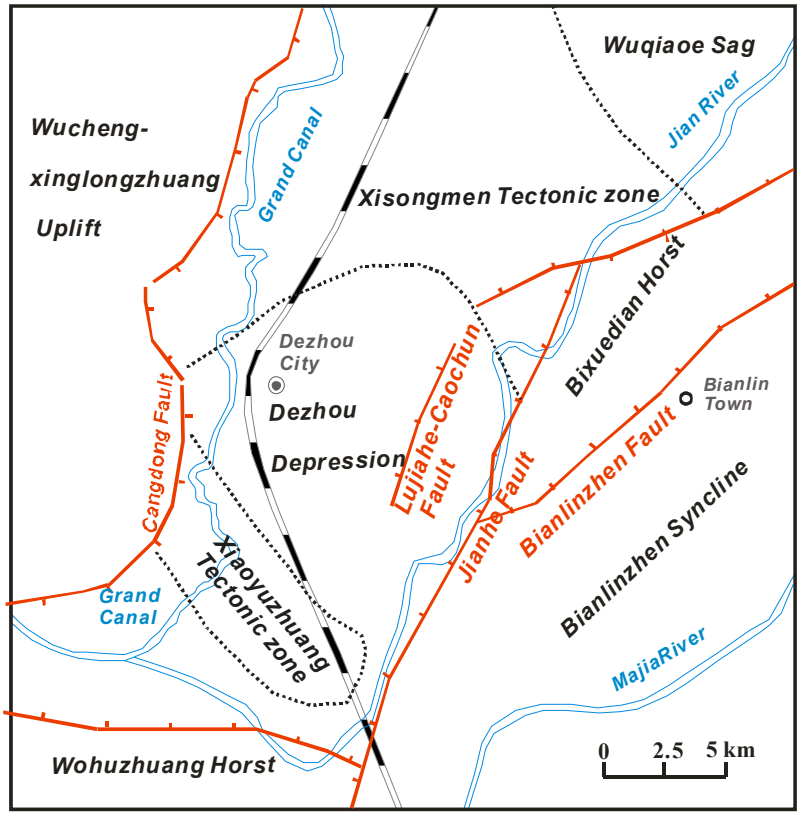

FIGURE 3: Tectonic settings of the Urban Dezhou reservoir (Zhang et al., 2015a)

exists because of the formation of fracture-controlled highly permeable sedimentary layers with an above average geothermal gradient. When it reaches great depth, below 1300 m approximately, the water is heated by thermal conduction. As shown in Figure 4, the depth of the Guantao Formation sandstone of the reservoir ranges from 1350 to 1650 m and thicknesses varies from 300 to 480 m.

The cap rock of the reservoir is upper Minghuazhen formation from the Neogene age, with a thickness of 900 m. It is composed of argillite and sandy argillite with interbedded sandstone. The main production aquifers of the reservoir are comprised of sandstone and conglomerate with high porosity, 24-35%. In the natural state, most of the wells in the Urban Dezhou reservoir are artesian, with an artesian water level height of 7-8 m above the ground surface and a free-flow rate of 8.3-11.1 l/s (Kang, 2000).

Layers below the Guantao formation in the Urban Dezhou reservoir are formations of Eogene age, such as Dongying formation, Shahejie formation and Kongdian formation (Figure 4). The aquifers of these formations are mainly sandstone. Because they are much deeper and the water-abundance is much less than in the Guantao sandstone in Dezhou area, they are not considered reservoirs for development yet. In the future, if the water level of the Guantao Formation aquifer decreases too much, the development of the reservoirs below might be considered. The reservoirs in formations of Eogene age are not considered in this report on the Urban Dezhou reservoir, however.

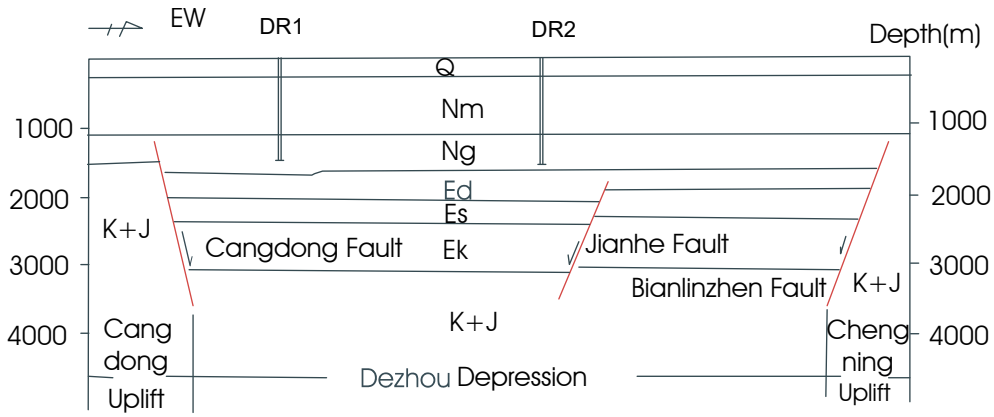

FIGURE 4: Tectonic cross-section of the Dezhou depression (Kang, 2000)

2.2 Geothermal reservoir properties

Figure 5 shows the thickness and the contours of the bottom depth of the Guantao formation in the Urban Dezhou reservoir, in which the depth ranges from 1350 to 1650 m and the thickness from 300 to 480 m. The main sandstone production aquifer of the reservoir has a thickness of 150-210 m, about 43-50% of the total reservoir thickness (Figure 6).

Figure 7 shows that the formation temperature increases quickly from 43 to 50°C below 1351 m depth. The main aquifer zone in well R34 is from 1400 to 1500 m depth with a stable temperature of 50°C. The average thermal gradient of the well is 3.05°C/100 m. It should be pointed out that this temperature log was taken during drilling when the well was cooler than later during production when temperature reached 52-55°C.

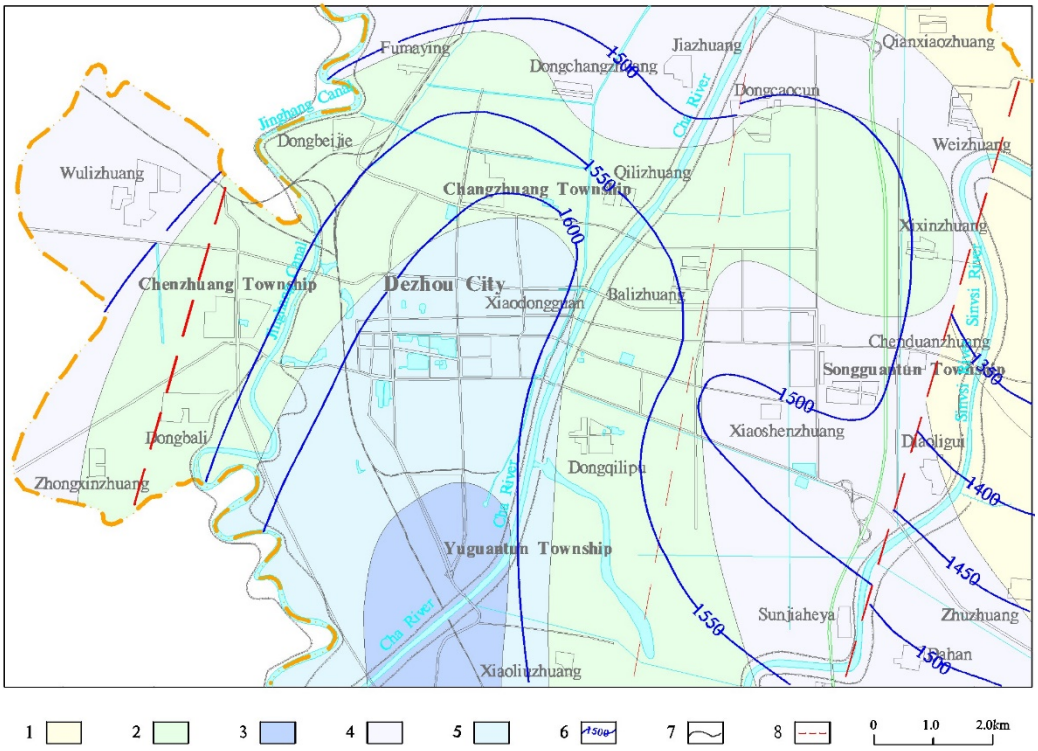

FIGURE 5: Thickness and contours of the bottom of the Guantao formation (Zhang et al., 2011)
(1: Thickness < 350 m, 2: Thickness 350-400 m, 3: Thickness 400-450 m, 4: Thickness 450-500 m,
5: Thickness > 500 m, 6: Bottom depth contour of the Guantao Formation,
7: Boundary of thickness zonation, 8: Main fault)

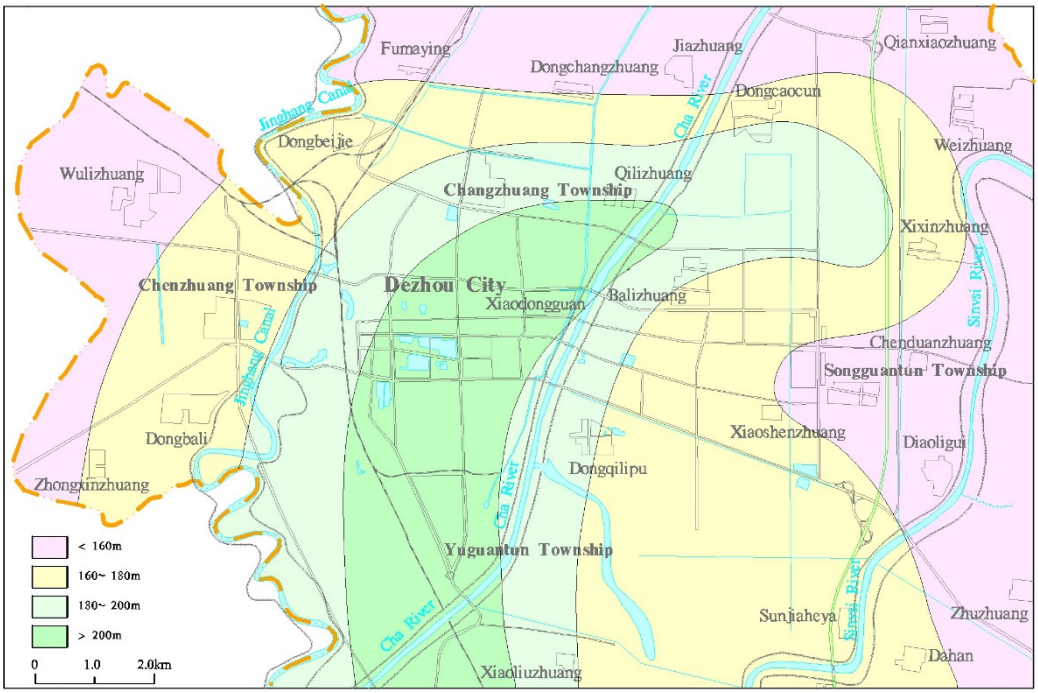

FIGURE 6: The thickness of the sandstone aquifer in the Guantao formation reservoir (Zhang et al., 2011)

In the Urban Dezhou reservoir, thermal gradient ranges from 3.0 to 3.1°C/100 m (Figure 8). The production temperature of the reservoir ranges from 52 to 59°C (Figure 9).

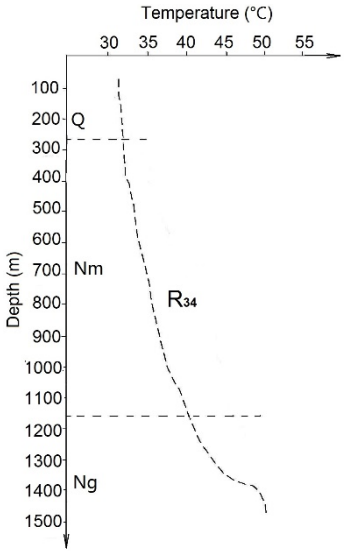

FIGURE 7: Temperature log in well R34 measured during drilling (Zhang et al., 2011)

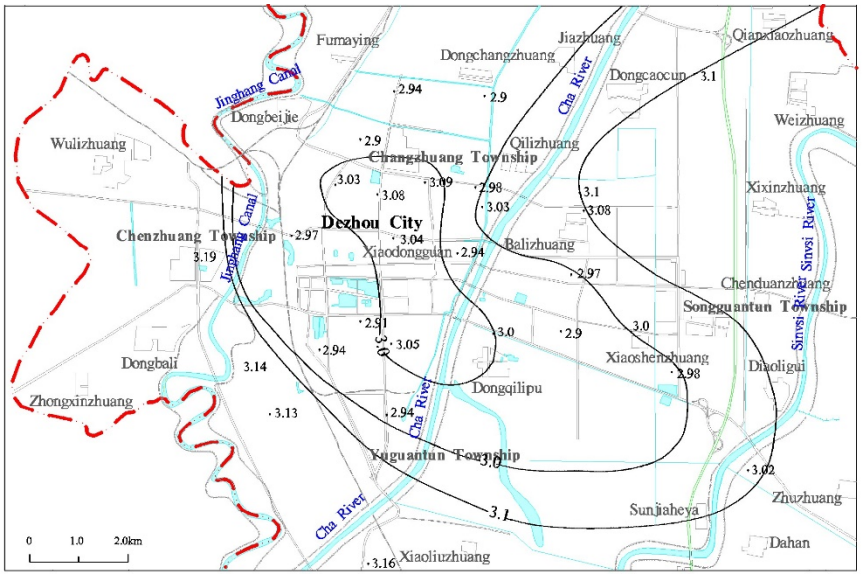

FIGURE 8: The geothermal gradient contour of the Guantao formation reservoir (°C/100 m) (Zhang et al., 2015b)

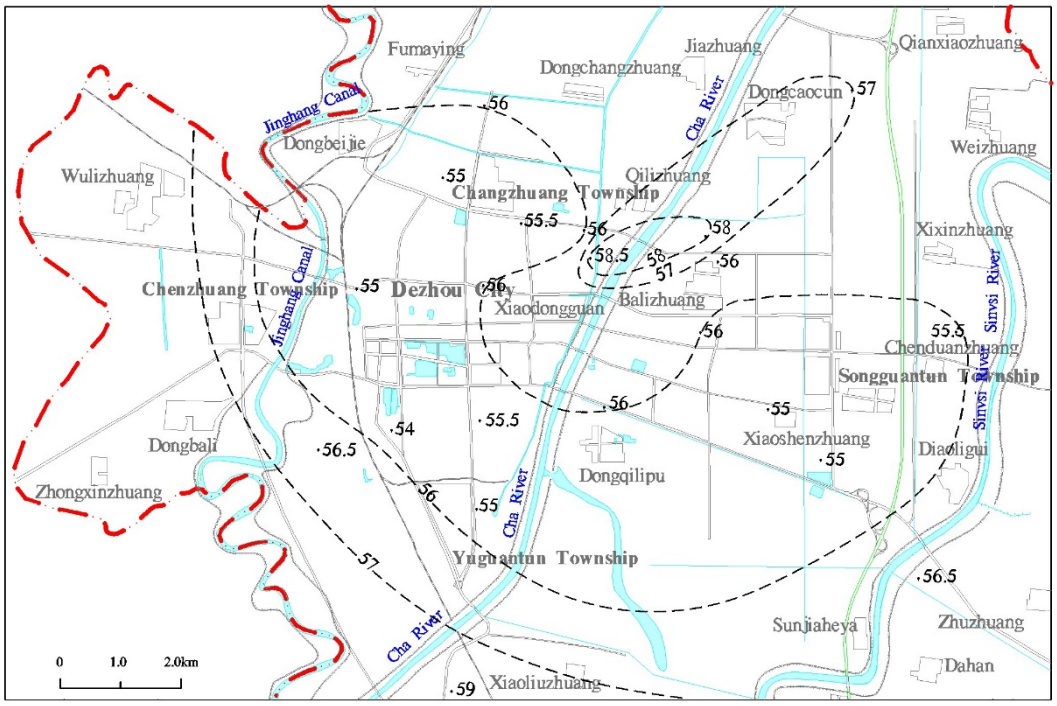

FIGURE 9: Geothermal temperature contours of the Urban Dezhou reservoir (°C) (Zhang et al., 2011)

2.3 Exploration and development history of the Urban Dezhou reservoir

The first geothermal well in the area (well R14) was drilled in 1997 and the second in 1998 (Kang, 2000). Nowadays there are 256 geothermal wells in Dezhou city, about 82 of which are located in the Urban Dezhou reservoir (Figure 10). The other wells are in outer parts of Guantao formation sandstone reservoirs in the outer areas of the Dezhou city. The total production rate of the Urban Dezhou reservoir

was 18.3 million m^3 in 2014, the depth of the wells ranges from 1400 to 2010 m and the production rate changes seasonally; 90% of the production is for the space heating demand from middle November until middle March. The main utilization of the geothermal fluid is for space heating, about 89.5% of the total. Bathing and entertainment use about 9% of the total. The other 1.5% is used in greenhouses. It should be kept in mind that large-scale production of geothermal fluid and geothermal energy used with low efficiency and without reinjection may produce environmental problems.

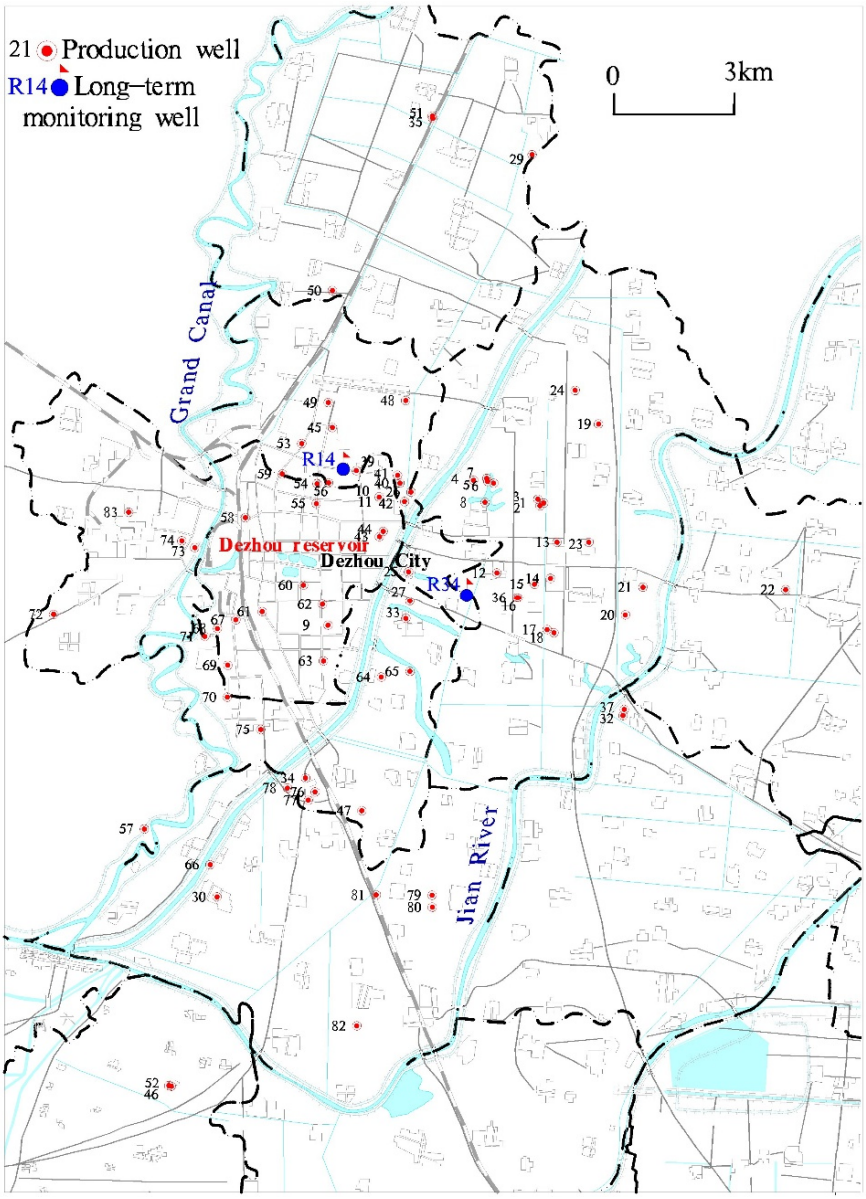

FIGURE 10: Distribution of production and monitoring wells in the Urban Dezhou reservoir (Zhang et al., 2015a)

2.3.1 Water level decline

Owing to its very low actual production, 2.9 l/s in 1999 (Kang, 2000), the Urban Dezhou reservoir, overall, was still in its natural state. However, after nearly 10-years of large scale of production, the water level of the whole Guantao sandstone geothermal aquifer has decreased significantly.

Figure 11 shows the initial water level of the complete north-western Shandong Guantao geothermal depression, before large scale production, and water level depth in 2015. It can be seen that the water level drawdown increases significantly after large-scale production started and that several water level depression cones have emerged. The water level depression cone in the Urban Dezhou reservoir can be seen in Figure 12 with the maximum water level depth of 70 m.

Wells R14 and R34 are located in the centre of the depression cone of the water level and are used for long term monitoring (Figures 10, 12 and 13). The water level depth in Dezhou reservoir has been decreasing from 8.3 m artesian height before 1997 to 70 m below ground surface in 2015, which corresponds to an annual decrease of 3.6 m (Figure 12).

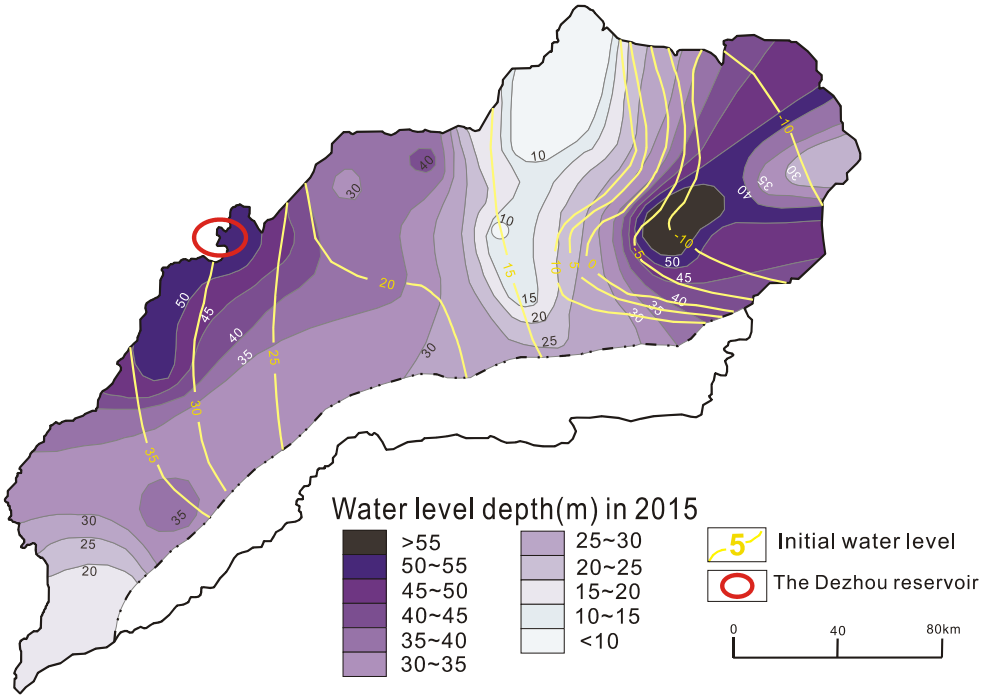

FIGURE 11: Observed water level changes in the north-western Shandong Guantao geothermal depression. Water level depth is measured in 2015 after large-scale production. The initial water level is measured before large-scale production. (Zhang et al., 2015b)

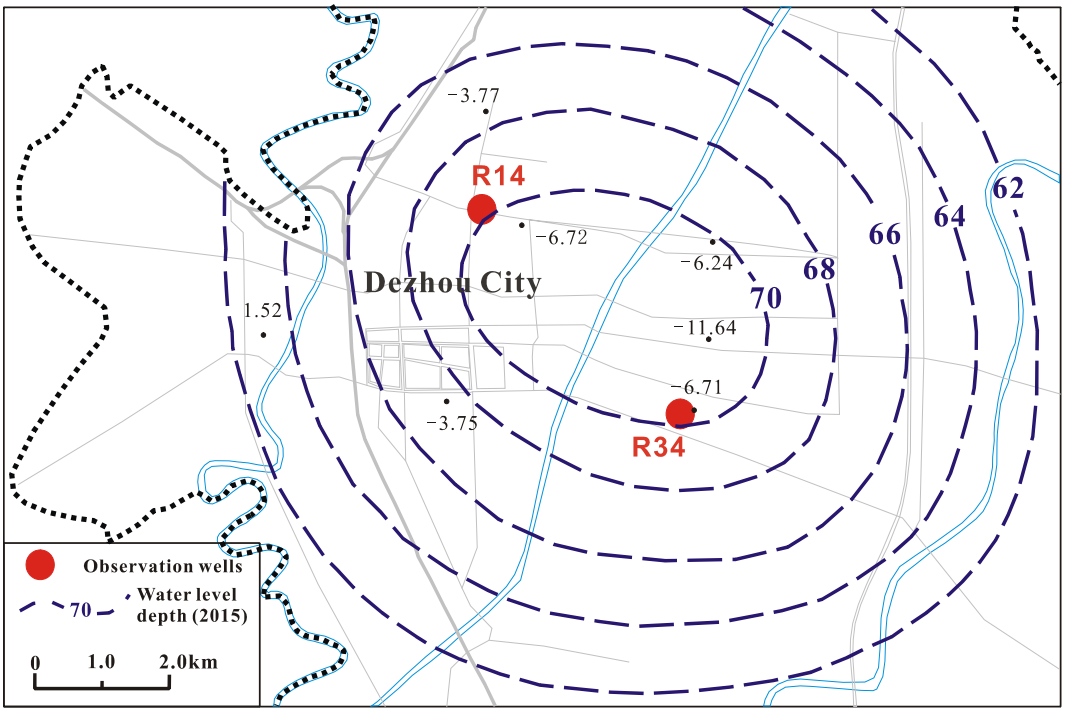

FIGURE 12: The water level depth of the Urban Dezhou reservoir, 2015

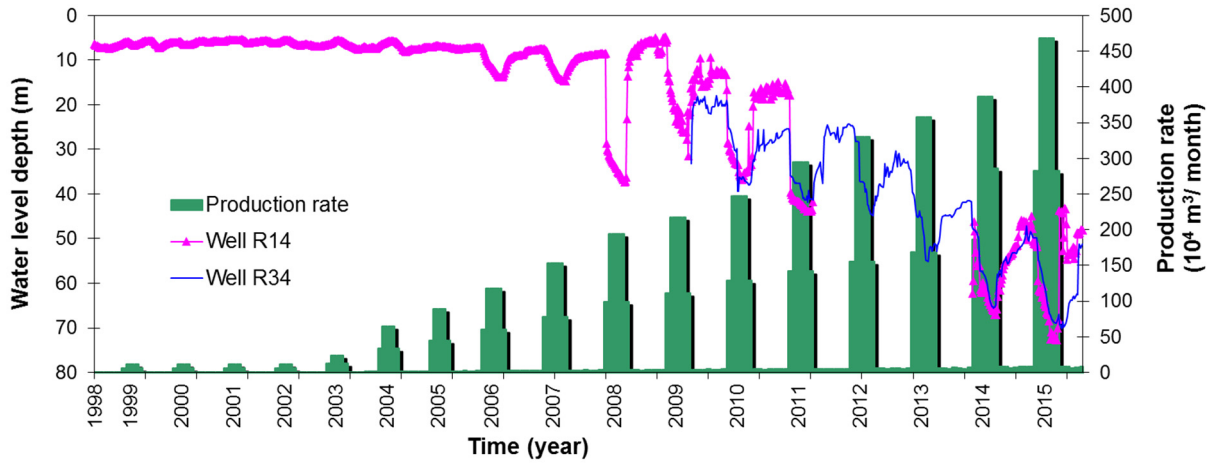

FIGURE 13: Measured long-term variations in water level depth with increasing production rate in wells in the Urban Dezhou reservoir (1998-2015) (Zhang et al., 2015b)

2.3.2 Cooling in reservoir

Temperature monitoring in well R14 from 1998 to 2015 (Figure 14) shows that the geothermal water temperature of the Urban Dezhou reservoir didn't changed significantly from 1998 to 2011. The temperature is between 52 and 55°C. From 2014 to 2015, the temperature in the well changed but this was because the well was closed and the water column in the well cooled down. When pumping was reinitiated in the well, the colder water was pumped out and the water temperature rose back to near 55°C, the same before the production break. From this it can be deduced that there appear to be no cooling problems due to large-scale production of geothermal water in the Urban Dezhou reservoir.

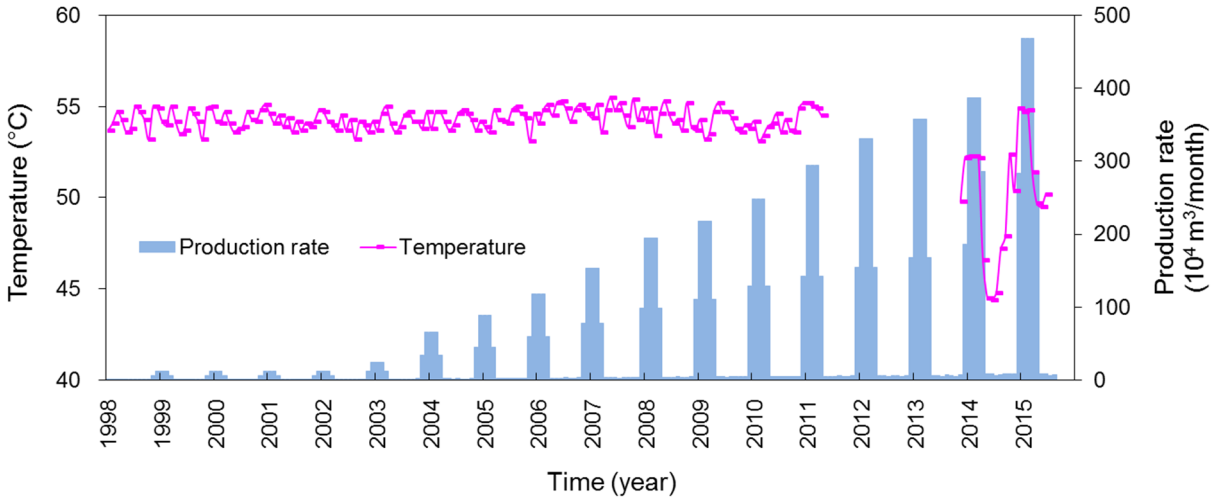

FIGURE 14: Measured long-term variations of water temperature for well R14 with the increase in production rate in the Urban Dezhou reservoir (1998-2015) (Zhang et al., 2015a)

2.3.3 Subsidence

Declining water level usually leads to other problems. Ground subsidence is one of the most common problems in the north-west part of the Shandong Province. Unfortunately, there is no data available measuring the subsidence caused by production of geothermal water in Dezhou. However, it is possible to infer some idea from the subsidence caused by cold groundwater production.

There is a colder groundwater aquifer in the Minghuazhen formation, above the geothermal aquifer, at a depth of 190-250 m. It is the main water supply of the city of Dezhou. This aquifer has been producing since 1965. The groundwater level has been declining at a rate of 3 to 4 m per year and has fallen from 2 to 140 m depth in response to extensive production of up to 7.0×10^4 m^3 per day. The cause of the subsidence is considered compression of high-porosity, low-permeability mudstone at 90-150 m depth (Kang et al., 2015).

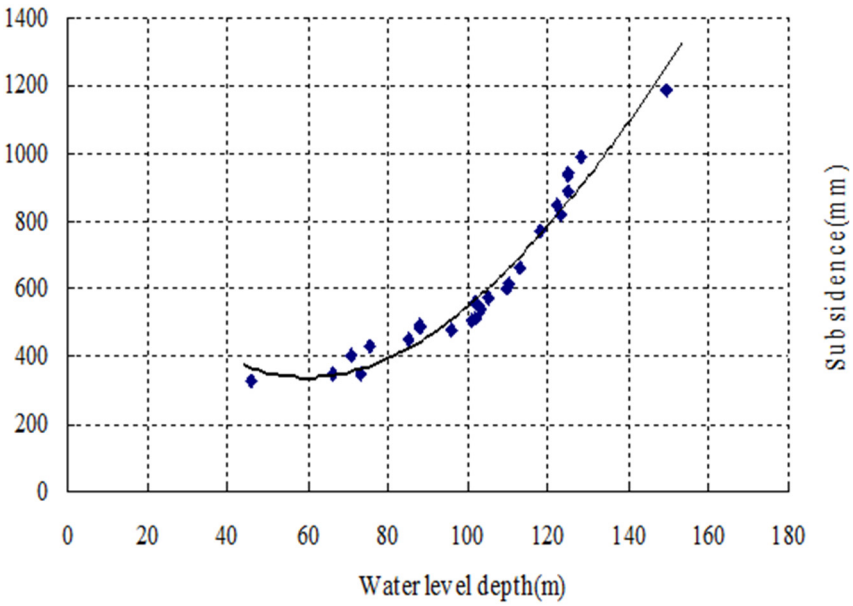

FIGURE 15: Relation between groundwater level depth and subsidence in Urban Dezhou (Kang et al., 2015)

Figure 15 shows the relationship between water level depth in the groundwater system and subsidence in Urban Dezhou. When the water level depth is between 100 and 150 m depth, the rate of subsidence increases to 14 mm for every metre of water level decrease. This is much higher than above the 100 m water level depth. From this conclusion, it is important to consider water level depth as a factor constraining conditions of both colder groundwater and geothermal water productions. To avoid subsidence caused by geothermal water level decline in Dezhou city in the future, it would be best to maintain the water level above 100 m depth. However, considering the demand of the city, the maximum allowable water level depth can be somewhat lower, or above 150 m depth. With this depth limit, further subsidence can be avoided and the demands of the city met. The relationship between water-level decline in the geothermal reservoir and land subsidence needs to be studied further, however.

The above emphasises the fact that reasonable assessment of production potential is a prerequisite for developing the geothermal resource perennially; and comprehensive management countermeasures should be adopted to assure sustainable development of the geothermal reservoir (Kang et al., 2015).

2.3.4 Thermal and chemical pollution

After its use for district heating, the waste geothermal water in Dezhou drains into surface water directly without reutilization or reinjection. The wastewater temperatures are around 30-35°C and the environment air temperature of -10-5°C (during heating season). The temperature difference between the geothermal wastewater and the environment may cause ecological unbalance in surface water. The total dissolved solids (TDS) of the Dezhou geothermal water is around 4000-5000 mg/l. The draining of wastewater into surface irrigation water may cause hardening and salinization problems in the soil. The fundamental countermeasure for solving these problems is reinjection, which can not only reduce the wastewater draining but also improve the efficiency of the geothermal exploitation.

3. REINJECTION TESTS AND ANALYSIS

Reinjection is the most effective solution to solve the water level decline problem in the Urban Dezhou reservoir. Geothermal reinjection involves returning some, or even all, of the water produced from a geothermal reservoir back into the geothermal system, after energy has been extracted from the water (Axelsson, 2013).

For the purpose of sustainable development of geothermal resources, especially for the Chinese sedimentary aquifers with very little geothermal water recharge, including sandstone aquifers, reinjection is increasingly becoming the means for sustainable and environmentally friendly geothermal utilization. It is efficient for wastewater disposal as well as to provide additional recharge to geothermal aquifers (Kang et al., 2015). Thus, reinjection counteracts pressure (water level) drawdown induced by heavy development and extracts more thermal energy from reservoir rocks (Axelsson, 2008), ideally maintaining the production capacity of the geothermal aquifers. Meanwhile, reinjection can also mitigate land subsidence and be used to maintain geothermal manifestations (artesian wells, natural hot springs) (Kang, 2015).

In China, the earliest geothermal reinjection experiments were successfully implemented in the urban area of Beijing in 1974 and 1975 in a dolomite aquifer. However, during the reinjection, the injectivity decreased quickly (Liu, 2008).

Three reinjection tests have been undertaken in Pingyuan Country, Dezhou City. The Pingyuan County is about 30 km south-east from Urban Dezhou, and is in the same sedimentary basin as the Urban Dezhou reservoir (Figure 16). Thus, the tests can be taken to represent the reinjection properties of the Urban Dezhou reservoir. There is one production well and one reinjection well, with 231 m distance between them. The static water level depth in the reinjection well was 30.7 m, and 31.8 m in the production well. The aquifers of the two wells are in the same sandstone formation, the Neogene Guantao formation at a depth at around 1130 mm (Figure 17).

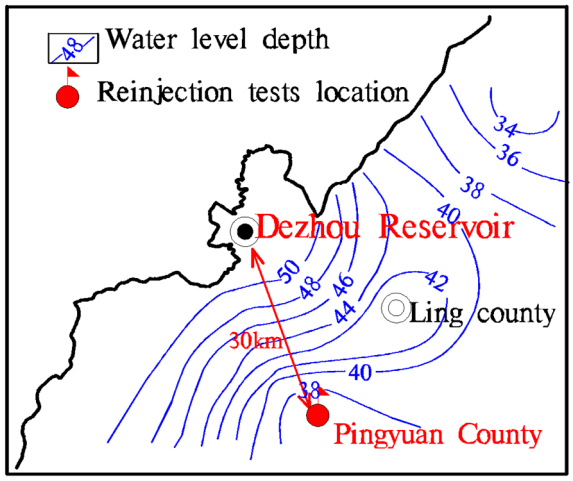

FIGURE 16: Location of reinjection tests in Pingyuan County, Dezhou

3.1 Reinjection test 1

The first reinjection test took place from October 13th to December 15th, 2012. The main purpose of this reinjection test was to assess how much water could be injected into the sandstone reservoir in natural condition, without artificial pressure. The geothermal water for reinjection in this test was taken directly from the production well with the same temperature, 50-52°C, without any utilization.

The methodology of this test is presented in Figure 18. After production and reinjection, a depression cone is observed around the production well and the water level inside the well is at a minimum, while there is a water level uplift cone around the reinjection well and water level inside the well is at a maximum. Artificial water level difference is created between the two wells and the reinjection water gets more potential energy to flow between them.

Figure 19 shows that the highest injection rate is about 70 m^3/h along with the maximum water level increase in the reinjection well of 28.7 m. The maximal stable water level increase in the production well is 3.6 m.

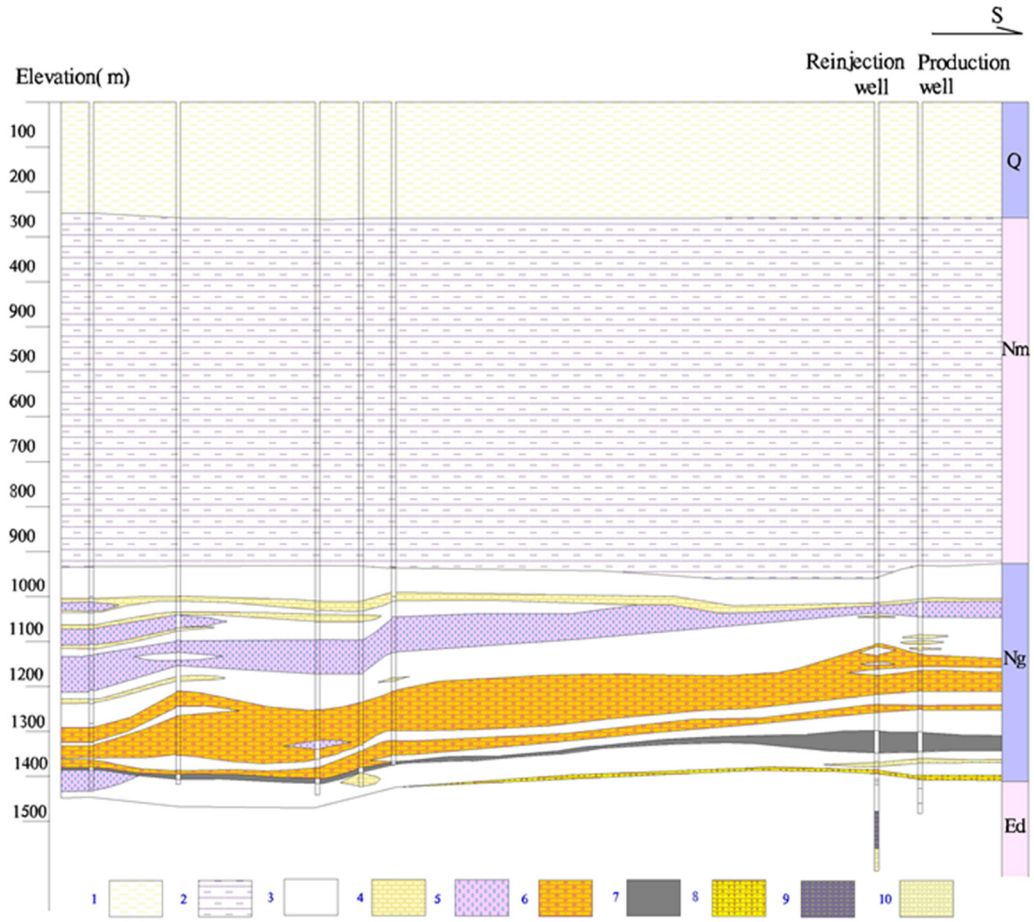

FIGURE 17: A borehole cross-section in the Dezhou geothermal field (Q-Pingyuan formation of Quaternary: 1-clay and sandy clay; Nm-Minghuazhen formation of Neogene: 2-upper section: mudstone, silt and fine sand, low diagenesis, lower section: argillite, silt and fine sand, high diagenesis; Ng-Guantao formation of Neogene: 3-argillite, 4-fine sandstone, 5-medium sandstone, 6-coarse sandstone, 7-intrusive rock, 8-conglomerate; Ed-Dongying formation of Eogene: 9-sandy argillite, 10-argillaceous sandstone) (Kang et al., 2015)

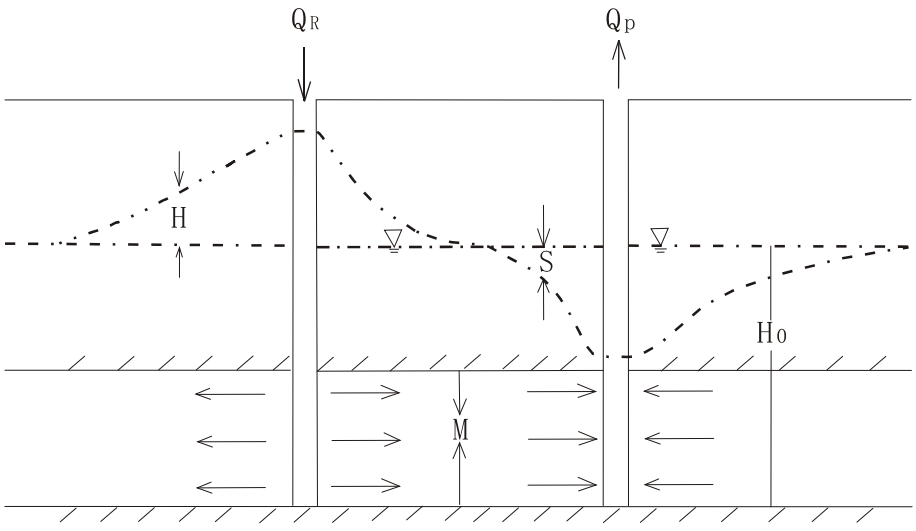

FIGURE 18 Methodology of reinjection under natural condition (Q_R- Reinjection rate, Q_P- Production rate, H- Water level increase, S- Water level drawdown, H_0- Initial water level, M- Aquifer thickness)

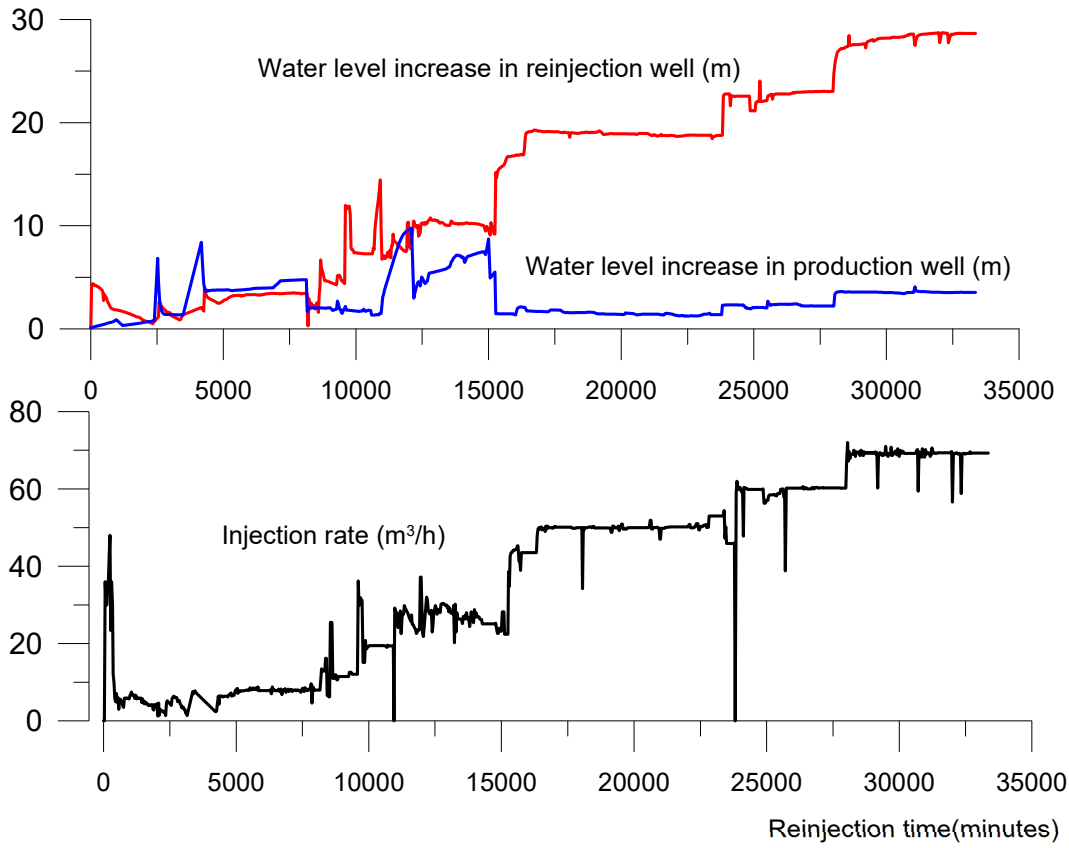

FIGURE 19: The reinjection rate changes and water level increase in production and reinjection wells during the period of October 13th - December 15th, 2012 (Kang et al., 2015)

Figure 20 shows the correlation between the reinjection rate and the water level increase in the reinjection well. It can be seen that the reinjection rate is positively correlated with water level increase. The linear equation of correlation as given in Figure 20 is:

$$y = 0.396x - 0.0856 \quad (R^2 = 0.99) \quad (1)$$

3.2 Reinjection test 2

The second test took place from November 14th, 2013 to March 14th, 2014. The reinjection test was implemented in the same wells also under natural condition, with the main purpose of assessing the temperature response of the reservoir to the test.

Figure 21 shows that the reinjection water, of temperatures about 30-32°C, does not influence temperature in the production well, which remains at 53°C during the whole space heating period of 120 days.

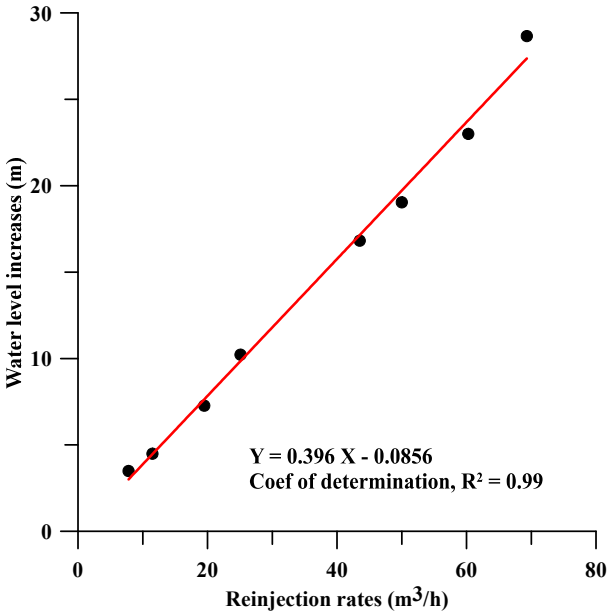

FIGURE 20: The relationship between reinjection rate and water level increase (dots: measured data, line: fitted line)

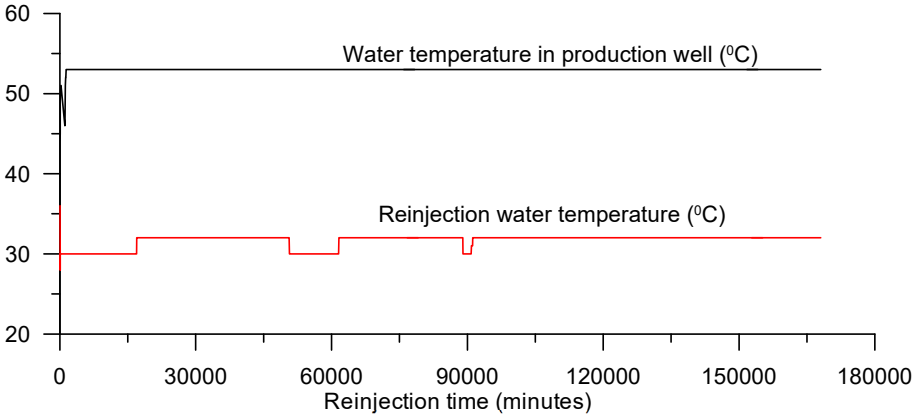

FIGURE 21: Comparison of reinjection water temperature to those in the production well during the period from Nov. 14, 2013 to Mar. 14, 2014 (Kang et al., 2015)

3.3 Reinjection test 3 with tracer test

3.3.1 Result of the tracer test

Tracer testing is an important tool for reinjection studies because tracer tests actually have a predictive power since tracer transport is orders of magnitude faster than cold-front advancement around reinjection boreholes. A simple and efficient method of tracer test interpretation, assuming specific flow channels connecting reinjection and production boreholes, is used here (Axelsson, 2013). The third reinjection test in the same place also implemented in the same wells. A tracer test was taken with the reinjection test.

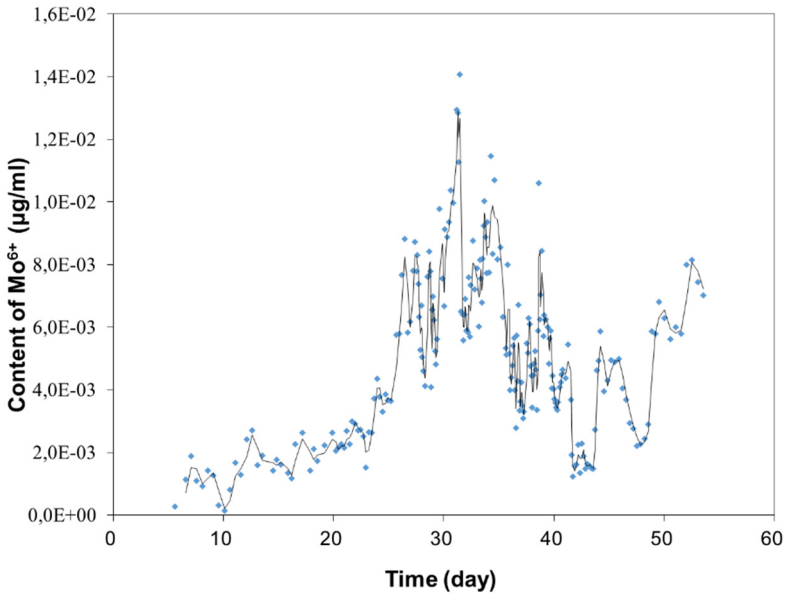

FIGURE 22: Changes of content of Mo^{6+} in the production well, during the test period

The tracer test started on January 20th, 2015 and concluded on March 16th, 2015 along with the third reinjection test. The reinjection also took place under natural conditions with an average production rate of 18.1 kg/s and reinjection rate of 4.5 kg/s. The water temperature in the production well was 53°C and the reinjection temperature was 32.8°C. The tracer chosen was ammonium molybdate, 50 kg of which were injected into the reinjection well. Comparing the content of Mo^{6+} in water samples taken before the tracer test and in the beginning of the test and considering the error in the analysis, the background content of Mo^{6+} is estimated to be 0.014 µg/ml. Figure 22 shows the changes in the content of the Mo^{6+} tracer in the water produced during the test period, after background value correction. The peak of the tracer concentration occurred about 32 days (755 hours) after tracer injection and the tracer recovery lasted 42 days (1000 hours). After this time, the tracer is considered to re-enter the production well through recirculation.

3.3.2 Tracer recovery modelling

The main purpose of tracer testing in geothermal studies and management is to predict possible cooling of production wells due to long-term reinjection of colder fluid (Axelsson et al., 2005). In order to quantify this cooling, interpretation of tracer data is needed and numerous models have been developed for that.

The method of tracer test interpretation used here is conveniently based on the assumption of specific flow channels connecting injection and production boreholes. These flow-channels may, in fact, be parts of near-vertical fracture-zones or parts of horizontal interbeds or layers. The channels may be envisioned as being delineated by the boundaries of these structures, on one hand, and flow-field streamlines, on the other hand. In other cases, these channels may be larger volumes involved in the flow between boreholes. In some cases, more than one channel may be assumed to connect an injection and a production borehole, for example connecting different feed-zones in the boreholes involved. In the case of one-dimensional tracer transport, the relevant differential equation simplifies to (Axelsson et al., 2005):

$$D\frac{\partial^2 C}{\partial x^2} = u\frac{\partial C}{\partial x} + \frac{\partial C}{\partial t} \tag{2}$$

where D = Dispersion coefficient of the material in the flow channel (m2/s);
C = Tracer concentration in the channel (kg/m3);
x = Distance along the channel (m);
u = Average transport velocity, $q/\rho A\emptyset$;
q = Injection rate (kg/s);
ρ = Water density (kg/m^3);
A = Average cross-sectional area of the flow-cannel (m^2);
$\emptyset$ = Flow-channel porosity.

Molecular diffusion is neglected in this simple model such that $D = \alpha_L u$ with α_L the longitudinal dispersivity of the channel (m). Assuming instantaneous injection of a mass M (kg) of tracer at time t = 0, the solution is given by Axelsson et al., (2005) as:

$$c(t) = \frac{uM\rho}{Q}\frac{1}{2\sqrt{\pi Dt}}e^{-(x-ut)^2/4Dt} \tag{3}$$

where $c(t)$ = Tracer concentration in the production borehole fluid;
Q = Production rate (kg/s);
x = Distance between the boreholes involved (m).

Conservation of the tracer according to c·Q = C·q, has been assumed. Such a simulation yields information on the flow channel cross-section area, actually A∅, the dispersivity α_L as well as the mass of tracer recovered through the channel (Axelsson et al., 2005).

This one dimensional flow-channel model for the Urban Dezhou reservoir tracer test can be applied by using the ICEBOX software package form UNU-GTP (Arason et al., 2004), including several programs which can be used for inversion of tracer test data and to predict cooling of production wells during long-term reinjection.

For the Urban Dezhou reservoir, it is assumed that there is one flow channel in the aquifer between the reinjection well and production well. Figure 23 shows the simulation curve of the model and Table 1 below shows the settings and parameters of the model.

Now, the result of one flow-channel obtained by the TRINV tracer programme is used to predict the production temperature during long-term production and injection. The surface area is assumed to have

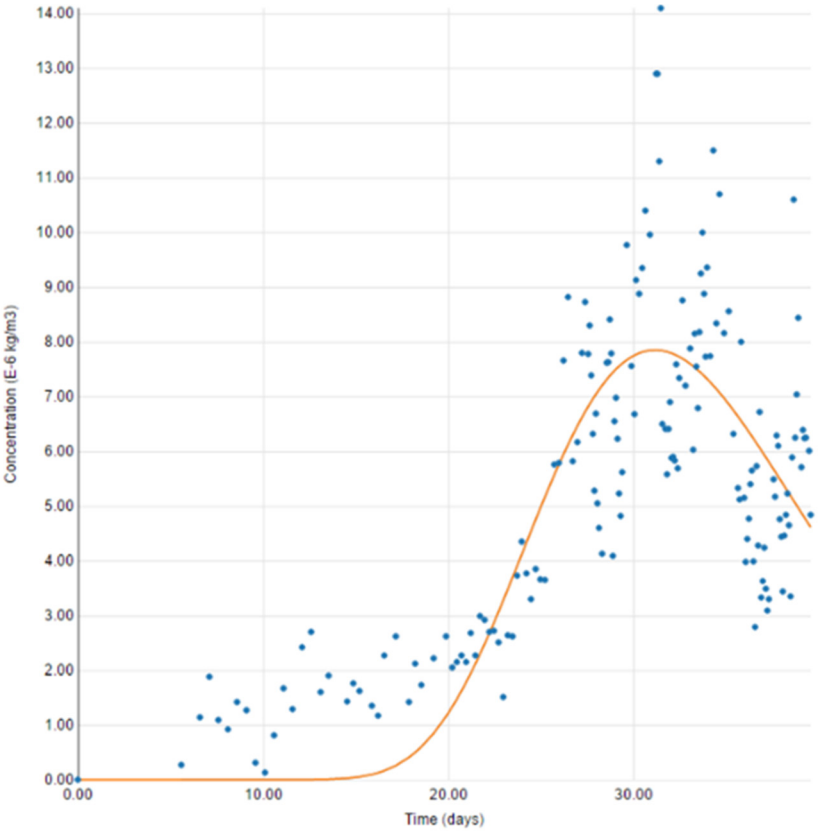

FIGURE 23: Simulation curve of the tracer model

equal width and height and porosity is assumed to be 32%. Because the calculated cross-section (area × porosity) is 0.25 m^2, the width and the height can be calculated, both of them are about 0.86 m. The result calculated by the programme shows there is no temperature change in the production well in 50 years, which remains constant at 53°C.

The predicted cooling of the production well is very little due to the low mass fraction recovered (0.46%). This low mass fraction may be caused by the fact that the tracer is added to the water level uplift cone of the reinjection well (Figure 18) and is thus diffused to all directions, with only a limited amount of the tracer received by the production well.

TABLE 1: The settings and parameters of the one dimensional flow-channel model of the connection between the injection well and production well

Setting	One channel	Parameter	One channel
Tracer mass (kg)	50.0	Velocity (m/s)	$8.36\times10^{-5} \pm 9.1\times10^{-7}$
Production rate (kg/s)	18.1	Dispersivity (m)	6.22 ± 0.76
Reinjection rate (kg/s)	4.5	Mass (kg)	0.23 ± 0.01
Reservoir temperature (°C)	53.0	Mass fraction (%)	0.46
Reinjection temperature (°C)	32.8	Cross-section (m^2)	0.25
Distance between 2 wells (m)	231		

3.4 Advancement of the reinjection tests

Poor injection performance for sandstone geothermal reservoirs has become an issue for many countries in the world (Liu, 2003; Axelsson, 2008). Known problems of reinjection in sandstone aquifers include the reinjection rates decreasing significantly with time due to problems in the wells or the equipment, such as scaling, clogging and corrosion. Many tests have e.g. been performed in different Guantao formation geothermal fields in China. To improve the reinjection performance in Guantao formation sandstone reservoirs, well completion is a key factor. Nowadays, the traditional option for well completion is perforation, which is adopted in many projects, such as in the Binhai and Wuqing reservoirs in Tianjin (Zhao et al., 2015). But these kind of methods are limited to actual industrial reinjection because they are expensive.

However, the reinjection tests in Pingyuan County provide possible new solution to overcome rapid clogging of aquifers next to reinjection wells in porous sandstone aquifers. The following measures may

be adopted: Large diameter reaming and gravel packing to enlarge the flow surface area and increase the permeability around the reinjection well, coarse filtering, fine filtering with 3-5 μm precision, gas escaping, back flushing when the pressure difference between the two sides of filtering equipment reaches 50-60 kPa, re-pumping for the reinjection well at an interval of reinjection for 7 days (Kang et al., 2015).

Three reinjection tests have been successfully implemented during different space heating periods from November to March, about 120 days, in three years. During these periods no obvious aquifer clogging occurred according to observed data. Similarly, the reinjection rates and water level increases in the reinjection well have been stable.

Because this method is not as costly as the perforation one, it has a potential to be used in actual reinjection projects in the future.

4. THERMAL BREAKTHROUGH

The thermal breakthrough is the most serious issue in long-term reinjection. Although there is no cooling of the Urban Dezhou reservoir during the reinjection tests, thermal diffusion is much slower than pressure diffusion, so cooling effect may occur in the long term. For this reason, it is necessary to predict the overall long-term thermal breakthrough time for the Urban Dezhou reservoir, in addition to the specific cooling prediction based on the tracer test results.

A porous model with cold recharge can be used for a simple estimate of the reinjection breakthrough time. This model involves an infinite, homogeneous, isotropic, fluid-saturated, hot (at temperature T_r), horizontal layer of porous material with porosity $\emptyset$ and thickness H. At time t= 0, injection of cold (at temperature T_0, cold relative to the initially hot layer) water at a rate Q (kg/s) is initiated at the location r = 0 (location of the injection well).

By assuming that heat transport by conduction is negligible compared to the advective heat transport, one can show that a cold front travels radially away from the reinjection well (two-dimensional flow). On the inside of the front, the temperature is T_0, while on the outside, the temperature is undisturbed at T_r. The distance to the cold front is then given by (Bödvarsson, 1972):

$$r_T = \sqrt{\frac{\beta_w Q t}{\pi H < \rho\beta >}} \tag{4}$$

So, the cold-front breakthrough time is given by:

$$t = \frac{R^2 \pi H < \rho\beta >}{\beta_w Q} \tag{5}$$

where t = Thermal breakthrough time (s);
R = Radial distance from reinjection well (m);
r_T = Radial distance of cold front (m);
H = Reservoir thickness (m);
$<\rho\beta>$ = Average volumetric heat capacity of reservoir, i.e. = $\emptyset \beta_w \rho_w + (1-\emptyset) \beta_r \rho_r$ (J/m^3/°C);
β_w = Heat capacity of water (J/kg/°C);
ρ_w = Water density (kg/m^3);
$\emptyset$ = Rock porosity;
β_r = Heat capacity of rock (J/kg/°C);
ρ_r = Rock density (kg/m^3);
Q = Injection rate (kg/s).

The geothermal production wells in the Urban Dezhou reservoir have different production rates. Here the 4 most common injection rates and corresponding production rates (including the maximum rate) are chosen for the calculation. It should be pointed out that these injection rates are based on the space-heating period (120 days). The annual average injection rate for calculation is shown in Table 2.

TABLE 2: Injection rate scenarios for the thermal breakthrough calculations of the Urban Dezhou reservoir

No.	Space heating time (kg/s)	Annual average (kg/s)
1	11.0	3.6
2	13.7	4.5
3	16.4	5.4
4	19.2	6.3

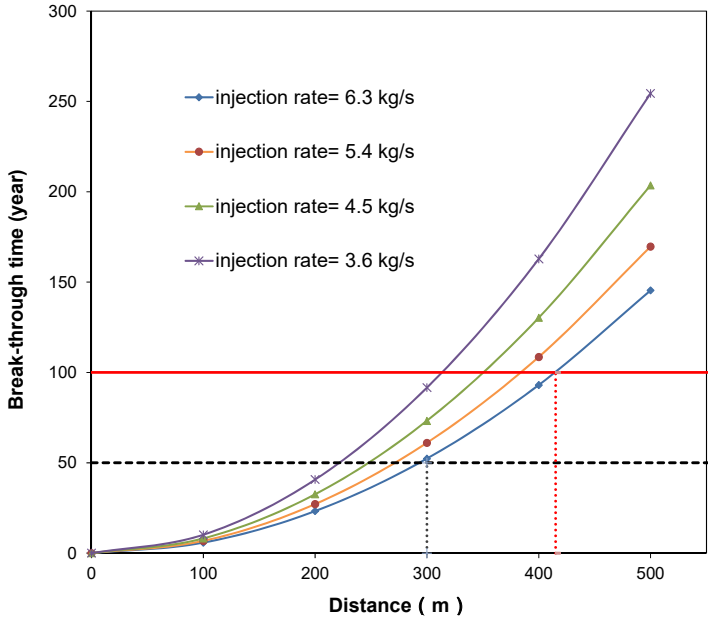

FIGURE 24: Estimated cold front breakthrough time as a function of distance between reinjection well and production well with different reinjection rates in Urban Dezhou reservoir

The breakthrough time is calculated as a function of the distance between reinjection and production wells. Here the annual average injection rates in Table 2 are used.

The results are presented in Figure 24. It should be pointed out that for the safety of the reservoir to avoid colder water intrusion through flow channels in feed-zones, the thickness of the reservoir used in the above equation is 50 m, approximately 33% of the actual thickness of the reservoir considering the porosity. To avoid thermal breakthrough in 50 years, the estimated safe distance between the reinjection well and the production well should be more than 300 m. To avoid thermal breakthrough in 100 years, the estimated safe distance should be more than 420 m.

The result of this model may, however, be too optimistic. Because, it considers the system to be homogeneous and isotropic. In reality, the aquifer may be influenced by fractures, which cause flow velocity variations in different directions.

5. VOLUMETRIC ASSESSMENT OF THE URBAN DEZHOU SANDSTONE GEOTHERMAL RESERVOIR

After avoiding cooling in the reservoir an assessment of the energy in reservoir should be made. A simple but useful method is volumetric assessment.

5.1 Methodology background

The volumetric method refers to the calculation of thermal energy in the rock and the fluid, which could

be extracted, based on specified reservoir volume, reservoir temperature and reference or final temperature.

The volumetric method is patterned from the work applied by the USGS (United States Geological Survey) to the Assessment of Geothermal Resources of the United States (Muffler, 1979). It is often used for first stage assessment, when data are limited. The main drawback of this method is that the dynamic response of a reservoir to production is not considered, such as pressure response, permeability, recharge, etc.

For a liquid-dominated reservoir, the equations used for calculating the thermal energy are as follows:

$$Q_T = Q_r + Q_w \tag{6}$$

in which

$$Q_r = A \cdot h \cdot (1 - \emptyset) \cdot \beta_r \cdot \rho_r \cdot (T - T_0) \tag{7}$$

$$Q_w = A \cdot h \cdot \emptyset \cdot \beta_w \cdot \rho_w \cdot (T - T_0) \tag{8}$$

where Q_T = Total thermal energy (kJ/kg);
Q_r = Heat in rock (kJ/kg);
Q_w = Heat in water (kJ/kg);
A = Area of the reservoir (m^2);
h = Average thickness of the reservoir (m);
$\emptyset$ = Rock porosity;
β_r = Specific heat of rock at reservoir (kJ/(kg°C));
β_w = Specific heat of water (kJ/(kg°C));
ρ_r = Rock density (kg/m^3);
ρ_w = Water density (kg/m^3);
T = Average temperature of the reservoir (°C);
T_0 = Cut-off temperature (°C).

Not all the energy can be extracted from the reservoir, so the recovery factor is defined to help estimate the energy that can be extracted. The thermal energy recoverable from the system can be calculated as follows:

$$Q_R = R \cdot Q_T \tag{9}$$

where Q_R = Recoverable thermal energy (kJ/kg);
R = Recovery factor.

The recovery factor represents how easily the heat contained in the reservoir can be extracted which mostly depends on the reservoir permeability. Muffler proposed a linear connection between the porosity and the recovery (Muffler, 1979) and Williams (2007) introduced models for fractured reservoir and proposed recovery in the range of 2-25%.

5.2 Monte Carlo volumetric assessment calculation

The parameters used in the Monte Carlo volumetric assessment calculation for the Urban Dezhou reservoir are presented in Table 3.

Area (km^2): The distribution of sedimentary reservoir aquifer is continuous. It is considered that the area is the same as the surface area of 169 km^2.

Thickness (m): The thickness of the sandstone aquifer in Guantao formation ranges from 100 to 300 m. For Monte Carlo calculations, use the most likely: 200 m; minimum: 100 m; maximum: 300 m.

Rock density (kg/m^3): The main type of rock is sandstone, which has a density of around 2800 kg/m^3. Therefore, the most likely estimate is 2800 kg/m^3; minimum: 2700 kg/m^3; maximum: 2900 kg/m^3.

Porosity (%): The average porosity of the sandstone aquifer is around 32%. In the Monte Carlo input cell, use the most likely: 32%; minimum: 24%; maximum: 35%.

Rock specific heat (J/(kg°C)): Usually this is about 950 J/(kg°C). For the Monte Carlo calculations use the most likely: 950 J/(kg°C); minimum: 910 J/(kg°C); maximum: 980 J/(kg°C).

Reservoir temperature (°C): The formation temperature of the conduction reservoir is not easy to obtain. The geothermal water temperature in wells is around 53°C. For the Monte Carlo calculations, it is assumed that the most likely value is 60°C; minimum: 53°C; maximum: 70°C.

Fluid density (kg/m^3): Water density is 983.2 (most likely), 977.8 (minimum) and 988.1 kg/m^3(maximum) at 60, 70 and 50°C, respectively.

Fluid specific heat (J/(kg°C)): It is about 4200 J/(kg°C) for pure water.

Recovery factor (%): The porosity of sandstone in Dezhou reservoir ranges from 24 to 35% with the average of 32%. Muffler (1979) proposed a linear correlation between porosity and recovery factor. However, it seems too optimistic for this reservoir. For a conservative estimate and referring to other sedimentary reservoirs in China (Huang, 2012), the estimated most likely recovery factor of Dezhou reservoir is 23%. For Monte Carlo calculations use the most likely: 23%, minimum: 20%, maximum: 25%.

Cut-off temperature (°C): One of the main reasons for cooling of reservoir is reinjection. Here the average reinjection temperature of 32.8°C is taken as the cut-off temperature.

TABLE 3: Parameters used for Monte Carlo volumetric assessment of the Urban Dezhou reservoir

Input Variables	Units	Minimum	Most likely	Maximum
Surface area	km^2	-	169	-
Thickness	M	100	200	300
Rock density	kg/m^3	2700	2800	2900
Porosity	%	24%	32%	35%
Rock specific heat	J/(kg°C)	910	950	980
Temperature	°C	52	55	59
Fluid density	kg/m^3	977.8	983.2	988.1
Fluid specific heat	J/(kg°C)	-	4200	-
Recovery factor	%	20%	23%	25%
Cut-off temperature	°C	-	32.8	-

The most likely estimate of the total energy of the reservoir is 2340 PJ (10^{15} J), and the most likely estimate for recoverable energy is 540 PJ.

To estimate for how long the energy of reservoir can be used, the following equation is used：

$$Q_0 = q \cdot \beta_w \cdot (T - T_0) \tag{10}$$

where Q_0 = Thermal heat taken by production annually (kJ/s or kWth);
q = Production rate of geothermal wells annually (kg/s);
β_w = Specific heat of water (kJ/(kg°C));
T = Average temperature of the reservoir (°C);
T_0 = Cut-off temperature (°C).

The current annual production rate of Dezhou reservoir is about 600 kg/s (q). The thermal heat of one year taken by production (Q_0) is 5.6×10^4 kWth. Based on the calculation, it will take about 300 years to extract all the recoverable energy (540 PJ) from the reservoir.

The thermal energy is usually plotted using the relative frequency distribution and the cumulative frequency distribution. The relative frequency of a value or a group of numbers is calculated as a percentage of the total number of data points.

For the 300-year lifetime of the reservoir, the relative frequency distribution and the cumulative frequency of the thermal power calculated by the Monte Carlo model are presented in Figure 25. The mean thermal power, the median thermal power, the standard deviation, 90% upper limit, and 90% lower limit could also be extracted from the results, shown in Table 4.

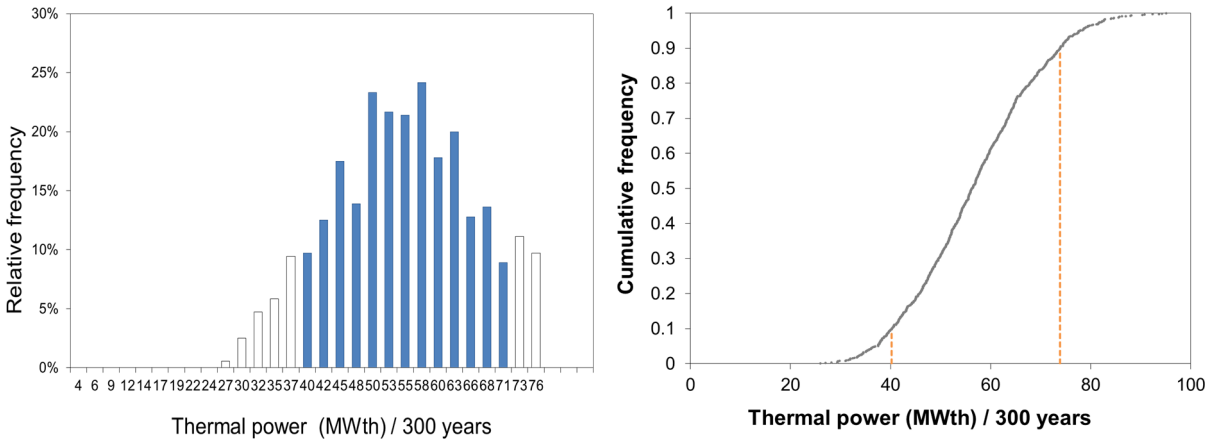

FIGURE 25: The relative and cumulative frequency distributions of thermal power for a 300-year utilization; the darker columns on the left indicate the 90% probability range while the dotted lines on the right indicate the 90% upper and lower limit of the cumulative distribution

TABLE 4: The results of the thermal power estimation for the Urban Dezhou reservoir by the Monte Carlo volumetric assessment

Results	Thermal power / 300 years
Most likely thermal power (MW_{th})	57
90% above (MW_{th})	41
90% below (MW_{th})	72

The result shows that the most likely thermal power for the direct use is 57 MW_{th} for a reservoir lifetime of 300 years. From the 90% acceptance range, the results of the simulations are that the estimated thermal power will range between 41 and 72 MWth, for 300 years. That means the resource capacity will be at least 41 MWth for 300 years. However, as mentioned before, the volumetric assessment can only build a static model. It cannot give a dynamic view. Also, it is not environmentally friendly to extract the total recoverable energy from the Urban Dezhou reservoir without sustainable development.

6. SUSTAINABLE YIELD OF THE URBAN DEZHOU SANDSTONE GEOTHERMAL RESERVOIR

6.1 Reservoir modelling

The main objective when modelling a geothermal system is to simulate the response of the reservoir to long-term and large-scale production. The reservoir model can be used to assess the production potential by predicting the water level response to different production scenarios.

6.1.1 Conceptual model

The conceptual model is the foundation of the reservoir model. The conceptual model of the Urban Dezhou reservoir can be described briefly as follows:

1) *Reservoir type:* Low-temperature sedimentary reservoir, water-dominated, heated by conduction of the thermal flow (with the average thermal gradient of 3.05°C/100m) (see Figures 7-9);
2) *Boundary and area:* Permeable fault boundaries, 169 km^2 (see Figure 3);
3) *Production aquifer:* Horizontal, homogeneous, and confined sandstone, with a thickness from 150 to 210 m at a depth between 1350 and 1650 m (Figures 4-7);
4) *Cap rock:* Upper Minghuazhen formation of Neogene period, composed of argillite and sandy mudstone (Figures 4 and 17);
5) *Underlying rock:* Eogene Dongying Formation composed of argillite, fine sandstone, and siltstone (Figures 4 and 17);
6) *Recharge*: Meteoric origin.

6.1.2 Lumped parameter modelling

The Urban Dezhou reservoir has a large area and about 82 production wells. The changes in water level and temperature of these wells show similar trends (Figure 13). Compared to numerical models, which requires large amounts of field data, lumped parameter modelling has the advantage of needing only production history and water level data. In addition, it is simpler and thus can give an estimate of the nature of the geothermal reservoir in a relatively short time. Thus in conclusion, lumped parameter model is a good choice for modelling the Urban Dezhou reservoir.

Lumped parameter models can simply be considered as distributed parameter models with a very coarse spatial discretization (Axelsson, 1989). A general lumped model consists of a few tanks and flow resistors as is shown in Figure 26. The resistors, controlled by permeability of rocks, simulate the flow resistance in a reservoir. The first tank simulates the innermost part of a geothermal reservoir, i.e. it represents the active well field; while the second and third tanks simulate outer and deeper parts of a system, i.e., they act as recharge parts from either deeper or outside parts of the main reservoir. If the third tank is connected by a resistor to a constant pressure source, which supplies recharge to a geothermal system, the model is open. Otherwise, without the connection to a constant pressure source the model would be closed (Axelsson, 1985).

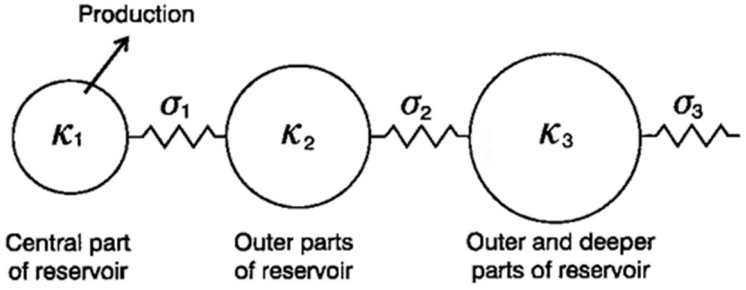

FIGURE 26: Schematic diagram of lumped parameter model (Axelsson et al., 2005)

The water level or pressure in the tanks simulates the water level or pressure in different parts of a geothermal system. The pressure response (p) of a general open lumped model with N tanks, to a constant production (Q) since time t=0, is given by the equation (Axelsson, 1985):

$$p(t) = p_0 - \sum_{j=1}^{N} Q \frac{A_j}{L_j}[1 - e^{-L_j t}] \quad (11)$$

The pressure response of an equivalent N tank closed model is given by the equation:

$$p(t) = p_0 - \sum_{j=1}^{N} Q \frac{A_j}{L_j}[1 - e^{-L_j t}] - QBt \quad (12)$$

The coefficients A_j, L_j and B are functions of the storage coefficients of the tanks (κ_j) and the conductance coefficients of resistors (σ_j) in the model.

The main problem when performing lumped parameter modelling is the estimation of the tank and conductor parameters. To tackle the simulation as an automatic inverse problem, a powerful and effective computer code LUMPFIT has been developed (Axelsson, 1985). Here the LUMPFIT programme is used to model the Urban Dezhou reservoir.

As mentioned previously, there are no obvious temperature changes in the reservoir and the main response of the reservoir for production is water level decreases. In order to predict future water level changes and to be able to suggest solutions to problems such as land subsidence caused by it, long term monitoring data is used as a basis for reservoir modelling using lumped parameter modelling. Two different models are compared: a two-tank closed and a two-tank open lumped parameter model.

The long term monitoring data used for the modelling is water level depth in wells R14 and R34 and the corresponding total production data of the reservoir (both shown in Figure 13) from 1998 to 2015. Figure 27 shows the simulated water level depth, the measured water level depth and the production. Both models present good agreements with the same coefficient of determination of 0.95.

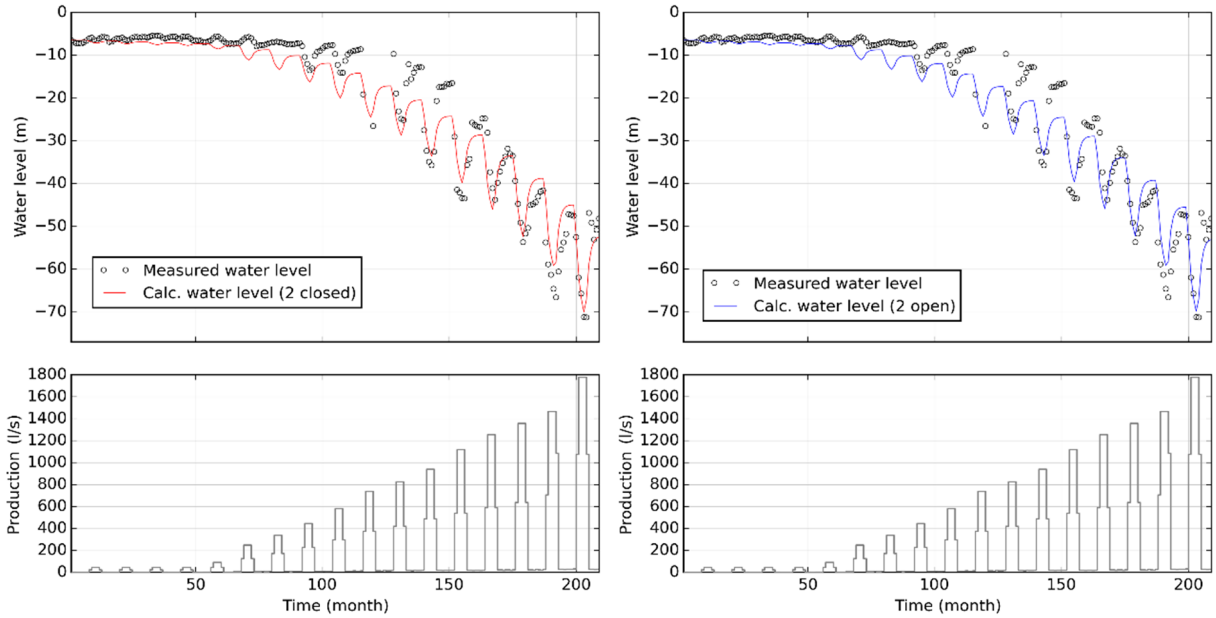

FIGURE 27: The results of the two-tank closed and open lumped parameter model of the Urban Dezhou reservoir

The reservoir properties calculated by the two models are presented in Table 5. The σ_2 represents the conductance of the second tank to the recharge from the boundary. It has very small number, which shows that the flow between the second tank and the open boundary is very limited. The monitoring data in Figure 13 shows that when production is halted, the water level rises and remains stable without recovering to the initial water level, which indicates that the recharge source is limited. These results indicate that the Urban Dezhou reservoir data fits better using a closed two-tank model than an open one. The closed two-tank model can thus be used to predict pressure changes in the reservoir for given production scenarios.

Before extensive exploitation of the Urban Dezhou reservoir, around the year 2000 the same method was used to model the reservoir. The result was different from the results presented here since a closed three-tank model fitted the data best. The data used for the modelling was from a pumping test during the period from Mar. 28 to Apr. 4, 1997 (Kang, 2000). Table 6 compares the parameters of the older model to the model presented here. The two-tank closed model shows larger storage (κ) and higher

TABLE 5: Parameters of the two types of lumped model of Dezhou

Parameter	Two-tanks closed	Two-tanks open
$A_1(10^{-3})$	9.4	9.2
$L_1(10^{-1})$	8.1	8.3
$A_2(10^{-4})$	-	9.7
$L_2(10^{-9})$	-	2.3
B	9.6×10^{-4}	-
κ_1 (ms^2)	25700	26200
κ_2 (ms^2)	252000	247000
σ_1 (10^{-5} ms)	720	750
σ_2 (10^{-10} ms)	-	2.4
Coefficient of determination: 0.95 κ: Capacitance (storage) σ: Conductivity		

permeability (σ) between the inner part and the outer part of reservoir based on long term monitoring data. The older model is based on data from the only production well at the time, R14. The model can thus be estimated to represent the properties of the reservoir in a near natural state. The two-tanks model presented in this report is based on long-term monitoring data, which better represents the large-scale production situation and can be used to predict the development of the reservoir under exploitation. It can be deduced that as the development of the reservoir increases, more storage is consumed by the reservoir and a larger area is influenced, which is a typical property of closed sedimentary reservoirs.

TABLE 6: Parameters of the lumped model of the Urban Dezhou reservoir during different periods

Parameter	Model 1 (two-tank closed)	Model 2 (Kang, 2000)
κ_1 (ms^2)	25700	0.023
κ_2 (ms^2)	252000	4.4
κ_3 (ms^2)	-	9520
σ_1 (10^{-4}ms)	72	6.2
σ_2 (10^{-4}ms)	-	54.4
κ: Capacitance (storage) σ: Conductivity		

6.2 Sustainable yield estimated by lumped parameter model

The prerequisite of calculating sustainable yield is to determine a reasonable maximum allowable drawdown of the production wells in the geothermal reservoir, within a given time frame (Kang, 2010). The constraints in the Urban Dezhou reservoir include the risk of cold-water inflow, the setting depths of production well pumps and especially the land subsidence caused by the water level decrease. Thus, the maximum allowable water level depth is defined as 150 m.

Using the maximum allowable drawdown and the lumped parameter model, water level predictions were calculated for 50 years for two different production scenarios.

6.2.1 Sustainable yield without reinjection

The water level predictions calculated by the lumped parameter model, are presented in Figure 28, which shows the water level depth changes for the next 50 years.

For the current production situation (Table 7) the water level depth will be below the 150 m limit in 10 years' time. The sustainable yield without reinjection is 25% of the current production rate (Table 7). That means the production of the reservoir cannot meet the demands of the city.

TABLE 7: Comparison of current and sustainable production rate without reinjection

Period	Current production rate (l/s)	Sustainable production rate (l/s)
Dec.-Feb.	1770	440
Mar.	1070	260
Apr.-Oct.	30	7.5
Nov.	1070	260
Space heating period	1490	370
The whole year	630	150

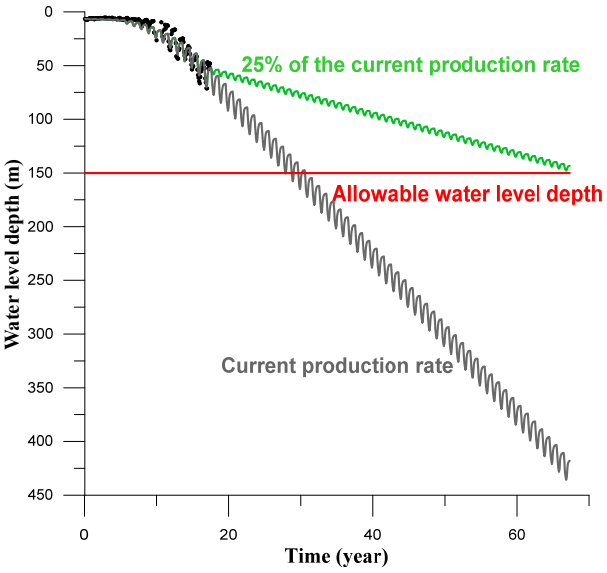

FIGURE 28: The water level depth predictions without reinjection, calculated with the lumped parameter model

6.2.2 Sustainable yield with reinjection

As discussed before, reinjection is an effective method for sustainable development of geothermal resources and according to the results of the reinjection tests with a 100% injection rate mentioned above, reinjection in the Urban Dezhou reservoir is feasible.

Figure 29 shows the predictions of water level depth changes for different reinjection rate scenarios. It shows that in order to maintain the current production rate, the reinjection rate should be more than 75% of the production rate. The maximum reinjection rate is assumed to be 80% of the production rate. That is due to having to consider the loss of the recycling water from space heating. In this situation, the sustainable yield can be up to 780 L/s annually and the average sustainable yield during the space heating period is 1860 L/s, which is about 1.25 times the current production rate. This means that the sustainable yield with reinjection cannot only meet the demands of the city but also has potential for further development of the reservoir.

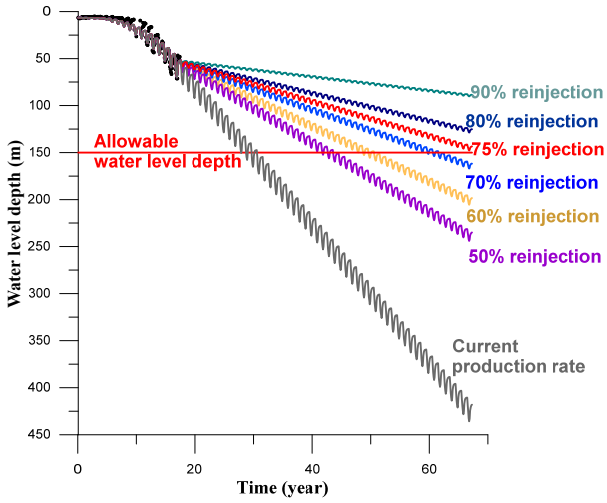

FIGURE 29: The water level depth predictions with reinjection, calculated with the lumped parameter model

It should be pointed out that the lumped parameter model can only predict water level changes in the reservoir. Further study of temperature and chemistry changes in the Urban Dezhou reservoir should be considered.

7. CONCLUSIONS

The main conclusions of the assessment of the Urban Dezhou reservoir are as follows:

1) The Urban Dezhou reservoir is a low-temperature sedimentary conduction controlled reservoir. The area of the reservoir is about 169 km^2 and the reservoir thickness ranges from 300 to 480 m at a depth between 1350 and 1650 m. Due to limited recharge and large amount of production, water level of Dezhou reservoir has been decreasing very quickly, from 8.3 m artesian height in 1998 to 70 m below ground surface in 2015, with an annual decrease of 3.6 m. However, the geothermal water temperature is generally stable around 52-55℃.

2) Three reinjection tests were undertaken in Pingyuan County from 2012 to 2015 without any clogging problems. The biggest reinjection rate without artificial pressure was about 70 m^3/h and 100% of the production water could be reinjected. From the reinjection test it can be concluded that reinjection does not lead to cooling in the reservoir during the space-heating period of 120 days. A tracer test model was built to predict the geothermal temperature changes, which shows the temperature remaining stable at 53°C for 50 years.

3) To give an idea of the minimum distance between reinjection wells and production wells, the thermal breakthrough was calculated. To avoid thermal breakthrough in 50 years, the minimum distance should be more than 300 m and to avoid a breakthrough in 100 years, the minimum distance should be over 420 m.

4) To estimate the total recoverable energy in the Urban Dezhou reservoir, Monte Carlo volumetric assessment was undertaken. The estimated total energy is 2340 PJ and the estimated recoverable energy is 540 PJ, with the estimated recovery factor of 23%. Based on the current annual production rate, the lifetime of the Urban Dezhou reservoir is estimated to be about 300 years. However, sustainable resource management should be considered here.

5) The sustainable yield of the Urban Dezhou reservoir based on the two-tank closed lumped parameter model is discussed given two production scenarios with the prerequisite of maximum allowable water level depth of 150 m and a 50 years' time frame. Without reinjection, the estimated sustainable yield is 25% of the current production rate, which cannot meet the demands of the city. A more sustainable situation was shown to be obtained keeping the current production rate but introducing systematic reinjection and a reinjection rate of over 75% of the production rate. The maximum reinjection rate is 80% of the production rate. At this reinjection rate, the sustainable yield is 1.25 times the current production rate. This means the sustainable yield with reinjection cannot only meet the demands of the city but also has the potential for increased development of the reservoir.

6) For sustainable yield, further research in Dezhou reservoir should focus on changes of temperature and the geochemistry contents of geothermal water caused by reinjection.

ACKNOWLEDGEMENTS

I would like to extend my sincere gratitude to Mr. Lúdvík S. Georgsson, director of the United Nations University Geothermal Training Programme (UNU-GTP) for offering me the opportunity to participate in the six-month training programme. To all the teachers, thank you for giving us such good lectures and sharing precious experiences. To the UNU-GTP staff, Mr. Ingimar G. Haraldsson, Mr. Markús A.G. Wilde, Ms. Málfrídur Ómarsdóttir, Ms. Thórhildur Ísberg, and Ms. María Gudjónsdóttir, thank you for your assistance, you really did a lot for us and I really appreciate it.

To my dear supervisors, Ms. Valdís Gudmundsdóttir and Dr. Gudni Axelsson, thank you very much for your patience, experienced guidance and huge support; my project would not be completed without your help. Special thanks to the teachers: Dr. Svanbjörg Helga Haraldsdóttir, Ms. Sæunn Halldórsdóttir and Ms. Helga Tulinius, for the help in the report presentation.

To my supervisor in China, Dr. Kang Fengxin, thank you for the recommendation for UNU-GTP, the effort to obtain essential data and supporting me in this study.

To my friend fellows, Fardaneh, Amali, Nuno, António and my fellow reservoir engineers and borehole geophysicists. Thank you for your help in the study and daily life.

To my directors in Shandong Provincial Institute of Geology and Mineral Resources. Thanks Mr. Li Changsuo, Mr. Zhao Changhe, Mr. Peng YuMing, Mr. Cheng Xuming, Mr. Qin Pinrui, Mr. Lin Guangqi and all the supporting directors and colleagues.

To the colleagues in the Lubei Institute of Geology and Mineral Resources, Shandong. Thank you for the precious data and material for my report.

To all the 2015 fellows, I am very glad for your company and hope our friendship lasts forever.

To my family and friends back home, thank you for the love and support, you are always with me in my heart wherever I am travelling in the world.

REFERENCES

Arason, Th., Björnsson, G., Axelsson, G., Bjarnason, J.Ö., and Helgason, P., 2004: *ICEBOX – geothermal reservoir engineering software for Windows. A user's manual.* ÍSOR – Iceland GeoSurvey, Reykjavík, Iceland, report 2004/014, 80 pp.

Axelsson, G., 1985: *Hydrology and thermomechanics of liquid-dominated hydrothermal systems in Iceland*. Oregon State University, PhD thesis, 291 pp.

Axelsson, G., 1989: Simulation of pressure response data from geothermal reservoir by lumped parameter models. *Proceedings of the 14th Workshop on Geothermal Reservoir Engineering, Stanford University, California,* 257-263.

Axelsson, G., 2008: Importance of geothermal reinjection. *Presented at "Workshop for Decision Makers on Direct Heating Use of Geothermal Resources in Asia", organized by UNU-GTP, TBLRREM and TBGMED, Tianjin, China*, 16 pp.

Axelsson, G., 2012: Role and management of geothermal reinjection. *Presented at "Short Course on Geothermal Development and Geothermal Wells", organized by UNU-GTP and LaGeo, Santa Tecla, El Salvador,* 21 pp.

Axelsson, G., 2013: Tracer tests in geothermal resource management. *EPJ Web of Conferences, 50,* article no. 02001, 8 pp.

Axelsson, G., Björnsson, G., and Montalvo, F., 2005: Quantitative interpretation of tracer test data. *Proceedings of the World Geothermal Congress 2005, Antalya, Turkey*, 12 pp.

Bödvarsson, G., 1972: Thermal problems in the siting of reinjection wells. *Geothermics, 1*, 63–66.

Huang J.C., 2012: *Assessment and management of sedimentary geothermal resources.* University of Iceland, MSc thesis, 63 pp.

Liu, J.R., 2003: The status of geothermal reinjection (in Chinese). *Hydrogeology and engineering geology, 30-3*, 100-104.

Liu, J.R., 2008: Experience of geothermal reinjection in Beijing and Tianjin. *Presented at "Workshop for Decision Makers on Direct Heating Use of Geothermal Resources in Asia", organized by UNU-GTP, TBLRREM and TBGMED, Tianjin, China*, 12 pp.

Kang, F.X., 2000: Assessment of sedimentary geothermal reservoirs in Dezhou, China and Galanta, Slovakia. Report 8 in: *Geothermal training in Iceland 2000.* UNU-GTP, Iceland, 139-163.

Kang, F.X., 2010: Sustainable development of geothermal resources in China. Proceedings of the World Geothermal Congress 2010, Bali, Indonesia, 5 pp.

Kang, F.X., Zhou, Q.D., Zhang, P.P., and Zheng, T.T., 2015: Reinjection experiment for a sandstone aquifer in Pingyuan, China. *Proceedings of the World Geothermal Congress 2015, Melbourne, Australia*, 8 pp.

Muffler, L.P.J. (editor), 1979: *Assessment of geothermal resources of the United States - 1978.* USGS Circular 790, Arlington, VA.

Williams, C.F., 2007: Updated methods for estimating recovery factors for geothermal resources. *Proceedings of the 32nd Workshop on Geothermal Reservoir Engineering, Stanford University, Stanford, Ca,* 7 pp.

Zhang, D.Z., Liu, Z.G., and Lu, H.L., 2013: *Geothermal in Hebei* (in Chinese). Geological Publishing House, Beijing, 275 pp.

Zhang, P.P., Zhao, J.C., Tan, Z.R., Bai, T., and Huang, X., 2015a: *Research report of reinjection technology in porous medium geothermal reservoir in Shandong Experimental Research Establishment.* Lubei Institute of Geology and Mineral Resources, Shandong, and Shandong Geology and Mineral Resources New Energy Company Ltd., report (in Chinese), 106 pp.

Zhang, P.P., Ai, Z.G., Bai, T., Yang, Y.B., Gao, Y.L., Huang, X., Liu, Y., Xia, Y., Yan, P.F., and Zhao, S.X., 2015b: *Research report of geothermal reinjection tests in Shandong.* Lubei Institute of Geology and Mineral Resources, Shandong, report (in Chinese), 164 pp.

Zhang, Z.Y., Wang, H., Zhang, J.Q., and Deng, R.Q., 2011: *Report of geothermal resources reinjection explorations for the urban area of Dezhou, Shandong*. Lubei Institute of Geology and Mineral Resources, Shandong, report (in Chinese), 96 pp.

Zhao, N., Wang, G., Feng, W., Li, Y. and Gao, L., 2015: Reinjection effect study of different geothermal well completion in porous sandstone reservoir in Tianjin, China. *Proceedings of the World Geothermal Congress 2015, Melbourne, Australia*, 6 pp.

Zheng, K.Y., Dong, Y., Cheng, Z.H., Tian, T.S., and Wang, G.L., 2015: Speeding up industrialized development of geothermal resources in China – Country update report 2010-2014. *Proceedings of the World Geothermal Congress 2015, Melbourne, Australia*, 9 pp.